SPONSE / ATC 161

Proceedings of

Fifth International Workshop on Seismic Performance of Non-Structural Elements (SPONSE)

ATC Applied Technology Council

SPONSE

Stanford | Blume Earthquake Engineering Center

EUCENTRE FOR YOUR SAFETY.

Applied Technology Council

The Applied Technology Council (ATC) is an internationally recognized non-profit corporation founded by the Structural Engineers Association of California in 1973 to protect life and property through the advancement of science and engineering technologies. With a focus on seismic engineering, and demonstrated capabilities in wind, coastal inundation, and blast engineering, ATC develops state-of-the-art, user-friendly engineering resources and applications to mitigate the effects of natural and other hazards on the built environment. ATC implements funded research and technology transfer projects through the development of nonproprietary consensus opinions on structural engineering issues. ATC also identifies and encourages needed research, and disseminates technological advancements through guidelines, manuals, seminars, workshops, forums, and electronic media.

ATC consists of a small group of in-house technical and support staff, assisted by highly qualified individuals engaged as consultants or subcontractors on specific projects. With this model, ATC is able to assemble teams of researchers and practitioners in diverse areas of expertise that would not otherwise be available through any one organization. Funding for ATC projects comes from federal, state, and local government entities, or from the private sector in the form of tax-deductible contributions to the ATC Endowment Fund.

ATC is guided by a nationally recognized Board of Directors consisting of representatives appointed by the American Society of Civil Engineers, the National Council of Structural Engineers Associations, the Structural Engineers Association of California, the Structural Engineers Association of New York, and five at-large members representing different areas of engineering practice. Each director serves a three-year term.

2022 Board of Directors

ATC Disclaimer

Cover image: Nonstructural damage in the Library at the University of Canterbury, 2010 Darfield earthquake (photo credit: Rajesh Dhakal).

SPONSE / ATC-161

Proceedings of Fifth International Workshop on Seismic Performance of Non-Structural Elements (SPONSE)

Prepared by
APPLIED TECHNOLOGY COUNCIL
201 Redwood Shores Parkway, Suite 240
Redwood City, California 94065
www.ATCouncil.org

in Association with
INTERNATIONAL ASSOCIATION FOR THE SEISMIC PERFORMANCE OF NON-STRUCTURAL ELEMENTS (SPONSE)
Pavia, Italy

and
EUCENTRE FOUNDATION
Pavia, Italy

2022

Preface

In 2019, at the invitation of the International Association for the Seismic Performance of Non-Structural Elements (SPONSE) and the EUCENTRE Foundation, the Applied Technology Council (ATC) Board of Directors attended the *Fourth International Workshop on the Seismic Performance of Non-Structural Elements* in Pavia, Italy. With its unique focus on nonstructural elements, and topics covering seismic demand estimation, design, retrofit, and loss estimation, the two-day program was found to be highly relevant to ongoing performance-based design needs and challenges in the United States. As a result of this experience, an ATC-SPONSE-EUCENTRE partnership was formed with a plan to bring the next SPONSE Workshop to a venue in the United States.

On December 5-7, 2022, the *Fifth International Workshop on the Seismic Performance of Non-Structural Elements* was jointly organized by ATC and SPONSE, and hosted by the Blume Earthquake Engineering Center at Stanford University in Stanford, California, USA. This 5th SPONSE Workshop assembled more than 140 participants from the United States and around the world to discuss the latest advancements in the state of research, practice, and knowledge on the experimental behavior and predicted performance of nonstructural elements. These *Proceedings* catalog the papers that formed the basis of the technical program.

ATC and SPONSE would like to acknowledge those who participated in the planning and conduct of the 5th SPONSE Workshop, including Bernadette Hadnagy and Daniele Perrone for their work on the Organizing Committee, Greg Deierlein and Racquel Hagen of the Blume Center for their efforts in arranging the venue, the members of the Steering Committee for their guidance in planning the event, the members of the Scientific Committee for their assistance in reviewing papers, Jan Stanway, Peter Fajfar, Bret Lizundia, and Keri Ryan for providing keynote addresses, and the many authors who took the time to submit papers and present their work.

ATC and SPONSE also gratefully acknowledge the many students who volunteered their time alongside ATC staff members, Chiara McKenney and Kiran Khan, who provided on-site logistical, presentation, and publication support. Finally, ATC and SPONSE would like to thank Degenkolb

Engineers, Hilti North America, Paradigm Engineering Inc., Silicon Valley Bank, and VIE Inc. as sponsors of the event.

The 5th SPONSE Workshop and these *Proceedings* would not have been possible without the contributions of all who generously provided their time, effort, and financial support.

Jon A. Heintz	Andre Filiatrault
5th SPONSE Co-Chair	5th SPONSE Co-Chair

Table of Contents

List of Figures

Chapter 1
Introduction

The seismic performance of nonstructural elements is recognized as a key factor in the performance of the built environment in earthquakes, and a key consideration in the performance-based design of new buildings and other structures. Reconnaissance reports following earthquakes, and recent scenario and loss estimation studies, have all shown that a significant portion of earthquake-related losses can be attributed to damage to nonstructural elements. Although inadequate performance of nonstructural systems has been observed repeatedly in past earthquakes, there is limited research and a scarcity of new information being made available to increase our understanding of nonstructural system behavior and improve performance in future earthquakes.

To promote the dissemination of research findings and technological developments related to the seismic performance of nonstructural systems and components, the International Association for the Seismic Performance of Non-Structural Elements (SPONSE) has been conducting a series of international workshops focused exclusively on nonstructural elements. Because of the relevance of nonstructural performance to U.S. performance-based seismic design practice, the Applied Technology Council (ATC) partnered with SPONSE, and its parent organization, the EUCENTRE Foundation, to bring the next workshop in the series to a venue in the United States.

1.1 About SPONSE

The Seismic Performance of Non-Structural Elements (SPONSE) Association is an international, nonprofit, technical society of engineers, architects, manufacturers, insurers, builders, planners, public officials, and social scientists, interested in the seismic performance of nonstructural elements. SPONSE welcomes members from a wide range of backgrounds including research and teaching institutions, insurance groups, manufacturers of nonstructural elements, and individuals including engineers, architects, builders, practicing professionals, educators, government officials, and building code regulators.

The objective of the SPONSE Association is to contribute to the improvement of the resilience of communities to earthquakes by:

(1) promoting research related to the seismic performance of nonstructural elements; (2) promoting education and training on subjects related to the seismic performance of nonstructural elements; (3) assisting with the dissemination of research findings and technological developments relevant to the seismic performance of nonstructural elements; and (4) facilitating collaboration between industry, academia, professionals and other parties interested in the seismic performance of nonstructural elements.

1.2 Past International SPONSE Workshops

There have been four previous International SPONSE Workshops:

- *First International SPONSE Workshop*, August 29-31, 2014, Harbin, China
- *Second International SPONSE Workshop*, May 13, 2015, Pavia, Italy
- *Third International SPONSE Workshop*, March 31, 2016, Christchurch, New Zealand
- *Fourth International SPONSE Workshop*, May 22-23, 2019, Pavia, Italy

In 2017, the Workshop was replaced by a Special Session on the Seismic Performance of Non-Structural Elements organized during the 16th World Conference on Earthquake Engineering (16WCEE) held in Santiago, Chile.

In 2018 the Workshop was replaced by two Special Sessions on the Seismic Performance of Non-Structural Elements, one organized during the 16th European Conference of Earthquake Engineering (16ECEE) held in Thessaloniki, Greece, and the other organized during the 11th National Conference on Earthquake Engineering (11NCEE) held in Los Angeles, California, USA.

1.3 Fifth International SPONSE Workshop

The *Fifth International Workshop on the Seismic Performance of Non-Structural Elements* was jointly organized by ATC and SPONSE, and hosted by the Blume Earthquake Engineering Center at Stanford University, on December 5-7, 2022, in Stanford, California, USA.

The Workshop assembled more than 140 participants from the United States and around the world. The technical program included four keynote presentations and more than 80 technical papers on the latest advancements in the state of research, practice, and knowledge on the experimental behavior and predicted performance of nonstructural elements. The *Fifth International SPONSE Workshop* Program is provided in Figure 1-1.

Stanford ENGINEERING | Blume Earthquake Engineering Center

EUCENTRE FOR YOUR SAFETY.

DETAILED PROGRAM

Monday, December 5, 2022

8:00-8:30 **REGISTRATION (Huang Engineering Center)**

8:30-9:15 **OPENING CEREMONY (MacKenzie Room, Huang Engineering Center)**

Background and Motivation – *A. Filiatrault*

Applied Technology Council – *J. Heintz*

International Association for the Seismic Performance of Non-Structural Elements – *R. Dhakal*

Stanford Blume Earthquake Engineering Center – *G. Deierlein*

9:15-10:00 **KEYNOTE 1 (Mackenzie Room, Huang Engineering Center)**
Seismic Performance of Non-Structural Elements in New Zealand – What Have We Learnt?
J. Stanway

10:00-10:30 **Coffee Break**

10:30-12:30 **PARALLEL SESSIONS:**

SESSION 1A – PERFORMANCE BASED-SEISMIC DESIGN OF NON-STRUCTURAL ELEMENTS
CO-CHAIRS: *Rajesh Dhakal – Daniele Perrone* (Y2E2 – 299 Conference Room)

1. Component-Based Simplified Framework to Assess Integrated Structural and Non-Structural Seismic Upgrade Strategies
A. Miliziano, L. Wiebe, S. Pampanin, D. Perrone, A. Filiatrault
2. The Impact of Nonstructural Damage on Building Function
D. Cook, S. Sattar
3. Seismic Evaluation of Existing Unreinforced-Masonry Partition Walls to Achieve Project Goals
A. Kurt, A. Rush
4. Seismic Performance of Pre-Fabricated Façade Panels
A. Itsekson, E. Guetter

SESSION 2A – EXPERIMENTAL STUDY RELATED TO THE SEISMIC PERFORMANCE OF NON-STRUCTURAL ELEMENTS
CO-CHAIRS: *Gennaro Magliulo – Tara Hutchinson* (Y2E2 – 111 Lecture Room)

1. New Testing Protocol for Acceleration-and-Drift-Sensitive Non-Structural Elements through the Innovative 9-DOFs Multi-Story Dynamic Testing Facility
I. Lanese, D. Bolognini, E. Brunesi, F. Dacarro, P. Dubini, L. Grottoli, S. Peloso, E. Rizzo Parisi, M. Rota
2. Experimental Facility for the Seismic Testing of Non-Structural Elements and Systems under Full-Scale Floor Motion
F. Dacarro, D. Bolognini, G.M. Calvi
3. Seismic Performance of Suspended Ceilings and Development of Floor Motion Responses for Experimental Testing
C. C.W. Flude, G.A. Davidson, D.T. Lau, J. Erochko, K. Kasai

Figure 1-1 Program – *Fifth International SPONSE Workshop*.

SPONSE | FIFTH INTERNATIONAL WORKSHOP ON SEISMIC PERFORMANCE OF NON-STRUCTURAL ELEMENTS

4. Numerical Simulation of Prefabricated Steel Stairs to be Implemented in the NHERI TallWood Building
   S. Sorosh, T.C. Hutchinson, K.L. Ryan, S. Wichman, K. Smith, R. Belvin, J.W. Berman
5. Numerical Simulation to Predict the Seismic Behavior of Continuous Plasterboard Suspended Ceiling Systems
   V. Patnana, D.C. Rai
6. Experimental Study to Validate an Improved Approach to Design Acceleration-Sensitive Nonstructural Components
   A. Elkady, D. Vamvatsikos, D. Lignos, A.K. Kazantzi, E. Miranda

SESSION 3A – MODELING/NUMERICAL SIMULATION TO PREDICT THE SEISMIC BEHAVIOR OF NON-STRUCTURAL ELEMENTS
CO-CHAIRS: ***Gilberto Mosqueda – Simona Bianchi*** **(Y2E2 – 300 Conference Room)**

1. Parametric Seismic In-Plane Fragility Models for Clay Masonry Infills in Low-to-Medium-Rise Reinforced Concrete Frames
   S. Peloso, E. Brunesi, D. Perrone, B. Chichino, G. Sinopoli, C. Moroni
2. Numerical Study on the Seismic Interaction between Innovative Ductile Masonry Infills and RC Elements
   S. Pelucco, R. Milanesi, P. Morandi, V. Bolis, A. Stavridis, G. Magenes, M. Preti
3. Development of a Simplified Modeling Technique for Seismic Performance Assessment of Gypsum Partition Walls
   I. Lotfy, M. Salkhordeh, S. Soroushian, E. Rahmanishamsi, M. Maragakis
4. Numerical Investigation of the Displacement Incompatibility between Masonry Infill Walls and Surrounding Reinforced Concrete Frames
   L. Pedone, S. Pampanin
5. Seismic Performance of Point Fixed Glass Facade Systems through Finite Element Modelling and Proposal of a Low-Damage Connection System
   S. D'Amore, S. Bianchi, J. Ciurlanti, S. Pampanin

12:30-1:30 Lunch

1:30-3:00 PARALLEL SESSIONS:

SESSION 1B – PERFORMANCE BASED-SEISMIC DESIGN OF NON-STRUCTURAL ELEMENTS
CO-CHAIRS: ***Bob Bachman – Brian Kehoe*** **(Y2E2 – 299 Conference Room)**

1. Case Study of a Rapid Assessment of Seismic Upgrade Viability using Performance Based Earthquake Engineering
   P. Steneker, L. Wiebe, A. Filiatrault, D. Konstantinidis
2. Review of Current Design Standards for Acceleration Sensitive Nonstructural Components
   P. Steneker, D. Arnold, D. Carson
3. Design for Enhanced Nonstructural Performance – Case Studies and Recommended Practices
   M. Phipps, S. Jumakuliyeva
4. A Snapshot of Societal Expectations for the Seismic Performance of Buildings in New Zealand – What This Reveals about Future Design Considerations for Non-Structural Elements
   H. Ferner, C. Brown, S. Horsfall, S. Abeling, H. Cowan

Figure 1-1 Program – *Fifth International SPONSE Workshop* (cont'd).

SESSION 2B – EXPERIMENTAL STUDY RELATED TO THE SEISMIC PERFORMANCE OF NON-STRUCTURAL ELEMENTS
CO-CHAIRS: *Timothy Sullivan – Emanuele Brunesi* (Y2E2 – 111 Lecture Room)

1. Component-Test-Informed Seismic Design Methodology for Façade Systems
   S. Peloso, E. Brunesi, E. Rizzo Parisi
2. Ongoing Extension of Systems for Seismic Securing of Masonry Facades through Refurbishment, Strengthening and Retrofitting
   S. Hine, M. Roik
3. In-plane Quasi-Static Reversed Cyclic Tests on Infilled Façades made of Lightweight Steel Drywall Systems
   S. Shakeel, L. Fiorino, R. Landolfo
4. Seismic Testing and Multi-Performance Evaluation of Full-Scaled Unitized Curtain Walls: Research Overview and Preliminary Results
   S. Bianchi, G. Lori, V. Hayez, R. Schipper, S. Pampanin, M. Overend, G. Manara, T. Klein

SESSION 3B – MODELING/NUMERICAL SIMULATION TO PREDICT THE SEISMIC BEHAVIOR OF NON-STRUCTURAL ELEMENTS
CO-CHAIRS: *Greg Deierlein – Roberto Nascimbene* (Y2E2 – 300 Conference Room)

1. Effect of Floor Slab Vibration on Seismic Performance of Suspended Ceiling Systems
   S. Gopagani, A. Filiatrault, A.J. Aref
2. Study the Effect of Aspect Ratio of Unbraced Suspended Ceiling Systems on their Dynamic Responses and Damage Failure Mechanisms
   R. Rezvani, S. Soroushian, A.E. Zaghi, M. Maragakis
3. On In-Plane Shear Stiffness of Ceiling Surface in JPN-US Suspended Ceiling
   R. Morohoshi, S. Motoyui
4. Numerical Analysis of Suspended Ceiling Considering Pounding Behavior between Ceiling Surface and Walls
   M. Li, S. Motoyui, Y. Wang, H. Jiang, K. Kasai

3:00-3:30 Coffee Break

3:30-5:00 PARALLEL SESSIONS:

SESSION 4A – EVALUATION OF THE SEISMIC DEMAND ON NON-STRUCTURAL ELEMENTS
CO-CHAIRS: *Daniele Perrone – Dave Welch* (Y2E2 – 299 Conference Room)

1. Absolute Acceleration Floor Response Spectra for Inelastic Buildings: Quantification of Amplitude Capping and Period Lengthening
   D. Rodriguez, D. Perrone, A. Filiatrault, E. Brunesi
2. Estimating Floor Acceleration Response Spectra for Self-Centering Structural Systems with Flag-Shaped Hysteretic Behavior
   B.K. Shrestha, A.C. Wijeyewickrema, H. Miyashita, N. Malla
3. A Practice-Oriented Floor Response Spectrum Prediction Method for Seismic Design of Non-Structural Elements
   K. Haymes, T.J. Sullivan, R. Chandramohan, L. Wiebe
4. Free-Field Earthquake Hazard Spectra to Establish Nonstructural Test Requirements for Global Code Compliances
   J.A. Gatscher, S.R. Littler

Figure 1-1 Program – *Fifth International SPONSE Workshop* (cont'd).

SPONSE | FIFTH INTERNATIONAL WORKSHOP ON SEISMIC PERFORMANCE OF NON-STRUCTURAL ELEMENTS

SESSION 2C – EXPERIMENTAL STUDY RELATED TO THE SEISMIC PERFORMANCE OF NON-STRUCTURAL ELEMENTS
CO-CHAIRS: ***Clemens Beiter – Jeff Eroshko*** **(Y2E2 – 111 Lecture Room)**

1. Shaking Table Tests of a Braced Outdoor Aircon Unit
   B. Huang, M. Cheng, W. Lu
2. Seismic Fragility Testing of Electrical Equipment for the Safe Operation of Hydroelectric Facilities
   A.M. Coughlin, K.M. Braman, B. Bergman
3. Seismic isolation of an Industrial Steel Rack using Innovative Modular Devices: Shake-Table Tests
   G. Guerrini, F. Graziotti, A. Penna
4. Quasi-Static Cyclic Testing of a Drift-Sensitive Sub-Assembly of Non-Structural Elements with Low-Damage Characteristics
   R. Clement, R.P. Dhakal, M. Tripathi, G. De Francesco, M. Rashid, T.J. Sullivan

SESSION 3C – MODELING/NUMERICAL SIMULATION TO PREDICT THE SEISMIC BEHAVIOR OF NON-STRUCTURAL ELEMENTS
CO-CHAIRS: ***Roberto Nascimbene – Shojiro Motoyui*** **(Y2E2 – 300 Conference Room)**

1. Numerical Simulation of Piping Systems Connected by Grooved Fit Joints
   T. Wang, L. Qiu, Q. Shang
2. Seismic Response Analysis of Irregular Piping Networks Accounting for Vertical Acceleration
   G. Blasi, D. Perrone, M.A. Aiello
3. Modelling One-Dimensional Rolling Response of Rigid Bodies on Casters using Physics Engine Simulation
   C. Xu, Q. Ma, M. Kurata
4. Seismic Response Analysis of Freestanding Building Contents Exhibiting Rocking, Sliding, and Wall Pounding
   Y. Bao, D. Konstantinidis

5:00 Adjourn

Tuesday, December 6, 2022

8:00-8:30 **REGISTRATION (Huang Engineering Center)**

8:30-9:15 **KEYNOTE 2 (MacKenzie Room, Huang Engineering Center)**
Floor Acceleration Spectra: from Research to Seismic Code Provisions
P. Fajfar

9:15-10:00 **KEYNOTE 3 (Mackenzie Room, Huang Engineering Center)**
Development of the New Nonstructural Seismic Design Provisions in ASCE/SEI 7-22 and Enhanced Seismic Resilience for Nonstructural Components
B. Lizundia

10:00-10:30 **Coffee Break**

Figure 1-1 Program – *Fifth International SPONSE Workshop* (cont'd).

10:30-12:30 PARALLEL SESSIONS:

SESSION 4B – EVALUATION OF THE SEISMIC DEMAND ON NON-STRUCTURAL ELEMENTS
CO-CHAIRS: *Derek Rodriguez Pacheco – Dimitrios Konstantinidis* (Y2E2 – 299 Conference Room)

1. Equipment Seismic Performance in the General Docente Ambato Hospital, Ecuador
   O.S. Saravia, A.G. Haro
2. Effect of Unequal Slab Levels in Adjacent Buildings on the Seismic Demand of Non-Structural Building Components
   P. Verma, Y. Aggarwal, S. Kumar Saha
3. Seismic Assessment of Acceleration-Sensitive Nonstructural Elements: Reliability of Existing Shake Table Protocols and Novel Perspectives
   D. D'Angela, M. Zito, C. Salvatore, G. Toscano, G. Magliulo
4. Development of a Code-Compliant Seismic Input for Shake Table Testing of Acceleration-Sensitive Nonstructural Elements
   M. Zito, D. D'Angela, G. Maddaloni, G. Magliulo

SESSION 2D – EXPERIMENTAL STUDY RELATED TO THE PERFORMANCE OF NON-STRUCTURAL ELEMENTS
CO-CHAIRS: *Maryann T. Phipps – Simone Peloso* (MacKenzie Room, Huang Engineering Center)

1. Seismic Cable Bracing of Sprinkler Piping
   J. Carl, H. Mostafaei
2. Numerical Analysis of Gypsum Board Subjected to Bending Moment using Fiber Model
   F. Sakyraba, A. Shegay, Y. Sato, S. Motoyui
3. A Zinc Sheeting such as a Shear Wall in a Mixed CFS Frame with Non-Structural Masonry
   X. Nieto-Cárdenas, C. Takeuchi, J. Tamasco
4. Dynamic Properties and Seismic Performance of an Innovative Cleanroom
   M. Zito, D. D'Angela, G. Magliulo
5. Shaking Table Experimental Campaign on Pre-Code Masonry Infills Subjected to In-Plane and Out-Of-Plane Loading
   M. Kurukulasuriya, R.R. Milanesi, D. Bolognini, I. Lanese, L. Grottoli, G. Magenes, F. Dacarro, P. Morandi
6. Evaluation of Nonstructural Walls with Drift-Compatible Details in a 10 Story Mass Timber Building Shake Table Test
   W. Roser, S. Wichman, Y. Ji, Sir L. Wynn, K.L. Ryan, J.W. Berman, T.C. Hutchinson, S. Pei

SESSION 3D – MODELING/NUMERICAL SIMULATION TO PREDICT THE SEISMIC BEHAVIOR OF NON-STRUCTURAL ELEMENTS
CO-CHAIRS: *Andre Filiatrault – Davide Bellotti* (Y2E2 – 300 Conference Room)

1. Evaluation of Seismic Demand on Bridge Nonstructural Components using ASCE 7
   N. Girmay, M. Tumbeva, T. Do, D. Ojala
2. Computational Modelling and Seismic Performance of Non-Traditional Automated Warehouse Storage System
   L. Mello, A. Coughlin
3. Case Study to Evaluate the Key Parameters of the Dynamic Response of Floor-Anchored Nonstructural Components
   T. Feinstein, J.P. Moehle
4. Effect of Spectral Shape on the Amplification of Peak Floor Acceleration Demands in Buildings
   G. Scagliotti, E. Miranda

Figure 1-1 Program – *Fifth International SPONSE Workshop* (cont'd).

FIFTH INTERNATIONAL WORKSHOP ON SEISMIC PERFORMANCE OF NON-STRUCTURAL ELEMENTS

5. Nonlinear Approach on Seismic Design Force of Non-Structural Components for Isolated and Fixed Base Buildings Comparison
S. Shakeri, J. Wong, T. Hart, M. Halligan

12:30-1:30 Lunch

1:30-3:00 PARALLEL SESSIONS:

SESSION 4C – EVALUATION OF THE SEISMIC DEMAND ON NON-STRUCTURAL ELEMENTS
CO-CHAIRS: ***Gianrocco Mucedero – Dustin Cook*** **(Y2E2 – 299 Conference Room)**

1. Mitigate Seismic Rocking Responses and Deformations on the Isolated Equipment-Platforms Sets by Wire Rope Isolators Mounted in Low-Rise Buildings
A. Al Jawhar
2. Seismic Demand on Sprinkler Piping Systems: Findings from a Shake Table Testing Program & Relevance to NZ Standards
M. Rashid, R.P. Dhakal, T.J. Sullivan, T.Z. Yeow
3. Analytical Studies in Support of an Improved Approach to the Design of Acceleration-Sensitive Nonstructural Elements
A.K. Kazantzi, E. Miranda, D. Vamvatsikos, A. Elkady, D. Lignos
4. Simple and Economical Details to Improve the Seismic Resiliency of Large Power Transformers
N.G. Moore

SESSION 2E – EXPERIMENTAL STUDY RELATED TO THE SEISMIC PERFORMANCE OF NON-STRUCTURAL ELEMENTS
CO-CHAIRS: ***Andrew Baird - Tal Feinstein*** **(MacKenzie Room, Huang Engineering Center)**

1. Seismic Demand on Power Actuated Fasteners (PAF) under In-Plane Loading of Drywall Partitions: an Approach
L. Fiorino, A. Campiche, P. Grzeisk, R. Lanfoldo
2. Failure Mode and Hysteretic Behavior of Steel Angles used for Floor-Mounting of Non-Structural Elements
C-J. Bae, C-H. Lee, S-C. Jun, S. Lee
3. Crack Widths in Concrete Floor Diaphragms, in Relation to Selected Power Actuated Fasteners used to Attach Interior Partition Walls
M.R. Eatherton, R. Avellaneda-Ramirez, P. Grzesik, C. Gill
4. Performance of Power Actuated Fastener Connections for Cold-Formed Steel Framing
A.E. Schultz, S.D. Overacker, D. Amori, P. Grzesik. C. Gill

SESSION 5 – INNOVATIVE TECHNIQUES TO MITIGATE DAMAGE TO NON-STRUCTURAL ELEMENTS
CO-CHAIRS: ***Snehasagar Gopagani – Alessandra Miliziano*** **(Y2E2 - 300 Conference Room)**

1. Seismic Performance Evaluation of Braced and Friction-Added Suspended Ceilings Based on Shake Table Testing
S-C. Jun, C-H.Lee, C-J. Bae, D-S. Lee
2. Seismic Response of a Braceless Seismic Restraint System for Suspended Nonstructural Elements
B. Chalarca, A. Filiatrault, D. Perrone, R. Nascimbene
3. Non-Structural Contents Mitigation: Design, Implementation, and Community Outreach Structures
G. Granholm, S. Austin, K. Briggs, M. Benthien

3:00-3:30 Coffee Break

Figure 1-1 Program – *Fifth International SPONSE Workshop* (cont'd).

3:30-5:00 **PARALLEL SESSIONS:**

SESSION 7 - LOSS ESTIMATION WITH SPECIAL FOCUS ON BUILDING REOCCUPANCY AND FUNCTIONAL RECOVERY
CO-CHAIRS: ***Paul Steneker - Bryan Chalarca*** **(Y2E2 - 299 Conference Room)**

1. The Influence of High-Dispersion Nonstructural Component Fragility Curves in Damage and Loss Uncertainty
J.V. Manousakis, D. Konstantinidis
2. Seismic Performance of Acceleration Sensitive Non-Structural Elements in Stiff Self-Centering Structural Systems
W.W. Carofilis, E. Kim, D. Jung
3. Impact of Masonry Infill Variability on the Seismic Demand of Non-Structural Elements
G. Mucedero, D. Perrone, R. Monteiro

SESSION 9A - IMPACT OF NON-STRUCTURAL ELEMENTS ON THE SEISMIC PERFORMANCE OF BUILDINGS
CO-CHAIRS: ***Jon Heintz - Andre Filiatrault*** **(Mackenzie Room, Huang Engineering Center)**

1. Seismic Response Analysis of Precast Structures with Closure External Panels
D. Bellotti, F. Cavalieri, R. Nascimbene
2. Assessment of the Effect of Non-Structural Walls (NSWs) on the Dynamic Properties and Inter-Story Drifts of a Case Study Building
A. Ramadan, R. Assi
3. Probabilistic Evaluation of Post-Earthquake Functional Recovery of a Seismically Isolated RC Building
J. Chavez, J. Murcia-Delso, F. Lopez-Almansa

5:00 Adjourn

Wednesday, December 7, 2022

8:00-8:30 **REGISTRATION (Huang Engineering Center)**

8:30-9:15 **KEYNOTE 4 (MacKenzie Room, Huang Engineering Center)**

Influence of Vertical Floor Accelerations on the Seismic Performance of Building Non-Structural Elements
K. Ryan

9:15-10:00 Coffee Break

10:00-12:00 **PARALLEL SESSIONS:**

SESSION 6 - STANDARDIZATION OF QUALIFICATION AND FRAGILITY TESTING AND DESIGN PROCEDURES
CO-CHAIRS: ***Jon Heintz - Bryan Chalarca*** **(Y2E2 - 299 Conference Room)**

1. Seismic Performance of Electrical Cabinets during Shake Table Testing
R. Merino, D. Perrone, A. Filiatrault, R. Nascimbene
2. A New Testing and Evaluation Method for Seismic Rating of Non-Structural Elements
N. Zamani, C. Beiter, D. Perrone, A. Filiatrault, D. Rodriguez, C. Tokas
3. Performance Assessment of Seismically Damaged Firestopping Systems: A Preliminary Framework
Z. Ye, A.K. Abu, C.M. Fleischmann, R.P. Dhakal

Figure 1-1 Program – *Fifth International SPONSE Workshop* (cont'd).

FIFTH INTERNATIONAL WORKSHOP ON SEISMIC PERFORMANCE OF NON-STRUCTURAL ELEMENTS

4. Seismic Qualification of Square D Relays Type KPD13 at Laguna Verde Nuclear Power Plant
   G. Jarvio, J. Guadarrama, V.A. Jarvio
5. Recent Developments in the Field of Anchoring Heavy Facades in Seismic Areas
   M. Roik, C. Piesker

SESSION 9B - IMPACT OF NON-STRUCTURAL ELEMENTS ON THE SEISMIC PERFORMANCE OF BUILDINGS
CO-CHAIRS: ***Rajesh Dhakal - Eduardo Miranda*** **(Mackenzie Room, Huang Engineering Center)**

1. Comparison of Seismic Loss and Floor Response Spectra of Low-Rise Buildings with Various Types of Braced Frames
   A. Banihashemi, L. Wiebe, A. Filiatrault
2. Wooden Infills Influence on the Seismic Performance of Steel Structures
   M. Calò, G. Mucedero, V. Nicoletti, G. Gabbianelli
3. Customized Tools for Assessing Nonstructural Element Vulnerabilities in Hospitals in Nepal and Myanmar
   J. Rodgers, H. Kumar, W. Holmes, Y. Lotay, D. Joshi, U. Ojha
4. Managing Seismic Risk in the San Francisco Legal Arena: Performance Gap Claims based on Curtain Walls and other Non-Structural Elements
   M. White

SESSION 8 - PRACTICAL IMPLEMENTATION/INSTALLATION OF NON-STRUCTURAL ELEMENTS IN BUILDINGS
CO-CHAIRS: ***Daniele Perrone - Derek Rodriguez Pacheco*** **(Y2E2 - 300 Conference Room)**

1. Overlooked Nonstructural Component Flexibility Design Issues
   B.E. Kehoe
2. Seismic Design Optimization of Sprinkler Piping Restraint Installations with Dynamo
   M. Casto, D. Perrone, R. Nascimbene, A. Filiatrault, M.A. Aiello
3. Improving Seismic Restraint Design Implementation
   A. Baird, C. A. Muir, A. Pourali, W.Y. Kam
4. Practical Considerations for Non-Structural Bracing Design of Multiple Suspended Utilities in Congested Areas of Facilities
   J. Masek, P. McMullin, B. Larsen

12:00 Adjourn

Figure 1-1 Program – *Fifth International SPONSE Workshop* (cont'd).

1.4 Technical Themes

Papers were separated into groups with similar topics, and organized into sessions with the following themes identified in the technical program:

1. Performance Based-Seismic Design of Non-Structural Elements
2. Experimental Study Related to the Seismic Performance of Non-Structural Elements
3. Modeling/Numerical Simulation to Predict the Seismic Behavior of Non-Structural Elements
4. Evaluation of the Seismic Demand on Non-Structural Elements
5. Innovative Techniques to Mitigate Damage to Non-Structural Elements
6. Standardization of Qualification and Fragility Testing and Design Procedures
7. Loss Estimation with Special Focus on Building Reoccupancy and Functional Recovery
8. Practical Implementation/Installation of Non-Structural Elements in Buildings
9. Impact of Non-Structural Elements on the Seismic Performance of Buildings

1.5 Sponsors

ATC and SPONSE recognize and thank the following organizations for their sponsorship of the *Fifth International SPONSE Workshop* (Figure 1-2).

Figure 1-2 Sponsors – *Fifth International SPONSE Workshop*.

Chapter 2

Technical Papers

Seismic Performance of Non-Structural Elements in New Zealand – What have we learnt?

Jan M. Stanway[1]

[1] WSP New Zealand
Christchurch, New Zealand
e-mail: Jan.Stanway@wsp.com

Abstract. The performance of buildings in recent New Zealand earthquakes, delivered stark lessons on seismic resilience. Most of our buildings, with a few notable exceptions, performed as our Codes intended them to with regard to safeguarding people from injury. Many buildings only suffered minor structural damage but were unable to be reused and occupied for significant periods of time due to the damage and failure of non-structural elements. The performance of our buildings has led many to ask if we have the right balance between designing to preserve life in extreme, infrequent events versus designing for lesser more frequent events that enable continued functional use of the buildings, in a way that meets the needs and expectations of our communities.

Improving the seismic performance of non-structural elements will minimise the need to close buildings for repair after smaller earthquakes which will lead to improved resilience of the organisations and entities that occupy the buildings. Reduced damage and need for repair and replacement of non-structural elements will also reduce the amount of waste generated to restore buildings and consequently reduce the Whole-of-Life embodied carbon emissions from our buildings.

This paper provides an overview of the design, coordination, and installation practices for non-structural elements in New Zealand prior to 2020 and discusses the changes that are currently occurring in the industry. The second part of this paper discusses how improving the seismic of performance of non-structural elements requires holistic design that considers the response and function of the building as a whole. It highlights the importance of understanding how the response of the structure affects the seismic performance of non-structural elements. Considerations for post-earthquake repair are discussed in the context of the impact of structural damage on the future performance of non-structural elements.

Keywords: non-structural elements, resilience, waste reduction, embodied carbon emissions, post-earthquake performance.

1. INTRODUCTION

Non-structural elements suffered extensive damage in the Canterbury [Dhakal, 2010], Cook Strait and Kaikoura earthquakes [Baird and Ferner, 2017]. Figure 1 illustrates a sample of some of the observed damage to non-structural elements. Greater damage occurred to non-structural elements than expected by building owners and insurers, especially where the earthquake intensity encountered for individual buildings was significantly lower than the design level earthquake (defined as an earthquake with a 10% probability of exceedance in 50 years).

Figure 1: Illustrating damage to non-structural elements observed in the Canterbury earthquakes (from Dhakal, 2010)

The cost of repair work for material damage and business interruption due to poor performance of non-structural elements in the Christchurch, Cook Strait and Kaikoura earthquakes was substantial, although difficult to quantify as the economic losses for structural damage and non-structural damage are not recorded separately by insurers, or the wider industry. The damage highlighted the potential for large consequential damage due to failure of a non-structural element such as a cladding system or sprinkler failure. It also highlighted the complexity and duration of repairs which significantly impacted business interruption.

There appears to be increasing awareness in the earthquake engineering community that improved seismic performance of non-structural elements is key to limiting the damage and disruption caused by earthquakes [Filiatrault & Sullivan, 2014]. It was learnt that consideration of the seismic performance of non-structural elements is not only important for buildings that need to continue operation post major earthquake (such as hospitals), but also how important it is for our school buildings, supermarkets, office buildings, apartment buildings, industrial buildings, and transportation links to be functional following moderate earthquake[1] events, as these are essential for the economy and wellbeing of our communities. Many people were immediately shut out of their homes and apartments, similarly businesses were affected where industrial buildings and offices were closed. There was also significant disruption to homeowners and businesses when they had to find alternative accommodation and places for their businesses to operate from when the extent of the repair works needed the premises to be vacated.

To better understand the underlying reasons for the poor seismic performance of non-structural elements in New Zealand, a strategic review of the New Zealand construction industry in relation to non-structural elements in both new and existing buildings was completed in 2020 [BIP, 2020]. The review found that the poor performance of non-structural elements was directly linked to much wider construction industry issues, including procurement methodologies for the design and construction teams where risk is poorly managed, limitations in the knowledge of code minimum performance compared with outcomes from resilient options, poor coordination between design disciplines and sub-trades on site, issues with the construction

[1] A moderate earthquake is that which represents an earthquake that is one-third as strong as the earthquake shaking that would be used to design a new building.

and installation behaviours involving inadequate or lack of seismic restraints, lack of independent QA, gaps in regulation and lack of knowledge, skills and training throughout the industry.

Improving the seismic performance of non-structural elements will reduce, to acceptable levels, the need to close buildings following earthquakes or to close them to enable the repairs to be completed. This will lead to improved social and economic recovery and therefore improved resilience of our communities. Reduced damage and resulting repair works will also reduce the amount of waste generated to restore the buildings and consequently reduce the Whole-of-Life embodied carbon emissions for our buildings. Waste is also a significant practical issue as the recycling industry simply cannot cope with the volumes generated in such a short period, nor can the construction industry cope with the demand on labour for deconstruction for recycling.

2. DESIGN FOR LIFE PRESERVATION vs RESILIENCE

Immediately following the major earthquakes of 2010 (Mw 7.1) and 2011 (Mw 6.2) in Canterbury there was a great deal of focus on determining the %NBS (percentage of New Building Standard for the Ultimate Limit State case) for buildings. Throughout New Zealand, banners appeared strung up on office buildings, advertising space for rent and proudly stating the %NBS [Ferner, 2018]. But the %NBS was solely a measure against the structural performance of the building in relation to the minimum criteria of 'preservation of life' and ignored the potential for loss of functionality/occupation of the building due to non-structural damage.

Following the major Canterbury earthquakes in 2010 and 2011, there was a Mw 6.5 earthquake in 2013 (Cook Strait) that generated shaking in Wellington close to, or slightly exceeding a 1 in 25-year earthquake event. Whilst there had been extensive damage and learnings regarding the seismic performance of non-structural elements in Christchurch there was a focus on the structural damage sustained by buildings in Canterbury. The Cook Strait earthquake put significant focus on the impacts of damage to non-structural elements in smaller, more frequent earthquake events where minimal structural damage occurred. One notable modern building sustained significant damage to the non-structural elements throughout the building including damage to a sprinkler head that led to significant flooding throughout the building requiring the tenant to immediately vacate the building for months until the repairs were completed.

It became evident that the seismic performance of non-structural elements (which account for 70 – 80% of the building's capital cost) can have a bigger impact on <u>operational disruption</u> for businesses and tenants than failure of structural elements. Consequently, following the 2013 Cook Strait earthquake the insurance industry called for there to be a shift in the debate from the baseline structural minimum 'preservation of life' to building and business resilience [Stanway and Curtain, 2017].

Historically performance objectives for new buildings have been framed by technical experts in structural engineering and building science [RBP, 2022]. The recently published white paper 'Societal expectations for seismic performance of buidings' [RBP, 2022], documented, from a community perspective, nationwide societal expectations for the seismic performance of buildings. This report acknowledged the importance of life safety in building performance expectations but also highlighted the importance of resilience for buildings beyond hospitals and critical infrastructure, including schools, aged care facilities, community meeting places, residential apartments and houses, supermarkets, and the like. Improving the seismic performance of non-structural elements across our building stock is key to the post-earthquake social and economic recovery of our communities.

We are starting to see more resilience conversations occurring in New Zealand with some clients requesting higher than New Zealand Building Code minimum performance requirements for new buildings. However, the code minimum requirements to achieve no damage that requires repair following a 1 in 25-year event, remains the dominant serviceability limit state performance requirement for most buildings. Following a 1 in 100-year seismic event this code minimum design practice can lead to significant damage and repair/replacement of the non-structural elements, which can result in business interruption, significant generation of waste and costs of repair.

The Ministry of Education owns one of the largest property portfolios in New Zealand and recognises that school buildings serve important roles in our communities that extend beyond teaching children including places to hold community fairs, community meetings, night classes for adults and welfare hubs following emergency events (floods, earthquakes etc.). Following the Canterbury earthquakes (2010 to 2011) the Ministry of Education prepared mandatory design requirements for school design that go above minimum code requirements [MOE, 2020]. The requirements include the need for simple, regular structures that limit building drift for improved holistic building performance. The requirements include qualitative performance requirements for non-structural elements (cladding, ceilings, partition walls and building services) such that they buildings remain usable following an SLS2 earthquake event (SLS2 event is defined by the MOE as being 1 in 100-year event for buildings with typically with less than 250 occupants, and 1 in 250-year event for buildings with typically 250 or more occupants).

3. DESIGN, COORDINATION, AND INSTALLATION OF NON-STRUCTURAL ELEMENTS

The following provides a high-level overview of the design, coordination, and installation of non-structural elements in New Zealand.

3.1 PROCUREMENT

The most common procurement practice is to use 'Design-Build' (often lowest price conforming) to procure the design and construction of non-structural elements. This procurement method attempts to transfer the risk of design, coordination, and construction of non-structural elements to the contracting teams even though the consultants now have exception tools available to them, such as BIM, to undertake this coordination. Typically, the consultants complete the building design without coordination of the final layout and sizing of the building services equipment, ducting and piping or the seismic restraints for the building services, ceilings and partitions which are documented for the contracting teams using Performance Specifications. The final design usually has significant changes to the layout and seismic bracing details once the building services design is completed and equipment chosen, compared to the basic details and layouts provided at consent and tender stage.

3.2 DESIGN AND COORDINATION

It is still common that not all non-structural elements and their seismic restraints are documented and coordinated in the design stages e.g., ICT, electrical for mechanical, small pipework, details of all tenancy walls etc. are often excluded from design documentation and BIM models. The design of these items are commonly procured as design-build and coordinated with the remainder of the building components during the construction phase.

In many instances, as the non-structural elements are first coordinated in the project during the construction phase, it is not uncommon for the capacity and geometry of the structure that has been provided to be insufficient to resist the seismic loads generated by the non-structural elements leading to the requirement to accommodate secondary steel within the building envelope to support the seismic restraint of non-structural elements. On top of this there are often significant implications when gussets, fly braces, collars, baseplates and the like are included in the coordination following shop drawing documentation (which is undertaken during the construction phase) [Stanway et al, 2021]. It is not uncommon to find that there is insufficient room to install code compliant non-structural elements and their seismic restraints within the space provided within the building envelope. Changes of this magnitude are often too difficult to make during the construction phase and this often leads to compromises in compliance with the potential to lower the expected seismic performance of the overall building.

There are a limited range of tested passive fire systems for fire rated ceilings. This can make it challenging to detail an unusual non-standard situation but with the additional requirement to accommodate seismic movement, an architect may require the input of a specialist passive fire engineer. Clients often don't want additional consultants, or this specific advice is excluded from the architect's scope. Without the experience and knowledge, these issues can result in non-code compliant outcomes [Stanway et al, 2021].

Multi-storey apartment buildings are a particularly challenging building type because they are heavily compartmentalised with walls that must perform to required fire and acoustic performance levels. In some cases, developer clients don't like to see movement joints in ceilings (or access hatches to inspect walls) and so request these to be omitted [Stanway et al., 2021]. Apartment bathrooms incorporate tiled walls and floors with waterproof membranes that may be easily torn in a seismic event. Proper isolation of the tops of walls from the floor slab above can be challenging especially at an intertenancy wall.

Different façade systems have different pros and cons. Curtain wall or unitised window systems tend to perform well with the preferred approach to have a rainscreen over a drained cavity. The issue with this is that damage to components of the waterproof line in the cavity may not be noticed for some time after an event. Also, a number of these products lack specific test information, or are suitable only for low-rise situations [Stanway et al, 2021].

3.3 CONSTRUCTION

For design-build procurement with performance specifications it becomes the contracting team's responsibility to adequately design, coordinate and install the non-structural elements. Contractor's take on the risk that if appropriate coordination for all non-structural elements has not been undertaken from project inception, that significant additional costs and work arounds may be required to achieve compliance with the New Zealand Building Code, or in a worst case compromises are required, noting that it can be very difficult to achieve a) seismic, b) acoustic and c) fire compliance and where these are required in a location it is often the case that only two of the three requirements can be achieved. This is because seismic considerations are generally driven by separation of components whilst the others are the reverse.

It is the contracting teams challenge to find sufficient room within the context of the already designed building, to adequately install, restrain and provide the required clearances for the non-structural elements.

To be competitive in a market driven by risk transfer and lowest cost, many subcontractors try to manage the cost risk by choosing the easiest and cheapest support points and reticulation routes without due consideration of the potential significant effects for other subcontractors or other elements of the building. An uncoordinated installation by one subcontractor can result in inadequate space to achieve a compliant installation for another subcontractor.

New Zealand contractors reported [BIP, 2020] that they want to construct and install fully resolved designs, but they are currently taking on design risk for the coordination of non-structural elements and their seismic restraints that is difficult to accurately assess and price at tender. They noted it is common for items to need to be reconfigured three or more times to get the installation right. It has been highlighted those subcontractors have limited knowledge of the seismic restraint subtrade themselves and those limitations in knowledge have led to mistakes and missing items during subcontract negotiation and construction. The seismic restraint of non-structural elements is commonly subcontracted to specialist seismic designers who are structural engineers by trade but have limited knowledge of the systems that they are restraining e.g., heating pipes, steam pipes, chilled water pipes, fire dampers. Functionality of these components is not currently well understood by the specialist seismic restraint designers, and restraint details are often provided that do not enable heating and chilled water pipes to expand or fire dampers to break away.

3.4 INDEPENDENT INSPECTION

Whilst it is starting to change, up until around 2020 it was typical that the design, coordination and installation of non-structural elements and their seismic restraints relied on self-regulation of the industry without formal review and signoff from independent authorities that the installations met the minimum requirements of the New Zealand Building Code. It is difficult for building consent authorities to confirm compliance with the Building Code once the building is complete when the seismic restraint of non-structural elements is provided by reference to a performance specification only. It was also common, but again now changing, that the design team was not typically responsible for undertaking inspections to confirm that the installed seismic restraint for the non-structural elements met the performance specifications.

The issues around self-regulation was highlighted in the research by Geldenhuys et al. [2016] who completed a survey of 20 commercial buildings in Wellington and Auckland, to assess the earthquake resilience and compliance of the existing stock of non-structural elements (mechanical, electrical, plumbing, fire sprinkler and internal fitout) in relation to the New Zealand Building Act objectives and current building standards (NZS4219, AS/NZS2785 and NZS4541). The survey found that most of the non-structural elements inspected do not have adequate restraint in accordance with the relevant standards and 80 to 90 % of the inspected partition walls, fire systems, HVAC systems and ceilings needed upgrade to comply with the relevant standard. In addition, it was found that many seismic restraints were compromised by poor fixing at the restraint, structure, or both.

3.5 PASSIVE FIRE DESIGN AND SEISMIC RESTRAINT

A greater level of awareness regarding passive fire aspects of building design and construction came about because of the investigations into the leaky building syndrome that occurred in timber-framed homes built between 1988 and 2004 that were not fully weathertight. In investigating these buildings, serious issues were found in passive fire construction [Stanway et al., 2021].

Knowledge and experience in the industry on how to appropriately incorporate seismic design into passive fire design has largely been driven by Importance Level 4 projects (facilities that need to continue function following a disaster, such as hospitals) which require that the passive fire components achieve operational continuity following a 1 in 500-year seismic event. For general building design (offices, apartment buildings, warehouses etc.), the only criterion for continued performance of passive fire required for building code compliance is following a 1 in 25-year return period event (SLS1).

It is most often by good luck rather than good management that seismic performance is appropriately incorporated into the passive fire design. The good luck component is that some firestop systems inherently have good firestop performance in a seismic event because they are already seismically isolated or restrained as part of normal design [Stanway et al., 2021]. Further research is required to support the seismic performance of various passive fire systems and detailing to enable appropriate detailing for various structural forms and to support post-earthquake damage and repair assessments.

4. STEPS TO IMPROVE THE SEISMIC PERFORMANCE OF NON-STRUCTURAL ELEMENTS

4.1 HOLISTIC BUILDING DESIGN FROM INCEPTION TO COMPLETION OF CONSTRUCTION

The single biggest change to improve the seismic performance of non-structural elements in New Zealand is expected to occur when the holistic consideration of non-structural elements from the project inception to completion of construction is embedded in our industry. It requires consideration of the following:

- Procurement - design consultants and contracting teams are procured such that risk is distributed to the various parties in an equitable way,

- Consultant scope of work – the expectations regarding the design, performance requirements and coordination of non-structural elements is clearly stated by the Principal so that the fees and timeframes can be appropriately estimated,

- Alignment of structural system with performance requirements for the building – the structural system must not only achieve the architectural intent but should be chosen such that the drift and floor accelerations of the building for either damage limitation or continued functionality, results in cost-effective choice of non-structural elements , e.g., what cladding system is to be used? What is the extent of partitions in the building? Should the partitions be fixed floor to floor or have a seismic slip joint just above the ceiling level? Are there multiple wet areas (e.g., membrane showers as is provided in multi-residential units)?

- Coordination of design disciplines throughout the design and construction phases – where architectural and building services components are to be design-build elements, the design should allow sufficient 'real estate' within the building design for not only the potential size of the components but also the required seismic restraint, such that when the contractor does the final design and coordination of these design-building components there is sufficient room to enable full coordination and achieve code compliance,

- Responsibility for installation – ideally one entity has ownership of the installation and coordination of non-structural elements and their seismic restraints during construction rather than each sub-trade doing their own seismic restraint and passive fire. Without overall coordination, one subcontractor can damage or compromise the seismic performance of other services and elements of the building,

- Product substitutions and bespoke equipment– alternative equipment may be cheaper, however the true cost, including knock-on implications, of installing the alternative equipment into the holistic building design can be better understood through interrogating a fully coordinated design model. It is recommended that where bespoke equipment is to be installed that a test to fit for alternative equipment from various suppliers is undertaken and the final detailing and coordination of spaces where bespoke equipment is to be provided is undertaken as late as possible in the design phase,

- Independent inspection – undertake independent QA to confirm that the installation of non-structural elements meets the design requirements.

4.2 RESEARCH AND TESTING

While research into the seismic performance of non-structural elements has been on-going for decades (e.g. Yancey and Camacho, 1978; Villaverde, 1997), recent research [BIP 2020] has demonstrated significant gaps in technical knowledge both nationally and internationally, especially with regard to how various non-structural elements respond to seismic accelerations and building drifts and the interaction, impact and damage of various building components during seismic events.

Since the 2010-11 Canterbury earthquake sequence, multiple research projects have progressed that seek to improve the wider understanding and to provide new and improved details for use in the construction industry [Dhakal et al 2014, 2016a, 2016b, 2019, Pourali et al 2017, Yeow et al 2018, Khakurel et al 2019, Bhatta et al 2020, Mulligan et al 2020, Arifin et al 2020a, 202b].

Sullivan et al. [2013] and others have demonstrated that international standards provide poor prediction of floor spectral demands, particularly for non-structural elements characterized by low levels of damping. In addition, there is little evidence from research or in-situ observations that the ductility reduction factors included in some codes (including NZS 1170.5) to allow reduction of elastic acceleration demands to design levels that allow for some non-linear response of components are appropriate.

There are a number of areas where research would benefit the industry, these include:

- The performance of passive fire protection systems and detailing under seismic loads,
- Testing to provide assurance and information on the expected post-earthquake performance of non-structural elements in various configurations and seismic restraint. In particular, the industry needs clearer understanding on the way forward to achieve low-damage and continued operation design objectives in relation to mechanical and electrical equipment as well as passive-fire ratings post-earthquake and detailing to facilitate ease of repair for minor damage,
- To develop testing methodologies and testing facilities to investigate the post-earthquake water/weathertightness and thermal/acoustic insulation of cladding systems, window systems, partitions, and other non-structural elements,
- Estimations of repair costs, repair time, environmental impact, and embodied carbon emissions,
- Database of the tested response of non-structural elements.

4.3 Seismic Classification System

It is proposed that non-structural elements are rated according to their drift and acceleration capacity [Sullivan et al. 2020]. The University of Canterbury is looking to develop a non-structural element seismic rating system which promises to:

- Help engineers to appropriately specify and detail non-structural elements for buildings of different importance levels in line with their expected performance in earthquakes,
- Help the design team choose the most cost-effective combination of various structural systems at concept design alongside the expected costs for the detailing for the non-structural elements to achieve the associated non-structural element Drift and Acceleration Element Class for each structural system considered.
- Assist in communicating the performance expectations for all categories of non-structural elements and restraints,
- Help facilitate inspection and compliance checks for sign-off of non-structural elements,
- Help facilitate inspection and assessment post-earthquake.

5. IMPACT OF STRUCTURAL DAMAGE ON THE FUTURE PERFORMANCE OF NON-STRUCTURAL ELEMENTS

Another important learning from the recent earthquakes is that structural damage can reduce the stiffness of structures, in particular concrete moment resisting frames. Research [Marder et al., 2020], found that epoxy-repaired plastic hinges can exhibit different behaviour from identical undamaged components in terms of reduced stiffness, increased strength and increased axial elongation but achieve comparable energy dissipation and deformation capacities. This is generally good news for the post-earthquake performance of concrete moment frames in terms of preservation of life, but in terms of the future performance of non-structural elements in smaller (more frequent) earthquake events engineers need to consider the impact of the damage and repair of the structure and the potential for the non-structural elements to be more vulnerable in future events.

Based on the damage sustained and the subsequent epoxy repair of the beam-column sub assemblages Marder et al. [2020] recommends using 80% of the stiffness of the undamaged beams for the post-repair stiffness as an appropriate effective secant stiffness to yield but notes that a larger stiffness reduction should be considered when the moment demands are less than Mn (nominal flexural strength of the beam). If the future performance of the non-structural elements does not meet the required performance expectations with the reduced stiffness of the structure, localised concrete breakout and repair may need to be considered or replacement of non-structural elements with components and detailing that can achieve the required seismic performance with the increased drift.

A particular issue for drift sensitive non-structural components was highlighted in the consideration of the restoration of a multi-storey multi-unit apartment building in Christchurch where the building had a residual drift of 0.5%. Unsurprisingly post-earthquake the solid plaster cladding system was damaged and leaking and the window joinery was leaking along with air gaps at the base of opening windows, allowing cold air into apartments. The damage required the full replacement of both the cladding and glazing systems. The challenge is how to replace the cladding and windows when the building has a 0.5% drift. Installing new windows to fit the existing shape of the opening with the 0.5% drift would likely damage the windows during the installation process [Arifin et al., 2020b], however installing the new cladding system and window joinery vertical would subject the cladding and windows to significantly more drift in future events, e.g., movement of the structure to 0.25% drift in the opposite direction would subject the new cladding and windows to 0.75% drift and almost certainly damage these components windows making them considerably more vulnerable to damage in future smaller earthquake events.

6. CONCLUSIONS

The performance of our buildings caused many to pause and consider if current design and construction practices were delivering the buildings that meet the resilience needs of our communities. In New Zealand we needed to ask if we have the right balance between designing to preserve life in extreme, infrequent events versus designing for lesser more frequent events that enable continued functional use of the buildings in a way that meets the needs and expectations of our communities and businesses. We have learnt that we need building and business resilience for all our building stock not just facilities that are expected to be operational in a post-disaster environment (e.g., hospitals).

Holistic design is expected to improve the seismic performance of non-structural elements. Design should consider the impact of the structural response on the detailing of the non-structural elements to achieve the seismic performance, provide sufficient real estate for contractors to appropriately design and install the non-structural elements, consider the seismic reactions from the restraint of non-structural elements and provide appropriate structure to resist those actions and consider the thermal, acoustic and passive fire requirements to achieve the performance expectations for the building as a whole.

The potential for increased vulnerability of non-structural elements to damage in future earthquake events as a result of an earthquake event that causes damage to the primary structure needs careful consideration during the initial design process and during post-earthquake assessments. Engineers need to ensure any post-event repair scheme, for the structural and non-structural elements, will achieve the seismic performance expectations of the overall building in future seismic events.

As more research is undertaken into the response of various non-structural element and configurations and this knowledge is embedded into the wider construction industry, we expect improved seismic performance of non-structural elements in future seismic events and consequent improvement in the resilience of our businesses and communities.

7.REFERENCES

Arifin, F., Sullivan, T.J., Dhakal, R., 2020, *Experimental Investigation into the Seismic Fragility of a Commercial Glazing System*, Bulletin of the New Zealand Society for Earthquake Engineering, (Accepted for Publication).

Arifin, F., De Francesco, G., Sullivan, T.J., Dhakal, R.P., 2020. *Developing guidelines for the seismic assessment of glazing systems.* Annual Conference of NZ Society for Earthquake Engineering (NZSEE20), Wellington, 10pp.

AS/NZS 2785:2020 "Suspended Ceilings – Design and installation". *Standards New Zealand*, Wellington, NZ

Baird, A., Ferner, H. [2017] "Damage to Non-structural elements in 2016 Kaikoura Earthquake", *Bulletin of the New Zealand Society of Earthquake Engineering*, Vol. 50, No. 2, pp. 187-193.

Bhatta, J., Dhakal, R.P., Sullivan, T.J. and Lanyon, M. (2020). "Low-damage rocking precast concrete cladding panels: Design approach and experimental validation". *Journal of Earthquake Engineering.* https://doi.org/10.1080/13632469.2020.1830201

Building Innovation Partnership (BIP), [2020], "Design, Construction and Seismic Performance of Non-Structural Elements", *Building Innovation Partnership*, bipnz.org.nz, https://bipnz.org.nz/design-construction-and-seismic-performance-of-non-structural-elements/

Dhakal, R.P. [2010] "Damage to Non- Structural Components and Contents in 2010 Darfield Earthquake", *Bulletin of the New Zealand Society of Earthquake Engineering*, Vol. 43, No. 4, pp. 404-411.

Dhakal, R.P., Pourali, A., Tasligedik, S., Yeow, T., Baird, A., MacRae, G., Pampanin, S. and Palermo, A. [2016]. "Seismic performance of non-structural components and contents in buildings: An overview of NZ research". Earthquake Engineering and Engineering Vibration, 15(1): 1-17. https://doi.org/10.1007/s11803-016-0301-9

Dhakal, R.P., MacRae, G.A., Pourali, A., Paganotti, G., [2016a], *Seismic Fragility of Suspended Ceiling Systems Used in NZ Based on Component Tests*, Bulletin of the New Zealand Society for Earthquake Engineering, Special Issue on Seismic Performance of Non-structural elements (SPONSE), Vol. 49, No. 1, pp. 45-63.

Dhakal, R.P., Pourali, A., Saha, S., [2016b], *Simplified Seismic Loss Functions for Suspended Ceilings and Drywall Partitions*, Bulletin of the New Zealand Society for Earthquake Engineering, Special Issue on Seismic Performance of Non-structural elements (SPONSE), Vol. 49, No. 1, pp. 64-78.

Dhakal, R.P., Pourali, A., Saha, S., [2016]. *Simplified seismic loss functions for suspended ceilings and drywall partitions*. Bulletin of the New Zealand Society for Earthquake Engineering, Special Issue on Seismic Performance of Non-Structural Elements (SPONSE), 49(1): 64-78, https://doi.org/10.5459/bnzsee.49.1.64-78

Dhakal, R.P., Rashid, M., Bhatta, J., Sullivan, T.J., MacRae, G.A., Clifton, G.C., Jia, L.J., Xiang, P., [2019]. *Shake Table Tests of Multiple Non-Structural Elements in a Low–Damage Structural Steel Building*. 4th International Workshop on Seismic Performance of Non-Structural Elements (SPONSE), 22-23 May, Pavia, Italy.

Ferner, H., [2018] "A seismic building rating system – The New Zealand experience", *17th U.S.-Japan-New Zealand Workshop on the Improvement of Structural Engineering and Resilience*, Queenstown, New Zealand, November 12-14, 2018.

Filiatrault, A., Sullivan, T., [2014] "Performance-based Seismic Design of Non-structural Building Components: The Next Frontier of Earthquake Engineering", *Earthquake Engineering and Engineering Vibration*, 13(Supp.1), pp. 17-46.

Geldenhuys, B., Szakats, G., Stuart, G., Burling, M. [2016] "Survey of seismic restraint of non-structural elements in existing commercial buildings – Report on Stage 2 – Full Study Volume 1", *KOA & MBIE Report*, November 2016, KOA, Wellington, New Zealand. https://www.mbie.govt.nz/assets/178a7534c9/survey-of-non-structural-elements-in-20-commercial-buildings.pdf , 35 pages.

Khakurel, S., Yeow, T.Z., Chen, F., Wang, A., Saha, S.K., Dhakal, R.P., 2019. *Development of cladding contribution functions for seismic loss estimation*. Bulletin of the New Zealand Society for Earthquake Engineering, 52(1): 23-43, https://doi.org/10.5459/bnzsee.52.1.23-43

Marder, K.J, Elwood, K.J., Motter, C.J., Clifton, G.C., [2020] "Quantifying the effects of epoxy repair of reinforced concrete plastic hinges", *Bulletin of the New Zealand Society for Earthquake Engineering*, Vol. 53, No. 1, March 2020, pp. 37-51.

Ministry of Education (MOE), [2020], "Designing Schools in New Zealand, Structural and Geotechnical Requirements", Version 3.0, October 2020, https://assets.education.govt.nz/public/Documents/Primary-Secondary/Property/Design/Design-guidance/Structural-and-Geotechnical-Requirements-Version-3.0.pdf

Mulligan, J., Sullivan, T.J., Dhakal, R.P., 2020. *Experimental seismic performance of partly sliding partition walls*. Journal of Earthquake Engineering, https://doi.org/10.1080/13632469.2020.1733139

NZS 1170.5:2004 "New Zealand Standard – Structural design actions – Part 5: Earthquake actions – New Zealand". *Standards New Zealand*, Wellington, NZ

NZS 4219:2009 "New Zealand Standard – Seismic Performance of Engineering Systems in Buildings". *Standards New Zealand*, Wellington, NZ

NZS 4541:2013 "New Zealand Standard Automated Fire Sprinkler Systems". *Standards New Zealand*, Wellington, NZ

Pourali, A., Dhakal, R.P., MacRae, G.A., 2014. *Seismic performance of suspended ceilings: Critical review of current design practice*. New Zealand Society for Earthquake Engineering Annual Conference (NZSEE2014), 21-23 March, Auckland, 8 pages

Pourali, A., Dhakal, R.P., MacRae, G., Tasligedik, S., 2017. *Fully-floating suspended ceiling system: Experimental evaluation of structural feasibility and challenges*. Earthquake Spectra, 33(4): 1627-1654, https://doi.org/10.1193/092916EQS163M

Resilient Building Project (RBP), [2022] "Societal expectations for seismic performance of buildings – Detailed report on focus groups", *NZSEE & EQC*, New Zealand, 2022. https://www.nzsee.org.nz/wp-content/uploads/2022/07/Focus-Group-Report-final.pdf

Sullivan, T., Dhakal, R., Stanway, J., [2020] "A framework for the seismic rating of non-structural elements in Buildings", *17th World Conference on Earthquake Engineering*, Sendai, Japan, 2020.

Sullivan, T.J., Calvi, P.M, Nascimbene, R., [2013] "Towards Improved Floor Spectra Estimates for Seismic Design", *Earthquakes and Structures*, Vol.4, No.1.

Stanway, J., Curtain B., [2017] "Economic Benefits of Code Compliant Non-structural elements in New Buildings", *Opus & MBIE Report* https://www.mbie.govt.nz/assets/decf694d37/economics-relating-to-the-seismic-performance-of-non-structural-elements-v2.pdf, 52 pages.

Stanway, J., Sullivan, T., Dhakal, R., Hinz, S., James, M., Davis, M., [2021] "Design, Construction and Seismic Performance of Non-Structural Elements in New Zealand – Current Challenges and Steps for the Future – August 2021", SESOC – SEAOC Paired Article, *SESOC newsletter*, April 2022.

Villaverde, R., [1997] "Seismic Design of Secondary Structures: State of the Art", *Journal of Structural Engineering*, Vol 123, Issue 8 – August 1997.

Yancey, C., Camacho, A., [1978] "Aseismic Design of Building Service Systems: The State of the Art, Volume 13", Department of Commerce, *National Bureau of Standards*, National Engineering Laboratory, Centre for Building Technology, 1978.

Floor Acceleration Spectra: From Research to Seismic Code Provisions

Peter Fajfar[1] and Vladimir Vukobratović[2]

[1] Faculty of Civil and Geodetic Engineering, University of Ljubljana
Jamova cesta 2, 1000 Ljubljana, Slovenia
e-mail: peter.fajfar@fgg.uni-lj.si
[2] Faculty of Technical Sciences, University of Novi Sad
Trg Dositeja Obradovića 6, 21000 Novi Sad, Serbia
vladavuk@uns.ac.rs

Abstract. Seismic design and evaluation of acceleration-sensitive nonstructural components is usually performed by using floor acceleration spectra. The concept was initially used mainly in the design of nuclear power plants. Much later, it was recognized that nonstructural components account for the majority of direct property losses due to earthquake damage in all buildings, and floor spectra attracted more attention of researchers, code developers and designers. In this paper, the main research results, which represented the base for the determination of seismic demand on nonstructural components in the latest generation of European (draft second-generation Eurocode 8) and US (ASCE 7-22) codes are summarized. The simplifications made in both code provisions are discussed, and a comparison between the procedures and results obtained by using both documents is made. A conceptual difference between the floor acceleration spectra in two codes exists. Eurocode 8 is based, to a large extent, on the dynamics of structures, whereas ASCE 7-22 relies more on empirical observations and judgement. Seismic design forces on nonstructural components according to Eurocode 8 are generally larger than those according to ASCE 7-22, mainly due to the difference in the assumed component damping (2% versus 5%).

Keywords: Floor acceleration spectra, Eurocode 8, ASCE 7-22, Nonstructural components.

1. INTRODUCTION

Floor response spectra in terms of acceleration, which are also known as in-structure spectra, are usually used for the seismic design and evaluation of acceleration sensitive nonstructural components and systems (mechanical, electrical, plumbing and architectural) and building contents, that are not part of the main or intended load-bearing structural system. The floor response spectra concept is based on a separate (uncoupled) analysis of the building structure and nonstructural components, which means that dynamic interaction between them is neglected. It is sufficiently accurate in cases of nonstructural components whose mass is significantly smaller than that of the primary structure. Floor spectra are influenced both by the characteristics of the ground motion and those of the building structure, and can be "accurately" determined by performing a response history structural analysis. Because this approach is time-consuming, it is only exceptionally used. In everyday design practice usually an approximate approach is used, where the floor spectra are determined directly from the ground motion spectra. There are several methods of different complexity and with different limitations which are based on this approximate approach. They are called direct methods.

Research on seismic analysis of nonstructural components started in 1960s and has been initially driven by the needs of nuclear industry. It was essential to guarantee the survivability of critical equipment in nuclear power plants. Only several decades later also a large economic impact of potential earthquake damage of nonstructural components in conventional buildings has been recognized. An early direct method for the determination of acceleration floor spectra was proposed by Biggs [1971]. The development which followed is described in a state-of-the-art paper on the seismic design of secondary structures by Villaverde [1997]. In this millennium, we are witnessing an exponential growth of articles in the field of floor spectra. A review paper by Filiatrault and Sullivan [2014], among others, summarized current knowledge on the seismic design and analysis of nonstructural building components. The most recent state-of-the-art review was published by Wang *et al.* [2021].

The most important research results have been, with some delay, continuously implemented in seismic provisions. In this paper the latest research, which represents the basis for the horizontal floor acceleration spectra in the draft of the new (second generation) Eurocode 8 (EC8) [CEN, 2022] and in ASCE 7-22 [ASCE, 2021], and its implementation in code provisions, are briefly summarized. A qualitative and quantitative comparison of the equations for seismic design forces on nonstructural components is made.

2. RESEARCH RELATED TO EC8

Research results obtained at the University of Ljubljana, Slovenia, represent the theoretical background for the floor acceleration spectra in the new EC8. The history of our research on floor spectra, which started already in 1980s, is summarized in [Fajfar, 2021]. The main results are presented in the PhD thesis of the second author [Vukobratović, 2015], and in three journal papers by the authors [Vukobratović and Fajfar, 2015, 2016, 2017]. In this section the simplified code-oriented version of the floor acceleration spectra which was, with some additional simplifications and modifications, adopted in EC8, is summarized.

The basis of our work was a direct method developed by Yasui *et al.* [1993] for elastic building structures. The method takes into account the dynamic characteristics of the primary structure and elastic ground response spectrum. It is based on the theory of structural dynamics. We found the method to be convenient for practical applications and reasonably accurate in the off-resonance regions. So, we decided to use it in our research with some modifications: (1) in order to extend the method to inelastic behaviour of primary structures, the elastic response spectrum was replaced by an inelastic response spectrum; (2) in the resonance region, the Yasui *et al.* [1993] formula produced overly conservative results, so it was replaced by empirically determined values; (3) in the post-resonance region, the Square Root of the Sum of the Squares (SRSS) modal combination was replaced with the algebraic sum (ALGSUM) of contributions of different modes, which has a better theoretical background [Vukobratović and Fajfar, 2016]; and (4) the inelastic behaviour of nonstructural components was taken into account by increasing the component damping.

The floor acceleration spectrum represents the acceleration of the secondary system S_{ap} as a function of its period T_{ap}. Floor acceleration spectra are determined separately for each considered mode of the primary structure, and are then combined in order to obtain the resulting floor response spectrum. For mode 'i' and floor 'j', the value of the floor acceleration spectrum is determined as (for a more detailed description see [Vukobratović and Fajfar, 2017] or [Fajfar, 2021], in this paper the EC8 notation is used):

$$S_{\mathrm{ap,ij}} = \frac{\Gamma_{\mathrm{i}}\phi_{\mathrm{ij}}}{\left|\left(T_{\mathrm{ap}}/T_{\mathrm{p,i}}\right)^2 - 1\right|}\sqrt{\left(\frac{S_{\mathrm{ep,i}}}{R_{\mu}}\right)^2 + \left\{\left(T_{\mathrm{ap}}/T_{\mathrm{p,i}}\right)^2 S_{\mathrm{eap}}\right\}^2} \tag{1}$$

$$\left|S_{\mathrm{ap,ij}}\right| \le AMP_{\mathrm{i}} \times \left|PFA_{\mathrm{ij}}\right| \tag{2}$$

$$PFA_{\mathrm{ij}} = \Gamma_{\mathrm{i}}\phi_{\mathrm{ij}}S_{\mathrm{ep,i}}/R_{\mu} \tag{3}$$

$$AMP_{\mathrm{i}} = \begin{cases} 2.5\sqrt{10/\left(5+\xi_{\mathrm{ap}}\right)}, & T_{\mathrm{p,i}}/T_{\mathrm{C}} = 0 \\ \text{linear between } AMP_{\mathrm{i}}\left(T_{\mathrm{p,i}}/T_{\mathrm{C}}=0\right) \text{ and } AMP_{\mathrm{i}}\left(T_{\mathrm{p,i}}/T_{\mathrm{C}}=0.2\right), & 0 \le T_{\mathrm{p,i}}/T_{\mathrm{C}} \le 0.2 \\ 10/\sqrt{\xi_{\mathrm{ap}}}, & T_{\mathrm{p,i}}/T_{\mathrm{C}} \ge 0.2 \end{cases} \tag{4}$$

The indices 'p' and 'ap' correspond to the primary (building) structure and the secondary element (i.e., nonstructural component), respectively. S_{ep} is a value in the elastic acceleration spectrum. $S_{ep,i} = S_e(T_{p,i}, \xi_{p,i})$ applies to the i[th] mode of the primary structure, whereas $S_{eap} = S_e(T_{ap}, \xi_{ap})$ applies to the component. The natural periods of the i[th] mode of the structure and component are denoted as $T_{p,i}$ and T_{ap}, respectively, whereas $\xi_{p,i}$ and ξ_{ap} denote the damping values of the structure (for the i[th] mode) and of the component, respectively. They are expressed as the percentage of critical damping. T_C is the characteristic period of the ground motion (which is equal to T_C in EC8). Γ_i is the modal participation factor for the i[th] mode, whereas ϕ_{ij} represents the i[th] mode shape value at the j[th] floor. AMP_i is the amplification factor (for the i[th] mode, it applies to all floors j), defined as the ratio between the peak value in the floor acceleration spectrum (the value in the plateau of the i[th] mode), $S_{ap,i}$, and the peak floor acceleration PFA_i. It depends only on the component damping ξ_{ap}. The results of the performed parametric studies indicated that this is the most important parameter influencing the amplification factor. The influence of hysteretic behaviour, ductility, and the ratio T_p/T_C (except when this ratio has small values) is small to moderate. Thus, the equation in the third line of Equation (4), proposed by Sullivan *et al.* [2013], is a simple and viable option for implementation in codes. More elaborate empirical formulae, which also take into account the effects of hysteretic behaviour, ductility and the ratio T_p/T_C, are presented in [Vukobratović and Fajfar, 2016].

In the case of the inelastic primary structure, in principle, a pushover analysis is needed in order to determine some parameters. The inelastic behaviour of the primary structure is taken into account by the ductility and period dependent reduction factor R_μ. The term ($S_{ep,i}/R_\mu$) represents the value in the inelastic acceleration spectrum for the primary structure. It can be replaced by the ratio of the yield force and the mass of the equivalent SDOF (single-degree-of-freedom) primary system (see, e.g., the N2 method [Fajfar, 2000]). It is assumed that the inelastic behaviour is related only to the fundamental mode, whereas all higher modes are treated as elastic. Thus, R_μ should be determined only for the fundamental mode, whereas for all higher modes (i > 1), R_μ amounts to 1. As an approximation, implemented also in the new EC8, the part of the force modification factor corresponding to the energy dissipation capacity of the building structure can be used as R_μ. The fundamental mode shape ϕ_1 is, in the case of an inelastic structure, approximated with the deformation shape determined in pushover analysis.

Inelastic behaviour of ductile nonstructural components can be approximately taken into account by increasing the damping of the component. Our study [Vukobratović and Fajfar, 2017] indicated that floor acceleration spectra for elastic components with 10% and 20% damping approximately correspond to the spectra for inelastic components in the case of a ductility demand μ_{ap} equal to 1.5 and 2.0, respectively, and the actual damping of the component equal to 1%. It was also found that, with increasing inelastic behaviour of the component, the influence of its damping rapidly decreases. Based on these observations we proposed to use ξ_{ap} = 10%, independently of the actual damping of component, as a preliminary conservative approach for taking into account the inelastic behaviour of ductile components.

The floor acceleration spectra calculated for individual modes should be combined in order to determine the resulting floor spectra. The modal superposition is a standard procedure in the case of elastic structures. As an approximation, it is often applied also for inelastic structures. In the case of the described direct method, the standard SRSS or CQC (Complete Quadratic Combination) modal combination rules are used for both elastic and inelastic primary structure, with the exception of the post-resonance region of the fundamental mode, where the algebraic sum (ALGSUM) is used, in which the relevant signs of individual modes are taken into account.

If a nonstructural component is attached to the ground floor of a building (without soil-structure interaction), it responds as if it was supported directly on the ground, thus the floor acceleration spectrum is equal to the ground motion acceleration spectrum corresponding to the component damping and ductility. This spectrum is taken as the lower limit of floor spectra along the height of the building.

Due to uncertainties in assessing natural periods of both the primary structure and nonstructural components, a broadening of the spectra in the resonance region is required by seismic codes and standards. A broadening is implicitly included in the described direct method, especially in the case of the fundamental mode.

The described direct method is based on the principles of structural dynamics. Empirical values obtained in a parametric study are used only in the resonance region in order to improve the accuracy of the peak values of floor acceleration spectra. All important influences identified by the US researchers (Section 4) are considered. Inertial forces on nonstructural components depend on the characteristics of the ground motion (intensity and frequency content), of the building (period, damping, ductility), and of the component itself (period, damping, ductility and vertical location in the building). Equations (1) to (4) take into account all above parameters. The ground motion characteristics are represented by response spectra. Periods and damping values of the building and the component are explicitly included in the equations. Of course, in order to develop a practice-oriented approach, some approximations were considered in the process of derivation of equations. In the linear range, the approximations are related to damping (see the derivation of the equations proposed by Yasui *et al.* [1993] in [Vukobratović, 2015]). Nonlinear effects due to the possible ductile response of the primary structure and nonstructural components are approximately taken into account by using well established concepts (inelastic spectra, equivalent damping).

Equation (1) indicates that the acceleration of a component depends both on the dynamic characteristics of the building and of the component. In the case of rigid components (relative to building), the vibration of the building prevails, whereas the vibration of the component is decisive in the case of flexible components. When $T_{ap} << T_p$, the response of the component is almost identical to the response of the building. In the opposite case, $T_{ap} >> T_p$, the component response is almost the same as it was attached to the ground.

As demonstrated in Figure 1 (and in several papers by the authors), the floor spectra obtained by Equations (1) to (4) match well with the floor spectra obtained by the more accurate approach based on nonlinear dynamic analysis.

3. FLOOR ACCELERATION SPECTRA IN THE NEW EC8

The existing version of EC8 was officially enforced in 2004 [CEN, 2004]. The new, second generation of Eurocodes is in the final stage of preparation. This paper is based on the latest draft of EC8 1-2 [CEN, 2022]. Major changes are not expected. The first author of this paper has participated in the EC8 development as a representative of Slovenia in the CEN/TC 250/SC 8 Committee, but he has not been a member of the project teams responsible for drafting the provisions.

It should be noted that in EC8 different notation is used than in ASCE 7-22. Nonstructural components are called ancillary elements, response modification (reduction) and importance factors are called behaviour and performance factors, respectively.

Floor acceleration spectra in the draft new EC8 are based mainly on the research results of the authors summarized in Section 2. The direct method, as defined in [Vukobratović and Fajfar, 2017], was, with some modifications, implemented in the informative Annex C, entitled Floor accelerations for ancillary elements, whereas a simplified version, limited to rigid nonstructural components in buildings with negligible higher mode effects, is provided in Subsections 7.1 and 7.2. Compared to the approach described in Section 2, some changes were made: (1) if the force-based approach is used for the design of the primary structure, R_μ is determined as a function of the ductility dependent behaviour factor q_D, provided in EC8 for different structural systems, so pushover analysis is not needed; (2) the effect of the inelastic behaviour of nonstructural components is taken into account, by analogy with buildings and following the approach in the existing EC8, by a behaviour (reduction) factor rather than by an increased damping value; and (3) for "ease of use", the standard combination rules (SRSS or CQC), typical for modal analysis of buildings, are used in the whole period range, rather than algebraic sum proposed in the original method in the post-resonance range.

The component damping "may be taken equal to 2%, unless greater values are demonstrated".

The horizontal design force on a nonstructural component may be determined by the formula

$$F_{\mathrm{ap}} = \gamma_{\mathrm{ap}} m_{\mathrm{ap}} S_{\mathrm{ap}} / q_{\mathrm{ap}}' \tag{5}$$

where γ_{ap} and m_{ap} are the performance factor (taken as equal to 1 in this paper) and the mass of the component, respectively. q_{ap}' is the period-dependent behaviour factor of the component

$$q_{\mathrm{ap}}' = q_{\mathrm{ap,S}}\, q_{\mathrm{ap,D}}' \tag{6}$$

where $q_{\mathrm{ap,S}}$ is the behaviour factor component accounting for all sources of overstrength which can be taken as equal to 1.3 unless another value is specified or documented for the ancillary element under consideration, and $q_{\mathrm{ap,D}}'$ is the frequency dependent behaviour factor component accounting for the deformation capacity and energy dissipation capacity of the ancillary element, defined as

$$q_{\mathrm{ap,D}}' = \begin{cases} 1, & T_{\mathrm{ap}} \le T_{\mathrm{B}} \\ \text{linear between 1 and } q_{\mathrm{ap,D}}, & T_{\mathrm{B}} \le T_{\mathrm{ap}} \le 0,8T_{\mathrm{p,1}} \\ q_{\mathrm{ap,D}}, & T_{\mathrm{ap}} \ge 0,8T_{\mathrm{p,1}} \end{cases} \tag{7}$$

$q_{ap,D}$ is equal to 1.0 for elements not able or not allowed to dissipate energy by inelastic deformations. For elements dissipating energy by inelastic deformations, $q_{ap,D}$ is equal to 2.0. $T_{p,1}$ is the period of the fundamental building mode, T_{ap} is the component period, and T_B is the corner period in the response spectrum at the beginning of the plateau.

S_{ap} is the value in the floor acceleration spectrum determined for the floor under consideration. For each floor j, floor spectra $S_{ap,ij}$ for each relevant vibration mode are determined with Equations (1) to (4). The period-dependent behaviour factor R_μ in Equation (1), taking into account the inelastic behaviour of the building structure, is denoted as $q_D{}'$ in the new EC8, and is defined as

$$R_\mu = q_D{}' = \begin{cases} 1, & T_{p,1} \le T_A \\ \text{linear between 1 and } q_D, & T_A \le T_{p,1} \le T_C \\ q_D, & T_{p,1} \ge T_C \end{cases} \tag{8}$$

where q_D is the component of the building behaviour factor accounting for the energy dissipation capacity, provided in EC8 for different structural systems and different materials. T_A and T_C are corner periods in the response spectrum: T_A is the period where the spectrum starts to linearly increase from the PGA value, and T_C is the period at the end of the plateau. Behaviour factor $q_D{}'$ is used only for the fundamental mode. For higher modes $q_D{}' = 1$.

At every floor, j, the resulting floor acceleration $S_{ap,j}$ should be calculated as a SRSS or CQC combination of values for all modes of vibration contributing significantly to the global response. $S_{ap,j}$ should not be smaller than the elastic ground motion spectrum value corresponding to the damping of the ancillary element.

Note that in EC8 the energy dissipation capacity and the overstrength of the component are not included in the floor acceleration spectrum S_{ap}. They are taken into account by the behaviour factor $q_{ap}{}'$ in Equation (5).

The described approach is defined in Annex C. If the ancillary element is rigid, i.e., if $T_{ap} \le T_B$, or if it is included in the group of rigid elements listed in EC8, a simpler approach, defined in Section 7 of draft EC8 1-2 may be used. The floor acceleration value can be determined as

$$S_{ap,j} = \Gamma_1 \frac{z_j}{H} \frac{\eta S_\alpha}{q_D{}'} \ge \frac{S_\alpha}{F_A} \tag{9}$$

Equation (9) represents a special case of Equation (1) corresponding to $T_{ap} = 0$ and accounting for the fundamental mode only. S_α is the value at the plateau of the elastic response spectrum, η is a coefficient accounting for building damping ($\eta = 1.0$ for 5% damping), and z_j/H defines the vertical position of floor j. The participation factor of the fundamental mode Γ_1 may be determined by the simplified formula $\Gamma_1 = 3N_s/(2N_s+1)$, where N_s is the number of storeys. The values of Γ_1 range from 1 to 1.5. F_A is the ratio between S_α and PGA, so PGA represents the lower bound of floor accelerations.

In Figure 1, floor acceleration spectra at the roof and at the first floor ($z_1/H = 0.33$) of a three-storey reinforced concrete frame, determined according to new EC8 (using 5% component damping), are compared with the spectra determined according to the original Vukobratović and Fajfar [2017] approach, as well as with the spectra obtained by using the nonlinear response history analysis (RHA). The structural and dynamic characteristics of the frame are presented in [Vukobratović and Fajfar, 2016]. The three natural periods are 0.3, 0.08 and 0.04 s. Structural damping of 5% was assumed in the analysis. The building response is inelastic ($q_D = 2$), nonstructural component has no energy dissipation capacity. The corner periods in the ground motion spectrum are $T_A = 0$ s (the start of linear increase), $T_B = 0.15$ s (the start of plateau), and T_C = 0.5 s (the end of plateau). The ratio between the maximum spectral acceleration of the elastic response spectrum S_α and peak ground acceleration PGA is equal to 0.4.

Figure 1 shows a reasonable agreement between the code- and more accurate RHA floor spectra. The original direct method [Vukobratović and Fajfar, 2017], which, in the post-resonance region, applies the ALGSUM combination of different modes, correlates better with the RHA results than the EC8 approach which uses the SRSS combination in the whole period region. The higher mode effects are clearly visible. Direct spectra are calculated without considering the lower bound. The lower bound values, represented by the ground response spectrum for 5% damping of the component, are shown as a separate graph. The figure indicates that the first floor acceleration spectra are in some period regions controlled by the lower bound values.

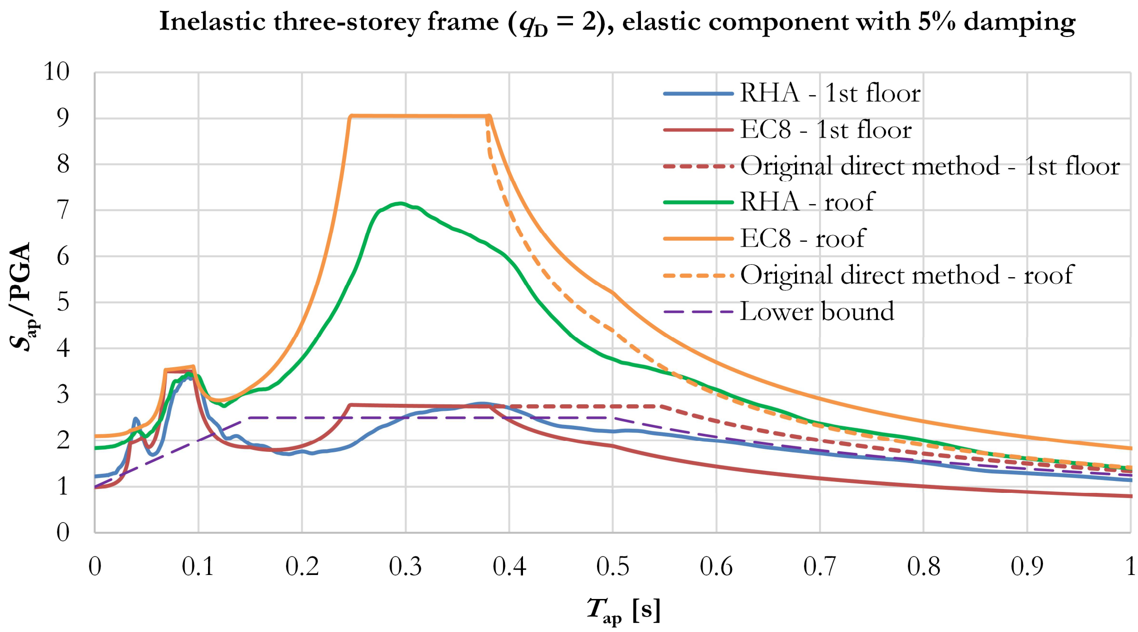

Figure 1. Comparison of normalized floor acceleration spectra according to the draft new EC8, original direct method and response history analysis (RHA)

4. RESEARCH RELATED TO ASCE 7-22

Nonstructural seismic design force equations in NEHRP provisions [FEMA, 2020] and ASCE 7-22 are mainly based on the research in the Applied Technology Council ATC-120 project [NIST, 2017, 2018]. This project reviewed the available literature, identified key parameters of interest, assessed their influence on component response, and proposed a design equation. Nonlinear analyses of archetype buildings and components, as well as the analyses of strong motion records from instrumented buildings, were used. An excellent overview of the project findings was prepared by Lizundia [2019]. The investigated parameters included: (1) peak ground acceleration PGA, (2) seismic force resisting system, (3) fundamental period of the building, (4) building ductility, (5) vertical location of the component within the building, (6) component period, (7) inherent component damping, (8) component ductility, (9) component reserve strength margin, (10) inherent building damping, (11) building configuration, and (12) floor and roof diaphragm flexibility. The parameters (1) to (9) were identified as the most influential and were included in the proposed design equation, as explained below. Three remaining parameters were not included either due to small influence on the component response (building damping) or due to the complexity of the issue (building configuration and floor flexibility). No attention has been paid to the effect of higher modes.

The proposed nonstructural design Equation (10) [NIST, 2018], which basically represents the nondimensional (note that accelerations are considered as a fraction of g) floor acceleration spectrum (design force divided by the weight), was formulated as a product of three independent individual terms, recognizing that the earthquake force on a nonstructural component depends on the level of ground shaking (parameter 1 above), the modification of shaking resulting from the building response (parameters 2-5), and a further modification of shaking associated with the component itself (parameters 6-9).

$$\frac{F_{\mathrm{p}}}{W_{\mathrm{p}}} = \mathrm{PGA} \times \left[\frac{\left(\frac{\mathrm{PFA}}{\mathrm{PGA}}\right)}{R_{\mu\mathrm{bldg}}}\right] \times \left[\frac{\left(\frac{\mathrm{PCA}}{\mathrm{PFA}}\right)}{R_{\mathrm{pocomp}}}\right] \times I_{\mathrm{p}} \tag{10}$$

I_{p} is the component importance factor which is everywhere in this paper set to 1.0. The level of ground shaking is represented by PGA. The influence of building response is captured by the PFA (peak floor acceleration) to PGA ratio, which is based on a detailed review of instrumented building strong motion records. The ratio is a function of the vertical location of the component (z/h) and of the fundamental period of the building T_{abldg}

$$\left(\frac{\mathrm{PFA}}{\mathrm{PGA}}\right) = 1 + a_1\left(\frac{z}{h}\right) + a_2\left(\frac{z}{h}\right)^{10}, \quad a_1 = \frac{1}{T_{\mathrm{abldg}}} \le 2.5, \quad a_2 = \left[1 - \left(0.4 / T_{\mathrm{abldg}}\right)^2\right] \ge 0 \tag{11}$$

PFA/PGA values at the top of the building range from 2.0 for very flexible buildings to 3.5 for very rigid buildings. So, the PFA/PGA ratio implicitly takes into account the characteristics of a typical response spectrum where the accelerations of rigid structures are larger than those of flexible ones.

The beneficial effect of the inelastic structural behaviour (building ductility) is taken into account by the reduction factor $R_{\mu\mathrm{bldg}}$ which is equal to the square root of the ductility-related building response modification coefficient R_{D}

$$R_{\mu\mathrm{bldg}} = \left(R_{\mathrm{D}}\right)^{1/2} = \left(1.1R / \Omega_0\right)^{1/2} \tag{12}$$

where R and Ω_0 are the response modification coefficient and the overstrength factor, respectively, provided for different structural systems in ASCE 7-22. Equation (12) is based on a series of archetype case studies using different seismic force-resisting systems, number of storeys, and overstrength assumptions. For selected building structures, Equation (12) yields values from 1.13 to 2.10 [NIST, 2018].

The influence of shaking associated with the component itself is included in the peak component acceleration (PCA) to peak floor acceleration (PFA) ratio. The PCA/PFA includes amplification due to possible resonance and depends on the component period (relative to the building period), component damping, and component ductility. Inherent component damping was fixed to 5%, although 2% damping has been also considered as an option [NIST, 2018]. In the resonance region, the component damping has a large influence on the peak component acceleration. Hysteretic damping, which is related to component ductility, has a similar effect. Both effects are captured in the proposed equation framework. The PCA/PFA ratios are provided in a table for two different vertical locations of the component (on ground floor and above it), for two different possibilities of being in resonance with building (more likely and less likely), and four different component ductilities (ranging from 1 to 2). When the ratio of the component period to the building period is relatively small or relatively large, resonance is unlikely, and the PCA/PFA ratio is set to 1.0, regardless of ductility. When the ratio is closer to unity, resonance is likely, and the PCA/PFA ratio is amplified to account for it. It is suggested to assume resonance in a quite broad region, where the ratio of the component to the building period is between 0.5 and 1.5. The PCA/PFA decreases with increasing ductility from 2.5 to 1.4 if the component is located at the ground floor or below, and from 4.0 to 1.4 for locations above the ground floor. The highest values correspond to elastic behaviour of components. They are used for reference only. It is assumed that typical nonstructural components used in practice have at least a ductility of 1.25. Thus, the maximum values of the PCA/PFA ratio in practical applications amount to 2.0 on the ground floor or below it, and to 2.8 above it. The proposed PCA/PFA values are based on archetype studies and account for some level of reduction from the theoretical peak value. They represent a highly simplified outcome of research performed in ATC-120.

The PCA/PFA ratio is divided by the factor $R_{pocomp} = 1.3$, which represents the inherent component reserve strength margin that occurs as a part of the design process.

Lower and upper bounds for design force ($I_p = 1$) are defined as $0.3\ S_{DS} \leq F_p/W_p \leq 2.0\ S_{DS}$, where S_{DS} is the design spectral acceleration at short periods.

5. NONSTRUCTURAL SEISMIC DESIGN FORCE IN ASCE 7-22

The design Equation (10) proposed in the ATC-120 project was, with some changes and with a different notation, adopted in NEHRP provisions and ASCE 7-22

$$F_p = 0.4 S_{DS} I_p W_p \left[\frac{H_f}{R_\mu}\right]\left[\frac{C_{AR}}{R_{po}}\right] \tag{13}$$

Peak ground acceleration PGA is replaced by $0.4S_{DS}$. A lower limit of 1.3 is placed on the value of R_μ ($R_{\mu bldg}$ in Equation (10)). C_{AR} and R_{po} values are provided in two tables for a large number of specific architectural, mechanical and electrical components, depending on the likelihood of being in resonance, on vertical location, and on the component ductility. They are “based on the collective judgment of the responsible committee” [FEMA, 2020]. For C_{AR}, the values proposed in ATC-120 are preserved, whereas R_{po} values are increased, in most cases to 1.5. The maximum value of the design force is decreased ($F_p/W_p \leq 1.6S_{DS}$).

6. COMPARISON OF FLOOR SPECTRA IN EC8 AND ASCE 7-22

Floor spectra in the new generation in both EC8 and ASCE 7 take into account, with some exceptions, the same influences/parameters, identified as important in previous research. The intensity of ground motion (PGA or S_{DS}), the fundamental period of the building, the vertical location of the component, the reduction factor due to inelastic building response (q_D' in EC8 and R_μ in ASCE 7), and the component (over)strength factor ($q_{ap,S}$ in EC8 and R_{po} in ASCE 7) are explicitly included in both documents. The component characteristics, i.e., the period, the damping, and the reduction factor due to inelastic response are explicitly included in EC8. In ASCE 7 all three parameters influence C_{AR}. In addition, the period influences also H_f. Note, however, that the recommended value of component damping is 2% in EC8 and is fixed to 5% in ASCE 7. The difference in the assumed damping values is the major source of quantitative differences between the two codes. Ground motion response spectrum is explicitly included in the EC8 equations, whereas in ASCE 7 it has some indirect influence on H_f. The damping of the building is explicitly included only in EC8. However, as a rule, 5 % damping is used. Higher mode effects, which are taken into account in EC8, are ignored in ASCE 7. It should be noted that these effects on component accelerations may be substantial, especially in lower storeys.

The way how the important effects are taken into account in the determination of seismic demand on nonstructural components is basically different in both documents. Floor spectra in EC8 are, to a great extent, based on the theory of the dynamics of structures, partly combined with empirical values and well established approaches for considering nonlinear effects. On the other hand, the ASCE 7 approach is based mainly on empirical results, experience and judgement. The effects of important parameters, identified in numerical and experimental investigations, are considered through a simple user-friendly equation, combined with tabulated coefficients. Neither the dynamic characteristics of the building (with the exception of the building period), nor those of the components are explicitly involved.

Seismic design forces on nonstructural components according to EC8 are generally larger than those according to ASCE 7, mainly due to the difference in the assumed component damping (2% versus 5%), which results in a factor of about 1.6 in the resonance region (see the third line of Equation (4)).

In order to demonstrate the quantitative differences, the EC8 and ASCE 7 spectra representing normalized seismic force at the roof and the first floor of the three-storey reinforced concrete frame, already considered in Section 3, are compared in Figures 2 and 3, respectively. Inelastic behaviour of both the building and the nonstructural component is taken into account.

In the case of EC8, q_D = 2. According to Equation (8), q_D' = 1.6. Γ and ϕ values are provided in [Vukobratović and Fajfar, 2016]. A nonstructural component (NSC) with energy dissipation ($q_{ap,D}'$ according to Equation (7) with $q_{ap,D}$ = 2) and overstregth factor $q_{ap,S}$ = 1.3 is considered. Two component damping values were used, 2% representing the recommended value in EC8, and 5%, i.e., the component damping value from ASCE 7.

According to the ASCE 7 approach, only two values in the whole spectrum can be calculated, one for the resonance region, and one for the rest of the period region. For comparison with EC8 spectra, we assumed the resonance region between $0.5T_1$ and $1.5T_1$, where T_1 is the fundamental period of the building, as proposed in ATC-120. For T_1 = 0.3 s, H_f = PFA/PGA (Equation (11)) amounts to 3.5 at the roof and 1.83 at the first floor. For a "special reinforced concrete moment frame" with R = 8 and Ω_0 = 3, Equation (12) leads to R_μ = 1.7. C_{AR} for a specific component is obtained from Tables 13.5-1 and 13.6-1 in ASCE 7-22. In the case of a high ductility component (with ductility equal to 2.0), C_{AR} = 2.2 for a component "likely in resonance", C_{AR} = 1.0 for other components, and R_{po} = 1.5. Upper and lower bounds of accelerations are 4.0 PGA and 0.75 PGA, respectively.

The floor spectra in Figure 2 show that design forces for a ductile component at the roof in EC8 have larger peaks than in ASCE 7, also if 5% component damping is used in EC8. At the first floor, shown in Figure 3, the design seismic forces are mostly comparable. However, as shown also in Figure 1, EC8 floor spectra predict a substantial peak in the resonance region of the second mode, both at first floor and at the roof, whereas the ASCE approach completely ignores the higher mode effects. At the first floor, the EC8 spectra are controlled by the lower bound spectra in a broad period range. The lower bound of the floor spectrum is represented by the elastic ground motion spectrum considering the component damping, divided by q_{ap}' (Equation (6)). In the case of ASCE 7, the lower bound practically coincides with the calculated spectrum at the first floor for components not likely in resonance.

The results presented in Figures 2 and 3 correspond to a component with the highest ductility. In the case of a component with the lowest ductility (μ =1.0 in EC8, resulting in $q_{ap,D}'$ = $q_{ap,D}$ = 1, and μ = 1.25 in ASCE 7), the EC8 floor spectrum increases by a factor of 2.0 in the period range over 0.24 s (based on Equation (7)), whereas the ASCE floor spectrum increases only in the resonance region for a factor of 2.8/2.2 = 1.27. Consequently, a substantial increase of EC8 floor spectra in comparison to ASCE spectra takes place.

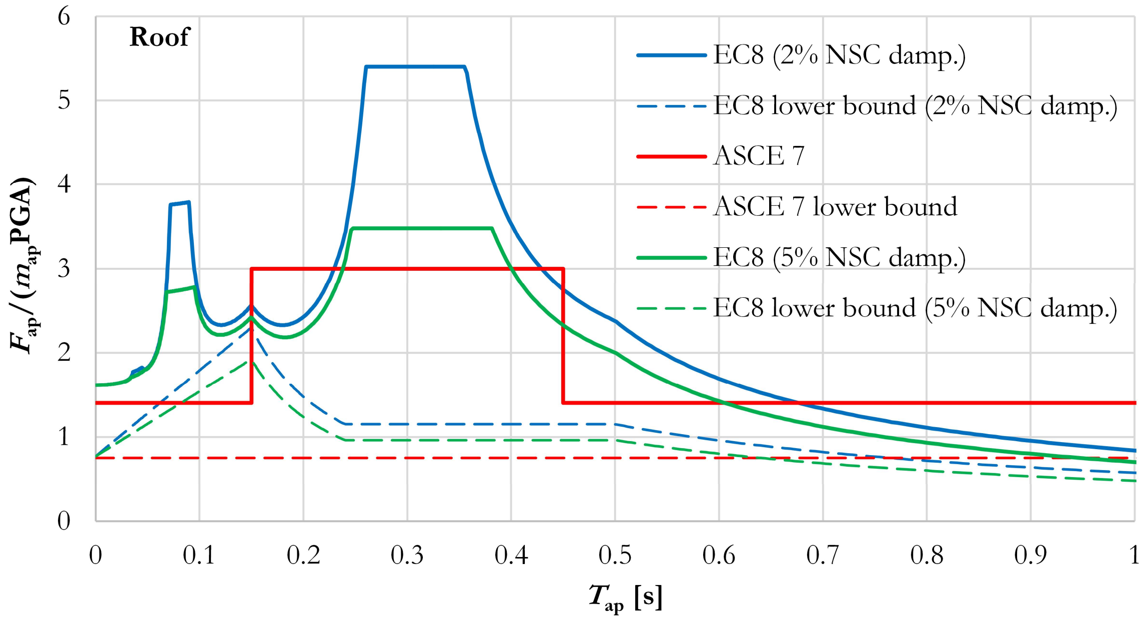

Figure 2. Comparison of normalized design force spectra at the roof of the three-storey frame according to the draft new EC8 and ASCE 7-22

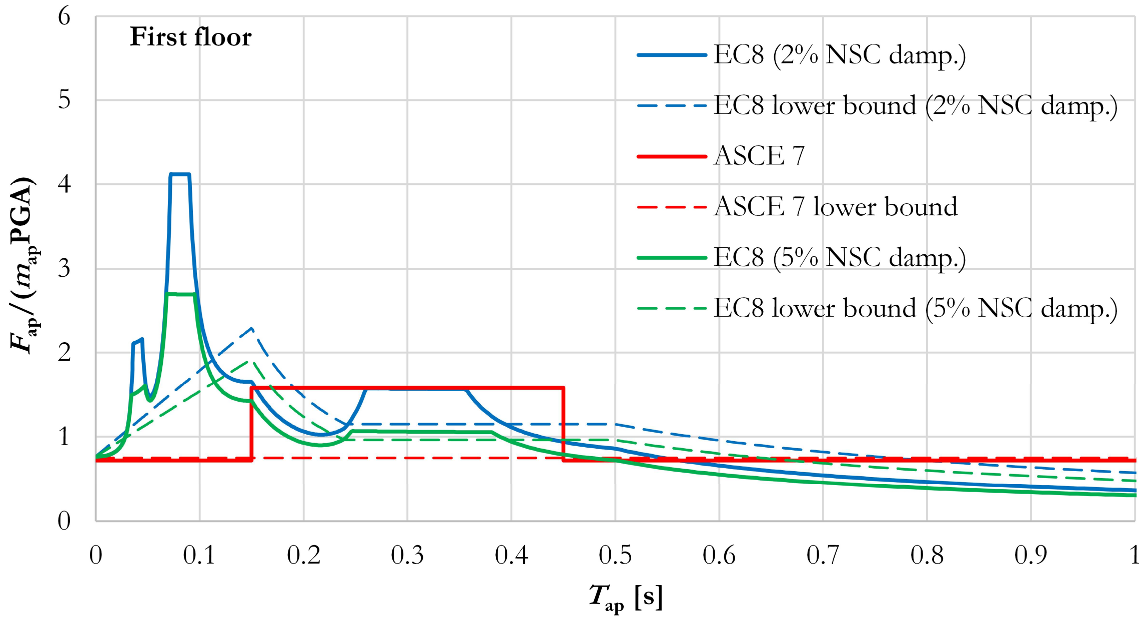

Figure 3. Comparison of normalized design force spectra at the first floor of the three-storey frame according to the draft new EC8 and ASCE 7-22

7. CONCLUSIONS

New seismic code provisions for nonstructural elements in Europe and USA have experienced substantial improvements, based on recent research results. The floor spectra in both new EC8 and ASCE 7-22 take into account the same influencing factors, which proved to have important effects on the shape and magnitude of the floor spectra, with the exception of higher mode effects which are included only in EC8.

However, a conceptual difference between the floor spectra in both codes exists. ASCE 7-22 relies mostly on empirical observations and "collective judgement of the responsible committee" (commentary in [FEMA, 2022]), and results in a very simple user-friendly equation, accompanied with tabulated values of some equation coefficients for a large number of nonstructural components. EC8 is mainly based on the dynamics of structures. It provides more "accurate" floor spectra, explicitly taking into account the ground motion spectra and the dynamic characteristics of buildings and components. The advantage of such an approach is its general applicability, provided that the main characteristics of the nonstructural components (period, damping, ductility) are known with a sufficient accuracy. For the time being, this is not (yet) the case. However, considering the exponentially growing research on nonstructural components, the situation may improve in the future, hopefully during the expected long life-span of the new generation of Eurocodes.

ACKNOWLEDGEMENT

The authors greatly appreciate kind cooperation of Pierre Labbe, the leader of the EC8 Project team PT1 and a member of the Management group (CEN/TC 250/SC 8/MG), who has always been open for discussion and has promptly provided the information needed for the preparation of this paper.

REFERENCES

ASCE [2021] Minimum Design Loads and Associated Criteria for Buildings and Other Structures, ASCE/SEI 7-22, Structural Engineering Institute of American Society of Civil Engineers, Reston, VA, USA.

Biggs, J.M., [1971] "Seismic response spectra for equipment design in nuclear power plants", Proceedings of SMIRT-1, Berlin, Paper K4/7.

CEN [2004] EN 1998-1 Eurocode 8: Design of structures for earthquake resistance. Part 1: General rules, seismic actions and rules for buildings. CEN, Brussels.

CEN [2022] prEN 1998–1–2 Eurocode 8: Design of structures for earthquake resistance. Part 1-2: Rules for New Buildings, Working Draft, CEN, Brussels.

Fajfar, P. [2000] "A nonlinear analysis method for performance based seismic design", Earthquake Spectra, Vol. 16, No. 3, pp. 573–592. https://doi.org/10.1193/1.1586128

Fajfar, P. [2021] The story of the N2 method, International association of earthquake engineering, Tokyo, https://www.iaee.or.jp/pdf/ReadMasters_CSI_IAEE_PETER_FAJFAR_2021.pdf

FEMA [2020] NEHRP Recommended Seismic Provisions for New Buildings and Other Structures, Volume 1: Part 1 Provisions, Part 2 Commentary, FEMA P-2082-1, Federal Emergency Management Agency, Washington, D.C.

Filiatrault, A., Sullivan, T. [2014] "Performance-based seismic design of nonstructural building components: the next frontier of earthquake engineering", Earthquake Engineering and Engineering Vibration, Vol. 13(S1), pp. 17–46. https://doi.org/10.1007/s11803-014-0238-9

Lizundia, B. [2019] "Proposed nonstructural seismic design force equations," *Proceedings of the Structural Engineers Association of California Convention (SEAOC 2019)*, Squaw Creek, CA, USA.

NIST [2017] Seismic Analysis, Design, and Installation of Nonstructural Components and Systems – Background and Recommendations for Future Work, NIST GCR 17-917-44, National Institute of Standards and Technology, Gaithersburg, MD.

NIST [2018] Recommendations for improved seismic performance of nonstructural components, NIST GCR 18-917-43, National Institute of Standards and Technology, Gaithersburg, MD.

Sullivan, T.J., Calvi, P.M., Nascimbene, R. [2013] "Towards improved floor spectra estimates for seismic design", Earthquakes and Structures, Vol. 4, No. 1, pp. 109–132. https://doi.org/10.12989/eas.2013.4.1.109

Villaverde, R. [1997] "Seismic design of secondary structures: state of the art", ASCE Journal of Structural Engineering, Vol. 123, No. 8, pp. 1011–1019. https://doi.org/10.1061/(ASCE)0733-9445(1997)123:8(1011)

Vukobratović, V. [2015] The influence of nonlinear seismic response of structures on the floor acceleration spectra. Doctoral dissertation, University of Ljubljana, Slovenia. http://drugg.fgg.uni-lj.si/5153/

Vukobratović, V., Fajfar, P. [2015] A method for the direct determination of approximate floor response spectra for SDOF inelastic structures. Bulletin of Earthquake Engineering, Vol. 13, No. 5, pp. 1405–1424. https://doi.org/10.1007/s10518-014-9667-0

Vukobratović, V., Fajfar, P. [2016] A method for the direct estimation of floor acceleration spectra for elastic and inelastic MDOF structures. Earthquake Engineering & Structural Dynamics, Vol. 45, No. 15, pp. 2495–2511. https://doi.org/10.1002/eqe.2779

Vukobratović, V., Fajfar, P. [2017] Code-oriented floor acceleration spectra for building structures. Bulletin of Earthquake Engineering, Vol. 15, No. 7, pp. 3013–3026. https://doi.org/10.1007/s10518-016-0076-4

Wang, T., Shang, Q., Li, J, [2021] "Seismic force demands on acceleration-sensitive nonstructural components: a state-of-the-art review", Earthquake Engineering and Engineering Vibration, Vol. 20, No. 1, pp. 39–62. https://doi.org/10.1007/s11803-021-2004-0

Yasui, Y., Yoshihara, J., Takeda, T., Miyamoto, A. [1993] "Direct generation method for floor response spectra", Kussmaul K (ed.), Transactions of the 12th International Conference on Structural Mechanics in Reactor Technology (SMiRT 12), Elsevier Science Publishers B.V.: Stuttgart, Germany: Paper K13/4, pp. 367–372.

Development of the New Nonstructural Seismic Design Provisions in ASCE/SEI 7-22 and Enhanced Seismic Resilience for Nonstructural Components

Bret Lizundia[1]

[1] Rutherford+Chekene, San Francisco
375 Beale Street, Suite 310
San Francisco, CA 94105, USA
e-mail: blizundia@ruthchek.com

Abstract. This paper (1) summarizes the applied research that underlies the development of the new nonstructural seismic design provisions in ASCE/SEI 7-22, (2) provides example comparisons of the differences between the new provisions and those in ASCE/SEI 7-16, and (3) highlights practical strategies for enhanced seismic resilience of nonstructural components.

Keywords: ASCE/SEI 7-22, Nonstructural Design Force Equations, Enhanced Seismic Resilience.

1. INTRODUCTION

In ASCE/SEI 7-22, significant revisions have been made to the nonstructural seismic design force equations. They are based on the proposed equations and underlying research in the Applied Technology Council ATC-120 project that resulted in NIST GCR 18-917-43 *Recommendations for Improved Seismic Performance of Nonstructural Components* (NIST, 2018). Lizundia (2019) summarizes the initial development in NIST (2018) and the revisions in the 2020 *NEHRP Recommended Seismic Provisions* (FEMA, 2020) The Section C13.3.1 commentary to ASCE/SEI 7-22 also provides a comprehensive summary of the issues and resulting ASCE/SEI 7-22 provisions. There is additional detailed discussion and a set of nonstructural design examples in FEMA P-2191-V1, *2020 NEHRP Recommended Seismic Provisions: Design Examples, Training Materials, and Dseign Flow Charts, Volume I: Design Examples* (FEMA, 2021). Much of this paper is taken verbatim or paraphrased from these sources.

The ATC-120 effort took a broad, but detailed, look at nonstructural design and developed many recommendations. One of the key goals of the ATC-120 effort was to develop nonstructural seismic design force equations that have a more rigorous scientific basis and capture the key parameters that can affect nonstructural component response and yet remain appropriate for use in design by practicing engineers. The ATC-120 project team reviewed the available literature, identified key parameters of interest, assessed the influence of these parameters individually on component response, focused on parameters shown to strongly affect response, and then tested a set of equations combining all the selected parameters of interest using an extensive set of nonlinear analyses of archetype buildings and components as well as analysis of strong motion records from instrumented buildings. Chapter 4 and Appendices B and C of NIST (2018) summarize the literature review, analysis approach and findings, and resulting equations.

This paper first reviews the new nonstructural seismic design force equation in ASCE/SEI 7-22, highlighting each of the variables of the equation and summarizing the associated applied research. Comparisons between ASCE/SEI 7-16 and ASCE/SEI 7-22 are provided both for the equation itself and for a specific example. Then there is a broader discussion of practical strategies for enhanced seismic resilience of nonstructural components that go beyond design forces, based on experience from different projects, seismic oversight committees, and seismic policy efforts.

2. NEW NONSTRUCTURAL DESIGN EQUATION

2.1 ASCE/SEI 7-22 NONSTRUCTURAL SEISMIC DESIGN FORCE EQUATION

The following seismic force equations are prescribed for nonstructural components in ASCE/SEI 7-22:

$$F_p = 0.4 S_{DS} I_p W_p \left[\frac{H_f}{R_\mu}\right]\left[\frac{C_{AR}}{R_{po}}\right] \qquad \text{(ASCE/SEI 7-22 Eq. 13.3-1)}$$

$$F_{p,max} = 1.6 S_{DS} I_p W_p \qquad \text{(ASCE/SEI 7-22 Eq. 13.3-2)}$$

$$F_{p,min} = 0.3 S_{DS} I_p W_p \qquad \text{(ASCE/SEI 7-22 Eq. 13.3-3)}$$

where:

F_p = horizontal equivalent static seismic design force centered at the component's center of gravity and distributed relative to the component's mass distribution

S_{DS} = five percent damped spectral response acceleration parameter at short period as defined in ASCE/SEI 7-22 Section 11.4.4

I_p = Component Importance Factor (either 1.0 or 1.5) as indicated in ASCE/SEI 7-22 Section 13.1.3

W_p = component operating weight

H_f = factor for force amplification as a function of height in the structure as determined by ASCE/SEI 7-22 Section 13.3.1.1

R_μ = structure ductility reduction factor as determined by ASCE/SEI 7-22 Section 13.3.1.2

C_{AR} = component resonance ductility factor that converts peak floor or ground acceleration into the peak component acceleration as determined by ASCE/SEI 7-22 Section 13.3.1.3

R_{po} = component strength factor as determined by ASCE/SEI 7-22 Section 13.3.1.4

Equation 13.3-1 is significantly revised from ASCE/SEI 7-16; Equations 13.3-2 and 13.3-3 are identical.

2.2 Comparison with ASCE/SEI 7-16

Table 1 summarizes the parameters that were studied in the ATC-120 effort and how they are—or are not—incorporated in the nonstructural seismic design force equations for both ASCE/SEI 7-16 and ASCE/SEI 7-22.

Table 1. Comparison of Parameters of Influence on Nonstructural Response

Parameter	ASCE/SEI 7-16	ASCE/SEI 7-22
Shaking intensity	Included	Same as ASCE/SEI 7-16, incorporated in S_{DS}
Component Importance Factor	Included	Same as ASCE/SEI 7-16, incorporated in I_p
Seismic force-resisting system	Not included	Included through C_{AR}
Building model period	Not included	Included through H_f
Building ductility	Not included	Included through R_μ
Inherent building damping	Not included	Not included – not a significant influence
Building configuration	Not included	Not included – not practical for general equation
Diaphragm rigidity	Not included	Not included – not practical for general equation
Vertical location of component	Included	Revised from ASCE/SEI 7-16, included in H_f
Component period	Indirectly included	Indirectly included in C_{AR}
Component and/or anchorage Ductility	Indirectly included	Indirectly included in C_{AR}
Inherent component damping	Indirectly included	Indirectly included in C_{AR}
Component overstrength	Not explicitly included	Included explicitly through R_{po}

The additional parameters included in the ASCE/SEI 7-22 equations were found to have a significant influence and are described in detail below. Inherent building damping was found to have a relatively small effect on component response. Building configuration and floor diaphragm rigidity can have a significant effect on component response, but, given the complexity of the issues involved and desire to keep code equations practical, building configuration and diaphragm rigidity were not included in final set of equations.

2.3 Key Features and Variables in ASCE/SEI 7-22 Equation

Using the above selected parameters, the proposed equations in NIST (2018) and in ASCE/SEI 7-22 Section 13.3.1 include a set of key features and variables. They are summarized in this section.

2.3.1 Seismic Coefficient at Grade, $0.4S_{DS}$

The short-period design spectral acceleration, S_{DS}, considers the site seismicity and local soil conditions. S_{DS} is determined in accordance with ASCE/SEI 7-22 Section 11.4.4 and is the used to design the primary structure. ASCE/SEI 7-22 approximates the effective peak ground acceleration as $0.4S_{DS}$, which is why 0.4 appears in ASCE/SEI 7-22 Equation 13.3-1.

2.3.2 Component Importance Factor, I_p

The Component Importance Factor, I_p, is determined per ASCE/SEI 7-22 Section 13.1.3. It has a value of either 1.0 or 1.5, and it is applied to the force and displacement demands on the component. I_p of 1.5 is applied to components with greater life safety or hazard exposure importance. The I_p of 1.5 is intended to improve the functionality of the component or structure by requiring design for a lesser amount of inelastic behavior and providing larger capacity to accommodate seismically induced displacements. It is assumed that reducing the amount of inelastic behavior will result in a component that will have a higher likelihood of functioning after a major earthquake.

2.3.3 Amplification at Height, H_f

Based on a detailed review of instrumented building strong motion records, a more refined equation was developed to relate the ratio of Peak Floor Acceleration (PFA) to Peak Ground Acceleration (PGA) at different heights in the building. The equation incorporates building period. This is accounted for in the variable H_f of Equation 13.3-1.

The H_f term scales the seismic coefficient at grade to the peak floor acceleration, resulting in values varying from 1.0 at grade to up to 3.5 at the roof level. This factor approximates the dynamic amplification of ground acceleration by the supporting structure. For nonstructural components supported at or below the grade plane, $H_f = 1.0$. For components supported above the grade plane by a building or nonbuilding structure, H_f is permitted to be determined by ASCE/SEI 7-22 Equation 13.3-4 or 13.3-5. Where the approximate fundamental period of the supporting building or nonbuilding structure is unknown, H_f is permitted to be determined by ASCE/SEI 7-22 Equation 13.3-5.

$$H_f = 1 + a_1\left(\frac{z}{h}\right) + a_2\left(\frac{z}{h}\right)^{10} \quad \text{(ASCE/SEI 7-22 Eq. 13.3-4)}$$

$$H_f = 1 + 2.5\left(\frac{z}{h}\right) \quad \text{(ASCE/SEI 7-22 Eq. 13.3-5)}$$

where:

$$a_1 = \frac{1}{T_a} \leq 2.5 \quad \text{(ASCE/SEI 7-22 Sec. 13.3.1.1)}$$

$$a_2 = [1 - (0.4/T_a)^2] \geq 0 \quad \text{(ASCE/SEI 7-22 Sec. 13.3.1.1)}$$

where:

- z = height above the base of the structure to the point of attachment of the component. For items at or below the base, z shall be taken as 0. The value of $\frac{z}{h}$ need not exceed 1.0;
- h = average roof height of structure with respect to the base; and
- T_a = the lowest approximate fundamental period of the supporting building or nonbuilding structure in either orthogonal direction. For structures with combinations of seismic force-resisting systems, the seismic force-resisting system that produces the lowest value of T_a shall be used.

In ASCE/SEI 7-16, the variation with height was linear, using the relationship $[1 + 2(z/h)]$. The dynamic characteristics of the building, as reflected by building fundamental period, were not incorporated. Shorter building periods have higher and more linear amplification. Figure 1 shows the relationship between (z/h) and T_a on the amplification factor as a function of height in the building, H_f. Longer building periods have lower amplification that is also more nonlinear. The H_f equation is based on both the recorded variation in PFA normalized by PGA in instrumented buildings and the mean (average) variation computed in simplified continuous models consisting of a flexural beam laterally coupled with a shear beam as adapted from Taghavi and Miranda (2006) and from Alonso-Rodríguez and Miranda (2016). Although the maximum value at the roof has increased from $[1 + 2(z/h)] = [1+2(h/h)] = 3$ in ASCE/SEI 7-16 to 3.5 in ASCE/SEI 7-22 for short period buildings, the values are lower in ASCE/SEI 7-22 in many other cases and other locations below the roof.

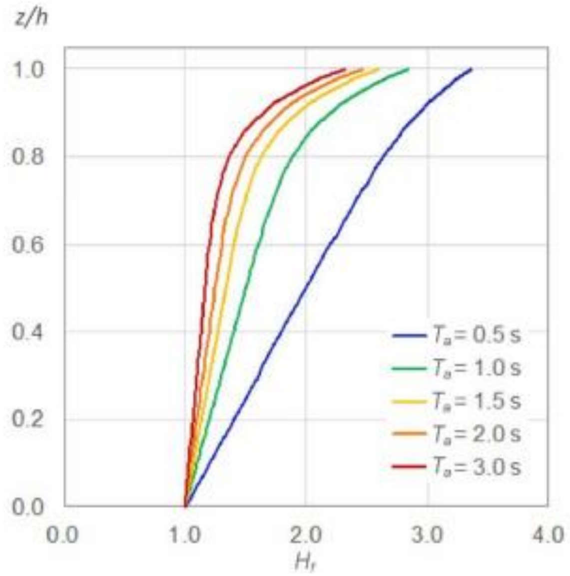

Figure 1. Relationship H_f (PFA/PGA) s. height (z/h) in ASCE/SEI 7-22

2.3.4 Structure Ductility Reduction Factor, R_μ

Typically, the ratio of Peak Component Acceleration (PCA) to PGA is larger when the building is elastic and lower when there is nonlinearity of the building. This is captured by the variable R_μ. The equation for determining R_μ is based on a series of archetype case studies using different seismic force-resisting systems, numbers of stories, and overstrength assumptions. Determination of the structure ductility reduction factor, R_μ, relies on the R and Ω_0 values in ASCE/SEI 7-22 Table 12.2-1, Table 15.4-1, and Table 15.4-2, and the Seismic Importance Factor, I_e, as prescribed in ASCE/SEI Section 11.5.1. R_μ need not be taken as less than 1.0. If a seismic force-resisting system is not listed in Table 12.2-1 or the seismic force-resisting system does not conform to the associated requirements for the system, then $R_\mu = 1.3$.

$$R_\mu = (1.1R / I_e\, \Omega_0)^{1/2} \qquad \text{(ASCE/SEI 7-22 Eq. 13.3-6)}$$

2.3.5 Component Resonance Ductility Factor, C_{AR}

The relationship between PCA and PFA, defined as C_{AR} in Equation 13.3-1, is affected by several parameters including the ratio of component period, T_{comp}, to building period, T_{bldg} (or T_a), and component ductility. When component and building periods are close, component response is increased due to resonance; when component ductility is larger, component response decreases.

Component Period and Building Period

Figure 2 illustrates the PCA/PFA amplification factor with the spectral ordinates of the average of eight different recorded motions based on T_{comp} and the same motions with the x-axis normalized to T_{comp}/T_{bldg}. These records come from eight different buildings and five different earthquakes and were selected from a suite of 86 records with 5% PCA values over 0.9g. The significant amplification of demand when the component period matches one of the building periods, typically referred to as resonance, was an important subject of investigation since the peak component accelerations can greatly exceed those typically used for design. ASCE/SEI 7-16 Equation 13.3-1 did not explicitly include a factor for T_{comp}/T_{bldg}. In the ATC-120 project, it was decided to include the effect of resonance and the presentation approach of normalizing response against T_{comp}/T_{bldg} as the basis of the new nonstructural design equation. For most nonstructural components, the component fundamental period, T_{comp}, can be obtained accurately only by expensive shake-table or pullback tests. As a result, the determination of a component's fundamental period by dynamic analysis, considering T_{comp}/T_{bldg} ratios, is not always practicable. Engineering judgment is needed.

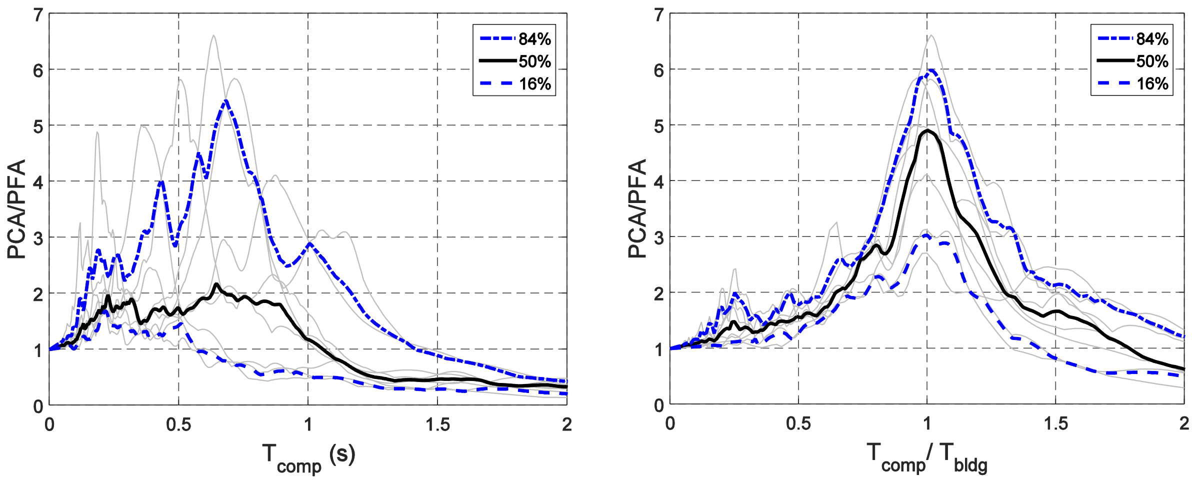

Figure 2. Relationship between PCA/PFA comparing spectra without (left) and with (right) normalization by T_{bldg}. An elastic component is assumed with inherent component damping = 5%. The dataset includes eight recordings with PCA > 0.9g. From Kazantzi et al. (2018) and FEMA (2021).

Component and/or Anchorage Ductility

ASCE/SEI 7-16 Equation 13.3-1 included the R_p factor which indirectly accounted for reductions in response that component ductility can provide, but there was not an explicit link in the code between the R_p factor and component ductility, μ_{comp}.

There can be ductility in the component, the attachment of the component to the anchor, the anchor itself, or a combination of any of the items. Anchorage ductility is often difficult or impossible to achieve given practical considerations of available substrate depth for anchor. ATC-120 project studies lumped these three potential sources of component and anchorage ductility together into one simple model where the single-degree-of-freedom (SDOF) oscillator representing a component yields and then continues to deform, providing a measure of component ductility. Component ductility was found to have a significant effect.

Figure 3 overlays the mean response for each component ductility level for β_{comp} = 5%. For β_{comp} = 5% at T_{comp}/T_{bldg} = 1 resonance, PCA/PFA drops from about 4.6 for an elastic component, to about 2.8 for a component with a ductility, μ_{comp}, of 1.25, to about 2.0 for μ_{comp} = 1.5, then to about 1.4 for μ_{comp} = 2. Note that for these "constant component ductility" PCA/PFA spectra, the strength of the component is different for each level of μ_{comp} at each value of T_{comp}.

Given the significant effect of component and/or anchorage ductility on component response, it was decided in the ATC-120 project to explicitly incorporate this effect into the new nonstructural component design equation.

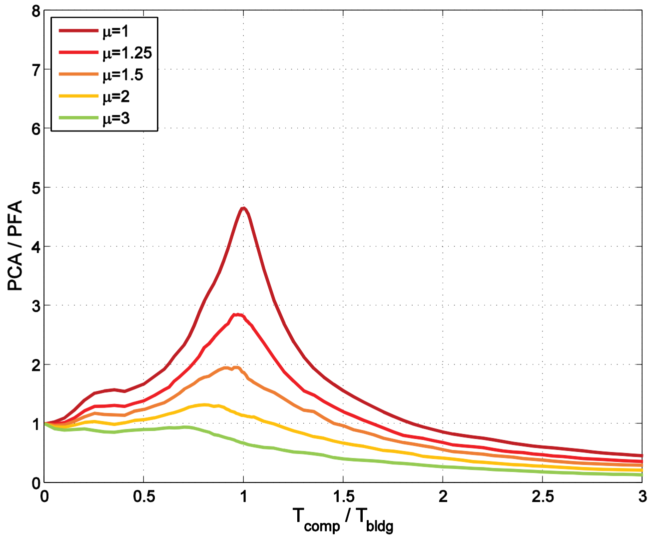

Figure 3. Comparison of mean response of PCA/PFA vs. T_{comp}/T_{bldg} for different levels of component ductility for β_{comp} = 5%. The dataset includes 86 recordings with PCA > 0.9g. From NIST (2018), Lizundia (2019), and FEMA (2021).

C_{AR} Categories

The effects of resonance and component ductility are captured by two concepts in the equation framework. The first concept is whether component response is likely or unlikely to be in resonance with the building response. When the ratio of component period to building period is relatively small or relatively large, resonance is unlikely, and C_{AR} is set to 1.0. When the ratio is closer to unity, resonance is likely, and C_{AR} is amplified to account for resonance. If the component period, T_{comp}, is less than 0.06 seconds, then resonance is unlikely regardless of building period, since the building period will typically be well above that level. In the 2016 and earlier editions of ASCE/SEI 7, components with T_{comp} (or T_p) ≤ 0.06 seconds were termed “rigid” and did not receive any amplification of PFA (while those with T_{comp} > 0.06 were termed “flexible” and received an increase of 2.5 times PFA). When the ratio of component period to building period is relatively low or relatively large, then resonance is also unlikely. A criterion of T_{comp} / T_{bldg} < 0.5 or T_{comp} / T_{bdlg} > 1.5 can be used, as suggested by NIST (2018) as well as extrapolation of results from Hadjian and Ellison (1986). Distribution systems may experience resonance, but its effect is judged to be minimized due to reduced mass participation caused by multiple points of support.

The second concept is to create low, moderate, or high component ductility categories for situations with likely resonance. C_{AR} values for low ductility are higher than those for high ductility. The selected C_{AR} values are based on archetype studies and account for some level of reduction from the theoretical peak value to address the probability of overlap between component and building periods. The amplification of PCA/PFA as the ratio of component to building period approaches unity comes from narrow band filtering of response by the dynamic properties of the building. Components that are ground supported can see dynamic amplification due to component flexibility, based on structural dynamics, but this amplification is typically less than what occurs in the building. Given that there are both theoretical and numerical differences between the ground and superstructure cases, it was decided to distinguish the two. See Table 2 for the theoretical basis of the C_{AR} values. As discussed in NIST (2018), the elastic category is used for reference only. It is assumed that typical nonstructural components and their attachments to the structure systems used in practice have at least the low level of component ductility. Thus, nonstructural components have been assigned to one of three categories of component ductility—low, moderate, and high—in ASCE/SEI 7-22 Tables 13.5-1 and 13.6-1. Engineering judgment has been used in the development of the table values.

Table 2. C_{AR} **(PCA/PFA) Categories**

		Component Ductility		
Location of Component	**Possibility of Building in Resonance with Building**	**Category**	**Assumed Ductility**	C_{AR} **(PCA/PFA)**[1]
Ground	More Likely	Elastic	$\mu_{comp} = 1$	2.5
		Low	$\mu_{comp} = 1.25$	2.0
		Moderate	$\mu_{comp} = 1.5$	1.8
		High	$\mu_{comp} \geq 2$	1.4
	Less Likely	Any	--	1.0
Roof or Elevated Floor	More Likely	Elastic	$\mu_{comp} = 1$	2.5
		Low	$\mu_{comp} = 1.25$	2.0
		Moderate	$\mu_{comp} = 1.5$	1.8
		High	$\mu_{comp} \geq 2$	1.4
	Less Likely	Any	--	1.0

[1] Inherent component damping of 5% is assumed.

2.3.6 Component Strength Factor, R_{po}

For *building* design, there is an inherent reserve strength margin between the design value and the eventual peak strength. This comes in part from capacity reduction factors, ϕ, but also as a result of other design factors, design simplifications, redundancy, and design decisions. This inherent reserve strength margin is a substantial part of the response modification coefficient, *R*, that is used to reduce elastic response levels down to design levels. See the discussion on R_o in the *SEAOC Recommended Lateral Force Requirements and Commentary* (SEAOC, 1999).

It is assumed that *components* also have some inherent reserve strength margin that occurs as part of the design process. This inherent reserve strength margin has traditionally been considered by code writers in the development of nonstructural design equations. While a component's inherent reserve strength margin factor has not been explicitly identified, effects have been considered as part of the R_p factor in previous versions of ASCE/SEI 7.

It was decided to explicitly incorporate a value for the effect of component reserve strength in the nonstructural component design equation. The ATC-120 project team decided to assume a placeholder value of 1.3 for the inherent component reserve strength margin in NIST (2018). This was termed R_{pocomp}. In the development of the code change that eventually was approved for ASCE/SEI 7-22, the term was changed to the component strength factor, R_{po}. Values of 1.5 and 2.0 were selected. Since R_{po} is in the denominator of the F_p equation, it serves to reduce the design force needed.

2.4 OTHER NOTABLE CHANGES IN ASCE/SEI 7-22 CHAPTER 13

There are several other notable changes in the nonstructural provisions of ASCE/SEI 7-22, including explicit load combinations and loading directions, explicitly accounting for the influence of the lateral force-resisting system types bracing MEP components, and an updated equation for nonlinear response history analysis.

2.4.1 Load Combinations for Nonstructural Design

The load combinations applicable to the nonstructural components chapter are now explicitly referenced in ASCE/SEI 7-22 Section 13.2.2. This clarifies that the load combinations for dead, live, earthquake, and overstrength used for structural design also apply to nonstructural design.

2.4.2 Loading Directions for Nonstructural Design

The seismic design force, F_p, is to be applied independently in the longitudinal and transverse directions. F_p should be applied in both the positive and negative directions if higher demands will result. Per ASCE/SEI 7-22 Section 13.3.1, the directions of F_p used shall be those that produce the most critical load effects on the component, the component supports, and attachments. Alternatively, it is permitted to use the more severe of the following two load cases:

- Case 1: A combination of 100% of F_p in any one horizontal direction and 30% of F_p in a perpendicular horizontal direction applied simultaneously.
- Case 2: The combination from Case 1 rotated 90 degrees.

2.4.3 Equipment Support Structures and Platforms and Distribution System Supports

Previous editions of ASCE/SEI 7 did not made a distinction in design forces between the component and the supporting structure. They required the nonstructural components and supporting structure to be designed with the same seismic design forces, F_p, regardless of their potential dynamic interaction, and the force was based on the component properties. For example, a platform supporting a pressure vessel was designed for pressure vessel forces regardless of whether the platform structure was made of concrete, steel braced frames, or steel moment frames. Or the trapeze assembly bracing a piping run was designed for the pipe force, regardless of the type of trapeze assembly. In some cases, this could produce comparatively weak component supports, especially for distribution systems which had relatively low design forces for certain types of piping.

In ASCE/SEI 7-22, a significant refinement has been made to distinguish the requirements for design of the component from the supporting structure. This permits a more accurate determination of forces that more realistically reflect the differences in dynamic properties and ductilities between the component and the support structure or platform. Definitions are given in ASCE/SEI 7-12 Section 11.2 for three different types of support. ASCE/SEI 7-22 Commentary Section C13.6.4 provides figures for each type. ASCE/SEI 7-22 Table 13.6-1 has been revamped to provide C_{AR}, R_{po}, and Ω_{op} values for each of the three types and subvariations.

- Integral equipment supports: This is where the supports, such as short legs, are directly connected to both the component and the attachment to the structure. Integral equipment supports are designed for the seismic design force computed for the component itself. Integral equipment supports include legs less than or equal to 24 inches in length, lugs, skirts, and saddles. The 24-inch length limit for legs was determined by judgment and experience to be a reasonable length, above which the leg will no longer likely respond in a manner similar to the component.
- Equipment support structures and platforms: These are assemblies of members or manufactured elements, other than integral equipment supports, including moment frames, braced frames, skids, legs longer than 24 inches, or walls. An equipment support structure supports one piece of equipment; an equipment support platform supports multiple pieces of equipment.
- Distribution system supports: These are members that provides vertical or lateral resistance for distribution systems, including hangers, braces, pipe racks, and trapeze assemblies.

2.4.4 Nonlinear Response History Analysis for Nonstructural Design Forces

The new ASCE/SEI 7-22 Equation 13.3-1 is easily adapted for use with nonlinear response history analysis (NRHA) per ASCE/SEI Section 13.3.1.5. NRHA provides the maximum floor accelerations (PFAs) in the Design Earthquake directly so they replace the $0.4S_{DS}$ [$H_f/R\mu$] terms in ASCE/SEI 7-22 Equation 13.3-1.

2.5 EXAMPLE

An example comparison between ASCE/SEI 7-16 and ASCE/SEI 7-22 is for interior walls and partitions. ASCE/SEI 7-16 Table 13.5-1 has two interior wall and partition categories: plain (unreinforced) masonry and all other partition types. Unreinforced masonry walls and partitions are now prohibited in ASCE/SEI 7-22 in areas with seismic shaking of significance. As such, the focus here is on the remaining wall and partition types, which in ASCE/SEI 7-16 Table 13.5-1 have a_p = 1 and R_p = 2.5. Thus, there is an implied presumption that dynamic amplification of floor acceleration is minimal, and the partitions have moderate ductility. However, per structural dynamic theory, component ductility does not reduce response for components as T_{comp} approaches zero.

There are several issues to consider with partitions.

- Partitions typically span out-of-plane between diaphragms. Thus, their displacements and accelerations are affected by two diaphragms that will have different dynamic response. Out-of-phase behavior between the two diaphragms is likely to reduce partition response.
- The behavior of reinforced concrete masonry unit (CMU) partitions is likely to be different from wood and metal stud partitions with gypboard finishes. CMU partitions are likely to have to have less flexibility and ductility than wood and metal stud partitions, and CMU partitions will weigh more. Out-of-plane cracking of gypboard may mean that wood and metal stud walls and partitions have higher damping which could reduce response.
- For wood and metal stud walls and partitions, height may impact dynamic amplification. As the walls and partitions get taller, the out-of-plane period lengthens, and there is more likelihood that the component could become more in resonance with the building.

Given these issues, four wall and partition categories have been placed in ASCE/SEI 7-22 Table 13.5-1.

- Short, light frame: These are assumed to be wood and metal stud partitions of 9 feet high or less. These walls and partitions are assumed to have relatively short periods and a comparatively low T_{comp}/T_{bldg} ratio, and thus are unlikely to be in resonance with the building.
- Tall, light frame: These are assumed to be wood and metal stud partitions of over 9 feet in height. They are assumed to have longer periods and a T_{comp}/T_{bldg} ratio moving toward a central value, and thus they have the potential to be in resonance with the building. They also are assumed to have desirable damping and a high level of ductility.
- Reinforced masonry: Reinforced masonry partitions are assumed to have short periods and a low T_{comp}/T_{bldg} ratio, and thus they are unlikely to be in resonance with the building.
- All other walls and partitions: These are conservatively assumed to be likely in resonance with low ductility to cover any other type of situation.

Per ASCE/SEI 7-16, for a site with S_{DS} = 1.0g, I_p = 1.0, a partition at midheight of the building (z/h = 0.5), and a_p = 1 and R_p = 2.5, F_p/W_p is 0.32g, which is just above the 0.30g minimum. With the proposed equations, for a six-story steel special moment resisting frame, a short, metal stud partition or a reinforced masonry partition with the assumption of “unlikely to be in resonance,” H_f = 1.54, R_μ =1.71, C_{AR} = 1, R_{po} = 1.5, and F_p/W_p =0.24g, so it is governed by the minimum value of 0.30g. For a tall, metal stud partition, with the assumption of "likely to be in resonance" and "high ductility," H_f= 1.54 and R_μ =1.71 as before, C_{AR} = 1.4 for high ductility, R_{po} = 1.5 and F_p/W_p =0.34g, which governs over the 0.30g minimum.

In order to review the impact of the code change proposals for the ASCE/SEI 7-22 nonstructural seismic design equations, extensive numeric comparisons were made. They were done for 30 architectural, mechanical, and electrical component categories supported by building structures covered by ASCE/SEI 7-16 Chapter 13 building structures and 26 component categories covered by ASCE/SEI 7-16 Chapter 15 nonbuilding structures, leading to a comparison document of over 200 pages of tables that accompanied the code change proposal. In some situations, the new ASCE/SEI 7-22 equations result in lower forces; in others, they result in higher forces.

3. ENHANCED SEISMIC RESILIENCE FOR NONSTRUCTURAL COMPONENTS

3.1 PERFORMANCE OBJECTIVES OF ASCE/SEI 7-22

Specific performance goals for nonstructural components are not explicitly defined in ASCE/SEI 7-22, although the ASCE/SEI 7-22 Commentary Section C13.1.3 provides expectations of the anticipated behavior of noncritical components in three levels of earthquake shaking intensity:

- *Minor earthquake ground motions—minimal damage; not likely to affect functionality;*
- *Moderate earthquake ground motions—some damage that may affect functionality; and*
- *Design Earthquake ground motions—major damage but significant falling hazards are avoided; likely loss of functionality.*

While the nonstructural design provisions focus on reducing the risk to life safety, in some cases, the provisions protect functionality and limit economic losses. For example, noncritical equipment units in mechanical rooms that are unlikely to topple in an earthquake still require anchorage, although they pose minimal risk to life safety. The flexible connections between unbraced piping and noncritical equipment are required but serve mainly to reduce the likelihood of leakage.

3.2 BEYOND SEISMIC FORCES

The most basic—and the most blunt—approach in the building code for achieving enhanced resilience beyond the typical expectations noted in Section 3.1 is to design for higher seismic forces by increasing the Component Importance Factor, I_p, from 1.0 to 1.5. However, there are many factors that contribute to success that are beyond just the seismic forces used on anchorage and bracing. These include both specific techniques (discussed in Section 3.3) and overall strategies (discussed in Section 3.4).

3.3 TECHNIQUES FOR ENHANCED SEISMIC RESILIENCE

Techniques for enhanced seismic resilience of nonstructural components include (1) enhanced design requirements for components like elevators, cladding, and stairs; (2) expanded use of special seismic certification; (3) more rigorous specification development, submittal review, structural observation, and special inspection and testing; and (4) application of capacity design to nonstructural components.

3.3.1 Enhanced Design for Elevators

Loss of elevator function following an earthquake can significantly reduce the usability of a building for extended periods of time. Studies of damage to elevators in earthquakes have identified several different types of damage. One key observation is that guiderail flexibility can lead to car and counterweight disengagement, potential injury, substantial damage, and loss of use of the elevators for extended periods of time. As a result, reducing guiderail deflection is believed to be an important and relatively affordable and effective way of improving performance. Experience has shown that project-specific seismic enhancements are difficult to implement and hard for elevator vendors to price. Thus, use of widely-available existing standards that have been used in past elevator procurement—and that provide for reduced guiderail deflection—are recommended.

ASCE/SEI 7-22 has elevator requirements and references ASME A17.1-19 *Safety Code for Elevators and Escalators* (2019). Enhancements for elevators can be found in the 2019 California Building Code (CBC) for community colleges, K-12 schools, and hospitals. K-12 requirements are similar to hospitals. CBC Section 1617.11.21 provides elevator seismic design requirements for community colleges including limitations for guiderail deflection, weight assumptions, and additional minimum seismic design force requirements. The CBC provides additional requirements for hospital elevators including use of a Seismic Component Importance Factor I_p = 1.5, Section 1617A for weights and minimum loads, Section 1617A.1.28 for retainer plates and guiderail deflections, Section 1705A.13.3.1 requirements for special seismic certification through shake table testing of elevator components, and Section 3009 for connection to the emergency generator and for a go-slow feature.

Enhancement techniques can include specifying one community college elevator or one hospital elevator instead of specifying all typical code elevators. A more unusual idea is in buildings with more than one elevator, where possible, orient the elevator door openings so that at least one elevator has a door that opens at 90 degrees with respect to the others. Earthquake reconnaissance reports indicate there is a strong correlation between the direction of earthquake shaking, damage to rails and rail brackets, and interstory drift locking up door movement. To enhance resiliency, it is thus desirable to orient the door openings so that not all are parallel to one another. This will be difficult in most buildings since the elevators are typically on one side of a lobby or on opposite sides so the doors are rotated at either zero degrees to another or 180 degrees to one another, and thus they all experience the same earthquake shaking direction. Orienting at least one elevator at 90 degrees to the other elevators means that at least one elevator will experience a lower level of shaking in the key direction of interest.

3.3.2 Enhanced Design for Cladding

Enhanced resilience techniques for cladding often focus on drift design and associated mockup testing. Cladding mockups can be tested to resist in-plane and out-of-plane interstory drift, per ASCE/SEI 7-22 Section 13.5.9, using standards such as AAMA 501.4 (AAMA, 2018a) and AAMA 501.6 (AAMA, 2018b). When this is done, the typical standard of practice has been that air and water tightness are intended to be provided at a serviceability level earthquake or a code level eaerthquake, and the goal is that there be no falling hazards at the Design Earthquake (DE) level. Many years ago, the serviceability earthquake was defined using allowable stress design and a value of 0.5% interstory drift. Enhanced resilience can come from increasing the drift used to target air and water tightness from code level to, say, 50% of DE. Or repairability can be targeted at the DE level, not just no falling hazards. Repairability is best proven by repairing the damage, and then rerunning the tests to the air and water tightness drift criterion to confirm the cladding can be recover its function.

3.3.3 Stairs

Egress stairs are already required by ASCE/SEI 7-22 to be designed using I_p = 1.5. However, they are typically designed by the stair subtractor's engineer using the subcontractor's preferred typical details, with limited margins of additional capacity. Enhancement techniques and issues including the following.

- Seismic design includes both inertial loading from the stair weight itself and loading induced on the stair by interstory drift of the building superstructure. Although ASCE/SEI 7-22 does not say this explicitly, these loads should be applied simultaneously.
- Stairs in areas of high seismicity are typically designed with a slip connection parallel to the stringers at the base or top of the stair run, but they have fixed restraints perpendicular to the stringers. These longitudinal slip connections are strongly recommended. However, even with them, three-dimensional analysis models of stairs show that demands on members and connections are highly dependent on geometry, boundary connections, and tread and riser modelling. With some assumptions, induced forces can get quite large. Modeling flexibility of stair connections at landings and to the primary structures can significantly reduce demands. Design models should include realistic assumptions for tread and risers and flexibility at connections.
- There is limited testing of stairs, despite their ubiquity. Tests at Oregon State University of steel stairs (Higgins, 2009) confirm the importance of yielding and fuses at connections. Designs should focus on providing ductile connection details where flexibility can be created, and energy can be absorbed.

3.3.4 Expanded Scope of Seismic Certification

ASCE/SEI 7-22 Section 13.2.3 provides requirements for special seismic certification of designated components, including active mechanical and electrical equipment that must remain operable after the Design Earthquake and components with hazardous substantances and I_p = 1.5. The seismic certification can be done through shake table testing and in some cases through rigorous analysis. For hospitals in California, this is a requirement in 2019 CBC Section 1705.A.13.3.1 which defines a long and specific list of systems, equipment, and components that must have certification. After successful completion of testing, the manufacturer receives an "OSP" certificate defining what was tested, how it was anchored, and the seismic design force limitations of the testing. One technique for enhancing resilience is to expand the scope of special seismic certification. For example, in a laboratory, project specifications could require certification for components important for the research but not triggered by the code life safety or hazardous material requirements.

3.3.5 More Rigorous Specification Development, Submittal Review, Structural Observation, and Special Inspection and Testing

More rigorous quality assurance can enhance resilience by increasing the likelihood that performance intent will be achieved. This begins with writing clear, achievable specifications that can be bid and built. Submittal of calculations stamped by a licensed civil or structural engineer can be required. Thorough review of submittals by the design team helps confirm proper, project-specific detailing and calculations have been provided. Additional field review by design-build subcontractor's engineer and by the submittal reviewer (which would typically be the building structural engineer of record) can provide confirmation the details were properly implemented and can discover and address unanticipated field conditions such as conflicts with other trades. Finally, special inspection and testing can be more rigorous and extensive, such as what is done for California hospitals and K-12 schools. Stair welding, for example, is not always inspected, but it can be required. Or the frequency of pull testing of anchors in concrete can be increased.

3.3.6 Capacity Design

The ATC-120 project explored the viability of requiring ductile or capacity design for nonstructural components to provide more energy dissipation and reliable behavior. While a noble goal, many practical challenges were found. However, concern remained about brittle elements being permitted in the load path from the nonstructural component to the primary structure. The following sentence based on the ATC-120 recommendations was placed in the ASCE/SEI 7-22 Commentary Section C13.3.1.

Anchors in concrete or masonry that cannot develop a ductile yield mechanism are required to use design forces increased by the Ω_{op} factor. Designers should consider amplifying design forces by an overstrength factor for elements in the load path between the component and the anchor that have limited ductility.

3.4 STRATEGIES AND ISSUES

Strategies and associated issues for enhanced nonstructural seismic resilience include the following: (1) target select occupancies for enhancement, (2) target select project-specific components for enhancement, (3) be wary of non-mandatory requirements, (4) establish a Nonstructural Seismic Coordinator for the project, and (5) develop typical institutional details for nonstructural seismic anchorage and bracing.

3.4.1 Target Select Occupancies for Enhanced Seismic Resilience

The *2021 International Building Code* (ICC, 2021) uses Risk Categories to vary the seismic performance objectives for both structural and nonstructural design.

- Building occupancies in Risk Category IV have the highest requirements, are termed essential facilities, and include hospitals that provide emergency surgery or treatment, fire stations, police stations, emergency operations centers, and emergency shelters.
- Occupancies in Risk Category III have the next highest requirements and include buildings with large numbers of occupants and toxic or explosive materials over minimum allowable levels.
- Risk Category II is for standard occupancy structures that are not assigned to one of the other risk categories, such as office buildings.
- Risk Category I is for buildings that represent a low hazard to human life such as agricultural facilities, temporary facilities, and minor storage facilities.

One strategy for enhanced seismic resilience is to shift occupancy types from Risk Category II to Risk Category III or IV. Risk Category IV increases the nonstructural design forces by 50%, using an I_p =1.5 There are proposals (ICC, 2022) under consideration for the *2024 International Building Code* to add occupancies such as the following to Risk Category IV.

- Buildings where loss of function represents a substantial hazard to occupants. These could include occupancies such as a 24-hour medical facility; residential care facility; public water, wastewater, or power utility; detention center with impeded egress; or critical supply chain facility.
- Food processing establishments or commercial kitchens, not primarily associated with dining facilities, with gross floor area exceeding 30,000 square feet, and retail or wholesale stores with gross floor area exceeding 30,000 square feet in which at least half of the usable floor area is used for the sale of food or beverages.

A similar approach is under development at the University of California, Berkeley (UCB) through its Seismic Review Committee (SRC) which would effectively add student housing, buildings with large classrooms, and buildings with high value research or high value collections to Risk Category III. The SRC believes that assigning these occupancies to have requirements similar to those of Risk Category III in the California Building Code plus other targeted nonstructural enhancement measures will reduce displacement of students, limit loss of research and high value collections, reduce loss of faculty, and have capital costs less than the savings from reduced damage. The UCB draft excerpted in Table 3 shows enhanced nonstructural resilience measures.

Table 3. Possible Nonstructural Enhancements for Targeted Occupancies in Higher Education Institutions

Occupancy Type	General Performance Goal	Required Enhanced Resiliency Measures	Potential Enhanced Resiliency Measures
Student Housing	Keep students housed on campus to reduce displacement and the need to find alternative housing sources	• Charging stations for phones and computers • Enhanced performance for water and sewer systems (I_p=1.5) • High performing cladding • One high performance elevator	• Cistern • Increased emergency generator capacity and quick connect for temporary generator
Buildings with Large Classrooms	Keep highly used large registrar-managed classrooms available for teaching	• Enhanced performance for nonstructural elements in large classrooms and their egress corridors (I_p=1.5) • Emergency generator support of classroom information technology • One high performance elevator if classrooms are not on ground floor	• Increased emergency generator capacity and quick connect for temporary generator
High Value Research	Minimize loss of high value research and the faculty and staff that work on the research	• Enhanced performance for nonstructural elements supporting high value research (I_p=1.5) • Emergency generator support of high value research • High performing cladding where needed for research thermal control • One high performance elevator where needed to evacuate high value research	• Increased emergency generator capacity and quick connect for temporary generator
High Value Collections	Minimize loss of high value collections	• Enhanced performance for nonstructural elements supporting high value collections (I_p=1.5) • Emergency generator support of high value collections • High performing cladding where needed for collection thermal control • One high performance elevator where needed to evacuate high value collections	• Increased emergency generator capacity and quick connect for temporary generator

3.4.2 Target Select Components for Enhanced Seismic Resilience

Section 3.4.1 described code or policy approaches for select occupancies. Enhancement strategies can be tailored to specific buildings, but involve multiple techniques, such as those described in Section 3.3. Table 4 shows some examples for a laboratory building, highlighting how some components that are part of the life safety system already have higher design requirements in the IBC and enhancement is not needed, some enhancements will improve the ability to reoccupy the building, and some will improve functional recovery.

Table 4. Example Targeted Component Enhancements for a Laboratory

Component	For Occupancy	For Function	Above IBC	I_p	Examples/Comments
Mechanical and Electrical Components					
HVAC typical	N	N	N	1	Office
HVAC life safety	Y	N	N	1.5	Supply and exhaust fans and ducts and fume hoods with toxic chemicals
HVAC lab special	N	Y	Y	1.5	Serving critical research
Electrical typical	N	N	N	1	Office
Electrical life safety	Y	Y	N	1.5	Exit lighting and emergency generators
Electrical lab special	N	Y	Y	1.5	Serving critical research
Plumbing Typical	N	N	N	1	Office, cafe, restroom
Plumbing Life Safety	Y	Y	N	1.5	
Plumbing Lab Special	N	Y	Y	1.5	Serving critical research
Fire sprinkler	Y	Y	N	1.5	
Equipment typical	N	N	N	1	
Equipment life dafety	Y	Y	N	1.5	
Equipment lab dpecial	N	Y	Y	1.5	Serving critical research
Architectural Components					
Elevator rail support tubes	Y	N	Y	1.5	
Elevator rails	Y	N	Y	1.5	
Elevator controller	Y	N	Y	1.5	
Elevator remainder	Y	N	Y	1.5	
Stair	Y	Y	N	1.5	Shop inspection
Stair railings	Y	Y	N	1.5	Shop inspection
Other railings	N	N	N	1	Shop inspection
Interior metal studs (non lab)	N	N	N	1	
Lab metal studs	N	Y	Y	1.5	
Cladding	Y	Y	Y	1	Specific performance criteria at different drift levels
Casework, equipment, ceilings					
Casework typical	N	N	N	1	
Casework wall-mounted lab special	N	Y	Y	1.5	
Casework moveable lab special	N	Y	Y	1.5	Done with removable anchors
Ceilings	N	N	N	1	

3.4.3 Aspirational vs. Mandatory Requirements

A number of institutions consider enhanced seismic resilience during the early design stages. Sometimes, there are two designs done—one to code and one with additional enhancements. Sometimes there is a base design and then a rough cost estimate is done to price aspirational enhancement strategies. Experience has shown that, without an owner commitment at the start of the project or a mandatory policy requiring enhanced design, the aspirational design usually is not selected because budgetary pressures and associated value engineering first cut items that are aspirational. This is leading to moves on many fronts to establish minimum enhanced seismic resilience requirements in policies and codes. An example is the Building Seismic Safety Council (BSSC) Provisions Update Committee (PUC) which writes the *NEHRP Recommended Seismic Design Provisions*, which are in turn the basis for the ASCE/SEI 7 seismic provisions. For the current PUC 2022-2026 cycle which will develop the *2026 NEHRP Provisions*, a large effort has been established to develop functional recovery and enhanced resilience provisions, including those for nonstructural components, that can eventually be part of the next ASCE/SEI 7 edition in 2028.

3.4.4 Nonstructural Seismic Coordinator

One of the problems with nonstructural seismic design is that there are many different parties, including the owner, design team, general contractor, subcontractors for different components, and the subcontractor's specialty engineer who typically provides seismic anchorage and bracing for specific components in their scope. This diversity and lack of an overall coordination can lead to varying degrees of quality and missed requirements and opportunities. The concept of a Nonstructural Seismic Coordinator (NSC) was identified at the University of California, Berkeley two decades ago to help address this situation and was applied to several buildings formally and informally. A similar "Nonstructural Coordinator" role is mentioned briefly in NIST (2018).

The NSC serves as a central point of responsibility to coordinate the design and construction administration of seismic bracing for nonstructural building components and systems. The structural engineer of record is a good choice for the NSC and would typically report to the architect. Tasks can include the following.

- Develop a list of nonstructural components or systems to be incorporated into the base project, the responsible design team member, and methods of specification of seismic protection planned by team member.
- Develop, in cooperation with each team member, improvements to methods of specification and presentation for each component or system. Revisions will be aimed at effecting improvements in implementation of seismic protection without exceeding the standard of practice or significantly increasing the contracted level of effort of the team members.
- Review specifications and design standards for compliance with project criteria.
- Provide assistance to the project team for presentation and specification of seismic protection measures. Actual documentation and specification could be by others.
- Review construction documents at appropriate stages including MEP subcontractor's documents.
- Formulate recommended revisions to owner's construction administration and management plan to improve compliance with nonstructural seismic protection specified by drawings.
- Monitor submittal of shop drawings or design calculations that are specified by the construction documents. Provide assistance to consultants for review of such submittals.
- Provide spot field reviews at key times during installation of nonstructural components and system.
- Provide written progress reports to the architect and owner at project submittal milestones and quarterly during construction of nonstructural components and systems.

3.4.5 Typical Institutional Details for Nonstructural Seismic Anchorage and Bracing

Some large institutions have developed typical nonstructural seismic anchorage and bracing details. The University of California, San Francisco is one example. The fifth edition of the *UCSF Preapproved Seismic Restraint Details* is nearing completion (UCSF, 2022, in draft). The purpose is stated as:

Preapproved seismic restraint details have been created to prevent serious injury, reduce losses, protect irreplaceable research and help restore use of UCSF facilities after an earthquake. They are intended to streamline the design and approval process by creating details for common installations, which eliminates the need to hire a Structural Engineer for each installation and for related plan review services.

Other universities have similar programs and the hospitals in California have long had a preapproved detail program for seismic anchorage and bracing.

4. RESEARCH NEEDS

Substantial analysis and engineering judgment went into the new nonstructural design equations, but additional research is desired, including these items below, some of which are from (NIST, 2018).

- In future earthquakes, collect detailed and comprehensive information about the performance of nonstructural components and impacts on component and building functionality to inform future developments of the nonstructural seismic performance objectives and code requirements.
- Conduct additional research and testing to better understand the response of nonstructural components in earthquakes and to refine nonstructural seismic design equations in the future. This includes research on component damping, ductility, and periods and additional archetype studies beyond the set done for the ATC-120 project.
- Conduct additional research linking design requirements with functional recovery times.
- Revise the building strong motion instrumentation protocols of the California Strong Motion Instrumentation Program (CSMIP) and the USGS to better provide information needed to understand nonstructural component response. Protocols should be expanded to record horizontal (and vertical) response to include selected nonstructural components in addition to structural elements so that in-situ measurements of peak component amplification, peak floor acceleration, and peak ground acceleration can be compared, and component damping levels can be better understood.

5. CONCLUSION

The updated nonstructural design equations in ASCE/SEI 7-22 are based on a more rigorous understanding of the influence of different parameters on seismic response of nonstructural components and should produce more reliable performance. Beyond design forces, there are many specific techniques and broacder strategies that are being employed and are under development for enhanced nonstructural seismic design.

6. REFERENCES

AAMA [2018a] *Recommended Static Test Method for Evaluating Window Wall, Curtain Wall and Storefront Systems Subjected to Seismic and Wind-Induced Inter-Story Drift*, AAMA 501.4-2018, American Architectural Manufacturers Association.

AAMA [2018b] *Recommended Dynamic Test Method for Determining the Seismic Drift Causing Glass Fallout from Window Wall, Curtain Wall and Storefront Systems*, AAMA 501.6-2018, American Architectural Manufacturers Association.

ASME [2019] *Safety Code for Elevators and Escalators*, A17.1-19, American Society of Mechanical Engineers.

Alonso-Rodríguez, A., and Miranda, E. [2016] "Dynamic behavior of buildings with non-uniform stiffness along their height assessed through coupled flexural and shear beams," *Bulletin of Earthquake Engineering*, Vol. 14, No. 12, pp. 3463-3483.

ASCE [2017] *Minimum Design Loads and Associated Criteria for Buildings and Other Structures*, ASCE/SEI 7-16, Structural Engineering Institute of the American Society of Civil Engineers, Reston, VA.

ASCE [2022] *Minimum Design Loads and Associated Criteria for Buildings and Other Structures*, ASCE/SEI 7-22, Structural Engineering Institute of the American Society of Civil Engineers, Reston, VA.

CBC [2019] *2019 California Building Code*, California Code of Regulations, Title 24, Part 2, Volume 2 of 2, California Building Standards Commission.

FEMA [2020] *NEHRP Recommended Seismic Provisions for New Buildings and Other Structures*, Volume I: Part 1 Provisions, Part 2 Commentary, FEMA P-2082-1 Report, prepared by the Building Seismic Safety Council for the Federal Emergency Management Agency, Washington, D.C., September.

FEMA [2021] *2020 NEHRP Recommended Seismic Provisions: Design Examples, Training Materials, and Dseign Flow Charts, Volume I: Design Examples,* FEMA P-2192-V1, prepared for the Federal Emergency Management Agency by the Building Seismic Safety Council, Washington, D.C.

Hadjian, A., and E. Ellison [1986] "Decoupling of secondary systems for seismic analysis," *J. of Press. Vessel Technol.* 108(1): 78–85. https://doi.org/10.1115/1.3264755.

Higgins, C. [2009] "Prefabricated Steel Stair Performance under Combined Seismic and Gravity Loads," *Journal of Structural Engineering,* American Society of Civil Engineers, Reston, VA.

ICC [2021] *2021 International Building Code*, International Code Council, Country Club Hills, IL.

ICC [2022] *IBC – Structural, 2022 Group B Public Comment Agenda*, September 14-21, 2002, International Code Council, Country Club Hills, IL.

Kazantzi, A., Vamvatsikos, D., and Miranda, E. [2018] "The effect of yielding on the seismic demands of nonstructural elements," *Proceedings of the 16th European Conference on Earthquake Engineering*, Thessaloniki, Greece.

Lizundia, B. [2019] "Proposed Nonstructural Seismic Design Force Equations," *2019 SEAOC Convention Proceedings*, Structural Engineers Association of California, Sacramento, CA.

NIST [2018] *Recommendations for Improved Seismic Performance of Nonstructural Components*, GCR 18-917-43, 2018, National Institute of Standards and Technology Gaithersburg, MD.

SEAOC [2009] *Recommended Lateral Force Requirements and Commentary*, Structural Engineers Association of California Seismology Committee.

Taghavi, S., and Miranda, E. [2006] "Probabilistic Seismic Assessment of Floor Acceleration Demands in Multi-Story Buildings," Technical Report 162, the John A. Blume Earthquake Engineering Center, Stanford University, Stanford, CA.

UCSF [2022] *UCSF Preapproved Seismic Restraint Details,* University of California, San Francisco, in draft.

Influence of Vertical Floor Accelerations on the Seismic Performance of Building Non-Structural Elements

Keri L. Ryan[1]

[1] University of Nevada Reno
Reno, NV, USA
e-mail: klryan@unr.edu

Abstract. Based on recent events, the structural engineering community has developed awareness that damage to building non-structural elements (NSEs) and contents can dominate losses incurred in frequent to moderately-large earthquakes in regions with modern building codes. In reality, all ground shaking is spatial or multi-directional; however, the vertical component of shaking is not understood to be a significant source of damage and can generally be accommodated by the structural gravity system. In contrast, acceleration-sensitive NSEs are sensitive to both horizontal and vertical accelerations. Nonetheless, the influence of vertical shaking on NSE damage is difficult to quantify, and it has not yet been the focus of much research.

The NEES TIPS/E-Defense test program on innovative isolation systems conducted in 2011 provided a first hand opportunity to observe and systematically evaluate the influence of vertical shaking on NSEs. The vertical structural acceleration demands and the correlation of NSE damage states to both horizontal and vertical shaking intensity during NEES TIPS/E-Defense were carefully evaluated. Several examples of NSE damage and failure states were attributed specifically to vertical shaking. Other evidence, in reconnaissance observations, experimental and analytical studies, can be found to corroborate the notion that some types of NSE damage are caused by vertical shaking. The ongoing large scale NHERI TallWood shake table experiment provides another opportunity to observe and quantify 2D versus 3D shaking demands and associated damage states to a varied class of NSEs, and evaluate next steps to advance practice.

Keywords: non-structural elements, vertical, shake table test, suspended ceilings, sprinkler piping

1. INTRODUCTION

In classic and more recent examples, non-structural elements (NSEs) have been recognized as a significant source of earthquake-related damage and economic losses, which in many cases have exceeded losses due to structural damage [e.g. Kircher, 2003; Dhakal, 2010; Miranda et al., 2012; Perrone et al., 2019]. There is limited information on seismic performance of NSEs in general, and the body of research has lagged behind structural performance, for which great strides have been made in recent decades. The influence of vertical shaking on NSE response in particular is not well understood, and perhaps underestimated or dismissed because the structural system is often claimed to be vertically rigid. Vertical rigidity is reasonable when considering propagation of seismic accelerations through columns or walls, but is not accurate for floor systems. Code guidance for design of NSEs consider vertical shaking in an ad-hoc way. A significant portion of experimental studies do not include vertical shaking.

The NEES TIPS/E-Defense test program in 2011 generated definitive evidence of the damaging potential of vertical ground motions on NSEs. Because the testbed building was tested in the base-isolated configuration, the horizontal shaking response was mitigated, which allowed seclusion of effects related to vertical shaking. With strong supporting evidence, it was concluded that certain damage states were specifically caused by vertical shaking, and at least for the levels of shaking in this experiment, the overall NSE damage classifications were more closely related to vertical shaking than horizontal shaking. The main objective of this paper is to share the story and synopsize what happened and what was learned from the test 11 years ago. Also, this paper aims to highlight other works that have led to progress in understanding the influence of vertical shaking on NSEs. Finally, a synthesis of needs, future directions and opportunities is provided.

2. FINDINGS FROM NEES TIPS/E-DEFENSE PROGRAM

2.1 PROGRAM FEATURES

NSEs and contents comprised a significant component of the NEES TIPS/E-Defense shake table test of a 5-story steel moment frame testbed building. The building was reused from a prior project on supplementary damping systems, and had been stored in the fabrication yard for 2 years. The building had been designed so that it could be hoisted by crane on and off the table. In this project, the building was tested in three different configurations: isolated with triple pendulum bearings (TPB configuration), isolated with a hybrid system of lead rubber bearings and tension capable cross-linear rolling bearings (LRB configuration), and fixed at the base.

Figure 1. 5-story testbed building

The building was approximately 16 m tall, asymmetric in plan with dimensions of 10 m x 12 m (2 bay x 2 bay), and weighed approximately 5220 kN (Figure 1). The floor system consisted of reinforced concrete slabs on corrugated metal decking on floors 2-5, and slightly thicker slabs cast on a flat steel deck on the roof. The slabs were connected to the sructural beams by shear studs that provided composite behaviour. Concrete blocks weighing 175-257 kN per floor were added on floors 2-5 to represent live load. Four steel plates weighing 535 kN were installed on the roof in an asymmetric configuration. The weight was justified as being representative of roof equipment, but was questioned by some observers as in total it was much larger than typical roof equipment. This weight amplified both the torsional response and the vertical vibration observed at the roof level.

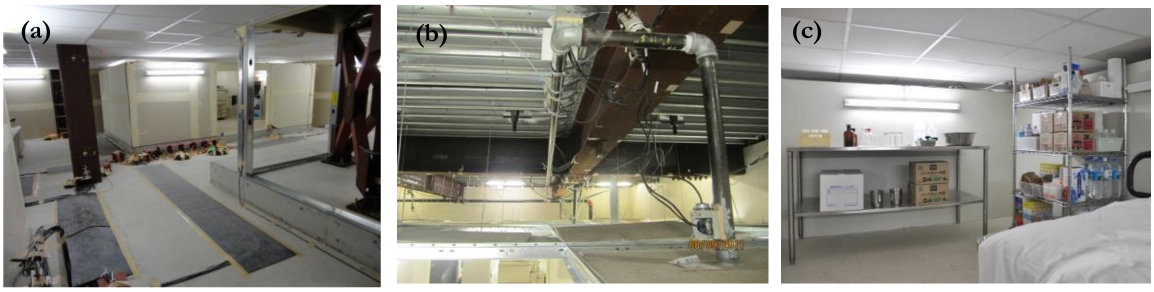

Figure 2. NSEs in the building: (a) ceilings and partitions, (b) sprinkler piping, (c) hospital equipment

With regard to NSEs, an integrated system of suspended ceilings, partition walls, and sprinkler piping was installed in the 4th and 5th stories of the building (Figure 2). The suspended ceiling system was U.S. style with main runners and cross tees, attached to the wall molding with seismic clips – tight on two sides and with 19 mm gap on two sides. Ceilings suspended from the 5th and roof slabs were identical except for the use of seismic bracing (compression posts with diagonal splay wires) on the roof only as required in the U.S. for ceiling areas larger than 93 m^2. Sprinkler piping suspended from the 5th and roof slabs included a main run extending from a riser pipe, three branch lines and a mix of straight and armover drops. A mix of grooved and threaded connections were used, and the system was supported by pipe hangers and sway bracing. A small number of flexible hose sprinkler heads were included. Partition walls were built from cold-formed steel framing and double sheathed with gypsum. Tracks and studs were fully connected to the slabs above and below on the 4th story, while the 5th story used a slip track connection that allowed sliding of the top track relative to the studs. Enclosed rooms with partial height walls was constructed, and staged with medical equipment and furniture on the 4th floor (Fig. 2(c)) and office equipment on the 5th floor.

A variety of motions at various intensities were applied without regard to the usual approach of systematically increasing intensity and directional input. The team was not expecting to observe damage and wished to maximize the number and variety of ground motions that could be applied within a limited testing timeframe. Since this paper aims mainly to share some overarching perspective on the test program, only minimal details have been included and the reader is referred to Ryan et al. [2015] and Soroushian et al. [2015] for more information.

2.2 NATURE OF VERTICAL RESPONSE

Next, the characteristics of vertical structural response are discussed to establish the nature of the shaking and vertical demands transmitted to NSEs. Whereas other publications have focused on intense vertical shaking (input at the table exceeding 1g [Ryan et al., 2015]), this paper focuses on a more typical range of intensity for a design event. Figure 3 plots recorded vertical acceleration histories at three different locations: the shake table, at the roof level next to a column, and at the roof level in the middle of the southeast (SE) floor slab; and for three different input motions: (a) 80% of 1978 Tabas – Tabas Sta in the TPB configuration (TAB80), (b) 175% of a synthetic motion at Vogtle nuclear power plant site in the LRB configuration (VOG175), and 35% of 1994 Northridge – Rinaldi Sta. in the fixed base building (RRS35). Note the difference in scale for the accelerations recorded in the slab compared to the table and column. Figure 4 plots spectral response generated from recorded accelerations at the column and SE floor slab at each floor level (table up to roof) for these same input motions.

The figures suggest that the acceleration is transferred essentially rigidly through the columns, which is expected because columns are rigid elements. The column spectral acceleration responses (Fig. 4(a)-(c)) exhibit the same frequency content as the ground acceleration. A moderate amplification of peak acceleration is observed from the table to the column in the two isolated configurations (Fig. 3(a) and (b)). Not much amplification is expected since in both systems the isolators are pretty rigid vertically. The amplification could be due to, for example, movement along the spherical surface in the TPB configuration.

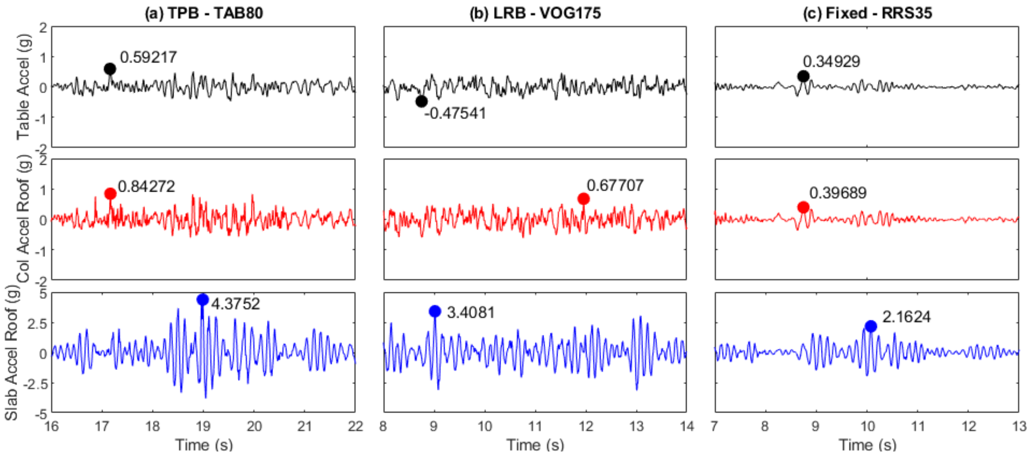

Figure 3. Recorded vertical accelerations at table, roof level column, and middle of slab for (a) TPB – 80% Tabas, (b) LRB – 175% Vogtle, (c) Fixed – 35% RRS

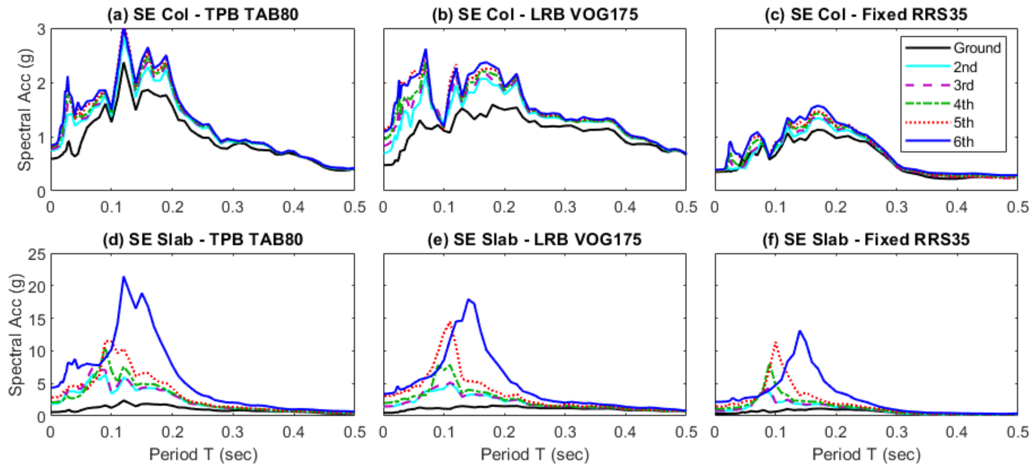

Figure 4. Vertical spectral accelerations at roof level southeast column and floor slab, (a),(d) TPB – 80% Tabas, (b),(e) LRB – 175% Vogtle, (c),(f) Fixed - 35% RRS

Regardless, significant amplification of accelerations is observed in the motion recorded in the SE floor slab, in all three configurations, and does not seem to depend on the configuration. Ryan et al. [2015] found that peak slab acceleration was amplified by an average factor of 3 at floor 2 to 6 at the roof. Moreover, it can be visually noted that the slab responses exhibit a lower frequency and more uniform frequency content (Fig. 3). In Figure 4(d)-(e), the slab spectra tend to exhibit a distinct peak with increasing period from the 2nd floor to the roof. This observation was supported by evidence in Ryan et al. [2015] that slab response tends to be single frequency (idealized as an SDOF osciallator between columns), and slab vibration frequencies in the test building were systematically characterized and varied from 7.7 to 12.5 Hz. The SE slab at the roof level is on the low end of that frequency range, due to the added mass plates at the roof level. Some observers questioned whether the slabs in the test building were excessively flexible; however, the observed frequencies are within the range found by others in vibration sensitivity studies [Murray et al., 1997], and in fact the slabs were somewhat stiff due to the small footprint of the building.

2.3 Observed Damage in NSEs and Correlation to Vertical Input

This section outlines some of the damage observed in the test and why it was believed to be specifically correlated to the vertical shaking. First, damage to the suspended ceiling system was observed in many of the trials. A couple fallen ceiling panels was considered light damage. More extensive damage was characterized by a large number of panels falling, which weakened the grid system and caused some of the

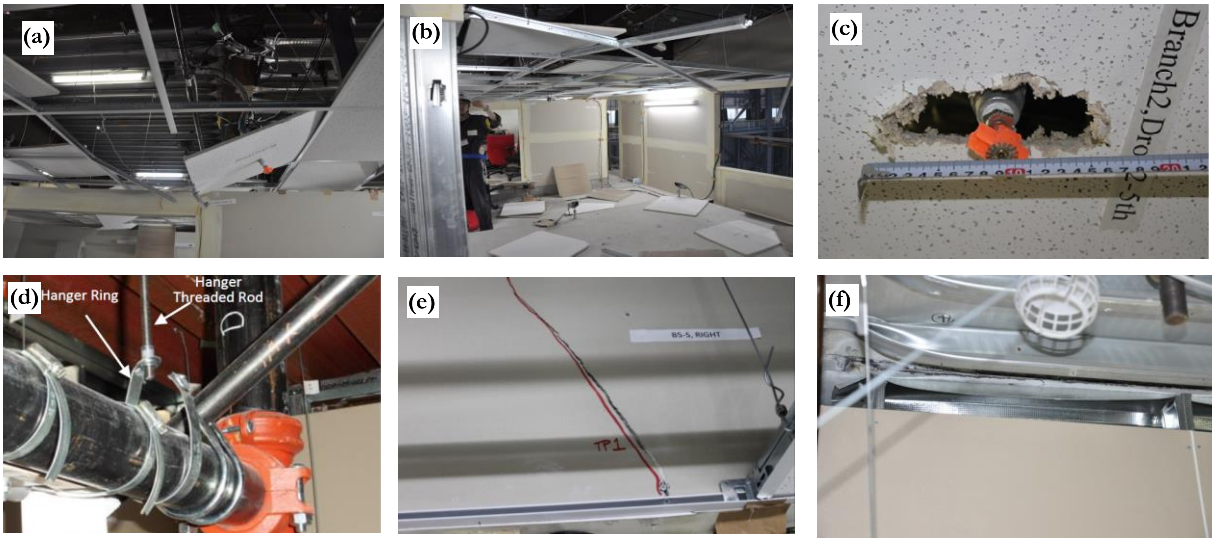

Figure 5. Representative NSE damage from E-Defense tests: (a),(b) ceiling grid damage and rotated armover pipe, (c) ceiling panel/sprinkerhead interaction, (d) failed pipe hanger, (e) partition wall cracks, (f) bent tracks

cross members to fail (Fig. 5(a) and (b)). After extensive damage, which occurred early in the test program, repairs were made (connections repaired and fallen tiles replaced), but the ceiling system was never restored to its original condition. The research team concluded that the large vertical accelerations specifically caused the panels to pop out of the grid, initiating much of the damage. Ironically, the damage was much more significant in the ceiling with seismic bracing than in the unbraced ceiling. Soroushian et al. [2015] theorized that when subjected to a large downward acceleration, the bracing forced the ceiling grid to move with the attached slab above that hence dislodged the unsecured ceiling panels. However, in the unbraced configuration, the grid system and panels could float together and be isolated from the sharp downward movement of the attached floor slab. While dislodged ceiling panels dominated the damage observations, damage was also observed at the ceiling perimeter on the edges with seismic gaps. It was theorized that horizontal gap opening first caused the ceiling grid to settle, and then collide with the wall molding on load reversal. This phenomenon was likely caused by horizontal movement, but perhaps exacerbated by the vertical shaking.

Several different types of damage were observed in the piping system. First, pounding interaction between the ceiling panels and piping sprinkler heads caused damage in the ceiling panels (Fig. 5(c)), even in situations where a 50 mm gap was provided between the panel and the sprinkler head by an oversized ring. This type of damage is fairly easily repaired and is not expected to be amplified by vertical shaking. However, other types of damage were thought to be caused or intensified by vertical shaking. First, the entire branch line with three armover drops was observed to twist around its connection point to the main run (Fig. 5(a)). The vertical acceleration caused the development of a large twisting moment around the branch line that loosened the connections of the threaded joints. Also, a pipe hanger connection failure was observed (Fig. 5(d)). The vulnerability at this connection was likely increased because the pipe hanger threaded rod was not detailed to extend all the way down to the pipe.

Partition walls are mostly drift sensitive, and while drift-related damage can occur at drifts as low as 0.3%, typical drift-related damage was not observed in the partition walls in this experiment, where maximum observed drifts were 0.78% in the 4th story and 0.62% in the 5th story. However, some atypical damage states attributed to strong vertical shaking were observed. Fully connected full height partition walls developed large vertical cracks in the gypsum board (Fig. 5(e)), and stud buckling of bulkhead partitions was observed. This illustrates the importance of detailing partition walls with a vertical gap or joint at the top of the wall to accommodate relative vertical movement. In the slip track configuration, studs were observed to move laterally or pop out from their constrained position within the track (Fig. 5(f)). This type of damage seems difficult to avoid, but some protection could be offered by increasing the seismic gap with longer track legs. However, the vertical gap opening in combination with a horizontal seismic force could easily bend the track leg. Overall, Ryan et al. [2015] categorized the overall NSE damage in every trial as None, Slight, Moderate, or Extensive and depicted these ratings on a 2D scatter plot against peak horizontal and peak vertical (slab) acceleration. Increasing damage was more closely associated to the vertical shaking intensity.

2.4 COUPLING OF HORIZONTAL AND VERTICAL RESPONSE

Although the intensity of the vertical shaking was found to be the dominating factor behind the NSE damage observed in the E-Defense test, another factor served to increase the overall seismic demands to NSEs. A horizontal-vertical coupling was observed that caused horizontal accelerations to be amplified during 3D shaking compared to horizontal shaking alone. The horizontal-vertical coupling sources were confirmed through computational simulation. In both fixed-base and LRB configurations, modal analysis showed that one of the higher structural modes included a significant contribution from slab vibration (Fig. 6(a)). Thus, vertical shaking caused the greater expression of the specific mode, which was proven by spectral analysis of the horizontal floor accelerations that showed the additional peak in 3D shaking compared to horizontal only shaking (Fig. 6(b)) [Guzman and Ryan, 2017]. In the TPB configuration, the predominant source of coupling was due to the friction pendulum bearings. The frequency of vertical shaking (correlated to slab vibration frequencies mentioned earlier) was shown to be tuned to one of the higher horizontal structural modes (Fig. 6(c)) [Ryan and Dao, 2015]. Due to the friction mechanism, the high frequency axial load variation on the bearings generated a proportional high frequency component in the isolator base shear, which caused the expression of the associated structural mode. The effect was significant, as the higher mode was exhibited in the peak acceleration profile plot and large modal peaks in the floor spectra only at floors 1, 3, 4 and 6 (Fig. 6(d)). Representation of these coupling effects as well as accurate simulation of the vertical slab vibration required finite element models with discretization of framing elements that allowed for improved resolution of the mass distribution. While a frame element model that included composite sections to represent the composite stiffness of the slab with the framing was successful in representing the horizontal-vertical coupling [Ryan and Dao, 2015], explicit representation of the slab using shell elements was the best approach to predict slab vibration [Guzman and Ryan, 2017].

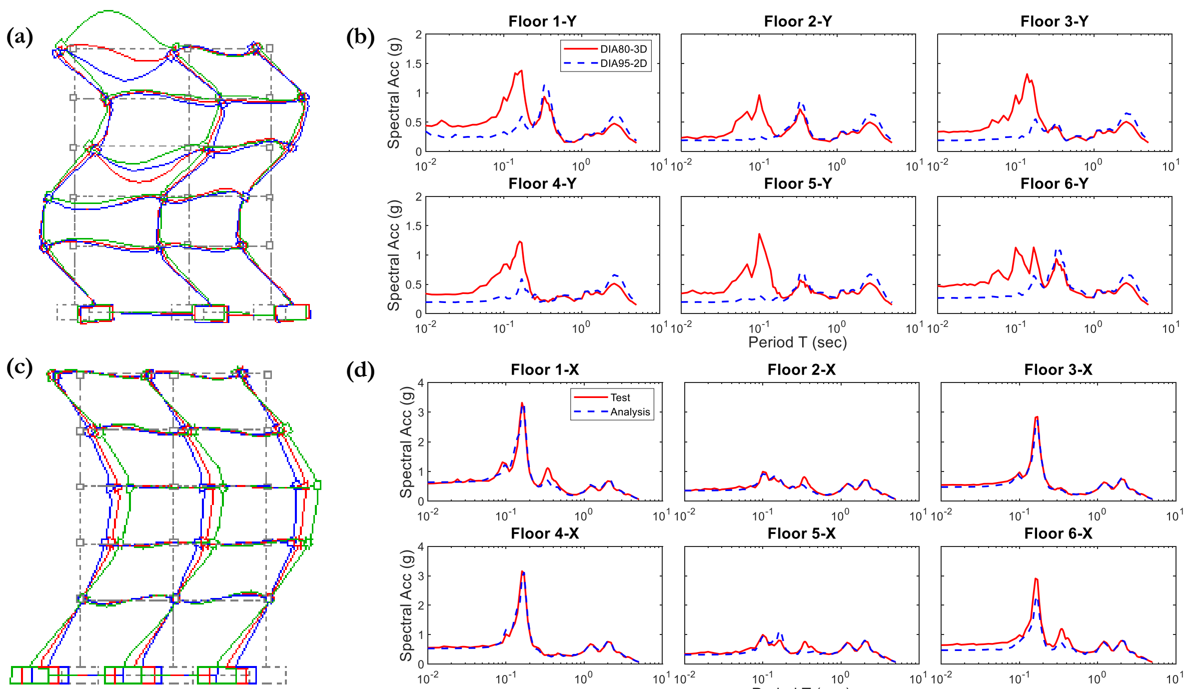

Figure 6. (a) H-V coupled model in LRB configuration, (b) additional spectral peaks for 3D input, (c) 2nd structural mode in TPB configuration, (d) spectral peaks corresponding to the mode shape, validated by analysis

3. OTHER EVIDENCE OF VERTICAL SHAKING INFLUENCE ON NSE PERFORMANCE

The following section represents an attempt to catalog other useful studies that provide insight on how vertical shaking affects the seismic response of NSEs. Meaningful examples from the body of work are highlighted, but this review is not intended to be comprehensive.

3.1 EXPERIMENTAL OBSERVATION

Shortly before the NEES/E-Defense tests extensively above, data became available from another E-Defense test on a 4-story base-isolated RC building [Furukawa et al., 2013]. The building was outfitted with medical equipment to assess functionality in both horizontal and 3D shaking. Similar amplification factors in peak vertical accelerations were observed compared to NEES/E-Defense: 1.5 from the table to the base level above the isolators, 1.5 from base to roof, and 1.8 to 2.6 from column lines to center of slabs, for total amplification factors of 4 to 6. Three distinct motions were executed that generated maximum vertical accelerations of up to 1*g*, 1*g* to 2*g*, and 2*g* to 4*g*., Disruptions were minimal for vertical accelerations <1*g*. Some disruption of equipment and furniture (jumping, toppling, sliding rocking) was noted in the range of 1*g* to 2*g*, but generally not catastrophic. Disruptions were significant beyond 2*g*. However, Japanese designed NSEs such as suspended ceiling, plumbing, sprinklers, walls and doors remained undamaged at all levels of shaking in the test. Recall that the building was base-isolated and limited to low horizontal accelerations.

Suspended ceilings are highlighted here as being among the more vulnerable multi-directional acceleration sensitive components, with a growing body of experimental research considering vertical and combined shaking. Shaking table tests of a 24 m^2 suspended ceiling with seismic bracing were performed in Gilani et al. [2010]. No damage was observed for shaking producing vertical acceleration in the frame up to 2*g*. Large vertical accelerations in the center of the frame (peaking at about 6*g*) led to large sections of panel fallout in the same location; however, no damage to the grid was observed. The authors noted that the damage pattern was inconsistent with field observations, may be due to the large vertical flexibility of the frame, and that further investigation was needed. However, the observations were similar to Soroushian et al. [2015]. Ryu and Reinhorn [2019] reported on a very extensive set of tests on 15 different ceiling cofigurations (93 m^2 and 37 m^2) subjected to 3D motions. They did not comment specifically on the effect of vertical shaking other than to note the test frame was very rigid in the vertical direction (22 Hz) compared to typical floor systems, limiting vertical acceleration amplification to about 1.5. Yu et al. [2018] reported on experiments of suspended ceilings attached to large span spatial structures, which are unique due to the large number of and complexity of the vibration modes. They considered both a rigid and flexible supporting structure. While large amplification of vertical acceleration was observed especially in the vertically flexible specimen, the characteristic damage states associated with vertical shaking were not. For example, extent of fallen panels was not significant until the horizontal acceleration reached 3g, and tended to originate at the perimeter and not the center of the grid where vertical accelerations are largest. In summary, a clear pattern of damage to suspended ceilings from vertical shaking is not apparent. The vulnerability inevitably depends on the detailing, and the findings give hope that solutions to minimize damage can be found.

3.2 INVESTIGATION OF VERTICAL ACCELERATION DEMANDS

With growing awareness of the issue, a handful of studies have investigated vertical acceleration demands in buildings through analytical simulation. Certainly, modelling assumptions are critical, wherein explicit 3D representation of floor slabs with discrete mass distribution is expected to be the best representation of reality. Two studies used equivalent stick models, intending to focus on accelerations near columns [Qu et al., 2014; Moschen et al., 2016]. They observed considerable amplification factors (on the order of 3 to 6 at the roof level). While effective techniques to create these equivalent stick models may be possible (as attempted in Moschen et al. [2016]), the large amplification near column lines is questionable, and may be a result of lumping the entire floor mass at the column, which is not representative of the vertical inertia that the column experiences. Gremer et al. [2019] and Francis et al. [2017] investigated the question using 2D frame models of steel moment frames and a concrete wall building, respectively. Both applied beam discretization and distributed mass along the beam length, and sampled vertical accelerations near column lines and at mid-beam. Gremer et al. [2019] found that amplification increased over height, and reached factors of 4-5 at the roof for both mid-beam and at exterior columns, while Francis et al. [2017] found amplification factors at mid-beam only up to 2. The source of discrepancy is unclear, but development of frame models for this purpose is tricky due to the potential for composite slab action and the general representation of the 3D slab effects. A few studies [Wieser, 2012; Tutuiana, 2019; Guzman Pujols and Ryan, 2020] examined vertical accelerations with 3D models of steel moment frame buildings. Wieser [2012] in particular combined the effects of secondary beam framing and slabs into a single shell element, and used pin connections to primary beam elements (representative of partially composite action). The first two studies found that vertical amplification factors from ground to mid-slab locations peaked out at about 2 or 2.5. Tutuiana [2019] also observed a unique C-shaped acceleration profile (highest accelerations near building top and bottom and lowest in the middle of the 20-story building). Using modelling techniques validated by the E-Defense test, Guzman Pujols and Ryan [2020] found slab amplification factors in a 3-story moment frame building varyied from 2.5 to 6.5, and recommended a factor of 4 or 5 to be applied in design. The studies should be examined more closely to understand the discrepancy in slab amplification.

Observations from instrumented buildings can also provide insight on vertical acceleration demands to NSEs, but such information proved difficult to find. The location of accelerometers (adjacent to column, middle of beam line, or middle of floor slab) is critically important and reports need to clarify where observations are made. Accelerometers in instrumented buildings are suspected to be generally near columns and not in the middle of floor slabs. Bozorgnia et al. [1998] observed vertical accelerations and amplification factors in 12 buildings shaken in the 1994 Northridge Earthquake. Amplification factors with respect to base varied from 1.1 to 6.4 depending on the instrument location, which wasn't always clear. Amplification factors were 2.4, 3.75 and 6.4 in three buildings with vertical accelerometers clearly located away from a column. Amplification factors from 1.08 to 2.86 (mean = 1.88) were recorded in seven buildings with rooftop accelerometers during the 1999 Chi Chi Taiwan Earthquake [Assi et al., 2017]. No information was given about the location of the accelerometers.

3.3 FIELD OBSERVATIONS

The author surveyed 15 papers that reported mainly or in depth on the performance of NSEs in specific earthquakes. Very few commented about effects related specifically to vertical shaking. Reitherman and Sabol [2005] commented that vertical accelerations affected sprinkler systems in the 1994 Northridge Earthquake, causing branch lines to move upward and sprinkler heads to push through the ceiling panels. Braga et al. [2011] commented that vertical motions seemed to exacerbate demands and induce crushing on masonry infill panels in the 2009 L'Aquila Earthquake. Both Dhakal et al. [2011] (2011 Christchurch Earthquake) and Hosseini [2004] (2003 Bam Earthquake) commented on the effect of vertical in exacerbating ceiling damage by dislodging ceiling panels or false ceilings. Free field vertical accelerations of up to 2.2*g* were measured in the Christchurch Earthquake. Distinguishing effects that could arise from vertical shaking is admittedly challenging without clear data or the ability to control the combination of horizontal and vertical shaking.

4. CURRENT CODE GUIDANCE AND SHORTCOMINGS

At the time, results from the E-Defense tests [Ryan et al., 2015; Soroushian et al. 2015] were interpreted in the context of current code guidance. For determining NSE anchorage force demands, the governing ASCE 7-10 [ASCE, 2010] required that horizontal forces be combined with a vertical force $\pm 0.2 S_{DS} W_P$, where S_{DS}

is the short period design spectral acceleration and W_P is the weight of the component. This implies that the component is subjected to one half of the horizontal peak ground acceleration (PGA) in the vertical direction, with no allowance for amplification over height or vertical component amplification factor. ICC-AC156 [ICC Evaluation Service, 2010], which provides guidance for seismic certification of NSEs, specified vertical spectral acceleration equal to 2/3 horizontal spectral acceleration, which allows for comparable component amplification factor for flexible components, but again no allowance for amplification over height. Since peak slab accelerations were amplified on average by factors of 3-6 with respect to the vertical PGA, the codes at the time were very inadequate with respect to the effects observed in the test. However, the state of knowledge to develop alternative code guidelines was acknowledged to be inadequate.

In 2014, the ATC-120 project was initiated to address shortcomings in seismic design of NSEs. The committee took a holistic look at state of knowledge and design practice related to NSEs and direct limited resources to addressing items that would have the largest impact to public safety and welfare. A significant revision to the anchorage force equation was recommended based on the current body of research and independent studies conducted by the ATC-120 team. The revised equation includes revised amplification of horizontal ground acceleration over height that depends on the building period, and depends on the structure ductility factor, component dutility factor, and a component strength factor. The findings and recommendations from this project were published in NIST GCR 18-917-43 [NIST, 2018]. Recommendations from the NIST report were adopted into ASCE 7-22 [ASCE, 2022]. Similar to E-Defense researchers, the ATC-120 team concluded that knowledge on vertical response of NSEs was insufficient to develop improved design guidance. The provision for determining the influence of vertical acceleration on NSE demand remain essentially unchanged from ASCE 7-10 to ASCE 7-22.

5. SUMMARY AND CONCLUSIONS

Prior to the E-Defense test, the nature of slab vibration amplification was not well understood. The test program demonstrated that amplification of vertical accelerations from columns out to middle of floor slabs can be substantial and with spectral content reflecting the flexiblilty of the floor system. The finding is significant because many attached NSEs will "feel" the shaking in the floor slab, and the slab frequency may be more closely matched to the NSE frequency. The review in Section 3 indicates that the body of knowledge on vertical response of NSEs is growing, but there is a lot of uncertainty and lack of consensus, especially on determining demands to NSEs.

Expanding the knowledge base to allow for the development of a refined approach for assessing vertical anchorage force demands is a top priority. This should include additional analytical studies on 3D structures with properly modelled floor systems, which admittedly leads to computationally intense analysis. Relevant variables such as floor system type, thickness, span length, structural type, height, and configuration irregularities should be considered. These analytical models should be validated, to the extent possible, from large scale shaking experiments of buildings. In addition, available data from well-instrumented buildings should be revisited and results should be synthesized.

An upcoming experiment, the NHERI Tallwood shake table test of a 10-story building, provides another opportunity to observe and quantify vertical acceleration demands. The floor systems are comprised of mass timber diaphragms made from several distinct materials. In addition, the influence of vertical shaking will be observed on a varied class of NSEs, mostly detailed for drift compatibility. The test specimen will include a 10-story stair scissor stair tower, various interior and exterior cold-formed steel subassemblies, and a glass curtain wall subassembly. The wall subassemblies have been designed to accommodate relative vertical movement. Construction of the test structure is ongoing at the time of this writing, with first shakes projected for December 2022.

ACKNOWLEDGMENTS

The NEES/E-Defense project was supported by NSF Grants CMMI-1113275 and CMMI-0721399, Contract NRC-HQ-11-C-04-0067 and NIED in Japan, and a number of industry suppliers. The author is indebted to the former graduate students that made the project successful: Camila B. Coria, Nhan D. Dao, Jean C. Pujols Guzman, and Siavash Soroushian, and the late Professor Stephen B. Mahin for his vision.

REFERENCES

ASCE [2010]. *Minimum Design Loads for Buildings and Other Structures: ASCE/SEI 7-10*, American Society of Civil Engineers, Reston, VA, USA.

ASCE [2022]. *Minimum Design Loads for Buildings and Other Structures: ASCE/SEI 7-22*, American Society of Civil Engineers, Reston, VA, USA.

Assi, R., Dliga, M., Yao G [2017] "Horizontal and vertical seismic acceleration demands in multi-storey buildings", *Structures Congress*, ASCE, Denver, Colorado, USA.

Bozorgnia, Y., Mahin, S.A., Brady, A.G. [1998] "Vertical response of twelve structures recorded during the Northridge Earthquake", *Earthq Spectra*, Vol. 14, No. 3, pp. 411-432.

Braga, F., Manfredi, V., Masi, A., Salvatori, A., Vona, M. [2011] "Performance of non-structural elements in RC buildings during the L'Aquila, 2009 earthquake", *Bull Earthq Eng*, Vol. 9, No. 1, pp. 307-324.

Dhakal, R.P. [2010] "Damage to non-structural components and contents in 2010 Darfield earthquake", *Bull of NZ Society for Earthq Eng*, Vol. 43, No. 4, pp. 404–411.

Dhakal, R.., MacRae, G.A., Hogg, K. [2011] "Performance of ceilings in the February 2011 Christchurch earthquake", *Bull of NZ Society for Earthq Eng*, Vol. 44, No. 4, pp. 377-387.

Francis T.C., Hendry, B.C., Sullivan, T.J. [2017] "Vertical spectral demands on building elements induced by earthquake excitation", *New Zealand Society for Earthquake Engineering Annual Conference*, Wellington, New Zealand.

Furukawa, S., Sato, E., Shi, Y., Becker, T., Nakashima, M. [2013] "Full-scale shaking table test of a base-isolated medical facility subjected to vertical motions", *Earthq Eng Struct Dyn*, Vol. 42, No. 13, pp. 1931-1949.

Gilani, A.S.J., Reinhorn, A.M., Glasgow, B., Lavan, O. and Miyamoto, H.K. [2010] "Earthquake simulator testing and seismic evaluation of suspended ceilings", *J. Archit. Eng.*, ASCE, Vol. 16, No. 2, pp. 1–11.

Gremer, N., Adam, C., Medina, R.A., Moschen, L. [2019] "Vertical peak floor accelerations of elastic moment-resisting steel frames", *Bull Earthq Eng*, Vol. 17, No. 6, pp. 3233-3254.

Guzman Pujols, J.C., Ryan, K.L. [2017] "Computational simulation of slab vibration and horizontal-vertical coupling in a full-scale test bed subjected to 3D shaking at E-Defense," *Earthq Eng Struct Dyn*, Vol. 47, No. 2, pp. 438-459.

Guzman Pujols, J.C., Ryan, K.L. [2020] "Slab vibration and horizontal–vertical coupling in the seismic response of low-rise irregular base-isolated and conventional buildings", *J Earthq Eng*, Vol. 24, No. 1, pp. 1-36.

Hosseini, M. [2004] "On the nonstructural elements and their behavior in the Bam Earthquake of 26 December 2003", *J Seism Earthq Eng*, Vol. 5, No. 4, pp. 169-196.

ICC-ES [2010] "AC156: Acceptance criteria for seismic certification by shake-table testing of non-structural components" International Code Council Evaluation Service, Brea, CA, USA.

Kircher, C. [2003] "It makes dollars and sense to improve non-structural system performance", *Proc. ATC 29-2 Seminar on Seismic Design, Performance and Retrofit of Nonstructural Components in Critical Facilities*, Newport Beach, CA, USA.

Lu, Y., Mosqueda, G., Han, Q., Zhao, Y. [2018] "Shaking table tests examining seismic response of suspended ceilings attached to large-span spatial structures", *J. Struct. Eng.*, Vol. 144, No. 9, pp. 04018152-1-15.

Miranda, E., Mosqueda, G., Retamales, G., Pekcan, G. [2012] "Performance of nonstructural components during the 27 February 2010 Chile earthquake", *Earthq Spectra*, Vol. 28, No. S1, pp. S453–S471.

Moschen, L., Medina, R.A., Adam, C. [2016] "Vertical acceleration demands on column lines of steel moment resisting frames", *Earthq Eng Struct Dyn*, Vol. 45, No. 12, pp. 2039–2060.

Murray, T.M., Allen, D.E., Ungar, E.E. [1997] "Floor vibrations due to human activity", *Steel Design Guide Series 11*, American Institute of Steel Construction (AISC), Chicago.

NIST [2018] *Recommendations for Improved Seismic Performance of Nonstructural Components: NIST GCR 18-917-43*, Applied Technology Council, Redwood City, CA, USA.

Perrone, D., Calvi, P.M., Nascimbene, R., Fischer, E.C., Magliulo, G. [2019] "Seismic performance of non-structural elements during the 2016 Central Italy earthquake", *Bull Earthq Eng*, Vol. 17, No. 10, pp. 5655-5677.

Qu, B., Goel, R.K., Chadwell, C.B. [2014] "Evaluation of ASCE/SEI 7 provisions for determination of seismic demands on nonstructural components", *10th US Nat Conf Earthq Eng*, EERI, Anchorage, AK, USA.

Reitherman, R.., Sabol, T. [1995] "Nonstructural Damage," in John Hall, (ed.), *Northridge Earthquake of January 17, 1994 Reconnaissance Report*, *Earthq Spectra*, Vol. 11, Supplement C, pp. 453-514.

Ryan, K.L., Dao, N.D. [2015] "Influence of vertical ground shaking on horizontal response of seismically-isolated buildings with friction bearings", *J Struct Eng*, ASCE, Vol. 142, No. 1, pp. 04015089-1-12.

Ryan, K.L., Soroushian, S., Maragakis, E.M., Sato, E., Sasaki, T., Okazaki, T. [2015] "Seismic simulation of an integrated ceiling-partition wall-piping system at E-Defense I: Three-dimensional structural response and base isolation", *J Struct Eng*, ASCE, Vol. 142, No. 2, pp. 040151301-1-15.

Ryu, K.P., Reinhorn, A.M. [2019] "Experimental study of large area suspended ceilings", *J Earthq Eng*, Vol. 23, No. 6, pp. 1001-1032.

Soroushian, S., Maragakis, E.M., Ryan, K.L., Sato, E., Sasaki, T., Okazaki, T., Mosqueda, G. [2015] "Seismic simulation of an integrated ceiling-partition wall-piping system at E-Defense. II: Evaluation of nonstructural damage and fragilities", *J Struct Eng*, ASCE, Vol. 142, No. 2, pp. 04015131-1-17.

Tutuiana, G. [2019] "Peak vertical floor accelerations of tall steel structures", *M.S. thesis*, Civil Engineering, University of New Hampshire Durham, New Hampshire, USA.

Wieser, J.D. [2012] "Assessment of floor accelerations in yielding buildings", *M.S. thesis*, Civil Engineering, University of Nevada Reno, Nevada, USA.

Component-based Simplified Framework to Assess Integrated Structural and Non-Structural Seismic Upgrade Strategies

Alessandra Miliziano[1], Lydell Wiebe[2], Stefano Pampanin[3], Daniele Perrone[4] and André Filiatrault[5]

[1] University School for Advanced Studies IUSS Pavia
Piazza della Vittoria 15, Pavia 27100, Italy
e-mail: alessandra.miliziano@iusspavia.it
[2] McMaster University
1280 Main St W, Hamilton, ON L8S 4L8, Canada
e-mail: wiebel@mcmaster.ca
[3] Sapienza University
Via Eudossiana 18, Rome 00184, Italy
e-mail: stefano.pampanin@uniroma1.it
[4]University of Salento
Piazza Tancredi 7, Lecce 73100, Italy
e-mail: daniele.perrone@unisalento.it
[5]University School for Advanced Studies IUSS Pavia
Piazza della Vittoria 15, Pavia 27100, Italy
e-mail: andre.filiatrault@iusspavia.it

Abstract. Recent studies have demonstrated the importance of harmonizing structural and non-structural performance levels when implementing strategies to reduce seismic risk. The benefit of a seismic structural upgrade may be reduced if it increases the demand on non-structural elements and, vice versa, a non-structural upgrade may not be as effective if the structural performance is inadequate. The aim of this study is to provide a framework for evaluating the impact of various integrated structural and non-structural upgrade strategies in a way that is straightforward and consistent with the limited resources available at the early design stage. Upgrade strategies for structural elements are represented in the framework by changes to the pushover curve, damping, and/or re-centering capacity of the building, whereas upgrades of non-structural elements are represented by changes to the element's EDP (Engineering Demand Parameter)-Loss functions. The framework's application to a case study steel moment-resisting frame building and comparison of the results with those obtained using the FEMA P-58 methodology demonstrates that it is able to capture the impact of various structural and non-structural upgrade strategies on the expected annual loss. This makes the proposed framework a straight-forward tool to be used by engineers to quantify the seismic risk associated with structural and non-structural elements for different upgrade strategies, improve the communication of that risk to other stakeholders early in the design process and narrow the number of feasible upgrade strategies on which to apply a more rigourus loss estimation methodology.

Keywords: Simplified loss estimation framework, component EDP-Loss functions, seismic upgrade strategies, non-structural elements, non-structural seismic upgrade strategies, nonstructural components.

1.INTRODUCTION

Recent earthquakes have demonstrated how a building's performance and functionality may be significantly reduced by the vulnerability of non-structural elements (NSEs) [Miranda *et al.*, 2012; Perrone *et al.*, 2019]. Even if the structural performance of a building meets the immediate occupancy performance objective after an earthquake, damage to its architectural, electrical or mechanical equipment and content may result in a safety risk, large monetary loss and functional loss. In order to design a building's seismic upgrades to harmonize the performance levels between structural and NSEs, it is crucial to consider that structural and non-structural responses are not independent. After a structural seismic upgrade, the seismic demand on NSEs changes as a result of the modified structural response. Therefore, the benefit of a structural upgrade may be reduced if the change in the structural response lowers the non-structural performance. Similarly, a non-structural seismic upgrade may not be as effective if the building's structural elements are damaged.

The performance-based earthquake engineering (PBEE) framework developed by the Pacific Earthquake Engineering Research Center [Cornell and Krawinkler, 2000; Miranda and Aslani, 2003] captures the relationship between the performance of structural and NSEs. The framework has been implemented in the FEMA P-58 methodology, and simplified loss estimation procedures have been developed incorporating aspects of PBEE [Bradley *et al.*, 2009; Zareian, 2012, Welch *et al.*, 2014, Ligabue *et al.*, 2018, Perrone *et al.*, 2019; O'Reilly and Calvi, 2020, Del Vecchio *et al.*, 2020]. The PBEE methodology allows designers to assess the performance of a building and deagreggate expected losses between different building elements. The information on the deaggregated sources of losses can be used as a guide for identifying structural and non-structural upgrade strategies. However, it is difficult to optimize an upgrade strategy because multiple combinations of structural and non-structural upgrades should be considered using a trial-and-error approach, which requires extensive structural analyses. To optimize both structural and non-structural seismic upgrades, Steneker *et al.* [2020] recently developed a general optimization procedure in which a genetic algorithm is used within the PBEE framework. A modified version of the PBEE method, known as the Median Shift Probability (MSP) method, was also proposed by Steneker et al. *et al.* [2022] to rapidly assess the effects of structural upgrades on NSEs by considering the impacts of structural modifications on the seismic demand on NSEs.

The objective of this paper is to provide a framework that can be used in the early stage of the design process (e.g., conceptual, preliminary) to evaluate the viability of multiple integrated structural and non-structural upgrade strategies without the need for extensive analyses. Structural upgrade strategies are represented by changes in the pushover curve, damping and/or re-centering capacity of the building, while non-structural upgrade strategies are represented by changes in non-structural element's Engineering Demand Parameter (EDP) – Loss functions. Using approaches developed in previous simplified loss assessment procedures, the Expected Annual Loss (EAL) associated with each integrated structural and non-structural upgrade is estimated and used as a metric to assess the feasibility of each building upgrade strategy. The motivation for this paper is to improve the communication of risk associated with NSE damage by providing a framework that can be used to easily quantify how critical it might be to upgrade NSEs as part of a building seismic upgrade. The framework is intended to help practitioners quickly identify the potential structural and non-structural upgrade strategies that are worth allocating the resources to in order to conduct a more accurate seismic loss assessment. The first part of the paper illustrates the main steps of the proposed framework. In the second part of the paper, the framework is applied to a six-storey case study steel moment-resisting frame building to demonstrate how it can be used to quickly assess the viability of different structural and non-structural upgrade strategies.

2.OVERVIEW OF THE PROPOSED FRAMEWORK

The main steps of the proposed framework are illustrated in Figure 1 and summarized below, with more detailed explanation thereafter. The first step requires the identification and assessment of the original building (as-built) condition. The building capacity is defined by its pushover curve, which can be obtained via numerical or simplified analytical methods [Del Vecchio et al. *et al.*, 2020]. Each structural and non-structural element is characterised by an EDP-Loss function and the demand at the site is represented by the site hazard curve.

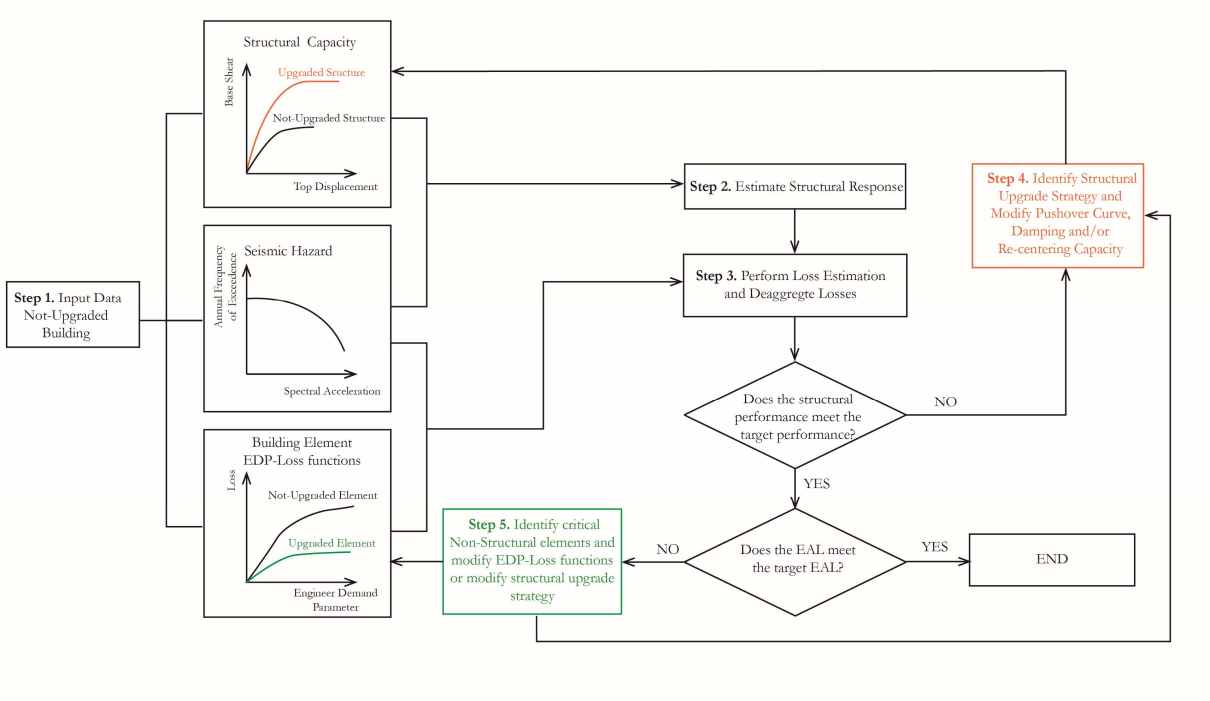

Figure 1 Overview of the proposed framework.

In the second step of the framework, the structural response for different intensity levels is obtained by combining the building's capacity with the seismic demand at the site. The loss estimation is conducted in Step 3 using the structural and non-structural element EDP-Loss functions along with the hazard curve and the structural response estimated in Step 2. The results from Step 3 can be used to determine if the structural performance satisfies that structural performance objective, which can be set by users of the framework, for example, in terms of probability of collapse. If the structural performance is judged to be inadequate, Step 4 should be followed. In this step, a structural upgrade strategy is identified and the input structural capacity is modified in accordance with the selected upgrade strategy. Typical structural upgrade strategies could take various forms such as increasing the structure's strength and stiffness, increasing its ductility, enabling the structure to self-center, adding viscous damping, or a combination of these. All these upgraded strategies can be easily addressed in the framework by modifying the pushover curve in Step 1 or the assumptions used to calculate damping and residual drift in Step 2. Once the structural performance has been determined to be adequate, the performance of both structural and NSEs should be assessed to quantify the impact of a change in the structural response on the building EAL. If the EAL does not meet the target performance objective, the critical NSEs should be identified (Step 5) and their EDP-Loss functions modified until an acceptable EAL is achieved. If this targeted performance cannot be met by retrofitting NSEs, a different structural upgrade strategy should be selected.

2.1 STRUCTURAL RESPONSE ESTIMATION

The structural response is estimated in terms of the EDPs of Peak Interstorey Drift (PID), Peak Floor Acceleration (PFA), and Residual Drift (RD), as well as collapse fragility, in accordance with the PBEE methodology. PID values are estimated using the Capacity-Spectrum approach [ATC, 1996]. In order to apply this approach, structural capacity and seismic demand both need to be plotted in the spectral acceleration versus spectral displacement domain. The pushover curve, which is described in terms of base shear and roof displacement, needs to be converted into a capacity spectrum, which is defined in terms of spectral acceleration and spectral displacement of an equivalent single degree of freedom (SDOF) system. The equivalent viscous damping at each intensity is calculated and a reduced Acceleration-Displacement Response Spectrum (ADRS) is plotted. The intersection between the reduced ADRS spectrum corresponding to a given intensity and the capacity spectrum represents the performance point of the building at that intensity (Figure 2a). After estimating the performance point at each intensity, the relationship between the pushover curve and capacity spectrum is used to calculate the corresponding roof displacements. This requires users of the framework to assume a displaced shape of the structure based on the expected failure mechanism. Results from numerical pushover analysis, or analytical methods such as those suggested by Welch *et al.* [2014] and Del Vecchio et al. *et al.* [2020], or engineering judgement can be employed for this purpose. Once a displaced shape is assumed, intersorey drift values at each intensity level are calculated. The PFA values are estimated using empirical approximations provided in the FEMA P-58-1 [2018] guidelines. Specifically, the peak floor acceleration for a given intensity level is estimated from the peak ground acceleration (PGA) using empirical coefficients that are provided for different structural systems, the estimated yield strength of the building in first mode response, the total weight and the 5% damped spectral acceleration at the fundamental period of the building. The approach suggested in FEMA P-58-1 [2018] is also used to estimate the residual drift at different intensity levels, which are calculated as a function of the peak interstorey drift ratio at that intensity and the interstorey drift ratio at yield.

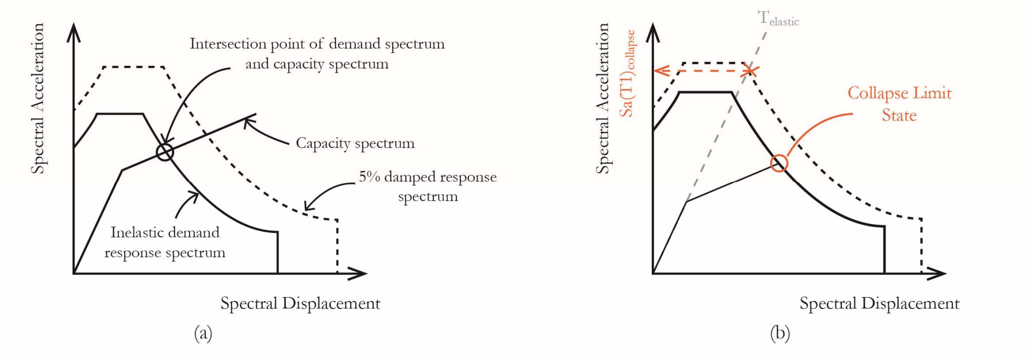

Figure 2 (a) Representation of building's capacity and demand in the spectral acceleration vs spectral displacement domain; (b) estimation of median spectral acceleration for collapse limit state.

In addition to EDP values, the collapse fragility curve of the building is required to perform the loss estimation. Several approaches have been proposed in the literature for analytical vulnerability assessment [D'Ayala *et al.,* 2015]. A simplified approach is used in this framework to estimate the median and dispersion of the collapse fragility curve. The proposed approach requires that the collapse limit state is identified on the pushover curve. In order to identify this collapse limit state, users of the framework can use the results from numerical pushover analysis or analytical considerations based on a P-delta stability coefficient and deformation/drifts limits provided for the collapse prevention limit state [Priestley *et al.,* 2007]. The intensity that will cause this collapse limit state to be exceeded can be identified in the spectral displacement-spectral acceleration domain by estimating the ADRS spectrum that intersects the last point of the bilinear pushover curve. This ADRS spectrum represents the inelastic demand on the building, and it must be scaled to obtain the 5% elastic response spectrum (Figure 2b). The elastic spectral acceleration at the first period of the structure estimated from the elastic ADRS spectrum is assumed as the 50th percentile value of the collapse fragility curve. Following the FEMA P-58-1 [2018] guidelines, a log-normal distribution is assumed for collapse and a large dispersion β equal to 0.6 is assumed as suggested for regular structures when a judgement-based collapse fragility is used.

2.2 LOSS ESTIMATION AND DEAGGREGATION

The loss estimation is performed using the approach of Ramirez and Miranda [2012]. The expected value of total economic loss in a building conditioned on ground motion intensity is calculated using the total probability theorem as the weighted sum of three mutually exclusive, collectively exhaustive scenarios: a) collapse does not occur and the building is repaired; b) collapse does not occur and the building is demolished; c) collapse occurs and the building is rebuilt. To apply the Ramirez and Miranda [2012] approach, the expected loss given that collapse does not occur and the building is repaired for a given ground motion intensity, $E[L_T|NC \cap R, IM]$, needs to be calculated. This can be done using a component-based approach [Aslani and Miranda, 2005; Mitrani-Reiser and Beck, 2007] or a storey-based approach, which uses cost distribution assumptions to estimate loss at each story [Ramirez and Miranda, 2009]. As the objective of the framework is to establish the benefit of upgrading each non-structural element, a component-based approach is used. For each element, the expected loss given that collapse does not occur and the building is repaired for a given ground motion intensity is calculated as a function of the EDP at that intensity, using component EDP-Loss functions. Peak floor acceleration or peak interstorey drift values are used as EDPs, depending on whether the non-structural element being assessed is acceleration-sensitive or drift-sensitive. The total loss due to repair of structural and NSEs is then calculated by summing up the loss from each element. Correlation between different components is neglected. Following the approach suggested by Steneker *et al.* [2020], each non-structural element is considered in the framework as either seismically or not seismically designed and thus, only two EDP-Loss functions are associated with each non-structural element. To generate each EDP-Loss function, the following equation is used:

$$E[L_j|NC, EDP_j] = \sum_{i=1}^{m} E[L_j|NC, DS_i] P(DS = ds_i|NC, EDP_j) \tag{1}$$

where m is the number of damage states in the jth element, $E[L_j|NC, DSi]$ is the expected value of loss for the jth element when it is in damage state DS_i and $P(DS= ds_i|NC, EDP_j)$ is the probability of the element being in ds_i given EDP_j. The probability of the element being in a specific damage state is calculated from the element fragility function, while the loss associated with a damage state is calculated using the element consequence function (Figure 3). To simplify the loss estimation process, the uncertainty in repair cost is neglected in the framework and an average unit repair cost URC_i is used to calculate the $E[L_j|NC, DS_i]$ as the product of the performance group quantity q_j and the average URC_i associated with each damage state:

$$E[L_j|NC, EDP_j] = \sum_{i=1}^{m} URC_i \cdot q_j \cdot P(DS = ds_i|NC, EDP_j) \tag{2}$$

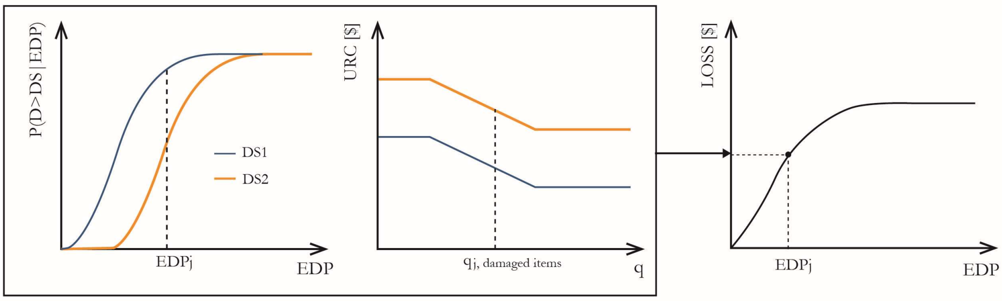

Figure 3 Key elements for developing component EDP-Loss functions: fragility functions, consequence functions and EDP-Loss functions.

The damage quantity input in the consequence function depends on how damages are aggregated to account for economies of scale. Different approaches can be used depending on aggregating damages across different floors and damage states [Banihashemi *et al.,* 2022]. In this paper, it is assumed that economies of scale are applied to all damaged items of a given non-structural element group, regardless of the degree of damage or the location of the items. Based on the selected approach, Equation 3 is used in this study to calculate the damage quantity to be input in the consequence function.

$$q_{j,damaged\ items} = \sum_{i=1}^{m} q_{j,tot} \cdot P\left(DS = ds_i \middle| NC, EDP_j\right) \quad (3)$$

where $q_{j,tot}$ is the component's quantity in the entire building.

The EAL is computed by combining the expected loss at each intensity IM estimated using the simplified framework with the site hazard curve. However, the estimation of losses as described so far neglects the uncertainty in the structural response as only a single EDP value is used to estimate expected losses for each intensity level. In order to incorporate this source of uncertainty in the estimation of EAL, the approach proposed by Sullivan and Calvi [2011] is used. The approach relies on a simplified form of the SAC/FEMA approach [Cornell *et al.*, 2002] initially proposed for use with simplified analysis by Dolšek and Fajfar [2007]. The probability of exceeding a given limit state with a certain confidence is estimated in this approach by scaling the median annual frequency for a given limit state with correction factors that account for difference between mean and median hazard, dispersion in demand and capacity and confidence level for the given limit state. As per the simplifying recommendations of Fajfar and Dolšek [2010, 2012], the correction coefficients are estimated in this study by neglecting the difference between mean and median hazard, assuming a 50% confidence level, a linear demand-intensity relationship and a dispersion factor $\beta^2_{DR}+\beta^2_{CR}$ for demand (record to record) and capacity (modeling) equal to 0.2025.

3.CASE STUDY BUILDING

The case study building used in this paper to evaluate the proposed framework is a six-storey steel moment-resisting frame with pre-Northridge Earthquake beam-to-column connections that was selected from the SAC project [ATC, 1994].

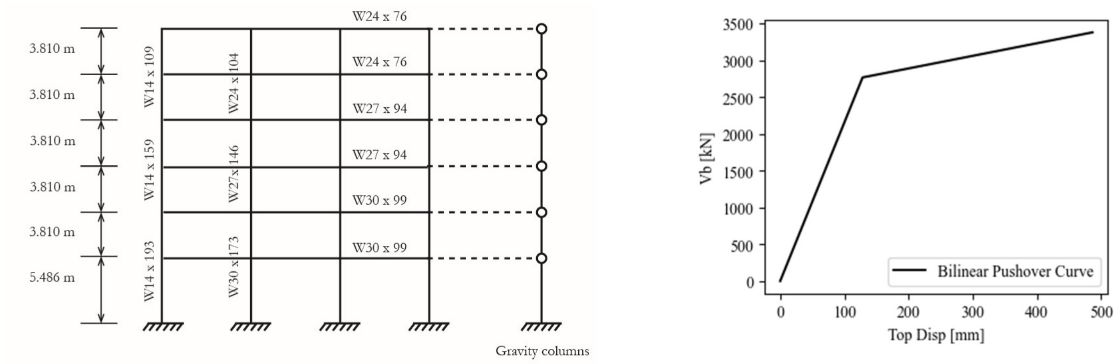

Figure 4 Case study building elevation view and bilinear pushover curve.

The building is located in the city of Los Angeles, United States, designed according to the 1994 Uniform Building Code [ICBO, 1994]. The hazard curve at the site was obtained using the USGS Uniform Hazard Tool [USGS, 2014]. The seismic force resisting system is composed of moment-resisting frames along the building's perimeter, while interior frames were designed to carry only gravity loads. The building has three bays in the North-South direction and four bays in the East-West direction, with a total floor area of 803 m^2. For this study, only the North-South direction was considered (Figure 4). The moment-resisting frames were modelled with OpenSees [McKenna *et al.,* 2000] according to a lumped plasticity approach, using *beamWithHinges* element and *Steel02* material, while the interior gravity frames were modelled using a leaning gravity column to account for P-Delta effects. Figure 4 shows the bilinear pushover curve of the building obtained through numerical investigation and bilinearization according to ATC-40 [1996]. For the purpose of this study, it was assumed as a structural performance objective that the probability of collapse at the maximum considered earthquake level should be less than 10%. The EAL targeted threshold was set at 0.2% of the building replacement cost.

3.1 SIMPLIFIED APPROACH

The response of the building was estimated following the procedure described in Section 2 for eight different intensity levels corresponding to 80%, 50%, 20%, 10%, 5%, 2%, 1%, and 0.5% probability of exceedance in 50 years. Fragility and consequence functions provided in the FEMA-P58 guidelines for Pre-Northridge beam-column joints were used to estimate the structural EDP-Loss functions. Table 1 summarizes the fragility and consequence functions used to develop the non-structural EDP-Loss functions for both seismically and not seismically upgraded configurations.

Table 1 Non-structural elements in the case study building and associated consequence functions from FEMA-P58.

Non-Structural Element	Not Seismically upgraded	Seismically upgraded	Non-Structural Element	Not Seismically upgraded	Seismically upgraded
Curtain Glazing	B2022.032	B2022.201	**Chiller**	D3031.011c	D3031.013h
Wall Partition	C1011.001a	C1011.001d	**Cooling Tower**	D3031.021c	D3031.023h
Raised Floor	C3027.001	C3027.002	**Air Handling Unit**	D3052.011d	D3052.013k
Suspended Ceiling	C3032.001d	C3032.004d	**HVAC Duct**	D3041.012a	D3041.012d
Elevator	D1014.012	D1014.011	**Motor Controller**	D5012.013a	D5012.013c
Domestic Water Piping	D2021.011a	D2021.014a	**Distribution Panel**	D5012.031b	D5012.033e
Domestic Water Piping Bracing	D2021.011b	D2021.014b	**Low Voltage Transformer**	D5012.021b	D5012.023e
Sanitary Piping	D2031.021a	D2031.024a	**Sprinkler Piping**	D4011.021a	D4011.024a
Sanitary Piping Bracing	D2031.021b	D2031.024b	**Sprinkler Head**	D4011.031a	D4011.034a

Figure 5 shows the expected loss at each intensity based on the proposed framework along with the deaggregation of losses from various sources calculated using the approach proposed by Ramirez and Miranda [2012]. The collapse probability at the maximum considered earthquake level was found to be higher than the 10% value assumed as a structural performance objective. Stiffening and strengthening of the building were chosen as structural upgrade strategies. After selecting an upgrade strategy, the structural response and the EAL of the upgraded building may be estimated by assuming a change in the pushover curve, which is considered to be achievable when implementing that upgrade strategy. Therefore, a detailed design of the upgraded building and its numerical modelling are not necessary in this phase. For the case study building, a modified pushover curve with an initial stiffness equal to twice the stiffness of the original (as-built) building was assumed, and the structural response and loss estimates associated with this modified pushover curve were calculated using the simplified framework. As illustrated in the next section, this structural upgrade strategy can be implemented by introducing a chevron braced frame in the central bay of the moment-resisting frame and installing hysteretic energy dissipating devices at one end of the bracing members. Figure 6 shows that a very small variation is obtained in the total EAL after the structural upgrade. However, the loss deaggregation shows a dramatic reduction in the EAL caused by collapse. The adopted upgrade strategy reduces the collapse probability of the building, which is now within acceptable bounds, but causes an increase in the demand on the acceleration sensitive NSEs. The loss due to repairs which comprise both structural and NSEs increases as a result of the stiffening of the building.

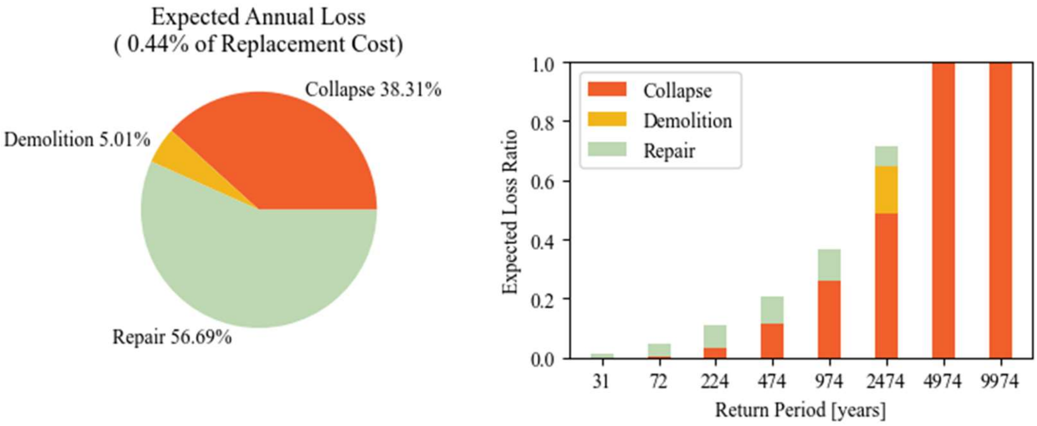

Figure 5 EAL and loss deaggregation of the case study building in as-built configuration.

To prioritize the NSEs to be upgraded, the loss estimation was performed considering a scenario in which all NSEs are seismically upgraded. The reduction in EAL due to the upgrade of each element was calculated and used as a metric for prioritization. The results in Figure 6 show that upgrades of heavy mechanical equipment may have the greatest impact on reducing the EAL. Therefore, the chiller and air handling units were selected as critical NSEs to be upgraded in order to meet the EAL performance objective. The EAL obtained by upgrading only these two elements is equal to 0.14% of the building replacement cost and thus the performance objective is achieved. Additionally, Figure 6 shows that there is only a marginal difference between the EAL values obtained when all NSEs were seismically upgraded and those obtained when only the critical NSEs were upgraded, confirming the cost-benefit value of implementing selective interventions.

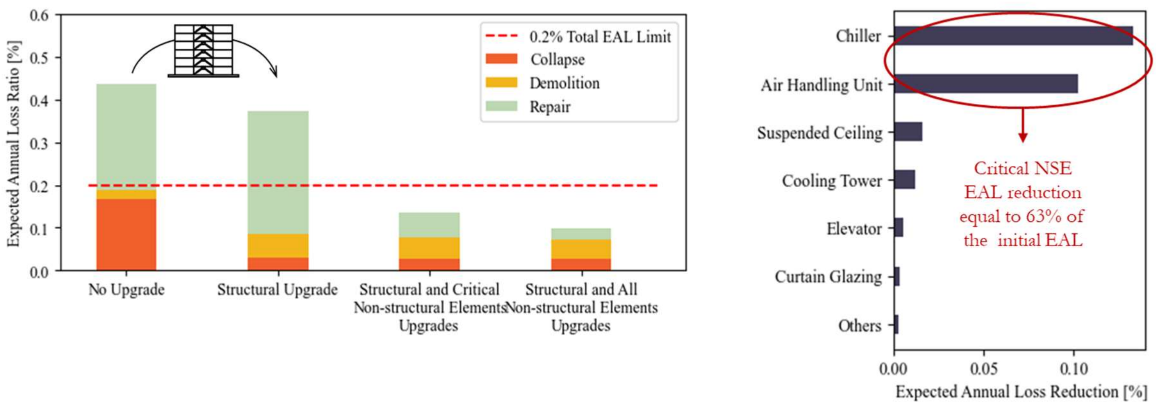

Figure 6 EAL deaggregation for different building configurations and contribution of NSE to EAL reduction.

3.2 DETAILED APPROACH

The results from the simplified framework were compared with those obtained using the FEMA P-58 methodology. As the FEMA P-58 methodology was applied using the structural response from time history analyses, it was necessary to develop a detailed design and model of the upgraded structure. The design was performed by introducing a chevron braced frame in the central bay of the moment-resisting frame and installing hysteretic energy dissipating devices at one end of the bracing members. The use of chevron braced frames and hysteretic dampers led to the pushover curve of the upgraded building that was used in the simplified framework. The retrofitted structure was modelled in OpenSees and incremental dynamic analyses were performed to estimate the response in both the original as-built and upgraded configurations. The FEMA P-695 [2009] far-field record set was used and the records were scaled so that the median spectrum of the records matches the spectral acceleration at the first period of the structure $Sa(T_1)$ at each of the eight considered intensity levels. To capture the failure of the beam-to-column connections in the numerical model, a flexural strength degradation model was introduced at the ends of the column and beam elements to capture the failure of the beam-to-column connections. As shown in Figure 7, the EAL estimated using the FEMA P-58 methodology was slightly lower than the one estimated using the proposed framework when the majority of the losses were coming from the collapse of the building (original building). When structural and non-structural upgrades were considered, the simplified framework resulted in a slight underestimation of the EAL. Overall, for the investigated case study building, the influence of various upgrade strategies on the EAL appears to be well captured by the framework, and the discrepancy between the results is considered satisfactory for a preliminary assessment approach.

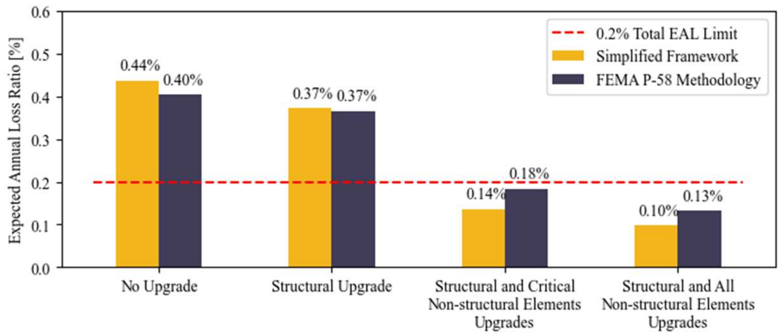

Figure 7 EAL comparison between the FEMA P-58 methodology and the proposed simplified framework.

4.CONCLUSIONS

In this paper, a simplified framework was proposed to easily compute the impact of various integrated structural and non-structural upgrade strategies on the building's Expected Annual Loss (EAL). Structural upgrade strategies are represented in the framework by changes in the building pushover curve, damping and/or re-centering capacity, while non-structural upgrades are represented by changes in the non-structural element Engineering Demand Parameter (EDP)-Loss functions.

The development of component EDP-Loss functions, which are tailored to the seismic design rating of each non-structural element, was found to be a practical and efficient method for identifying NSEs that are critical for improving the performance of a building. The results from this study show the potential of the framework as a simplified tool for quantifying the seismic risk associated with NSEs and communicating the benefit of upgrading them to stakeholders at an early stage of the design process. The framework may also help engineers to conduct a preliminary assessment and reduce the number of potential integrated structural and non-structural upgrade strategies to consider by excluding upgrade solutions that cannot achieve the target performance objectives. Although the framework's application to a case study building yielded promising results, the framework still needs to be comprehensively validated by investigating more archetype buildings and structural upgrade strategies. Furthermore, the EAL was used as a metric in this study to identify critical NSEs, but other relevant metrics, such as a net present value or a benefit-cost ratio, should be considered to perform a more comprehensive cost-benefit analysis. Future work should include incorporating the framework into a more robust optimization methodology that could benefit from the framework's ease of application to provide optimal structural and non-structural upgrade strategies based on the metrics of interest while using the limited resources available in the early design stages.

REFERENCES

ATC [1994] *Proceedings of the Invitational Workshop on Steel Seismic Issues*, Applied Technology Council and Structural Engineers Association of California. United States.

ATC [1996] *Seismic Evaluation and Retrofit of Reinforced Concrete Buildings*, ATC-40, Applied Technology Council, United States.

Aslani, H., Miranda, E. [2005] "Probabilistic Earthquake Loss Estimation and Loss Disaggregation in Buildings," *Report No. 157*. Stanford, CA: John A. Blume Earthquake Engineering Center, Stanford University.

Banihashemi, A., Miliziano, A., Zsarnóczay, A., Wiebe, L., Filiatrault, A. [2022] "Modeling Repairs in FEMA P-58: Different Interpretations and their Influence on Loss Estimates," *12th National Conference on Earthquake Engineering*, Salt Lake City, Utah.

Bradley, B., Dhakal, R., Cubrinovski, M., MacRae, G., Lee, D. [2009] "Seismic loss estimation for efficient decision making" *Bulletin of the New Zealand Society for Earthquake Engineering*, 42 (2), 96-110.

Cornell., C. A., Krawinkler, H. [2000] "Progress and Challenges in Seismic Performance Assessment," *PEER Center News*, 3, 1–3.

Cornell, C. A., Jaylayer, F., Hamburger, R. O., Foutch, D. A. [2002] "Probabilistic basis for 2000 SAC Federal Emergency Management Agency Steel Moment Frame Guidelines," *Journal of Structural Engineering* 128(4), 526–553.

D'Ayala, D., Meslem, A., Vamvatsikos, D., Porter, K., Rossetto, T. [2015] *Guidelines for analytical vulnerability assessment: Low/mid-rise*, *GEM vulnerability and loss modelling.* Global Earthquake Model (GEM) Foundation, Pavia.

Del Vecchio, C., Gentile, R., Di Ludovico, M., Uva, G., Pampanin, S. [2020] "Implementation and validation of the simple lateral mechanism analysis (SLaMA) for the seismic performance assessment of a damaged case study building," *Journal of Earthquake Engineering*, 24(11), 1771-1802.

Dolšek, M. and Fajfar, P. [2007] "Simplified probabilistic seismic performance assessment of plan- asymmetric buildings," *Earthquake Engineering and Structural Dynamics* 36, 2021–2041.

Fajfar, P., & Dolšek, M. [2010] "A practice-oriented approach for probabilistic seismic assessment of building structures," *Advances in performance-based earthquake engineering* Springer, Dordrecht, 2010. p. 225-233.

Fajfar, P. and Dolšek, M. [2012] "A practice-oriented estimation of the failure probability of building structures," *Earthquake Engineering and Structural Dynamics* 41, 531–547.

FEMA [2009] *Quantification of building seismic performance factors FEMA P695*, Federal Emergency Management Agency. United States.

FEMA [2018] *Seismic Performance Assessment of Buildings Volume 1 – Methodology (2nd Edi*t.), FEMA P-58-1, Washington, D.C.: Federal Emergency Management Agency.

ICBO. [1994] *Uniform Building Code*, International Conference of Building Officials. United States.

Ligabue, V., Pampanin, S., Savoia, M. [2018] "Seismic performance of alternative risk-reduction retrofit strategies to support decision making," *Bulletin of Earthquake Engineering*, 16(7), 3001-3030.

McKenna, F., Fenves, G.L. and Scott, M. [2000] "Open System for Earthquake Engineering Simulation." University of California Berkeley, CA.

Miranda, E., Aslani, H., [2003] "Probabilistic Response Assessment for Building-Specific Loss Estimation" *Report No. 3*, Pacific Earthquake Engineering Research Center, University of California Berkeley, CA.

Miranda E., Mosqueda G., Retamales R., Pekcan G. [2012] "Performance of nonstructural components during the 27 February 2010 Chile earthquake," *Earthquake Spectra*, 28 (1_suppl1), 453-471.

Mitrani-Reiser, J., Beck, J. [2007] "An Ounce of Prevention: Probabilistic Loss Estimation for Performance-based Earthquake Engineering," *PhD Thesis*. California Institute of Technology.

O'Reilly, G. J., Calvi, G. M. [2020] "Quantifying seismic risk in structures via simplified demand–intensity models," *Bulletin of Earthquake Engineering*, 18(5), 2003-2022.

Perrone D., Calvi P. M., Nascimbene R., Fischer E. C., Magliulo G. [2019] "Seismic performance of non-structural elements during the 2016 Central Italy earthquake," *Bulletin of Earthquake Engineering,* 17(10), 5655-5677.

Perrone, G., Cardone, D., O'Reilly, G. J., Sullivan, T. J. [2019]. "Developing a direct approach for estimating expected annual losses of Italian buildings," *Journal of Earthquake Engineering*, 26(1), 1-32.

Priestley, M. J. N., Calvi, G. M., Kowalsky, M. J. [2007] *Displacement-Based Seismic Design of Structures,* IUSS Press, Pavia, Italy.

Ramirez, C. M., Miranda, E. [2009] "Building-Specific Loss Estimation Methods & Tools for Simplified Performance-Based Earthquake Engineering," *Technical Report No. 156* Stanford, CA: John A. Blume Earthquake Engineering Center, Stanford University.

Ramirez, C. M., Miranda, E. [2012] "Significance of residual drifts in building earthquake loss estimation," *Earthquake Engineering & Structural Dynamics*, 41(11), 1477-1493.

Steneker, P., Filiatrault, A., Wiebe, L., Konstantinidis, D. [2020] "Integrated Structural–Nonstructural Performance-Based Seismic Design and Retrofit Optimization of Buildings" *Journal of Structural Engineering,* 146(8), 04020141.

Steneker, P., Wiebe, L., Filiatrault, A., Konstantinidis, D. [2022] "A framework for the rapid assessment of seismic upgrade viability using performance-based earthquake engineering," *Earthquake Spectra*, 87552930211065771.

Sullivan, T. J., Calvi, G. M. [2011] "Considerations for the seismic assessment of buildings using the direct displacement-based assessment approach*," Proceeding of the 2011 ANIDIS Conference*, Bari.

USGS [2014] *United States Geological Survey*, Unied Hazard Tool, 14 Version 4.1.9.

Zareian, F., Krawinkler, H. [2012] "Conceptual performance-based seismic design using building-level and story-level decision support system," *Earthquake engineering & structural dynamics*, 41(11), 1439-1453.

Welch DP, Sullivan TJ, Calvi GM [2014] "Developing direct displacement-based procedures for simplified loss assessment in performance-based earthquake engineering," *Journal of Structural Engineering* 18(2):290–322.

The Impact of Nonstructural Damage on Building Function

Dustin Cook[1] and Siamak Sattar[1]

[1] National Institute of Standards and Technology
100 Bureau Dr., Gaithersburg, MD 20899
e-mail: dustin.cook@nist.gov, siamak.sattar@nist.gov

Abstract. To reduce the impacts of disasters on communities, recent initiatives have focused on improving the performance of the building stock by designing for limited damage and downtime. Through these initiatives, researchers and engineers have highlighted the key role that nonstructural damage plays in building performance, especially in terms of maintaining or regaining the post-earthquake functionality of a building. While new performance-based frameworks have emerged that allow the functional recovery of a building to be probabilistically estimated based on the vulnerability of the various structural and nonstructural components within the building, it is unclear which types of nonstructural components or configurations have the largest impact on building function and the types of nonstructural system that need further research to better define vulnerability and reduce uncertainty in the assessment.

To quantify the impact of nonstructural damage on building function, we perform a sensitivity analysis on nonstructural component vulnerability using the latest performance-based frameworks. More specifically, this study investigates how variation in fragility capacity and uncertainty impacts estimates of post-earthquake building function. The sensitivity study is performed on a set of simplified structural response models covering shear-type (frames) and flexure-type (cantilever walls) response behavior and considering uncertainties in ground motion, structural response, and component performance.

This study provides key insights into the design and assessment of nonstructural components, targeting functional recovery, and helps focus the next efforts in nonstructural research. Results from the study are compared with documented empirical data on nonstructural performance in previous earthquakes and recommendations are made for future studies to improve our understanding of nonstructural performance in the areas that are most critical for recovery.

Keywords: Functional Recovery, Nonstructural Loss Analysis, Performance-Based Earthquake Engineering.

1. Introduction

The performance of nonstructural components within a building plays a crucial role in maintaining building function and mitigating downtime after earthquakes. As engineers and policymakers consider new design standards for functional recovery, the use of new performance-based methods to probabilistically quantify the functional recovery of a building, explicitly considering the performance of the building's nonstructural components, instead of just structural performance, is becoming more prevalent. However, the component fragility and consequence data that these methods rely on are sparse compared to the actual variation in nonstructural components and often not based on extensive empirical or experimental observations.

Therefore, to reduce uncertainty in recovery-based modeling, future studies should further investigate nonstructural seismic vulnerability and consequences and improve upon the readily available data. But where should we start? Which nonstructural components and systems have the largest potential impact on building function? Which nonstructural fragilities have the largest uncertainties or are based on limited data sources?

To answer these questions and to identify critical nonstructural components for future investigation, this study reviews the literature to identify the most vulnerable systems and gaps in data and performs a sensitivity study, using state-of-the-art recovery modeling methods to identify nonstructural systems and components that have the highest impact on expected post-earthquake building function. We identify the most critical components for future study as the overlap between components with the highest analytical impact on building function, those that have frequently impacted building function in previous earthquakes, and component fragility models based on the most limited data sources.

2. Nonstructural Damage in Previous Earthquakes

While post-earthquake reconnaissance and disaster failure investigations have traditionally focused on structural damage to buildings and infrastructure, recent studies have documented important nonstructural damage in earthquakes over the last few decades. From a review of these studies, we highlight commonalities among the types of nonstructural damage that impacted building function in past events. A summary of the most prevalent sources of nonstructural damage is provided in Table 1.

In review of recent earthquakes, we observe the two most common sources of nonstructural damage to be dislodging of suspended ceilings, creating a falling hazard, and water damage from burst pipes or fire sprinklers. Other common sources include elevator damage and broken windows and glazing. In this review, we specifically omitted damage to tenant contents, damage to unreinforced masonry components such as chimneys and parapets, and loss of use due to failure of an external utility or lifeline; all of these sources of damage have been shown to be prevalent in previous earthquakes and can have a major impact on building function but are outside the scope of this study.

The 1994 Northridge Earthquake in southern California caused widespread damage to nonstructural components across a large metropolitan area; there were many examples of buildings with only minor structural damage that had to be evacuated or left unoccupied due to severe nonstructural damage [EERI, 1995]. After the Northridge Earthquake, 9 % of the hospitals in Los Angeles County evacuated patients, citing nonstructural damage as a primary reason [Schultz et al., 2003]; common types of damage leading to evacuation were water damage from burst pipes, fire sprinklers, and rooftop water tanks. Other types of nonstructural damage affecting hospital function were failure of backup power systems, damage to partitions and suspended ceilings, proper ventilation, failed fire suppression systems, and damaged elevators [Yavari et al., 2010]. Among other building types, common sources of nonstructural damage impacting building function included broken windows, dislodged suspended ceilings, and perhaps most prevalent, pipe breakage and water damage, including fire sprinkler, chilled water (HVAC), and domestic water piping. Additionally, elevator damage was quite common, with 688 documented occurrences of elevators counterweight damage (EERI, 1995).

Table 1. A summary of common sources of nonstructural damage affecting building function from recent earthquakes

Earthquake	Prevalent Nonstructural Damage	Reference(s)
Northridge (CA), 1994	**Pipes (domestic, fire, and chilled) and fire sprinkler heads**, liquid storage tanks, windows, HVAC/ventilation systems, backup electrical systems, suspended ceiling, partition walls, **elevator counterweights**.	EERI, 1995 Schultz et al., 2003 Yavari et al., 2010
Nisqually (WA), 2001	**Suspended ceilings**, interior and exterior wall cracking, windows, water-line damage causing flooding.	Filiatrault et al., 2001
Maule (Chili), 2010	**Suspended ceilings, fire suppression systems, elevators,** cable trays, poorly anchored equipment.	Miranda et al., 2012 Mitrani-Reiser et al., 2012
Christchurch, (NZ), 2011	**Suspended ceilings and lightings, stairs**, elevators, rooftop equipment, partitions and fire separations, windows.	Jacques et al., 2014 CERC, 2012 Kam et al., 2014
Tohoku, (Jpn), 2011	**Suspended ceilings.**	Motosaka & Mitsuji, 2012
Napa (CA), 2014	**Storefront glazing, façades, small diameter fire sprinkler pipes, sprinkler heads**, pendant lighting, rooftop equipment.	FEMA, 2015
Kaikoura (NZ), 2016	**Suspended ceilings,** other suspended services such as lights and conduit, HVAC equipment, **glazing**.	Baird & Ferner, 2017

In the 2001 Nisqually Earthquake in Washington state, Filiatrault et al. [2001] reported that a large portion of the damage from the earthquake was due to nonstructural damage, even for buildings with well-behaved structural systems. In particular, suspended ceilings were one of the most common types of damage observed. Glass window failure shut down the SEA-TAC airport for 4 hours, and several cases of pipe damage, both mechanical and domestic, caused flooding in some buildings. Additionally, there were many reports of cracking of interior and exterior walls, but typically not significant enough to affect building function.

The 2010 Maule Earthquake in Chili caused widespread nonstructural damage disrupting the post-earthquake occupancy and functionality of many buildings, even in buildings with limited structural damage. Damage to suspended ceilings was commonly observed; most notably, in the Santiago International Airport and the San Carlos Hospital, causing major disruptions to building function [Miranda et al., 2012]. Other frequent occurrences of nonstructural damage included fire sprinkler systems–water leakage was observed in 50 % of the inspected fire suppression systems–and elevators–more than 50 % of the inspected elevators were damaged by the earthquake. Additionally, other sources of nonstructural damage included damage of cable trays (often from interactions with other systems) and poorly anchored equipment. Building facades were noted to have performed quite well due to a rigorous design process; backup power systems also performed well. Mitrani-Reiser et al. [2012] noted that in seven hospitals with relatively undamaged structural systems, the presences of significant nonstructural damage limited hospital function. In particular, damaged elevators impeded patient transport, collapsed ceilings hindered the use of certain areas and patient rooms, and minor flooding shut down surgical rooms and other services.

From the 2011 Christchurch Earthquake in New Zealand, Jacques et al. [2014] reported that much of the hospital function interruptions came from nonstructural damage; sources of loss of function included broken windows, partition wall damage (which affected function during repairs), floor coverings, and in particular, dislodged suspended ceilings and light fixtures. Other notable damage included damage to rooftop equipment causing flooding, stair damage that needed to be temporarily repaired to remain operational, and non-functional elevators. Beyond hospital facilities, damage to fire separation, ceilings, and lighting was widely observed [CERC, 2012]. Fire suppression systems were noted to have performed generally well. Of particular concern., was the collapse and severe damage of staircases in many multi-story buildings [Kam et al., 2014].

While most modern buildings in the 2014 Napa Earthquake in northern California sustained little or no structural damage, many buildings had significant nonstructural damage, resulting in some building closures for over 6 months [FEMA, 2015]. Perhaps the costliest nonstructural type of damage that occurred during the earthquake was from the rupture of fire sprinklers and the flooding that followed; these ruptures were often due to failure of small diameter piping and interactions of sprinkler heads or pipe fittings with adjacent suspended components and ceilings. Other major sources of nonstructural damage included exterior cladding, broken storefront glazing, rooftop equipment, and pendant lighting.

In the 2016 Kaikoura Earthquake in New Zealand, Baird and Ferner [2017] observed that nonstructural damage was significantly more widespread compared with structural damage. Notable damage included suspended services–such as lighting, HVAC equipment and ducts, pipework, and electrical conduit–and ceilings damage, especially where components interacted. Other widely reported damage included glazing and interior partitions, however, partition damage was mostly comprised of minor cracking, typically not significant enough to cause major disruptions in function.

3. The FEMA P-58 Nonstructural Fragility and Consequence Database

Recent performance-based assessment methods have emerged to allow the probabilistic quantification of building function and recovery given damage to structural and nonstructural components [Cook et al., 2022; Molina-Hutt et al., 2022; Terzic & Villanueva, 2021]. Following the FEMA P-58 assessment framework [FEMA, 2012] and the Porter et al. [2001] assembly-based vulnerability procedure, these methods quantify the performance of nonstructural components, in terms of their damage fragility, using data collected in the FEMA P-58 fragility database [FEMA, 2018]. This database collects fragility functions for over 700 structural and nonstructural components to help facilitate performance-based assessments. However, the source of the data forming the basis for each component fragility model varies significantly; some models come from experimental testing, some from earthquake experience data (i.e., post-earthquake field observations), some are derived from prescribed code requirements, and others are based on expert opinion. Along with the lognormal dispersion assigned to the damage states of each fragility, the source of data implies the degree of confidence that assessors should have when using these fragilities, i.e., fragility models derived from experimentation should elicit higher confidence than models derived from sparse earthquake experience data or expert opinion.

To identify the data needs among the nonstructural components within the FEMA P-58 fragility database, Table 2 lists the types of nonstructural components provided in the database according to their fragility source models. In Table 2, even when similarly labeled, the data forming the base of fragility are not necessarily equal, e.g., the experimental data for glazing and interior partition fragilities are based on a larger set of experimental tests than the stair and suspended ceiling fragilities, as indicated by the Number of Observations column.

From a review of the fragility database provided in Table 2, we observe that while many of the architectural components are derived from experimental data, many MEP (mechanical, electrical, and plumbing) components are based on limited data sources, especially distributed MEP components, whose basis of fragility is formed entirely from expert opinion. Other studies have developed fragility models based on finite element models, for example, for historic masonry infill frames with terra-cotta cladding [Dutta et al., 2009], or more recently for suspended ceilings systems [Gopagani et al., 2022]; however, these are not formally part of the FEMA P-58 database and are, therefore, not included in Table 2.

Table 2. Summary of nonstructural fragility models available in the FEMA P-58 database.

Component Type	Fragility Id Group(s)	System	Basis of Fragility	Number of Observations	Average Dispersion (β)
Cladding (precast)	B201	Exterior	Code-defined**	N/A	N/A
Glazing	B202	Exterior	Experimental	44	0.36
Tile Roofing	B301	Exterior	Experimental	24	0.35
Interior Partitions	C101	Interior	Experimental	74	0.39
Suspended Ceilings and Recessed Lighting	C303	Interior	Experimental	13	0.28
Pendant lighting	C3034	Interior	Experimental	18	0.4
Stairs	C201	Stairs and Egress	Experimental	9	0.55
Elevators	D101	Elevators	Earthquake experience	206*	0.375
Domestic and Sanitary Piping	D202, D203	Plumbing	Expert opinion	N/A	0.4
Distributed HVAC	D205, D206, D304	HVAC	Expert opinion	N/A	0.41
HVAC Equipment	D303, D304.1, D305, D306	HVAC	Earthquake experience	1305*	0.45
Fire Suppression	D401	Fire Suppression	Expert opinion	N/A	0.4
Transformers	D5011	Electrical	Earthquake experience	245*	0.5
Distribution Panels	D5012	Electrical	Earthquake experience	199*	0.425
Low Voltage Switchgear	D5012	Electrical	Earthquake experience	196*	0.4
Motor Control Center	D5012	Electrical	Earthquake experience	283*	0.425
Backup Power Equipment	D5092	Electrical	Earthquake experience	631*	0.4

**Most of the earthquake experience datapoints forming the basis for the fragility curves are from observations on non-damage in non-instrumented shaking conditions.*
***The median capacity and uncertainty for precast cladding units are derived by the user according to prescriptive code requirements and recommendations from FEMA P-58.*

4. Sensitivity Analysis: Methods

To identify the nonstructural component and fragility models with the greatest potential impact on building function, we perform a sensitivity analysis using the performance-based functional recovery method outlined in Cook et al. [2022]. This functional recovery method leverages the component fragility models and damage simulation within the FEMA P-58 framework to simulate loss of building function through a series of a fault trees, which relate component damage to system performance; component damage and building function is simulated probabilistically using a Monte Carlo simulation. To estimate loss of building function for a given shaking intensity, the method requires users to estimate the structural response to the expected ground shaking and develop a FEMA P-58-type performance model, representative of the building's vulnerable structural and nonstructural components.

For this study, we quantify the impact of variation in nonstructural component capacity and uncertainty on a set of 20 simplified performance models. Models are developed for buildings ranging from 2-10 stories, of office and multi-unit residential occupancies, and assuming two distinct response behaviors: cantilever-type and frame-type response. The functional recovery performance of each model is defined in terms of building robustness [Molina-Hutt et al., 2022], where robustness is the probability that a building maintains its basic intended function [NIST, 2021], post-event, e.g., a robustness of 0.9 is equivalent to a 90 % probability that the building will still be functional following the earthquake. We quantify the robustness of each model across eight shaking intensities, ranging from elastic response to highly nonlinear response.

The structural response of each model is estimated using the simplified response procedure outlined in the FEMA P-58 method [FEMA, 2012]. The method requires simplified inputs such as fundamental period, base shear strength, shaking intensity, mode shape, and peak ground acceleration (PGA). For each model, we assume the fundamental period of the building (T1), in seconds, is equal n/10, where n represents the number of stories. All models are assumed to have a base shear strength (Vy) of 0.2 g and are assessed for eight shaking intensities ranging from shaking equal to the base shear strength, to shaking equal to eight times the base shear strength. The shaking intensity metric is quantified as the strength ratio (S), where S equals Sa (T1) over Vy; Sa (T1) is the spectral acceleration at the fundamental period, in g's. The mode shape for each model is calculated using the approximate formula developed by Miranda [1999], assuming flexure response for the cantilever-type models and pure shear response for the frame-type models; we populate the structural components and select the nonlinear correction assuming the cantilever-response models are reinforced concrete shear walls, and the frame-type response models are reinforced concrete frames. To estimate peak floor accelerations, the PGA is calculated from Sa (T1) using the uniform hazard spectra from a site in Los Angeles California (latitude = 34.05 deg, longitude = -118.25 deg), assuming a Site Class C. The nonstructural components in each building model are populated using the FEMA P-58 normative quantities sheet [FEMA, 2018], assuming modern construction practices and anchorage requirements. Chapter 13 of ASCE 7-16 [ASCE, 2016] is used to calculate the anchorage of select nonstructural components where required by the fragility models.

To quantify the impact of variation in nonstructural component fragility on building function, we assess two sensitivity cases: (1) where we vary the median capacity of each fragility and hold constant the distributional model (e.g., lognormal) and dispersion (i.e., beta) as defined by FEMA P-58, and (2) we vary the dispersion of each fragility but leave the distributional model and the median capacity unchanged. The goal of investigating the two cases separately is to uniquely understand the impact of two separate actions: (1) modifying the failure point of a nonstructural component and (2) reducing uncertainty in nonstructural component performance. For both cases, we assess a status quo (i.e., per FEMA P-58), an upper-, and a lower-bound condition; upper- and lower-bound conditions are defined by +/- 50 % modifications to the component's median capacity or lognormal dispersion, depending on the case. Based on judgment, we select 50 % to represent a reasonable range of variation of the status quo fragility data.

To assess the sensitivity of building function to nonstructural component variation for each case, we quantify the building's robustness assuming only one major system is damageable at a time and that all components within that system are adjusted together to create the upper- and lower bound conditions; this assumption allows us to isolate any dependencies between systems and components that might hide certain impacts of fragility variation. We then repeat this process for nine major buildings systems (eight system in Table 2 and one structural system) to help identify which systems and component most impact building function.

5. Sensitivity Analysis: Results

In this study, we quantify the impact of nonstructural fragility variation on building function in terms of the building robustness, given the simulated distribution of damage. We do not quantify the time to recover building function, which is influenced by factors such as impeding times, long lead times, and repair schedule; instead, building robustness is more directly related to the fragility of the nonstructural components. The tornado plots in Figure 1a and 1b show the sensitivity of building robustness to the upper- and lower-bound modifications to the system fragility capacity and fragility uncertainty, respectively, averaged across all models for a single shaking intensity at a strength ratio equal to three (representing the point of highest overall variation in robustness). The outcomes show that variation in the fragilities of the HVAC system, electrical system, stairs, exterior, and the fire suppression system all had a major impact on building robustness. Variation in structural, plumbing, and interior fragilities had consistently less of an impact.

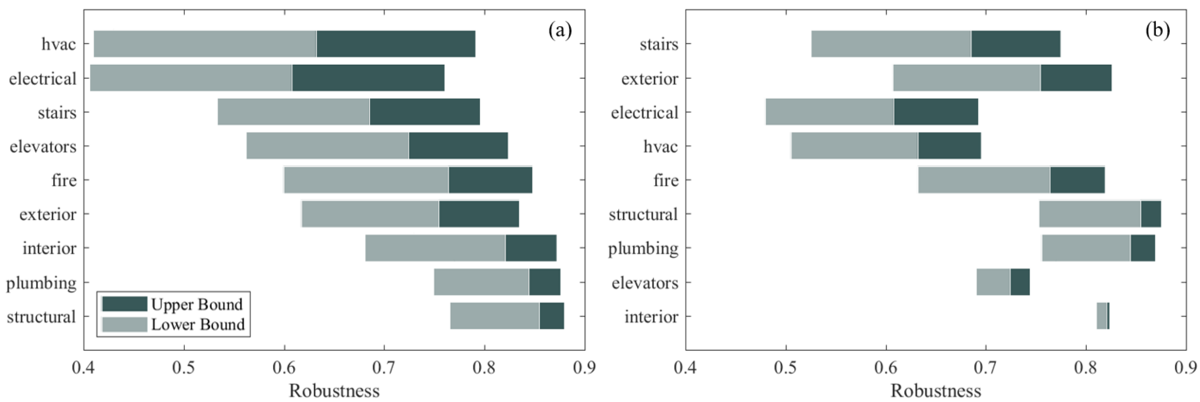

Figure 1. Tornado plots showing the impact of variation of (a) median fragility capacity (case 1) and (b) fragility uncertainty on building robustness (case 2), averaged across all models, for S = 3.

5.1 TREND WITH SHAKING INTENSITY

Figure 1 above shows the average impact of variation in component fragility models on building robustness for a single shaking intensity. However, as shaking intensity changes, so too does the relative impact of various systems on robustness. Figure 2 shows the total change in building robustness (upper bound - lower bound) as shaking intensity ranges from a strength ratio of one (essentially elastic) to a strength ratio of eight (highly nonlinear). At low shaking intensity, variation in component median capacity has only a relatively minor impact on robustness. However, as shaking amplifies, the sensitivity of robustness to the fragility model increases; the sensitivity reaches its peak around a strength ratio of three. After this, the impact begins to saturate as damage becomes so severe that even increasing the component's median capacity by 50 % is unlikely to provide many benefits. Additionally, as shaking intensity increases, the relative impact of variability in structural component capacity significantly increases compared to nonstructural damage; as structural components reach more severe damage states, the likelihood of unsafe and unstable structural conditions dramatically increases. The standard deviation in the total change in building robustness tends to range from about 0.09 at a strength ratio of three to about 0.02 at a strength ratio of eight.

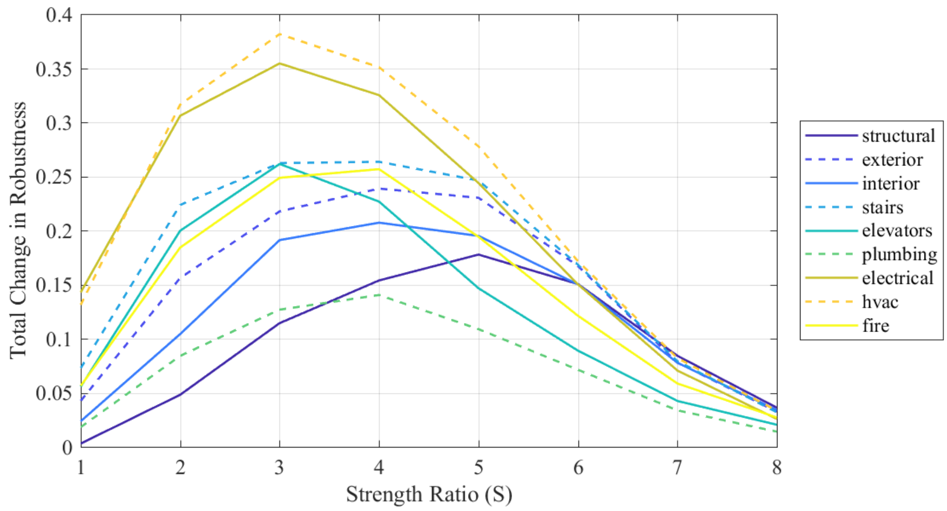

Figure 2. Total change in building robustness (upper bound – lower bound) due to variation in fragility medians (case 1) for each system, averaged across all models.

5.2 FRAME VS CANTILEVER RESPONSE

Breaking down the results among the models assessed in this study, Figure 3 shows the impact of variation in fragility median capacity on the building robustness for both the frame-type and cantilever-type response models. Both response types are similarly sensitive to variation in the fragility models of the HVAC and electrical systems. However, overall, the cantilever-type response models are less robust at the baseline and less sensitive to variation in fragility median capacities compared to the frame-type models. This difference is likely due to the amplification of accelerations and drifts throughout the building in the cantilever-type response models, compared to the tendency for a concentration of deformation demands on a single story in the frame-type response models. As a reminder, for these models, the frame-type and cantilever-type response models share the same period and base shear strength, the only difference is their response profile and structural component fragilities.

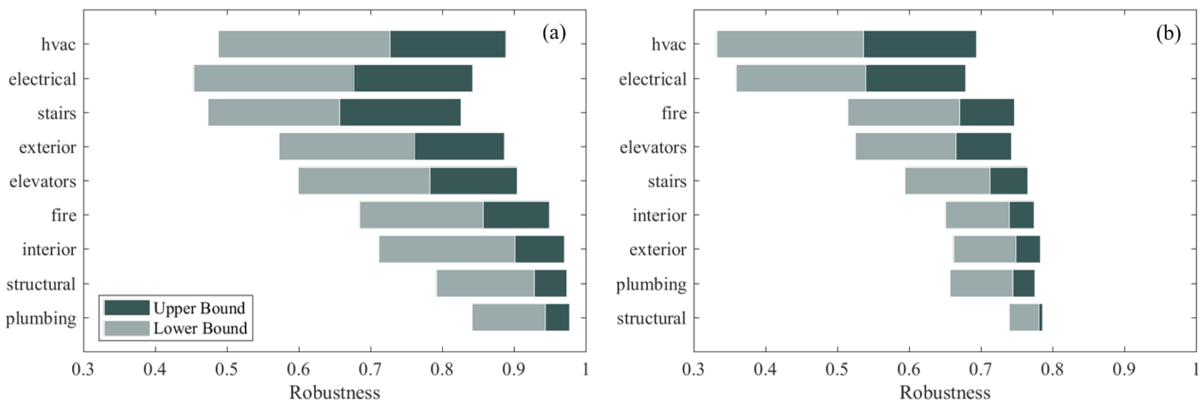

Figure 3. Tornado plots showing the impact of variation of median fragility capacity on building robustness (case 1), averaged across (a) all frame-type models and (b) all cantilever-type models, for S = 3.

5.3 OFFICE VS RESIDENTIAL OCCUPANCY

The overall influence of variation in the nonstructural fragility model on building robustness is very similar between the office and residential occupancies assessed in this study, as shown in Figure 4. The biggest difference between the models is the sensitivity of office occupancies to variations in interior component fragility models, compared to residential occupancies. This difference is directly stemming from a modeling assumption in the performance-based recovery method; the method assumes that to establish tenant function in a residential building, there is a higher tolerance for interior damage, compared to office buildings (i.e., people are more likely to continue to use their homes for their basic intended function than an office building, given the same level of interior damage).

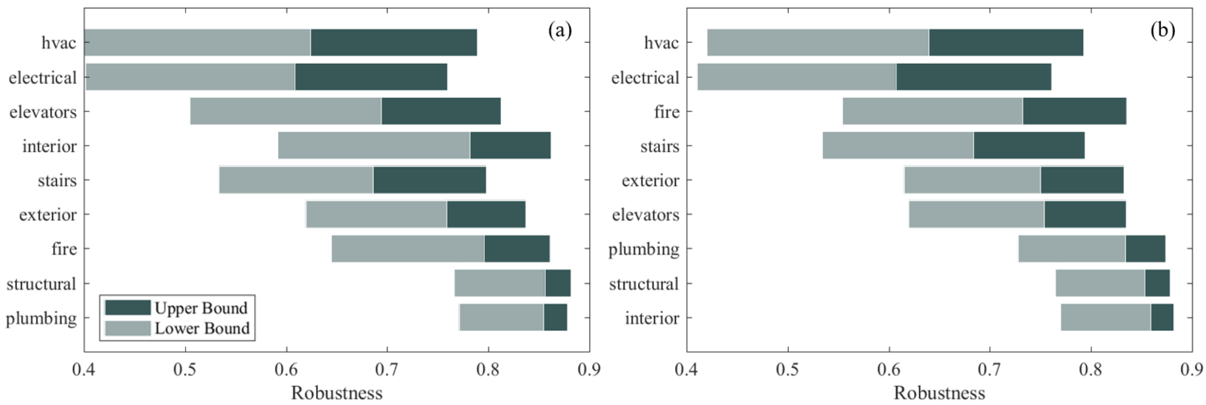

Figure 4. Tornado plots showing the impact of variation of median fragility capacity on building robustness (case 1), averaged across (a) all office occupancy models and (b) all residential occupancy models, for S = 3.

5.4 BUILDING HEIGHT

Many of the results above are presented at a strength ratio of three, representing the shaking intensity with the highest average impact on building function. However, the point of peak impact changes with the height of the building; taller buildings are more likely to lose function at lower shaking intensities compared with shorter buildings due to the increased size of the building and subsequent building systems, i.e., in a probabilistic sense, the bigger the building, the larger the systems (more components), the more possible points of failure. Figure 5a and 5b show the impact of variation in fragility median capacity for 4-story and 10-story models, respectively. Even at a lower shaking intensity (S = 2) the baseline 10-story models are generally less robust compared to the 4-story models at higher shaking intensity (S = 4). In particular, the taller buildings are more sensitive to variation in stair capacity compared to the shorter buildings.

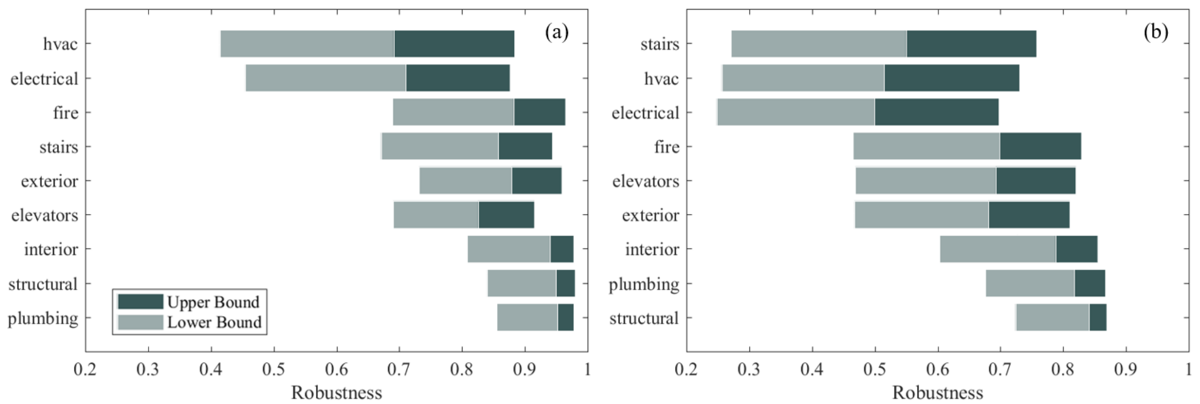

Figure 5. Tornado plots showing the impact of variation of median fragility capacity on building robustness (case 1), averaged across (a) all 4-story models at S = 4 and (b) all 10-story models at S = 2.

6. Summary and Future Work

To identify key research gaps in nonstructural seismic performance quantification, we investigated the impact of nonstructural components and fragility models on building function. In particular, we reviewed evidence of common nonstructural impacts on building function from previous earthquakes, summarized the source models and data quality forming the basis of the nonstructural fragility models in the FEMA P-58 fragility database, and performed a sensitivity analysis quantifying the impact of variation in fragility model capacity and uncertainty on building robustness using a state-of-the-art probabilistic recovery modeling framework.

From our review of earthquake damage, we observe the dislodging of suspended ceilings and broken pipes or fire sprinklers to be common sources of damage impacting building function in past earthquakes, alongside elevator damage and broken windows and glazing. From the review of the FEMA P-58 database, we found most MEP fragility models to be based on limited data, particularly for distributed components such as HVAC ducts, pipes, and fire suppression systems. Finally, results from the sensitivity analysis indicate that variability in the fragility models (median capacity and uncertainty) for HVAC and electrical components have the largest impact on building function, followed by stairs, exterior cladding and glazing, fire suppression systems, and elevators.

Taking all of these observations into consideration, we recommend that future studies focus efforts to improve the seismic performance quantification of piping components—particularly for mechanical and fire suppression systems—as these types of components were shown to have the highest impact across all sources investigated in this study. Additionally, we recommend that future studies look to improve seismic fragility models for stairs, elevators, and MEP equipment. Future studies can improve upon the fragility models in the FEMA P-58 database through a literature review of recent experimental programs that are unaccounted for in the fragility database, perform analytical failure analysis using advanced finite element models, or through an experimental testing program.

While the literature review and sensitivity analysis performed in this study was not exhaustive, this study identifies key gaps and next steps in improving quantitative analysis and prediction of nonstructural behavior and building function. While many building components common to U.S. construction were considered in this study, other nonstructural components, not explicitly considered herein, may indeed be critical for building function and susceptible to seismic excitation, and therefore, important for consideration in future studies.

REFERENCES

Baird, A., & Ferner, H. [2017]. Damage to Non-Structural Elements in the 2016 Kaikoura Earthquake. Bulletin of the New Zealand Society for Earthquake Engineering, Vol. 50, No. 2.

CERC [2012]. Final Report: Volume 2. The Performance of Christchurch CBD Buildings. Canterbury Earthquakes Royal Commission.

Cook, D. T., Liel, A. B., Haselton, C. B., & Koliou, M. [2022]. A framework for operationalizing the assessment of post-earthquake functional recovery of buildings. Earthquake Spectra, Vol. 1, No. 36.

Dutta, A., Hamburger, R. O., Citipitioglu, A., & Bono, S. T. [2009]. Advance Performance Based Analysis for Seismic Retrofit of a Historic High Rise Building. SEAOC Convention, San Diego, USA.

EERI [1995]. Northridge, California, 1994 Earthquake: Reconnaissance Report. Earthquake Engineering Research Institute

FEMA [2015]. FEMA P-1024: Performance of Buildings and Nonstructural Components in the 2014 South Napa Earthquake. Federal Emergency Management Agency.

FEMA [2012]. FEMA P-58: Seismic Performance Assessment of Buildings. Federal Emergency Management Agency.

FEMA [2018]. FEMA P-58: Seismic Performance Assessment of Buildings: Second Edition. Federal Emergency Management Agency.

Filiatrault, A., Uang, C.-M., Folz, B., Chrstopoulos, C., & Gatto, K. [2001]. Reconnaissance report of the February 28, 2001 Nisqually (Seattle-Olympia) Earthquake. Pacific Earthquake Engineering Research Center,

Gopagani, S., Perrone, D., Filiatrault, A., & Aref, A. [2022]. Finite Element Modelling for Seismic Damage Estimation of Suspended Ceiling Systems. 12th National Conference on Earthquake Engineering. Salt Lake City, USA.

Jacques, C. C., McIntosh, J., Giovinazzi, S., Kirsch, T. D., Wilson, T., & Mitrani-Reiser, J. [2014]. Resilience of the canterbury hospital system to the 2011 Christchurch earthquake. Earthquake Spectra, Vol. 30, No. 1.

Kam, W. Y., Pampanin, S., & Elwood, K. J. [2014]. Performance-Based Issues from the 22 February 2011 Christchurch Earthquake. Geotechnical, Geological and Earthquake Engineering, Vol. 32, pp. 159–175

Miranda, E. [1999]. Approximate Seismic Lateral Deformation Demands in Multistory Buildings. Journal of Structural Engineering, Vol. 125, No. 4.

Miranda, E., Mosqueda, G., Retamales, R., & Pekcan, G. [2012]. Performance of nonstructural components during the 27 February 2010 Chile earthquake. Earthquake Spectra, Vol. 20, No. S1.

Mitrani-Reiser, J., Mahoney, M., Holmes, W. T., de La Llera, J. C., Bissell, R., & Kirsch, T. [2012]. A functional loss assessment of a hospital system in the Bío-Bío province. Earthquake Spectra, Vol. 20, No. S1.

Molina-Hutt, C., Vahanvaty, T., & Kourehpaz, P. [2022]. An Analytical Framework to Assess Earthquake Induced Downtime and Model Recovery of Buildings. Earthquake Spectra. Vol. 38, No. 2.

Motosaka, M., & Mitsuji, K. [2012. Building damage during the 2011 off the Pacific coast of Tohoku Earthquake. Soils and Foundations, Vol. 52, No. 5, pp. 929–944.

NIST (2021). NIST-FEMA Special Publication FEMA P-2090/NIST SP-1254: Recommended Options for Improving the Built Environment for Post-Earthquake Reoccupancy and Functional Recovery Time. National Institute of Standards and Technology.

Porter, K., Kiremidjian, A., & LeGrue, J. [2001]. Assembly-Based Vulnerability of Buildings and Its Use in Performance Evaluation. Earthquake Spectra, Vol. 17, No. 2.

Schultz, C. H., Koenig, K. L., & Lewis, R. J. [2003]. Implications of Hospital Evacuation after the Northridge, California, Earthquake. The New England Journal of Medicine. Vol. 348.

Terzic, V., & Villanueva, P. K. [2021]. Method for probabilistic evaluation of post-earthquake functionality of building systems. Engineering Structures, Vol. 241.

Yavari, S., Chang, S. E., & Elwood, K. J. [2010]. Modeling post-earthquake functionality of regional health care facilities. Earthquake Spectra, Vol. 26, No. 3, pp. 869–892.

Seismic Evaluation of Existing Unreinforced-Masonry Partition Walls to Achieve Project Goals

Atilla Kurt[1] and Adam Rush, P.E. [2]

[1] Simpson Gumpertz & Heger Inc.
1625 I St. NW, Suite 900, Washington, D.C., 20006
e-mail: akurt@sgh.com
[2] Simpson Gumpertz & Heger Inc.
1625 I St. NW, Suite 900, Washington, D.C., 20006
e-mail: arush@sgh.com

Abstract. Unreinforced-masonry partition walls – be they brick, concrete, or terra-cotta – are commonly encountered in existing buildings. Due to their relatively high mass and brittle properties, these walls are particularly susceptible to damage during seismic events. When renovating a building with masonry partition walls, code requirements or observed conditions may trigger a need for the structural engineer to evaluate their stability and capacity. Examples of observed conditions include lack of original detailing to brace or support the tops of walls, unaccounted-for wall penetrations, and poorly executed modifications from earlier renovation projects. While it can sometimes be easier to replace masonry partitions with more contemporary types of construction, less destructive mitigation efforts, such as demonstrating adequate capacity or minor repair/strengthening, can help to achieve project goals. This is especially true in buildings of historic significance where preservation of these walls may have wider value. This paper provides examples of a previous renovation project to demonstrate common code triggers and in-situ conditions that necessitate evaluation and possible strengthening of masonry partitions in existing buildings. It will also describe multiple analysis techniques (ranging from simple to nonlinear/performance-based) successfully deployed in this project.

Keywords: Masonry, Partitions, Code, Renovation, Seismic, Evaluation, Analysis

1. Introduction

Non-structural unreinforced masonry (URM) partitions are commonly encountered in existing buildings. These walls are typically slender and not specifically engineered to resist external loads. These characteristics combined with plain masonry's characteristically brittle qualities, make these walls susceptible to damage due to out-of-plane loads during seismic events. When renovating a building with URM partitions, code requirements and/or observed conditions may trigger the need for the Engineer of Record (EOR) to evaluate their ability to resist out-of-plane seismic loads. This paper discusses some of the existing conditions and code requirements (within the context of governing building codes in the United States) that warrant analysis and potential retrofit. This paper also provides project examples of as-built conditions, analysis techniques, and creative in-situ strengthening solutions.

2. Code Provisions

Unreinforced masonry (URM) partition walls present a common and well-understood fall hazard during a seismic event. Recognizing this hazard, modern building codes require that new construction projects provide details to laterally brace partition walls and provide specific guidance to design those of details, and, as a result, this hazard is greatly reduced in code-compliant new construction and renovation projects. Interestingly, not all renovation projects require seismic evaluation of existing URM partition walls. Minor interior renovations often fall below the code provisions triggering seismic analysis and retrofit of URM partition walls. This paper will review code provisions from the International Existing Building Code dated 2018 (IEBC 2018) [ICC, 2018b] related to URM partition walls and will offer examples on how to respond.

In the United States, local jurisdictions adopt versions of model design codes produced by the International Code Council (ICC) as the basis of their local building codes (such as the IEBC 2018). Each city, state, or county may then elect to make changes to specific provisions within the adopted code. While these variations may be significant, using the IEBC 2018 code provisions for this paper provides sufficient guidance to a broad audience.

Renovation projects involving buildings with existing URM partition walls typically fall under two categories: Repairs or Alterations. Code compliance for Repair projects is straightforward: re-establish the original existing capacity or bring it up to modern codes. For Repair projects, only URM partition walls with existing damage require retrofit. Code compliance for Alteration projects under the IEBC 2018 provisions is less straightforward, with three broad compliance options available.

i. Prescriptive Compliance Method: A simplistic method intended to prescribe the minimum requirements for modifying existing buildings.

ii. Work Area Method: A flexible method intended to encourage reuse of existing buildings by allowing different levels of compliance based on the level of work occurring.

iii. Performance Compliance Method: A complicated method intended to provide a rational, numerical scoring system to evaluate the safety of existing buildings that otherwise would not satisfy modern code standards.

Specific code provisions governing URM partition walls are included with each compliance method as noted below:

- Prescriptive Compliance Method: Section 503.10 "Anchorage of unreinforced masonry partitions in major alterations"
    - "Where the work area exceeds 50 percent of the building area, and where the building is assigned to Seismic Design Category C, D, E or F, unreinforced masonry partitions and nonstructural walls within the work area and adjacent to egress paths from the work area shall be anchored, removed or altered to resist out-of-plane seismic forces, unless an evaluation demonstrates compliance of such items. Use of reduced seismic forces shall be permitted."
- Work Area Method: Section 906.7 "Anchorage of unreinforced masonry partitions"
    - Level 3 Alteration: Work area exceeds 50 percent of gross area of building.
    - "Where the building is assigned to Seismic Design Category C, D, E or F, unreinforced masonry partitions and nonstructural walls within the work area and adjacent to egress paths from the work area shall be anchored, removed, or altered to resist out-of-plane seismic forces, unless an evaluation demonstrates compliance of such items. Use of reduced seismic forces shall be permitted."
- Performance Compliance Method: Section 1301.4.1 "Structural analysis"
    - If read loosely, this provision requires assessment of URM partition walls to satisfy the bracing requirements for new construction.

Comparing the URM partition wall code provisions across the three compliance methods is useful to understand the intent of the code. Taken together, IEBC 2018 requires evaluation of existing URM partition walls under specific circumstances:

i. Major renovations (work areas exceeds 50 percent of building area AND seismic design category of the existing building is C, D, E or F (Alteration projects), OR

ii. Existing damage to URM partition walls (Repair projects)

The result of these provisions is that small renovation projects in low seismic zones often do not trigger code provisions requiring seismic evaluation of existing URM partition walls. This is not too surprising because the seismic demand on these walls in low seismic zones are close to loads from internal wind pressures, as the example project included later in this paper will demonstrate. That said, seismic evaluation of existing URM partition walls may be warranted due to uncovered existing conditions during construction or project modifications to the walls (e.g., new mechanical penetrations). The intention of the code is to improve public safety with larger projects as made clear by the levels where assessment of URM partition walls becomes required.

3. Evaluation

3.1 COMMON CONSTRUCTION

URM partition walls comprise many individual masonry units connected via mortar joints. Brick, concrete, and terra-cotta are a few commonly encountered base materials for these walls. Each of these materials are relatively dense, inherently weak in tension and much stronger in compression.

URM partition walls do not support gravity loads from the floor framing, and therefore are often built to be relatively slender (large height-to-thickness ratio). To maintain general stability, these walls are laterally braced to supporting structure. Examples of this include walls constructed with the base on a structural floor slab and the top tight to the underside of framing above (friction providing lateral support) (see Figure 1) or intermittently braced laterally (tie-backs) to a structural back-up wall (Figure 1).

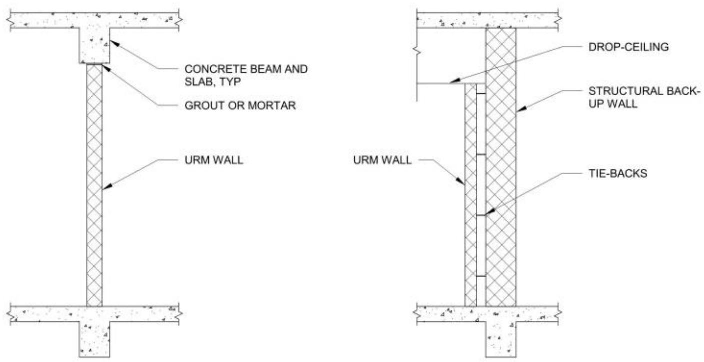

Figure 1. URM Partition Wall Support Conditions

In the absence of closely-spaced and sufficiently stiff lateral supports, slender, relatively heavy, and brittle URM partition walls are highly susceptible to damage due to out-of-plane seismic loading. Flexural tensile stresses that develop due to the out-of-plane loads may exceed the masonry's capacity, resulting in damage that may compromise the integrity of the partitions.

3.2 EVALUATION PROCEDURE – LOAD CALCULATION

After establishing that the existing partitions require evaluation per IEBC, the next rational step is to generate the demands and check the URM partition wall capacities. A useful resource to follow is ASCE 41 – *Seismic Evaluation and Retrofit of Existing Buildings* [ASCE, 2017] Chapter 13, which broadly establishes provisions for evaluating architectural components, including URM partition walls. Prior to analysis, the engineer must first gain an understanding of the existing conditions. To achieve this, the engineer would first review all available documentation (existing design drawings, previous reports, etc.) which may provide information on partition wall construction. Next, the engineer would conduct a visual survey of the existing partitions in accordance with ASCE 41 Section 13.2.1. The authors note that in some instances, condition assessments of existing URM partitions may reveal instabilities, material deficiencies, or otherwise unsafe conditions that compel the engineer to address existing conditions through strengthening/retrofit or removal and replacement regardless of whether the IEBC requires evaluation of URM partition walls.

The analytical procedure outlined in ASCE 41 Section 13.4.1 is a good resource to calculate the seismic demand on URM partition walls. ASCE 41 Table 13.1 requires that both force analysis (Section 13.4.3) and deformation analysis (Section 13.4.4) be performed for URM partitions. Engineers in higher seismic zones should not neglect reviewing the performance of URM partition walls subjected to large seismic story drifts. The project example included in this paper did not have significant story drifts and therefore this paper will only focus on the force analysis methods from ASCE 41. The lateral seismic force on URM partitions, F_p, applied at mid-height shall be calculated in accordance with ASCE 41 equation 13.1 (Equation 1 below), but must not be greater than

ASCE 41 Equation 13.2 (Equation 2 below) and less than ASCE 41 Equation 13.3 (Equation 3 below). Refer to Table 1 below for variable descriptions and to ASCE 41 for further limitations.

$$F_p = \frac{0.4 a_p S_{XS} W_p \left(1 + \frac{2x}{h}\right)}{\left(\frac{R_p}{I_p}\right)} \tag{1}$$

$$F_{p,max} = 1.6 S_{XS} I_p W_p \tag{2}$$

$$F_{p,min} = 0.3 S_{XS} I_p W_p \tag{3}$$

Table 1. ASCE 41 Equation 13.1 Variables

Variable	Description
a_p	Component amplification factor from ASCE 41 Table 13.5-1 or 13.6-1 of ASCE 7
S_{XS}	Spectral response acceleration parameter at short periods for the Seismic Hazard Level associated with the Structural Performance Level for the building determined in accordance with Section 2.4.1.6 or 2.4.2.1 of ASCE 41
W_p	Component operating weight
x	Elevation in structure of the average point of attachment of the component to the structure.
h	Average roof elevation of structure, relative to grade elevation
R_p	Component response modification factor from Table 13.5.1 or 13.6-1 of ASCE 7
I_p	Component importance factor as set forth in Sections 13.6-13.8 of ASCE 41

As can be seen from the equations – and as would be expected – the seismic loads generally increase with increasing wall weight, seismicity, building importance level, and wall elevation relative to building height. Interestingly, we have found that for buildings with low importance factors (I or II) located in low seismic zones, the lateral seismic load calculated as shown above may not control over the code-prescribed [ICC, 2018a] internal wind pressure of 5 psf. This is true even for relatively heavy URM partitions.

3.3 Evaluation Procedure – Out-Of-Plane Capacity

Understanding common failure mechanisms of URM partition walls is important to guide the analysis and capacity review of these walls. For example, walls that lack sufficient lateral restraint at their top are prone to tipping over in large sections compared to walls with the top restrained, which commonly fail around wall openings (or at mid-span in the absence of openings). When subject to out-of-plane lateral loads, URM partitions experience several stresses. These stresses primarily consist of shear and flexural tensile stresses within mortar joints. Mortar joint shear stresses are resisted by friction and chemical bond between masonry units and the mortar. TMS 402-13 – *Building Code Requirements for Masonry Structures* [TMS, 2013] chapter 9.2 provides linear-elastic calculation procedures for determining shear and bending capacities of unreinforced masonry elements. For flexure, this reference utilizes the limit state of flexural tensile stresses (assuming linear stress distributions) within the mortar to determine the ultimate bending capacity. The resisting flexural tensile stresses of mortars are based on the modulus of rupture test and generally considered conservative. However, this code is primarily focused on the design of new structures. Beckmann and Bowles [2004] state that the tensile capacity of joints in most historic structures is often negligible. Furthermore, they state that cracking of a bed joint does not immediately trigger a failure. Beckmann and Bowles describe that URM walls with cracked bed joints can still resist flexure, with the primary resisting mechanism resulting from the cross-section's compressive stress distribution's net eccentricity relative to the section's centroid (see Figure 2). Thus, limiting the out-of-plane flexural capacity to the product of the axial load (i.e., self-weight only for URM partition walls) and the maximum eccentricity (half of wall thickness) that can be developed within the thickness of the masonry unit.

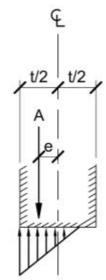

Figure 2. Free-body diagram of Masonry Unit Subject to Flexure and Compression Neglecting Tensile Stresses

This simplified theory, while generally valid, is based on static equilibrium, effectively neglecting beneficial kinematic effects that can reasonably be justified in dynamic events, such as earthquakes. The most prevalent such kinematic mechanism for masonry walls is arching. In short, arching assumes that after the development of tension cracks at both the centre and ends of the wall, two separate rigid bodies compress as they rotate due to sufficiently rigid boundary conditions (see Figure 3). Thus, the arching capacity of URM walls is mostly limited by their compressive properties and the rigidity of the supports, rather than their inherently weak tensile properties. EQE International [1998] describes a method for using the arching mechanism to calculate out-of-plane capacity for URM walls. This method iteratively calculates lateral load-resisting capacity resulting from arching that develops due to out-of-plane displacement/rocking of the wall confined by supporting structures at the top and bottom of the wall (for vertically-spanning walls). While somewhat complex, spreadsheets and modern solvers are sufficiently capable of efficiently performing this calculation. This method is further described in Section 4.1.2 below.

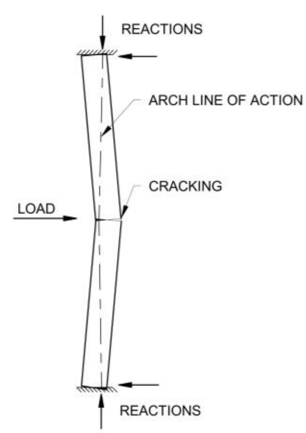

Figure 3. Section of URM Wall Showing Arching Mechanism

4. Project Example

The following project example is provided to demonstrate the application of the building code provisions to a specific project and highlight the need to adapt to existing conditions as they present themselves. The example project consists of the renovation of gallery and storage spaces within the Baltimore Museum of Art (BMA) in Baltimore, MD, USA. The goal of the project was to improve the storage and accessibility of the museum's prized collection by creating a Prints, Drawings, and Photographs (PDP) Center for academic study and renovating an existing library space for the museum staff.

The BMA began with the originally constructed John Russell Pope Building (1927) to serve as the central building, with a series of additions including the Jacobs Wing (1936), the May Wing (1949), the Cone Wing (1955), the East Wing (1980), and the West Wing (1990). The entire museum space is 275,861 square-feet in area (25,628 square meters) and is three stories tall with a maximum height of roughly 58 feet (17.7 meters) above grade (plus partial basements and penthouse spaces). Though not specified on the original drawings, the building's existing lateral system consist of unreinforced masonry load bearing walls.

The PDP Center renovation project occurs in the centre cluster of buildings, specifically within the Pope Building and the Cone Wing. The area impacted by this renovation is 20,445 square-feet (1899 square-meters) which is 7.5% of the total building area. This is clearly below the 50% work area limit for a Level 2 alteration as described in IEBC 2018. The structural work did not increase that lateral loads on the building nor decrease the lateral capacity of the building and, therefore, no seismic upgrades or interventions were required for the project. The building risk category was 2 with low ground accelerations leading to a seismic design category = B. With the work area being less than 50% and the seismic design category = B, the IEBC did not require evaluation of the existing URM partition walls for seismic performance. Because the project scope did not include significant modifications to the existing URM partition walls, they were not reviewed for seismic performance for out-of-plane motion during design.

4.1 Evaluation Of Existing Conditions

Removal of existing finishes during construction exposed a few URM partition wall conditions that warranted seismic assessment for stability. These conditions were not apparent during the design phase and required immediate action during construction. One goal of this paper is to share lessons learned from this project with design professionals encountering a similar situation. Below, we discuss three specific examples from this project that required evaluation and potential remedial action.

4.1.1 Case 1 – Short URM Partition Wall Without Bracing to Back-Up Wall

Case 1 presented herein represents a short, 4 in. (10 cm) thick unreinforced CMU wall whose as-constructed condition after removal of architectural finishes was devoid of lateral restraint (Figure 4). Prior to removal of finishes, there existed a heavily reinforced ornamental plaster ceiling that we suspect acted as lateral restraint for the top of the wall. Though adjacent to a load bearing wall, there were no tie-backs to the structural back-up wall resulting in an unstable condition, necessitating stabilization or removal and replacement. In this situation, we were incentivized not to go through the costly process of removal and replacement. Therefore, we decided to evaluate the wall for its out-of-plane capacity and potential retrofit solutions.

Figure 4. Short Unbraced Unreinforced 4 in. CMU Wall

In these instances, we generally find that starting the evaluation with simple, conservative methods can be both cost and time effective. In the context of URM walls subject to out of plane lateral loads, without sufficiently stiff boundary conditions to develop arching, this typically means conventional simple beam analysis as described herein. In this scenario, we analysed the wall as a vertically-spanning simply-supported member, assuming that at a minimum we would also have to design a strengthening solution to laterally brace the top of the wall.

As described above, first the lateral loads are calculated in accordance with Chapter 13 of ASCE 41. Next the flexural and shear demands are calculated based on simply-supported beam analysis, by considering a vertically-spanning design "strip." These demands are then compared to the wall's capacity.

To determine the flexural capacity of the wall, we assumed a conservative mortar tensile rupture stress normal to the bed joints and calculated the maximum ultimate moment based on an elastic stress distribution, as described by TMS 402. We also checked the wall for out-of-plane shear per TMS 402, as well as the ability for base friction to laterally restrain the wall at its base. We find that shear generally does not control the wall's capacity. Due to the short height of this specific wall, we were able to justify adequate capacity of this wall using simplified analysis.

In the context of this case study, once the wall was deemed to have adequate shear and bending capacity, the post-installed top of wall restraint had to be designed to satisfy the lateral support requirements. Our project team came up with a cold-formed steel "z-clip" solution (see Figure 5 below), which proved to be effective and easy to construct.

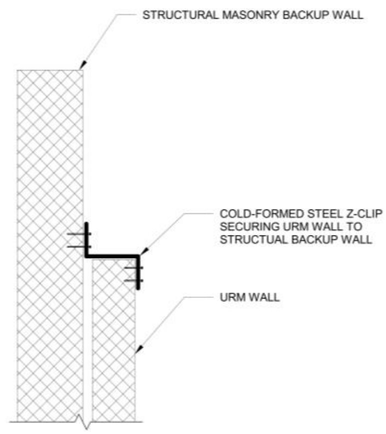

Figure 5. Z-Clip Securing URM Wall to Structural Back-up Wall

4.1.2 Case 2- Tall URM Partition Wall Built Tight to Underside of Structure Above

Case 2 presented herein represents a tall, slender URM infill wall bearing on structure at its base and built tight to the underside of structure above (see Figure 1). While general stability of this wall is not of concern, the detailing of attachments, or lack thereof, brings into question its ability to resist out-of-plane loads. Again, presented with the cumbersome and costly process of removal and replacement, we were incentivized to demonstrate that the wall had adequate capacity. In cases of infill walls, TMS 402 [TMS, 2013] explicitly states that it is inappropriate to base the out-of-plane flexural capacity on the flexural tensile capacity of the mortar joints, stating that arching acts as the primary resisting mechanism. TMS 402 provides arching capacity equations, which rely on specific detailing requirements. Thus, we considered the non-linear arching behaviour of the wall in accordance with the procedure described by EQE International [1998], which we found to contain less stringent detailing requirements and to generally be more broadly adaptable to different as-built conditions.

As described previously, first the lateral loads are calculated in accordance with Chapter 13 of ASCE 41. Next, we rely on EQE International [1998] to calculate the wall's capacity resulting from its ability to arch vertically between supports. This arching develops due to out-of-plane displacement/rocking of the wall, which is confined by supporting structures at the top and bottom of the wall. Thus, both the properties of the wall as well as the boundary conditions afforded by the confining structure are considered in this analysis. We provide a brief outline of this method below – refer to EQE International [1998] for a more detailed description. Note that the calculations described conceptually below have corresponding equations that can be found in the referenced text.

i. First, parameters related to assumed crushing at the supports are calculated. These parameters include the effective thickness of the masonry that crushes, as well as the local crushing capacity.

ii. Next, factors related to the eccentricity of the wall reaction relative to its support are calculated. These parameters are related to the torsional stiffness of the supports.

iii. Finally, the maximum out-of-plane capacity for vertical arching is calculated using the reserve energy method. This process involves a system of equations through which the maximum arching force is calculated via incrementing the lateral displacement of the wall. During this incrementing process, the maximum distance of which the wall is in contact with its supports (typically beams or slabs above/below) is calculated. Due to the relationship between the compression within the wall and its contact with its confining supports, the actual arching value can be controlled by the support's stiffness and/or its strength.

While this calculation was developed with empirical relationships demonstrated to be acceptable, there are some assumptions required. These include the material properties of masonry, as well as the gap between the masonry wall and its top support. Therefore, we stress the importance of assessing the condition of the wall being analysed to justify said assumptions. For example, during our renovation of the BMA cone wing, we required the contractor to dry-pack mortar at the tops of all walls whose capacity to resist out-of-plane seismic loads was justified utilizing this arching action calculation.

The demand-to-capacity ratio from the arching analysis was more than twice as high as that from linear-elastic analysis based on flexural tensile capacities commensurate with new construction. Although this comparison is partially flawed (see above), in the absence of proper detailing allowing one to rely on arching per modern codes, it is the next logical method of calculating out-of-plane capacity. Furthermore, this case study proves the premise that while simple, conservative analyses have their place in practice, the capability to perform higher-order non-linear analyses can significantly enhance project delivery.

4.1.3 Case 3 – Cold-Formed Steel Back-up Stud Wall Retrofit

In some cases, simple analysis does not prove sufficient wall capacity and the boundary conditions are not conducive to arching of the wall. One such example is shown in Figure 6, which features a URM partition wall below a clerestory window laterally tied back to concrete-encased steel beams. While the tie-backs provide lateral support, they are not sufficiently stiff/strong to develop arching. Additionally, the tie-backs were spaced such that substantial bending and shear would develop between supports when the wall is subject out-of-plane loads.

Our chosen solution for this condition was laterally supporting the wall with a cold-formed steel (CFS) stud wall (see Figure 6). The CFS stud wall was designed to resist out-of-plane seismic loads from its and the URM partition wall's weights. Intermittent tie-backs between the CFS stud wall to the URM wall were spaced such that insignificant demands would develop within the URM wall.

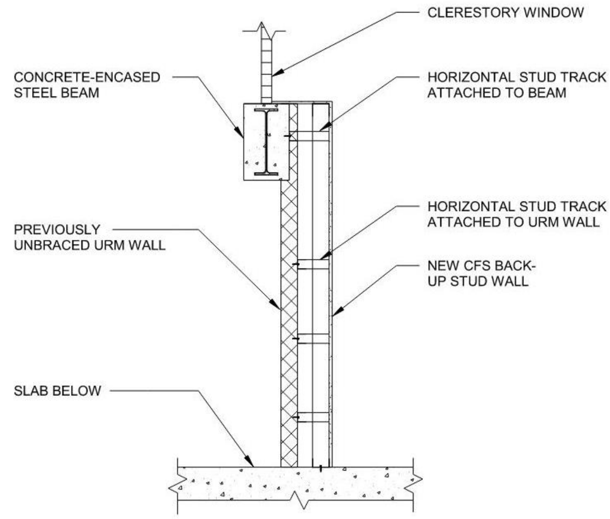

Figure 6. CFS Back-up Stud Wall Retrofit

While this solution accompanied a fair amount of trade-off (reduced floor space, considerable amounts of new materials, etc.), it still proved to be the most cost- and time-effective solution since it eliminated the need to remove and replace the entire wall, thus helping to meet the desired project delivery goals.

5. Conclusions

This paper demonstrated that there are both building code-related and in-situ condition-related triggers that necessitate evaluation of URM partition walls. Understanding the code provisions that require seismic evaluation of URM partition walls allows engineers to plan accordingly with larger projects. Evaluating the seismic capacity of non-structural components is time-consuming and can overwhelm project budgets if not addressed early. The examples included in this paper cover simple, linear and complex, nonlinear analysis techniques that may be used to evaluate these walls, both of which have their place in general structural engineering practice. Ultimately, evaluation and/or savvy retrofit can help achieve project delivery goals, be they primarily driven by cost, construction time, or both.

REFERENCES

ASCE [2017] *Seismic Evaluation of Retrofit of Existing Buildings*, American Society of Civil Engineers, US.

ASCE [2016] *Minimum Design Loads and Associated Criteria for Buildings and Other Structures*, American Society of Civil Engineers, US.

EQE International [1998] "Development of Seismic Evaluation Criteria for URM Infill Frames Including Independent Review of Oak Rice HCTW Test Program," *Research*, Center for Natural Phenomena Engineering, US.

Beckmann, P. and Bowles R. [2004] *Structural Aspects of Building Conservation*, Elsevier Butterworth Heinemann, Oxford, UK.

ICC [2018a] *International Building Code*, International Code Council, USA.

ICC [2018b] *International Existing Building Code*, International Code Council, USA.

TMS [2013] *Building Code Requirements for Masonry Structures*, The Masonry Society, USA.

Seismic Performance of Pre-Fabricated Façade Panels

Alexander (Sasha) Itsekson, S.E. [1]**, Eric Guetter, P.E.** [2]

[1] Principal, Sr. Façade Structural Specialist, RDH Building Science
405 14th Street, Oakland, CA, USA
sitsekson@rdh.com
[2] Associate, Project Engineer, RDH Building Science
405 14th Street, Oakland, CA, USA
eguetter@rdh.com

Abstract: A combination of factors including budget constraints, reduced construction timelines, and higher energy performance targets are pushing project teams to pursue large format prefabricated exterior wall assemblies, often referred to as megapanels. Similar in scale to large-format architectural precast facades, megapanels provide design flexibility with many available cladding types, relative ease of integrating preinstalled glazing systems, flexibility to meet increasingly stringent thermal performance targets, and ability to incorporate a highly reliable water management strategy. Megapanels are typically constructed with light gauge non-loadbearing steel stud walls with structural steel at select locations; however, recent innovations have expanded secondary structural material options to mass timber and extruded aluminum components in lieu of light gauge steel.

Structural detailing within the panels themselves and in the connections back to the primary structure dictate how the panels respond to seismic loads. Panels can be designed to respond to primary structure displacement through translating, racking, rocking, or a combination of these strategies. By selecting the appropriate movement strategy early in the project design, architectural, structural, firesafing, and building enclosure design intent can be coordinated to achieve successful results in construction and throughout the useful service life of the building. Selection of the movement strategy will also dictate the required analysis required to validate the seismic performance of the megapanel; more complicated designs often necessitate a performance mockup to AAMA 501.4, while relatively simpler designs can be validated with a combination of calculations and well-planned joint detailing. Emphasis on understanding and predicting seismic movement of the megapanel system is critical when detailing connections, vertical and horizontal panel joints, inside and outside corners, transitions to dissimilar wall assemblies, and other conditions. This paper will discuss the constraints, benefits, and shortcomings of these design decisions through several case studies which highlight innovative techniques and practical implementation of these solutions.

Keywords: Modular construction, Façade Engineering, Connection details, Joint detailing, Performance mock-up

1.INTRODUCTION

1.1 Seismic Movement of Facades

In order to understand the seismic response of façade megapanels to primary structure seismic movement, one must be aware of the three mechanisms in which the façade can move: translating, racking, and rocking. Figure 1 below shows these three mechanisms.

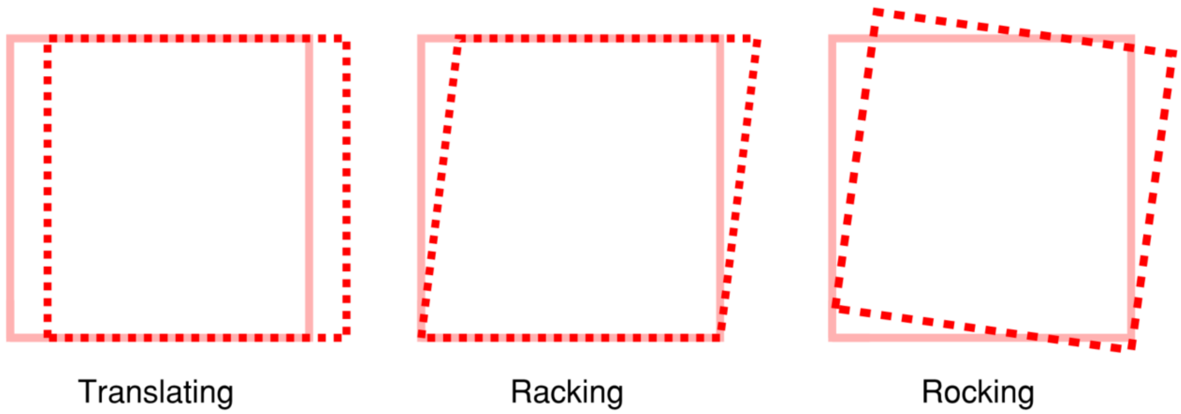

Figure 1. Types of façade motion; faint solid line shows initial shape and location of panel, dotted line shows final shape and location with applied seismic force/movement to the right.

As the building responds to seismic accelerations, its shape changes such that each successive story moves relative to the story above and below. Normally facades of the building are non-structural elements and are designed to allow for the movement of the building without structurally constraining movements such as live load deflections and lateral force induced inter story drifts. Depending on the type of façade structure, facades are forced to respond to seismic movement with a combination of the above three mechanisms. For example, the framing members in stick-built curtain wall may rack, while the glass unit within the framing will rock around the setting blocks, and precast concrete panels translate with the floor that they are attached to.

In buildings with multiple façade systems, it is critical to understand the movement of each system and the implications of each type of movement when adjacent to a system with a differing movement mechanism. For example, a precast system, which typically translates, adjacent to a stick-built curtain wall system, which typically racks will often require a vertical seismic separation joint; either a flexible expansion joint or sacrificial "crush joint". Crush panels are typically fabricated from sheet metal with multiple bends to allow the metal to easily deform without restricting façade movement. The challenge with crush panels is that once they experience a significant seismic event, they require replacement. However, if one can change the curtain wall to a unitized curtain wall with the stack joint that allows for translating movement, detail the floor line joint of both systems at the same datum, and force the curtain wall to rack rather than translate, such joints may be avoided. Rocking motion is typically preferred for panels with tall and skinny aspect ratios, such as unitized curtain walls, while translating motion is preferred for wide and short panels, such as architectural precast. Additionally, as panel width and therefore weight grows, the ability for a single dead load anchor to support a panel in rocking motion becomes challenging. Racking is commonplace in site-built construction with wood and steel studs, along with stick-built curtain walls, and is also possible with prefabricated megapanel systems depending on backup structure. This paper will not discuss racking megapanels in depth but will use racking motion as a reference to differentiate between different façade movement types.

Two levels of lateral force drifts are typically considered. The lesser is an elastic seismic or wind interstory drift, the greater is the inelastic seismic drift. Because the seismic response is a primary focus of this paper and the fact that both elastic and inelastic drifts generated by earthquake forces are generally larger than those by wind in the Western regions of the USA, this paper will concentrate on seismic drifts. The building code design criteria for the façade's performance typically requires that facade remains damage free as well as water- and airtight after a small or moderate size earthquakes at the elastic drift level. At the larger inelastic seismic drifts, the building code allows for some damage to the façade, provided no components become detached and fall off and does not require the facade to be water- and airtight after the design seismic event. Some higher Risk Category buildings such as hospitals and emergency centers require full enclosure performance even at the inelastic drifts which puts the detailing of the joints into a higher focus.

One additional consideration related to structural support of megapanel systems is that due to the length of the panel there can be significant and variable live load deflection of the support structure over the length of the panel. This necessitates to limit the number of the attachments supporting the self-weight of the panel (dead load anchors) to two, normally located towards the ends of the panel. To help resist wind loads, additional anchors specifically detailed to allow the vertical live load movement can be added in between. Because the panel needs to be allowed to expand and contract thermally relative to the support structure, one of the dead load anchors is usually detailed to allow for the in-plane movement while the other is fixed. That fixed anchor is often required to be designed to resist the entire seismic load generated by the weight of the megapanel.

1.2 Joint Detailing Considerations for Seismic Performance

This section discusses how seismic performance requirements and the selected seismic response of the façade to primary structure movement impacts the joint detailing of megapanel facades. Joint detailing is critical for structural, water, and air performance of the façade, and selection of the appropriate system is dependent on many factors, such as required performance after seismic events, fabrication options, and installation sequence, The two most common types of joints used to connect megapanels are sealant joints outboard of structural connections (Figure 2) and gasketed interlocking metal components, which are commonly referred to as stack joints (Figure 3).

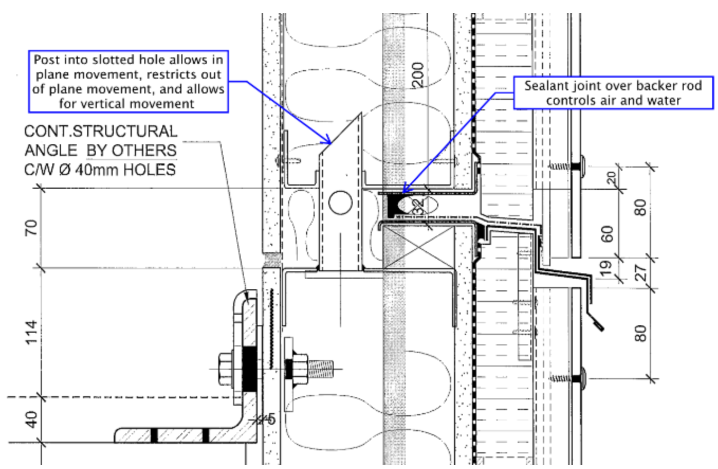

Figure 2. Horizontal section detail of sealant joint outboard of structural connection

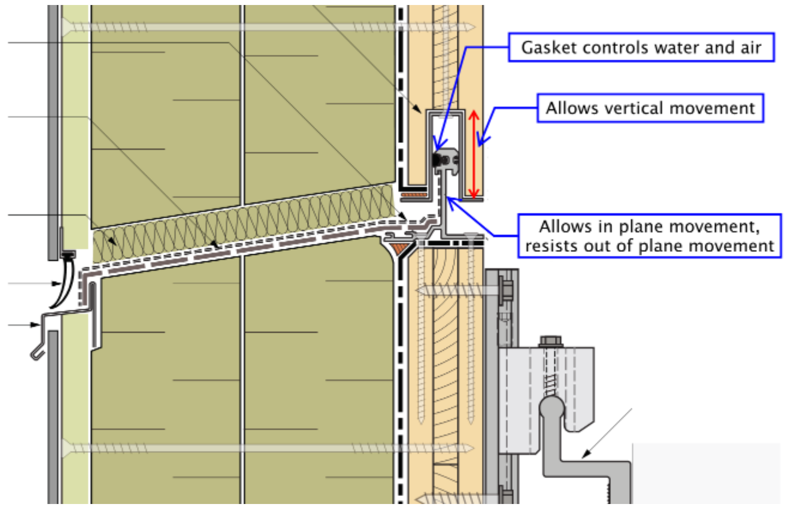

Figure 3. Horizontal section detail of gasketed interlocking metal components

1.2.1 Translating Systems

Typical joint detailing for translating systems requires the following considerations: Relative displacement between the upper and lower panel at the horizontal panel joints, geometric interference at the inside and outside corners, and geometric interference at adjacent dissimilar systems. A schematic of a typical set of 4 panels is shown below to illustrate the relative displacement of the horizontal joint in a translating system.

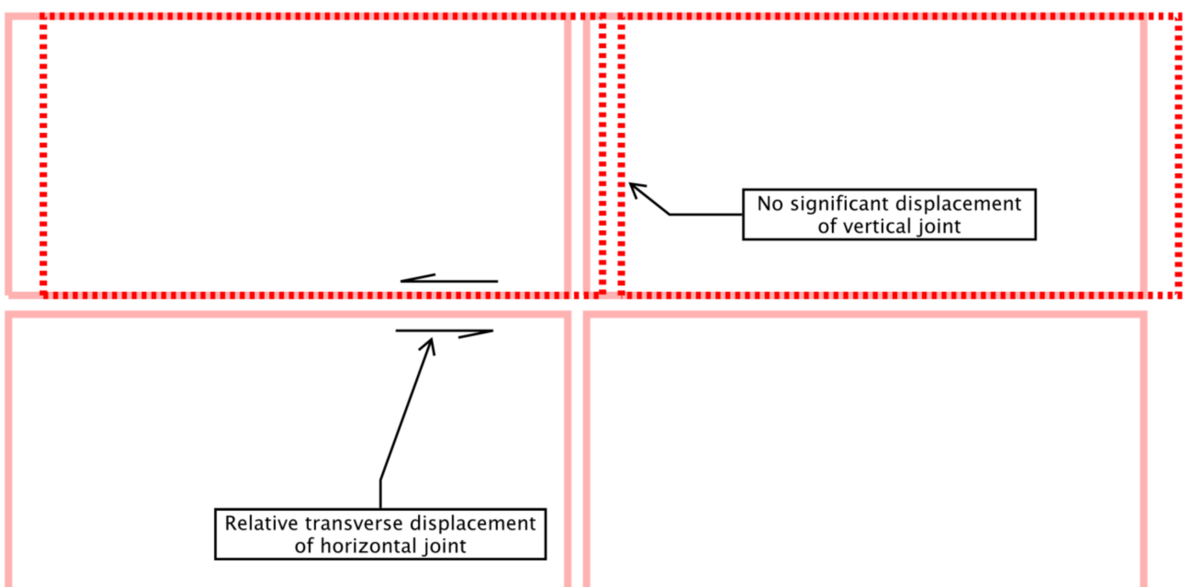

Figure 4. Joint forces applied to translating panels

Transverse displacement of the horizontal joint has minimal effect on gasketed interlocking metal joint systems, as the top and bottom components of the joints independent components and do not connect in a manner that would impart meaningful stress on the joint. However, if a backer rod and sealant joint is used for the horizontal joint, the relative displacement will introduce shear stress into the joint, as the sealant is attached to both the top and bottom panel. At large displacements, the shear stress can cause the sealant joint to exceed its maximum elongation, resulting in joint failure. Larger seismic movement will require wider sealant joints, which become challenging to install and unsightly from an architectural standpoint and in these scenarios, a sealant joint over backer rod may not be feasible. For translating panels on projects with high seismic performance targets or large floor to floor dimensions such as office spaces, an alternative solution such as a gasketed interlocking metal stack joint may be required for the horizontal joint.

1.2.2 Rocking Systems

When the layout of the panels or higher seismic drift demands require using a rocking solution with horizontal and vertical stack joints, it is relatively easy to calculate the requirements for the joint sizes based on using geometric proportions of the panel. In rocking motion, the horizontal joint can either grow on one end and shrink on the other, or displace in the transverse direction horizontally, depending on the surrounding construction and the slab movement. The vertical joint is displaced in the transverse direction vertically. The typical vertical stack joints for gasketed interlocking metal components readily allow for in plane displacement while providing out of plane structural load transfer between the panels.

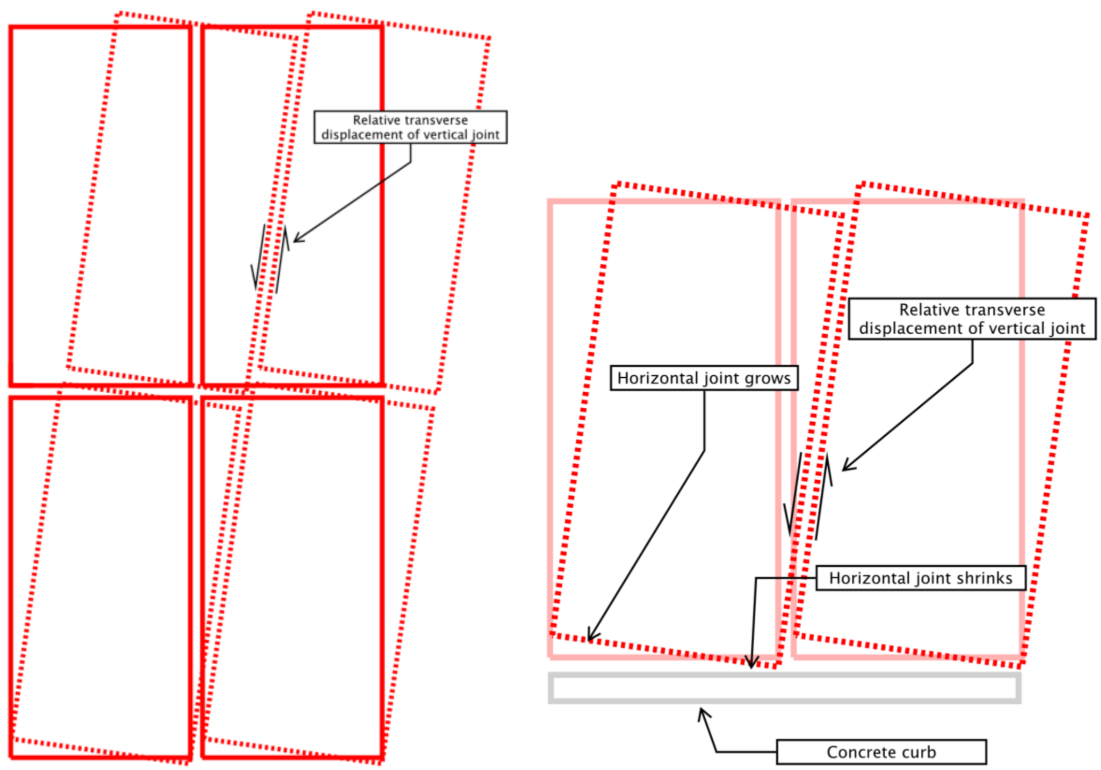

Figure 5. Joint forces applied to rocking panels

For the horizontal joint, the relationship between the vertical displacement of the growing stack joint is a function of dead load anchor location, panel width, and horizontal displacement of the moving floor. Assume a typical 2 ½" inches of inelastic seismic drift example and assume a 5-foot-wide panel with the 10 ft story height that is dead loaded near its corners. The resultant upwards displacement of the stack joint will be equal to the ratio of the width to height times the floor displacement (Figure 6).

$$\Delta_{stack} = \left(\frac{w}{h}\right)\Delta_{floor}$$

$$\Delta_{stack} = \left(\frac{5}{10}\right)2.5$$

$$\Delta_{stack} = 1.25$$

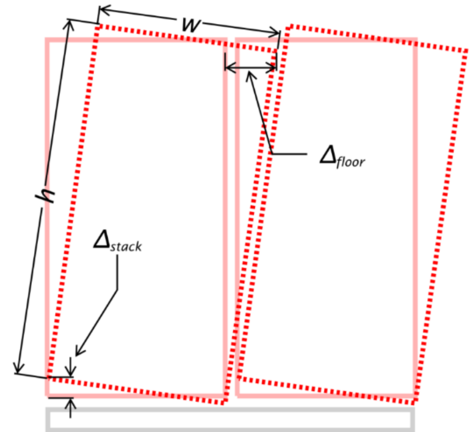

Figure 6. Example calculation of stack joint displacement with rocking motion

This example also shows that rocking solutions are generally preferred for panels with tall and skinny panels (low width/height), as with a long and wide panel the upwards horizontal joint can significantly exceed the horizontal floor displacement.

Provided there is enough overlap at the stack joint between the lower panel and upper panel to maintain compression of the gaskets, the joint will remain functional during the seismic displacement (Figure 7).

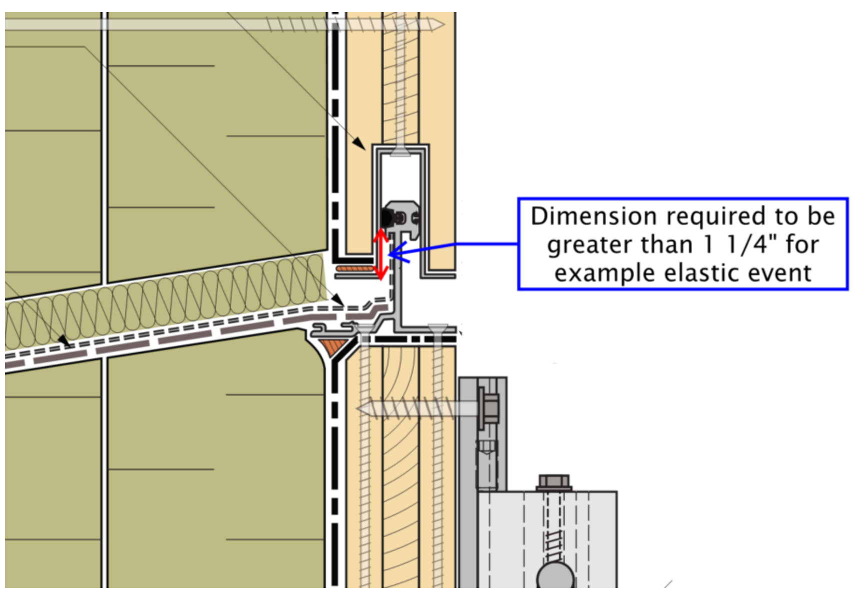

Figure 7. Stack joint sizing for rocking panels

Custom fabricators are able to size the stack joint components to remain serviceable during even relatively large elastic seismic movements by simply lengthening the vertical dimensions of the interlocking pieces and making it strong enough with transfer the out of plane wind loads. If the panels are supported for dead load at the quarter points rather than the edges, the displacement of the stack joint can be reduced proportionally using basic trigonometry. Note that larger megapanels generally result in correspondingly larger dead loads per panel. Therefore, rocking solutions that generally require the entire dead load of the panel to be supported from one anchor during seismic events become less feasible as panel size increases, as the anchor size and cost becomes prohibitive.

A fine balance between panel size, cost, and desired panel size is required to determine the appropriate joint detailing in response to seismic movement for megapanel facade systems. To summarize, sealant joints are preferred where cost and fabrication capabilities are the major constraints, while gasketed interlocking metal stack joints are a more versatile solution that generally allow for serviceability at higher elastic displacements and faster building dry-in.

2. CASE STUDY #1

The first megapanel system discussed in this paper is comprise of a 4” thick mass plywood panel (MPP) backup structure with rainscreen cladding and integrated punched windows. MPP is a mass timber structural component, comprised of numerous layers of plywood adhered together. Due to the rigidity of MPP, these megapanels are not capable of achieving racking motion, and thus must be designed to translate or rock. For this project, the MPP megapanels were designed with a much larger width than height, therefore translation was decided to be the most practical solution for façade movement in response to in plane lateral seismic drift. Due to installation considerations and drift requirements, a gasketed interlocking metal stack joint was selected for the horizontal joint system. The stiff translating panels require careful corner design to avoid collision between the two panels when significant seismic interstory drift occurs. At the corner, the in-plane panel translates laterally for the full amount of seismic drift for its entire height, and the perpendicular panel rocks out of plane such that the top of the panel moves in the amount of the interstory drift, while the bottom of the panel remains relatively stationary. In order to avoid, the collision at the bottom of these panels, three concepts were explored for the condition near the corner of the building (Figure 8)

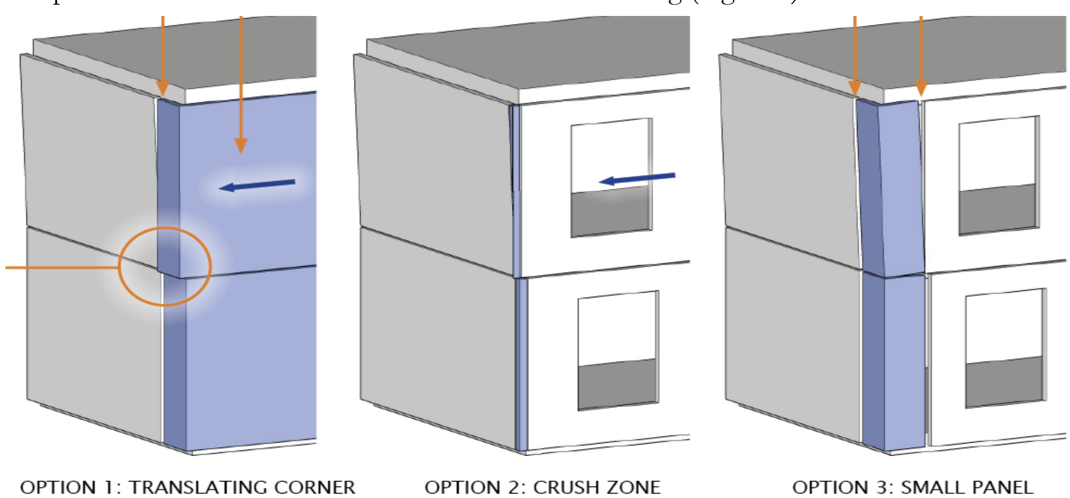

Figure 8. Three concepts for corner condition explored

Option 1 utilized a translating corner, which requires out of plane displacement of the return portion of the panel in relation to the panel above and below. This approach is feasible with sealant joints, and flexible preformed expansion joints, provided they are appropriately sized to accommodate drift. However, the system designed by the selected megapanel supplier utilized a continuous rigid aluminium extrusion at the floor line stack joint, commonly referred to as a chicken head in unitized curtain wall, which restricts out of plane movement. Therefore, Option 1 was deemed not feasible for the project.

Option 2 utilized a corner crush panel, which is further discussed in the previous section. This approach was determined to be feasible for the project, however, concerns were noted about the impact on architectural design intent and repair requirement after a significant seismic event. This approach also requires considerably more site work, as the crush panel needs to be installed after the panels have been lifted in to place and set.

Option 3 utilized a small corner panel that was designed to rock between the two adjacent translating panels. Due to the narrow width (30 inches) of the corner panel, the in-plane motion is accommodated by rocking on the chicken head, and the out of plane motion is also accommodated by out of plane rocking around the chicken head. After calculating panel size and vertical and horizontal joint size to perform feasibility analysis on this approach, the team proceed to select this option for the AAMA 501.4 test.

The results of the AAMA 501.4 test were successful, particularly the interstory horizontal displacement at both the service level elastic drift and the inelastic drift; after the elastic displacement, the performance mockup was able to withstand the specified air and water penetration criteria, and during the inelastic displacement movement, no elements detached from the façade and no glass breakage occurred.

Figure 9. Corner panel displacement under interstory drift

3. CASE STUDY #2

The second megapanel system discussed in this paper is a conceptual design of a cross laminated timber (CLT) wall panel with rainscreen cladding and integrated punched windows. CLT is a mass timber structural component, comprised of alternating layers of dimensional lumber adhered together. Common thicknesses of CLT are 3-, 5- and 7- ply depending on structural requirements. 5- and 7- ply are typically used in slab applications, while 3-ply are typically suitable for exterior wall wind loading. Due to the rigidity of CLT, these megapanels are not capable of achieving racking motion, and thus must be designed to translate or rock.

The prototype building is a 40-foot tall 2-story project in a high seismic zone. To span the high floor to floor heights and accommodate the large inelastic drift requirements, tall and skinny panels with rocking movement were selected. Typically, without a rigid connection or member to resist translation, such as a curtain wall lifting lug that remains in place (often referred to as a "bayonet" or "sword"), rigid panels will naturally be inclined to initially respond to seismic movement by translating. On this project, the team explored innovative options to force the CLT megapanels to respond to seismic movement by rocking. Panels were envisioned to be dead loaded at the top of the panel, requiring the restraint to occur at the base of the panels. A solution was developed incorporating a steel T-shaped member that restrained in plane movement but allowed vertical movement, which allowed for the panels to rock and restricted translation.

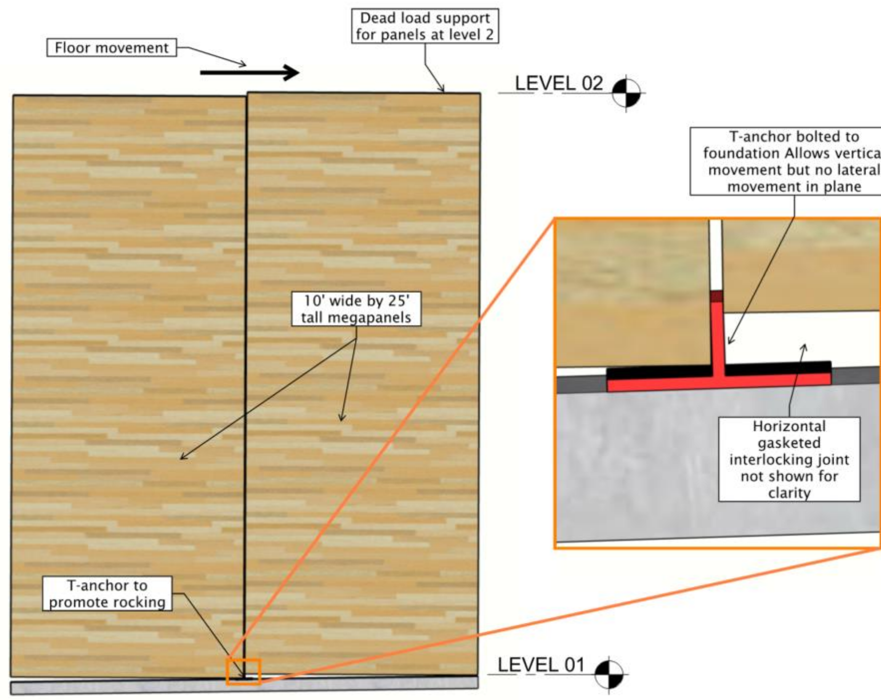

Figure 10. T-anchor concept

The height of the vertical leg of the T-anchor was determined using the project drift and the aspect ratio of the panel as discussed in Section 1. Due to the rocking motion of the panels and the desire for the system to be utilized in various seismic regions, a gasketed interlocking metal stack joint was selected as the joint system for further exploration.

4.CASE STUDY #3

The third megapanel system discussed in this paper is a steel stud framed wall panel with integrated punched windows. The megapanel system design was envisioned by the design team and designed by the design build subcontractor through the permitting process as a translating system. The elastic seismic drift was relatively small at 3/8" and the project was a low income housing development with significant budget constraints, therefore the horizonal and vertical panel joints were designed with sealant over backer rod. The panels were designed to be dead loaded at the base of the panel to accommodate balcony thresholds, as top hung units would move differentially to the floor below and result in ADA issues. The panels were designed to translated relative to the panels above through slotted connections, which allow for in plane movement and restrict out of plane movements.

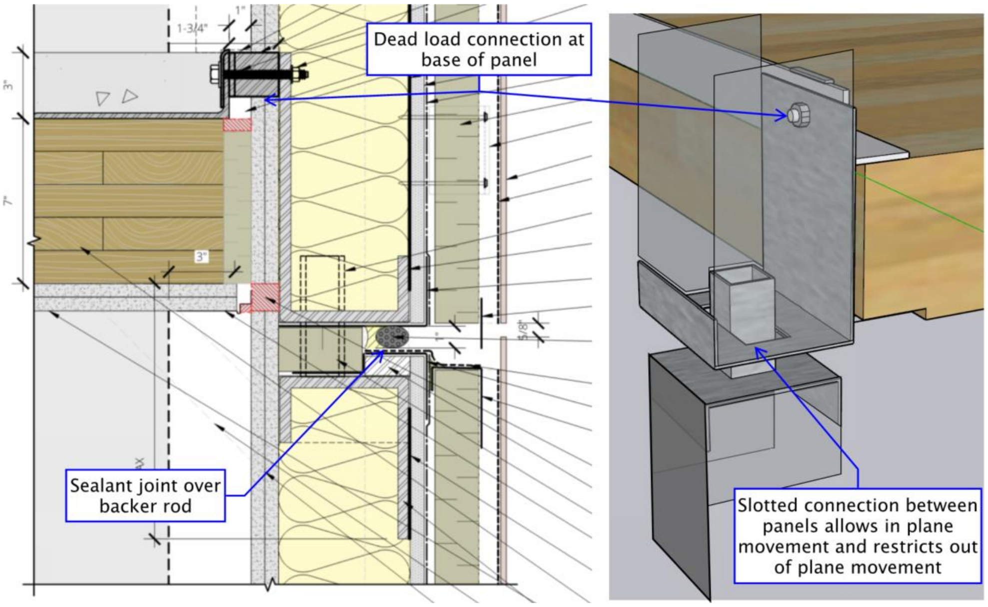

Figure 11. Proposed panel connections and joint detailing

During design, the subcontractor proposed a proprietary preformed silicone extrusion joint system which appeared to reduce labour requirements of installing sealant joints. The product data sheet for the joint system included test results that met the project specifications, including testing to AAMA 501.4 at project inelastic seismic displacement. Upon review of the full test report that detailed the results for the joint system, it became apparent that the test for the joint system that was reported on the data sheet was performed utilizing racking panels rather than translating panels. The movement of a racking system subjected the horizontal to vertical joints to minimal deformations and stresses, while the movement of a translating system would impart significantly more force on the intersection of the horizontal and vertical panel joints, potentially causing seal failure. The two largest areas of concern for the project team were the capability for the horizontal joint to withstand the shear stress due to relative motion of the upper and lower panels and at the vertical to horizontal intersection, where the vertical joint is bed in sealant onto the horizontal joint. The joint had not been previously tested in shear, and its response to this type of movement was unknown. Bedding seals are intended to be static joints, in contrast to dimensional sealant joints over backer rod which are dynamic joints with clearly defined elongation and compression limits. If the bedding seal were to fail prior to the horizontal joint deforming to accommodate shear stress, the system would not be serviceable in an inelastic seismic event.

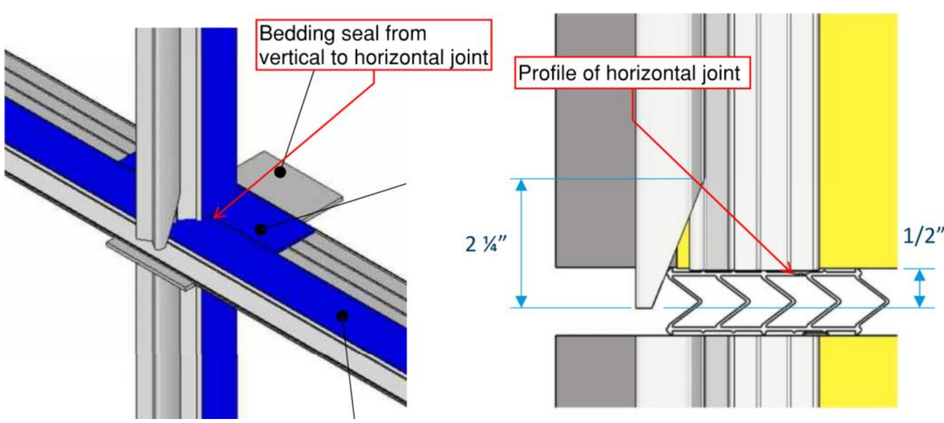

Figure 12. Preformed silicone joint system

To resolve the issue, the manufacturer of the joint system performed an informal test to validate the performance of the vertical to horizontal joint intersection and the shear response of the horizontal joint with the effects of a translating panel rather than a racking panel. Results of the informal test proved adequate to proceed with the joint system and move forward with formal testing. Unfortunately, the project was placed on hold in early 2022 due to budgetary constraints.

Figure 13 – Informal testing showing translating joint

5.CONCLUSION

Megapanel facades systems will continue to gain momentum in the North American construction market. Being aware of the options for seismic response of megapanels and their relative pros and cons, along with the joint systems and their relative pros and cons is critical to mitigate damage to non-structural elements during seismic events. Translating systems are generally preferred where panels are designed with short and wide configurations, where physical analysis such as PMU testing to AAMA 501.4 is not desired for cost or schedule reasons, and for very large panels, as a rocking system may require the entire dead load of the panel to be supported from one anchor during seismic events. Conversely, rocking systems are generally preferred where panels are designed with tall and skinny configurations, for building requiring higher levels of seismic drift, and when the design intent does not allow for large crush zones at corners. Regarding joint detailing, sealant joints are preferred where cost and fabrication capabilities are the major constraints, while gasketed interlocking metal stack joints are a more versatile solution that generally allow for serviceability at higher elastic displacements and faster building dry-in and can also be cheaper depending on size of the building and exterior access. With innovative techniques, a combination of conceptual analytical evaluation, informal proof of concept testing, and formal laboratory testing are required to ensure project success.

CASE STUDY OF A RAPID ASSESSMENT OF SEISMIC UPGRADE VIABILITY USING PERFORMANCE BASED EARTHQUAKE ENGINEERING

Paul Steneker[1], Lydell Wiebe[2], Andre Filiatrault[3], and Dimitrios Konstantinidis[4]

[1]WSP Canada Inc.
150 Slater, Ottawa, Canada
e-mail: paulsteneker@gmail.com
[2] Department of Civil Engineering, McMaster University
1280 Main St. West, Hamilton, Canada
e-mail: wiebel@mcmaster.ca
[3] University School of Advanced Studies IUSS
Palazzo del Broletto, Piazza della Vittoria, Pavia, Italy
e-mail: andre.filiatrault@iusspavia.it
[4] Department of Civil and Environmental Engineering, University of California, Berkeley
760 Davis Hall, Berkeley, CA, United-States
e-mail: konstantinidis@berkeley.edu

Abstract. The development of Performance Based Earthquake Engineering (PBEE) provides designers with a tool to quantify expected seismic losses in a building at an individual structural and nonstructural component level. However, it is difficult to use even deaggregated sources of loss to optimize upgrade strategies for a structure due to the relationship between the structural and nonstructural responses, such that it is generally only possible to compare competing upgrade options based on time-consuming detailed analysis. Recent research has aimed to address this challenge by proposing a modified version of the PBEE method, namely the median shift probability (MSP) method, which guides the assessment of the viability of both structural and nonstructural upgrade strategies. This method accepts the limited resources that are likely available in the early stages of the design process, allowing designers to quickly quantify the impact of structural and/or nonstructural upgrade decisions on estimated seismic losses. This paper presents a case study analysis of a structure for which multiple seismic upgrade options are assessed using the MSP method to rapidly summarize the effects of structural upgrades on nonstructural components. The case study demonstrates how the MSP method utilizes the deaggregation of loss across different source categories to identify the benefit of combined structural and nonstructural upgrades, increasing a designer's understanding of the impact of structural decisions on losses and allowing for the rapid determination of optimized upgrade strategies based on the owner's unique conditions. Ultimately, the case study demonstrates that the MSP method provides a pathway to further component-specific optimization, which can be achieved using a genetic algorithm once the number of considered structural upgrade options is more limited.

Keywords: Performance-based earthquake engineering, holistic seismic design, cost-benefit analysis, rapid design optimization, structural and nonstructural upgrades.

1.Introduction

The Performance-Based Earthquake Engineering (PBEE) methodology allows the estimation of earthquake-induced losses using metrics beyond structural performance. While this methodology has highlighted the importance of considering both structural and nonstructural seismic losses in seismic design and retrofit (Bradley et al. 2009; Perrone et al. 2019; O'Reilly and Calvi 2020), the relationships between the structure and nonstructural components must be considered when attempting to optimize the seismic improvements of a specific building. The effect of these relationships can include:

- A reduction of expected benefits from the implementation of higher performing seismic force-resisting systems if seismic upgrades to the nonstructural components are not considered.
- The benefits provided by upgrading the nonstructural components not being wholly achieved if the structure is not similarly robust.
- The effect of changes in the dynamic properties of a structure due to structural upgrades impacting the engineering demand parameters (EDPs) imposed on the nonstructural components.

As current PBEE evaluation methodologies capture these relationships implicitly through scenario-based evaluations, they do not facilitate the implementation of an integrated and optimized seismic force protection strategy, herein referred to as a strategy, because they require a trial-and-error approach aided only by guidance from experienced designers. Recently, Steneker et al. (2020) presented a method of using a genetic algorithm to systematically determine optimal strategies when considering modifications or upgrades to both structural and nonstructural components. The algorithm targets the maximization of the net present value (*NPV*), determined using Eq. (1), where EAL_O is the expected annual loss of the original strategy (or existing building), EAL_U is the expected annual loss of the upgraded strategy, *r* is the desired rate of return, *t* is the occupancy time, and *UC* is the total strategy cost. The flexibility of the algorithm allowed multiple target metrics, such as minimizing economic costs or downtime, including both strategy costs and reduction in seismic losses.

$$NPV = (EAL_O - EAL_U)\left(1 - \frac{1}{(1+r)^t}\right)r^{-1} - UC \qquad (1)$$

While a genetic algorithm provides a systematic way of determining optimal strategy, and significantly reduces the computational effort when compared to a brute force approach, its implementation can still be onerous during the preliminary phases of a feasibility study. Therefore, the genetic algorithm was integrated as the final level of a three-level framework in Steneker et al. (2022). The goal of this framework is to provide a more accessible evaluation for practicing engineers and stakeholders who use PBEE to evaluate and optimize seismic resisting strategies with increasing layers of analytical complexity. As shown in Figure 1, the first two levels of this framework utilize a novel and rapid modification to the PBEE evaluation process, referred to as the median shift probability (MSP) method, which was presented in detail in Steneker et al. (2022).

	Level 1: Preliminary Analysis with MSP	Level 2: Validation of Approximations with MSP	Level 3: Optimization
Objective:	-Identify viable strategy	-Validate viability of strategy	-Optimize strategy
Actions:	-Estimate strategy costs as a fraction of repair costs -Use response of original structure, strategy cost and strategy dynamic behaviour to estimate required scope	-Design strategy and determine cost independantly of repair cost -Perform analysis on strategy design to validate strategy dynamic behavior	-Implement Monte Carlo loss model and use stochastic optimization -Determine holistic costs for each strategy
Benefits:	-Limited time investment	-Moderate time investment -Increased reliability of structural dyanmic behavior	-Includes shared costs and uncertainties for more precise optimization
Limitations:	-Heavy use of approximations	-Increased use of structural analysis	-Significant analytical investment required

Figure 1: Overview of Framework for Upgrade Optimization

This paper presents brief descriptions of each of the three framework levels. Integrated with each description is an application to a case study building, illustrating the insights that can be achieved using this framework at different design stages.

2. Level 1: Use of MSP Method for Preliminary Analysis

The Level 1 analysis of the framework consists of a preliminarily evaluation of the benefits of a proposed strategy versus its potential cost when compared to an original baseline strategy (or existing building). At this initial stage in the design process, only the seismic performance of the original structure is known, and the objective of this level is to apply engineering judgment in a systematic way to quantify if a series of alternative structural strategies are viable. The MSP method aids this process by providing a simplified way to quantify the influence of changes of a structure or its nonstructural components to the total expected annual loss (EAL). Where typical implementations of the PBEE assessment are conducted using Monte Carlo scenario-based analyses (FEMA 2012), the MSP method consists of a simplified implementation of the PBEE methodology that integrates the various probability distributions directly. The simplification of each step of the PBEE methodology via probabilistic functions is shown in

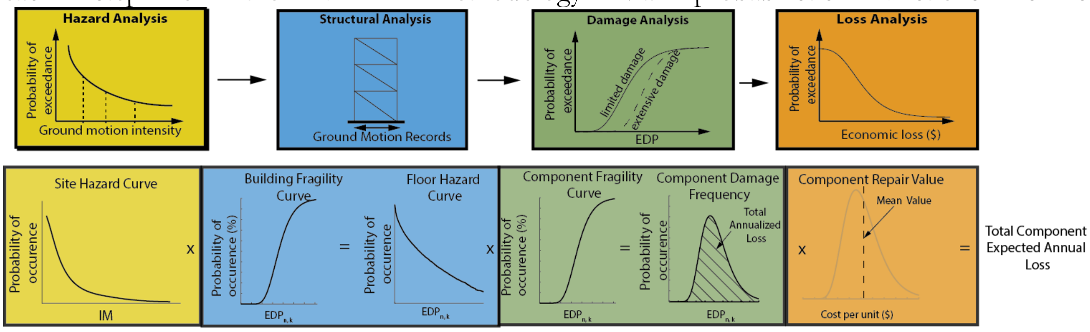

for a component n with damage state k. The hazard analysis is captured by the integration of the probability of occurrence of a ground motion intensity. The impact of the structural analysis on the nonstructural component is represented similarly by a floor hazard curve, which accounts for the probability of occurrence of the engineering demand parameter ($EDP_{n,k}$) within a structure before replacement. The damage analysis is captured by the product of the component fragility curve and the floor hazard curve, resulting in component damage frequency as a function of EDP. Finally, the loss analysis is represented by the multiplication of the mean repair cost and integral of the component damage frequency curve. This allows for the comparison of changes to the loss associated with a component based on changes to either that component's frequency of hazard exposure its probability of failure, but relies on the deterministic assumptions of component mean repair costs. A detailed explanation of this method is available in Steneker et al. (2022).

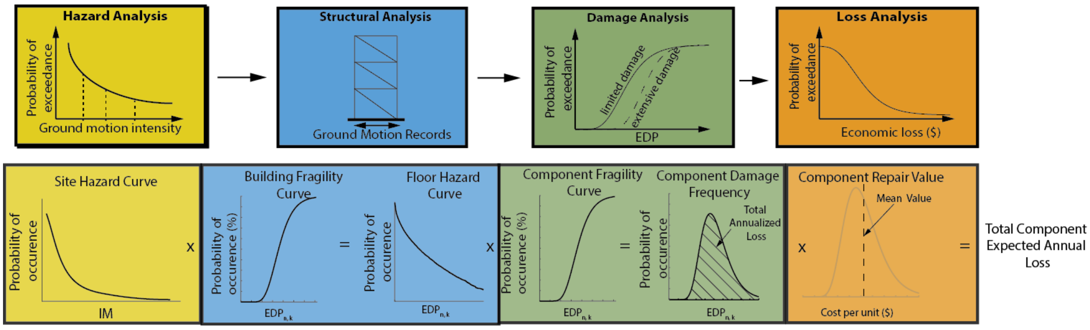

Figure 2: Example of Simplified Implementation of PBEE Methodology for Each Step of PBEE

This representation allows the MSP method to determine the viability of each modification to structural and nonstructural components by using Eq. (1). The viability of each nonstructural upgrade can be quickly determined by calculating the NPV resulting from changes to the component's damage state fragility curves against the upgrade cost, while the simplification also enables practitioners to predict the effect of structural modifications on the losses by modifying the median values of four curves:

1. The structural collapse fragility curve, which impacts the structural EAL and occupant casualty EAL;
2. The non-repairable residual inter-story drift curve, which impacts the structural EAL value;
3. The floor acceleration hazard curve, which impacts the nonstructural component EAL; and
4. The inter-story drift hazard curve, which impacts the nonstructural component EAL.

By only changing the median value of these four curves, a practitioner can obtain the total change in EAL and a list of the beneficial nonstructural upgrades. However, two significant assumptions are made at this level: (1) no changes in the dispersion of the curves, and (2) completely independent upgrade costing, which overestimates the overall strategy cost because the potential benefits of cost sharing across adjacent upgrades are not considered. A visualization of the process is shown in *Figure 3*, and the steps to this process for a Level 1 analysis are described in the following subsections.

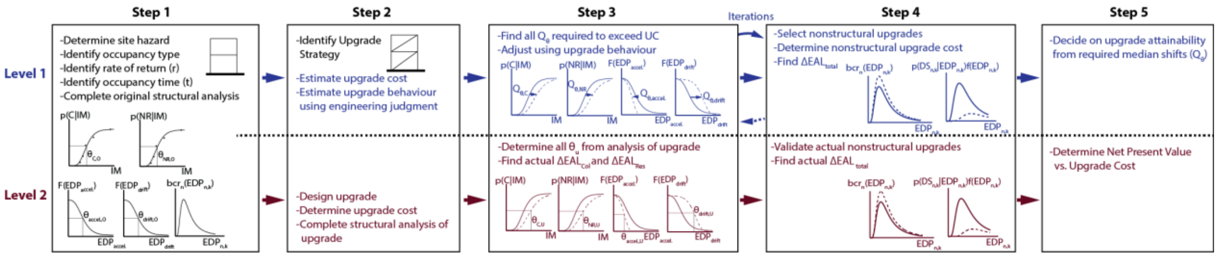

Figure 3: Flow Chart of Level 1 and Level 2 Analysis

2.1 STEP 1: IDENTIFY BASELINE STRATEGY OF CASE STUDY

The objective of this first step is to identify the original baseline strategy including structural system, nonstructural population, owner parameters, and site hazard to determine median (θ) and dispersion (β) values for collapse, residual drift, and floor hazard curves for the original structure. The case study for this paper consists of a seismic retrofit assessment of an original archetype structure. The building is a three-story steel moment resisting frame (MRF) with an office occupancy, and is located on site class B soil in Seattle, Washington. The structure was designed according to the seismic provisions of the 1994 Uniform Building Code (UBC 1994) and also satisfies current seismic design requirements (ASCE 2016, AISC 2016), with the exception of the pre-Northridge Earthquake beam-to-column connections. The building is assumed to have no irregularities and plan and elevation views for this frame are shown in *Figure 4*. The frame model of this structure was assembled in OpenSees (McKenna et al. 2000), with concentrated zero-length springs capturing element nonlinearity using the Ibarra-Medina-Krawinkler hysteretic model (Ibarra et al. 2005) and the nonlinear behaviour of the panel zones was modeled using the Krawinkler Spring Box model with a trilinear backbone curve (Gupta and Krawinkler 1999). The resulting computed fundamental period of the frame was 0.87 seconds. Further details of the modelling of the archetype structure are provided by Steneker (2020). The owner profile used for the analysis is assumed to target a 4% rate of return and 40-year occupancy time. The population of nonstructural components included in this archetype structure consists of 26 components identified by the FEMA P-58 Normative Quantity Tool (FEMA 2012), which included elevators and rooftop mechanical systems.

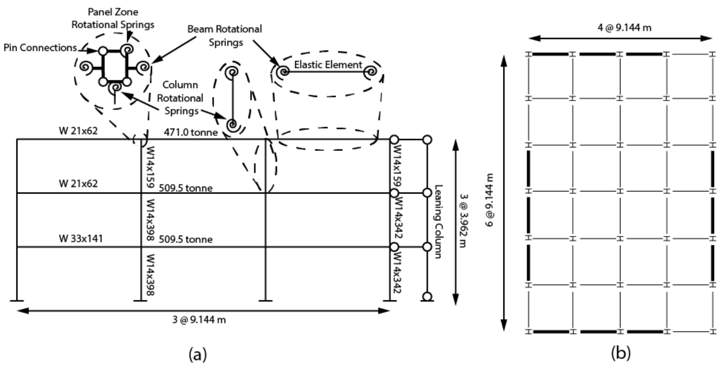

Figure 4: (a) Elevation View of Structure with Modelling Details, (b) Plan View of Structure

The seismic hazard analysis for the archetype building's site was obtained using the USGS Uniform Hazard Tool (USGS 2014). Since the MSP method requires a baseline set of curves, a multiple stripe analysis (Baker 2015) was conducted to evaluate the structural performance of the original frame, with nine intensity stripes, each with 40 ground motions selected and scaled to match different conditional mean spectra (Baker and Lee 2017). For each stripe, ground motions were selected from the far-field NGA-West2 Database (PEER 2013) to match rupture parameters identified by the site seismic hazard deaggregation information corresponding to the frequency of occurrence of each stripe's intensity. Details on the ground motion selection is provided by Steneker (2020). The results of the multiple stripe analysis provided the median values for the collapse fragility curve, the non-recoverable residual displacement curve, the floor acceleration hazard curve, and the floor inter-story drift hazard curve.

2.2 STEP 2: UPGRADE COST AND STRUCTURAL BEHAVIOUR

This step begins by selecting an alternative strategy and estimating if the strategy will increase or decrease the median of both the collapse and non-recoverable residual drift cumulative probability curves and the median of the two annual frequency of occurrence of floor acceleration or drift curves. This shift in a the probability curve is represented by a multiplier of the curve's median value (Q_θ) being greater than or less than one, as well an estimate of the modified structural cost of the strategy as a fraction of the building value (BV). As mentioned, the Level 1 analysis assumes no change in the curves' dispersion (Q_β=1), an assumption which will be verified in the Level 2 analysis. For this case study example, four alterative structural strategies are considered, as well as one retrofit strategy that is limited to upgrades of the nonstructural components. The first column of Table 1 provides a qualitative estimate of the expected influence of each structural change on the four curves, and the second column provides an approximation of the structural upgrade cost.

Table 1: Results of Level 1 Assumptions

Strategy -Expected Change in Performance	Structural Cost Estimate (% of BV)	Total Cost Estimate (% of BV)	Collapse Q_θ	Residual Drift Q_θ	Floor Acceleration Q_θ	Floor Drift Q_θ	Rank from Eq. 2
1. Increase in Strength and Stiffness with Braces -Improve collapse and residual drift performance -Increase Accelerations -Decrease Drifts	5%	11%	1.4	1.2	1.4	0.5	13.6
2. Increase in Ductility/Self-Centering with Connections -Improve collapse and residual drift performance -Increase Accelerations -Increase Drifts	10%	14%	1.6	1.8	1.1	1.1	11.4

3. Addition of Supplemental Viscous Damping -No change in collapse or residual drifts -Decrease Accelerations -Decrease Drifts	15%	17%	1.0	1.0	0.7	0.8	2.9
4. Base Isolation -Improve collapse and residual drift performance -Decrease Accelerations -Decrease Drifts	75%	75%	2.5	2.8	0.1	0.1	6.8
5. Upgrade of Nonstructural Components -No change in any curve	0%	6.6%	1.0	1.0	1.0	1.0	N/A

2.3 STEP 3 & STEP 4: REQUIRED CHANGE IN EAL AND APPROXIMATION OF Q_θ VALUES

These steps are an iterative approach to determine the required change in the four curves based on the assumed strategy cost, or alternatively by determining the maximum permissible strategy cost if the expected performance is known. For this case study, the values of Q_θ are estimated to quantify the expected effect of each structural upgrade. These estimates are then adjusted until the changes in EAL due to modifications of the four curves, as well as the benefit of all nonstructural component upgrades deemed viable based on the modified floor hazard curves, exceeds the estimated total cost. The total cost is a summation of the costs required for structural and nonstructural modifications. The upgrade of individual nonstructural components is selected when the NPV of upgrading the individual component is positive, which is determined by the change in EAL for an upgraded over a non-upgraded component. The EAL is quickly calculated using the deterministic method shown in Figure 2 using the modified floor hazard curve. The relevant nonstructural repair and upgrade costs are included in Steneker et al. (2022). Table 1 lists all the Q_θ values assumed in Level 1 of the MSP method.

2.4 STEP 5: DETERMINATION OF ATTAINABILITY OF Q_θ VALUES AND RANKING OF STRATEGIES

In this step, engineering judgment is used to determine if the final Q_θ values are attainable for the strategy. The values shown in Table 1 were considered achievable based on engineering judgment except for the base isolation strategy, which required unrealistic reductions in floor accelerations and drifts to offset the major costs of construction. Therefore, except for base isolation, all other strategies were considered for a Level 2 analysis. Furthermore, while the results of this level do not explicitly identify the optimal structural strategy, the strategy with the smallest ratio of the total deviation of required Q_θ from 1 over the total strategy cost would be the strategy considered likely to be the most efficient. This is shown in Eq. (2) and the results are summarized in Table 1. The results of Eq. 2 identify supplemental damping as the likely optimal structural strategy.

$$Structural\ Strategy\ Rank = \frac{\sum |Q_\theta - 1|}{Total\ Cost} \quad (2)$$

Further research can provide more accurate guidance on estimating Q_θ for each upgrade strategy. While this case study focused on an owner profile with only a 4% target rate of return and a long occupancy time, owners with shorter occupancy times and higher rates of return would require more significant shifts in median values for a viable upgrade as a smaller NPV would be determined in Eq. (1) from the same shift in median value. This would result in the upgrades being deemed less attainable. Finally, owners with alternative target metrics, such as downtime, would obtain differing Q_θ values for each strategy.

3. Level 2: Use of MSP Method for Validation

A Level 2 analysis, which requires an increase in computational resources, can be justified to confirm the viability of a shortlist of strategies that were identified as achievable in Level 1. This Level 2 validation is completed using the same MSP method as in Level 1, but using probability curves obtained from NLTHA of the structural strategy, a more precise estimate of cost obtained through further design development, and possibly including additional nonstructural upgrades selected considering cost sharing benefits determined using an iterative approach. The steps are summarized in the following subsections.

3.1 STEP 1: ORIGINAL CONDITIONS

A detailed model of the original building was used in the Level 1 analysis for this case study and therefore no further refinement was used for this step of the Level 2 analysis.

3.2 STEP 2: UPGRADE SCHEMATIC DESIGN

The increase in stiffness and strength was implemented by adding buckling restrained braces (BRBs) designed using the equivalent lateral force procedure as outlined in ASCE 7-16, where the design period of the structure was determined from modal analysis of the combined MRF/BRB system, but with the BRBs designed to take 100% of the lateral loads. The increase in ductility and addition of self-centering behaviour were implemented by replacing the pre-Northridge connections with low-damage self-centering sliding hinge joint (SCSHJ) connections (Khoo et al. 2012) without changing the beam section. The design of the SCSHJ connections targeted 100% self-centering capability in each beam-column connection, and the activation moment was set to allow for the full connection mechanism to develop before yielding of the existing beam (Steneker 2020). The addition of supplemental damping was realized using diagonal linear viscous dampers (VD) that were designed to provide an equivalent damping ratio of 25% of critical in the first mode of vibration of the structure using the process outlined in Christopoulos and Filiatrault (2006). The upgrade costs estimated using the details of the final schematic design of each strategy are summarized in Table 2.

3.3 STEP 3: ANALYSIS OF UPGRADED DESIGN PERFORMANCE

The performance of each structural upgrade design was evaluated using the same multiple stripe analysis process used for the original structure but with updated first mode periods when required. Table 2 summarizes the obtained Q_θ values for each structural upgrade design and includes the values of Q_β to demonstrate the validity of approximating Q_β as 1.0 in the Level 1 MSP method. As shown, the assumption of small changes in the deviation of the curves is reasonable given the values of Q_β near unity.

Table 2: Structural Strategy Cost and Calculated Q Values for Level 2 MSP Method

Structural Strategy Design	Structural Strategy Cost (% of BV)	Collapse $Q_{\theta,C}$ (Q_β)	Residual Drift $Q_{\theta,NR}$ (Q_β)	Floor Acceleration $Q_{\theta,accel}$ (Q_β)	Floor Drift $Q_{\theta,drift}$ (Q_β)	Total Strategy Cost (% of BV)	NPV (% of BV)
BRB	6.6	1.45 (1.03)	1.31 (1.07)	1.45 (1.14)	0.41 (1.07)	13.0	2.6
SCSHJ	10.0	1.51 (0.79)	1.54 (0.90)	1.25 (1.02)	1.31 (1.05)	16.6	-3.5
25% VD	12.2	2.39 (0.95)	1.96 (0.91)	0.43 (1.02)	0.16 (1.01)	15.0	21.9
Nonstructural Only	0.0	1.00 (1.00)	1.00 (1.00)	1.00 (1.00)	1.00 (1.00)	6.4	11.9

3.4 STEP 4: USE FLOOR HAZARD CURVES TO DETERMINE NONSTRUCTURAL UPGRADES

The identification of viable upgrades to nonstructural components for each strategy was identical to Step 4 of Level 1, but using the floor hazard curves obtained with the more sophisticated analysis mentioned above. Once obtained, the accuracy of a Level 2 analysis is enhanced using an iterative evaluation process to account for the shared upgrade tasks across component types. To identify nonstructural components for upgrade at this stage, shared costs are considered in the MSP method using an iterative approach where the cost of upgrading a component within Eq. 1 is reduced by the value of any common tasks that are associated with upgrades that have already been selected in the previous iteration. This iterative process is repeated until no new upgrades are identified. The upgrade cost of the non-structural components for each structural strategy is added to the estimated structural strategy cost of each of the strategies, as shown in Table 2. Large differences between the total strategy cost and the structural strategy cost indicates that significant investments in nonstructural upgrades are beneficial to the overall strategy, such as in the case of adding BRBs.

3.5 STEP 5: EVALUATION OF NPV

The NPV of each of the four strategies is calculated using Eq. 1 with the EALs obtained from the MSP method and the corresponding total strategy cost. These are shown in Table 2, where positive values indicate that the structural strategy has a net benefit for the given owner parameters of the case study. The largest NPV indicate that the optimal structural strategy for this case study is the addition of viscous dampers. Furthermore, as the NPV of the SCSHJ strategy of this case study is negative, the strategy is not considered for further optimization in Level 3.

4. Level 3: Use of Genetic Algorithm for Optimization

Once the structural analysis of Level 2 has verified the viability of each structural strategy, further computational effort can be justified to obtain an optimal overall strategy. For this purpose, a genetic algorithm is used to optimize the three strategies that were identified as viable in Level 2. As presented in Steneker et al. (2020), the algorithm has five steps:

4.1 STEP 1: FORMULATION OF GENETIC CODE

The formulation of the genetic code defining each individual strategy within a population is implemented with a string of bits, where each nonstructural component is represented with its own binary bit, as shown in Fig. 2. A zero bit represents a non-upgraded status, and a unity bit represents an upgraded status captured in the PBEE Monte Carlo loss model by a modification of the component's fragility curves. The inclusion of a particular structural strategy is captured by two separate bits, where the value of the first bit varies from unity to N, where N is the maximum number of structural strategies being considered. The implementation of the chosen structural strategy is then represented by one binary bit for each floor of the building (with a value of unity indicating an implementation at that floor) if deemed possible for this strategy. An example of a single population of three individuals within a generation for the case study building is shown in Fig. 5, capturing three different structural strategies and 26 different nonstructural components. The total number of bits composing the string of a particular individual of this building is 30: 26 nonstructural bits, 1 "structural option" bit with three different structural options and 3 structural bits, one for each floor. The initial population is formed by individuals having randomly assigned bit values. This provides an initial diversity to the population before selective optimizing begins.

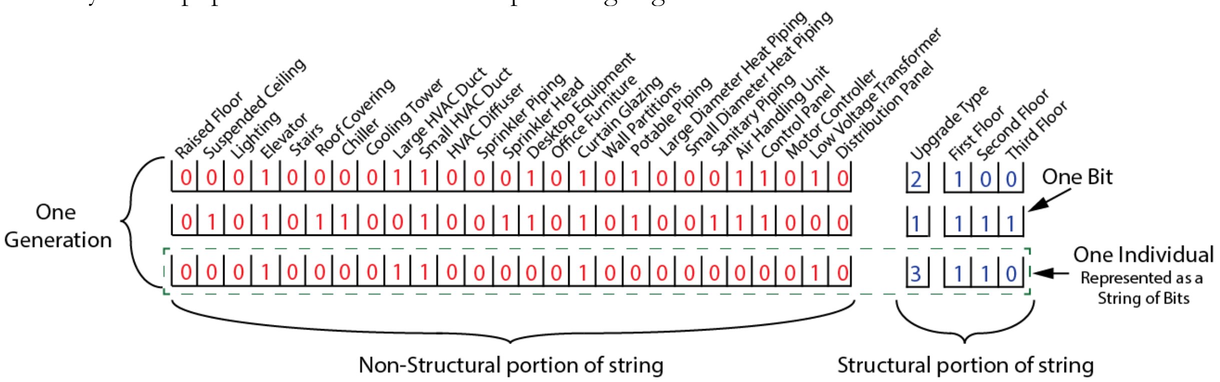

Figure 5: Examples of Genetic Code for an Individual Upgrade Strategy (Modified from Steneker et al. 2020)

4.2 STEP 2: EVALUATION OF THE PERFORMANCE

The evaluation of the performance of each individual using a ranking function for a specific target metric is implemented using Eq. 1, where each individual strategy is ranked based on its NPV. This includes a calculation of the EAL using the Monte Carlo PBEE implementation, and therefore includes any repair cost reductions due to economies of scale, as well as all shared upgrade savings in the upgrade cost.

4.3 Step 3: Selection and Mixing of Individuals

The selection and mixing of individuals to form a new generation seeking higher performing individuals is completed by a crossover, where two individuals are randomly selected with a weighted preference according to their rank. The strings of these highly ranked individuals are spliced and mixed to form a new generation of the same population size as the previous generation. A carryover percentage is used to guarantee the existence of a certain number of the best performing individuals from the previous generation moving into the next generation without undergoing splicing.

4.4 Step 4: Mutation of Individuals

The mutation of individuals to ensure genetic diversity is implemented based on a pre-determined mutation rate. If a bit mutates, its value is randomly reassigned using a uniform distribution. The new generation is then evaluated and ranked again.

4.5 Step 5: Convergence to an Optimum Solution

The determination of an optimum solution is done using single or multiple convergence criteria. The two convergence criteria used for this study were: 1) a change of less than 1% in the rank of the optimal solution (individual) between the current and the previous generation, and 2) the population of the current generation consists of at least 25% of individuals having the highest ranked genetic code (i.e., 25% of optimal individuals). Due to the randomness built into both the selection and mutation of individuals, as well as the uncertainty of the Monte Carlo loss estimation, the genetic algorithm was repeated 100 times, resulting in a sample of 100 optimum solutions.

5. Result Comparison

The components identified in the optimal strategy of all three framework levels is shown in Figure 6, where modifications included in the optimum strategy are colored and with a numerical value indicating the certainty of selection varying from 0 to 100%. As the MSP method is purely deterministic, the solutions obtained for Level 1 and Level 2 indicate a selection certainty value of either 0 or 100%. The certainty values obtained in the Level 3 results vary, as lower percentage values indicate that a component is not always selected in the optimal solution. For this case study, the optimal individual consists of upgrading the structure with viscous dampers to target 25% of critical viscous damping and upgrading 11 of the 26 nonstructural typologies included in the building. The main nonstructural upgrades included in the optimal solution are large mechanical and electrical systems, for which damage translates into large EAL values and upgrade costs are relatively minor. The optimal solution obtained reduces the EAL of the original archetype building by 89%, with a corresponding structural strategy cost of 15% and a nonstructural strategy cost of 4% of the building value. The differences in optimum strategy obtained across all three levels indicate that the Level 1 approach identifies the optimal structural strategy but does not completely identify all upgrades. By taking advantage of cost sharing and refined estimations of the losses, the Levels 2 and 3 identified several additional nonstructural upgrades as optimal. Furthermore, since the Level 3 analysis uses a Monte Carlo approach to determine loss analysis, it identifies additional nonstructural upgrades which have a positive return if upgraded as a group due to each component causing the same damage consequence.

		Level 1	Level 2	Level 3
No Structural Upgrades	First Floor			
	Second Floor			
	Third Floor			
Increase Stiffness & Strength	First Floor			
	Second Floor			
	Third Floor			
	First Floor	100	100	90

		Level 1	Level 2	Level 3
Plumbing	Potable Piping			35
	Large Diam. Heat Piping			100
	Small Diam. Heat Piping			35
	Sanitary Piping			35
	Sprinkler Piping			70
	Sprinkler Head			70
Contents	Lighting			100

Increase Damping	Second Floor	100	100	90
	Third Floor	100	100	70
Mech. Equip.	Chiller	100	100	100
	Cooling Tower	100	100	100
	Air Handling Unit	100	100	77
	Control Panel		100	100
	Motor Controller		100	100
	Low Voltage Transformer		100	75
	Distribution Panel		100	100
Egress	Stairs			
	Elevator			

	Desktop Equipment			
	Office Furniture			
Finishes	Suspended Ceiling			
	Raised Floor			
	Curtain Glazing			
	Wall Partitions			
	Roof Covering			
HVAC	Large HVAC Duct			
	Small HVAC Duct			
	HVAC Diffuser			

Figure 6: Comparison of Selected Upgrades (Rate of Return 4%, Occupancy Time 40 Years)

6. Conclusions

This paper presented a framework to identify and assess the viability of seismic upgrades considering both structural and nonstructural components options. The framework is structured to provide quantifiable milestones of the viability of a considered seismic force protection strategy with relatively low computational resources at early design stages. A case study was presented and demonstrated how this framework can be used to determine the optimal strategy for an individual building and unique owner's desired rate of return and occupancy time. Since this framework initially uses an estimated interpretation of the impact of structural modifications on the viability of seismic upgrades, continued research is required to provide guidance on the influence of various structural strategies on the four curves. The assumed shift in performance due to an upgrade (Q_θ) is a critical step in determining the viability of a structural upgrade and developing guidance. Conducting further case studies would allow a more accurate estimate of the behaviour associated with an upgrade during preliminary design. This would allow for more certainty of the Level 1 results before conducting a Level 2 and 3 analysis.

7. References

AISC (American Institute of Steel Construction). (2016) "Specification for Structural Steel Buildings." AISC 360-16, Chicago, IL.

ASCE (American Society of Civil Engineers). (2017) "Seismic Evaluation and Retrofit of Existing Buildings." ASCE 41-17, Reston, VA.

Baker, J. W. (2015) "Efficient Analytical Fragility Function Fitting Using Dynamic Structural Analysis." Earthq. Spectra 31(1): 579–599.

Baker, J. W., and Lee, C. (2017) "An Improved Algorithm for Selecting Ground Motions to Match a Conditional Spectrum." J. of Earthq. Eng. 22 (4): 708-723.

Bradley, B., Dhakal, R., Cubrinovski, M., MacRae, G., and Lee, D. (2009) "Seismic loss estimation for efficient decision making" Bulletin of the New Zealand Society for Earthquake Engineering 42(2): 96-110.

Christopoulos, C., and Filiatrault, A. (2006) Principles of Passive Supplemental Damping and Seismic Isolation, IUSS Press, Pavia, Italy.

FEMA (2012). "Seismic Performance Assessment of Buildings - Methodology." Report P-58 Federal Emergency Management Agency, Washington, DC.

Gupta, A., and Krawinkler, H. (1999). Seismic Demands for Performance Evaluation of Steel Moment Resisting Frame Buildings. Department of Civil and Environmental Engineering, Stanford University, Report No. 132.

Ibarra, L., Medina, R., and Krawinkler, H. (2005) "Hysteretic Models That Incorporate Strength and Stiffness Deterioration." Earthq. Eng. and Struct. Dyn. 34: 1489-1511.

Khoo, H.-H., Clifton, C., Butterworth, J., MacRae, G., Gledhill, S., and Sidwell, G. (2012). "Development of the self-centering Sliding Hinge Joint with friction ring springs." J. Constr. Steel Res., 78: 201–211.

McKenna, F., Fenves, G. L., and Scott, M. (2000). Open System for Earthquake Engineering Simulation. University of California Berkeley, CA.

O'Reilly, G., and Calvi, G., (2020) "Quantifying Seismic Risk in Structures via Simplified Demand-Intensity Models" Bulletin of Earthq. Eng., 18: 2003-2022.

PEER (2013) PEER NGA-West2 Database. PEER Report No. 2012/03, Pacific Earthquake Engineering Research Center, Berkeley, CA, USA.

Perrone, G., Cardone, D., O'Reilly, G., Sullivan, T. (2019) "Developing a Direct Approach for Estimating Expected Annual Losses of Italian Buildings" Journal of Earthq. Eng, 26(1), 1-32.

Steneker, P., (2020). Towards More Optimized and Resilient Seismic Design of Buildings with Steel Moment Resisting Frames Ph.D. Thesis, McMaster University, CAN.

Steneker, P., Filiatrault, A., Wiebe, L., Konstantinidis, D. (2020) "Integrated Structural-Nonstructural Performance-Based Seismic Design and Retrofit Optimization of Buildings." J. Struct. Eng., 146(8).

Steneker, P., Filiatrault, A., Wiebe, L., Konstantinidis, D. (2022) "A Framework for the Rapid Assessment of Seismic Upgrade Viability Using Performance-Based Earthquake Engineering" Earthq. Spec., 38(3), 1761-1787.

2022UBC (Uniform Building Code) (1994) Structural Engineering Design Provisions vol. 2, International Conference of Building Officials, Lansing, Michigan.

USGS (2014). "Unified Hazard Tool" Version 4.1.9, (Lat: 47.6, Long: -122.3, T: 1.0 Sec), United States Geological Survey, Reston, VA, USA.

REVIEW OF CURRENT DESIGN STANDARDS FOR ACCELERATION SENSITIVE NONSTRUCTURAL COMPONENTS

Paul Steneker[1], David Arnold[1], and Daniel Carson[1]

[1] WSP Canada Inc.
e-mail: Paul.steneker@wsp.com
David.arnold@wsp.com
Daniel.carson@wsp.com

Abstract. The design of seismic protection for acceleration sensitive non-structural components requires the calculation of component acceleration demand and most building codes provide simple, approximate methods for this purpose. Typically, these methods do not explicitly consider the dynamic characteristics of either the base building or non-structural component. Whilst convenient for design office use, these methods are inadequate when a refined estimate of non-structural component acceleration demand is desired, such as for the design of buildings with high value contents or when post-disaster functionality is required. To address this shortcoming, various authors have developed alternate methods that generate floor acceleration spectra with explicit consideration of base building and non-structural component dynamic characteristics. This paper reviews the current building code non-structural component acceleration methods and discusses their advantages and limitations. A summary of several alternative methods is provided, followed by an evaluation of their implementation complexity. Finally, recommendations for new methods and/or modifications to existing methods are made for future building code revisions.

Keywords: Non-structural component seismic acceleration, Floor acceleration spectra.

1. Introduction

The design of acceleration sensitive non-structural component seismic protection requires the quantification of expected seismic force. Building codes (ASCE 7 2016, ASCE 7 2022, NBCC 2020, NZS 1170.5, EN 1998-1) address the quantification of seismic component force with equations that use empirical values and scenario specific parameters.

However, several researchers have identified shortcomings with these equations (Filiatrault and Sullivan 2014, Rashid et al. 2021). The shortcomings include; 1) an assumed non-structural component behaviour, independent of its restraint design, 2) an assumed modal structural response, independent of the structural design, and 3) an assumed independence of the structure and non-structural component dynamic behaviour. Furthermore, the increased implementation of high performance and low damage seismic force resisting systems, such as supplemental damping or isolation systems, provides significant potential reductions in the imposed floor accelerations due to the dynamic behaviour of these systems when compared to the behaviour of more traditional structural systems (Constantinou & Symans (1993), Christopoulos & Filiatrault (2006), Kelly and Marsico (2015)). This reduction in acceleration is not materialized when determining non-structural forces from design standards but more accurate design forces can be obtained from the analytical models, which are often already required to complete the design of the structural systems. Furthermore, these models are typically created by the consulting structural engineer, while the design of seismic restraints for most components is delegated by the component installer to a specialty structural engineer (SSE) who may not be as familiar with the unique dynamic properties of the structure. No formal process for sharing the dynamic information of the structure from the structural engineering to the SSE is currently outlined in any design standards.

This paper summarizes the parameters that influence non-structural component seismic design force and identifies those that are considered by five existing design standard equations. This paper then includes a summary of four alternative methods of determining the seismic forces imparted on non-structural components which include most or all of the influencing parameters. These methods were selected based on their ability to address the identified shortcomings of the design standard equations, as well as their varying degrees of complexity of implementation. The complexity of implementation assumed a method of seismic structural design which included dynamic structural analysis, such as a response spectrum analysis (RSA), as even RSA has become standard practice for most seismic design. Further information on the exact development, validation, and implementation of each methodology can be found at the relevant references. Finally, the paper discusses additional considerations for the implementation of these methods in practice, including the additional analytical effort and the effective transmission of the additional information between engineering stakeholders.

2. Review of Existing Design Standard Equations

As discussed by Rashid et al (2021), the values used in current design standard equations to determine the design acceleration typically capture six unique design characteristics, which are shown in Figure 1. These are either explicitly determined, or approximated using empirically derived values:

- **Site Ground Hazard**: The site-specific hazard at the base of the supporting structure is captured with a combination of terms which include the spectral acceleration at a specific return period, as well as factors for various local effects, such as soil type. In design standards, the hazard is obtained as a spectral acceleration at a singular and static period of vibrations ($S_a(T)$), which is then further reduced to values equivalent to peak ground acceleration (PGA) in the case of the ASCE and NBCC design equations (Filiatrault 2014).

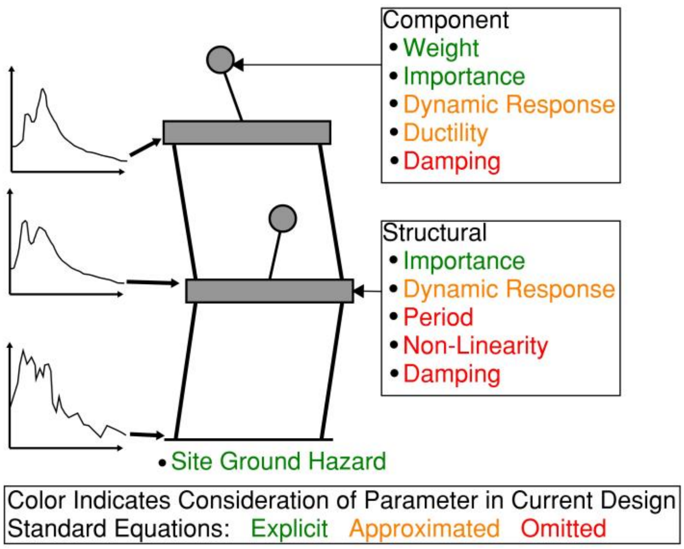

Figure 1: Parameters Influencing Design Forces for Non-Structural Components

- **Structural Dynamic Response**: As the response of the structure is determined by the contribution of the structural modes, the dynamic behavior of the structure filters the floor spectral accelerations values to peak at the periods of the first few modes of the structure. While the higher modes typically cause the maximum spectral acceleration at intermediate floors, the fundamental period often causes the largest amplifications of the floor spectral accelerations at the highest floors (Rodriguez et al. 2002). The effect of the acceleration amplification caused by these higher modes is not included in any of the five design equations, including the influence of fundamental torsional modes. Only a first mode behavior is included in these five design equations, captured as a function of the component's elevation within the total height of the structure, therefore assuming a first mode only amplification.
- **Component and/or Structure Importance**: As with most seismic loads, the forces are amplified based on the importance of the structure and/or the component. In design standards, this is a singular value. (I_e for structures and $I_{e,c}$ for components)
- **Component Dynamic Response**: Like a structure, the dynamic response of a component affects the magnitude of the imposed forces, where components with fundamental periods near the structural periods being vulnerable to resonance with the dynamic behavior of the supporting structure. This would increase the applied accelerations to the component. As such, the ratio of the structural period and the component period is a critical characteristic when determining non-structural component loads. However, only the design equation in the EuroCode currently considers this relationship (EC8 2006) and only to the first mode of the structure, while other design equations typically represented this with an empirical amplification term. Furthermore, this empirical dynamic response amplification is obtained independently of the supporting structure's dynamic response and is based on a limited number of component categories assigned from the perception of either "rigid" or "flexible" behaviour. This binomial option provides limited flexibility when designing a component anchorage, or to adjust the forces based on potential resonances between the component and structure.
- **Component Ductility**: The forces imparted on a component can be reduced based on the perceived ductility of a component. In design standards, this is typically represented by an empirical term which reduces the applied forces.
- **Component Weight**: The design forces are obtained from accelerations which cause inertial forces on the component as a function of the components weight.

Each of these six factors is included for consideration in the five design equations included for comparison in this paper. These five equations are summarized in Table 1, which identifies the variable of the relevant equation associated with each of the six characteristics. However, while these equations provide a simplified approach to determining design loads, most of these current design equations omit several characteristics which are either already explicitly considered during the structural design of the supporting structure or are inherently selected based on the non-structural component. These other characteristics should be considered when determining the loads applied to an acceleration sensitive non-structural component:

- **Structural Period**: The period of the structure will dictate the magnitude of the structural response to a specific seismic intensity. Therefore, identical components located in structures with differing fundamental periods would experience different forces. However, the five design equations only consider the spectral ground acceleration at a singular and ubiquitous structural period for all structures.
- **Structural Non-linearity**: The non-linearity of the structure affects the floor accelerations since yielding of the structural elements limits the possible maximum floor accelerations, while simultaneously lengthening the period range at which the largest spectral floor acceleration occurs (Steneker et al. 2022)). This nonlinearity is not included in any of the design equations.
- **Structural Damping:** While exact values are often not available, differing structural seismic force resisting systems have recommended values ranging from 1 to 5% (Anajafi and Medina 2019)). Current

design standards assume a consistent use of 5% structural damping as the ground spectral acceleration values are obtained from a 5% damped spectrum.

- **Component Damping**: While the known values of damping for non-structural components is limited, recent research has indicated that most non-structural components have inherent damping values between 0.5% and 4% (Anajafi and Medina 2019). Since all five current design equations specify utilizing the 5% damped spectral acceleration from the ground site hazard, the reduced component damping value would result in an amplification of forces ranging from 1 to 3 times current force values.

Table 1: Current Design Standard Equation Characteristics

	ASCE 7-16 Clause 13.3.1.1 $F_p = \frac{0.4a_p S_{DS} W_p I_P}{R_p}\left(1+\frac{2z}{h}\right)$ $\geq 0.3S_{DS}I_pW_p$ $\leq 1.6S_{DS}I_pW_p$	**NBCC Clause 4.1.8.18** $V_p = \frac{0.3S_a(0.2)I_E C_p A_r \left(1+\frac{2h_x}{h_n}\right)W_p}{R_p}$	**ASCE 7-22 Clause 13.3.1.1** $F_p = 0.4a_p S_{DS} W_p I_P \frac{\left(1+\frac{1}{T_s}\left(\frac{z}{h}\right)+\left(1-\frac{0.4}{T_s}\right)^2\left(\frac{z}{h}\right)^{10}\right)}{\sqrt{\frac{1.1R}{I_E\Omega_O}}}\left(\frac{C_{AR}}{R_{po}}\right)$ $\geq 0.3S_{DS}I_pW_p$ $\leq 1.6S_{DS}I_pW_p$	**EuroCode 8** $F_a = \alpha S\left(\frac{3\left(1+\frac{z}{H}\right)}{1+\left(1-\frac{T_c}{T_{s,1}}\right)^2}-0.5\right) W_a\gamma_a q_a^{-1} \geq \alpha S W_a\gamma_a q_a^{-1}$	**New Zeland Standard 1170.5** $F_{ph} = C_h(0)ZRN(T_s,D)C_{Hi}C_i(T_c)C_{ph}R_pW_p \leq 3.6W_p$
Site ground hazard	S_{DS}	$S_a(0.2)$	S_{DS}	S and α	$C_h(0)$, Z, R, and N(T,D)
Structural period			$T_{s,1}$	$T_{s,1}$	
Structural non-linearity			R and Ω_O		
Structural damping					
Structural/Component importance	I_p	I_E	I_E and I_p	γ_a	R_p
Structural dynamic response	z and h	h_z and h_n	z and h	z and H	C_{Hi}
Component dynamic response	a_p	C_p	a_p	q_a and T_c	C_{ph} and $C_i(T_c)$
Component weight	W_p	W_p	W_p	W_a	W_p
Component ductility	R_p	R_p	R		
Component damping					

3. Alternate Methods to Determine Seismic Forces on Components

To address the shortcomings of current building code design equations for non-structural component seismic force determination, several authors have proposed alternate analytically based methods which have been validated empirically (Calvi and Sullivan 2014, Welch and Sullivan 2017, Vukobratovic and Fajfar 2017). Three of these empirical methods are summarized in the following sub-sections, and a method using the direct results from non-linear time history analysis (NLTHA) is also presented. All four methods involve the generation of a floor acceleration spectrum, from which spectral accelerations at specific component periods can be obtained. These accelerations can be multiplied by the non-structural component weight, as well as other parameters such as component importance and ductility, to determine design forces.

3.1 CALVI AND SULLIVAN

The Calvi and Sullivan (2014) method predicts the floor acceleration spectrum of a multi-degree of freedom (MDOF) linear system based on a method of estimating acceleration spectrums on single degree of freedom systems (SDOF) which was previously proposed by Sullivan et al. (2013). The original SDOF method relies on an empirical dynamic amplification factor (DAF) which links the floor spectral acceleration (a_m) at a given period to the maximum acceleration of the SDOF (a_{max}) based on the ratio of the component period (T_c) and the effective period of the structure ($T_{e,i}$). The value of a_m is determined differently for various component period ranges in relation to the structures natural period ($T_{s,i}$) and the structures effective period.

$$a_m(T_c) = \frac{T_c}{T_{s,i}}\left[a_{max}(DAF_{max}-1)a_{max}\right] \text{ for } T_c < T_{s,i} \quad (1)$$

$$a_m(T_c) = a_{max}DAF_{max} \quad \text{for } T_{s,i} \leq T_c < T_{e,i} \quad (2)$$

$$a_m(T_c) = a_{max}DAF \quad \text{for } T_c \geq T_{e,i} \quad (3)$$

$$DAF = \frac{1}{\sqrt{\left(1-\frac{T_c}{T_{e,i}}\right)^2+\xi_c}} \qquad DAF_{max} = \frac{1}{\xi_c^{0.5}} \quad (4) \text{ and } (5)$$

Since this SDOF method provides the ability to estimate the floor accelerations for singular modes, the method is then extended to a MDOF system by using modal combination rules analogous to determining floor forces when completing response spectrum analysis, such as shown in Chopra (2000), and the value of a_{max} are determined from the spectral acceleration of a mode $S_{a,i}(T_{s,I},\xi_s)$ using the mass normalized (m) eigen shape for each mode at each floor (j).

$$a_{max} = a_{j,i} = \frac{\varphi_{j,i}m_{e,i}}{\sum \varphi_{j,i}m_j}S_{a,i}(T_{s,i},\xi_s) = \varphi_{j,i}\Gamma_{j,i}S_{a,i}(T_{s,i},\xi_s) \quad (6)$$

As such, this method requires knowledge of the modal properties of the structure since it combines the response of each of the structure's modes at each of the floors (or degrees of freedom) to form an envelope. This information is readily available from commonly used structural analysis software. Furthermore, the ground spectrum is required as it is used as a lower bound limit of the acceleration spectrum at the lower floors.

3.2 WELCH AND SULLIVAN WITH ADDITIONS BY MERINO ET AL.

The Welch and Sullivan method (Welch and Sullivan 2017) extends the Calvi and Sullivan method to account for the non-linearity of the structural system. This extension is shown in Equation (7), where the ductility demand on the supporting structure (μ) is included and the value of α as empirically derived which varies based on the structural system and the mode. Welch and Sullivan (2017) also specify a method of obtaining the structural effective period $T_{e,i}$ of mode i based on the anticipated ductility of the structural system, an example of which is shown in Equation (8) and (9) for reinforced concrete cantilever shear walls.

$$a_{j,i} = \frac{\varphi_{j,i}\Gamma_{j,i}S_a(T_i,\xi_s)}{\mu^{\alpha_i}} \quad (7)$$

$$T_{e,1} = T_{s,1}\sqrt{\frac{\mu}{1+r(\mu-1)}} \qquad T_{e,2} = T_{s,2}\left(1+0.5\left(\frac{\mu}{5}\right)\right) \; for\ RC\ walls\ with\ 1.0 < \mu < 5.0 \quad (8) \text{ and } (9)$$

The Welch and Sullivan method adjusted Equations (1), (2), and (3), initially presented by Calvi and Sullivan, but further refinement of these equations was completed by Merino et al. (2019) and included considerations for the relationship between peak floor displacements ($\Delta_{R,j,i}$) and spectral accelerations, as well as the peak ground displacement (PGD). A detailed description of the adjusted equations is included in Merino et al. (2019), but the structure of the equations is included for clarity of comparison here:

$$a_m(T_c) = \left(\frac{T}{T_{s,i}}\right)^2(a_{j,i}DAF - a_{j,i}) + a_{j,i} \quad \text{for } T_c < T_{s,i} \quad (10)$$

$$a_m(T_c) = a_{j,i}DAF \quad \text{for } T_{s,i} \leq T_c < T_{e,i} \quad (11)$$

$$a_m(T_c) = \frac{4\pi^2}{T_c^2 g}\sqrt{\sum_{i=1}^{n}\Delta_{R,j,i}^2 + PGD^2} + \frac{4\pi^2}{g}\left(\frac{T_{e,i}}{T_c^2}\right)^2\left(\frac{T_{e,i}^2}{4\pi^2}a_{j,i}DAFg - \sqrt{\sum_{i=1}^{n}\Delta_{R,j,i}^2 + PGD^2}\right) \quad \text{for } T_c \geq T_{e,i} \quad (12)$$

Where g is the gravitational constant. The value of the peak floor displacement ($\Delta_{R,j,i}$) is determined using an iterative procedure which closely mirrors those of the Direct Displacement Based Design (DDBD) introduced by Priestley et al. (2007) (outlined in Merino et al. (2019)) and is independently determined for specific expected quantities of non-linear behavior. Merino et al. (2019) demonstrate that the result of this method provides an accurate estimation of both floor spectral accelerations and displacements for structures whose non-linear behavior is well defined.

3.3 VUKOBRATOVIC AND FAJFAR

Another method for determining floor spectral acceleration was proposed by Vukobratovic and Fajfar (2017), which is similar in application to the method proposed by Calvi and Sullivan (2014). It relies on determining the floor spectral acceleration using a modal combination of the spectral acceleration (S_a) estimated at floor j from the i^{th} mode for a specific structural damping (ξ_s). The method is focused on the ratio between the component period (T_c) and the structural modal period ($T_{s,i}$). Finally, the method does account of the non-linearity of the structure by reducing the applied ground spectral acceleration by a response modification factor R_μ.

$$a_{m,i,j}(T_c) = \frac{\Gamma_i \varphi_{i,j}}{\left|\left(\frac{T_c}{T_{s,i}}\right)^2 - 1\right|} \sqrt{\left(\frac{S_a(T_{s,i},\xi_s)}{R_\mu}\right) + \left[\left(\frac{T_c}{T_{s,i}}\right)^2 S_a(T_c,\xi_c)\right]^2} \leq AMP_i \Gamma_i \varphi_{i,j} \left(\frac{S_a(T_{s,i},\xi_s)}{R_\mu}\right) \quad (13)$$

$$AMP_i = 2.5\sqrt{\frac{10}{5+\xi_c}} \quad \text{for } \frac{T_{s,i}}{T_c} = 0 \quad (14)$$

$$AMP_i \text{ Linear between } AMP_i \text{ values at } \frac{T_{s,i}}{T_c} = 0 \text{ and } \frac{T_{s,i}}{T_c} > 0.2 \quad (15)$$

$$AMP_i = \frac{10}{\sqrt{\xi_c}} \quad \text{for } \frac{T_{s,i}}{T_c} > 0.2 \quad (16)$$

3.4 DIRECT RESULTS FROM NLTHA

Many building codes state that non-structural component seismic forces may be determined using alternate methods of rational analysis but provide limited additional guidance. An exception is ASCE 7-22 which provides Equation (17) to determine non-structural component seismic forces from non-linear time history analysis (NLTHA):

$$F_p = I_p W_p a_i \left(\frac{C_{AR}}{R_{po}}\right) \quad (17)$$

where a_i is the maximum acceleration at floor level i, I_p is an importance factor, W_p is the component weight, R_{po} is the component ductility, and C_{AR} is an empirical component response amplification factor. This approach, while allowing the dynamic non-linear behaviour of the base structure to be incorporated still does not attempt to explicitly quantify component response amplification due to resonance between a component and the structure.

This can be derived from NLTHA results by outputting mean floor acceleration spectrum directly from acceleration time history records at nodes across the structural model. A floor acceleration spectrum can then be calculated from each acceleration record at each node of interest, and a mean or mean plus the standard deviation of the floor spectrum can be used to determine design accelerations. In structures with no torsional irregularities and relatively stiff diaphragms, the resulting design spectrum of all nodes at a single floor should be similar and could be simplified to a single design floor acceleration spectrum. The design floor spectral acceleration at the expected component period is then multiplied by the component weight, importance factor, and a ductility reduction factor to determine the expected component design forces, as shown in Equation (18). To avoid regenerating floor spectrums for each component damping value, an amplification factor (D_p) can be attributed to various component categories based on their assumed reduced damping value compared to the 5% used to generate the floor spectrum. A schematic summary of this method is shown in Figure 2.

$$F_p = \frac{I_p W_p D_p S_{a,c}(T_c, \xi_c = 5\%)}{R_{po}} \quad (18)$$

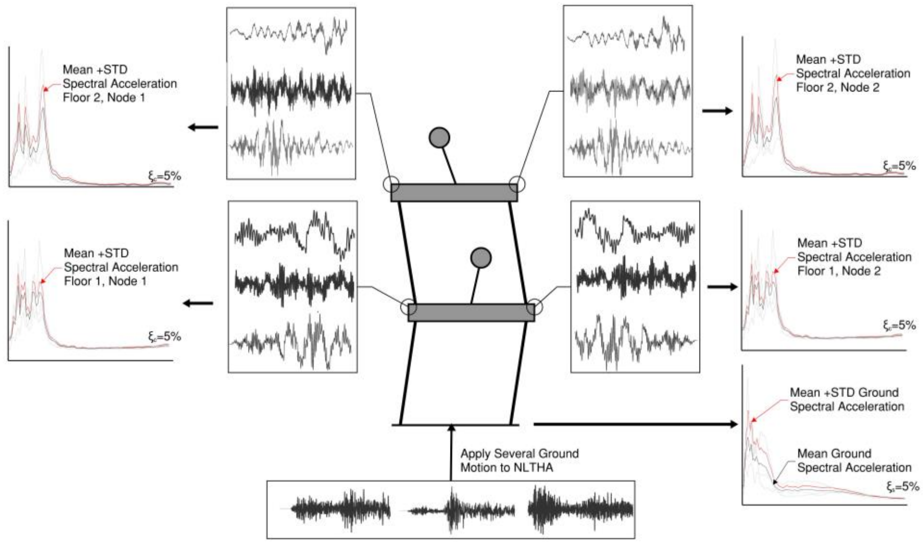

Figure 2: Generation of Floor Spectral Accelerations from NLTHA

3.5 Comparison of the Analytical Based Methods

All three empirically developed methods capture several parameters not included in the design standard equations, a summary of which is shown in Table 2Table 2. However, the three methods vary when attempting to capture the impact of the non-linear behaviour of the structure. While the Calvi and Sullivan method does distinguish between a structural elastic period and effective period, the floor accelerations are not limited by the non-linearity of the structure, as $a_{j,i}$ is determined using a linear relationship to the ground acceleration with only the mass and modal values. This disadvantage is overcome by the modifications made by Welch and Sullivan (2017), and later Merrino et al. (2019), but includes several underlying assumptions including determining a seismic displacement, assuming negligible contribution of higher modes to floor displacements, and adjusting Equations (8) and (9) based on knowledge of the hysteretic behaviour of the elements. Finally, the Vukobratovic and Fajfar method does simplify the inclusion of the non-linear behaviour by accounting for it with a singular structural force reduction factor. However, this static value is determined empirically and does not vary based on the magnitude of forces. The Fajfar method also imposes a limit on the floor spectral accelerations enforced around the periods of the structure to also account for ductility, leading to a plateau of accelerations which can underestimate the floor accelerations (Merino et al. 2019). Finally, using the results of the NLTHA explicitly includes all the characteristics as they are captured by the analytical model and, therefore, the values are only sensitive to the assumptions and uncertainties inherent to any model.

3.6 Practical Considerations when Utilizing Analytical Based Methods

As highlighted in Section 2, the refinement of current design standard equations is required to determine more accurate non-structural component design forces by considering additional parameters not included in current design standards, particularly those related to the structural behaviour. This requirement becomes increasingly relevant when seeking to utilize the efficiencies provided by high performance systems, such as seismic isolation and supplemental damping, as these systems significantly modify the dynamic behaviour of the structure. As such, these systems can reduce the imposed floor accelerations on non-structural components when compared to those determined with existing standards, providing an additional source of design efficiency. However, none of the newly developed methods can consider this structural behaviour without required additional information from a dynamic analysis of the structure. This requirement highlights two main practical considerations for adjusting the design method:

Table 2: Characteristics of Recently Developed Methods for Determining Design Acceleration

	Calvi and Sullivan $S_{a,c}(T_c) = f(S_a(T_s), T_s, T_c, \Gamma, \varphi, \xi_c)$ $F_p = I_p W_p S_{a,c}(T_c) R_{po}^{-1}$	**Welch and Sullivan with Merino et al. correction** $S_{a,c}(T_c) = f(S_a(T_s), T_s, T_c, \Gamma, \varphi, \xi_c, \xi_S, R, \mu, \alpha)$ $F_p = I_p W_p S_{a,c}(T_c) R_{po}^{-1}$	**Vukobratovic and Fajfar** $S_{AF}(T_c) = f(S_a(T_s, \xi_s), T_c, \Gamma, \varphi, \xi_c, R_\mu)$ $F_p = I_p W_p S_{AF}(T) R_{po}^{-1}$	**Spectra from Direct NLTHA** $F_p = I_p W_p S_{a,c}(T_c) R_{po}^{-1}$
Site ground hazard	$S_a(T_s)$	$S_a(T_s)$	$S_a(T_s)$	Ground Motion Selection
Structural period	T_s	T_s	T_s	Analytical Model Modal Analysis
Structural ductility		R, μ, α	R_μ	Non-linear Model Elements
Structural damping	ξ_s	ξ_s	ξ_s	Modeled damping
Structural/Component importance	I_p	I_p	I_p	I_p
Structural dynamic response	Γ,φ	Γ,φ	Γ,φ	Modal Responses
Component dynamic response	$S_{a,c}(T_c)$	$S_{a,c}(T_c)$	$S_{a,c}(T_c)$	$S_{a,c}(T_c)$
Component weight	W_p	W_p	W_p	W_p
Component ductility	R_{po}	R_{po}	R_{po}	R_{po}
Component damping	ξ_c	ξ_c	ξ_c	ξ_c

3.6.1 The Additional Analysis Effort

- Both the Calvi and Sullivan method and the Vukobratovic and Fajfar method could be implemented within any software conducting linear RSA, where the floor spectrums would be an additional output. The only additional design effort required is the specification of either the effective period of the structure, or the response reduction factor, which could be assigned conservative values to neglect the non-linear effects. Either of these methods would provide accurate estimations of the acceleration demands at seismic intensities which do not cause large quantities of structural non-linear behaviour, such as ground motions with higher return periods. This performance level has increased relevance as design standards begin targeting immediate occupancy performance objectives for seismic events with higher return periods (ex: NBCC 2020). However, the limited integration of non-linear structural behavior can cause these methods to overestimate the floor accelerations at higher intensity ground motions, as well as floor accelerations in isolated structures or those with supplemental damping.
- The considerations for non-linear structural behavior captured by the Welch and Sullivan method requires that the designer specify the quantity of expected non-linearity at the specified seismic intensity. While this requires some additional effort, the quantity of non-linear behaviour (or ductility) is often already determined at a specific seismic intensity for regular structures due to current capacity design mandated in design standards. Updated versions of equations (8) and (9) are also required for different structural systems and some examples of these equations can be found in Priestley et al. (2007). However, more complex seismic force resisting systems may not be adequately captured by these simplifications (Priestley et al. 2007). An implementation of this method could integrate the generation of floor response spectrums from RSA, where each seismic intensity load case would require specific inputs by the designer, limiting the potential use of this method to a single or select number of seismic intensities which are expected to cause large quantities of non-linear structural behaviour, such as when targeting life safety or collapse prevention.

- The use of NLTHA to generate floor response spectra is also possible, particularly when the effort to perform the analysis has already been expended for the main seismic force resisting system design, such as typically required by codes when seismic isolation or supplemental damping is in incorporated (ASCE 2022, NBCC 2020). The generation of floor response spectrums would then only require the extraction of acceleration time histories from the model.

3.6.2 The Transfer of Design Accelerations to the SSE

The design of seismic restraints of non-structural components is often not completed by the structural engineer but is assigned to a specialty structural engineer (SSE) who is accountable to the contractor and/or installer of the various components. Currently the structural engineer provides the SSE with a limited number of structural parameters required for design, such as the site seismicity, building height, and fundamental period when following EC8. The SSE then performs the design of the components with the remaining component specific parameters. However, the use of any of the four newly developed methods requires detailed information about the dynamic behavior of the structure to generate a floor acceleration spectrum and could be best provided by the structural engineer.

The transfer of entire spectral accelerations would result in a large quantity of information being sent from the structural engineer to the SSE since a minimum of one spectrum would be required for each floor. This level of detail may not be required to capture the various parameters presented in Section 2 and could lead to inaccuracies or additional significant effort as an SSE would have to determine an exact component period. A proposed simplified method to transfer this information would include only two acceleration values and a period range, as shown in Figure 3 (a). The two acceleration values are for components expected to either experience some resonance with the structure or for components with estimated periods outside of the resonance range, defined from a rigid value (T_R) to an extremely flexible value (T_L). These periods would be determined by the structural engineer based on the shape of the acceleration spectrum and would therefore be a function of the structural periods ($T_{s,1,2,etc.}$). The chosen acceleration value would then be used by the SSE in Equation (18) to determine the design force. This simplification results in a streamlined design process as the SSE must decide if a component is considered extremely rigid, or extremely flexible, and choses the amplified value of spectral acceleration. The approximation of a component's rigidity omits the requirement to determine the exact period of a component. This information would be transferred to the SSE via a table of acceleration values for each floor, shown in Figure 3 (b).

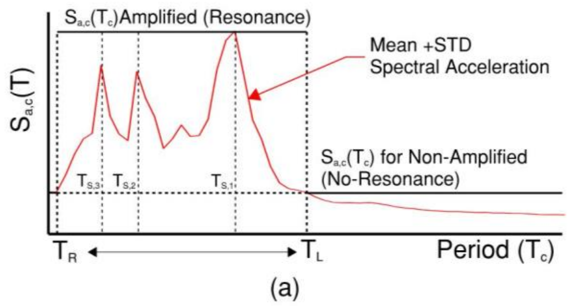

Level	T_R	T_L	$S_{a,c}(T_c)$ Amp.	$S_{a,c}(T_c)$ No Amp.
1				
2				
3				

(b)

Figure 3: (a) Example of Simplified Floor Acceleration Spectrum, and (b) Example of acceleration value table

4. Conclusions

This paper outlined the parameters which impact the design forces for acceleration sensitive non-structural components and explicitly identified the parameters which are not currently included in four design standard equations. The paper then summarises three recently developed methods, Calvi and Sullivan (2014), Welch and Sullivan (2017) with additions from Merino et al. (2019), and Vukobratović and Fajfar (2017); all of which generate a floor acceleration spectrum that captures the influence of the dynamic properties of the supporting structure and its interaction with the component. This paper proposes that the Calvi and Sullivan (2014) and the Vukobratović and Fajfar (2017) methods are the most appropriate for lower intensity seismic events where limited structural non-linearity is expected, while the Welch and Sullivan (2017) method is better suited to regular structures undergoing larger quantities of non-linear behaviour. A method using NLTHA to determine floor accelerations was also discussed and is considered practical when the main seismic force resisting system design requires NLTHA, such as when seismic isolation or supplemental damping is incorporated. Finally, a simplified method of transmitting the design floor acceleration spectrums obtained from any of the four methods to the SSE is presented, which captures the influences of the supporting structure while not requiring the transfer of complex analytical results.

5. References

Anajafi H, Medina R., (2019) "Damping Modification Factor for Elastic Floor Spectra" *Bull. Earthq. Eng.* 17: 6079-6108.

ASCE. (2016) "Minimum design loads for buildings and other structures", ASCE/SEI Standard 7-16. Reston: American Society of civil engineers.

ASCE. (2022) "Minimum design loads for buildings and other structures", ASCE/SEI Standard 7-22. Reston: American Society of civil engineers.

Calvi PM, Sullivan TJ. (2014) "Estimating floor spectra in multiple degree of freedom systems." *Earthquake Struct.* 2014;7(1):17-38.

Chopra, A.K. (2000), "Dynamics of structures", Pearson Education, USA.

Christopoulos, C., and Filiatrault, A. (2006) "Principles of passive supplemental damping and seismic isolation", IUSS Press, Pavia, Italy.

Constantinou, M.C., and Symans, M.D. (1993) "Seismic response of structures with supplemental damping." *The Structural Design of Tall Buildings*, 2: 77–92.

EC8 (2006) "Design of structures for earthquake resistance" *EuroCode 8*, CEN, Brussels

Filiatrault A, Sullivan T. (2014) "Performance-based seismic design of nonstructural building components: The next frontier of earthquake engineering" *Earthq Eng & Eng Vib*, 13: 17-46.

Kelly, J.M. and Marsico, M.R. (2015) "The influence of damping on floor spectra in seismic isolated nuclear structures." *Structural Control Health Monitoring*, 22: 743–756.

Merino RJ, Perrone D, Filiatrault A. (2019) "Consistent floor response spectra for performance-based seismic design of non-structural elements", *Earthq. Eng. Struct. Dyn.*

NZS (2004). "NZS1170.5: Structural Design Actions. Part 5: Earthquake Actions-New Zealand (Incorporating Amendment No. 1)". Standards New Zealand, Wellington, NZ, 86 pp.

Priestley MJN, Calvi GM, Kowalsky MJ. Direct displacement-based seismic design of structures. Pavia: IUSS Press; 2007.

Rashid M., Dhakal R., Sullivan T. (2021) "Seismic design of acceleration-sensitive non-structural elements in New Zealand: State-of-practice and Recommended Changes" *Bull. Of NZ Society for Earthq. Eng.* 54(4)

Rodriguez, M.E., Restrepo, J.I. and Carr, A.J. (2002), "Earthquake-induced floor horizontal accelerations in buildings", *Earthq. Eng. Struct. Dyn.*, 31, 693-718.

Sullivan TJ, Calvi PM, and Nascimbene R. (2013) "Towards Improved Floor Spectra Estimates for Seismic Design" *Earthquakes and Structures*, 4(1): 109-132.

Vukobratović V, Fajfar P. (2017) "Code-oriented floor acceleration spectra for building structures." Bull Earthquake Eng., 15:3013-3026.

Welch DP, Sullivan TJ. (2017) "Illustrating a New Possibility for the Estimation of Floor Spectra in Nonlinear MDOF Systems." Proceedings of the 16WCEE, Paper N° 2632, Santiago, Chile.

Design for Enhanced Nonstructural Performance – Case Studies and Recommended Practices

Maryann Phipps[1] and Solmaz Jumakuliyeva[2]

[1,2] Estructure Inc.
1144 65th St, Suite A
Oakland, CA 94608
[1] e-mail: mphipps@estruc.com
[2] e-mail: solmazj@estruc.com

Abstract. Transforming communities to better achieve earthquake resilience is an aspirational goal that will take time and resources to accomplish. It will require a collective call to action and a willingness to adopt building codes that not only protect life safety, but also address functional recovery. While debate continues about whether and how to implement enhanced seismic performance objectives on a broad scale, some knowledgeable building owners understand the limitations of most modern building codes and are eager to explicitly design their own buildings for low damage right now. Structural design for enhanced performance can be accomplished using tools such as ASCE/SEI 41 *Seismic Evaluation and Retrofit of Existing Buildings*. Nonstructural design for enhanced performance, however, is less straightforward because of the vast number of nonstructural components and systems in any building, their interrelationship, and their roles in supporting needed post-earthquake functions, which vary from building to building. When resources are limited, yet enhanced performance is desired, a common question from building owners is "What are the most cost-effective nonstructural improvements that will enhance post-earthquake recovery?" Or in other words, "Where do I get the most return on my nonstructural investment?" A strategy is needed to determine which nonstructural components should be targeted for enhanced performance and what design approaches are available to increase the likelihood of achieving project objectives.

This paper describes approaches for enhanced design of selected nonstructural systems and provides case studies of projects where enhanced nonstructural performance was an explicit performance objective. It explores both the process used and strategies implemented to achieve the desired post-earthquake recovery objectives. Since different occupancy types have different post-earthquake needs, a range of nonstructural systems and project types is presented. The goal of the paper is to advance the practical implementation of low damage/enhanced performance nonstructural design.

Keywords: Nonstructural, Enhanced, Performance, Resilience, Case Study

1. ENHANCED NONSTRUCTURAL PERFORMANCE

1.1 INTRODUCTION

Reconnaissance of past earthquakes and loss estimates for future earthquakes both highlight the fact that for modern engineered buildings, most future earthquake losses in most earthquakes will be predominated by nonstructural damage. It is also well known that consequences of nonstructural damage can include extended building closure while repairs are undertaken. In light of this, code requirements for buildings housing essential services – those defined as Risk Category IV in the International Building Code (IBC) - include enhanced design requirements for nonstructural components and systems. These requirements are intended to improve the likelihood that essential facilities remain functional following an earthquake.

For buildings not designated essential, however, the minimum requirements of the building code are intended to reduce risks to occupants. Property protection is neither a stated nor an implied goal of the building code [ASCE-SEI, 2022]. For building owners interested in quickly regaining use of their facilities following an earthquake, intentional design of nonstructural systems is needed to reduce the possibility of extended building closure resulting from avoidable nonstructural damage. One approach to enhanced nonstructural design is to implement code requirements for essential buildings. This would generally require all components and systems to be designed for 50% higher design forces and for more nonstructural components to be explicitly designed for earthquake demands. Structural design could limit drift as is required for Risk Category IV buildings or the components, in particular cladding, could be designed to accommodate higher drifts without damage. For many building owners the level of desired nonstructural performance does not rise to that associated with essential facilities since they can accept limited downtime following an earthquake until city or regional utilities are restored. However, they often do desire to reduce the risk associated with closure that could extend for many months.

In order to address a building owner's desire for enhanced nonstructural performance, designers are often asked to recommend specific measures that can be undertaken to reduce nonstructural damage. This requires the explicit consideration of the consequences of nonstructural damage on the specific building occupancy. It also requires collaboration with the owner, as well as other design professionals, because of the interdependencies among most nonstructural systems. Since most enhancements also come at added cost, the relative cost-benefit of enhancements is needed to guide decision-making. The process of identifying and implementing nonstructural enhancements can be cumbersome as there is little practical guidance available.

1.2 NONSTRUCTURAL DESIGN FOR ENHANCED PERFORMANCE

The process of designing for enhanced nonstructural performance starts with understanding the building occupancy and the conditions associated with functional recovery. For example, in a research laboratory, loss of use of dry labs and offices may be acceptable for extended periods following an earthquake. However, loss of access to research specimens may be unacceptable as decades of research could be lost. For a disadvantaged or elderly housing project, the desire may be to allow residents to continue occupying their spaces. The question then becomes what services are deemed essential for continued occupancy? An understanding of what is judged to be critically important, and what is not, is needed to guide design development in each case.

When nonstructural systems are targeted for enhanced design, there is still a need to determine what enhancements are best suited for the project. Enhancements may include designing for higher demands, selecting more robust equipment, adding details that accommodate relative movement, and/or implementing enhanced inspection, for example. Probabilistic assessments of building performance, such as those based on the FEMA P-58 methodology, can be used to help identify the most vulnerable components and establish priorities for nonstructural enhancements. Practical approaches for enhanced design of selected nonstructural systems are described in the next section on a system-by-system basis. Each is intended to summarize the consequences of damage and highlight the range of options available for design enhancements. Case studies in the following section spotlight strategies and methods utilized to achieve such design enhancements.

2. NONSTRUCTURAL COMPONENTS AND SYSTEMS

While there are countless nonstructural components and systems within a building that may be critical for post-earthquake recovery of a specific building, most buildings are vulnerable to nonstructural damage associated with the following nonstructural systems. Design strategies for reducing the likelihood and/or severity of earthquake damage are described for each.

2.1 CLADDING

The building envelope is typically one of the most expensive systems installed in a building. Heavy cladding systems are vulnerable to becoming dislodged and have the potential to cause death or serious injury. Most cladding systems are vulnerable to earthquake damage that could cause extended building closures to implement repairs. Building code requirements have evolved over the years and current US seismic codes are believed to be sufficient to prevent death or serious injury in most seismic shaking. However, while the codes include design provisions addressing drift compatibility of cladding and the structural framing, these requirements are not well-defined and are often not the subject of plan review. Consequently, some buildings are vulnerable to cladding damage that could render them unusable for extended periods following an earthquake.

In recognition of the potential vulnerability posed by cladding, enhanced measures can be implemented to improve the reliability of the cladding performance. These measures may include:

- Cladding selection – Some cladding systems are inherently more resilient than others due to their lightweight nature and inherent deformability. Some are easier to design and install. For example, well-designed curtain wall systems have been shown to accommodate substantial interstory drift without damage requiring significant repairs.

- Cladding design – An essential aspect of cladding design is identifying the manner in which interstory drift is addressed. A single cladding system with a simple, well-defined and well-designed mechanism for accommodating drift generally has the best potential for limiting damage. The damage potential increases when different cladding systems are installed on a building, particularly if the cladding systems behave substantially differently. For example, installing a sliding system immediately adjacent to a rocking system complicates the waterproofing, fireproofing and seismic detailing. Performance is usually more reliable when the cladding systems installed on a building are compatible, designed by engineers experienced in seismic design of cladding, and when they are easy to construct and inspect.

- Structural stiffness – While cladding is sensitive to both seismic floor accelerations and interstory drifts, accommodating drift is generally more challenging and has been the source of most earthquake damage to cladding. When the structural system is being chosen and proportioned, the ability of the cladding system to accommodate the anticipated structural drifts should be considered. Sometimes it is cost-advantageous to reduce structural drift rather than use special cladding detailing to accommodate large drifts. It is critically important that the coordination of cladding and structural design occur early in the structural design process when decisions about the primary lateral force resisting systems are being made. The relative advantages of reducing drift with a stiffer lateral system versus reducing accelerations with a more flexible system should be considered.

- Mock-up tests – One way to increase the reliability of the cladding system is to build and test full size replicas under anticipated building drifts. Acceptance criteria at various stages would be established in advance of the testing, such as no damage at 50% Design Earthquake (DE), repairable damage at DE, no dislodging at the Maximum Considered Earthquake (MCE).

- Peer review – Since most building departments focus primarily on protection of life, cladding design to limit damage may not be reviewed. In order to gain confidence in the design, some owners elect to have their designs peer reviewed by an independent third party experienced in the design of similar systems. Such a review is generally focused on limiting damage to satisfy the project performance objectives.

2.2 ELEVATORS

Elevators are an important means of safe emergency egress in many buildings. They are particularly important in high-rise buildings and essential facilities, such as hospitals, where emergency egress can be impaired due to the long egress distances or occupant immobility. They are also important in any building housing individuals with mobility restrictions or in buildings for which continued post-earthquake occupancy is desired. Earthquake damage to elevator systems has often hindered building operability and emergency response following earthquakes [Wang *et al.*, 2017].

Elevators can be classified into one of two major categories depending on the type of hoist mechanisms: 1) hydraulic elevators, which utilize a fluid pumping system to lift the cabin, or 2) traction elevators, which consist of a cabin attached to one end of hoist ropes and a counterweight attached to the opposite end to balance the cabin weight. Traction elevators used in all high-rises and buildings over about 7 stories have historically been more susceptible to earthquake damage than hydraulic elevators [Brinkman *et al.*, 2017].

Counterweight derailment has accounted for the most prominent damage in past earthquakes largely as a result of excessive impact loading imposed on the supporting guiderail systems. Other common types of damage included bent guiderails, guiderail anchorage failure, collision of counterweights and cabins, machine-drive anchorage failure, jumped or twisted ropes, falling counterweight blocks and damage to hoistway elevator doors [Wang *et al.*, 2017].

ASME A17.1 provides seismic design guidelines for elevator guiderail systems [2019]. The design guidelines require that the stresses imposed on the guiderails remain in the elastic range when subjected to seismic impact loading of the cabin and counterweight. In addition, deflections of the guiderails and their attachment points are limited to prevent cabins and counterweights from derailment. The design criteria set forth in ASME A17.1 are intended to protect life safety in the Design Earthquake. However, if high level of reliability for post-earthquake use is desired, additional measures are often undertaken, which include the following:

- Design criteria - Increasing the design forces and/or imposing stricter deflection requirements on guiderails will increase the threshold for common types of damage to elevators.

- Limit building drift – Damage associated with elevator doors and frames is directly related to building drift. There will generally be less likelihood of doors jamming if subjected to lower interstory drifts.

- Elevator switches – Much elevator system damage and subsequent repair can be attributed to the elevator's continued movement within the hoistway while undergoing seismic motion. An elevator not in motion at the start of a seismic event and one that is not operated until the seismic motion has subsided will have far greater probability of post-earthquake functionality [Brinkman *et al.*, 2017]. Modern elevator control systems can be utilized to create algorithms requiring at least one elevator to always be stationary to ensure that at least one remains at rest during a seismic event.

- Post-EQ plan – Should elevator service be lost as a result of earthquake damage, service restoration can be expedited by stocking on-site critical elevator replacement parts and contracting in advance for priority response for elevator mechanics.

Some owners investing in enhanced seismic performance have elected to design at least one elevator using the design criteria specified for California hospitals as set forth in the California Building Code (CBC) Section 1617A.1.27 [2022; ASME, 2019]. Increasing the reliability of at least one elevator will increase the potential for building re-occupancy following an earthquake.

2.3 Mechanical and Electrical Equipment

In order for most buildings to function after an earthquake, the basic infrastructure providing ventilation, water, sewer, and power must remain functional or be quickly returned to service. For complex buildings and functions, the list of essential utilities can be expansive. These systems rely on a vast array of building equipment. US building code seismic design requirements for equipment deemed non-essential are intended to prevent the equipment from moving during an earthquake - they are not designed to maintain functionality. Equipment deemed "essential", including equipment containing sufficient hazardous material, are designed for higher forces (Importance Factor of 1.5) and must be demonstrated to function following strong earthquake shaking [ASCE-SEI, 2022].

When enhanced nonstructural performance is desired, the consequences of loss of equipment must be considered and measures need to be undertaken to reduce risks judged unacceptable. These may include:

- Design demands – Equipment judged to be needed for post-earthquake operations can be designed for higher forces (Importance Factor of 1.5).

- Special Seismic Certification – Equipment that has been certified for earthquake shaking via shake table testing can be specified when post-earthquake functionality is needed.

- Location – Since floor accelerations generally increase over the height of the building, more reliable performance can generally be achieved by locating critical equipment at or below grade.

- Back-up systems – Planning for interruptions of electrical and water service is part of achieving enhanced seismic performance. Essential facilities provide emergency generators for back-up power, reserve water and other utilities deemed essential to operations.

2.4 Suspended Piping Systems

Earthquake damage to suspended piping rarely represents a life safety concern unless piping contains a sufficient amount of hazardous material. However, damage to piping systems can cause water release which, if not shut off quickly, can cause damage resulting in building closure for an extended period. This is particularly true for pressurized water piping systems.

In recognition of the severe consequences of damage to piping systems, piping systems can be explicitly designed to limit earthquake damage. Some enhancement measures include:

- Design demands – Components designed with an Importance Factor of 1.5 are expected to remain in place, sustain limited damage and increase the likelihood of functioning after an earthquake. Where enhanced performed is desired, suspended piping can be designed for these higher demands. This will tend to result in the installation of bracing at closer spacing and/or stronger bracing.

- Design scope – The building code exempts some pipes from bracing based on size, ductility and/or weight. Where a higher level of seismic performance is desired, more pipes can be braced.

- Pipe connections – Pipes tend to be most vulnerable at locations of high stress concentration such as at the connection to equipment or at any location where differential movement is expected. For enhanced performance, greater attention is paid to likely vulnerable locations. Flexible connections can be used to reduce the potential for damage caused by differential movement. Material selection and connection design are also important factors. More ductile material and robust connections will tent to limit damage.

- Analysis – Piping systems requiring a high degree of reliability, such as those in power plants, can be analytically modelled and analysed to more accurately evaluate stresses in piping, connections and restraints. Such analyses are not currently common in the U.S. building industry, but could be considered for design of critical piping systems.

- Shut-off valves – One way to reduce the consequential damage of pipe breakage, particularly for pressurized piping, is by increasing the number of shut-off valves, improving access to them and maintaining trained on-site staff available for immediate post-earthquake response.

2.5 CEILINGS

Ceilings designed for conformance with modern building codes are expected to protect building occupants from serious injury. Ceiling damage will range based on ceiling type and could consist of fallen ceiling tiles in a suspended acoustic tile ceiling to cracked gypsum wallboard in a joisted gypsum wallboard ceiling. Such damage may be acceptable, even when post-earthquake occupancy is desired. If a higher level of performance is desired, additional measures such as these may be considered:

- Brace spacing – Decreasing the spacing of suspended ceiling bracing will tend to reduce damage. For example, in California hospitals, ceiling bracing is installed every 96 sf, compared with 144 sf for some jurisdictions and 1000 sf in ASTM E580 [2022; California Building Standards Commission, 2022].

- Strength of the suspended grid system – Systems rated "heavy duty" by ASTM E580 will tend to provide enhanced seismic performance due to increased strength.

- Ceiling subdivision – Large ceiling areas can be subdivided into smaller areas, each independently braced. This will tend to result in more reliable performance.

- Ceiling elimination – Open ceiling designs eliminate ceiling damage.

2.6 PARTITIONS

Most modern commercial partitions consist of metal stud walls sheathed with gypsum wallboard. Such partitions are vulnerable to damage, primarily as a result of interstory drift. Cracked gypsum wallboard may be acceptable for post-earthquake occupancy of some buildings. In other cases, cracked gypsum wallboard may impact critical room pressurization or compromise fire ratings. If limiting damage to partitions is desired, the following measures can be considered:

- Building drift – Stiffer buildings resulting in less interstory drift will cause less partition damage than more flexible buildings.

- Top track detailing – Full height studs extended floor-to-floor can be provided with "slip tracks" or "nested tracks", which allow for relative in-plane movement at the track, thereby protecting the gypsum wall board from cracking. These details are less effective at corner conditions and unlikely to prevent all cracking.

- Partial height walls – Stud terminated just above the ceiling and braced to the floor above may be somewhat less vulnerable to gypsum wallboard cracking as a result of interstory drift.

- Box-in-a-box – Designing self-braced rooms with walls connected to ceilings without connection to the floor above can significantly improve partition performance by eliminating the need to accommodate interstory drift.

3. CASE STUDIES

Examples of practical implementation of nonstructural design for reduced damage are described below. These case studies are intended to highlight both the process used to establish nonstructural design goals as well as the strategies employed.

3.1 HCAI'S THREE-PRONGED APPROACH

California's department of Healthcare Access and Information (HCAI), formerly known as Office of Statewide Health Planning and Development (OSHPD), is the authority having jurisdiction for hospitals in California. Recognizing the importance of continued operations of hospitals after an earthquake, OSHPD is charged with developing the regulations and building standards, as well as enforcing them for these essential facilities. OSPHD was formed by Senate Bill 519 in 1973 in direct response to life loss incurred due to the collapse of hospitals in the 1971 Sylmar Earthquake [OSHPD, 2021]. For over two decades, OSHPD developed and enforced strict seismic design standards – this led to hospitals built in accordance with these standards to survive the 6.7 magnitude Northridge earthquake in 1994. However, some essential nonstructural components in these hospitals incurred substantial damage rendering vital systems inoperable. Observed hospital damage in the Northridge Earthquake resulted in Senate Bill 1953 that emphasized the necessity of having both structural *and* nonstructural components survive a major earthquake. The Northridge Earthquake demonstrated the limitations of the nonstructural code provisions and enforcement, and was the catalyst behind OSHPD's emphasis on design of nonstructural components.

In order to fulfil its task of ensuring hospital functionality following a major earthquake, HCAI adopted stringent seismic design requirements for nonstructural components post-Northridge earthquake, similar to those adopted for structural systems post-Sylmar earthquake. HCAI's three-pronged approach to ensuring nonstructural component post-earthquake functionality consists of: 1) implementation of strict seismic design requirements through amendment and promulgation of California Building Standards Code (CBSC), 2) enforcement of these requirements through comprehensive plan reviews, and 3) thorough and continuous construction inspection and material testing.

1) HCAI makes extensive amendments to ASCE/SEI 7 in the California Building Code (CBC), which adopts seismic design requirements for nonstructural components (chapter 13 of ASCE/SEI 7) by reference. HCAI enforces stringent seismic design provisions to minimize damage to nonstructural systems, the most notable of which is the use of component Importance Factor equal to 1.5 in all hospitals. This results in higher seismic design forces on nonstructural components, which leads to

more reliable performance during and after an earthquake. Additionally, HCAI routinely conducts research to achieve reduced seismic hazards in essential facilities that then inform the HCAI code amendments. A recent example of such a research effort is the simulation of the seismic performance of nonstructural systems, Nonstructural Grand Challenge at University of Nevada, Reno, sponsored by the National Science Foundation [OSPHD, 2021].

2) Upon receipt of construction documents, which primarily include plans and construction specifications, HCAI Architects, Engineers, and Fire and Life Safety Officers review each submittal to enforce compliance with the requirements of the CSBC and goals of unimpaired hospital operations after an earthquake. To aid designers, HCAI runs multiple pre-approval programs designed to achieve reliable nonstructural performance. One of these is the Special Seismic Certification Preapproval (OSP), which HCAI voluntarily established to streamline special inspection certifications [OSPHD, 2021] required by ASCE/SEI 7 for those components that must remain operable following the design earthquake. This program requires components to be shake table tested to assure structural stability and functionality of the component. Another notable program is Pre-Approved Details (OPD) which contains standard partition, suspended ceiling, and gypsum board ceiling details that have been designed in accordance with the CSBC and have been reviewed and pre-approved by HCAI. As such, these details are deemed code-compliant if shown in construction documents without modification. These and other HCAI preapproval programs serve to establish and enforce engineering practices that reduce seismic damage of nonstructural components.

3) After plan review and approval, HCAI oversees construction activities to verify project compliance with the approved construction documents and the CBSC. This oversight lasts from building permit issuance to the issuance of a certificate of occupancy. To this end, HCAI runs Hospital Inspector of Record Certification Program to ensure that inspectors of record (IORs) who shall continuously inspect all construction work are appropriately certified. Structural Observation by the Structural Engineer of Record is also required.

All of these HCAI regulations and practices establish an important standard for nonstructural component structural design and a useful model for designing essential facilities needed to be operational immediately following an earthquake. Examples where lesser performance is acceptable, yet intentional low-damage design was desired, are described in subsequent case studies.

3.2 UCSF Wayne and Gladys Valley Center for Vision

The University of California, San Francisco Wayne and Gladys Valley Center for Vision is an example of a new non-HCAI design project where the owner's desire for seismic resilience led to thoughtful consideration of nonstructural component design. The building is located on UCSF's Mission Bay campus and consists of a 12-story office tower, a 5-story ophthalmology clinic, and a 3-story conference center. Forrell/Elsesser served as the Structural Engineer of Record (SEOR) and focused on reducing both structural and nonstructural damage after a major earthquake.

The design process started by determining aspects of seismic resilience that were important to the client. Through guided discussions, the design team and the client narrowed the nonstructural focus to reducing repair costs and recovery times, and limiting or eliminating casualties [Marusich, 2021]. Having identified the desired performance goals, the choice of the structural system was driven by nonstructural considerations. Steel buckling-restrained brace frame (BRBF) and concrete shear wall systems were both identified as viable systems during early stages of design and both systems were evaluated against pre-determined criteria. The nonlinear response history analysis performed early in the design process allowed for best estimates of performance and system comparisons. In comparing the two systems, the concrete shear wall structure was determined to have lower building drifts as well as being more conducive to nonstructural anchorage compared to its steel BRBF counterpart. These advantages, along with others (Figure 1), resulted in the selection of concrete shear walls as the building's lateral force-resisting system. Selection of a structural system that resulted in reduced drifts allowed for a cheaper, but still robust, cladding system to be chosen and installed. This alone was a source of considerable cost savings since the necessity for complicated cladding detailing was waived and consequent material and installation were less costly.

Analysis	Factor	STRUCTURAL STEEL	CONCRETE
	PERFORMANCE:		
	Structural seismic performance:	Better in large events ADVANTAGE	Better in small to moderate events ADVANTAGE
	Nonstructural seismic performance:		Lower building drifts ADVANTAGE
	Vibration performance:	EQUAL	EQUAL
	Acoustic comfort:		ADVANTAGE
	Thermal comfort:	EQUAL	EQUAL
	Daylighting:	EQUAL	EQUAL
	FLEXIBILITY:		
	Interior workspace design efficiency:	Smaller structural columns ADVANTAGE	Open core with core offset ADVANTAGE
	Finishing options for exposed interiors:		ADVANTAGE
	Nonstructural anchorage:		ADVANTAGE
	Future structural modifications:	ADVANTAGE	
	Floor flatness and levelness:		ADVANTAGE
	LOGISTICS & SCHEDULE:		
	Permit schedule:	EQUAL	EQUAL
	Fabrication schedule:		ADVANTAGE
	Field schedule:	ADVANTAGE	
	Flexibility in design schedule:		ADVANTAGE
	Construction hoisting:	EQUAL	EQUAL
	Construction logistics:	EQUAL	EQUAL
	COST:		
	Initial (construction) cost:		More cost effective (less $2.6M) ADVANTAGE
	Post earthquake repair cost:		See the "mean repair" chart ADVANTAGE

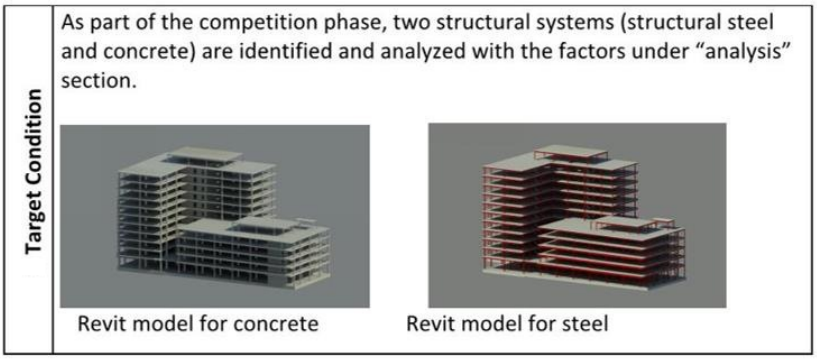

Figure 1: Comparison of two viable lateral force-resisting systems [Marusich, 2021]

Among other nonstructural considerations was specification and installation of automatic seismic shut-off valves and flexible connections between stationary/anchored equipment and MEP distribution lines. Displacement compatibility of nonstructural systems with structural elements and with each other was explicitly examined and clearances were prescribed to avoid contact damage. Furthermore, distribution systems containing hazardous materials were routed out of emergency egress paths to maintain clear and safe evacuation route. In order to provide more reliable functionality of electrical, data and telecom equipment after an earthquake, water piping was also routed away from such essential devices.

3.3 STANFORD BIOMEDICAL INNOVATIONS BUILDING

Another example of a project where enhanced nonstructural performance was desired and explicitly designed for is the Stanford Biomedical Innovations Building located in Palo Alto, CA. The building is located on Stanford University's campus and houses 27 biomedical research labs across four levels above grade and basement. Rutherford + Chekene served as the SEOR and worked closely with the client and users of the space to design the structure to achieve desired structural and nonstructural performance goals.

The building's structure was designed to be a buckling-restrained brace frame (BRBF) with concrete-filled metal deck diaphragms above grade with shear walls in the basement. The foundation system consists of strip and spread footings with grade beams and soil anchors at BRBFs. The building was designed with Importance Factor (I_e) of 1.25 to achieve Stanford's seismic performance objectives for this facility (Class 2).

Nonstructural performance objectives were defined early on in collaboration with the client and users to reduce nonstructural damage, with the ultimate goal of reduced downtime for faster re-occupancy and return to function after an earthquake [Lizundia, 2021]. However, as in almost every project, translating target performance objectives into select cost-effective and biddable design and construction standards presented a considerable technical challenge.

Various approaches to achieving nonstructural enhanced performance were employed by the designer to achieve cost-effectiveness. As a result, select nonstructural elements that required to maintain their functionality reliably (e.g., elevators and stairs) were identified and designed to higher design forces by increasing component Importance Factor (I_p). These elements were identified through a performance objective summary table (Table 1) which was the result of coordination and collaboration between the structural engineer, architect, MEP engineers, users, and peer reviewer. To ensure reliable performance of nonstructural components, rigorous submittal review, field and shop inspections were employed in the project.

Table 1: Performance objective summary table [Lizundia, 2021]

Component	Importance		Above	I_p	Comment
	Occupancy	Function	CBC		
Ceilings	N	N	N	1	
Electrical Typical	N	N	N	1	
Electrical Life Safety	Y	Y	N	1.5	Enhanced submittal review or field observation
Electrical Lab Special	N	Y	Y	1.5	Support components critical to lab function on emergency power? Enhanced submittal review or field observation
Elevator Rail Guiderails & Support Framing	Y	N	Y	1.5	Limit deflection to 0.5"
Other Elevator Components	Y	N	Y	1.5	
Non-stair Railings	N	N	N	1	
Stairs and Stair Railings	Y	Y	N	1.5	Shop inspection of welding
Interior Stud Framing (Non-Lab)	N	N	N	1	
Cladding and Supporting Stud Framing	Y	Y	Y	1	Specific performance criteria at different drift levels

In addition to this, nonlinear response history analysis (NHRA) was performed to obtain reliable drift estimates. These drift estimates were then used to run full scale mock-up tests to ensure that the cladding system was designed to have desired performance at drifts even larger than project NHRA results. Desired performance for this project was identified as remaining watertight at BSE-1N drifts and no contact across joints at BSE-2N drifts.

3.4 UC Berkeley Student Housing

A new student housing project currently underway at the University of California, Berkeley, promises to exhibit all the advantageous aspects of nonstructural component design in a residential project. Tipping Structural Engineers is the SEOR working on project construction documents at the time of writing. The project is set to include a 12-story north and a 9-story south structure, both concrete shear wall buildings with south structure including steel moment frames. There is an enclosed bridge connecting the two structures on levels three through nine, which has seismic joints that allow movement between the structures. The flexible foundations are planned to be auger-cast piles. The project will be designed in accordance with ASCE/SEI 7-22 to take advantage of reduced wall shear demands and to use nonlinear time history (NLTH) analysis.

Due to the project bid schedule, the development of seismic criteria for nonstructural elements has been pushed to the beginning of the construction documents phase. As is a very common practice in California and all across the US, numerous nonstructural systems have already been delegated as deferred submittals at this stage in the project to ensure that all nonstructural systems are accounted for [Tipping Structural Engineers, 2022]. Unlike many projects, however, the process of determining nonstructural design criteria and deferred submittal schedule involved a few rounds of review and commentary with the peer reviewer (Rutherford + Chekene). Among deferred submittals are seismic bracing and anchorage of MEP equipment and distribution systems, building envelope (cladding), stairs and elevators, as well as structural attachments for window washing, exterior building maintenance and fall protection (Figure 2). Importantly, all life-safety elements (fire protection, stairs, etc.) have been flagged to be designed using component Importance Factor of 1.5 – this information will be communicated to the delegated designers via construction specifications and/or structural general notes. Additionally, a critical elevator was identified to require more reliable post-earthquake functionality, and as such, delegated designers will be specified to design one elevator to stringent HCAI essential facility standards.

Utility connections between structures are being made at the lowest possible level to limit the drift demands. The building is almost nearly all electric and emergency outlets will be provided at select locations throughout the building to enable residents to charge phones and laptops after an earthquake. Bathrooms are designed to have independent risers so that individual risers can be shut off and isolated as required to maintain at least one operational bathroom in the event of damage (earthquake or otherwise).

Criteria for cladding performance have been identified as a) accommodating interstory drifts at 50% DE and remaining weathertight, and b) accommodating interstory drifts at DE & meeting “immediate occupancy performance” where some breakage may occur but it must be repairable. A mock-up and testing program for the cladding system is required to demonstrate the weathertight requirements and is fully described in construction specifications.

DELEGATED-DESIGN DEFERRED SUBMITTALS REVIEWED BY SEOR[1]			
	DEFERRED SUBMITTAL	OBSERVATION BY CEOR[2]	SPECIAL INSPECTION
FOUNDATION DEFERRED SUBMITTALS			
1. TEMPORARY SHORING	☒	☒	☒
2. AUGER-CAST PILES	☒	☒	☒
3. CRANE MAT FOUNDATION	☒	☒	☒
INTERIORS DEFERRED SUBMITTALS			
4. INTERIOR METAL STUD PARTITIONS	☒	☐	☐
5. MEP SLAB PENETRATIONS	☒	☐	☐
6. GRAVITY SUPPORT, SEISMIC BRACING, AND ANCHORAGE OF SUSPENDED CEILING ASSEMBLIES	☒	☒	☐
7. MEPFS LATERAL BRACING AND ANCHORAGE FOR EQUIPMENT AND DISTRIBUTION SYSTEMS	☒	☒	☒
CORE AND SHELL DEFERRED SUBMITTALS			
8. BUILDING ENVELOPE, INCLUDING:			
A. CLADDING & GLAZING (INCLUDING CURTAINWALLS & SUNSHADES) W/ ASSOCIATED ATTACHMENTS	☒	☒	☒
B. METAL STUD FRAMING FOR EXTERIOR CLADDING SUPPORT	☒	☒	☒
9. STAIRS, INCLUDING STRINGERS, TREADS, RISERS & ATTACHMENTS	☒	☒	☒
A. ASSOCIATED HANDRAILS/GUARDRAILS AND ATTACHMENTS	☒	☒	☒
10. STRUCTURAL ATTACHMENTS FOR WINDOW WASHING, EXTERIOR BUILDING MAINTENANCE AND FALL PROTECTION	☒	☒	☒
11. ELEVATORS, INCLUDING EQUIPMENT AND GUIDE-RAILS	☒	☒	☒
12. PV PANELS, INTERNAL FRAMING AND ATTACHMENT TO PRIMARY STRUCTURE	☒	☒	☐
13. SEISMIC JOINT COVERS	☒	☒	☐

NOTES:
1. AFTER REVIEW BY SEOR, DEFERRED SUBMITTALS SHALL BE SUBMITTED TO THE CAMPUS BUILDING DEPARTMENT FOR REVIEW.
2. COMPONENT ENGINEER OF RECORD

Figure 2: Deferred submittal and responsibility matrix [Tipping Structural Engineers, 2022]

4. CONCLUSION

Many building owners are interested in implementing nonstructural enhancements to reduce the cost and disruption associated with potential nonstructural earthquake damage. The question is, where is it best to focus nonstructural improvement investments? There is no single answer to the question since it is dependent on many factors including the building occupancy and the consequences of downtime following an earthquake. Probabilistic assessments of building performance can be used to help identify the most vulnerable components and establish priorities for nonstructural enhancements. However, regardless of occupancy, the following measures are expected to reduce the risk of nonstructural damage:

1. Implementing enhanced design review and inspection requirements to ensure that the minimum code and project requirements are properly satisfied.

2. Enhancing protection of suspended water pipes, particularly those under pressure.

3. Specifying critical equipment that has been certified for earthquake resistance.

Additional measures have been presented on a system-by-system basis and case studies have illustrated design strategies for a range of occupancies.

Owners should be informed of options and strategies for reducing nonstructural damage - design professionals are well-positioned to provide insight and guidance.

REFERENCES

ASCE-SEI [2016] *ASCE/SEI 7-16: Minimum Design Loads and Associated Criteria for Buildings and Other Structures – Commentary*, Reston, Virginia: American Society of Civil Engineers.

ASCE-SEI [2022] *ASCE/SEI 7-22: Minimum Design Loads for Buildings and Other Structures,* Reston, Virginia: American Society of Civil Engineers.

ASME [2019] *ASME A17.1/CSA B44-19: Safety Code for Elevators and Escalators,* New York, New York: American Society of Mechanical Engineers

ASTM [2022] *ASTM E580/E580M-22: Standard Practice for Installation of Ceiling Suspension Systems for Acoustical tile and Lay-in Panels in Areas Subject to Earthquake Ground Motions,* West Conshohocken, Pennsylvania: American Society for Testing and Materials

Brinkman K.L, Horne B.W., Lamb M., Shelton T. Mueller M. [2017] "Elevator Post Seismic Functionality in Hospital Applications," *OSHPD White paper submitted on behalf of the National Elevator Industry, Inc. (NEII) dated November 1, 2017.*

California Building Standards Commission [2022] *CBC: California Building Code*, Sacramento, California: International Code Council.

Marusich, S. [2021] "UCSF Wayne and Gladys Valley Center for Vision," *PowerPoint presentation for SEAONC 2021 Summer Seminar dated July 15, 2021.*

OSHPD [2021] "Seismic Compliance Program and Product Report in Accordance with Assembly Bill 100," *dated August 31, 2021.*

Lizundia, B. [2021] "Design of the Stanford BRBF Biomedical Innovations Building," *PowerPoint presentation for SEAONC 2021 Summer Seminar dated July 15, 2021.*

Tipping Structural Engineers [2022] "People's Park Student Housing," *PowerPoint presentation for UCSF Seismic Review Committee (SRC) dated July 18, 2022.*

Wang, X., Hutchinson, T.C., Astroza, R., Conte, J.P., Restrepo, J.I., Hoehler, M.S., & Ribeiro, W.Q. [2017] "Shake table testing of an elevator system in a full-scale five-story building," *Earthquake Engineering & Structural Dynamics,* Vol. 46, pp. 391 - 407.

A Snapshot of Societal Expectations for the Seismic Performance of Buildings in New Zealand – What This Reveals about Future Design Considerations for Non-Structural Elements

H. Ferner[1], C. Brown [2], S. Horsfall[2], S. Abeling[3], and H. Cowan[4]

[1] New Zealand Society for Earthquake Engineering
helenmferner@gmail.com
[2] Resilient Organizations
{charlotte.brown, sophie.horsfall}@resorgs.org.nz
[3] University of Auckland
shannonabeling@gmail.com>
[4] Hugh Cowan Consulting
hugh@hughcowan.com

Abstract.

New Zealand has just experienced its most sustained period of disruption caused by earthquakes since the mid-20th century. The impact of the recent earthquakes has been widely observed and commented upon by stakeholders, policy makers and the general public. The recent events caused extensive structural and non-structural damage with wide ranging social, economic and environmental impacts.

Structural engineers in New Zealand (NZ) historically have designed buildings to meet life safety objectives during and following earthquakes but there has been limited regard to usability following such events. This approach has been effective in reducing loss of life – fulfilling a core objective of the current NZ building code, but questions have arisen whether the observed levels of damage and disruption warrant a rethink of seismic performance objectives. Research to explore societal expectations and tolerance toward seismic risk has been completed as part of a programme of work to inform future performance objectives for the design of new buildings. The findings reveal the importance to NZ communities of restoring building functions following an earthquake, and therefore highlight the performance of non-structural elements as a key determinant of outcomes.

Keywords: seismic risk objectives, non-structural, seismic design, impact on seismic performance of buildings

1. INTRODUCTION

How do New Zealanders in the 2020s want buildings to perform during and after an earthquake? Do New Zealand's current systems and approaches provide buildings that meet these expectations? If not, what changes may be appropriate?

The impacts of the recent NZ earthquakes have been observed and commented upon by stakeholders, policymakers and the public, including both the direct and wider social impacts [CERC, 2012]. Design standards and the subsequent performance of our buildings have consequences for all.

Minimizing the likelihood of death and injury in earthquake and fire has been a fundamental imperative for building design standards for over 50 years. However, other performance outcomes have risen to prominence during recent years in New Zealand and abroad, including, for example, the ability to shelter in place in multi-storey residential buildings after a significant event and to reduce waste and carbon emissions by constructing repairable buildings.

The Resilient Buildings Project (RBP), a New Zealand Society for Earthquake Engineering (NZSEE) initiated project, was conceived to lay the groundwork for resilient building design, informed by the perspectives and expectations of building users. It complements the work currently underway updating New Zealand's National Seismic Hazard Model (NSHM) Both inputs will inform a planned series of updates to the seismic loadings standard NZS1170.5.

NZSEE undertook research to explore societal expectations and tolerance toward seismic risk [Brown et al., 2022] as part of the Resilient Buildings Project. Through a series of interviews and focus groups with diverse stakeholders across New Zealand, the research sought to understand perspectives on the seismic performance of buildings. The participants did not differentiate between different building components but considered the overall performance of a building hightlighting the importance of non-structural elements for stakeholders in addition to the structural elements when considering the performance expectations for seismic designs.

2. SOCIETAL EXPECTATIONS RESEARCH

This work is the first time in New Zealand that researchers have sought to document from a community perspective nationwide societal expectations for the seismic performance of buildings. The approach entailed a series of interviews and focus groups with diverse stakeholders across New Zealand to sample perspectives on the future seismic performance of buildings. The team interviewed 32 individuals who represented a range of experiences and interests across different seismic hazard zones, geographies, socioeconomic groups, and cultural contexts. The interviews focussed on understanding each participant's current role, background, and earthquake experience and their expectations of new building performance during a significant earthquake and during minor to moderate earthquakes.

A series of six geographically based focus groups were then convened, covering three urban centers and three smaller towns with differing levels of seismic hazard. The focus groups each comprised three to seven individuals representing different community perspectives (local civil defence, business community, health sector, welfare sector, environmental interests, and indigenous Māori). The research findings are summarised in a research report [Brown et al., 2022a], a detailed report on interviews [Abeling et al., 2022a] and a detailed report on focus groups [Horsfall et al., 2022].

3. WHAT DO NEW ZEALANDERS WANT FROM THEIR BUILDINGS?

The research findings show that life safety remains of primary importance when considering building performance in earthquakes. It is an expected outcome, indeed was assumed by the research participants. This focus on life safety aligns with New Zealand's current code settings for the building structure.

Participants in the research framed their responses in terms of expectations of overall building performance, but the expectations expressed bear directly on the performance of non-structural elements which has been attributed to 61% of all earthquake-related injuries in New Zealand between 2010 and 2014 [Yeow et al., 2020].

The research found the priorities for life safety are not simply about the number of people occupying a building but include consideration of the types of individuals likely to be in the building. Participants identified vulnerable people and those with essential skills for response and recovery (including economic recovery) as requiring protection. Another consideration the research participants identified was avoiding the potential for mass casualty events or areas with the potential for panic or chaos.

Participants agreed that prioritizing buildings with post-disaster functions, such as hospitals, was important but considered priority should be extended to more buildings, including supermarkets and food production facilities as well as multi-purpose spaces that can be used to support disaster recovery. Locations likely to experience or attract large numbers of people immediately after an earthquake, such as schools and community centers, were also identified as locations where higher building performance is expected due to the danger of aftershocks.

The findings indicate that New Zealanders want more than life safety, with social and economic recovery identified as important objectives following an earthquake.

Equitable access to essential goods and services, sustaining social connection and restoring normalcy that supports cultural identity and economic wellbeing were all noted as important for social and economic recovery. Different types of buildings were identified as high-priority gathering locations depending on the community. These ranged from community centres and places of worship to retail shops and restaurants in cities, and pubs, sports grounds and clubrooms in smaller towns.

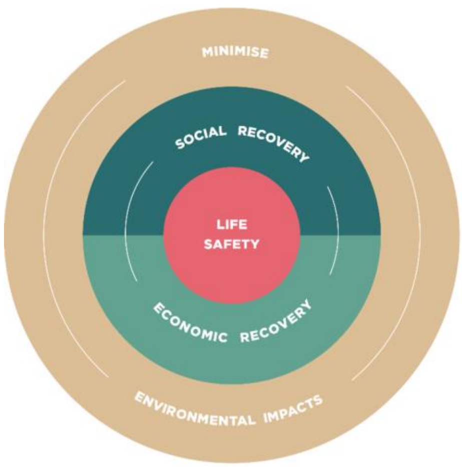

1: LIFE SAFETY

Avoid mass casualty events
Protect vulnerable persons
Ensure safety at mass gathering points
Preserve high value skills and resources
Support immediate response activities
Maintain a perception of safety

2: SOCIAL RECOVERY

Ensure equitable access to essential goods and services
Enable effective governance
Have places to connect
Return sense of normalcy
Retain sense of place and cultural identity

3: ECONOMIC RECOVERY

Restore enabling services and industries
Enable people to work
Build business confidence

4: MINIMISE ENVIRONMENTAL IMPACT

Minimise waste generation
Avoid hazardous waste or potential public health risks
Reduce embodied carbon

Figure 1. Seismic Resilience Performance Objectives

3.1 Expectations of Earthquake Recovery

The research identified safe housing and confidence and certainty in the recovery process as core expectations of the period immediately following a major earthquake. This framing of expectations included prioritizing mental wellbeing and enabling conditions for individuals to contribute to the social and economic recovery of their community.

Participants considered the ability to shelter in place in their homes important and desired an early return of electricity, internet, and telecommunications even if water and sanitary systems were not functional. This expectation is based on the recent Christchurch experience, where many people continued to live in their damaged single-family homes, despite not having access to indoor plumbing, throughout the 14-month-long earthquake sequence.

Participants emphasized the importance of being able to retrieve essential belongings from damaged buildings. This could include allowing people to return to their apartments to collect important documents or their workplaces to collect essential business supplies, all of which depend on the post-earthquake integrity of non-structural elements.

The research highlighted the very strong synergies between economic and social recovery and that many buildings support both. The need for households to generate income soon after an earthquake was identified as important, along with schools reopening quickly, both to enable parents to return to work and to reduce stress on families. Schools also provide a vital function in assisting students in regaining a sense of normality by attending class and seeing their peers thus contributing to mental wellbeing.

Many participants identified the importance of electricity, internet, and telecommunications systems to support businesses to function after an earthquake but noted flexibility about requirements for a physical building for many businesses. Clearly, the recent experience of Covid-19 pandemic has shaped people's expectations of what is needed to support business functionality.

"Returning to normal" is considered a critical factor for recovery. While "normalcy" may look different for different communities, reopening schools, retail and arts and recreation facilities and access to buildings that support cultural wellbeing and identity are noted as key parts of the return to normalcy.

The research identified a significant intolerance to a long-drawn-out recovery, noting the adverse impacts on people's wellbeing and mental health when recovery is slow or uncertain. Many of the functions identified by participants as important for rapid recovery involve the non-structural components of buildings, suggesting that extensive damage to elements that preclude rapid recovery does not meet societal expectations.

This intolerance to disruption following an earthquake points to an expectation of no damage or minimal damage in all but the largest earthquakes, an expectation at variance with the current code settings in New Zealand.

3.2 How Quickly Do Communities Want Different Types of Buildings to be Available After an Earthquake?

Continued building functionality is expected for critical infrastructure and for buildings such as hospitals and emergency service facilities with critical post-disaster functions. This expectation matches the current New Zealand building code settings.

Expectations of time for other buildings to function again after an earthquake vary by building type but show that the expectation is days and weeks rather than months or years. Speed of return to function was identified as a particular priority for some building types that are not currently a priority, including supermarkets, aged care facilities, community centres and homes, refer Figure 2 below.

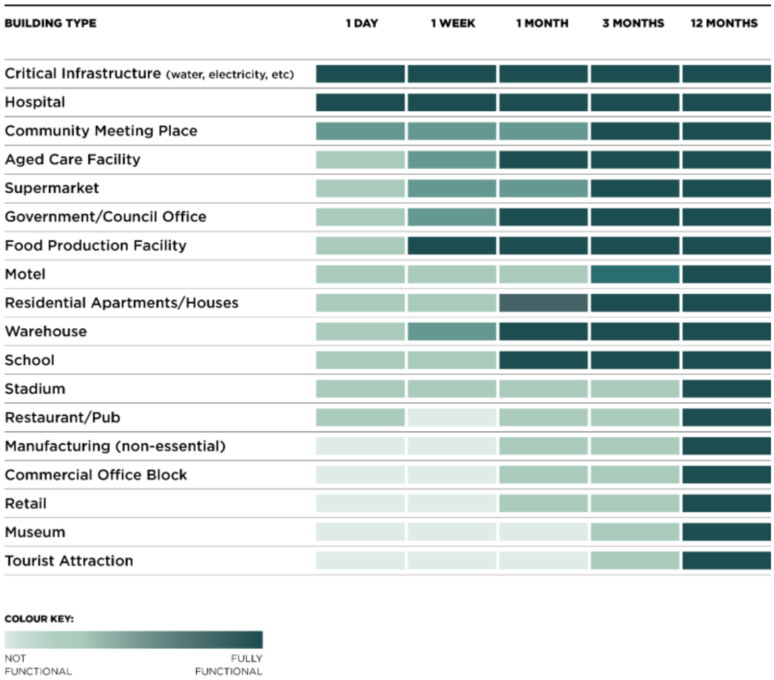

Figure 2. Time to Restore Building Function

In a review of the findings held in March 2022 [Abeling, 2022b], a group of New Zealand's earthquake standards and design experts expressed surprise about people's perceptions of acceptable recovery times for different building types. It was noted that the focus groups' expectations for timelines to return to function were significantly shorter than those anticipated by the 'experts' and were, perhaps, unattainable. The group also noted the need to avoid or limit damage to non structural elements if these expectations for return to function are to be in any way realised. The engineering community has acknowledged that the schema for prioritizing buildings for rapid return to function needs review, particularly with regard to vulnerable groups (e.g., aged care residents).

3.3 What Levels of Damage are Acceptable?

The research sought to explore the extent to which people are willing to accept different levels of disruption due to earthquake damage. While tolerance for disruption due to earthquake damage can be subjective and influenced by factors such as previous earthquake experience, the vulnerability of the building occupants, and the primary use of the building, general trends for people's willingness to accept damage emerged.

The findings indicate that people are generally accepting of minor earthquake damage (defined in the research as repairs needed but minimal disruption to services).

Moderate damage (defined in the research as repairs needed with minor disruption to services – in the order of weeks) was also considered to be generally acceptable, but the descriptions of moderate damage provided by participants were similar to those provided for types of minor damage (e.g., cosmetic damage to paint, plaster and plasterboard and other superficial cracks) suggesting a lower level of acceptability to moderate damage than the initial responses indicated. This finding aligns with the research participants' expectations for a rapid return to function.

One participant reflected on moderate damage at a community level and noted. "*It shouldn't be more than 10% of buildings that would require a week-long remediation.*"

Significant damage (defined in the research repairs needed with significant disruption to services – in the order of months) was identified as less acceptable, with people noting that significant damage would likely require a building to be closed while repairs are planned and undertaken, significantly disrupting occupants and normal building function.

Major damage (defined in the research unoccupiable, possibly requiring replacement) within a nominal 50-year lifecycle was generally considered to be unacceptable..

3.4 WHAT ABOUT MODERATE EARTHQUAKES?

The research shows that in addition to an expectation of safety in smaller earthquakes people expect minimal or no impact on building functionality and limited damage to the non structural elements that support building functionality. In homes, the expectation is that kitchens and bathrooms should remain usable. In offices, building systems (e.g., HVAC systems, telecommunications, and emergency systems such as fire protection systems) should continue to work uninterrupted. Buildings are expected to remain watertight. It is typically expected that the building contents will have moved around and there may be some cosmetic cracking (e.g., cracks in plasterboard). However, any damage should be both minor in nature and limited in extent such that it will be easily repairable and not include any structural damage.

The psychological impacts of ground shaking and earthquake induced building damage is a particular concern. Participants often noted they wanted to "feel safe" within their buildings following an earthquake. Even small earthquakes can cause anxiety, triggering recollection of past events or concern that another larger earthquake is going to follow. Visual reminders of past earthquakes through damage (e.g., cracked plasterboard) can cause anxiety to building occupants. Prevention or remediation of minor damage can reduce unease about building safety.

Participants noted that damage to non-structural elements can be both costly and time-consuming to repair. Buildings may be demolished in the worst-case scenario if they become economically infeasible to repair despite being structurally sound. Maintaining building weathertightness, a key expectation in a moderate earthquake, relies to a great extent on the cladding system in many buildings. Damage to infrastructure service connections or the services themselves can also cause disruptions, such as power outages and damage to pipes that affect water supply will affect a building's ability to function.

3.5 ARE SEISMIC RISK PRIORITIES UNIFORM ACROSS NEW ZEALAND COMMUNITIES?

Mass casualties and impacts that cause intergenerational effects are perceived to be intolerable for communities throughout New Zealand. The community context though was found to deeply influence risk tolerance, with restoration priorities and timeframes for the return to function of various assets and industries dependent on community-specific priorities. This variance in building risk prioritization demonstrates that buildings are part of broader social and economic systems that support community resilience.

The seismic hazard, level of geographic isolation, density of the built environment, and the capacity for a community to recover from disruption all influence the risk tolerance of communities. In addition, the social and economic context of a community directly influence their risk mitigation priorities.

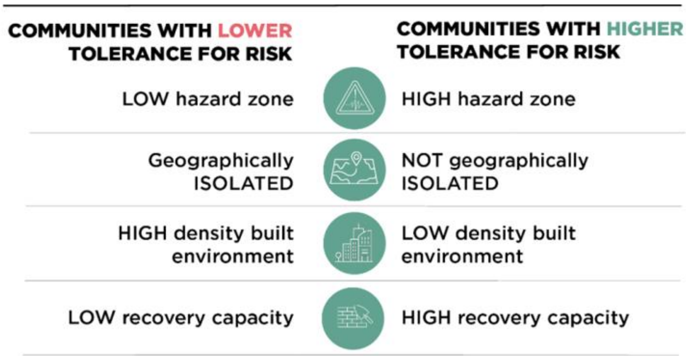

Figure 3. Factors affecting risk tolerance of communities

Communities with dominantly agricultural economies prioritize buildings related to agricultural employment and production. (e.g., food production facilities and transport/logistics hubs) while such facilities are perceived to be less important in urban centres.

While not assessed directly, overall tolerance for seismic risk appears to have declined as a consequence of recent earthquake impacts on NZ urban centers. This is reflected in the recommendations of an official inquiry into the Canterbury Earthquakes to "both explore the performance of buildings in Christchurch in the earthquakes and the adequacy of the current legal and best practice requirements for the design, construction and maintenance of buildings in central business districts in New Zealand to address the known risk of earthquakes" [CERC, 2012].

3.6 What Influences Willingness to Reduce Seismic Risk in Buildings?

The research on societal expectations explored qualitative trade-offs between the benefits and costs of reducing seismic risk. This revealed that building owners with a long-term perspective of their buildings are more likely to invest in reducing seismic risk to reduce whole-of-life costs and enhance return on investment over the longer term. Other benefits identified are to protect reputation, attract tenants, obtain and maintain insurability, reduce downtime and rebuild costs in the event of an earthquake, and support the local community.

Many factors were also identified as a deterrent or hindrance to the construction of buildings with enhanced seismic resilience. Some participants expressed concern that higher building standards for enhanced seismic risk mitigation are likely to be prohibitively expensive, and the benefits may not exceed the costs, especially over a typical debt repayment period of about 20 years. There was also concern that the market may not understand or be able to adequately value the benefits of seismic resilience, with building owners and tenants unwilling to pay for enhanced levels of building performance. Additionally, the expected performance of neighbouring buildings was identified as a significant inhibitor. Building owners were concerned they may not be able to realize the benefits of a seismically enhanced building due to damage to surrounding infrastructure or damage to neighbouring buildings resulting in mandatory exclusion and perceptions of lack of safety in the area.

The availability and affordability of earthquake insurance also influence building owners' willingness to build more seismically resilient buildings. Some participants described how, instead of building to higher standards, risk could be mitigated given the current (high) availability of earthquake insurance in New Zealand and assumed government support for post-event recovery. Similarly, some larger businesses selfinsure and/or rely on their geographic spread to manage risk. These businesses have calculated that a disruption in one region or the loss of one site can be compensated by other parts of their operations.

The study also identified a lack of trust in engineering and the construction sector to design a building to a given performance outcome, manage building sites to ensure that what is designed is built and for contractors to build quality products. These perceptions may be influenced by damage to relatively modern buildings following the 2016 Kaikōura earthquake.

3.7 How Important is Seismic Risk Relative to Other Aspects of the Built Environment?

Seismic resilience is one among many competing demands on the built environment. The research sought to contextualize seismic risk relative to other key performance objectives and found that safety is considered the most important performance objective. Safety includes the safety of building users' day-to-day, fire safety, as well as life safety during an earthquake. User health and wellbeing and building functionality are considered important and are supported by factors such as acoustics, lighting temperature, air quality, accessibility, usability, and access to amenities.

Longevity and sustainability of buildings are also seen as important design objectives. There was considerable surprise that earthquake design considerations are expressed in relation to a nominal 50-year building design life. Many thought buildings should (and already do) last much longer than 50 years and that earthquake-related design should contemplate longer timeframes, given that reducing building damage will support economic recovery by reducing recovery costs and business disruption. Improving the longevity of buildings would also improve building sustainability and reduce the carbon footprint of the built environment by minimizing the demolition of damaged buildings following an earthquake.

Architectural values and heritage both scored significantly lower in terms of importance. It was noted though that effective architectural design is a key component of building performance if it provides a functional and aesthetically pleasing space and supports the wellbeing of users, and if material choices and design detailing support building durability, sustainability, and longevity.

The research highlighted the highly interconnected nature of the drivers and the strong links between seismic resilience and wellbeing of users, longevity, and environmental sustainability.

4. WHAT'S NEXT FOR SEISMIC DESIGN AND ESPECIALLY FOR NON-STRUCTURAL ELEMENTS?

These social science findings indicate that engineers have been relatively successful designing for earthquakes in New Zealand thereby reducing life safety risk. This represents a significant advance from 50 years ago when the concepts of ductile design and a hierarchy of failure intended to protect life were first introduced into the building codes. Like the impact of vaccines, which have largely eliminated the horrors of once-common diseases, the codified requirements for earthquake-resistant design now underpin expectations of safety for buildings. The societal focus for building seismic performance now extends to reducing social and economic impacts.

The findings also identified that members of the public may sometimes conflate life safety with lack of damage and functionality. While engineers have a clear understanding that life safety means to escape from a building without loss of life or injury in an earthquake, even though the building may be significantly damaged and no longer functional, this may not be sufficient for some. Societal expectations as expressed by the research participants are for very limited damage and a swift return to reoccupancy and full functionality.

The expectation of a rapid return to function for most buildings (days and weeks) is causing surprise amongst the engineering community in New Zealand. Engineers have noted these expectations for return to function are significantly shorter than anticipated and are questioning if they are obtainable. This view is, of course, informed by current design and construction approaches and practices in New Zealand and the observations of building performance in the recent earthquakes. It presents a challenge to structural engineers that New Zealand's current building codes are not well aligned with societal expectations for the onset of damage and implications for building performance.

The relevance of these findings for the design of non-structural elements is clear – an expectation of a rapid return to function and full recovery with minimal disruption. This effectively means avoiding or limiting damage to minimal or minor effects in all but very large earthquakes, including and perhaps especially for all the non-structural elements.

These expectations align with observations of the economic impact of damage to non-structural elements in recent past earthquakes. Analyses of the losses due to the 1994 Northridge earthquake indicated that of the approximate US$6.3 billion of direct economic losses to non-residential buildings, only about US$1.1billion was due to structural damage [Kircher, 2003]. A similar study completed in 2004 suggested that losses associated with damage to non-structural elements and building contents represents 50% of the total costs of an earthquake in a developed country [Bachman, 2004].

The Canterbury Earthquakes Royal Commission [CERC, 2012] identified the need to improve the performance of non-structural elements in earthquakes (recommendation 70), and this research indicates a clear imperative to improve the seismic performance of non-structural elements. An associated challenge is determining how to meet these expectations for improved seismic performance while also meeting the expectation that building resilience can be improved without significantly increasing building costs.

5. LESSONS FOR NON-STRUCTURAL ELEMENTS IN THE DESIGN PROCESS

The performance of non-structural elements in earthquakes are dependent on a range of intersecting factors, from the location of the element within the building to the rigidity of the element itself and its response to shaking, allowances for its movement, and connection detailing.

Design considerations of the individual elements are not sufficient. The interconnectedness between non-structural elements and building functionality points to the need for building design to be a much more integrated process between different parts of the building and different design disciplines, including for example building services, fire, architecture, and structural design. The performance of suspended ceilings is influenced by in-ceiling services and above-ceiling services and vice versa as well as the structure itself [Chen et al, 2012]. Alarm systems are supported by the ceilings, egress route fire ratings are dependent on the integrity of the plasterboard walls lining the corridors and stairways [Ferner et al, 2016].

Work currently underway in New Zealand to codify the updated national seismic hazard model (NSHM) highlights the uncertainty of earthquake demands. Ground shaking at a site is unavoidably uncertain, so the consistent application of earthquake engineering design principles is essential. NZSEE has recently published guidance for structural engineers on earthquake design for uncertainty [NZSEE, 2022]. This advisory emphasizes that focusing on designing for specific code-defined specific hazard levels is not sufficient.

"Certainty of building performance is best achieved by scheming structures so that they behave in a controlled, predictable manner during earthquakes even when subjected to shaking that is more intense than anticipated. This means more reliable and less fragile buildings. This approach ***manages the actual risk holistically****, rather than just the hazard (loads) specifically."*

Designing non-structural elements to behave in a controlled and predictable manner during earthquakes, even when subjected to shaking that is more intense than anticipated, is important to meet societal expectations for buildings.

Reducing building drifts and avoiding torsional response through considered and careful design will reduce the likelihood of drift-induced damage to both the structure and non-structural elements. There is also a need for greater attention to the possible effects of accelerations in the design of non-structural elements and their fixings to limit possible impacts. Careful detailing that is demonstrably compatible with deformations such as drifts and second order effects such as geometric (or plastic) elongations is vital. Other options include designing out or relocating some non-structural elements to reduce the potential for damage. Questions designers should consider include: "Are the hung ceilings necessary, or is there another option?" and "Can the building services plant be located in a basement rather than on the roof while still managing other threats such as possible flooding?"

This interconnectedness of building elements for building seismic performance suggests a much more integrated design approach is required [Ferner and Baird, 2016]. Tradition dictates that non-structural elements and their bracing are designed after the building consent process for the main structure and by a designer employed by the subcontractor installing the element. Integrating consideration of the non-structural elements into the main design process for the building would focus all parties on achieving cost-effective performance outcomes that align with contemporary societal expectations of building performance in earthquakes.

6. CONCLUSIONS

The presented research on societal expectations of building performance in earthquakes reveals that New Zealand people want more resilient buildings and expect a rapid return to functionality in large earthquakes. They also expect no or minimal damage and no loss of functionality in moderate earthquakes. The performance of non-structural elements within a building is key to meeting these expectations.

Integrating the design of non-structural elements into the design process of the main structure would focus the design (and construction) team on the importance of the non-structural elements and would seem to point the way forward to better meet these societal expectations.

ACKNOWLEDGEMENTS

The authors gratefully acknowledge the New Zealand Society for Earthquake Engineering (NZSEE) for initiating the Resilient Buildings Project that this research was completed for, the funding support of the New Zealand Earthquake Commission (EQC) and the contributions of the steering group to its design and delivery: Sarah Beaven (University of Canterbury), Dave Brunsdon (Kestrel), Caleb Dunne (EQC), Ken Elwood (University of Auckland), Derek Gill (NZIER), John Hare (Holmes), Jo Horrocks (EQC), and Rob Jury (Beca). We also gratefully acknowledge the contribution of those who participated in the interviews and focus groups.

REFERENCES

Abeling, S., Brown, C., Horsfall, S., Ferner, H., Cowan, H., [2022a] "Societal expectations for seismic performance of buildings: detailed report on interviews". The Resilient Buildings Project Report. NZSEE. June 2022; https://www.nzsee.org.nz/news-activities/technical-activities/resilient-buildings-project/

Abeling, S., [2022b] "Resilient Buildings Project Workshop: Integrating societal expectations into the seismic design of buildings", Proceedings of the QuakeCoRE Annual Meeting 2022, Napier, New Zealand.

Bachman, Robert E. [2004]. "The ATC 58 Project, Plan for Non-structural Components, Performance – Based Seismic Design: Concepts and Implementation", proceedings of the International Workshop, Bled, Slovenia 28 June - 1 July 2004, Peer Report 2004/05, Pacific Engineering Research Centre, University of California.

Brown, C., Abeling, S., Horsfall, S., Ferner, H., Cowan, H., [2022] "Societal expectations for seismic performance of buildings". The Resilient Buildings Project. NZSEE March 2022, https://www.nzsee.org.nz/news-activities/technical-activities/resilient-buildings-project/

CERC, [2012] "Canterbury Earthquakes Royal Commission Final Report"

Chen, M., Pantoli, E., Wang, X.., Espino, E., Mintz, S., Conte, J., Walsh, K., Englekirk, R., Faghihi, M., & Hoehler, M [2012] "Design and Construction of a Full Scale 5-Story Base Isolated Building Outfitted with Non-structural Components for Earthquake Testing at the UCSD-NEES Facility" Structures Congress 2012 (pp 1349-1260), ASEC

Ferner, H., Jury, R., King, A., Wemyss, M., & Baird, A. [2016]. "Performance objectives for non-structural elements". Bulletin of the New Zealand Society for Earthquake Engineering, 49(1), 79–85. https://doi.org/10.5459/bnzsee.49.1.79-85

Ferner, H., Baird, A., [2016] The Next Frontier – Improving the Seismic Resilience of Non-structural Components, 16th US, Japan, NZ joint workshop on Improvement of Structural Engineering and Resiliency, Japan, 2016

Horsfall, S., Brown, C., Abeling, S., C Ferner, H., Cowan, H., [2022], "Societal expectations for seismic performance of buildings: detailed report on focus groups". The Resilient Buildings Project Report. NZSEE. June 2022; https://www.nzsee.org.nz/news-activities/technical-activities/resilient-buildings-project/

Kircher, C. [2003]. "It makes Dollars and Sense to Improve Non-structural System Performance," ATC-29-2

NZSEE, [2022] “Earthquake Design for Uncertainty: Guidance”, New Zealand Society for Earthquake Engineering, July 2022. https://www.nzsee.org.nz/db/PUBS/Earthquake-Design-for-Uncertainty-Advisory_Rev1_August-2022-NZSEE-SESOC-NZGS.pdf

Yeow, T., Baird, A., Ferner, H., Ardagh, M., Deely, J., Johnston, D., “Cause and level of treatment of injuries from earthquake damage to commercial buildings in New Zealand, EERI Earthquake Spectra, 36(3): 1254-1270

New Testing Protocol for Acceleration-and-Drift-Sensitive Non-Structural Elements through the Innovative 9-DOFs Multi-Story Dynamic Testing Facility

I. Lanese, M. Bazzini, D. Bolognini, E. Brunesi, F. Dacarro, P. Dubini, L. Grottoli, S. Peloso, E. Rizzo Parisi, M. Rota

European Centre for Training and Research in Earthquake Engineering (EUCENTRE)
Via Ferrata, 1 – 27100 Pavia (PV) - Italy
E-mail: {igor.lanese, miriam.bazzini, davide.bolognini, emanuele.brunesi, filippo.dacarro, paolo.dubini, luca.grottoli, simone.peloso, elisa.rizzoparisi, maria.rota}@eucentre.it

Abstract. The importance of an appropriate seismic response of non-structural components is nowadays widely recognized. The need to match the same target levels for structural and non-structural (NS) response is a compulsory requirement for an effective seismic design. Several national and international codes and guidelines (e.g. ICC ES AC156, IEC 60068, IEEE std 693) provide protocols and recommendations for NSEs testing, typically target spectra to reproduce on the shake table; however, the provisions regarding relative displacements do reduce only to different limit values for the considered NS typologies (e.g. infill walls).

Current codes typically provide acceleration floor spectra derived from analyses on linear single degree of freedom systems, which are suitable for acceleration-sensitive NSEs. NSEs belonging to typologies which are drift-sensitive or both drift-and-acceleration-sensitive (e.g. inner office partitions, piping running through different floors and suspended ceilings with surrounding elements), instead, require different specific testing and qualification procedures.

The above reasons led to the design and implementation of an innovative 9-DOFs multi-story dynamic testing facility at EUCENTRE laboratories in Pavia (Italy). This new testing facility allows reproducing the actual conditions of any couple of adjacent floor levels within a building, both in terms of acceleration and displacement. The focus of this paper is to contribute to the definition of a realistic and general qualification testing protocol for drift-and-acceleration-sensitive NSEs, to be adopted for experimental tests on this new testing facility. This protocol should allow defining appropriate levels of drift and absolute acceleration at the two adjacent stories, for a given seismicity and target performance, to accurately reproduce the actual complex dynamic environment, through a generally applicable testing method.

Keywords: Experimental Testing, Drift-sensitive, Acceleration-sensitive, Shake Table, Innovative Testing Protocol.

1. INTRODUCTION

The crucial role of NSEs in the seismic response of a building system is nowadays widely recognized. Not only NSEs represent, particularly in offices, hotels and hospitals, more than 80% of the total monetary investment in a building, as shown by Taghavi and Miranda [2003], but they are also the cause of the main economic losses and service interruption, even in case of low intensity seismic events [Miranda and Taghavi, 2003; Taghavi and Miranda, 2004; Miranda *et al.*, 2012; Calvi *et al.*, 2015; Sullivan *et al.*, 2015; Perrone *et al.*, 2019; Perrone *et al.*, 2020]. Not considering NSEs in the design phase may lead to an overall inadequate seismic performance, not corresponding to what is considered in the structural design process. On the opposite, a robust and effective performance-based design must ensure the desired performance level of the building system as a whole.

In the last decades, standard and code requirements have moved a big step forward ensuring an adequate seismic response of NSEs. Notwithstanding an uneven approach between different countries, NSEs manufacturers are now getting more and more used to deal with seismic requirements. Experimental qualification tests on shake table oftern considered in the standards aim at demonstrating the uninterrupted usability of NSEs during and after a seismic event. Seismic codes typically define the acceleration response spectrum to be adopted for this kind of tests, referring to single-degree-of-freedom systems anchored to a single structural level.

However, many NSEs are actually either drift-sensitive, or both acceleration- and drift-sensitive and they can be anchored to different levels within a structure. In other cases, they can be made as an assembly of several components, some of which are drift-sensitive and some are acceleration-sensitive, so that the system is globally both acceleration- and drift-sensitive. Literature and code provisions for drift-and-acceleration-sensitive NSEs (e.g. office inner partitions, infill walls, piping and plants running through the floors, etc.) are still limited [Retamales *et al.*, 2008; Petrone *et al.*, 2014; Petrone *et al.*, 2017] and experimental tests are currently lacking. The latter is also due to the lack of experimental facilities allowing tests on this type of elements, with the exception of the Nonstructural Component Simulator (NCS) at the University at Buffalo, USA [Mosqueda *et al.*, 2008]. The strong impact on society resilience and the need for a deeper understanding and better consideration of the seismic performance of these very common NSEs pushed the design and implementation of the innovative 9D Testing System at EUCENTRE laboratories (Pavia, Italy). Along with the testing equipment implementation, a new multi-story dynamic testing protocol for distributed restraints NSEs is proposed in this paper and compared with the results of a large set of non-linear parametric numerical analysis.

2. INNOVATIVE 9D TESTING SYSTEM

The innovative facility located in the EUCENTRE 6DLab is a complex 9-DOFs system, consisting of two independent shaking platforms placed at different heights (Figure 1); more in detail, the bottom platform is the 4.8 m x 4.8 m 6-DOF shake table of the EUCENTRE 6DLab, and the top platform is a 7 m x 5 m lightweight frame, consisting of welded aluminum tubular elements placed about 4 m over the lower table. Four steel columns, whose ends are equipped with spherical swivels, connect the two platforms to each other and allow their relative horizontal displacement. An additional removable 0.8 m high steel frame can be connected to the lower table and used for specimens requiring special mounting configurations. The lower and upper tables are each controlled by four horizontal actuators. The actuators of the lower table directly react on the strong floor, which is a 1200 tons post-tensioned reinforced concrete mass with base isolation, thus dynamically decoupled from the laboratory. The reaction system of the four actuators controlling the upper platform consists of two steel frame towers (Figure 1), connected to the floor of the laboratory. The vertical motion, which is common to the two platforms, is provided by a system of 6 single action actuators (i.e. 4 pushing up and 2 pulling down), placed under the lower table. A more detailed description of the EUCENTRE 9D Testing System can be found in a companion paper [Dacarro *et al.*, 2022].

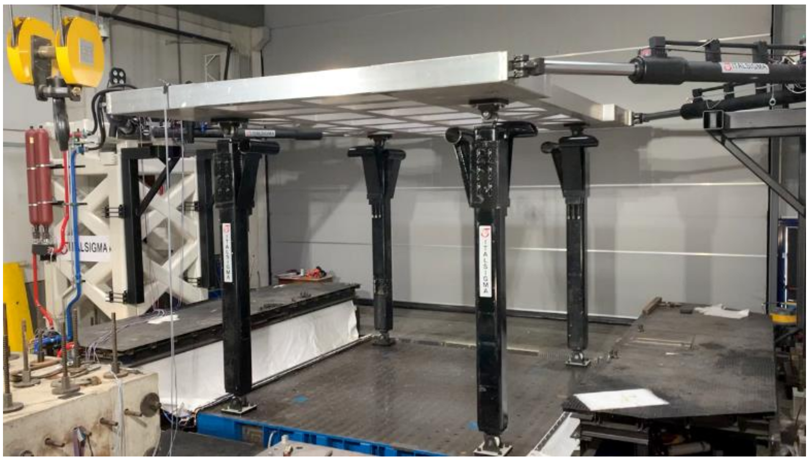

Figure 1. Overview of the EUCENTRE 9D Testing System

3. EXISTING TESTING PROTOCOLS FOR NSEs AND PROPOSAL FOR SYSTEM-SPECIFIC DYNAMIC TESTING

Requirements and testing provisions for NSEs currently available in literature and codes worldwide are still heterogeneous. Some standards and references providing guidance on seismic qualification/characterization of electrical and mechanical equipment, as well as NSEs in general include: ISO 13033 [2013], ICC ES AC156 [2020], IEEE 693 [2018], IEC EN 60068 [IEC EN 60068-2-57, 2013; IEC EN 60068-3-3, 2019], TELCORDIA-GR-63-CORE [2006], ANSI/AHRI Standard 1271 [2015] and FEMA 461 [2007]. The aim of these standards is typically to provide indications on seismic qualification of NSEs, meaning the ability of the element to be subjected to a target seismic level, with no (or limited) damage and without loss of operation. In addition to the assessment criteria for seismic certification, they typically include prescriptions on technical aspects, such as applicability conditions, test and specimen setup, testing procedures, testing protocols and content of technical report. Specifically, IEEE 693 is a reference for electrical substations, IEC EN 60068 for electro-technical components and equipment, TELCORDIA-GR-63-CORE for communication networks, ANSI/AHRI Standard1271 for HVACR equipment, while other standards such as ISO 13033, ICC ES AC156 and FEMA 461 are not NSE-specific.

All the above codes allow to achieve seismic qualification through shake table tests. The approach generally includes pre-test and post-test specific verifications and dynamic identification. The shake table test requires the actual Test Response Spectrum (TRS), i.e. the spectrum of the signal actually applied by the shake table, to reproduce the Required Response Spectrum (RRS), with a tolerance specified by the code, which could be for example in the range -10% to +30%. The RRS is related to the specific site – or reference – seismicity, possibly modified and/or amplified depending on the building characteristics, installation height, etc.

The selection of the most suitable seismic qualification procedure is based on different parameters, including static and dynamic characteristics of the specimen, boundary conditions and type of mounting system, reference seismic input and required performance, which can range from the basic capacity to withstand the applied load, to the requirement of remaining fully operational during and after the test.

In most cases, code provisions address acceleration-sensitive NSEs with a single connection to the structure, meaning that the NSE can even have a redundant connection system, but with a single excitation (e.g. series of bolts on a floor/base plate), hence excluding the possibility of having a relative displacement between different anchorage points. This is typically the case for example of electrical cabinets, data center server racks, uninterruptible power supply units, suspended ceilings and floating floors, if not connected to the vertical walls (which is actually often the case). Nevertheless, a wide variety of NSEs has boundary conditions more articulated than a single connection point; this is the case, among others, of infill walls, inner office partitions, piping and distribution systems running through the floors, etc. In these cases, structural deformations imply distortion in the elements due to relative displacement between connection points at different levels. In case of NSEs sensitive and subjected to relative displacements, code provisions reduce significantly and are in most cases limited to imposing a simple drift limitation in the structural design phase, assumed to indirectly ensure a satisfactory performance. Obviously, this is often not sufficient, since the seismic performance depends on the characteristics and deformation capacity of the specific non-structural element.

Few testing recommendations for drift-sensitive NSEs are included in the American standard AAMA 501-4 [2018], AAMA 501-6 [2018], aiming to evaluate the inter-story drift element response, respectively with quasi-static and faster but not "real dynamic" testing. AAMA 501-4 [2018] considers both elastic and inelastic displacement tests with different performance criteria, to determine the failure mode of e.g. exterior curtain wall systems and to compare the design demand with the NSE drift performance/capacity. AAMA 501-6 [2018] is more oriented to the evaluation of dynamic effects. The test methodology includes a dynamic crescendo displacement in the plane of the facade elements. Concatenated crescendo series include ramp up intervals and constant amplitude intervals, each of four sinusoidal cycles. The test shall be performed on three identical specimens and must be run without interruption until either the end of the test or failure of the specimens. FEMA 461 [2007] provides testing protocols which are not specifically intended for seismic performance qualification tests, even if they could be used to this end if indicated by local building codes. Other than shake table tests, FEMA 461 [2007] includes quasi-static cycle testing, whose protocol consists in the application of load or deformation with a target cycling loading history of step-wise increasing amplitude.

While the above standards somehow cover ideal displacement-sensitive NSEs, the real dynamic environment in which such elements are integrated – and to which they can be sensitive to – induces simultaneous in-plane and out-of-plane distortions and a certain range of frequency strong vibrations. A typical example, certainly the one that received more attention from the researchers in the last decades, is constituted by infill walls [e.g. Morandi *et al.*, 2021, Milanesi *et al.*, 2021]. During a seismic event, infill walls are typically subjected to drift-dependent in-plane damage, significantly reducing the out-of-plane resistance and triggering their collapse. Other examples of NSEs which are both drift-and-acceleration-sensitive are inner partitions, such as office glass and panels partitions (Figure 1), plumbing components and distribution piping systems running through floors with multi-point connection to the structure, glass facades, curtain walls, ventilated facades, etc.

Figure 2. Full-scale inner office partitions tested at the EUCENTRE 9D Testing System

All these elements are then characterized by peculiar excitation and feature-specific distributed boundary conditions, which need to be properly reproduced in the qualification testing.

The need to reproduce the actual seismic response of this kind of NSEs led to the design and realization of the new 9D Testing System (Figure 2) and highlighted the need of developing an *ad-hoc* experimental protocol, to fill the gap in the existing literature and standard provisions. Indeed, to the Authors's knowledge, the only existing testing protocol for acceleration and drift-sensitive NSEs is the one adopted at the University at Buffalo, which is based on the use of properly calibrated double sine-sweep multi-story uniaxial motion [Retamales *et al.*, 2011].

This paper hence proposes a new multi-story and multi-axial qualification testing protocol for drift-and-acceleration-sensitive NSEs, to be implemented for tests carried out at the 9D Testing System of EUCENTRE. The two shake tables of the system are independently controlled, with the exception of the vertical motion, allowing high flexibility in the choice of the input motion.

The input for the lower table (i.e. building n^{th} story) is defined using the well consolidated ICC ES AC156 [2020] provisions and consists of independent and uncorrelated accelerograms for the two horizontal DOFs (longitudinal X and transversal Y displacements), generated from the specific RRS described in the code. The seismic input of the upper table (i.e. building $n+1^{th}$ story) is then generated by amplifying the acceleration time-histories of the lower table by a factor allowing the specimen to reach the desired drift level. The target drift level could be chosen for example based on the maximum drift limit imposed by local seismic design codes for the specific limit state under consideration and/or structural typology. As an example, the Italian code [NTC18, 2018] indicates a range of 0.5% - 0.75% for the maximum inter-story drift at the damage control limit state.

From an operational point of view, the accelerogram of the lower table (e.g. in X direction) is numerically integrated to obtain the corresponding velocity and displacement time-histories. From the displacement time-history (filtered and base-line corrected if needed), the maximum displacement value is detected and the corresponding maximum displacement value of the upper table is derived by imposing the desired drift level. This allows computing the amplification factor, defined as the ratio of the two maximum displacements, to be applied to the displacement time-history of the lower table to obtain the required upper table displacement time-history (Figure 3). Consequently, the acceleration time-history of the upper table is derived, as it is needed for shake table control purposes.

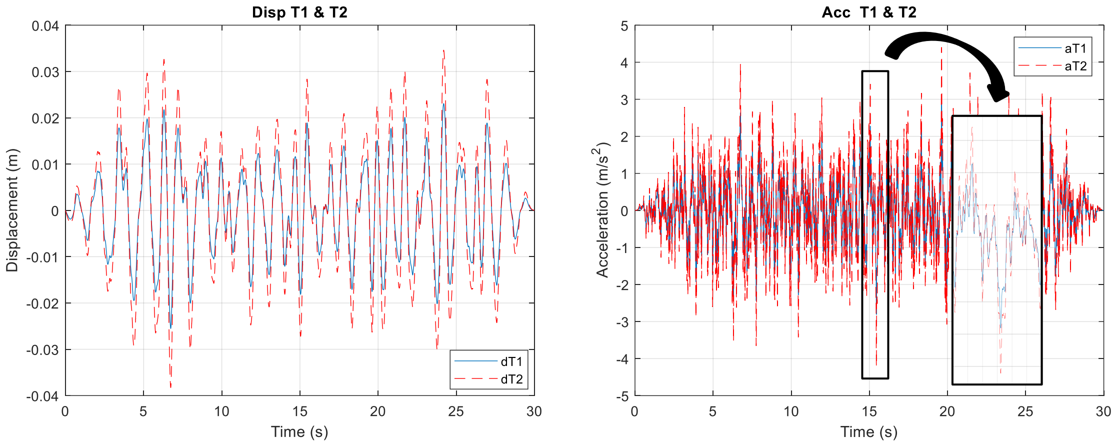

Figure 3. Displacement (left) and acceleration (right) time-histories of the lower (T1) and upper (T2) tables (X direction)

The proposed approach relies on the assumption that the signals applied to the two shake tables (i.e. the accelerations experienced by two consecutive stories of a given structure) are in phase, with peak drift and peak displacement occurring at the same time. Although this assumption is supported by the results of the numerical analyses discussed in the following chapter, it is recognized that, whenever the building response is not governed by the first vibration mode (e.g. in case of irregular structures), this assumption may not hold true.

It is also worth noting that, based again on the results of the large set of nonlinear numerical analyses discussed in the next chapter, a limit value of 1.5 was imposed to the amplification factor, to avoid having excessively large and unrealistic acceleration values at the upper table, in order to achieve the target drift limit in case of low-seismicity sites.

4. MULTI-STORY BUILDING RESPONSE

To substantiate the proposed seismic qualification testing protocol, a series of time-history analyses was carried out on a set of buildings, to evaluate the evolution of seismic demand along the height of a building and better justify some of the assumptions embedded in the proposed approach. A set of low-to-mid-rise reinforced concrete building prototypes was used for structural analyses. These prototypes were extracted from the building portfolio generated in Perrone *et al.* [2020], via complete Monte Carlo simulation, and used by Rodriguez *et al.* [2021] to derive a probabilistic strong floor motion duration model for seismic performance assessment of non-structural building elements.

The considered structures, which are simple masonry-infilled reinforced concrete plane frames featuring bare frame model counterparts, have a number of stories varying from two to six, and are meant to resemble key characteristics of newly built frame systems designed for gravity loads and earthquake resistance in Italy and, more generally, in the Mediterranean area. Geometrical and mechanical properties, along with gravity loads, were selected accordingly, and result from a complete Monte Carlo simulation in conjunction with a simulated design procedure, which relies upon European seismic provisions [CEN, 2004] for the so-called medium ductility class. All structures are assumed to be located near the city of Cassino, in a medium-high seismicity zone of Italy, with a design peak ground acceleration of 0.21g for the life safety limit state (i.e. return period of 475 years).

An example of the structural system is presented in Figure 4, together with key items of the implemented finite element modelling approach and assumed random variables (RVs). The latter are (i) the number of stories n_f, (ii) the inter-story height h_i, (iii) the number of bays n_b, (iv) the length of the bays L_b, (v) the dead loads g_T, (vi) the live loads q_k, (vii) the yielding strength of reinforcing rebars f_y, and (viii) the concrete compressive strength f_c. To provide an idea of the building-to-building variability, numerical values associated with each RV are collected in Table 1. Interested readers are also referred to Peloso *et al.* [2022a; 2022b], wherein the same frame structures were used to produce infill-specific fragility functions, and to Chichino *et al.* [2021], who selected the five-story building model, namely M4, to check the accuracy and suitability of Italian code-compliant methodologies for the calculation of acceleration floor response spectra.

Structural models were developed using the open source finite element platform OpenSees [Mazzoni *et al.*, 2006]. Both beams and columns were modelled by means of nonlinear beam-column elements, with a force-based distributed-plasticity approach. The uniaxial uniform-confinement model proposed by Chang and Mander [1994], *Concrete07*, was assigned to concrete fibres, and *Steel01*, a bilinear constitutive material model with isotropic strain hardening, was assumed for the longitudinal steel bars of beams and columns. Masonry infills were modelled by an equivalent triple-truss model, in which the global stiffness of the panel was distributed among three parallel diagonal inelastic trusses by assigning a rate of stiffness and strength equal to 50% to the central truss and equal to 25% to each of the off-diagonal truss elements. The *pinching4* unixial material model was considered and calibrated based on pseudo-static cyclic tests by Cavaleri and Di Trapani [2014], namely experimental test data on specimen S1B-1, which is representative of clay masonry.

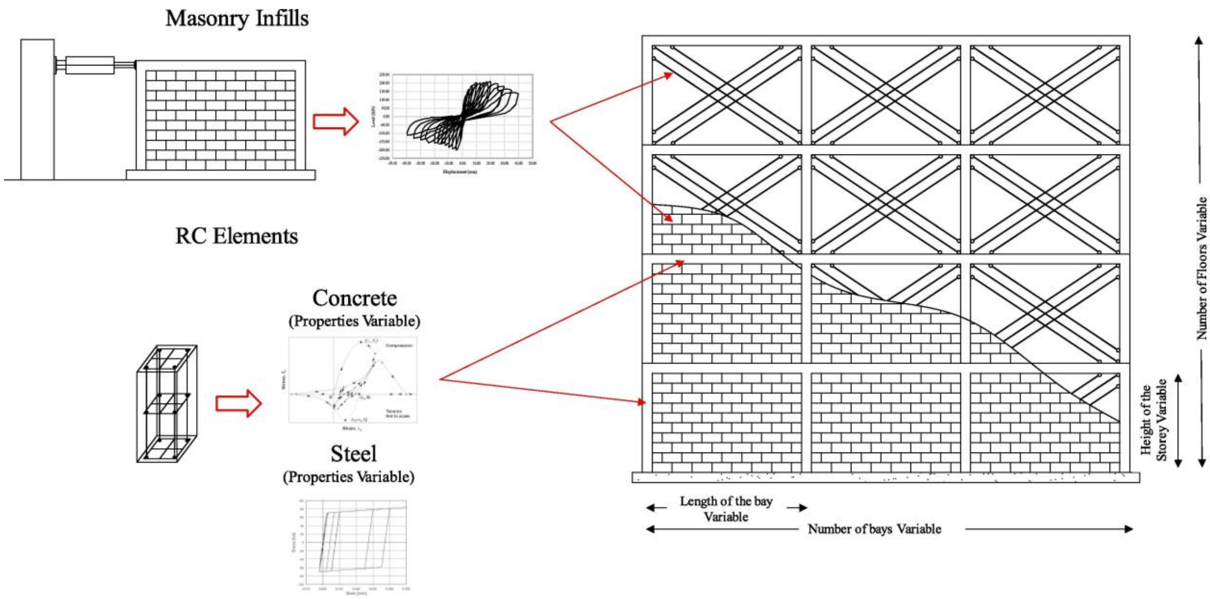

Figure 4. Numerical model concept for nonlinear dynamic building response assessment

Table 1. Values of RVs for the selected case-study structures

Model	n_f (-)	h_i (mm)	n_b (-)	L_b (mm)	g_T (N/mm)	q_k (N/mm)	f_y (N/mm^2)	f_c (N/mm^2)
M1	2	3250	3	3500	22.32	12.25	375.0	32.0
M2	3	3000	3	4000	24.01	11.00	430.0	39.0
M3	4	2750	6	3750	22.34	9.38	430.0	40.0
M4	5	2750	3	4500	25.60	10.13	375.0	39.0
M5	6	3000	6	3750	22.75	10.31	430.0	41.0

Nonlinear time-history analyses were performed considering a suite of 20 earthquake ground motions per each of the 10 return periods selected to characterize structural behavior in the elastic and inelastic range of response. All these records – selected from the PEER NGA-West database – resulted from a hazard-consistent selection undertaken based on spectral compatibility with a conditional mean spectrum according to the methodology detailed in Jayaram *et al.* [2011]. Acceleration time-history response at all floors (and ground) was processed to calculate floor response spectra and the ratio at two consecutive floors, as illustrated in Figure 5, for instance, for the 475-year return period case. More specifically, Figure 5 shows mean as well as mean plus/minus one standard deviation of these ratios, which are plotted against T_{NSE} (i.e., the non-structural period) and T_{NSE}/T_1 (i.e., non-structural period normalized by the fundamental period of each single frame structure). Note that red dots indicating the T_1 range are overlapped in Figure 5a, whereas the dimensionless-dimensionless plot of Figure 5b permits a more immediate interpretation of the obtained numerical data referring to spectral amplification. Figure 6 shows the time occurrence of peak drift and peak displacement, showing a very good correlation, wich justifies the assumption of simultaneous occurrence of the two peaks.

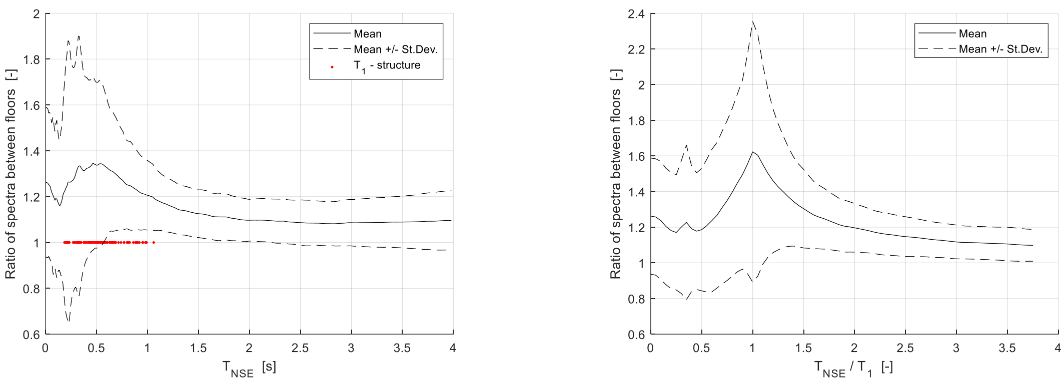

(a) (b)

Figure 5. Ratios of acceleration floor response spectra versus (a) T_{NSE} and (b) T_{NSE}/T_1

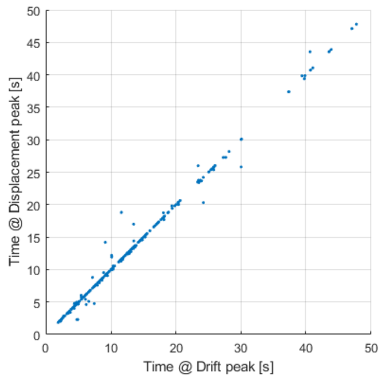

Figure 6. Time correlation between drift and displacement peaks

5. CONCLUDING REMARKS

The proposed testing protocol extends the consolidated spectrum-based excitation included in several seismic qualification standards - e.g. ICC ES AC156 [2020] - to the case of drift-and-acceleration-sensitive NSEs anchored at multiple levels within a structure. The protocol aims at consistentently reproducing the dynamic conditions of this type of NSEs, taking advantage of the specific capabilities of the new EUCENTRE 9D Testing System.

The frequency content of the considered artificial accelerograms is consistent with the selected standard provisions, so that possible relevant element resonances are duly triggered. The applied inter-story drift level is consistent with the results of a large set of parametric nonlinear numerical analyses and the drift target is typically imposed by design codes. Unrealistic upper floor amplifications, which could be required to obtain relatively large drifts (e.g 0.5% – 0.75%) with minor ground excitation (i.e. in low-seismicity sites), are prevented by applying a limit of 1.5 to the amplification factor.

This field is however still quite unexplored and deeper understanding, as well as further refined analysis and procedures, are certainly needed. As an example, the number of drift cycles, both at high and low-to-medium amplitude, at which the element is subjected through the proposed procedure is higher than the typical hysteresis generated by actual seismic events. This aspect may be of concern, especially in case of elements sensitive to the number of cycles (low-cycle fatigue) due to strength and stiffness degradation and/or accumulation of damage. Possible modifications to the reference spectrum are currently under investigation and will be included in future works. Moreover, further building typologies, featuring for example plan and/or elevation irregularities and/or including buildings realized with different construction materials, could be considered to extend the numerical analysis campaign, in view of specific recommendations for future testing guidelines, with or without the support of *ad hoc* case-specific numerical simulation.

AKNOWLEDGEMENTS:

The work presented in this paper has been developed within the framework of the project "Dipartimenti di Eccellenza", funded by the Italian Ministry of University and Research (MIUR) at the University School for Advanced Studies IUSS Pavia, and within the activities of the CADS Project, PON Grant n.1735/2017, funded by MIUR.

This work has been also developed thanks to the activities of the Eucentre-DPC 2019–2021 Research Programme, WP14 "Caratterizzazione della Risposta Sismica di Elementi Nonstrutturali", funded by the Italian Department of Civil Protection.

REFERENCES

AAMA 501-4 [2018] *Recommended Static Test Method for Evaluating Window Wall, Curtain Wall and Storefront Systems Subjected to Seismic and Wind-Induced Inter-Story Drift*, American Architectural Manufacturers Association, USA.

AAMA 501-6 [2018] *Methods of Test for Exterior Wall – Recommended Dynamic Test Method for Determining the Seismic Drift Causing Glass Fallout fro Window Wall, Curtain Wall and Storefront Systems*, American Architectural Manufacturers Association, USA.

ANSI/AHRI Standard 1271 [2015] *Standard for Requirements for Seismic Qualification of HVACR Equipment*, Air-Conditioning, Heating and Refrigeration Institute approved by ANSI, USA.

Calvi, P. M., Moratti, M., Filiatrault, A. [2015] "Studio della risposta di elementi non strutturali di edifici scolastici soggetti ad eventi sismici," *Progettazione Sismica*, Vol. 6.

Cavaleri, L., Di Trapani, F. [2014] "Cyclic response of masonry infilled RC frames: Experimental results and simplified modelling," *Soil Dynamics and Earthquake Engineering*, Vol. 65, pp. 224-242.

CEN, European Committee for Standardisation [2004] *EN 1998-1. Eurocode 8: Design of structures for earthquake resistance - Part 1: General rules, seismic actions and rules for buildings*, Brussels, Belgium.

Chang, G.A., Mander, J.B. [1994] *Seismic energy based fatigue damage analysis of bridge columns: Part 1 – Evaluation of seismic capacity*, NCEER Technical Report, no. NCEER-94-0006 State University of New York, Buffalo, NY, USA.

Chichino, B., Peloso, S., Bolognini, D., Moroni, C., Perrone, D., Brunesi, E. [2021] "Towards seismic design of nonstructural elements: Italian code-compliant acceleration floor response spectra," *Advances in Civil Engineering*, Vol. 2021, No. 4762110.

Dacarro, F., Bolognini, D., Calvi, G.M. [2022] "Experimental Facility for the Seismic Testing of Non-Structural Elements and Systems Under Full-Scale Floor Motion," *Proceedings of Fifth International Workshop on the Seismic Performance of Non-Structural Elements (SPONSE.*), Palo Alto (CA), USA.

EN IEC 60068-3-3 [2019] *Enviromental testing - Part 3-3: Supporting documentation and guidance – Seismic test methods for equipment*, International Electrotechnical Commission.

EN IEC 60068-2-57 [2013] *Enviromental testing - Part 2-57: Tests – Test Ff: Vibration - Time-history and sine-beat method*, International Electrotechnical Commission.

FEMA 461 [2007] *Interim Testing Protocols for Determining the Seismic Performance Characteristics of Structural and Nonstructural Components*, Federal Emergency Management Agency, Washington D.C., USA.

ICC ES AC 156 [2020] *Acceptance criteria for seismic certification by shake-table testing of nonstructural components*, International Code Council Evaluation Service.

IEEE SA 693 [2018] *Recommended Practice for Seismic Design of Substations*, Institute of Electical and Electronic Engineers Standards Association, New York, USA.

ISO 13033 [2013] *Bases for design of structures – Loads, forces and other actions – Seismic actions on nonstructural components for building applications*, International Organization for Standardization.

Jayaram, N., Lin, T., Baker, J.W. [2011] "A computationally efficient ground-motion selection algorithm for matching a target response spectrum mean and variance" *Earthquake Spectra*, Vol. 27, No. 3, pp. 797-815.

Mazzoni, S., McKenna, F., Scott, M.H., Fenves, G.L. [2006] *OpenSees Command Language Manual*, Pacific Earthquake Engineering Research (PEER) Center, Berkeley (CA), USA.

Milanesi R.R., Morandi P., Hak S., Magenes G. [2021] "Experiment-based out-of-plane resistance of strong masonry infills for codified applications", *Engineering Structures*, 242 (2021) 112525.

Miranda, E. and Taghavi, S. [2003] "Estimation of seismic demands on acceleration-sensitive nonstructural components in critical facilities," *Proceedings of the Seminar on Seismic Design, Performance, and Retrofit of Nonstructural Components in Critical Facilities*, Applied Technology Council (ATC 29–2), Newport Beach, USA.

Miranda, E., Mosqueda, G., Retamales, G., Pekcan, G. [2012] "Performance of nonstructural components during the 27 February 2010 Chile earthquake," *Earthquake Spectra*, Vol. 28, No. S1, pp. S453–S471.

Morandi P., Hak S., Milanesi R.R., Magenes G. [2021] "In-plane/out-of-plane interaction of strong masonry infills: From cyclic tests to out-of-plane verifications", *Earthquake Engineering and Structural Dynamics* 2021; 00 1– 25.

Mosqueda, G., Retamales, R., Filiatrault, A., Reinhorn, A. M. [2008] "Testing facility for experimental evaluation of nonstructural components under full-scale floor motions," *Journal of Structural Design of Tall and Special Buildings*, Vol. 18, No. 4, pp. 387–404.

NTC18 [2018] *Aggiornamento delle Norme tecniche per le costruzioni*. Ministero delle Infrastrutture e dei Trasporti; Roma, Italia.

Peloso, S., Brunesi, E., Perrone, D. [2022a] "Derivation of in-plane seismic fragility models for clay masonry infills in reinforced concrete frames," New Boundaries of Structural Concrete - NBSC 2022, proceedings of the workshop.

Peloso, S., Brunesi, E., Perrone, D., Chichino, B., Sinopoli, G., Moroni, C. [2022b] "Parametric seismic in-plane fragility models for clay masonry infills in low-to-medium-rise reinforced concrete frames," *Proceedings of the Fifth International Workshop on the Seismic Performance of Non-Structural Elements (SPONSE).*

Perrone, D., Calvi, P. M., Nascimbene, R., Fischer, E. C., Magliulo, G. [2019] "Seismic performance of non-structural elements during the 2016 Central Italy Earthquake," *Bulletin of Earthquake Engineering*, Vol. 17, No. 10, pp. 5655–5677.

Perrone, D., Brunesi, E., Filiatrault, A., Nascimbene, R. [2020] "Probabilistic estimation of floor response spectra in masonry infilled reinforced concrete building portfolio," *Engineering Structures*, Vol. 202, No. 109842.

Petrone, C., Magliulo, G., Manfredi, G. [2014] "Shake table tests for the seismic assessment of hollow brick internal partitions," *Engineering Structures*, Vol. 72, pp. 203-214.

Petrone, C., Magliulo, G., Manfredi, G. [2017] "Shake table tests on standard and innovative temporary partition walls," *Earthquake Engineering and Structural Dynamics*, Vol. 46, No. 10, pp. 1599-1624.

Retamales, R., Mosqueda, G., Filiatrault, A., Reinhorn, A. M. [2011] "Testing protocol for Experimental Seismic Qualification of Distributed Nonstructural System," *Earthquake Spectra*, Vol. 27, No. 3, pp. 835-856.

Rodriguez, D., Perrone, D., Filiatrault, A., Brunesi, E. [2021] "A probabilistic strong floor motion duration model for seismic performance assessment of non-structural building elements," *Earthquake Engineering and Structural Dynamics*, Vol. 50, No. 15, pp. 4161-4179.

Sullivan, T., Calvi, P. M., Bolognini D. [2015] "Valutazione degli spettri di piano per la progettazione sismica di elementi non strutturali," *Progettazione Sismica*, Vol. 6.

Taghavi, S. and Miranda, E. [2003] *Response Assessment of Nonstructural Building Elements*, Pacific Earthquake Engineering Research (PEER) Center, Berkeley (CA), USA.

Taghavi, S. and Miranda, E. [2004] "Estimation of seismic acceleration demands in building components," *Proceedings of the 13th World Conference on Earthquake Engineering*, Vancouver, Canada.

TELCORDIA-GR-63-CORE [2006] Network Equipment-Building System (NEBS) Requirements: Physical Protection, Telcordia Technologies Generic Requirements, USA.

Experimental Facility for the Seismic Testing of Non-Structural Elements and Systems under Full-Scale Floor Motion

F. Dacarro[1], D. Bolognini[1], and G.M. Calvi[2]

[1] Researcher, European Centre for Training and Research in Earthquake Engineering
Via Ferrata, 1 – 27100 Pavia (PV) - Italy
e-mail: filippo.dacarro@eucentre.it
e-mail: davide.bolognini@eucentre.it

[2] Professor, University School for Advanced Studies IUSS Pavia
Piazza della Vittoria, 15 – 27100 Pavia (PV) - Italy
e-mail: gm.calvi@iusspavia.it

Recent earthquakes worldwide have highlighted the influence of the non-structural elements on direct economic losses and building's operability. The need of experimental facilities able to evaluate accurately the seismic response and conduct seismic qualification tests on non-structural elements is recognized in many seismic prone countries. At the 6D-Lab of the Eucentre Foundation, a six-degree of freedom (DOFs) 4.8 x 4.8 m shaking table able to perform triaxial seismic qualification tests, has been recently upgraded to an innovative 9-DOFs dynamic interstory simulator capable of doing real-time experimental tests on both drift and acceleration sensitive non-structural components and systems. This paper focuses on the design, installation and acceptance tests of this machine, which consists of two platforms at different heights, with clear interstorey distance of 4.1 m, whose horizontal movements are controlled by eight hydraulic actuators. The 9-DOFs system can impose realistic full-scale floor motions expected at any couple of adjacent levels of a multistorey building. The maximum longitudinal and transversal relative displacements are equal to ±1.7 m and ±1.1 m, the peak relative velocity and acceleration is equal to 4.6 m/s and 4.2 g. The proposed system has a high level of flexibility; free-standing elements that are influenced mainly by horizontal accelerations can be positioned indifferently on one of the two testing platforms. Architectural components that are mainly influenced by inter-story drifts, such as partition walls, can be anchored between the two testing platforms. Finally, nonstructural elements that are both acceleration and drift sensitive, such as pressurized piping systems or suspended ceilings, can be tested in various geometrical configurations and anchored to various support points of both testing platforms.

Keywords: Non-structural elements, seismic qualification, experimental test, testing facility, shaking table, drift sensitive, acceleration sensitive.

1. INTRODUCTION

Recent earthquakes worldwide have highlighted the relevant influence that non-structural components may have on direct economic losses and interruptions of building's functionality. Critical situations, particularly for strategic buildings (e.g. hospitals) may arise in case of both high and low intensity earthquakes. Even when the structural elements have been properly designed, the possibility of an immediate occupancy after a seismic event is limited by the damage of the non structural components, which causes not only the interruption of the functionality, but may hinder the movement of occupants as they evacuate the building. Also in case of low intensity earthquakes, when it is expected that the structures do not suffer evident damages, the inability of non structural components to withstand the seismic demand may lead to interruption of functionalities and to direct economic losses anyway. Always these situations must be considered; structures and non structural components share the same dynamic environment during an earthquake, so that it is crucial that their responses are harmonized in the seismic design of buildings.

The importance of experimental information, in particular coming from seismic qualification tests on shaking table of mechanical, electrical and architectural non structural components is justified by the need to ensure their functionality during and after seismic events. This need is currently recognized by the scientific community and by some seismic prone countries, which have adopted specific codes. Among them, AC156 [ICC-ES, 2007] FEMA461 [FEMA, 2006] and IEEE standards [IEEE, 2006] have become very popular, so that, due to the lack of specific harmonized standards, it is not unusual they can be adopted as a reference also in European countries, which prefer this solution, rather than to rely only on past experiences and designer's intuition. A peculiarity of such codes is that they are based on acceleration response spectra of linear single degree of freedom (SDOF) systems and are thought mainly for experimental tests on acceleration-sensitive non structural elements which are anchored to a single level of a building (e.g. suspended ceiling systems, mechanical and electrical equipment). [Retamales *et al.*, 2011; Filiatrault *et al.*, 2014]. Within FEMA461, some protocols specifically defined for drift sensitive non structural elements were also proposed. The problem is that real cases are not only acceleration sensitive or displacement sensitive. Non structural elements of common use, which can be easily found in residentiual buildings, offices or strategical buildings (hospitals, police stations, fire stations, municipal offices or even nuclear power plants) may consist of different components. Each one of them can be sensitive only to acceleration or drift, but their combination is sensitive to both. Very common examples of drift and acceleration sensitive non structural elements are piping systems that develops on more levels of a building, elevators, or non structural elements fixed to a partition wall (monitors, thermostats, hospital machinery), which are acceleration sensitive, while the partition wall is drift sensitive in plane and acceleration sensitive out-of-plane.

This is the reason why a testing machine capable of performing real-time experimental investigation on both drift and acceleration sensitive non-structural systems is necessary in the execution of qualification tests and, more generally, in the development of the research on the seismic response of non structural elements. This paper focuses on the design, installation and acceptance of a similar testing machine, whose construction was completed at the 6D-Lab of the Eucentre Foundation in the first months of 2022. A first attempt to develop reliable and effective testing protocols concerning the aforementioned seismic qualification tests is the subject of a companion paper [Lanese *et al.*, 2022].

2. THE 9-DOFS TESTING MACHINE

The Eucentre Foundation aims to support training and research activities in risk engineering; among them, numerical and experimental projects concerning seismic engineering represent an important share in terms of funds and interests of the community. Their experimental laboratories, facilities and equipment, independently designed and developed by the researchers over the years, make a significant contribution to such activities. One of the major current research topic concerns the seismic response of non-structural elements. The design and construction of a new facility specifically thought to perform effective dynamic tests on non-structural elements have to be set in this subject matter. Substantially, the facility is a complex 9-DOF system, consisting of two independent shaking platforms placed at different heights, able of imposing realistic full-scale displacements and accelerations at any couple of adjacent floor levels of any multistory building. More in detail, the bottom platform is the 4.8 m x 4.8 m – 6 DOF shaking table of the 6D-Lab, currently used for tri-axial dynamic tests on non-structural elements and specimens of mass up to 30 tons. The top platform is a 7 m x 5 m lightweight spatial frame consisting of welded aluminum tubular elements placed above the bottom platform with a clear height of 4.10 m (Figure 1). Four steel columns, whose ends are equipped with spherical low friction swivels, connect the two platforms between them and allow their relative horizontal displacements (Figure 2 and Figure 3). A second removable testing grid can be installed on the bottom shaking table and used for tests needing special configurations (e.g. elements influenced by inter-story drifts).

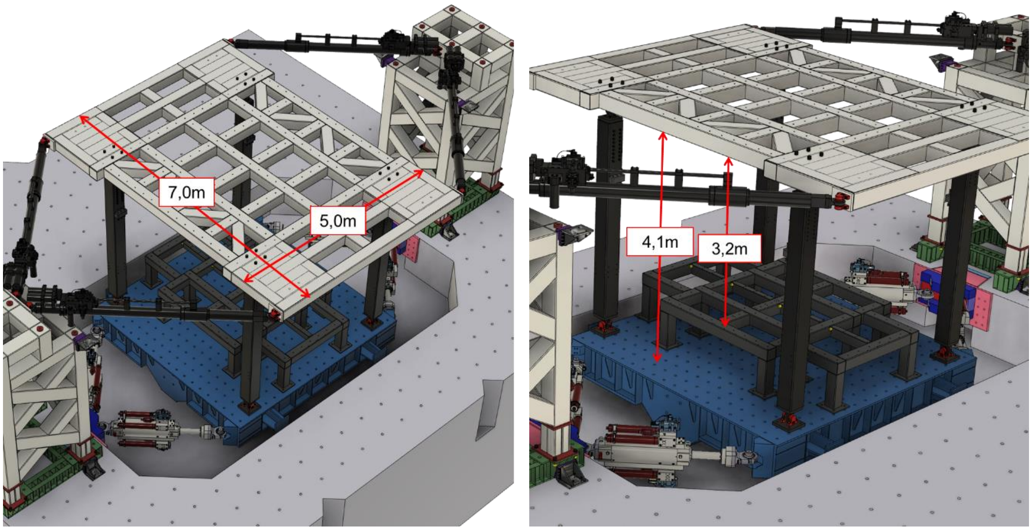

Figure 1. Three-dimensional representation of the 9 DOF system: in-plane dimensions and clear heights between the lightweight aluminum spatial frame, the surface of the existing shaking table and the steel removable testing grid.

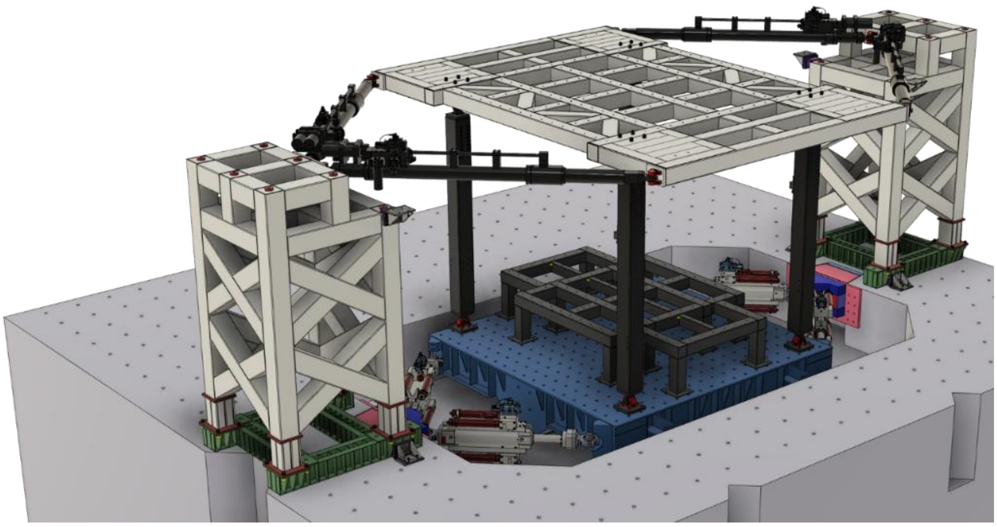

Figure 2. Three-dimensional representation of the 9 DOF system: overview of the steel towers on the base-isolated strong floor and of the vertical hinged steel columns between the two platforms.

Figure 3. Picture of the 9-DOF system during its construction.

The horizontal orthogonal displacements of the bottom shaking table and of the above aluminum platform are controlled by eight double-ended actuators, whilst the vertical movement is controlled by four single-ended actuators counteracted by two hold-down actuators. The four actuators of the bottom shaking table react on the strong mass, which is a 1600 tonn - post tensioned - reinforced concrete block isolated at the base. The reaction systems of the four actuators controlling the upper platform consist of two specifically designed framework steel towers, connected to the strong mass at the base through a system of post-tensioned steel beams and bolted steel plates. The maximum horizontal longitudinal and transversal relative displacements of the resulting system of platforms are ±1700 mm and ±1100 mm, respectively (Figure 4). The peak capacities of relative velocity and acceleration are about 4.6 m/s and 4.2 g, respectively. Although the new maximum payload is about 20 ÷ 22 tons, instead of 30 tons, depending on the configuration of the system, this is not a real limitation, since the non structural elements that required to be tested with the 9-DOF system usually have a limited weight. The design of the system was addressed to obtain a good compromise between stability, stiffness, lightness and optimization of the materials; in order to include a very wide range of cases, it was assumed that minimum reliable reference values regarding displacement, velocity and acceleration at the top of general reference buildings could be ±1 m, 2 m/s, 1.5 m/s^2, respectively. Moreover, very particular care was devoted to check the kinematics and the control strategy, the latter consisting of a real-time controller with a loop closed on degrees of freedom. The total accumulation and peak flow rate capacities of the original hydraulic system were improved to match the capability of the new testing rig and the existing piping system have been upgraded by means of new hardlines, manifolds and flexible hoses.

The input of the 9-DOF system consists of different acceleration or displacement time-histories, which can be imposed separately to the bottom and to the top platforms. Such time histories may be obtained from floor motions, which may have been recorded during past earthquakes, or from numerical simulations concerning the response of two adjacent levels of a building excited by a ground motion at the base.

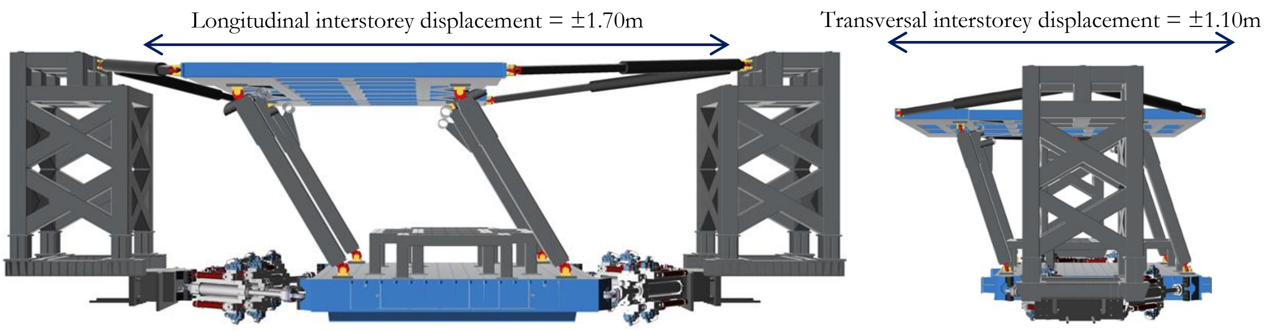

Figure 4. Design of the 9 DOF system: longitudinal and transversal interstorey drift.

More in detail, for what concerns the single components of the 9-DOF system, the upper platform was designed to satisfy minimum vertical and horizontal stiffness requirements necessary to allow the appropriate conditions for the execution of the tests. Several solutions, with both steel profiles and aluminum tubes, were studied. The advantage of the aluminum solution is the reduced weight, which is about three times lower than the steel; however, also their masses has the same proportion, so that what is gained in terms of weight, it is lost in terms of frequency of vibration. The final solution, characterized by a spatial frame of welded aluminum tubular elements with section 250 x 260 mm and thickness of 10 mm (Figure 5), represented a good compromise, essentially for its transportability due to the reduced weight (24 kN instead of 80 kN). The frame has a vertical deformation less than 1 mm under the combination of the self-weight and a concentrated vertical force of 10 kN acting in the middle; the vertical and horizontal minimum frequency values are greater than 30 Hz and 140 Hz, respectively. The aluminum used for the construction of the frame was 6000 series (magnesium and silicon alloy), hardened and weldable; it is not trivial, anyway, to highlight that the weldings of aluminum elements required particular care and expertize respect steel elements. Both specimens and intermediate plates can be connected to the platform by vertical through holes provided in the aluminum elements.

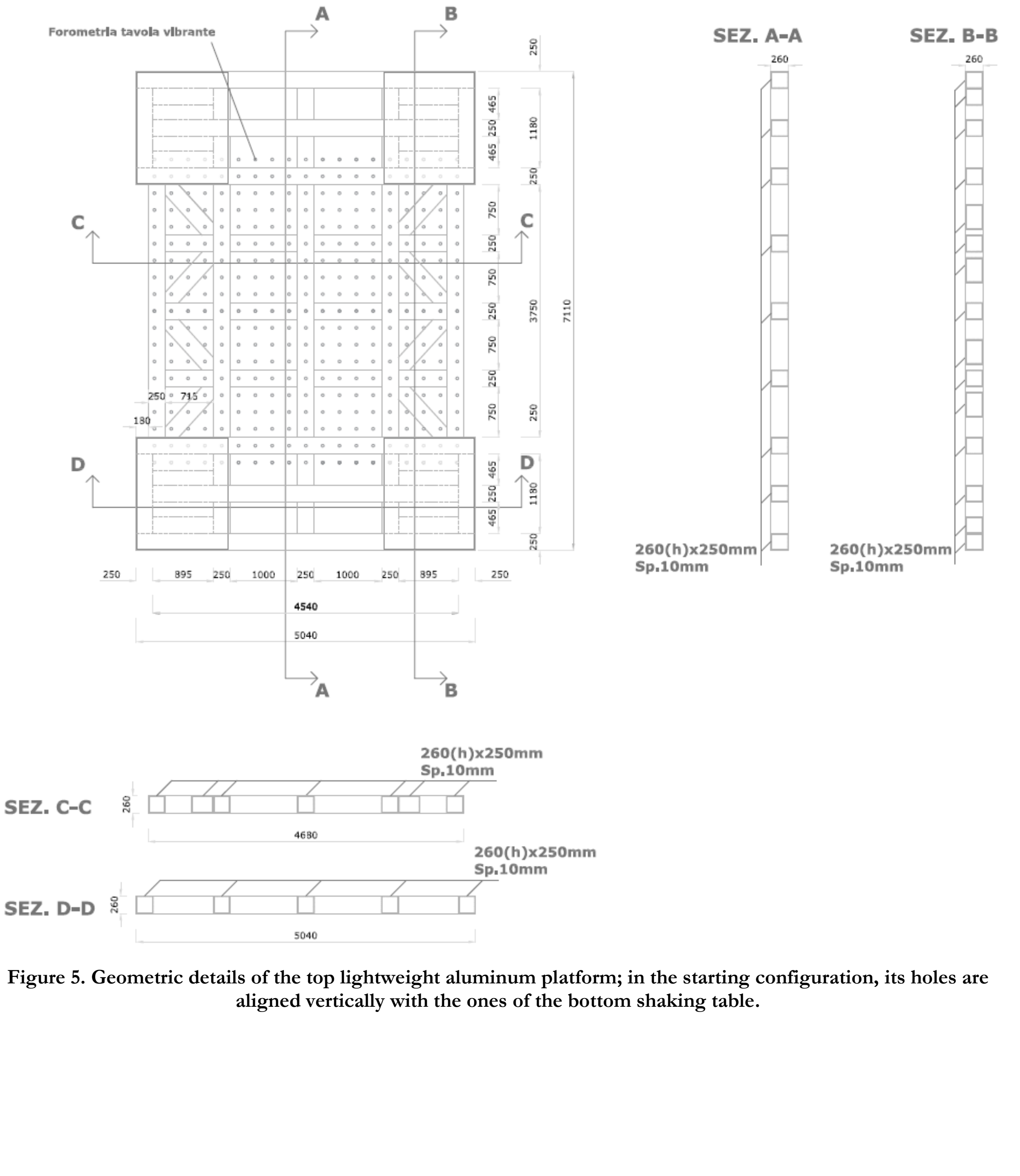

Figure 5. Geometric details of the top lightweight aluminum platform; in the starting configuration, its holes are aligned vertically with the ones of the bottom shaking table.

The main role of the towers is to be the reaction elements of the four actuators at the top; they were designed to satisfy minimum frequency requirements, depending on their stiffness and mass. The final solution, defined among several different attempt configurations, consists of European S355JR tubular steel profiles 300 x 300 mm, with a thickness of 16 mm, welded between them. The towers, having in-plan dimensions of 2.10 x 2.10 m, are about 4.40 m height. A steel plate of dimensions 320 x 1200 x 70 mm is welded to the profiles at the top of each tower to connect each couple of horizontal actuators to the upper aluminum platform. Each foundation consists of four orthogonal steel beams, which are made by two stiffened welded profiles (European UPN400), post-tensioned to the strong floor of the laboratory. The towers are connected to the foundation through systems of bolted steel plates (Figure 6). The resulting frequencies of each tower are about 70 Hz along both longitudinal and transversal horizontal directions. The maximum horizontal displacement of a tower due to the two actuators acting contemporaneously at their maxim loading capacity is about 0.3 mm.

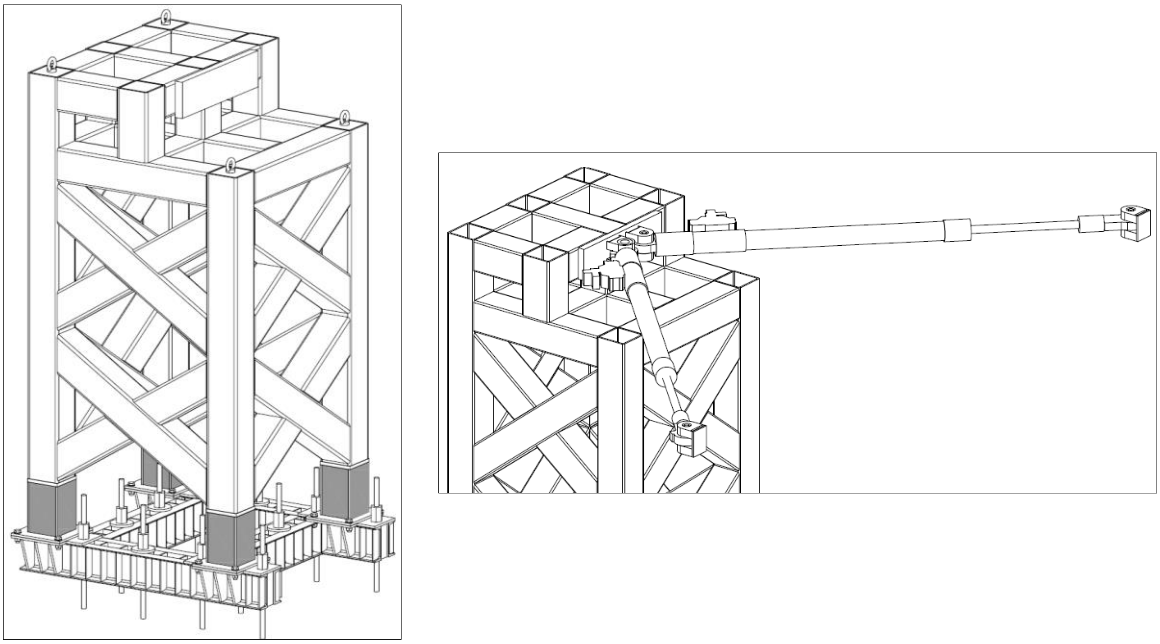

Figure 6. Details of the steel towers: system of connection at the base (left); connection of the actuators with the reaction steel plate at the top (the initial configuration of the actuators is characterized by an angle of 90 degrees).

The shaking table at the bottom is also a stand alone system able of doing tri-axial tests on both non structural components and general structures, with a payload of about 300 kN. Its acceptance tests were executed in acceleration control with a target Required Response Spectrum (RRS) obtained from the AC156 standards [ICC-ES, 2007] for z/H = 1 and SDS = 2.5 g (Figure 7). This configuration was chosen since it represents the most severe condition, with a large allowance, for the shaking table. The tests were performed by imposing various successive steps at increasing amplitudes up to the attainment of one of the limit related to the functioning of the system. Both uniaxial and biaxial configurations gave acceptable results in terms of RRS vs. Test Response Spectrum (TRS) comparisons; in the case of triaxial tests, the deviation between reference and feedback spectra was greater (Figure 8), also due to the increased severity of the imposed conditions. The results of the past acceptance tests on the shaking table induced to improve the capabilities of the hydraulic equipment during the design of the 9-DOF system. In order to perform real-time seismic testing of nonstructural components, in fact, the main requirements is represented by the ability of the actuators to reproduce the multi-directional floor motions at each couple of adjacent levels of a building excited by the earthquake ground motion. This capability, in turn, relies on the performance of the servo-hydraulic equipment and on both flow rate capacity and peak capacity of the system. The characteristics of the upgraded hydraulic power system, depicted in Figure 9, are also resumed in Table 1.

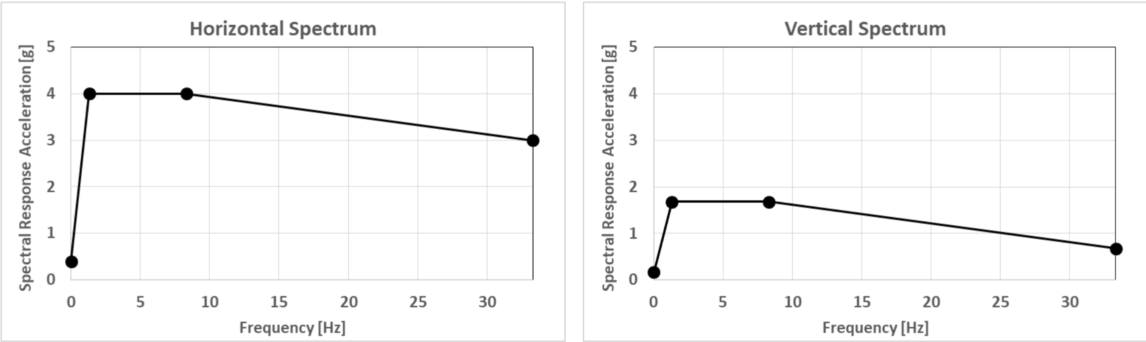

Figure 7. Horizontal and vertical spectra (SSR) obtained from AC156 standard for z/H = 1 and SDS = 2.5 g.

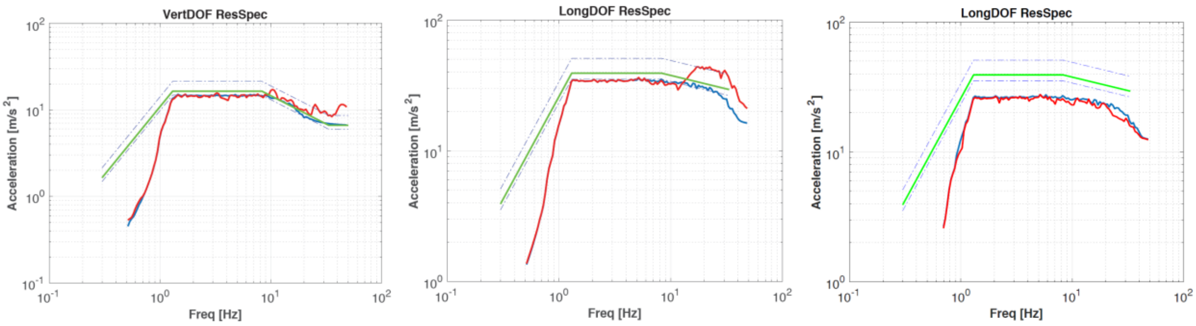

Uniaxial (vertical) test | Biaxial (horizontal) test | Triaxial (horizontal and vertical) test

Figure 8. Uniaxial, biaxial and triaxial acceptance tests of the lower shaking table with the original configuration of the hydraulic system: comparisons in terms of RRS (green line with relative upper and lower tolerance bound) and TRS (red and blue lines, which refer to the reference and the feedback spectra, respectively).

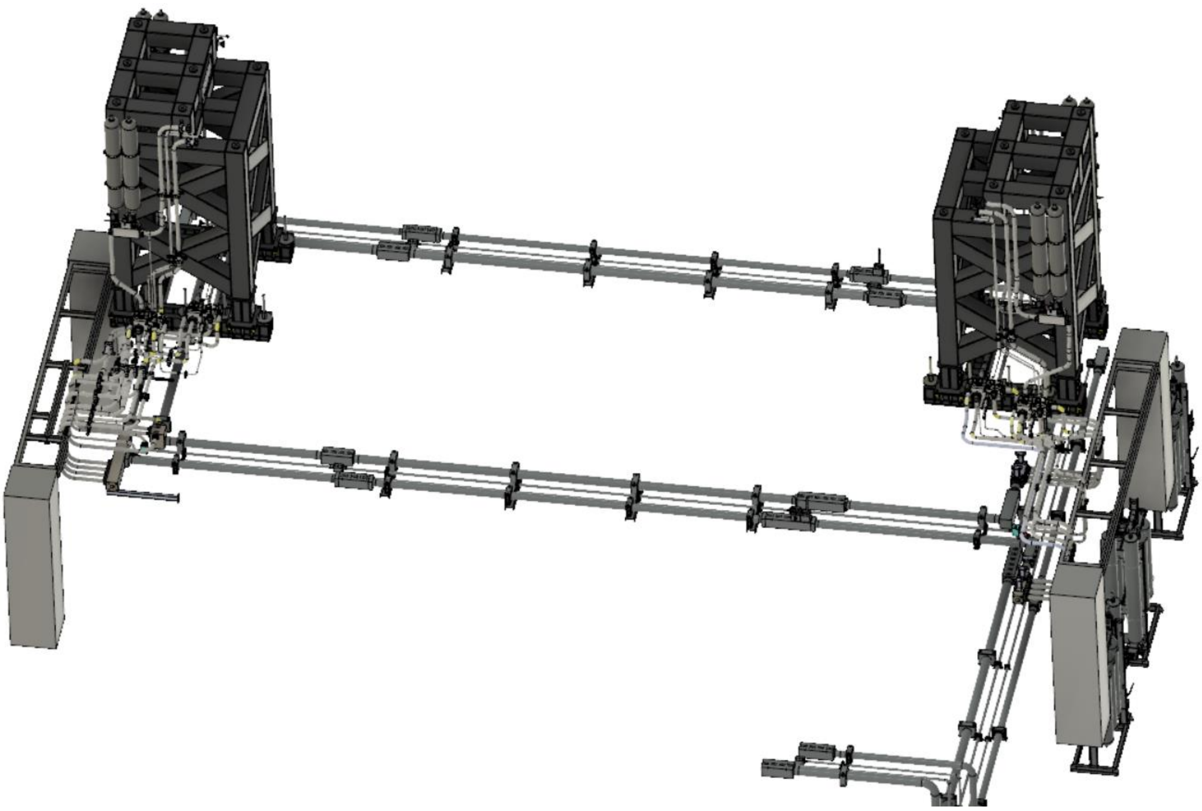

Figure 9. Scheme of the upgraded hydraulic power system.

Table 1. Components and characteristics of the upgraded hydraulic power system

Reservoir of 5.000 l
Four main pumps of 150 l/min at a maximum working pressure of 280 bar
Recirculating, filtering and cooling system of 500 l/min at 20 bar
One pilot pump of 65 l/min at 230 bar
Eight field manifolds of 300 l of nitrogen + 100 l of oil with a pre-charge of 200 bar
Eight embedded bladder manifolds of 50 l with a pre-charged of 200 bar

3. ACCEPTANCE TESTS OF THE SYSTEM

A series of new experimental acceptance tests and high level seismic simulations (Figure 10) [Petrone *et al.*, 2014; Filiatrault *et al.*, 2021] were performed on actuators, bare system and finally on a real setup which included piping and steel supports, different typologies of partition walls, floating floors and office furnishings. The goal of the multi-level acceptance test was to check, in a first stage, the compliance of the actuators and of the whole system with the target performance in terms of capacity and kinematics. A second stage was focused on the accuracy of the system in reproducing accelerations and interstory drifts, keeping in mind that the control strategy consists of a closed loop on the acceleration degrees of freedom, which means that the displacements are not directly controlled unless by means of numerical evaluations. A very accurate matching was achieved on both acceleration and interstory drifts. The results are depicted below in terms of RRS vs. TRS (Figure 11) and interstory drift time history compared with target maximum values (Figure 12) for three different values of target drift (0.5%, 1.0% and 3.0%) at each one of the two levels along the two orthogonal horizontal directions.

Figure 10. Experimental set-up before and after one of the first high level seismic simulations using the 9-DOF system.

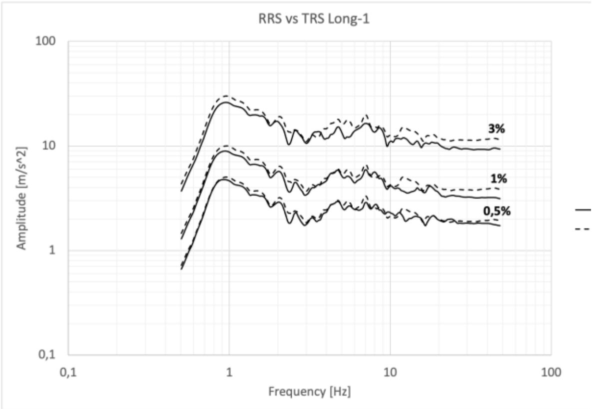

(Longitudinal dof – Level 1)

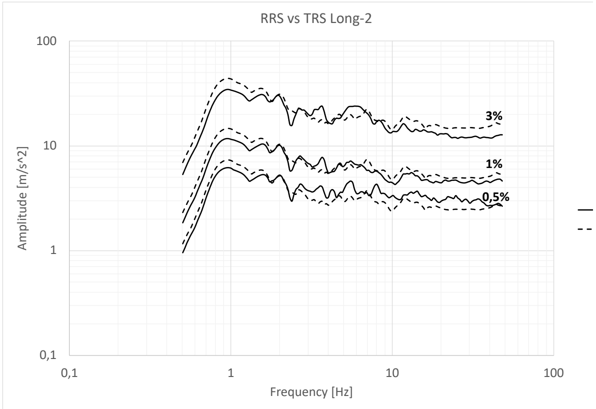

(Longitudinal dof – Level 2)

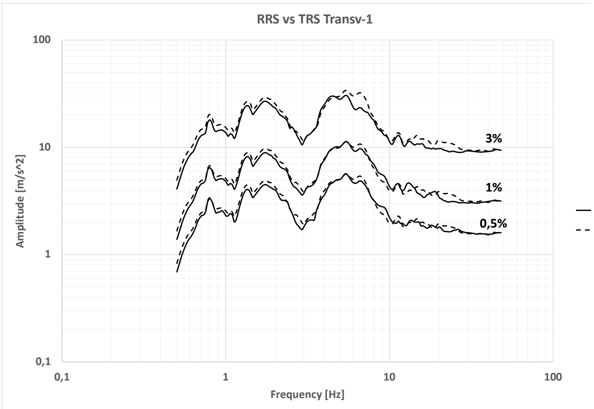

(Transversal dof – Level 1)

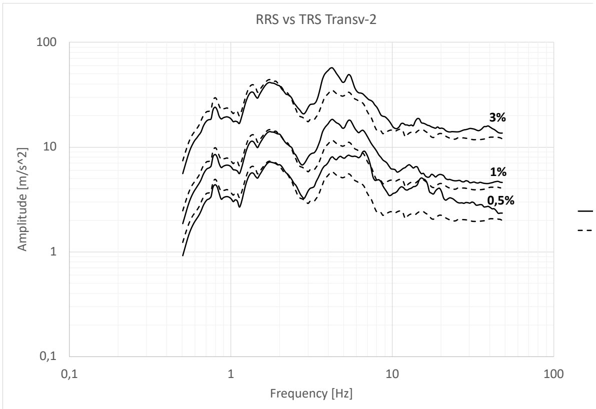

(Transversal dof – Level 2)

Figure 11. First results of new acceptance tests for three different values of drift levels expressed in terms of Required Response Spectrum (RRS) vs. Target Response Spectrum (TRS) along the two orthogonal horizontal directions for each level.

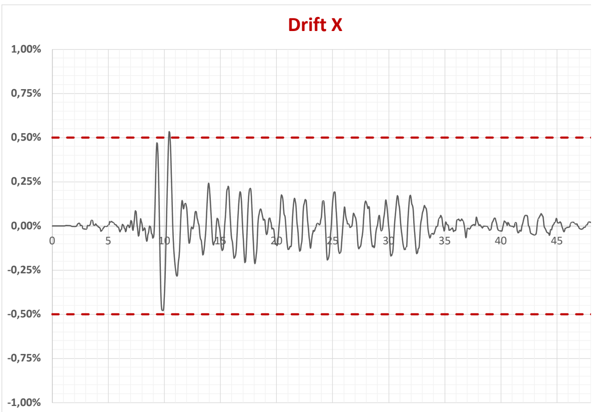

(Longitudinal Target Drift: 0.5%)

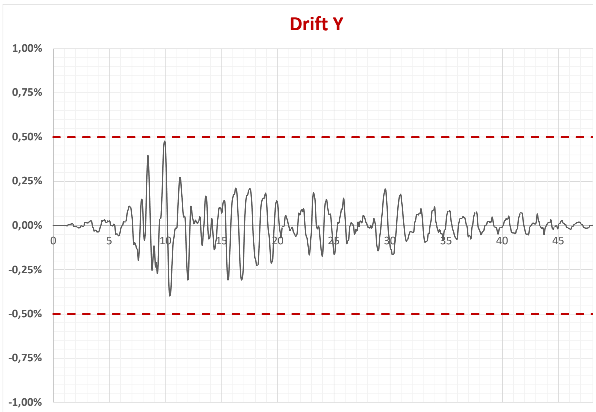

(Transversal Target Drift: 0.5%)

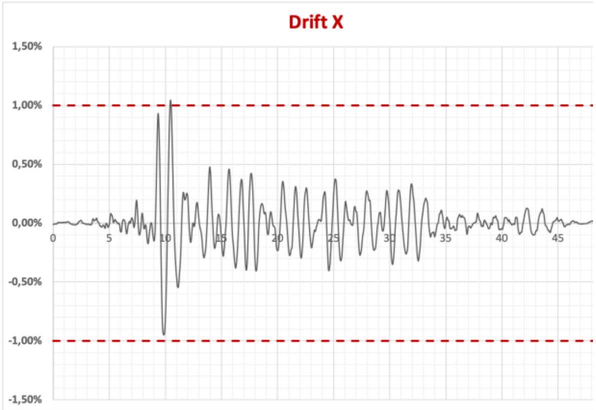

(Longitudinal Target Drift: 1.0%)

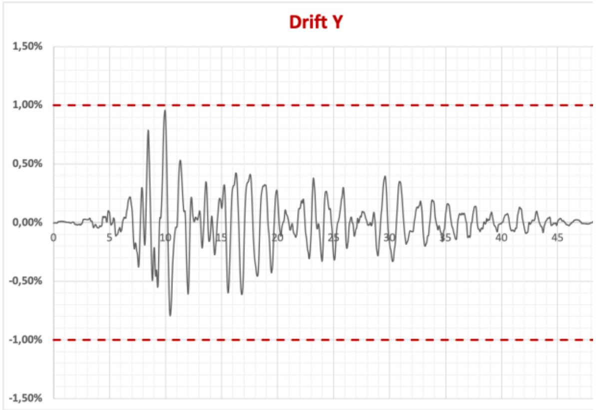

(Transversal Target Drift: 1.0%)

(Longitudinal Target Drift: 3,0%)

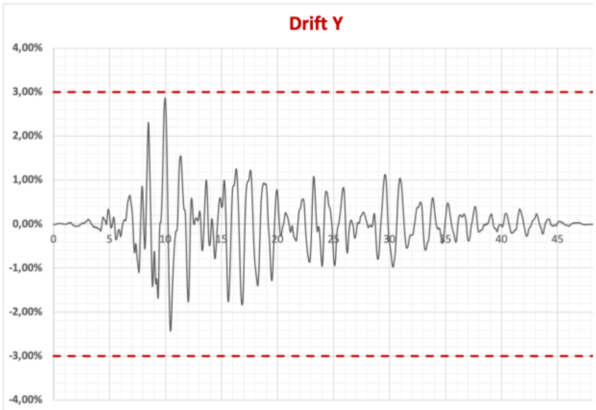

(Transversal Target Drift: 3.0%)

Figure 12. First results of new acceptance tests expressed in terms of interstory drift time history (continuous line) vs. target maximum and minimum values (dashed lines) along the two orthogonal horizontal directions for each level.

4. CONLUSIONS

In this contribution the aim, the design assumptions, the characteristics and details of the construction pahses of an innovative 9-DOF testing machine for seismic tests on non structural components have been described. The results of first acceptance tests have been also reported. Moreover, the first development of an effective protocol for seismic qualification tests was the subject of a companion paper [Lanese *et al.*, 2022].

The 9-DOF testing system consists of a 6-DOF shaking table and an upper platform at two different heights, with a clear interstorey height of about 4.1 m. The resulting system is capable of imposing acceleration and drift time histories along the two horizontal ortoghonal directions at each level, that is to say independent seismic input signals at the bottom and at the top levels can be imposed. Such time histories may be obtained by floor motions recorded during past earthquakes or by the response of two given adjacent levels of a building excited by an earthquake ground motion coming from numerical simulations.

The importance of this experimental facility relies not only in the fact that it is able to impose realistic full-scale interstory drifts and accelerations of any adjacent floor levels of any multistory building. This system is able of doing what a single shaking table can not control, that is to say to experimentally investigate the seismic response of non-structural systems, which components are both acceleration sensitive and drift sensitive. More in detail, free-standing components that are influenced mainly by horizontal accelerations can be anchored indifferently on one of the two platforms; architectural components, which are heavily influenced by interstory drifts, such as partition walls and glazed walls, can be anchored between the two testing platforms. Non-structural elements that are influenced by both accelerations and drifts, such as pressurized piping systems and suspended ceilings, can be tested in various different geometrical configurations and anchored to various support points of both testing platforms.

Acceptance tests on actuators, bare system and real setup, including different typologies of non structural elements, gave good results in terms of compliance of the responses of actuators and whole system with the target performance levels for what concerns both capacity and kinematics. Furthermore, a good accuracy in reproducing acceleration and interstory drift time histories at different intensity levels was achieved.

AKNOWLEDGEMENTS:

The work presented in this paper has been developed within the framework of the project "Dipartimenti di Eccellenza", funded by the Italian Ministry of University and Research (MIUR) at the University School for Advanced Studies (IUSS) of Pavia.

REFERENCES

Federal Emergency Management Agency (FEMA) [2006] *FEMA 461: Interim Protocols for Determining Seismic Performance Characteristics of Structural and Nonstructural Components through Laboratory Testing*, Applied Technology Council.

Filiatrault, A., Sullivan, T. [2014] "Performance-based seismic design of nonstructural building components: The next frontier of earthquake engineering," *Earthquake Engineering and Engineering Vibration*, Vol. 13, No. 1, pp. 17-46.

Filiatrault, A., Perrone, D., Merino, R. J., Calvi, G. M. [2021] "Performance-based seismic design of nonstructural building elements," *Journal of Earthquake Engineering*, Vol. 25, No. 2, pp. 237-269.

International Code Council Evaluation Service (ICC-ES) [2007] *AC156: Acceptance Criteria for Seismic Qualification by Shake-Table Testing of Nonstructural Components and Systems*.

Institute of Electrical and Electronic Engineers (IEEE) [2006] *IEEE Standard 693: IEEE Recommended Practice for Seismic Design of Substations*, New York.

Lanese, I., Bazzini, M., Bolognini, D., Brunesi, E., Dacarro, F., Dubini, P., Grottoli, L., Peloso, S., Rizzo Parisi, E., Rota, M. [2022] "New Testing Protocol for Acceleration-and-Drift-Sensitive Non-Structural Elements through the Innovative 9-DOFs Multi-Story Dynamic Testing Facility," *Proceedings of Fifth International Workshop on Seismic Performance of Non-Structural Elements (SPONSE)*, Palo Alto (CA), USA.

Petrone, C., Magliulo, G., Manfredi, G. [2014] "Shake table tests for the seismic assessment of hollow brick internal partitions," *Engineering Structures*, Vol. 72, pp. 203-214.

Retamales, R., Mosqueda, G., Filiatrault, A., & Reinhorn, A. [2011] "Testing protocol for experimental seismic qualification of distributed nonstructural systems," *Earthquake Spectra*, Vol. 27, No. 3, pp. 835-856.

Seismic Performance of Suspended Ceilings and Development of Floor Motion Responses for Experimental Testing

Cameron C.W. Flude[1], Geoffrey A. Davidson[2], David T. Lau[3], Jeffrey Erochko[4] and Kazuhiko Kasai[5]

[1] Carleton University
Ottawa, ON, Canada
e-mail: cameronflude@cmail.carleton.ca
[2] Carleton University (Former Student)
Ottawa, ON, Canada
e-mail: geoffreydavidson@cmail.carleton.ca
[3] Carleton University
Ottawa, ON, Canada
e-mail: davidlau@cunet.carleton.ca
[4] Carleton University
Ottawa, ON, Canada
e-mail: jeffreyerochko@cunet.carleton.ca
[5] Tokyo Institute of Technology
Tokyo, Japan
e-mail: kasai@serc.titech.ac.jp

Abstract. Damage to suspended ceilings is one of the most observed types of earthquake damage to non-structural components. Despite the extensive damage observed in past earthquakes, there is still a lack of thorough investigation on understanding the behaviour and failure mechanisms of suspended ceilings during earthquakes. This paper describes the development of a new testing program to investigate the failure mechanisms and seismic performance of suspended ceilings, including the influence of the vertical and rotational components of building floor motions. While there have been previous shake table tests on suspended ceilings, most of these tests considered only the horizontal motions and only limited studies have also included the vertical component of floor motions. New state-of-the-art testing facilities at Carleton University utilize four mobile shake tables which allow for movement in all six degrees-of-freedom and can more realistically simulate the configuration and support conditions and seismic excitations of complex suspended ceiling layouts. Behaviour and performance of suspended ceilings in buildings of different heights including super-tall buildings are investigated. Super-tall buildings are more flexible and deflect more as part of their design strategy to dissipate seismic energy during earthquakes. As a result, especially at high floor levels, the floor vibration response includes more pronounced vertical and rotational components. Consequently, the vertical and rotational floor motion component may have a significant impact on the performance of suspended ceilings in super-tall buildings making them more vulnerable to seismic damage and failure.

Keywords: Suspended Ceiling, Non-structural Component, Shake Table, Floor Motion, Tall Buildings.

1. INTRODUCTION

Over the past decades there have been significant advancements in earthquake engineering in building design, resulting in stronger, more resilient, and safer structures. However, over the same period there has not been a parallel development of improvement in other areas concerning building safety, especially in the performance of non-structural building components during earthquakes. A modern structure designed in accordance with current building codes can be expected to survive a significant earthquake, remaining intact even though it may suffer a controlled amount of damage. In contrast, experiences from recent major earthquakes, such as the 1994 Northridge [Norton et al., 1994], 2011 Christchurch [Dhakal et al., 2011], 2011 Tohoku [Motosaka & Mitsuji, 2012], and 2018 Anchorage earthquakes [Rodgers et al., 2021], have clearly demonstrated that non-structural components are susceptible to suffer significant damage which affect the performance of their hosting structures. For example, Norton et al. [1994] observed that of the commercial buildings within the epicentral area of the 1994 Northridge earthquake, only 2% experienced structural damage whereas 15% suffered non-structural damage significant enough to deem the building unoccupiable. Similarly, during the 2011 Christchurch earthquake severe non-structural damage was observed in low-medium rise buildings despite only minor structural damage [Dhakal et al., 2011]. In a survey study, Taghavi and Miranda [2003] pointed out that non-structural components represent significant asset value which can account for 65% to 85% of the total cost of commercial buildings. Filiatrault and Sullivan [2014] noted that earthquake losses from damage to non-structural components has been shown to exceed losses from structural damage, resulting in billions of direct (damage) and indirect (business disruption and downtime) economic losses.

Suspended ceilings are among the many types of non-structural components commonly used in commercial, office and institutional buildings such as schools and some medical facilities. Ceiling failure poses a major life safety hazard as falling ceilings are a serious threat to building occupants and can cause significant damage to other collocated components like electrical wiring or gas lines, resulting in loss of building function or possibly starting fires within the building. Furthermore, fallen ceilings create additional hazards as they can severely impede evacuation of the building and subsequent emergency search and rescue response. Damage to suspended ceilings has been reported as one of the most commonly observed types of damage to non-structural components even in moderate earthquakes that have higher probability of occurrence [Phan and Taylor, 1996]. Examples of ceiling failure causing detrimental business disruption include the shut down of the San Francisco International Airport during the 1989 Loma Prieta earthquake [Yao, 2000] and school closures after the 2018 Anchorage earthquake [Rodgers et al., 2021]. Despite their observed poor performance and the impact of failure to life safety, there is a lack of thorough investigation on understanding the behaviour and failure mechanisms of suspended ceilings during earthquakes.

A suspended ceiling is typically attached to the underside of a floor slab in a multi-storey high-rise building. The acceleration motion imparted to the suspended ceiling is influenced by the building's dynamic vibration characteristics and its response to the earthquake ground motions at its foundations. Consequently, the location of the ceiling in relation to the height of the building and the stiffness of the ceiling systems relative to the building can significantly influence the performance of the ceilings during earthquakes. Earthquake ground motions are three dimensional, but typically in earthquake engineering design practice, only the effects of the usually dominant horizontal ground motion components are considered. This ignores the potential significance of the vertical ground motion component. However, recent near-fault earthquakes have recorded vertical ground shaking components that are greater than the horizontal ground motion components [Chang et al., 1995]. Recent studies on seismic performance of suspended ceilings show that the vertical component of earthquake shaking may have a significant effect on the behaviour of suspended ceilings [Gilani et al., 2010; Ryu and Reinhorn, 2019; Soroushian et al., 2016]. The extent and severity of dislodgement of ceiling panels from the supporting grid may be influenced by the direct vertical motion of the building. As the ceiling panels are critical in maintaining the in-plane rigidity of the suspended ceiling system, the loss of ceiling panels can lead to failure of the ceiling grid and complete collapse of the entire suspended ceiling system.

Because of advances in design and construction technologies in recent years, a new generation of super-tall buildings are being constructed in major cities around the world. Because most of these super-tall buildings have not been subjected to any major earthquakes [Lu and Guan, 2021], there is limited information regarding the performance of suspended ceilings in super-tall buildings. These super-tall buildings are more flexible and deflect more as part of their design strategy to dissipate seismic energy during earthquakes. As a result, especially at high floor levels, the floor vibration response includes more pronounced rotational components. Consequently, this rotational floor motion component together with the vertical motion component may have a significant impact on the performance of suspended ceilings in super-tall buildings making them more vulnerable to seismic damage and failure.

This paper describes the development of a new testing program to investigate the failure mechanisms and seismic performance of suspended ceilings. This includes the development of appropriate floor response motions from a typical super-tall building to determine the influence of the vertical and rotational components of building floor motions. The research is being performed as part of a joint research project with Tokyo Institute of Technology and Tongji University which includes larger scale bi-directional suspended ceiling tests performed at Tongji University. The goal of the present research is to further advance the knowledge of seismic performance of suspended ceilings, including the understanding of the effects of rotational motions, which has not been included in any previous studies. This is particularly important for determining the resilience of suspended ceilings in super-tall buildings that experience significant rotation on the high floors during earthquakes.

2. SEISMIC PERFORMANCE OF SUSPENDED CEILING SYSTEMS

Suspended ceilings are any ceilings that are hung from the structure above, typically from a floor or roof slab. Two common types are suspended drywall ceilings or suspended lay-in tile ceiling systems, but other more specialized types exist as well. In the context of this paper, the term suspended ceiling will typically refer to suspended lay-in tile ceiling systems which are commonly known as T-bar ceilings. These systems consist of a light gauge metal grid system suspended from the structure with hanger wires and lightweight ceiling panels which are laid into the grid system typically without any physical connection. They are typically supported at the perimeter by a light gauge metal angle fastened to the partition walls. It is common in areas of moderate or high seismicity to have more robust or stringent seismic requirements at the perimeter connections and/or lateral braces for the ceiling grids. The lateral braces typically consist of a compression post (such as a light gauge steel stud) and four 45° splay wire braces as shown in Figure 1.

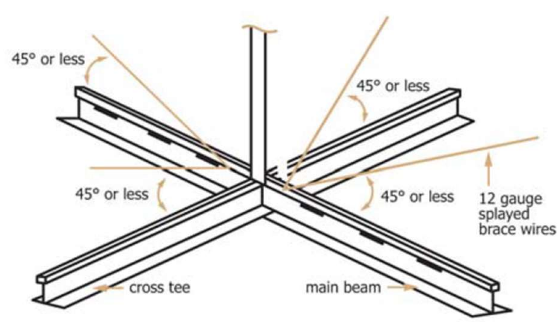

Figure 1: Seismic later brace for suspended ceilings [ASTM, 2020]

Failures of suspended ceilings have been observed in many past earthquakes and are often identified as the most common type of damage to non-structural components. The types and severity of the damage observed have varied between earthquakes and the types of buildings the suspended ceilings were located in. It has been observed after several earthquakes including the 1994 Northridge earthquake [Norton et al., 1994], 1998 earthquake in southern Taiwan [Yao, 2000], and the 2011 Christchurch earthquake [Dhakal et al., 2011], that damage is often initiated by failure at the perimeter connection. Suspended ceiling earthquake damage has also been attributed to strong vertical accelerations of the supporting structure. Ceiling damage observed during the 2011 Tohoku earthquake by Motosaka and Mitsuji [2012] included the loss of ceiling boards in large span structures. They investigated the vibration characteristics of one of these structures and found that significant vertical motions were induced in the roof structure from horizontal input motions. They noted that based on the observed damage it appeared that the ceiling design did not account for the vertical motions experienced.

Various studies including experimental testing of the seismic performance of suspended ceilings have been performed throughout the years. The studies have included a range of ceiling types, sizes, configurations, and input motions. While the studies explore many different aspects of seismic performance of suspended ceilings, they have tended to focus on the effectiveness of lateral braces and have produced conflicting results regarding their effectiveness. Yao [2000] found that lateral braces did not increase the seismic performance of the suspended ceilings, but the installation of transverse supports at the perimeter of the ceiling that prevented the lateral spread of the grid system did. Gilani et al. [2010] observed the dislodgement of ceiling panels at the center of their test specimen and almost no damage at the perimeter. The observed damage was largely attributed to the flexibility of the test frame which resulted in amplification of the vertical input motions and unexpected large vertical accelerations at the center of the test frame. During tests performed with a full-scale five-storey building, Soroushin et al. [2016] observed that when subjected to vertical accelerations greater than 1g, the lateral braces, originally intended to enhance the seismic performance of the suspended ceiling, actually had a negative impact. This was observed to be because the lateral braces provide a rigid connection between the floor structure and the ceiling grid. When the floor structure acceleration is greater then 1g downwards, the floor and ceiling grid move together but the unconnected ceiling panels only experience acceleration due to gravity and become separated from the grid system. When acting together with acceleration motions in the horizontal direction, this results in the ceiling panels becoming easily dislodged. In contrast, Ryu and Reinhold [2019] found that the use of lateral restraints improved the performance of the suspended ceiling in their large-scale ceiling tests but noted that the effects of the vertical amplification of the supporting structure was not assessed due to the relatively high stiffness of the test frame in the vertical direction.

The observations of ceiling performance from past earthquakes and previous experimental seismic testing of suspended ceilings have indicated that the perimeter connections are a vulnerable component of the suspended ceiling system. They have also shown that vibration characteristics of the supporting structure can result in large vertical accelerations that have a significant impact on the performance of the suspended ceiling. This emphasizes the importance of the proper determination of the floor motion responses which ceilings could be subjected to, including the potential significant influence of the vertical motion component imparted to the ceiling system from the supporting structure as well as the importance of proper test setup and equipment that can realistically and accurately replicate the proper floor response motions. While previous studies have included the effects of vertical accelerations, there have been no studies that have also included the effects of rotations.

3. TEST SETUP

Testing will be performed using a newly developed shake table system consisting of four independent mobile shake tables by MTS Systems Corporation and their subsidiary E2M Technologies B.V.. Each table can duplicate motions in six degrees-of-freedom. The four tables can be controlled such that they move individually, each table's movement independent of the movement of the other tables, or such that they move together as a single large platform in translation and rotation about one reference location. Since there are four separate mobile tables, they can be positioned in any configuration depending on the specimen shape and size being tested. For the suspended ceiling tests to be performed, the four independent tables are positioned in a square layout to support a 5.4m x 5.4m steel test frame from which the ceiling specimen is suspended.

The test frame, specially designed for testing non-structural components [Davidson, 2021] is shown in Figure 2. The test frame is a steel braced structure with perimeter beams and open web steel joists forming the roof/floor structure. Steel angles can be installed on the perimeter of the test frame at varying heights below the underside of the joists to simulate the perimeter support conditions for suspended ceilings and allow for different suspension heights. The test frame was designed with the intention to reduce the amplification of the input excitations in both the vertical and horizontal directions and as such the bare frame's fundamental frequency in the horizontal and vertical directions was designed to be greater than 20 Hz. The relatively high stiffness of the frame will reduce amplification and therefore allow desired floor motion responses to be inputted directly and give greater control of the response motion to the researchers. In addition, if a lower vertical frequency is desired for specific testing, weight can be added to the roof of the frame to lower the frequency.

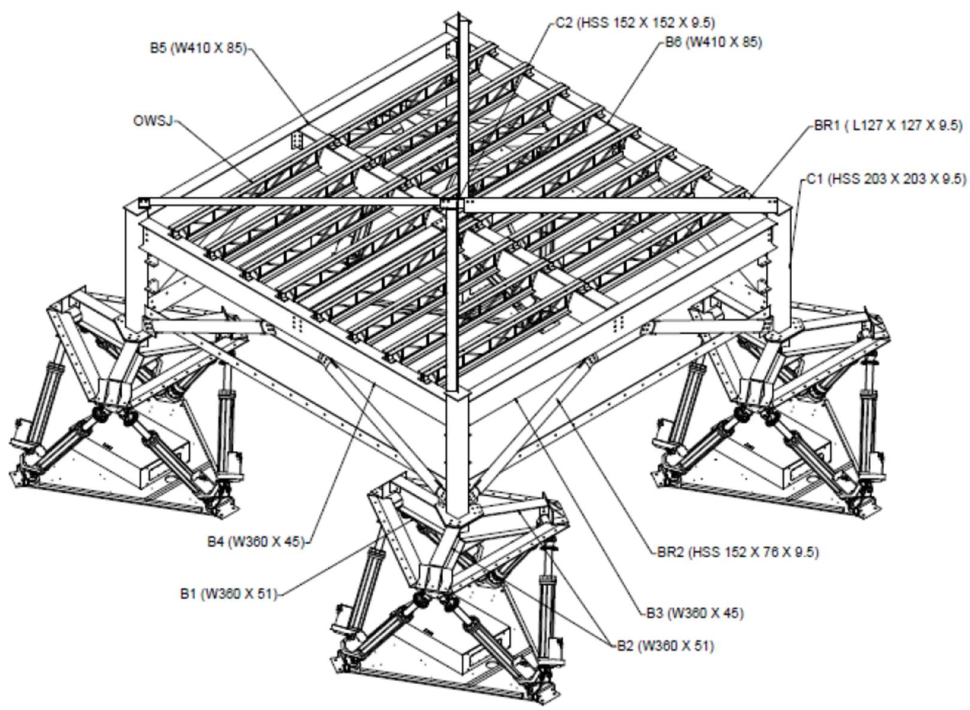

Figure 2: Test frame setup [Davidson, 2021]

4. FLOOR MOTION RESPONSES

In order to properly simulate earthquake motions experienced by suspended ceilings it is essential to consider also the vibration characteristics of the test frame and the input motions applied to the test frame to reproduce the floor response motion at the support locations of the structure where the suspended ceiling is attached.

As mentioned previously, there have been no field experience of super-tall buildings subjected to major earthquakes [Lu and Guan, 2021] and, therefore, there is limited information regarding the response of super-tall buildings to actual seismic events. In this study, two prototype building models were used to produce the simulated floor response motions for the suspended ceiling tests. The first is a model of the 128-storey Shanghai Tower, one of the tallest buildings in the world. The second is a model of a ten-storey building located on the Carleton University campus in Ottawa, Ontario, Canada. The buildings were chosen as representatives of a typical super-tall and a mid-rise building, respectively. The intention of these two models is to observe the different characteristics in floor responses between mid-rise and super-tall buildings in order to determine the impact of the influence of the characteristics of super-tall buildings on the seismic performance of suspended ceilings.

The model of the Shanghai Tower is a nonlinear model using PERFORM-3D software developed by Lu et al. [2015] as a benchmark model for seismic performance of super-tall buildings. The structure consists of a central core made of reinforced concrete shear walls with steel embedded reinforced concrete columns at its perimeter, and steel outrigger trusses in between [Lu and Guan, 2021]. Analysis of the building found that the fundamental vibration modes were approximately 8.93s in both horizontal directions and 0.60s in the vertical directions.

The model of the 10-storey building [Davidson, 2021] is a linear model created in ETABS software. The structure consists of reinforced concrete slabs supported by reinforced concrete shear walls to provide lateral load resistance in both directions. Analysis of the building found that the fundamental vibration modes in the long, short and vertical directions were approximately 0.47s, 0.31s and 0.08s respectively.

Both models were subjected to two ground motion records [Lu et al., 2015]. The first, SHW6, is an artificial seismic wave that was used for the Tongji tests and has only horizontal components. The second is a ground motion record from the 1985 Mexico City earthquake which contains components in both horizontal directions and the vertical direction. For the simulation study here, the ground motions were scaled to different peak acceleration levels with the horizontal X, Y, and vertical Z components at 100%, 85% and 65% of the peak value respectively. The roof level response was analyzed for both building models. The displacement and acceleration time histories were recorded at nodes which represent the top of vertical supports at the sides of each building. The differences in the vertical position at opposite sides of the building were used to estimate the overall rotation of the roof level at each time step to create a rotation time history. The rotation time history was repeatedly differentiated to obtain the floor rotational velocity and acceleration time histories.

The rotation and rotational acceleration time histories in the weak direction of each building subjected to the two ground motions at a peak acceleration of 0.4g are shown in Figures 3 through 6. The maximum elevation difference between the two sides of the buildings at their maximum rotation are highlighted on the figures to give an indication of the magnitude of the associated vertical deflection of the floor at the perimeter of the building.

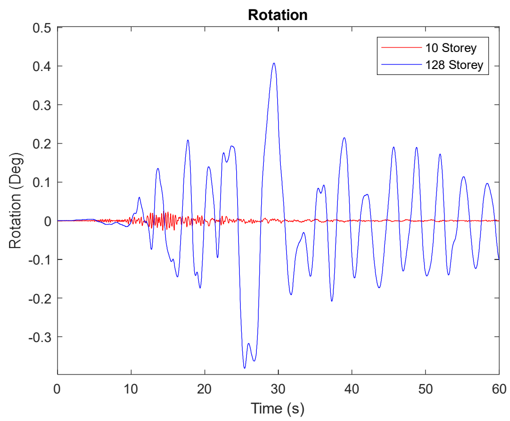

Figure 3: Building rotation due to SHW6 wave

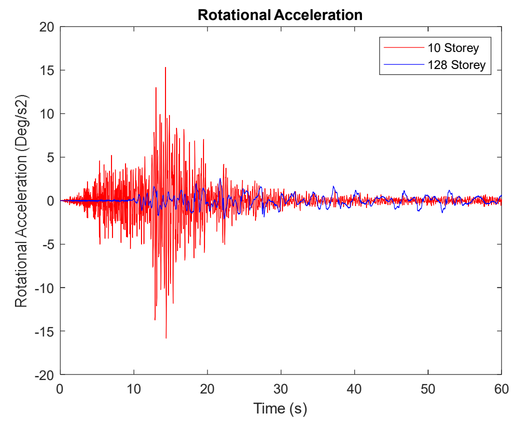

Figure 4: Rotational acceleration due to SHW6 wave

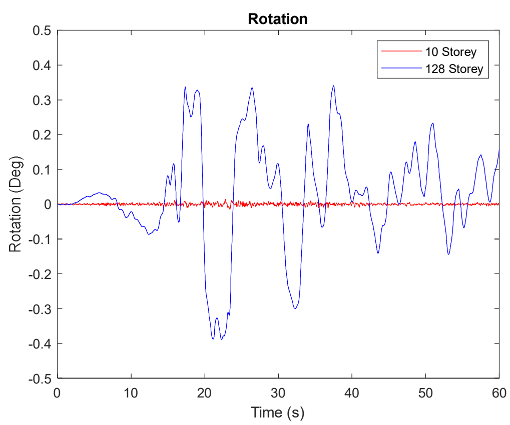

Figure 5: Building rotation due to Mexico City wave

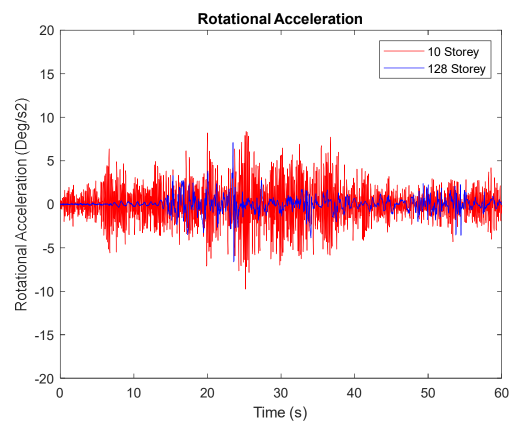

Figure 6: Rotational acceleration due to Mexico City wave

The rotation of the building results in the floor being at an angle to the horizontal plane, while the rotational acceleration of the floor also has the effect of increasing the vertical acceleration at every point on the floor except the point of rotation. This effect will be the greatest at the exterior of the building where the rotation of the floor leads to the largest vertical movement of the floor and was calculated based on the rotational acceleration and the distance from the center of the building. The amount of vertical acceleration caused by the rotations at the perimeter of the buildings are shown in Figures 7 and 9. For comparison, the total vertical accelerations (including the accelerations caused by rotations) at the same locations are shown in Figures 8 and 10.

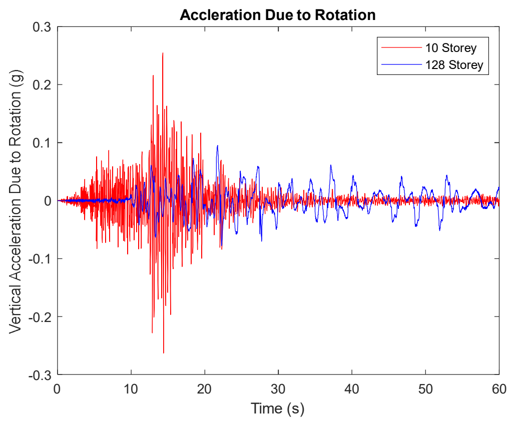

Figure 7: Vertical acceleration due to rotation (SHW6)

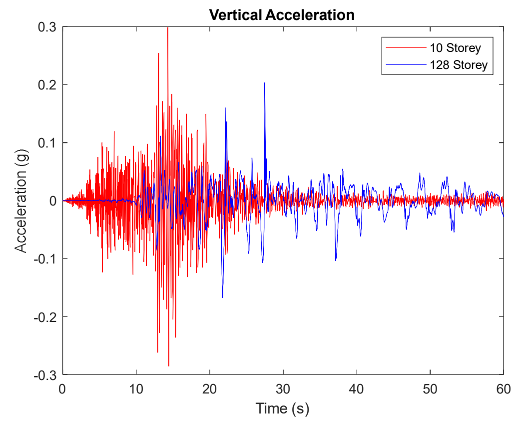

Figure 8: Total vertical acceleration (SHW6)

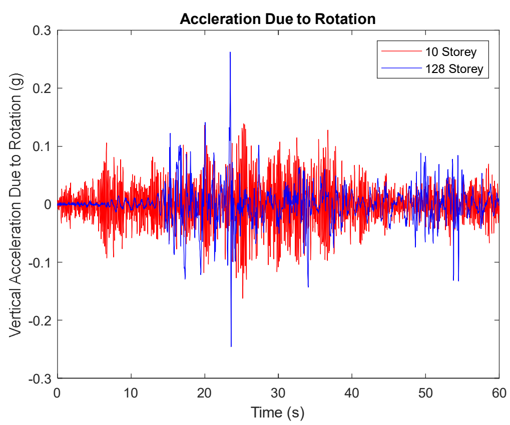

Figure 9: Vertical acceleration due to rotation (Mexico City)

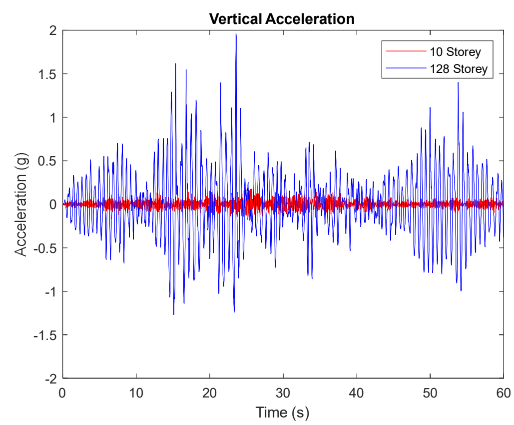

Figure 10: Total vertical acceleration (Mexico City)

When subjected to the SHW6 wave, vertical accelerations are observed at the top of each building even though there is no vertical component in the ground motion excitation. The vertical accelerations caused by rotations at the top of the 10-storey building are almost equal to the total vertical accelerations while the 128-storey building experiences total vertical accelerations approximately two times the vertical acceleration caused by rotations. This indicates that the vertical movement at the roof level of the 128-storey building is due to not just the rotation of that level but also the vertical movement of the entire building.

The vertical accelerations observed in the buildings when subjected to the Mexico City ground motion indicate that there is very significant vertical amplification in the 128-storey building resulting in vertical accelerations that were several times higher than the peak vertical acceleration of the ground motion excitation and only a small portion of these accelerations were due to the rotation of the building. In contrast, the vertical accelerations at the top of the 10-storey building were less than the peak vertical acceleration of the ground motion excitation and were mostly due to the rotation of the building. To further evaluate the effect of the vertical ground motion component to the rotational response of the floor and the associated vertical floor displacement at the building perimeter, the building models were subjected to the Mexico City ground motion record with and without the vertical component of the ground motion excitation. The results of this and several additional analyses performed on the models and the results are summarized in Table 1.

Table 1. Results of ground motion analysis of building models

Building Model		Peak Ground Acceleration			Floor Response				
Storeys	Ground Motion	X (g)	Y (g)	Z (g)	Floor Level	Rotation (Deg)	Rotational Acc. (Deg/s^2)	Acc. Due to Rotation (g)	Vertical Acc. (g)
128	SHW6	0.2	0.17	0	128	0.33	1.8	0.07	0.09
128	SHW6	0.4	0.34	0	128	0.46	2.6	0.10	0.20
128	SHW6	0.4	0.34	0	70	0.28	1.0	0.05	0.13
128	Mex. City	0.2	0.17	0.13	128	0.28	4.1	0.15	0.72
128	Mex. City	0.4	0.34	0.26	128	0.39	7.1	0.26	1.94
128	Mex. City	0.4	0.34	0.26	70	0.30	6.5	0.30	1.49
128	Mex. City	0.4	0.34	0	128	0.40	4.1	0.14	0.14
10	SHW6	0.4	0.34	0	10	0.02	15.8	0.26	0.30
10	Mex. City	0.4	0.34	0.26	10	0.02	9.8	0.16	0.20
10	Mex. City	0.4	0.34	0	10	0.02	4.0	0.07	0.08

It was observed that without the vertical component of the ground motion excitation there was only a small vertical acceleration which was entirely due to the rotations. This also indicates that most of the vertical acceleration experienced by the 128-storey building when subjected to the ground motion excitation with a vertical component was due to the amplification of this vertical component.

The floor response was also recorded at the 70th floor of the 128-storey building to observe how the response varies along the height of the building. The results show that both the rotation and vertical amplifications are higher at the top compared to the mid-height, indicating that they generally increase along the buildings height as would be expected.

5. CONCLUSIONS

Previous earthquake experience has shown that earthquake damage to non-structural components, and especially suspended ceilings, can be a significant hazard to life and the continuing function of the building. Damage to suspended ceilings has commonly been the most reported type of damage to non-structural components and has resulted in large economic losses due to property damage and often more significantly the extended closure of business. Suspended ceiling performance in previous earthquakes and in experimental testing has shown that ceilings are susceptible to damage at their perimeter connections and that vertical acceleration of the supporting structure has a significant impact on the ceiling's performance.

A seismic testing system was designed specifically for experimental testing of the seismic performance of non-structural components including suspended ceilings. The test system consists of six degree-of-freedom mobile shake tables supporting a rigid steel frame which can be used to accurately simulate the floor response of super-tall buildings including the rotational components of the motion.

Models of a typical super-tall and mid-rise building were used to develop floor response motions. The floor responses indicate that suspended ceilings at the top of super-tall buildings could be susceptible to earthquake damage. Large amplifications of the vertical component of the ground motion excitation were observed resulting in large vertical accelerations which suspended ceilings have been shown to be vulnerable to. In addition, floor rotations of up to almost 0.5 degrees were observed. This amount of rotation would result in the support location of a ceiling suspended 1200mm below the floor structure to move approximately 10mm away from the original location. This combined with the effects of the building drift, the additional vertical accelerations due to the rotations and the amplification of the vertical component of the ground motions will add stresses to the perimeter connections or cause more pronounced movements of the ceiling making them more susceptible to damage during earthquakes. The floor response motions determined from building models of different height from low-rise to high-rise and super-tall buildings will be used in shake table test of suspended ceilings to determine the effects of the vertical and rotational components of floor response motions to performance of suspended ceilings during earthquakes.

ACKNOWLEDGEMENTS

The authors would like to acknowledge the technical assistance of providing the numerical model of the Shanghai Tower by Xilin Lu, Huanjun Jiang and Y. Wang of Tongji University, China and the assistance provided by S. Motoyui of Tokyo Institute of Technology, Japan for this research.

REFERENCES

ASTM International [2020] "ASTM E580/E580M-20: *Standard Practice for Installation of Ceiling Suspension Systems for Acoustical Tile and Lay-in Panels in Areas Subject to Earthquake Ground Motions*."

Chang, S. W., Bray, J.D., & Seed, R.B. [1995] "Ground motions from the Northridge Earthquake," *Proceedings: Third International Conferences on Recent Advances in Geotechnical Earthquake Engineering and Soil Dynamics*, St. Louis, Missouri, United States.

Davidson, G.A. [2021] "Development of testing facilities and procedures for seismic performance of suspended ceilings," *Master's thesis*, Department of Civil Engineering, Carleton University, Ottawa, Ontario, Canada.

Dhakal, R.P., MacRae, G.A., & Hogg, K. [2011] "Performance of ceilings in the February 2011 Christchurch earthquake," *Bulletin of the New Zealand Society for Earthquake Engineering*, Vol. 44, No. 4, pp. 379-389.

Filiatrault, A., & Sullivan, T. [2014] "Performance-based seismic design of nonstructural building components: The next frontier of earthquake engineering," *Earthquake Engineering and Engineering Vibration*, Vol. 13, Supp. 1, pp. 17–46.

Gilani, A. S. J., Reinhorn, A. M., Glasgow, B., Lavan, O., & Miyamoto, H. K. [2010] "Earthquake simulator testing and seismic evaluation of suspended ceilings," *Journal of Architectural Engineering*, Vol. 16, No. 2, pp. 63–73.

Lu, X., & Guam, H. [2021] "Earthquake Disaster Simulation of Civil Infrastructures," *Springer Singapore.*

Lu, X., Jiang, C, Jiang, H. [2015] "The benchmark model of super high-rise building structure and its seismic response analysis," *Structural Engineer*, Vol. 31, No. 4, pp. 100-107.

Motosaka, M., & Mitsuji, K. [2012] "Building damage during the 2011 off the Pacific coast of Tohoku Earthquake," *Soils and Foundations*, Vol. 52, No. 5, pp. 929–944.

Norton, J. A., King, A. B., Bull, D. K., Chapman, H. E., McVerry, G. H., Larkin, T. J., & Spring, K. C. [1994] "Northridge earthquake reconnaissance report," *Bulletin of the New Zealand Society for Earthquake Engineering*, Vol. 27, No. 4, pp. 235-344.

Phan, L. T., & Taylor, A. W. [1996]. "State of the art report on seismic design requirements for nonstructural building components," *U.S. Department of Commerce. National Institute of Standards and Technology*.

Rodgers, J., Hassan, W., Motter, C., & Thornley, J. [2021] "Impacts of the 2018 M7.1 Anchorage earthquake on schools," *Earthquake Spectra*, Vol. 37, No. 3, pp. 1849–1874.

Ryu, K. P., & Reinhorn, A. M. [2019] "Experimental study of large area suspended ceilings," *Journal of Earthquake Engineering*, Vol. 23, No. 6, pp. 1001–1032.

Soroushian, S., Maragakis, E. M., Ryan, K. L., Sato, E., Sasaki, T., Okazaki, T., & Mosqueda, G. [2016], "Seismic simulation of an integrated ceiling-partition wall-piping system at E-Defense. II: Evaluation of nonstructural damage and fragilities," *Journal of Structural Engineering*, Vol. 142, No. 2.

Taghavi, S., & Miranda, E. [2003] "Response assessment of non-structural building elements," *Pacific Earthquake Engineering Research Centre.*

Yao, G. C. [2000] "Seismic performance of direct hung suspended ceiling systems," *Journal of Architectural Engineering*, Vol. 6, No. 1, pp. 6–11.

Numerical Simulation of Prefabricated Steel Stairs to be Implemented in the NHERI TallWood Building

Shokrullah Sorosh[1], Tara C. Hutchinson[1], Keri L. Ryan[2], Sarah Wichman[3]
Kevin Smith[4], Robert Belvin[4], and Jeffrey W. Berman[3]

[1] Dept. of Structural Engineering, UC San Diego, La Jolla, CA 92093
e-mail: ssorosh@ucsd.edu, tara@ucsd.edu

[2] Dept. of Civil and Environmental Engineering, University of Nevada, Reno
e-mail: klryan@unr.edu

[3]Dept. of Civil and Environmental Engineering, University of Washington
e-mail: wichman@uw.edu, jwberman@uw.edu

[4]Construction Specialties, Inc., Muncy, PA
e-mail: ksmith@c-scgroup.com, rbelvin@c-sgroup.com

Abstract. During extreme events such as earthquakes, stairs are the primary means of egress in and out of buildings. Therefore, understanding the seismic response of this non-structural system is essential. Past earthquake events have shown that stairs with a flight to landing fixed connection are prone to damage due to the large interstory drift demand they are subjected to. To address this, resilient stair systems with drift-compatible connections have been proposed. These stair systems include stairs with fixed-free connections, sliding-slotted connections, and related drift-compatible detailing. Despite the availability of such details in design practice, they have yet to be implemented into full-scale, multi-floor building test programs. To conduct a system-level experimental study using true-to-field boundary conditions of these stair systems, several stair configurations are planned for integration within the NHERI TallWood 10-story mass timber building test program. The building is currently under construction at the UC San Diego 6-DOF Large High-Performance Outdoor Shake Table (LHPOST6). To facilitate pre-test investigation of the installed stair systems a comprehensive finite element model of stairs with various boundary conditions has been proposed and validated via comparison with experimental data available on like-detailed single-story specimens tested at the University of Nevada, Reno (UNR). The proposed modelling approach was used to develop the finite element model of a single-story, scissor-type, stair system with drift-compatible connections to be implemented in the NHERI TallWood building. This paper provides an overview, and pre-test numerical evaluation of the planned stair testing program within the mass timber shake table testing effort.

Keywords: Steel stairs, non-structural components, and systems, finite element analysis, dynamic analysis, seismic response

1. INTRODUCTION

Stairs, spanning floor-to-floor and subject to seismic interstory drift demands, are displacement-sensitive non-structural systems. Previous earthquakes and experimental studies consistently document the significant damage, including total failure possible for these non-structural systems. For example, Li and Mosalam [2013] reported significant damage to concrete stairs during the 2008 Wenchuan earthquake. In addition, Bull [2011] summarized damage to both concrete and steel stairs during the 2011 Christchurch earthquake.

Previous experimental studies showed that the overall response of the stair system significantly depends on the flexibility of the connection. Notably, Higgins [2009] studied the behavior of steel stairs under quasi-static load, achieving a drift of 2.5%. However, at this design targeted drift, large local deformations of stair to landing connection were observed. In subsequent studies, prefabricated steel stairs were tested as part of a full-scale five-story reinforced concrete building at UC San Diego [Hutchinson *et al.*, 2013]. In these shake table tests, connection and slab-embedded weld fractures were seen even before reaching the design target peak inter-story drift ratio (PIDR) of 2.0-2.5 % [Wang *et al.* 2013, 2015; Pantoli *et al.* 2013].

Observing the performance of stairs during past earthquake events and experimental studies, it is understood that stairs with fixed flight-to-landing connections are understood to be prone to damage. Therefore, ASCE 7-16 [2017], Section 13.5.10 requires that egress stairs not part of a seismic force-resisting system be detailed to accommodate the relative displacement between two levels without loss of gravity support. To this end, two shake table testing programs of full-scale prefabricated steel stairs with a variety of connection details were conducted at the University of Nevada Reno Earthquake Engineering Laboratory [Black *et al.*, 2017, 2020]. In these testing programs, the stair flight to landing connection was detailed using several strategies, notably, fixed at the top and free sliding at the bottom (fixed-free configuration), longitudinal slots at the top, and transverse slots at the base (slotted connection), an industry-designed drift-compatible connection at the top and fixed connection at the base (fixed-drift compatible configuration). The stair system with a fixed-drift compatible configuration performed well and sustained no damage when subjected to a target MCE-scaled earthquake. However, the stair systems with fixed-free configurations sustained significant damage under MCE-level earthquake. The stairs with slotted connections performed well under earthquakes with smaller amplitudes, but sustained binding at the connection during earthquake tests with larger amplitudes.

To further investigate the seismic performance of stairs with drift-compatible connections, at a system level, a 10-story operable steel stair system with various connection details is being planned to be tested as part of the NHERI Tallwood 10-story mass timber building at the UC San Diego 6-DOF Large High-Performance Outdoor Shake Table (LHPOST6). The NHERI Tallwood project is a multidisciplinary industry-university research program, which aims to advance the use of a new seismic resilient lateral system using post-tensioned mass timber rocking walls along with U-shaped flexural plates (UFP) as a means to dissipate energy. The design methodology was validated through testing a full-scale 2-story mass timber building in 2017 [Pei *et al.*, 2019]. The 10-story mass timber building is the centrepiece of this project. Seismic resiliency of both the structural and non-structural systems is considered in this 10-story building.

Prefabricated steel stairs incorporated into the 10-story mass timber building consist of eight stories of Modular Stair Systems (MSS), and two stories representing Traditional Construction (TC) [Sorosh *et al.*, 2022] (see Figure 1). Considering the flight to landing connections, six stories will have drift-compatible connections installed at the flight to mid-landing connections, with the other end of the flights fixed. Two stories will have longitudinal slots at the bottom connections of each flight and transverse slots at the top connections of each flight. Two stories will have fixed-free configurations with the bottom connections of each flight free and the top connections fixed. The details of each connection are shown in Figure 1. With exception of story 1, which is 13', all story heights are 11'.

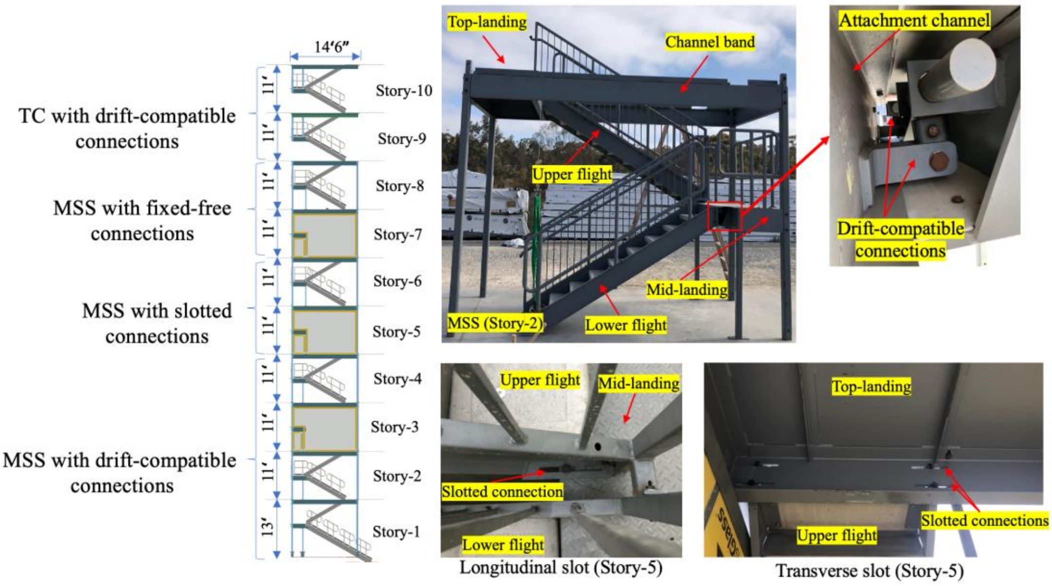

Figure 1. 10-story stair tower (Left), and a sample of stair connection details (Right)

1.1 SCOPE OF PRESENT PAPER

In an effort to prepare for the 10-story testing program, a high-fidelity finite element model of steel stairs with various boundary conditions has been proposed and validated through comparison with the aforementioned experimental studies at UNR [Sorosh *et al.*, 2022] The proposed modelling approach is used to develop the finite element model of steel stairs with drift-compatible connections to be tested as part of the 10-story building. This paper discusses the development of the finite element model and the dynamic characteristics of these stair systems.

2. FINITE ELEMENT MODEL DESCRIPTION

Using Abaqus [2020], the finite element model of the prefabricated steel stairs with various flight-to-landing connection details was developed and validated through comparison with test data. The same procedure is followed to develop the finite element model of modular stair systems with drift-compatible connections to be incorporated in the NHERI Tallwood mass timber building. To obtain the dynamic characteristics of these stair systems, a modal analysis is conducted. In addition, to determine the load capacity of each stair unit, a pushover analysis is performed.

2.1 GEOMETRY AND MESH GENERATION

Figure 2 shows the dimensions, element types, and approximate global mesh size (AGMS) of each stair component. Note that both solid and shell elements are used in this finite element model. The components that have complex geometry such as columns with bolt holes, drift-compatible connections, and bolts are modelled using solid elements. Components with simple geometry and smaller thickness-to-width ratio such as landings, risers, and stringers are modelled using shell elements. Table 1 summarizes the steel section, material, element type, and mesh size of each component. Abaqus provides many types of shell and solid elements with various formulations, integration points, and accuracy levels. Sun [2006] discusses the performance of different finite elements in this commercial software. As listed in Table 2, stairs components are modelled using various finite elements. The selection of the finite element types noted in Table 1 is based on Sun [2006] and the FEM previously developed and validated through experimental data.

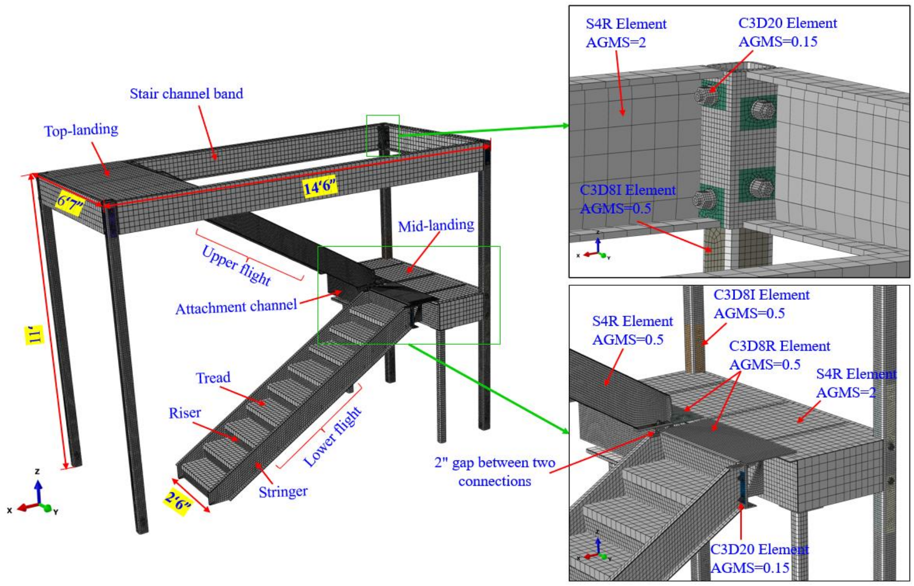

Figure 2. Geometry and mesh details of the finite element model

Table 1. Material, element type and mesh size

Component	Section	Material	Element	Mesh Size (AGMS)
Stair channel band	C12×30	A36	S4R Linear Quadrilateral	2
Column	HSS4×4×3/8	A500 Grade B	C3D8I Linear Hexahedron	0.5
Stringer	MC10×8.4	A36	S4R Linear Quadrilateral	1
Drift-compatible connection	Various	A36	C3D8R Linear Hexahedron	0.2 - 0.5
Aluminum plate	PL5'-10"×13-3/4"×3/16"	Aluminum	C3D8R Linear Hexahedron	0.5
Riser	PL2'-6"×5-7/16"×1/16"	A36	C3D8R Linear Hexahedron	1
Tread	2'-6"×12"×2-1/4"	Concrete	C3D8R Linear Hexahedron	1
Bolt	Various	A325	C3D20 Quadratic Hexahedron	0.15
Mid-landing	PL6'-7"×2'-6"×1/4"	A36	S4R Linear Quadrilateral	2
Top-landing	PL6'-6 1/2"×3'-1 1/2"×1/4"	A36	S4R Linear Quadrilateral	2

2.2 MATERIALS

As listed in Table 1, the stair components are made of various materials. Based on the preliminary analysis, bolts and concrete do not experience inelastic deformations. Therefore, a linear material model is assigned for concrete treads and bolts. The stair components made of A36 and A500 Grade B steel have nonlinear material models. In Abaqus, a plastic material model with combined cyclic hardening rules is used to model the sections with A36 and A500 Grade B steel materials. Ramberg-Osgood's material model [1943] is used to define the stress-strain relation of A36 and A500 Grade B steel materials. Figure 3 shows the response of a single shell element with A36 and A500 Grade B steel material models under uniaxial displacement controlled monotonic and cyclic loads.

2.3 BOUNDARY CONDITIONS AND CONTACT ELEMENTS

In this FEM, the column bases, and bottom connection of lower-flight have fixed (Encastre) boundary conditions, in which all rotation and translation degrees of freedom are constrained. In modal analysis, to represent a rigid diaphragm around the stair channel band, the movement of the stair channel band is restrained.

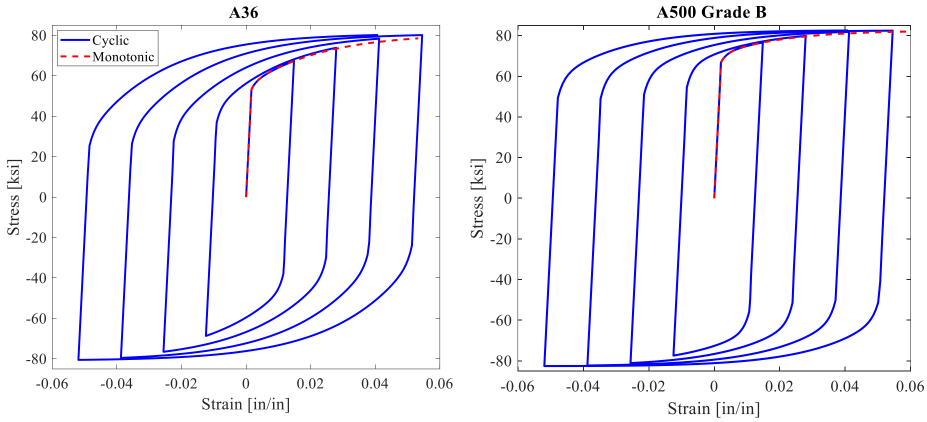

Figure 3. Stress-strain relation of A36 steel (Left) and A500 Grade B steel (Right) adopted for the FEs used herein

Welded connections are not modelled explicitly. Instead, a tie constraint is defined in all welded sections. The interaction between stair components such as the bolted connections and the drift-compatible connections are modelled using surface-to-surface contact elements with a friction model. The ideal friction model results in a convergence issue. Therefore, in this FEM, the penalty formulation with isotropic directionality, and 0.005-unit elastic slip is used to model the frictions in all surfaces in contact. Figure 4 shows the shear stress-slip relation in penalty and ideal friction models. In addition, for better illustration purposes, meshed drift-compatible connections and surfaces with contact elements highlighted are shown in Figure 4.

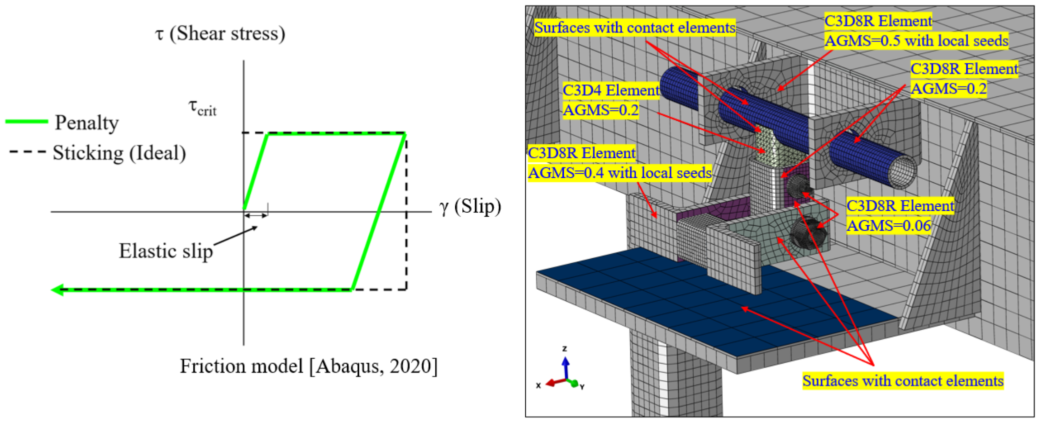

Figure 4. Friction model (Left), and meshed drift-compatible connection with contact elements highlighted (Right)

3. DYNAMIC CHARACTERISTICS OF STAIR SYSTEMS

This paper discusses the dynamic characteristics of modular stair systems (MSS) with drift-compatible connections. In the 10-story mass timber building, two types of MSS with drift-compatible connections will be tested. In the first three stories, at the mid-landing level, two drift-compatible connections are attached to a single attachment channel (see Figure 1). The lower flight is bolted to this channel using four 1/2"-diameter ASTM A325 tension control bolts. The upper flight is bolted to the same channel using two 1/2"-diameter ASTM A325 tension control bolts. In the fourth story, to allow free movement of each stair flight and corresponding drift-compatible connection, two attachment channels are installed. There is a two-inch gap between attachment channels (see Figure 2).

In the dynamic response of the stair system, both the local and global vibration modes are essential to fully characterize the stair subsystem. The local vibration modes manifest within each stair largely along the flights, see Figure 5. To determine the local mode in Abaqus modal analysis is conducted on each stair unit separately. The global mode of the stair system consists of the vibration modes of the stair tower at the system level. The structural non-structural interaction primarily depends on the global modes of the stair tower. The global modes of stair systems are calculated based on a simplified shear-frame model of a 10-story stair tower. The story stiffness is based on the pushover analysis of the proposed FEM.

3.1 Stair System with Drift-Compatible Connections

In Abaqus, linear perturbation analysis is conducted to obtain the modal properties of the modular stair systems with drift-compatible connections. During linear perturbation analysis, the model's response is defined by its linear elastic stiffness at the base state. The mode shapes and corresponding vibration frequencies of the stair system with a single attachment channel are shown in Figure 5. The first mode of this stair system corresponds to the vibration of stair flights transverse to the stair run direction (in Y-direction). The second local mode of the stair system corresponds to the buckling of stringers because of the single attachment channel.

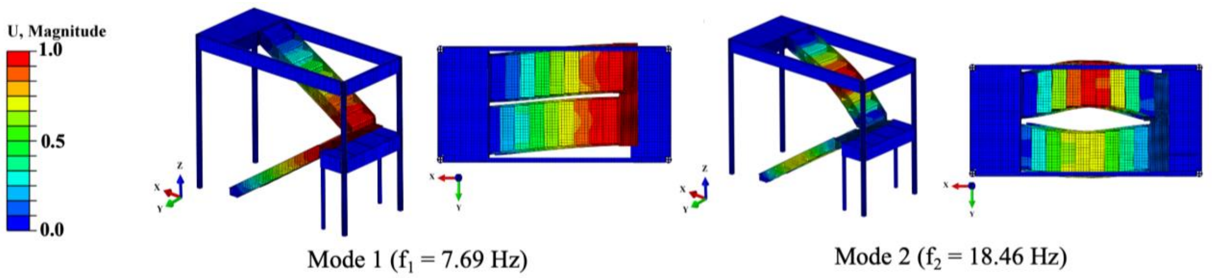

Figure 5. First two local modes of stair system with a single attachment channel

In the stair system with two attachment channels at the mid-landing level, the movement of the lower flight is independent of that of the upper flight. Therefore, as is seen in Figure 6, the vibration modes of the stair flight are not continuous throughout the stair height, rather each flight vibrates in distinct vibration modes. The first vibration mode of this stair unit corresponded to the vibration of upper flight in the gravity direction. The vibration of lower flight in transverse to the stair run direction (in Y-direction) corresponds to the second mode of the stair unit. The stair system with two attachment channels at the mid-landing connections is more flexible than the one with a single attachment channel. The natural periods corresponding to the local modes of the stair systems are much lower than the building period. However, as discussed in Section 3.2.3, the natural periods corresponding to the global vibration modes of the stair tower are closer to the building vibration period.

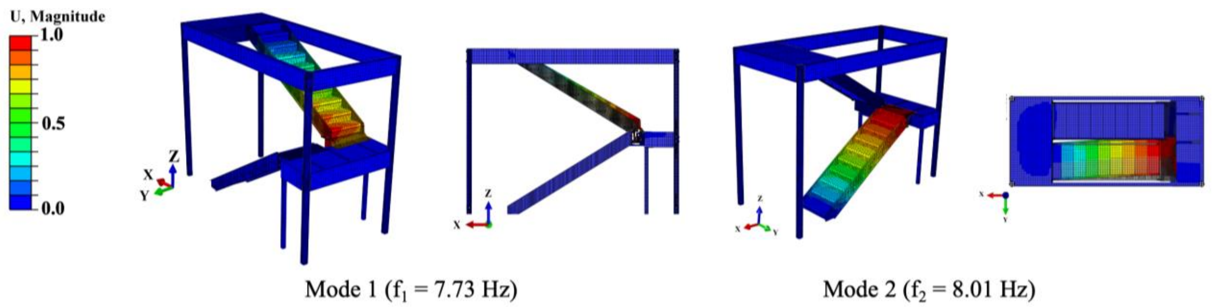

Figure 6. First two local modes of stair system with two attachment channels

3.2 Global Modal Properties of 10-Story Stair Tower

To determine the global modes of the stair tower, a 10-story shear frame is assumed for characterizing the 10-story stair tower. Specifically, a lumped mass model of the shear frame is developed. The stair mass is distributed throughout the stair tower height such that mass at each level accounts for 50% of the story mass above and below the specific level. The stiffness of the lumped mass model is based on the initial stiffness of the pushover analysis of the developed FEM.

3.2.1 Pushover Analysis of Stair System with Drift-compatible Connections

To determine the lateral load-displacement relation of the stair system, a pushover analysis is conducted. In the pushover analysis, after applying the boundary conditions as stated in Section 2.3, monotonic, slow application of displacement-controlled load is applied at the stair channel band in each of the X and Y directions. The target interstory drift ratio (IDR) for the stair system with two attachment channels is 4%. However, the target IDR for the stair system with a single attachment channel was set as 3.5% as convergence issues are observed at the large in-elastic response of the attachment channel. Figures 7 and 8 show the pushover analysis results of the stair systems with one and two attachment channels, respectively. Griffis [1993] states that the typical interstory drift ratio (IDR) corresponding to the serviceability limit state is 0.17% to 0.5%. Therefore, in this study, the initial stiffness of the stair system is calculated based on a secant line from IDR=0 to 0.5%. Both stair systems showed higher stiffness in the longitudinal direction (X-direction) compared to the lateral direction (Y-direction). It is worth noting that the stair system with two attachment channels performed well and sustained no material yielding. This high-fidelity FEM captures the interaction between each component and the friction response between each surface in contact. Therefore, the nonlinearity in the pushover curve is due to the interaction between stair components (Figure 8). However, during pushover analysis of the stair system with a single attachment channel in the X-direction, the upper flight of the stair system freely slides until an IDR of 1.25% (See Figure 7). Beyond IDR=1.2% the torsion of the attachment channel about the Y axis was observed.

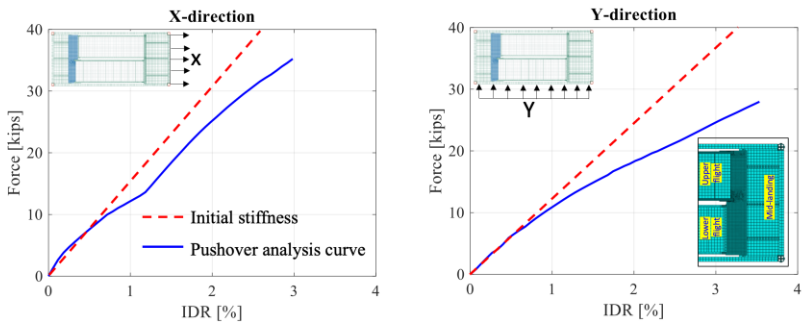

Figure 7. Pushover analysis results of stair system with single attachment channel

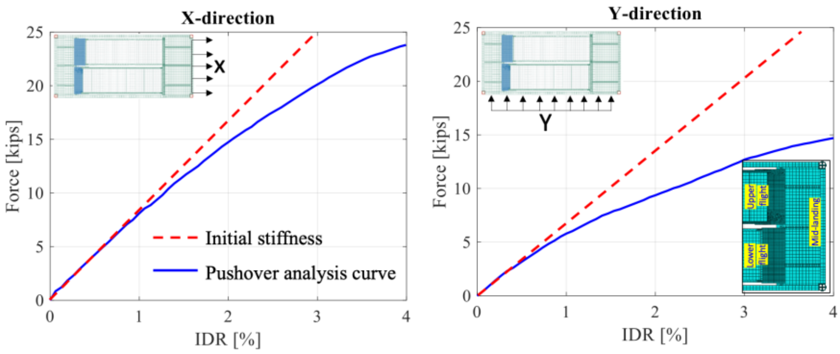

Figure 8. Pushover analysis results of stair system with two attachment channels

3.2.2 Modal Properties of the 10-story Stair Tower

Eigenvalue analysis of the lumped mass model is conducted to determine the global mode shapes and corresponding natural vibration periods of the 10-story stair tower. The developed finite element model of the stair systems represents the modular stair systems on the 2nd, 3rd, and 4th stories of the NHERI Tallwood building as shown in Figure 1. The stairs on the 1st, 9th, and 10th stories have the same connection details. However, the first story is 2 ft taller than all other stories, and the stairs on the 9th and 10th stories represent traditional construction. Therefore, the initial stiffness of the 1st, 9th and 10th stories, which are based on the 2nd and 4th stories, are adjusted to consider the change in the configuration of the stair systems. These adjustments are based on the stiffness of stair columns with fixed boundary conditions at the bottom and top connections. The initial stiffness calculated based on the pushover analysis of the stair system with a single attachment channel is applied at the 5th -8th stories. Figure 9 summarizes the lumped mass model properties and associated eigenvalue analysis results of the 10-story stair tower.

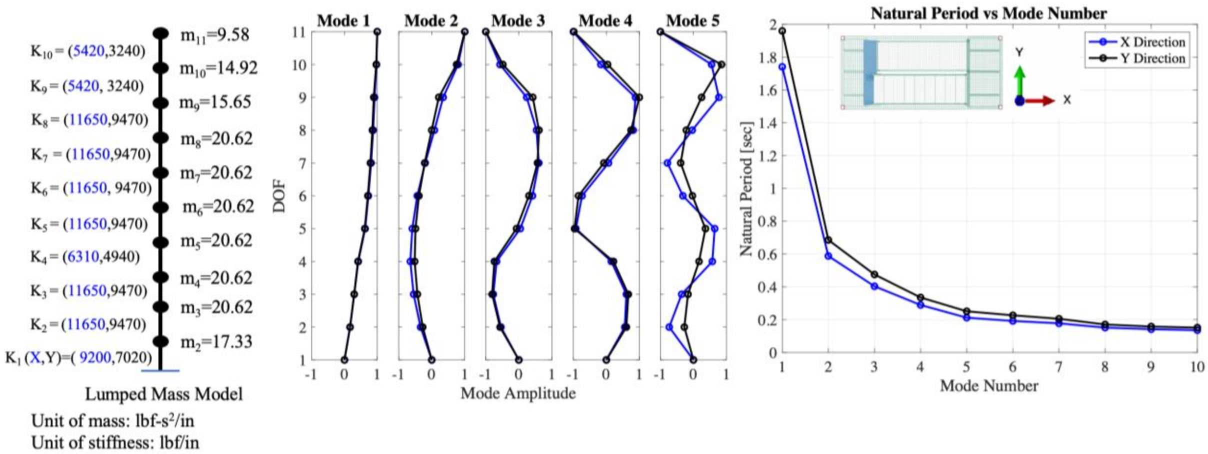

Figure 9. Global modal properties of the 10-story stair tower

The stair systems with slotted connections (stories 5 and 6) and those with fixed-free configurations (Stories 7 and 8) are stiffer than the stair system with drift-compatible connections. At this time the exact initial stiffnesses of these four stories are unknown. Figure 10 shows the natural periods corresponding to the first 10 modes and the first mode shape of the 10-story stair tower considering various stiffness values for these four stories. In this eigenvalue analysis, the stiffness of stories 5 through 8 is defined in terms of the percentage of the stiffness of the stair system at story 2. The figure illustrates that stiffness values beyond 100% do not have a significant effect on the modal properties, while stiffness values below 100% have a significant effect.

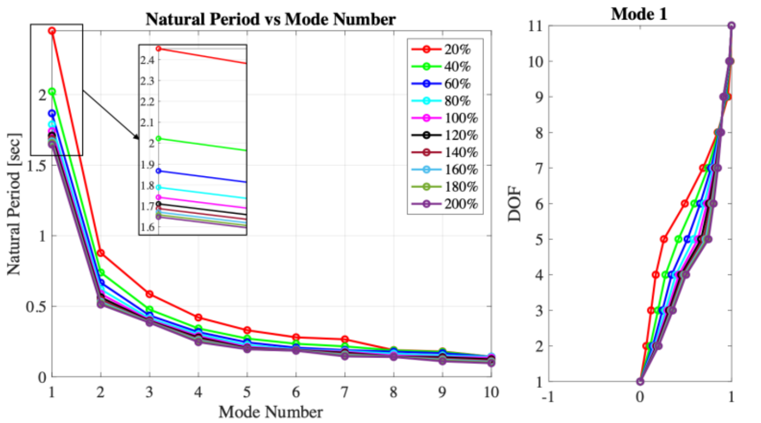

Figure 10. Global modal properties of 10-story stair tower with varying stiffness at story 5 to 8

3.2.3 Relation Between Modal Properties of the Building and the Stair Tower

The modal properties of the stair tower can be compared to the modal properties of the building acquired from the 3D non-linear OpenSees numerical model presented in Wichman *et al.* [2022a-b]. This model was initially developed and utilized to conduct non-linear response history analyses for the design of the lateral force resisting system of the test building. As a result, the model is a simplified representation of the building, including only the four post-tensioned structural walls, absent the stairs, and other non-structural building components. Figure 11 summarizes the natural periods of the building and the stair tower. The first, second, and third mode periods are shown for each of the two orthogonal directions in the building as well as the torsional response. As seen from this figure, the natural periods corresponding to the first mode of the stair tower in both the x- and y-directions are close to that of the building. Thus, it is anticipated that the stair tower will oscillate nominally with the building when this vibrational period is excited. However, the second and third modes of the stair tower are much larger than those of the building. Thus, it can be anticipated that at higher modes the two systems will be out of phase. It should be mentioned that the proposed lumped mass model of the stair tower does not capture the torsional modes of the stair tower, however, it is notable that none of the stair tower predicted translational modes are close to the first torsional mode of the building (~1.1sec), implying minimal interaction when the building is excited at this mode.

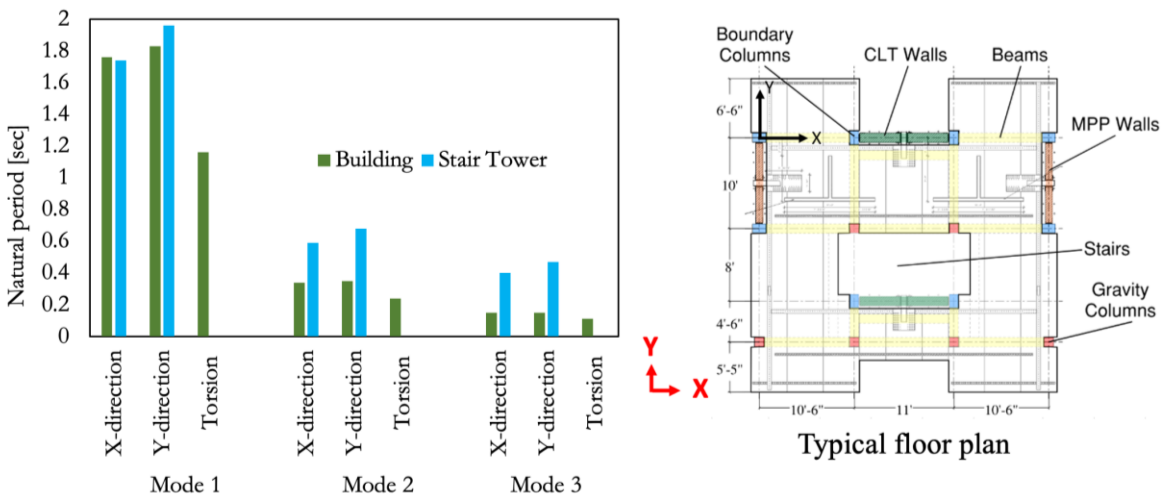

Figure 11. Natural periods of the building and the stair tower (Left), and a typical floor plan (Right (Wichman *et al.* 2022b))

At the time of writing this paper, the NHERI Tallwood 10-story mass timber building is under construction. Currently, the floor panels at level 6 are being constructed. According to the current state of knowledge, the shake table testing of this building will happen in January 2023.

4. CONCLUSIONS

This paper describes a high-fidelity finite element model of a modular stair system with drift-compatible connections to be tested as part of the NHERI Tallwood 10-story mass timber building. The modelling approach is based on a methodology previously proposed and validated through comparison with experimental data [Sorosh et al., 2022]. Of particular interest herein, are the dynamic characteristics of the modular stairs, considering drift compatible details, with two different attachment strategies. Using modal analysis and nonlinear static pushover analysis, it was shown that stair systems with two attachment channels at the flight to mid-landing connections are more flexible than those detailed with a single attachment channel. In addition, in the case of a stair system with two attachment channels, during pushover analysis with a target IDR of 4%, no damage to the stair components was observed. However, the bending of an aluminum plate and yielding of the associated attachment channel is expected on the stairs with a single attachment channel.

In stair systems, the local modes account for the vibration of stair components within each stair unit. The design and performance of stair components and connections depend on the local modes. However, the design and performance of connections between the stair system and the floor diaphragm and the interaction between the stair systems and the supporting building strongly depend on the global modes of the stairs. Therefore, in this study, a simplified lumped mass model of the 10-story stair tower was developed using data from the nonlinear static pushover analysis and the geometry of the stair system.

The NHERI Tallwood 10-story mass timber building is currently under construction. Parallel to the construction phase, each stair system is being tested under man-loaded walking excitation, wind excitation, and low amplitude impact loading. Analysis of these system identification tests is ongoing and may be available for comparison to the high-fidelity FEM discussed herein at the time of the workshop.

ACKNOWLEDGMENTS

The nonstructural component scope of this project is sponsored by NSF Grant No. CMMI-1635363, USFS Grant No. 19-DG-11046000-16, Softwood Lumber Board, Computers and Structures Inc, a first-year UC San Diego graduate student fellowship (first author), and a variety of industry sponsors. The use and operation of the NHERI shake table facility are supported by NSF through Grant No.1520904. Materials and in-kind support for the stair system are provided by Construction Specialties. The authors appreciate the aforementioned support. The opinions and findings of this study are of the authors and do not necessarily reflect those of the sponsors.

REFERENCES

Abaqus [2020] Abaqus documentation, Software Manual, Dassault Systems.

ASCE-16 [2017] *Minimum Design Loads and Associated Criteria for Buildings and Other Structures*, Standard ASCE/SEI 7-16, Structural Engineering Institute of American Society of Civil Engineers, Reston, V A. USA.

Black, C., Aiken, A., Smith, K., Belvin, R., Peachey, A. [2017] "Seismically-Resilient Stair Systems for Buildings." *Proceeding of Structural Engineers Association of California Annual Convention (SEAOC 2017)*, San Diego, CA.

Black, C., Aiken, I., Smith, K., Belvin, R., and Peachey, A. [2020] "Shake table testing of seismically resilient stair systems for buildings" *Proceeding of 17th world conference on earthquake engineering,* Sendai, Japan.

Bull, DK. [2011] *Stair and access ramps between floors in multi-storey building*. A report at the Canterbury Earthquake Royal Commission, Christchurch, New Zealand.

Griffis L.G. [1993] "Serviceability limit states under wind load." *AISC Engineering Journal*, 1st Qtr:1–16.

Higgins, C. [2009] "Prefabricated steel stair performance under combined seismic and gravity loads." *ASCE Journal of Structural Engineering*, Vol. 135 No. 2, pp. 122-129.

Hutchinson, T.C., Restrepo, J.I., Conte, J., Meacham, B. [2013] "Overview of the building nonstructural component and systems (BNCS) project." *Proceeding of ASCE 2013 Structures Congress, Pittsburg*, PA, 1485-1498.

Li, B., Mosalam, K.M. [2013] "Seismic performance of reinforced concrete stairways during the 2008 Wenchuan earthquake." *ASCE Journal of Performance of Constructed Facilities*, Vol. 27 No. 6, pp. 721-730.

Pantoli E., Wang X., Chen M., Hutchinson T.C., Meacham B., Park H.J. [2013] "Shake table testing of a full-scale five story building: performance of the major nonstructural components-egress and façades." *Proceeding of ASCE 2013 Structures Congress*, Pittsburg, PA.

Pei S., van de Lindt J.W., Barbosa A.R., Berman J.W., McDonnell E., Dolan J.D., Blomgre H.E., Zimmerman R.B., Huang D., Wichman S. [2019] "Experimental seismic response of a resilient 2-story mass-timber building with post-tensioned rocking walls" *ASCE Journal of Structural Engineering,* Vol. 145 No. 11 :04019120

Ramberg, W., Osgood, W. R. [1943] *Description of stress–strain curves by three parameters*. Technical Note No. 902, National Advisory Committee for Aeronautics, Washington DC

Sorosh S., Hutchinson T.C., Ryan K.L. [2022] "NHERI TallWood 10-story Test Nonstructural, Part 4 of 4: Prefabricated Steel Stair Subassemblies" *Proceedings of the 12th National Conference in Earthquake Engineering*, Earthquake Engineering Research Institute, Salt Lake City, UT.

Sorosh S., Hutchinson T.C., Ryan K.L. Smith K., Belvin R., Black C. [2022] "High fidelity finite element simulations of the seismic response of steel stairs." *Earthquake Engineering and Structural Dynamics*, (in preparation).

Sun, E.Q., [2006] "Shear locking and hourglassing in MSC, Nastran, ABAQUS." *MSC Software Users Meeting.*

Wang, X., Astroza, R., Hutchinson, T.C., Conte, J.P., Restrepo, J.I. [2015] "Dynamic characteristics and seismic behavior of prefabricated steel stairs in a full-scale five-story building shake table test program." *Earthquake Engineering and Structural Dynamics*, Vol. 44 No. 14, pp. 2507-2527.

Wang, X., Ebrahimian, H., Astroza, R., Conte, J., Restrepo, J., Hutchinson, T.C. [2013] "Shake table testing of a full-scale five-story building: pre-test simulation of the test building and development of a nonstructural component and systems design criteria." *Proceeding of ASCE 2013 Structures Congress*, Pittsburg, PA.

Wichman, S., Berman, J. W., and Pei, S. [2022a] "Experimental investigation and numerical modelling rocking cross laminated timber walls on a flexible foundation," *Earthquake Engng Struct Dyn*, Vol 51, No. 7, pp. 1697-1717.

Wichman, S., Berman, J., Zimmerman, R., Pei, S. [2022b] "Lateral Design of a 10-Story Building Specimen with Mass Timber Rocking Walls," *Proceedings of 12th National Conference on Earthquake Engineering*, Salt Lake City, Utah, USA.

Numerical Simulation to Predict the Seismic Behavior of Continuous Plasterboard Suspended Ceiling Systems

Venkatesh Patnana[1], Durgesh C. Rai[2]

[1] Doctoral Student, Dept. of Civil Engineering, IIT Kanpur
Kanpur, Uttar Pradesh, 208016, India
e-mail: vpatnana@iitk.ac.in

[2] Professor, Dept. of Civil Engineering, IIT Kanpur
Kanpur, Uttar Pradesh, 208016, India
e-mail: dcrai@iitk.ac.in

Abstract. Evaluating the performance of ceiling systems for every change made in the connections is not always feasible because of the expenses incurred in conducting the full-scale shake table testing. Conversely, the general dynamic behavior of a variety of ceilings for various random loadings can be efficiently traced from numerically verified critical experimental ceilings. In this paper, two continuous plasterboard ceiling systems, namely, (a) vertical strut suspended ceiling system with all edges fixed and (b) vertical strut and lateral brace suspended ceiling system with all edges free, were considered for the full-scale shake table testing and sub-assemblage testing of their critical components and connections. From the components and connections test data, nonlinear (multilinear) models were developed from the initial and post-yield behavior of backbone curves. These multilinear models were idealized to get linearized connection models (linear stiffnesses), namely, peak stiffness, average stiffness, and effective stiffness, that can be used to obtain comprehensibly rational responses from the linear structural analyses. Numerical models of floor acceleration simulator (test frame) and plasterboard ceiling systems were developed in SAP2000 to validate the experimentally evaluated responses at the ceiling and floor/roof of the test frame. Nonlinear and linear response history analyses were conducted on the corresponding numerical models, and the results are presented in the form of a comparison of experimental and numerical behavior: (1) peak ceiling and floor/roof accelerations for eleven increased intensities and (2) response spectra at the ceiling for different intensities of shake table generated motions. From the observed responses, it was noted that instead of evaluating the mechanical behavior of plasterboard ceilings for nonlinear models, linear analyses could be conducted to predict reasonably rational results.

Keywords: Continuous plasterboard suspended ceiling, Shake table, Nonlinear, Linearization, Numerical response.

1. INTRODUCTION

Suspended ceiling systems are one of the most vulnerable nonstructural features of modern buildings, and the two prominent ceilings are lay-in tile and continuous plasterboard systems. The expensive task of testing and verifying the performance of all the configurations of a particular topology of a ceiling can be avoided by numerically verifying the experimental response of critical ceilings through detailed modeling of connections and components. Modeling of suspended ceilings was initiated to estimate the natural frequencies of sway and non-sway fully floating lay-in tile ceiling systems [Yao, 2000]. Many advanced numerical ceiling models have been developed recently for dynamic performance verification [Paganotti, 2010; Soroushian *et al.*, 2014; Rahmanishamsi *et al.*, 2014; Pianigiani *et al.*, 2014; Ryu and Reinhorn, 2014, 2019]. These models produced invaluable knowledge on modeling and parameters that influence ceilings' performance. In addition, to fill the lack of experimentally validated numerical models, modeling methodologies have been established for future numerical studies on tile suspended ceiling systems, and expected that these models could substitute expensive shake table tests [Zaghi *et al.*, 2016]. Even though the performance evaluation of suspended ceilings is an active research area, no advanced nonlinear and linearized models are available for continuous plasterboard ceilings, which have different boundary conditions and lateral force-resisting mechanisms. The plasterboard ceilings differ from lay-in tile ceilings in connection and component layouts, and in addition, limited numerical models are available for the plasterboard ceiling systems; besides, the model had fixed boundaries and was suspended by hanger elements [Gilani *et al.*, 2015]. This study focuses on the modeling of the two experimentally evaluated continuous plasterboard ceiling systems that had fixed (fixed at all around the perimeter) and free (gap to accommodate displacement demands) boundaries with different lateral force-resisting mechanisms [Patnana and Rai, 2022]. These systems replaced the traditional hanger and splay wires by vertical struts (ceiling angles) and rigid braces (channel braces), respectively.

2. DEVELOPMENT OF NUMERICAL MODELS FOR CONTINUOUS PLASTERBOARD SUSPENDED CEILING SYSTEMS

Two continuous plasterboard ceiling systems (Figures 1a-b) that were considered for the full-scale shake table testing and sub-assemblage testing of components and connections are (a) vertical strut suspended ceiling system with all edges fixed (AFX_S) and (b) vertical strut and lateral brace suspended ceiling system with all edges free (AFR_{SB}). The critical components and connections and their location in the AFX_S and AFR_{SB} systems are shown in Figures 1d-h and 1j-q. In this paper, all the components and connections forming the ceiling grid were considered to behave elastically; however, all other connections, struts, and braces were assumed to behave inelastically. The identified critical connections are classified as (1) connections at perimeter, (2) connections to roof, and (3) connections to ceiling. The connections at perimeter include the (i) fixed connection to perimeter channel (Figure 1d), (ii) interaction at perimeter (Figure 1m), (iii) intermediate channel to wooden ledge connection (Figure 1f), and (iv) plasterboard to perimeter channel connection (Figure 1e). Connections to roof include the (i) strut to roof (Figures 1h and 1n) and (ii) brace to roof connection (Figures 1p-1q), and the connections to ceiling include the (i) brace to ceiling (1o) and (ii) strut to ceiling connection (Figures 1g and 1n-o). Owing to the similarities in the connections, one set of testing data was sufficient to approximately assess the behavior of other connections. The identified connections were tested by selecting a certain portion of the joint as a sub-assemblage to derive their nonlinear behavior. However, to test the struts and braces exclusively without failing the connection well before the member, the full length of the members along with the approximated boundary conditions were considered. The number of identical specimens' configurations was selected according to the specifications given in the ASTM E580/E580M-20 [ASTM, 2020]. Both the monotonic tension and/or compression and cyclic tests were conducted using a uniform ramp and increasing sinusoidal cyclic displacement loading protocols [Retamales *et al.*, 2011], respectively, at a rate of

12.7 mm/min (0.5 in./min). The complete details of the behavior of components and connections along with their idealizations (Figures 2 and 4), were presented in Patnana and Rai [2022]. The numerical modeling parameters derived for all the critical connections and components considering the pivot and isotropic hysteresis models are given in Table 1, and as an example, a comparison between numerical and experimental responses of strut to roof connection is shown in Figure 3. In addition, the linearized models of the connections are given in Table 2.

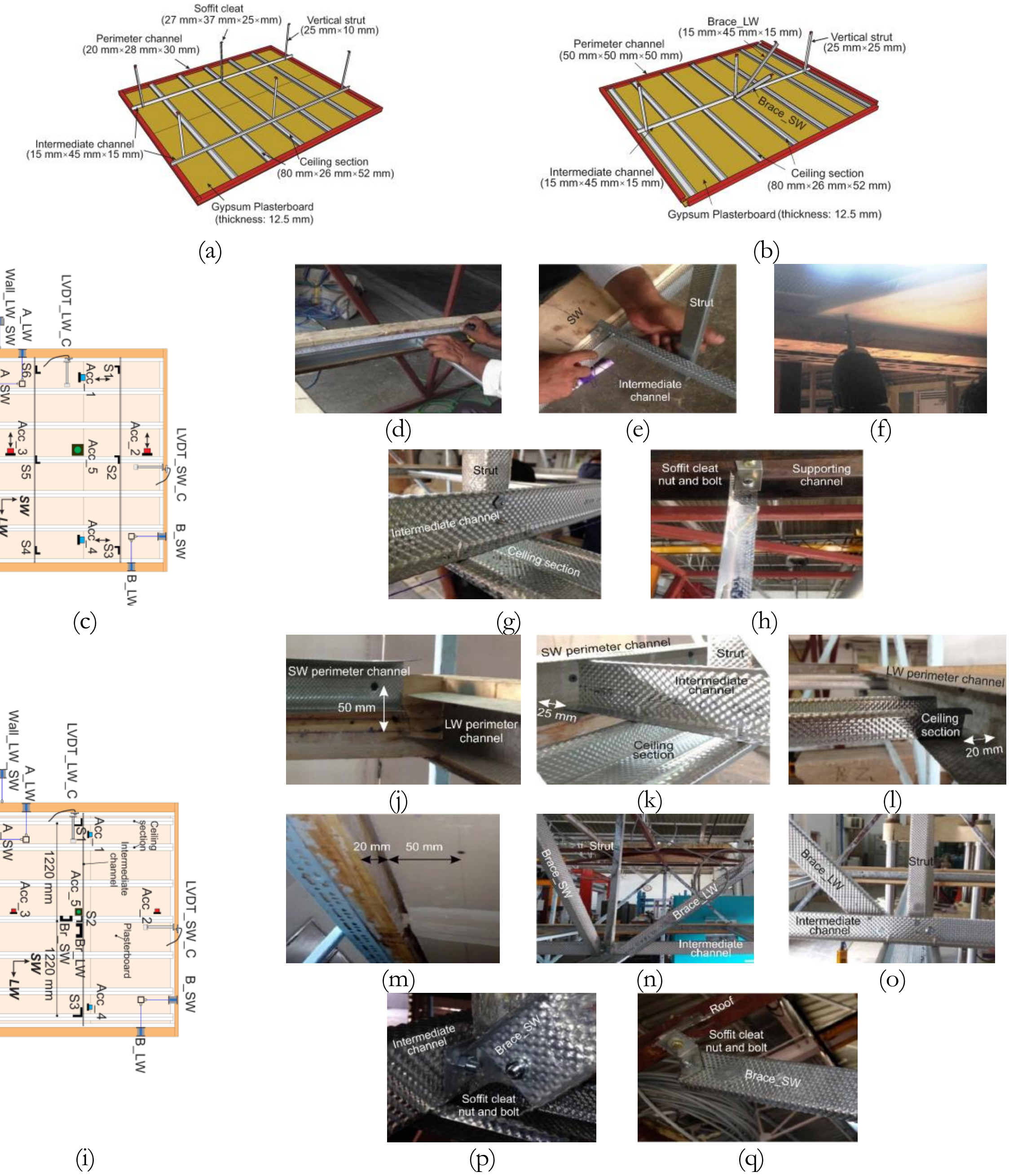

Figure 1. (a) Schematic of AFX$_S$ (b) Schematic of AFR$_{SB}$; AFX$_S$ (c) plan view (d) connecting ceiling sections to perimeter channel (e) intermediate channel connected to shortwall wooden ledge through soffit cleat and nut and bolt (f) plasterboard to perimeter channel attachment (g) intermediate channel to strut and ceiling section connection (h) strut to roof connection; AFR$_{SB}$ (i) plan view (j) level difference between longwall (LW) and shortwall (SW) perimeter channels (k) intermediate channel end resting on SW perimeter channel (l) positioning of ceiling sections and 20 mm gap with perimeter channel webs (m) drywall screw positioned at 50 mm from the LW plasterboard edge (n) braces and strut joint on the intermediate channel (o) LW brace to intermediate channel connection (p) soffit cleat connecting SW brace and intermediate channel (q) soffit cleat connecting LW or SW brace to the roof of the test frame (Patnana and Rai, 2022)

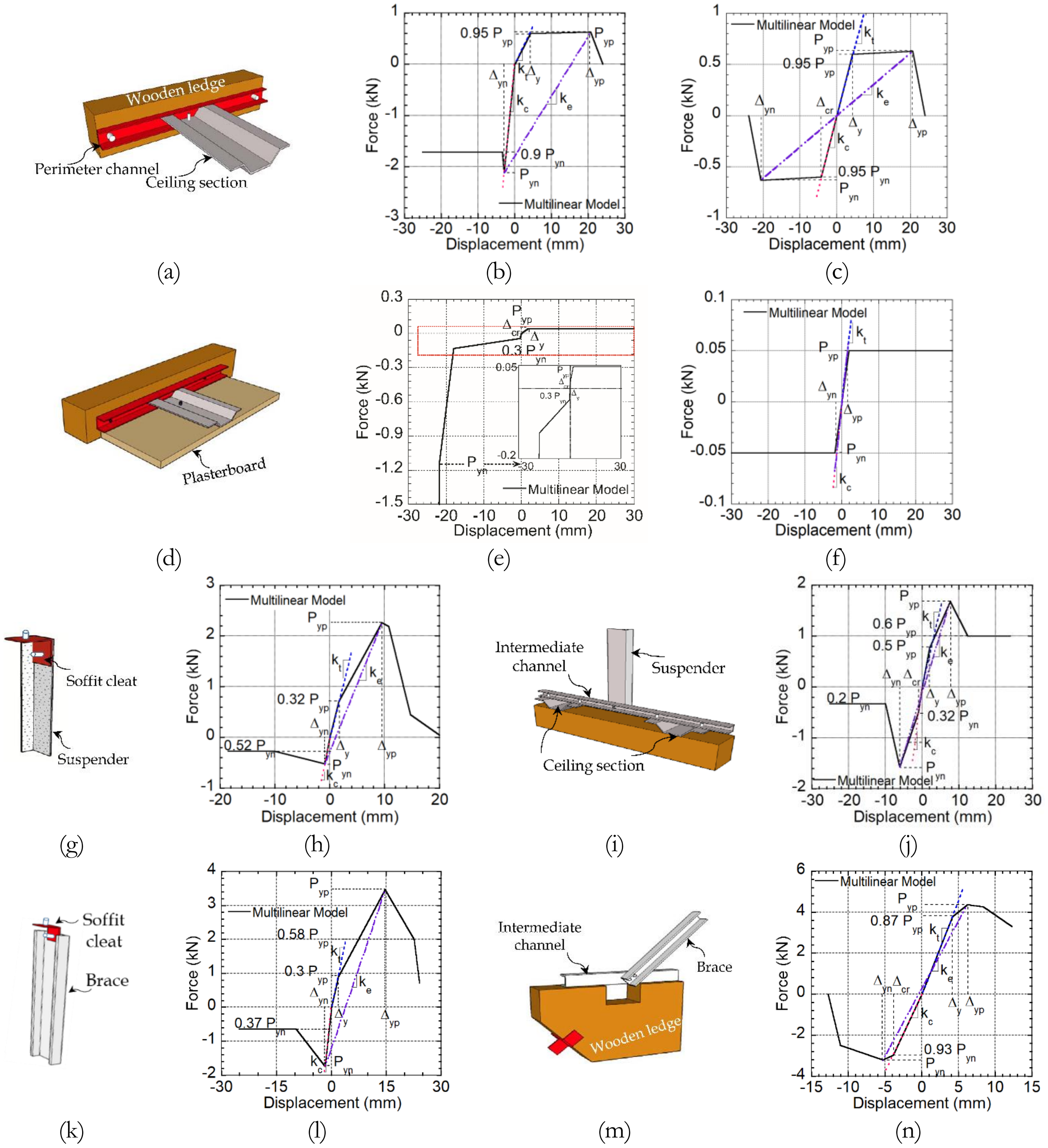

Figure 2. Schematic of connections and multilinear models for (a)-(c) fixed connections to perimeter channel (d)-(f) interaction at perimeter (g)-(h) strut to roof (i)-(j) strut to ceiling (k)-(l) brace to roof (m)-(n) brace to ceiling

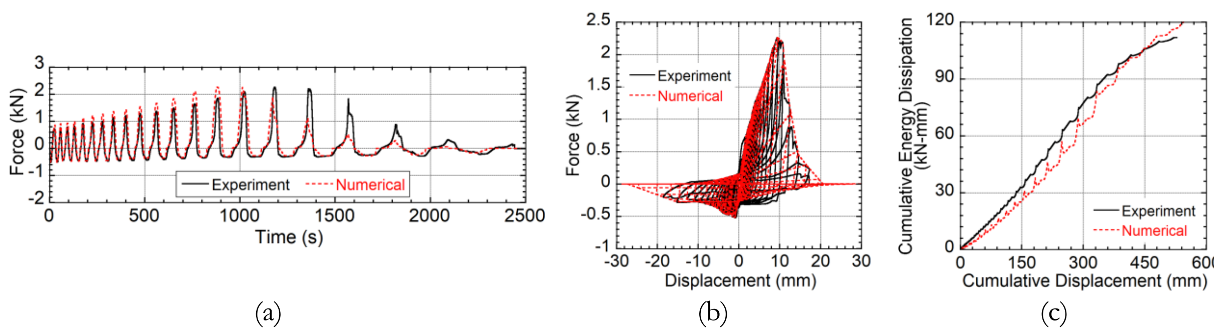

Figure 3. (a)-(c) Comparison of experimental and numerical responses of strut to roof connection

2.1 VERTICAL STRUT SUSPENDED CEILING SYSTEM WITH ALL EDGES FIXED (AFX_S)

In modeling the AFX_S system, connections between the test frame and wooden ledges were considered rigid to avoid relative motion, as shown in Figure 5. To model the fixed connections at the perimeter with properties mentioned in Figures 2b and 2c, a spacing of 10 mm was modeled to draw links between the ceiling sections and the wooden ledges, as shown in Figure 5b. As the fixed connection details are given in the form of links and assigned at the required zones, the perimeter channels were not modeled. In addition, the other degrees of freedom for these connections were restrained (U3 = R1 = R2 = R3 = 0). The connections joining the perimeter channels and the plasterboard (Figure 1c) were neglected due to their brittle behavior. However, these zones were assigned with restraining boundary conditions (U3 = R1 = R2 = R3 = 0) to replicate the restraining of the edges of the ceiling from uplift or vertical movement along the LW and SW, as shown in Figures 5b-c.

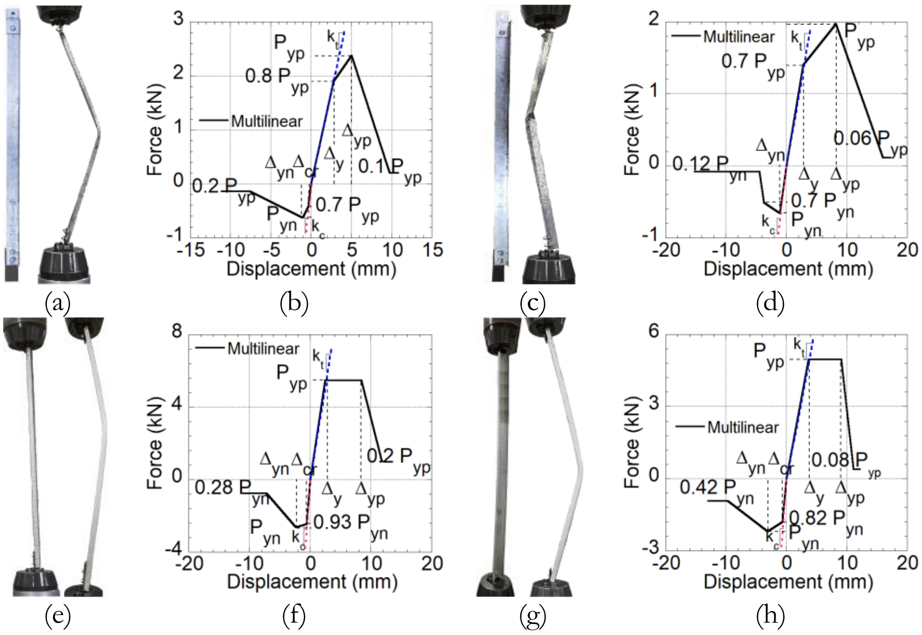

Figure 4. Test specimens and multilinear and linearized models of (a)-(b) struts in AFX_S (c)-(d) struts in AFR_{SB} (e)-(f) longwall brace in AFR_{SB} (g)-(h) shortwall brace in AFR_{SB}

Table 1. Pivot and isotropic hysteresis parameters for numerical models of components and connections

Component/Connection		Direction	α_1	α_2	β_1	β_2	γ
Strut in AFX_S Strut in AFR_{SB} Brace_LW Brace_SW		U1	1000	1000	0.00	0.143	0
Connections at perimeter	Fixed connection to perimeter channel	U1 U2	1000	1000	0.20	0.20	0
	Interaction at perimeter	U1 U2	Isotropic hysteresis model - No parameters are required				
	Intermediate channel to wooden ledge connection	U1 U2	1000	1000	0.46	1.00	0
Connections to roof	Strut to roof	U1	1000	1000	0.22	1.00	0
	Brace to roof	U1	1000	1000	0.46	1.00	0
Connections to ceiling	Brace to ceiling	U1	1000	1000	0.30	0.80	0
	Strut to ceiling	U1	1000	1000	0.34	1.00	0

Note1: direction along the length of the component: U1; perpendicular to the length of the component: U2

Note2: α_1 and α_2 define pivot points for unloading (degradation) to zero from positive and negative force; β_1 and β_2 define pivot points for reverse loading (pinching) from zero towards positive and negative force; γ controls degradation of elastic stiffness after plastic deformation [Dowell *et al.*, 1998; CSI 2019]

Table 2. Linearized models for critical connections

Connection		Direction	Peak stiffness, (k_t or k_c) (N/mm)	Average stiffness, $(k_t+k_c)/2$ (N/mm)	Effective stiffness (P_{yp}-P_{yn}/Δ_{yp}-Δ_{yn}) (N/mm)	Equivalent damping (%)
Connections at perimeter	Fixed connection to perimeter channel	U1	729	436	117	0.08
		U2	142	142	30.5	0.10
	Interaction at perimeter	U1	185	105	275	0.04
		U2	25.5	25.5	25.5	0.07
	Intermediate channel to wooden ledge connection	U1	1333	898	494	0.04
		U2	1333	898	494	0.04
Connections to roof	Strut to roof	U1	578	504	268	0.05
	Brace to roof	U1	1042	752	319	0.06
Connections to ceiling	Brace to ceiling	U1	907	837	658	0.13
	Strut to ceiling	U1	467	430	236	0.13

Along the SW direction, there were two intermediate channels, and their connections to SW wooden ledges were modeled as links along and perpendicular to the intermediate channel (Figure 5c) with the connection properties derived from the brace to roof connection similarity (Figure 2l). The connections between the struts and the intermediate channels and struts and roof channels were modeled (Figure 5d) using the properties mentioned in Figures 2h and 2j, respectively, along the length of the struts. These link ends were considered to have translational restraints (U2 = U3 = 0) because all the nonlinearity developed from the connection and eccentricity was condensed to have only a U1 degree of freedom, leaving the rotations unchecked to have pinned connections. In addition, nonlinear hinges were assigned at the center of the struts. The plasterboard of 12.5 mm thick (density: 668 kg/m^3; Young's modulus: 2.5 GPa) was modeled as a shell element and joined to the frame members (ceiling sections and intermediate channels) at their intersecting nodes so that there won't be any independent movement among these members. The complete numerical model of the AFX$_S$ ceiling system modeled in the test frame is shown in Figure 5e.

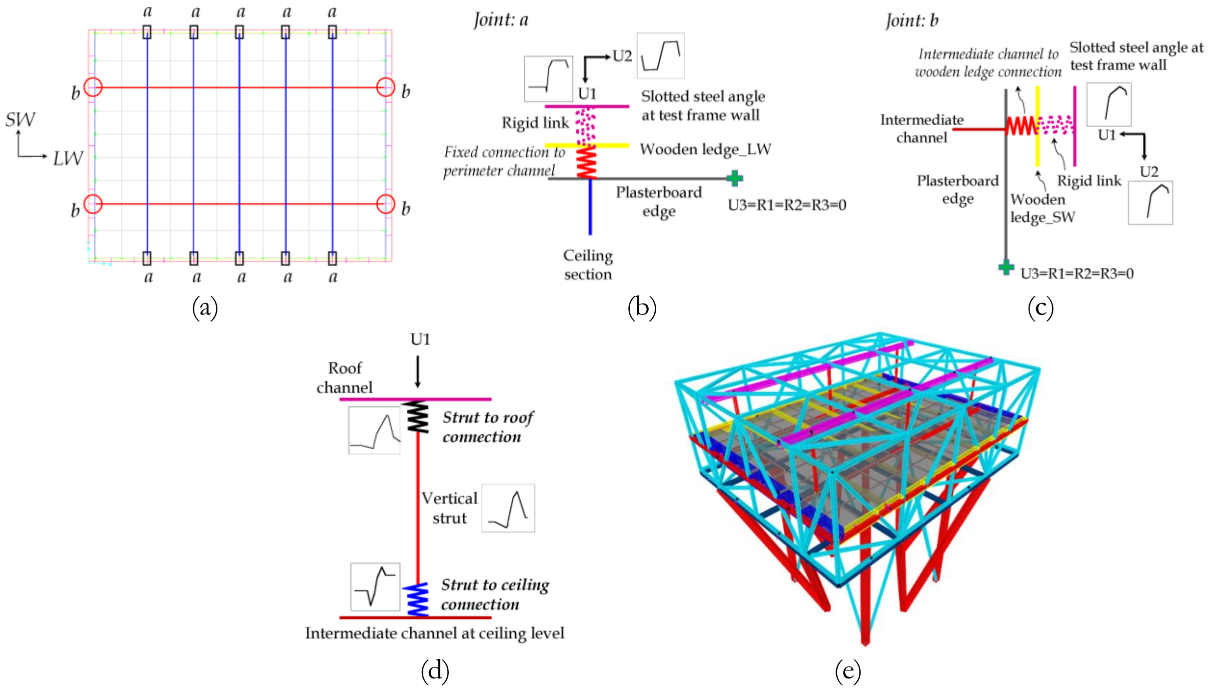

Figure 5. (a) Plan view of AFX$_S$ and critical connections at the perimeter; joint details of the (b) ceiling section to perimeter channel connection (c) intermediate channel to shortwall wooden ledge connection; (d) details of the strut to roof and ceiling connections (e) numerical model of AFX$_S$ system

2.2 VERTICAL STRUT AND LATERAL BRACE SUSPENDED CEILING SYSTEM WITH ALL EDGES FREE (AFR$_{SB}$)

Contrary to the AFX$_S$, the degrees of freedom for the interaction at perimeter connections were restrained (U3 = R1 = R2 = 0) to model the rotation of the plasterboard within its plane. Along the LW, the plasterboard boundaries were modeled with the restraining conditions (U3 = R1 = R2 = 0) to restrict their movement vertically and rotation about any horizontal axis (Figure 6b). However, along SW, there is neither interaction nor any connection between the perimeter channels and the plasterboard because of the level difference between the LW and SW perimeter channels, as shown in Figures 1j and k, so these joints can move in any direction (unrestrained 6-degrees of freedom). The intermediate channel at the center of the ceiling was supported over the bottom flanges of the SW perimeter channel, as shown in Figure 1k, and it can slide along and rotate about any axis; therefore, body constraints were assigned between the perimeter channel and ends of the intermediate channel (U3-direction), as shown in Figure 6c.

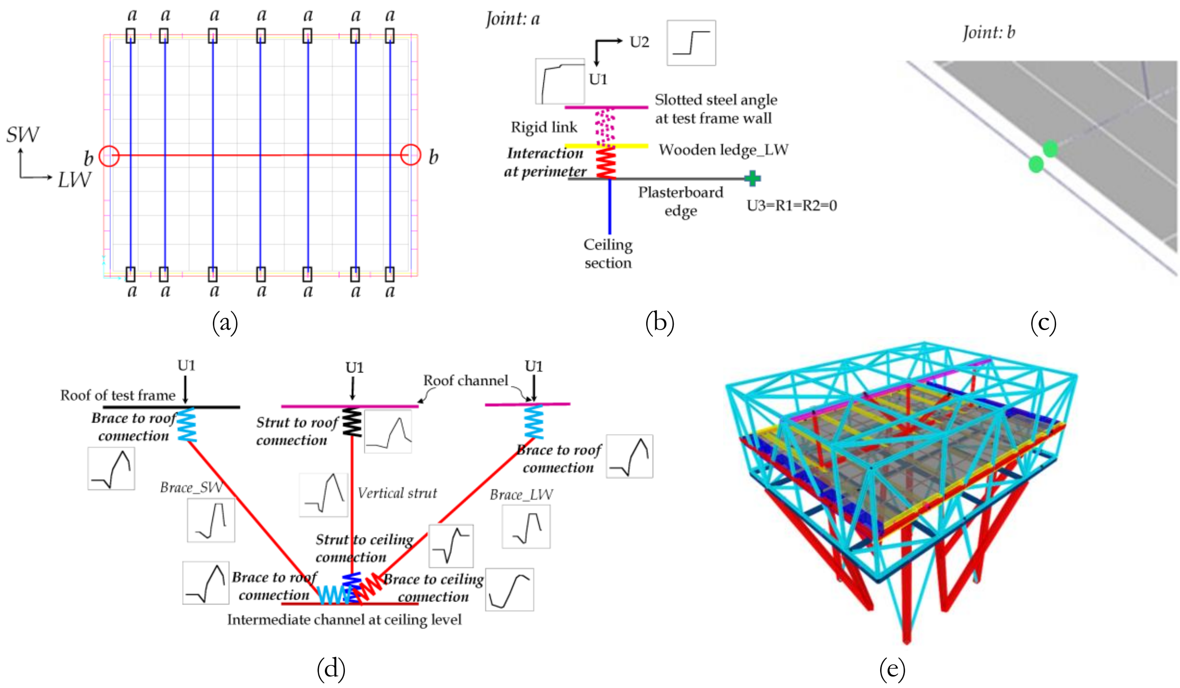

Figure 6. (a) Plan view of AFR$_{SB}$ and critical connections at the perimeter; joint details for the (b) ceiling section to perimeter channel interaction connection (c) roller supports at the end of the intermediate channel (d) braces and central strut and their connection to roof and ceiling (e) numerical model of AFR$_{SB}$ system

The brace to roof and ceiling connections were modeled as inline and inclined links (45^0 with the member), as shown in Figure 6d. The struts and their connections to the roof and the ceiling were the same as that of the AFX$_S$ system. As the struts and braces were assumed to resist the imposed vertical and horizontal forces at the ceiling along their axis, properties of all other translational degrees of freedom were restrained (U2 = U3 = 0) except the axial properties, leaving the rotations unchecked to have pinned connections. The complete numerical model of the AFR$_{SB}$ ceiling system along with the test model, which has been verified separately [Patnana and Rai, 2020], is shown in Figure 6e. In all the models and at eight supports of the test frame, springs with stiffnesses of 5787.6 kN/m were assigned to model the effect of oil column stiffness, as, i.e., $2\beta A/l$ [effective piston area (A) of actuator: 25.2 × 10^{-4} m^2; bulk modulus of hydraulic oil (β): 689 × 10^5 kN/m^2; half stroke length of the actuator (l) = 0.075 m]. The experimentally evaluated damping values at resonance frequencies (0.55% - 1.81%) were incorporated in all the models to derive the mass and stiffness proportional damping coefficients, which in turn prescribe the damping values at the other frequencies.

3. EXCITATION

IBC 2015 design spectrum comparable to Taft 1952 ground motion was considered for the full-scale shake tables tests (Figure 7), and this ground motion was scaled to derive eleven levels (L1 to L11) of intensities in terms of PGA, i.e., 0.05g, 0.1g, 0.15g, 0.2g, 0.25g, 0.3g, 0.35g, 0.4g, 0.5g, 0.6g, and 0.7g.

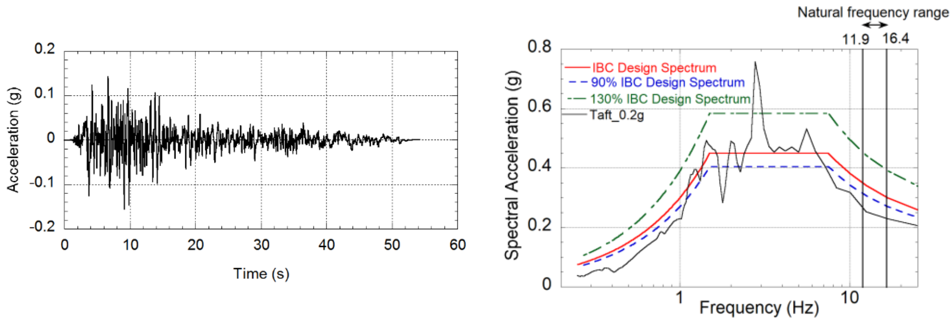

(a) (b)

Figure 7. (a) N21E component of the 1952 Kern County earthquake (Taft 1952) (b) comparison of IBC design spectrum with Taft 0.2g spectrum

Due to the interaction of the test frame with the shake table, the resultant modified motion at the shake table was considered as the shake table-generated motion. A total of 176 nonlinear and linear response history analyses were conducted on the respective numerical models of AFX_S and AFR_{SB}, and the roof and ceiling responses were noted.

4. RESULTS AND DISCUSSION

4.1 RESPONSE OF AFX_S SYSTEM

Peak acceleration responses at the center of the ceiling and roof of the test frame were obtained and compared with the experimental responses, as shown in Figures 8a-d, along the LW and SW directions for all the levels of intensities of shake table generated motion. It was observed that all the numerical responses of models were in good agreement with the experimental responses; however, there was a considerable deviation for certain loading, which was also expected because the numerical model may not completely mimic the experimental response. Similar to the experimental responses (Figures 8b and d), all the ceiling models predicted large roof accelerations, and the ceiling accelerations were smaller than the roof accelerations along the LW and SW for all the intensities of input motion, as shown in Figures 8a and c. In addition, there observed a negligible difference between the multilinear and all the linearized model responses because of the large capacity and stiffness of connections available at the perimeter edges (Figures 9e-j).

4.2 RESPONSE OF AFR_{SB} SYSTEM

Peak accelerations observed by the AFR_{SB} ceilings and roof of the test frame noted that the numerical responses were in good agreement with the experimental responses along the LW; however, for certain intensity levels, the numerical responses were smaller than the experimental responses, as shown in Figures 9. Also, for most of the loading levels, the nonlinear ceiling models produced large accelerations at the ceiling and roof than the linearized models. Even though the connections' stiffnesses varied significantly from the peak to effective stiffness, the linearized models produced approximately the same peak responses along the LW, similar to the responses observed along the LW and SW for the AFX_S. The acceleration responses of the AFR_{SB} ceiling models were smaller than the roof accelerations along the LW, similar to that of the experimental response. Along the SW, the peak roof accelerations predicted by both the nonlinear and linearized models were smaller compared to the experimental values of accelerations, as shown in Figures 9c and d. The flexibility of the weak connections and the reduction in stiffness of overall connections (nonlinear and average stiffness) around the perimeter and other locations led to large numerical accelerations at the ceiling level than the experimental ceiling accelerations, as shown in Figure 9c. However, the experimental ceiling accelerations at L10 (0.6g PGA) shown in Figure 9d suggested that ceiling accelerations are prone to be larger than roof accelerations. The comparison of the experimental and numerical responses and response spectra are shown in Figures 9e-j.

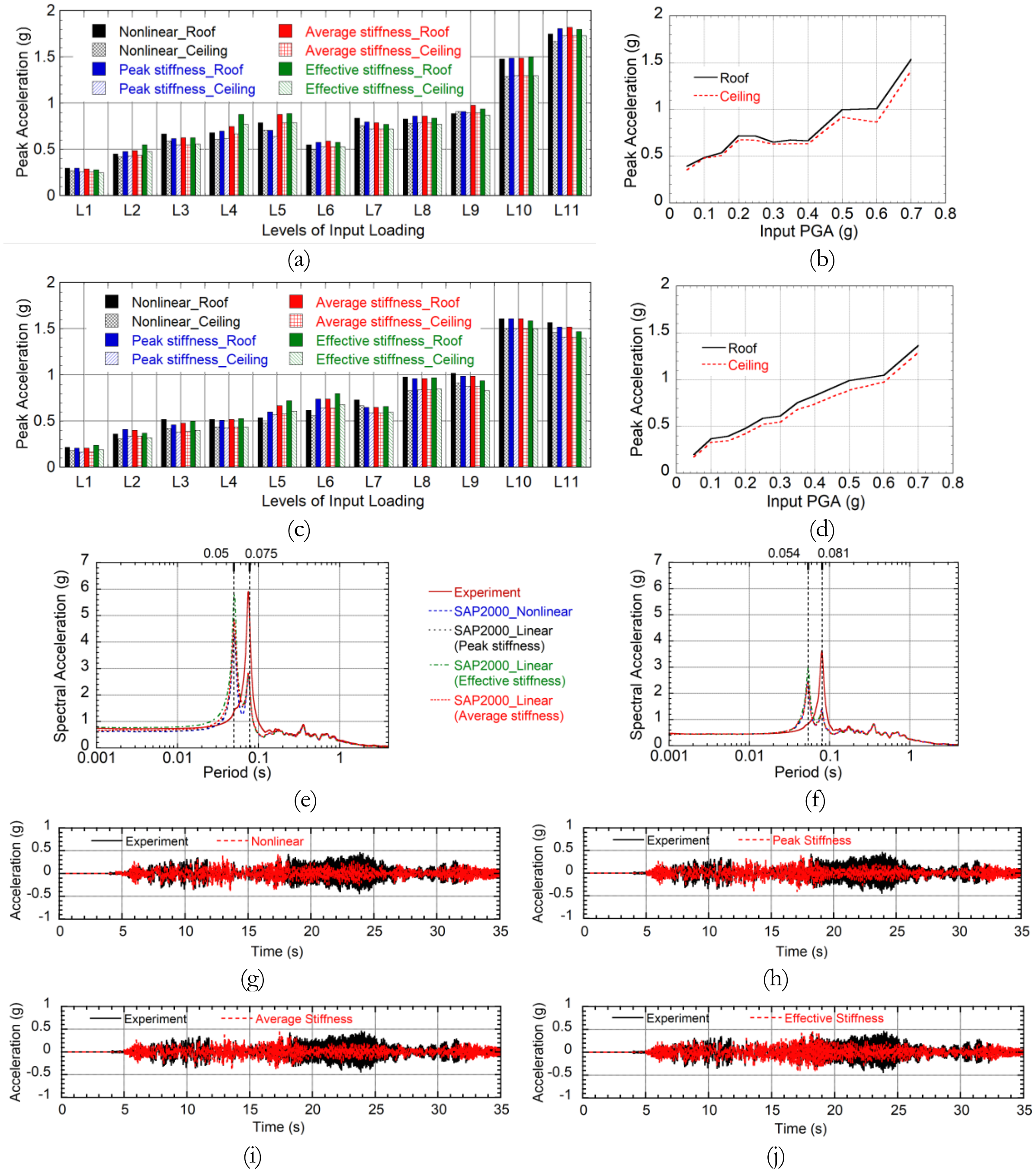

Figure 8. Comparison of peak roof and ceiling accelerations of experimental and numerical models along the (a)-(b) LW and (c)-(d) SW; Response spectra comparison for experimental and numerical responses for (e) L4_LW (f) L4_SW; (g)-(j) comparison for experimental and numerical responses for L4_SW for AFX$_S$ system

Models with effective stiffnesses experienced approximately the same response as that of the other models because of the inclusion of connections equivalent dampings. It was also noted that the deviation between the ceiling and roof accelerations of the effective stiffness ceiling model was smaller than that of the nonlinear, peak, and average stiffness models, and the difference was exceptionally large in the case of the nonlinear and average stiffness model. These results suggest that instead of evaluating the mechanical behavior of a vertical strut and lateral brace ceiling system developing for nonlinear analysis, linear analysis can be conducted on the linearized models to effectively predict reasonably rational results.

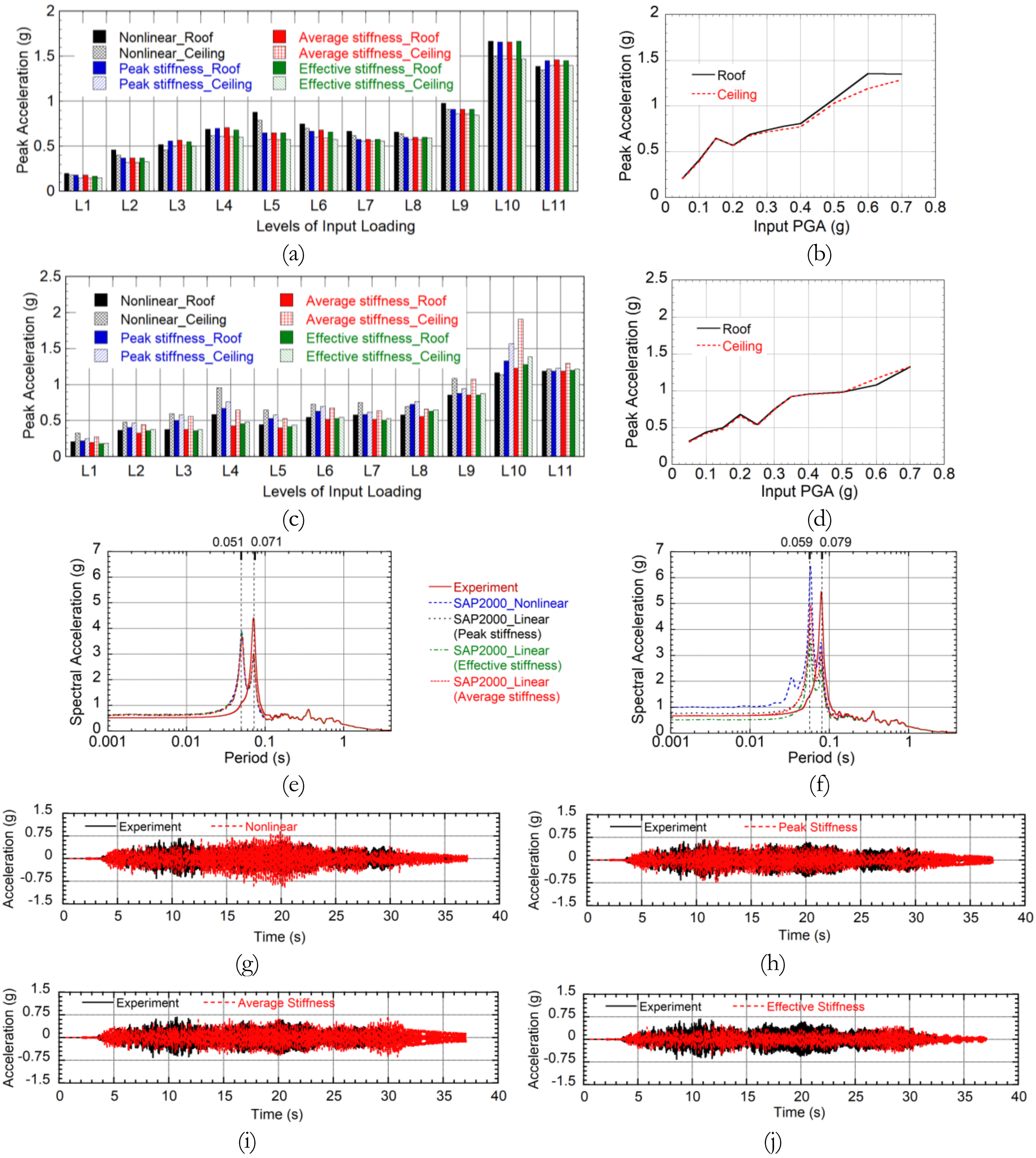

Figure 9. Comparison of peak roof and ceiling accelerations of experimental and numerical models along the (a)-(b) LW and (c)-(d) SW; Response spectra comparison for experimental and numerical responses for (e) L4_LW (f) L4_SW; (g)-(j) comparison for experimental and numerical responses for L4_SW for AFR$_{SB}$ system

5. CONCLUSIONS

For all the AFX_S models, similar to the experimental responses, ceiling accelerations were smaller than the roof accelerations along the longwall and shortwall because of the influence of the perimeter connections over the roof connections. As the system was rigidly fixed all around the perimeter, there observed no or negligible deviation among the nonlinear and linearized ceiling responses. However, for the AFR_{SB} models, in the shortwall direction, the ceiling accelerations are larger than the roof accelerations because of the flexibility of the perimeter connections over the roof connections. But along the longwall, similar to experimental responses, for certain intensities, the roof and ceiling observed approximately the same acceleration, while for the other loading, the ceiling accelerations were smaller than the roof accelerations. Numerical models of the ceiling with linearized behavior of connections can predict the dynamic responses due to ground motions reasonably well.

6. ACKNOWLEDGMENTS

The authors sincerely acknowledge the Saint-Gobain Research India (SGRI) Pvt. Ltd. for providing ceiling system components and current knowledge on suspended ceiling systems. Any opinions, findings, and conclusions or recommendations expressed in this material are those of the authors and do not necessarily reflect the views of Saint-Gobain Research India.

7. REFERENCES

ASTM E580/E580M [2020] *Standard Practice for Installation of Ceiling Suspension Systems for Acoustical Tile and Lay-In Panels in Areas Subject to Earthquake Ground Motions*, American Society for Testing and Materials, USA.

CSI [2019] *SAP2000 Integrated Software for Structural Analysis and Design* (version 20), Computers Structures Inc., USA.

Dowell, O.K., Frieder, S., Edward, L.W. [1998] "Pivot hysteresis model for reinforced concrete members," *ACI structural journal*, Vol. 95, No. 5, pp. 607-617.

Gilani, A.S., Takhirov, S.M., Straight, Y. [2015] "Seismic evaluation of drywall suspended ceilings using shake table testing and the finite element analysis." *Proceedings of Improving the Seismic Performance of Existing Buildings and Other Structures,* San Francisco, California.

Paganotti, G. [2010] "Behaviour of suspended ceiling system during seismic events: Development of fragility," *MS Thesis*, Politecnico Di Milano, Milano, Italy.

Patnana, V., Rai, D.C. [2020] "Seismic performance of plasterboard suspended ceilings under shaking-table generated motions, " *Proceedings of 17th World Conference on Earthquake Engineering*, Sendai, Japan.

Patnana, V., Rai, D.C. [2022] "Experimental testing on nonstructural continuous plasterboard suspended ceiling systems under shake table-generated motions," *Earthquake Spectra*, pp. 87552930221085298.

Patnana, V., Rai, D.C. [2022] "Sub-assemblage testing on critical connections of continuous plasterboard suspended ceiling systems," *Proceedings of 12th US National Conference on Earthquake Engineering*, Salt Lake City, Utah.

Pianigiani, M., Pourali, B.A., Dhakal, R.P. [2014] "Seismic evaluation of suspended ceilings in a hospital building: A case study." *Proceedings of New Zealand Society for Earthquake Engineering (NZSEE) Conference,* Auckland, New Zealand.

Rahmanishamsi, E., Soroushian, S., Maragakis, M. [2014] "System-level experiments on ceiling/piping/partition systems at UNR-NEES site." *Proceedings of 10th US National Conference on Earthquake Eng*ineering, Anchorage, Alaska.

Retamales, R., Mosqueda, G., Filiatrault, A., Reinhorn, A. [2011] "Testing protocol for experimental seismic qualification of distributed nonstructural systems," *Earthquake Spectra,* Vol. 27, No. 3, pp. 835-856.

Ryu, K.P., Reinhorn, A.M. [2014] "Simplified analytical modelling of a suspended ceiling system," *Proceedings of 10th US National Conference on Earthquake Engineering,* Anchorage, Alaska.

Ryu, K.P., Reinhorn, A.M. [2019] "Analytical Study of Large-Area Suspended Ceilings," *Journal of Earthquake Engineering,* Vol. 23, No. 4, pp. 592-624.

Soroushian, S., Maragakis, M., Jenkins, C., Zaghi, A.E., Echevarria, A. [2014] "Analytical simulation of the performance of ceiling-sprinkler systems in shake table tests performed on a full-scale 5-story building," *Proceedings of Structures Congress*, Boston, MA.

Yao, G.C. [2000] "Seismic performance of direct hung suspended ceiling systems," *Journal of Architectural Engineering,* Vol. 6, No. 1, pp. 6–11.

Zaghi, A.E., Soroushian, S., Echevarria, H.A., Maragakis, M., Bagtzoglou, A. [2016] "Development and Validation of a Numerical Model for Suspended-Ceiling Systems with Acoustic Tiles," *Journal of Architectural Engineering,* Vol. 22, No. 3, pp. 1-13.

Experimental Study to Validate an Improved Approach to Design Acceleration-Sensitive Nonstructural Components

Ahmed Elkady[1], Dimitrios Vamvatsikos[2], Dimitrios Lignos[3], Athanasia K. Kazantzi[2] and Eduardo Miranda[4]

[1] University of Southampton, Southampton SO16 7QF, United Kingdom
a.elkady@soton.ac.uk

[2] National Technical University of Athens, Athens, Greece
divamva@mail.ntua.gr, kazantzi@mail.ntua.gr

[3] École Polytechnique Fédérale de Lausanne, Lausanne CH-1015, Switzerland
d.lignos@epfl.ch

[4] Stanford University, Stanford, CA 94305, USA
emiranda@stanford.edu

Abstract. Nonstructural components in buildings can be subjected to very large acceleration and deformation demands during earthquakes. This is particularly true for flexible components that are tuned or nearly tuned to one of the modal frequencies of the supporting structure. To control the seismic demands in these situations, the authors have proposed a new design approach in which the connections between the structure and the nonstructural element are designed and detailed to experience nonlinearities to limit force and deformation demands. This paper summarizes an experimental campaign sponsored by the Seismology and Earthquake Engineering Research Infrastructure Alliance for Europe (SERA) aimed at validating the proposed design approach. The research project involved subjecting 14 different specimens representing nonstructural elements, with masses ranging from approximately 200 kg to 800 kg, to severe floor motions recorded during the 1989 Loma Prieta and the 1994 Northridge earthquakes in three instrumented buildings in California. A total of 45 individual tests were carried out. The tests were conducted at the EQUALS laboratory shake table at the University of Bristol. Mass and stiffness were carefully selected in each specimen to have vibration periods that resulted in both non-tuned and tuned components to modal frequencies of the supporting structure. Furthermore, some of the tuned tests involved components tuned to the fundamental mode while others were tuned to the second mode of vibration of the supporting structure to examine possible differences. Lateral strength and primary energy dissipation were provided by two steel plates with rotations restrained at both ends and loaded out-of-plane. The tests demonstrated how the proposed approach greatly reduces force and acceleration demands while also reducing lateral displacement demands. Furthermore, tests also demonstrated that the proposed approach reduces the response sensitivity to the period ratio of the nonstructural element to that of the supporting structure leading to a reduction in seismic demands uncertainty.

Keywords: Nonstructural components, Shake table tests, New design approach, Recorded narrowband motions, Nonlinearity.

1. INTRODUCTION

Recent seismic events have highlighted the damage vulnerability of nonstructural components. This has been observed even in seismic events with low or moderate intensities; that occur far more frequently than design-basis ones. Thus, community-critical buildings, such as hospitals, telecommunication facilities or fire stations, often face lengthy functionality disruptions despite having suffered little or no structural damage during an earthquake. Notable examples of the aforementioned seismic performance are the Sylmar County Hospital in the aftermath of the 1994 Northridge earthquake [Naeim 2004] and the Santiago and Concepcion airports during the 2010 Maule earthquake in Chile, which sustained very little structural damage but massive nonstructural damage [Fierro et al. 2011; Miranda et al. 2012]. Similar observations have been made after recent earthquakes in New Zealand [Dhakal 2010; Ferner et al. 2014]

To this end, the engineering community in countries with modern seismic codes has shifted its attention to the development of robust methodologies for the evaluation of acceleration demands, that are imposed on nonstructural components, during an earthquake. An accurate absolute acceleration demand assessment could lead to an effective design strategy of nonstructural components. Recently, Kazantzi et al. [2020b] conducted a numerical study that evaluated the elastic/inelastic floor acceleration spectra for single-degree of-freedom (SDF) secondary systems with linear/bilinear non-degrading hysteretic behavior. The study identified important characteristics of floor spectra of actual recorded motions as related to nonstructural components performance:

i. The building amplifies and filters ground motions leading to floor motions characterized by narrowband spectra. Therefore, acceleration demands imposed to nonstructural components can be strongly amplified if the component's fundamental period (T_p) is close to the building's fundamental, or higher mode, period (T_{bldg}); i.e. $\tau_m = T_p / T_{bldg} = 1$. This amplification, which is quantified as the ratio of the peak component acceleration (PCA) to the peak floor acceleration (PFA), can approach on average values close to eight and close to five for such tuned components with damping ratios of 2% and 5%, respectively.

ii. Allowing for some inelasticity to occur, either in the support or the bracing of the nonstructural component installed above ground on buildings, can substantially reduce acceleration demands with reductions much larger than those that occur from ground motions recorded on rock or firm soils which are characterized by wideband spectra; a conclusion that was initially introduced by Miranda et al. [2018]. This suggests that the well-known strategy of allowing nonlinearities to take place in structures during moderate and strong earthquakes can be even more effective in reducing force and deformation demands when used for nonstructural components if the nonlinearity occurs between the structure and the nonstructural element.

iii. Benefits of using an inelastic support system to protect nonstructural components from damage was later carefully quantified in Kazantzi et al. [2020a]; Kazantzi et al. [2020b] who conducted statistical studies of strength reduction factors and inelastic floor spectral ordinates by using motions recorded in instrumented buildings in California. They showed that allowing nonlinearity to occur in the component's support system results in acceleration demands that are much less sensitive to changes in the period of the component relative to the modal periods of the supporting structure (τ_m ratio), since even small level of nonlinearity lead to inelastic floor spectra that are substantially flatter compared to their elastic counterparts.

As part of a project sponsored by the Seismology and Earthquake Engineering Research Infrastructure Alliance for Europe (SERA), an experimental testing program was undertaken to confirm the aforementioned numerical observations. The experimental testing program involved dynamic tests conducted at the shake table facility of the University of Bristol. The main short and long term objectives of the testing program were: (a) to demonstrate the -undesirable- potential for large amplified acceleration demands for components tuned to periods of modes of vibration strongly contributing to the seismic response of the supporting structure; (b) to demonstrate the conceptual validity of using nonlinear ductile steel fuses for decoupling and significantly reducing these acceleration demands; and (c) to show that the proposed approach leads to a reliable and inexpensive solution for the protection of acceleration sensitive nonstructural elements.

2. DESCRIPTION OF THE EXPERIMENTAL PROGRAM

2.1 DESCRIPTION OF THE TEST SETUP

The experimental testing program was conducted on the shake table within the Earthquake and Large Structures (EQUALS) laboratory at the University of Bristol. The shaking table at the EQUALS LABORATORY has a 3m by 3m platform supported by eight hydraulic actuators. The table can carry up to 15 tonnes and depending on the loading can reach acceleration levels up to about 5g with peak displacements of ±150mm, making it ideal for testing specimens to destruction.

Fig. 1 shows an overview of the test setup and its components. The setup mainly comprises of a mass carrying rigid steel carriage that is resting on two cylindrical rollers; meant to represent the lateral movement of a non-structural component. The rollers rests on two track rails that are securely bolted to the shake table adapter plate. Four L-shaped guide sliders, installed on the carriage, are set in close contact with the grooves of the track rails to enforce unidirectional movement of the carriage and to block out-of-plane displacement and potential uplift during shaking.

The carriage is connected to the top end of two fuse plates (i.e., the deformable yielding element between the mass of the nonstructural element and the supporting structure) using a rigid assembly with double 20mm pins and shrink-fitted ball joints. Fig. 2b shows the typical geometry of the deformable fuse plates. The fuse plate comprises of three regions forming a dog-bone shape. The bottom region is clamped using pre-tensioned high-strength M16 bolts to a rigid block that is securely fastened to the shake table (i.e., fixed end). Similarly, the top zone is also clamped to the rigid pin assembly (i.e., free end). The middle zone is the deformable zone, which has a varying height, width and thickness, i.e., *h*, *b* and *t*, respectively in order to adjust the strength and stiffness of the lateral bracing of the carriage simulating the nonstructural component. Essentially, the carriage and fuse plates represent a single-degree-of-freedom (SDF) system ... nstrated in Fig. 2a based on the deformed configuration during a test.

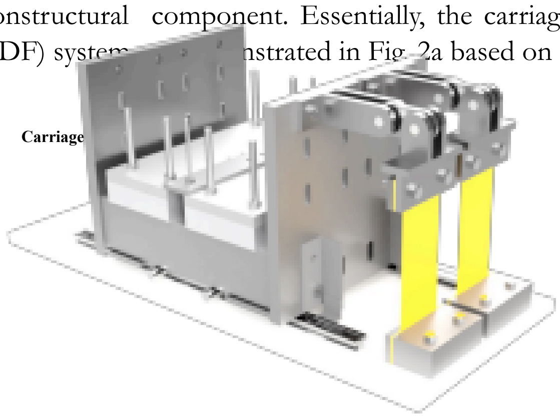

Fig. 1 Test setup overview

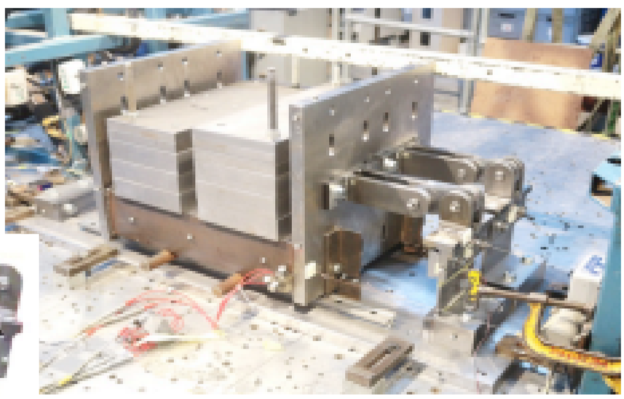

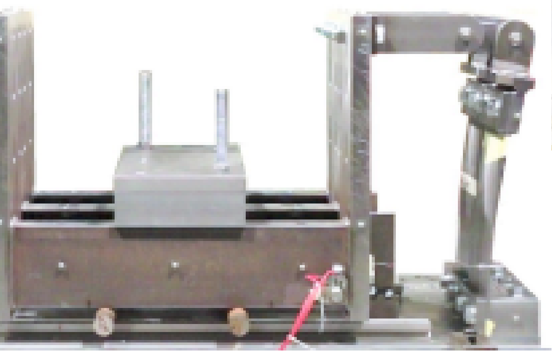

Fuse relative disp.
Inertia force = mass * carriage acceleration

60
R5
Clamped zone
Clear zone
b h
Clamped zone
60
180

(a) (b)

Fig. 2 Test setup overview and typical fuse dimensions

2.2 INPUT FLOOR MOTIONS

Unlike most prior shake table tests of nonstructural elements which typically have made use of artificial (synthetic) motions, this testing program made exclusive use of floor motions recorded in instrumented buildings in California to represent realistic severe motions that nonstructural components can be subjected to. Three recorded floor motions, labeled as FM14, FM21 and FM93 were selected to be used as input motions for the uniaxial shake table tests. These floor motions were recorded during the 1989 Loma Prieta and the 1994 Northridge earthquakes in three instrumented buildings in the United States [Kazantzi et al. 2022]. The details of each record are summarized in Table 1. For the first two cases, the floor acceleration spectra are characterized by large amplifications at or close to the fundamental period of the instrumented building (see Fig. 3a and 3b, i.e. T_1=0.33sec and T_1=0.25sec for FM14 and FM21, respectively) whereas the third case has its maximum floor acceleration spectral ordinate at the second modal period of the supporting structure (see Fig. 3c, i.e. T_1=0.45sec).

Table 1. Summary of floor records

Record ID	Earthquake event	Building type	Building height	T_{bldg} [sec]	Recorded floor	Duration [sec]	PFA [g]
FM14	1989 Loma Prieta	RC shear walls	4-story	0.33	Roof	40	1.20
FM21	1989 Loma Prieta	RC tilt-up walls	2-story	0.19	Roof	60	0.58
FM93	1994 Northridge	Steel frames	6-story	0.45	Roof	60	0.45

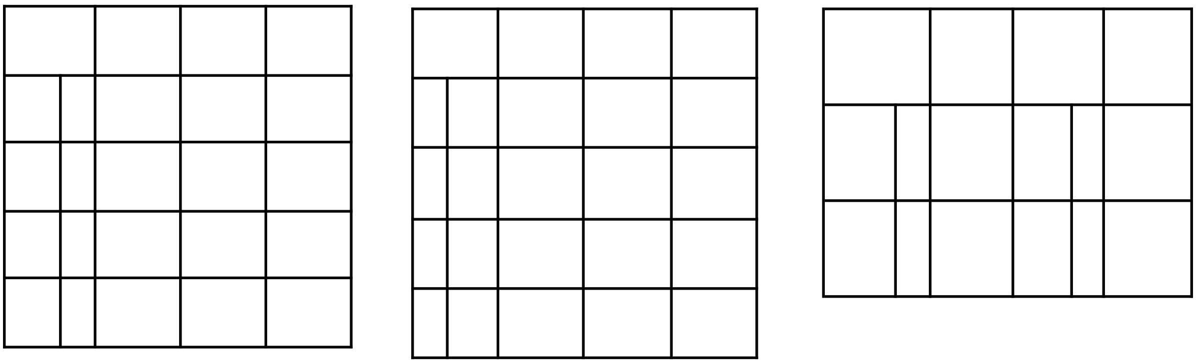

(a)FM14 (b) FM21 (c) FM93 **Fig. 3 Acceleration response spectra for the three employed unscaled ground motion records.**

2.3 TEST MATRIX

The carriage mass and fuse plate dimensions were modified in order to achieve specific target tuned periods of vibration and lateral strength on each test. As summarized in Table 2, the experimental program involved a total of 45 individual tests conducted on 14 specimens (i.e., 14 different combinations of fuse plate sizes and masses). As shown in this table in some cases, the target period was selected to be perfectly tuned to that of the modal period of interest of the supporting structure where the motion was recorded but some of the tests involved slightly shorter periods or slightly longer periods to investigate the sensitivity to the uncertainty in the period ratio, $\tau_m = T_p / T_{bldg}$. Each different specimen was then subjected to a single specific recorded floor motion scaled by different factors.

Table 2. Testing matrix and measured dynamic properties

Specimen ID	Fuse dimensions [b x b x t in mm]	Mass [kg]	Record ID	Scaling [%]	T_{target} [sec]	T_{actual} [sec]	ζ [%]
A1-01	150 x 150 x 8	202	FM21	50, 100, 150	0.15	0.15	1.18
A1-02		331		50, 100	0.19	0.20	2.96
A1-03		570		50, 100, 150	0.22	0.26	5.46
A1-04		202		20, 50, 100, 150	[illegible]	[illegible]	[illegible]

A1-05 357 20, 50, 100, 150 0.33 0.35 3.16
200 x 180 x 6 FM14

A1-06 454 20, 50, 100, 150 0.39 0.40 5.73

A2-01 80 x 38 x 10 806 30, 80, 150 0.26 0.28 1.11

A2-02
150 x 150 x 5 199 30, 50, 100 0.33 0.32 3.88
FM14

A2-04 199 40, 80, 150 0.33 0.32 4.52

A2-05 80 x 38 x 8 806 50, 75, 100, 150 0.36 0.39 1.66

A2-06
260 x 180 x 5 228 75, 100, 120, 140 0.45 0.47 3.81
FM93

A2-08 219 50, 140 0.45 0.46 2.61 A3-01 95 x 150 x 6 648 FM14 40, 80, 150 0.27 0.28 3.98

A3-02 806 40, 80, 150 0.31 0.32 1.07

2.4 INSTRUMENTATION

An instrumentation scheme was developed to capture accelerations and displacements at various locations. The instrumentation layout is shown in Fig. 4 which includes a combination of accelerometers, string potentiometers and a wireless displacement tracking system. In particular, two accelerometers are employed to measure the shake table and carriage absolute accelerations in the three orthogonal directions X, Y and Z. Eight string potentiometers are used to measure the in-plane (i.e., X-direction) displacements of the carriage and at the top end of each fuse plate relative to the table. For measurement redundancy, and to track possible uplift or twisting of the carriage, a wireless system with 12 light-emitting diodes (LED) targets was also employed to track absolute displacements of the shake table, carriage and fuse plate in the three dimensional space.

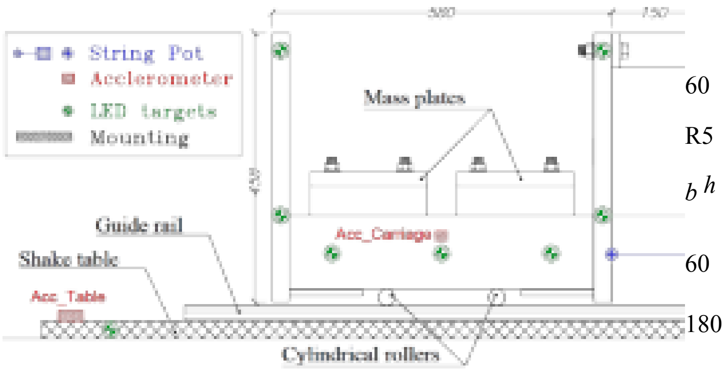

Fig. 4 Instrumentation layout

2.5 TESTING PROCEDURE

For each specimen, and prior to running the main test (i.e., shaking with recorded floor motions), a free vibration test was conducted in order to identify the system's dynamic properties; that is, its fundamental period of vibration (T_{actual}) and its equivalent viscous damping coefficient (ζ). Fig. 5 shows a sample of the decaying motion of the carriage displacement in one of the characterization tests as tracked by the wireless tracking system. As demonstrated in the figure, the system period is obtained as the difference in time between two consecutive decaying cycles' peaks or as the difference in time to complete a certain number of cycles divided by the number of cycles. The equivalent viscous damping coefficient is obtained based on the linear regression fit slope of the logarithm of the decayed carriage motion. When necessary, the mass was fine-tuned by slightly increasing it or slightly decreasing it in an iterative process to get closer to the target period (T_{target}). The values of the target and achieved (measured) periods and inferred equivalent damping ratios are summarized in Table 2. Typical inferred damping ratios ranged between 1 to 5 %. Damping in the test set up was mainly due to the interaction/friction between the carriage and the guiding rails, cylindrical rollers and pins. As such, higher damping values are generally observed in specimens with large mass due to the increased contact between the carriage, the rollers and the guide rails (see Table 2). In all tests, carriage twisting, and uplift was negligible. Out-of-plane accelerations were practically zero and vertical accelerations were below 0.1g.

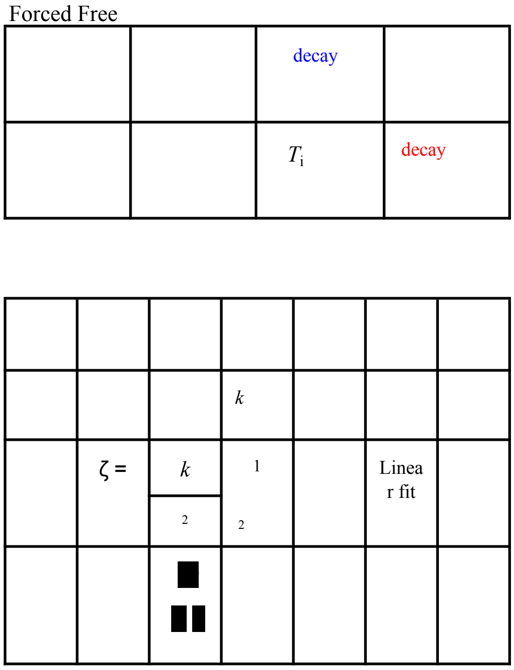

Fig. 5 Illustration of system period and damping coefficient inferred from the free vibration tests

2.6 MEASURED QUANTITIES

In addition to baseline correction, a second-order low-pass Butterworth filter was applied to all recorded signals (accelerations and displacements) with a frequency cutoff at 10Hz. The chosen filter type and parameters were efficient in removing noise from recorded signals without compromising the amplitude or main frequency content characteristics of the signals. This is demonstrated in Fig. 6 which shows a comparison of the acceleration history and Fourier amplitude spectrum (FFT) of the original and filtered time series.

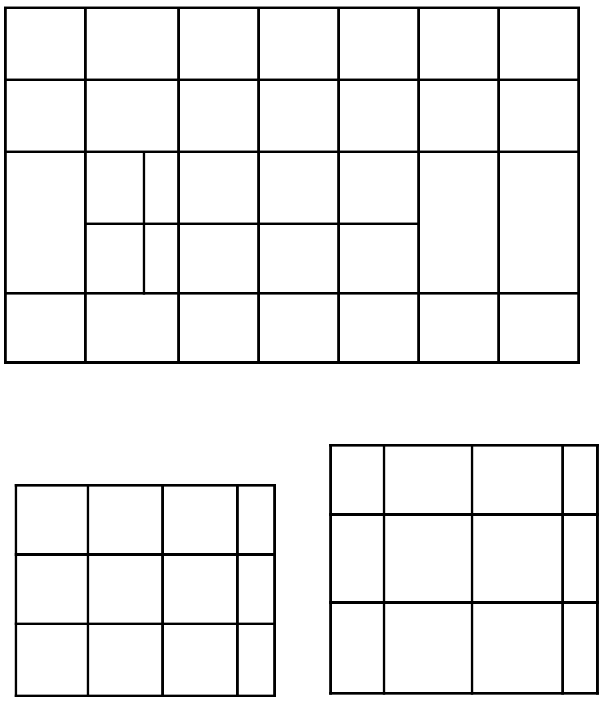

Fig. 6 Illustration of signal filtering using a 2nd-order low-pass Butterworth filter

3. TEST RESULTS

Figure 7a-c shows the inertia force versus the relative displacement fuse plate response of specimen A3-02 when subjected to the FM14 floor motion for three different intensity scaling factors. In the same figure, the elastic stiffness (dashed red line) and the plastic force (dashed blue line) are superimposed for reference. The elastic stiffness was deduced from the force-displacement curves, using data fitting, and validated using the period measured during the characterization tests. The plastic force is computed using Equation (1), where Z is the fuse plate plastic modulus about the axis of bending, f_y is the plate material's measured yield

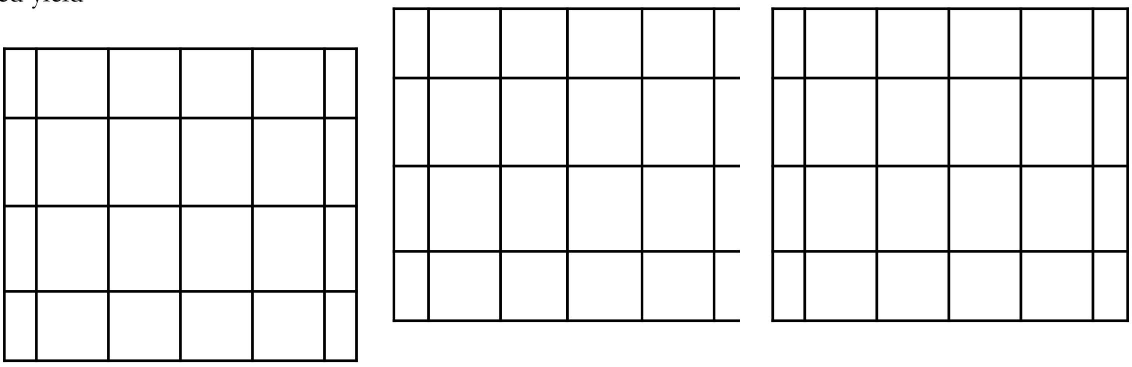

(a) FM scale = 40% (b) FM scale = 80% (c) FM scale = 150% **Fig. 7 Summary of force-displacement response for specimen A3-02**

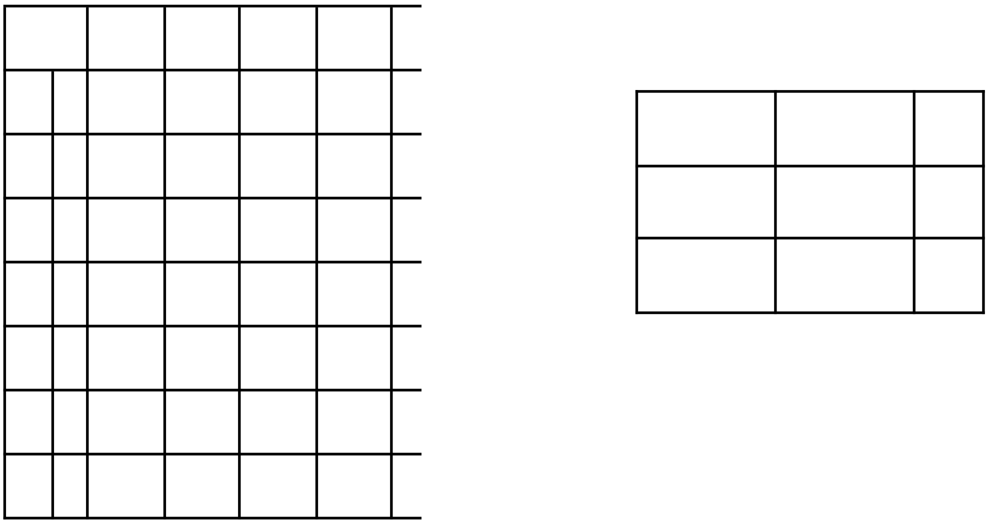

Fig. 8 Summary results for specimen A3-02

stress based on coupon testing and h_{eff} is the effective plate height which is taken as the plate clear length of the plate plus 140mm (distance to top pin center). Based on the computed K_e and F_p, the yield displacement of this plate was 20mm. This yield displacement was exceeded during the shaking at 40%, 80% and 150% scale factor as shown in Figure 7a-c, with peak displacements of 28, 38 and 59mm, respectively. This resulted in ductility ratios, μ, (ratio of peak to yield displacement of the carriage) that ranges from 1.5 to 3.

$$F_p = \frac{Z f_y}{h_{eff}} \quad (1)$$

A summary of the reductions in peak acceleration (and force) measured on the carriage on all specimens as a function of the level of nonlinearity is shown in Figure 9. It can be seen that, consistent with the analytical studies [Kazantzi et al. 2022], by allowing even relatively small levels of nonlinearity−such as ductility demands of two−significant reductions in force are achieved. The largest reductions are obtained for specimens whose period of vibration was perfectly tuned to that of the supporting structure where the record was obtained. This was true whether the carriage was tuned to the fundamental mode of the supporting structure or tuned to the second mode. Figure 8 shows the reductions in acceleration demands on the carriage as the level of ductility demand was increased. In the left-hand figure, the floor spectrum shown in red corresponds to the elastic acceleration ordinates normalized by the peak ordinate, whereas the figure superimposes -in blue dashed lines- the measured peak accelerations of the carriage, normalized by the peak ordinate of corresponding elastic spectrum; represented by the factor α_p. The extend of the reduction in acceleration demands with respect to increasing ductility in specimen A3-02 is plotted on the right-hand side of Figure 8. The figure demonstrated that by roughly doubling the ductility demand (from μ=1.5 to μ=3), the acceleration amplification is reduced by about two thirds.

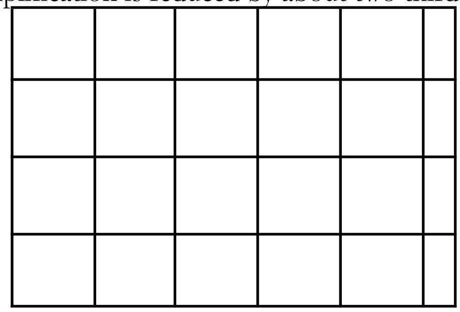

Fig. 9 Measured reductions in force demands as a function of ductility demand

4. SUMMARY AND CONCLUSIONS

This paper has summarized an experimental program that was undertaken to evaluate a novel approach to the design of nonstructural elements in which the bracing elements between the structure and the nonstructural element are designed and detailed to experience nonlinearities during moderate and strong earthquakes. The tests were conducted at the EQUALS laboratory shake table at the University of Bristol. The research project was sponsored by the Seismology and Earthquake Engineering Research Infrastructure Alliance for Europe (SERA).

The experimental program involved the uniaxial shake table testing of 14 different specimens representing nonstructural elements, with masses ranging from approximately 200 kg to 800 kg. Rather than using synthetic motions developed to match a certain floor spectrum specified in a seismic code or in a loading standard, specimens were subjected to motions recorded at the roof level of three instrumented buildings in California, thus the input motions that were used represent realistic intensities, frequency content and durations that nonstructural components can be subjected to. The mass, lateral stiffness and lateral strength of each specimen was modified to obtain specific periods of vibration to obtain perfectly tuned or nearly tuned components relative to the modal period of interest of the supporting structure. Eleven specimen had periods of vibration equal or close to the fundamental period of vibration of the building where the record was obtained, while three of the specimens had periods of vibration equal or close to the period of vibration of the second mode of building where the record was obtained, whereas the lateral strength was selected to obtain specific relative strengths compared to those required to maintain the component elastic. Each specimen was carefully instrumented with accelerometers, string potentiometers and optical (wireless) displacement tracking devices to measure absolute motions of the carriage and motions relative to those occurring in the shake table.

The tests demonstrated how by allowing nonlinearity to occur in the bracing elements, results in the forces acting on the nonstructural element being significantly reduced with respect to those that would occur if the bracing and component were to remain elastic. In particular, consistent with analytical studies conducted by the authors and reported elsewhere prior to the testing program, even small levels of nonlinearity such as a ductility ratio of two, are sufficient to produce significant reductions in the accelerations and the lateral forces acting on nonstructural elements. Reductions are larger for perfectly tuned components than those in nearly tuned components. Therefore, tests also validated that the proposed approach reduces the response sensitivity to the period ratio of the nonstructural element to that of the supporting structure leading to a reduction in seismic demands uncertainty.

ACKNOWLEDGEMENTS

The project was sponsored by the Seismology and Earthquake Engineering Research Infrastructure Alliance for Europe (SERA). This funding is greatly appreciated. Special thanks are also given to Profs

Anastasios Sextos and George Mylonakis, Dr. Raffaele De Risi and laboratory personnel at the University of Bristol for their assistance during the shaking table testing.

5. REEFERENCES

Dhakal, R. P. [2010]. "Damage to non-structural components and contents in 2010 darfield earthquake." *Bulletin of the New Zealand Society for Earthquake Engineering*, 43(4), 404-411, DOI: 10.5459/bnzsee.43.4.404-411

Ferner, H., Wemyss, M., Baird, A., Beer, A., and Hunter, D. (2014). "Seismic performance of non-structural elements within buildings." *Proc., New Zealand Society for Earthquake Engineering Conference*, Aucklan, New Zealand, 21-23.

Fierro, E. A., E., M., and Perry, C. L. (2011). "Behavior of nonstructural components in recent earthquakes." *Proc., Architectural Engineering Conference (AEI) 2011*, Oakland, California, USA, 369-377.

Kazantzi, A. K., Miranda, E., and Vamvatsikos, D. [2020a]. "Strength reduction factors for the design of light nonstructural elements in buildings." *Earthquake Engineering and Structural Dynamics*, 49(13), 1-15, DOI: 10.1002/eqe.3292.

Kazantzi, A. K., Vamvatsikos, D., and Miranda, E. [2020b]. "Evaluation of seismic acceleration demands on building nonstructural elements." *Journal of Structural Engineering* 146(7), 04020118, DOI: 10.1061/(ASCE)ST.1943-541X.0002676.

Kazantzi, A.K., Miranda, E., Vamvatsikos, D., Elkady, A., Lignos, D.G. [2022]. "Analytical studies in support of an imrpoved approach to the design of acceleration-sensitive nonstructural elements." *Proc., Fifth International Workshop on the Seismic Performance of Non-Structural Elements*, Stanford University, Stanford, CA, USA.

Miranda, E., Kazantzi, A. K., and Vamvatsikos, D. (2018). "New approach to the design of acceleration-sensitive non-structural elements in buildings." *Proc., 16th European Conference on Earthquake Engineering*, Thessaloniki, Greece, 18-21.

Miranda, E., Mosqueda, G., Retamales, R., and Pekcan, G. [2012]. "Performance of nonstructural components during the 27 february 2010 chile earthquake." *Earthquake Spectra*, 28(1_suppl1), 453-471, DOI: 10.1193/1.4000032.

Naeim, F. [2004]. "Impact of the 1994 northridge earthquake on the art and practice of structural engineering." *The Structural Design of Tall and Special Buildings*, 13(5), 373-389, DOI: 10.1002/tal.280.

Component-Test-Informed Seismic Design Methodology for Façade Systems

Peloso S.[1], Brunesi E.[1], and Rizzo Parisi E.[1]

[1] European Centre for Training and Research in Earthquake Engineering, Pavia, Italy
E-mail: simone.peloso@eucentre.it; emanuele.brunesi@eucentre.it; elisa.rizzoparisi@eucentre.it

Abstract. This paper presents key steps towards the derivation of a simple, yet effective, seismic design methodology for façades, which are complex non-structural systems that compose the building system. Firstly, brackets connecting the panel elements were identified as the crucial components that drive the response of the entire system typology of interest, and hence were tested in pseudo-static cyclic fashion to characterise experimentally their nonlinear behaviour up to failure for both in-plane and out-of-plane panel actions. Secondly, test data were processed to inform component modelling – for different bracket length and size – to be used/implemented in system modelling, the latter being a helpful tool for capacity verification/check under earthquake-induced in-plane extra distortions. The procedure is showcased with reference to a case-study façade system, and relies upon i) FEMA461 for the assumed testing protocol, ii) European rules for calculation of seismic demand, and iii) parametric linear/elastic models, given a target displacement.

Keywords: façade systems, component testing, experimentally informed numerical modelling, design methodology.

1. INTRODUCTION

Both moderate and large seismic events in urban regions of countries with well-established seismic design codes have repeatedly demonstrated the importance and vulnerabilities of non-structural elements (NSEs) [Filiatrault *et al.*, 2001; Chock *et al.*, 2006; Gupta and McDonald, 2008; Ricci *et al.*, 2011; Belleri *et al.*, 2015; Perrone *et al.*, 2019], thus triggering significant interest in seismic demand/design and performance-related issues [Filiatrault and Sullivan, 2014; Perrone *et al.*, 2020; Rodriguez *et al.*, 2021]. Special relevance has been gained in recent years due to recent advancements in performance-based earthquake engineering and the economic losses attributed to NSEs, which is ascribed to the higher vulnerability of NSEs at lower seismic intensities in comparison with structural systems as well as to the higher investment associated with NSEs (with respect to the total structural cost counterpart).

NSEs, usually not designed to be part of the load-bearing system of a building in spite of being subjected to the same dynamic environment as the supporting structure during a seismic event, include architectural elements, building utility systems as well as building contents, and ventilated façade systems are certainly a very interesting example owing to not only inertia effects but also those related to building distortions and separation as well as to non-structural interaction [Rodriguez *et al.*, 2021; Peloso *et al.*, 2022]. On one hand, window wall, curtain wall and storefront systems are regulated by both American and European standards [AAMA 501.4-18, 2018; AAMA 501.6-18, 2018; EN 13830:2015+A1:2020, 2020] whilst ventilated façades are not covered. On the other hand, European Assessment Documents (EADs) that cover them do exist [EAD 090062-00-0404, 2018; EAD 090034-00-0404, 2016] but provisions for earthquake-induced actions are not included therein.

Accordingly, experimental seismic response characterisation of ventilated façade systems and components is of paramount importance, as test data could permit performance evaluation and could inform numerical modelling efforts towards definition of seismic design methodology for façades, which are complex NSEs integrated in the building system, the latter being intended as a unique system that combines together both structural skeleton/components and non-structural items. Pseudo-static cyclic tests, aimed at investigating the load and displacement capacity of brackets connecting panel elements for both in-plane (IP) and out-of-plane (OoP) seismic actions, were carried out and results, feeding component-test-based nonlinear and linear/elastic modelling, are described hereinafter. Single-degree-of-freedom (SDoF) models developed by means of the open source finite element (FE) platform OpenSees [Mazzoni *et al.*, 2006] were calibrated to reproduce the nonlinear response of tested systems up to failure as well as solely the elastic stiffness given a target displacement. Finally, pivotal steps of a seismic design methodology, which is currently missing in technical literature as well as codes and standards, are discussed considering a simple case-study façade.

2. CRITICAL REVIEW OF EAD REQUIREMENTS

With the aim of identifying the best approach for the execution of tests and, hence, for characterisation of the brackets to be tested, a review of relevant EADs is provided hereinafter. This is not only the first and, perhaps, the most relevant step for the identification of behaviour and response mechanisms of the façade systems but it also provides guidance for the design of the experimental methods for the products to test and, eventually, qualify.

EAD 090034-00-0404 [2016] and EAD 090062-00-0404 [2018] are thus the two most significant EADs to be brought into discussion. The latter is applicable to kits for mechanically fixed external wall claddings – or external wall claddings mechanically fixed as referred to as therein – composed by i) cladding elements, ii) cladding fixings, iii) sub-frame components, iv) thermal insulation products, as well as v) other ancillary components. Although the effects of seismic actions are not covered by EAD 090062-00-0404 [2018], this document sets the working life of the cladding kit (i.e. 25 years or shorter depending on the environmental conditions to which the kit is subjected) and identifies methods and criteria for performance assessment, out of which the most relevant are for i) wind load resistance, ii) mechanical resistance and, specifically iii) for bracket resistance.

The test method for the assessment of wind load resistance shall be in line with Annex E of EAD 090062-00-0404 [2018], which provides two test types: wind suction and pressure. In both cases, the principle is to establish the effects on the assembled cladding kit. The mechanically weakest case, at least, shall be tested with uniformly distributed loads applied in subsequent steps on the surface of the assembled cladding kit until failure, the latter being determined by breaks or permanent deflection of any cladding element, fixing, profile or bracket, or by falling of detached component or by failure or detachment of the kit sub-frame.

For mechanical resistance, key items are identified as follows: i) cladding element, ii) connections between the cladding element and fixing, iii) cladding fixing, and iv) sub-frame components. More in detail, bracket resistance – as per §2.2.12.16 of EAD 090062-00-0404 [2018] – shall be tested in accordance with Annex L of this EAD. The test specimen shall consist of one brackets (i.e. asymmetric layout) or two brackets, in which case testing can be undertaken by means of two brackets in opposition on both sides of the profile. The weakest bracket configuration shall, at least, be tested (for example, when several lengths of wings are available), and the profile defined for the system shall be used in the test. Whenever this is not possible, a square or rectangular section steel tube of 1.5 mm minimum thickness may be adopted alternatively. Also the profile-bracket fixing must correspond to that considered in the system, and the worst fixing position shall be assumed. The bracket-substrate fixing must be selected in accordance with the type of substrate. When no manufacturer specifications are available for the fixings, bolts of at least 6 mm diameter shall be used in conjunction with washers, and shall not represent the weakest link of the specimen. The maximum specified distance from the profile of the fixing anchor on the support shall be considered.

For what concerns the execution of tests, load and displacement should be carefully measured so that the load-displacement capacity curve of the tested specimen could be obtained. The test procedure for vertical and horizontal loads relies upon a semi-cyclic test protocol: in each cycle an increasing load is applied, at a constant load or displacement rate, to the profile and then returned to zero. Constant load/displacement rate is imposed to avoid mobilising a dynamic failure in the test specimen. For load-controlled tests, EAD 090062-00-0404 [2018] suggests increasing steps of 100 N for vertical load tests and 200 N for horizontal load tests, both with a constant rate < 5000 N/min. For displacement-controlled tests, increasing steps of 0.25 mm, 0.5 mm or 1.0 mm are suggested, with a constant rate ≤ 5 mm/min.

EAD 090034-00-0404 [2016], which is applicable to kits composed of sub-frame and fixings for fastening cladding and external wall elements, includes the following items, in addition to sub-frame brackets: i) skin element fixing, ii) sub-frame metallic vertical profiles, iii) sub-frame metallic skin element fixings, as well as iv) ancillary components. Concerning the assessment of bracket resistance, criteria are given in §2.2.11 and §2.2.12, with Annex H that specifies how to assess the load bearing capacity and wind resistance. The test procedure provided therein is the same as the one described in EAD 090062-00-0404 [2018].

3. EXPERIMENTAL TESTING

As reported in Table 1, the chosen test matrix includes 15 different specimens, combination of three sizes (i.e. small, medium and large), and five lengths, thus implying a total of 195 tests, when considering that (i) each bracket type was tested twice, namely for IP and OoP loading/direction, and that (ii) five cyclic tests were carried out per each, accompanied by three monotonic tests for the purpose of calibrating the cyclic loading protocol. More in detail, a single monotonic test was undertaken for the IP direction, whereas two monotonic tests were performed for the OoP direction, one in tension and one in compression.

Table 1. Sizes and lengths of test specimens

Size	Length [mm]
Small (S)	40 – 80 – 140 – 220 – 300
Medium (M)	40 – 80 – 140 – 220 – 300
Large (L)	40 – 80 – 140 – 220 – 300

A brief overview regarding the rationale behind the design of the test setup as well as the definition of the assumed, displacement-controlled loading protocol is proposed in Section 3.1, so as to highlight the main assumptions that were considered for the execution of the tests. Test results are then presented in Section 3.2, thus giving account of observed behaviour and trends.

3.1 TEST SETUP AND LOADING PROTOCOL

As can be gathered from Figure 1, which shows three-dimensional views of test setup for the IP and OoP directions together with labels to facilitate identification of each single component, a decision was made to opt for an asymmetric layout consisting of a single bracket (rather than a pair of brackets in opposition on both sides of the profile) so that interaction one another could be avoided. Testing one bracket at a time, which is in accordance with §L.3.2 of EAD 090062-00-0404 [2018], was favoured (i) to simulate the actual bracket-profile interaction, and (ii) to identify the weakest point in the bracket-screwed-connection-profile chain, all with their own possible failure mechanisms.

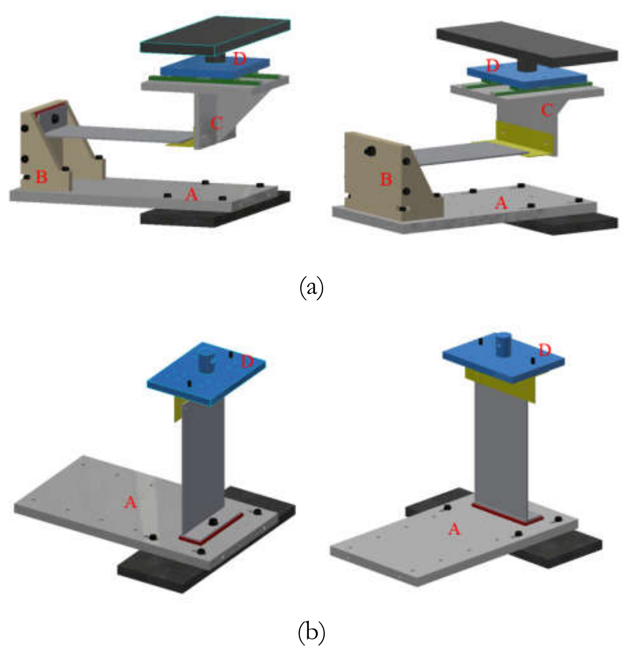

Figure 1. Schematics of test setup for (a) IP testing and (b) OoP testing

Tests were performed by means of an electromechanical MTS machine with a load cell of 10 kN capacity, and the setup, consisting in four main steel components, was designed in such a way that the same plates could be used for both IP and OoP tests.

- a base plate for connection to the bottom part of the machine, wherein brackets are also fixed for OoP tests (A);
- a vertical plate with stiffeners for fixing the brackets for IP tests (B);
- a bottom piece composed by horizontal and vertical plates with stiffener, which is used for fixing the two rails (above the horizontal plate) and the profile (on the vertical plate) for IP tests (C);
- an upper horizontal plate to be connected to the mobile part of the testing machine, wherein the aluminium profile is fixed for OoP tests and for fixing the guides for IP tests (D);

It is worthwhile to note that, for IP testing, component C and component D were connected together by means of two linear guides that allow for displacement in the direction perpendicular to that of the test so as to avoid axial tension being mobilised in the specimen. Further and more specific details regarding the setup and how it easily accommodates different bracket lengths can be found in Peloso *et al.* [2022].

For what concerns the loading protocol, IP and OoP pseudo-static cyclic tests were undertaken assuming FEMA461 [2007] provisions – see e.g. Filiatrault *et al.* [2018] for more insights into its definition as well as for comparative analysis of this displacement-controlled protocol with other force- or displacement-based ones available in the literature. In this case, ten displacement amplitudes were selected and two cycles were performed for each of them, by making use of (i) a symmetric displacement history for IP tests, and (ii) an asymmetric one for OoP tests, as a different behaviour in the two directions was expected (and confirmed by monotonic test results). Note that monotonic tests that accompanied cyclic ones for evaluation of the ultimate displacement of each specimen and, hence, for calibration of target displacement for cyclic testing were carried out imposing a constant displacement rate of 5 mm/min, in line with EAD 090062-00-0404 [2018] and EAD 090034-00-0404 [2016].

3.2 TEST RESULTS

The normalised force-displacement response curves obtained experimentally for an M80 specimen, that is, a short-length/mid-size bracket-profile system, are presented in Figure 2, which collects both IP and OoP test results. Counterpart response curves for a specimen M140, namely a mid-length/mid-size one, and a specimen M220, or a long-length/mid-size one, are provided in Figure 3 and Figure 4, respectively.

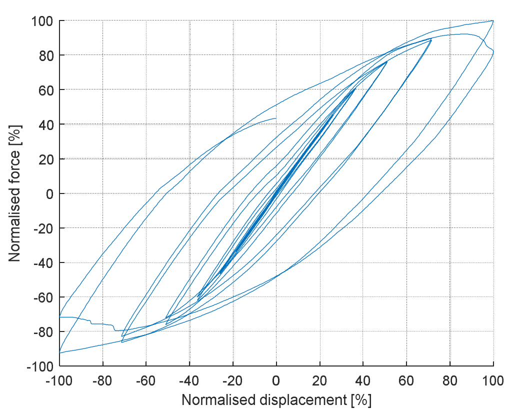

(a)

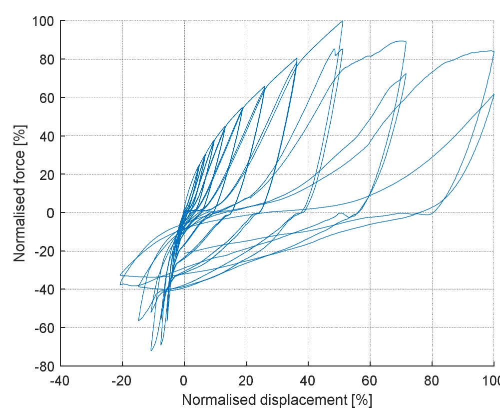

(b)

Figure 2. Normalised force-displacement response of an M80 specimen: (a) IP testing; (b) OoP testing

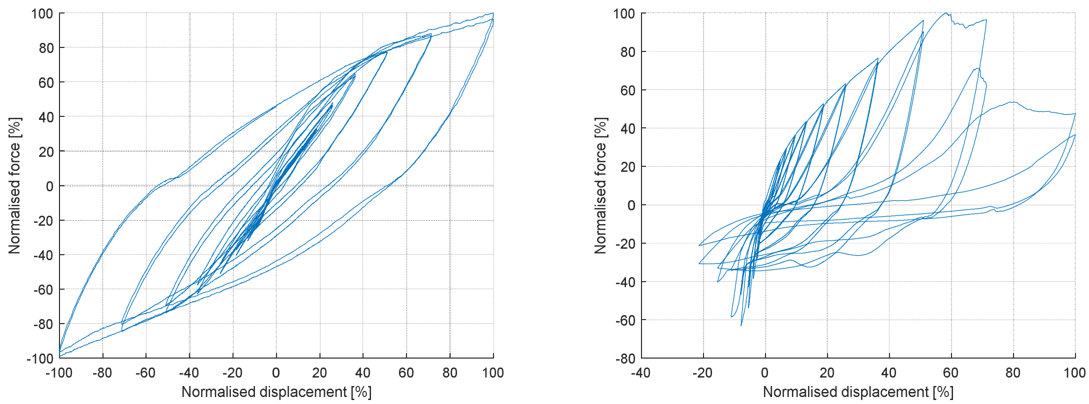

(a) (b)

Figure 3. Normalised force-displacement response of an M140 specimen: (a) IP testing; (b) OoP testing

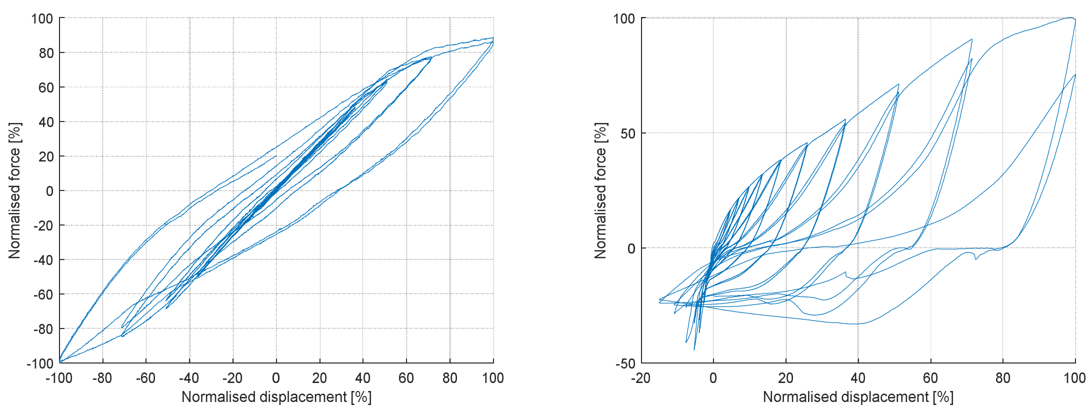

(a) (b)

Figure 4. Normalised force-displacement response of an M220 specimen: (a) IP testing; (b) OoP testing

Response curves such as those presented in Figure 3 – as well as Figure 2 and Figure 4 – were processed to obtain stiffness decay with the imposed displacement and to calculate the dissipated energy (as the area of the hysteresis loops resulting from testing). An example of obtained trends is shown in Figure 5 for one of the tested mid-length/mid-size specimens (i.e. M140 – Figure 3), and these are useful data not only for experimental response characterisation or interpretation but also for inelastic numerical modelling efforts, which should be targeted to minimisation of discrepancy between experimental and numerical response in terms of stiffness decay and dissipated energy.

As can be gathered for instance from Figure 3a, the IP response is approximately symmetric and hardened in character, with hysteresis loops showing a fairly stable unloading branch, whose stiffness resembles the loading one. As far as the OoP behaviour is concerned instead, the hysteretic force-displacement response curve is highly asymmetric, as expected, due to the fact that different damage mechanisms were mobilised in tension and compression (i.e. yielding/plasticisation and buckling, respectively), with the displacement capacity corresponding to buckling being approximately one fifth of the tensile displacement at which the peak force is recorded. Further, peak compressive resistance-to-peak tensile resistance ratio is roughly two thirds. These trends are reflected by normalised stiffness decay curves (see Figure 5a and Figure 5b), with an almost linear decrement for IP testing, as opposed to a pair of curves showing two different slopes for the OoP test case. Lastly, it is worthwhile to note that, somehow expectedly, the – normalised – dissipated energy increases as the imposed displacement increases (Figure 5c and Figure 5d), with small-deformation cycles associated with the IP response that is characterised by minor energy dissipation capacity, as can be seen in Figure 5c as well.

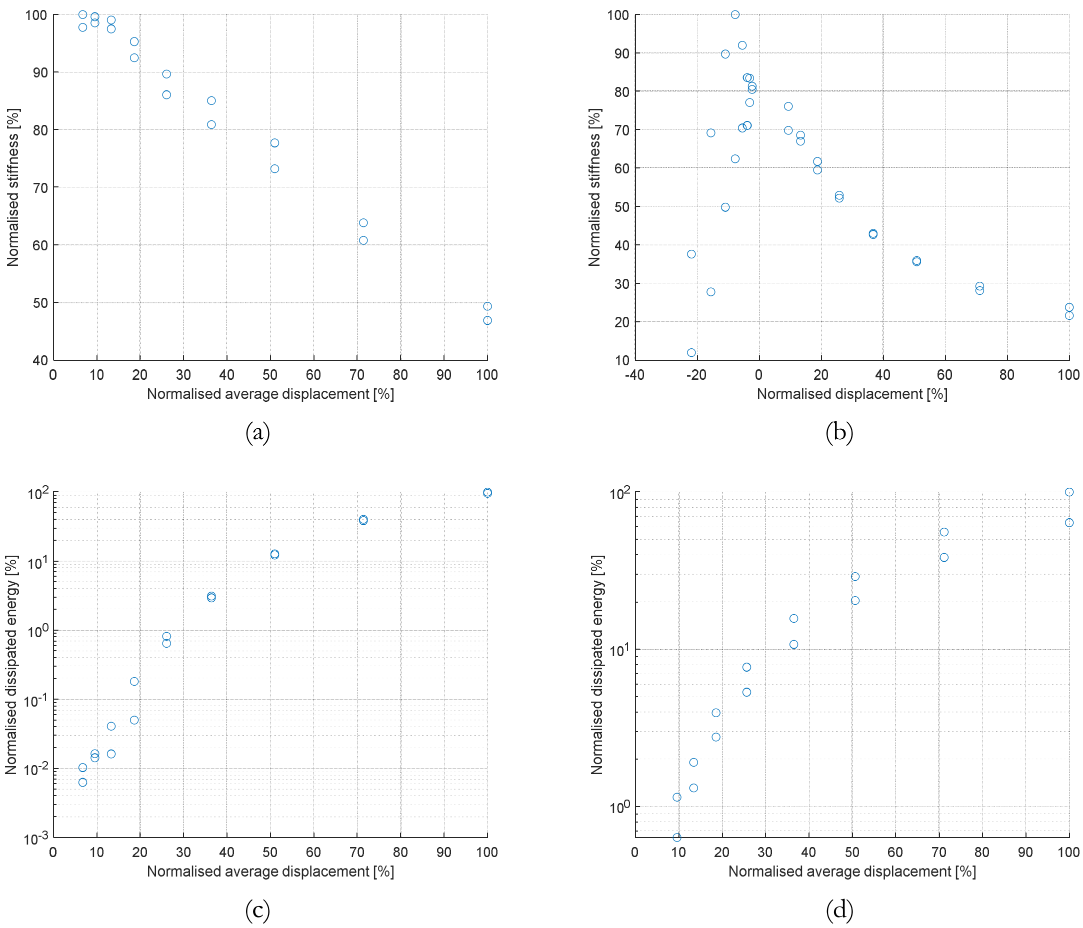

Figure 5. Experimental characterisation, M140 specimen: normalised stiffness decay from (a) IP response and (b) OoP response, and normalised dissipated energy increase obtained from (c) IP response and (d) OoP response

4. NUMERICAL MODELLING AND DESIGN METHODOLOGY

Although the Pinching4 uniaxial material model available in OpenSees [Mazzoni *et al.*, 2006] can certainly be a promising and viable tool to reproduce the inelastic response of tested systems, regardless of whether the IP or OoP response is concerned (Figure 6), different modelling approaches are likely to be envisaged for design purposes, especially when considering the computational burden implied by nonlinear dynamic analysis and the fact that, even though SDoF models are quite agile and efficient, FE models for ventilated façades could involve many of them together with other model elements/items, as shown by Figure 7 for instance.

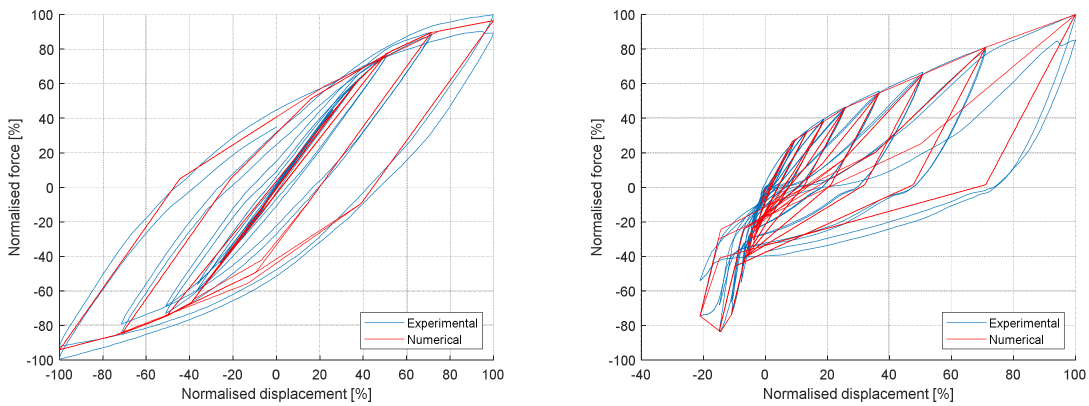

(a) (b)

Figure 6. Comparison between experimental and numerical response curves for an M80 specimen (involving the Pinching4 material [Mazzoni *et al.*, 2006] for SDoF bracket modelling): (a) IP testing; (b) OoP testing

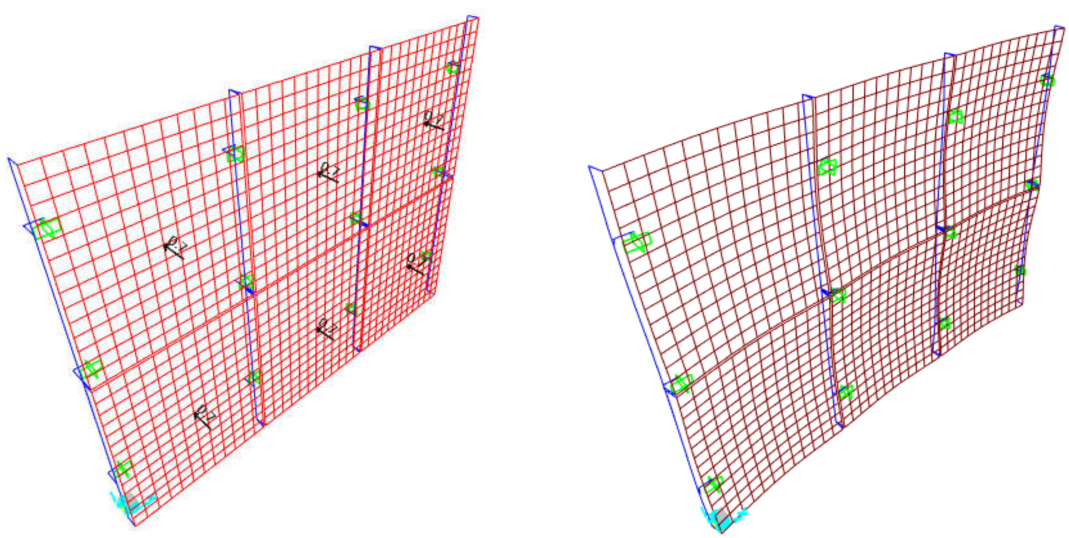

(a) (b)

Figure 7. Example of elastic, shell-beam-link, numerical model for a case-study façade system: (a) undeformed configuration; (b) deformed configuration for OoP loading

Therefore, designers could be, understandably, tempted to opt for the linear elastic case – both in terms of modelling and analysis – which strategy however implies either turning the Pinching4 material model into the elastic material model counterpart or calibrating another elastic material model whose stiffness is taken via linearisation or bilinearisation of experimental force-displacement response envelope, for a given target displacement Δ_T. The latter can be set according to issues of displacement/deformation compatibility with other items or portions of the façade of interest, and can be defined by varying Δ_T parametrically in such a way that the estimated stiffness k_b is stable and the corresponding force capacity $F^* = k_b \cdot \Delta_T$ is evaluated in accurate or conservative manner. Note that Δ_T could either be selected independently of bracket size or length, relying only upon construction issues or available distance with other façade portions, or could be brackt-length/bracket-size-specific. It is also worthwhile to mention that response linearisation adapts well the purposes of interpolation and regression analysis, thus leading to simple closed-form models or curves accounting for different bracket geometry and target displacement.

That said, the following key steps are envisaged for a conscientious (and easy-to-implement) design:

- Step1: evaluate seismic demand, which step implies estimation of panel weight, tributary area, and floor acceleration. Amongst others, reference can be made to European rules [CEN, 2004] for the calculation of spectral acceleration amplification at a given normalised height of the building.
- Step 2: select bracket size and length, according to geometry of the façade system of interest and by checking IP capacity F^* be greater than demand ($F^* > F_{IP}$). This also means that extra capacity resources ΔF could be evaluated subtracting F_{IP} from F^*.
- Step 3: develop FE model of the entire façade of interest with proper stiffness for brackets k_b and impose inter-storey displacements δ suitable to the considered design limit state so as to obtain F_δ or the inter-storey-displacement-driven actions on the brackets.
- Step 4: check IP capacity and OoP capacity, and possibly iterate. The most conservative approach is to check $F_\delta + F_{IP} < F^*$ and $F_{OoP} < F^*_{OoP}$ separately, where F_{OoP} is the OoP sesmic demand set to be equal to the IP one ($F_{OoP} = F_{IP}$) and F^*_{OoP} is the target capacity in the OoP direction.

For the sake of clarity and completeness, it is noted that the numerical model in Figure 7, as developed for a case-study façade system featuring profiles spaced approximately 600 mm apart, can be implemented in any FE software with capabilities for linear static analysis. Indeed, thin-shell elements were assumed to be linear with the elastic properties of the panel (and its weight), whereas the vertical profiles were modelled as series of linear-elastic Bernoulli beams with the elastic stiffness of the chosen profile(s), the latter being connected to the panel by means of rigid links. Linear-elastic link elements were also used for all brackets with properties corresponding to the equivalent stiffness approximation (k_b) of the selected bracket type.

5. CONCLUSIONS

This paper has laid down some foundations to design ventilated façade systems by means of component-test-informed numerical modelling. Following a critical review of relevant EADs on brackets and bracket-profile systems, the latter being identified as key components driving the behaviour of entire façades, tests were carried out, in pseudo-static cyclic fashion, to characterise the IP and OoP response of a wide range of brackets with different length and size up to failure. Behavioural changes as a consequence geometrical variations in the bracket were quantified, and trends were shown in terms of stiffness decay and dissipated energy increase with increasing the imposed displacement. Use was made of data collected to also calibrate SDoF models implementing the Pinching4 uniaxial material model for reproducing the hysteretic response of tested bracket-profile systems up to failure, as well as other design-oriented linear/elastic SDoF models, whose stiffness resulted from linearisation of experimental force-displacement response envelope, given a target displacement. The latter, treated parametrically, could either be set to be brackt-length/bracket-size-specific or could only be targeted to meet displacement compatibility criteria that are inherently related to the adopted construction system. All of the above led to produce tools and items for developing a seismic design methodology for the ventilated façades under investigation herein.

The following conclusions were drawn from this study:

- The IP response was flexural-dominated, with stable and fairly symmetric hysteresis loops that are hardened in character, whilst the OoP response was driven by issues of yielding/plasticisation and buckling in tension and in compression, respectively.
- Stiffness reduction and energy dissipation capacity were quantified and proven to be characterised by stable trends with the imposed displacement, which outcome helped calibrating inelastic SDoF models to reproduce both IP and OoP hysteretic response for different bracket geometry.
- Design-oriented linear/elastic SDoF models with stiffness calibrated via linearisation of hysteretic response envelope were also produced for varying target displacement levels, thus allowing readily implementation into a simple, yet effective, procedure for seismic design of façade systems.
- The proposed design framework was introduced and applied to a case-study façade configuration, which was modelled as an assembly of fully linear/elastic thin-shells, Bernoulli beams, and links in order to undertake linear static analysis for both IP and OoP actions (as well as distortions).

Although the presented seismic design procedure was tested promising, non-structural system level testing would be envisaged for further validation in parallel with the development of nonlinear numerical models of various façade typologies to be subjected to multi-directional dynamic excitation. Thus, to verify further the framework discussed herein, new design information on façades with enough details and specificity to identify permissible ranges of applications could be obtained, as adequately simulated and reliably assessed by nonlinear time-history analyses.

REFERENCES

AAMA 501.4-18 [2018] *Recommended static test method for evaluating window wall, curtain wall and storefront systems subjected to seismic and wind-induced inter-story drift*, American Architectural Manufacturers Association (AAMA); Schaumburg, IL, USA, 11 pp.

AAMA 501.6-18 [2018] *Recommended dynamic test method for determining the seismic drift causing glass fallout from window wall, curtain wall and storefront systems*, American Architectural Manufacturers Association (AAMA); Schaumburg, IL, USA, 15 pp.

Belleri, A., Brunesi, E., Nascimbene, R., Pagani, M., Riva, P. [2015] "Seismic performance of precast industrial facilities following major earthquakes in the Italian territory," *Journal of Performance of Constructed Facilities*, Vol. 29, No. 5, 04014135.

CEN, European Committee for Standardisation [2004] *EN 1998-1. Eurocode 8: Design of structures for earthquake resistance - Part 1: General rules, seismic actions and rules for buildings*, Brussels, Belgium.

Chock, G., Robertson, I., Nicholson, P., Brandes, H., Medley, E., Okubo, P., Hirshorn, B., Sumada, J., Kindred, T., Linurna, G., Sarwar, A., Dal Pino, J., Holmes, W. [2006] *Compilation of observations of the October 15, 2006, Kiholo Bay (Mw 6.7) and Mahukona (Mw 6.0) earthquakes, Hawaii*, Earthquake Engineering Research Institute, Oakland, 53 pp.

EAD 090062-00-0404 [2018] *Kits for external wall claddings mechanically fixed*, European Organisation for Technical Assessment (EOTA); Brussels, Belgium, 81 pp.

EAD 090034-00-0404 [2016] *Kit composed by subframe and fixings for fastening cladding and external wall elements*, European Organisation for Technical Assessment (EOTA); Brussels, Belgium, 37 pp.

EN 13830:2015+A1:2020 [2020] *Curtain walling – Product standard*, European Committee for Standardisation (CEN); Brussels, Belgium, 94 pp.

FEMA461 [2007] *Interim testing protocols for determining the seismic performance characteristics of structural and nonstructural components*, Federal Emergency Management Agency (FEMA); Washington, DC, USA, 138 pp.

Filiatrault, A., Uang, C.M., Folz, B., Christopoulos, C., Gatto, K. [2001] *Reconnaissance report of the February 28, 2001 Nisqually (Seattle-Olympia) earthquake*, Structural Systems Research Project Report No. SSRP-2000/15, Department of Structural Engineering, University of California, San Diego, La Jolla, CA, USA, 62 pp.

Filiatrault, A., Sullivan, T.J. [2014] "Performance-based seismic design of nonstructural building components: The next frontier of earthquake engineering," *Earthquake Engineering and Engineering Vibration*, Vol. 13, No. 1, pp. 17-46.

Filiatrault, A., Perrone, D., Brunesi, E., Beiter, C., Piccinin, R. [2018] "Effect of cyclic loading protocols on the experimental seismic performance evaluation of suspended piping restraint installations," *International Journal of Pressure Vessels and Piping*, Vol. 166, pp. 61-71.

Gupta, A., McDonald, B.M. [2008] "Performance of building structures during the October 15, 2006 Hawaii earthquake," *Proceedings of the 14th World Conference on Earthquake Engineering*, Beijing, China, 8 pp.

Mazzoni, S., McKenna, F., Scott, M.H., Fenves, G.L. [2006] *OpenSees Command Language Manual*, Pacific Earthquake Engineering Research (PEER) Center, Berkeley (CA), USA.

Peloso, S., Brunesi, E., Rizzo Parisi, E. [2022] "Experimental seismic response characterisation of brackets for use in ventilated façade systems," *Proceedings of XIX ANIDIS Conference, Seismic Engineering in Italy*, Torino, Italy, 8 pp.

Perrone, D., Calvi, P.M., Nascimbene, R., Fischer, E. C., Magliulo, G. [2019] "Seismic performance of non-structural elements during the 2016 Central Italy earthquake," *Bulletin of Earthquake Engineering*, Vol. 17, No. 10, pp. 5655-5677.

Perrone, D., Brunesi, E., Filiatrault, A., Nascimbene, R. [2020] "Probabilistic estimation of floor response spectra in masonry infilled reinforced concrete building portfolio," *Engineering Structures*, Vol. 202, 109842.

Ricci, P., De Luca, F., Verderame, G.M. [2011] "6th April 2009 L'Aquila earthquake, Italy: Reinforced concrete building performance," *Bulletin of Earthquake Engineering*, Vol. 9, No. 1, pp. 285-305.

Rodriguez, D., Perrone, D., Filiatrault, A., Brunesi, E. [2021] "A probabilistic strong floor motion duration model for seismic performance assessment of non-structural building elements," *Earthquake Engineering and Structural Dynamics*, Vol. 50, No. 15, pp. 4161-4179.

Ongoing Extension of Systems for Seismic Securing of Masonry Façades through Refurbishment, Strengthening and Retrofitting

Samuel Hine[1], Matthias Roik[2]

[1] Leviat Limited
9 President Way, President Park, Sheffield, S4 7UR, United Kingdom
e-mail: Sam.hine@leviat.com

[2] Leviat GmbH
Liebigstr. 14, 40764 Langenfeld, Germany
e-mail: Matthias.roik@leviat.com

Abstract. Recent earthquakes show that existing, older buildings are not sufficiently secured against seismic loads. This applies to both structural and non-structural elements of a building. Damage to so called 'heavy' façade structures is of particular concern, as falling components can cause personal injury and block important traffic and escape routes.

Heavy façades typicall consist of masonry, natural stone cladding or concrete panels with a dead load of more than 100 kg/m² and are usually fixed to the supporting structure with steel anchors that transfer the loads from the cladding panel back to the structural frame. This paper will focus on masonry façades but many of the topics covered are also applicable to other heavy façade constructions.

While newly constructed façades can be very well secured against seismic events, there is little experience in the field of seismic retrofitting for existing façades, although there are some product systems on the market that allow repair or strengthening. These systems are investigated for their suitability to carry additional loads from earthquakes.

Progressive testing is expanding a fastening system that is not only suitable for repair but also for retrofitting masonry façades. This will draw on experience published at previous SPONSE conferences. In our own test series, knowledge gained from previous tests can be translated to the repair product range.

This paper presents methods for the subsequent repair of masonry façades on existing buildings. This method can be used to preserve historic building fabric, but it can also be used to strengthen the façade with the aim of meeting seismic design requirements such as protecting life and enabling rescue work after an earthquake. As an alternative to large shake table tests, 'meso-scale' tests are described for checking the load-bearing capacity. The technical background is explained, and the test results are presented.

Keywords: Façades, Fixing Constructions, Heavy Façade Systems, Non-structural Elements, Testing Methods.

1. INTRODUCTION

A building facade serves numerous purposes: it affects the appearance of the building – allowing it to blend in with or stand out from other buildings – but also protects the internal structure and its occupants from weather influences such as rain and wind. The façade design can also enhance the physical properties of a building; for instance ventilation can be provided by an open cavity space and thermal performance can be improved by incorporating an insulating layer.

Façade fixings are an integral part of this construction and must safely transfer dead loads (the façade itself) and imposed loads (e.g. wind, seismic) back to the structure whilst also maintaining the distance between the supporting and façade layers. 'Heavy' façades such as brickwork, natural stone or concrete, typically feature dead loads in excess of 100kg/m^2 which place high demands on the façade fixings. Not only must the fixings transfer high point loads back to the structure but, due to the nature of construction, the distance that the fixings span between the inner and outer layers can be large (300mm or more).

BS EN 1998-1 [2013] classifies façades and façade fixings as non-load-bearing components i.e. masses without any inherent stiffness, attached to the load-bearing structure. Such items can be designed for seismic load by using static equivalent horizontal loads acting in the most unfavourable direction.

In the following, only masonry façades are considered, as – in a first step – the range of these repair products were examined. Nevertheless, the lessons learned could also be applied to other façade materials such as natural stone and concrete.

Hairline cracking and other minor damage to masonry façades can be caused by earthquakes. Whilst detrimental to the aesthetics of the building, this type of damage does not typically present any immediate danger. More significant damage causing partial or complete collapse of a façade presents much higher levels of risk and danger – both to building occupants trying to escape and to emergency services trying to access a building. Not only is there the imminent risk posed by falling masonry, but vital access routes in and around the building can become blocked. Damage to façades and fallen masonry are clear to see in photographs taken in the aftermath of earthquakes in Christchurch (2011) and more recently in Zagreb (2020) – see Figure 1.

Figure 1. Masonry façade damage – Zagreb 2020 (Photo credit REUTERS/Antonio Bronic)

Façade damage could be an indicator that the structure itself has also been weakened – reducing the potential seismic performance during aftershocks and subsequent earthquakes. Assessment of the damage (both to the structure and the façade itself, including any associated fixings) needs to be carried out quickly to identify areas requiring repair so the seismic resistance of the building and the integrity of the façade can be restored.

Whilst repair can help to restore the seismic performance of a building once it has been damaged, retrofitting existing façades with new components presents a way to raise the seismic resistance and help to limit damage being incurred in the first place. This helps to reduce the risk to people during an earthquake and can save time and money during the repair process (if repairs are even required).

Seismic retrofitting is particularly applicable to older, historical façades which were constructed before the introduction of modern standards so typically do not contain any seismic fixings. Retrofit methods with minimal or no visual impact are available which allow seismic performance to be upgraded whilst preserving the façade aesthetics.

Rather than assessing a façade fixing in isolation, the interaction of the fixing with other components such as the structural frame and façade itself should be considered. Analysing the fixing in this way allows load-bearing capacity and ductility to be assessed. In addition, the system load-bearing behaviour can be evaluated for a variety of scenarios by using tests at different scales. Macro-scale tests present the opportunity to replicate site conditions exactly but require large, expensive test facilities and can be very time-consuming. Smaller scales such as meso- or micro-scale testing offer viable alternatives where representative results can be obtained at a lower cost.

This paper discusses methods for seismic repair and retrofitting of existing masonry façades. Different approaches to testing façade fixings are presented and evaluated.

2. BRICKWORK FAÇADES

Modern buildings with brickwork façades typically rely on a number of layers to provide the required weather proofing, thermal performance and ventilation. The external facing façade layer is generally separated from the insulation layer by a clear air gap or cavity, with the structural frame located behind the insulation layer. Shelf angles or brickwork support brackets (Figure 2) are used to carry the dead load of the brickwork façade and these must therefore span between the layers, penetrating the insulation and fixing securely back to the frame. Typically these components are designed as cantilevers or tensions members with spacers and are fixed using suitable anchor bolts or channels.

Loads acting perpendicular to the façade such as wind loading are accommodated separately by horizontal restraints. These components transfer tensile and compressive loads between the masonry façade and the structure and limit movement between the two. The fixing examples shown in Figure 2 are not designed to transfer loads parallel to the façade layer. Where seismic loads are expected, additional bearing components should be included – this is important for new build constructions as well as for repair and refurbishment.

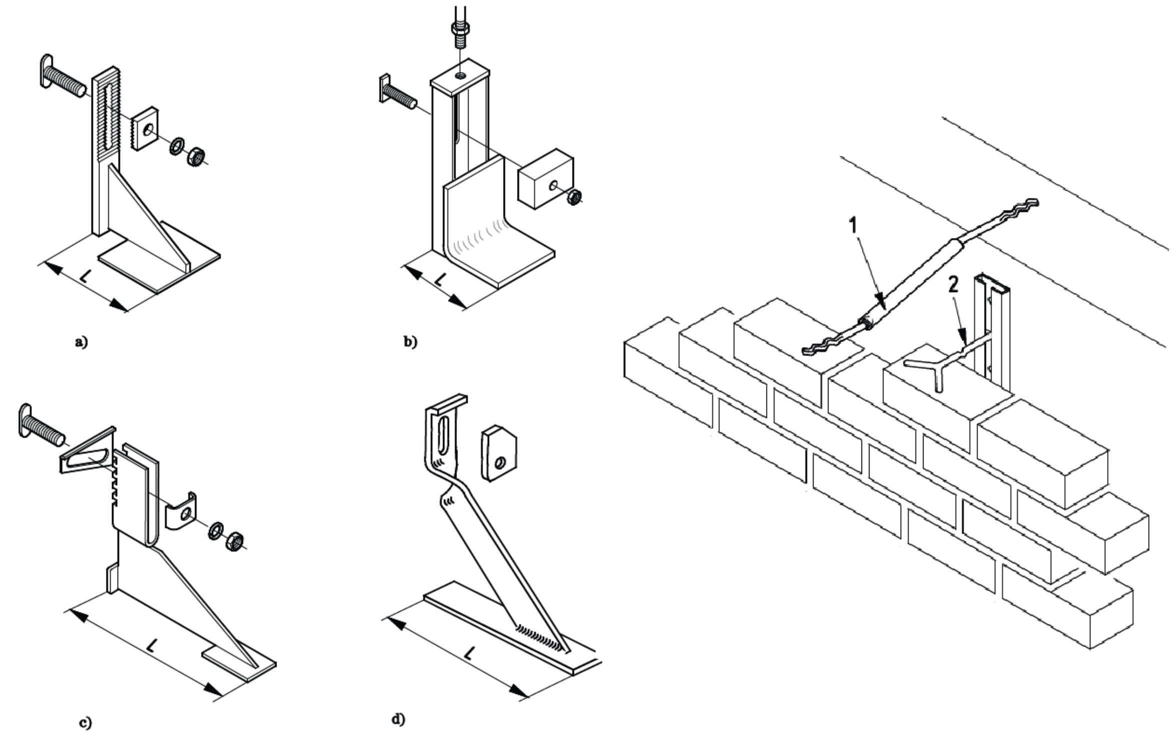

Figure 2. Examples of brickwork support brackets and movement-tolerant wall ties [BS EN 845-1, 2016]

3. SEISMIC STRENGTHENING METHODS

Strengthening methods broadly fall into two categories; repair and retrofit. BS EN 1990 [2005] defines repair as '*Activities performed to preserve or to restore the function of a structure that fall outside the definition of maintenance*'. Whereas repair methods are employed in response to damage being sustained to a building, retrofit is a more pro-active approach and is carried out in anticipation of an event, such as an earthquake, occurring. Ultimately the aim is to reduce or completely eliminate the damage being caused in the first place. This has the dual benefit of lower risk to health during an event and reducing the amount and cost of repairs required after the event. Various retrofit strategies exist; from simple single components to more complex linked systems. Many methods can be installed sympathetically and with minimum disruption to the existing façade – this can be of great importance when working with older buildings of historic significance. A number of such methods are presented below and assessed for their ability to secure masonry façades against seismic loads.

3.1 REPAIR METHODS FOR MASONRY FAÇADES

Repair methods for masonry façades are vital for restoring structural integrity after damage has been incurred. The longer a building is left in a damaged state, the greater the chance of a subsequent earthquake occurring which, due to the reduced seismic resistance of the damaged façade, could cause much greater damage and pose an increased risk to life. It is therefore imperative that damage such as cracked, broken or collapsed masonry is repaired as soon as possible.

One such method of repair for cracked masonry is the use of long, twisted (helical) stainless steel bars inserted into the horizontal mortar joints and grouted in place – see Figure 3. This is known as 'crack stitching' and provides near-surface reinforcement to masonry panels – the helical bars and thixotropic cementitious grout form a strong bond with the existing masonry, allowing tensile loads to be redistributed along the length of the panels and helping to minimise any further crack development. With careful consideration of the mortar used for repointing, a façade can be repaired using this technique in a very aesthetically sympathetic manner.

Figure 3. Thixotropic cementitious grout applied to a horizontal slot in preparation for insertion of helical bar

Another use of helical stainless steel bar for façade repair is the creation of deep masonry beams. In a similar way to crack stitching, bars are grouted in place in horizontal slots cut in the mortar joints. By using pairs of bars installed a number of courses apart, structural integrity and load-bearing capacity of the façade can be restored.

Masonry façades which are bowing out of plane can be repaired by using threaded or helical stainless steel bars to reinstate the connection between the façade and the structural frame – see Figure 4. By driving the bars through the façade and into the internal timber joists (either into the ends or the sides), the masonry can be stabilised and further movement prevented. As external spreader plates are not required, this method is again easily concealed and presents a quick, permanent repair solution.

For masonry façades which have suffered more significant damage or have high load applications, a more robust system of threaded stainless steel bar, heavy duty mesh fabric sleeves and cementitious grout may be required. The bars and sleeves are inserted into the walls through drilled holes, grout is then pumped into the sleeves which expand and form a strong chemical/ mechanical bond with the existing masonry ad internal structure – see Figure 4. Again, with good detailing and workmanship to fill the drilled cores this solution is fully concealed and can leave the façade looking virtually un-touched.

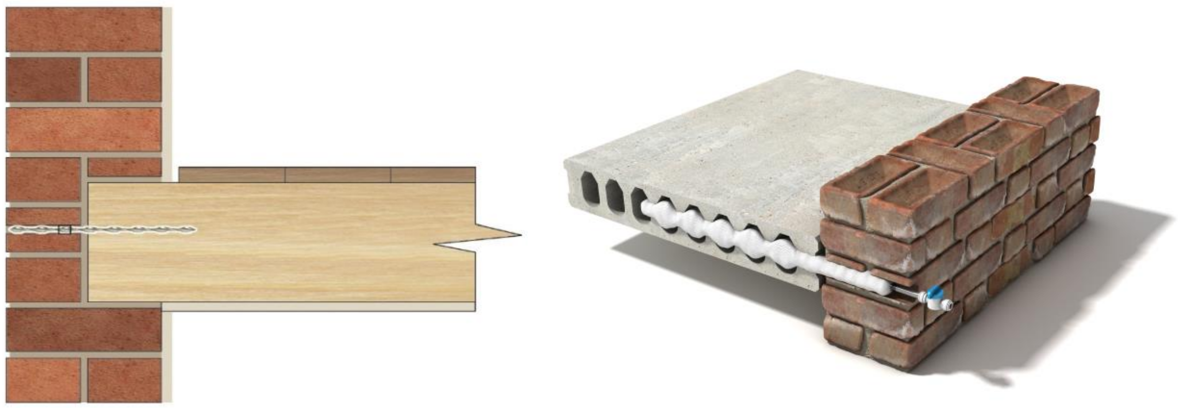

Figure 4. Brickwork façade restrained from bowing out of plane and heavy duty repair to masonry façade.

If complete masonry collapse has occurred and the façade is to be re-built, cavity wall ties can be employed to join the leaves of masonry together. This improves the wall stability by tying the layers together and allowing them to act as one homogenous unit. Many different wall tie profiles and end types are available to suit different applications – ties can be bedded in mortar at both ends, mechanically fixed using screws or bolts, or resin-bonded directly to the masonry. Typically wall ties are made from stainless steel but pultruded basalt fibre ties are also available when even lower thermal conductivity is required.

3.2 RETROFIT METHODS FOR MASONRY FAÇADES

Retrofitting masonry façades to improve seismic performance utilises a different philosophy – rather than simply waiting for damage to occur and then repairing it, retrofit is a pro-active approach where time and money are spent up-front with a view to reducing expenditure in the future.

In a similar way to crack stitching, long lengths of helical stainless steel bar can be installed into horizontal mortar joints in a brickwork façade. These long lengths of bar can be connected via a stainless steel component to shorter, helical ties which are driven into the inner structure perpendicularly through the façade – see Figure 5. By connecting the bars and ties in this way, long runs of remedial masonry reinforcement can be installed to improve the in- and out-of-plane performance of the facade with minimal addition to the seismic mass. Fixing security can be easily tested in-situ using a simple pull test where required.

Another use of helical stainless steel ties for retrofitting is mechanically (or chemically) pinning brickwork façades, render and masonry features back to the structural frame. The ties can be driven through small pilot holes into the inner leaf to tie the layers together and prevent masonry from falling due to seismic activity – see Figure 5. Depending on the application, cementitious grout and fabric sleeves can be used alongside the ties. This is a versatile retrofit technique which can be used with both cavity and solid wall constructions and is suitable for fixing to brickwork, blockwork, concrete and timber.

Testing has shown the use of retrofitted helical stainless steel ties to be an effective way of improving the out-of-plane performance of masonry walls [EQ Struc. 2013]. Newcastle Innovation [2010] also showed that the requirements for an earthquake medium duty tie to Australasian standard AS/NZ2699.1 can be met using this method.

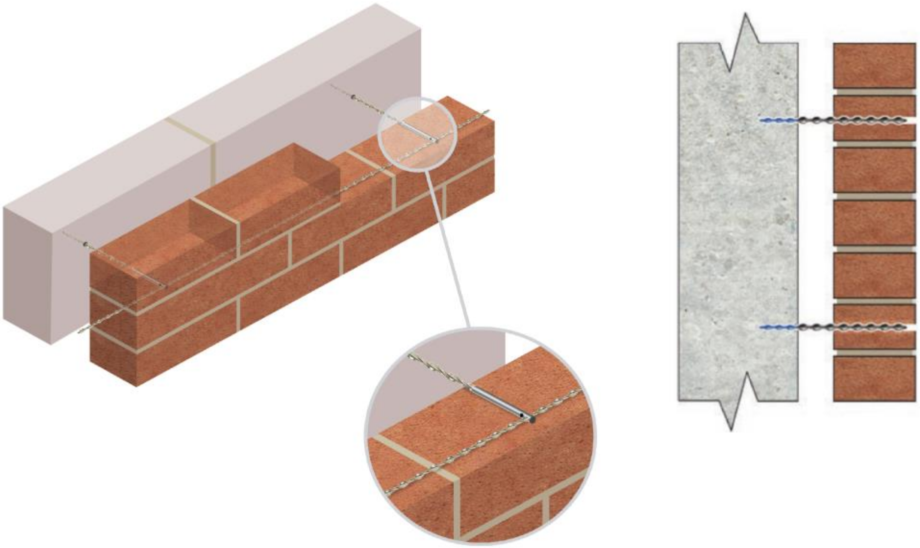

Figure 5. Long helical bars connected to perpendicular helical ties and a mechanically pinned masonry façade

Seismic performance can be further improved by the use of 'rigid' and 'ductile' anchors. Typically these require more invasive installation procedures; individual masonry support brackets ('rigid' anchors) can be installed to carry horizontal seismic loads whilst angled wall ties ('ductile' anchors) can transfer both transverse and longitudinal loads back to the structure. This has been shown to be an effective method of limiting damage to heavy façades during shake-table testing [Roik and Piesker, 2017].

4. TESTING OF REPAIR & RETROFIT FOR MASONRY FAÇADES

4.1 INTRODUCTION

Roik and Piesker [2019] describe the different test scales that are suitable for heavy façade fixings; macro, meso and micro. Each scale has various advantages and disadvantages but, generally, the larger the scale, the greater the expense and time required. For this reason, meso-scale testing presents a good compromise where the full representative façade system and inter-linked components can be evaluated without requiring large-scale testing facilities.

4.2 MESO-SCALE TESTING

Meso-scale testing utilises a representative façade area of around $1m^2$ and as such can be much more accessible than large, full-scale shake table tests. Critically, an area of $1m^2$ still allows all components of a façade fixing system to be assessed together so potentially vital interaction between the elements is not lost. Due to the lower cost, it is more feasible to carry out project-specific testing with relevant pre-determined static equivalent loads.

Due to the lack of specific regulation of test procedures for façade systems subject to seismic loading, the regulations of ETAG 001, Annex E [2013] are proposed. The only exception is that the calculated horizontal equivalent loads (taken from relevant seismic design standards) are used as the maximum loads N max for tension and compression and V max for shear force.

Figure 6 shows an example of a meso-scale test using a $1m^2$ masonry façade area supported on brickwork support brackets and fixed back to a concrete frame. Perpendicular wall ties were installed as the brickwork was built with the mortar then left to cure. Once at design strength, 2No. helical bars were driven through the brickwork at an angle into the concrete frame and resin-fixed in place to accurately represent a retrofit scenario with 'ductile' anchors. Horizontal load was applied in the plane of the wall, at a continuous load speed and in accordance with ETAG 001, Annex E [2013] in increasing load steps. Horizontal displacement of the façade was measured using displacement transducers.

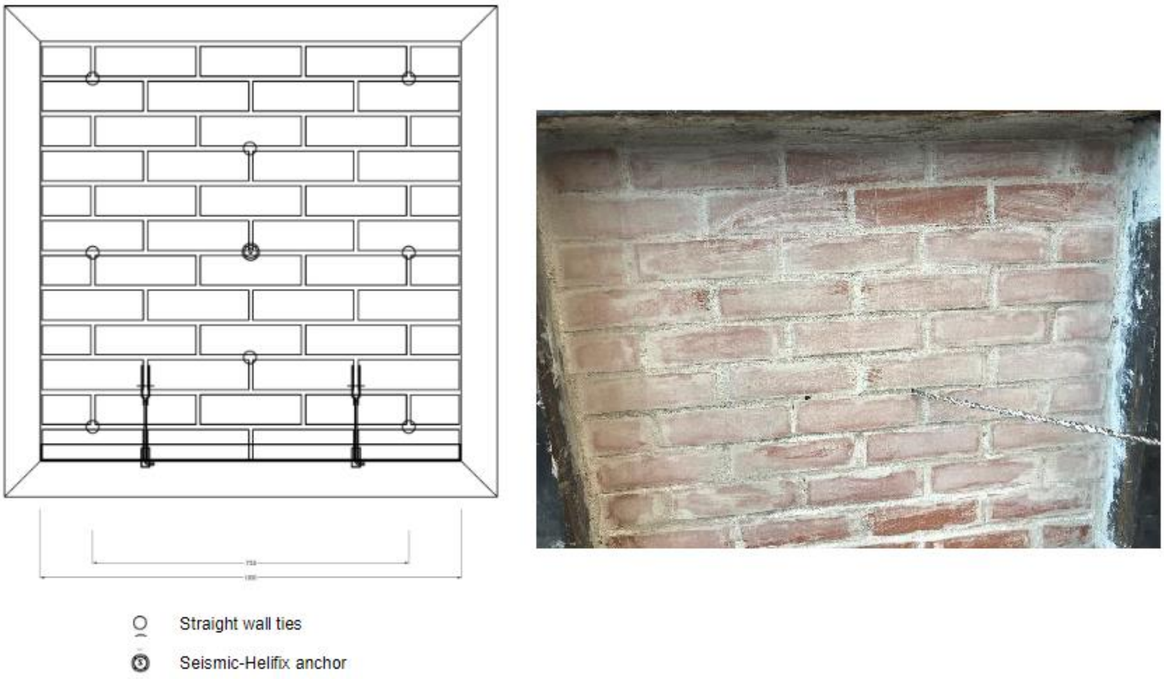

Figure 6. Meso-scale test concept and installation of helical bar through brickwork

The test results show minimal horizontal displacement (less than 1mm) is exhibited with load application Vmax = ±2.0kN (equivalent to 1 x G). Plastic deformation starts to become apparent around Vmax = ±4.0kN (2 x G) with horizontal displacement of ±9mm. With further load increases the displacement grows strongly up to around 50mm (applied loading in the region of 4 x G). However, even at 'failure' when the wall ties have buckled and bent the masonry is still held together and does not collapse – suggesting that in the event of an earthquake such a design would reduce the risk of falling masonry.

4.3 MACRO- & MICRO-SCALE TESTING

Macro-scale tests are carried out at a 1:1 scale, typically on a shake-table, and allow the whole façade & fixing system to be tested in an as-built state. Behaviour under load can be examined accurately and gives a very good representation of building performance in the 'real world'. However, due to the scale of the testing, it is very expensive to repeat for new scenarios and is also time-intensive.

Micro-scale tests on the other hand focus solely on a single component and analyse behaviour and performance in isolation. They can be carried out easily in a laboratory or on site and are quick and inexpensive, meaning many different scenarios can be tested. Results however do not take into account any interaction with other building components so need to be carefully considered.

5.CONCLUSION

The latest seismic design standards classify façades and façade fixings as non-structural components. Static equivalent horizontal loads, acting in the most unfavourable direction, are used to design these elements.

The severity of damage caused to façades from seismic events can range from minor hairline cracking to much more dangerous partial or total collapse. It is vital that major damage is prevented to reduce the risk of injury to persons in and around the building and to aid rescue efforts in the immediate aftermath. Any and all damage to masonry façades should be assessed following an earthquake and repairs carried out as soon as possible. Even damage that appears to be only aesthetic in nature can indicate a reduction in the seismic resistance of a building and therefore needs to be dealt with promptly. The longer a building remains in a damaged state, the increase in risk posed by future earthquakes – both in terms of danger to life and increase in repair costs. Various repair techniques exist to suit a variety of masonry applications.

By taking action before damage is sustained, retrofitting existing buildings to upgrade their seismic performance presents a way to reduce risk to life and, at the very least, decrease the amount of repair work required after an earthquake has occurred. Combinations of components such as stainless steel helical bars, resins, grouts and sleeves can be used to create appropriate retrofit systems which can be installed quickly and with minimal disruption.

When evaluating façade fixings for seismic performance, the interaction of all components within the system needs to be considered. Elements such as the façade fixing, the façade itself and the structural frame all need to be included in the assessment to ensure load-bearing capacity and ductility meet requirements. Theoretical calculations can give a partial picture but physical tests present a valuable method of determining the actual performance of an element or system. Tests can be conducted based on regional standards where required and specifications can be altered to suit specific project conditions.

Tests can be conducted at various scales depending on the space, time and cost restrictions that are applicable. Macro-scale tests carried out at 1:1 can provide very accurate representations of overall load-bearing behaviour but are very time and cost intensive. Micro-scale tests tend to be much easier and cheaper to carry out but only focus on an isolated component and can miss important system interactions. Meso-scale tests present a compromise between the two – using a façade test area of around 1m^2 to keep costs low but still allowing the interaction between various elements to be analysed.

Tests carried out at the meso-scale have been used to show the success of retrofitted façade fixings in limiting deflection of brickwork when subjected to cyclical horizontal loading. Even when taken to 'failure' with large plastic deformations, the façade fixings were able to provide sufficient integrity to the test wall to prevent any collapse of the masonry.

REFERENCES

BS EN 845-1 [2016] *Specification for ancillary components for masonry - Part 1: Wall ties, tension straps, hangers and brackets,* British Standards Institution, UK.

BS EN 1990 [2005] *Eurocode: Basis of structural design,* British Standards Institution, UK.

BS EN 1998-1 [2013] *Eurocode 8: Design of structures for earthquake resistance - Part 1: General rules, seismic actions and rules for buildings,* British Standards Institution, UK.

[2013] "Seismic performance of twisted steel bars used as wall ties and as remedial wall stitching: 2010/2011 Canterbury Earthquakes", *Commissioned report*, New Zealand.

ETAG 001, Annex E [2013] *Metal Anchors for Use in Concrete, Annex E: Assessment of Metal Anchors under Seismic Action*, European Organization for Technical Approvals, Belgium.

Roik, M., Piesker, C. [2017] "A concept for fixing "heavy" façades in seismic zones", *Proceedings of 16th World Conference on Earthquake Engineering*, Santiago de Chile, Chile.

Roik, M., Piesker, C. [2019] "Streamlining the Test Methods for Seismic Verification of Façade Anchors", *Fourth International Workshop on the Seismic Performance of Non-structrual Elements (SPONSE),* Pavia, Italy.

Simundic, G. [2011] "Helifix wall ties testing", *Individual Study,* University of Newcastle, NSW, Australia.

In-plane quasi-static reversed cyclic tests on infilled façades made of lightweight steel drywall systems

Sarmad Shakeel[1], Luigi Fiorino[2], and Raffaele Landolfo[2]

[1] NUST Institute of Civil Engineering, School of Civil and Environmental Engineering, National University of Sciences and Technology (NUST), Pakistan
e-mail: sshakil@nice.nust.edu.pk
[2] University of Naples "Federico II", Department of Structures for Engineering and Architecture, Italy
lfiorino@unina.it, landolfo@unina.it

Abstract. A lightweight steel (LWS) drywall façade is one of the most widely used architectural non-structural components in a building. This paper presents the results of in-plane quasi-static tests carried out on 14 different full-scale façades made with LWS framing. The main goal of the study is to investigate the effect of various construction details on the seismic response of the selected facades. The investigated parameters include: single or double frame walls, type of sheathing panels, presence of finishes, variation in surrounding structural elements, absence of track members, type of connection to the surrounding structural elements, and presence of offset. The effect of the construction parameters on the lateral response of the façades was examined in terms of strength, stiffness, and force-displacement hysteretic response. Furthermore, the main damage phenomena observed during the tests are also reported, associating them with the three damage limit states based on the level of damage and the related repair actions. For the definition of the seismic vulnerability, the fragility curves for different façade typologies are also presented

Keywords: infilled façades, lightweight steel, cold-formed steel, cyclic tests

1. INTRODUCTION

Non-structural elements can collapse, endangering human lives and creating damage comparable to structural parts collapsing. Non-structural components may lead buildings to fail even if a proper seismic design assures satisfactory structural performance. This is owing to a lack of established design requirements for non-structural systems, as the study of non-structural seismic response has received less attention in the past than structural systems. Traditional methodologies, such as detailed numerical simulations or analytical approaches, are incapable of forecasting the seismic response of these systems. In this context, at the University of Naples Federico II, an experimental campaign was conducted to evaluate the in-plane seismic response of façade walls composed of lightweight steel (LWS) drywall systems, and the results are reported in this article.

The terms façade wall and external wall are used interchangeably here. Façade walls differ from curtain walls and cladding in that they are joined to the building face with metal connectors, are not infilled in the building structure, and are non-load bearing systems. Curtain walls and cladding are held up by the building face to which they are attached. Façade or external walls, on the other hand, are typically infilled or partially infilled in the building structure. They are not load bearing, however, and are always supported by the lowest structural element: a beam or floor slabFaçade walls composed of LWS framing are very similar to LWS internal partition walls, with the exception that the panels used in façades on the outer face are normally cement-based panels, which give greater outdoor performance due to being waterproof and impact resistant.

The current state of the art on LWS facade walls is fairly restricted, with only two experimental studies completed in the past. [Wang et al. 2015] performed shaking-table testing on a five-story reinforced concrete structure with LWS façades. The tested façades' were not infilled and were fastened to the floor slabs with steel clips. Distinct types of damage to the façades, as well as drifts, were identified and classified into different damage states. [Fiorino et al. 2019] used shaking-table tests to assess the seismic response of LWS non-structural architectural components. Loading was applied on the specimens' in-plane direction. During the testing, various damage states were detected, and force-displacement responses were examined. For comparison, a similar façade wall as tested on the shake-table by [Fiorino et al. 2019] is included in the experimental investigation on façades reported here.

The present experimental study on façades focuses on the in-plane seismic performance of infilled façades and analyses the impact of various construction parameters on their performance via quasi-static reversed cyclic tests. It's also worth mentioning that there are only minimal modifications if the LWS façade walls and internal partition walls are completely infilled in a structural frame. The behaviour of façade walls and interior partition walls can be contrasted in this situation.

2. EXPERIMENTAL PROGRAM

2.1 SPECIMENS DESCRIPTION

The experimental programme included 14 full-scale infilled façade wall specimens, referred to as "walls" or "specimens" hereafter. All of the walls were 2400 mm x 2700 mm (length x height) with a total thickness ranging from 75 mm to 211 mm depending on the type of configuration. The walls were erected in accordance with contemporary metal stud non-structural wall construction norms [SCI 2015]. Table 1 shows the entire experimental programme. The specimens were chosen to investigate the impact of the following constructional characteristics on the overall seismic behaviour of walls: (1) Interaction between exterior and interior frames: partition wall with double frame vs. partition wall with single external frame or partition wall with double frame vs. partition wall with single internal frame (2) The type of surrounding structural elements: steel box profiles vs. concrete blocks; (3) the presence of further finishing on the external face: a wall with no additional finishing vs a wall with additional finishing on the exterior face; (4) Sheathing panel types: GKB vs. Diamant, Aquapanel vs. Guardex, and Aquapanel vs. Vidiwall [Knauf 2022]; (5) presence of a protrusion: wall totally contained within the width of the surrounding constructional elements vs. wall with a protrusion with regard to surrounding elements; (6) External frame type: wall with C-shaped stud profiles and U-shaped track profiles vs. wall with U-shaped slotted stud profiles and slotted L-brackets; (7) the existence of additional cladding on the outside face: wall without additional cladding vs wall with additional cladding on the exterior face; (8) The sort of connections between the wall and the surrounding elements: "fixed" connections vs. "sliding" connections. Based on these characteristics, fourteen distinct walls were defined for testing.

Table 1. Experimental program.

Label	Protusion / offset (mm)	Material	Studs spaced at 600mm	Tracks / Brackets	External frame Interior face	External frame Exterior face	Internal frame Exterior face	Additional Finishing
W-01	No	Steel box profiles	C 75x50x0.6	U 75x40x0.6	1 x Diamant	1 x Aquapanel	2 x Diamant	No
W-02	No	Concrete blocks	C 75x50x0.6	U 75x40x0.6	1 x Diamant	1 x Aquapanel	2 x Diamant	No
W-03	No	Steel box profiles	C 75x50x0.6	U 75x40x0.6	1 x Diamant	1 x Aquapanel	2 x Diamant	Yes
W-04	No	Steel box profiles	C 75x50x0.6	U 75x40x0.6	1 x Diamant	1 x Aquapanel		No
W-05	No	Steel box profiles					2 x Diamant	No
W-06	No	Steel box profiles	C 75x50x0.6	U 75x40x0.6	1 x GKB	1 x Aquapanel		No
W-07	No	Steel box profiles	Slotted KAW C 150x45x1.0	1.0 mm thick. slotted L-brackets	1 x GKB	1 x Aquapanel		No
W-10	No	Steel box profiles					2 x GKB	No
W-11	Yes / 38	Steel box profiles	C 75x50x0.6	U 75x40x0.6	1 x Diamant	1 x Aquapanel		No
W-12	No	Steel box profiles	Slotted U 75x50x2.0	2.0 mm thick. slotted L-brackets	1 x Diamant	1 x Aquapanel		No
W-14	No	Steel box profiles	C 75x50x0.6	U 75x40x0.6	1 x Diamant	1 x Guardex		No
W-15	No	Steel box profiles	C 75x50x0.6	U 75x40x0.6	1 x Diamant	1 x Vidiwall		No
W-18	No	Steel box profiles	Slotted KAW C 150x45x1.0	1.0 mm thick. slotted L-brackets	1 x GKB	1 x Aquapanel		No
W-20	No	Steel box profiles	C 75x50x0.6	U 75x40x0.6	1 x GKB	1 x Aquapanel		No

The internal frame was made of C-shaped stud profiles with a cross section of 50 mm x 50 mm x 0.6 mm (height x width x thickness) spaced at 600 mm in the centre and attached to the top and bottom ends to U-shaped track profiles with a cross section of 50 mm x 40 mm x 0.6 mm (height x width x thickness). Except for slotted U-shaped profiles made of S 250GD+Z275 steel grade and slotted L-brackets made of S220GD steel grade, all cold-formed steel components, i.e., studs and tracks, were manufactured with DX51D+Z steel grade. Except for slotted KAW C shaped and U shaped studs, which were fixed to slotted L-brackets with 4.8 mm x 20 mm screws, studs and tracks were usually connected by punching.

External frames had one layer of sheathing panels on both the exterior and inner faces, while internal frames had two layers of sheathing panels only on the outside face. Except for sheathing panels, some walls were essentially the same. Except for wall W-10, where the frame was coated with two layers of GKB board, other internal frames were sheathed with two layers of Diamant board. Three distinct kinds of sheathing panels—Aquapanel (the reference sheathing panel), Guardex, or Vidiwall—were utilised for the external faces of the external frames. There were various finishing techniques utilised for each type of sheathing panel. For the GKB, Diamant, and Vidiwall boards, joints between adjacent panels were filled with tape and gypsum-based plaster; for the Aquapanel board, glass mesh tape and cement-based plaster; and for the Guardex board, a hybrid polymer-based glue.

Depending on the type of sheathing panels used, the steel profiles were fastened to the sheathing panels using self-piercing screws of various typologies: (1) 3.5 mm x 25 mm (diameter x length) or 3.5 mm x 35 mm for GKB boards; (2) 3.9 mm x 23 mm or 3.9 mm x 38 mm for Diamant boards and Guardex boards; (3) 4.2 mm x 25 mm for Aquapanel boards

With the exception of the wall W-11, which protrudes from the surrounding elements, all walls, minus any additional cladding, had their whole thickness completely contained within the breadth of the surrounding elements. The protrusion was roughly 38 mm in size. Except for wall W-07, which had a cladding made of -profiles with a cross section measuring 27 mm by 40 mm by 0.6 mm (height, breadth, and thickness) put on the outside face of the external frame, none of the walls had any additional cladding. Note that the additional external frame cladding was not regarded as a cause of protrusion from the surrounding elements.

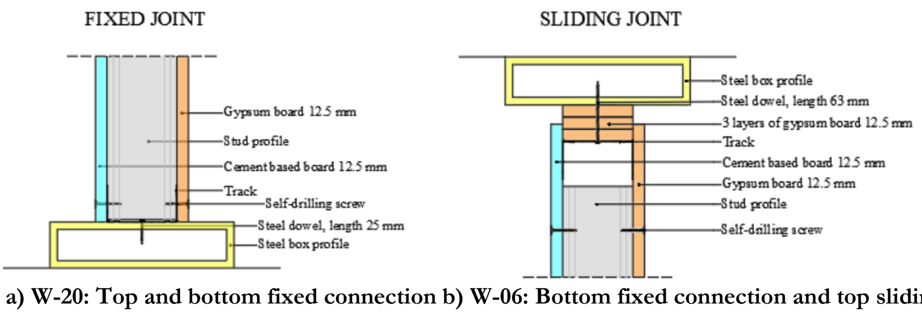

Figure 1. a) W-20: Top and bottom fixed connection b) W-06: Bottom fixed connection and top sliding connection

All walls had "fixed" connections with surrounding elements, i.e. connections which restrained both in-plane and out-of-plane displacements between the wall and surrounding elements (Figure 1a), except for wall W-06 (Figure1b), where a "sliding" connection was adopted to connect the top side of the wall to surrounding elements. Only the out-of-plane displacements between the wall and the surrounding elements were constrained by the "sliding" connection; while in-plane displacements were permitted. In particular, studs and sheathing panels in the "sliding" connection were not fastened to the tracks, leaving a gap of 20 mm between the panels and the adjacent structural components.

2.2 TEST SETUP AND LOADING PROTOCOL

As a test setup, a particular 2D hinged steel frame was used (Figue 2). Using the bottom beam of the steel frame, the walls were held to the sturdy floor of the lab. The steel frame's loading beam, which is the top beam, was subjected to horizontal displacements. In order to mimic the behaviour of vertical surrounding constructional elements of a building, two hinged rectangular hollow vertical profiles were positioned at either end of the wall. Two steel portal frames with roller wheels helped control the out-of-plane displacements. Additionally, to prevent any vertical load transfer, a sliding hinge was positioned between the loading actuator and the loading beam.

Tests were performed by subjecting the wall specimens to the loading protocol given by FEMA 461 [FEMA 2007], where the following parameters were adopted: step number *n*=16; targeted smallest deformation amplitude Δ_0 =0.0015; targeted maximum deformation amplitude Δ_m =0.03. Note that deformation amplitudes are shown in terms of IDR (Interstorey Drift Ratio) in Fig.3. The loading was continued till 8.4% IDR to observe significant damages in the wall specimens.

Figure 2. Test set-up. a) Without a specimen b) With specimen

3. EXPERIMENTAL RESULTS

3.1 LOAD VS. INTER-STOREY DRIFT CURVE

Figure 3a shows the experimental response as obtained from the load (F) vs. IDR curves for a typical wall specimen. All walls had a lateral response that was completely nonlinear, pinched in nature, and exhibited stiffness and strength degradation as displacement amplitudes increased.

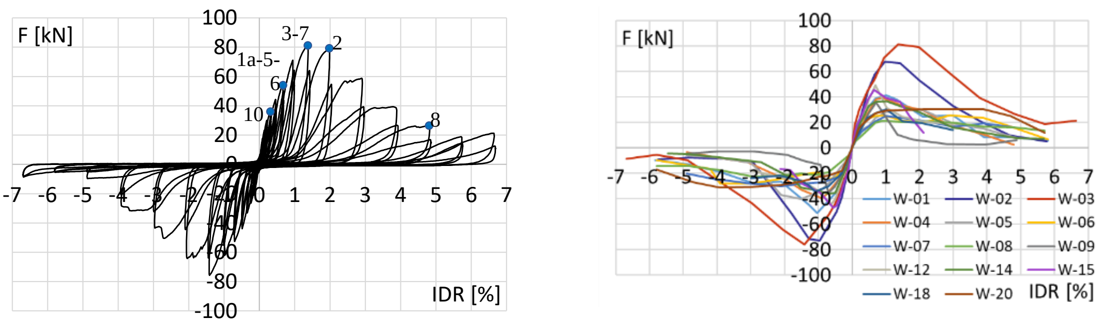

Figure 3. Load vs. IDR curves for all tests.

Different types of damage are experienced by specimens during the tests, which take place at various IDR values, as discussed in Section 3.2. In Figure 3a, each type of detected damage's trigger is represented by a dot and a number from 1 to 11. (the number from 1 to 11 corresponds to the type of damage, as defined in Table 2). Figure 3b displays the backbone envelopes for each load vs. IDR curve generated from testing.

The walls W-04 and W-05 represented the two frames that made up the wall W-01 and were tested separately to assess their contribution to the overall response of the wall W-01. Walls W-04 and W-05, in particular, constituted the exterior and interior frames of wall W-01, respectively. As can be observed from the results, wall W-01 had stiffness and strength values that were somewhat higher (by 1.2 times) than those recorded for wall W-04 and greater stiffness and strength values (by 2.0 and 1.3 times, respectively) than those recorded for wall W-05. Therefore, the contributions of the exterior (W-04) and external (W-05) frames cannot be added to yield the response of the double frame wall (wall W-01).

Specimens W-01 and W-02 were nominally similar walls except for the surrounding constructional elements, which were composed of steel box profiles for W-01 and concrete blocks for W-02. The results indicated that the wall W-02 had 1.6 times the stiffness and 1.5 times the strength of the wall W-01.

Specimens W-01 and W-03 were nominally identical walls except for the external finishing, which was formed of glass mesh and cement-based plaster on the outer Aquapanel board in wall W-03. The inclusion of a cement-based plaster reinforced by a glass mesh boosted both stiffness and strength by 1.2 and 1.7 times, respectively.

According to the results, the specimens made using Diamant boards had higher stiffness and strength values than those built with GKB boards (by 2.8 and 2.1 times, respectively, if walls W-10 and W-05 are compared, and by 3.5 and 1.3 times, respectively, if walls W-20 and W-04 are compared). The specimens constructed using Aquapanel boards had stiffness and strength values equivalent to those constructed with Guardex boards (differences between walls W-14 and W-04 were less than 10%) and lower stiffness and strength values than those constructed with Vidiwall boards (by 1.8 and 1.2 times, respectively). Finally, the specimens constructed using Vidiwall boards demonstrated stronger stiffness and strength than a wall constructed with Guardex boards (by 1.3 and 1.8 times respectively).

Specimens W-04 and W-11 were nominally identical walls, except for the presence in wall W-11 of a protrusion from the surrounding elements, whereas wall W-04 was completely contained within the width of the surrounding elements. Results showed small differences in terms of stiffness and strength (differences between walls W-14 and W-04 less than 10%).

The effect of the different external frames was investigated by comparing the response of a wall having slotted U-shaped studs connected to the surrounding elements by slotted L-brackets (W-12) or a wall having slotted KAW C-shaped studs connected to the surrounding elements by slotted L-brackets (W-18) with relevant nominally identical walls, except for the frame, made of typical C-shaped studs and U-shaped tracks, i.e. W-12 vs. W-04 and W-18 vs. W-20. According to the findings, walls with slotted U-shaped or KAW C-shaped studs and L-brackets were stiffer (by 1.7 to 2.5 times) and marginally stronger (differences less than 20%) than walls with conventional studs and tracks.

When specimens W-07 and W-18 were compared, it was discovered that adding a cladding formed of -profiles sheathed with Aquapanel panels on the outer face increased both stiffness and strength by 1.6 and 1.2 times, respectively. The inclusion of -profiles screwed to studs may have increased the overall number of fixings between Aquapanel boards and studs, resulting in an increase in stiffness. The higher number of fixings produced a limited increase in the strength due to the position of the Aquapanel boards belonging to the additional cladding, which protruded from the surrounding elements by limiting their interaction when the level of IDR increased.

Except for the connections between the wall and the surrounding constructional materials, specimens W-06 and W-20 were nominally similar walls. Walls W-20 and W-06 had "fixed" connections to the surrounding elements, whilst Wall W-20 featured a "sliding" connection between the top side of the wall and the surrounding elements. The results showed that the stiffness of the wall with "sliding" connections was 1.3 times more than the stiffness of the wall with "fixed" connections, but the strength values were equivalent (difference equal to 10 percent). As a result, "sliding" connections used on the top side of the wall had a very limited effect in terms of "isolation" between non-structural and surrounding parts. Usually, reduction in stiffness in walls with sliding connections can be achieved, if the sliding connections are provided at both sides of wall.

3.2 DAMAGE STATES AND DAMAGE MECHANISMS

The visual inspection of the specimens was used to assess the damage done to the walls during the testing. According to the existing literature [Pali et al. 2018; Restrepo and Bersofsky 2011; Retamales et al. 2013], the observation of damages was connected with three Damage States (DSs) defined according to the damage level in terms of necessary repair action and safety.

(1) DS1, characterized by superficial wall damage and no threat to life safety.
(2) DS2 is distinguished by local damage, primarily finishing, sheathing panels, and panel fixings, as well as modest damage in steel frame profiles and a moderate risk to life safety.
(3) DS3, characterized by serious wall damage and a substantial risk to life safety.

The detected damages in the tested walls are correlated to the identified DSs in Table 2. The triggered DS for panel section rupture, crushing, or spalling relied on the level of damage, i.e., this damage could correlate to DS1, DS2, or DS3 depending on the size of the implicated panel (DS1 if it was less than 25 cm², DS2 if it was from 25 to 100 cm², or DS3 if it was higher than 100 cm²). Except for the residual detachment, which was measured by the LVDTs, the damages were noticed and documented during the tests based on a visual assessment. The IDR value at which the single damage phenomenon occurred was recorded for each specimen.

Table 2. Correlation between observed damage phenomena and DSs.

Observed damage phenomena		DS1	DS2	DS3
Sheathing panels	Rupture, crushing or spalling of panel portions, Limited for DS1: less than 25 cm²; intermediate for DS2: from 25 to 100 cm²; Severe for DS3: more than 100 cm²	✓	✓	✓
	Crack in panel > 10 cm		✓	
	Out-of-plane collapse of panels without falling down of panels		✓	
	Falling down of panels			✓
Finishing	Detachment of joint cover / crack in joint finishing	✓		
Sheathing fixings	Screw tilting > 10%	✓		
	Screw breaking on panel edge or screw pull out/trough > 10%		✓	
Steel elements	Plastic deformation of studs/tracks			✓
	Stud-to-track fixing failure > 10%			✓
Global level	Residual detachment between wall and surrounding elements between 1 and 5 mm	✓		
	Wall-to-surrounding element connections failure > 10%			✓

4. SEISMIC FRAGILITY ANALYSIS

The behaviour of tested walls was influenced only by a few structural parameters, namely the presence of Diamant boards (in the case of an external frame), the protrusion of the wall with respect to surrounding elements, and the sliding connection between the top side of the wall and surrounding elements; all other design variations were ignored, and the walls were divided into three groups for developing the fragility analysis:

(1) Group I, double frame or external frame walls with common tracks and studs, Diamant boards, fixed upper connections, and no protrusion and extra finishing (W-01, W-02, W-04, W-14, W-15);

(2) Group II, external frame walls with GKB sheathing boards, fixed upper connections, and no protrusion (W-07, W-18, W-20);

(3) Group III, internal frame walls with fixed upper connections and no protrusion (W-07, W-18, W-20 (W-05, W-10).

Walls W-03 (with additional finishing), W-06 (with sliding upper connections), and W-11 (with slotted U-shaped studs and slotted L-brackets) were excluded from the above-mentioned groups due to the criterion used to group the walls with comparable behaviour.

The experimental results have been refined for the goal of determining seismic vulnerability by developing fragility curves using the approach given by Porter et al., Method A [Porter et al. 2007]. The fragility curves were created for the three defined limit states (DS1, DS2, DS3) and wall groups (I, II, III). Figure 4 a, b, and c depict fragility curves and parameters, as well as the IDR limitations (0.5, 0.75, 1.0 percent) for ductile non-structural elements defined by Eurocode 8: EN 1998-1 [CEN 2004].

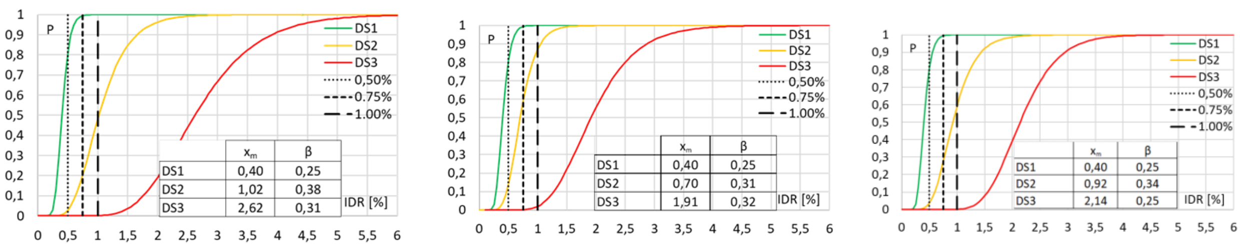

a) Group A b) Group B c) Group C

Figure 4. Fragility curves.

The study of the fragility curves reveals that each group exhibits the same behaviour for the first limit states (DS1), with log-normal distribution average values equal to 0.40 percent. For DS2, the average log-normal distribution value ranges from 0.70 percent to 1.02 percent for Group II and Group I, respectively; for DS3, the average log-normal distribution value ranges from 1.91 percent to 2.62 percent for Group II and Group I, respectively.

5. Conclusion

The experimental results and fragility analysis of lightweight steel (LWS) drywall systems are presented in this paper. In plane quasi-static cyclic loading is applied to wall specimens. The results of the experiments were directly translated into hysteretic load vs. interstory drift curves and statistics on damage development. The specimens were chosen to investigate the effect of various constructional parameters such as single or double frame walls, sheathing panels, the presence of finishes, variations in surrounding constructional structural elements, the absence of track members, the type of connection to the surrounding constructional elements, and the presence of protrusion. Fourteen distinct walls were defined for testing based on these factors.

The influence of constructive factors on the seismic response influences mainly the triggering of Damage States DS2 and DS3, whereas Damage State DS1 was always triggered for the same IDR=0.40 percent. The presence of a protrusion of the wall with respect to surrounding elements or the presence of an external frame made with U-shaped slotted studs and slotted L-brackets caused a premature triggering of damages, whereas a "sliding" connection between the top side of the wall and surrounding elements, as well as additional finishing, resulted in a premature triggering of damages. The other constructive parameters under investigation did not significantly affect the evolution of damages during the tests.

For the fragility analysis, three groups of homogeneous walls were defined: (I) double frame or external frame walls with tracks and studs, Diamant sheathing boards, fixed upper connections, and no protrusion and additional finishing (W-01, W-02, W-04, W-14, W-15); (II) external frame walls with GKB sheathing boards, fixed upper connections, and no protrusion (W-07, W-18, W-20); and (III) internal frame walls with (W-05, W-10). The evaluation of fragility reveals that Group I performed best (xm=1.02, IDR 0.78 percent to 1.53 percent for DS2 and xm=2.62, IDR from 2.14 percent to 3.00 percent for DS3), while Group II performed worst (xm=0.70, IDR 0.56 percent to 0.78 percent for DS2 and xm=1.91, IDR from 1.53 percent to 2.14 percent for DS3).

REFERENCES

CEN. [2004] *EN 1998-1 Eurocode 8: Design of Structures for earthquake resistance-Part 1: General rules, seismic actions and rules for buildings*, European Committee for Standardization, Brussels.

FEMA. [2007] *FEMA 461 : Interim testing protocols for determining the seismic performance characteristic of structural and non-structural components*, Federal Emergency Managment Agency, Washigton, D.C.

Fiorino, L., Bucciero, B., and Landolfo, R. [2019] "Evaluation of seismic dynamic behaviour of drywall partitions, façades and ceilings through shake table testing," *Engineering Structures*, Vol. 180, pp. 103–123.

Knauf, "Kanuf Product Catalog, " https://www.archiexpo.com/prod/knauf-50767.html, accessed on 02 October, 2022.

Pali, T., Macillo, V., Terracciano, M. T., Bucciero, B., Fiorino, L., and Landolfo, R. [2018] "In-plane quasi-static cyclic tests of nonstructural lightweight steel drywall partitions for seismic performance evaluation," *Earthquake Engineering & Structural Dynamics*, Vol. 47, No.6, pp. 1566–1588.

Porter, K., Kennedy, R., and Bachman, R. [2007] "Creating Fragility Functions for Performance-Based Earthquake Engineering," *Earthquake Spectra*, Vol. 23, No.2, pp. 471–489.

Restrepo, J. I., and Bersofsky, A. M. [2011] "Performance characteristics of light gage steel stud partition walls," *Thin-Walled Structures*, Vol. 49, No.2, pp. 317–324.

Retamales, R., Davies, R., Mosqueda, G., and Filiatrault, A. [2013] "Experimental Seismic Fragility of Cold-Formed Steel Framed Gypsum Partition Walls," *Journal of Structural Engineering*, Vol. 139, No.8, pp. 1285–1293.

SCI_P402. [2015] "Light Steel Framing in Residential construction, " Steel Construction Institute.

Wang, X., Pantoli, E., Hutchinson, T. C., Restrepo, J. I., Wood, R. L., Hoehler, M. S., Grzesik, P., and Sesma, F. H. [2015] "Seismic Performance of Cold-Formed Steel Wall Systems in a Full-Scale Building," *Journal of Structural Engineering*, Vol. 141, No.10, p. 04015014.

Seismic testing and multi-performance evaluation of full-scale unitized curtain walls: research overview and preliminary results

Simona Bianchi[1], Guido Lori[2], Valerie Hayez[3] , Roel Schipper[1], Stefano Pampanin[4], Mauro Overend[1], Giampiero Manara[2], Tillman Klein[1]

[1] Delft University of Technology, Delft, Netherlands
{S.Bianchi, H.R.Schipper, M.Overend, T.Klein}@tudelft.nl
[2] Permasteelisa S.p.A., Vittorio Veneto, Italy
{g.lori, g.manara}@permasteelisagroup.com
[3] Dow Silicones, Seneffe, Belgium
valerie.hayez@dow.com
[4] Sapienza University, Rome, Italy
stefano.pampanin@uniroma1.it

Abstract. Unitized curtain walls are glazing facade systems widely used in modern architecture for mid and high rise buildings, due to their benefits in terms of lightness, quality control, ease of construction and quick installation. However, recent earthquake surveys have shown damages to these non-structural elements. Slight-to-moderate damage can cause loss of facade functionality, moderate-to-major damage can provoke severe post-earthquake economic losses and pose a life-threatening danger to both building occupants and pedestrians. Despite recent studies on the seismic behavior of unitized curtain walls, research in this field is still limited and experimental investigations typically neglect the study of the overall facade performance as well as the identification of the full sequence of damage states and the ultimate resistance of the facade components.

This paper presents the extensive experimental campaign carried out at the laboratory of Permasteelisa Group, in Vittorio Veneto (Italy), to investigate the seismic behaviour of full-scale unitized curtain walls from a holistic and multi-performance perspective. The research aims at providing information about the serviceability performance and the ultimate limit state of alternative facade designs. The tests involve various facade configurations consisting of dry (gasket) vs. wet (structural silicone) glazing systems with different construction details for glass, frame and joints (dimensions and type). The testing sequence consists of displacement-control dynamic cyclic loading and/or time histories at increasingly seismic intensity levels, accounting for in-plane, out-of-plane and vertical movements. Air infiltration tests, water leakage tests and wind resistance tests are performed before and after the low-intensity seismic tests to study the post-earthquake facade serviceability. This paper discusses the research objectives, the specimen details and the test setup, and provides preliminary experimental results.

Keywords: Glass facades, Structural silicone, Experimental testing, Seismic loads, Serviceability.

1. INTRODUCTION

Unitized curtain walls are widely used by architects and system manufacturers especially for high-rise buildings (Figure 1a), due to their multiple advantages such as lightness, ease of construction, weather tightness, thermal performance and quality of detailing. Unitized systems enable straightforward processing through serial production and pre-assembly of the facade units under controlled working conditions, therefore allowing for improved quality of assembly, reduced fabrication lead-time and rapid installation.

(a) (b) (c)

Figure 1. (a) Application of unitized curtain walls to high-rise buildings - GIOIA 22 tower in Milan, Italy (by Permasteelisa S.p.A.). Seismic damage to glazed facades: (b) 2010 Chile earthquake [FEMA E-74, 2011], (c) 2011 Christchurch earthquake [Baird *et al.*, 2011]

These non-structural components consist of glass panels within metal frames anchored to the main load-bearing structure by means of connections at the floor levels. During earthquakes these glazed facades are affected directly by inter-storey drift ratios and possible displacement incompatibilities (mainly in-plane) as well as by inertia forces (mainly out-of-plane). Seismic movements can initially (if small) be sustained by the facade through internal gaps and deformations, then, if deformations become larger, local stresses concentrate in specific parts of the system and damage develops. Past earthquake events have repeatedly shown damages to unitized curtain walls (Figure 1b) and the damage mechanisms observed were: (a) gasket degradation, leading to air and/or water infiltrations; (b) glass breaking, not compromising life-safety whilst allowing even further air leakage, water infiltration and other indirect damages; (c) glass fallout, posing potential life safety hazard and causing huge economic consequences [Baird *et al.*, 2011]. Glass breaking was often due to the presence of an insufficient movement capacity of the panels. Another typical damage consisted of warping of the aluminum frame and its total or partial disconnection from the structure in case of inadequately designed connections.

Different experimental studies have been conducted to assess the seismic performance of glazing systems over the past decades. These studies focused on the investigation of the in-plane movement and drift capacity of the glass panels through in-plane monotonic and cyclic racking testing [e.g., Memari *et al.*, 2004; Caterino *et al.*, 2017] as well as through shake table testing [e.g., Wang *et al.*, 2015; Lu *et al.*, 2016], in order to study the influence of different glass typologies, clearance values and connection systems. Bi-directional tests were also performed [e.g., Behr *et al.*, 1995; Lu *et al.*, 2016] to properly identify the damage patterns and study the in-plane/out-of-plane action. It is worth noting that also the out-of-plane behaviour of glazed facades may limit the overall seismic performance, as observed in the experimental campaign carried out by Bianchi *et al.* [2021]. Furthermore, recent experimental tests performed by Arifin *et al.* [2020] aimed at studying the post-earthquake serviceability of glazed curtain walls in terms of water tightness, observing that this property was lost at a median inter-storey drift ratio as low as 0.35%. In most cases, experimental results were also used to calibrate finite element models (solid elements/shells) able to describe the facade in-plane behaviour [e.g., Memari *et al.*, 2011] or macro-models (lumped plasticity) to be used in numerical simulations of building systems [Casagrande *et al.*, 2019].

Despite previous works on the seismic performance of unitized curtain walls, research in this field is still limited and, particularly, research efforts are needed to study the facade performance from a multi-performance perspective. Towards this goal, an extensive experimental campaign is currently ongoing at the laboratory of Permasteelisa Group, in Vittorio Veneto (Italy), to investigate the overall performance of full-scale unitized curtain walls subjected to increasingly earthquake intensity levels. Air infiltration, water leakage and wind resistance tests are performed before/after the low-intensity seismic tests to study the post-earthquake facade serviceability. This paper discusses the research objectives, the specimen details and the test setup, and provides preliminary experimental results.

2. RESEARCH MOTIVATION

A series of full-scale mockup performance tests must be carried out before starting the production and the on-site assembly of a facade, in order to verify that the final product complies with the project specifications. The facade system can in fact be accepted only if it fulfills all the performance requirements. When dealing with seismic performance, specimens are typically subjected to specified horizontal displacements representing the earthquake and the seismic safety of the facade architectural components is assessed through visual inspection. Nevertheless, both the post-earthquake serviceability and the ultimate performance should be analyzed to properly identify the behaviour of the facade and its components. To this end, the proposed research aims at evaluating the performance of unitized curtain walls from a multi-performance perspective. Moreover, the following main objectives are pursued:

i. *Influence of facade detailing on the seismic behaviour*. Experimental tests are carried out on specimens consisting of dry-glazed (with rubber gasket, DG) and wet-glazed (structural silicone glazing, SSG) systems, different glass units (panel dimensions, double-pane or triple-pane glass) and joints (aspect ratio, type of silicone). This allows to investigate the influence of alternative details on the facade response. By comparing the performance of all the alternative solutions, adequate strategies/materials/elements can be proposed to enhance the facade behaviour.

ii. *Calibration of numerical modelling*. Numerical simulations represent the main tool for a designer to validate the facade performance prior to the experimental testing, especially in case of bespoke curtain wall manufacturing. However, enhanced modelling strategies should be developed to support the numerical study of unitized curtain walls. The research aims at developing finite element models (FEM) able to describe either the local (joint/connection) response or the global (facade) behaviour. Furthermore, equivalent spring models for both joints and facades (lumped plasticity models) are developed based on FEM and experimental results. These models could be useful to assess the expected facade seismic response at early design stage.

iii. *Investigating the facade modes of failure*. As mentioned above, during the seismic testing protocol required for a specific building project, the only intent is to prove that the facades comply with the project requirements. The ultimate resistance and the different mode of failures of the facade are generally unknown. For this reason, in addition to the serviceability performance at lower seismic intensities, the experimental campaign aims at collecting relevant information regarding the maximum seismic levels that the facade is able to resist prior to its structural failure. This would allow to identify design and application issues related to the structural and infiltration performances that might arise during their life cycle. Therefore, this study could provide useful indications on how to improve the existing guidelines/codes in terms of displacement verifications and seismic (displacement) demands to be considered in order to verify the façade functionality and safety.

3. EXPERIMENTAL CAMPAIGN

3.1 TEST FACILITY

The experimental campaign is carried out at the Permasteelisa laboratory in Vittorio Veneto, Italy, where full-scale facades up to about 10m width and height can be tested. The specimens can be anchored to the available steel support structure at three levels: two upper and lower fixed beams and an intermediate moving beam (Figure 2a). By means of a hydraulic actuator able to apply a maximum displacement of ± 75 mm in the in-plane horizontal (X) and vertical (Y) directions and ± 50 mm in the out-of-plane (Z) direction, a range of velocities (11-60mm/s) can be applied to impose the displacement history at low-to-higher frequencies (0.25-1Hz). The actuator is interfaced with a digital controller and a control panel to apply the desired displacement. Specimens can be tested in two different layouts (Figure 2b): (a) L1, to test single-storey glazed units or units in a row; (b) L2, to test facades on two levels. L1 allows to study and compare the behaviour of alternative facade systems. Although not representing a real scenario where different inter-story drift ratios are expected at the two floor levels, L2 is generally used in performance tests to study the facade movement at the horizontal joint and verify compliance with the project requirements.

(a)

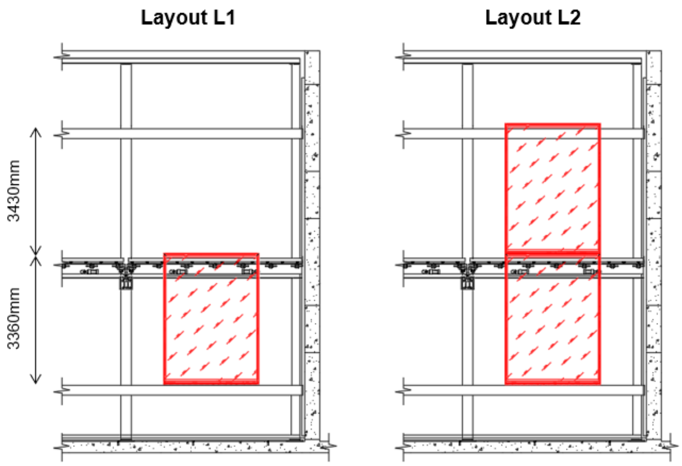

(b)

Figure 2. (a) Seismic performance test facility, highlighting the blue "seismic beam" and the in-plane X horizontal and Y vertical directions. (b) Possible testing layouts for the facade specimens (assuming one unit at each level)

3.2 SPECIMEN CONFIGURATIONS

Four full-scale unitized curtain walls are available for the experimental testing (Figure 3), each designed for a specific building project. *Facade T1* is composed of two SSG modules of 3430mm height and 1267.5mm width and one large dry-glazed module of 2535mm width. *Facade T2* is a full DG system comprising four identical units, all characterized by 3500mm height and 2700mm width. *Facade T3* is a SSG system consisting of eight units of 3850mm height, four with 1500mm width and four with 2250mm width. *Facade T4* is another SSG system consisting of eight units of 3850mm height, four with 1500mm width and four with 2691mm width. In addition to the units dimensions, the four alternative facades are characterized by different aluminum profiles (material type, cross-section of mullions and transoms, male-female joint connection), glass panels (double or triple panes), thermal bridging solutions, presence or absence of openings in the units, type and dimension of gasket and structural sealant. Moreover, the systems can be tested in layout L1 or L2 assembled in their original configuration and/or a modified experimental arrangement, i.e. joint modifications in order to transform a DG system into a SSG module or to test different conditions of structural silicone (material type and aspect ratio). This system variability creates a set of parametric configurations to be tested and compared in terms of performance during the entire experimental campaign, therefore allowing to investigate the influence of the construction details on the facade behaviour.

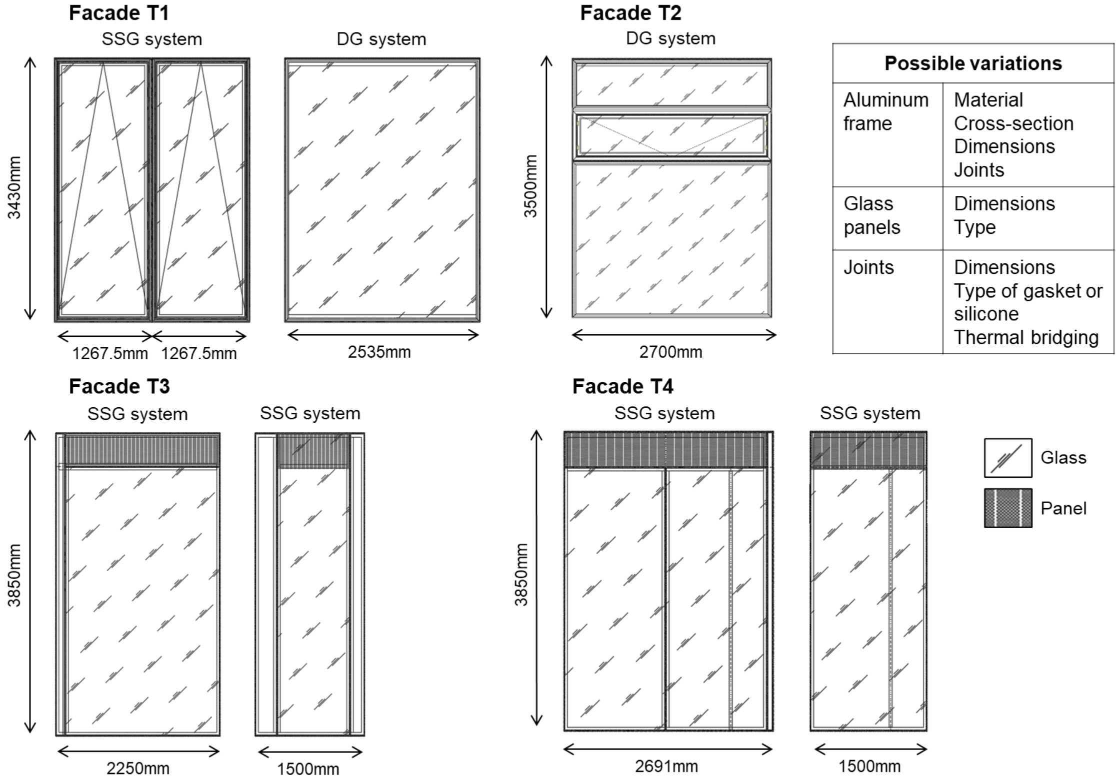

Figure 3. Facade types available for testing

3.3 TESTING PROTOCOL

The testing protocol involves a series of experiments applied on the same test chamber, in order to assess the facade overall performance in terms of air infiltration, water penetration, wind resistance and seismic resistance. Air infiltration test is carried out under static pressure to determine the air leakage through the facade specimen at specified differential pressures induced across the assemblies [EN 12153, 2000]; the air leakage rates are compared against the acceptable rates identified for the specific project. Water penetration test is performed under static pressure by applying a differential pressure across the curtain wall assembly, while simultaneously applying water spray on the exterior facade surfaces [EN 12155, 2000]; the water leakage is checked through simple visual inspection. Wind resistance test is carried out based on both serviceability and safety requirements by applying positive and negative pressure increments to the specimen, then the pressure is dropped to zero [EN 12179, 2000]; frontal deflections are recorded on both glass and frame to verify that the deformation limits are not exceeded. During the experimental campaign, air permeability test, water leakage test and wind resistance test are performed before and after the low-intensity seismic tests to study the facade functionality.

Concerning the seismic resistance test, this is typically applied following a code-compliant procedure [e.g. JASS14, 1996] which involves the application of in-plane horizontal drift levels, representing earthquakes with different return periods. To properly analyse the seismic response of unitized curtain walls, seismic displacements are applied in all the directions of the moving beam (horizontal X and vertical Y in-plane, Z out-of-plane) at increasingly intensity levels. Moreover, to study the failure mechanism for specific facade configurations, the displacement demand is increased till the maximum displacement capacity of the test rig (± 150 mm, to be achieved by modifications to the existing seismic beam).

Based on the discussion above, Table 1 shows a typical test matrix to be followed during each experiment.

Table 1. Test matrix

ID	Type	Description
1	Air	Pre-seismic: Air infiltration test (procedure for fixed joints and openings, pressure/suction)
2	Water	Pre-seismic: Water penetration test (pressure/suction)
3	Wind	Pre-seismic: Wind resistance test at serviceability level (pressure/suction)
4	Seismic	Seismic level 1 (H/300 displ. for X, Z directions, 30-50% intensity Y direction): cyclic loading or real time-history (separately and/or simultaneously in all the directions)
5	Air	Seismic level 1: Air infiltration test (procedure for fixed joints and openings, pressure/suction)
6	Water	Seismic level 1: Water penetration test (pressure/suction)
7	Wind	Seismic level 1: Wind resistance test at serviceability level (pressure/suction)
8	Seismic	Seismic level 2 (H/200 displ. for X, Z directions, 30-50% intensity Y direction): cyclic loading or real time-history (separately and/or simultaneously in all the directions)
9	Air	Seismic level 2: Air infiltration test (procedure for fixed joints and openings, pressure/suction)
10	Water	Seismic level 2: Water penetration test (pressure/suction)
11	Wind	Seismic level 2: Wind resistance test at serviceability level (pressure/suction)
12	Seismic	Seismic level 1 (H/100 displ. for X, Z directions, 30-50% intensity Y direction): cyclic loading or real time-history (separately and/or simultaneously in all the directions)
13	Wind	Seismic level 3: Wind resistance test at safety level (pressure/suction)
14	Seismic	Seismic level 4 (failure test): monotonic or cyclic loading (in-plane X direction)

4. PHASE 1 - PRELIMINARY RESULTS

4.1 SPECIMEN DETAILS

The first experiments were conducted on *Facade T1*, which was assembled in two different configurations: (a) SSG units only and (b) overall *Facade T1*, both tested in layout L1 as shown in Figure 4 (a,b).

(a) (b) (c)

Figure 4. Facade specimens tested in the first experimental phase: (a) SSG units of *Facade T1* in layout L1, (b) *Facade T1* in layout L1. (c) Joint detailing of *Facade T1*

The facade framing consists of aluminum (type 6063 T6) extruded profiles, where mullions and transoms are connected through screwed joints while mullions of different units by male-female joints, including thermal breaks and anti-buckling local components. Figure 4c shows the typical joint detailing of the dry (with rubber gasket) and wet (with structural sealant) triple-glazing units. The SSG units embed DOWSIL™ 993 structural glazing silicone with dimensions of 26mm bite and 8mm thickness for both mullions and transoms. The fastening system to the main steel structure consists of hooks, brackets and adjusting bolts for the connection to the upper (moving) beam, while brackets and bolts for connecting the starter sill to the lower (fixed) beam. The starter sill is, in turn, connected to the bottom transom of the units by means of screwed allignment blocks and shear keys. Each unit requires two hooks for the upper anchorage to the structure. These hooks have different constraints in the horizontal in-plane direction: one hook is fixed (by using screws) while the other hook is free to move; this constraint scheme is applied to allow the unit to accommodate thermal and building differential movements. In addition to the rotation, the hooking connections also allow to accommodate construction tolerances. Vertical tolerance is accommodated using adjusting bolts, while horizontal tolerance is provided by the clearance between the hook and the steel plate.

It is worth noticing that, in order to perform the other performance tests (air/water/wind) on the same testing chamber, after the assembly of the facade units by their uplifting through a crane and subsequent fastening to the support steel structure, wooden panels were installed and connected to the glazed units by a waterproofing shealth to make the full mock-up airtight (as shown in Figure 4).

4.2 MONITORING SYSTEM

Instrumentation layouts were properly designed for both specimens to capture the in-plane and out-of-plane facade movements under cyclic loading. The monitoring system of the first configuration (SSG units) included a total of 24 potentiometers (PT, 50mm or 100mm stroke) and 3 laser sensors (LS, 200mm or 500mm detection). These sensors were used to record the vertical and horizontal displacements of glass panels and framing system (Figure 5), as well as the displacements of the upper central bracket/hook, the lower central bracket and the seismic beam.

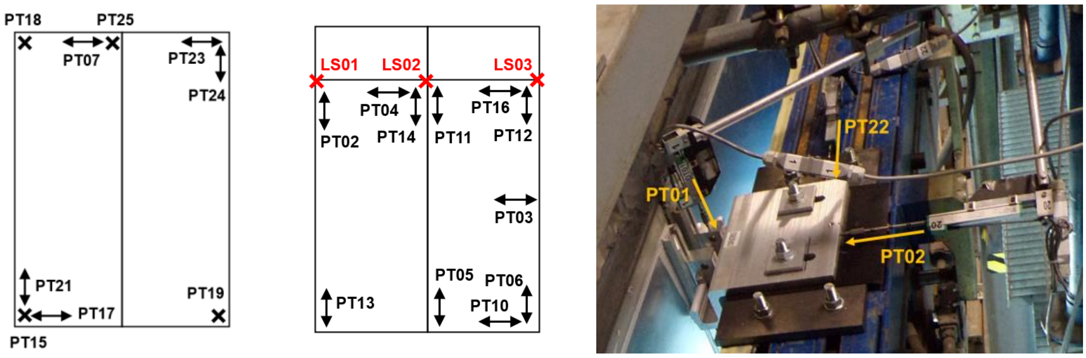

(a) (b) (c)

Figure 5. Monitoring system used for Specimen 1 (SSG units): (a) glass panels (external view), (b) frame system (internal view), (c) upper bracket connection

The monitoring system of the second configuration (*Facade T1*) included additional sensors: 6 linear transducers (200mm stroke), 4 draw wires (50mm measurement range) and 6 bi- or tri- directional accelerometers (± 6g). The displacement sensors were placed following a similar configuration as per Specimen 1, but focusing on the large dry glazed unit and the internal SSG unit. Draw wires were used to monitor the diagonal and corner elongations of the frame, while accelerometers measured the accelerations at the centre of the panels, at the bracket connections and on the seismic beam. Measurements were acquired through the same data acquisition device and controller and adjusted by applying calibration factors to consider the measurement accuracy. A second order Butterworth low-pass filter was applied to the recorded acceleration data to eliminate noise outside of the range of response.

In addition to videos recording front/elevation/joint views, two cameras (Pentax K70) were used to capture multiple scans and acquire repeated point clouds during the seismic testing. These set of recordings enabled to detect deformations at specific locations of the glass panels through Digital Image Correlation.

4.3 TESTING SEQUENCE

The first experimental phase served as validation of the proposed testing protocol involving air infiltration, water leakage, wind resistance and seismic resistance tests. As the calibration of the numerical modeling of both specimens (with DG vs. SSG units) was one of the main objectives of this phase, cyclic tests were only performed at two different seismic intensities, namely: a) *Seismic Level 1*, corresponding to 10 cycles at ± 12mm displacements (around 0.35% drift), signal frequency of 0.24Hz, applied separately in the horizontal directions X (in-plane) and Z (out-of-plne), plus ±6mm for the vertical Y direction for Specimen 2 only; b) *Seismic Level 2*, simulated by 10 cycles at ± 24mm displacements (0.70% drift), signal frequency range of 0.24-0.45Hz, applied separately in both horizontal directions X and Z (and increased to ± 36 mm in the X direction for Specimen 2, for which ± 12mm was also applied in the vertical Y direction). All the other performance tests (air infiltration test up to a pressure of 600 Pa, water penetration test up to a pressure of 900 Pa, wind resistance test up to a pressure of 1500/1900Pa for pressure/sunction) were carried out in the pre-seismic and post-seismic conditions for Specimen 2 (after *Seismic Level 1* only, representing the serviceability limit state for the specific project), while the air permeability test was only performed for Specimen 1. It is worth noting that, due to the presence of the openings in the SSG units, the air permeability test was also conducted after the application of tape at the internal perimeter of the frame (simulating the case of fixed joints) in order to investigate the influence of the openings. A wind test at safety level (wind load amplified by a safety factor of 1.5) was finally performed after *Seismic Level 2* for Specimen 2.

4.4 PRELIMINARY RESULTS

The displacements recorded on the facade components (glass panels, internal frame, connection systems) allow to study the global behaviour of the specimens under cyclic dynamic motions. Focusing on Specimen 1 (SSG units only), the rotational behaviour of the facade units is evident when the horizontal in-plane displacement is applied to the seismic beam (Figure 6). To adapt to the inter-storey drift, the whole facade unit first rotates rigidly, then the aluminum frame undergoes deformations by rotations in the corners, the structural silicone sealant between the glass and the aluminum frame deforms in shear to accommodate the inter-storey drift and the glass panel rotates as a result of forces imposed by the structural silicone. By elaborating the displacement data (+X direction) and accounting for geometrical considerations, it is found that the glass panels rotates by 0.12-0.30° while the frame by 0.21-0.40° (diagonal elongations of 1.6-2.0mm) during Seismic Level 1-2, where the rotations are measured referring to the component diagonal. When the horizontal -X displacement is analyzed, it is observed a reduced rotation of the glass panels when compared to the +X direction for both Seismic Level 1 and 2 (rotations become 0.01-0.18°) and a sliding of the glass on the support blocks is also recorded. As highlighted in a previous study by Galli (2011), this behaviour is due to the alignment screw in the bottom transom representing a restraint in the horizontal translation: (a) during the positive motion, it enables the mixed rotational and deformational behaviour of the unit, (b) during the negative motion, it induces a total deformational behaviour of the unit (rhomboidal shape).

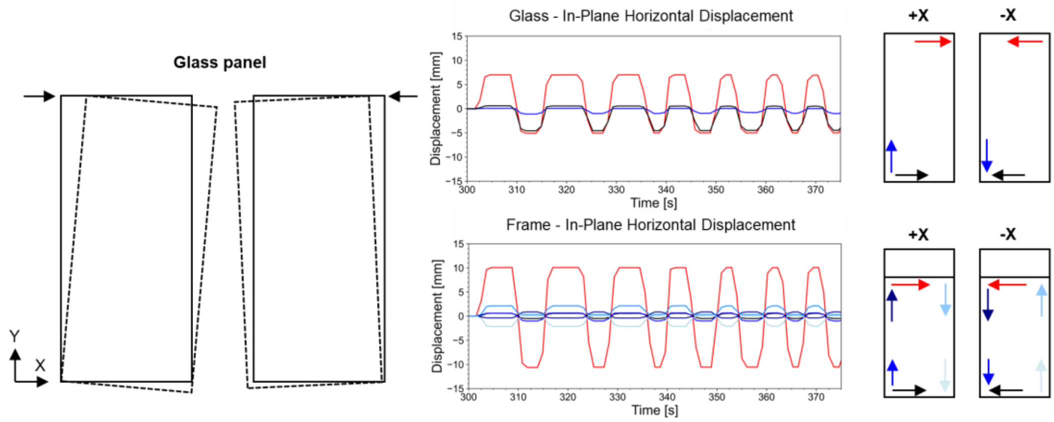

Figure 6. Rotations of the glass panel during Seismic Level 1, ± 12mm X direction, and displacements recorded

During the seismic motion, the aluminum frame deforms and its male-female mullions are slightly able to slip vertically relative to each other. It should be highlighted that the vertical measurements at the bottom corner of the frame could be used (indirectly) to calibrate spring models describing the behaviour of the sill/transom connection (free to uplift whilst resisting to the movement in the negative direction). The same consideration applies to the measurements at the hook/bracket, useful to calibrate spring models to simulate the connection to the seismic beam. In addition to the independent dynamic behaviour of facade attached to the main frame structure, the hook-bracket system contributes in reducing the seismic displacements of around 25% from the beam to the glass. When referring to the out-of-plane Z direction, the rotation of the units is facilitated by the hook and the clearance in the sill/transom. A maximum tilt of around 0.20-0.40° is recorded on the glass panels for both the positive and negative directions. It is finally highlighted that negligible residual displacements are recorded (less than 1mm in all directions) meaning that the frame behaved in the elastic domain, while glass-frame relative displacements achieve a maximum of 4.9mm (glass/frame clearance is 8mm). Table 2 summarizes the displacements measured for Specimen 1.

Table 2. Displacements (max/min) recorded for Specimen 1 (SSG units)

	Glass		**Frame**		**Glass**		**Frame**	
	X dir. (±12mm)	Z dir. (±12mm)	X dir. (±12mm)	Z dir. (±12mm)	X dir. (±24mm)	Z dir. (±24mm)	X dir. (±24mm)	Z dir. (±24mm)
Displ. [mm]	Max/Min	Max/Min	Max/Min	Max/Min	Max/Min	Max/Min	Max/Min	Max/Min
IP_H_Top	9.4/9.4	0.0/0.1	10.6/10.1	0.2/0.0	20.8/19.2	0.2/0.1	20.5/20.0	0.1/0.3
IP_H_Bot	4.6/0.6	0.0/0.0	0.5/0.6	0.1/0.0	5.5/1.5	0.0/0.0	0.5/1.2	0.0/0.2
IP_V_Top	0.9/2.8	1.2/1.1	0.4/2.1	0.2/0.3	1.1/6.5	3.2/2.2	5.5/0.8	0.9/0.3
IP_V_Bot	1.1/0.1	1.2/1.1	2.1/0.7	0.2/0.1	3.9/0.4	1.7/2.7	0.5/5.3	0.1/0.7
OOP_Top	0.5/0.3	11.8/12.2	0.6/0.3	6.4/6.5	1.2/0.4	22.1/24.5	0.8/0.2	12.6/12.6
OOP_Bot	0.0/0.7	0.4/0.3	-	-	0.4/0.7	0.7/0.9	-	-

Note: 1) IP = In-Plane, OOP= Out-Of-Plane, H = Horizontal, V = Vertical; 2) max/min refer to the local axes of the sensors.

Regarding Specimen 2 (*Facade T1*), the following main conclusions can be drawn. Although characterized by different geometrical dimensions, Specimen 2 allows to compare the behaviour of the DG and SSG units. The different rotations of the glass panels in the positive and negative direction are still observed for both units, although more limited than the previous test. For smaller X displacements, the glass panels undergo rotations less than 0.1° while for higher displacements the SSG units rotate more than the DG unit (0.52° for SSG, 0.46° for DG). Vertical displacements at the bottom corners of the glass panels are higher for the larger DG unit (16.1mm) when compared to the smaller SSG unit (7.3mm), as shown in Table 3.

Table 3. Displacements (max/min) recorded for Specimen 2 at Seismic Level 2 (DG vs. SSG)

	Glass - DG		**Frame - DG**		**Glass - SSG**		**Frame - SSG**	
	X dir. (±36mm)	Z dir. (±24mm)	X dir. (±36mm)	Z dir. (±24mm)	X dir. (±36mm)	Z dir. (±24mm)	X dir. (±36mm)	Z dir. (±24mm)
Displ. mm]	Max/Min	Max/Min	Max/Min	Max/Min	Max/Min	Max/Min	Max/Min	Max/Min
IP_H_Top	33.5/32.5	1.9/1.2	26.7/29.2	0.3/0.4	32.4/33.5	0.4/0.2	23.5/29.4	0.5/0.3
IP_H_Bot	2.5/6.9	0.7/0.3	1.4/5.0	0.2/0.1	4.1/5.1	0.6/0.1	2.2/2.6	0.4/0.0
IP_V_Top	-	-	21.1/3.5	1.2/3.1	-	-	8.8/1.1	1.1/0.8
IP_V_Bot	1.5/16.1	4.1/2.4	3.1/19.7	2.9/0.5	0.8/7.3	2.9/3.3	2.2/9.5	1.0/1.3
OOP_Top	1.9/0.6	23.6/25.2	2.4/8.7	21.6/19.6	4.3/4.8	23.5/26.7	1.4/1.7	22.2/18.9
OOP_Bot	0.3/0.6	1.0/0.9	0.3/0.1	0.6/0.7	0.4/1.2	1.0/1.1	-	-

Note: 1) IP = In-Plane, OOP= Out-Of-Plane, H = Horizontal, V = Vertical; 2) max/min refer to the local axes of the sensors.

Focusing on the frame behaviour, higher vertical displacements are recorded for the larger unit, also experiencing defomations in the out-of-plane direction (8.7mm), while the different behaviour in the positive/negative direction is due to the sill/transom and hook/bracket connections, as previously discussed. Referring to the draw wire located at the corner of the large frame, a maximum elongation of 2mm is found which confirms the rotational behaviour of the corner instead of a full rigidity. Residual displacements are below 2mm thus the frame still behaved in the elastic domain, and the frame/glass relative displacements are less than 7mm (higher in the vertical direction). When the out-of-plane Z and vertical Y motions are analyzed, a similar behaviour is found for the SSG and DG units.

Although Specimen 2 experienced an inter-storey drift of 1% (representing the design drift level for the building project), the facade behaved very well due to its detailing and internal gaps and no potential damage mechanism was observed. The only negligible damage noticed during the disassembly phase was the distortion of the anti-buckling components located between the vertical mullions. Concerning the post-earthquake serviceability of the specimens, the facades maintained their performance after Seismic Level 1 (0.35% drift level). Specifically, performance tests on Specimen 2 highlighted that: (a) the air leakage - measured per unit length of openings, $m^3/h\ m$ - was negligible in case of pressure, while higher losses were measured in the suction phase for the no tape scenario (with openings), probably due to the units subjected to other performance tests before the planned campaign; overall, the air tightness was preserved and the facade maintained the same class A4; (b) no water penetration was observed after Seismic Level 1; (c) frontal deflections slightly increased for the frame when the wind test was performed in the post-earthquake scenario. For the wind test at safety level, despite the expected noise in the suction phase due to the presence of the openings, out-of-plane displacements reached 5mm and 7mm for glass and frame, respectively, that are deflection values which highly satisfy the deflection limits (around 18mm for the glass and 16mm for the frame) as defined in UNI EN 13830 (2022).

5.CONCLUSIONS

The paper describes the experimental campaign currently ongoing at the laboratory of Permasteelisa Group, in Vittorio Veneto (Italy), to investigate the serviceability and ultimate seismic performance of unitized curtain walls. The research project aims at pursuing multiple objectives, namely: (a) the study of the influence of various facade details on the overall behaviour (b) the calibration of proper numerical modelling (distributed and lumped plasticity), (c) the study of the damage mechanisms developing until failure. The paper describes the alternative facade designs available for testing, consisting of various architectural features for glass/frame/joints, to be compared from a holistic perspective. The paper discusses the testing protocol involving seismic tests at increasingly intensity levels, and air permeability, water resistance and wind resistance tests at the lower intensities. Preliminary results are provided for two specimens composed of structural silicone sealant and dry glazed units. Experimental data are elaborated to investigate the seismic response of the facade units in all the directions, by deriving max./min. displacements and accelerations, rotations, frame elongations, residual displacements and relative glass-frame displacements. Both specimens behaved well and maintained their serviceability performance in the post-earthquake scenario (drift level of 0.35%). As further investigation, the whole facade will be converted into a fully structural silicone glazed system and tested either following the same protocol, for comparison purposes, or until failure.

6. ACKNOWLEDGEMENTS

This study has received funding from the European Union's Horizon 2020 research and innovation programme under the Marie Skłodowska-Curie grant agreement No. 101029605 (H2020-MSCA-IF-2020 - SAFE-FACE - Seismic SAFety and Energy efficiency: Integrated technologies and multi-criteria performance-based design for building FACadEs) for Simona Bianchi. The Authors also acknowledge the valuable contribution and support provided by the technicians Matteo Dazzan and Gianluca Casagrande.

7. REFERENCES

Arifin, F.A., Sullivan, T.J., Dhakal, R.P. [2020] "Experimental investigation into the seismic fragility of a commercial glazing system," *Bulletin of New Zealand Society and Earthquake Engineering*, Vol. 15, No. 3, pp. 144-149.

Baird, A., Palermo, A., Pampanin, S. [2011] "Facade damage assessment of multi-storey building in the 2011 Christchurch earthquake," *Bulletin of New Zealand Society and Earthquake Engineering*, Vol. 44, No. 4, pp. 368–376.

Behr, R.A., Belarbi, A., Culp, J.H. [1995] "Dynamic racking tests of curtain wall glass elements with in‐plane and out‐of‐plane motions," *Earthquake Engineering and Structural Dynamics*, Vol. 24, No. 1, pp. 1-14.

Casagrande, L., Bonati, A., Occhiuzzi, A., Caterino, N., Auricchio, F. [2019] "Numerical investigation on the seismic dissipation of glazed curtain wall equipped on high-rise buildings," *Engineering Structures*, Vol. 179, pp. 225-245.

Caterino, N., Del Zoppo, M., Maddaloni, G., Bonati, A., Cavanna, G., Occhiuzzi, A. [2017] "Seismic assessment and finite element modelling of glazed curtain walls," *Structural Engineering and Mechanics*, Vol. 61, No. 1, pp. 77-90.

EN 12153 [2000] "Curtain Walling – Air Permeability – Test Method," European Committee for Standardization.

EN 12155 [2000] "Curtain Walling – Watertightness – Laboratory Test Under Static Pressure," European Committee for Standardization.

EN 12179 [2000] "Curtain Walling – Resistance to Wind Load," European Committee for Standardization.

FEMA E-74 [2011] *Reducing the Risks of Nonstructural Earthquake Damage – A Practical Guide*, Federal Emergency Management Agency, Washington, USA.

Galli, U. [2011] "Seismic behaviour of curtain wall facades – A comparison between experimental mock-up test and finite element method analysis," *Individual Study*, Technical University of Milan, Italy.

JASS14 [1996] "Japanese Architectural Standard Specification Curtain Wall," Architectural Institute of Japan.

Lu, W., Huang, B., Mosalam, K.M., Chen, S. [2016] "Experimental evaluation of a glass curtain wall of a tall building,"*Earthquake Engineering and Structural Dynamics*, No. 45-7, pp. 1185-1205.

Memari, A.M., Behr R.A., Kremer P.A. [2004] "Dynamic racking crescendo tests on architectural glass fitted with anchored pet film," *Journal of Architectural Engineering*, Vol. 10, No. 1, pp. 5-14.

Memari, A.M., Shirazi, A., Kremer, P.A., Behr, R.A. [2011] "Development of Finite-Element Modeling Approach for Lateral Load Analysis of Dry-Glazed Curtain Walls," *Journal of Architectural Engineering*, pp. 17-1.

UNI EN 13830 [2022] "Curtain walling - Product standard," European Committee for Standardization.

Wang, X., Pantoli, E., Hutchinson, T.C., Restrepo, J.I., Wood, R., Hoehler, M.S., Grzesik, P., Sesma, F.H. [2015] "Seismic performance of cold-formed steel wall systems in a full-scale building," *Journal of Struct. Engineering*, Vol. 141, No. 10.

Shaking Table Tests of a Braced Outdoor Aircon Unit

Baofeng Huang[1], Meng Cheng[2], and Wensheng Lu[3]

[1] College of Civil Engineering, Shanghai Normal University, Shanghai 201418 China, email: baofeng@shnu.edu.cn
[2] College of Civil Engineering, Nanjing Tech University, Nanjing 211800 China, email: cm@njtech.edu.cn
[3] College of Civil Engineering, Tongji University, Shanghai 200092 China, email: wally@tongji.edu.cn

Abstract.

The split-system aircons are widely used in many building structures. The seismic performance of the outdoor unit is not well understood so that extensive seismic damage appeared in recent earthquakes. To investigate the seismic performance of the outdoor aircon unit, a campaign of shaking tables tests was carried out. A rigid steel frame was built and fixed on the shaking table to host the aircon unit and impose the possible earthquake motions generated by the shaking table. The aircon unit was installed on a pair of triangular steel braces, which is a typical support type. The finite element model of the rigid frame and the braced aircon unit was built with OpenSees, where the aircon unit was modelled with a converged mass and simplified spring model. Four artificial motions namely AC156, FEMA 461 and sine-sweep motions were generated as the input motions for the shaking table tests. The seismic responses such as the acceleration, displacement, and stress of the aircon unit were observed and compared to those obtained from the analytical results. The experimental and analytical results matched with each other well. The seismic responses to the input motions generally increased with the with increasing input peak accelerations (IPAs). Yielding of the steel braces appeared at IPA > 0.3 g. For the codified testing protocols, the seismic responses to the sine-sweep motions were obviously larger than those generated with AC156 and FEMA461. This study is beneficial to understand the seismic qualification of the aircon unit and other nonstructural components in buildings.

Keywords: Aircon unit, Seismic response, Nonstructural component, Shaking table, Floor motion.

1. INTRUDUCTION

A significant advancement in the seismic deign of the building structures has been made in the past century. While the seismic performance of the nonstructural components (NCs) is relatively not well understood. In comparison to the structural components such as columns, beams, and slabs, NCs do not share the load in the primary structural system. However, during an earthquake, they must subject the inertia load and/or the story drift passing from the structure they are attached to. For the properly designed and constructed buildings, it has been demonstrated that the economic losses resulting from the nonstructural damage exceed the structural losses in most recent earthquakes [Filiatrault *et al.*, 2021]. In modern buildings particularly the hotel, office, and hospital buildings, NCs account for most of the economic cost [Miranda and Taghavi, 2003]. Consequently, in the community of earthquake engineering, extensive attention has been paid to the seismic performance of the NCs particularly recently [Soong, 1995; Filiatrault and Christopoulos, 2002]. The NCs consist of pipelines, ductworks, cable trays, building envelopes, equipment, and so on. It is more complicated than the building structures in terms of structural types and seismic responses. As a result, the code provisions on seismic design of various NCs are not so advanced like those on the structural components. To fill this gap, comprehensive analytical and experimental works should be carried out to understand the seismic behavior of the NCs. Then the seismic design procedures should be developed to ensure the seismic safety of the NCs in the expected earthquake excitations. According to the intensity of the seismic response of the NCs to the earthquake excitations, NCs are classified into three categories namely acceleration, velocity, and displacement sensitive NCs [FEMA, 2012]. The computation method of the equivalent seismic design force is specified in ASCE 7-16 [ASCE, 2017]. However, it is applicable only to the acceleration sensitive NCs. To verify the seismic performance of the NCs, shaking table test is one of the reliable approaches to investigate the seismic performance of the NCs [Huang *et al.*, 2017]. For the acceleration sensitive NCs mounting on floors, roofs, and other locations of the buildings, earthquake excitations are easily reproduced by the shaking table when the NCs are fixed on the table. Insufficient anchorage of NCs was supposed to be the main cause of the earthquake damage, Mahrenholtz *et al.* [2014] carried out shaking table tests of an idealized suspended NCs anchored in crack concrete component. Feinstein and Moehle [2022] developed a novel yielding anchor for the connection between the floor and the floor mounted NC. The flexibility of the connection led to the increment of the displacement due to rotation of the NC. The nonstructural infill wall, cladding, and buttoned glass façade were supposed to be drift sensitive NCs. They were installed in a ½ scaled reinforced concrete frame fixing on a shaking table [Bianchi *et al.*, 2021]. Damage to the partition walls were found under high-level earthquake excitation. Whereas the building envelope system behaved well without visible damage in the whole test campaign. In modern industrial buildings, complex equipment is installed in the building structure due to their functionalities. Shaking table tests of the multi-framed equipment such as tanks, pipelines with specific fasteners were carried out with spectrum-compatible motions in Butenweg *et al.*, [2021]. The relatively heavy NCs in comparison to the steel frame caused the dynamic interaction between the two systems. For the light NCs such as ceiling, cladding, and aircon unit, the dynamic interaction can be ignored. The shaking table tests on the aircon unit are rarely report in literature.

In this study, a full-scale external aircon unit was installed in a rigid steel fame fixing on a shaking table. A pair of steel braces were employed to provide structural support for the aircon unit. Free vibration tests of the braced aircon unit were performed to obtain the dynamic properties of the bracing system. Four motions were generated following the protocols following the code provisions namely AC156, FEMA 461 and Retamales *et al.* [2011] on shaking table testing of the NCs. Seismic responses of the braced aircon unit were measured for evaluation of its seismic performance. Numerical model of the testing system was built with OpenSees [Mazzoni *et al.*, 2006]. The experimental and numerical results were in agreement with each other. This work is beneficial to understand the seismic performance of the aircon unit under code-compatible motions. It is also referable to the shaking table qualification testing and seismic evaluation of the various NCs.

2. SPECIMEN AND METHODOLOGY

2.1 TEST SPECIMEN

The external aircon unit is widely used in China and the rest of the world (Figure 1a). It is generally supported by two triangular steel braces anchoring on the façade of the buildings. Each steel brace simply consists of three angle steels with bolt connections (Figure 1b). The vertical angle steel is fixed on the façade wall of the building with anchor bolts (Figure 1c). The horizontal angle steel provides structural support for the aircon unit with bolt connections at the bottom of the aircon. The inclined angle steel provides vertical support of the aircon. The cross section of the angle steels is thin and concise (Figure 1d). Its seismic performance should be verified with shaking table tests. A rigid steel frame was constructed with rectangular steel tube (200 mm × 180 mm × 10 mm). The dimension of the frame is 2300 mm × 2100 mm × 3200 mm (Figure 2a). As indicated in Lu *et al.* [2017], the function of the frame is to impose the input motions of the shaking table to the aircon unit fixing on the frame with negligible flexible deformation. The aircon unit was installed on the frame with the two braces as shown in Figure 1b,c,d.

(a). Onsite layout

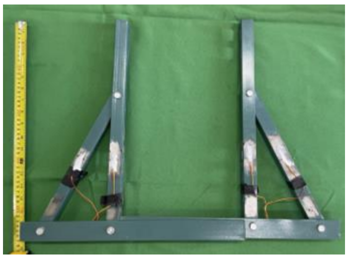

(b). Steel braces

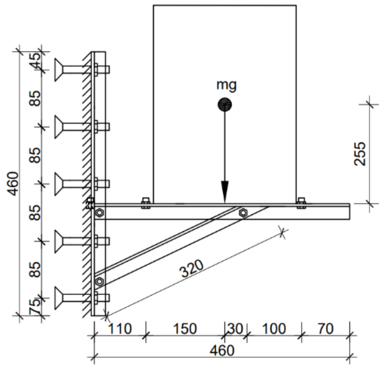

(c). Structural configuration

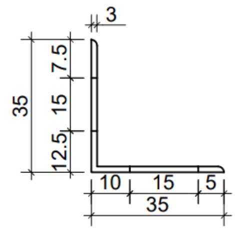

(d). Cross section of angle steel

Figure 1. Typical braced external aircon unit

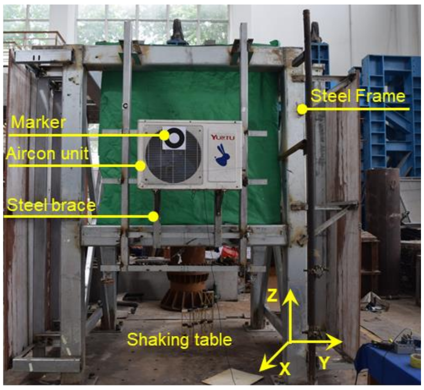

(a). Experimental layout

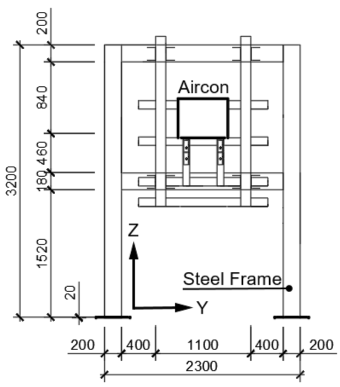

(b). Configuration of the aircon

Figure 2. Layout of the shaking table test

To measure the dynamic response of the aircon, sensors were employed and placed to the locations where the responses are critical. Markers were placed at the center of the aircon in the front and side surface to measure the displacement response (Figure 3a,b). Two accelerometers were placed at the same locations to measure the acceleration response. To observe the strain response of the braces, strain gauges were attached to the middle of each angle steel. Additional markers and accelerometers were place at the steel frame at the location corresponding to the aircon specimen.

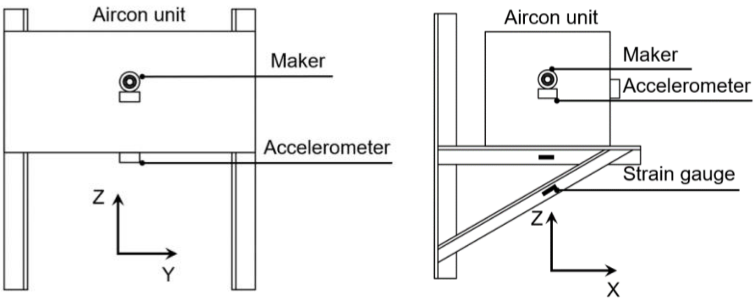

(a). Front view (b). Side view

Figure 3. Layout of the sensors

Numerical model of the testing system was built with OpenSees [Mazzoni et al., 2006]. The converged mass model was considered to represent the whole mass of the braced aircon unit (Figure 4a). For the uniaxial shaking table test in this study, only horizontal stiffness of the brace was considered. Further, computational results shows that the stiffness in direction X is smaller than that of the direction Y. Accordingly, the analytical spring k_2 = 1.67 kN/m, and $k_1 = k_3 = 0$ kN/m were defined in the OpenSees model. BoucWen material was employed to model the simplified triangular brace, namely the uniaxial spring. The hysteretic curve is shown in Figure 4b. The yield stress if the material is 210 N/mm^2.

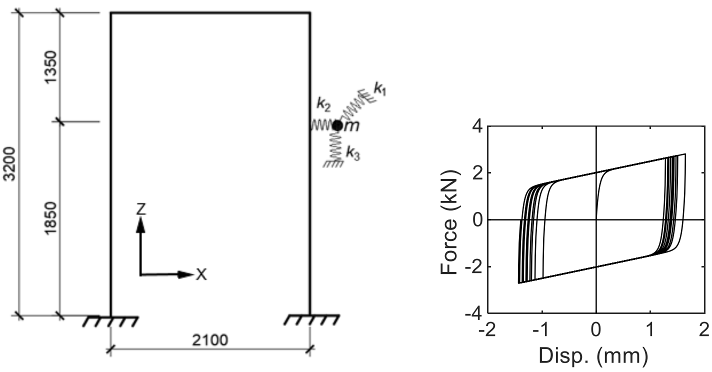

(a). Numerical model in OpenSees (b). BoucWen model

Figure 4. Numerical model

2.2 INPUT MOTIONS

Four motions were generated in accordance to the methods suggested in code provisions [ICC-ES, 2016; ATC, 2006] and literature [Retamales *et al.*, 2011; Gilani and Takhirov, 2011]. AC156 [ICC-ES, 2016] is currently one of the basic references for seismic qualification testing of nonstructural components or systems. It is applicable to shaking table experimental verification of nonstructural systems. The aircon unit was assumed to be installed in a building at Shanghai, where the spectral response acceleration at short period is 0.17 g [Huang *et al.*, 2018]. Conservatively, the relative height (z/h in AC156) was taken as 1.0. Accordingly, based on the recommended target spectra in AC156, two artificial motions were generated. One was generated following the procedure in Huang *et al.* [2018]. It has time duration of 60 sec (AC156-LT in Figure 5a), which was used to investigate the response of an aircon unit on tall buildings. The other was generated following the procedure in [Gilani and Takhirov, 2011]. It has time duration of 30 sec (AC156-ST in Figure 5b), which was used for aircons in other buildings.

FEMA 461 [ATC, 2006] provided a shaking testing protocol for seismic assessment of NCs. The testing procedure is based on the work by the Construction Engineering Research Laboratory [Wilcoski *et al.*, 1997]. It is actually a frequency-sweep motion with random floor accelerations. The input motions consist of 60 sec long narrow-band random sweep acceleration records scaled to produce motions which have relatively smooth response spectra. The bandwidth is one third octave and the center frequency of the record sweeps from 32.0 Hz down to 0.5 Hz at a rate of 6 octaves^2/min. It slightly differs from the recommendation of AC156 (3.3 to 33.3 Hz) [ICC-ES, 2016]. A sweep from high to low frequencies is used to first excite higher vibration modes that have associated failure modes at smaller amplitudes compared to low frequency failure modes. A 60-sec-long time history and corresponding response spectrum developed by the authors of this paper is shown in Figure 5c.

Retamales *et al.* (2011) developed a testing protocol to investigate the seismic performance of distributed nonstructural systems with multiple attachment points. The motion time histories exhibit an instantaneous testing frequency transitioning from high to low frequencies, and then back again to high frequencies. The final high frequency sweep is intended to capture possible high frequency acceleration-induced failure modes of nonstructural systems. In this study, only the horizontal excitation was considered. According to this method the sine-sweep motion time history at the bottom level of the aircon is calculated for a given story height, where the frequency content of the sine-sweep motion ranges from 1.0 to 30 Hz which covers the fundamental vibration frequencies of the braced aircon unit. The time duration is 50.0 sec (Figure 5c), and the constant frequency sweep rate is 0.5 octaves per second. The corresponding response spectra of the four motions are shown in Figure 5e.

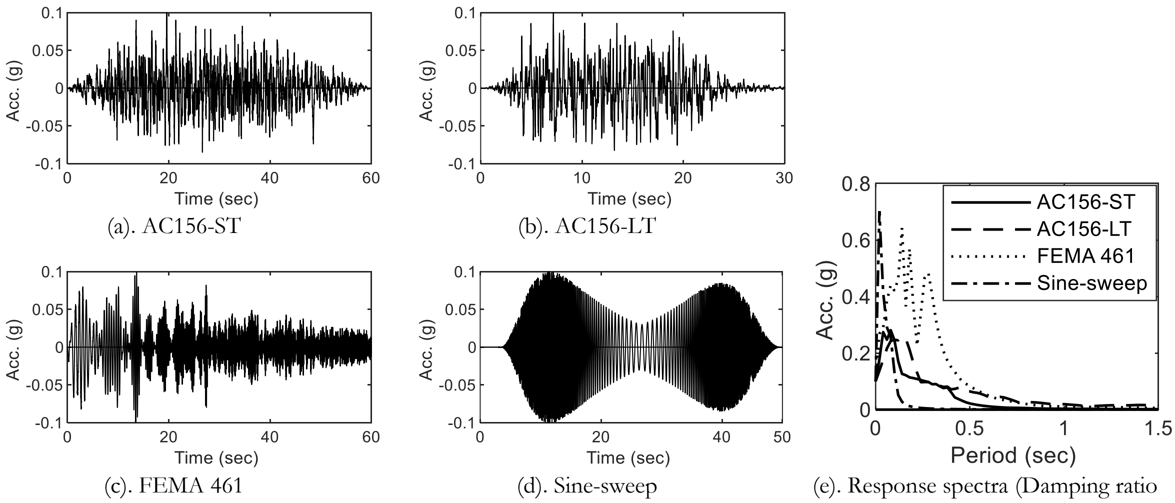

(a). AC156-ST

(b). AC156-LT

(c). FEMA 461

(d). Sine-sweep

(e). Response spectra (Damping ratio = 0.05)

Figure 5. Input motions

2.3 TEST PROGRAM

The dimension of the uniaxial shaking table is 3.3 m × 4.8 m, with a peak acceleration of 1.0 g at payload = 15.0 ton. Prior to the formal test, the four motions were reproduced by the shaking table with a peak acceleration of 1.0 g, indicating that all the motions can be generated in the subsequent shaking table tests. The test matrix is listed in Table 1, where five earthquake intensity levels were considered in the tests. The four motions were input to the shaking table in a sequence as shown in Table 1. While noise with peak acceleration of 0.05 g and time duration of 60 sec were input to the shaking table to obtain the dynamic parameters of the specimen such as the vibration frequency and damping ratio. Variation of these two parameters demonstrates different levels of damage due to earthquake excitations.

Table 1. Test matrix

Case #	Motion	IPA (g)
1	AC156-ST	0.1
2	AC156-LT	
3	FEMA 461	
4	Sine-sweep	
5	AC156-ST	0.2
6	AC156-LT	
7	FEMA 461	
8	Sine-sweep	
9	AC156-ST	0.3
10	AC156-LT	
11	FEMA 461	
12	Sine-sweep	
13	AC156-ST	0.4
14	AC156-LT	
15	FEMA 461	
16	Sine-sweep	
17	AC156-ST	0.5
18	AC156-LT	
19	FEMA 461	
20	Sine-sweep	

Note: IPA = input peak acceleration, WN = white noise.

3. TEST RESULTS

3.1 ACCELERATION RESPONSE

The acceleration responses were measured by the accelerometers attached at the center of the aircon unit. The acceleration time histories of the aircon unit under different earthquake excitation intensities are shown in **Figure 6**. It is evident that the magnitude of peak acceleration increased with increasing IPAs. However, the increment of the peak acceleration was negligible at IPA > 0.3 g, indicating that the nonlinear responses of the braces must have been occurred. The impact of the input motions on the acceleration response of the aircon unit was clearly demonstrated in Figure 7. The FEMA 461 and sine-sweep motions generated larger acceleration responses than those of AC156. For the AC156 compatible motions, the acceleration response under the AC156-LT were smaller than those of the AC156-ST. The experimental results matched to those of the numerical as demonstrated in Figure 7f.

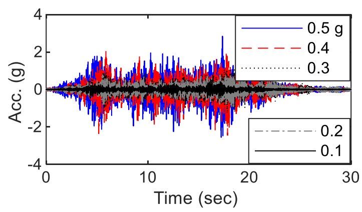

(a). AC156-ST

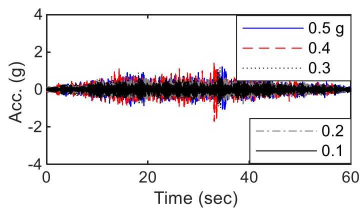

(b). AC156-LT

6

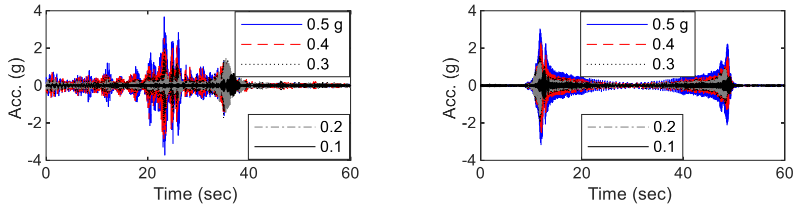

(c). FEMA 461 (d). Sine-sweep

Figure 6. Acceleration response at different IPAs

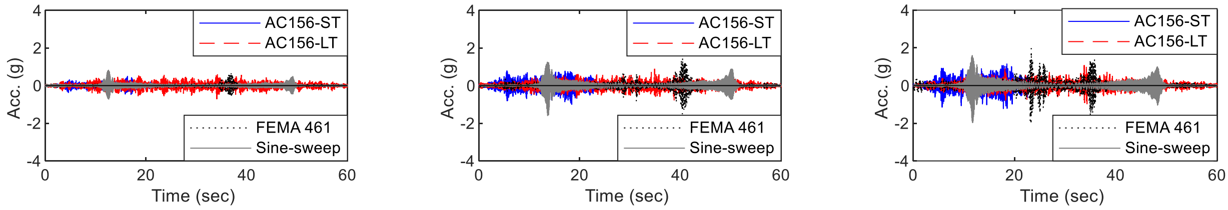

(a). IPA = 0.1 g (b). IPA = 0.2 g (c). IPA = 0.3 g

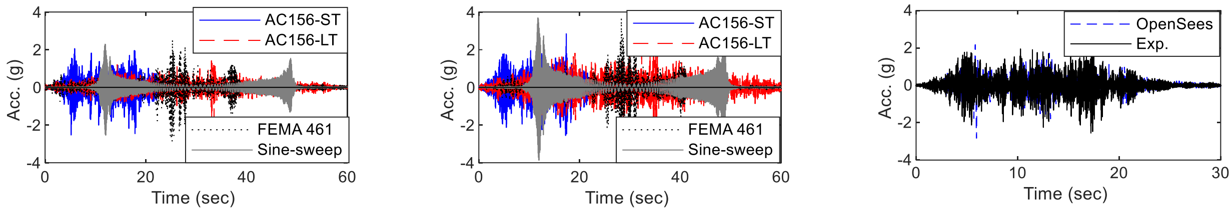

(d). IPA = 0.4 g (e). IPA = 0.5 g (f). AC156-ST at IPA = 0.5 g

Figure 7. Acceleration response to different input motions

3.2 RELATIVE DISPLACEMENT RESPONSE

The displacement response of the aircon unit was measured the markers at the center of the aircon unit and rigid frame. The two displacements observed by means of the markers were employed to compute the relative displacement. It is an indicator to represent the dynamic response level. The relative displacement responses under each type of motions are shown in Figure 8. Like those of the acceleration responses (**Figure 6**), the magnitude of the peak relative displacement increases with increasing IPAs. The increment was negligible at IPA > 0.3 g for the AC156-ST, AC156-LT, and FEMA 461 motions, while the increment was still considerable for the sine-sweep motion. In Figure 9, one can find that the braced aircon unit was quite sensitive to the AC156-LT motion. The resulting peak relative displacements were the largest among the four input motions. This trend is different from those of the acceleration responses. The experimental and numerical results were in agreement with each other (Figure 9f).

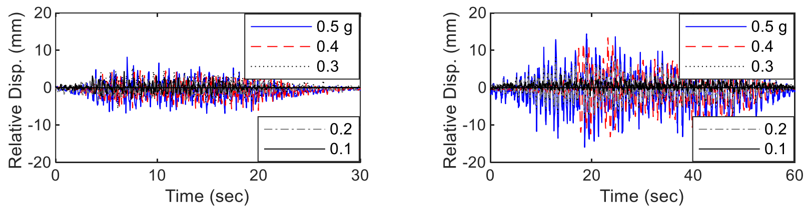

(a). AC156-ST (b). AC156-LT

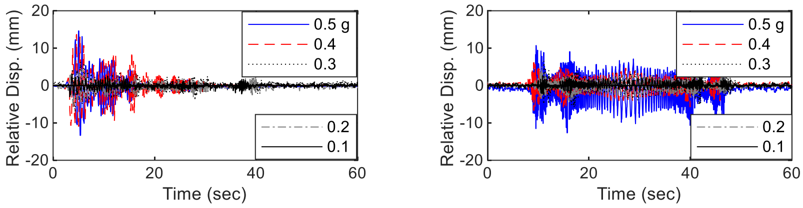

(c). FEMA 461 (d). Sine-sweep

Figure 8. Relative displacement response to different IPAs

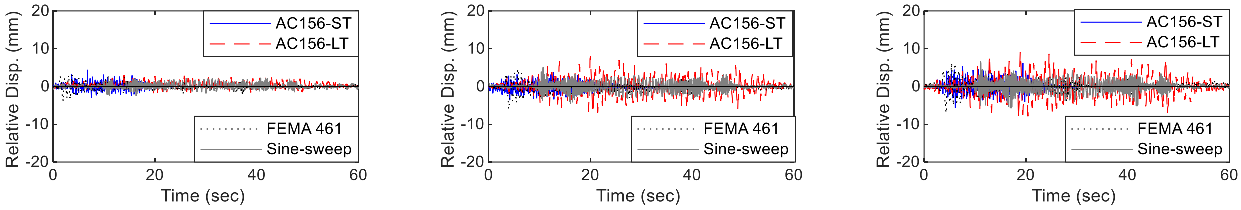

(a). IPA = 0.1 g (b). IPA = 0.2 g (c). IPA = 0.3 g

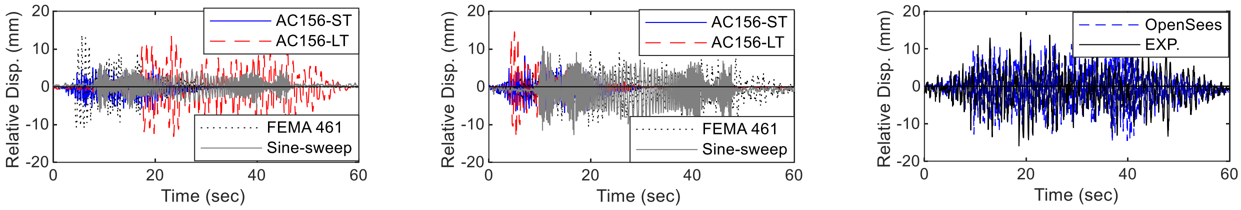

(d). IPA = 0.4 g (e). IPA = 0.5 g (f). AC156-LT at IPA = 0.5 g

Figure 9. Relative displacement response to different input motions

3.3 Strain and Stress Response

The strain response of the brace supporting the aircon unit was measured by the stain gauges fixing on the angle steels. The nominal stress was computed using the elastic modulus times by the measure strain. The resulting times histories of the stress and strain are shown in Figure 10. The horizontal and inclined braces maintained elastic at IPA ≤ 0.3 g (Figure 10a,b). The peak stresses under the four motions were all smaller than 210 N/mm², which is the yielding stress of the steel material. Whereas nonlinear responses appeared at IPA > 0.3 g (Figure 10c-f). Where the yield stress was exceeded both in the two braces. Residual strains appeared at IPA = 0.5 g, indicating that the failure of the two braces. The sine-sweep motion generated largest stresses and strains than the other three motions. As shown in Figure 10g,h, the yielding of the braces were reproduced in the OpenSees model.

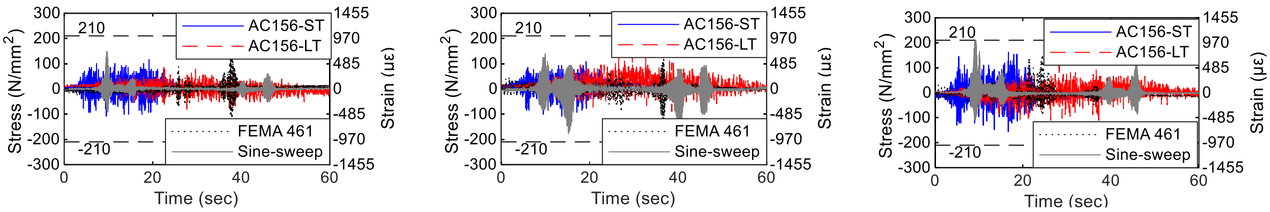

(a). Horizontal brace at IPA = 0.3 g (b). Inclined brace at IPA = 0.3 g (c). Horizontal brace at IPA = 0.4 g

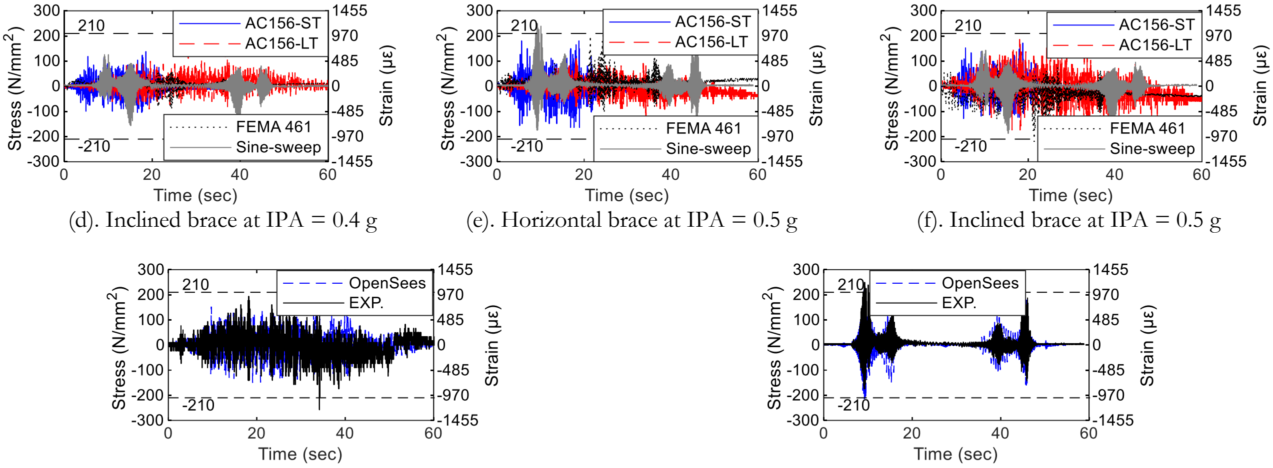

(d). Inclined brace at IPA = 0.4 g (e). Horizontal brace at IPA = 0.5 g (f). Inclined brace at IPA = 0.5 g

(g). AC156-LT at IPA = 0.5 g (h). Sine-sweep at IPA = 0.5 g

Figure 10. Stress and strain responses

4. CONCLUSIONS

To investigate the seismic safety of the braced external outdoor aircon unit, a campaign of shaking tables tests was carried out. A rigid steel frame was built and fixed on the shaking table to host the aircon unit and impose the possible earthquake motions generated by the shaking table. The aircon unit was supported by a pair of triangular steel braces, which is a typical support type. The finite element model of the rigid frame and the braced aircon unit was built with OpenSees [Mazzoni *et al.*, 2006], where the aircon unit was modelled with a converged mass with simplified spring model. The codified motions were generated and employed in the shaking table tests. Some conclusions are addressed below:

1) The seismic responses to the input motions generally increased with the increasing IPAs. The braces maintained elastically at IPA < 0.3 g, while yielding of the steel braces appeared at IPA ≥ 0.3 g.

2) For the codified testing protocols, the seismic responses to the sine-sweep motions were obviously larger than those generated with AC156 and FEMA461.

3) The seismic responses such as the acceleration, displacement, and stress of the aircon unit were in agreement with those obtained from the analytical results.

4) The seismic response of the braced aircon unit varied with different testing protocols. Conservatively, the most vulnerable response is suggested to represent the seismic performance of the specimen. However, the available protocols should be re-evaluated further to reach a uniform experimental result of a NC.

REFERENCES

Filiatrault, A., Perrone, D., Merino, R.J., Calvi, G.M. [2021] "Performance-based seismic design of nonstructural building elements," *Journal of Earthquake Engineering*, Vol. 25, No. 2, pp. 237-269.

Miranda, E., and Taghavi, S. [2003] "Estimation of seismic demands on acceleration-sensitive nonstructural components in critical Facilities," *Proc. of the Seminar on Seismic Design, Performance, and Retrofit of Non-structural Components in Critical Facilities*, ATC 29−2, Newport Beach, California, pp. 347-360.

Soong, T.T. [1995] "Seismic behavior of nonstructural elements-state-of-the-art-report," *Proc. Of the 10th European Conference on Earthquake Engineering*, Vienna, Austria, pp. 1599-1606.

Filiatrault, A., and Christopoulos, C. [2002] "Guidelines, specifications, and seismic performance characterization of nonstructural building components and equipment," Report PEER 2002/05, Pacific Earthquake Engineering Research Center, Berkeley, CA, pp. 102.

Huang, B., Chen, S., Lu, W., and Mosalam, K.M. [2017] "Seismic demand and experimental evaluation of the nonstructural building curtain wall: A review," *Soil Dynamics and Earthquake Engineering*, 2017, Vol. 100, No. 7, pp. 16-33.

FEMA P-58-1. [2012] *Seismic Performance Assessment of Buildings: Volume 1 - Methodology* (P-58-1), Federal Emergency Management Agency, Washington, DC.

ASCE 7-16. [2016] *Minimum Design Loads for Buildings and Other Structures*, American Society of Civil Engineers, Reston, Virginia.

Mahrenholtz, T.C., Hutchinson, T.C., and Eligehausen, R. [2014] "Shake table tests on suspended nonstructural components anchored in cyclically cracked concrete," Journal of Structural Engineering, Vol. 140, No. 11, 04014079.

Feinstein, T., Moehle, J.P. "Seismic response of floor-anchored nonstructural components fastened with yielding elements," *Earthquake Engng Struct Dyn*., 2022, Vol., 51, No. 1, pp. 3-21.

Bianchi, S, Ciurlanti, J, Perrone, D, et al. [2021] "Shake-table tests of innovative drift sensitive nonstructural elements in a low-damage structural system," *Earthquake Engng Struct Dyn*., 2021, Vol. 50, No. 9, pp. 2398–2420.

Fathali, S., Filiatrault, A. [2008] "Effect of elastomeric snubber properties on seismic response of vibration-isolated mechanical equipment: an experimental study," *Earthquake Spectra,* Vol. 24, No. 2, pp. 387-403.

Mazzoni, S., McKenna, F., Scott, M.H., Fenves, G.L. [2006] *OpenSees Command language manual*. Pacific Earthquake Engineering Research Center, Berkeley, California.

Lu, W., Huang, B., Chen, S., and Mosalam. K.M. [2017] "Shaking table test method of building curtain walls using floor capacity demand spectrum," *Bulletin of Earthquake Engineering*, Vol. 15, No. 8, pp. 3185-3205.

International Code Council Evaluation Service (ICC-ES). [2016] *Acceptance Criteria for Seismic Qualification by Shake-table Testing of Nonstructural Components and Systems*. AC156, Whittier, CA.

Applied Technology Council (ATC). [2006]. *Interim Protocols for Determining Seismic Performance Characteristics of Structural and Nonstructural Components*, FEMA Report No. 461, Federal Emergency Management Agency, Washington, DC.

Retamales, R., Mosqueda, G., Filiatrault, A., and Reinhorn, A.M. [2011] "Testing protocol for experimental seismic qualification of distributed nonstructural systems," *Earthquake Spectra*, Vol. 27, No. 3, pp. 835-856.

Gilani, A., and Takhirov, S. [2011] "Current U.S. practice of seismic qualification of suspended ceilings by means of shake table tests," *Ingegneria Sismica Journal*, Vol. 28, No. 1, pp. 26-42.

Huang, B., Lu, W., and Mosalam, K.M. [2018] "Shaking table testing of the granite cladding with undercut bolt anchorage," *Engineering Structures*, Vol. 171, pp. 488-499.

Wilcoski, J., Gambill, J.B., and Smith, S.J. [1997] *The CERL Equipment Fragility and Protection Procedure (CEFAPP)*, USACERL Technical report No. 97/58, U.S. Army Corps of Engineers, Champaign, Ill.

Seismic Fragility Testing of Electrical Equipment for the Safe Operation of Hydroelectric Facilities

Andrew M. Coughlin[1], Katie M. Braman[1], and Brent Bergman[2]

[1] Structural Integrity Associates, Inc.
233 SW Wilson Ave., Suite 101, Bend, OR 97702, USA
e-mail: {acoughlin,kbraman}@structint.com
[2] BC Hydro
6911 Southpoint Dr., Edmonds A02, Burnaby, BC V3N 4X4, Canada
Brent.Bergman@bchydro.com

Abstract. Safe dam operation requires the continued operation of various types of electrical equipment to control gates and spillway water flow levels. Anomalies resulting from loss of structural support, relay chatter, or loss of functionality could affect the integrity of the dam and the safety of communities and ecosystems downstream.

A recent BC Hydro project commissioned a seismic fragility test program for all the electrical equipment identified as critical in the fault tree. While most seismic test programs test unpowered equipment at a single qualification level, this program tested powered equipment, monitored voltage on numerous channels during testing, and subjected the equipment to up to five levels of IEEE 693-2018 compliant time-histories targeted to subduction zone motions. A system of tracking functional and structural limit states demonstrated which equipment was inherently rugged and what seismic fragility existed in the remaining equipment. In some cases, relay chatter and electrical shorts occurred that would not have been detected during unpowered seismic testing.

The results of this study are being used by BC Hydro to build resilience and safety into their systems. They will also be valuable to other dam and critical facility operators using similar equipment to inform the operational state estimation after varying levels of seismic events.

Keywords: Fragility Testing, Electrical Components, Hydroelectric, Relay Chatter, IEEE 693

1. INTRODUCTION

Reliable operation of spillway gates is critical to controlling reservoir levels and preventing uncontrolled release following a seismic event. Many BC Hydro facilities are located in high seismic hazard regions putting particular importance on the post-seismic reliability of gate power and control equipment.

This research seeks to benchmark the performance of powered hydroelectric gate control equipment for functional and structural anomalies resulting from in-service shaking during an earthquake. These test results are intended to be useful for dam operators in seismic regions to estimate the system-level impacts of earthquakes in gate control. Larger themes of seismic fragility and robustness can also be inferred for application in a variety of essential facilities due to the unique test program described below.

1.1 PROJECT BACKGROUND

BC Hydro is the main electricity provider in the Canadian province of British Columbia, providing service to over four million customers and operating thirty hydroelectric plants [BC Hydro 2021]. As part of the larger efforts to seismically upgrade several facilities, BC Hydro is procuring equipment that allows precise flow control of the water going over the spillways, such as the one shown at Ladore Dam in Figure 1. Reliable post-seismic operation of equipment is needed to prevent possible overtopping or unwanted opening that would allow uncontrolled water flow through the spillway. To confirm the seismic resilience of their primary system of gate control, BC Hydro sponsored a seismic test program as described below.

Figure 1. Ladore Dam Spillway, part of the Campbell River System

1.2 EXPERIMENTAL PROGRAM

BC Hydro's test program focused on qualifying the equipment for a target seismic level and increasing demand to determine the seismic level at failure. Additionally, all electrical equipment was to be energized during testing and its voltage was monitored on one or several channels to determine the state of relays, switches, and other electrical signals of interest.

The test plan for each unit under test (UUT) consisted of the following:

i. Visual inspection of each UUT

ii. Resonant frequency search in three axes via sine sweep method (repeated after each test)

iii. Seismic test at 100% reference level

iv. Seismic test at 125% reference level

v. Seismic test at 150% reference level

vi. Seismic test at 200% reference level

vii. Seismic test at 250% reference level

The reference level for seismic tests was at 1.0g PGA and 2.5g peak spectral response with 5% of critical damping. More detail of the time histories is discussed in Section 2. Vertical required response spectra were taken as 80% of the horizontal.

2. TIME HISTORY DERIVATION

The seismic time histories were based on an adapted framework of IEEE 693-2018 [IEEE 2018] and IEC/IEEE 60980-344:2020 [IEEE/IEC 2020].

Based on seismology studies conducted by BC Hydro, an adapted response spectrum was derived, in which the amplified portion of the spectra fell between 2.2 Hz and 16 Hz, double the upper and lower limits of the standard IEEE 693 spectrum. The required response spectra are plotted in Figure 2.

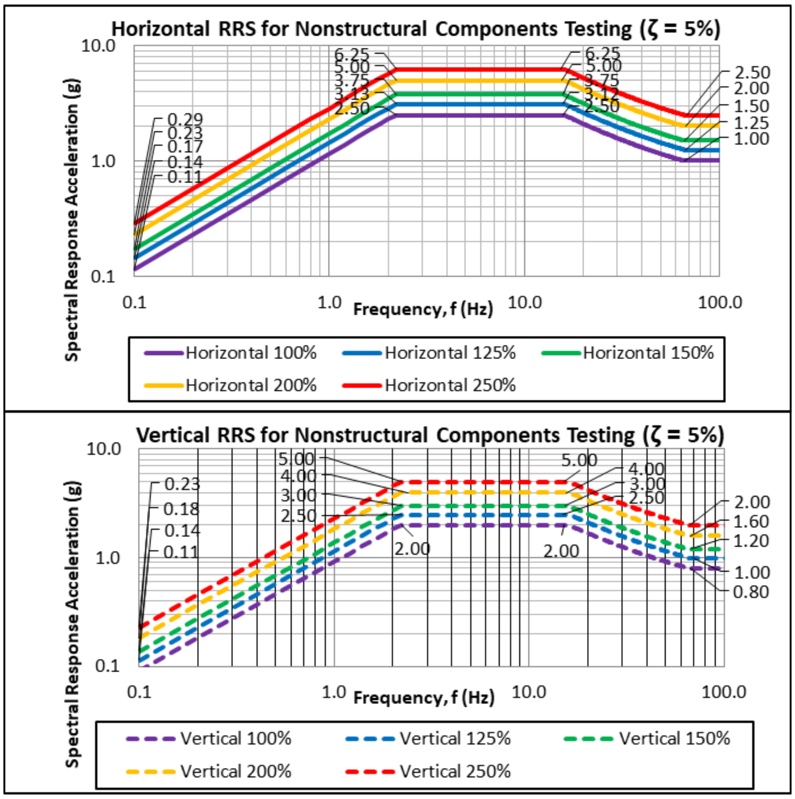

Figure 2. Required response spectra for seismic testing: horizontal (top) and vertical (bottom)

The time histories were derived from subduction zone records in three perpendicular directions from the February 27, 2010 Constitucions/N4598 Chile earthquake record. The record was shaped by Takhirov et al. (2017) to match the IEEE 693 target response spectrum. The original record was 200 seconds long, but the duration was artificially shortened to 100 seconds to match the required response spectra required by BC Hydro. The resulting acceleration time histories and 5% damped response spectra are shown in Figure 3. The resulting time-histories were confirmed to meet the IEEE 693 requirements for bounding the target spectrum, strong motion duration, strong part ratio, peak displacement, and low frequency filtering effects.

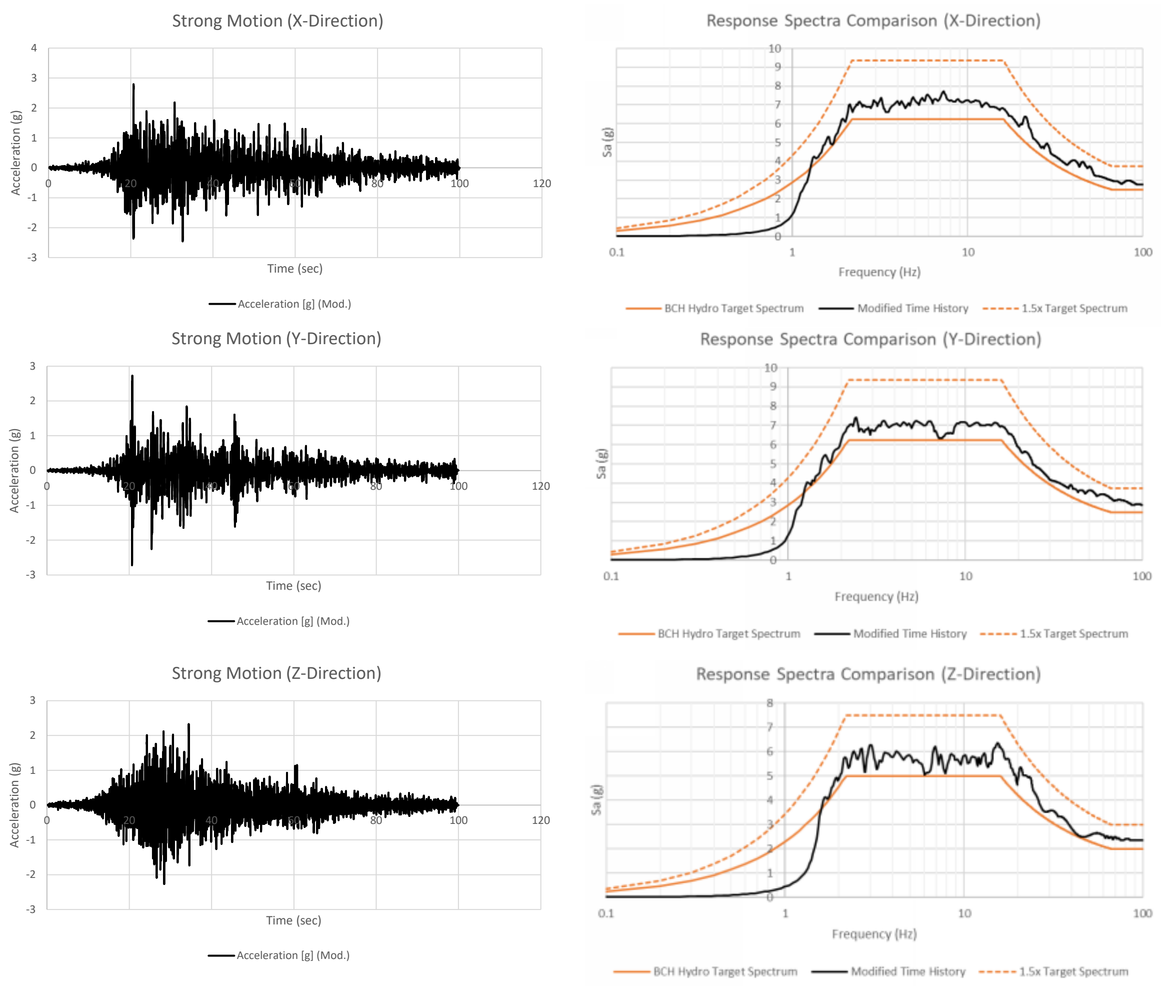

Figure 3. Acceleration-time histories (left) and 5% damped response spectra (right) from seed motions for 250% of reference level

3. TEST METHODOLOGY

3.1 TEST EQUIPMENT

Seismic testing was completed at Environmental Testing Laboratory (ETL) in Dallas, Texas during four test windows in July, September, November, and December of 2021. All testing was performed on an ANCO Model R250.6 Shaker System, which is a triaxial vibration shake table driven by six (6) servo-hydraulic actuators described in Table 1.

Table 1. ETL shake table size and capacity

ETL ANCO R250.6 Shaker System	
Frequency Range	1-100 Hz
Force Capacity	(6) 107 kN actuators
Maximum Stroke	± 25cm
Maximum Velocity	1.9 m/sec
Maximum Acceleration	7g
Maximum Payload	6,800 kg
Mounting Plate	3m x 3m

Acceleration of the shake table was captured with calibrated triaxial accelerometers and each UUT was instrumented with a triaxial accelerometer mounted on top of most units and at the centre of gravity of some units. Voltage monitoring equipment fastened to key parts of the equipment tracked the state of internal relays and other key voltage signals. The data was logged in a National Instruments data acquisition system. Each test was recorded with a video camera at multiple angles. A typical test setup is shown in Figure 4.

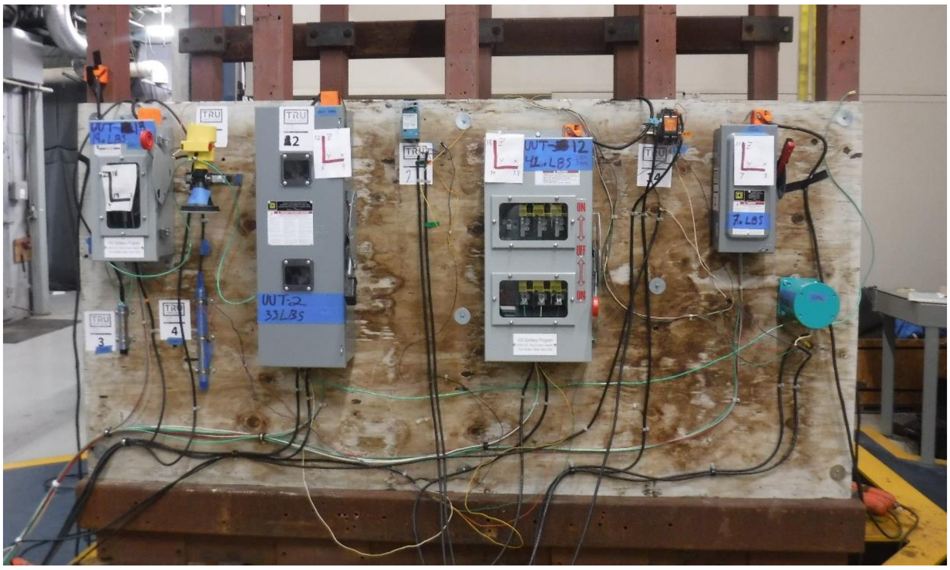

Figure 4. Test setup 1

3.2 UNITS UNDER TEST

The twenty-two units under test (UUT's) comprise key equipment required for gate operation and ranged from less than 1 kg to over 3,000 kg. The UUT's are summarized in Table 2.

Table 2. Unit under test details

UUT No.	Set Up No.	Product Name	Manufacturer	Dimension(mm)			Weight (kg)	Mounting[1]
				Depth	Width	Height		
1	1	Low Voltage Safety Disconnect Switch	Square D	124	193	378	3.2	W

UUT No.	Set Up No.	Product Name	Manufacturer	Dimension(mm)			Weight (kg)	Mounting[1]
				Depth	Width	Height		
2	1	Low Voltage Manual Transfer Switch	Square D	178	292	762	15.0	W
3	1	Pressure Transducer - Analog	KPSI	25	25	191	0.5	W
4	1	Pressure Transducer - Digital	KPSI	25	25	191	0.5	W
5	1	Gate Position Optical Rotary Encoder	Rittmeyer	130	130	207	2.5	W
6	1	Gate Position Radar Indicator	Vega	114	114	267	1.4	W
7	2	Main Control Station	Surtek	914	648	1,829	254.1	B
8	2	Backup Control Station	Surtek	914	648	1,829	251.8	B
9	2	Emergency Control Station	Surtek	762	457	1,829	189.1	B
10	2	Rotary Limit Switch	Ametek-Gemco	262	508	140	14.3	W
11	5	Low Voltage AC Distribution Panel Board	Eaton	292	978	1,880	151.1	W
12	1	Low Voltage Manual Transfer Switch	Eaton	76	127	495	18.6	W
13	1	Low Voltage Safety Disconnect Switch	Eaton	290	333	709	8.6	W
14	1	Load Cell Transducer	Weidmuller	112	46	99	0.5	W
15	4	Motor Control Center	Eaton	533	4,572	2,311	1,993.6	B/W[2]
16	6	Battery Inverter System - UPS/Inverter	RIC	1,041	671	2,385	470.0	IW/B[3,4]
17	6	Battery Inverter System - Power Distribution Unit	RIC	1,029	914	2,177	258.2	IW/B[3]
18	6	Battery Inverter System - Battery Disconnect Switch	RIC	315	599	1,427	60.5	W
19	6	Battery Inverter System - Step-down Transformer	Hammond	686	719	914	293.6	B
20	6	Battery Inverter System - Step-up Transformer	Hammond	686	719	914	297.7	B
21	1	Gate Position Limit Switch	Honeywell	51	38	119	1.8	W

UUT No.	Set Up No.	Product Name	Manufacturer	Dimension(mm)			Weight (kg)	Mounting[1]
				Depth	Width	Height		
22	3	Low Voltage Power Circuit Breaker Switchgear	Eaton	1,981	1,880	2,438	3,090.9	B

Notes: [1]B = base mounted-rigid, W = wall mounted – rigid, IW/B-Isolated at wall and base mounted rigid, [2]Initial run unit was base mounted only. Subsequent runs unit was base and wall mounted, [3]Mounted without factory base isolators, [4]Addition bracing added to unit after initial shake test.

3.3 TEST PROCEDURE

The test procedure generally followed the test plan prescribed by BC Hydro and introduced in Section 1.2. Similar table capacity limits precluded the 250% level test for heavier test setups. Resonant frequency sine sweeps were completed after each successful run in the frequency range of 1 Hz to 50 Hz in three orthogonal directions with a 1 octave/min maximum. The acceleration level used was 0.1g ± 0.05g.

A log of seismic test runs performed is given in Table 3. Unit modifications were made during the course of testing and are summarised in the results section.

Table 3. Seismic test run log

UUTs	Test Date	Test Level	Modification Required?	Units Passed Test?
Test Window 1				
UUT 1, 2, 3, 4, 5, 6, 12, 13, 14, 21	07/21/2021	100%	No	Yes
	07/21/2021	125%	No	Yes
	07/21/2021	150%	No	Yes
	07/21/2021	200%	No	Yes
	07/21/2021	250%	No	Yes
UUT 7, 8, 9, 10	07/23/2021	100%	No	Yes
	07/23/2021	125%	No	Yes
	07/24/2021	150%	No	Yes
	07/24/2021	200%	No	Yes
	07/24/2021	250%	No	Yes
Test Window 2				
UUT 22	09/28/2021	100%	No	Yes
	09/29/2021	125%	No	Yes
	09/29/2021	150%	No	Yes
	09/29/2021	200%	Yes	No
	09/30/2021	200%	Yes	No
	09/30/2021	200%	Yes	Yes
UUT 15 (Without Wall Fixture)	10/1/2021	100%	No	No
	10/1/2021	100%	Yes	Yes
Test Window 3				
UUT 15 (With Wall Fixture)	11/9/2021	125%	Yes	Yes
	11/10/2021	150%	Yes	Yes
	11/10/2021	200%	Yes	No
	11/10/2021	200%	Yes	No
	11/11/2021	200%	Yes	Yes
UUT 11	11/11/2021	100%	No	Yes
	11/11/2021	125%	No	Yes

UUTs	Test Date	Test Level	Modification Required?	Units Passed Test?
	11/11/2021	150%	No	Yes
	11/12/2021	200%	No	Yes
	11/12/2021	250%	No	Yes
		Test Window 4		
UUT 16, 17, 18, 19, 20	12/02/2021	100%	UUT 19 & 20	Yes
	12/03/2021	125%	UUT 16, 19 & 20	Yes
	12/03/2021	150%	UUT 16, 19 & 20	Yes
	12/03/2021	200%	UUT 16, 19 & 20	Yes
	12/03/2021	250%	UUT 16, 19 & 20	No

3.4 DATA PROCESSING

In addition to standard plots for transmissibility, acceleration-time history, response spectra, and voltage-time history, a fragility limit state system was developed to document structural and functional anomalies and failures, which can be correlated to system-level consequences such as downtime. Table 4 describes the limit states, which by necessity are somewhat qualitative.

Table 4. Limit states for documenting equipment seismic damage

Limit State	Structural Integrity	Functionality
0	-No visible damage	-No observed anomalies
1	-Limited yielding of force resisting system. Limited fracture of non-force resisting system	-Anomalies observed during testing, but unit maintains functionality after test. No hazardous conditions. May require maintenance.
2	-Significant permanent deformation (includes door opening). Failure or fracture of force resisting system.	-Electrical hazard formed during or after test. Electrical anomaly repairable without subcomponent replacement.
3	-Failure of mounting. Structural collapse (total or partial)	-Functional failure after test requiring replacement or major repair

4. TEST RESULTS

4.1 RESONANT FREQUENCIES

Not all units were large enough to support a triaxial accelerometer on them to track resonance. Those units whose transmissibility functions were captured were processed to determine the lowest natural frequency, as summarized in Table 5.

Table 5. Resonant frequencies

UUT No.	Set Up No.	Product Name	Mounting[1]	Resonant Frequency (Hz)		
				Front-Back	Side-Side	Vertical
1	1	Low Voltage Safety Disconnect Switch	W	>33	>33	>33

UUT No.	Set Up No.	Product Name	Mounting[1]	Resonant Frequency (Hz)		
				Front-Back	Side-Side	Vertical
2	1	Low Voltage Manual Transfer Switch	W	>33	>33	11.8
7	2	Main Control Station	B	14.3	15.1	>33
8	2	Backup Control Station	B	12	16.5	>33
9	2	Emergency Control Station	B	12.6	14.4	>33
10	2	Rotary Limit Switch	W	>33	>33	>33
11	5	Low Voltage AC Distribution Panel Board	W	>33	>33	>33
12	1	Low Voltage Manual Transfer Switch	W	>33	>33	>33
13	1	Low Voltage Safety Disconnect Switch	W	>33	>33	>33
15	4	Motor Control Center	B	4.3	7.4	23.2
15	4	Motor Control Center	B/W	8.7	>33	>33
16	6	Battery Inverter System - UPS/Inverter	IW/B	5.6	11.5	6.4
17	6	Battery Inverter System - Power Distribution Unit	IW/B	7.3	11.5	9.3
18	6	Battery Inverter System - Battery Disconnect Switch	W	16.1	11.5	>33
19	6	Battery Inverter System - Step-down Transformer	B	24.4	21.5	>33
20	6	Battery Inverter System - Step-up Transformer	B	16.5	>33	27.6
22	3	Low Voltage Power Circuit Breaker Switchgear	B	7.1	6.3	21.3

Notes: [1]B = base mounted-rigid, W = wall mounted – rigid, IW/B-Isolated at wall and base mounted rigid

4.2 Unit Modifications and Anomalies

Those units that experienced significant anomalies were considered failed units. Where reasonable measures could be taken to improve the seismic performance, equipment was modified and testing was resumed. Details of each modification are not included in this paper but were provided to BC Hydro for potential implementation in hydroelectric plants.

Significant anomalies and modifications were present in UUT 15 (motor control centre), UUT 19 (step-down transformer), UUT 20 (step-up transformer), UUT 16 (battery inverter), and UUT 22 (low voltage switchgear). Notably these were the five heaviest pieces of equipment tested among the twenty-two test units. Other test units either experienced no anomalies or minor anomalies that did not require modification. Each of the modified units is discussed below.

4.2.1 Motor Control Centre (UUT 15)

UUT 15 was initially base mounted only, as shown in Figure 5. Manufacturer-supplied angles were welded to the unit for extra base support, which is an installation condition that is not always implemented. During the initial run at 100% the vertically cantilevered portion of the bus contacted an interior panel wall. The contact with the bus and cabinet caused the bus to arc which resulted in the shake table's current overprotection to stop the test run. The 100% run was repeated with the interior wall removed and the unit passed the test.

Due to the improbability of UUT15 passing seismic testing at higher levels, a wall fixture was added behind the unit and a manufacturer-supplied top angle fastened the top of the UUT to the fixture for the 125% level run and higher (also shown in Figure 5). The removed internal panel wall from the 100% test was not replaced. With this modification UUT15 passed the 125% and 150% tests. The first attempt at the 200% shake test was aborted. The table overcurrent protection shut the table down. A spark was observed coming from the bus section of the cabinet. Upon opening the bus cabinet scorch marks from the centre bus connection were observed along with scorch marks near the top of the integrated dry-type transformer cores, shown in Figure 6.

Figure 5. Motor control centre (UUT 15) base mounted (left) and with top support fixture (right)

Figure 6. Scorch marks from arc after 200% level test on frame (left) and near transformer (right)

Several significant modifications were made to UUT15, including supplementing the bracing mechanism for the top of the transformer cores. After these modifications the third attempt at the 200% test was successful.

4.2.2 Transformers (UUT's 19 and 20)

Prior to shake testing the bases of the transformers were modified. Four stiffeners were welded to each side of the base rail of the transformers as shown in Figure 7. In this condition the units experienced no anomalies for the 100%, 125%, 150%, and 200% shakes. At the 250% level shake, the internal mounting system for the transformer cores failed in both UUT's and the test was aborted. Figure 8 shows the damaged state after the test.

Figure 7. UUT19 and 20 mounting flange modification prior to testing

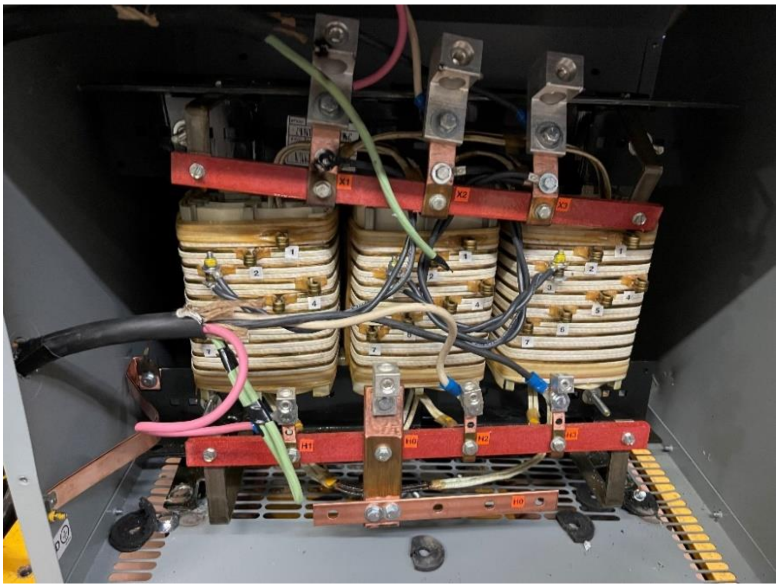

Figure 8. UUT20 damage after 250% level shake (UUT19 similar)

4.2.3 Battery Inverter (UUT 16)

The battery inverter (UUT 16) was tested in a base mounted configuration with a manufacturer-supplied wire rope isolator connecting the top to a wall fixture as shown in Figure 9. The unit passed the 100% level test, but small fractures were identified near the base mounting hardware. For the higher-level tests, mounting angles on each side provided additional top support to the cabinet. The unit did not experience any other anomalies in the 125%, 150%, and 200% level shakes. The 250% level test was aborted due to other units on the table and was not retested.

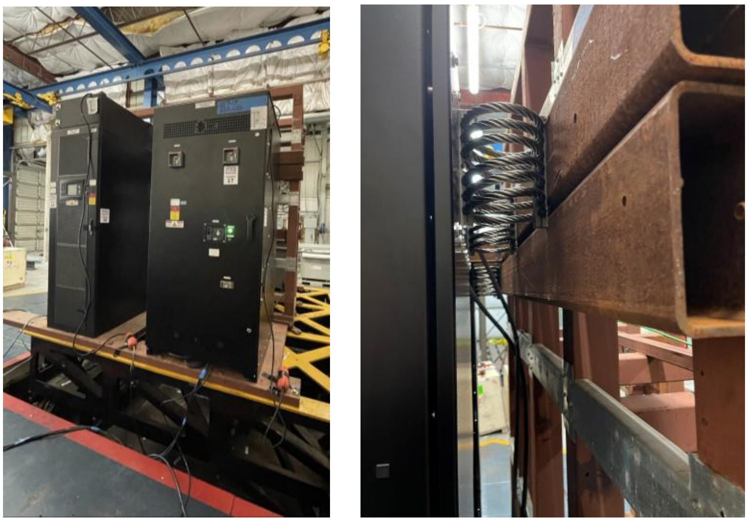

Figure 9. Battery inverter mounting with isolator connection to wall fixture (inverter/UPS is the narrow cabinet)

4.2.4 Low Voltage Switchgear (UUT 22)

The low voltage switchgear (UUT 22) was base mounted only, as shown in Figure 10. It successfully passed seismic runs at 100%, 125%, and 150% of reference levels. On the first attempt at the 200% shake test level, the table shut down into the strong motion of the shake, about 20 to 25 seconds into the shake. Video shows a spark at the table's grounding system. Upon inspection of the unit after the aborted shake, it was determined that during the shake the bus bar came close enough to the vertical metal support in Cabinet 1 that the bus was able to arc. This resulted in the shake table shutting down due to the table's overcurrent protection system.

Multiple significant modifications were made to the switchgear before it passed the 200% level test on the third attempt. The modifications included removal of portions of busbars near the exterior enclosure, replacement of mounting washers with thick plate washers, movement of internal vertical channels, and addition of extra internal bolts.

Figure 10. Low voltage switchgear (UUT 22) on shake table

4.3 FUNCTIONAL AND STRUCTURAL LIMIT STATE RESULTS

To summarize the levels of functional and structural anomalies experienced by the equipment, simple fragility plots were created with limit states from Table 4 plotted versus peak ground acceleration (PGA) of the test. Note that most seismic qualification test standards define passing as limit state 0 or 1 as defined in this paper.

Most equipment experienced no anomalies up to the 2g or 2.5g PGA level as shown in Figure 11, indicating it is very seismically rugged. A second class of equipment was found to be prone to minor structural or functional anomalies such as yielding of supports or relay chatter. This equipment is shown in Figure 12. The final category of equipment is prone to high consequence failure, shown in Figure 13. These equipment types are also those with the highest mass.

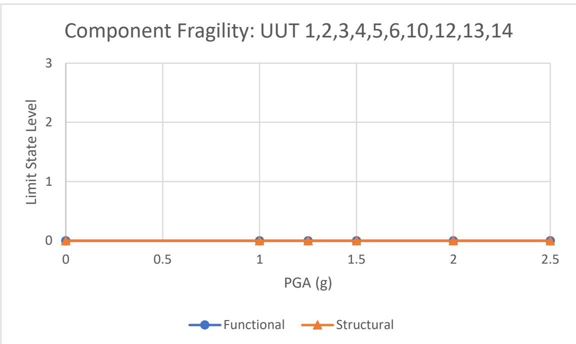

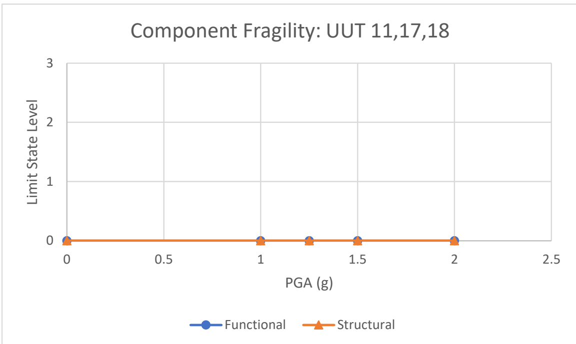

Figure 11. Fragility of seismically rugged equipment

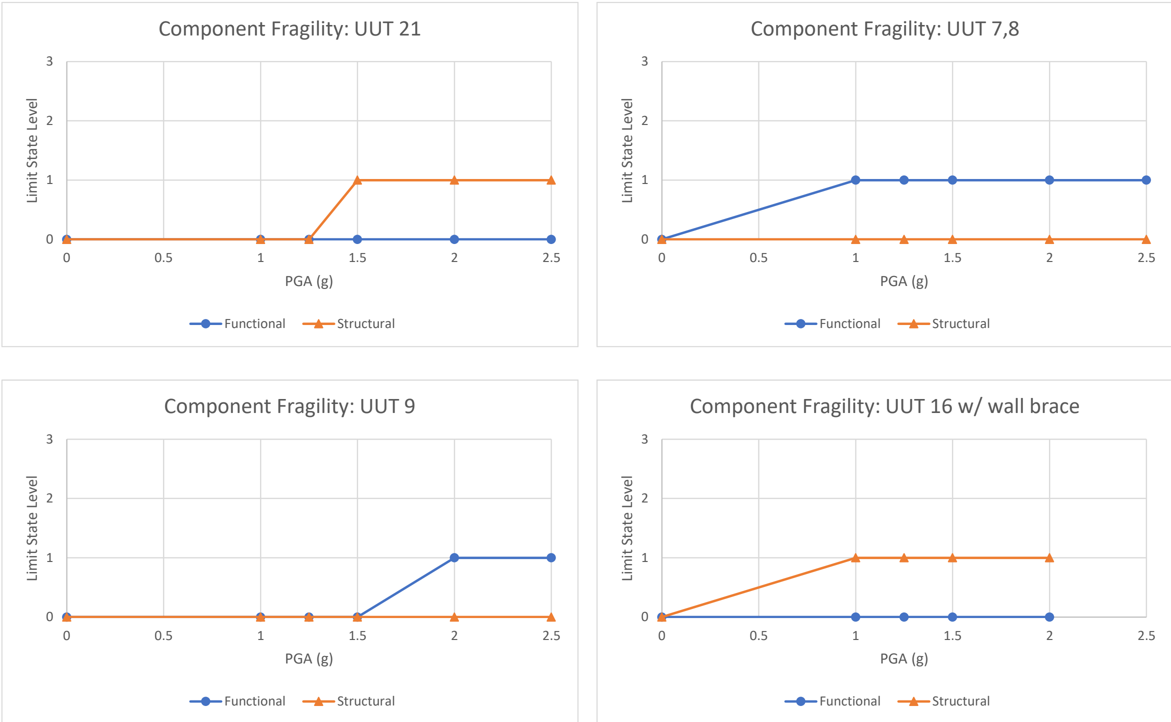

Figure 12. Fragility of equipment that is prone to minor anomalies

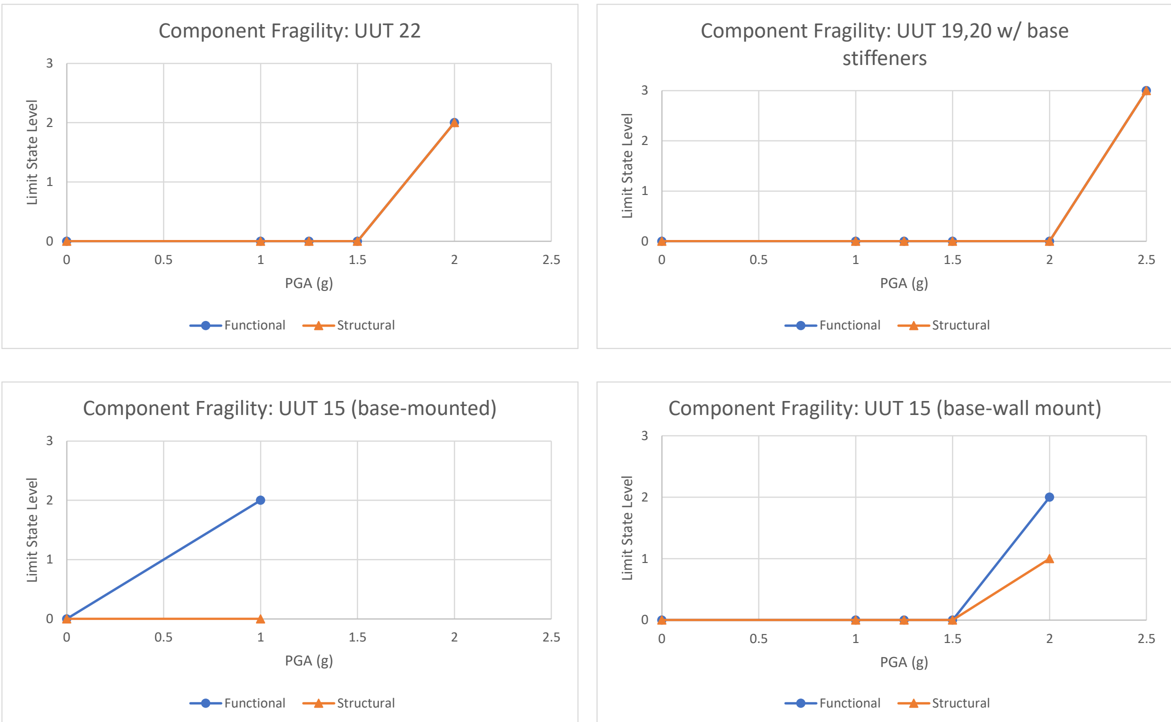

Figure 13. Fragility of equipment with major seismic failure modes

5.CONCLUSIONS

Though this roster of tested equipment is not necessarily representative of all hydroelectric gate control facilities, it is a useful reference to dam operators and other essential facility stakeholders as to the vulnerability of equipment to seismic motions. This testing was unique because it tested the equipment energized and monitored voltages, such that arcs could occur or changes in state of relays could be detected. This is not typically completed in seismic qualification testing. Furthermore, the tests were conducted at increasing levels until failure, or until table capacity was reached. This has allowed rough fragility curves to be presented showing the onset of different failure limit states for functional and structural performance.

This testing could be expanded to other hydroelectric components to inform a more comprehensive view of seismic dam safety from an operability perspective.

REFERENCES

BC Hydro. [2021]. "BC Hydro Quick Facts," 2020/21 Annual Service Plan Report, <https://www.bchydro.com/content/dam/BCHydro/customer-portal/documents/corporate/ accountability-reports/financial-reports/annual-reports/bchydro-quick-facts-2021.pdf>, Accessed 27 Jul 2022.

IEEE [2018] *IEEE Std 693™-2018: IEEE Recommended Practice for Seismic Design of Substations*, Institute of Electrical and Electronics Engineers, Inc., New York, USA.

IEC/IEEE [2020] *IEC/IEEE 60980-344:2020: Nuclear facilities – Equipment important to safety – Seismic qualification*, International Electrotechnical Commission, Geneva, Switzerland and Institute of Electrical and Electronics Engineers, Inc., New York, USA.

Takhirov, S.M., Fujisaki, E., Kempner, L., Low, B. [2017]. "Time Histories for IEEE693 Testing and Analysis: A Summary of Unfiltered and Filtered Versions." Structures Laboratory Report 2017/01. University of California, Berkeley.

Seismic Isolation of an Industrial Steel Rack using Innovative Modular Devices: Shake-Table Tests

Gabriele Guerrini[1,2], Francesco Graziotti[1,2], and Andrea Penna[1,2]

[1] University of Pavia, Department of Civil Engineering and Architecture (DICAr)
Via Ferrata, 3 - 27100 Pavia (PV) - Italy
e-mail: {gabriele.guerrini, francesco.graziotti, andrea.penna}@unipv.it

[2] European Centre for Training and Research in Earthquake Engineering (EUCENTRE Foundation)
Via Ferrata, 1 - 27100 Pavia (PV) - Italy

Abstract. This paper discusses the experimental results from dynamic shake-table tests conducted at the University of Pavia and at the EUCENTRE Foundation (Pavia, Italy) on an industrial steel rack seismically isolated with innovative devices. In fact, targeted protection of nonstructural building components can play a significant role in earthquake loss mitigation. While traditional elastomeric or friction-pendulum isolators are surely effective at reducing seismic accelerations transmitted to the supported structure, their application to nonstructural systems might be hindered by intrinsic cost, durability, and mechanical issues. To overcome these drawbacks, an innovative seismic isolator based on a multiple articulated quadrilateral mechanism and named "Kinematic Steel Joint (KSJ)" has been patented by Kyneprox S.r.l. This device can be manufactured by simply cutting, folding, and pinning metal sheets. Stainless or galvanized steel can be adopted to mitigate corrosion issues. The modular nature of the basic mechanism allows tailoring it to a variety supported masses. The trajectory imposed by the KSJ isolator to the superstructure results in a self-centering, pendulum-type motion. Friction within the pinned joints provides some energy dissipation to the device, and replaceable fuses can be added to limit displacement demands before reaching the maximum range. In this study, KSJ devices were installed below the columns of a five-shelf, two-bay industrial steel rack. Isolation was provided in the cross-aisle direction, while the rack was braced in the down-aisle one. Incremental uniaxial shake-table tests were performed in the isolated direction under three different loading scenarios: empty, half-loaded, and fully loaded rack. The beneficial effects of the KSJ devices on the dynamic response of the rack are discussed in terms of elastic demands on the isolated superstructure.

Keywords: Energy dissipation; Industrial steel rack; Kinematic Steel Joint; Seismic isolation; Self-centering; Shake-table test.

1. INTRODUCTION

Isolation can be used in seismically active regions as an integrated system for new structures, as a retrofit solution for existing structures, and as a passive protection for nonstructural components. In fact, protecting buildings from earthquakes requires not only preventing collapse, but also limiting the economic and social cost of post-event disruption, repair, and reconstruction. Nonstructural elements, including architectural, mechanical, or electrical components and contents, constitute most of the total investment in a typical building, and can suffer damage under earthquake intensities much lower than those producing structural damage [Taghavi and Miranda, 2003]. Consequently, losses from nonstructural damage often exceed those from structural damage, and even if a building structural performance is satisfactory enough to allow immediate occupancy after a seismic event, nonstructural element failures can lower the overall performance level and functionality of the building system [Filiatrault and Sullivan, 2014].

The 2012 Emilia, Italy earthquake sequence caused failure of steel racking systems in several industrial facilities, resulting in the loss of valuable contents and, in many cases, in the subsequent collapse of warehouse cladding [Bournas et al., 2014]. The 2016 Central Italy earthquake sequence also produced extensive damage to shelves and storage racks, with overturning of entire racks or buckling of their vertical members [Perrone et al., 2019]. However, the same seismic sequence highlighted the importance of proper designing and detailing these components to limit damage to industrial facilities: for example, an effective solution combined a bracing system with a special base connection, that allowed relative movement at the floor level. The latter observation encourages sesmic isolation of storage racks.

Seismic isolation filters the dynamic input transmitted to the superstructure (i.e., the rack) above the isolation layer, reducing acceleration, displacement, and deformation demands, and potential damage to steel members and stored goods. Common elastomeric and friction-pendulum devices are effective at reducing the seismic accelerations transmitted to isolated structures, but they might not be fully suitable for protecting nonstructural systems. In fact, on one hand their material and manufacturing costs can make them uneconomical, on the other hand they may need maintenance or replacement over time, to control elastomer aging, steel corrosion, sliding surface degradation, and other effects that could impair their performance [Lee, 1981; Kauschke and Baigent, 1986; Clark et al., 1996; Morgan et al., 2001; Constantinou et al., 2007].

To overcome these drawbacks, Kyneprox S.r.l. has conceived and patented a new isolator device, based on a double articulated-quadrilateral mechanism, named "Kinematic Steel Joint" (KSJ) [Guerrini et al., 2019, 2020]. This device can be manufactured by simply cutting, folding, and pinning metal sheets, possibly employing stainless or galvanized steel to mitigate corrosion issues. Its modular nature allows tailoring it to different payloads and displacement demands. The KSJ imposes a self-centering pendulum-type motion to the superstructure, associating horizontal with upward displacements and resulting in a restoring force proportional to the slope of the trajectory. Friction within the pinned connections grants some energy dissipation, and replaceable hysteretic fuses can be added to act as brakes when approaching the maximum displacement range.

This paper presents the main results from a shake-table test conducted at the University of Pavia, Italy, and at the EUCENTRE Foundation laboratories on a five-shelf, two-bay industrial steel rack, equipped with KSJ isolators in the cross-aisle direction [Filiatrault et al., 2008] and braced in the down-aisle one. Incremental uniaxial shake-table tests were conducted in the isolated direction under three different loading scenarios, applying a ground motion recorded in Norcia, Italy, during the 2016 Central Italy earthquake sequence and progressively scaling its acceleration amplitude. The trajectories and force-displacement relationships recorded on the isolators, as well as the elastic response spectra calculated above and below the isolation layer, are examined to prove the effectiveness of the KSJ solution.

2. EXPERIMENTAL CAMPAIGN

2.1 SPECIMEN OVERVIEW

The industrial steel rack had the layout and dimensions shown in Fig. 1a: it consisted of five shelves divided in two bays, supported by three cross-isle frames. Each frame rested on a pair of aligned KSJ isolators, moving in the cross-isle direction only (Fig. 1b and c). Vertical bracing was provided in the down-isle direction, while horizontal bracing at the first, third, and fifth shelves. The KSJ isolators were fastened to 50-mm-thick steel plates, which were in turn tied to the shake-table by four M20 threaded rods. A steel frame sourrounded the specimen, serving as a safety restraint against collapse.

Each pair of devices was equipped with two or four replaceable hysteretic fuses made of S355 steel (Fig. 2), with lateral flexural strength of 480 N and stiffness of 150 N/mm. The fuses were engaged at displacements of ±145 mm to dissipate some kinetic energy by flexural plasticization before reaching the maximum allowable range of ±180 mm.

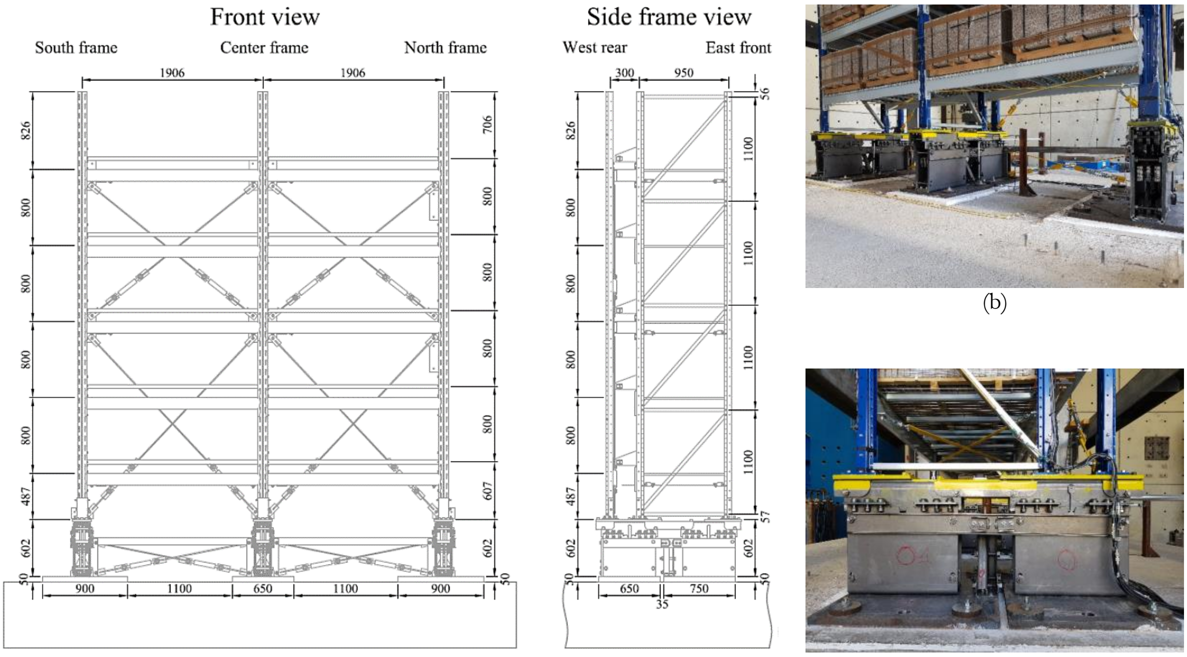

(a) (c)

Figure 1. Test specimen: (a) dimensions [mm]; (b) isolation layer; (c) KSJ pair supporting the North frame.

(a) (b) (c)

Figure 2. Hysteretic fuse: (a) dimensions [mm]; (b) individual fuse; (c) fuse inserted in the North KSJ pair.

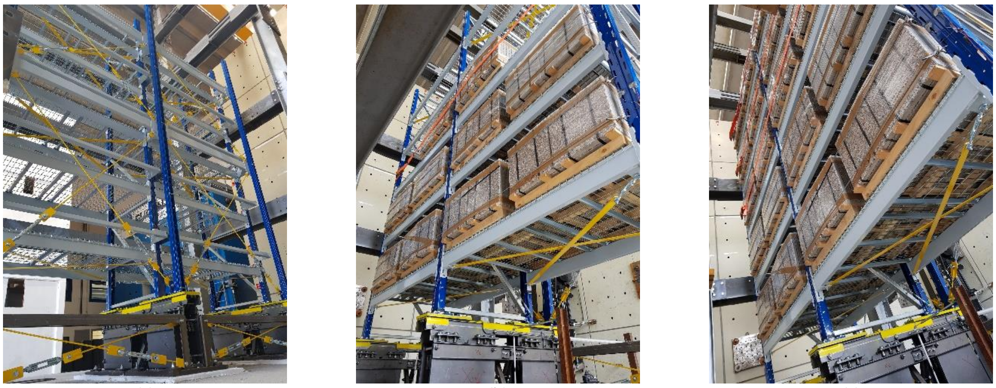

(a) (b) (c)

Figure 3. Loading configurations: (a) unloaded; (b) half-loaded; (c) fully loaded.

2.2 MASSES AND LOADING CONFIGURATIONS

The mass provided by a KSJ pair was about 400 kg, half of which participating in the specimen dynamic response. The rack mass was about 575 kg, and any bay could accommodate two 1000-kg pallets. Three loading configurations were obtained through different pallet distributions on the shelves, to investigate the repeatability and stability of the KSJ isolation response:

i. unloaded configuration, with no pallets at all (Fig. 3a), corresponding to a dynamic mass of 1.175 t and an estimated fundamental period in the cross-isle direction of 0.09 s;

ii. half-loaded configuration, with two pallets on both bays of shelves 1 and 2, one pallet on each bay of shelf 3, and no pallets on shelves 4 and 5 (Fig. 3b), corresponding to a mass of 11.175 t and an estimated period of 0.38 s;

iii. fully loaded configuration, with two pallets on both bays of all shelves (Fig. 3c), corresponding to a mass of 21.175 t and an estimated period of 0.53 s.

2.3 INPUT GROUND MOTION

The rack was excited only in the isolated cross-isle direction, defined longitudinal with respect to the imposed shake-table motion. Accordingly, the down-isle direction was identified as transverse. The East-West component recorded during the M_w 6.5 event of October 30th, 2016, at the NRC station in Norcia, Italy, was selected as input signal for the incremental dynamic shake-table test. This record is characterized by epicentral distance of 4.6 km and peak ground acceleration (PGA) of 4.76 m/s² (Fig. 4a).

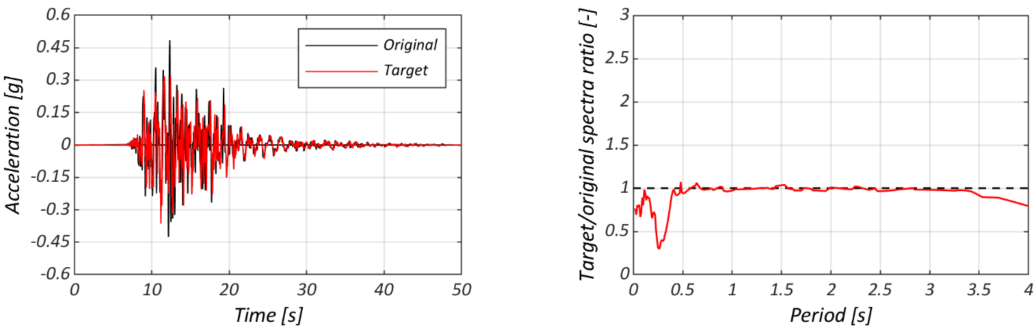

(a) (b)

Figure 4. Original and target input motions: (a) acceleration time series; (b) 5%-damped elastic response spectra ratio.

The original signal was processed with a band-stop 4^{th} order Butterworth filter between 3.2 Hz and 4.6 Hz. This operation was necessary to avoid resonance issues with the safety steel frame mounted on the shake-table, characterized by natural period of about 0.25 s. The frequency range was chosen to minimize the consequences on the elastic response spectrum for periods longer than 0.4 s, where the fundamental period of the loaded, fixed-base rack was expected to be found. The target (filtered) acceleration time history is compared with the original one in Fig. 4a. The ratio between the corresponding 5%-damped elastic response spectra is plotted in Fig. 4b. It should be noted that filtering the signal at high frequencies resulted in a 25% reduction of PGA from 4.76 m/s^2 to 3.57 m/s^2.

2.4 TESTING SEQUENCE

The target signal was applied through the shake-table by progressively scaling up its acceleration amplitude, with factors 25%, 50%, 75%, 100%, and 125%. In all loading configurations the entire test sequence was performed with 2 hysteretic fuses per KSJ pair (total 6 fuses). However, in the fully loaded configuration the 50%, 75%, 100%, and 125% tests were run also with 4 fuses per pair (total 12 fuses). This allowed to investigate the effect of the different braking force on the isolator response when approaching the maximum displacement allowance.

Low-intensity random noise tests were performed between the seismic runs with the selected natural record, for dynamic identification and damage correlation purposes. Moreover, low-intensity seismic and random noise tests were performed to calibrate the shake-table controller and to check the instrumentation recordings.

2.5 INSTRUMENTATION

The dynamic response of the specimen was recorded through a dense distribution of sensors, including 27 accelerometers, 13 potentiometers, 15 wire potentiometers, and 24 strain gages.

Strain-gage recordings were used only during the test execution to detect possible local buckling of the cold-formed steel columns. Because the rack was loaded while the data acquisition system was offline, these strain measurements did not include gravity load effects, and are deemed not interesting for the analysis and interpretation of the experimental response.

Fig. 5a shows the potentiometer triplet installed to obtain the 3D trajectory of a KSJ pair, and Fig. 5b the accelerometer to record the signal transferred by a KSJ pair to the base of the supported frame. Because any displacement affects all three potentiometers at the same time, a routine was implemented to extract the three orthogonal displacement components from the combined sensor recordings.

(a) (b)

Figure 5. Instrumentation for a pair of KSJ isolators: (a) potentiometer triplet; (b) accelerometer.

3. EXPERIMENTAL RESULTS

3.1 BEHAVIOR OF THE KSJ ISOLATORS

Fig. 6 through Fig. 8 show the variable-curvature trajectories recorded atop the KSJ isolator pairs under the 125%-scaled input acceleration amplitude for the three loading configurations, confirming previous analytical and experimental findings [Guerrini et al., 2019, 2020]. Variable-curvature trajectories result in a nonlinear restoring force-displacement response at the isolation level, characterized by the following correspondences: positive/negative force with positive/negative trajectory slope; zero force with trajectory horizontal-tangent points; positive/negative stiffness with positive/negative trajectory curvature; and zero stiffness with trajectory inflection points.

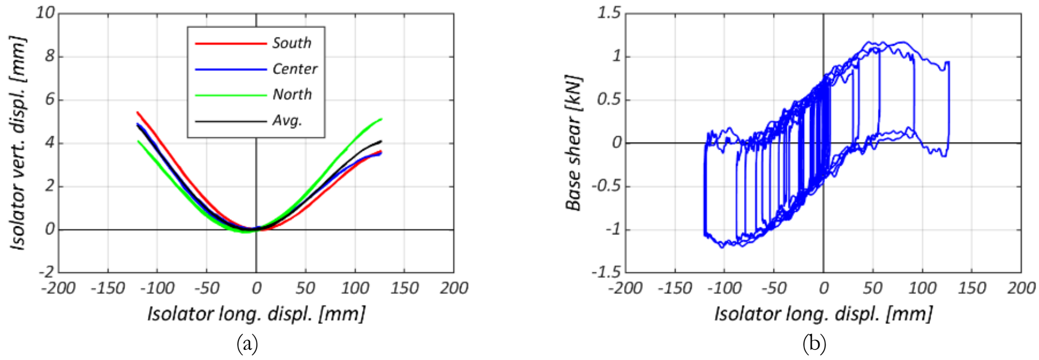

Figure 6. Unloaded rack, 6 fuses, 125%-scaled input: (a) KSJ trajectories; (b) force-displacement response.

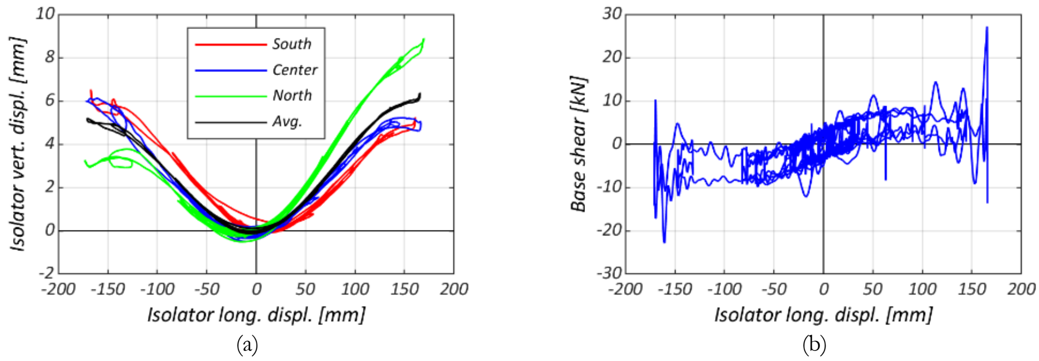

Figure 7. Half-loaded rack, 6 fuses, 125%-scaled input: (a) KSJ trajectories; (b) force-displacement response.

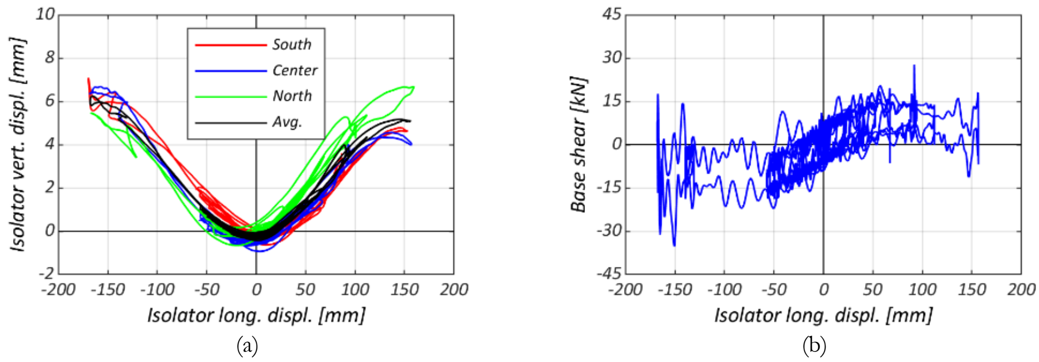

Figure 8. Fully loaded rack, 6 fuses, 125%-scaled input: (a) KSJ trajectories; (b) force-displacement response.

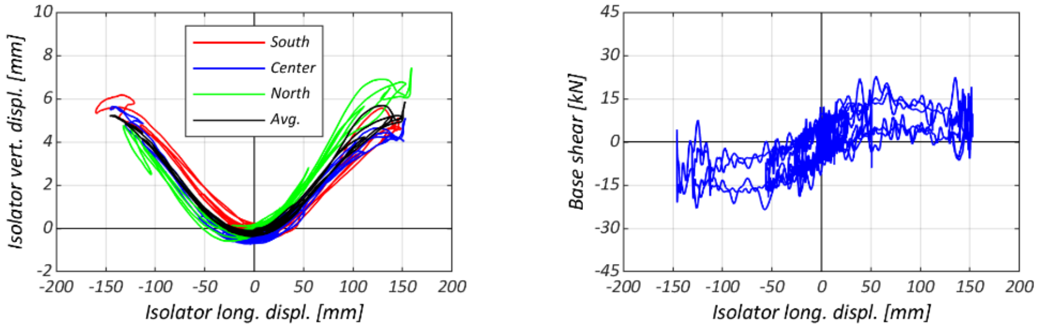

(a) (b)

Figure 9. Fully loaded rack, 12 fuses, 125%-scaled input: (a) KSJ trajectories; (b) force-displacement response.

As with friction-pendulum devices, the KSJ restoring force was proportional to the dynamic mass. It achieved a maximum value of about 4.5% of the dynamic weight in all loading configurations, net of frictional effects within pinned joints. The latter were responsible of energy dissipation, making the force-displacement response fatter, and included two components: one independent of the supported mass (around 0.3 kN) and one equal to about 3% of the dynamic weight.

Spikes in the hysteretic curves at maximum displacements denote impact upon achievement of the isolator maximum range. In the unloaded configuration this was never reached; indeed, under the 25%-scaled input the KSJ isolators barely moved as joint friction kept them locked. In the half-loaded configuration, it was achieved during the test run scaled to 100%, only in the positive verse, and during the one scaled to 125%, in both positive and negative verses. Finally, with the fully loaded rack the displacement allowance was reached under the 125%-scaled runs in both positive and negative verses.

The 50%, 75%, 100%, and 125%-scaled runs were repeated in fully loaded configuration increasing the number of fuses from 2 to 4 per isolator pair (6 to 12 total fuses). Comparing Fig. 9 and Fig. 8 shows that doubling the number of hysteretic fuses, and the associated braking effect, resulted in some reduction of the acceleration or force demand on the specimen upon impact at maximum displacement range.

Overturning moment at the specimen base and higher modes of rack vibration caused some irregularities in the KSJ trajectories and more visible wobbles in the force-displacement curves. These effects were more pronounced under higher gravity loads. Moreover, minor discrepancies between the trajectories of the three pairs of isolators can be attributed to installation misalignments, which caused little deviations from the at-rest positions.

3.2 Effectiveness of the Isolation System

Fig. 10 through Fig. 12 plot the ratios between the elastic spectral ordinates for the acceleration time series recorded atop the isolators and for the one imposed to the shake-table. This operation was repeated for the test runs with scale factors of 25% and 125%. Because the signal recorded above the isolators acts as input motion for the superstructure, this ratio informs about the isolation effectiveness: values smaller than 1.0 denote desirable input reductions. For superstructure periods approaching or exceeding the average isolation period, undesirable amplification was obtained as typically observed also with other devices, due to resonance with the isolated system.

More pronounced spectral reduction was obtained under higher-intensity input signals, as indicated by wider period ranges over which the spectra ratio was smaller than 1.0. In fact, this range was limited to an upper-bound period of about 1.25 s in the 25% test runs and extended up to about 2.25 s in the 125% ones. Moreover, in unloaded conditions the 25%-scaled input did not even activate the isolators, with spectral ratios oscillating around 1.0 for any period. These observations can be attributed to two factors:

i. the variable curvature of the KSJ trajectories results in average isolation periods increasing with the displacement demand [Guerrini et al., 2019, 2020];

ii. the KSJ frictional resistance keeps the isolators locked under small lateral accelerations and dynamic masses.

Spikes in the response spectra ratio at periods of about 0.1 s correspond to the actuator oil column frequency. Other spikes around the fixed-base natural period of the rack were more evident under higher gravity loads because the superstructure dynamic response interfered more with the isolator motion. The spectra ratios were only slightly affected by the increased number of hysteretic fuses (Fig. 13), mainly around the fixed-base natural period of the rack (about 0.4 s), which was less excited by the softer impact.

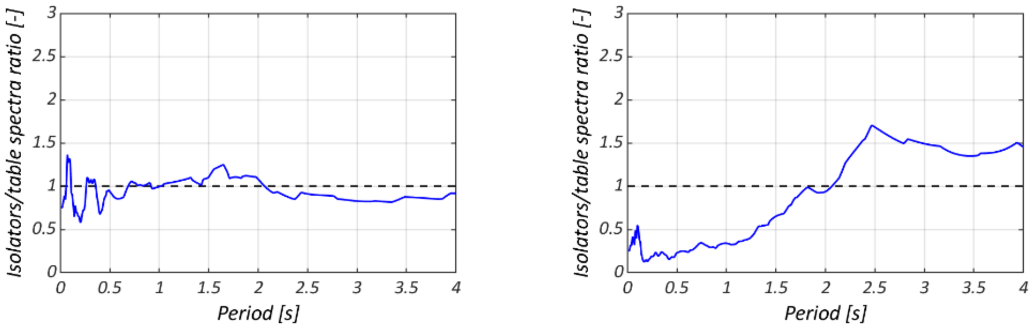

(a) (b)

Figure 10. Unloaded rack, 6 fuses, 5%-damped response spectra ratios: (a) 25%-scaled input; (b) 125%-scaled input.

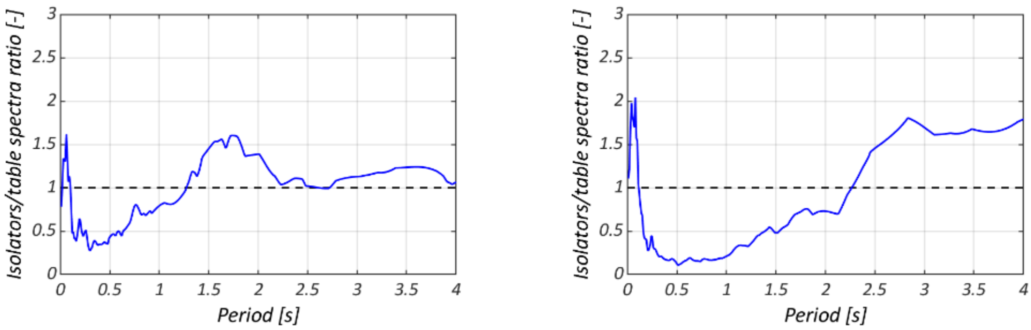

(a) (b)

Figure 11. Half-loaded rack, 6 fuses, 5%-damped response spectra ratios: (a) 25%-scaled input; (b) 125%-scaled input.

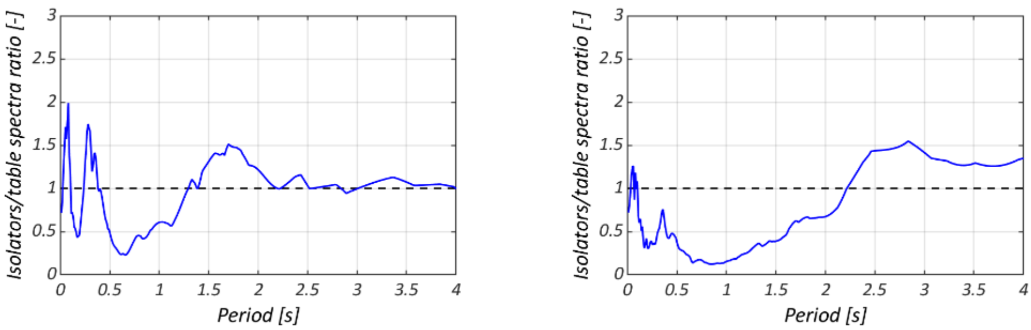

(a) (b)

Figure 12. Fully loaded rack, 6 fuses, 5%-damped response spectra ratios: (a) 25%-scaled input; (b) 125%-scaled input.

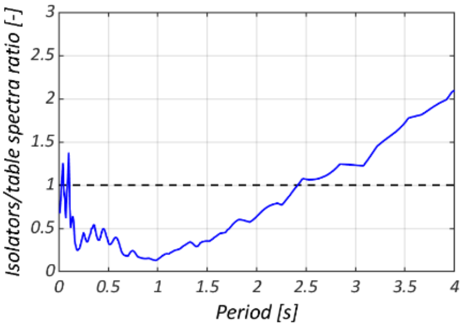

Figure 13. Fully loaded rack, 12 fuses, 5%-damped response spectra ratio under the 125%-scaled input.

4. CONCLUSIONS

This paper discussed the findings from an experimental campaign on an industrial steel rack, seismically isolated with an innovative device in the cross-isle direction. The isolator, named "Kinematic Steel Joint" (KSJ), consists of a double articulated-quadrilateral mechanism. Compared to more conventional elastomeric and friction-pendulum isolators, the KSJ offers the advantages of competitive fabrication costs and low-maintenance requirements, if made of galvanized or stainless steel.

Incremental dynamic shake-table tests were performed on the specimen in the isolated cross-isle direction, under three loading configurations: unloaded, half-loaded, and fully loaded. The experimental results confirmed the behavior of the KSJ devices obtained from previous investigations. The isolators imposed a pendulum-type, self-centering motion to the superstructure base, with a trajectory characterized by variable curvature.

Consistently with friction-pendulum devices, restoring forces at the isolation layer were proportional to the slope of the trajectory and to the weight of the supported rack. KSJ isolators also provided some energy dissipation thanks to friction within pinned joints. Replaceable hysteretic fuses allowed dissipating part of the kinetic energy when approaching the maximum displacement range of the isolators, slightly softening the impact, and thus reducing superstructure accelerations.

The KSJ devices reduced seismic effects on the superstructure over a fixed-base period range varying with the displacement demand imposed to the isolators. In fact, the period of the isolated system depends on the average curvature of the trajectory, which is not constant but decreases as the lateral displacement increases. Consequently, the upper bound of the period range of effectiveness increases with the displacement demand.

If the fixed-base period of the superstructure approaches or exceeds the average isolation period for the given displacement demand, undesirable amplification of the effects on the rack are expected because of resonoance, as typically observed also with other isolators. Under low-intensity input motions and small dynamic masses the KSJ devices remained locked, due to frictional resistance within the pinned joints. Some interference occurred between rack and isolation responses, especially under high gravity loads.

The results of this study confirmed the effectiveness of the KSJ technology at isolating industrial racks and encourage further developments and applications to other nonstructural components. Geometric optimizations will allow to obtain different lateral displacement ranges and trajectory curvatures, compatible with a variety of superstructure configurations. For instance, research is in progress to extend the application of KSJ isolators to museum artworks, electrical cabinets, and server racks.

ACKNOWLEDGMENTS

The authors would like to thank Kyneprox S.r.l. for the financial and material support to the experimental campaign. The fundamental contribution of Giovanni Ausenda (Kyneprox S.r.l.) is duly acknowledged, as well as the help provided by the staff of the EUCENTRE Foundation and of the Department of Civil Engineering and Architecture of the University of Pavia.

REFERENCES

Bournas, D.A., Negro, P., Taucer, F.F. [2014] "Performance of industrial buildings during the Emilia earthquakes in Northern Italy and recommendations for their strengthening," *Bulletin of Earthquake Engineering*, Vol. 12, No. 5, pp. 2383–2404. DOI 10.1007/s10518-013-9466-z

Clark, P.W., Kelly, J.M., Aiken, I.D. [1996] "Aging studies of high-damping rubber and lead-rubber seismic isolators," *Proc. 4th U.S.-Japan Workshop on Earthquake Protective Systems for Bridges, Technical Memorandum No. 3480*, pp. 75–89, Public Works Research Institute, Ministry of Construction, Tokyo, Japan.

Constantinou, M.C., Whittaker, A.S., Kalpakidis, Y., Fenz, D.M., Warn, G.P. [2007] "Performance of Seismic Isolation Hardware under Service and Seismic Loading;" *Technical Report MCEER-07-0012*, Multidisciplinary Center for Earthquake Engineering Research, University at Buffalo, The State University of New York, Buffalo, NY, USA.

Filiatrault, A., Higgins, P.S., Wanitkorkul, A., Courtwright, J.A., Michael, R. [2008] "Experimental seismic response of base isolated pallet-type steel storage racks," *Earthquake Spectra*, Vol. 24, No. 3, pp. 617–639. DOI: 10.1193/1.2942375

Filiatrault, A., Sullivan, T. [2014] "Performance-based seismic design of nonstructural building components: The next frontier of earthquake engineering," *Earthquake Engineering and Engineering Vibration*, Vol. 13, No. S1, pp. 17–46. DOI:10.1007/s11803-014-0238-9

Guerrini, G., Ausenda, G., Graziotti, F., Penna, A. [2019] "An innovative seismic isolation device based on multiple articulated quadrilateral mechanisms: analytical study and shake-table test," *Proc. 18th ANIDIS Conference*, Ascoli Piceno, Italy.

Guerrini, G., Tomassetti, U., Graziotti, F., Rota, M., Penna, A. [2020] "Effect of an innovative isolation system on the seismic response of cultural heritage building contents," *Proc. 17th World Conference on Earthquake Engineering*, Sendai, Japan.

Kauschke, W., Baigent, M. [1986] "Improvements in the long-term durability of bearings in bridges, especially of PTFE slide bearings," *Proc. 2nd World Congress on Joint Sealing and Bearing Systems for Concrete Structures, Publication SP-94*, Vol. 2, pp. 577–612, American Concrete Institute, Detroit, MI, USA.

Lee, D.J. [1981] "Recent experience in the specification, design, installation, and maintenance of bridge bearings," *Proc. World Congress on Joint Sealing and Bearing Systems for Concrete Structures, Publication SP-70*, Vol. 1, pp. 161–175, American Concrete Institute, Detroit, MI, USA.

Morgan, T., Whittaker, A.S., Thompson, A. [2001] "Cyclic behavior of high-damping rubber bearings," *Proc. 5th World Congress on Joints, Bearings and Seismic Systems for Concrete Structures*, Rome, Italy.

Perrone, D., Calvi, P.M., Nascimbene, R., Fischer, E.C., Magliulo, G. [2019] "Seismic performance of non-structural elements during the 2016 Central Italy earthquake," *Bulletin of Earthquake Engineering*, Vol. 17, No. 10, pp. 5655–5677. DOI: 10.1007/s10518-018-0361-5

Taghavi, S., Miranda, E. [2003] "Response assessment of nonstructural building elements," *PEER Report 2003/05*, Pacific Earthquake Engineering Research Center, University of California Berkeley, Berkeley, CA, USA.

Quasi-static cyclic testing of a drift-sensitive sub-assembly of non-structural elements with low-damage characteristics

Robert Clement[1], Rajesh P. Dhakal[2], Mayank Tripathi[3] Giovanni De Francesco[2], Muhammad Rashid[2], and Timothy J. Sullivan[2]

[1] University of Canterbury
Christchurch, New Zealand
{robert.clement}@pg.canterbury.ac.nz
[2] University of Canterbury
Christchurch, New Zealand
{rajesh. dhakal, giovanni.defrancesco, muhammad.rashid, timothy.sullivan}@canterbury.ac.nz
[3]Mayank.tripathi@gib.co.nz

Abstract. As an ongoing effort to improve the seismic performance of non-structural elements (NSEs), a precast concrete cladding system with novel rocking connections has been recently developed at the University of Canterbury, New Zealand. In this system, cladding panels are attached to the structure through steel-embeds with vertical slots placed at four corners of the panel. The panels sit on the structure at the locations of weld-plates in the panels. The steel embeds allow the panels to rock under inter-storey drifts while the weld-plates transfer the gravity loads to the structure. This allows for the accommodation of significant drift demands, delaying and minimising damage to the cladding system. This design has been validated as a low-damage solution, but its interaction with other drift-sensitive non-structural elements such as partition walls and glazed curtain walls has not been investigated. Moreover, as air and watertightness are desired attributes of cladding systems, satisfactory weather-tightness performance of the cladding system is also essential. This study investigates interactions between a sub-assembly of low-damage internal partition walls, glazed curtain walls and the novel cladding system. The test results will provide essential information on the applicability and effectiveness of this cladding system as an alternative to conventional systems. For this purpose, a test specimen replicating a typical external wall segment of a commercial building including cladding panels, window glazing, and plasterboard internal walls has been designed to examine the interaction of these non-structural elements under quasi-static cyclic drift demands. In addition to seismic testing, weather-tightness tests will also be conducted to ensure that the cladding system and its interfaces with glazing and internal partition walls are not only structurally sound but also satisfy the serviceability requirements. These tests are expected to provide a holistic view of the interactions between these drift-sensitive non-structural elements and identify shortcomings (if any) arising due to their mutual interaction.

Keywords: non-structural interactions, weather-tightness, quasi-static cyclic testing.

1. INTRODUCTION

It has been repeatedly observed that the performance of non-structural elements (NSEs) is crucial to the performance of a building facility. After the 2010-2011 Christchurch Earthquake sequence, there was significant damage observed to NSEs [Dhakal, 2010, Baird *et al.,* 2011]. This included injuries due to broken glass [Arifin *et al.,* 2020], and connection failures of several precast concrete panels [Kam *et al.,* 2011]. Figure 1 shows some of the damage to NSEs observed during the 2011 Christchurch earthquake. This shows that despite current design provisions within New Zealand focusing on ensuring life safety and requiring non-structural elements to be secured such that they do not present a falling hazard [Baird *et al.,* 2011], a risk is still presented by the poor performance of these components during seismic excitation. Even for the cases where the seismic performance proved sufficient to meet the life-safety requirements, the serviceability performance can still be compromised. This can present a series of issues, such as a loss of weather-tightness [Arifin *et al.,* 2020] which can lead to further damage, limiting access for emergency and recovery services. This leads to a loss of building functionality and high economic losses [Mulligan *et al.,* 2020]. For residential and commercial structures, NSEs contribute about 80% of the building value [Khakurel *et al.,* 2020] and comprise the majority of the expected economic losses from earthquake damage [Bradley *et al.,* 2009]. With this in mind, this research intends to examine both the seismic and serviceability performance of NSEs. Drift-sensitive components, such as precast concrete panels, glazing systems, and internal plasterboard walls, are the focus of this research.

Figure 1: Photos of NSEs damage during the 2011 Christchurch Earthquake. a) and b) indicate damage to glazing systems [Baird *et al.,* 2011], c) and d) show damage to precast concrete panels [Kam *et al.,* 2011].

In order to address the weaknesses found in the connections between precast concrete cladding panels and the building structure that led to some dangerous cladding damage during the Christchurch Earthquake, Bhatta *et al.,* [2020] developed a precast concrete panel with novel rocking connections, which enable the panels to displace vertically and horizontally, as well as rotate, under seismic loading. The rocking mechanism is facilitated by four steel embeds cast into each concrete panel, with each consisting of a vertical slot and a cap filled with grease which facilitates the sliding of the bolt connected to the panel. There are also two weld plates flushed with the bottom of the panel, which act as the points of contact for the rocking motion to prevent spalling and chipping of the concrete. A schematic layout of precast concrete panels with these connections is shown below in Figure 2. These panels were tested under quasi-static loading to an interstorey drift of 4.2%, and it was found that up to this drift level, no damage occurred to the panels or the rocking connections. Nevertheless, some damage was sustained by the silicone sealant used between the panels. The first damage state (DS1) was partial tearing of the sealant over a short length of the joint (and may not be easily perceived), which was observed at 1.92% interstorey drift. The second damage state (DS2) was visible tearing over much of the length of the joint, which occurred at 2.7% interstorey drift. These damage states are shown in Figure 3 below. These results were compared to other prevalent connection types used for precast concrete panels, and it was shown that this novel rocking design possessed "superior seismic resilience" when compared to other conventional connections [Bhatta *et al.,* 2020].

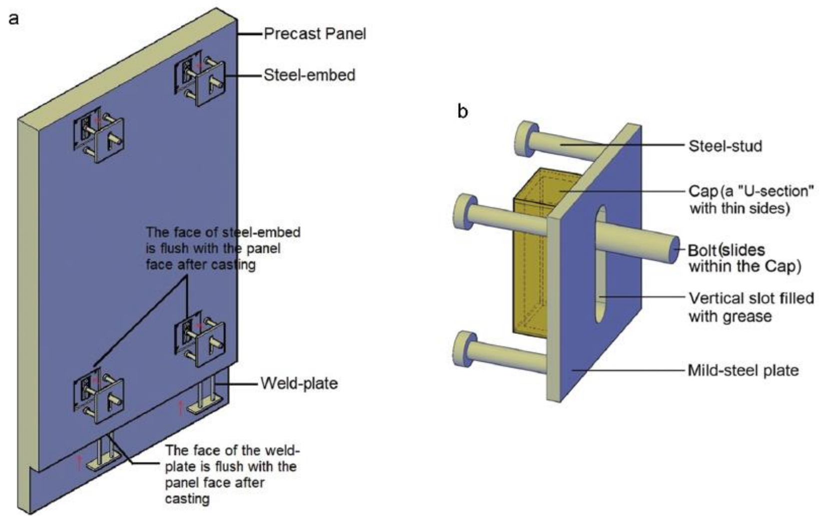

Figure 2: Renders of a) The precast panel with the embeds and weld plates, and b) The steel-embed [Bhatta *et al.,* 2020].

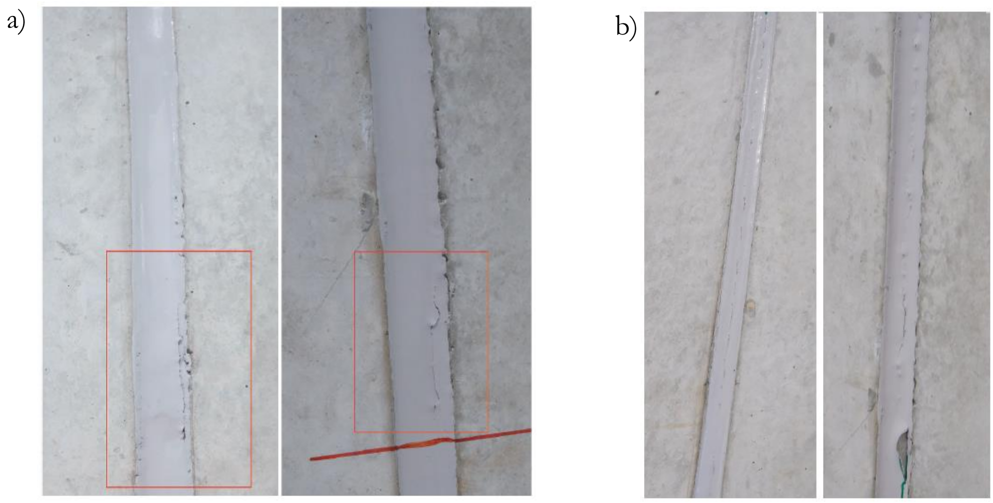

Figure 3: Photos taken showing a) DS1 (small tearing over a short length of the joint) and b) DS2 (visible tearing over much of the length of the joint) in the sealant [Bhatta *et al.,* 2020].

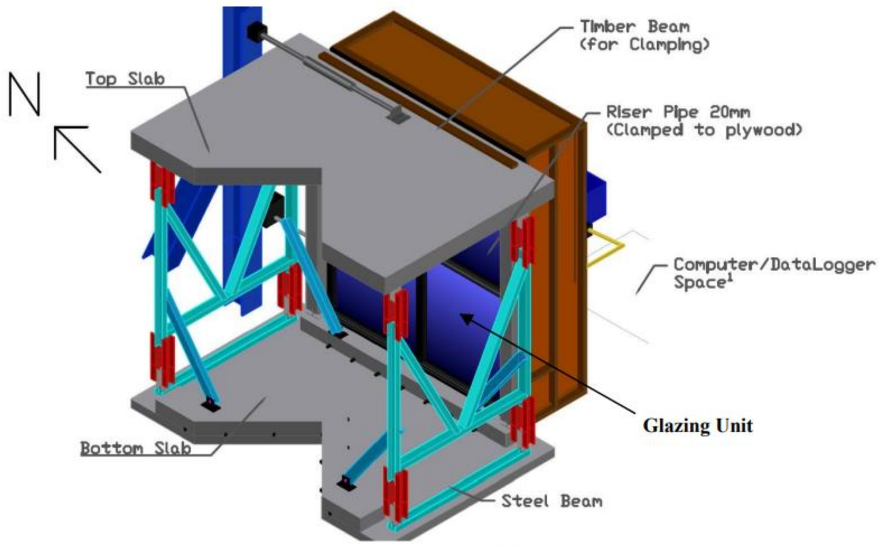

Figure 2: 3D render of glazing experimental setup with Waterbox [Arifin *et al., 2020].*

In 2020, Arifin *et al.,* investigated the seismic fragility of New Zealand-manufactured commercial glazing systems. These tests investigated the deformation limits at which the tested glazings exceeded the defined damage states. These damage states were water leakage, gasket failure, and glass/frame failure. To achieve this objective, Arifin *et al.,* [2020] simultaneously conducted weather-tightness and seismic tests on glazings. To test the weathertightness, a wooden waterbox was designed and assembled to the recommendations set out by NZS4211:2008 Specification for the performance of windows, as well as NZS4284:2008 Testing of building facades [SAS/NZ, 2008]. This waterbox has four spray nozzles spaced 1800mm apart, along with a microcontroller that was used to regulate the air pressure as required by the testing standards. The overall set-up of the experiment is shown in Figure 4. Within this testing rig, three specimens with a standard glazing frame and three specimens with seismic frames were tested [Arifin *et al.,* 2021]. These tests demonstrated that while glazing with standard frames are vulnerable to leakage at low drifts (at around 0.5%), applying the seismic frame systems delays the onset of the first damage state (defined as water leakage) until at least 1.5% interstorey drift. On the other hand, the improvements to the other two damage states (gasket failure and glass/frame failure, respectively) by using seismic frames were insignificant. Using these results, a comparison was made between the gains in weather-tightness performance versus the additional costs incurred from using the seismic glazing system. This was accomplished using the Pacific Earthquake Engineering Research – Performance-Based Earthquake Engineering (PEER – PBEE) process on three case buildings, and then undertaking a FEMA P58 loss assessment process. By using these processes, it was possible to determine the expected annual losses (EAL), and it was found that "seismic glazing systems are likely to be beneficial, especially in active seismic areas such as Christchurch and Wellington" [Arifin *et al.,* 2021].

The seismic performance of plasterboard partition walls with seismic gaps was investigated by Tasligedik *et al.,* [2013] and Mulligan *et al.,* [2020]. Tasligedik *et al.,* [2013] proposed the use of a series of seismic gaps (both internal and external) to provide a cumulative spacing over the partition, which was found to delay the onset of minor damage to 2.0% in both steel and timber framed partitions. This was an improvement in performance, up from 0.3% and 0.75% in the standard steel- and timber-framed partitions with no gaps. These findings were further examined and expanded upon by Mulligan *et al* in 2020 to examine the interactions with return wall partitions (both at 45 and 90 degrees to the base wall), the out-of-plane performance, and the impact of using a filler material in the seismic gaps. The test setup used by Mulligan *et al., [2020]* is shown in Figure 5. This involved loading the configuration at an angle of 35 degrees from the base wall, resulting in all components experiencing both in and out-of-plane loading. From this, it could be determined that the out-of-plane displacements and the return wall configuration did not have a significant impact on the onset of damage and that the filler material caused the earlier onset of the first damage state but provided beneficial re-centring behaviour for the panels post-lateral loading.

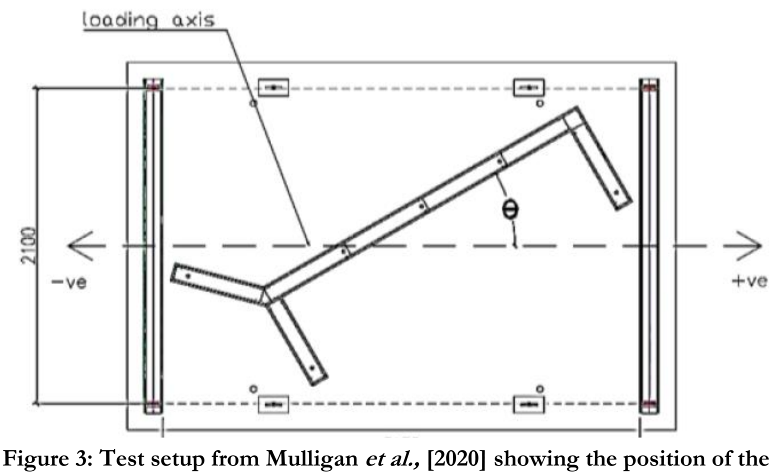

Figure 3: Test setup from Mulligan *et al.,* [2020] showing the position of the return walls and the loading axis.

Bhatta [2022] developed this concept further by implementing detailing which allowed the internal partition walls to accommodate structural deformations through a rocking motion. This involved the use of dual-slot tracks (DSTs), created by screwing two tracks of different widths, to provide two different slots for the plasterboards and the studs. Section drawings of the top and bottom connections are shown in Figure 6. Three different wall specimens, which had different configurations of stud and joint detailing, were subjected to quasi-static testing. From this, it was shown that the use of boxed end-studs with timber planks and a sealant joint (which was a combination of the results from the different wall specimens) presented the best arrangement for delaying damage to the end-studs and aluminium angles. This prompted the testing of a 'y' shaped partition wall, similar in premise to the test setup shown in Figure 5, to investigate these combined features, along with the in-plane and out-of-plane performance. Further tests were also done with these rocking partition panels in mind, such as the following:

- The use of sacrificial L-trim (SLT) joints, which make use of two GIB® paper-faced external 90-degree metal trims (L-trims) bedded by three layers of joining, causing the separation of the partitions once the vertical gap in the DST was exhausted.
- Replacing the SLT joints with traditional plaster, along with replacing the studs at the ends and junctions of the partition walls with boxed end-studs. This also included a 50mm horizontal gap between the wall and the vertical columns to avoid interaction between these elements.
- Investigating the behaviour of L and T-shaped walls configured based on the detailing in Mulligan *et al.,* [2020], to compare the performance to that of the rocking details.
- Implementing the rocking details within planar walls with standard steel studs and aluminium angles. This was further expanded upon by using boxed end-studs with timber planks when it was found that the aluminium angles resulted in bending of the steel studs (as well as screw failure at the junctions). This also re-used the aluminium angles to observe the difference in performance between new and re-used angles. A further test was done with the internal partition walls in an 'L' shaped arrangement.

These tests provided a series of recommendations on how to improve the seismic performance of the rocking partition specimens, as well as showing that this design "exhibits a comparable seismic performance to other low-damage partition walls" Bhatta [2022].

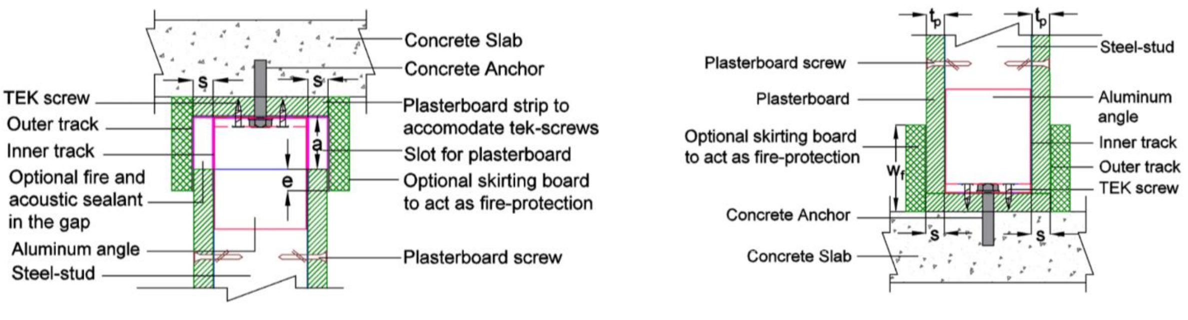

Figure 4: Section drawings of the top and bottom DST connections [Bhatta, 2022]

These series of tests demonstrate that large improvements can be made to non-structural elements by providing them with the ability or the capacity to deform, displace or rock under seismic displacements. However, the NSEs of a building are not exclusively made up of only one of these components, but rather a combination of panels, glazing and partitions, along with other non-structural elements. While the performance of each of these low-damage elements in isolation is known, an understanding of how these various drift-sensitive components would perform if they interact during seismic excitation will provide valuable information on the low-damage characteristics of these novel systems and potentially highlight the extent to which damage to NSEs in a building can be minimised by using these systems. Further, it will provide an opportunity to assess if a combination of these elements has any effect on the functionality or serviceability of the components, either positively or negatively, due to their combined response to seismic excitation. Additionally, the precast rocking panels are a newly developed system and their ability to be installed in conjunction with other NSEs in a building is yet to be examined. Therefore, this research intends to:

- Develop an experimental sub-assembly that incorporates low-damage plasterboard partitions and precast concrete rocking panels, and a curtain wall glazing.
- Take this sub-assembly and subject it to quasi-static testing, to investigate the interactions between these multiple drift-sensitive NSEs.
- Investigate the weather-tightness of the sub-assembly to evaluate the post-earthquake serviceability performance of this system.

2. EXPERIMENTAL SETUP

2.1 EXPERIMENTAL FRAME AND REACTION WALL

The testing rig which will be used for this experiment is an adapted version of the experimental setup used in Arfiin *et al.,* [2020], as shown in Figure 4 above. The setup consisted of a top and bottom concrete slab connected by pinned steel v-braced frames, with diagonal supports to provide stability. The setup also makes use of two square hollow section columns, which support the curtain wall glazing.

To evaluate the water-tightness, the wooden waterbox developed for the glazing experiment will also be reused. As mentioned, this waterbox (shown in Figure 7) makes use of several water sprinklers and a microcontroller to meet the building facade testing requirements. For seismic testing, a reaction wall made from a series of precast reinforced concrete blocks will be used. A series of threaded rods were inserted into the blocks both vertically (directly into the strongfloor) and horizontally, which are then tensioned to lock the blocks into place. To ensure no stress concentrations occur in the concrete blocks during testing, a layer of grout is placed between each vertical layer of blocks. This reaction wall is shown in Figure 8.

2.2 SPECIMEN DESIGN

The specimen sub-assembly is illustrated from different angles in Figure 9 below. As can be seen, three precast concrete rocking panels will be used, with one full-height panel and two half-height panels. This is to examine the effects of stacking the panels on top of each other in the case of multiple storeys, as well as the effect on the glazing in the centre of the front face. These half-height panels are separated by a 20mm gap, which will be sealed using a one-stage silicone sealant, as was done by Bhatta *et al.,* [2020]. The concrete panels are supported by angle sections with stiffeners, either bolted into the bottom concrete slab or welded to the added steel beam. The steel embeds, which enable the rocking motion, are supported by connections on the top and bottom slab, as well as the steel beam. These slotted connections have the same horizontal spacing on all the panels but differ in their vertical spacing. The construction dimensions for the panels are shown below in Table 1.

Between the cladding panels, a full-height curtain wall glazing unit with a seismic frame will be appropriately affixed to the cladding panels and the top and bottom slabs. A seismic frame will be used in this experiment to better accommodate the deformations that will be imposed on the glazing frame due to the applied lateral deformations. The size of the panels and glazing is such that the waterbox used for the weather-tightness testing will be able to form a seal with no exposed areas. These dimensions are shown below in Table 1. Additionally, the front of the glazing system will be positioned towards the front of the panels, to provide a flat finish.

Figure 5: Photos of the Waterbox used for the watertightness testing, showing the front of the apparatus.

Figure 6: Photo of the completed reaction wall.

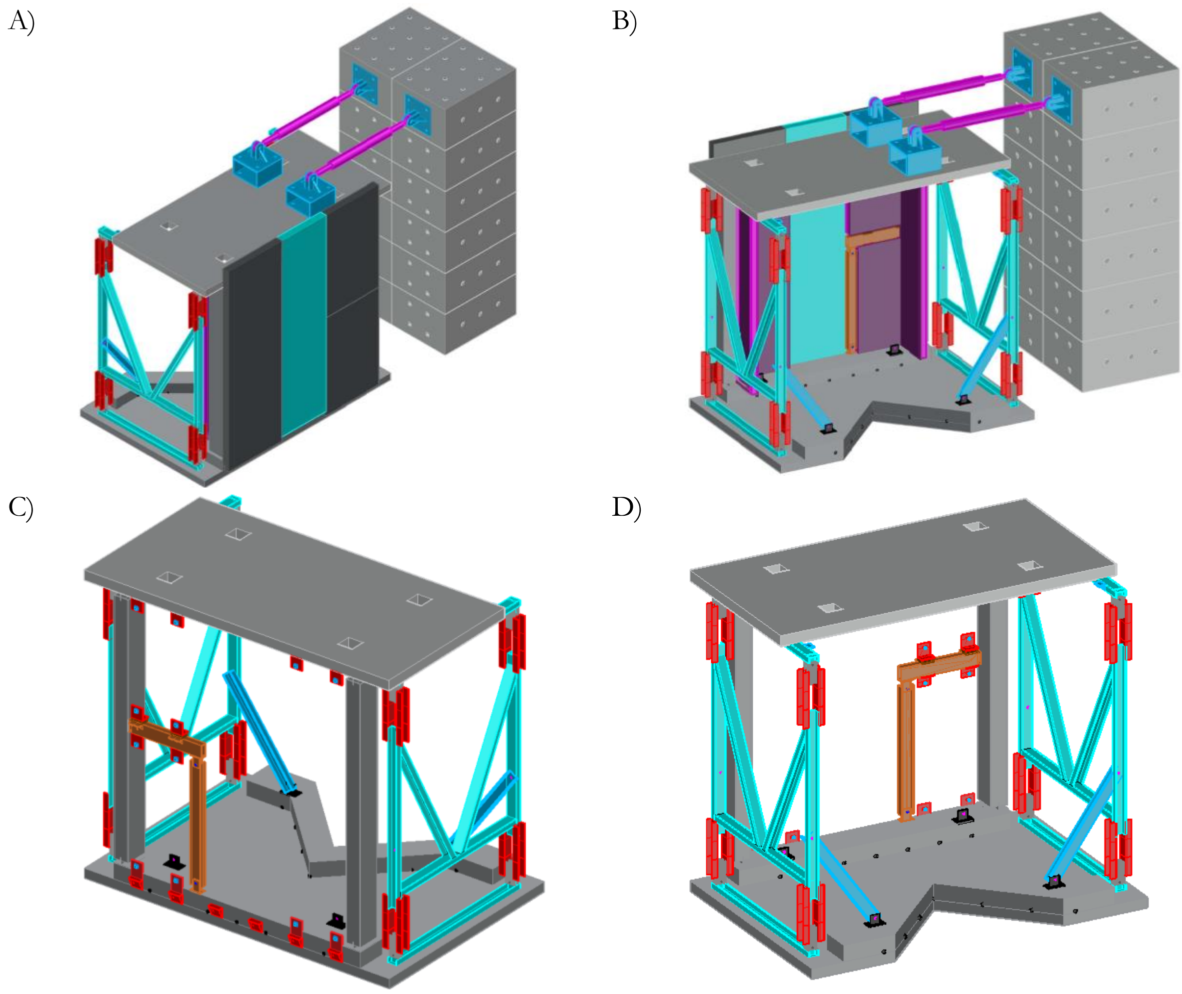

Figure 7: 3D views of the experiment setup, A) Specimens included (front), B) Specimens included (back), C) Specimens excluded (front), D) Specimens excluded (back).

Table 1: Table showing the dimensions of the experimental components.

Component	Length (mm)	Width (mm)	Depth (mm)
Precast Concrete Panel 1 (Top-Left)	1993mm	1200mm	120mm
Precast Concrete Panel 1 (Bottom-Left)	1935mm	1200mm	120mm
Precast Concrete Panel 1 (Right)	3902mm	1200mm	120mm
Seismic Frame Glazing	3820mm	1000mm	120mm
Plasterboard Partition Wall 1 (Top-Left)	1425mm	950mm	104mm (13mm board and 91mm studs)
Plasterboard Partition Wall 2 (Bottom-Left)	1640mm	800mm	104mm
Plasterboard Partition Wall 3 (Right)	3290mm	1000mm	104mm
Partition Return Walls	3310mm	600mm	117mm (two 13mm boards)
Note: The widths of the horizontal sealant joints between the two half-height panels, and the vertical joints between the partitions and the return walls, are 20mm and 6mm, respectively.			

Plasterboard partition walls will sit behind the precast panels and will be attached to the panels such that when the panels rock the partitions will also rock. This aims to ensure that there is no incompatibility between the plasterboard and the panels at any stage of loading. To do this, a spacer (whose dimensions will be determined during construction) will be placed in between the panels and the partitions, such that there will not be any interference with the panel rocking connections. The dimensions of these panels are shown below in Table 1. To allow for this movement, the plasterboard partition wall design will follow the detailing suggested in Bhatta [2022], making use of the concealed gaps inside the DSTs to provide the deformation capacity. In addition, return walls will be constructed with the same detailing to examine the interaction between different low-damage partition wall segments. At the vertical joint between these elements, a 6mm gap will be provided, which will be filled with a one-stage polyurethane sealant, similar to what was done in the experiments performed by Bhatta [2022].

2.3 TESTING PROTOCOLS

The quasi-static testing to be undertaken in this study will use the slightly modified version of the FEMA461 [FEMA, 2007] loading protocol adopted by Bhatta *et al.,* [2020]. In-plane cyclic loading will be applied to the test specimen through two actuators attached to the top slab of the experimental frame. Between each drift cycle, weather-tightness tests will be performed to see if the serviceability of the sub-assembly has been compromised. This cyclic pressure testing will immediately follow the static pressure test. A visualisation of this procedure is shown in Figure 10.

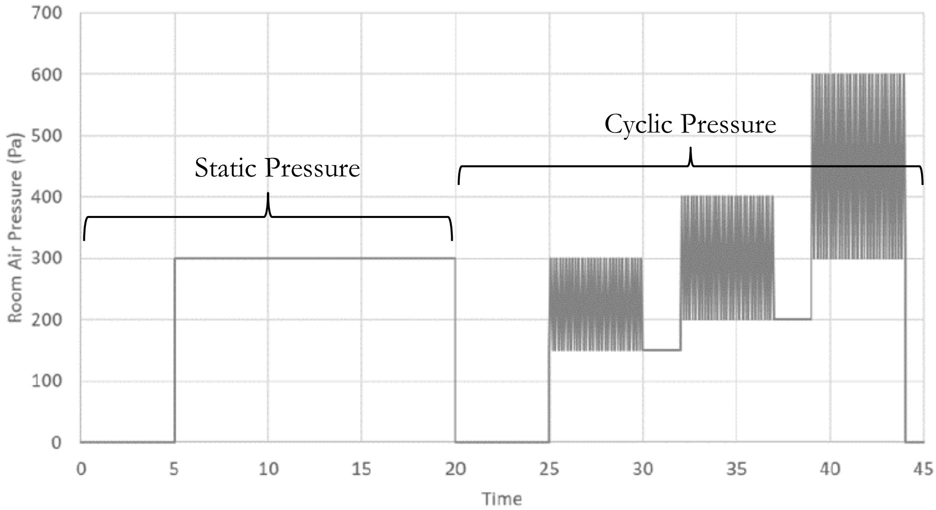

Figure 10: Visualization of differential air pressure imposed as per NZS4281 ***[Arifin et al., 2020].***

2.4 INSTRUMENTATION

The instrumentation for this experiment will focus on measuring the relative horizontal and vertical displacements between the various NSEs within the experimental rig. The horizontal joint between the two precast concrete panels, the interface between the panels and the glazing system, and the connections between the internal partition and return walls are of particular interest for examining potential incompatibilities. These measurements will be taken using linear potentiometers across the horizontal and vertical joints, and string pots when the expected displacement is large. Visual measuring techniques such as drawing horizontal and vertical lines across the connections will also be used to measure the offset during the loading procedure. A comparison will also be made between the measured displacement of the precast panels and the attached partition walls, to assess if or when the displacement of these elements begins to differ.

3.CONCLUDING REMARKS

This paper presents an overview of the quasi-static test currently being undertaken at the University of Canterbury Structural Engineering Laboratory (SEL) to estimate the seismic performance of multiple drift-sensitive NSEs. At the time of writing this paper, the specimens are being fabricated, and assembly has begun of the experimental frame. A photo of the in-progress assembly is shown in Figure 11 below. Work on assembling this frame is progressing as expected, and with prompt delivery of the specimens, the experimental testing will begin in the near future. These tests will set out to examine the seismic and weather-tightness performance of a sub-assembly of NSEs comprising of drywall partition walls, seismic curtain wall glazing, and low-damage rocking precast concrete cladding panels. The test is expected to provide a holistic view of the interactions between these drift-sensitive NSEs in terms of seismic performance as well as in terms of serviceability performance. Additionally, it will provide an opportunity to identify incompatibilities that may arise from the interactions, as well as potential issues that may warrant further investigation.

Figure 11: Photo of the in-progress assembly.

4. ACKNOWLEDGEMENTS

The work described in this paper is part of the research being done by QuakeCoRE, a New Zealand Tertiary Education Commission-funded Centre. This work is part of Disciplinary Theme 2: Whole-of-Building Seismic Performance with a focus on the key research thrust regarding non-structural component demands. The authors also wish to gratefully acknowledge the support provided by Jitendra Bhatta and Fransiscus Arifin in the development and running of this experiment. Partial funding has been provided via a QuakeCoRE scholarship.

5. REFERENCES

Arifin, A.F., Sulivan, T.J., Dhakal, R.P., [2021] "Performance Comparison of Standard and Seismic Glazing Systems:" *Paper presented at the New Zealand Society of Earthquake Engineering Annual Technical Conference,* Christchurch, New Zealand

Arifin, A.F., Sullivan, T.J., Dhakal, R.P., [2020] "Experimental Investigation into the Seismic Fragility of a Commercial Glazing System." *Bulletin of the New Zealand Society of Earthquake Engineering,* Vol. 53, No. 3, pp. 144-149.

Baird, A., Ferner, H. [2017] "Damage to Non-Structural Elements in the 2016 Kaikoura Earthquake" *Bulletin of the New Zealand Society for Earthquake Engineering,* Vol. 50, No. 2, pp. 187-193.

Baird, A., Palermo, A., Pampanin, S. [2011] "Facade Damage Assessment of Multi-storey Buildings in the 2011 Christchurch earthquake." *Bulletin of the New Zealand Society for Earthquake Engineering,* Vol. 44, No. 4, pp. 368-376.

Bhatta, J., [2022] "Development and Verification of Seismically Resilient Drift-Sensitive Non-Structural Elements in Buildings." *PhD Thesis*, Department of Civil and Natural Resources Engineering, University of Canterbury, New Zealand.

Bhatta, J., Dhakal, R.P., Sullivan, T.J., Lanyon, M., [2020] "Low-Damage Rocking Precast Concrete Cladding Panels: Design Approach and Experimental Validation." *Journal of Earthquake Engineering,* DOI: 10.1080/13632469.2020.1830201.

Dhakal, R.P., [2010] "Damage to non-structural components and contents in 2010 Darfield earthquake" Bulletin of the New Zealand Society for Earthquake Engineering, Vol.43, No.4, pp.404-411. DOI: https://doi.org/10.5459/bnzsee.43.4.404-411

FEMA [2007] 461: Interim Testing Protocols for Determining the Seismic Performance Characteristics of Structural and Nonstructural Components, Applied Technology Council, USA.

Kam, W.K., Pampanin, S., Elwood, K., [2011] "Seismic Performance of Reinforced Concrete Buildings in the 22 February Christchurch (Lyttelton) Earthquake" *Bulletin of the New Zealand Society of Earthquake Engineering,* Vol. 44, No. 4, pp. 239-278.

Khakurel S., Dhakal, R.P., Yeow, T.Z., Saha, S.K., [2020] "Performance Group Weighting Factors for Rapid Seismic Loss Estimation of Buildings with Different Usage" *Earthquake Spectra,* Vol.36, No. 3, pp. 1141-1165.

Mulligan, J.G., Sullivan, T.J., Dhakal, R.P., [2020]. "Experimental Study of the Seismic Performance of Plasterboard Partition Walls with Seismic Gaps." *Bulletin of the New Zealand Society of Earthquake Engineering,* Vol. 53, No. 4, pp. 175-188.

SAS/NZ [2008]: AS/NZS4281 Testing of Building Facades. Standards Australia/New Zealand.

Tasligedik, A.S., Pampanin, S., Palermo, A. [2013]. "Low Damage Seismic Solutions for Non-Structural Drywall Partitions." *Paper presented at the Vienna Congress on Recent Advances in Earthquake Engineering and Structural Dynamics 2,* Vienna, Austria.

Seismic Cable Bracing of Sprinkler Piping

Jochen Carl[1], Hossein Mostafaei[2]

[1] Lead Research Scientist
FM Global, Research Division, Norwood, Massachusetts
e-mail: jochen.carl@fmglobal.com
[2] Principal Research Scientist
FM Global, Research Division, Norwood, Massachusetts
e-mail: hossein.mostafaei@fmglobal.com

Abstract. Cable braces are easy to install, are light, and are less costly than rigid seismic braces.

Unlike rigid seismic braces, cables don't fatigue through plastic deformation but instead fail in a brittle manner. In a series of tension tests, the cables showed a nonlinear elastic behavior until close to failure, and failed consistently about 30% above the minimum breaking strength rating of ASTM A1023. The breaking strength was not affected by the loading speed and was even maintained when a sudden, pulse-like load was applied to a slack cable.

However, concerns arose in shake table tests with full cable brace assemblies, which consist of a hanger and two cables. While cables are very stiff and stretch little under earthquake loads, the fittings and the slack in the cable may allow the sprinkler pipe to move before being resisted by the cables. Under dynamic loading, the pipe gains energy during unrestricted swing that causes an impact load on the cables. These impact loads may require increasing the design strength of the cables, especially if the pipe can swing upwards and gain potential energy that is then released in a shock load on the cables when the pipe drops. Both numerical simulations and shake table tests showed that impact loads increase with larger cable slack and larger allowable pipe upswing.

The shake table tests also verified that failure of one cable usually triggers failure of other cables because the seismic load redistributes to fewer cables.

Keywords: Cable braces, Sprinkler pipe bracing, Seismic cable bracing, Pipe uplift, Cable brace failure

1. Introduction

Cables commonly used in seismic sway braces are also called “aircraft cables” due to their original use in the aircraft industry. Per ASCE 19, these cables must be corrosion resistant, are prestretched, are color coded according to strength, and have a minimum breaking strength that is defined by ASTM A1023. The fittings vary among the manufacturers and may induce premature failure in the cable. Therefore, many manufacturers rate the cable with and without fittings, and most seek a UL 203A rating.

Cable braces are readily adjustable in length, are easy to install, are light, and are less costly than rigid seismic braces. A cable consists of several strands of metal wire laid (twisted) into a helix. In this type of assembly, flaws in a wire can be balanced out by the other wires, and friction between the individual wires and strands, because of their twist, further compensates for any flaws. Steel wires for wire ropes are made of improved plow steel, which is non-alloy carbon steel with a carbon content of 0.4% to 0.95%.

All relevant code requirements about seismic cable braces can be found in ASCE 19 [2016] and NFPA 13 [2019] (Figure 1). Table 7 of ASTM A1023 [2019] lists the minimum breaking force of cables commonly used in seismic sway braces of sprinkler piping; these are galvanized, have diameters up to 3/8 in. and have 7 strands with either 7 or 19 wires. UL 203A [2019] rates cable assemblies based on a tension test.

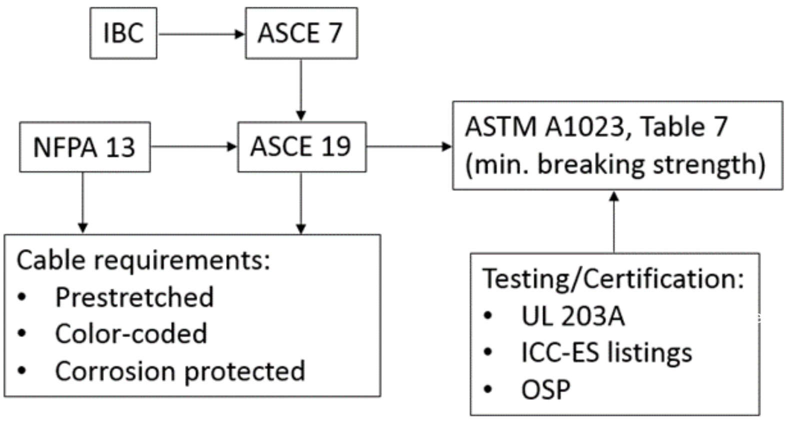

Figure 1. Most relevant codes for cable bracing.

In addition to the UL 203A listing, some manufacturers seek certification by the International Code Council Evaluation Service (ICC-ES). The ICC-ES product certification system uses external laboratories such as Intertek to test samples taken from the market or supplier’s stock, or a combination of both, to verify compliance with the applicable codes and standards. The system also involves factory inspections, and assessment and surveillance of the listee’s quality system.

The California Department of Health Care Access and Information (HCAI), also known as the Office of Statewide Health Planning and Development (OSHPD), established a voluntary Special Seismic Certification Preapproval Program (OSP) that is limited to components that require special seismic certification in accordance with CBC [2019], Section 1705A.13.3. or ASCE 7-16 [2016], Section 13.2.2. The “Certificate of Compliance” assures that after a Design Earthquake the equipment maintains structural integrity and functionality. OSHPD requires special seismic certification for fire sprinkler/fire protection systems in OSHPD 1 and 2 buildings (Hospitals and Skilled Nursing Facilities). An OSP is issued based on shake table tests in accordance with AC156 [2010] or equivalent shake table testing criteria approved by the building official.

In summary, the manufacturing process and minimum strength of cables, and the seismic design of cable braces is regulated. However, few data are available on the performance of cable braces for sprinkler systems during earthquakes. This study presents static and dynamic testing, and finite element simulations of cable braces. Section 2 describes the tensile tests on the cables and their fittings, performed to determine the breaking strength and failure type under different load rates. Section 3 summarizes shake table tests including clevis hangers and different installation angles that were performed to investigate possible pipe uplift and resulting shock loads on cables, potentially leading to unanticipated cable failure. Section 4 describes a finite element model of a full cable brace assembly, and simulations of the effect of cable slack was simulated.

2. Tension tests with cables and fittings

A test setup was built in the FM Global load frame (Figure 2a). The 3/16 in. diameter cable with 920 lb breaking strength was wrapped twice around a pipe with a 2.5 inch nominal pipe size (DN 65) on the bottom (Figure 2a, b), and attached to a seismic anchoring fitting (SAF) on the top (Figure 2c). The sleeves were crimped twice with a hand swaging tool (Figure 2c). The same test setup is used in UL 203A to rate the load capacity of seismic cable braces including their fittings.

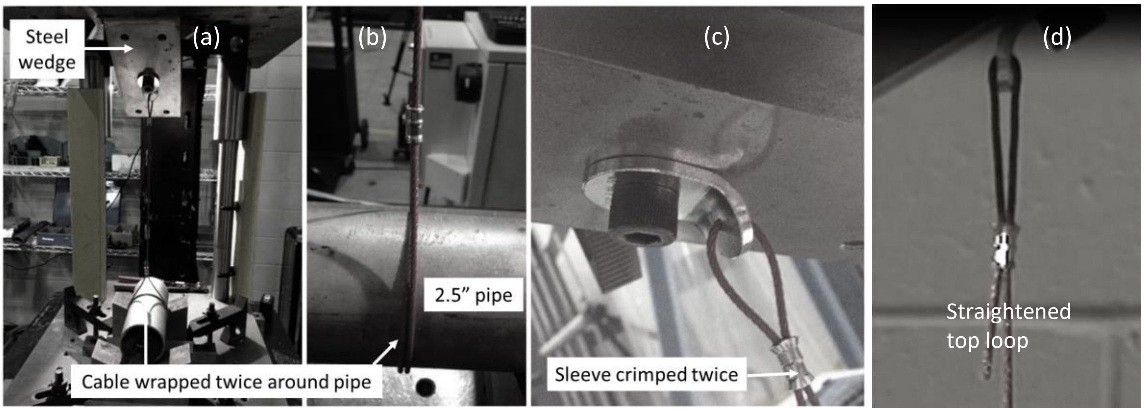

Figure 2. Tension test setup following the setup used in UL 203A.

Nine monotonic tension tests were performed until failure. Figure 3 shows the force-displacement curves, and Table 1 summarizes the failure loads.

The first three tests were performed with a slow load speed of 20 lb/s (black curves in Figure 3). The second three tests were performed with a fast load speed of 1000 lb/s (red curves in Figure 3). In the third three tests (green curves in Figure 3), the cables were slack at the test start and the actuator was commanded to apply a very fast, shock type load (> 10,000 lb/s).

At the beginning of each test, the actuator movement first straightened the cable loop in the fittings (Figure 2d). Because the length of these cable loops varied, the actuator displacements needed to straighten these loops varied (Figure 3a). Then, the cables showed a nonlinear-elastic force-displacement behavior until close to the failure load. The slopes of Tests 7-9 differ because the tests were so short that only a few data points (green diamond markers) were collected. Figure 3b shows the similar slopes of the force-displacement curves for Tests 1-6 after removal of the loop straightening. Due to variations in the total cable length during the tests, the small variations between the force-displacement curves were expected.

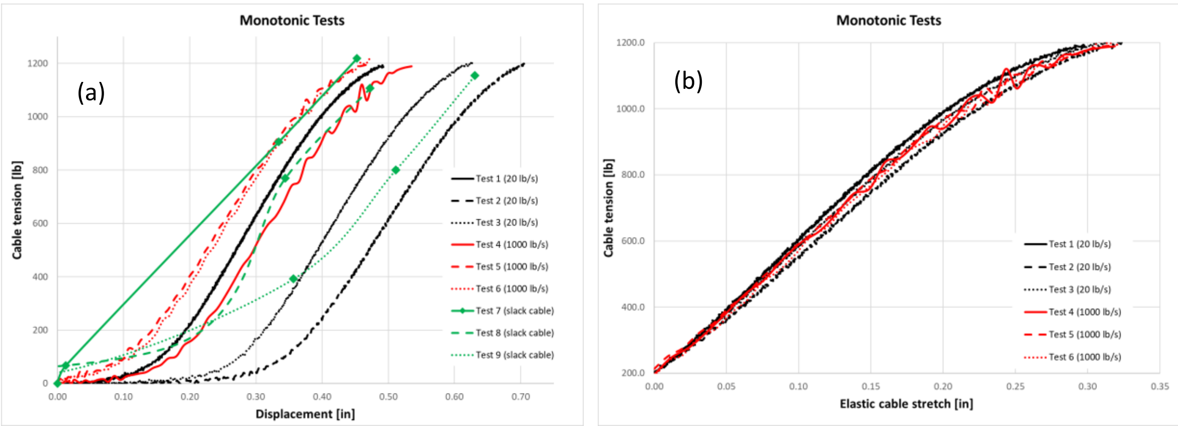

Figure 3. Force-displacement plots for all monotonic tests.

Table 1. Failure loads and modes during monotonic tests.

Monotonic loading	Test #	Failure load [lb]	Colors in Figure 3
Slow loading (20 lb/s)	1	1,187	
	2	1,108	
	3	1,201	
Fast loading (1,000 lb/s)	4	1,189	
	5	1,194	
	6	1,222	
Slack cable (>10,000 lb/s)	7	1,219	
	8	1,107	
	9	1,153	
All tests	**Mean [lb]**	**1,176**	
	COV	**4.3%**	

Conclusions from the tension tests:

- The cable performance was consistent. The coefficient of variation (COV) of the breaking strengths was only 4.3%.
- The cables are elastic and break in a brittle manner. Unlike rigid seismic braces, cables don't fatigue through plastic deformation.
- The mean breaking strength of all cables (1,176 lb) was 28% higher than the minimum breaking strength in ASTM A1023, Table 7 (920 lb).
- The breaking strength was not affected by the load rate. The cables maintained their breaking strength, even when a slack cable was loaded instantly.
- Depending on the installation and the fittings, cable loops can allow some pipe movement before the cable starts to resist the load.

To include the effects of a hanger and dynamic loading, the study was extended to shake table tests with full cable brace assemblies.

3. Shake table tests with cable brace assemblies

3.1 Shake table setups including cables and hangers

A 24 ft long, water-filled, six in. diameter, schedule 40 steel pipe was suspended by two cable brace assemblies from the steel frame shown in Figure 4. This test setup was designed to allow pipe uplift prior to cable failure, as further explained in Section 3.2. Hangers were installed six in. from the cables, within the two ft limit defined in NFPA 13. The pipe motion and the loads in the cables and hangers were measured (Figure 5). The cables, hangers, and transducers were designated according to their location using the compass directions (Figure 6).

Figure 4. Steel frame with six in. steel pipe installed using two hangers and cable brace assemblies on the FM Global shake table.

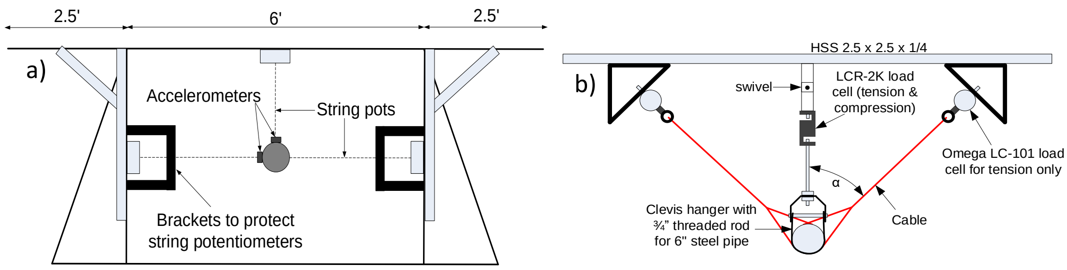

Figure 5. Sketches of the end-on view of the shake table setup. (a) Accelerometers and string potentiometers were used to measure the pipe motion. (b) Load cells (LC) measured the loads in the cables and hangers. Note the Clevis hanger attaching the pipe to the hanger.

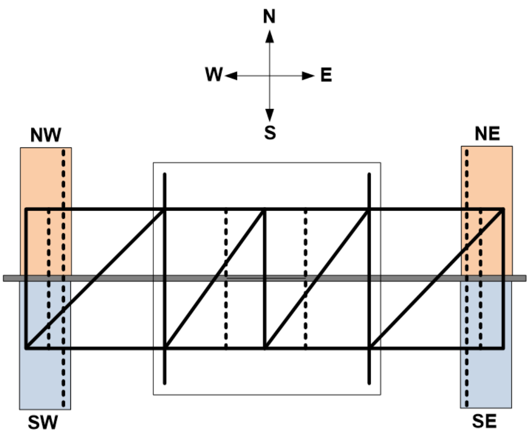

Figure 6. Plan view of the setup with the compass direction designations of transducers, cables, and hangers.

3.2 CRITICAL UPLIFT ACCELERATIONS

In a Clevis hanger (Figure 5b), there is a gap between the pipe and the cross-bolt, and the pipe can bounce up and down within this gap. The pipe uplift force due to the pipe's horizontal inertia load is $W_p \tan\alpha$, where α is the installation angle (Figure 5b). Uplift initiates when this uplift force is higher than the pipe's weight W_p. The critical lateral acceleration that uplifts the pipe is thus $g(\tan\alpha)$. Note that a different pipe size or cable strength would not change the critical uplift accelerations. Assuming a restricted pipe uplift and taut cables, the horizontal force resistance of an assembly is $F_{cable}\sin\alpha$, and the maximum acceleration needed to break the cables is $F_{cable}\sin\alpha/W_p$. The cable's breaking strength was conservatively assumed to be the nominal minimum breaking strength (F_{cable}=920 lb). In this design, pipe uplift thus occurred prior to cable failure (Table 2).

Table 2. Estimated accelerations that lead to pipe uplift.

	Installation angle α		
	30°	45°	60°
Uplift acc.=$g(\tan\alpha)$	0.6g	1g	1.7g
Max acc. = $F_{cable}\sin\alpha/W_p$	1.2g	1.7g	2.1g

When the pipe lifts by a distance h, it stores a potential energy of $W_p h$. When the pipe drops, this energy transfers to strain energy in the hangers, cables, or both. This raises the question if the bouncing of the pipe could lead to premature failure of the stiff, brittle cables.

For example, assume the pipe with tributary weight W_p = 380 lb swings upward by h and stores the potential energy PE=$W_p h$. Then, the pipe drops and the potential energy transfers into strain energy of a 2 ft long cable. Assuming the cable breaks at ~1% stretch at the minimum breaking strength of 920 lb, the maximum strain energy the cable can take prior to failure is SE=0.5 x 1% x 2ft x 920 lb=110 lb-in. The pipe uplift leading to such critical strain energy is h=SE/W_p=0.3 in. (PE=SE). Depending on the hanger type and pipe size, the gap between pipe and cross-bolt can exceed 0.3 in. In the shake table tests with a six-in. pipe, the gap was 3/4 in. Minor pipe uplift within the hanger may therefore lead to premature cable failure.

3.3 SHAKE TABLE TEST MATRIX FOR CABLE ASSEMBLIES USING A SINESWEEP RECORD

Thirty-six shake table tests were performed (Table 3) with a one-dimensional sinesweep record where the accelerations increased from 0.25 g to 2 g by linearly sweeping from 2.5 in. at 1 Hz to 5 in. at 2 Hz. The record was designed to gradually approach the critical uplift accelerations calculated in Table 2. Each test setup was repeated three times to increase the statistical significance of the results. Tests without hangers were performed to simulate a scenario where the hangers fail.

Table 3. Shake table test matrix for cables assemblies with and without hangers.

# of tests / setup		Installation angles α		Vertical member		Total # of tests
3	X	30° 45° 60°	X	• 1 ft clevis hanger • 1 ft hanger removed • 2 ft clevis hanger • 2 ft hanger removed	=	36

Figure 7 shows the test setup for a 45-degree installation angle. A swivel was used as top connection of the hanger to prevent a lateral resistance from the hanger to require the cables to resist all lateral loads. A load cell was aligned with the hanger rod to measure tension and compression in the hanger. Due to the pipe's weight, each hanger resisted W_p=380 lb in tension at the beginning of the tests. Following the manufacturers' installation requirements, the cable was wrapped twice around the pipe and the loop closure was placed approximately 9 in. (1.5 x pipe diameter) away from the pipe. Load cells to measure the cable tension were rigidly connected to the frame. The pipe could move upwards 3/4 in. before hitting the cross-bolt of the clevis hanger.

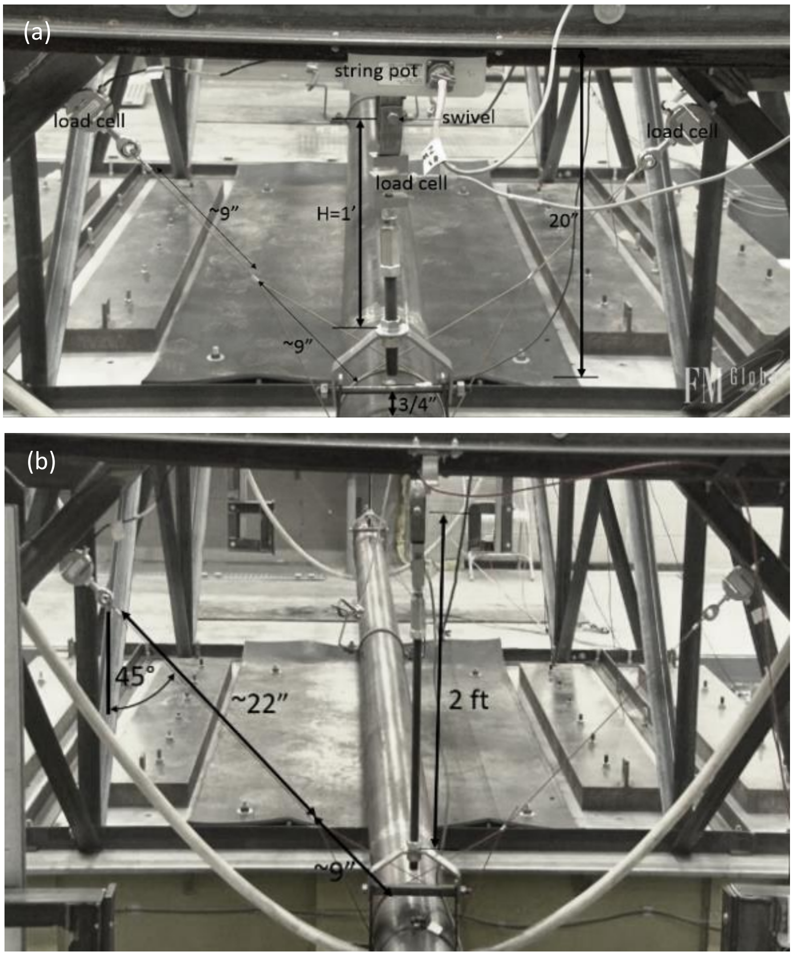

Figure 7. Cross-view of the shake table test setup with α=45° for 1 ft (a) and 2 ft (b) Clevis hangers.

3.4 EVALUATION OF TEST RESULTS

For each test, the vertical and horizontal pipe displacements and accelerations, the loads in the cables and hangers, and the acceleration of the shake table platen were recorded. The interpretation of the test results is explained by an example (Figure 8) that shows all transducer outputs for a test conducted with the setup shown in Figure 7a.

The test was stopped after a cable failure was observed. Usually, failure of one cable was instantly followed by failure of the other cables~~,~~ so that it was difficult to visually determine which cable failed first. The cable load cell data allowed us to identify at what time and under what load the first cable failed (Figure 8, rows f and g).

The horizontal pipe swing was documented to estimate the typical deflections of the cable assemblies and to evaluate the effect of the installation angle and hanger length. The horizontal accelerations of the shake table (e.g., 0.8 g in the example of Figure 8, row a, left) were compared with the pipe uplift acceleration of Table 2 (e.g., 1.0 g for α=45°).

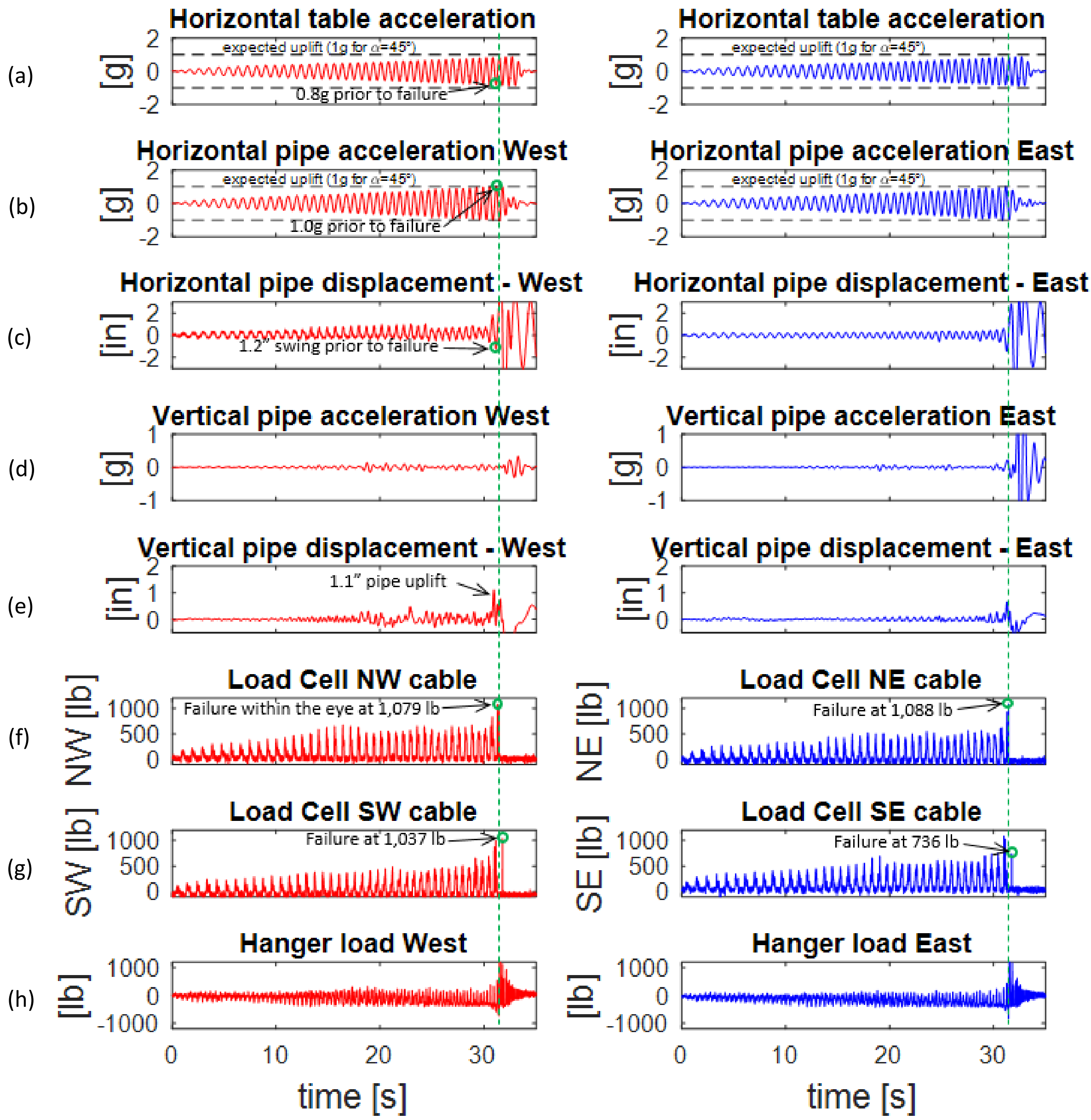

Figure 8. Example for a test output with α=45° and 1 ft hanger. The hanger loads were tared to zero prior to each test.

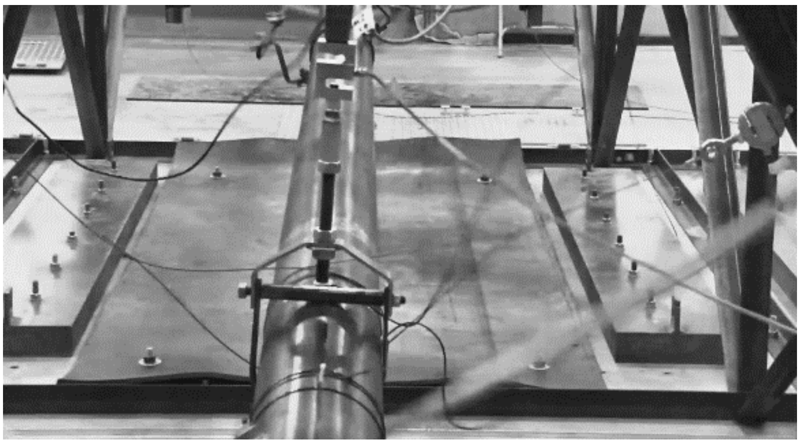

Figure 9. Uplift of the pipe in tests with α=60° using 1 ft hanger.

Pipe uplift occurred in all 36 tests prior to cable failure, as confirmed from the measurements of the vertical pipe motions (Figure 8, row e) and from videos (Figure 9). Clearly, Clevis hangers cannot prevent pipe uplift and the subsequent cable failure due to impact loads. Figure 10 correlates the (1-2 Hz bandpass filtered) table accelerations at failure with the installation angle α. The top panel in Figure 10 shows the measured, filtered shake table accelerations in the time domain. The bottom panel in Figure 10 shows the measured, filtered shake table accelerations at or just before cable failure.

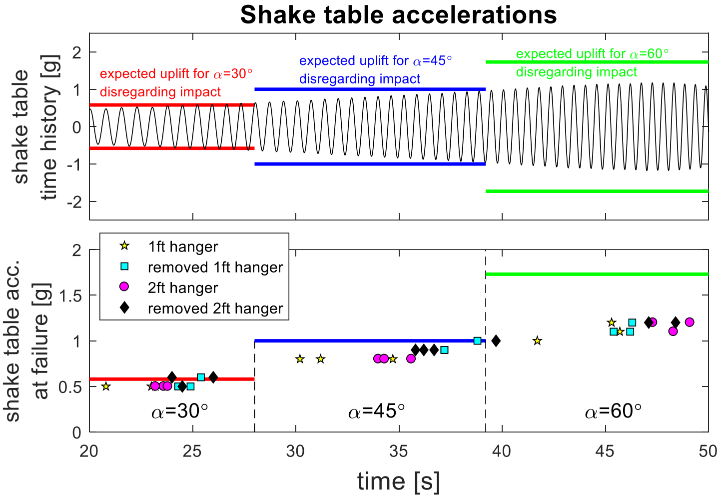

Figure 10. Accelerations (filtered) and swing at cable failure. The red, blue, and green lines represent the uplift accelerations for cable assemblies with α=30°, 45°, and 60°, respectively.

Note that all test setups with α = 30° fail the earliest during the tests (between 20 s and 26 s) and under table accelerations of 0.5 g-0.6 g. Tests with α = 45° fail between 30 s and 39 s under table accelerations of 0.8 g-1 g. Tests with α=60° fail above 39 s under table accelerations of 1 g-1.2 g.

3.5 EFFECT OF IMPACT LOADS

If pipe uplift is restricted and the cables are taut, the cable brace assembly ideally behaves like a truss and the trigonometric relationship in Figure 11 can be assumed.

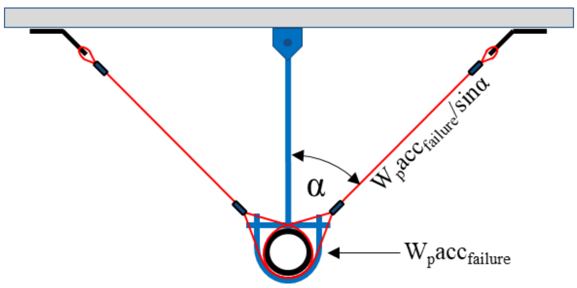

Figure 11. Theoretical cable load assuming there are no impact loads due to cable slack or pipe uplift.

Table 4 lists the estimated cable loads for the tributary pipe weight of W_p=380 lb and the shake table accelerations at cable failure from Figure 10. The shock loads due to a bouncing pipe did not weaken the cables' load capacity. The tension tests in Section 2 showed that the cables failed at similar loads regardless of the loading rate. It is assumed that the mean failure load of 1,176 lb (Table 1) also holds true for shake table tests. (In the example of Figure 8 the failure load is 1,079 lb). Note that the estimated cable loads under the assumption of Figure 11 are less than half of the mean cable breaking strength. Clearly, the pipe uplift within the hanger imposed critical shock loads to the cables.

Table 4. Estimated cable loads disregarding any impact loads.

	Installation angle α		
	30°	45°	60°
Expected uplift acceleration: acc_{uplift}=g(tanα) (Table 2)	0.6g	1g	1.7g
Acceleration measured at failure: $acc_{failure}$ (Figure 10)	0.5-0.6g	0.8-1g	1-1.2g
Estimated cable loads without impact loads: $W_p acc_{failure}/\sin\alpha$	380-456 lb	430-537 lb	439-527 lb
Fraction of mean cable breaking strength of 1,176 lb	32-39%	37-46%	37-45%

4. Finite element simulations of a cable brace assembly

A finite element model was built in Abaqus, mimicking the shake table test setup with the 1 ft long hanger and a 45° installation angle (Figure 9). First, the assembly with tight cables was simulated (Figure 12a). Second, some cable slack was introduced by dropping the ceiling supports of the cables by 10 mm (Figure 12b).

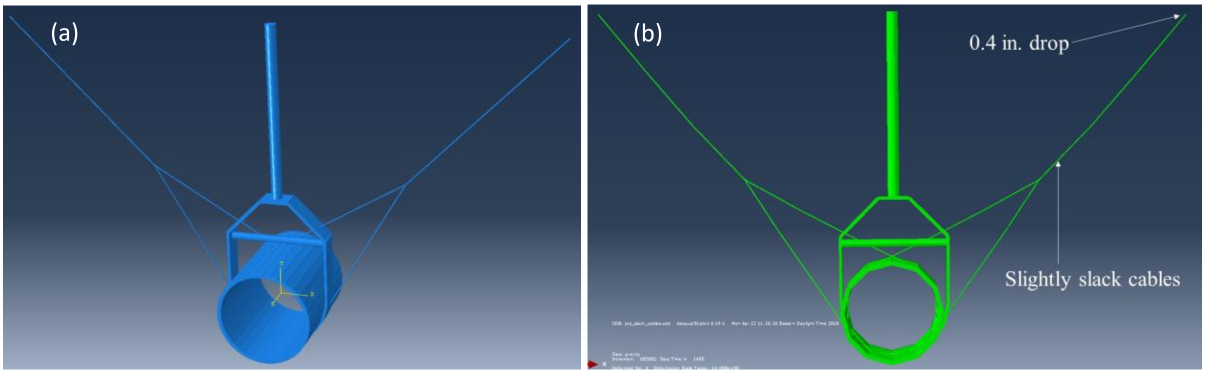

Figure 12. Abaqus model mimicking the shake table setup with a 1 ft long hanger and α=45°. (a) Taut cables. (b) Slightly slack cables.

Figure 13 compares both Abaqus simulations with the shake table measurements. The Abaqus simulations with taut cables (black) are reasonably close to the measurements (red). The slight slack roughly doubled the simulated cable loads in comparison to the model without slack (green vs. black in Figure 13). In addition to pipe uplift, cable slack can cause critical shock loads in cables because the pipe absorbs kinetic energy during its unrestricted motion.

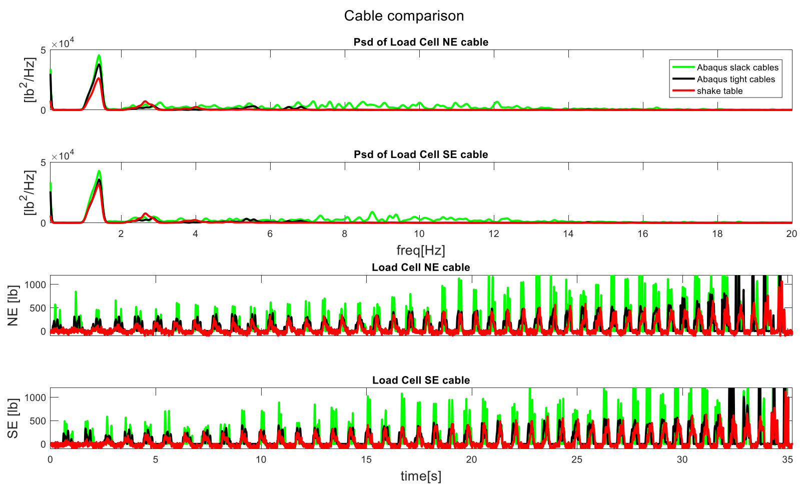

Figure 13. Increased cable loads due to cable slackness.

5. Conclusions

In the tension tests, the cables showed a nonlinear elastic force-displacement behavior and failed in a brittle way at a higher force than the minimum breaking strength in ASTM A1023. The cable strength was not affected by the loading speed and was even maintained when a sudden, pulse-like load was applied to a slack cable.

However, the dynamic loading in shake table tests revealed new challenges for cable assemblies that are not present for rigid assemblies. Cables allow for a small, unrestricted pipe swing and the hangers allow for some pipe uplift. The pipe can gain potential and kinetic energy which transforms into impact loads in the cables. ASCE 19 and ASCE 7 do not address the impact loads in the design of seismic cable bracing and therefore may underestimate the load demand on cable assemblies. The shake table tests also verified that failure of one cable is usually followed by failure of other cables because after the brittle failure of the first cable, the seismic energy redistributes to the remaining cables. Abaqus simulations moreover showed that even a small amount of slack can significantly increase cable loads.

To prevent impact loads, the following three aspects are critical in the design of cable brace assemblies:

- Hangers need to restrict pipe uplift and be designed properly for compressive loads.
- Installations must ensure taut cables without cable slack.
- Fittings should be designed such that no additional cable slack occurs under loads.

References

AC156 [2010] *Acceptance Criteria for Seismic Certification by Shake-Table Testing of Nonstructural Components*, Evaluation Services.

ASCE 7-16 [2016] *Minimum Design Loads for Buildings and other Structures*, American Society of Civil Engineers.

ASCE 19 [2016] *Structural Applications of Steel Cables for Buildings*, American Society of Civil Engineers.

ASTM A1023 [2019] *Standard Specification for Stranded Carbon Steel Wire Ropes for General Purposes*, American Society for Testing and Materials.

CBC [2019] *California Building Code*, California Code of Regulations.

NFPA 13 [2019] *Standard for the Installation of Sprinkler Systems*, National Fire Protection Agency.

UL 203A [2015] *Standard for Sway Brace Devices for Sprinkler System Piping*, Underwriters Laboratories, Inc.

Numerical analysis of gypsum board subjected to bending moment using fiber model

Fumihiko Sakuraba[1], Alex Shegay[2], Yasuaki Sato[3] and Shojiro Motoyui[4]

[1] Corporate Officer, Someno Construction Materials Co., Ltd.
648 Shishiko-cho, Ushiku-shi, Ibaraki 300-1231, Japan
sakuraba@someno.co.jp
[2] Assistant Professor, Tokyo Institute of Technology, Japan
G5, 4259 Nagatsuta, Midori-ku, Yokohama, Kanagawa 226-8502, Japan
shegay.a.aa@m.titech.ac.jp
[3]Researcher, Research&Development, Takenaka Corporation
1-5-1 Ohtsuka, Inzai-shi,Chiba 270-1395, Japan
satou.yasuaki@takenaka.co.jp
[4] Professor, Tokyo Institute of Technology, Japan
G3, 4259 Nagatsuta, Midori-ku, Yokohama, Kanagawa 226-8502, Japan
motoyui.s.aa@m.titech.ac.jp

Abstract. The in-plane force and bending moment simultaneously occur on gypsum boards which are used in the drywall partition walls, due to the composite beam effect. The mechanical performance of gypsum boards has been tested for pure compression/tension, but the behavior when subjected to simultaneous in-plane force and out-of-plane bending moment demands is unclear. In this paper, a model is proposed to predict the bending behavior of gypsum boards using the results obtained from pure compressive/tensile tests. The purpose of this study is to establish a method to simulate the behavior of gypsum boards subjected to simultaneously axial and bending moment demands. Particularly, the gypsum board is a composite material consisting of gypsum (core material) and base papers. Similar to calculation of non-linear bending behavior of reinforced concrete members, a fiber modelling approach is adopted to perform numerical analysis of gypsum boards subjected to bending moment. This model can also simulate the post cracking behavior macroscopically. On applying the fiber model to the gypsum board, three stress-strain curves are necessary: two curves of gypsum boards in compression/tension and one curve of the base paper in tension. The "effective" curves of pure gypsum in compression/tension were obtained as the difference between the performance of the composite gypsum board and that of the base paper in isolation. The effective stress-strain curve of gypsum, especially one in tension, was found to be higher than that obtained by testing the pure gypsum in isolation. This difference is attributed to the so-called tension stiffening effect in the gypsum material. Finally, to validate the proposed fiber model we show that the numerical results are in good agreement with experimental data.

Keywords: Gypsum board, Base paper, Tension stiffening effect, Numerical analysis.

1. INTRODUCTION

Following the April 16, 2016 M7.0 Kumamoto earthquake and the March 16, 2022 M7.3 Fukushima earthquake, several accounts of ceiling and partition wall damage were confirmed in media (Figure 1). Eleven years have passed since the 2011 Tohoku Earthquake, but there are still issues with the earthquake resistance of walls and ceilings due to the lightweight steel base material (LGS). Although the breaking load of the gypsum board that composes the LGS wall/ceiling surface has been confirmed by the bending test of JIS A 6901 [JIS, 2013], the data for defining the stress-strain curve of the gypsum board has not been provided. In addition, while in-plane force and bending moment generally act simultaneously on the gypsum board mounted on the LGS (due to the composite beam effect), most existing experimental data have only considered the characteristics of uniaxial compression or tension of the gypsum board [Y. Sato *et al.*, 2020]. Abdelhalim [1995] has previously examined the basic mechanical properties of gypsum boards by uniform compression/tensile testing and bending testing. The study attempted to use statistical methods to address the inconsistency between the stress-strain relationship obtained from bending tension and from uniform tension; however, only qualitative results were obtained. Therefore, there are still many unclear points about the behavior when in-plane force and bending act on the gypsum board at the same time. In considering the earthquake resistance of LGS walls and ceilings, it is important to develop a mechanical understanding of the above points. The objective of this study is to develop a modelling approach for gypsum boards subjected to bending moment demands, founded on experimental results obtained from uni-axial material testing. The focus will be on interpretation and implementation of material test data with consideration to composite action effects, with less focus on the exact material properties and their expected statistical variation.

(a) Kumamoto earthquake (April 2016)

(b) Fukushima earthquake (March 2022)

Figure 1. Example of earthquake damage of non-structural elements following earthquakes in Japan.

2. UNIFORM LOADING TEST

2.1 OUTLINE OF TEST

Axial testing was carried out on the gypsum board (t = 9.5 mm) to establish mechanical properties. The gypsum board is a three-layer composite board in which two surfaces of the core gypsum material are covered with base paper. Presently, there is no unified standard in Japan for the characteristics of the gypsum board material components, so properties can differ from maker to maker. For the gypsum board adopted in this study, the unit weight was measured to be 6.7 kg/m^2, and the base paper grammage was measured to be 173 g/m^2. The base paper thicknesses are listed in Table 1. It is generally considered that the base paper has anisotropy derived from the fiber direction of the paper during the papermaking process by a paper machine ([T. Yokoyama *et al.*, 2007]). Therefore, the uniaxial loading test of the gypsum board was carried out in the longitudinal and transverse direction of the base paper. Considering the length of the gypsum board as the parallel direction of the base paper fibers and the short side as the orthogonal direction of the base paper fibers, three test pieces are sampled as shown in Figure 2. A separate set of test pieces were prepared for each tensile and compressive testing.

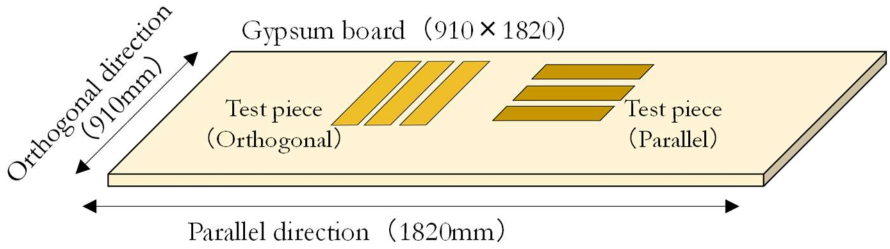

Figure 2. Sampling the test pieces

The tensile test piece of the gypsum board is dogbone-shaped (Figure 3 (a)), and the compression test piece is strip-shaped [Y. Sato et al., 2020]. The base paper test pieces were collected from the gypsum board by separating them with a band saw. The base paper test pieces were taken both from the front (yellow paper) and back (gray paper) of the gypsum board. Figure 3 (b) shows the shape of the tensile test piece of the base paper. All test pieces are shown in Table 1. The width *B* and thickness *t* of the test piece are average values measured at the center and both ends of the test piece with a caliper. The measured quantities included the load, *F*, as measured by the testing machine; the displacement, *δ*, of the chuck that grips the test piece and the strain from the strain gauges attached to the center of the test piece. All gypsum board test pieces had strain gauges on the front and back surfaces. For the test piece of the base paper, the strain gauge was attached only on the outer surface. It is noted that unlike the base paper, the gypsum material does not possess anisotropic properties due to its random crystalline structure.

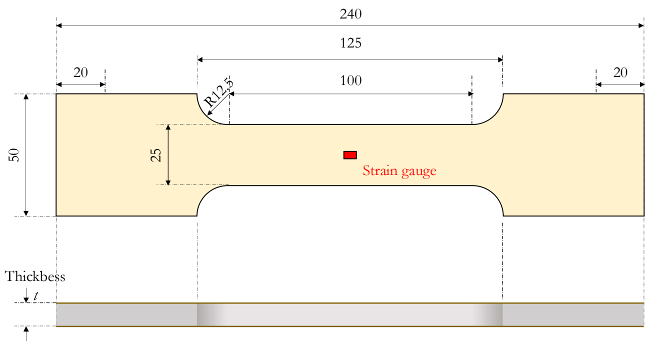

(a) Gypsum board

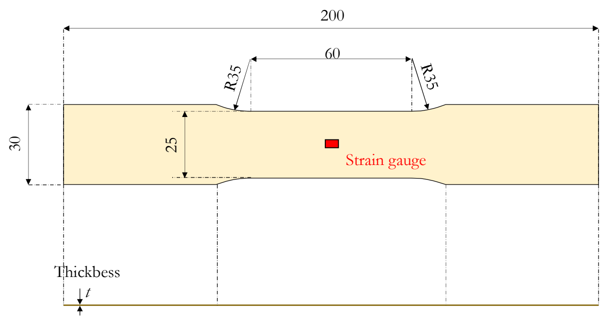

(b) Base paper

Figure 3. Size of tensile test pieces.

Table 1. List of the test pieces.

No.	Name	Material	Load type	Fiber Direction	Average [mm]	
					Width (B)	Thickness (t)
1	Cp-T-P-1	Gypsum board (Composite board)	Tensile	Parallel	24.53	9.74
2	Cp-T-P-2				24.49	9.71
3	Cp-T-P-3				24.79	9.70
4	Cp-T-O-1			Orthogonal	24.72	9.70
5	Cp-T-O-2				24.66	9.70
6	Cp-T-O-3				24.51	9.69
7	Cp-C-P-1		Compression	Parallel	49.53	9.71
8	Cp-C-P-2				49.78	9.72
9	Cp-C-P-3				49.74	9.71
10	Cp-C-O-1			Orthogonal	49.85	9.73
11	Cp-C-O-2				49.74	9.67
12	Cp-C-O-3				48.72	9.70
13	Pa-f-T-P-1	Yellow paper (Front)	Tensile	Parallel	25.06	0.24
14	Pa-f-T-P-2				25.11	0.29
15	Pa-f-T-P-3				25.17	0.24
16	Pa-f-T-O-1			Orthogonal	24.66	0.26
17	Pa-f-T-O-2				25.26	0.24
18	Pa-f-T-O-3				24.47	0.23
19	Pa-b-T-P-1	Gray paper (Back)	Tensile	Parallel	25.15	0.23
20	Pa-b-T-P-2				24.77	0.23
21	Pa-b-T-P-3				25.09	0.23
22	Pa-b-T-O-1			Orthogonal	24.99	0.22
23	Pa-b-T-O-2				24.78	0.23
24	Pa-b-T-O-3				24.96	0.23

2.2 RESULTS OF UNIFORM LOADING TEST

First, the results of the tensile test of the base paper in the parallel and orthogonal direction are shown in Figure. 4 (a) and 5 (a), respectively. Considering the uncertainty of the thickness of the base paper, the vertical axis is expressed as the load F divided by the width B of the test piece. The horizontal axis is the longitudinal strain, ε_P, measured by the strain gauges. Data is shown up until the test piece breaks. It is clear that the stiffness and strength of the base paper are higher in the parallel direction than in the orthogonal direction due to the material anisotropy. On the other hand, the difference between the base paper properties from the front (yellow paper) and back (gray paper) of the gypsum board are small. This result is also consistent with previous research results [Abdelhalim, 1995]. The average of the stress-strain curves in Figures 4 (a) and 5 (a) are approximated by a cubic function (in the range $0 \leq \varepsilon_P \leq 7500$), represented by the black dotted line. Next, the results of the tensile test of gypsum board and gypsum are shown in Figure 4 (b)~(c), 5 (b)~(c). The horizontal axis is the strain ε obtained by dividing the displacement recorded by the test machine, δ, (excluding the deformation of the loading jig) by the total length, L, of the test piece. The "effective" stress-strain curve of the gypsum (Figure 4 (c), 5 (c)) is obtained by subtracting the curves of the two sheets of base paper approximated by a cubic function (black dotted line) from the stress-strain curve of the gypsum board (Figure 4 (b), 5 (b)). The solid black lines in Figure 4 (c) and 5 (c) are the results of the tensile test of the gypsum in isolation, after removal of the base paper. By comparing Figure 4 (b) and 5 (b), it can be recognized that the gypsum board has anisotropy similar to that of the base paper. Comparing the black solid lines in Figure 4 (c) and 5 (c), it can be seen that the difference depending on the fiber direction is small. From this, it is considered that the anisotropy of the gypsum board may be influenced by the anisotropy of the base paper. The "effective" gypsum properties (blue line) in Figure 4 (c) and 5 (c) clearly shows tougher performance in tension compared to when the gypsum is tested in isolation (solid black line). It is considered that the tension stiffening effect [H. Yoshikawa *et al.*, 1986], analogous to that seen in RC members, is the reason the gypsum material is tougher when in the gypsum board configuration than in isolation. The results of the compression test are organized in the same way as in Figures 4 and 5, assuming that compressive properties of the base paper are identical to the tensile properties (Figure 6). It can be confirmed that the influence of the anisotropy of the base paper on the performance of the gypsum board is smaller in compression than in tension. Figure 6 shows a softening response of the gypsum board after the maximum compressive strength is reached.

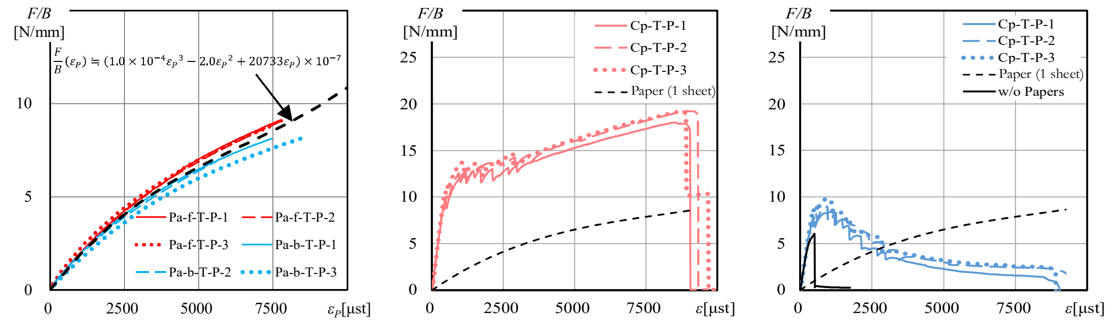

(a) Base paper (b) Gypsum board (c) Gypsum

Figure 4. The relationship between F/B and ε of each material against the tensile load in the parallel direction.

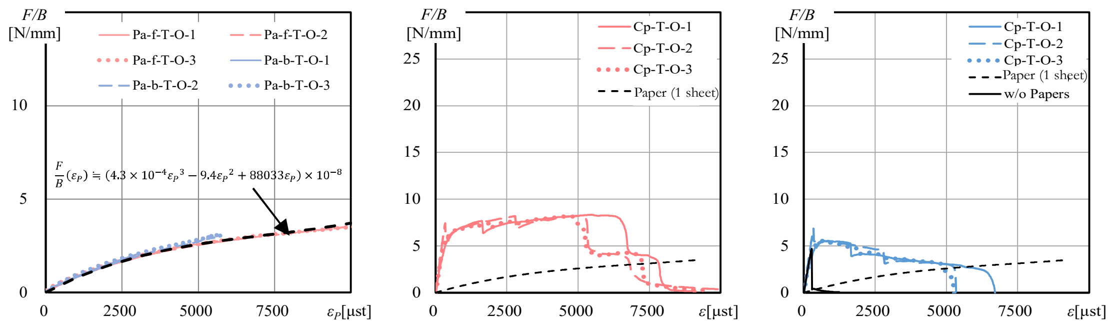

(a) Base paper (b) Gypsum board (c) Gypsum

Figure 5. The relationship between F/B and ε of each material against the tensile load in the orthogonal direction.

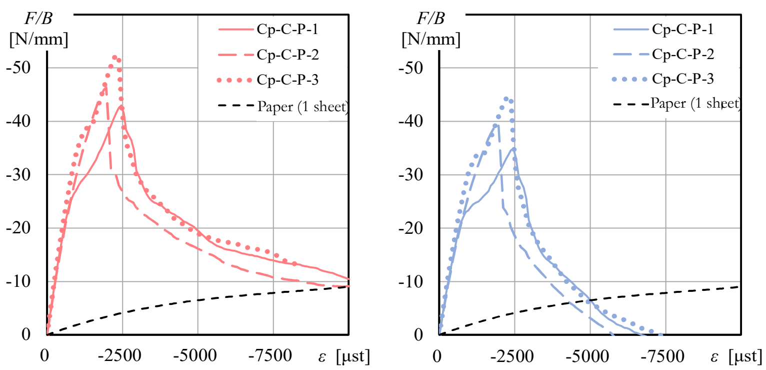

(a) Parallel direction

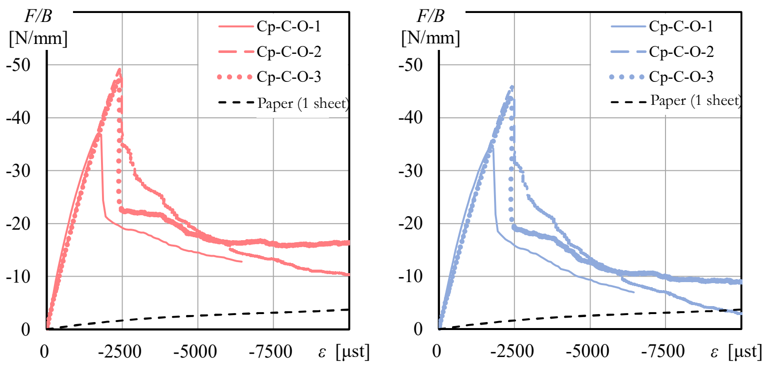

(b) Orthogonal direction

Figure 6. The relationship between F/B and ε of each material against the compressive load.

3. NUMERICAL ANALYSIS OF GYPSUM BOARD

3.1 OUTLINE OF FIBER MODEL

Figure 7 shows the gypsum board subjected to pure out-of-plane bending. Considering the gypsum as the concrete and the base paper as the reinforcing bar, the gypsum board composite can be analgous to the composition of RC members. In the relationship between the moment and the curvature in the cross section of the RC member, the flexural stiffness gradually decreases due to the progression of cracks. Therefore, the fiber model is often used as a method for evaluating the non-linear flexural behavior of RC members. In this section, the fiber model is also used to perform cross-sectional analysis of the gypsum board.

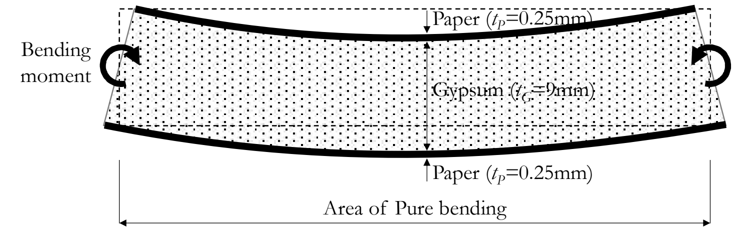

Figure 7. Gypsum board in pure bending.

When the cross section is divided into multi-layered fiber elements as shown in Figure 8, the total bending moment is obtained by the following equation.

$$M = \int_A \sigma y \, dA = \sum_{i=1}^{n} \sigma_{G,i} \cdot y_i \cdot A_{G,i} + \sum_{j=1}^{m} \sigma_{P,j} \cdot y_j \cdot A_{P,j} \tag{1}$$

Here, σ : stress of each fiber element, A : section area of each fiber element, y : distance from the centroid of each fiber element to the section centroid, n : number of divisions of gypsum cross section, m : number of base papers, lower right subscript i, j : element number, lower right subscript G, P : gypsum and base paper. The total axial force on the section is as follow.

$$R_G = \sum_{i=1}^{n} \sigma_{G,i(\varepsilon_{G,i})} \cdot A_{G,i} = C_G + T_G \tag{2}$$

$$R_P = \sum_{i=1}^{m} \sigma_{P,j(\varepsilon_{P,j})} \cdot A_{P,j} = C_P + T_P \tag{3}$$

Where, C : total compression force, T : total tensile force, R : sum of C and T. Then, the force balance equation in the cross section is as follows, and the convergence calculation is performed while changing the neutral axis position y_0 until section force equilibrium ($N = 0$) is reached.

$$N = R_G + R_P \tag{4}$$

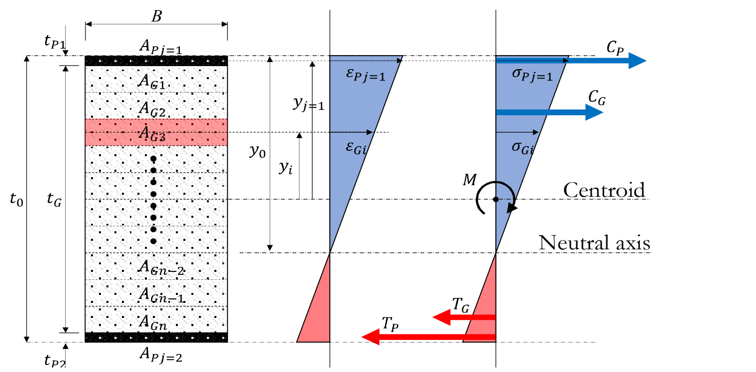

(a) Section area (b) Strain distribution (c) Stress distribution

Figure 8. Distribution of strain and stress of gypsum board in pure bending.

3.2 Model of Mechanical Property

The material properties of gypsum and base paper used for cross-sectional analysis of gypsum board subject to bending moment are obtained from the results of uniform tensile and compression tests of gypsum board, base paper, and gypsum shown in Figure 9 and 10. The tensile characteristics of the base paper are approximated by a cubic function (thick black line in Figure 9 and 10). The compressive characteristics of the base paper are taken to be equal to the tensile characteristics. The gypsum material model (blue solid line in Figure 9 and 10) is assigned to trace the experimental results. The solid red line shown in Figure 9 and 10 is the sum of gypsum and base paper material model curves, and represents the response of the gypsum board. The cross-section analysis is performed using these material models.

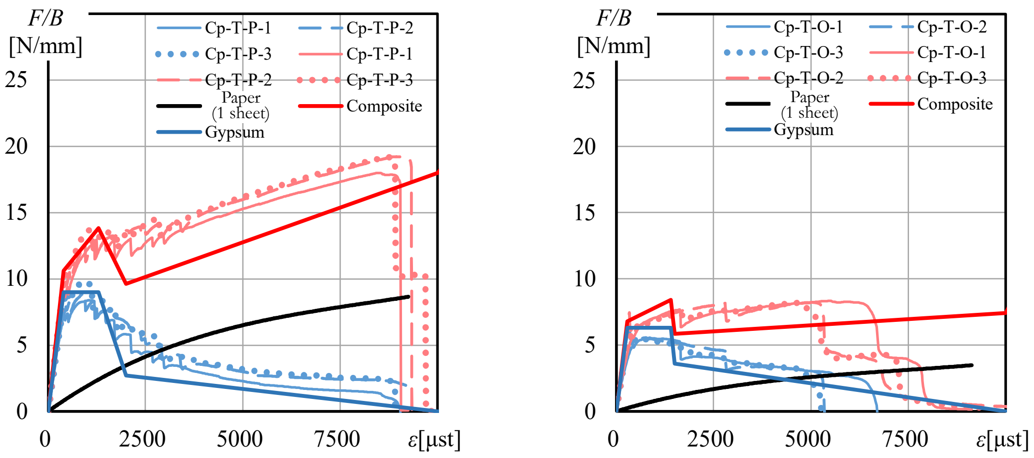

(a) Parallel direction **(b) Orthogonal direction**

Figure 9. Model of the relationship between *F/B* and *ε* (Tensile)

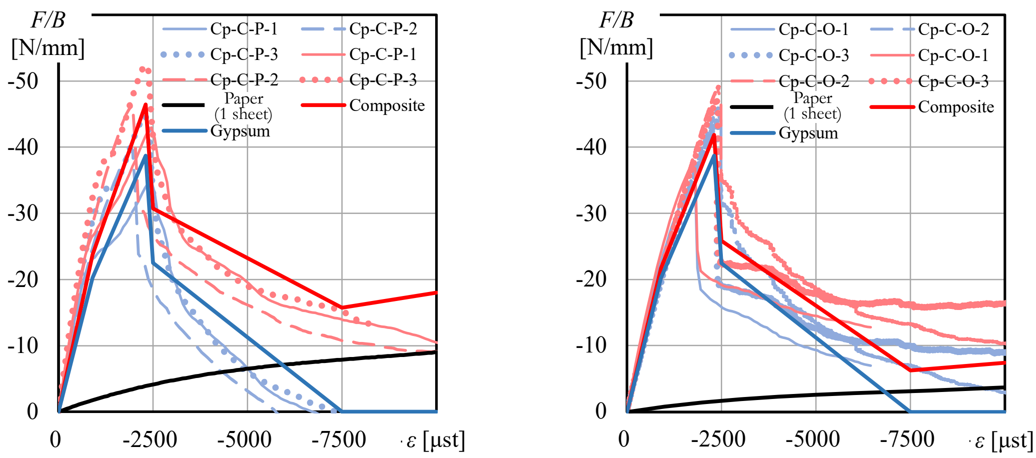

(a) Parallel direction **(b) Orthogonal direction**

Figure 10. Model of the relationship between *F/B* and *ε* (Compression)

3.3 Validity of Numerical Analysis

The 4-point bending test of a gypsum board shown in Figure 11 is the target of cross-section analysis. The test piece has strain gauges installed in the center of the pure bending section (front surface: ε_f, back surface: ε_b). The curvature $\varkappa$ is obtained by dividing the strain difference by the thickness t of the gypsum board. The moment M is obtained by using the loading force P and the support distance L. Two types of gypsum boards with different thicknesses (t = 9.5 mm, 12.5 mm) were each tested in two fiber direction configurations (parallel/orthogonal). Two test pieces were tested under each of these configurations.

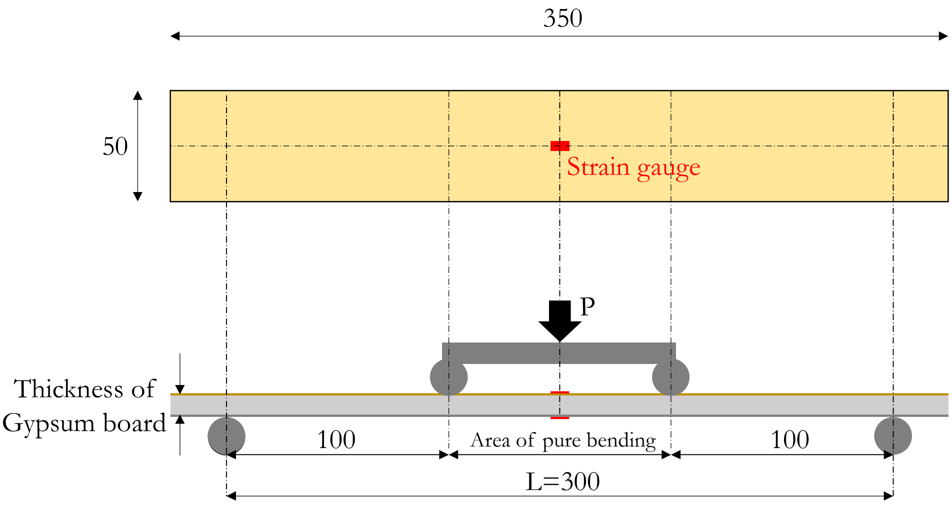

Figure 11. Set up and dimensions of a 4-point bending test of the gypsum board (units: mm).

The moment-curvature (M'-κ) relationship obtained from cross-sectional analysis of the gypsum board test pieces is compared with the experimental results in Figure 12. Here, the vertical axis of Figure 12 is the moment M' [Nmm/mm] per unit width of the gypsum board. The material properties used for the cross-sectional analysis of t = 12.5 mm are considered to be identical to those obtained from testing of the t = 9.5 mm test piece shown in Figure 10. Figure 13 shows the relationship diagram between the surface strain measured on the front of the gypsum board, ε_f (horizontal axis) to the strain measured on the back surface ε_b (vertical axis) of the gypsum board. The analysis result is represented by the symbol ◯ for t = 9.5 mm and Δ for t = 12.5 mm. Results in red correspond to bending with the gypsum board oriented in the parallel direction, and those in blue correspond to the orthogonal direction. The experimental results are shown by solid and dotted lines (black: t = 9.5 mm, gray: t = 12.5 mm). Figures 12 and 13 show that the analysis results are in good agreement to the experimental results; thus, and the validity of the cross-sectional analysis of the gypsum board using a fiber model is confirmed. The first analysis data point, excluding the origin (zero) in Figure 12, is the elastic limit at which the gypsum first cracks.

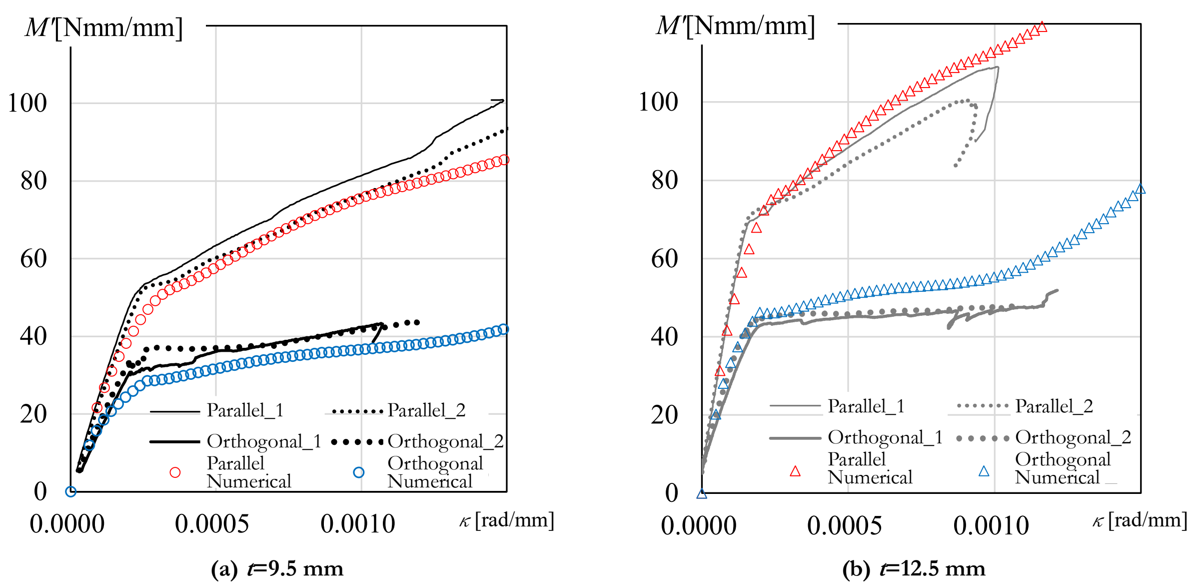

Figure 12. Comparison of of experimental and analytical results for the gypsum board moment-curvature relationship.

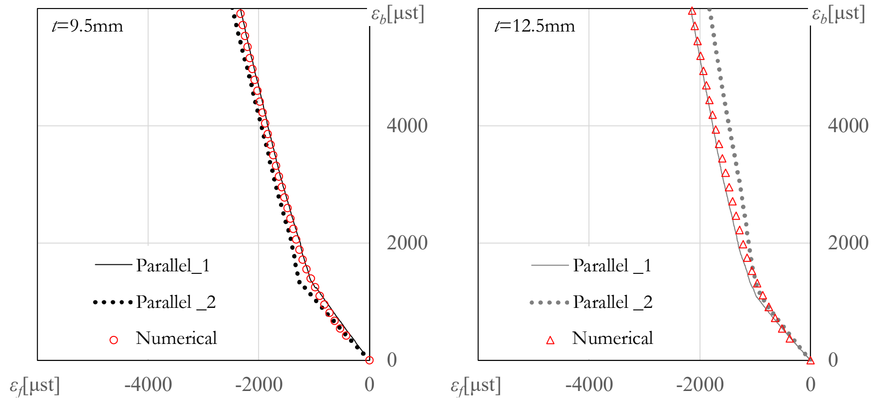

(a) Parallel direction

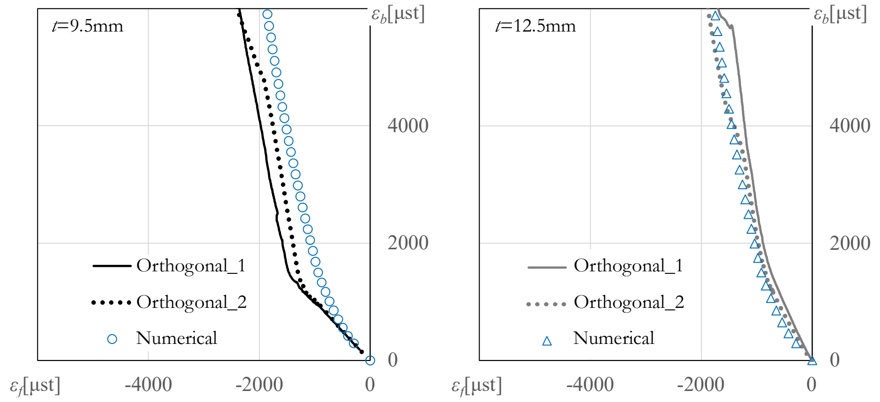

(b) Orthogonal direction

Figure 13. Comparison of experimental and analytical results for the front and back strain correlation

The distribution of stress through the gypsum board cross-section is shown in Figure 14 for the t = 9.5 mm (fiber parallel direction) test piece. The distribution is shown at the elastic limit (Figure 14 (a)), the first break point (i.e., instance at which the flexural stiffness changes significantly; Figure 14 (b)), and the point at which gypsum crushing begins (Figure 14 (c)). From Figure 12 and 14, it is probable that the initial gypsum board crack propagates to half the board thickness. Furthermore, it is also possible that the gypsum board enters the non-linear region at a bending moment magnitude that is about half of the bending moment magnitude at the first break point; thus, the exact elastic region is relatively narrow.

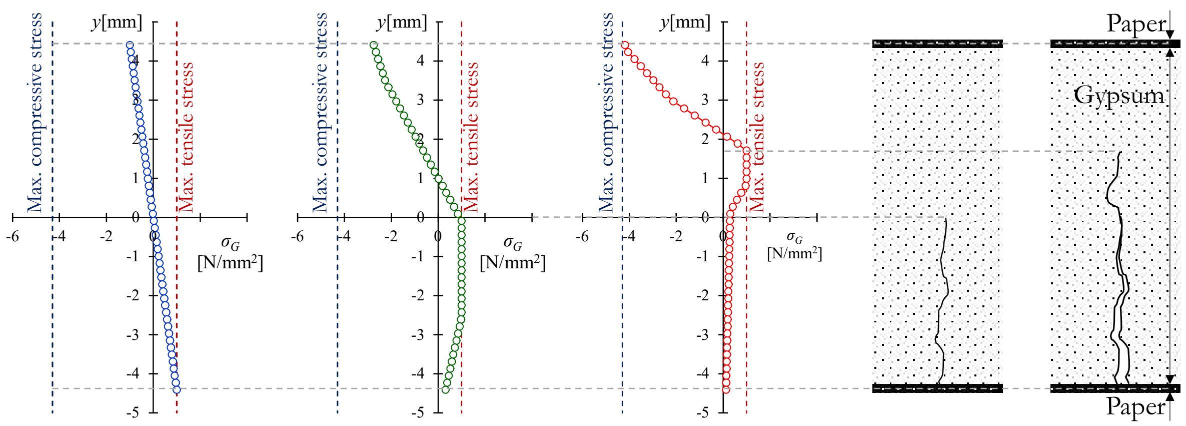

(a)Elastic limit **(b)Flexural stiffness changes** **(c)Gypsum crushing begins** **(d) Crack pattern**

Figure 14. Distribution of stress of the gypsum board (t=9.5 mm, Parallel direction)

4. CONCLUSION

In this paper, cross-sectional analysis of the gypsum board using the fiber model was carried out in order to investigate the mechanical properties of the gypsum board subjected to an out-of-plane bending moment. The analysis results were able to reproduce the experimental results well, and the fiber model was effective for cross-sectional analysis of the gypsum board. In the future, the behavior of the gypsum board when in-plane force and bending act on the gypsum board at the same time will be examined.

ACKNOWLEDGEMENTS

This work was supported by JST Program on Open Innovation Platform with Enterprises, Research Institute and Academia and JSPS KAKENHI Grant Number JP16H02375.

REFERENCES

H. Yoshikawa, T. Tanabe. [1986] "An analytical study for the tension stiffness of reinforced concrete members on the basis of bond-slip mechanism," *Journal of Japan Society of Civil Engineers*, Vol. 4, No. 366, pp. 93-102.

Abdelhalim Benouis. [1995] "Comportement mecanique des ouvrages en plaques de platre sur ossature metallique," *Phd thesis*, Sciences et Techniques du Bâtiment, École nationale des ponts et chaussées, France.

T. Yokoyama, T. Odamura, K. Nakai. [2007] "Empirical response spectral attenuation relations for shallow crustal earthquakes," *Journal of the Japanese Society for Experimental Mechanics*; Vol. 7, No. 2, pp. 129-135.

JIS [2013] *Japanese Industrial Standards*, Japanese Industrial Standards Committee, Japan.

Y. Sato, F. Sakuraba, S. Motoyui. [2020] "Structural Behavior of the Dry Partition Wall with Light-Gauge Steel," *Proceedings of 17th World Conference on Earthquake Engineering*, Sendai, Japan.

A zinc sheeting such as a shear wall in a mixed CFS frame with non-structural masonry

Xavier Nieto-Cárdenas[1], Caori Takeuchi[2], Juan Tamasco[3]

[1] National University of Colombia, jnietoc@unal.edu.co
[2] National University of Colombia, cptakeuchit@unal.edu.co
[3] National University of Colombia, jtamascot@unal.edu.co

Abstract. This document presents an experimental program to study the in-plane seismic behaviour of non-structural elements such as cold-formed steel (CFS) frames (CFS-F) and horizontal hollow clay bricks. The test specimens for this study were half-scale, single-story, single-bay, and were either unreinforced or reinforced with a zinc sheeting with a 1,07 aspect ratio. In order to build the frame of all specimens, we welded together channel-type sections of ASTM A1011 steel (100x50x15x1,5 mm) into beams and channel-type sections of the same material (120x60x15x1,5 mm) into columns. Then, we built the infilled masonry with #4 clay bricks (330x230x90 mm). The zinc sheeting that we used for the reinforced specimen was 0,15 mm thick and took a third part of their surface area, in both sides. All specimens were subjected to a quasi-static cyclic lateral load and their stiffness variations and failure modes were measured until they reached a lateral drift of 1%. Comparing the characteristic curve of combined walls (CW) and that of combined walls with a zinc sheeting (CWZ) showed that the latter material had a higher stiffness. Moreover, the tested CWZ had a greater deformation before failure. The failure mode for the CW was local buckling in its nodes and web-face columns. However, the failure mode for the CWZ was in its bolted connections. Additionally, an x-shaped deformation appeared on the zinc sheeting of this wall. The first cracks in the mortar appeared at 0,5% lateral drift in the CW and at 0,7% lateral drift in the CWZ. Furthermore, as opposed to the CW, which was significantly damaged at 1% lateral drift, the CWZ remained without meaningful damage and no out-of-plane failure at that point. Thus, we were able to conclude that the latter type of wall is an alternative for medium-hazard seismic zones.

Keywords: Cold-formed Steel, Shear wall, Non-structural element, Non-structural masonry, Stiffness.

1. INTRODUCTION

1.1 INTRODUCTION

Inequality in Latin America has produced an enormous housing gap that low-income households have tried to bridge by building or expanding their own houses by their own limited means. This has led to an increase in the number of cheap-yet-vulnerable constructions built without proper technical control [Nieto-Cárdenas & Gamón, 2012]. [Nieto-Cárdenas et al., 2021].

(a) (b)

Figure 1. Informal housing in general: (a) Extension structure in CFS-F. (b) Combined wall collapsed in Pedernales Earthquake 2016 (Ecuador). [Nieto-Cárdenas et al., 2021 , Carrillo et al., 2020].

Figure 1 (b) shows one type of the informal constructions being used in Latin America. It consists of a cold-formed steel frame (CFS-F) infilled with non-structural masonry (NSMI). This kind of combined wall (CW) is vulnerable to earthquakes according to previous research carried out by [Carrillo et al., 2020 and Nieto-Cárdenas & Takeuchi, 2019].

In order to better understand the behavior of these CWs under certain conditions, the present experimental work subjected two sample models —an unreinforced CFS-F wall and a CFS-F wall reinforced with a zinc sheeting— to various tests. The walls used for this purpose were half-scale, single-story, single-bay, and had a 1,07 aspect ratio. Moreover, they were built with materials commonly used in informal housing in Colombia and Ecuador.

The tests showed that the stiffness of the combined wall with a zinc sheeting (CWZ) was 60% higher than that of the CW.

2.EXPERIMENTAL WORK

2.1 DESCRIPTION OF TEST SPECIMENS

2.1.1 Description of test specimens

Figure 2 shows a diagram of the walls used for the experiments carried out in this study. Both types of walls were built by making a CFS frame, made up of thin sheet profiles welded together to form a box section, and filling it with horizontally hollow clay bricks. Additionally, one of the walls was reinforced on both sides with a zinc sheet that covered approximately 1/3 of its masonry area. The dimensions of the zinc sheet were 420x1235mm. Finally, an IPE300 beam was included in the setup to simulate a fixed foundation. The global aspect ratio of the walls was of 1,07; while that of the masonry was of 1,02 (1,26m x 1,23m).

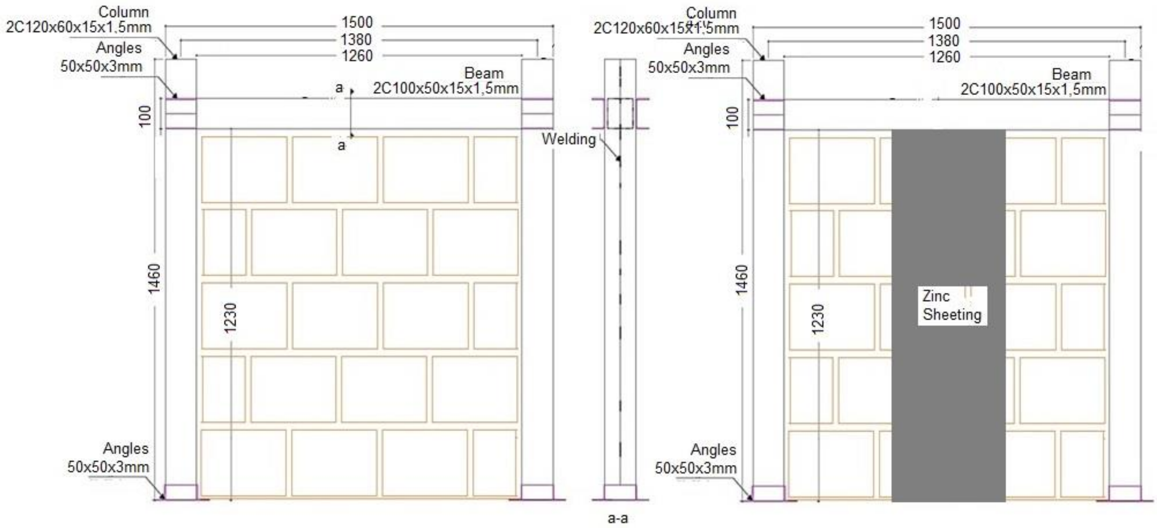

(a) (b)

Figure 2. Specimens for testing: (a) CW specimen and (b) CWZ specimen. Edited from [Nieto-Cárdenas et al., 2021b].

2.2 MATERIAL PROPERTIES OF THE TESTED SPECIMENS

The materials used in this study are indicated below:

i. Steel: The CFS-F were built of ASTM A1011 steel with factory values of *fy*=350 MPa and *fu*= 450 Mpa. The laboratory tests showed a resistance mean of *fy*=309,50 Mpa and *fu*=400 Mpa.

ii. Steel: The reinforcements in the nodes were made with ASTM A36 steel angles with fy=250 Mpa and were connected through SMAW welding with an E6011 electrode. (Naspud et al., 2021).

iii. Mortar: A paste mortar commonly used by teachers was used. It had a cement-sand ratio of 1:3 and an average resistance of f'cp=9,61 Mpa. Finally, it was classified as a type N mortar according to table D.3.4-1 of the NSR-10 (Colombian Seismic Code, NSR-10: Norma Sismo Resistente 2010) .

iv. Horizontal hollow clay brick: Non-structural 23x33x9-cm clay bricks known as No. 4 blocks. Their mean average in axial compression tests was *f'cu*=3,75 Mpa.

v. Zinc sheet: It was marketed as a 0,28mm thick sheet, but in their mean average measured in the laboratory was of 0,15mm. The mean yield stress was *fy*=556 Mpa.

vi. Portland cement: General use cement, under NTC 121 code – type UG.

vii. Sand: Yellow sand, under NTC 2240 or ASTM – C 33 code.

2.3 TEST SETUP AND INSTRUMENTATION

Figure 3 presents the set-up for the tests of this study, which were designed based on general the recommendations proposed by [Tasnimi & Mohebkhah, 2011].

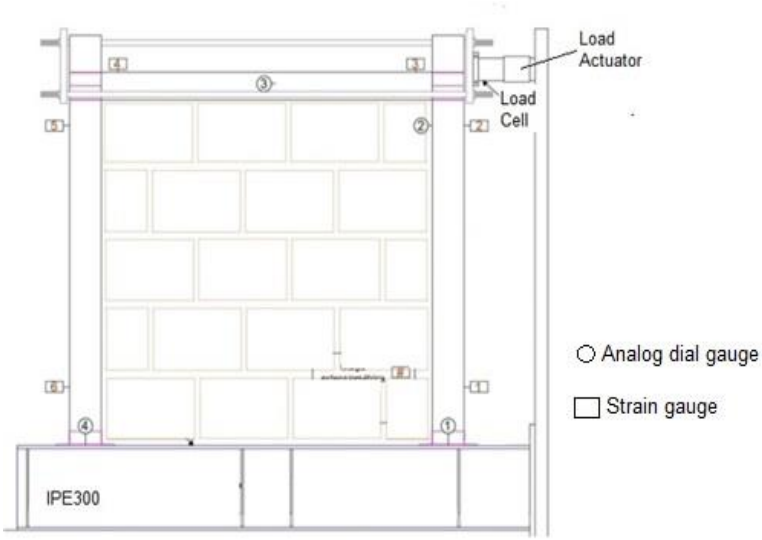

Figure 3. General scheme of testing.

The displacement during the tests was controlled by means of analog dial gauges (marked with a 3 inside a circle in Figure 3). On the other hand, the lateral quasi-static load to which the walls were subjected was applied through an actuator with a maximum load cell of 196 kN. Finally, there were strain gauges installed in the metal frame for stress control.

(a) (b)

Figure 4. Pictures of testing: (a) CW specimen and (b) CWZ specimen. Structural Laboratory of National University of Colombia. Edited from [Nieto-Cárdenas et al., 2022].

2.4 Displacement history pattern

The tests were carried out in several steps, each of which entailed a drift increase of 2 mm. In this paper we only show the results of the tests between 0 mm and 12mm (1% of drift).

3.EXPERIMENTAL RESULTS

3.1 Stiffness

The stiffness (*K*) value measured for each specimen at 12-mm lateral displacement (1% of drift) is presented in Table 1.

Table 1. CW and CWZ stiffness values at 12-mm lateral displacement.

Specimen	Stiffness mean (kN/mm)
CW	2,11
CWZ	3,61
(Naspud et al., 2021) Bare Frame (BF) Bare Frame model (BF-MEF)	1,63 1,81

The values of *K* were calculated by dividing the maximum load by the amount of displacement:

$$\boldsymbol{K} = {}^{\boldsymbol{P}}/_{\Delta_{\boldsymbol{lateral}}} \qquad \text{(Eq. 1)}$$

To deformation energy was calculated by Equation 2 and for the area under the curve in Figure 5 and Figure 6 respectively.

The EI values by Equation 3.

$$\boldsymbol{U} = \frac{\boldsymbol{P^2 \times L^3}}{\boldsymbol{6 \times E \times I}} = \qquad \text{(Eq. 2)}$$

$$\Delta = \frac{\boldsymbol{P \times L^3}}{\boldsymbol{3 \times E \times I}} = \qquad \text{(Eq. 3)}$$

3.2 Behaviour of the CW Specimen

Figure 5 shows the load-displacement relation of the CW specimen. The blue lines represent the two cyclic lateral displacements measured in the test. The maximum lateral displacement was of 12,0 mm.

The mean stiffness value of CW is 2,11 kN/mm average from similar values in the positive and negative field (2,07 and 2,16 respectively).

The deformation energy is 156 Joules and the EI=1,514x10^{12} N*mm^2.

3.3 SPECIMEN CWZ BEHAVIOUR

Figure 6 shows the load-displacement relation of the CWZ specimen. The blue lines represent the two cyclic lateral displacements. The maximum lateral displacement was of 12,0 mm.

The mean stiffness value of CWZ is 3,61 kN/mm average from similar values in the positive and negative field (3,72 and 3,50 respectively).

The deformation energy is 270 Joules and the $EI=2{,}621 \times 10^{12}$ N*mm^2.

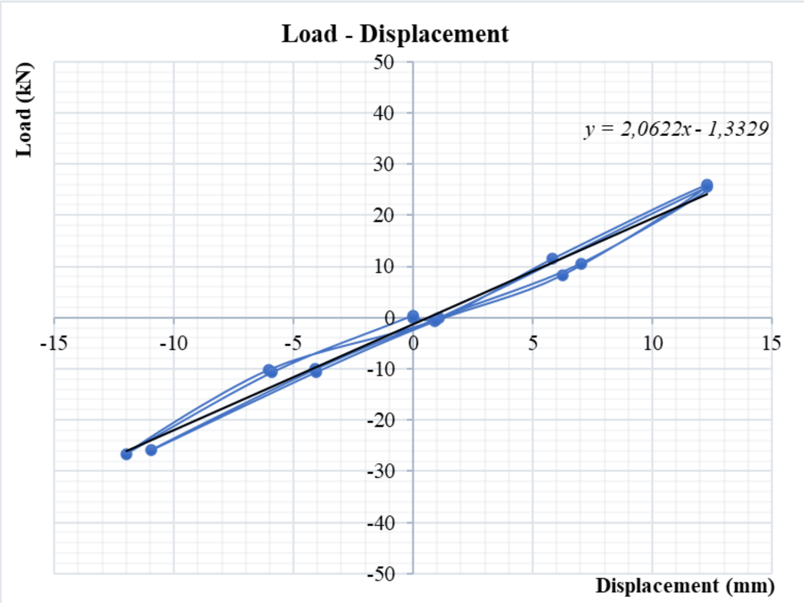

Figure 5. Load-displacement relation for specimen CW.

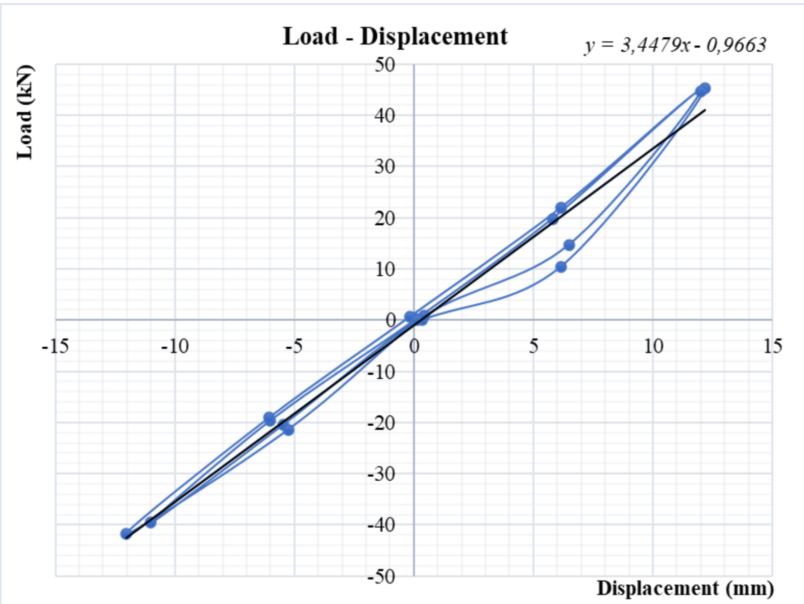

Figure 6. Load-displacement relation for specimen CWZ.

3.4 Comparation Behaviour

Figure 7 shows a comparison between the slopes of the CW and the CWZ curves. From this comparison we can conclude that the zinc sheeting with which the CWZ specimen is reinforced leads to a displacement curve with more amplitude than the CW curve. This difference in amplitude is, however, only noticeable in the positive range, between the ascendant line and the falling line of the cyclic load at the 1% drift point. The amplitude curves of both types of walls are quite similar in the negative range.

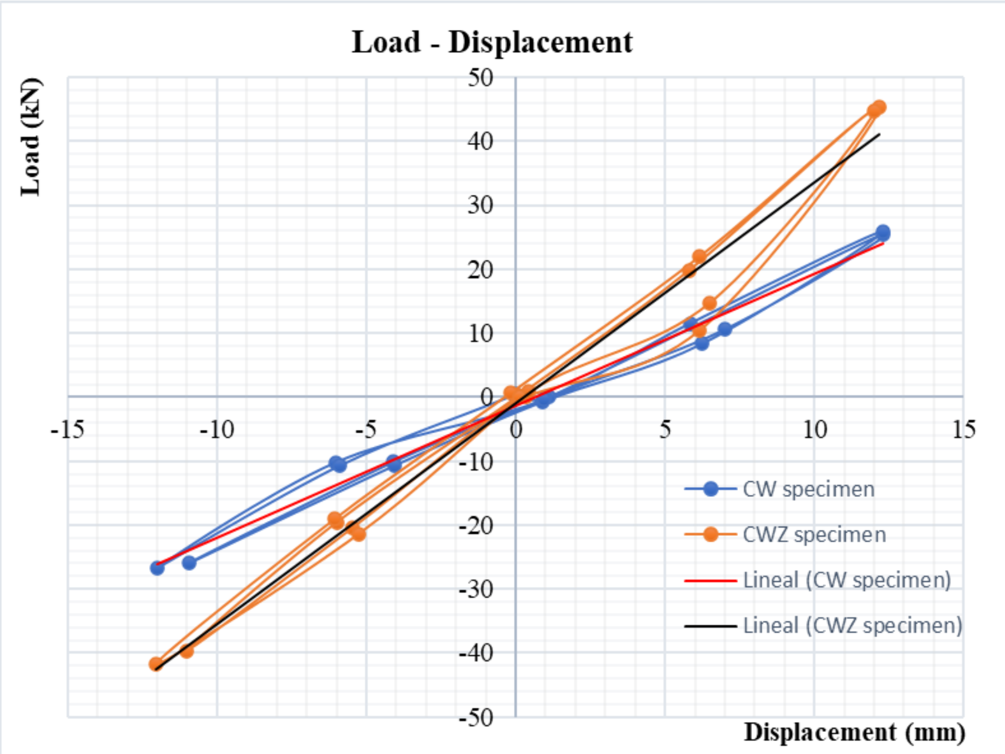

Figure 7. Load-displacement curve comparison of CW and CWZ specimens.

3.5 Failure Mode

Figures 8-10 show the damages sustained by both types of walls at the 1% drift point. The failure modes of the CW and the CWZ can be glimpsed from these first signs of damage.

Figure 8. Failures in the CW specimen corners in 1% drift.

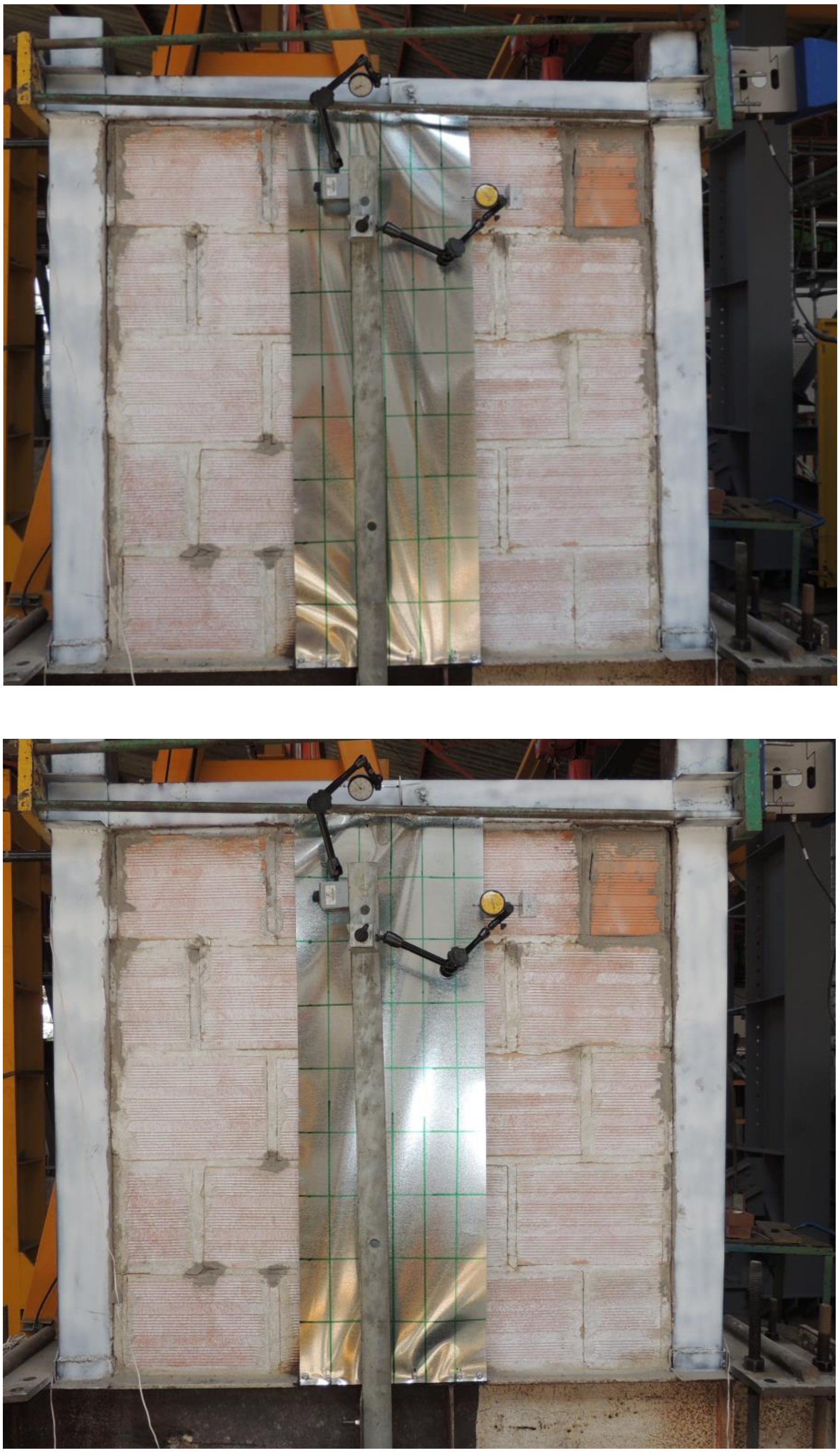

Figure 9. CWZ test in 1% drift. General view in both directions. (a "X" shape is identified in the zinc sheeting).

Figure 10. Failures in the CWZ specimen corners in 1% drift.

4. CONCLUSIONS

i. The stiffness difference between the CW and the CWZ specimens is of around 60%. This difference is due to the effects of the zinc sheeting with which the CWZ is reinforced.

ii. At the 1% drift point, neither specimen presents meaningful in-plane or out-plane damages. However, some cracks appear in the mortar used for joining the bricks of the walls and an x-shaped deformation appears in the zinc sheeting of the CWZ.

iii. This kind of reinforcement may be used in certain seismic hazard zones (low and intermediate) in order to reduce the vulnerability of low-cost housing and informal buildings.

iv. Zinc sheeting is a cheap and easy solution to reinforce light structures.

5.RECOMMENDATIONS

After carrying out these experiments and evaluating their results we came up with the following recommendations:

Fabricating recommendations:

i. In order to weld the channel-type profiles into a box section, we recommended the use of the GMAW welding method to prevent higher temperature in the steel due to electrode use.

ii. Welding ought to be organized and the parts being welded must be kept equidistant.

iii. The beam-column connections must be reinforced to avoid local buckling.

iv. Welding quality control is necessary in all steel structures, specially if the welding work involves thin-sheet elements.

v. In order to install the zinc sheeting we recommend the use of bolts with neoprene washer to reduce damage.

Research recommendations:

i. Test other specimens with zinc sheets of various thicknesses, different configurations, and different positions.

ii. Replicate this research with the finite element method (FEM).

iii. Test other specimens built with openings and another types of bricks.

6. ACKNOWLEDGMENTS

The authors would like to thank the "Apoyo a proyectos de investigación y creación artística de la sede Bogotá de la Universidad Nacional de Colombia – 2019" fund for the funding of the "Tipología constructiva mixta de muros para viviendas de interés social" project, from which the present study is derived. We are also grateful to Andrés Delgadillo and Pilar Naspud, as well as to the staff of the structure laboratory, for their collaboration to this project. In addition, we would like to thank Ladrillera Santafé, Gerdau Diaco and Proalco Bekaert for providing the materials used for the tests carried out in this study.

REFERENCES

Carrillo, J., Artete, C., Cano, W., & Vera, X. (2020). Post earthquake safety evaluation of buildings and schools after the 2016 Ecuador earthquake. *Earthquake Spectra*.

Naspud, P., Nieto-Cárdenas, X., Delgadillo, E., & Takeuchi, C. (2021). Simulación numérica de un pórtico con perfiles de acero formado en frío (CFS) ante carga lateral. *XXII Jornadas Estructurales*, 10. https://sci.org.co/wp-content/uploads/file/me_jornadas_2021/articulo_11.pdf%0A

Nieto-Cárdenas, X., & Gamón, R. (2012). *Diseño de una vivienda de dos plantas con soluciones prefabricadas.* Universidad de Cuenca.

Nieto-Cárdenas, X., & Takeuchi, C. (2019). Experimental behavior of combined frame under lateral load. In (Colombia) : ACOFI Bogotá (Ed.), *Encuentro Internacional de Educación en Ingeniería EIEI ACOFI 2019. Retos en la formación de Ingenieros en la era digital: Memorías ACOFI* (pp. 1–8). ACOFI ISSN:2665-5918. https://acofipapers.org/index.php/eiei/article/view/272

Nieto-Cárdenas, X., Takeuchi, C., & Carrillo, J. (2021a). Ampliación en edificaciones informales con pórticos de acero en perfilería tubular. *VIII Congreso Internacional de La Construcción Con Acero.*, 8.

Nieto-Cárdenas, X., Takeuchi, C., & Carrillo, J. (2021b). Estudio experimental de un sistema de mampostería confinada por un pórtico de lámina delgada. Enfoque de Laboratorio. *IX Encuentro de Investigacion de Estudiantes de Postgrado 2021.*, 8.

Nieto-Cárdenas, X., Takeuchi, C., & Carrillo, J. (2022). Rigidez de un muro mixto de mampostería y pórtico de lámina delgada. *XXIII Congreso Nacional de Ingeniería Sísmica.*, *1*, 1–8.

Tasnimi, A. A., & Mohebkhah, A. (2011). Investigation on the behavior of brick-infilled steel frames with openings, experimental and analytical approaches. *Engineering Structures*, *33*(3), 968–980. https://doi.org/10.1016/j.engstruct.2010.12.018

Dynamic properties and seismic performance of an innovative cleanroom

M. Zito[1], D. D'Angela[1], and G. Magliulo[1,2]

[1] Department of Structures for Engineering and Architecture, University of Naples Federico II
Via Claudio, 21, I-80125 Naples, Italy
address
e-mail: martino.zito@unina.it
[2] Construction Technologies Institute, National Research Council (ITC-CNR)
Via Claudio, 21, I-80125 Naples, Italy
address
{danilo.dangela, gmagliul}@unina.it

Abstract. A cleanroom or white room is a constructed facility having a controlled environment in terms of cleanliness, temperature, humidity, and pressure. Cleanrooms are used in various industrial contexts to implement activities that require strictly controlled environment and minimum air contamination. Typical applications refer to food, pharmaceutical, and electronic industry, as well as to healthcare facilities. Cleanrooms are considered nonstructural elements (NEs) since they are not part of the structural systems of the buildings; they are extremely complex and include architectural, mechanical, hydraulic, and electrical/electronic components. Several recent earthquakes in Italy and worldwide highlighted the potential vulnerability of complex NEs such as the cleanrooms. In particular, their damage potentially results in heavy economic losses related to both direct losses (e.g., repair cost) and indirect losses (e.g., downtime) and casualties. No literature studies investigated the seismic performance of cleanrooms, and no regulations or guidelines define reliable methods for assessing their dynamic properties and seismic capacities. This study investigates the seismic response of an innovative cleanroom, in terms of both dynamic properties and seismic performance. Shake table tests are performed on a full-scale innovative cleanroom under operation conditions. In particular, the cleanroom testing setup included walkable ceiling system and ventilation/electrical/piping network systems. The experimental investigation consists in both dynamic identification and incremental seismic performance tests, according to ICC-ES AC156 protocol. The cleanroom was proven to have high seismic capacities under operation conditions. The developed construction and technologic solutions, including innovative devices, represent guidance towards the implementation of seismically safe cleanrooms.

Keywords: Nonstructural elements, Cleanroom, Shake table test, Seismic performance, Earthquake engineering.

1. INTRODUCTION

The cleanroom or white room is an atmosphere-controlled environment, which characteristics, in terms of relative humidity, temperature, pressure, and particle contamination, allow the workability of specific products and the execution of some parts of the process [ISO, 2016]. Cleanrooms with high requirements for control of contamination are widely used in pharmaceutical, food, and electronic manufacturing industries [Loomans et al., 2020; Shao et al., 2022] and in healthcare and hospital facilities (e.g., operating theater) [Andersson et al., 2012; Can et al., 2021]. Cleanrooms consist in complex architectural systems integrating mechanical, electrical, electronic, and hydraulic facilities and equipment [ASCE 7-16, 2016; FEMA E-74, 2012]. Cleanrooms can be classified as nonstructural elements (NEs) since they are not part of the structural system of buildings and facilities. The cleanrooms, as NEs, are not typically designed considering seismic actions, and relatively frequent earthquakes might even cause significant losses and functioning disruption, which are extremely critical for production and manufacturing facilities. The cleanroom partitions exhibited major seismic damage in the 2012 Emilia earthquake [Petruzzelli, 2016]. This response caused significant damage to room's content and required major restoration intervention in terms of facilities and equipment prior to reinstate the production. Indeed, the seismic damage of cleanrooms can threaten life safety and can cause severe economic losses due to property loss and downtime [FEMA E-74, 2012; Taghavi and Miranda, 2003].

Several studies investigated architectural NEs such as partitions and ceiling systems [Arifin et al., 2020; Jun et al., 2022; Magliulo et al., 2014], electrical/mechanical/hydraulic equipment and components [Butenweg et al., 2021; Ghalibafian et al., 2004], freestanding elements housed within critical facilities [D'Angela et al., 2021; Filiatrault et al., 2004; Di Sarno et al., 2019; Wittich and Hutchinson, 2017], and objects/contents having historical/cultural significance [Blasi et al., 2018; Prota et al., 2022; Tran et al., 2021]. However, to the authors' knowledge, no literature studies focused on the seismic performance of complex NEs that integrate architectural and electrical/electronic/mechanical/hydraulic systems, especially under functioning conditions, such as cleanrooms. The present study represents a first step carried out to address the abovementioned research gap. This paper presents the results of an experimental investigation on the seismic performance of a full-scale cleanroom with walkable ceiling system, by means of shake table tests. The cleanroom was designed with innovative construction solutions to maximize seismic performance. The tests were carried out under full functioning conditions, including ventilation, air conditioning, pressure, and electronic opening control, in order to meet the requirements of a cleanroom with ISO Class 7 [CEN, 2016]. Both dynamic identification and seismic performance evaluation tests were carried out, according to ICC-ES AC156 protocol [ICC-ES, 2012]. The study was developed in the framework of an agreement between the Mangini srl (Italy) and the Department of Structures for Engineering and Architecture (DIST) (University of Naples Federico II, Italy).

2. METHODOLOGY

2.1 SPECIMEN

The specimen was a real-scale cleanroom consisting in the assembly of base/flooring, lateral partition system, ceiling, and electric/ventilation facilities. The plan dimensions of the cleanroom are about 2.8 x 2.8 m, while its height is about 3.0 m. The dimensions of the specimen are representative of a typical cleanroom used within food, pharmaceutical and healthcare facilities. The panels of the cleanroom were formed by two stainless and prepainted steel outsides layers each 0.8 mm thick and clad on the inside with rock wool. The steel layers were bonded with a Two-Part Polyurethane Adhesives Cure (2C PUR). The external perimeter of the panels was stiffened by aluminum frames. Also, in the inside corners of the frame of the panels were placed the brackets. The panels have a total thickness of 62 mm and a weight of 0.24 kN/m^2. The overall weight of the cleanroom including the weight of the ceiling system (1.96 kN) is 13.4 kN. As shown in Figure 1, the cleanroom was installed with four different walls: i) wall with pass-box (south side), ii) wall with glass and steel panels (east side), iii) wall with door (north side), and iv) blind wall (west side).

Figure 1. View of the specimen: i) wall with pass-box (south side), ii) wall with glass and steel panels (east side), iii) wall with door (north side), and iv) blind wall (side west).

In the following, the main components of the cleanroom are described, and the mounting procedure is briefly reported. The geometrical details of the elements and the technical specifics of the assembly are omitted for the sake of brevity since they are available within the technical reports [Magliulo and Zito, 2021]. The base layout of the cleanroom was composed by the assembly of extruded aluminum 6060-T5 elements, i.e., stiffened rectangular cross-section profiles, flanged floor rail profiles, and angular bracket profile elements. The rectangular profiles were fastened to the wood slab with wood screws. The telescoping flanged floor rail profiles were installed on the rectangular profiles to obtain a horizontal plane on which to position the walls of the cleanroom when the floor has unevenness and surface irregularities. Moreover, the shear key at the top of the telescoping track provides a restraint at the base of the walls of the cleanroom. The telescopic tracks were fastened to the rectangular profiles and angular bracket profile with screws on both sides. Finally, the angular bracket profiles were fastened to the wood slab with wood screws.

The lateral partition system of the cleanroom mainly consists of steel panels, curved angular profiles, vertical splice profiles, pass-box, and glass panels. The panels were positioned on the telescoping tracks and have different dimensions. The curved angular profiles were installed at the ends of the walls as well as inside the cleanroom at the corner of the pass-box and air hole. Two vertical splice profiles were connected on both sides of the curved angular profile before each was installed. The panels of walls of the cleanroom were spliced through the vertical splice profiles. Especially, the vertical splice profile with two gaskets was placed in the gap of 4 mm of the edges of panels. This gap is needed to allow for the replacement operation of panels of the walls. The pass-box was fastened to neighboring panels with screws on the four sides of the inside and outside frame of the pass-box. The final step was to install the shell profiles inside and outside of the cleanroom and the flooring. The shell profiles are used primarily for architectural and technological purposes. The shell profiles were installed on the snap-on angular bracket profiles and by adding a layer of neutral silicone sealant. Moreover, to prevent air pressure loss in the cleanroom, the walls were completed by filling the splices of the panels with a layer of neutral silicone sealant. Finally, a PVC flooring was positioned and bonded with adhesive glue.

The ceiling system consist of the T-shape profile, angular joint connector, loadbearing panels, stiffened suspension connection profile elements. The loadbearing panels have a variable length from 1500 to 3000 mm, variable width from 600 to 1200 mm, and a thickness of 62 mm. Some panels had holes to layout the frame of the ceiling light and air filter. The ceiling system was placed at 2.80 m level above the floor level of the cleanroom. At this level, the T-shape profiles were fastened to the walls of the cleanroom with two rows of screws. The ends of the T-shape profiles were fixed with the angular joint connector. Once the installation of the T-shape profiles was completed, the loadbearing panels of the ceiling system were placed. The panels were spanned in the north-south direction. The panels of the ceiling system were connected by the stiffened suspension connection profile elements to the ceiling suspension system. Lastly, two ceiling lights and two air filters were placed to complete the ceiling system.

2.2 TESTING SETUP AND INSTRUMENTATION

The testing setup was defined in order to replicate a realistic and typical arrangement of the cleanroom within the hosting facility, with particular attention to the functioning/service facilities/systems. The height of cleanrooms is typically lower than the hosting inter-story height, and a plenum space of variable height (ranging in 40 to 400 cm) is typically arranged between the top of the cleanroom and the upper floor of the building. Most functioning facilities and equipment (e.g., pipeline and electrical networks) are located within this plenum space and connect the external supply to the cleanroom, according to the functioning conditions of the cleanroom.

The shake table was representative of a building floor of installation of the cleanroom; in particular, a wood slab was used as an interface between shake table and cleanroom. A steel test frame was designed and constructed to simulate the upper building floor that supports the plenum space facilities and the ceiling of the cleanroom. Figure 1 shows the testing setup. Electrical and ventilation systems were installed and made fully operative during the tests to recreate the functioning condition of the cleanroom in realistic conditions (i.e., serviceability) [CEN, 2005]. In particular, the ventilation system (Figure 2) consisted in an air treatment unit (ATU system) provided with high-efficiency particulate air filters (HEPA), a galvanized sheet metal piping system, necessary to circulate air, cleanroom supplies and sensors (pression control). The system was able to keep the pressure in the cleanroom constantly equal to at about 40 Pascal, with tolerance of ±5 %, according to the relevant requirements [ISO, 2016; Yang et al., 2021]. The electrical system consisted of a control unit for the operation of the cleanroom opening system (a door and a pass-box), internal pressure sensor, and lighting system. Both service units were placed in an external area that was isolated from the shake table area, and the related network systems were realized through a duct system, flexible pipes, and cable trays. The network system was realized favoring flexible connections among the different components, in order to minimize the transfer of the dynamic actions and the associated deformations from the cleanroom to the units.

(a) (b)

Figure 2. Testing setup: (a) global view and (b) UTA system with HEPA filter [Zito et al, 2023].

Monitoring instrumentation consisted of eleven accelerometers (Acc) (Figure 3), eight displacement laser sensors (Las) (Figure 3), four wire potentiometers, and four video cameras. The accelerometers were three-axis piezoelectric devices, with a measurement range of ±10 g and a sampling rate of 100 Hz. Four accelerometers were positioned at the middle point of the cardinal side lateral panels of the cleanroom, on the external side. Three accelerometers were located at the top of the lateral panels (middle width), corresponding to south, east, and west side panels; an additional accelerometer was installed on the west side panel, corresponding to the bottom of the lateral panel (middle width). An accelerometer was installed on the wood slab (middle width), corresponding to the west side. Two accelerometers were placed on the ceiling system, i.e., corresponding to suspension connection element and (b) panel frame. The shake table was monitored by internal accelerometers (AccTX and AccTY, not depicted in Figure 3). "Luchsinger" e "Wenglor" type laser sensors were used (LasL and LasW); the former (latter) had a measurement range of 600 (200) mm at high resolution, i.e., 80 μm (50 μm), with maximum sampling frequency equal to 1.5 kHz (100 Hz); both sensor types were unaffected by materials, colors, and brightness issues. Five laser sensors were installed on the south side and two on the east side; displacement of the shake table along X and Y direction were monitored by one laser for along each direction. The top displacements of the test frame (Figure 1 and 2a) were monitored by four wire potentiometers (two along each direction).

The pressure within the cleanroom was monitored in real time by means of air pressure sensors with accuracy of up to ± 0.5 Pa and measurement of minimal differential pressures from 0 to 50 Pa according to DIN EN ISO 14644-3 [CEN, 2019]. In particular, a differential pressure transducer connected externally to the control unit was installed inside the cleanroom.

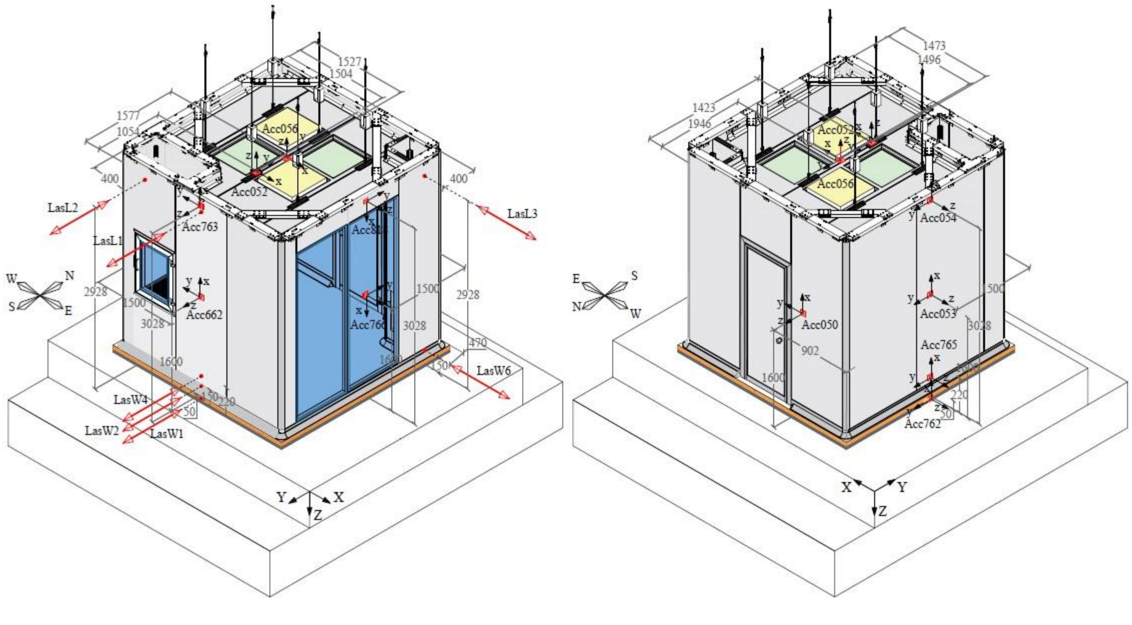

Figure 3. Perspective view of the instrumentation arrangement associated with the specimen [Zito et al, 2023].

2.3 TESTING PROCEDURE AND LOADING INPUTS

The testing procedure consisted of a series of shaking tests, including both dynamic identification tests and incremental seismic performance evaluation tests, according to a consolidated testing and seismic qualification approach [FEMA 461, 2007; ICC-ES, 2012]. The former tests were aimed at assessing the initial and final dynamic properties of the system and their evolution along the incremental tests, whereas the latter were carried out to assess the seismic capacities of the system as the intensity measure increases. In particular, the dynamic identification tests were performed through monodirectional low-intensity excitation along both horizontal directions, and the seismic performance tests were bidirectional (horizontal). Dynamic identification tests were performed considering initial configuration, between seismic incremental tests, and corresponding to final configuration (after incremental tests).

Dynamic identification inputs corresponded to low-amplitude random vibration acceleration time histories (RAN tests) [Di Sarno et al., 2019], whereas seismic performance inputs corresponded to scaled AC156 input tests (AC tests) [ICC-ES, 2012]. The testing program consisted of incremental bidirectional AC tests from S_{DS} equal to 0.10 g to 1.50 g, through 0.10 g S_{DS} increments, performing unidirectional RAN tests (along both directions) prior to, between, and after AC tests. Further details regarding the generation of both RAN and AC inputs and main details about the considered signals can be found in [Magliulo et al., 2012; Petrone et al., 2017].

2.4 DYNAMIC IDENTIFICATION METHODS

The dynamic properties of the cleanroom were assessed by using the transfer function method [Clough and Penzien, 2003]. In particular, the transfer curves and associated vibration modes of the specimen were assessed considering RAN tests. The natural frequencies and damping ratios were estimated, and their evolution along the incremental tests was assessed. The transfer functions were defined as the ratio of the Fourier transforms related to acceleration time histories recorded at the cleanroom top and on the shake table. Acc054z and Acc054y were considered as output accelerometers for X and Y directions, respectively. The equivalent damping ratio was evaluated according to the half-power bandwidth method [Chopra, 1995; Clough and Penzien, 2003], typically used to assess structures and components assumed to have linear viscous damping [Papagiannopoulos and Hatzigeorgiou, 2011]. The damping ratio associated with the first mode of the cleanroom was evaluated by assessing the transfer functions obtained by RAN tests.

3. RESULTS

The cleanroom did not exhibit damage or critical response even corresponding to very high seismic intensities, i.e., up to S_{DS} equal to 1.50 g. The full functioning of the cleanroom was not disrupted over the incremental tests. In the following, two key aspects of the seismic response of the cleanroom are discussed: (1) dynamic identification, i.e., transfer curves, natural frequencies, and damping ratio and (2) acceleration peaks and acceleration amplifications. Only key results are reported here for the sake of brevity.

The natural frequency of the cleanroom associated with the X (Y) direction is equal to 17.8 Hz (20.3 Hz), as shown in Figure 4. Also, the natural frequencies associated in both directions present an approximately constant trend, confirming that the cleanroom did not exhibit any damage. The damping ratio associated with the X (Y) direction ranges in about 6 – 8 % (8 – 13 %), showing that the specimen has higher damping properties along the Y direction. The evolution of the damping ratio over the incremental tests is monotonic; in particular, the ratio overall increases along with both X and Y directions, even though the increment related to the Y direction is more significant than along the X direction. Given the unicity of the tested specimen, it is not meant to make quantitative comparisons with literature results. However, the trends and the ranges of the fundamental periods and damping ratios are consistent with previous literature studies [Petrone et al., 2017].

Figure 5 shows the peak component acceleration (PCA) evolution over peak floor accelerations (PFA) related to multiple component locations and the peak floor acceleration (PFA) corresponding to the incremental test IDs. The acceleration amplification response is almost the same at the cleanroom panel's top (Figure 5a) and at in the vicinity of the ceiling suspension device (Figure 5b); in particular, PCA is approximately proportional to PFA and very minor differences are observed along X and Y direction. The out of plane accelerations related to the lateral partition panels is more dispersed.

(a) 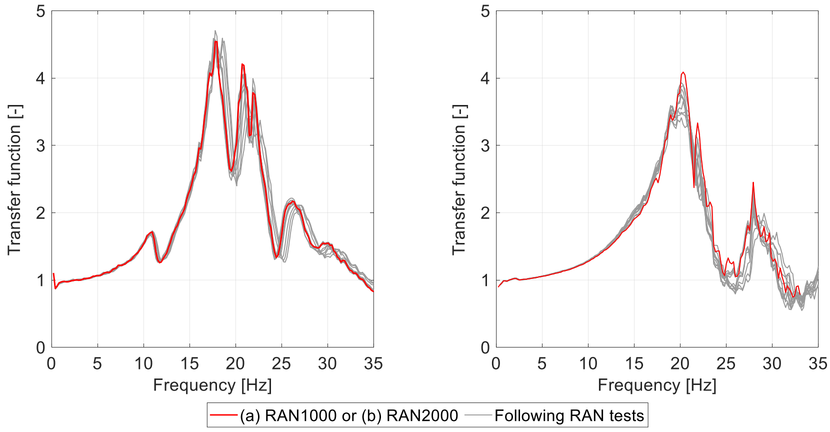 (b)

Figure 4. Transfer curves and fundamental frequencies related to all dynamic identification (RAN) tests along (a) X and (b) Y directions. RAN1000 and RAN2000 correspond to first RAN tests along X and Y directions, respectively.

The most amplified response is associated with East side, which corresponds to the glass panels; in this case, PCA is approximately linearly increasing with PFA, especially over lower to medium seismic intensities (e.g., up to PFA equal to about 1.0 g). The amplification response associated with North side (Figure 5c) (corresponding to the door side, where the accelerometers is located on the panel at the right of the door) is quite similar to the East side (glass panels) up to a PFA equal to about 0.75, whereas the slope of PCA to PFA significantly decrease for larger PFA values. The responses associated with West (blind partition side) and South (pass-box partition side) sides are significantly less amplified than the ones related to North and East panels. In particular, PCA is approximately halved or even lower. PCA associated with West and South sides (Figure 5c) is almost coinciding up to PFA equal to about 0.75 g and is quite similar from 0.75 g to about 1.5 g; for larger PFA values, PCA related to West side is larger than South one.

4.CONCLUSIONS

The paper reported the key results of an experimental campaign aimed at assessing the dynamic properties and the seismic performance of an innovative cleanroom. The cleanroom was tested on the shake table, including the presence of a ventilation system, an electrical system, and a walkable false ceiling system. The cleanroom did not exhibit damage or critical seismic response. In particular, the whole system remained operational until maximum accelerations higher than those expected on the Italian sites (e.g., S_{DS} equal to 1.5 g). The main dynamic properties of the specimen were estimated, and the accelerations recorded on the specimen were assessed, estimating the peak values and the acceleration amplifications. These parameters are essential for an accurate and reliable estimation of seismic demands on similar components and systems.

The study highlights the critical response of the cleanroom and stresses the need for further studies investigating the operation of the cleanroom under seismic action also controlling the increase in cost due to the addition of innovative components. In particular, further studies should be performed to assess the performance of cleanrooms through a performance-based engineering approach, also implementing and validating analytical and/numerical methods for design and assessment of cleanrooms.

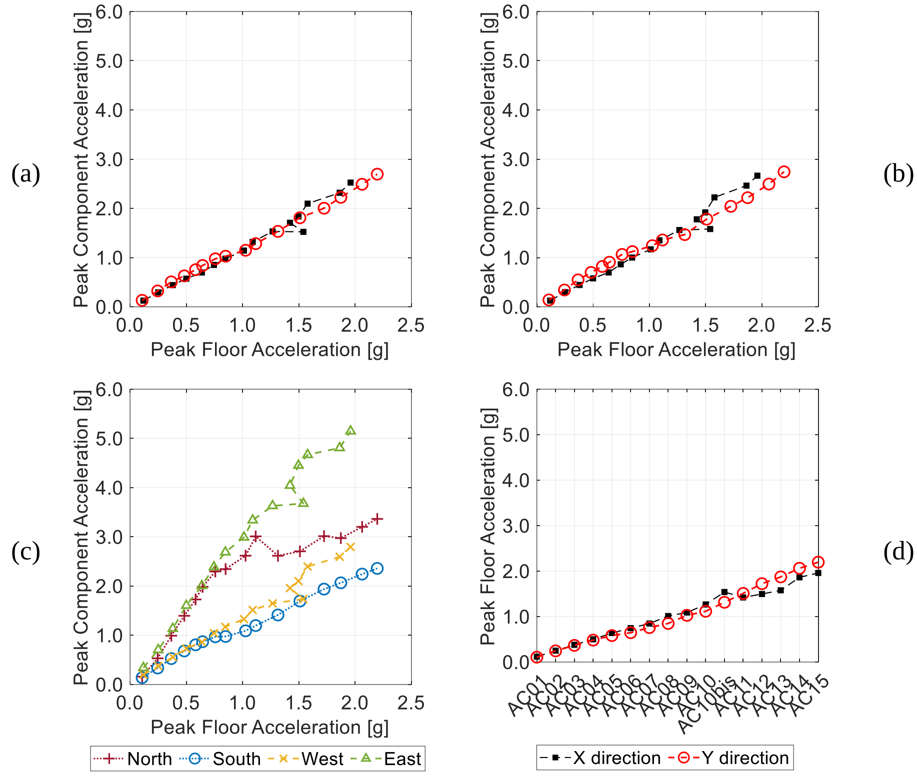

Figure 5. **Peak component acceleration evolution over peak floor acceleration, corresponding to (a) cleanroom panel's top, (b) ceiling suspension device, (c) lateral partition panel (middle point) and (d) peak floor acceleration associated with incremental tests.**

ACKNOWLEDGMENTS

This study was funded by Mangini Srl, which also provided materials and assembly of the specimens, by the Italian Ministry of University and Research (MUR) in the framework of PRIN 2020 project titled "ENRICH project: ENhancing the Resilience of Italian healthCare and Hospital facilities" and by Regione Campania in the frame of the national project POR GRISIS 2014-2020 Gestione dei Rischi e Sicurezza delle Infrastrutture a Scala regionale, Cup: B63D18000280007). The experimental tests were performed at the laboratory of the Department of Structures for Engineering and Architecture of the University of Naples Federico II under the technical and scientific supervision of Prof. Giuseppe Maddaloni.

REFERENCES

Andersson, A. E., I. Bergh, J. Karlsson, B. I. Eriksson, and K. Nilsson. 2012. "Traffic flow in the operating room: An explorative and descriptive study on air quality during orthopedic trauma implant surgery." Am J Infect Control, 40 (8): 750–755. https://doi.org/10.1016/j.ajic.2011.09.015.

Arifin, F. A., T. J. Sullivan, and R. P. Dhakal. 2020. Experimental investigation into the seismic fragility of a commercial glazing system. Bulletin of the New Zealand Society for Earthquake Engineering.

ASCE 7-16. 2016. Minimum Design Loads and Associated Criteria for Buildings and Other Structures. 1–889. American Society of Civil Engineers (ASCE).

Blasi, G., M. A. Aiello, G. Maddaloni, and M. R. Pecce. 2018. "Seismic response evaluation of medical gas and fire-protection pipelines' Tee-Joints." Eng Struct, 173: 1039–1053. Elsevier Ltd. https://doi.org/10.1016/j.engstruct.2018.07.045.

Butenweg, C., O. S. Bursi, F. Paolacci, M. Marinković, I. Lanese, C. Nardin, and G. Quinci. 2021. "Seismic performance of an industrial multi-storey frame structure with process equipment subjected to shake table testing." Eng Struct, 243: 112681. https://doi.org/10.1016/j.engstruct.2021.112681.

Can, A., H. Ö. Divarci, and E. Buyruk. 2021. "Design principles of the hospital clean rooms." Transactions of FAMENA Special issue 1, XLV (1): 1–15. https://doi.org/https://doi.org/10.21278/TOF.45Si1008521.

Chopra, A. K. 1995. "Dynamics of Structures: Theory and Applications to Earthquake Engineering." Prentice Hall, NewJersey.

Clough, R. W., and Penzien, J. 2003. "Dynamics of Structures". Computers & Structures, Inc. University Ave. Berkeley, CA 94704, USA.

European Committee for Standardization (CEN). 2005. Eurocode 8: "Design of structures for earthquake resistance".

D'Angela, D., G. Magliulo, and E. Cosenza. 2021. "Seismic damage assessment of unanchored nonstructural components taking into account the building response." Structural Safety, 93. https://doi.org/10.1016/j.strusafe.2021.102126.

European Committee for Standardization (CEN). 2016. "Cleanrooms and associated controlled environments - Part 1: Classification of air cleanliness by particle concentration". Brussels, Belgium. https://store.uni.com/.

European Committee for Standardization (CEN). 2019. "Cleanrooms and associated controlled environments - Part 3: Test methods. European Committee for Standardization". Brussels, Belgium. https://store.uni.com/.

FEMA 461. 2007. Interim Testing Protocols for Determining the Seismic Performance Characteristics of Structural and Nonstructural Components. Federal Emergency Management Agency (FEMA), Washington, D.C.

FEMA E-74. 2012. Reducing the Risks of Nonstructural Earthquake Damage-A Practical Guide. Federal Emergency Management Agency (FEMA), Washington, D.C.

Filiatrault, A., S. Kuan, and R. Tremblay. 2004. "Shake table testing of bookcase – partition wall systems." Canadian Journal of Civil Engineering .

Ghalibafian, H., G. S. Bhuyan, C. Ventura, J. H. Rainer, D. Borthwick, R. P. B. Stewart, and E. Zhai. 2004. "Seismic Behavior of Flexible Conductors Connecting Substation Equipment—Part II: Shake Table Tests." IEEE Transactions on Power Delivery, 19 (4): 1680–1687. https://doi.org/10.1109/TPWRD.2004.832387.

ICC-ES AC156. 2012. Acceptance criteria for seismic certification by shake-table testing of nonstructural components.

Jun, S.-C., C.-H. Lee, and C.-J. Bae. 2022. "Shake table testing of braced and Friction-Added suspended ceilings and associated numerical study." Eng Struct, 252: 113724. https://doi.org/10.1016/j.engstruct.2021.113724.

Loomans, M. G. L. C., T. B. J. Ludlage, H. van den Oever, P. C. A. Molenaar, H. S. M. Kort, and P. H. J. Joosten. 2020. "Experimental investigation into cleanroom contamination build-up when applying reduced ventilation and pressure hierarchy conditions as part of demand controlled filtration." Build Environ, 176: 106861. https://doi.org/10.1016/j.buildenv.2020.106861.

Magliulo, G., V. Pentangelo, G. Maddaloni, V. Capozzi, C. Petrone, P. Lopez, R. Talamonti, and G. Manfredi. 2012. "Shake table tests for seismic assessment of suspended continuous ceilings." Bulletin of Earthquake Engineering, 10 (6): 1819–1832. Kluwer Academic Publishers. https://doi.org/10.1007/s10518-012-9383-6.

Magliulo, G., C. Petrone, V. Capozzi, G. Maddaloni, P. Lopez, and G. Manfredi. 2014. "Seismic performance evaluation of plasterboard partitions via shake table tests." Bulletin of Earthquake Engineering, 12 (4): 1657–1677. Kluwer Academic Publishers. https://doi.org/10.1007/s10518-013-9567-8.

Magliulo, G. and Zito, M. 2021. "Prove su tavola vibrante per l'analisi della prestazione sismica di una cleanroom serie 62 acciaio". Rapporto di prova 202001-01, Dicembre 2021. (in Italian).

Papagiannopoulos, G. A., and G. D. Hatzigeorgiou. 2011. "On the use of the half-power bandwidth method to estimate damping in building structures." Soil Dynamics and Earthquake Engineering, 31 (7): 1075–1079. https://doi.org/10.1016/j.soildyn.2011.02.007.

Petrone, C., G. Magliulo, and G. Manfredi. 2017. "Shake table tests on standard and innovative temporary partition walls." Earthq Eng Struct Dyn, 46 (10): 1599–1624. John Wiley and Sons Ltd. https://doi.org/10.1002/eqe.2872.

Petruzzelli, F. 2016. Seismic risk assessment of an industrial plant struck by the Emilia 2012 earthquakes. Int. J. Forensic Engineering.

Prota, A., M. Zito, D. D'Angela, G. Toscano, C. Ceraldi, A. Fiorillo, and G. Magliulo. 2022. "Preliminary Results of Shake Table Tests of a Typical Museum Display Case Containing an Art Object." Advances in Civil Engineering, 2022: 1–18. https://doi.org/10.1155/2022/3975958.

Di Sarno, L., G. Magliulo, D. D'Angela, and E. Cosenza. 2019. "Experimental assessment of the seismic performance of hospital cabinets using shake table testing." Earthq Eng Struct Dyn, 48 (1): 103–123. John Wiley and Sons Ltd. https://doi.org/10.1002/eqe.3127.

Shao, X., Y. Hao, S. Liang, H. Wang, Y. Liu, and X. Li. 2022. "Experimental characterization of particle distribution during the process of reducing the air supply volume in an electronic industry cleanroom." Journal of Building Engineering, 45: 103594. https://doi.org/10.1016/j.jobe.2021.103594.

Taghavi, S., and E. Miranda. 2003. Response Assessment of Nonstructural Building Elements – technical report PEER 2003/05.

Tran, T. T., K. Salman, and D. Kim. 2021. "Distributed plasticity approach for nonlinear analysis of nuclear power plant equipment: Experimental and numerical studies." Nuclear Engineering and Technology. Korean Nuclear Society. https://doi.org/10.1016/j.net.2021.03.017.

Wittich, C. E., and T. C. Hutchinson. 2017. "Shake table tests of unattached, asymmetric, dual-body systems." Earthq Eng Struct Dyn, 46 (9): 1391–1410. https://doi.org/10.1002/eqe.2860.

Yang, Z., Y. Hao, W. Shi, X. Shao, X. Dong, X. Cheng, X. Li, and X. Ma. 2021. "Field test of pharmaceutical cleanroom cleanliness subject to multiple disturbance factors." Journal of Building Engineering, 42: 103083. https://doi.org/10.1016/j.jobe.2021.103083.

Zito, M., D'Angela D., and Magliulo G. 2023. "Shake-table performance evaluation of an innovative cleanroom with walkable ceiling system under operation conditions". Earthq Eng Struct Dyn. (in preparation)

Shaking table experimental campaign on pre-code masonry infills subjected to in-plane and out-of-plane loading

M. Kurukulasuriya[1], R.R. Milanesi[2], D. Bolognini[2], I. Lanese[2], L. Grottoli[2], G. Magenes[3], F. Dacarro[2], P. Morandi[2]

[1] IUSS Pavia
Piazza della Vittoria, 15 – Pavia (Italy)
e-mail: maithree.kurukulasuriya@iusspavia.it

[2] Eucentre Foundation
Via Ferrata, 1 – Pavia (Italy)
e-mail:
{riccardo.milanesi,davide.bolognini,igor.lanese,luca.grottoli,filippo.dacarro,paolo.morandi}@eucentre.it

[3] University of Pavia
Via Ferrata, 3 – Pavia (Italy)
e-mail: guido.magenes@unipv.it

Abstract. Masonry infills represent widely adopted solutions in existing and newly designed enclosures in r.c. and steel framed buildings. However, such elements, usually considered as non-structural, were found to be very vulnerable to seismic actions, as reported in many earthquake surveys. Although the seismic behaviour of infills has been studied for decades, the wide variety of construction techniques, masonry materials, and details still require further studies to fully understand their response. In particular, despite one of the most common masonry infill typologies in existing buildings is made of horizontal hollowed thin clay units (usually 8-12 cm thick), no experimental study through dynamic tests on shaking table has been conducted yet, and the influence of the in-plane damage to the out-of-plane dynamic behaviour on this masonry infill typology is still debated. Therefore, within this framework, a wide experimental campaign has started at the Eucentre Foundation with the aim to study the seismic performance of existing weak masonry infills with horizontal hollowed clay units through dynamic tests on shaking table. Five full-scale infills have been constructed within a steel-concrete frame designed to perform equivalently to a r.c. frame and having a concrete side at the infill/frame interface. Four out of five specimens were built in full adherence with the frame elements, whereas one specimen has been realized with a gap between the infill and the columns in order to investigate the case of pure vertical bending/arching mechanism in the out-of-plane test. The experimental campaign has consisted of three in-plane quasi-static cyclic tests at different target drifts, and four dynamic out-of-plane tests up to the collapse of the infill. The three in-plane tests have been conducted before the out-of-plane shaking table ones. The experimental investigation, that also includes mechanical characterization tests on units and masonry specimens, has allowed to define the influence of bidirectional effects in the out-of-plane behaviour and the degradation of the out-of-plane stiffness and resistance due to the in-plane damage (and drift), considering the out-of-plane dynamic response.

Keywords: Masonry infills, weak/thin masonry, seismic response; shaking-table tests, in-plane/out-of-plane interaction.

1. INTRODUCTION

The seismic behaviour of masonry infill walls has been widely investigated in the past few decades, as their vulnerability has been repeatedly highlighted in many post-earthquake surveys. Extensive damage has been observed in masonry infills during earthquakes such as Molise (Italy, 2002), L'Aquila (Italy, 2009), Lorca (Spain, 2011) and Central Italy (2016) implicating that the failure of infill walls may lead to considerable economic losses [Chiozzi et al., 2017, Rossi et al., 2021] and even pose a significant threat to life safety [Decanini et al., 2004a, Braga et al., 2011 and Hermanns et al., 2013]. The collapse of masonry infills could be mainly attributed to the reduction of the expected out-of-plane capacity as a consequence of interaction with in-plane damage. Therefore, investigating the seismic behaviour of masonry infill walls is of utmost importance to limit in-plane damage and prevent out-of-plane collapse. The investigation reported in the present paper is inherently complex due to many aspects that need to be addressed although studies have been conducted to explore the in-plane behaviour [Calvi and Bolognini, 1999, Morandi et al., 2018], out-of-plane behaviour [Abrams, 1996, Milanesi et al., 2021] and in-plane and out-of-plane interaction [Angel et al., 1994, Morandi et al., 2013, da Porto et al., 2013, Furtado et al., 2016, Di Domenico et al., 2018, Ricci et al., 2018, Morandi et al., 2022] considering different infill typologies with different boundary conditions and aspect ratios. Furthermore, the role of infills in the global structural response [Decanini et al., 2004b], infill-frame interaction and local effects [Hak et al., 2013, Milanesi et al., 2018] and innovative infill solutions [Butenweg et al., 2019, Milanesi et al., 2022] have also been topics of interest.

In current seismic design codes, for example, European seismic code EC8: part 1 [2004] and the Italian code NTC18 [2018], infill walls are considered as non-structural elements (NSE) and should be evaluated as such. However, the guidelines provided for the damage limitation, resistance verification and seismic demand evaluation of masonry infill walls are rather general and not specific to the infill typology or structural configuration [Hak et al., 2012]. Thus, expanding the current experimental database [Sassun et al., 2016, De Risi et al., 2018, Liberatore et al., 2020, Anic et al., 2020] could be beneficial for improvements in the current rules for assessment of masonry infills. Furthermore, while there are well-established testing protocols for the in-plane and out-of-plane testing of NSE [FEMA 461, 2007], the rules are not specific for infill walls, especially for dynamic tests in the out-of-plane direction that have been barely carried on in past experimental campaigns. The lack of well-defined testing protocols has resulted in a wide variety of experimental setups in previous studies; for example, application of monotonic uniform pressure [Angel et al., 1994, Milanesi et al., 2021, Dawe and Seah, 1989], quasi-static cyclic uniform pressure [Furtado et al. 2022], application of four point loads [Calvi and Bolognini, 1999, Ricci et al., 2018], line cyclic loads [Morandi et al., 2022] and dynamic tests on shaking table [Carydis et al., 1992, Lanese, 2012, Milanesi et al., 2022]. Such variations could lead to difficulties in comparing and interpreting the experimental results and arriving at common conclusions.

In this context, an extensive experimental campaign was initiated at the Eucentre Foundation, with the aim of investigating the seismic behaviour of an infill typology that was commonly used as enclosures and partitions in existing reinforced concrete frame structures built in Italy between the 1960s-1980s. The infills were usually constructed with horizontally perforated hollow clay masonry units of 8- 12 cm thickness, and often in two layers of walls with a cavity in between; within the present study 12 cm thick clay masonry infill with a layer of plaster only on one side have been considered. Such an infill typology can be classified as "weak" infills due to its high percentage of perforation and slenderness introduced from the small thickness. The tests consisted of five specimens, the infill wall built fully in contact with the surrounding frame except for one specimen which was only bound to the frame at the top and bottom edges. Out of the four specimens fully bound to the frame, one was tested purely in-plane and another purely out-of-plane. The remaining two were first subjected to different levels of in-plane drifts and subsequently to out-of-plane motion to study the in-plane/out-of-plane interaction. The specimen with only two edges bound to the frame was tested in the out-of-plane direction, to investigate the out-of-plane arching mechanism in a single vertical bending wall. All in-plane tests were displacement-controlled pseudo-static cyclic tests at increasing target drifts and all out-of-plane tests were shake table dynamic tests with incremental peak floor accelerations applied until collapse. Following a detailed description of the experimental set up, testing protocols and mechanical characterisation, the results of the experiment are discussed in terms of damage propagation, force-displacement response, drift capacity and performance levels for in-plane tests and recorded accelerations and displacements, failure mechanisms and relations to the previous in-plane damage for out-of-plane tests.

2. DESCRIPTION OF THE TESTING CAMPAIGN

2.1 DESCRIPTION OF THE SPECIMENS

The masonry infills have been constructed within a structural frame with composite sections made of steel elements and grouted high-performance concrete (Figure 1a). The structural frame has been designed to behave as an existing r.c. frame structure and, simultaneously, remain undamaged during the tests. The specimens were in real-scale and the masonry panel has a length of 3.50 m, a height of 2.75 m and a thickness 13 cm including about 10 mm of plaster on one side only.

Four out of five specimens (T1, T2, T3, T4) were identical (Figure 1b) and built in full adherence with the structural frame by filling the interface joint at the edges with mortar. Meanwhile, T5 had a vertical gap (Figure 1c) of about 25 mm between the masonry panel and the structural columns to promote the vertical bending/arching resisting mechanism and avoid any influence of the horizontal/bidirectional bending/arching resisting mechanism. The masonry mortar bed-joint had a thickness of approximately 10 mm, meanwhile the mortar head-joints had been barely filled to resemble the Italian construction techniques of the 1960s-1980s.


(a) (b) (c)

Figure 1. (a) Structural frame before the construction of the masonry infill; (b) masonry infill at the end of the construction; (c) detail of the vertical gap between the masonry panel and the frame column of T5.

2.2 RESULTS OF THE TESTS OF MECHANICAL CHARACTERISATION

A comprehensive test series was conducted to determine the properties of units, mortar, and the masonry. From compressive tests conducted on clay blocks, the mean compressive strength of blocks parallel to holes was found as 6.16 MPa with a standard deviation of 0.35 MPa, and the strength perpendicular to holes was found as 1.22 MPa with a standard deviation of 0.23 MPa, with 10 blocks tested in each direction. Mean compressive strength and flexural tensile strength of mortar was 4.18 MPa with a standard deviation of 1.01 MPa, and 1.21 MPa with a standard deviation of 0.43 MPa, respectively. Compressive strength tests were performed on three-course-high masonry wallets [EN 1052-1], with and without plaster, and in vertical and lateral directions, and the results are summarized in Table 1.

To characterize the shear sliding parameters in the plane of masonry bed joints, a series of triplet tests were performed under three pre-compression levels applied perpendicular to bed joints [EN 1052-3]. From the triplet tests, the initial shear strength without precompression was deduced as 0.15 MPa, and the friction coefficient as 0.98. The relationship between the precompression and shear stress is shown in Figure 2.

Furthermore, diagonal compression tests were carried out on 3 specimens of 1.29 m x 1.29 m to determine the diagonal tensile strength (0.21 MPa with a standard deviation of 0.02 MPa) and the shear modulus (922 MPa with a standard deviation of 159 MPa) of the masonry [ASTM E519-02].

Table 1. Summary of compression tests on wallets

Wallet	Compressive strength (MPa)			Elastic modulus (MPa)		
	Mean	St. Dev.	C.o.V.	Mean	St. Dev.	C.o.V.
Vertical (Perpendicular to holes)	1.93	0.28	15%	2888	492	17%
Vertical- Plastered	2.26	0.08	3%	4168	667	16%
Horizontal (Parallel to holes)	4.07	0.62	15%	2482	462	19%
Horizontal - Plastered	3.56	0.58	16%	2876	413	14%

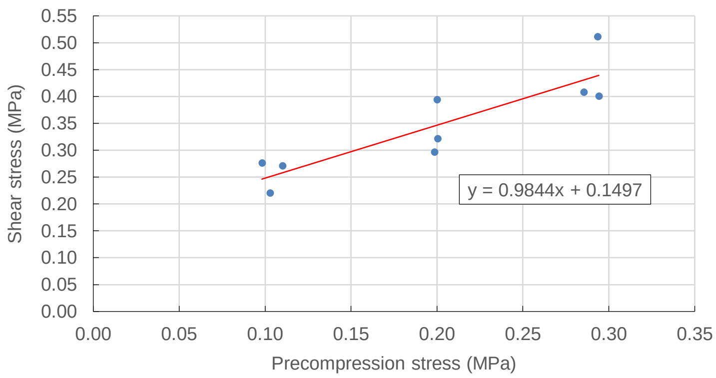

Figure 2. Shear stress vs precompression of triplet tests.

2.3 DESCRIPTION OF THE EXPERIMENTAL SET-UP AND INSTRUMENTATION

2.3.1 Experimental set-up

Two different experimental setup configurations (Figure 3) have been adopted for in-plane and out-of-plane tests. In both cases the specimens have been fixed to the shaking table in order to avoid any relative displacement between the foundation beam of the specimens and the shaking table. The location of the specimen remained constant for the whole duration of every in-plane and out-of-plane test conducted on a single infilled frame.

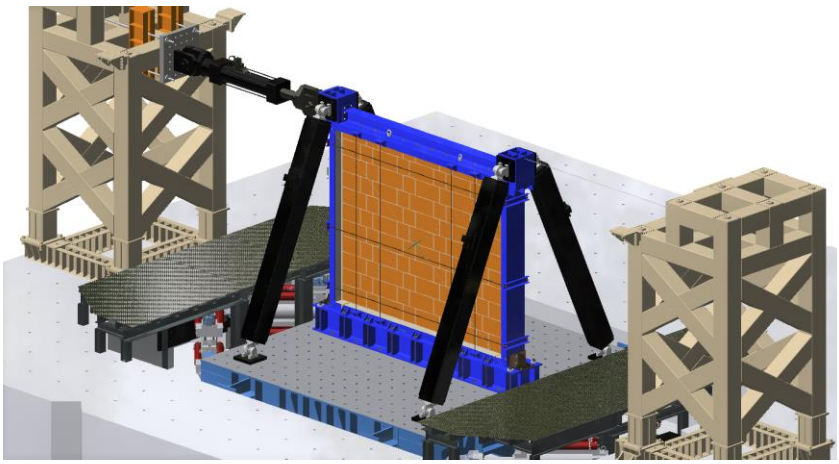

Figure 3. Sketch of the experimental setup adopted for the cyclic in-plane and dynamic out-of-plane tests.

The pseudo-static cyclic in-plane tests have been governed by a servo-hydraulic actuator restrained to strong steel structure and set into displacement control. Additionally, four inclined bracing systems were utilized to avoid any out-of-plane movement of the frame nodes. During the cyclic in-plane tests the shaking table has been used as a strong floor with an active control to stand still. During the out-of-plane tests, the servo-hydraulic actuator was disconnected from the specimen and the out-of-plane restraints remained attached to the specimen while the ground motion was applied through the shaking table.

2.3.2 Description of the instrumentation

The instrumentation installed differed depending by the tests conducted; in some cases, where the specimen was close to collapse, some instruments have been uninstalled to preserve them from damage, which otherwise would have led to erroneous data. The in-plane and the out-of-plane tests have different instrument configurations; in both types of tests, accelerometers (up to 10g), linear transducers and strain gauges have been adopted. Moreover, an optical acquisition with markers and high-resolution infrared cameras were used specifically for out-of-plane tests. The instruments were installed with the aim to monitor the whole specimen, the behaviour of the structural frame and the response of the masonry infill. In Figures 4 and 5, the instrumentations adopted for cyclic in-plane tests and the dynamic out-plane tests are shown, respectively.

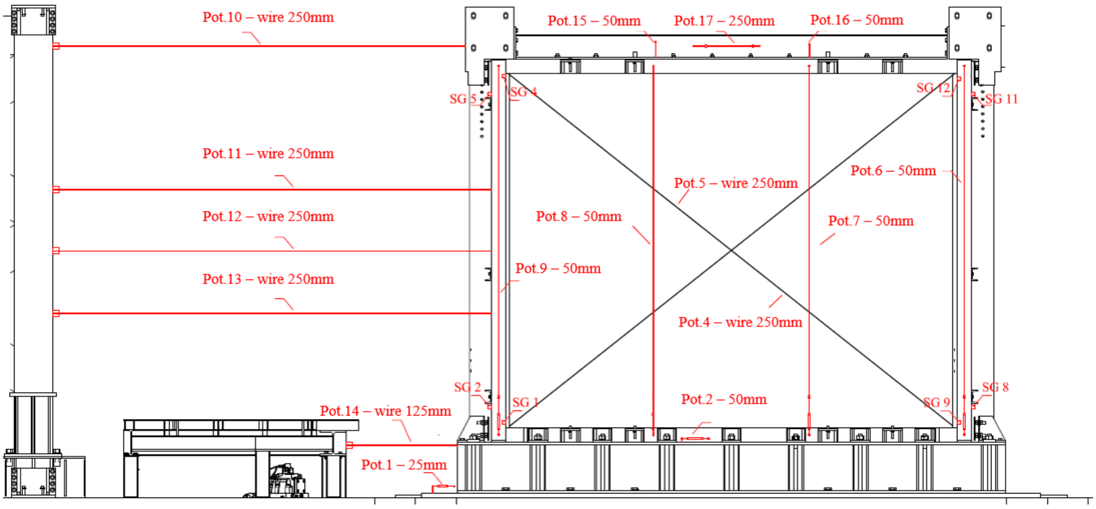

Figure 4. Instrumentation installed for in-plane cyclic pseudo-static tests

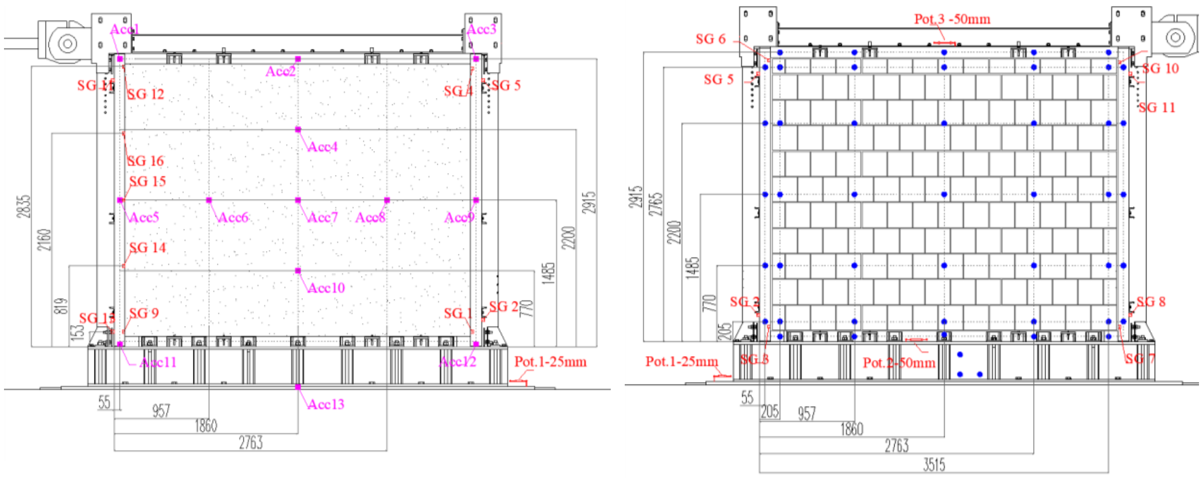

(a) (b)

Figure 5. Instrumentation installed for out-of-plane dynamic shaking table tests: (a) plastered side (accelerometers in pink); (b) unplastered side (displacement markers in blue)

2.4 DESCRIPTION OF THE EXPERIMENTAL LOADING PROTOCOLS

2.4.1 Preliminary in-plane pseudo-static cyclic tests on bare frames

Firstly, preliminary tests on bare frame configurations have been conducted on all frames with the scope to attain the same level of damage and stiffness among them before the tests on infilled frames are carried out. The tests also allowed to obtain the force-displacement response of the bare frame in order to be able to directly compare the infill contribution between all the specimens herein discussed and also any future infill that would be studied with the same set-up. The preliminary tests on bare frames were displacement controlled in-plane cyclic tests up to a maximum nominal drift of 1.50% according to the expected maximum in-plane drift of the infilled configuration. In Figure 6 the adopted loading protocol is reported: every bare frame has been tested according to the loading protocol shown in Figure 6a; moreover, bare frame 1 has been tested also according to the loading protocol reported in Figure 6b with the scope to obtain the cyclic force-displacement curve of the bare frame configuration to directly compute the cyclic infill contribution.

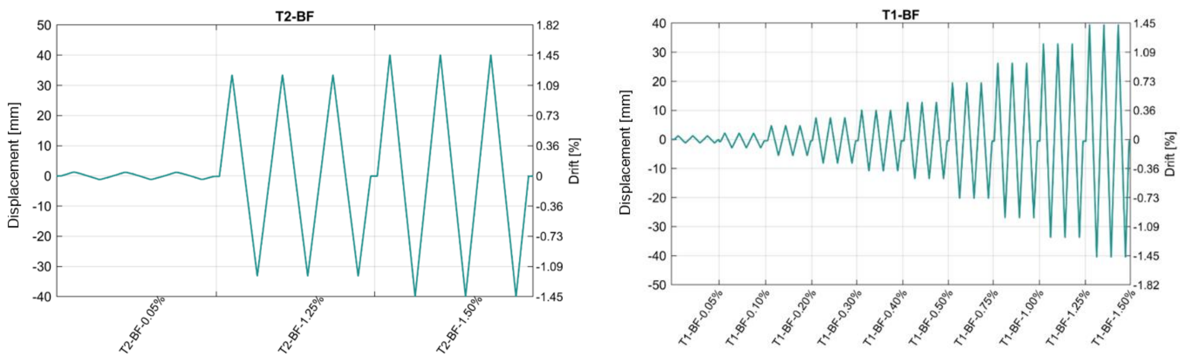

(a) (b)

Figure 6. Preliminary loading protocol on bare frame: (a) tests conducted on every frame; (b) test on frame 1

2.4.2 In-plane pseudo-static cyclic tests on masonry infilled frames

Three out of five specimens, named T1, T2 and T3, have been tested in-plane through a cyclic pseudo-static loading protocol where the in-plane drift was imposed through a servo-controlled actuator in displacement control. The target drifts had an incremental order and have been repeated three times each, keeping the duration of the test approximately the same for all tests. In the absence of standard in-plane loading protocols specific to infills as a non-structural element, the pseudo-static cyclic test protocol implemented in Milanesi et al. [2017] was used as a reference, which is deriving from past experiments on load-bearing walls [Tomazevic *et al.,* 1996, Magenes *et al.,* 2008] and later adapted for infills [Calvi and Bolognini, 2001, Morandi et al., 2018, da Porto et al., 2013].

While the tests on panel T1 were in-plane only, the in-plane tests of specimens T2 and T3 were followed by out-of-plane dynamic tests. The ultimate target drift of each panel was defined with the aim to reach a unique limit state; therefore, the infill T1 has been tested up to an Ultimate Limit equal to 1.00% nominal drift, meanwhile T2 and T3 tests have been stopped at 0.30% and 0.65% nominal drifts, respectively.

2.4.3 Out-of-plane dynamic tests on masonry infills

The out-of-plane seismic behaviour of the masonry infills has been investigated through dynamic tests on shaking table where the seismic excitation was applied in the out-of-plane direction only. All specimens have been tested out-of-plane except for panel T1, since the ultimate conditions had already been reached after the in-plane test. Every out-of-plane test has been indeed performed up to the ultimate capacity/collapse of the infill.

The ground motion was applied with an incrementally increasing nominal peak acceleration as reported in Table 2. The dynamic input signal has been selected according to Required Response Spectrum (RRS) method of the AC156 with some modifications in the definition of the plateau of the target spectrum. The frequency range of the plateau was chosen according to the methodology proposed in Milanesi et al. [2017], based on a series of nonlinear dynamic analyses accounting for the response of infills located in different types of buildings at different heights, and the fundamental frequency of the infill panel. In some cases, the variation of the fundamental frequency was higher than expected and a redefinition of the target plateau, and consequently of the ground motion, was needed. Figure 7 shows an example of a RRS spectrum adopted for the definition of the ground motion for T3 specimen.

Table 2. Out-of-plane loading protocol for each specimen.

Nominal amplification [g]	0.10	0.20	0.30	0.40	0.50	0.60	0.70	0.75	0.80	1.00	1.25	1.50	1.80	2.00	2.25	2.50
T1-IF	In-plane test only															
T2-IF	X	X	X	X	X	-	-	X	-	X	X	X	X	X	X	X
T3-IF	X	X	X	X	X	-	-	X	-	X	X	X*	-	-	-	-
T4-IF	X	X	X	-	X	-	-	X	-	X	X	X	X	-	-	-
T5-IF	X	X	X	X	X	X	X	-	X	X	-	-	-	-	-	-
**test repeated 3 times*																

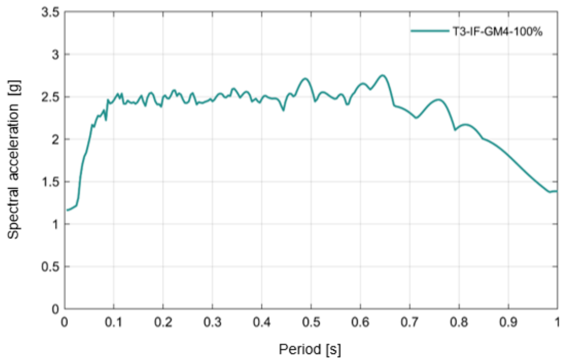

Figure 7. RRS defined for T3 specimen.

3. EXPERIMENTAL RESULTS

The experimental results are discussed in terms of force-displacement hysteresis curves for in-plane cyclic tests, and accelerations and displacements of the infill for out-of-plane dynamic tests, along with a description of damage propagation of all tests.

3.1 IN-PLANE CYCLIC TESTS

Specimen T1 has been subjected to in-plane cyclic loading protocol up to the achievement of the ultimate limit state. At the end of the test the damage was mainly characterised by several diagonal stepped cracks along the mortar joints and a horizontal zone of damage which was formed around the bottom 2nd and 3rd courses. The final damage pattern includes a wide area where the plaster has been spalled and some zones where clay units were heavily damaged (Figure 8a). In Figure 8b the force-displacement curves for increasing target drifts are reported along with the backbone curves of the structural frame, the infilled frame, and the infill contribution.

Specimens T2 and T3 were subjected to in-plane nominal drift levels of 0.30% and 0.65% respectively, prior to being subjected to out-of-plane motions. The damage patterns and force-displacement curves were consistent with the response of T1 up to 0.30% and 0.65% drifts. In Figure 9a and Figure 9b the specimens T2 and T3, at the end of the in-plane tests are shown, respectively.

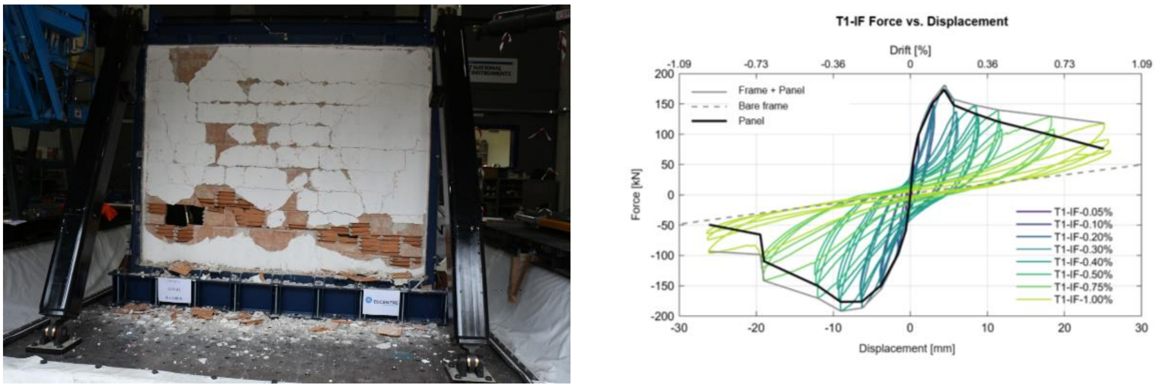

(a) (b)

Figure 8. (a) T1-IF damaged at the end of the in-plane cyclic tests up to 1.00% nominal drift; (b) in-plane force-displacement experimental response

(a) (b)

Figure 9. (a) T2-IF damaged at the end of the in-plane cyclic tests up to 0.30% nominal drift; (b) (a) T3-IF damaged at the end of the in-plane cyclic tests up to 0.65% nominal drift

3.2 OUT-OF-PLANE DYNAMIC TESTS

A summary of the recorded accelerations during the out-of-plane dynamic tests on the panel at the centre at mid-height and the amplification with respect to the recorded peak floor acceleration of the input motion is presented in Table 3 for specimens T2, T3, T4 and T5. Infills T2 and T3 collapsed at nominal peak floor accelerations (PFA) of 2.5 and 1.5g, respectively. T5 reached its peak capacity at 0.6g nominal PFA but did not collapse, whereas T4 was not tested up to its capacity due to limitations of the test set up.

The out-of-plane damage propagation was greatly influenced by the level of previous in-plane damage and the boundary conditions. Infill T3, which was subjected to a higher level of in-plane damage (0.65%) had a significant reduction in the out-of-plane capacity compared to T2 with the lower level of in-plane damage (0.30%) in terms of acceleration, with the maximum acceleration recorded at the centre reducing by 42%. The damage due to out-of-plane shaking in T2 and T3 continued extending from the previous in-plane damage, meanwhile for undamaged infills (T4 and T5) the cracks appears according to a pure flexural/arching resisting mechanism. T2 infill collapsed at a nominal PFA of 2.5g, with the severely damaged upper courses collapsing completely out-of-plane, and the bottom four courses remaining intact. T3 collapsed at PFA 1.5g, at which the motion was repeated three times. During the repeated floor motions, damage to the centre increased with most of bricks expelling out. Courses 6th to 8th completely detached and fell out, during which the upper and lower courses appeared to be bending horizontally while being connected to the columns. Subsequently, the upper three courses collapsed leaving the bottom five courses intact.

Table 3. Summary of recorded accelerations.

Ref PFA [g]	T2			T3			T4			T5		
	Rec. PFA /g	Rec. Accn. /g	Amplification	Rec. PFA/g	Rec. Accn. /g	Amplification	Rec. PFA/g	Rec. Accn. /g	Amplification	Rec. PFA/g	Rec. Accn. /g	Amplification
0.1	0.14	0.79	5.82	0.15	0.48	3.17	0.17	0.91	5.51	0.14	0.35	2.47
0.2	0.28	1.49	5.38	0.27	0.90	3.32	0.26	1.57	5.95	0.29	1.11	3.88
0.3	0.41	2.12	5.14	0.41	1.36	3.32	0.39	2.20	5.60	0.40	2.45	6.07
0.4	0.53	2.56	4.87	0.53	1.81	3.44	-	-	-	0.47	4.01	8.51
0.5	0.63	2.72	4.30	0.64	2.33	3.64	0.61	3.51	5.72	0.57	4.45	7.83
0.6	-	-	-	-	-	-	-	-	-	0.69	4.57	6.65
0.7	-	-	-	-	-	-	-	-	-	-	-	-
0.75	0.93	3.97	4.28	0.93	3.31	3.57	0.87	5.54	6.37	0.81	4.14	5.15
0.8	-	-	-	-	-	-	-	-	-	0.82	-	-
1.0	1.21	5.18	4.30	1.13	4.51	3.99	1.07	6.74	6.28	**0.98**	**-**	**-**
1.25	1.53	9.76	6.39	1.40	5.88	4.21	1.35	7.62	5.65			
1.5	1.77	10.71	6.04	1.71	6.18	3.60	1.65	9.55	5.80			
				1.71	6.25	3.65						
				1.69	**5.75**	**3.40**						
1.8	2.21	10.13	4.59				1.95	11.22	5.75			
2.0	2.34	10.34	4.43									
2.25	2.56	10.76	4.21									
2.5	**2.75**	**10.76**	**3.91**									

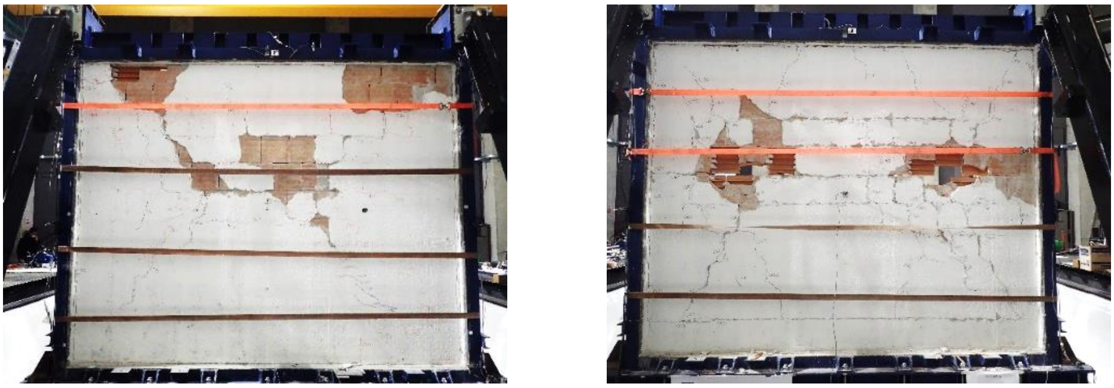

(a) (b)

Figure 10. (a) T2 after the 2.25g nominal PFA ground motion; (b) T3 after the 1.25g nominal PFA ground motion.

Specimen T4 showed a double flexural/arching (vertical and horizontal) resisting mechanisms that has been observed with acceleration and displacement vertical and horizontal profiles. Furthermore, the acceleration profiles recorded in T4 along the height and length at the centre of the panel are presented in Figure 11. This leads to an important observation that the distribution of accelerations, and consequently out-of-plane forces, are not uniform on the wall surface but close to triangular with maximum force acting at the centre. Such a trend of acceleration distribution was also observed in the other specimens.

The infill of specimen T5, which was constructed with a gap at the columns such that the wall was only bonded to the frame at top and bottom edges, has been subjected to out-of-plane loading without any previous in-plane damage to investigate the vertical single bending behaviour under dynamic forces, and to characterise the one-way arching mechanism which may develop under such conditions. The response has been vertical flexural for low levels of PFA, pure vertical arching mechanisms once that the horizontal cracks developed at the top-bottom edges and along the bed joint between 7th and 8th course, and vertical arch with gap at latest ground motions where the top of the infill was completely detached from the structural beam.

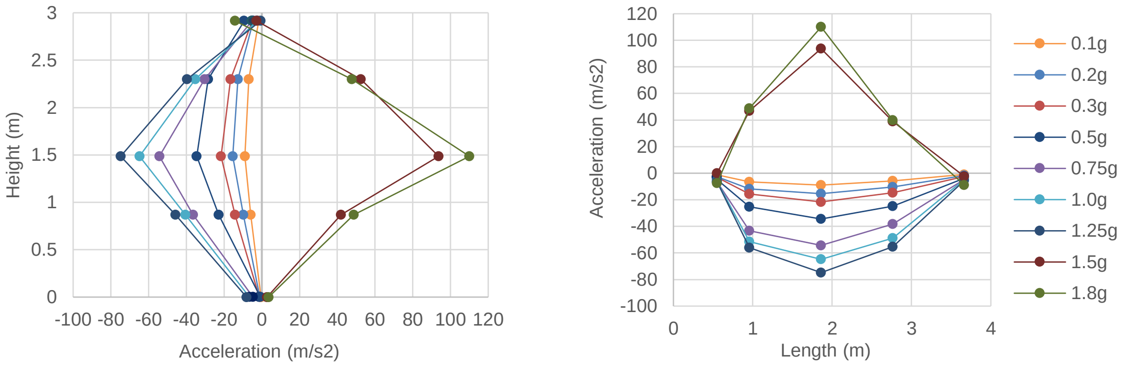

(a) (b)

Figure 11. Acceleration profiles of T4 (a) along the height; (b) along the length

3.3 PRELIMINARY INTERPRETATION OF THE RESULTS

The results have demonstrated the influence of previous in-plane damage on the out-of-plane resistance, with the peak acceleration reducing for increasing levels of in-plane damage. The acceleration and the displacement recorded at the centre of the panel when the panel response was maximum (except for a few instances, the maximum response was always observed at the panel centre) with respect to the recorded PFA (peak floor acceleration) of the ground motion are presented in Figure 12a and 12b, respectively.

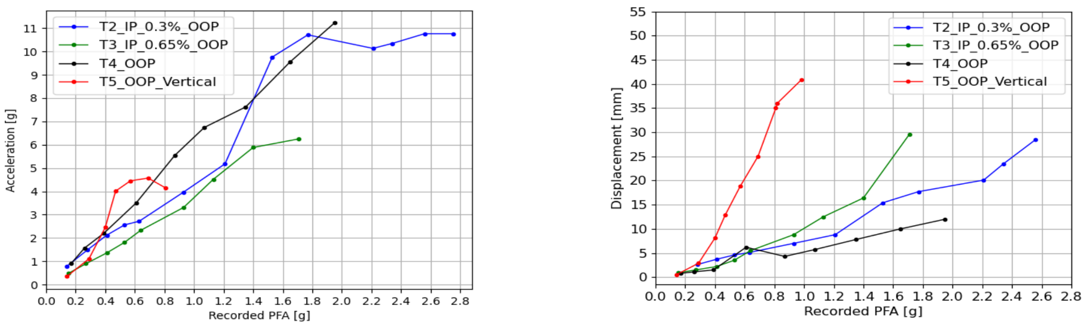

(a) (b)

Figure 12. (a) max acceleration at the centre vs recorded PFA; (b) max displacement at the centre vs recorded PFA.

Comparing the behaviour of the fully infilled specimens T2, T3 and T4, the measured accelerations and displacements seem to be affected by the damage state of the infill, as well as the stiffness of the panel at a certain PFA. The stiffer specimen T4 with the least damage generally exhibited lower displacements and higher accelerations, especially in comparison with heavily damaged T3 infill. T3 seems to have a level of damage that jeopardises the out-of-plane capacity, reaching higher displacement values at an earlier stage than T2 or T4. Specimen T5, that has a different boundary condition in the horizontal direction, has shown a sensibly different behaviour in terms of both the maximum acceleration and displacement recorded. All the specimens have shown an evolution of the damage that included the detachment of the top of the masonry panel from the structural beam, in some cases also with local damages of the masonry units. Finally, for every test, a triangular distribution of the acceleration along the height (and along the span for T2, T3 and T4) has been observed.

4. CONCLUSIONS

A comprehensive experimental campaign was conducted to explore the seismic behaviour of weak clay masonry infills, involving five full scale specimens. In the scope of this study, 12 cm thick horizontally perforated clay unit panels surrounded by a composite steel/r.c. frame were subjected to in-plane cyclic drifts and out-of-plane ground motions, with the aim of investigating the in-plane and out-of-plane behaviour, and their interaction. The details of the experimental set up have been reported, including a description of the five specimens and mechanical characterisation of the materials, and a summary of the instrumentation and loading protocols for the in-plane and out-of-plane tests. The main observations from the experiment have been discussed in terms of the damage propagation, failure mechanisms, force-displacement relationships, and acceleration profiles. The specimen T1 was subjected to increasing in-plane target drift levels until an ultimate damage state was reached at 1.00%. Specimens T2 and T3 were subjected to target drift levels of 0.30% and 0.65%, respectively, and subsequently out-of-plane floor motions with increasing peak floor acceleration were applied until collapse. The maximum peak acceleration which was observed at the centre of the panel was 42% less for the highly damaged infill (T3) than the slightly damaged infill (T2), emphasizing the importance of accounting for the in-plane/out-of-plane interaction in the assessment of masonry infills. The out-of-plane response of the undamaged fully attached infill T4 was stiff and robust with no significant damage observed compared to the damaged infills at a nominal PFA of 1.8g. The specimen T5 with two gaps between the wall vertical edges and the columns exhibited a vertical bending/arching mechanism with multiple horizontal cracks along bed joints, whereas the previous fully infilled walls developed the double bending/arching mechanism characterized by horizontal cracks in the middle from which diagonal cracks propagated towards the corners of the wall.

The present work described hereto lays a foundation for many future developments. In addition to the two boundary conditions explored in this study, infills with different boundary conditions, for instance, panels supported on three edges consisting of a gap between the wall top edge and the beam could be tested utilizing the reusable frames. Similarly, the influence of the presence of openings on the panel behaviour could also be experimentally investigated. Based on such extensive experimental database, numerical models could be developed and calibrated, then be used to conduct parametric studies to explore the influence of masonry material properties, aspect ratio, and frame properties, and to expand on enhanced solutions for infills and behaviour of double leaf enclosures. Subsequently, improved assessment formulations for code applications could be introduced with a wider understanding, and simplified procedures for efficient verification of infills in field applications could be innovated.

ACKNOWLEDGEMENTS

The work presented in this paper has been developed within the framework of the project "WP11 – Caratterizzazione della risposta sismica in piano e fuori piano di tamponamenti in muratura", funded by the Italian Department of Civil Protection, at Eucentre.

REFERENCES

Abrams, D. P., Angel, R., Uzarski, J. [1996] 'Out-of-Plane Strength of Unreinforced Masonry Infill Panels," *Earthquake Spectra,* Vol.12, No.4, pp. 825–844.

AC 156 [2010] *Acceptance criteria for seismic certification by shake-table testing of nonstructural components,* International code council. (n.d.).

Angel, R., Abrams, D. P., Shapiro, D., Uzarski, J., Webster, M. [1994] "Behavior of reinforced concrete frames with masonry infills," University of Illinois Engineering Experiment Station, College of Engineering, University of Illinois at Urbana-Champaign.

Anić, F., Penava, D., Abrahamczyk, L., Sarhosis, V. [2020] "A review of experimental and analytical studies on the out-of-plane behaviour of masonry infilled frames," *Bulletin of Earthquake Engineering*, Vol. 18, No. 5, pp. 2191-2246.

ASTM E519-02 [2017] *Test Method for Diagonal Tension (Shear) in Masonry Assemblages,* ASTM International.

Braga, F., Manfredi, V., Masi, A., Salvatori, A., Vona, M. [2010] "Performance of non-structural elements in RC buildings during the L'Aquila, 2009 earthquake," *Bulletin of Earthquake Engineering*, Vol. 9, No. 1, pp. 307–24.

Butenweg, C., Marinković, M., Salatić, R. [2019] "Experimental results of reinforced concrete frames with masonry infills under combined quasi-static in-plane and out-of-plane seismic loading," *Bulleting of Earthquake Engineering*, Vol. 17, pp. 3397–3422.

Calvi, G. M., Bolognini, D. [2001] "Seismic response of reinforced concrete frames infilled with weakly reinforced masonry panels," *Journal of earthquake engineering*, Vol. 5, No. 2, pp. 153–85.

Carydis, P.G., Mouzakis, H.P., Taflambas, J.M., Vougioukas, E.A. [1992] "Response of infilled frames with brick walls to earthquake motions," *Proc. 10th World Conference in Earthquake Engineering*, Rotterdam, Netherland.

CEN [2004] *Eurocode 8 - Design of structures for earthquake resistance, Part 1: General rules, seismic actions and rules for buildings, EN 1998-1*, European Committee for Standardisation, Brussels, Belgium.

Chiozzi, A., Miranda, E., [2017], "Fragility functions for masonry infill walls with in-plane loading", *Earthquake Engineering and Structural Dynamics*, Vol. 46, pp. 2831-2850.

da Porto, F., Guidi, G., Dalla Benetta, M., Verlato, N. [2013] "Combined in-plane/out-of-plane experimental behaviour of reinforced and strengthened infill masonry walls," *Proc. 12th Canadian Masonry Symposium*, Vancouver, Canada.

Dawe, J. L., Seah, C. K. [1989] "Out-of-plane resistance of concrete masonry infilled panels," *Canadian Journal of Civil Engineering*, Vol. 16, No. 6, pp. 854-864, https://doi.org/10.1139/l89-128.

De Risi, M. T., Del Gaudio, C., Ricci, P., Verderame, G. M. [2018]. "In-plane behaviour and damage assessment of masonry infills with hollow clay bricks in RC frames". *Engineering Structures*, Vol. 168, pp. 257-275.

Decanini, L. D., De Sortis, A., Goretti, A., Liberatore, L., Mollaioli, F., Bazzurro, P. [2004a] "Performance of Reinforced Concrete Buildings during the 2002 Molise, Italy, Earthquake," *Earthquake Spectra*, Vol. 20, No. S1, pp. 221–255.

Decanini, L., Mollaioli, F., Mura, A., Saragoni, R. [2004b] "Seismic performance of masonry infilled R/C frames," *Proceedings of 13th world conference on earthquake engineering*, Vancouver, Canada.

Di Domenico, M., Ricci P., Verderame G. M. [2018] "Experimental assessment of the influence of boundary conditions on the out-of-plane response unreinforced masonry infill walls," *Journal of Earthquake Engineering*, pp. 1–39.

EN 1052-1 [2001] *Methods of test for masonry – Determination of compressive strength*, Brussels, Belgium: CEN.

EN 1052-3 [2001] *Methods of test for masonry – Determination of initial shear strength*, Brussels, Belgium: CEN.

FEMA 461 [2007] *Interim testing protocols for determining the seismic performance characteristics of structural and nonstructural components*, Washington, DC: FEMA.

Furtado, A., Rodrigues, H., Arede, A., Varum, H. [2016] "Experimental evaluation of out-of-plane capacity of masonry infill walls," *Engineering Structures*, Vol.111, pp. 48-63.

Furtado, A., Rodrigues, H., Arede, A., Varum, H. [2022] "Experimental investigation on the possible effect of previous damage, workmanship and test setup on the out-of-plane behaviour of masonry infill walls," *Journal of Earthquake Engineering*, Vol. 26, No. 11, pp. 5647-5678.

Hak, S., Morandi, P., Magenes, G., Sullivan. T.J. [2012] "Damage control for clay masonry infills in the design of RC frame structures," *Journal of Earthquake Engineering,* Vol. 16, No.1, pp. 1-35.

Hak, S., Morandi, P., Magenes, G. [2013] "Local effects in the seismic design of RC frame structures with masonry infills," *Proceedings of the 4th International Conference on Computational Methods in Structural Dynamics and Earthquake Engineering*, Kos Island, Greece.

Hermanns, L., Fraile, A., Alarcón, E., Álvarez, R. [2012] "Performance of masonry buildings during the 2011 Lorca earthquake," *Proceedings of 15th World Conference on Earthquake Engineering,* Lisbon, Portugal.

Lanese, I. [2012] "Seismic vulnerability of an infilled frame structure designed for gravity loads and evaluation of the EC8-based assessment procedures," master's degree dissertation, IUSS Pavia.

Liberatore, L., AlShawa, O., Marson, C., Pasca, M., Sorrentino, L. [2020]. "Out-of-plane capacity equations for masonry infill walls accounting for openings and boundary conditions". *Engineering Structures*, Vol. 207, pp.110198.

Magenes, G., Morandi, P., Penna, A. [2008] "Experimental in-plane cyclic response of masonry walls with clay units", *Proceedings of 14th WCEE,* Beijing, China.

Milanesi, R. R., Morandi, P., Dacarro, F., Albanesi, L., Magenes, G. [2017] "In-plane cyclic and out-of-plane dynamic testing procedures for infilled RC frames" *Proc. 7th International Conference on Advances in Experimental Structural Engineering*, Pavia, Italy.

Milanesi, R. R., Morandi, P., Magenes, G. [2018] "Local effects on RC frames induced by AAC masonry infills through FEM simulation of in-plane tests" *Bulleting of Earthquake Engineering*, Vol. 16, pp. 4053–4080.

Milanesi, R. R., Morandi, P., Manzini, C. F., Albanesi, L., Magenes, G. [2022] "Out-of-plane Response of an Innovative Masonry Infill with Sliding Joints from Shaking Table Tests," *Journal of Earthquake Engineering*, Vol. 26, No. 4, pp. 1789–1823.

Milanesi, R. R., Morandi, P., Hak, S., Magenes, G. [2021] "Experiment-based out-of-plane resistance of strong masonry infills for codified applications," *Engineering Structures*, Vol. 242, p. 112525.

Morandi, P., Hak, S., Magenes, G. [2013] "Simplified Out-of-plane Resistance Verification for Slender Clay Masonry In-fills in RC Frames," *Proceedings of 15th ANIDIS Conference*, Padova, Italy.

Morandi, P., Hak, S., Magenes, G., [2018] "Performance-based interpretation of in-plane cyclic tests on RC frames with strong masonry infills", *Engineering Structures*. Vol. 156, No. 1, pp. 503–521. https://doi.org/10.1016/j.engstruct.2017.11.058.

Morandi, P., Hak, S., Milanesi, R. R., Magenes, G. [2022] "In-plane/out-of-plane interaction of strong masonry infills: From cyclic tests to out-of-plane verifications," *Earthquake Engineering Structural Dynamics*, Vol. 51, No. 3, pp. 648–672.
NTC [2018] *Istruzioni per L'applicazione Delle "Nuove norme Tecniche per le Costruzioni" di Cui al Decreto Ministeriale 17 Gennaio 2018*, Ministero delle Infrastrutture e dei Trasporti, Circolare 20 Febbraio 2018, Italy. (In Italian)
Ricci, P., Di Domenico, M., Verderame, G. M. [2018] "Experimental assessment of the in-plane/out-of-plane interaction in unreinforced masonry infill walls," *Engineering Structures*, Vol.173, No.1, pp. 960-978, doi 10.1016/j.engstruct.2018.07.033.
Rossi, A., Morandi, P., R.R., Magenes, G., [2021]. "A novel approach for the evaluation of the economical losses to seismic actions on RC buildings with masonry infills", *Soil Dynamics and Earthquake Engineering*, vol. 145, pp. 106722, doi 10.1016/j.soildyn.2021.106722.
Sassun, K., Sullivan, T. J., Morandi, P., Cardone, D. [2016] "Characterising the in-plane seismic performance of infill masonry," *Bulletin of the New Zealand Society for Earthquake Engineering*, Vol. 49, No. 1, pp. 98-115.
Tomazevic, M., Lutman, M., Petkovic, L., [1996] "Seismic Behaviour of Masonry Walls: Experimental Simulation", *Journal of Structural Engineering*, Vol. 122, pp. 1040-1047.

Evaluation of Non-structural Walls with Drift-Compatible Details in a 10-Story Mass Timber Building Shake Table Test

William Roser[1], Sarah Wichman[2], Yi-En Ji[1], Sir Lathan Wynn[1], Keri Ryan[1], Jeffrey W. Berman[2], Tara C. Hutchinson[3], and Shiling Pei[4]

[1] University of Nevada, Reno
MS 258, 1664 N. Virginia Street, Reno, NV 89557, USA
e-mail: wf.roser@gmail.com, sirwynn1104@ gmail.com, klryan@unr.edu
[2] University of Washington
201 Moore Hall, Box 352700 Seattle, WA 98195, USA
e-mail: wichman@uw.edu, jwberman@uw.edu
[3] University of California, San Diego
9500 Gilman Dr., MC 0085, La Jolla, CA 92093, USA
tahutchinson@eng.ucsd.edu
[4] Colorado School of Mines
1500 Illinois St., Golden, CO 80401, USA
spei@mines.edu

Abstract. Mass timber is a sustainable option for building design compared to traditional steel and concrete building systems. A shake table test of a full-scale 10-story mass timber building with post-tensioned mass timber rocking walls will be conducted as part of the NHERI TallWood project. The rocking wall system is inherently flexible and is expected to sustain large interstory drifts. Thus, the building's vertically oriented non-structural components, which include cold-formed steel (CFS) framed exterior skin subassemblies that use platform, bypass, and spandrel framing, a stick-built glass curtain wall subassembly with mechanically captured glazing, and CFS framed interior walls, will be built with a variety of innovative details to accommodate the large drift demands.

This paper will describe these innovative details and the mechanisms by which they mitigate damage, provide an overview of the shake table test protocol, and present performance predictions for the non-structural walls.

Keywords: non-structural walls, cold formed steel framing, drift-compatible details, shake table testing.

1. INTRODUCTION

Mass timber is a potentially more sustainable alternative to traditional concrete and steel construction. To make mass timber construction more viable for tall buildings, the NHERI TallWood project is underway at the outdoor shake table facility at the University of California, San Diego. A 10-story mass timber building will be erected on the shake table and subjected to ground motions of increasing intensity. This test building will employ mass timber rocking walls as its primary lateral force resisting system. Mass timber rocking walls can sustain large interstory drifts without damage [Hasani and Ryan, 2021], so it is desirable to provide and validate detailing options for non-structural systems that can likewise sustain large drifts without damage.

Non-structural walls, being interstory components, are particularly susceptible to damage from interstory drift. Furthermore, they often suffer extensive damage during earthquakes, causing significant economic loss and threats to human safety [Di Lorenzo and De Martino, 2019]. To mitigate drift-induced damage, the four exterior subassemblies used in this test will incorporate drift-compatible details designed to reduce or limit damage. Three subassemblies will use cold-formed steel (CFS) framing and use horizontal joints to accommodate relative horizontal movement between floors. The fourth subassembly, a stick-built curtain wall, accommodates drift though racking of the framing members and rotation of the glass within the frame. This paper describes these subassemblies and predicts their performance based on expected drift demands.

2. Project Description

2.1 Description of Mass-Timber Building Test Specimen

The test specimen will be built at the large-scale outdoor shake table facility at the University of California, San Diego. The 10-story test specimen, displayed in Figure 1, will be the world's tallest full-scale mass timber building ever tested. The test building will utilize a variety of mass timber products for the floor, gravity frame, and rocking wall components. Post-tensioned mass timber rocking walls, made of cross-laminated timber (CLT) and mass plywood panels (MPP), serve as the lateral force resisting systems in the building in the east-west and north-south directions, respectively. U-shaped flexural plates (UFPs) connected between the rocking wall and the bounding columns dissipate energy. The building's gravity framing consists of laminated veneer lumber (LVL) beams and columns detailed with pinned connections. Several types of mass timber components are utilized for floor diaphragms including CLT, veneer-laminated timber (VLT), glue-laminated timber (GLT), nail-laminated timber (NLT), and dowel-laminated timber (DLT).

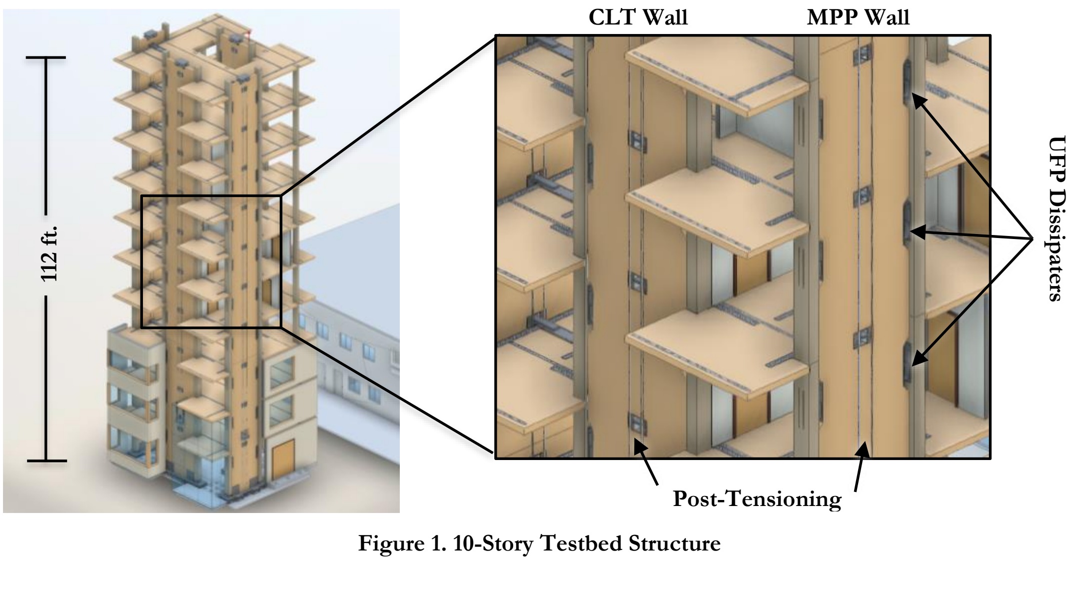

Figure 1. 10-Story Testbed Structure

2.2 DESCRIPTION OF SUBASSEMBLIES

The testbed structure will have four non-structural exterior wall subassemblies. Three of these are CFS framed systems and the fourth is a stick-built curtain wall. Each of these subassemblies employs innovative details to mitigate drift-induced damage. All of the subassemblies have windows, which vary in size and aspect ratio.

2.2.1 Subassembly 1: Platform-Framed CFS Exterior Wall

The first subassembly (Figure 2a) is L-shaped and uses platform framing, wherein studs bear directly on the floor below and are connected to the floor above via an inverted “header” track. Drift is accommodated using a joint at the header track. The first and third stories use double (nested) slip tracks (Figure 2b) where slip occurs between a header track connected to the floor above and a lower header track connected to the wall studs and sheathing. For comparison, the second floor uses CEMCO’s CST Brand Slotted Slip-Track (Figure 2c). Slotted slip tracks are attached directly to the floor above and slip occurs between the header and floor due to slotted holes for fasteners. Slotted slip tracks are easier to install and require less material than double slip track assemblies; however, the slip mechanism needs to be verified through experimental testing.

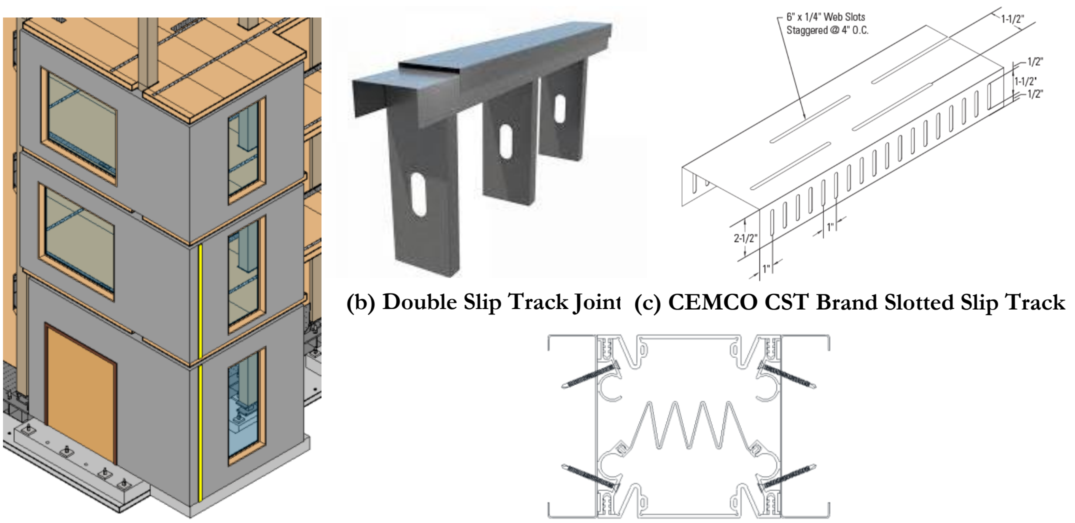

(b) Double Slip Track Joint (c) CEMCO CST Brand Slotted Slip Track

(a) Platform-Framed Assembly (d) SF-600 Expansion Joint Cover by Construction Specialties

Figure 2. Platform-framed CFS subassembly (a) and drift-compatible details (b-d)

Research has shown that damage is prevented when interior CFS partition walls, which are constructed similarly to platform-framed walls, are constructed with double slip tracks; however, increased damage occurs at wall intersections [Hasani and Ryan, 2021]. To address the drift incompatibility at the corners, the first and second stories will use SF-600 expansion joint covers supplied by Construction Specialties (Figure 2d), which are intended to separate the movement of adjoining walls. The vertical expansion joints provide 4 in. relative movement between adjoining perpendicular walls in both directions. The third story serves as a control specimen and lacks an expansion joint. However, the interior framing layout at the corner was designed to be more flexible than typical construction, which should delay or reduce the severity of damage. The corner of the third story could suffer significant damage while the other two stories should accommodate in-plane drift without significant damage.

2.2.2 Subassembly 2: Bypass-Framed CFS Exterior Wall

The second subassembly (Figure 3a) is an L-shaped subassembly with bypass framing, wherein long studs span multiple stories outside of the diaphragm envelope. Damage in bypass-framed walls is typically concentrated at the clips used to attach studs to the structural system [e.g. Wang *et al.*, 2015; Schafer *et al.*, 2016]. Therefore, drift can be accommodated by connecting the studs to the floor diaphragm via a clip that is free to slide laterally. This will be accomplished using a DSSCB clip from Simpson Strong-Tie installed into standard U-track (Figure 3b). This connection resists out-of-plane loads while permitting in-plane movement of the clip within the U-track.

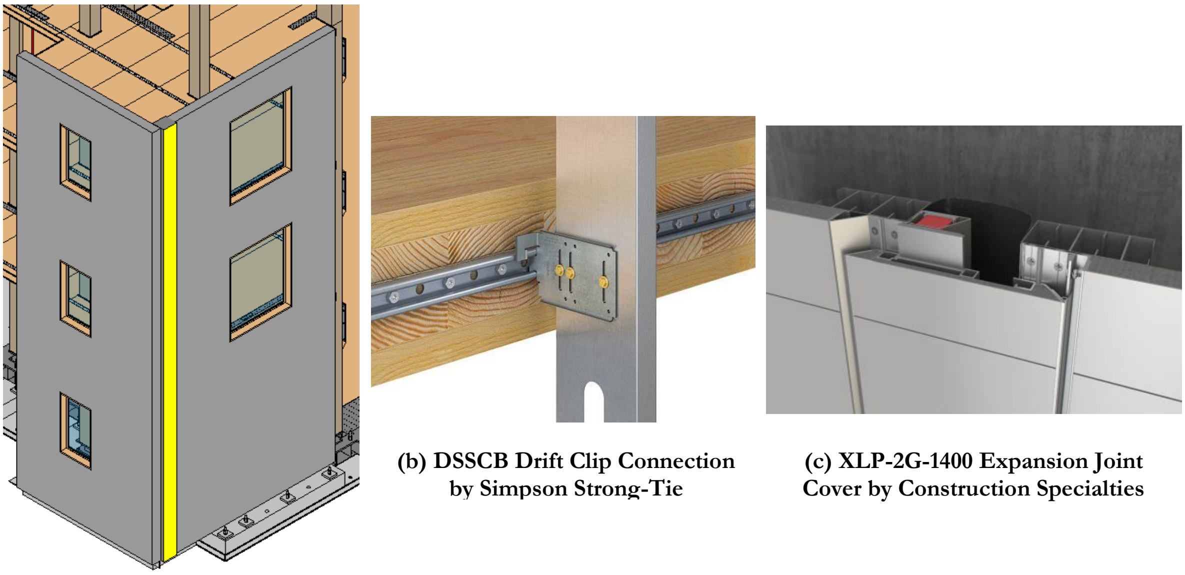

(b) DSSCB Drift Clip Connection by Simpson Strong-Tie

(c) XLP-2G-1400 Expansion Joint Cover by Construction Specialties

(a) Bypass-Framed Subassembly

Figure 3. Bypass-Framed CFS Subassembly and Details

Because this subassembly is continuous over three stories, interstory drifts accumulate over multiple floors and a relatively large gap is needed to separate adjacent walls. This gap is covered by an XLP-2G-1400 expansion joint cover supplied by Construction Specialties, a 14 in. cover with vertical hinges to allow it to open and close when the walls move relative to one another (Figure 3a and 3c). Magnets keep the cover closed under normal operation and reset the assembly after shaking. This joint is sized to allow an average of 2.3% drift in each direction over the height of the wall.

Without means to transfer in-plane forces to the structure, inertial forces are collected over the entire height of the subassembly, so special attention is required for shear design, especially given the high height to width ratio of the walls. The subassembly was designed as a shear wall and uses large holdowns at the ends of each wall and CEMCO Sure-Board® for enhanced shear strength.

2.2.3 Subassembly 3: Spandrel-Framed CFS Exterior Wall

The third subassembly, which uses spandrel framing, is C-shaped with two corners (Figure 4a). Spandrel framing consists of bands of short studs rigidly to a floor diaphragm via rigid metal clips (Figure 4c) and kicker studs (Figure 4b). Loads from the spandrel are transferred directly to the diaphragm to which it is attached. The space between spandrels can be filled with windows or infill studs. Drift compatibility is achieved by placing a double slip track (Figure 2b) between the window and the spandrel above. At the base of the wall, the lowest spandrel cannot use a kicker stud, so it is instead anchored to the foundation using a moment-resisting connection (Figure 4d).

Spandrel framing is often used so that a “ribbon” of windows can extend around the entirety of the structure without interruption. Thus, the windows in this subassembly wrap around its corners (Figure 4a) for aesthetic appeal. This will demonstrate whether typical window framing is flexible enough to permit perpendicular wall motion without damage. For comparison, the second floor instead incorporates a SF-600 joint between perpendicular windows to fully separate their movement (Figure 2d, 4a).

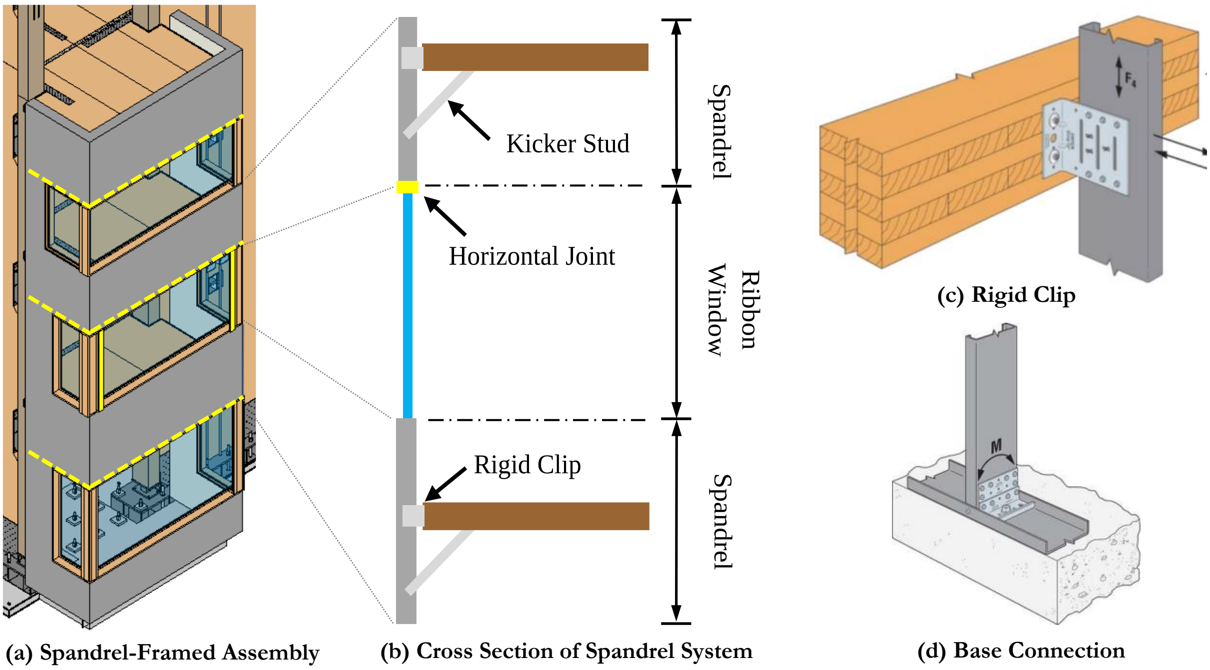

Figure 4. Spandrel-Framed Subassembly and Details

2.2.4 Subassembly 4: Stick-Built Curtain Wall

The fourth subassembly is a C-shaped curtain wall that spans the first two stories of the building and utilizes 1-1/16" 60-minute fire-rated glazing. The framing consists of heavy fire-rated S235JR steel horizontal and vertical mullions that support the glass lites. The subassembly is secured to the foundation and the edges of the 2nd and 3rd floor diaphragms of the building. To accommodate drift during seismic loading, the curtain wall system utilizes a stick-built system in which the framing racks (or distorts) to displace with the floor diaphragms. Because the curtain wall is C-shaped, the subassembly also utilizes a soft corner detail with a fire-rated fill to allow for independent movement of the perpendicular wall sections.

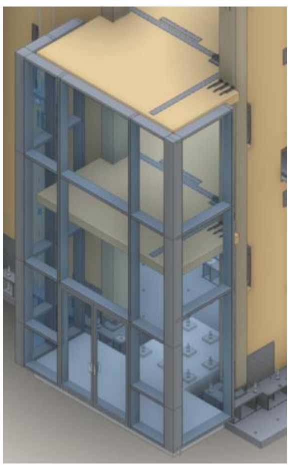

Figure 5. Curtain Wall with Stick-Built Framing

The glass panels in the curtain wall system are held in place using mechanically captured glazing, which consists of gasketed pressure plates mechanically secured to the mullions through the glazing pocket to hold the glass in place. The panels are designed to rotate within the frame and avoid frame-to-glass contact, which causes concentrated stresses at the corners of the panels and lead to crushing of the glass. The curtain wall system must satisfy the provisions of ASCE 7-16 Section 13.5.9 to prevent glass fallout at the peak drift, in which the glass fallout displacement is determined in accordance with AAMA 501.6 or by engineering analysis.

2.3 Description of Model

A model of the structural system was developed in OpenSees by Wichman *et al.* [2022b] for performing non-linear response history analyses for the design of the lateral-force resisting system. The performance of the non-structural walls is estimated herein by comparing the interstory drift demands computed by the Wichman *et al.* [2022b] model to the respective drift capacities of each subassembly.

Figure 6 shows details of the numerical model of the building specimen. As shown in Figure 6e, the model includes the four structural rocking walls with their boundary columns and a rigid diaphragm constraint at all floors. Figure 6a shows a detailed schematic of the typical structural wall modelling methodology, based on techniques similar to those presented in Wichman *et al.* [2022a]. The post-tensioning (PT) bars were modelled using corotational truss elements with a bi-linear tension-only material model that accumulates damage after yielding (Figure 6b). The initial post-tensioning of the walls was modelled by applying an initial strain wrapper to the PT truss elements. At each story, the UFPs were modelled using zero-length spring elements with the uniaxial Giuffre-Menegotto-Pinto steel material model shown in Figure 6c.

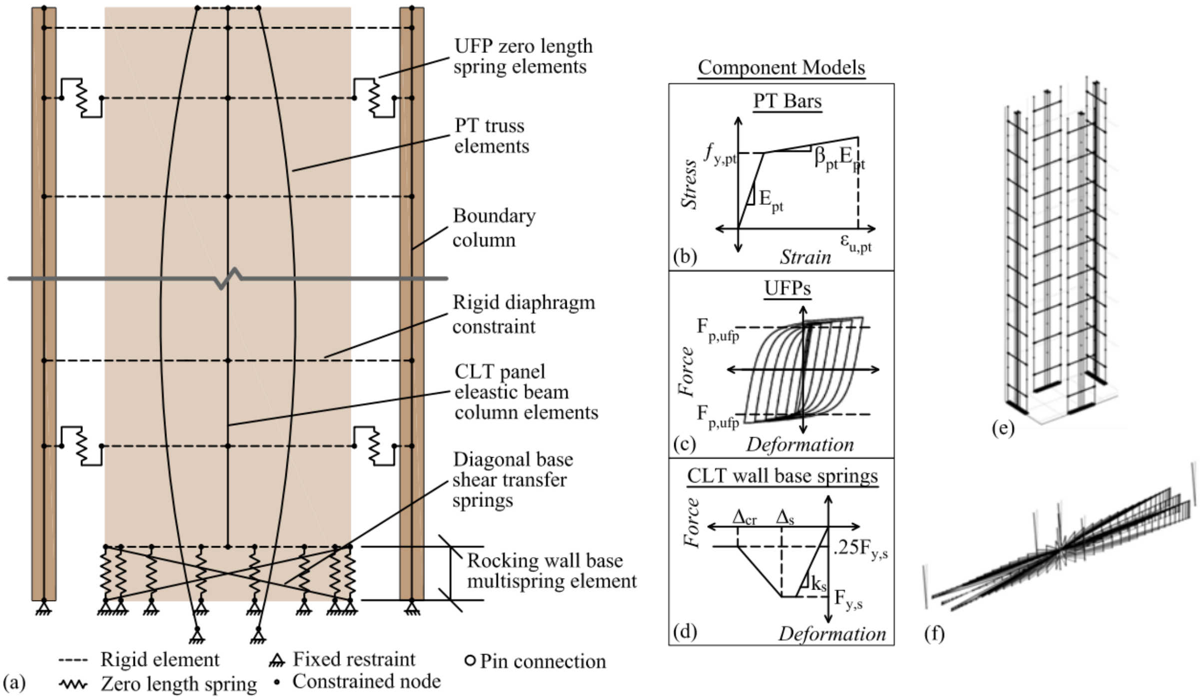

Figure 6. Numerical model schematic and material models used to model the 10-story building [Wichman *et al.*, 2022b]

To model the mass timber wall panels, a series of elastic beam-column frame elements were used. These elements included axial, flexural, and shear deformations. The inelastic compressive deformation at the base of the walls was modelled using a multispring contact element, initially developed by Spieth *et al.* [2004]. In this element, zero-length springs are distributed in parallel along the length and width of the wall base such that in-plane and out-of-plane rocking can be modelled. Figure 6f shows an isotropic view of these springs while the wall is rocking. The top of each spring is rigidly connected to the base of the wall and each spring uses the compression-only hysteretic material model shown in Figure 6d.

2.4 TESTING PROTOCOL

The specimen was designed to meet seismic demands computed per ASCE 7-16 for a location in Seattle, Washington with a Class C soil site. For design and test planning, suites of eleven 3D ground motions were selected and scaled to five hazard levels. The hazard levels included four return periods (43-year, 225-year, 475-year, and 975-year) and a risk-targeted maximum considered earthquake (MCE_R), all defined and scaled in accordance with ground motion scaling procedures outline in ASCE 7-16. From the original suites of eleven ground motions, five records, representative of suite mean behaviour, were selected at each hazard level for shake table preconditioning. The results presented here are for those five ground motion records. While the exact motions and sequencing will be adjusted as the test program progresses, they will likely be selected from the sets of five motions presented here.

As test planning is ongoing at the time of writing, only high-level details of the TallWood team's preliminary test plan are presented here, with the understanding that adjustments may be needed based on real time observations. First, about six weeks is planned for testing, and two trials (shakes) can be executed per day allowing adequate time for inspection and recharging the shake table after shutting down. Second, several trials at each of the hazard levels are desired. The intention behind repeating trials at a given hazard level is to develop fragilities for various structural and non-structural elements, albeit recognizing the limitations of having only a single specimen for most of the unique details. Trials will include motions applied in X-direction (east-west), Y-direction (north-south), bidirectionally (XY) and tridirectionally (XYZ). Note, results presented in this paper are all bidirectional application of the five records for each hazard level. Caution will be applied when executing vertical motions based on understanding of the sensitivity of non-structural elements to vertical shaking along with the desire to initially isolate the effect of the lateral motion for each intensity level; thus, vertical shaking is not considered in this analysis.

3. Damage Predictions

The model produced a time history of the displacements of the centerlines of each rocking wall, which were then used to calculate rigid body motion of the diaphragm at each floor level and the peak drift demands for the exterior wall subassemblies at each corner of the building. The interstory drift demands are shown in Figure 7 with horizontal lines indicating the drifts where the onset of damage is expected in each subassembly. These drifts and a description of expected damage are given in Table 1.

Peak building interstory drift ratios remain under 1.75% in the east-west direction, where the CLT walls resist lateral loads, and 2.25% in the north-south direction, parallel to the MPP walls. This difference in drift demands is due to minor differences in the CLT and MPP lateral force resisting systems, eccentricities in mass distribution, and relative magnitudes of the input earthquake motions in the two orthogonal directions.

3.1 SUBASSEMBLY 1: PLATFORM-FRAMED CFS EXTERIOR WALL

The first subassembly is expected to remain relatively undamaged on the first two floors. The vertical joint provides 2.5% interstory drift before onset of damage, above the maximum drift predicted by any of the simulations (2.25%, north-south MCE_R ground motions in Figure 7). Should drift exceed 2.5%, sheathing crushing and fastener tearing are the first types of damage that would be expected.

The third floor does not use a corner joint and its damage can be better predicted by previous research. Davies *et al.* [2011] showed that walls with friction connections (a close analogue to slip track walls) and perpendicular walls start suffering damage at 0.59% drift; however, this damage is limited to sheathing separation at the wall intersection and localized crushing of the gypsum sheathing. This limit is shown by the lowest horizontal line in Figure 7e and 7f. This limit may be exceeded by some 225-year ground motions and is certain to be exceeded at ground motions with longer recurrence intervals.

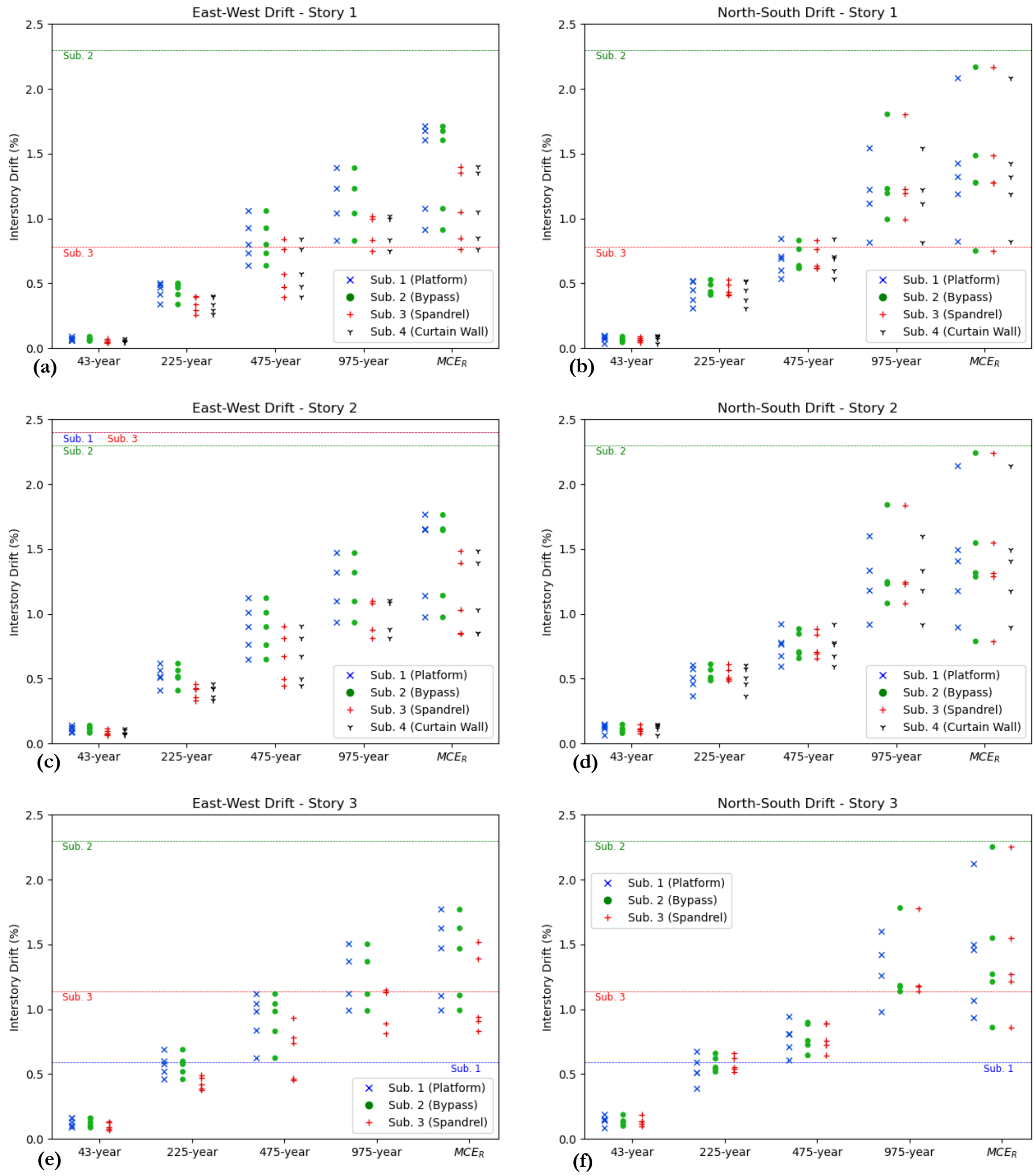

Figure 7. Building peak interstory drift demands and damage limits

Two design improvements may increase the drift limit of the third floor compared to previous research on platform framed CFS walls. Davies *et al.* [2011] suggested that gypsum crushing may be reduced by providing a small vertical gap between the gypsum and upper floor. This subassembly incorporates such a gap and will show whether it reduces damage or delays its onset. To further lessen damage at the corner, the CFS framing was designed to be flexible at the corner by using few studs and not connecting them to one another.

The slotted slip track on the second floor has a hard limit on its in-plane drift capacity, whereas the double slip track assemblies do not. The limited length of the slots in the header track will cause damage to the screws and track at drifts greater than 2.4%. However, the slotted slip track may be advantageous compared to double slip tracks under extreme out-of-plane drifts where a double slip track wall may unseat and fall over while a slotted slip track would be held in place, preventing a component collapse threat.

Table 1. Summary of damage predictions

Subassembly	% Drift at Onset of Damage	Expected Damage
Sub. 1 – Floor 1	2.5%	No damage under any hazard level.
Sub. 1 – Floor 2	2.4%	No damage under any hazard level.
Sub. 1 – Floor 3	0.59%	Damage possible for 225-year and damage expected more severe earthquakes.
Sub. 2 – All Floors	2.3%	No damage under any hazard level.
Sub. 3 – Floor 1	0.78%	Minor damage to window framing under 475-year earthquake. Window cracking and framing distortion expected under 975-year and MCE_R.
Sub. 3 – Floor 2	3.00%	No damage under any hazard level.
Sub. 3 – Floor 3	1.14%	Window framing damage under 225-year earthquake and cracking under more severe hazard levels.
Sub. 4 – Floor 1	2.50% EW 3.05% NS	Damage in the north-south direction possible only at MCE_R. No glass fallout expected.
Sub. 4 – Floor 2	2.50% EW 3.42% NS	

3.2 Subassembly 2: Bypass-Framed CFS Exterior Wall

The drift limit for this subassembly is based on the XLP-2G-1400 joint cover capacity and represents an average drift over the height of the three-story assembly (i.e., the limit can be locally exceeded on one floor as long as the total is not exceeded.) As can be seen in Figure 7, no ground motion has a predicted drift that exceeds this sub assembly's expected drift at damage initiation. Thus, the bypass-framed subassembly is expected to remain undamaged under most hazard levels. One MCE_R does near this wall's drift limit in the north-south direction (Figure 7d and 7f), so there is very little conservatism in the design. However, the three-story subassembly is isolated from the building's motion in the in-plane direction, so the building's motion may be a poor predictor of the wall's response. The subassembly may respond to the ground motion according to its own dynamic properties, potentially resulting in larger drifts than predicted here.

A previous test with bypass framed CFS walls with slotted clips by Wang *et al.* [2015] showed that damage usually commences with deformation of the clips. However, the drift clips used in this experiment are specifically designed to avoid this kind of damage, so damage is instead expected to be redirected to the wall end zones, namely via sheathing cracking and end stud distortion.

3.3 Subassembly 3: Spandrel-Framed CFS Exterior Wall

The vertical joint covers on the second story of the platform-framed subassembly provide sufficient drift capacity to avoid damage under the selected suite of ground motions (Figure 7c and d). However, due to framing limitations, the exterior sheathing may interfere with the slip track assembly's motion on all three stories. Depending on final, as-built details, this may cause some limited damage to the corners of the exterior sheathing on the north side of the subassembly; however, this damage should remain localized.

Conversely, the first and third stories have no mechanism to accommodate corner drift incompatibility other than the inherent flexibility of the windows themselves. The windows are designed to be somewhat flexible, and their drift capacities were estimated by performing a detailed examination of construction drawings. Figure 7a-b shows that damage may occur at the third story during 475-year earthquakes, and Figure 7e-f shows that damage may occur in the east-west direction and is very likely to occur in the north-south direction during the 975-year earthquakes. Window frame distortion and glass cracking are likely to be the first types of damage this subassembly experiences.

3.4 SUBASSEMBLY 4: STICK-BUILT CURTAIN WALL

The drift that corresponds to the onset of damage in curtain walls can be taken as a function of the aspect ratio of a window and the clear space between the glass lite and surrounding framing. A window's drift capacity increases as its aspect ratio increases [Memari *et al.,* 2011]. The drift limits shown in Table 1 represent the drift limits at which the window with the smallest aspect ratio reaches its drift capacity. Framing yielding and minor glass cracking occur when this drift limit is exceeded [Memari *et al.*, 2007]. No damage is expected; these drift limits fall just outside of the range shown in Figure 7.

If the drift limit of the curtain wall is exceeded too far, glass shatter or fallout may occur, which is particularly dangerous and undesirable. Fallout may be assumed to occur when the design drift is exceeded by 25% [Memari *et al.*, 2007, 2011]. While the curtain wall's drift limit is somewhat close to drifts imposed by certain MCE_R ground motions, sufficient excess capacity is provided to minimize risk of glass fallout.

4. Conclusions

The upcoming NHERI TallWood 10-story shake table test will include four non-structural, exterior wall subassemblies. The subassemblies are designed to accommodate interstory drift, and certain walls are designed to overcome drift incompatibilities at wall corners. This paper correlates predicted peak interstory drift to drift limit states of the non-structural walls to identify when damage is likely to occur. The CFS-framed walls which use vertical joints to avoid corner damage will remain undamaged under all but the most extreme hazard levels whereas CFS wall construction that incorporates drift-compatible detailing for in-plane motions but does not account for drift incompatibilities at wall corners is expected to avoid damage at most service-level earthquakes, but significant corner damage may occur at design-level earthquakes.

4.1 FUTURE WORK

At the time of writing, construction of the test building is underway. Shake table testing is expected to commence in January 2023. The upcoming test will verify whether or not these details successfully mitigate non-structural wall damage due to interstory drift. Physical testing is essential because the subassemblies incorporate new details that have not yet been studied in publicly available seismic testing programs. The seismic behaviour of these walls, which use novel details, may be far different from the more typical construction used in the references cited in this paper.

For instance, a key question is whether the subassemblies will suffer damage due to the vertical deflection of the diaphragms. The CFS-framed exterior wall subassemblies were generally designed to allow 0.75 in. vertical deflection. The model used in this study does not account for diaphragm rigidity, so physical testing is needed.

ACKNOWLEDGEMENTS

The authors acknowledge Aleesha Busch for developing the Revit model for the 10-story structure (Figure 1). The structural system scope of NHERI TallWood Project is sponsored by NSF Grants No. 1635227, 1634628, 1634204. The use and operation of NHERI shake table facility is supported by NSF through Grant No.1520904. The non-structural component scope of this project is sponsored by NSF Grant No.

CMMI-1635363, USFS Grant No. 19-DG-11046000-16, Softwood Lumber Board, Computers and Structures Inc, the GAANN Fellowship Program at UNR, and industry sponsors. Materials and in-kind support for the wall subassemblies discussed in this paper are provided by CEMCO® Steel, Construction Specialties, Ehmcke Sheet Metal, Innotech Window and Door, Simpson Strong-Tie, Winco Window and USG. The authors appreciate this support. This material is based upon work supported by the NSF Graduate Research Fellowship under Grant No. 1937966. Any opinion, findings, and conclusions or recommendations expressed in this material are those of the authors and do not necessarily reflect the views of the National Science Foundation.

REFERENCES

Davies, R. D., Retamales, R., Mosqueda, G., Filiatrault, A. [2011] "Experiemental seismic evaluation, model parameterization, and effects of cold-formed steel-framed gypsum partition walls on the seismic performance of an essential facility," *Technical Report MCEER-11-0005*.

Di Lorenzo, G., De Martino, A. [2019] "Earthquake response of cold-formed steel-based building systems: an overview of the current state of the art," *Buildings*, Vol. 9, Iss. 11.

Hasani, H., Ryan, K.L. [2021] "Experimental Cyclic Testing of Reduced Damage Detailed Drywall Partition Walls Integrated with a Timber Rocking Wall," *Journal of Earthquake Engineering*, Vol. 26, Iss. 10, pp. 5109-5129.

Memari, A. M., O'Brien, W. C., Harnam, K. J. Kremer, P. A., Behr, R. A. [2011] "Architectural Glass Seismic Behavior Fragility Curve Development," *FEMA P-58/BD-3.9.1*, Federal Emergency Management Agency, Washington D. C., USA.

Memari, A. M., Shirazi, A., Kremer, P. A. [2007] "Static finite element analysis of architectural glass curtain walls under in-plane loads and corresponding full-scale test," *Structural Engineering and Mechanics*, Vol. 25, No. 4, pp. 365-382.

Miranda, E., Mosqueda, G. [2011] "Seismic Fragility of Building Interior Cold-Formed Steel Framed Gypsum Partition Walls," *FEMA P-58/BD-3.9.2*, Federal Emergency Management Agency, Washington D. C., USA.

Schafer, B.W., Ayhan, D., Leng, J., Liu, P., Padilla-Llano, D., Peterman, K.D., Stehman, M., Buonopane, S.G., Eatherton, M., Madsen, R., Manley, B., Moen, C.D., Nakata, N., Rogers, C., Yu, C. [2016] "Seismic Response and Engineering of Cold-formed Steel Framed Buildings," *Structures*, Vol. 8, Part 2, pp. 197-212.

Spieth, H. A., Carr, A. J., Pampanin, S., Murahidy, A. G., Mander, J. [2004] "Modeling of precast prestressed concrete from structures with rocking beam-column connections," Report No. 2004-01, University of Canterbury, Christchurch, New Zealand.

Wang, X., Pantoli, E., Hutchinson, T.C., Restrepo, J.I., Wood, R.L., Hoehler, M.S., Grzesik, P., Sesma, F.H. [2015] "Seismic Performance of Cold-Formed Steel Wall Systems in a Full-Scale Building," *Journal of Structural Engineering*, Vol. 141, Iss. 10.

Wichman, S., Berman, J. W., and Pei, S. [2022a] "Experimental investigation and numerical modeling of rocking cross laminated timber walls on a flexible foundation," *Earthquake Engng Struct Dyn.*, Vol 51, No. 7, pp. 1697-1717.

Wichman, S., Berman, J., Zimmerman, R., Pei, S. [2022b] "Lateral Design of a 10-Story Building Specimen with Mass Timber Rocking Walls," *Proceedings of 12th National Conference on Earthquake Engineering*, Salt Lake City, Utah, USA.

Seismic demand on Power Actuated Fasteners (PAF) under in-plane loading of drywall partitions: an approach

Luigi Fiorino[1], Alessia Campiche[2], Peter Grzesik[3], Raffaele Landolfo[4]

[1,2,4] Department of Structures for Engineering and Architecture, University of Naples "Federico II", Naples, Italy

[3] Hilti Corporation, Schaan, Principality of Liechtenstein

e-mail: [1] lfiorino@unina.it, [2] alessia.campiche@unina.it, [3] peter.grzesik@hilti.com, [4] landolfo@unina.it

Abstract. Non-structural architectural components often suffer from significant seismic damage, and they can affect the seismic response of structural systems. As a result, the demand for non-structural architectural components specifically qualified against seismic actions becomes bigger and bigger.

In this context, the seismic performance evaluation of drywall partitions plays a key role. It is well known that the in-plane seismic behaviour of drywall partitions is characterised by a displacement-sensitive response, and many investigations were done on this topic. Available studies often focus on the global seismic behaviour of drywall partitions, neglecting the behaviour and impact of fasteners connecting drywalls to supporting elements. However, guidelines for the seismic qualification of typically used redundant light duty fasteners, including Power Actuated Fasteners or plastic anchors, are not available.

The main objective of the study presented in this paper is the evaluation of the seismic demand on fasteners connecting drywalls to supporting elements under in-plane cyclic loading. In particular, the seismic displacement demand on Power Actuated Fasteners (PAF) is obtained through quasi-static in-plane cyclic tests on full-scale drywall partitions. An available test setup at the University of Naples has been used for this purpose and a specific task has been devoted to study the optimal instrumentation layout to allow to capture the significant measurements on PAFs.

A summary of the literature review and goals of the study, together with the description of experimental program, prototypes, test set up, loading protocol, instrumentation layout and preliminary results are described in this paper.

Keywords: Drywall partitions, in-plane behaviour, partition walls; power actuated fasteners, seismic demand.

1. INTRODUCTION

Non-structural architectural components often suffer from significant seismic damage. As a result, the demand of non-structural architectural components specifically qualified against seismic actions continuously increases.

In this context, the seismic performance evaluation of drywall partitions can play a key role. Taghavi, Miranda et al [2003] investigated the cost of seismic damage to non-structural elements, and classified partitions generally as “drift sensitive” elements. Subsequently, the in-plane seismic behaviour of drywall partitions, characterised by a displacement-sensitive response, was investigated in various studies.

Available research often focuses on the global seismic behaviour of drywall partitions. To investigate the global behaviour in typical buildings, drywall partitions were part of the investigations using shake table tests by Rahmanishamsi, Soroushian & Maragakis [2014], Maglilo et al [2014] and Wang et al [2015]. More specific experimental and numerical sub-system studies by Retamales et al [2009], Woods & Hutchinson [2012] as well as Pali et al [2018] illustrate the behaviour of typical sub-systems. Such investigations derive fragility curves as well as an assessment of various damage states, including limited damage to fasteners connecting the partition system to the surrounding structure.

The behaviour of partitions and their attachment to the structure typically depends on the configuration and stiffness of the partition wall system, and resistance can be derived for an entire system. Often, these systems include fasteners to the structure, like light duty plastic anchors and power actuated fasteners, that are not specifically tested or evaluated for seismic demands. In fact, criteria to qualify such systems for seismic demands do not exist to date

To derive potential qualification criteria for power actuated fasteners, as one of the globally most preferred fastening methods for metal stud drywall partitions, most existing experimental studies lack important data. Demands on such fasteners are strongly depending on actual drift ratios, connection details and the stiffness of the entire partition system. A few first sub-system studies under selected application conditions were carried out by Ramirez and Laboube [2013] and Rahmanishamsi et al [2016] to estimate the capacity of power actuated fasteners under in-plane loading in non-cracked concrete. However, it remains unclear, what forces such fasteners will have to withstand under interstory drift demands.

An available test setup at the University of Naples from previous similar research has been used to study the optimal instrumentation layout to allow to capture the significant measurements on the demand on power actuated track fasteners (PAF).

A summary of the literature review and goals of the study, together with the description of experimental program, prototypes, test set up, loading protocol, instrumentation layout and preliminary results are described in the paper.

2. RESEARCH PROJECT

2.1 GENERAL

The main objective of the study presented in this paper is the evaluation of the seismic demand on fasteners connecting typical drywall configurations to supporting structural concrete elements under in-plane cyclic loading. In particular, the seismic displacement demand on PAF is obtained through quasi-static in-plane cyclic tests on full-scale drywall partitions, with varying common connection details:

- Fixed connections for bottom and top wall tracks, and wall sides – typical demand on fasteners expected

- Sliding connections for top wall track (gypsum type and non-gypsum type) and fixed connections for bottom wall track and wall sides - lowest demands expected on track fasteners.

- Fixed connections for bottom and top wall tracks and wall sides not connected to the surrounding structure – highest demand expected on track fasteners.

2.2 TEST CONFIGURATIONS

The test program followed FEMA 461 protocols, and damage states, as well as relevant measurements to derive demands on fasteners, were recorded at increasing drift levels between 0% and 4.5%. In particular, demands and damage states at 0.5% to 1% were of interest, in relation to the limits set by EN 1998-1 (EuroCode 8, Part 1), 4.4.3.2 [CEN, 2016], which specifies drift limits for damage control, depending on the sensitivity of non-structural elements and their connections. In comparison, drift levels are limited to a maximum of 1.5% per AS 1170.4 [2007] in Australia.

Test specimen consisted of 2285 mm long and 2600 mm high partition walls. The tested partitions were made of a single LWS frame, i.e., lipped channel section stud profiles connected at the ends with unlipped channel section track profiles, sheathed with double layer of 12.5 mm thick standard gypsum (GWB) boards installed on both wall faces. The total wall thickness was equal to 125 mm. Six different configurations were developed and seven specimens were tested, as summarized in Table 1, in which the main parameters investigated were:(a) type of top connections; (b) fastener system; (c) fastener spacing. For each test a specific instrument layout was adopted (Tab. 1). Further information about instrument layouts is given in Section 2.4.

The connection of all perimeter tracks and studs to the concrete base material was carried out with Power Actuated Fasteners (PAF) with a nominal shank diameter of 4 mm and a shank length of 27 mm (Figure 1-a). The gypsum type sliding connection was fastened with Power Actuated Fasteners with the same diameter, but with a shank length of 62 mm only for the top gypsum type sliding connection, as shown in Figure 1-b.

All Power Actuated Fasteners were installed with the setting tool recommended by the manufacturer, as shown in Figure 1-c.

1-a: Power Actuated Fasteners for Track and stud attachment

1-b: Power Actuated Fasteners for gypsum type sliding connection – top track (Specimen CONN Sw/G)

1-c: Power Actuated Fastening Tool

Figure 1. Fasteners installed and setting tool

Specimen configuration (label)	Type of top / bottom track connections	Track fastener system	Track fastener spacing - top & bottom	Wall side connections	Instrument layout
Reference (REF1)	Fixed / Fixed	Hilti X-X 27 MX	30 cm	Connected	LAYOUT 1
Reference (REF2)	Fixed / Fixed	Hilti X-X 27 MX	30 cm	Connected	LAYOUT 2
Reference (REF3)	Fixed / Fixed	Hilti X-X 27 MX	30 cm	Connected	LAYOUT 3
Top connection effect: sliding with gypsum strips (CONN Sw/G)	Sliding with gypsum strips / Fixed	Top track: Hilti X-X 62 MX Bottom track: Hilti X-X 27 MX	30 cm	Connected	LAYOUT 3
Top connection effect: sliding without gypsum strips, with fire sealant (CONN Sw/oG)	Sliding without gypsum strips, with Fire stop seal Hilti TTS / Fixed	Hilti X-X 27 MX	30 cm	Connected	LAYOUT 3
Maximum force on top and bottom connections: no side connection (SIDE-1)	Fixed / Fixed	Hilti X-X 27 MX	30 cm	Not connected	LAYOUT 4
Maximum force on top and bottom connections: no side connection (SIDE-2)	Fixed / Fixed	Hilti X-X 27 MX	~ 50 cm	Not connected	LAYOUT 4
Stud fastening on the side of the wall to concrete Hilti X-X 27 MX; fastener spacing both sides: 50 cm					

Tab. 1 Specimen configurations and instrumentation layouts

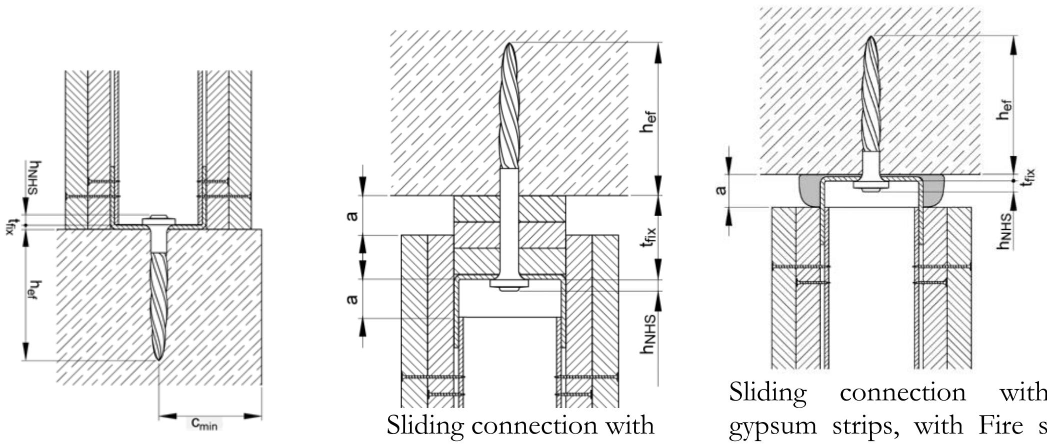

Fixed connection

Sliding connection with gypsum strips (Sw/G)

Sliding connection without gypsum strips, with Fire stop seal Hilti TTS (Sw/oG)

Figure 2. Track connection typologies

2.3 TEST SET-UP

A specific test set-up was designed to carry out the in-plane cyclic tests (Fig.2). The test set-up, which replicated the behaviour of a typical storey of a building structure, was a bi-dimensional frame made of S355JR steel grade hot-rolled profiles. The testing frame was made of a bottom beam, a top beam and two hinged columns and three different wall layouts were used to perform tests (REF, CONN, SIDE, see Table 1). Two steel portal frames were used for avoiding the out-of-plane displacements of test set-up. The testing frame was completed with C25/30 strength class 100 mm thick concrete blocks for simulating the interface with a reinforced concrete structure.

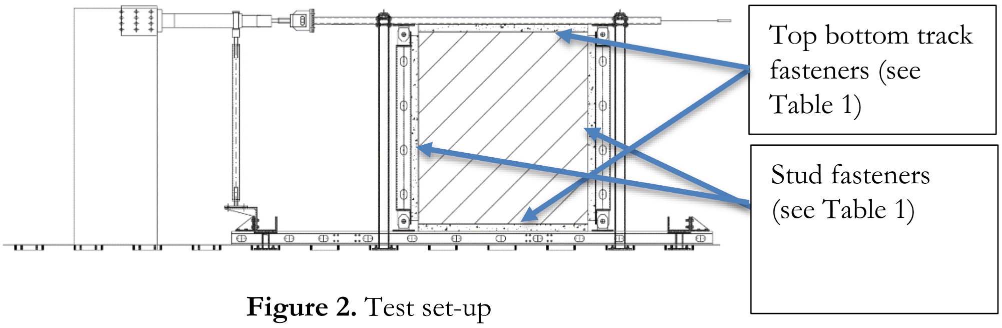

Figure 2. Test set-up

2.4 LOADING PROTOCOL

The in-plane quasi static reversed cyclic tests were performed by subjecting the wall specimens to the loading protocol defined by FEMA 461 [FEMA 461, 2007].

FEMA 461 provides a loading history that consists of repeated cycles of step-wise increasing deformation amplitudes. Two cycles for each amplitude (or step) and a specific relationship between consecutive step amplitudes are provided. The loading history, with a step number n generally greater than 10, is defined by several parameters:

- Δ_0 = targeted smallest deformation amplitude, and its recommended value in terms of inter-storey drift ratio (Δ=d/h, in which d is the lateral displacement at the wall top and h is the wall height set equal to 2700 mm) is 0.05%;
- Δ_m = targeted maximum deformation amplitude equal to 4.5%;
- a_i = inter-storey drift amplitude of the cycles in the step ith;
- a_{i+1} = inter-storey drift amplitude of the cycles in the step i+1th, given by:

$$a_{i+1} = 1.4a_i$$

According to FEMA 461, the first amplitude a_1 should be equal to Δ_0 and the last one should be equal to Δ_m. The loading history should be continued by using increments of amplitude of $0.3\Delta_m$ until reaching the load capabilities of test setup.

By imposing that a_n is exactly equal to Δ_m, the code provides the ratio a_i/a_n. In particular, the loading protocol used for performing the cyclic tests on the investigated walls was defined by imposing $a_1 = \Delta_0 = 0.05\%$ and $a_{12} = \Delta_m = 4.5\%$ for a total number of steps equal to 16.

Figure 3 shows the adopted cyclic protocol. The displacement-controlled test procedure involves displacements at rates of 0.25 mm/s up to displacements of 3.6 mm, 0.50 mm/s for displacements from 3.6 mm to 9.8 mm, 0.75 mm/s for displacements from 9.8 mm to 26.9 mm, 1.50 mm/s for displacements from 26.9 mm to 68.2 mm, 3.00 mm/s for displacements higher than 68.2 mm.

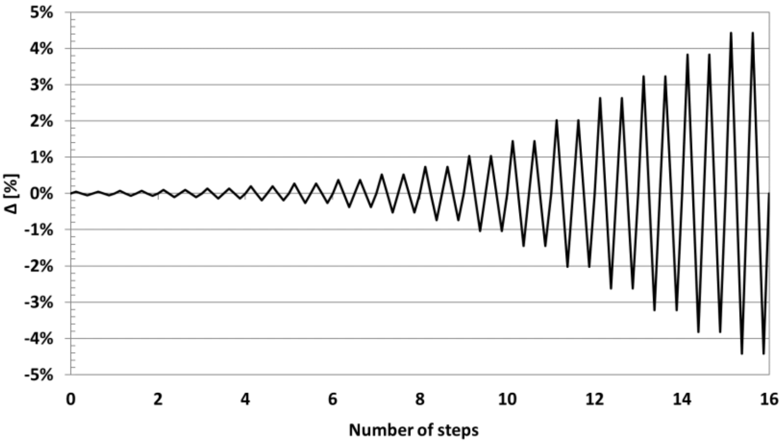

Figure 3. Loading protocol

2.5 INSTRUMENTATION

Five different instrumentation layouts were defined for the experimental tests, as shown in Figure 4:

- LAYOUT 1, used for the specimen configuration REF_01;
- LAYOUT 2, used for the specimen configuration REF_02;
- LAYOUT 3, used for the specimen configurations REF_03, CONN Sw/G and CONN Sw/oG;
- LAYOUT 4, used for the specimen configurations SIDE-1 and SIDE-2.

All the instrumentation layouts for tests included one potentiometer (P1) for measuring the wall top horizontal displacement (i.e., wall lateral drift) and a variable number of linear variable differential transducers (LVDTs) to measure relative horizontal and vertical displacements.

In particular, horizontal LVDTs were used for measuring the relative horizontal displacement between bottom concrete block interface and bottom beam of test set-up, the relative horizontal displacements between bottom concrete block interface (concrete slab) and bottom track, the relative horizontal displacements between top concrete block interface (concrete slab) and top track and the relative horizontal displacement between top concrete block interface (concrete slab) and top beam of test set-up.; vertical LVDTs were used for measuring relative vertical displacements between bottom concrete block interface (concrete slab) and wall steel frame (track or stud) and relative vertical displacements between top concrete block interface (concrete slab) and wall steel frame (track or stud).

Moreover, for LAYOUT 3 and 4 eight strain gauges (SG) were employed to measure the strain of the cold formed steel track in between fastener.

A load cell was used to measure the loads applied to the entire frame and assembly.

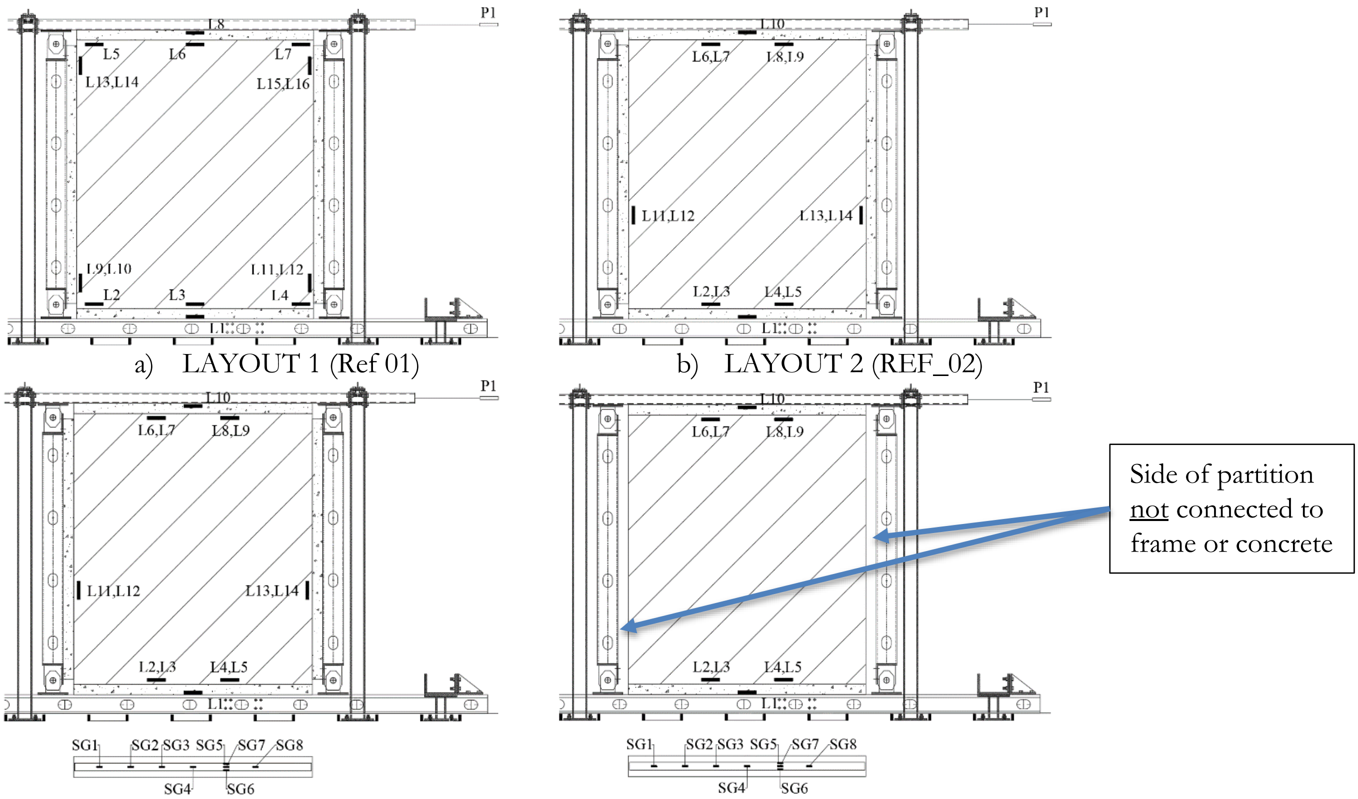

a) LAYOUT 1 (Ref 01)

b) LAYOUT 2 (REF_02)

c) LAYOUT 3 (REF_03. CONN Sw/oG & CONN Sw/G)

d) LAYOUT 4 (SIDE_01 & SIDE_02)

Figure 4. Instrument layouts

3. PRELIMINARY RESULTS

Experimental response in terms of load (F) vs. IDR curves obtained for all tests is shown in Fig. 5. As usual for this kind of tests, specimens were characterised by a fully nonlinear, pinched lateral response. Peak strength and secant stiffness evaluated at 0.5%, 1.0% and 1.5% IDR and at 40% of the peak load are given in Fig. 6 for each test for both positive and negative cycles.

From examination of results in terms of Load (F) vs. IDR curves and strength and stiffness it can be observed that:

(1) walls REF_02 and REF_03 showed similar response (differences of strength and stiffness less than 10%);

(2) holes in the panels affected the response of wall REF_01 (results showed higher stiffness, by about 2 times, of the walls REF_02 and REF_03 compared to the wall REF_01, whereas the values of the strength were not significantly different, i.e., difference less than 20%). As a result, walls REF_02 and REF_03 are used as reference of walls with top fixed connections and restrained side connections;

(3) type of top sliding connection did not affect the response (walls CONN Sw/G and CONN Sw/oG showed same value of strength and differences of stiffness less than 20%); as a result, walls CONN Sw/G and CONN Sw/oG are assumed as reference of walls with top sliding connections and restrained side connections;

(4) spacing of power actuated fasteners did not affect the response (walls SIDE_1 and SIDE_2 showed same value of stiffness and differences of strength less than 10%); as a result, walls SIDE_1 and SIDE_2 are assumed as reference of walls with top fixed connections and no restrained side connections;

(5) top sliding connections reduced the stiffness (results showed higher stiffness, by about 2 times, of the walls REF_02 and REF_03 with respect to the walls CONN Sw/G and CONN Sw/oG, whereas the values of the strength were not significantly different, i.e., difference less than 20%);

(6) having no restrained side connections significantly reduced strength and stiffness (results showed higher strength, by about 5 times, and stiffness, from 1.5 to 11 times, of the walls REF_02 and REF_03 with respect to the walls SIDE_1 and SIDE_2).

(7) No significant damage was observed related to the track to concrete connection using power actuated fasteners, regardless of the used wall or connection configuration.

The evaluation of the damages exhibited by the walls during the tests was carried out through visual observation of the specimens. The type of damage phenomena observed during the tests are shown in Fig. 7. The observation of damages is usually associated to three Damage States (DSs) defined in literature [Restrepo et al 2011, Retamales et al 2013] according to the damage level in terms of required repair action and safety: (1) DS1, characterized by superficial damage to the wall and no risk for life safety; DS2, characterized by local damage and moderate risk for life safety; (3) DS3, characterized by severe damage to walls and high risk for life safety. Fig.7 correlates observed damages in the tested walls to the defined DSs, i.e., (DS1), (DS2), and (DS3) is also given for each type of damage.

The correlation between observed damage phenomena and IDRs, the evaluation of the seismic demand on power actuated fasteners at different relevant drift levels, as well as the development of fragility curves will represent the next steps of the ongoing interpretation of test results and will be summarized in a separate publication. However, preliminary results for maximum displacement demand on top and bottom track connections with power actuated fasteners for drift level up to 1% show that (Fig. 8):

(1) Reference walls (REF_01, REF_02, REF_03) exhibited lower values of the maximum displacement demand (from 0,1 to 0,2 mm), because part of horizontal force acting on the wall was transferred through the contact between the wall and the surrounding structure. Note that the maximum horizontal force acting on the walls for the same range of drift level (no more than 1%) was from 18 to 39 kN for the reference walls.

(2) Walls with top sliding connections (CONN Sw/G, CONN Sw/oG) and walls having no restrained side connections (SIDE_1, SIDE_2) exhibited higher values of the maximum displacement demand (from 0,2 to 0,5 mm), because they were less restrained by the surrounding structure. However, if the maximum displacement demand is related to the maximum horizontal force acting on the wall for the same range of drift level (no more than 1%), it can be noted that power actuated fasteners of walls CONN Sw/G, CONN Sw/oG, SIDE_1 and SIDE_2 were subjected to the same displacement demand even if the horizontal force acting on the walls CONN Sw/G and CONN Sw/oG (from 18 to 21 kN) was significantly higher than that acting on the walls SIDE_1 and SIDE_2 (from 8 to 10 kN). This was due to the fact that no or only very limited horizontal forces was transferred through the contact between the wall boards and the surrounding structure in the tests SIDE_1 and SIDE_2, compared to the other tests.

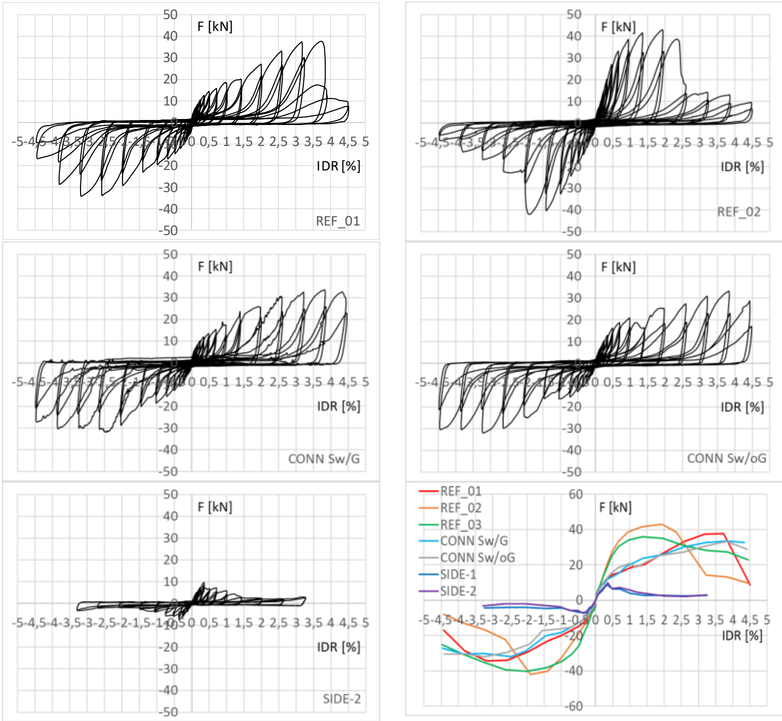

Figure 5 Load (F) vs. IDR curves

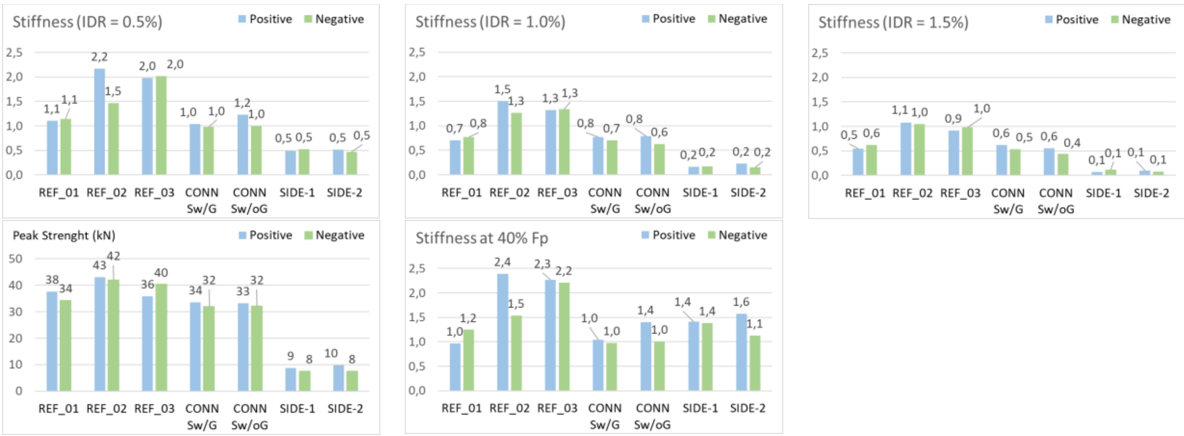

Figure 6 Strength (kN) and stiffness (kN/mm)

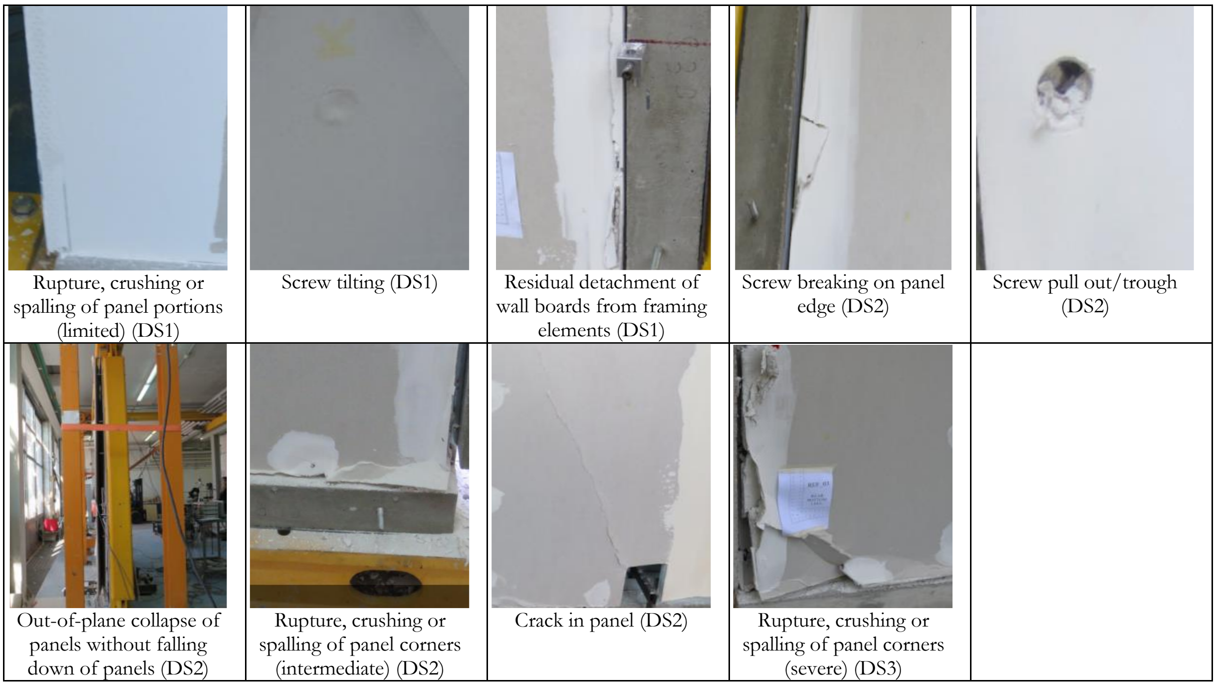

Figure 7 Types of damage observed during the tests

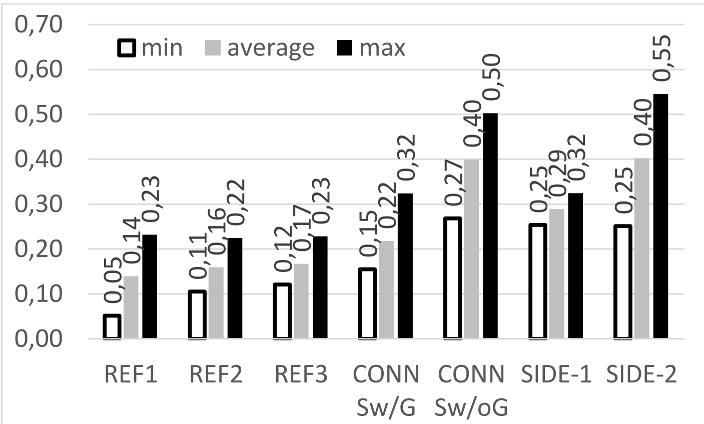

Figure 8 Displacement demand (mm) on top / bottom track fasteners for drift levels up to 1%.

4. CONCLUSIONS AND FUTURE DEVELOPMENTS

Seven different sets of wall partition wall configurations were tested to evaluate possible instrumentation for the assessment of track fastener demands. Damage states under cyclic in-plane loading simulation inter story drift were collected, as well as extensive sensor data.

In conclusion, it could be shown, that the selected instrumentation can be used without significantly influencing the behaviour of the tested wall systems. This allowed for the collection of a lot of useful sensor data. In addition, it could be shown, that Power Actuated fasteners may be suitable for cyclic demands caused by expected story drift at the design level earthquake in different typical partition wall configurations.

The ongoing assessment of the collected data will be used to quantify the estimation of demands on track fasteners, and to derive potential qualification criteria for cyclic demands to allow for an assessment of products by interested parties. A final assessment of all sensor data was not yet available at the time this paper was submitted and may be subject to future publications. However, the tests indicate higher demands on track fastening for walls with sliding connections or walls lacking vertical side connections to structural elements or return walls.

REFERENCES

AS 1170.4 [2007] "Structural design actions - Part 4: Earthquake actions in Australia", Standards Australia, 2007

CEN [2006] "Eurocode 8: Design of structures for earthquake resistance – Part 1: General rules, seismic actions and rules for buildings", EN 1998-1:2004, European Committee for Standardization, Brussels.

Magliulo G., Petrone C., Capozzi V., Maddaloni G., Lopez P., Manfredi G [2014] "Seismic Performance Evaluation of Plasterboard Partitions via Shake Table Tests", University of Naples Federico II, Department of Structures for Engineering and Architecture, Naples, Italy, 2014

Miranda E. [2003] "Response Assessment of Non-Structural Building Elements", PEER Report 2003/05, University of California Berkeley, Berkeley, USA.

Pali T., Macillo V., Terracciano M.T., Bucciero B., Fiorino L., Landolfo R. [2018] "In ‐ plane quasistatic cyclic tests of nonstructural lightweight steel drywall partitions for seismic performance evaluation," *Earthquake Engng Struct Dyn*. Vol. 47, pp. 1566–1588. https://doi.org/10.1002/eqe.3031.

Rahmanishamsi E., Soroushian S., Maragakis E. [2014] "Seismic Response of Ceiling/Piping/Partition Systems in NEESR-GC System level Experiments", *ASCE Structures Congress*, American Society of Civil Engineers ASCE, 2014,

Rahmanishamsi E., Soroushian S., Maragakis E. [2016] "Capacity Evaluation of Typical Track-to-Concrete Power-Actuated Fastener Connections in Nonstructural Walls", *Journal of Structural Engineering*, American Society of Civil Engineers ASCE, 2016, DOI: 10.1061/(ASCE)ST.1943-541X.0001472.

Ramirez R., Laboube R.A. [2013] "Report on Laboratory Testing of Fastening of CFS Track to concrete base materials with PAFs", *Research report* RP13-3, American Iron and Steel Institute AISI, Washington D.C., USA.

Restrepo J. I.; Bersofsky A. M. [2011] "Performance characteristics of light gage steel stud partition 5 walls", *Thin-Walled Struct.* 49, 317–324.

Retamales R., Davies R, Mosqueda G., Filiatrault A. [2009] "NEESR Nonstructural Grand Challenge Project Simulation of the Seismic Performance of Nonstructural Systems - Experimental Phase 1: Seismic Performance of Partition Wall Subsystems", University of Buffalo, New York, USA.

Retamales R., Davies R., Mosqueda G., Filiatrault A. [2013] "Experimental Seismic Fragility of 12 Cold-Formed Steel Framed Gypsum Partition Walls", *J. Struct. Eng.* 139, 1285–1293.

Wang X., Pantoli E., Hutchinson T. C., Restrepo J. I., Wood L. R., Hoehler M. S., Grzesik P., Sesma F. H., [2015] "Seismic Performance of Cold-Formed Steel Wall Systems in a Full-Scale Building", *Journal of Structural Engineering*, American Society of Civil Engineers ASCE, 2015, DOI: 10.1061/(ASCE)ST.1943-541X.0001245

Woods R.L., HutchinsonT.C. [2012] "A numerical Model for capturing the in-plane seismic response of interior metal stud partition walls", *Technical Report* MCEER-12-0007, University of Buffalo, New York, USA.

Failure Mode and Hysteretic Behavior of Steel Angles Used for Floor-Mounting of Non-Structural Elements

Chang-Jun Bae[1], Cheol-Ho Lee[2], Su-Chan Jun[2], and Seungjun Lee[2]

[1] Dept. of Architecture and Architectural Engineering, Seoul National University,
Seoul 08826, Republic of Korea
e-mail: changjun0125@snu.ac.kr
[2] Dept. of Architecture and Architectural Engineering, Seoul National University,
Seoul 08826, Republic of Korea
ceholee@snu.ac.kr (corresponding author)
corrora90@snu.ac.kr
wnstmd804@snu.ac.kr

Abstract. In earthquake events, non-structural elements (NSEs) are usually subjected to strong floor motions amplified by the supporting structure. For this reason, it is desirable to provide a ductile fuse in the load path between the supporting structure and NSEs to reduce seismic demand on NSEs. For floor-mounted NSEs, such as steel racks housing communication and mechanical equipment, L-shaped steel angles have been preferred as a floor-mounting element. In this case, the mounting angle should function as a major energy-dissipating element in the event of high seismic demand. Despite their critical importance as a potential ductile fuse, studies regarding the ductility and hysteretic behavior of the base angles have been rare. In this study, in order to investigate failure mode and hysteretic behavior of the base mounting angles, a series of shake-table tests on steel racks with diverse mounting conditions were conducted. Two steel racks having different slenderness were utilized. It was observed that dynamic behavior and failure mode of the angles were governed by the slenderness of rack, absence or presence of a gap (l_{gap}) between the rack and the floor, and the gauge length from the angle corner to anchor point (l_b). As the slenderness of the rack and l_b increased, the mounting angle's capacity to restrain rigid body rotation of the rack became weaker, thus resulting in uplift failure. For specimens with enlarged l_{gap}, the restraint to translational motion of the rack was not strong enough, thus leading to distorsional failure of the angles. Symmetric hysteretic behavior with a negative post-yielding stiffness caused by gravity force was observed when the rigid body rotation motion was involved. However, pinched asymmetric hysteresis behavior was dominant when the translational motion governed, which seemed to be caused by the clearance around the bolt hole and one-sided accumulation of inelastic deformation of the crushed angle.

Keywords: shake-table test, floor-mounted non-structural element, ductile design, floor mounting angles, hysteretic behavior.

1. INTRODUCTION

In earthquake events, non-structural elements (NSEs) are usually subjected to strong floor motions amplified by the supporting structure. Very high acceleration amplification can occur especially when the fundamental period of NSEs is located near the fundamental period of the supporting structure. Previous studies have indicated that the narrowband amplification can be reduced significantly by allowing nonlinearity on the NSE with a modest amount of ductility [NIST, 2018]. Based on this research, the component resonance ductility factor to account for acceleration reduction by component ductility was proposed in recently published ASCE 7-22 [2022]. However, this result was obtained from an analytical study with assuming the NSE hysteretic model as ideal bilinear hysteresis model with 3% strain hardening. Thus, it is necessary to verify the validity of the response reduction based on actual hysteretic behavior of the NSEs.

To satisfy performance objective (position retention or operational) of NSEs and secure convenient repair or retrofit, it is more appropriate to provide ductility to the bracing or mounting elements rather than the NSE itself. For floor-mounted NSEs, such as steel racks housing communication and mechanical equipment, L-shaped steel angles have been preferred as a floor-mounting element. In this case, the mounting angle should function as a major energy-dissipating element in the event of high seismic demand. Despite their critical importance as a potential ductile fuse, studies regarding the ductility capacity and hysteretic behavior of base angles have been rare while continued research has been conducted on the hysteretic behavior provided by concrete anchors [Quintana Gallo *et al.*, 2018, 2019; Ciurlanti *et al.*, 2022]. Feinstein and Moehle [2022], one of the rare studies focusing on the mounting attachment, investigated the contribution of base angles to dynamic response and seismic force demand on NSEs, but they also didn't address the hysteretic behavior of mounting angles.

In this study, failure mode and hysteretic behavior of the floor mounting angles were investigated through a series of shake-table tests on steel racks with diverse mounting conditions.

2. EXPERIMENTAL PROGRAM

2.1 Test Specimens

Floor-mounted NSEs are subjected to translational or rotational inertia forces during earthquakes. Governing dynamic motion is affected by the slenderness of the NSE. Thus, two steel racks, representing floor-mounted NSEs, with similar weight but different aspect ratio were fabricated as shown in Figure 1. The rack specimens were designed to remain essentially elastic without damage and severe deformation during tests. Table 1 summarizes two rack types tested.

Steel angles used for floor-mounting of NSEs restrains aforementioned dynamic motions at the base. The restraining action highly depends on the mounting conditions as well as the size of the angles as shown in Figure 2. A gap (l_{gap}) may exist between the rack bottom and floor because of the presence of wheels or supports for ease of installation and transportation. Also, the gauge length from the angle corner to the anchor bolt (l_b) is a very important design parameter since it determines uplift stiffness of the angle.

In this study, shake table tests were conducted for a total of 6 specimens in order to investigate failure modes and hysteretic behavior depending upon different mounting conditions. The key specimen information is summarized in Table 2. Two angles of the size described in Table 2 were arranged on each side of the rack as shown in Figure 1(c). The angle, bolted connection of the rack bottom with angle, and

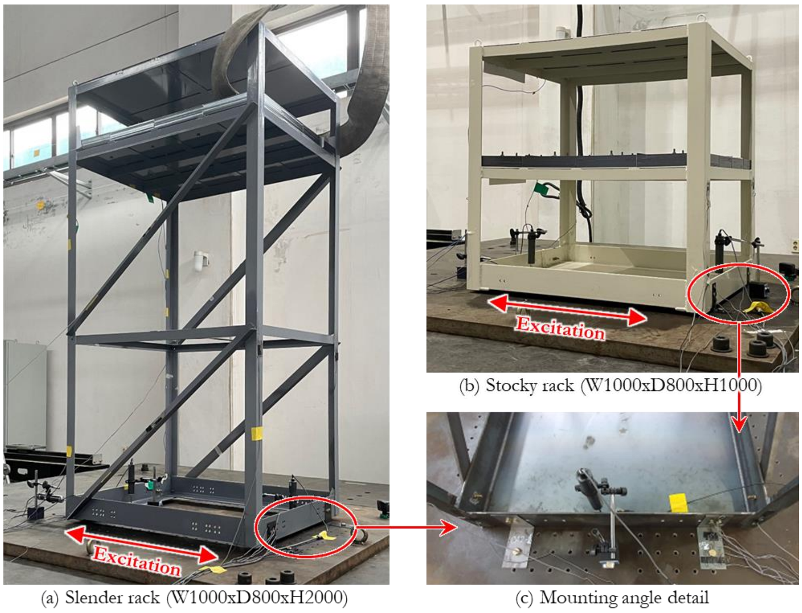

Figure 1. Steel rack specimens and mounting angle attachment

Table 1. Two rack types tested

Rack type	Rack size (mm) (width × depth × height)	Height of center of mass (mm)	Weight (kN)
Stocky (ST)	1,000 × 800 × 1,000	500	4.16
Slender (SL)	1,000 × 800 × 2,000	1,400	4.0

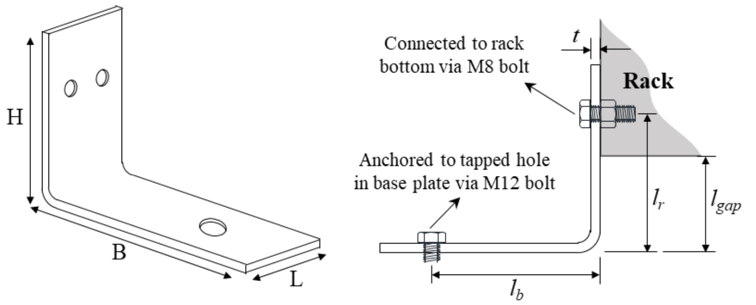

(a) Steel angle **(b) Key dimensions in connecting area**

Figure 2. Configuration of mounting steel angle

Table 2. Key properties of test specimens

Specimen	Rack type	Angle size (L - H × B × t × L)	l_{gap} (mm)	l_b (mm)	l_r (mm)
ST-S-NG	Stocky	L – 100 × 50 × 2 × 20	0	25	45
ST-S-G	Stocky	L – 100 × 50 × 2 × 45	15	25	60
SL-S-NG	Slender	L – 100 × 50 × 2 × 45	0	25	60
SL-L-NG	Slender	L – 100 × 120 × 2 × 70	0	75	60
SL-S-G	Slender	L – 100 × 50 × 2 × 60	20	25	60
SL-L-G	Slender	L – 100 × 120 × 2 × 70	20	75	60

*Note: ST = stocky, SL = slender, S = short l_b (=25mm), L = long l_b (=75mm), G = gap, and NG = no gap

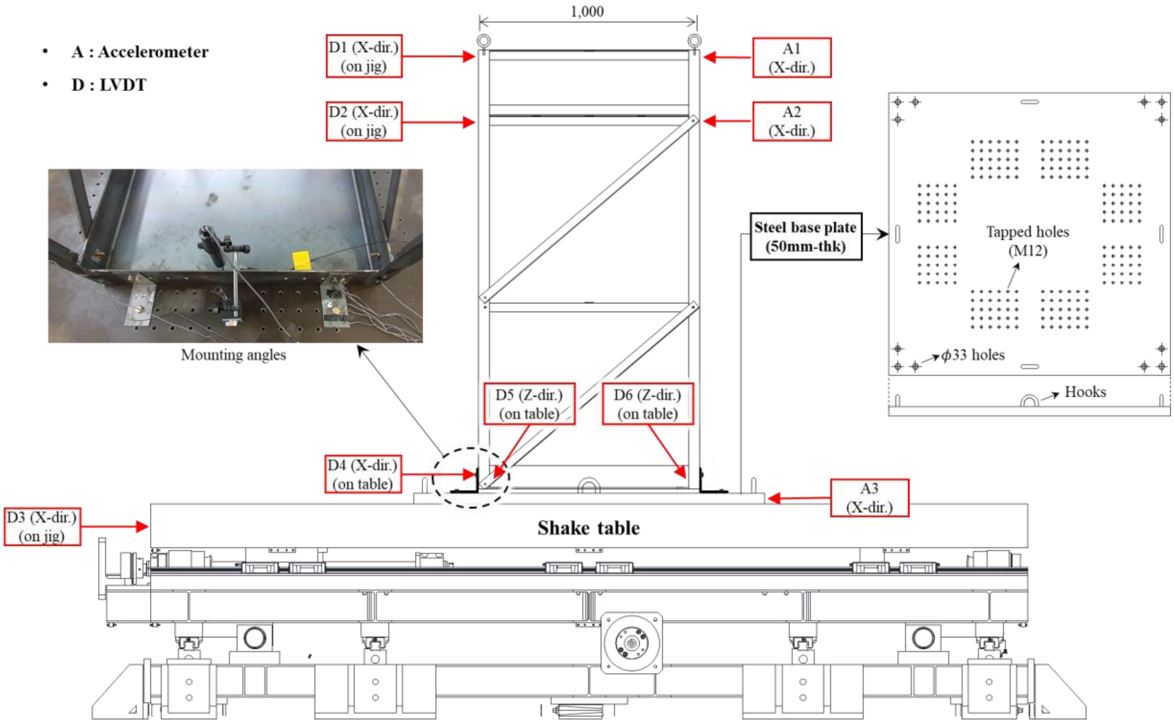

Figure 3. Test setup and measurement plan

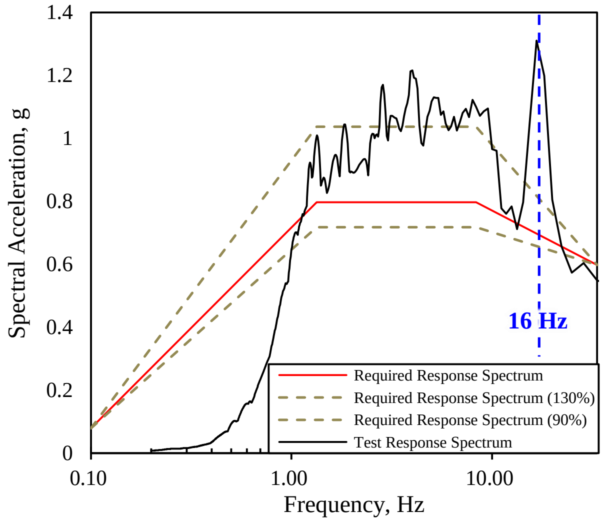

Figure 4. Test Response Spectrum (TRS) measured at shake table

anchorage were designed based on equivalent static procedure considering lateral force acting on center of the mass of racks. Angles were designed to be remain elastic under gravity force of the rack. Bolts used on the rack-angle connection and anchorage were designed to ensure tensile or shear fracture do not occur. In order to impose all the load acting on the rack to the mounting angles, there were no additional casters or supports between the rack and the base for specimens with the gap.

2.2 Test Setup

Figure 3 shows the test setup and measurement plan. Additional steel plate was fabricated to provide connectivity between test specimens and shake table. Various measuring devices including accelerometers and LVDTs were installed to monitor both horizontal and vertical responses of the test specimen. The installation locations are shown in Figure 3. LVDTs D4, D5, and D6 are installed on the table and they were used to measure relative displacement at bottom of the racks respect to the table motion. Also, the displacements obtained from D4, D5, and D6 can be regarded as the displacement of the mounting angle itself since the bottom of the rack was designed to be rigid enough such that no local deformation occurs. The hysteretic curves were obtained using the displacement of the mounting angle and the acceleration measured at accelerometer A2.

2.3 LOADING PROTOCOL

Testing was conducted one way using artificial floor input motion to capture failure modes and hysteretic behaviors of mounting angles. Artificial floor motions were generated to match the required response spectrum (RRS) required by ICC-ES-AC 156 [ICC, 2010], which has been widely used to evaluate the seismic performance of non-structural elements. The RRS was developed from the two parameters, the story height ratio (z/h = 1.0) and the design spectral response acceleration at short periods (S_{DS} = 0.5g), which corresponds to the highest seismic demand according to Korean Design Standard [AIK, 2019]. Figure 4 shows the RRS and the test response spectrum (TRS) obtained using the table acceleration measured via accelerometer A3. Although the TRS in this study did not satisfy the requirements by ICC-ES-AC 156, especially near 16 Hz due to the fundamental period component of the shake table itself, this does not matter since the main purpose of this study is to investigate the failure mode and hysteretic behavior of the mounting angles. Incremental-intensity shake table tests were conducted from 50% TRS until severe damage or deformation of the mounting angles were observed or the shake table reached its maximum capacity (250% TRS).

3. TEST RESULTS

3.1 STOCKY RACK

3.1.1 Failure Mode

Since stocky racks have very small aspect ratio lateral response was more pronounced than vertical response.

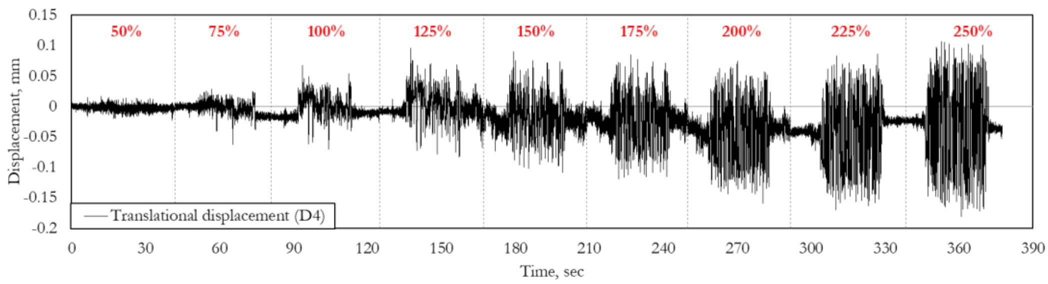

(a) ST-S-NG

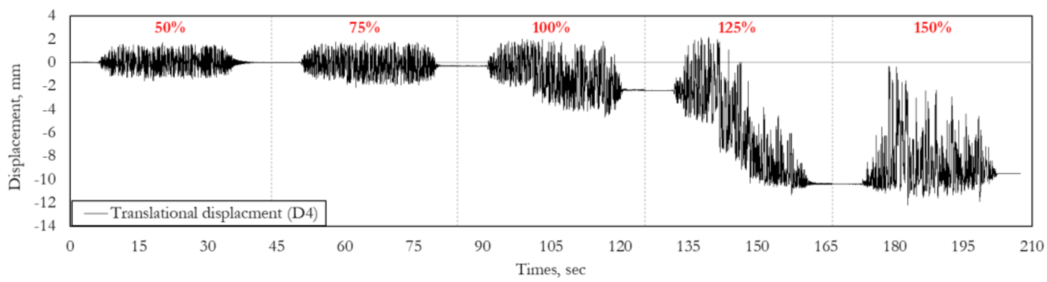

(b) ST-S-G

Figure 5. Lateral displacement history of mounting angle measured from stocky specimens

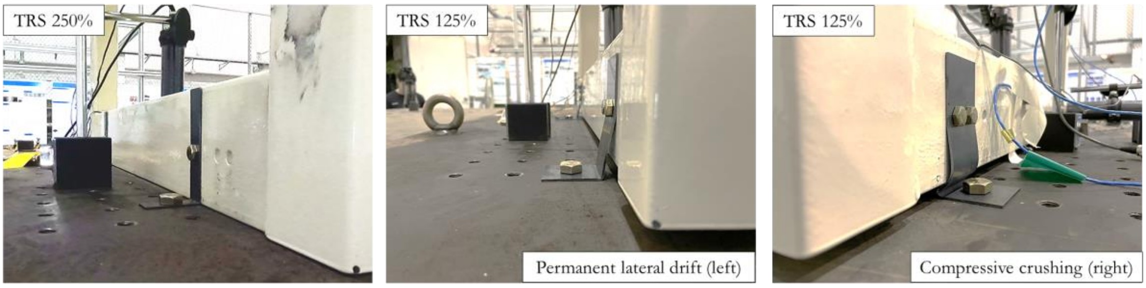

(a) ST-S-NG (TRS 250%) **(b) ST-S-G (TRS 125%)**

Figure 6. Angle damage observed in stocky (ST) specimens

Figure 5 indicates that permanent lateral deformation was accumulated in both stocky specimens as the input motion intensity increased. However, the displacements of ST-S-NG (no gap specimen) were significantly small compared with ST-S-G (gap specimen) and the deformation could not be observed with naked eyes as shown in Figure 6(a). This was because the axial stiffness of the bottom leg of the mounting angle provided sufficient restraint to dynamic motion, seismic load being directly transferred to the bottom leg of the angle due to absence of the gap in ST-S-NG. In addition, the rack of the ST-S-NG was directly in contact with the base plate so that translational motion could be suppressed by larger friction force than ST-S-G. On the other hand, in ST-S-G, the bending stiffness of the angle, which is more flexible than axial stiffness of the bottom leg, provided weaker restraint because upper leg of the angle was bolt-connected to the bottom of the rack. As shown in Figure 6(b), one side of the angle was pushed (crushed) and the other side was pulled, resulting in the distortional failure of the angle. Thus, permanent deformation of ST-S-G was accumulated to the side of the crushed angle until TRS 125%.

3.1.2 Hysteretic Behavior

Figure 7 shows hysteretic behavior of stocky specimens for all excitation steps. Hysteretic curves for ST specimens were determined by the lateral displacement of angles (D4) and the acceleration measured at the center of mass level of the rack (A2). Hysteretic curves from both specimens indicate inelastic behaviour occurred from 100% TRS. ST-S-NG showed symmetric hysteretic behavior similar to that used in previous analytical studies for the effect of component ductility. However, significantly pinched asymmetric hysteretic behavior was observed from ST-S-G. The pinching and asymmetric behavior seemed to be caused by the clearance around the bolt hole and the accumulated deformation on the side of the crushed angle.

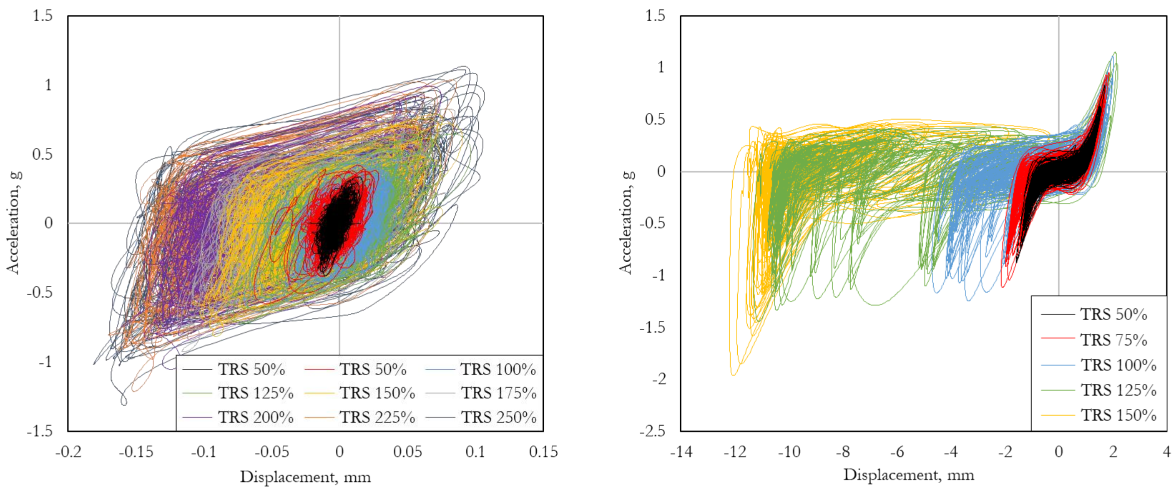

(a) ST-S-NG **(b) ST-S-G**

Figure 7. Observed hysteretic behavior of stocky specimens

3.1.3 Acceleration Amplification

Figure 8 shows the acceleration amplification measured from stocky specimens. The amplifications were determined by normalizing the peak acceleration measured at the mass level (A2) of the rack by the peak acceleration measured at the steel base (A3). The amplification of ST-S-G were much higher than those of ST-S-G since the lateral stiffness provided by the mounting angle is much smaller in ST-S-G. Both specimens showed that the amplification decreases as peak floor acceleration increases due to inelastic behavior of mounting angles. In the case of ST-S-NG, lateral stiffness was very high and the acceleration of the rack was almost equal to the base acceleration, so significant decrease did not occur.

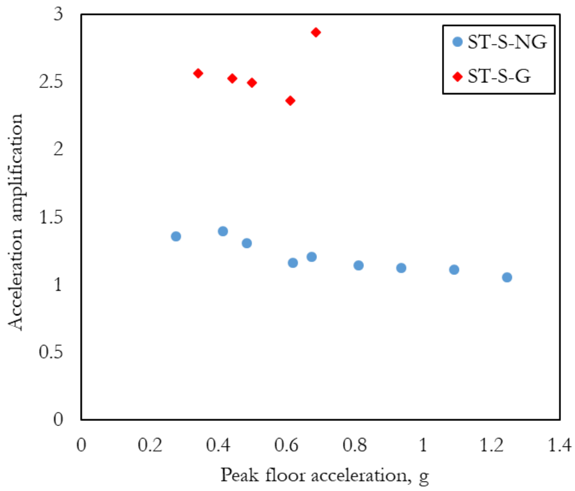

Figure 8. Measured acceleration amplification of stocky specimens

3.2 SLENDER RACK

3.2.1 Failure Mode

The uplift force, induced by overturning moment acting on the slender rack, was large enough to overcome the weight of the rack and lifted up the mounting angle as shown in Figure 9. Thus, rocking motion occurred for all slender specimens. Table 3 summarizes the maximum uplift displacement measured from LVDTs D5 and D6. Vertical displacements of SL-S series were much smaller than SL-L series due to stronger (short l_b) restraint to rigid body rotation. Nonetheless, the maximum uplift displacement of SL-S-NG at TRS 250% was significantly large compared with all other SL specimens since tensile fracture occurred at the angle corner as shown in Figure 9(a). Tests of SL-S-G and SL-L-G were terminated after TRS 200% and 175%, respectively, since translational distortional failure was observed as shown in Figure 10; the same as ST-S-G. Horizontal response was more dominant than vertical response in SL-S-G as shown in Figure 11, unlike SL-L-G which was governed by rocking motion because of weak restraint to uplift.

Table 3. Vertical displacement response of slender specimens

Specimen	Maximum uplift displacement (D5/D6), mm								
	TRS 50%	TRS 75%	TRS 100%	TRS 125%	TRS 150%	TRS 175%	TRS 200%	TRS 225%	TRS 250%
SL-S-NG	0.09/0.11	0.19/0.19	0.28/0.25	0.55/0.35	2.03/2.48	2.41/3.79	3.21/5.41	4.35/9.46	15.3/40.5
SL-S-G	0.24/0.13	0.50/0.44	0.62/0.72	0.87/1.42	1.37/2.44	1.69/3.38	1.99/4.52	-	-
SL-L-NG	0.69/0.52	1.72/1.87	3.02/4.49	10.7/9.87	18.8/21.7	23.8/27.8	33.9/37.9	-	-
SL-L-G	0.89/1.36	2.07/1.75	3.27/4.89	8.40/11.1	17.0/17.4	20.2/20.5	-	-	-

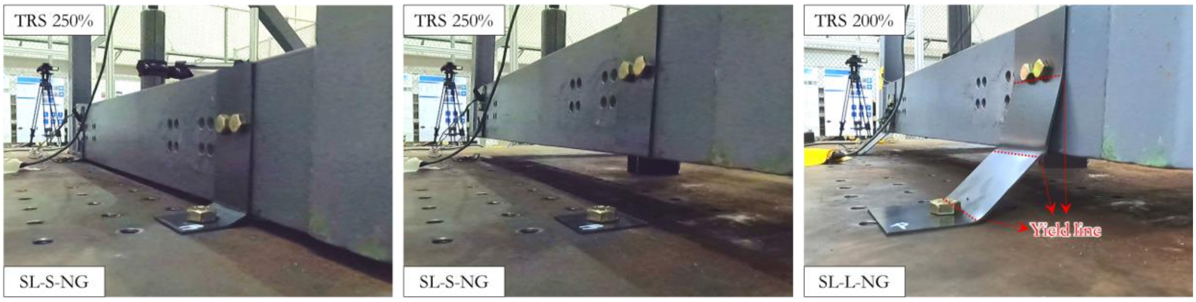

(a) SL-S-NG (TRS 250%, left: uplift, right: fracture of angles) **(b) SL-L-NG (TRS 200%)**

Figure 9. Failure mode of slender specimens with no gap

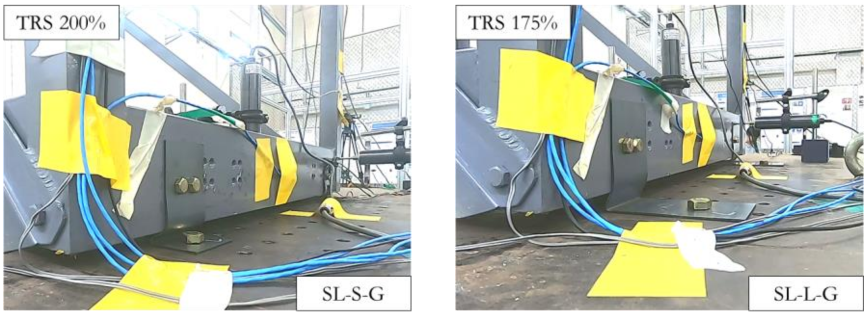

(a) SL-S-G **(b) SL-L-G .**

Figure 10. Translational distortional failure observed from slender specimens with gap

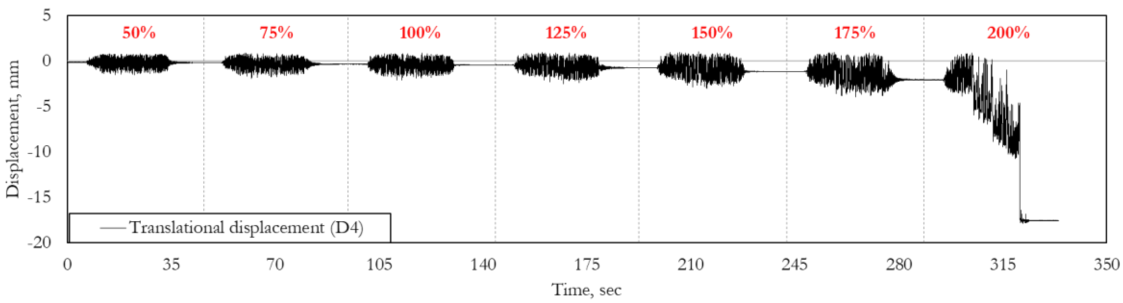

Figure 11. Lateral displacement history of mounting angle measured from specimen SL-S-G (D4)

3.2.2 Hysteretic Behavior

Figure 12 and Figure 13 shows hysteretic behavior of SL specimens for all excitation steps except TRS 250% of SL-S-NG because of the fracture. Hysteretic curves for SL-S-G were determined by the same way as the section 3.1.2 because its governing motion was translational motion. Hysteretic curves for other SL specimens, governed by rocking motion, were determined by the rotation angle calculated from the difference between D5 and D6 divided by the width of the rack and the acceleration measured at lead mass level of the rack (A2).

Symmetric hysteretic behaviors with a negative post-yielding stiffness caused by gravity restoring force were observed from SL-L series (Figure 12). These behaviors were similar to the moment-rotation curve of rocking block with ductile anchor proposed by Makris and Zhang [2001]. Similar hysteretic behavior was also observed in SL-S-NG, although the length of the negative stiffness region was short due to small vertical displacement resulted from short h_b (Figure 13(a)).

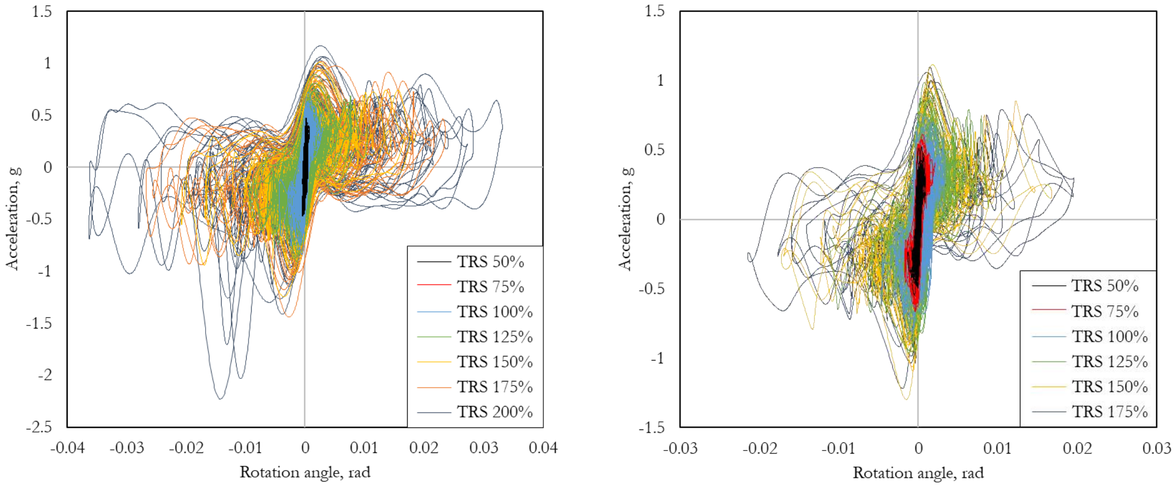

(a) SL-L-NG **(b) SL-L-G**

Figure 12. Observed hysteretic behavior of slender specimens with long l_b

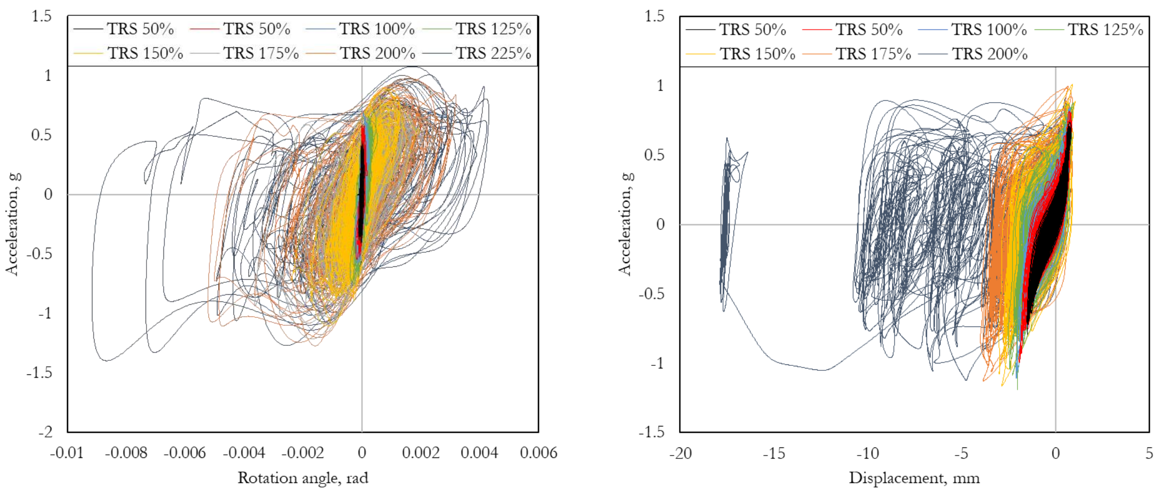

(a) SL-S-NG **(b) SL-S-G**

Figure 13. Observed hysteretic behavior of slender specimens with short l_b

Figure 13(b) shows hysteretic behavior of SL-S-G. Asymmetric hysteretic behavior was also observed from SL-S-G due to the same reason as in ST-S-G and pinched behavior was observed during TRS 50% and 75%. The notable point in SL-S-G is that the area of the hysteretic curve gradually increased as the input motion intensity increases until TRS 200%, when significant lateral displacement of the mounting angles occurred. This increasing energy dissipation capacity seemed to be caused by the friction force produced between bolt head and angle during pinching behavior due to vertical displacement.

3.2.3 Acceleration Amplification

Figure 14 shows the acceleration amplification measured from SL specimens. The amplifications were determined by the same way as the section 3.1.3. SL-S-G showed that the amplification decreases significantly as the peak floor acceleration increases; this seemed to be caused by additional energy dissipation due to friction as mentioned in section 3.2.2, not by the component ductility effect. Other specimens, governed by rocking motion, exhibited amplification decrease up to peak floor acceleration of 0.6g, but the amplification increased beyond 0.6g. Especially, significant increase was observed in SL-L-NG due to hard pounding with the floor which occurred during rocking motion.

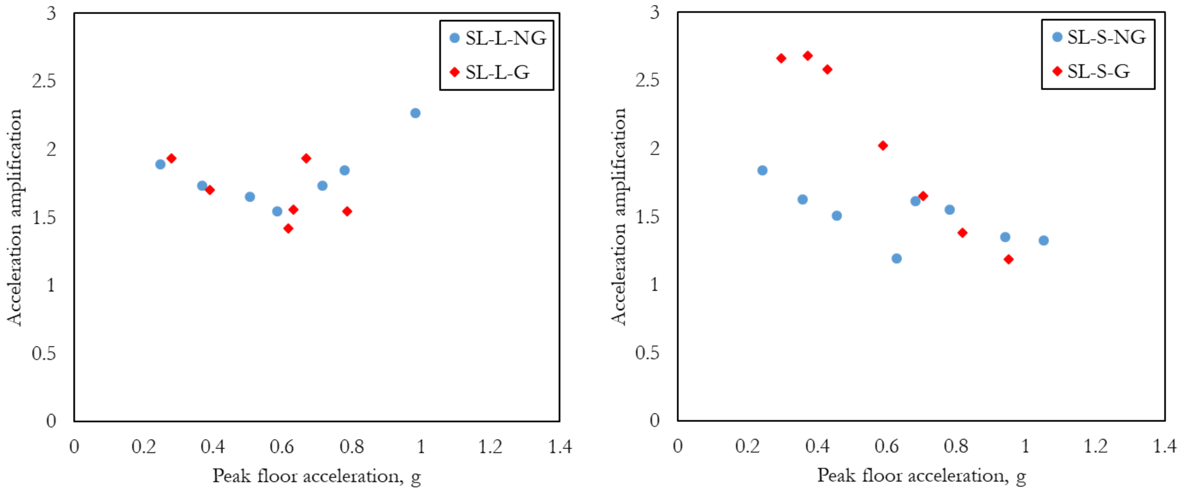

Figure 14. Acceleration amplification measured from slender specimens: left: SL-L series, right: SL-S series

4. SUMMARY AND CONCLUSIONS

In this study, shake-table tests were conducted using two types of steel racks having different slenderness with various configurations of mounting angles to investigate possible failure modes and hysteretic behaviors of floor-mounted NSEs. The results of this experimental study can be summarized as follows:

i. The failure mode and hysteretic behavior varied significantly depending on the slenderness of the steel rack and the connection configuration of the mounting angles such as the gauge length of the angle corner to the anchor bolt, l_b, and gap between the floor and the rack, l_{gap}.

ii. The translational distortional failure of the mounting angle was observed when l_{gap} was long. Under the translational distortional failure mode, the hysteretic behavior was asymmetric and highly pinched. This behavior was seemed to be caused by the clearance around the bolt hole and the accumulated deformation on the side of the crushed angle. Additional energy dissipation by the friction between the angle and the bolt head was observed when the slenderness of the rack was high.

iii. When the slenderness of the rack is high, the behavior was governed by rocking motion and uplift failure of the mounting angle occurred. Symmetric hysteretic behavior with negative post-yielding stiffness caused by gravity force was observed during the rocking-motion, and the acceleration response was amplified due to the pounding with the floor.

iv. The acceleration amplification decreased as the peak floor acceleration increased in all specimens, except when hard pounding with the floor occurred during rocking motion. The reduction in acceleration amplification was largest in specimen SL-S-G in which additional energy was dissipated by the friction between the angle and the bolt head.

v. To develop the ductile design method for floor-mounted NSEs, further experimental and analytical study is needed to identify the major parameters affecting the failure mode and hysteretic behavior.

ACKNOWLEDGEMENT

This work was supported by the National Research Foundation of Korea(NRF) grant funded by the Korea government(MSIT). (No. 2021R1A2C200983)

REFERENCES

AIK [2019] "Seismic Building Design Code, KDS 41 17 00," Seoul, Korea: Architectural Institute of Korea (in Korean).

ASCE/SEI, 7-22 [2022] *Minimum design loads and associated criteria for buildings and other structures*, Reston, VA: American Society of Civil Engineering.

Ciurlanti, J., Bianchi, S., Pürgstaller, A. [2022] "Shake table tests of concrete anchors for non-structural components including innovative and alternative anchorage detailing," *Bulletin of Earthquake Engineering*, Vol. 20, pp. 3971–3993.

Feinstein, T., Moehle, J.P. [2022] "Seismic response of floor-anchored nonstructural components fastened with yielding elements," *Earthquake Engineering Structural Dynamics*, Vol. 51, pp.3– 21.

ICC [2010] *AC 156 Acceptance Criteria for Seismic Certification by Shake-Table Testing of Non-Structural Components*, International Code Council Evaluation Service, Whittier, CA.

Makris, N., Zhang, J. [2001] "Rocking Response of Anchored Blocks under Pulse-Type Motions," *Journal of Engineering Mechanics*, Vol.127, No. 5, pp.484-493.

NIST [2018] "Recommendations for Improved Seismic Performance of Nonstructural Components," *NIST GCR 18-917-43*, National Institute of Standards and Technology.

Quintana Gallo, P., Moghaddasi, M., Pampanin, S., Bergmeister, K. [2018] "Shake Table Tests of Post-Installed Anchors with Supplemental Damping," *ACI Structural Journal*, Vol. 115, No. 3, pp.595-606.

Quintana Gallo, P., Moghaddasi, M., Pampanin, S., Carr, A.J. [2019] "Hysteresis Model for Concrete Anchors Subjected to Shear Loading," *ACI Structural Journal*, Vol. 116, No. 1, pp. 5-16.

Crack widths in concrete floor diaphragms, in relation to selected Power Actuated Fasteners used to attach interior partition walls

Matthew R. Eatherton, S.E. Ph.D.[1], Raul Avellaneda-Ramirez[1], Peter Grzesik[2] and Christopher Gill[3]

[1] Civil and Environmental Engineering, Virginia Tech
750 Drillfield Drive, Blacksburg, VA 24060
e-mail: meather@vt.edu; rear93@vt.edu
[2] Hilti AG, Feldkircherstrasse 100
9494 Schaan, Liechtenstein
e-mail: peter.grzesik@hilti.com
[3] Hilti Inc. 7250 Dallas Pkwy #1000, Plano, TX 75024
e-mail: christopher.gill@hilti.com

Abstract. The damage of non-structural elements is a primary source of economic losses during earthquakes. In particular, interior partition walls are subject to earthquake damage, and they represent a substantial investment. Metal stud drywall partition walls are typically attached to concrete floors using redundant fastening systems, such as light duty anchors and power actuated fasteners (PAF). Currently, ASCE 7 commentary suggests that PAF may be susceptible to pull-out when the concrete slab cracks during seismic excitation, although insufficient data exists to evaluate this concern, especially for applications dominated by short term shear forces, such as cold formed steel track fastening. Furthermore, seismic qualification criteria do not currently exist for such fastening systems and applying criteria for single point anchors may not adequately address the behavior and use of such fastening systems. A detailed investigation to determine crack widths for floor slabs subjected to diaphragm action is not available and therefore required. This paper starts with a discussion of the context and background for issues related to PAF attachment of interior wall partitions to floor slabs. A two-part experimental program is then described including a) crack width measurements for seven concrete-filled steel deck diaphragm specimens and b) evaluation of crack widths around PAF installed in a reinforced concrete slab diaphragm specimen. All specimens were tested in a cantilever diaphragm configuration with 15'x12' between beam centerlines and subjected to cyclic in-plane displacement histories. Crack patterns and crack widths were measured at times during the test, corelated with selected earthquake hazard levels. The second part of the experimental program involved one reinforced concrete slab specimen with PAF installed in various patterns on both faces, representing a range of interior partition wall attachments. The number of PAF crossed by a crack and the associated crack widths are evaluated.

Keywords: Concrete attachment, cracked concrete, floor diaphragm, floor slab, lightweight concrete, interior partitions, Power Actuated Fasteners, redundant fasteners, non-structural systems

1. Introduction

Two of the most common floor systems for non-residential buildings are concrete-filled steel deck for steel buildings and cast in place reinforced concrete slabs for concrete or masonry buildings. These floor slabs serve many critical purposes in the building from structural functions such as supporting gravity loads and acting as a diaphragm to transfer lateral loads to vertical frames, to other functions such as fire protection and acoustical separation. Another, perhaps less studied function of floor slabs is to provide a solid surface to attach non-structural components of the building such as partition walls, ceilings, and building contents.

An efficient way to attach objects to concrete slabs in buildings are Power Actuated Fasteners (PAF). The ease of use, speed of installation, and resulting anchor strength have made PAF a popular fastening method to steel or concrete for light duty applications. Some references suggest, however, that there may be a concern that the pullout strength of PAF may be compromised during extreme loading on the building as the concrete substrate cracks (ASCE 2016). For that reason, building codes limit the strength and use of PAF in concrete for buildings subjected to extreme loads such as earthquakes, due to the absence of relevant research.

In a building system subjected to an earthquake ground motion, the floor slabs act as diaphragms that transfer lateral forces to and between vertical elements of the seismic force resisting system (SFRS). Previous studies have shown that diaphragms designed using conventional methods such as Section 12.10.1 in ASCE 7 (ASCE, 2016) will likely be subject to inelastic deformation demands during the design level earthquake (e.g., Rodriguez et al, 2007, Wei et al. 2020). It may be expected, therefore, that concrete floor slabs acting as diaphragms will experience some cracking during design level seismic events. However, there is little data available about the expected crack sizes and distribution of cracking in building floor slabs during seismic events, and how these cracks might interact with PAF attachments.

The objective of this paper is to fill in some of the research gap by providing data about the size and distribution of cracks in concrete floor diaphragms at several displacement demands that might be related to specific earthquake hazard levels. An experimental study was conducted on eight total cantilever diaphragm specimens, seven constructed using concrete-filled steel deck floor assemblies and one using a cast-in-place reinforced concrete slab. The distribution and width of cracks were measured and recorded at three times during the test.

2. Context and Background

Power Actuated Fasteners (PAF) are commonly used in light duty applications on steel and concrete. The system typically consists of a nail like fastener, a setting tool, and an energy source like powder cartridges, gas cans or batteries (See Figure 1a). The tool and driving energy are used to drive fasteners directly into a suitable base material like concrete, without the need for a drilled pilot hole. The systems contain multiple safety features ensuring safe and productive job site use.

As a result, attachments can be made very fast and efficiently. Compared to drill in single concrete anchors, the capacity of PAF varies more and redundancy, achieved by use of multiple fasteners, is generally recommended. Redundancy may be assumed for applications where forces can be redistributed by the attached system to neighboring fasteners, in case of failures of individual fasteners. Typical examples are light acoustical suspended ceilings, electrical distribution systems or metal stud partitions (See Figure 1b). Often, these systems are mainly attached to concrete floor slabs for load transfer from the non-structural element to the structure.

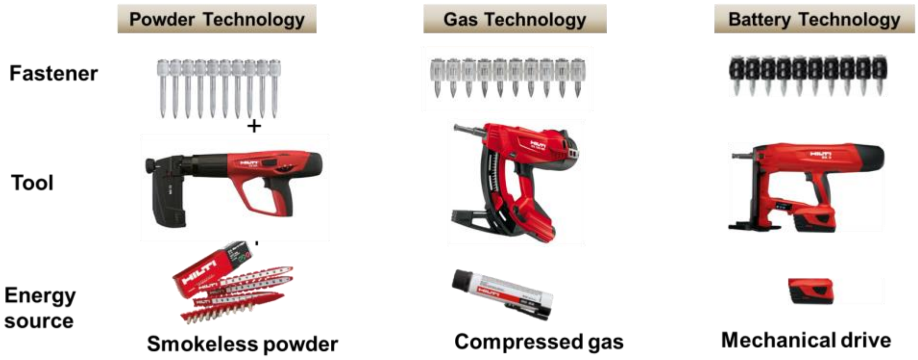

a) Power Actuated Fastener (PAF) systems

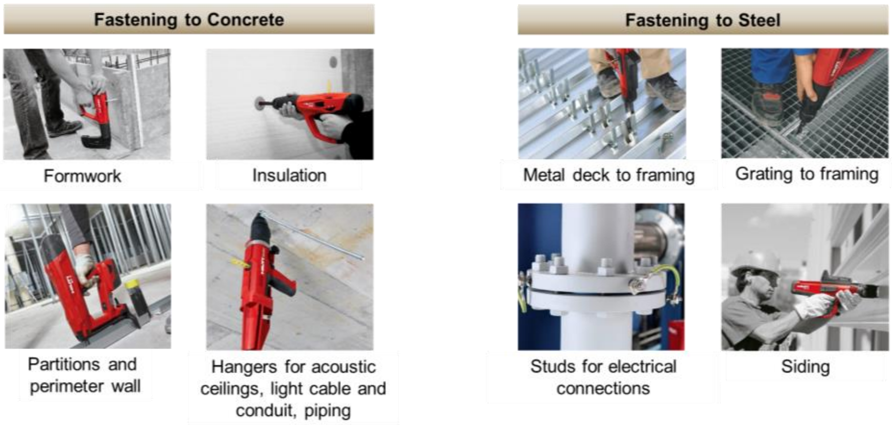

b) Typical applications for power actuated fasteners

Figure 1. Power Actuated Fastener (PAF) systems and applications

Per ASCE (2010, 2016 and 2022), PAF cannot be used for applications in seismic regions under sustained tension loads. An exception is granted for distributed systems (i.e., redundant applications), where the design loads do not exceed 90 lbf per fastener in concrete, or 250 lbf in steel. Such applications are exempt from seismic design. For higher design loads, the approval of the Authority Having Jurisdiction is required, but due to the lack of independent criteria, such approval is typically not requested or granted. While Annex A of ICC-ES AC70 (2021) contains provisions for seismic testing and evaluation of PAF on steel, that allows to qualify PAF for loads higher than 250 lbf, such provisions do not exist for PAF in concrete.

In addition, ASCE (2010, 2016 and 2022) is silent about the use of PAF in applications subject to seismic short term shear loads, like interior partition walls. ICC-ES AC70 (2021), allows for application of the limits in ASCE (2010, 2016) to non-structural elements under (short term) shear loads as well.

Consequently, PAF are used in US seismic regions only for attachments to concrete within the limits set by ASCE (2010, 2016). For example, the California Department of Health Care Access and Information (HCAI) publishes guidance for the use of PAF to attach partitions in hospitals in California in OPD 0001-13, Karim (2014), considering the limitations in ASCE (2010).

On the other hand, where higher or heavier wall configurations are used, or where wall mounted equipment is present, forces can easily exceed the current design capacity limit for PAF in concrete, and seismically qualified concrete anchors are used. Also, the seismic demand calculations for non-structural elements have changed in ASCE (2022), which may lead to an increase of demands for partitions under various conditions. It is expected that ASCE (2022) will be referenced by future building codes in seismic regions.

Since no independent criteria for the seismic qualification of PAF for specific and common applications exist, research is needed to understand relevant boundary conditions. This paper is intended to cover expected shear cracking of concrete floor diaphragms, and the interaction with installed PAF.

Cracking of structural concrete members was investigated by Hoehler (2006) with focus on beams and columns under flexural loading close to plastic hinges. However, cracking in floor slabs may be different, and a related study with a detailed crack analysis is not available. It is the intent of this paper to help investigate this subject in more depth, with a focus on diaphragm shear cracking.

Important factors when evaluating cracking in concrete diaphragms are the typical limit states and the associated areas of the diaphragm subject to cracking. With an idealized uniformly distributed lateral force as shown in Figure 2, the shear force diagram for the diaphragm is linearly varying with maximum shear experienced at the edges of the diaphragm, while the moment diagram reaches maximum at the middle of the diaphragm span. Figure 2a schematically shows the two most common limit states for concrete-filled steel deck diaphragms, perimeter fastener failure (failure of the headed shear studs on the collector), and diagonal tension cracking, both of which are associated with regions of maximum diaphragm shear. Because there are typically steel beams in the floor system perpendicular to the lateral force, and due to the extremely high moment of inertia of the floor slab in the horizontal axis, damage associated with chord forces in a regular building such as shown in Figure 2a are expected to be very rare. Conversely, cast-in-place reinforced concrete diaphragms (Figure 2b) may experience flexural cracking associated with chord forces (diaphragm moment) in addition to diagonal shear cracking, but failure of the lateral force transfer to the shear wall is not expected to be a controlling limit state (unlike perimeter fastener failure in concrete-filled steel deck diaphragms). The width of the zone of diagonal cracking at the end of the diaphragms can vary based on the floor framing, but a review of the literature for steel deck diaphragms suggested that the zone might be 10% of the diaphragm span length (O'Brien et al., 2017), while a recent computational study suggested the width may be limited to one bay (Wei et al., 2020).

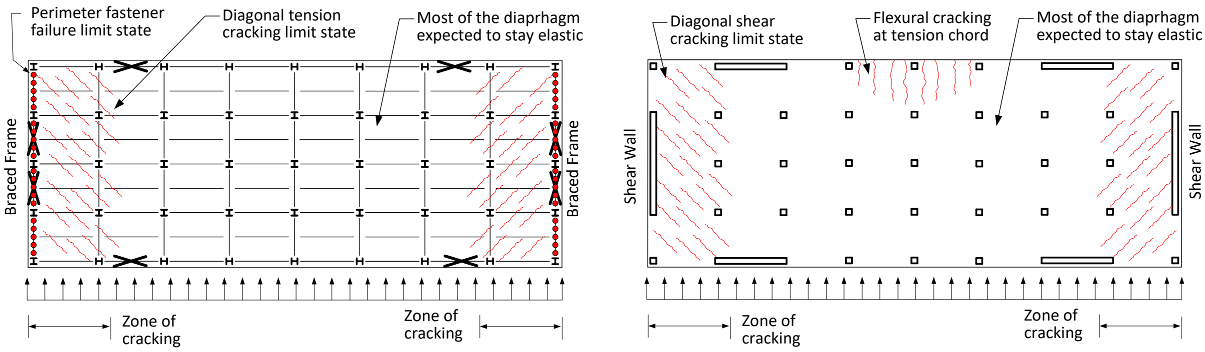

a) Concrete-filled steel deck diaphragm **b) Cast-in-place reinforced concrete diaphragm**

Figure 2. Typical limit states and zones of cracking for floor slab diaphragms

3. Description of the Experimental Program

3.1 SPECIMENS

A total of eight cantilever diaphragm specimens were tested as described in the test matrix given in Table 1. The first seven specimens were concrete-filled steel deck diaphragms which are typical in steel buildings. The steel deck was either 2 in. deep or 3 in. deep Verco FormLok deck. Concrete had a nominal 28-day strength of 4000 psi, and the measured concrete strengths are given in Table 1. Diaphragm specimens were tested 28 days after concrete placement. The first two specimens listed in Table 1 represent floor assemblies that have a 2-hour unprotected fire rating. Four of the concrete-filled steel deck specimens were unreinforced, while three of them had reinforcing steel from welded wire reinforcing steel to #4@12" each way. Both normal weight and lightweight concrete were tested because the use of lightweight concrete is prevalent in seismic zones to reduce building mass.

With the range of variables explored in Table 1, it is expected that the associated tests represent the range of possible cracking that might be expected in concrete-filled steel deck diaphragms whether they are unreinforced or reinforced, have lightweight or normalweight concrete, and experience diagonal tension cracking limit state or perimeter fastener failure. This set of seven specimens was part of a large research project called the Steel Diaphragm Innovation Initiative (SDII) (Avellaneda-Ramirez et al. 2021).

The last specimen listed in Table 1 was a solid reinforced concrete slab that was 5 in. thick with #3 bars at 12 in. spacing each way in the top and bottom of the slab with 3/4 in. cover. This specimen allows the examination of a floor slab that is representative of reinforced concrete and masonry buildings, but also included a total of 113 PAF in both the top and bottom surfaces to examine the number and size of cracks crossing the fasteners. For additional details on the specimens, see Avellaneda-Ramirez et al. (2021a), Avellaneda-Ramirez and Eatherton (2021), and Eatherton et al. (2019).

Table 1. Test matrix

Specimen Name	Concrete Type	Measured Concrete Strength (psi)	Steel Deck Height (in.)	Total Slab Depth (in.)	Comment
3/6.25-4-L-NF-DT	LW	3990	3	6.25	2 Hour fire rated assembly, unreinforced
3/7.5-4-N-NF-DT	NW	3940	3	7.5	2 Hour fire rated assembly, unreinforced
2/4-4-L-NF-DT	LW	3800	2	4	
2/4.5-4-L-RS-DT	LW	3950	2	4.5	#4 bars at 12 in. spacing each way
3/6.25-4-L-RS-DT	LW	4350	3	6.25	6x6 D2.1xD2.1 welded wire reinforcement
3/7.5-4-N-RS-DT	NW	4070	3	7.5	#3 bars at 18 in. spacing each way
3/7.5-4-N-NF-P	NW	4820	3	7.5	Shear studs at 36 in. spacing to fail studs
5-3.5-N-SOLID	NW	3700	5 in. solid slab		#3 bars at 12 in. each way top and bottom

LW = lightweight concrete, NW = normalweight concrete

3.2 Test Setup

The test setup is shown in Figure 3 wherein one edge of the specimen is attached to reaction frames and the opposing edge is subjected to a cyclic displacement history by two actuators. These cantilever specimens represent a portion of the diaphragm in the end region (zone of cracking) of the diaphragm span shown in Figure 2. Figure 3b shows the solid slab specimen with PAF typically used to attach cold formed steel framing members to concrete that were installed in the top surface of the specimen.

The same PAF were installed in the bottom face of the specimen, but with different locations (See Avellaneda-Ramirez and Eatherton (2021) for additional details).

The load was introduced into the testing frame using a pair of servo-controlled hydraulic actuators working in tandem. The control actuator was displacement-controlled while the following actuator was force-controlled to apply a force in the opposite direction with a magnitude equal to the force in the master actuator multiplied by the ratio of following to master actuator force capacities.

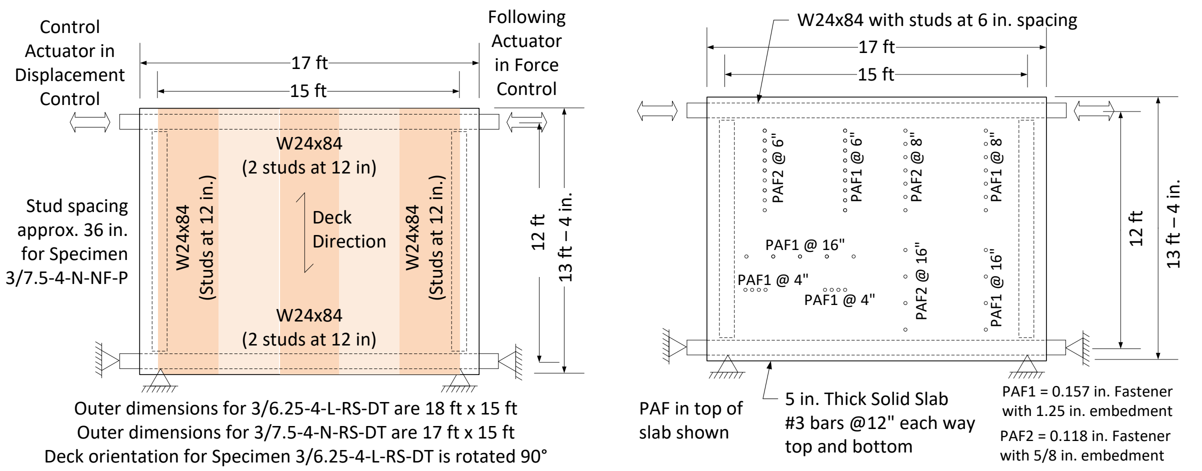

a) Concrete-filled steel deck specimens **b) Cast-in-place reinforced concrete specimen (top of slab)**

Figure 3. Test specimen and test setup details

3.3 LOADING PROTOCOL AND HAZARD LEVELS

The cyclic loading protocol was based on FEMA 461 (FEMA 2007), Section 2.9.1, and included at least six cycles before reaching the elastic limit. The loading protocol includes two cycles for every displacement step with a 40% increase in amplitude between displacement steps.

Crack patterns and crack widths were typically measured and documented at four times during the test: 1) before testing, 2) at approximately 2/3 the peak shear strength, 3) at approximately the peak shear strength, and 4) at a displacement that was two times the diagonal tension cracking displacement.

The second point at 2/3 peak shear strength is loosely associated with the design earthquake (DE) hazard level based on the following logic demonstrated graphically in Figure 4a. Concrete-filled steel deck diaphragms use a resistance factor, ϕ=0.5, and have a nominal strength that is approximately 2/3 of the expected max strength calculated using AISI S310-16 (O'Brien et al. 2017). According to Rodriguez et al. (2007), the elastic diaphragm design forces can be two to three times larger than what would be predicted using conventional diaphragm design. Assuming a factor of two, the expected DE diaphragm force demands would be approximately equal to the nominal diaphragm strength, V_n, because the factor of two offsets the resistance factor.

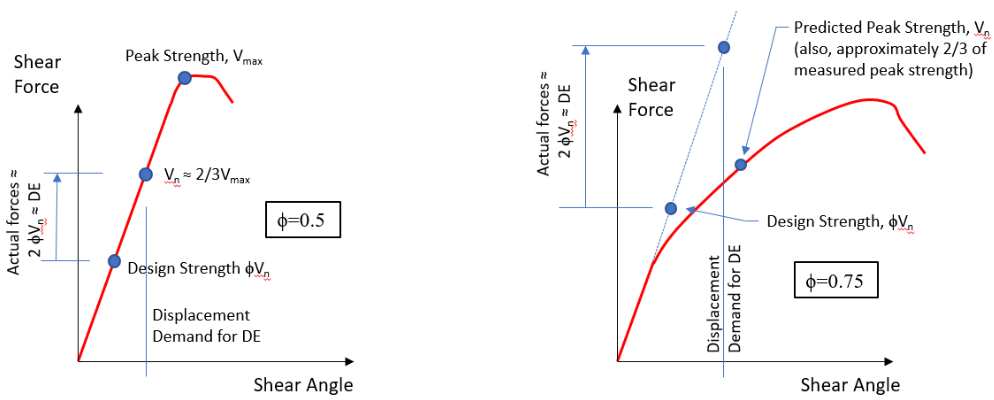

a) Unreinforced concrete-filled steel deck specimens **b) Cast-in-place reinforced concrete specimen**

Figure 4. Graphical explanation for correlation to design earthquake Level

For the cast-in-place reinforced concrete slab, the force vs. shear angle behaviour is nonlinear and the correlation between the point at 2/3 peak shear strength is associated with DE hazard level for a different reason. The equal displacement concept, first formulated by Newmark and Hall (1982), states that the peak displacement of a long period structure subjected to an earthquake ground motion will be similar regardless of the whether the system is elastic or inelastic. A DE displacement demand is therefore calculated as shown in Figure 4b as the expected diaphragm force of $2\phi V_n$ divided by the initial stiffness. The DE displacement demand was found to be similar to the displacement at 2/3 peak shear force as shown in Figure 4b. For specific values, see Avellaneda-Ramirez et al. (2021b).

It is sometimes assumed that the maximum considered earthquake (MCE) level forces are 3/2 the DE level forces (e.g., ASCE 7). Since the DE level forces are approximately 2/3 of the peak shear strength of the diaphragm, the point in the test at peak shear strength is assumed to be loosely associated with the MCE hazard level.

4.Crack Patterns and Widths

The experimental program generated a substantial amount of useful data about the cyclic behaviour of concrete-filled steel deck and solid slab diaphragms. The focus of this paper is on distribution of cracks and associated crack widths. For more information about diaphragm behaviour see Avellaneda-Ramirez et al. (2021b; 2022). Cracks were marked on the slab and crack widths were measured using one of three methods: a crack card with increments of crack width from 0.005 in. to 0.1 in., a crack microscope, or a digital calliper with 6 in. range when cracks exceeded 0.1 in. in width.

4.1 CONCRETE-FILLED STEEL DECK DIAPHRAGMS

For unreinforced concrete-filled steel deck diaphragms, the specimens stay relatively elastic and diagonal tension cracking is associated with a sharp drop in shear strength as shown in Figure 5a. Several diagonal tension cracks form in each direction when this occurs as shown in Figure 5b, but the typical crack widths are between 0.004 in. to 0.03 in. while the maximum crack width is up to 0.075 in. as given in the first three rows of Table 2. As the cyclic displacement protocol continues, a few new cracks form, but a subset of the cracks grow substantially in width compared to others such as Specimen 3/7.5-4-N-NF-DT where one of the cracks opened to 1.4 in. width at a specimen displacement that was twice that at peak load (Table 2).

With the addition of reinforcing steel, there are generally more cracks and cracks are more distributed across the specimen. As shown in Figure 5a, there is additional strength gain after diagonal tension cracks form (shown as change in slope in shear force vs. shear angle response), and additional cracks continue to form and propagate. To see the effect of reinforcing steel on crack patterns, Figure 5c which shows the crack pattern at peak load for Specimen 3/7.5-4-N-RS-DT having #3 @18" each way, is compared with Figure 5b which is nominally identical but without reinforcing steel. Although the specimen with reinforcing steel has more cracks, the crack widths shown are not smaller at peak load (Table 2 and Figure 6) because the specimen with reinforcing steel goes through larger shear angle to get to peak load than the unreinforced specimen. Reinforcing steel does reduce the crack widths during post-peak displacements as shown in Table 2 and Figure 6.

When the controlling limit state for the concrete-filled steel deck diaphragm is perimeter fastener failure (i.e., failure of the headed shear studs), there is little cracking and cracks, and related damage, are typically concentrated along the edge as shown in Figure 5d. The few cracks that do form can be of similar width as the specimens experiencing diagonal tension cracking as described in Table 2 and Figure 6.

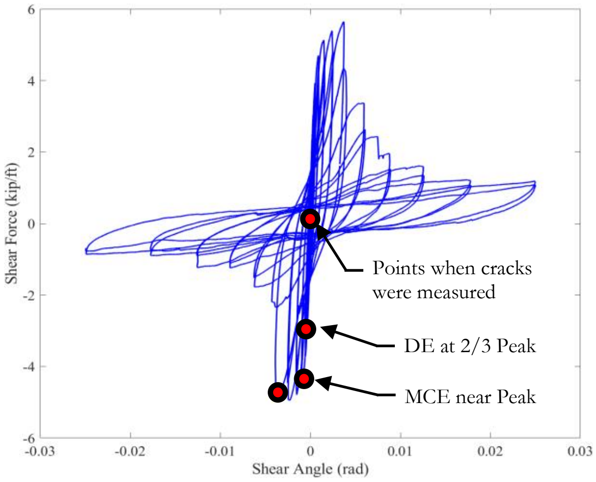

a) Specimen 3/7.5-4-N-RS-DT behaviour

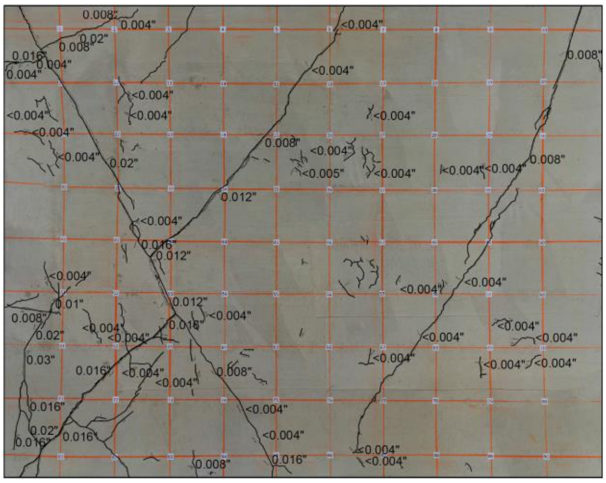

b) Specimen 3/7.5-4-N-NF-DT at peak load (MCE)

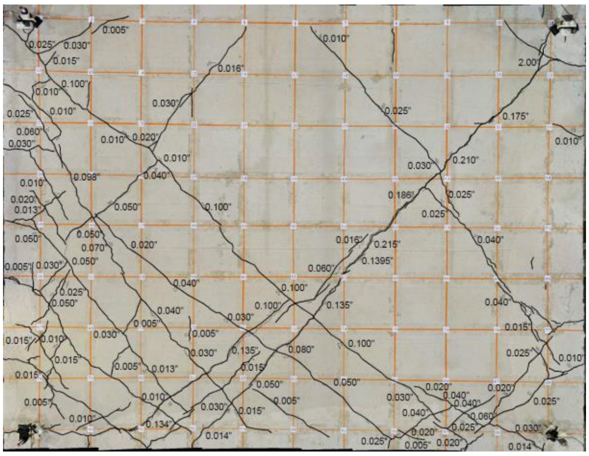

c) Specimen 3/7.5-4-N-RS-DT at peak load (MCE)

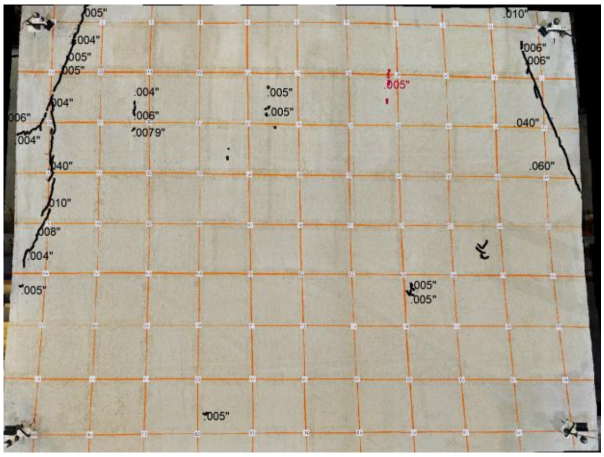

d) Specimen 3/7.5-4-N-NF-P at peak load (MCE)

Figure 5. Example cracking patterns and crack widths for concrete-filled steel deck diaphragms

Table 2. Results for concrete-filled steel deck diaphragm specimens

	Before Test		2/3 Peak (DE)		Peak Load (MCE)		2X Displ. At Peak Load	
Specimen Name	Max Width (in.)	Typical Width (in.)	Max Width (in.)	Typical Width (in.)	Max Width (in.)	Typical Width (in.)	Max Width (in.)	Typical Width (in.)
3/6.25-4-L-NF-DT	0.018	0.002 to 0.004	0.025	0.005 to 0.01	0.075	0.005 to 0.032	0.25	0.005 to 0.2
3/7.5-4-N-NF-DT	None Found	None Found	0.008	0.002 to 0.004	0.03	0.004 to 0.016	1.4	0.004 to 0.3
2/4-4-L-NF-DT	0.02 in.	0.005 to 0.015	0.02	0.005 to 0.02	0.075	0.005 to 0.03	0.1	0.005 to 0.075
2/4.5-4-L-RS-DT	0.01	0.004 to 0.006	0.016	0.004 to 0.016	0.02	0.004 to 0.02	0.025	0.004 to 0.025
3/6.25-4-L-RS-DT	<0.004	<0.004	0.004	0.004	0.08	0.004 to 0.08	0.122	0.004 to 0.122
3/7.5-4-N-RS-DT	None Found	None Found	None Found	None Found	0.215	0.005 to 0.215	0.825	0.01 to 0.825
3/7.5-4-N-NF-P	None Found	None Found	None Found	None Found	0.06	0.004 to 0.06	1.077	0.004 to 1.077

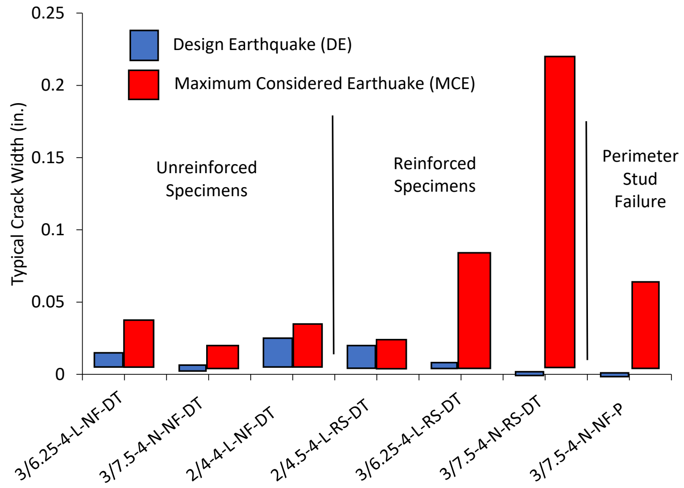

Figure 6. Range of typical crack sizes for each specimen, representing a bay at the end of a diaphragm span

4.2 CAST-IN-PLACE REINFORCED CONCRETE DIAPHRAGM

The goals for the cast in place reinforced concrete diaphragm were a) to evaluate cracking patterns in this type of diaphragm assembly, and b) to understand the likelihood of cracks crossing locations where PAF were installed on the top and bottom surfaces of the specimen. The PAF were not subjected to load in this testing program.

As shown in Figure 7a, the reinforced concrete diaphragm can hold strength through larger shear angles (i.e., larger ductility), and larger deformation capacity. In the positive loading direction, the specimen held a strength near its peak load through 1% shear angle. Many cracks formed over the surface of the specimen as shown in Figure 7b, but the cracks did not seem to be drawn to the PAF locations. That is, some cracks formed or propagated near the PAF, but did not deviate from their path to reach the PAF. Figure 7b shows the cracking pattern on the top of the slab at the peak load and PAF locations where a crack crossed the PAF are identified with a red circle and red plus sign (+). As given in Table 3, 55% of the PAF had cracks going through their location at peak load, but the crack widths were smaller than the concrete-filled steel deck specimens because the specimen had a higher reinforcing ratio with two mats of reinforcing steel compared to one or none in the other specimens. Crack widths averaged 0.02 in. with a range of 0.006 in. to 0.03 in. at the peak load as given in Table 3 and shown in Figure 8.

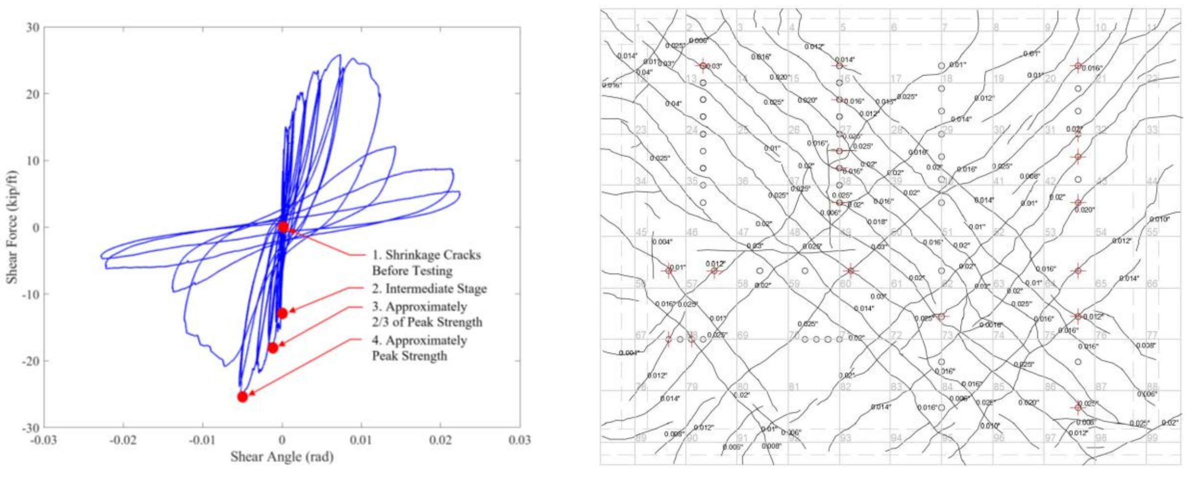

a) Hysteretic behaviour specimen 5-3.5-N-SOLID **b) Specimen 5-3.5-N-SOLID at 2/3 peak load (DE) top of slab**

Figure 7. Example cracking patterns and crack widths for concrete-filled steel deck diaphragms

Table 3. Results for Cast-In-Place Reinforced Concrete Diaphragm Specimen[1]

	Top of Slab		Bottom of Slab		Percent of Total	Minimum Crack Width (in)	Maximum Crack Width (in)	Average Crack Width (in)
Time During Test [2]	PAF2 [1]	PAF1 [1]	PAF2 [1]	PAF1 [1]				
At Intermediate Stage	0	3	1	3	6%	0.004	0.03	0.012
At 2/3 of Peak Load (~DE)	2	17	4	20	38%	0.006	0.03	0.02
At Peak Load (~MCE) [3]	8	21	NA	NA	55%	0.014	0.25 [4]	0.04

[1] PAF1=0.157in. fastener with 1.25 in. embedment; PAF2=0.118 in. fasteners with 5/8 in. embedment

[2] No shrinkage cracks were observed at the start of the test.

[3] Cracks at bottom of slab at or above peak load not measured for safety considerations

[4] Maximum crack width was related to one crack in one corner; next largest crack was 0.1 in.

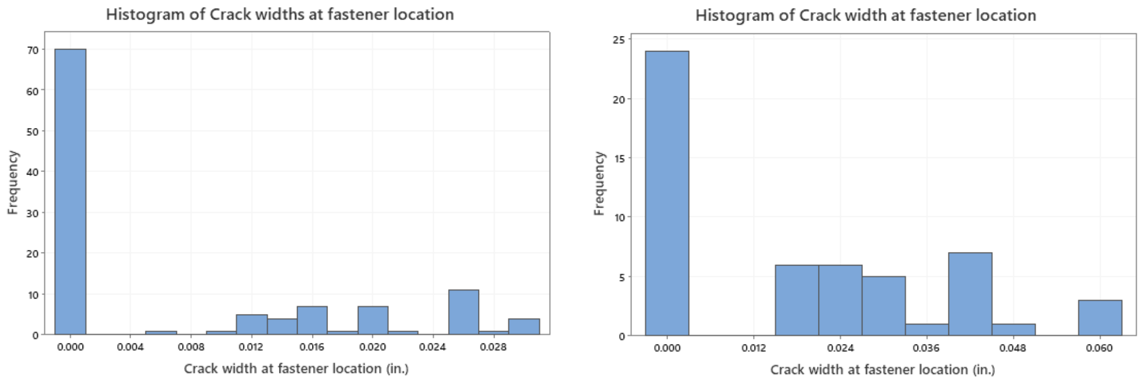

a) Design Earthquake Level (DE) **b) Maximum Considered Earthquake Level (MCE)**

Figure 8. Crack width distribution at fastener location, representing a bay at the end of a diaphragm span

After achieving the peak load, associated with the MCE level, the PAF were generally intact, without showing signs of loosening or falling out. However, the impact of concrete cracking on the tension or shear capacity of PAF in redundant applications, were not investigated in this program. It is recommended to investigate this subject in additional research.

5. Summary and Conclusions

A set of eight cantilever diaphragm tests were conducted to examine the distribution and widths of cracks that form as the diaphragm is subjected to shear angles that are loosely associated with design earthquake (DE) and maximum considered earthquake (MCE) hazard levels. The importance of this type of data is discussed in the context of understanding how non-structural attachments using systems like power actuated fasteners (PAF) might interact with diaphragm shear cracks in concrete floors caused by an earthquake. The cracking behaviour of unreinforced and reinforced concrete-filled steel deck diaphragms, as well as a cast-in-place reinforced concrete diaphragm were presented and discussed.

ACKNOWLEDGEMENTS

The measurement of crack patterns and widths, along with the subsequent processing and crack mapping was supported by Hilti Corporation. The diaphragm tests were supported by the National Science Foundation under Grant No. 1562669 and the Steel Diaphragm Innovation Initiative, which is funded by AISC, AISI, SDI, SJI, and MBMA. In-kind support was provided by Nelson, a Stanley Engineered Fastening Brand. Any opinions expressed in this paper are those of the authors alone, and do not necessarily reflect the views of the National Science Foundation or other sponsors.

REFERENCES

AISI. (2016). North American Standard for the Design of Profiled Steel Diaphragm Panels, AISI S310-16. American Iron and Steel Institute.

ASCE (2010, 2016, 2022). Minimum Design Loads and Associated Criteria for Buildings and Other Structures ASCE/SEI 7-10, -16, -22, American Society of Civil Engineers (ASCE).

Avellaneda-Ramirez, R. and Eatherton, M.R. (2021) Cantilever Diaphragm Test of a Solid Reinforced Concrete Slab with Hilti Power Actuated Fasteners, Virginia Tech Structural Engineering and Materials Report No. CE/VPI-ST-21/03

Avellaneda-Ramirez, R., Bise, E., Laferney, R. and Eatherton, M.R. (2021a) Crack Mapping and Measurements for Concrete-Filled Steel Deck Diaphragms – Phase 2, Virginia Tech Structural Engineering and Materials Report No. CE/VPI-ST-21/01

Avellaneda-Ramirez, R. E., Eatherton, M. R., Easterling, W. S., Schafer, B., and Hajjar, J. (2021b). Cantilever Testing of Concrete-Filled Steel Deck Composite Diaphragms Using Various Types of Steel Reinforcing. Cold-Formed Steel Research Consortium Report Series. CFSRC R-2021-02.

Avellaneda-Ramirez, R. E., Eatherton, M. R., Easterling, W. S., Schafer, B., and Hajjar, J. (2022). Stiffness of Concrete-Filled Steel Deck Composite Diaphragms. Cold-Formed Steel Research Consortium Report Series. CFSRC R-2022-01.

Eatherton, M.R., McEntee, A., and Avellaneda-Ramirez, R. (2019) Crack Mapping and Measurements for Concrete on Metal Deck Diaphragms, Virginia Tech Structural Engineering and Materials Report No. CE/VPI-ST-19/01

FEMA. (2007). Interim Testing Protocols for Determining the Seismic Performance Characteristics of Structural and Nonstructural Components, FEMA 461. Applied Technology Council, Federal Emergency Management Agency.

Hoehler, M. (2006). Behavior and Testing of Fastenings to Concrete for Use in Seismic Applications, University of Stuttgart, 2006

ICC-ES AC70 (2021). Acceptance Criteria for Power Actuated Fasteners driven into Concrete, Steel, and Masonry Elements, International Code Council – Evaluation Services (ICC-ES), 2021

Karim, M (2014): OPD 0001-13: 2013 CBC Standard Partition Details, Department of Healthcare Access and Information (HCAI), 2014

Newmark, N M, and W J. Hall (1982). Earthquake Spectra and Design. Berkeley, Calif: Earthquake Engineering Research Institute.

O'Brien, P., Eatherton, M. R., & Easterling, W. S. (2017). Characterizing the load-deformation behavior of steel deck diaphragms using past test data. Cold-Formed Steel Research Consortium, Report Series, CFSRC R-2017-02.

Rodriguez, M. E., J. L. Restrepo, and J. J. Blandon (2007). Seismic design forces for rigid floor diaphragms in precast concrete building structures. J. Struct. Eng. 133 (11): 1604–1615.

Wei, G., Eatherton, M.R., Foroughi, H., Torabian, S., and Schafer, B.W. (2020). "Seismic Behavior of Steel BRBF Buildings Including Consideration of Diaphragm Inelasticity", Cold-Formed Steel Research Consortium, Report Series, CFSRC R-2020-04.

Performance of Power Actuated Fastener Connections for Cold-Formed Steel Framing Elements

Arturo E. Schultz[1], Scott D. Overacker[2], David Amori[3], Peter Grzesik[4], Chris Gill[5]

[1] University of Texas at San Antonio
One UTSA Circle, San Antonio, TX 78249
e-mail: arturo.schultz@utsa.edu
[2] Ulteig Engineers, Inc., 4285 Lexington Ave N, St. Paul, MN 55126
e-mail: overa16@umn.edu
[3] University of Texas at San Antonio
One UTSA Circle, San Antonio, TX 78249
e-mail: david.amori@utsa.edu
[4] Hilti AG, Feldkircherstrasse 100
9494 Schaan, Liechtenstein
e-mail: peter.grzesik@hilti.com
[5] Hilti Inc. North America
7250 Dallas Pkwy #1000, Plano, TX 75024
e-mail: christopher.gill@hilti.com

Abstract. Proper evaluation of non-structural components is essential in seismic design to ensure safety and damage control. Of interest here are cold formed steel (CFS) framing applications, such as drywall partitions and exterior walls, which are sensitive to damage at lower levels of seismic demand. Research on the seismic behaviour of typical fasteners (PAF's) for attachment to concrete is rare. Consequently, the use of seismically qualified single-use post installed expansion, screw or similar anchors may be preferred, given the limited knowledge of PAF performance. To meet this need, a multi-phase investigation is ongoing to address: the influence of concrete aggregate, behaviour and redundancy effects of fastener groups, the influence of concrete cracks and the behaviour under cyclic shear loading. The ultimate goal is to develop a database and test criteria for PAF connections in seismic conditions. The first phase focused on monotonic performance of single PAFs and PAF groups, in uncracked concrete, under out- of-plane loading, with a focus on the influence of concrete aggregate. The second phase focuses on PAFs in normal and lightweight concrete with cracks under simulated seismic motion. The intent is to validate boundary conditions for use of PAFs in seismic conditions for track fastening to concrete with a view toward more economic installation and to improve clarity on the boundaries for such use. This paper demonstrates, by experiment, the influence of aggregate type on performance under monotonic demand of single PAFs and PAF groups loaded out-of-plane in uncracked concrete. Lastly, the paper presents the experimental program in the ongoing phase to address cyclic loading of PAF groups in cracked concrete.

Keywords: Concrete, Cold-formed steel, Experiments, Out-of-plane, Power actuated fastener, seismic.

Introduction

Despite the importance of the behaviour and capacity of PAF attachments on the performance of dry-wall) systems, there is precious little information available in the technical literature. Thus, the project summarized here is intended to begin to fill this knowledge gap. This paper offers highlights of the first phase of a research program focused on the performance of PAF attachments between cold-formed steel track and concrete slabs, in which drywall partitions and the connected track are loaded out-of-plane. In this phase, the monotonic performance of single PAFs and PAF groups in a track in uncracked concrete are investigated with a focus on the influence of concrete mix with an emphasis on the aggregate. The second phase of the investigation, which is currently ongoing, focuses on PAF groups in cracked concrete under simulated seismic motion and in both normal and lightweight concrete. The intent is to validate boundary conditions for use of PAFs in seismic conditions for track fastening to concrete with a view toward more economic installation and to improve clarity on the boundaries for such use. This paper demonstrates, by experiment, the influence of aggregate type on performance under monotonic demand of single PAFs and PAF groups loaded out-of-plane in uncracked concrete. Additionally, fastener group tests are shown to have significant redundancy effects. Lastly, the paper discusses a planned experimental program in the ongoing phase to address cyclic loading of PAF groups in cracked concrete.

Role of Aggregates

Current acceptance criteria [1] for the use of power-actuated fasteners (PAFs) primarily define concrete compressive strength (f_c'), relative concrete density (e.g., lightweight or normalweight), fastener type, and embedment depth to determine the allowable loads for PAFs installed in concrete for non-seismic conditions. It is assumed herein that key influence factors on the performance of PAFs such as the impact of concrete aggregate on PAF performance are not fully captured by the limited set of parameters covered by the criteria [1]. In particular, the composition, properties, and distribution of the coarse aggregate is believed to have a substantial impact on the capacity of a PAF installed in concrete. However, only a very generic concrete aggregate specification is provided in current acceptance criteria [1] which are used by the labs that perform qualification tests of PAFs.

Overacker [2] investigated the potential applicability of various characteristics of concrete aggregate and the corresponding ASTM standards for testing aggregate to be used in concrete mixes for PAF qualification tests [3-9]. Of the parameters investigated the following were found to be relevant for the performance of PAFs in concrete: Unit Weight, Voids between Particles, Deleterious substances, Specific Gravity and Absorption, Resistance to Degradation by Abrasion and Impact, and Gradation and Maximum Aggregate Size. He further surmised that Unit Weight, Specific Gravity, Absorption, and Resistance to Degradation by Abrasion and Impact would depend on the mineralogic composition of the aggregate; Voids between Particles would be controlled by the Gradation of the aggregate; and those Deleterious substances would be controlled by requiring that aggregate and mixing water meet ASTM requirements. Overacker [2] also investigated the mineralogic composition commonly found for aggregate sources regionally in the US using geographical maps developed by tool producers for concrete drills.

Prototype Concrete Mixes

One the basis of the foregoing, Overacker [2] proposed three concrete mixes (Table 1) for PAF qualification tests: Tough Normal-weight concrete (NWC), Standard Normal-weight concrete (NWC), and Sand Lightweight concrete (LWC). These mixes vary mainly due to the aggregate type, with limestone, gravel/river rock, granite/trap rock, respectively, being described in a relative manner as soft-to-medium soft, medium-to-medium hard, and hard-to-very hard. It was further deemed that sources of hard-to-very hard aggregate are scarce in regions where most labs that perform qualification tests are found. Thus, the hard-to-very hard category was dropped from further consideration. Additionally, lightweight concrete is used frequently in regions of high seismic hazard, so it was added to the test program. Strength development of the used concrete specimens is shown in Figure 1.

Table 1 - Concrete mix designs and aggregate properties used for testing

Mix Designation	Tough NWC	Standard NWC	Sand LWC
Mix Properties			
Target Strength	4,000 psi (27.6 MPa)	4,000 psi (27.6 MPa)	4,000 psi (27.6 MPa)
Cement Type	Type I/II	Type I/II	Type I/II
Unit Weight	148 pcf (2,370 kg/m^3)	149 pcf (2,390 kg/m^3)	120 pcf (1,920 kg/m^3)
Admixtures	None	None	None
W/C ratio	0.57	0.68	0.64
F/C Weight Ratio	0.79	0.92	2.08
Coarse Aggregate Properties			
Supplier	Aggregate Industries	Falkstone	Trinity
Quarry or Plant	St. Croix	Trenhaile	Baton Rouge
Location	Shafer, MN	Northwood, IA	Baton Rouge, LA
Classification	Gravel/River Rock	Limestone	Expanded Shale/Clay
LA abrasion loss [7]	16%	22%	n/a
Gradation [9]	#67	#57	2.36 mm to 9.5 mm

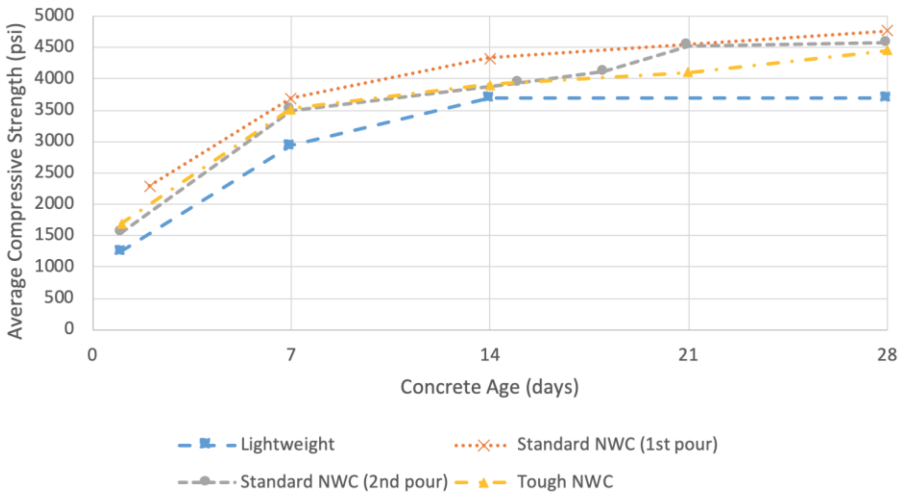

Fig. 1 Concrete strength gain with time curves

In all tests, slabs were cast using one of the three mixes listed in Table 1 were used. Strength and relative weight (lightweight, normal weight) are currently the main concrete properties considered for PAF testing, and existing acceptance criteria [1] define an acceptable strength range of +1,000 psi (6.9 MPa)/-400 psi (2.8 MPa) relative to the desired strength based on field-cured cylinders. The target strength for this project was 4,000 psi, so field-cured cylinders with strengths between 3,600 and 5,000 psi at the time of testing were deemed acceptable per existing requirements. Concrete aggregate complied with ASTM C33 [9], which offers a large variety of gradations. Concrete strengths at 28 days were determined to be 3,700 psi (21.2 MPa), 4,570 psi (31.5 MPa) and 4,460 psi (30.7 MPa), respectively for the Sand LWC, Standard NWC (2nd pour) and Tough NWC concrete mixes. Concrete strength gain curves are shown in Fig. 1 For the Standard NWC, a second pour was done because the first pour was expected to exceed target strengths based on the 7- and 14-day breaks. Only the slabs cast from the second pour of Standard NWC were used in the PAF tests.

Test Parameters

Given that concrete strength was kept within acceptable bounds of the 4,000 psi (2.76 MPa) target, the test variables were test type, nail type, track thickness and installation tool type. Both single nail tests (Fig. 2a) and PAF group tests (Fig. 2b) utilizing cold-formed steel track were conducted. In both cases the PAFs were driven into concrete slabs that were large enough to permit multiple tests, and to exclude any influences of close edges. Testing of single PAFs in shear was done at Element Materials Technology (Element) in St. Paul, Minnesota with a shear loading device in which a loading actuator pulled a cold-formed steel sheet, and displacements were measured using a string potentiometer. The group tests (Fig. 2a) were conducted at the University of Minnesota, Twin Cities, and the steel track was engaged by a steel crosshead that attached to two steel members which were supported on low-friction bearing tracks and were activated by a hydraulic actuator. The concrete slabs were approximately 8 ft (2.44 m) long, 4 ft (1.22 m) wide and 6.5 in. (165 mm) thick. The slabs were cast using the concrete mixes identified in Table 1 and ready-mixed concrete sources will be used to supply the mixes. Each slab accommodated up to ten tracks that were fastened to the concrete using four (4) PAFs each. All fasteners were driven by Hilti tools powered by powder cartridges or an electro-mechanical drive.

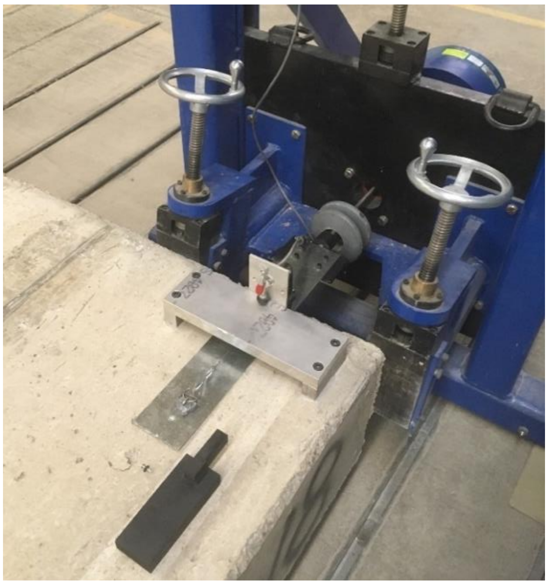

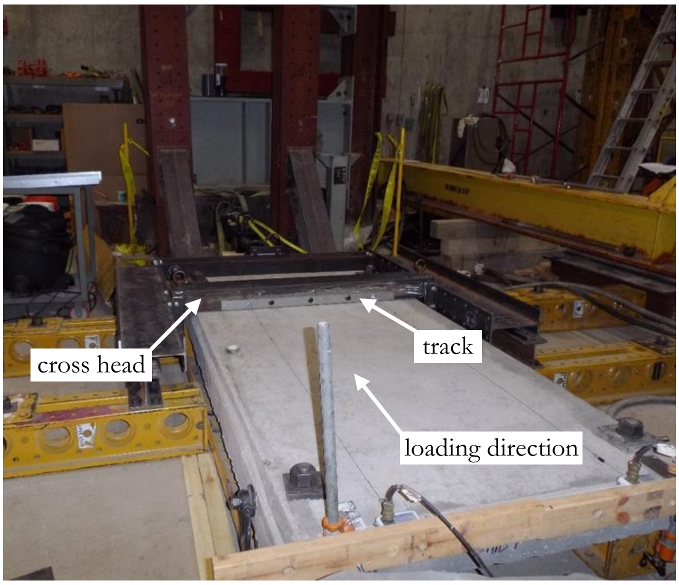

a) Single nail test b) PAF group Test

Fig. 2 PAF Test Setups

Two types of nails were used in the tests, with one type being PAFs with a 1-1/6 in. (27.0 mm) length, a 0.157 in. (4.0 mm) shank diameter, a Long Conical point profile and a Rockwell Hardness of 59. The other type had a 25/32 in. (19.8 mm) length, a 0.118 in. (3 mm) shank diameter, a Ballistic point profile and a Rockwell Hardness of 57.5. The 0.157 in. diameter fasteners were driven with a powder tool (Hilti DX5), while the 0.118 in. diameter PAFs were driven by a battery-operated tool (Hilti BX3). Note that the 0.118 in. diameter fasteners were not tested in the tough NWC due to manufacturer recommendations.

Four PAFs were used to attach a single cold-formed steel track segment to the concrete slab in each group test. All tracks had a 6" (152 mm) web, 2" (51mm) flange, and 3' (914 mm) length with either a 16-gauge (54 mils) thickness for use with 0.157 in. diameter fasteners, or 20-gauge (33 mil) thickness for use with 0.118 in. diameter fasteners. The 16-gauge steel tracks were made from steel with a nominal yield strength of 50 ksi (345 MPa), and the 20-gauge steel tracks had a nominal yield strength of 33 ksi (228 MPa). These are the highest material strengths typically available for steel tracks of these thicknesses. The PAFs were placed with the spacing and edge distances shown in Fig. 3.

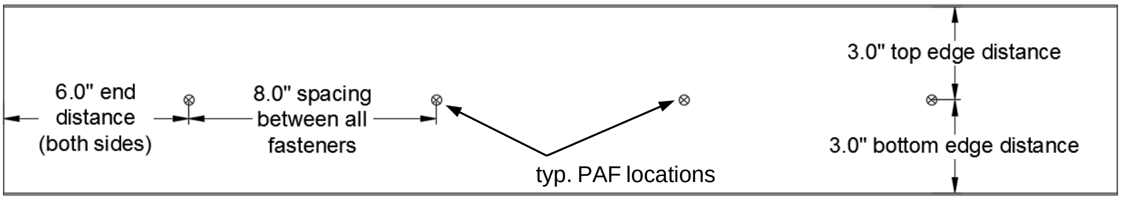

Fig. 3 Spacing and edge distances for PAFs in the cold-formed steel tracks

Test Results

All fasteners in both the single fastener tests and the track group tests experienced pull-out failure. That is, the fasteners break away from the concrete and do not shear prior to reaching their ultimate capacity, as intended when evaluating fastener behaviour in concrete. Figure 4 shows the average ultimate loads obtained from track group tests (Fig. 4a) and single fastener tests (Fig. 4b). For each test type, the results are further organized by the combination of concrete mix and nail/tool type. For any given test type, the influence of the nail type and installation tool combination is seen to be very large, as expected. For a given nail/tool type, there is a measurable difference depending upon concrete mix type. Figure 4 clearly indicates that the tougher the concrete, by virtue of aggregate hardness, the lower the average ultimate shear loads.

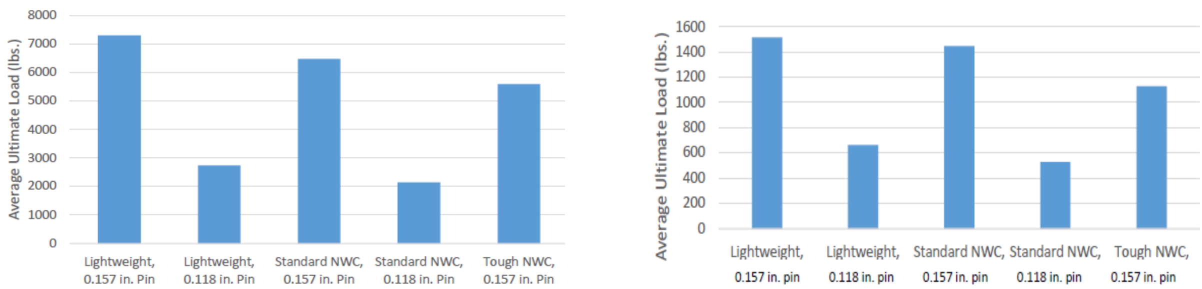

a) Track group tests

b) Single fastener tests

Fig. 4 Average ultimate load categorized by coarse aggregate and fastener type

The test data can also be organized in a way to show in a clear manner the range of mean ultimate shear load values that was determined for each concrete mix and for each combination of tool type and nail type. The results are shown in Fig. 5 which shows measurable differences between the minimum median and

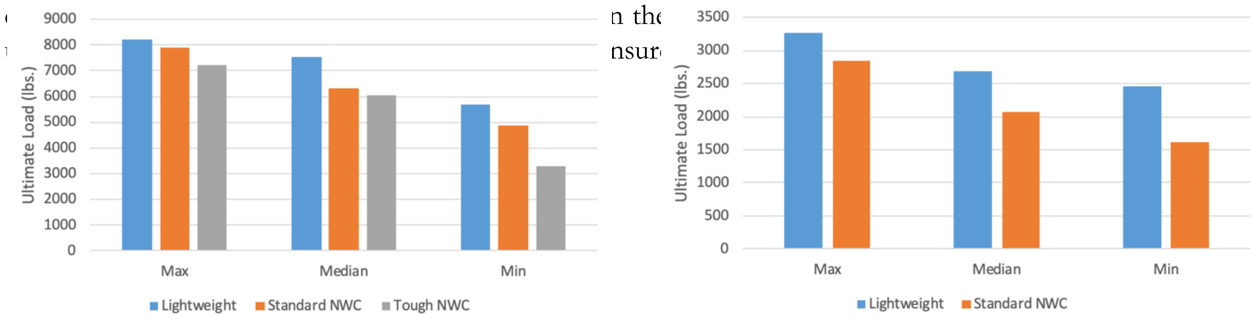

a) 0.157 in. diameter fastener

b) 0.118 in. diameter fastener

Fig. 5 Median and extreme ultimate loads for track group tests

Figure 6 shows the distributions expressed as the percentile of fasteners with loads below a given ultimate value. For the track tests, the individual fastener loads are calculated assuming that the load was evenly distributed all fasteners in a track group. The data is further organized by concrete mix and tool/nail type. Figure 6 shows marked differences in the distributions for single fastener tests and track tests, with the former being flatter and therefore less desirable. Flatter distributions imply a larger variation of failure loads. A steeper distribution as shown for group tests indicates a lower variation, and therefore the positive effect of using groups of nails (redundancy).

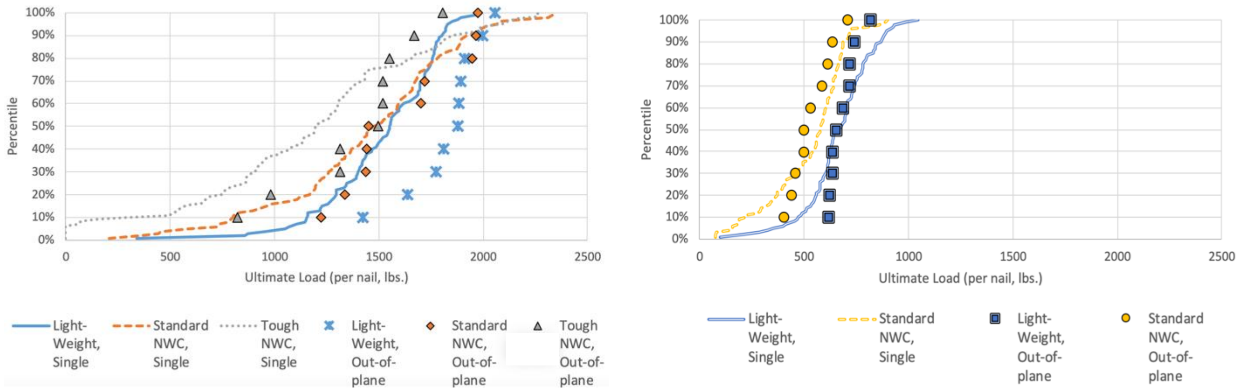

a) 0.157 in. diameter fastener b) 0.118 in. diameter fastener

Fig. 6 Distribution of fastener ultimate loads

The enhancement in performance observed from these distributions for track groups is attributable to the redundancy offered by the so-called "group effect". When a nail in a track becomes distressed and begins to slip, it will lose stiffness and enable the other fasteners to continuing loading. The track will not fail until multiple fasteners have failed. This is very different from a single nail test in which a nail will lose stiffness and begin to shed load in rapidly. This can also be understood as the variation of single fasteners decreasing as they are grouped together in a redundant track system, because the individual fastener variability is averaged out with the other fasteners in the track.

The variability in average ultimate loads per nail for the various test groups in the program that are listed in Table 2 support the different distributions given in Fig. 6. Coefficients of variation (CV) are much larger for single fastener tests than for the corresponding track group tests. This observation holds regardless of concrete mix and tool/nail type. Table 2 also indicates that the tougher the aggregate, the higher the variation in failure loads. This observation stands to reason as tougher aggregate is more likely to impede a straight embedment of the nail.

Table 2 – Average ultimate load per nail and coefficient of variation for all tests

Fastener Diameter		**0.157 in**	**0.118 in.**	**0.157 in.**	**0.118 in.**	**0.157 in.**
Concrete		**Sand LWC**	**Sand LWC**	**Standard NWC**	**Standard NWC**	**Tough NWC**
Single	Mean (lbs.)	1517	664	1447	526	1142
	CV	18%	24%	30%	35%	48%
Track	Mean (lbs.)	1827	684	1620	537	1399
	CV	10%	8%	17%	18%	22%

The data in Table 2 shows that mean ultimate loads increase only slightly on average by 12% from single or group tests, while the variation of capacities is significantly reduced by about 50% for nail group tests. This indicates a positive redundancy effect of using fastener groups on reliability

In addition, the results within a given combination of installation tool, nail type, track thickness, and concrete mix is, in part, a function of the ability of the tool to install the nails properly. A good measure of that notion is the embedment depth to which the nails were driven in each installation. Embedment was obtained by subtracting the offset dimension of the nails from the total length. Table 3 indicates that embedment decreased with aggregate toughness, as well as with the power delivered by the installation tool. Thus, the battery tool consistently resulted in smaller embedment than the powder tool. Additionally, the variability increased with increasing concrete toughness and decreased with increasing installation power.

Table 3 – Average and coefficient of variation of embedment for all fasteners

Fastener Diameter		**0.157 in**	**0.118 in.**	**0.157 in.**	**0.118 in.**	**0.157 in.**
Concrete		**Sand LWC**	**Sand LWC**	**Standard NWC**	**Standard NWC**	**Tough NWC**
Single	Mean (in.)	0.995	0.710	0.949	0.632	0.939
	CV	4.3%	5.9%	4.4%	7.3%	7.7%
Track	Mean (in.)	0.937	0.597	0.894	0.535	0.876
	CV	3.0%	6.1%	4.4%	10.4%	6.0%

Bending of the nails upon installation was assessed based on visual observation of the nails at the following the tests after the tracks were removed. A simple qualitative visual assessment as shown in Table 4 was made and the nail bending configuration was made based on the deviation of the shank with respect to its initial axis. Any deviation in the shank was assumed to have occurred during installation because the pull-out action during testing did not bend the nails any further given the strength and stiffness differences between the nail material and those of the concrete.

Table 4 shows some example fasteners taken from the testing program and illustrating these bending classes. Bending class 1 indicated less than 5° of deviation, whereas bending class 5 indicated 80 to 100° of deviation. A linear relationship is assumed between the assigned discrete bending values. Bending classes in Fig. 7 are seen to be greatly affected by concrete mix and the combination of nail and tool types.

Table 4 Example bending classes for track fasteners

Bending Class	**1**	**2**	**3**	**4**	**5**
0.118-in Pin Diameter Example			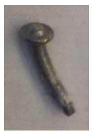	(none)	
0.157-in Pin Diameter Example				(none)	

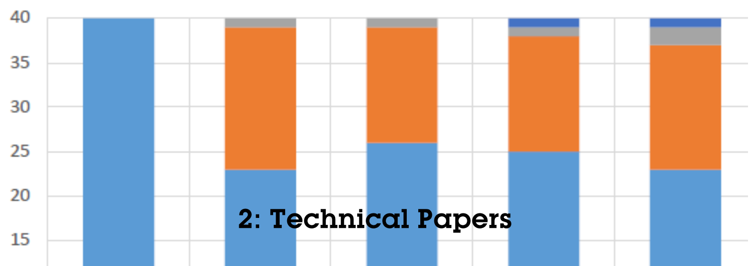

The harder the aggregate, the more likely that a larger deviation of the shank will occur upon installation. Similarly, the more power available from the installation tool, the smaller the deviation in shank position during nail driving.

Planned Cyclic Tests for Cracked Concrete

Testing activities are currently underway to include cyclic loading, a protocol for tracks loaded out-of-plane, and the influence of cracked concrete in the research base. The track tests and interpretation of the data they generate is designed to develop recommendations for seismic qualification testing and evaluation for track testing in seismic applications subjected to out-of-plane shear loads. A test setup like the one used at the University of Minnesota (Fig. 2b) has been designed, fabricated, and assembled at the University of Texas at San Antonio to investigate the failure behaviour of nail groups under out-of-plane cyclic shear loading. The FEMA 461 [10] quasi static, deformation-controlled cyclic load protocol described in FEMA 461 will be used (Fig. 8). The behaviour of PAF attachments to concrete are typically dominated by pull-out and spalling of the concrete, thus the FEMA 461 option will be employed here with a 20% increase between steps and 3 cycles per step.

The UTSA tests will feature longer tracks (40 in.) than was used in the University of Minnesota tests with 5 nails per track (8-in. spacing), but otherwise the test setup is very similar. Some tests will be conducted with the concrete being cracked prior to testing using crack wedges to 0.02 in. crack widths (0.5 mm). Goals of the testing include: measuring the entire load-displacement response, studying the statistics of the failure loads, studying the statis ing the influence of individual nail failure be ing PAF behaviour under cyclic loads in cra

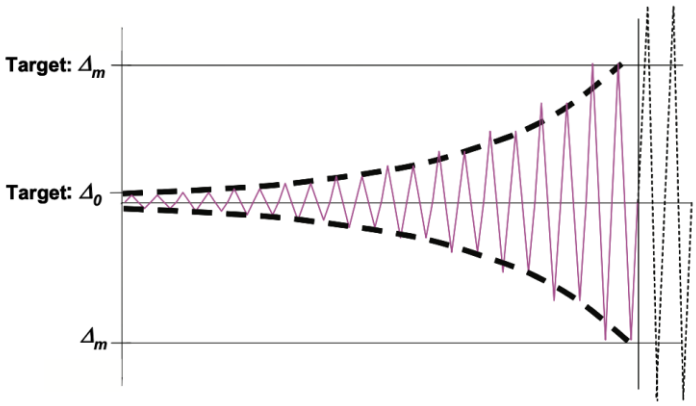

Fig. 8 FEMA 461 deformation-controlled cyclic loading protocol [10]

Fig. 9 shows fragility curves constructed based on preliminary data from tested track attachments to normal-weight concrete. Log-normal distributions have been fitted to statistical data obtained for monotonic and cyclic loading in both uncracked and cracked concrete specimens. The fragility curves indicate that for higher failure probabilities, the ultimate load per nail is generally higher for monotonic tests. However, variability is higher for monotonic tests than for cyclic tests, giving a larger range of ultimate loads for monotonic loading than for cyclic loading. Additionally, ultimate loads for PAF attachments in cracked concrete are on the order of one-half to two-thirds of the loads for attachments to uncracked concrete.

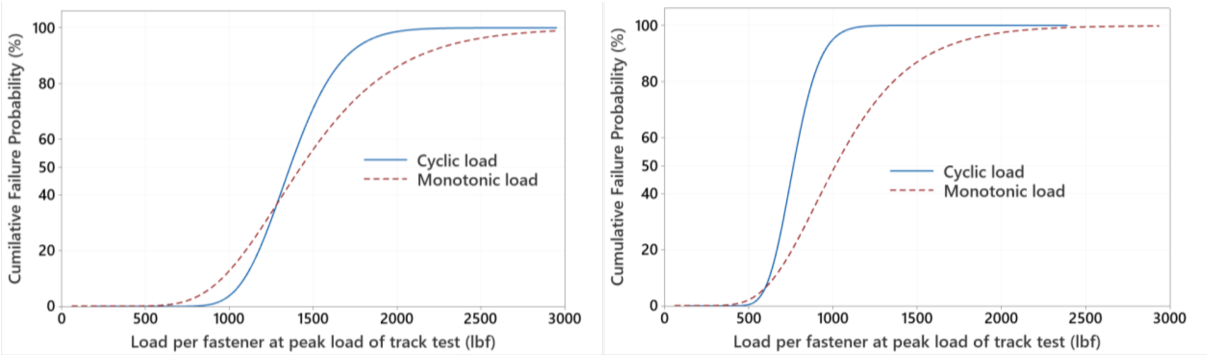

a) Tests on non-cracked concrete　　　　　　b) Tests on cracked concrete

Fig. 9 Fragility curves based on log-normal distribution of preliminary test data

Summary

From a series of experiments on cold-formed steel track fastened to concrete slabs using either powder actuated or electro-mechanical drive installations tools, the following conclusions were drawn.

1. Aggregate hardness, and the resulting concrete toughness, will vary across the country due to the minerals available from local geologic conditions.
2. PAFs installed in concrete with harder aggregate resulted in lower shear strength and greater variability than similar installations in less tough concrete.
3. The previous observation was supported by measured embedment depths and by observed bending configurations of the nails.
4. The steel track was observed to introduce redundancy which reduced variability substantially, while only slightly increasing average ultimate shear loads per fastener.
5. A series of experiments featuring cyclic loading of cold formed steel track attached with PAF groups in cracked concrete is planned to investigate seismic performance of tracks attached to concrete using PAFs, and to develop recommendations for seismic qualification tests.

Acknowledgements

The research described here was supported in part by the Hilti Corporation of North America, and partial student support was provided by the University of Minnesota, Twin Cities for the second author and by the University of Texas at San Antonio for the third author.

References

1. The ICC Evaluation Service, *AC70: Acceptance Criteria for Power-Actuated Fasteners Driven into Concrete, Steel and Masonry Elements*, Brea, 2017.
2. Overacker, S.D. and Schultz, A.E. (2021). *Influence of Concrete Coarse Aggregate Properties on the Shear Capacity of Power-Actuated Fasteners*. Final Report, Department of Civil, Environmental and Geo-Engineering, University of Minnesota, Twin Cities, August, 115 pp.
3. ASTM Standard C117, "Standard Test Method for Materials Finer than No. 200 Sieve in Mineral Aggregates by Washing," ASTM International, West Conshohocken, 2017.
4. ASTM Standard C123, "Standard Test Method for Lightweight Particles in Aggregate," ASTM International, West Conshohocken, 2014.
5. ASTM Standard C142, "Standard Test Method for Clay Lumps and Friable Particles in Aggregates," ASTM International, West Conshohocken, 2017.
6. ASTM Standard C127, "Standard Test Method for Relative Density (Specific Gravity) and Absorption of Coarse Aggregate," ASTM International, West Conshohocken, 2015.

7. ASTM Standard C131, "Standard Test Method for Resistance to Degradation of Small-Size Coarse Aggregate by Abrasion and Impact in the Los Angeles Machine," ASTM International, West Conshohocken, 2014.
8. ASTM Standard C136, "Standard Test Method for Sieve Analysis of Fine and Coarse Aggregates," ASTM International, West Conshohocken, 2014.
9. ASTM Standard C33, “Standard Specification for Concrete Aggregates,” ASTM International, West Conshohocken, 2018.
10. FEMA 461. *Interim testing protocols for determining the seismic performance characteristics of structural and nonstructural components*. FEMA 461. Washington, DC, 2007.

Parametric Seismic In-Plane Fragility Models for Clay Masonry Infills in Low-to-Medium-Rise Reinforced Concrete Frames

Peloso S.[1], Brunesi E.[1], Perrone D.[2], Chichino B.[1], Sinopoli G.[1], and Moroni C.[3]

[1] European Centre for Training and Research in Earthquake Engineering, Pavia, Italy
E-mail: simone.peloso@eucentre.it; emanuele.brunesi@eucentre.it; beatrice.chichino@eucentre.it; giuseppe.sinopoli@eucentre.it

[2] University of Salento, Lecce, Italy
E-mail: daniele.perrone@unisalento.it

[3] Italian Department of Civil Protection (DPC), Rome, Italy
E-mail: claudio.moroni@protezionecivile.it

Abstract. This study aims at deriving multi-damage state fragility functions for clay masonry infills in low-to-medium-rise reinforced concrete (RC) frames designed for earthquake resistance. Different structural archetypes were identified and modelled numerically by means of distributed plasticity approaches in order to undertake incremental dynamic analysis (IDA) and derive the parameters, namely median and standard deviation, along with the coefficient of determination, of the seismic lognormal fragility models through regression analysis involving least-squares fitting techniques. Both infilled and bare frame configurations were simulated and compared, providing fragility curves corresponding to immediate occupancy (SLO), damage prevention (SLD), and, ultimately, life safety limit states (SLV), all of which can be integrated in general frameworks for seismic risk/loss assessment and management. To this end, fragility models are given in terms of three different intensity measures (IMs), namely peak ground acceleration (PGA), peak floor acceleration (PFA), and peak floor spectral acceleration (PFSA), considering also two different methods for the calculation of the probability of occurrence/exceedance, that is, i) first occurrence over the building, and ii) first occurrence at the floor level. Sensitivity to IM and calculation method could thus be gathered accordingly, with a view to address a threefold scope involving also the sensitivity to the explicit modelling of the infills. Lastly, generalised parametric fragility functions are presented, thus bringing in a paradigm that relates mean and standard deviation with IM for varying limit state threshold values.

Keywords: masonry infills, reinforced concrete frames, seismic fragility analysis, sensitivity assessment, parametric fragility models.

1. INTRODUCTION

The most suitable numerical modelling choice for masonry infills, part of reinforced concrete (RC) frame systems is still a cause of concern, owing to several factors including but not limited to those following. On one hand, RC frames with masonry infills constitute a vast portion of both existing and newly built buildings in Italy as well as other Mediterranean countries and places around Europe and the world. On the other hand, infill walls are certainly part of the lateral-force resisting system of a building, most likely influencing the dynamic properties of the building system as a whole, despite being usually not designed according to modern seismic codes [Crisafully *et al.*, 2000; Calvi and Bolognini, 2001; El-Dakhakhni *et al.*, 2006; Celarec *et al.*, 2012; Hak *et al.*, 2012; Cavaleri and Di Trapani, 2014; Sussan *et al.*, 2016; Morandi *et al.*, 2018; Surana *et al.*, 2018; De Risi *et al.*, 2018; Ricci *et al.*, 2018; Perrone *et al.*, 2020; Mucedero *et al.*, 2020; Furtado *et al.*, 2021]. The fact that current design practice for these buildings generally does not consider the influence of masonry infills, which are rather treated as non-structural elements with the only scope of providing thermal insulation from the outdoors, worsens the seismic assessment problem, with issues of damage and losses being aspects that can no longer be ignored nowadays [Manfredi *et al.*, 2014; Cardone and Perrone, 2017; O'Reilly *et al.*, 2018; Mucedero *et al.*, 2021].

With the above in mind, this paper presents a framework for deriving seismic fragility models for clay masonry infill walls in RC frames, relying upon a simple, yet reliable fibre-based finite element (FE) modelling concept that makes use of a triple-strut method, whose calibration is carried out in accordance with past experimental test data [Cavaleri and Di Trapani, 2014]. After selecting structural archetypes representative of medium-to-low-rise framed buildings designed – for earthquake resistance according to Eurocode 8 [CEN, 2004] provisions – for a medium-to-high seismicity site in Italy, nonlinear FE models were developed considering both bare and infilled frame configurations, thereby obtaining as many sets of fragility curves – via incremental dynamic analysis (IDA) for different return periods (RPs) of the seismic intensity – with a view to single out the effects associated with the explicit modelling of the infill walls. As clarified thereinafter, different intensity measures (IMs) were considered to provide multi-damage state fragility models suited to different contexts of seismic risk/loss assessment and management, with the probability of exceeding a certain limit state condition being computed – for the same purpose/reason – in two separate manners, one of which considers the position of a damaged infill along the frame height and the other assumes the damage threshold being exceeded for the entire structure once exceeded in a single infill wall, regardless of its position and whether the other infills are actually to be tagged as "damaged" or not. Finally, generalised parametric fragility functions are showcased, thus bringing in a paradigm that relates mean and standard deviation with IM for varying limit state threshold values.

2. METHODOLOGY

Figure 1 shows key steps of the proposed seismic fragility analysis framework, whereas noteworthy aspects and assumptions underlying it are described in what follows.

Firstly, once a building class is selected (i.e. low-to-medium-rise masonry-infilled RC frames designed for medium ductility class in line with European rules [CEN, 2004] in this case), a reliable computational model has to be defined, able to account for significant damage/response mechanisms for the building class of interest. The FE model has to be accurate enough and, at the same time, computationally efficient to sequence non-linear dynamic analyses one another – thus integrating the structural response over time – in a reasonable amount of time. To this end, force-based fibre modelling was chosen, combining nonlinear beam-column elements for both beams and columns with truss elements for the infills.

Secondly, structural prototypes representative of the building class or portfolio under investigation have to be identified in such a way that building-to-building variability could be taken into account properly, along with record-to-record variability, which is given by ad-hoc ground motion selection. For this application, five structural archetypes with different number of floors – varying from two to six – were selected from a portfolio of 100 buildings randomly sampled via complete Monte Carlo simulation in Perrone *et al.* [2020]. As previously mentioned, infilled frames have a counterpart bare frame configuration, for a total of ten structural FE models, all of which developed using the open source FE platform OpenSees [Mazzoni *et al.*, 2006].

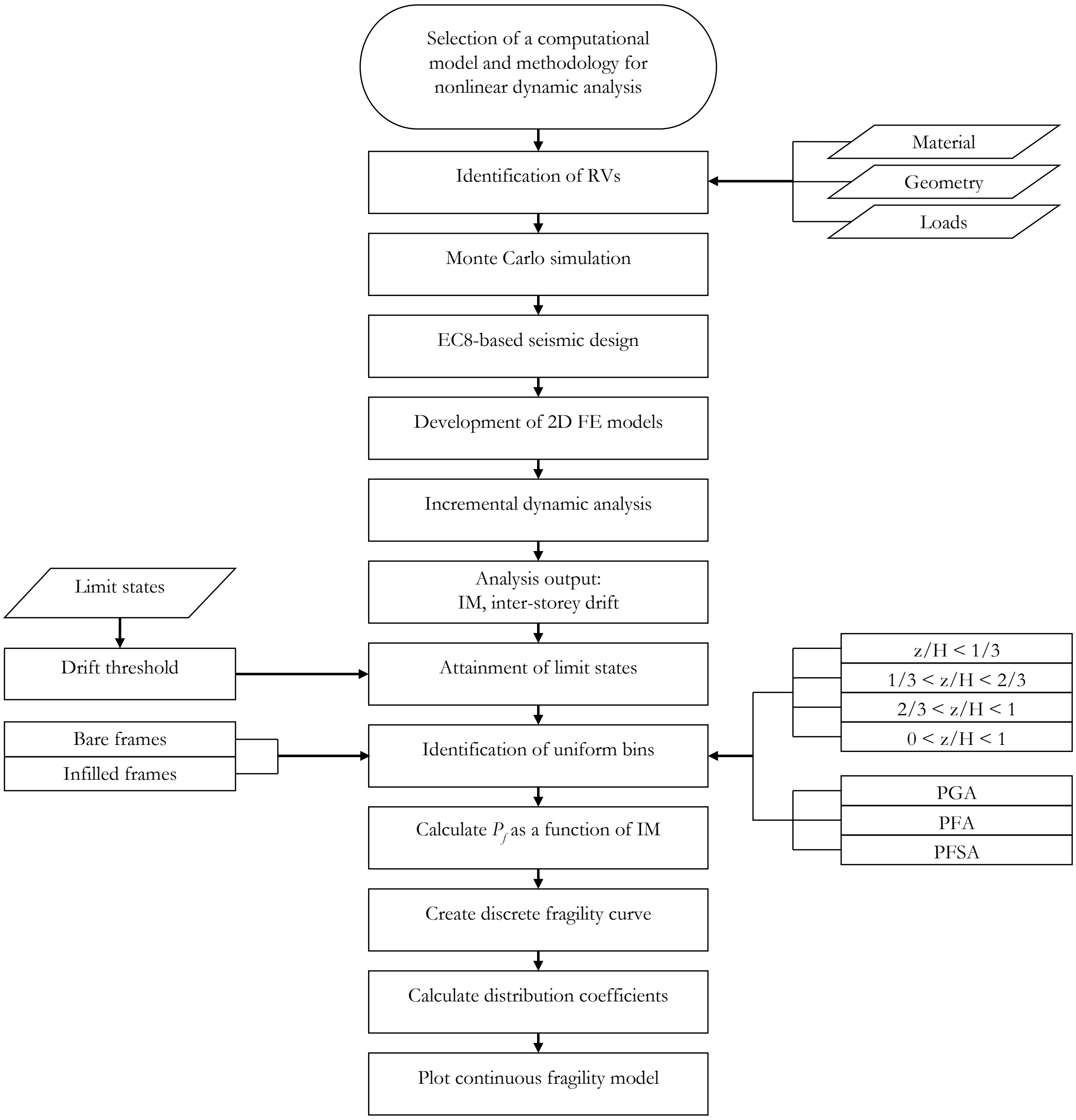

Figure 1. Flowchart of the proposed infill-specific seismic fragility analysis

Thirdly, following identification of random variables (RVs) to account for variability in building geometry, material, and gravity loads to use for seismic design according to Eurocode 8, referred to as EC8 hereon [CEN, 2004], and following both simulated design and modelling phases, the latter of which relies upon in-plane pseudo-static test results by Cavaleri and Di Trapani [2014] for the calibration of triple-strut inelastic infill model, IDA was carried out for different RPs ranging from 30 to 9975 years (i.e. 30, 50, 70, 140, 200, 475, 975, 2475, 4975 and 9975 years) in order to record acceleration and displacement time histories at each floor and characterise the nonlinear response of each case-study frame, also for rare earthquakes implying structural and non-structural damage. As described in the following Section, a site close to the city of Cassino, in Italy, was chosen for the ground motion selection, this site being characterised by a peak ground acceleration on stiff soil equal to 0.21 g for a 10% probability of exceedance in 50 years (or 475-year RP).

Fourthly, a damage probability matrix was assembled following identification of limit state thresholds for as many limit states, which in this application were three: immediate occupancy limit state (termed as SLO to follow the Italian nomenclature available in the Italian building code [MIT, 2018], henceforth called NTC18), damage prevention limit state (referred to as SLD for the same reason), and, ultimately, life safety limit state (or SLV to comply with NTC18 [MIT, 2018] terminology). To do so, drift thresholds were selected merging information available in the NTC18 [MIT, 2018] with other in international seismic codes [CEN, 2004; FEMA356, 2000] and infill-specific experimental observations [Cavaleri and Di Trapani, 2014].

Fifthly, and lastly, lognormal multi-damage fragility models providing the probability of occurrence/exceedance of multi-limit damage conditions for a given level of seismic shaking, in closed-form and continuous fashion, were calculated by simply iterating the above-described procedure (see Figure 1) as many times as the combinations of selected IMs and methods for evaluating the probability of damage state exceedance. For what concerns the former issue, three different IMs were considered, which are: i) peak ground acceleration (PGA), ii) peak floor acceleration (PFA), and peak floor spectral acceleration (PFSA) or peak spectral acceleration at the floor, thus resulting into three sets of fragility models (for comparison and correlation), each of which doubles when considering the methodology for damage state attainment and probability computation. Regarding the latter issue, two criteria were selected, namely i) first occurrence assumption, meaning that the limit state is said to be attained when the corresponding threshold is breached or exceeded in one single infill, as opposed to ii) first occurrence at each storey, in which case occurrences were computed separately, and the corresponding fragilities were grouped – conventionally – into three sets based on the dimensionless parameter z/H.

Clearly, the dimensionless height z/H is taken as the height at which the infill is located z normalised by the entire frame height H, and the following ranges were set: i) $0 < z/H < 1/3$, or lower storeys, ii) $1/3 < z/H < 2/3$, or mid storeys, and iii) $2/3 < z/H < 1$ or upper storeys. As can be inferred from Figure 1, the first occurrence case is identified by $0 < z/H < 1$, in which the dimensionless parameter z/H simply spans the entire range of possible outcomes.

It is noteworthy that the so-derived fragility functions allow a three-fold comparison be driven for analysts/designers or eventually decision-makers, i) between fragilities of the same kind (or limit state) for the same IM – and considering infill walls placed at the same height over the structure – but coming from bare and infilled frame simulation results, ii) between fragilities of the same kind for different IMs, which refer to shaking of a different nature, and iii) between fragilities associated with infills located at different positions up to the building height, for the same modelling option (infilled or bare case) and assumed IM.

3. CASE-STUDY STRUCTURES AND DAMAGE ANALYSIS

The analysed case-study buildings are simple masonry-infilled RC plane frames extracted from the portfolio randomly generated in Perrone *et al.* [2020]. These structures, with number of floors varying from two to six, were meant to resemble all characteristics of newly built frame systems designed for gravity loads and earthquake resistance in Italy and the Mediterranean area. Geometry and mechanical properties, together with gravity loads, were selected accordingly, as a result of a complete Monte Carlo simulation process in conjunction with a simulated design procedure, which relies upon European seismic provisions [CEN, 2004] for the so-called ductility class B, assuming all structures be located near the city of Cassino, a medium-high seismicity zone in Italy with a design PGA of 0.21g for SLV (or life safety limit state, i.e. RP = 475 years in this case).

Figure 2 shows an example of the structural system, along with key items of the implemented FE modelling approach and selected RVs, namely i) the number of floors n_f, (ii) the inter-storey height h_i, iii) the number of bays n_b, iv) the length of the bays L_b, v) the dead loads g_T, vi) the live loads q_k, vii) the yielding strength of reinforcing rebars f_y, and viii) the concrete compressive strength f_c. For the sake of clarity and completeness, Table 1 summarises numerical values for every RV, thereby providing an idea of building-to-building variability involved in the undertaken infill-specific fragility analysis. More information regarding the assumptions underlying these buildings and their design can simply be found in Perrone *et al.* [2020].

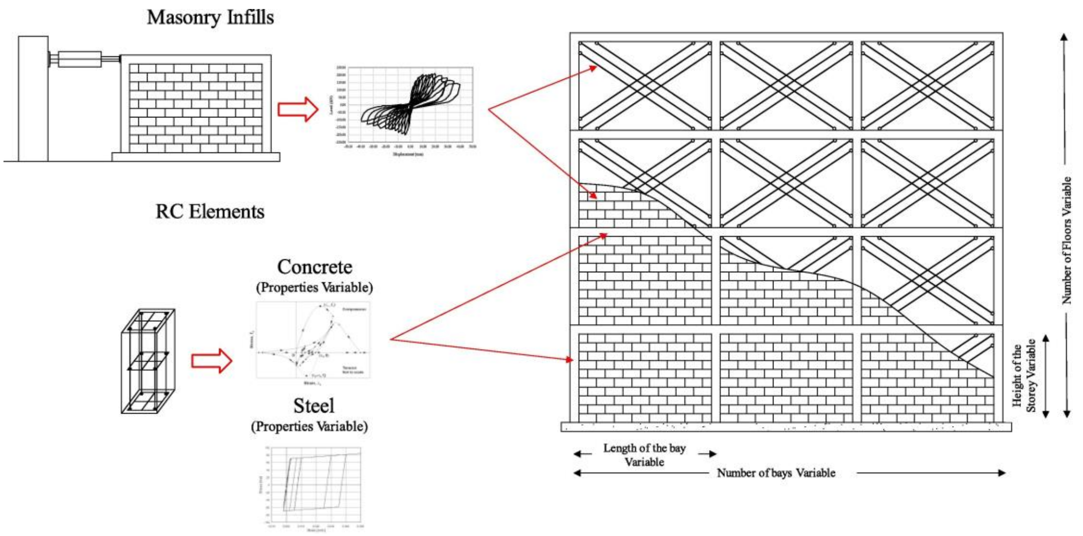

Figure 2. Numerical model concept for infill-specific seismic fragility analysis

Table 1. Characteristics of the case-study structures and values of RVs

Model	n_f (-)	h_i (mm)	n_b (-)	L_b (mm)	g_T (N/mm)	q_k (N/mm)	f_y (N/mm^2)	f_c (N/mm^2)
M1	2	3250	3	3500	22.32	12.25	375.0	32.0
M2	3	3000	3	4000	24.01	11.00	430.0	39.0
M3	4	2750	6	3750	22.34	9.38	430.0	40.0
M4	5	2750	3	4500	25.60	10.13	375.0	39.0
M5	6	3000	6	3750	22.75	10.31	430.0	41.0

All FE models were developed by making use of the open platform OpenSees [Mazzoni *et al.*, 2006] assuming a distributed-plasticity approach to simulate the onset and propagation of damage in the structure and its key portions. Both beams and columns were modelled by means of the nonlinear beam-column element available in OpenSees [Mazzoni *et al.*, 2006], meaning a force-based formulation was assumed for fibre modelling. More in detail, Concrete07, the uniform confinement model implemented by Chang and Mander [1994], was assigned to concrete fibres, and Steel01, a bilinear constitutive material model with isotropic strain hardening, was assumed for the longitudinal steel bars of beams and columns.

For what concerns the infills, they were modelled by an equivalent triple-truss model, in which the global stiffness of the panel was distributed amongst three parallel diagonal inelastic truss elements by assigning a rate of stiffness and strength equal to 50% to the central truss and equal to 25% to each of the off-diagonal trusses. The pinching4 material model available in OpenSees [Mazzoni *et al.*, 2006] was considered to mimic the cyclic behaviour of a clay masonry infill tested by Cavaleri and Di Trapani [2014], namely specimen S1B-1. For the sake of completeness, it is worth noting that vertical and horizontal Young's moduli were taken equal to 6401 and 5038 MPa, respectively, whilst the compressive and shear strength values were taken equal to 8.66 and 1.07 MPa, respectively, in agreement with material characterisation tests undertaken by the same authors [Cavaleri and Di Trapani, 2014].

Nonlinear time-history analyses (NLTHAs) were performed assuming a suite of 20 earthquake ground motions per each of the ten RPs selected to characterise nonlinear structural behaviour. All these records – from the PEER NGA-West database – resulted from a hazard-consistent selection undertaken based on spectral compatibility with a conditional mean spectrum according to the methodology proposed by Jayaram *et al.* [2011]. IDA results were processed to evaluate occurrences relying upon the drift thresholds reported in Table 2, as per Italian and international prescriptions [MIT, 2018; FEMA356, 2000] as well as infill-specific outcomes from testing [Cavaleri and Di Trapani, 2014].

Table 2. Assumed drift thresholds for performance evaluation

	SLO	SLD	SLV
Drift	0.15%	0.3%	0.8%

In closing, for the sake of clarity, it is worthwhile to mention that the above-reported drift levels are in line with §7.3.6.1 of the NTC18 [MIT, 2018] as well as Table C1-3 in FEMA356 [2000] for "Unreinforced Masonry Infill Walls".

4. SEISMIC FRAGILITY FUNCTIONS

Seismic fragility models were derived according to the flowchart presented in Section 2 and the assumptions concerning numerical modelling and damage analysis described in Section 3. Figure 3 and Figure 4 provide discrete/empirical fragility data along with continuous lognormal models, for the three limit states assumed, in terms of PGA, for bare and infilled frame cases, respectively. Moreover, Table 3 summarises the parameters of PGA-based functions, namely the mean of logPGA (denoted as μ), standard deviation of logPGA (denoted as σ) and coefficient of determination (R^2).

It can be clearly seen from a comparison between Figure 3 and Figure 4, or alternatively from Table 3, that the fragility of the infills for the bare frame configuration is higher than that associated with the infilled case counterpart. The fact that the vulnerability reduces if moving to mid (or intermediate) and upper storeys (the latter denoted as "Upp" in Table 3) can also be noted, which in turn affirms that the vulnerability of the entire structure (referred to as "all z/H values" in Figure 3 and Figure 4, or shortly as "All" in Table 3) is driven by that of the lower storeys ($z/H < 1/3$ in Figure 3 and Figure 4 or "Low" in Table 3), regardless of whether the bare or infilled configuration is concerned. As an example, the PGA associated with the 50% probability of SLD being exceeded changes from approximately 1.73 to 2.35 m/s^2, when passing from $0 < z/H < 1/3$ to $2/3 < z/H < 1$. Similarly, for the infilled frame case, the PGA changes from 2.78 to 4.68 m/s^2.

Another noteworthy aspect is that no fragility models could be fitted and provided for SLV at the top storeys simply because of no occurrences, meaning that the drift threshold corresponding to this limit state (i.e. 0.8% drift) has never been reached or exceeded during the series of NLTHAs for RPs ranging between 30 and 9975 years. Finally, it has to be pointed out that less variability is observed for what concerns the dispersion, as far as different limit states are compared together or if the comparison is made between the bare and infilled cases for the same limit state.

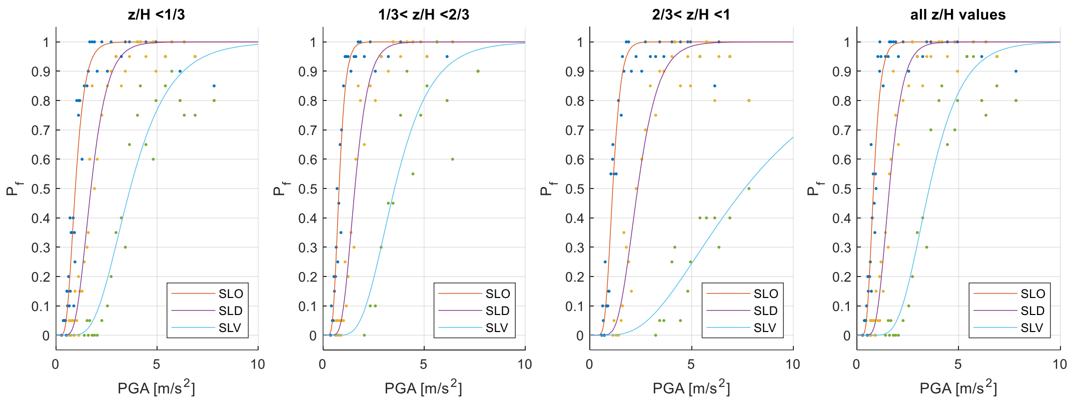

Figure 3. Fragility curves for the bare frame case in terms of PGA

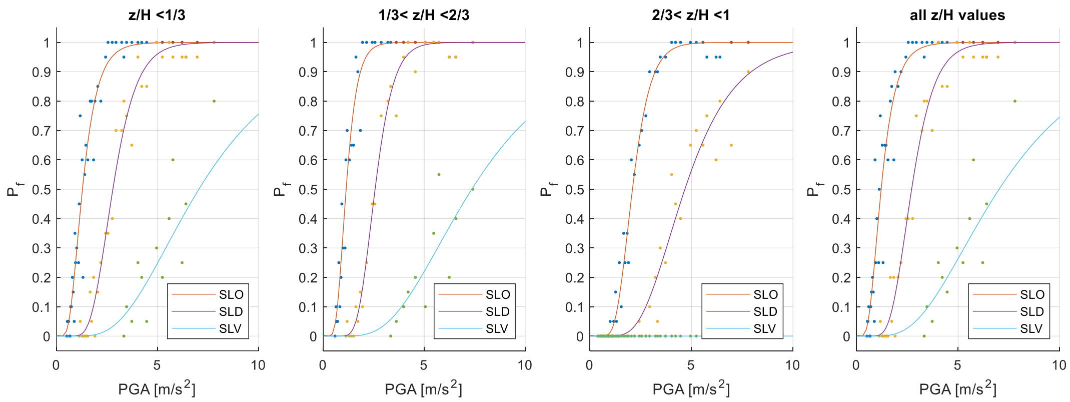

Figure 4. Fragility curves for the infilled frame case in terms of PGA

Table 3. Parameters of PGA-based fragility models

		SLO			SLD			SLV		
B/I	z/H	μ	σ	R^2	μ	σ	R^2	μ	σ	R^2
Bare	Low	0.954	1.485	0.940	1.726	1.455	0.953	3.667	1.525	0.908
	Mid	0.793	1.385	0.956	1.574	1.405	0.957	3.539	1.491	0.804
	Upp	1.118	1.331	0.953	2.345	1.416	0.940	7.598	1.830	0.727
	All	0.811	1.410	0.941	1.592	1.397	0.954	3.549	1.436	0.919
Infilled	Low	1.278	1.586	0.948	2.784	1.395	0.975	7.045	1.657	0.532
	Mid	1.131	1.461	0.955	2.564	1.325	0.987	7.354	1.648	0.669
	Upp	2.094	1.396	0.981	4.675	1.512	0.905	-	-	-
	All	1.209	1.595	0.929	2.710	1.390	0.971	7.018	1.711	0.541

For the sake of brevity, PFA- and PFSA-based fragility models are shown only for the bare frame configuration, in Figure 5 and Figure 6, respectively, whereas μ and σ corresponding to both bare and infilled frame configurations are given in Table 4 and Table 5. As an example, it can be seen that the 50% probability of SLD being reached or exceeded is attained for 1.59 m/s², 2.64 m/s² and 12.41 m/s² in terms of PGA, PFA and PFSA, respectively. Again considering the $0 < z/H < 1$ case, this time for the infilled frame configuration, this limit state is characterised by 2.71 m/s², 7.83 m/s² and 43.83 m/s², as far as PGA, PFA and PFSA are concerned, respectively.

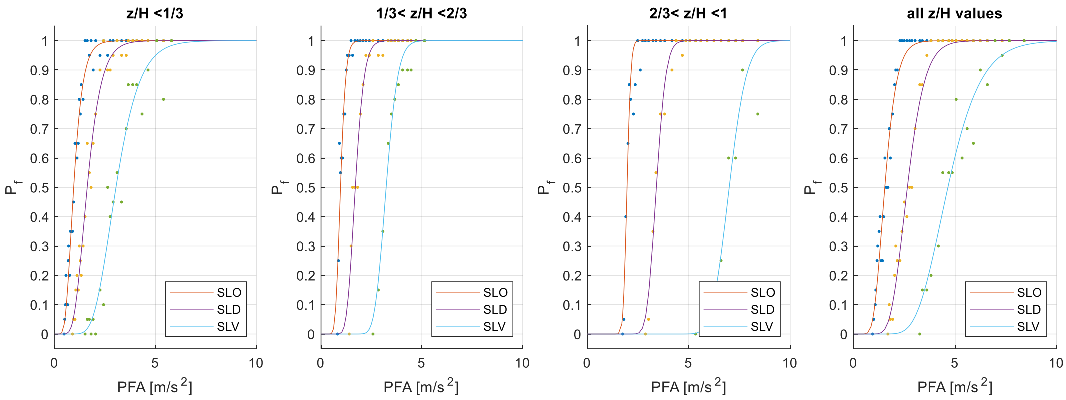

Figure 5. Fragility curves for the bare frame case in terms of PFA

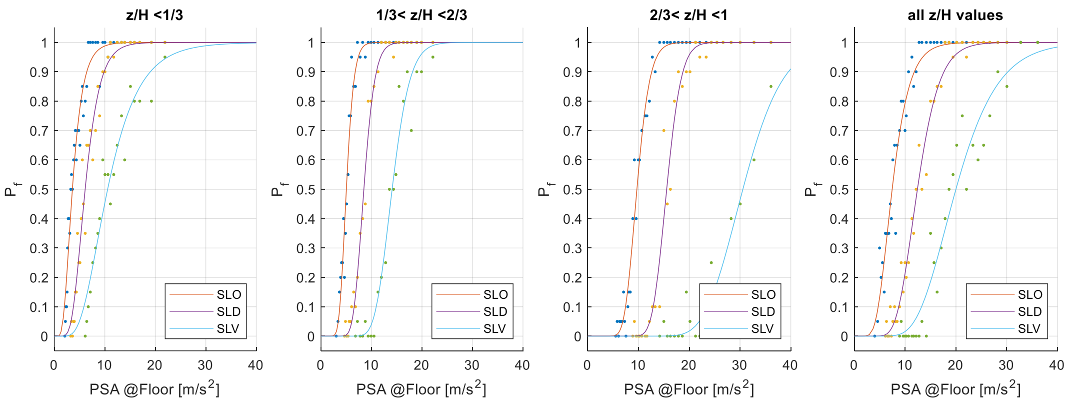

Figure 6. Fragility curves for the bare frame case in terms of PFSA or PSA at the floor

Table 4. Parameters of PFA-based fragility models

		SLO			SLD			SLV		
B/I	z/H	μ	σ	R^2	μ	σ	R^2	μ	σ	R^2
Bare	Low	0.942	1.461	0.982	1.612	1.408	0.978	3.039	1.354	0.944
	Mid	0.965	1.235	0.925	1.699	1.224	0.953	3.229	1.151	0.995
	Upp	1.955	1.080	0.947	3.400	1.116	0.982	6.993	1.102	0.958
	All	1.530	1.351	0.972	2.643	1.292	0.983	4.642	1.316	0.938
Infilled	Low	1.977	1.729	0.917	4.056	1.538	0.908	10.79	2.135	0.456
	Mid	2.747	1.235	0.974	5.435	1.231	0.942	10.84	1.397	0.481
	Upp	6.349	1.302	0.954	11.84	1.449	0.682	-	-	-
	All	4.030	1.430	0.953	7.828	1.375	0.936	16.57	1.966	0.206

Table 5. Parameters of PFSA-based fragility models

B/I	z/H	SLO μ	SLO σ	SLO R^2	SLD μ	SLD σ	SLD R^2	SLV μ	SLV σ	SLV R^2
Bare	Low	3.582	1.579	0.960	6.110	1.454	0.965	10.56	1.583	0.923
	Mid	5.019	1.263	0.974	8.488	1.222	0.991	14.09	1.218	0.965
	Upp	9.688	1.228	0.985	15.56	1.157	0.972	30.56	1.222	0.944
	All	7.432	1.434	0.962	12.41	1.316	0.985	19.99	1.381	0.942
Infilled	Low	9.858	1.860	0.920	19.22	1.702	0.888	99.14	5.479	0.233
	Mid	17.04	1.369	0.964	30.74	1.292	0.973	64.34	1.612	0.618
	Upp	37.22	1.332	0.974	68.58	1.783	0.714	-	-	-
	All	24.76	1.521	0.973	43.83	1.395	0.940	127.0	2.640	0.401

These latter sets of fragility functions or models could help interpreting the sensitivity of infill-specific vulnerability to the IM, thus creating a paradigm that involves parameters of shaking of a different kind/type. Notably, with the same response data at hand, extension is possible to the bi-variate or three-variate cases, thereby the probability of reaching or exceeding a certain limit state could be traced, conditioned upon reaching two or more triggers in terms of seismic shaking.

In closing, it is noted, and shown in Figure 7, that generalised fragility models can be provided – for different IMs and methods for calculating the probability of limit state occurrence – by simply varying, in a parametric fashion, the target drift assumed for capacity/demand convolution. As can be inferred from Figure 7, for instance for the PGA case combined with $0 < z/H < 1$, simple interpolants fit and provide μ and σ of a lognormal, continuous model. More in detail, in this case, the target drift assumed as threshold value to evaluate whether demand meets or exceeds capacity was selected to range from 0.025% to 0.8%, with steps of 0.025% each, meaning in turn that the calculations detailed in Figure 1 was repeated multiple times to obtain multiple closed-form fragility models, whose μ and σ are plotted continuously in Figure 7. The latter shows a fairly linear increase of μ with the target drift, whilst σ tends to remain fairly constant.

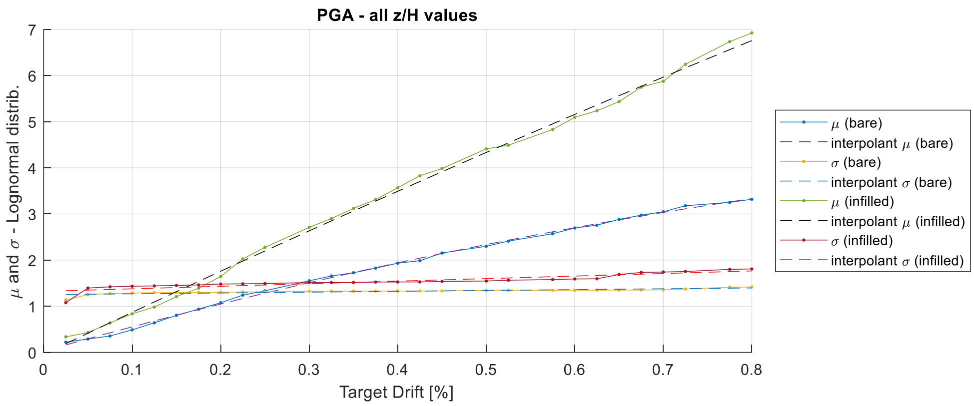

Figure 7. Example of mean and standard deviation – of a lognormal fragility model – for different target drifts

5. CONCLUSIONS

In this paper, IDAs were carried out to derive multi-damage state fragility models for clay masonry infills lodged in RC frame systems designed for earthquake resistance. A framework was developed and proposed involving i) the explicit modelling of infills in terms of stiffness and strength, as well as obviously mass, ii) different IMs, and iii) the position of infill walls along the height of the archetype framed building – and, similarly, a criterion for evaluating the probability of limit state occurrence/exceedance. In particular, the first occurrence over the building and the first occurrence at the floor level were both considered and compared together.

Sets of NLTHAs were undertaken for five structural archetypes, representative of Italian masonry-infilled frames, considering ten RPs ranging from 30 to 9975 years (i.e. 30, 50, 70, 140, 200, 475, 975, 2475, 4975 and 9975 years) in such a way that lognormal fragility functions could be obtained (and eventually integrated within frameworks for seismic risk and loss assessment and management).

The main conclusions drawn from this study can be summarised as follows:

- The lognormal model was proven a good fit/approximation of empirical fragility curves, with R^2 values close to 0.90 or even higher being observed for the vast majority of the cases.
- The PGA-, PFA- and PFSA-based, closed-form fragility models – expressed either in terms of median and standard deviation or their ratios – allow correlation of different fragility estimates and seismic intensity parameters.
- The non-negligible influence of stiffness and strength of the infills was quantified by simply comparing fragility models for bare and infilled configurations, both of which could be valid depending on purpose and time.
- Criteria other than the first occurrence in an entire building could be promising and worth trying not only in relation to position but also with impact on issues of repair and loss.
- Promising trends are also shown via generalised fragility functions, to obtain which limit state thresholds were parametrised, thus allowing a paradigm to be brought in relating mean and standard deviation with IM for varying limit state threshold values.

REFERENCES

Calvi, G.M., Bolognini, D. [2001] "Seismic response of reinforced concrete frames infilled with masonry panels weakly reinforced," *Journal of Earthquake Engineering*, Vol. 5, No. 2, pp. 153-185.

Cardone, D., Perrone, G. [2017] "Damage and loss assessment of pre-70 RC frame buildings with FEMA P-58," *Journal of Earthquake Engineering*, Vol. 21, No. 1, pp. 23-61.

Cavaleri, L., Di Trapani, F. [2014] "Cyclic response of masonry infilled RC frames: Experimental results and simplified modelling," *Soil Dynamics and Earthquake Engineering*, Vol. 65, pp. 224-242.

Celarec, D., Ricci, P., Dolšek, M. [2012] "The sensitivity of seismic response parameters to the uncertain modelling variables of masonry-infilled reinforced concrete frames," *Engineering Structures*, Vol. 35, pp. 165-177.

CEN, European Committee for Standardisation [2004] *EN 1998-1. Eurocode 8: Design of structures for earthquake resistance - Part 1: General rules, seismic actions and rules for buildings*, Brussels, Belgium.

Chang, G.A., Mander, J.B. [1994] *Seismic energy based fatigue damage analysis of bridge columns: Part 1 – Evaluation of seismic capacity*, NCEER Technical Report, no. NCEER-94-0006 State University of New York, Buffalo, NY, USA.

Crisafulli, F.J., Carr, A.J., Park, R. [2000] "Analytical modelling of infilled frame structures - A general review," *Bulletin of the New Zealand Society for Earthquake Engineering*, Vol. 33, No. 1, pp. 30-47.

De Risi, M.T., Del Gaudio, C., Ricci, P., Verderame, G.M. [2018] "In-plane behaviour and damage assessment of masonry infills with hollow clay bricks in RC frames," *Engineering Structures*, Vol. 168, pp. 257-275.

El-Dakhakhni, W.W., Hamid, A.A., Hakam, Z.H.R., Elgaaly, M. [2006] "Hazard mitigation and strengthening of unreinforced masonry walls using composites," *Composite Structures*, Vol. 73, No. 4, pp. 458-477.

FEMA356 [2000] *Prestandard and commentary for the seismic rehabilitation of buildings*, Federal Emergency Management Agency, Washington D.C., USA.

Furtado, A., Rodrigues, H., Arêde, A. [2021] "Effect of the infill panels in the floor response spectra of an 8-storey RC building," *Structures*, Vol. 34, pp. 2476-2498.

Hak, S., Morandi, P., Magenes, G., Sullivan, T.J. [2012] "Damage control for clay masonry infills in the design of RC frame structures," *Journal of Earthquake Engineering*, Vol. 16, No. S1, pp. 1-35.

Jayaram, N., Lin, T., Baker, J.W. [2011] "A computationally efficient ground-motion selection algorithm for matching a target response spectrum mean and variance," *Earthquake Spectra*, Vol. 27, No. 3, pp. 797-815.

O'Reilly, G.J., Perrone, D., Fox, M., Monteiro, R., Filiatrault, A. [2018] "Seismic assessment and loss estimation of existing school buildings in Italy," *Engineering Structures*, Vol. 168, pp. 142-162.

Manfredi, G., Prota, A., Verderame, G.M., De Luca F., Ricci, P. [2014] "2012 Emilia earthquake, Italy: reinforced concrete buildings response," *Bulletin of Earthquake Engineering*, Vol. 12, No. 5, pp. 2275-2298.

Mazzoni, S., McKenna, F., Scott, M.H., Fenves, G.L. [2006] *OpenSees Command Language Manual*, Pacific Earthquake Engineering Research (PEER) Center, Berkeley (CA), USA.

MIT, Ministero delle Infrastrutture e dei Trasporti [2018] *Aggiornamento delle Norme Tecniche per le Costruzioni*, G.U., in Italian.

Morandi, P., Hak, S., Magenes, G. [2018] "Performance-based interpretation of in-plane cyclic tests on RC frames with strong masonry infills," *Engineering Structures*, Vol. 156, pp. 503-521.

Mucedero, G., Perrone, D., Brunesi, E., Monteiro, R. [2020] "Numerical modelling and validation of the response of masonry infilled rc frames using experimental testing results," *Buildings*, Vol. 10, No. 10, pp. 1-30, 182.

Mucedero, G., Perrone, D., Monteiro, R. [2021] "Nonlinear static characterisation of masonry-infilled RC building portfolios accounting for variability of infill properties," *Bulletin of Earthquake Engineering*, Vol. 19, No. 6, pp. 2597-2641.

Perrone, D., Brunesi, E., Filiatrault, A., Nascimbene, R. [2020] "Probabilistic estimation of floor response spectra in masonry infilled reinforced concrete building portfolio," *Engineering Structures*, Vol. 202, No. 109842.

Ricci, P., Di Domenico, M., Verderame, G.M. [2018] "Experimental assessment of the in-plane/out-of-plane interaction in unreinforced masonry infill walls," *Engineering Structures*, Vol. 173, pp. 960-978.

Sassun, K., Sullivan, T.J., Morandi, P., Cardone, D. [2016] "Characterising the in-plane seismic performance of infill masonry," *Bulletin of the New Zealand Society for Earthquake Engineering*, Vol. 49, No. 1, pp. 98-115.

Surana, M., Pisode, M., Singh, Y., Lang, D.H. [2018] "Effect of URM infills on inelastic floor response of RC frame buildings," *Engineering Structures*, Vol. 175, pp. 861-878.

Numerical study on the seismic interaction between innovative ductile masonry infills and RC elements

Simone Pelucco[1], Riccardo Milanesi[2], Paolo Morandi[3], Valentino Bolis[1], Andreas Stavridis[4], Guido Magenes[2] and Marco Preti[1]

[1] Dept. of Civil, Environmental, Architectural Engineering and Mathematics, University of Brescia
via Branze 43, Brescia (BS), Italy
e-mail: s.pelucco@unibs.it, valentino.bolis@unibs.it, marco.preti@unibs.it

[2] Dept. of Civil Engineering and Architecture, University of Pavia
via Ferrata 3, Pavia (PV), Italy
riccardo.milanesi@unipv.it, guido.magenes@unipv.it

[3] Eucentre
via Ferrata 1, Pavia (PV), Italy
paolo.morandi@eucentre.it

[4] Dept. of Civil, Structural and Environmental Engineering, University at Buffalo
NY 14260, United States of America
astavrid@buffalo.edu

Abstract. Innovative masonry infill solutions have been proposed in the last decade to mitigate the damage observed in "traditional" infilled frame structures. The insertion of sliding joints in the masonry infills has been experimentally investigated with different layouts and technologies, proving the efficiency of the solution in mitigating the infill damage. However, uncertainties remain regarding the local trust exerted by the infill on the surrounding frame. That is challenging to measure during tests, but it is of critical importance for safe design of these structures. The present work describes the results obtained from a detailed numerical modelling effort focusing on the assessment of the effect of the infill-frame interaction. The numerical model, based on a validated and well-established approach, is calibrated with the mechanical properties of a previously tested RC frame with masonry infill with sliding joints. The results of a parametric analysis on the role of the design parameter in the local infill-frame interaction are presented and their design implications are discussed. In particular, the shear behaviour and damage of the RC columns is assessed and design guidelines resulting from the study are proposed.

Keywords: Local effects, infill-frame interaction, innovative ductile infills, sliding joints, fem modelling of infills.

1. INTRODUCTION

The interaction of masonry infills with the bounding frame is recognised as a source of significant post-earthquake damage (Braga et al. [2011]; Fikri et al. [2019]). Solutions to mitigate this interaction have been proposed in the last decade. Most methods focus on increasing the strength, while some of them aim at a deformable and ductile response of the infill. One option to make the infill in-plane response ductile is to subdivide it into subpanels through the introduction of sliding joints which allow mutual sliding. Preti et al. [2015] proposed to subdivide the infill by sliding joints opportunely shaped to allow the horizontal in-plane sliding. In that test, sliding joints were implemented with wooden boards, one located at the infill base and three at intermediate heights to subdivide the infill into four subpanels. At the lateral boundary of the infill to the columns, wood boards were placed to protect the masonry from local crushing. At the top of the infill, a gap was ensured to avoid the confinement effect of the top beam and to foster sliding along the horizontal joints. Morandi et al. [2018] proposed a similar ductile solution with different details. The infill was subdivided into four panels by means of polymeric sliding joints implemented with a male/female unit to allow the sliding without involving masonry; at the base, the infill was laid on a traditional mortar joint. The lateral vertical interfaces with the columns were filled with deformable mortar to reduce the stress concentration, as were the infill-to-the-top-beam interface. In Figure 1, the geometry of the specimen is reported. A first numerical parametric analysis on the response of infill with sliding joints was proposed by Bolis et al., [2017]. In this paper, the parametric study is further developed, focusing on the role of the deformable mortar joints at the infill-frame interface on the solution proposed in Morandi et al. [2018].

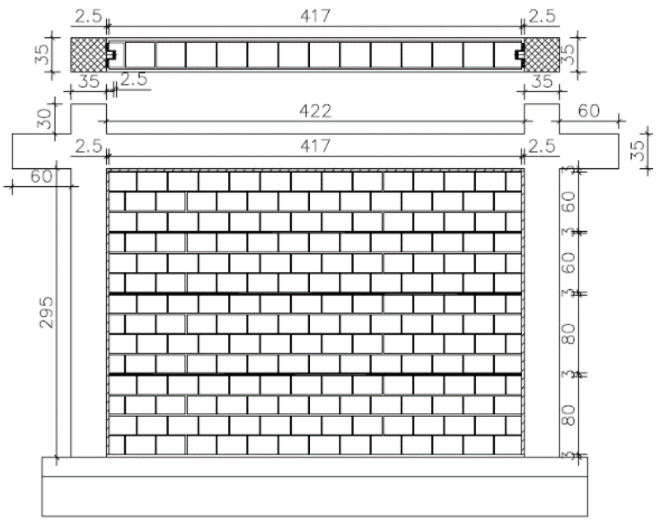

Figure 1: Layout of the fully infilled specimen represented without plaster (Morandi et al. [2018]).

2. SIMULATION OF THE EXPERIMENTAL TEST

2.1 REFERENCE STRUCTURE AND MODELLING SCHEME

The reinforced concrete (RC) frame infilled with the ductile masonry panel considered in this work is the specimen called TSJ1 (solid, without opening) tested in the experimental campaign carried out by Morandi et al., [2018] within the European FP7 "INSYSME". The masonry of the infill was realized with vertically perforated hollowed clay units and general-purpose mortar bed-joints and head-joints. An in-plane quasi-static test followed by a "high-velocity" test were conducted on TSJ1; in the present study, only the quasi-static test has been taken into account. The reference test was a full-scaled single-storey and single-bay RC frame infilled by a ductile masonry infill, where the vertical loads were applied at the top of the columns to simulate the upper floors, and cyclic displacement-controlled horizontal loads were applied to the top beam. The global force-displacement curve and the local deformations of the deformable mortar joints at the lateral vertical interfaces were measured through linear potentiometers. Two linear transducers located at each subpanel-end allowed the estimation of the subpanel-to-column contact length. Further information on the mechanical characterization of the materials, the experimental behaviour, and other details are reported in Morandi et al. [2018] and Milanesi et al. [2022].

Within the present study, the behaviour of the test structure is numerically simulated by a two-dimensional finite element model in the FEAP (Taylor and Govindjee [2014]) environment. The modelling scheme adopted is the one proposed by Stavridis and Shing, [2010] to model traditional masonry infilled frames and recently adapted by Bolis et al., [2017] to model the ductile infill proposed by Preti et al. [2015]. The masonry and the concrete are modelled by means of a combination of continuum smeared-crack elements (Lotfi and Shing [1991]) and interface discrete-crack elements (Lotfi and Shing [1994]). This modelling scheme allows the simulation of the diffused flexural cracks and dominant shear cracks in the RC elements, the mixed-mode fracture of the mortar joints, as well as the crushing of the masonry units and RC members. The modelling frameworks has been extensively validated with data from single-bay single-storey infilled frames tested quasi-statically, as well as two three-storeys specimens tested on the shake-table (Stavridis [2009]), and instrumented structures in the field (Bose et al. [2019]). The modelling scheme was then extended by Bolis et al. [2017] to account for the sliding joints, which are simulated by interface elements to allow local sliding between each sub-panel. The main material parameters are reported in Milanesi et al., [2021] and are also briefly presented in Table 1 and

Table 2. The schematic representation of the model is reported in Figure 2.

Table 1: Smeared-crack elements properties (Milanesi et al. [2021]).

Material	**SMEARED-CRACK ELEMENTS**					
	E [MPa]	**G [MPa]**	**ν [-]**	**t [mm]**	**f_c [MPa]**	**f_t [MPa]**
Concrete	25000	10417	0.20	350	37	1
Masonry	2600	1150	0.13	250	2.9	0.6
Deformable Mortar top	5	2	0.38	100	10.0	2.0
Deformable Mortar lateral	8	2.9	0.38	250	10.0	2.0

E: Young Modulus, G: shear modulus, ν: Poisson ratio, t: thickness, f_c: Compression resistance, f_t: Tensile resistance

Table 2: Interface elements properties (Milanesi et al. [2021]).

Material	**INTERFACE ELEMENTS**					
	s_0 [MPa]	**μ_0 [-]**	**μ_r [-]**	**r_0 [MPa]**	**r_r [MPa]**	**t [mm]**
Bed joints	0.45	0.88	0.75	0.005	0.005	250
Brick head joints	0.70	1.00	0.80	0.28	0.21	250
Mortar vertical joints	0.90	0.862	0.75	0.005	0.005	250
Concrete joints	1.00	0.90	0.70	0.25	0.20	350
Lateral joints	0.05	0.50	0.45	0.10	0.10	250
Top joint	0.05	0.25	0.20	0.10	0.10	250
Sliding joints	0.15	0.361	0.361	0.02	0.02	250

s_0: initial tensile strength, μ_0: initial yield surface asymptote slope, μ_r: residual yield surface asymptote slope, r_0: initial yield surface apex radius, r_r: residual yield surface apex radius, t: thickness

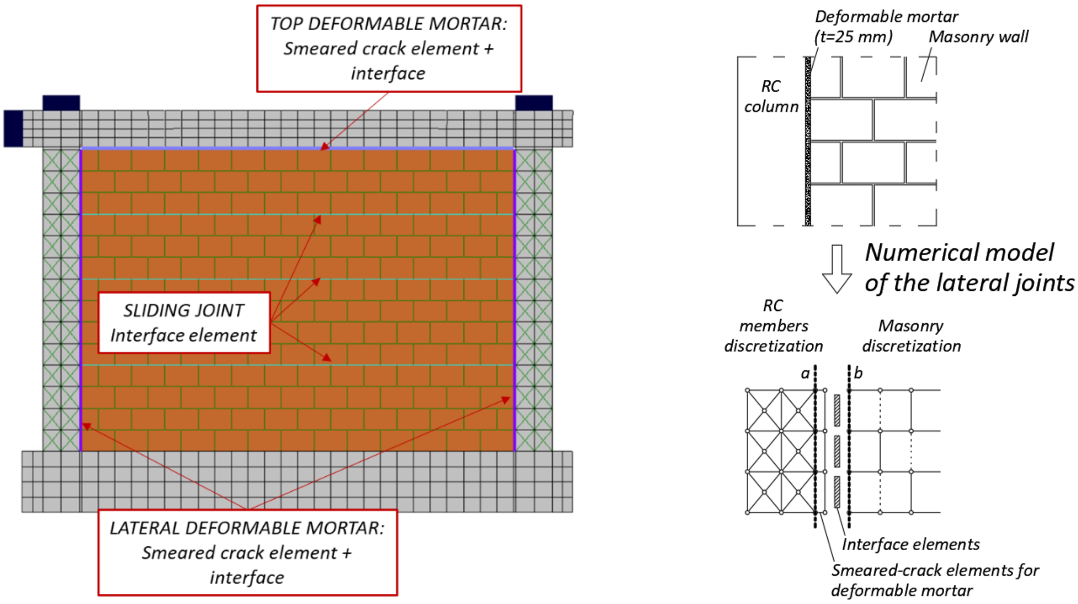

(a) (b)

Figure 2: (a) Infill frame mesh and detail of the sliding and contact joints; (b) detail of the contact joint modeling. (Milanesi et al. [2021])

2.2 COMPARISON OF THE RESULTS

The numerically obtained monotonic base-shear vs. top displacement curve is compared to the envelope of the experimental cyclic response (Figure 3). The initial stiffness is well captured, and the maximum strength is less than 10% higher with respect to the experimental one. This difference could be justified by the experimental strength degradation due to the cyclic load, which is not considered in the numerical simulation.

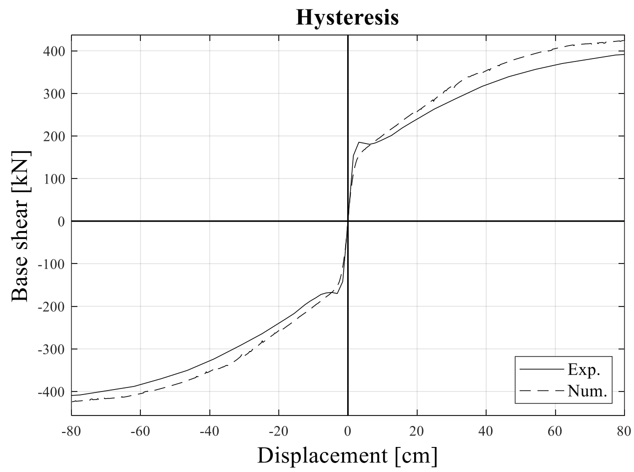

Figure 3: Experimental and numerical hysteresis (Milanesi et al. [2021])

To further assess the ability of the numerical model to simulate the behaviour of the test structure, the experimental local average deformation of the lateral deformable mortar is considered. This is estimated by dividing the deformation measured by the linear transducer by the thickness of the mortar joint. This assumption is possible as long as the masonry is significantly stiffer than the deformable mortar. Given the presence of two instruments for each sub-panel, the deformation profile along the height is evaluated assuming a linear trend in each sub-panel. The numerical one is evaluated considering the difference in displacement between the nodes of the masonry and those of concrete at the same height. Figure 4 represents the comparison of the two deformation profiles of the column/panel joint for both windward and leeward columns corresponding to the experimental cycle at 2.0% of imposed drift. The experimental results are well reproduced by the numerical modelling, in particular with regard to the contact length.

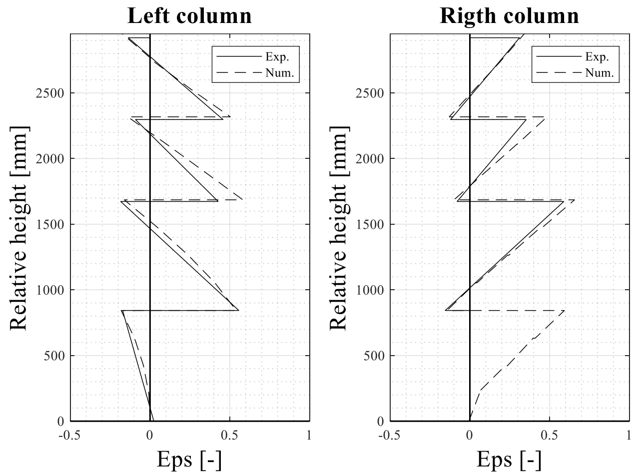

Figure 4: Lateral joint deformation profile for each column at 2.0% drift (Milanesi et al. [2021]).

3. PARAMETRIC ANALYSIS

3.1 Design parameters object of the parametric analysis

The parametric analysis focuses on the main design parameters influencing the in-plane response of the infill, including the stiffness of the deformable mortar joints, the number and layout of the sliding joints, the boundary condition at the top of the infill, and the length of the infill.

The influence of the deformable mortar joint stiffness, which is modelled with a simplified linear-elastic behaviour, is explored by increasing the reference value up to eight times, within a range considered realistic for the practical application. Different numbers, ranging from 0 to 13, and layouts of sliding joints are considered to investigate if different number or configurations of sliding joints could improve the behaviour observed during the experiments. Furthermore, the solution without sliding joints and with a deformable contact material at the lateral and top interfaces is also considered to provide a baseline comparison. The length of the infill is also varied to consider different aspect ratios to address a range of lengths that could be found in real applications. Finally, in addition to the masonry with hollowed clay units used in the reference test, other masonry types of different mechanical properties and thickness are taken into account, as analysed in Bolis et al., [2017]. Details of the different parameters are reported in Table 3.

Table 3: Design parameters considered in the parametric analysis

Param.	Model name	Geometry		Materials						
				Masonry prism					Top joint	Lateral joint
		L	n. sliding joint	Material	E	fc	ft	Thick	E	E
		[m]			[MPa]	[MPa]	[MPa]	[mm]	[MPa]	[MPa]
Baseline	***Baseline***	***4200***	***3***	***Hollow clay***	***2600***	***2.9***	***0.6***	***250***	***5***	***8***
	E7.5l									**7.5**
	E15l									**15.0**
Lat. joint stiff.	E30l	4200	3	Hollow clay	2600	2.9	0.6	250	5	**30.0**
	E45l									**45.0**
	E60l									**60.0**
	E7.5s								**7.5**	
	E15s								**15.0**	
Top joint stiff.	E30s	4200	3	Hollow clay	2600	2.9	0.6	250	**30.0**	8
	E45s								**45.0**	
	E60s								**60.0**	
	J0		0							
	J2_455		2							
	J2_545		2							
	J2_554		2							
N. sliding joints	**J3_3443**	4200	3	Hollow clay	2600	2.9	0.6	250	5	8
	J3_4334		3							
	J4		4							
	J5		5							
	J6		6							
	J13		13							
JX_ABCD: X=n. of sliding joints, ABCD: n. of courses between each sliding joints, i.e. baseline is J3_4433 (see Figure 1*)*										
	H295L320	**3200**								
Aspect ratio	H295L520	**5200**	3	Hollow clay	2600	2.9	0.6	250	5.0	8
	H295L610	**6100**								
	AAC200			**AAC200**	1600	1.8	0.5	200		
Masonry properties	AAC300	4200	3	**AAC300**				300	5	8
	CU1			**Solid CU1**	27579	23.44	4.82	190.5		
	Mehrabi9			**Mehrabi 9**	15168	14.2	1.72	92.5		

3.2 PARAMETRIC ANALYSIS RESULTS

In this section, the response of each case is compared to the response of the baseline model ("B"). The base shear vs. drift curve, the shear action acting on the columns, and the crushing of the first subpanel corner are reported.

3.2.1 Base shear – Drift response

As illustrated in **Errore. L'origine riferimento non è stata trovata.**, all the analyses show a ductile and hardening behaviour. From the Figure 5a, it is evident that the increase in the lateral joint stiffness has an insignificant influence on the global response. However, the lateral strength increases as the top joint stiffness increases (Figure 5b). This can be expected as the normal action acting on the infill and the joints increases as the joint stiffness increases. As indicated in previous studies (Bolis et al. [2017]), a reduction in the strength and stiffness of the infill occurs by increasing the number of the sliding joints when only a few joints are included (Figure 5c). A number of sliding joints equal or higher than three does not seem to affect the response. The absence of sliding joints led to a brittle failure characterised by the diagonal cracking of the infill. The length of the infill frame does not seem to affect the results (Figure 5d). The lateral strength reduces by reducing the masonry strength and thickness (AAC200 and Mehrabi9) (Figure 5e).

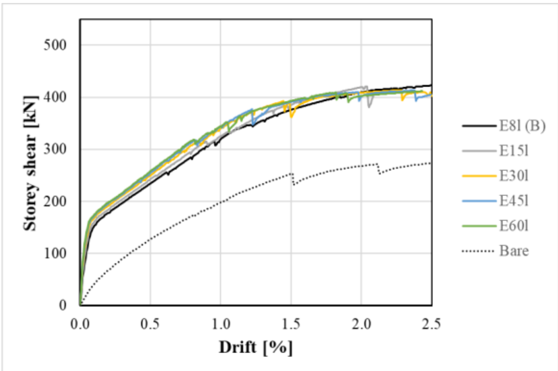

a) Lateral joints stiffness

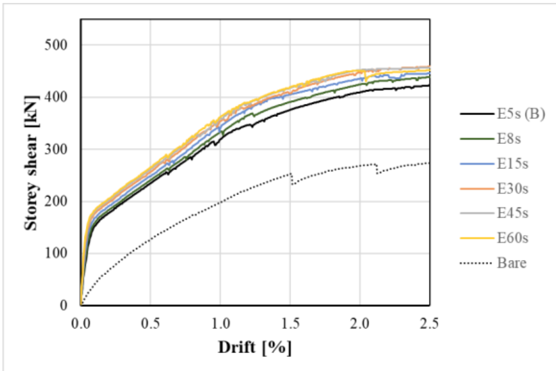

b) Top joint stiffness

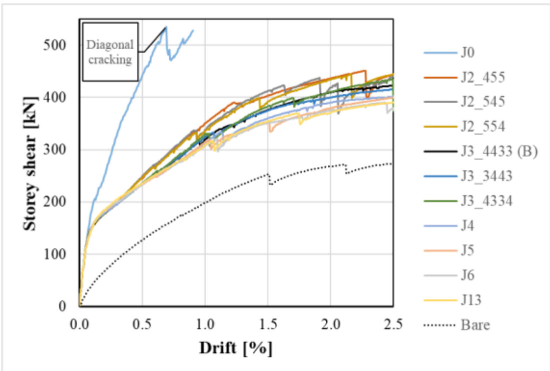

c) Number of sliding joints

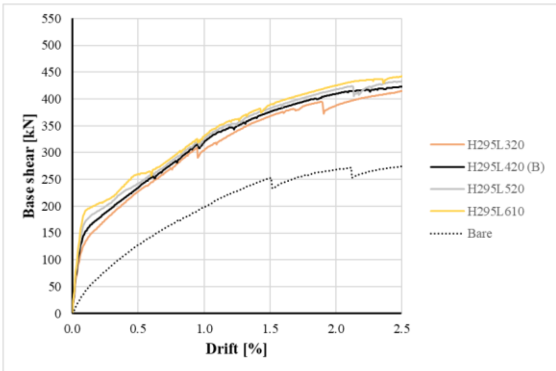

d) Infills length

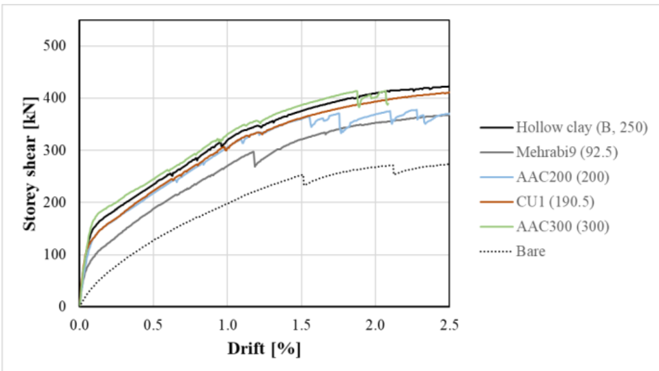

e) Masonry type and thickness

Figure 5: Base shear vs Drift response for the different design parameters considered. For the nomenclature, refer to Table 3.

3.2.2 Shear action on the columns

The maximum shear action in the columns occurs at the top of the windward column and at the base of the leeward one. In general, the shear action is higher than the shear acting on the columns of the bare frame, estimated as equal to half the frame base shear. The parametric analysis shows that the maximum shear action is sensitive to the number of sliding joints and the stiffness of the lateral joints. The stiffness of the top joint and the length of the infill do not considerably affect the column shear action. **Errore. L'origine riferimento non è stata trovata.** shows the trends of the maximum shear action acting on the top of the windward column and at the base of the leeward column for the two most influential design parameters.

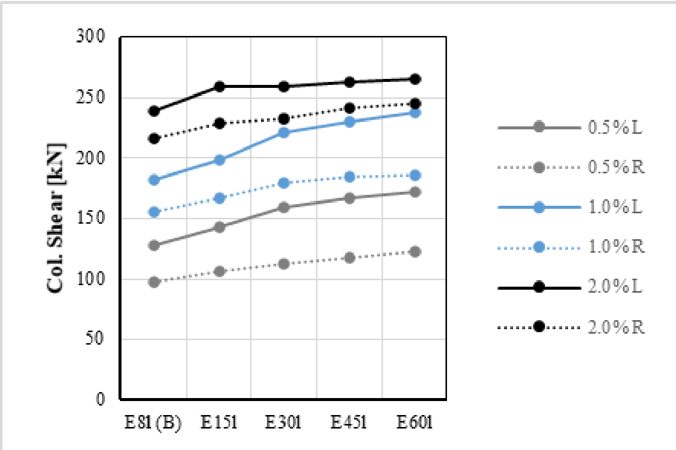

Lateral joint stiffness

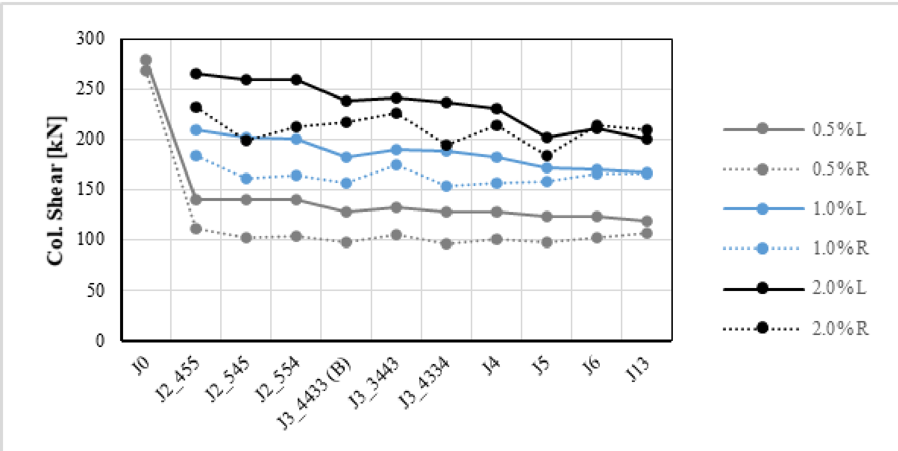

Number of sliding joints

Figure 6: Max shear action acting on the top of the left (L) and the base of the right (R) columns for different levels of drift.

3.2.3 Local crushing of the masonry

In Figure 7, the base shear vs. drift responses of all the parametric analyses are reported, and the point corresponding to the first crushing of the subpanel edge is highlighted. The crushing is identified at the reaching of the compressive strain corresponding to the masonry peak strength evaluated at an integration point of the smeared crack element. In red, the lateral deformable mortar stiffness varying cases are highlighted; in black, all the other cases where crushing occurred for drift values lower than 2.5% are indicated.

As the stiffness of the lateral contact interfaces increases, the masonry local crushing progressively occurs at lower drift levels. A minimum of three sliding joints is required to avoid local crushing at a drift level lower than 2.5%. Only the configuration with the larger subpanels at the base and the top of the infill led to a local crushing for drift level slightly lower than 2.5%. Very weak materials like AAC must be considered cautiously because their resistance may be too low to prevent anticipated crushing.

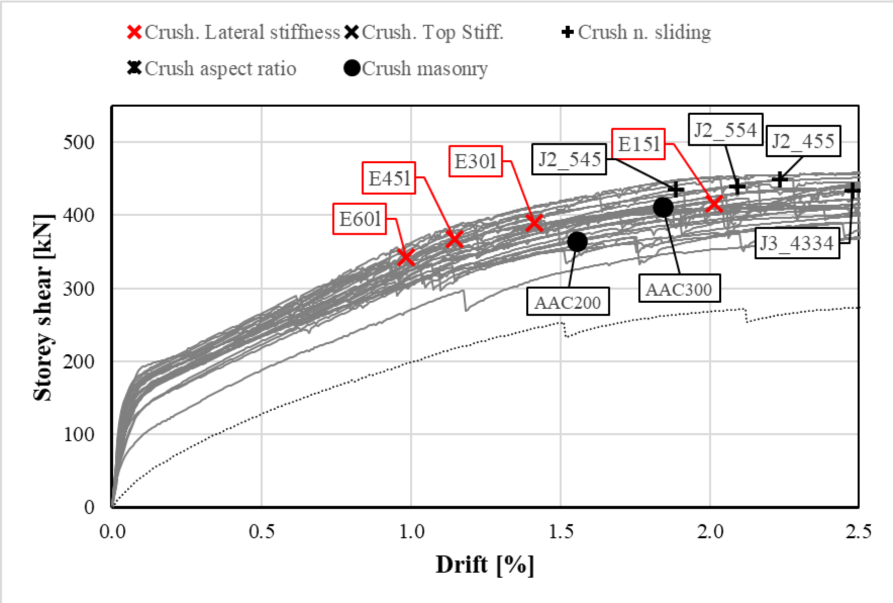

Figure 7: Local crushing of the edge of the subpanels for the different analyses.

3.3 Results discussion and proposed design provisions

According to the parametric analysis, the minimum number of sliding joints which ensures ductile behaviour and local crushing of the masonry subpanels for drift levels greater than 2.5% is equal to three. This is also in agreement with the experimental campaign conducted by Mohammadi et al. [2010], where the adoption of a single sliding joint at half of the panel height and two sliding joints has demonstrated a worse in-plane performance with respect to more recent tests, where at least three sliding joints have been included within the infill.

The stiffness of the lateral contact material seems to influence the local damage of the masonry and the drift at which it occurs. In particular, the activation of the local damage is influenced by the ratio between the stiffness of the lateral joint (E_{lat}) and the compressive strength of the masonry in the horizontal direction (f_m). With a simplified approach, it is possible to derive a limit for the ratio E_{lat} over f_m in order to avoid an anticipated corner crushing. By assuming a linear distribution of the deformations along the contact material characterised by an inclination equal to the drift, it is possible to evaluate the contact stress by multiplying the deformation by the stiffness of the lateral contact material. This stress must be lower than the horizontal strength of the masonry to avoid its damage (Eq. 1a). As shown in Eq. 1b, it is possible to define a limit for this ratio which prevents the local damage of the masonry for a target interstorey drift level δ.

$$\frac{\delta \cdot (\lambda h) \cdot E_{lat}}{s} < f_m \tag{1a}$$

$$\left(\frac{E_{lat}}{f_m}\right)_{lim} < \frac{s}{\delta \cdot (\lambda h)} \quad , \quad \lambda = \frac{1}{2} \tag{1b}$$

where λ defines the ratio of the contact depth over the mean subpanel height, *h*, and *s* is the thickness.

In Figure 8, the curve of the drift where the local damage occurs, as obtained by Equation 1b, is represented. The variation of the contact material stiffness, the number of sliding joints and the masonry properties are considered. The representation of the analytical curve for two (J2) and three joints (J3) is reported.

It is important to highlight that, for design purposes, a minimum strength of the masonry must be defined since, in case the masonry resistance is too low, the sliding mechanism could not be activated due to the anticipation of the masonry failure. The proposed formulation should be considered as a preliminary proposal that needs to be further investigated through future studies.

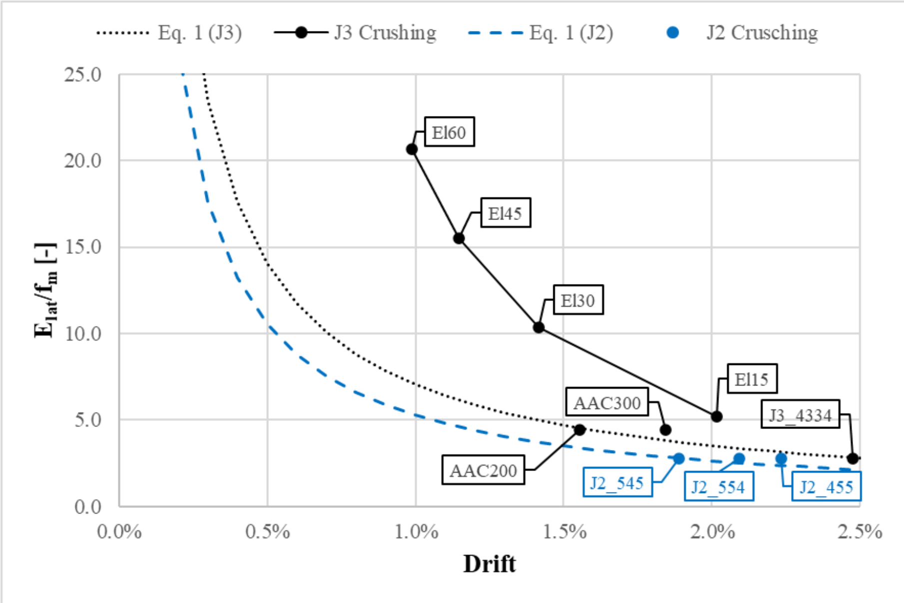

Figure 8: comparison between the numerical and the analytical prevision of the activation of the masonry damage.

4. CONCLUSIONS

An experimental test of a ductile masonry infill has been simulated in a detailed FEM environment and the results have been compared with the experimental ones both at a global and local level. The model has been therefore used to investigate the influence of the main design parameters on the lateral strength and the local damage of the infill through a parametric study. The design parameters that have been studied had both the aim to increase the knowledge of the new infill system and determine, if necessary, some limits that should not be exceeded in real applications.

The increase in the length of the infill does not affect the response, meanwhile a minimum of three sliding joints is required to have ductile behaviour and to prevent local masonry damage at low drift levels. The shear action acting on the columns is higher than the bare frame, and it is not negligible since an interaction with structural elements occurs. However, the shear action can be somehow controlled since it reduces as the stiffness of the lateral joints decreases and the number of sliding joints increases.

The increase in the stiffness of the top joint contact material leads to an increase in the global lateral strength, but it does not affect the local damage of the masonry. On the other hand, the stiffness of the lateral contact materials influences only the local damage of the infill by the crushing of the subpanel edges. In fact, as the stiffness increases, the contact force is localised, and the masonry crushing is anticipated. The activation of the local damage is affected by the ratio between the elastic modulus of the lateral contact material and the horizontal strength of the masonry. In conclusion, a simple equation, which may be adopted in the design process, is proposed as a preliminary procedure to estimate a limit ratio that allows for the prevention of local masonry damage at a defined drift level; however, further studies to improve some design processes and investigate the possibility to refine the proposed formulation are planned as a future development of the present research.

ACKNOWLEDGEMENTS

The work has been conducted within the framework of DPC/ReLUIS project 2019-2021 and 2022-2023, WP10, where both the University of Brescia and the University of Pavia are involved.

REFERENCES

Bolis, V., Stavridis, A., and Preti, M. [2017] "Numerical Investigation of the In-Plane Performance of Masonry-Infilled RC Frames with Sliding Subpanels," *Journal of Structural Engineering*, Vol. 143, No.2, p. 04016168.

Bose, S., Martin, J., and Stavridis, A. [2019] "Simulation Framework for Infilled RC Frames Subjected to Seismic Loads," *Earthquake Spectra*, Vol. 35, No.4, pp. 1739–1762.

Braga, F., Manfredi, V., Masi, A., Salvatori, A., and Vona, M. [2011] "Performance of non-structural elements in RC buildings during the L'Aquila, 2009 earthquake," *Bulletin of Earthquake Engineering*, Vol. 9, No.1, pp. 307–324.

Fikri, R., Dizhur, D., Walsh, K., and Ingham, J. [2019] "Seismic performance of Reinforced Concrete Frame with Masonry Infill buildings in the 2010/2011 Canterbury, New Zealand earthquakes," *Bulletin of Earthquake Engineering*, Vol. 17, No.2, pp. 737–757.

Lotfi, H. R., and Shing, P. B. [1991] "An appraisal of smeared crack models for masonry shear wall analysis," *Computers & Structures*, Vol. 41, No.3, pp. 413–425.

Lotfi, H. R., and Shing, P. B. [1994] "Interface Model Applied to Fracture of Masonry Structures," *Journal of Structural Engineering*, Vol. 120, No.1, pp. 63–80.

Milanesi, R. R., Bolis, V., Pelucco, S., Morandi, P., Magenes, G., and Preti, M. [2021] "Local effects due to the seismic interaction between innovative ductile masonry infills and RC elements," *Proceedings of the 8th COMPDYN 2021*, pp. 899–912.

Milanesi, R. R., Morandi, P., Manzini, C. F., Albanesi, L., and Magenes, G. [2022] "Out-of-plane Response of an Innovative Masonry Infill with Sliding Joints from Shaking Table Tests," *Journal of Earthquake Engineering*, Vol. 26, No.4, pp. 1789–1823.

Mohammadi, M., and Akrami, V. [2010] "An engineered infilled frame: Behavior and calibration," *Journal of Constructional Steel Research*, Vol. 66, No.6, pp. 842–849.

Morandi, P., Milanesi, R. R., and Magenes, G. [2018] "Innovative solution for seismic-resistant masonry infills with sliding joints: in-plane experimental performance," *Engineering Structures*, Vol. 176, pp. 719–733.

Preti, M., Migliorati, L., and Giuriani, E. [2015] "Experimental testing of engineered masonry infill walls for post-earthquake structural damage control," *Bulletin of Earthquake Engineering*, Vol. 13, No.7, pp. 2029–2049.

Stavridis, A. [2009] "PhD_Th_Stavridis, 2009.pdf," *Ph.D. thesis*, Univ. of California.

Stavridis, A., and Shing, P. B. [2010] "Finite-Element Modeling of Nonlinear Behavior of Masonry-Infilled RC Frames," *Journal of Structural Engineering*, Vol. 136, No.3, pp. 285–296.

Taylor, R. L., and Govindjee, S. [2014] "FEAP - - A Finite Element Analysis Program," Vol. University of California, Berkeley, p. 705.

Development of a simplified modeling technique for seismic performance assessment of gypsum partition walls

Iraj Lotfy[1], Mojtaba Salkhordeh[2], Siavash Soroushian[3], Esmaeil Rahmanishamsi[4], and Manos Maragakis[5]

[1] K. N. Toosi University of Technology
1346, ValiAsr Street, Mirdamad cross, Tehran, Iran
Irane-mail: I.lotfy@mail.kntu.ac.ir
[2] K. N. Toosi University of Technology
1346, ValiAsr Street, Mirdamad cross, Tehran, Iran
m-salkhordeh@email.kntu.ac.ir
[3] K. N. Toosi University of Technology
1346, ValiAsr Street, Mirdamad cross, Tehran, Iran
ssoroushian@kntu.ac.ir
[4] Chief Engineer-R&D, MiTek USA Inc., Corona, California, USA
erahmanishamsi@unr.edu
[5] University of Nevada, Reno, Nevada, USA
maragaki@unr.edu

Abstract. Recent studies proposed some complicated finite element modeling procedures to simulate the seismic performance of partition walls. However, the proposed modeling procedures include a detailed configuration of the walls using various types of nonlinear elements and springs that made it difficult to lay these micro-models into the macro-models of the whole building. In this regard, the present study proposed a simplified modeling technique to consider the seismic performance of gypsum partition walls in the macro-models of buildings. To do so, the nonlinear behavior of the wall is simulated by a nonlinear spring representing the hysteresis behavior of the wall using the "pinching4" element in the Opensees platform. The cyclic performance of the proposed technique is validated by the micro-model of the walls developed by previous researchers. Another problem raised for simulating the gypsum partition walls is related to numerous geometric and mechanical variables of these walls. This study presents some simple relationships to determine the "pinching4" parameters for the walls with different aspect ratios.

Keywords: Gypsum partition walls, Modelling technique, Pinching4, Cyclic performance, Nonlinear behavior.

1. INTRODUCION

Experiences gained from previous earthquake events clarified the importance of nonstructural elements due to their significant contribution to the total exposed risk to the buildings. These systems include approximately 48% to 70% of the total cost of building construction [Davies et al., 2012]. The vulnerability of the nonstructural components of the building was significant as these elements suffer damage at drift ratios much less than those required to initiate structural damage. Gypsum partition walls are one of the nonstructural components that were significantly damaged during recent earthquakes [Taghavi and Miranda, 2003]. These ground motions and experimental tests implemented on the partition walls reveal the damage mechanisms of these elements. Damage to the studs and track elements (e.g., bending of studs and failure of the joint between the track and stud elements), cracking at the openings of gypsum boards, and crashing at the corners of the wall are from common damage mechanisms of the partition walls. As an example, Figure 1 shows some damage mechanisms imposed on the gypsum partition walls in recent events and experimental tests. More information on the seismic damage mechanisms of partition walls can be found in [Fiorino, Pali and Landolfo, 2018; Araya-Letelier, Miranda and Deierlein, 2019; and Kim and Shin, 2021].

(a) Detachment of stud and track elements [Fiorino, Pali and Landolfo, 2018]

(b) Crack at the corner of opening [Salmasi Javid et al., 2020]

(c) Breaking of the wall (photo courtesy of S. Soroushian)

Figure 1 Damage mechanisms of gypsum partition walls; (a) and (b) from experiments, and (c) from Kermanshah 2016 earthquake

The vulnerability and economic costs related to these walls reveal the importance of investigating their seismic performance. Several studies were carried out to evaluate the cyclic performance of gypsum partition walls. Davies et al. [2011] implemented experimental tests to evaluate the cyclic performance, model parametrization, and effect of cold-formed steel-framed gypsum partition walls on the seismic performance of essential facilities. Fiorino, Pali and Landolfo [2018] investigated the out-of-plane behavior of lightweight partition walls by conducting experimental cyclic tests. Jenkins et al. [2016] evaluated the out-of-plane behavior of partition walls by conducting a series of experimental tests on the full-scale system-level braced-frame structure. Wang et al. [2015] investigated the seismic performance of two types of cold-formed partition walls by implementing shaking table tests using earthquakes with different peak ground accelerations. Such experimental studies pave the way for developing numerical models by which different aspects of seismic performance of gypsum partition walls can be evaluated. Several numerical models are developed for gypsum partition walls using the results derived from experimental tests. Kanvinde and Deierlein [2006] provided numerical models for estimating the lateral shear strength and initial stiffness of wood-framed gypsum partition walls. Davies et al. [2012] investigated the in-plane cyclic behavior of thirty-six full-scale experimental cold-formed gypsum partition walls. Rahmanishamsi et al. [2016] proposed a numerical modeling technique for simulating the seismic behavior of full connection cold-formed gypsum partition walls importing the effect of all variable parameters into the model. Wood and Hutchinson [2012] developed a simplified spring-based modeling technique for the cold-formed steel framed gypsum partition walls. These models were developed based on a finite number of experimental walls with a limited number of aspect ratios. Salmasi Javid et al. [2020] presented an approach for developing the fragility curves for the full connection gypsum partition walls. Recently, Salmasi Javid et al. [2022] investigated the effect of wall aspect ratio on the cyclic performance of cold-formed gypsum partition walls.

Although extensive studies are implemented to develop numerical simulation techniques for gypsum partition walls, the proposed methods include complicated modeling assumptions resulting in high computational costs. Besides, the spring-based modeling methodology developed by previous researchers was founded on a finite number of partition walls, which could not cover the behavior of walls with different design categories and construction quality. Therefore, the lack of generalized simplified models applicable for a wide range of partition walls is a clear research gap in the scope of nonstructural systems. This study proposed a spring-based modeling technique for simulating the cyclic performance of full connection gypsum partition walls based on the numerical models introduced by Rahmanishamsi et al. [2016] and developed by Salmasi Javid et al. [2020]. These numerical models were created for walls with different aspect ratios, geometrical properties, and construction qualities. According to the study of Salmasi Javid et al. [2020], the main parameter that affects the cyclic performance of gypsum partition walls is their aspect ratio. Herein, a regression procedure is implemented to calculate the parameters of the proposed simplified models between the known aspect ratio intervals.

In this paper, first, the micro modeling technique of the walls is reviewed. Then, the geometrical and design properties of the basic numerical modes are described. The proposed spring-based simplified modeling technique is explained in the next section. Afterward, the specimens are categorized into three types of minimum, median, and maximum capacity to pave the way for selecting an appropriate wall based on the force boundaries. Finally, the regression models are developed for the walls with an aspect ratio between the defined intervals.

2. REVIEW OF THE MICRO-MODELING PROCEDURE

The micro-models used in this study to construct the proposed spring-based simplified models are based on the numerical modeling technique developed by Rahmanishamsi et al. [2016]. These numerical models were simulated in the "Opensees" platform and validated using the results of experimental tests conducted by Davies et al. [2011] at the University of New York at Buffalo. The behavior of gypsum boards was simulated by four-node *ShellMITC4* element defined by "*ElasticMembranePlateSection*" command. The poisson's ratio and the modulus of elasticity of these boards were considered 0.3 and 144*ksi,* respectively. The studs and tracks were modeled by the "foceBeamColumn" element along with the "steel02" material command, which assumes the "Giuffre-Menegotto-Menegotto-Pinto"[McKenna, Fenves and Scott, 2006] uniaxial strain hardening material behavior. The distributed mass of elements was defined as the concentrated nodal mass in the model. The yield strength, modulus of elasticity, and strain hardening ratio of studs were respectively defined as 47.9ksi, 31763.3ksi, and 0.1% based on the manufacturer catalog. Also, the yield strength, Young's modulus, and strain-hardening slope of the trak elements were defined as 52.1ksi, 22190.8ksi, and 2.0%, respectively. The default values recommended for the steel02 material model were considered for the rest parameters of this command. The nonlinear interactions between different components (e.g., gypsum to studs connection) were defined using the "*Pinching4"* material model assigned to the *"twoNodeLink"* element. Figure 2 shows the controlling parameters of the *"Pinching4"* constitutive model.

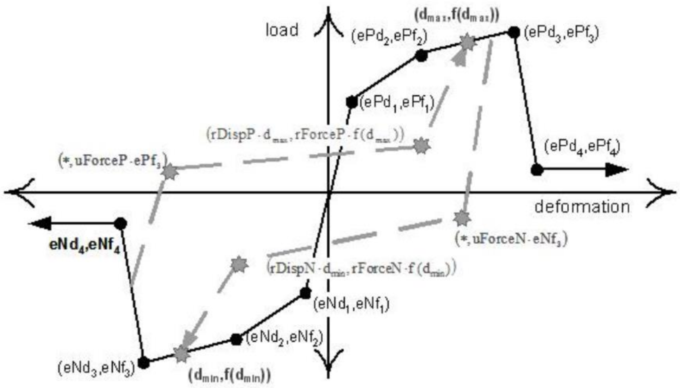

Figure 2 Variable parameters of the Pinching4 constitutive model [McKenna, Fenves and Scott, 2006]

The values considered for "*Pinching4*" parameters of the stud-to-track, track-to-concrete, and gypsum board-to-stud/track can be found in Salmasi Javid et al. [2020]. The gypsum board components were discritized into subcomponents with the size of $11.8in \times 11.8in$ to create additional nodes at the position of gypsum-to-track/stud joints and increase the accuracy of the simulation process. A rigid element was defined for the out-of-plane direction of the wall, while the "*twoNodeLink*" element was considered for the in-plane direction. The behavior of the mentioned "*twoNodeLink*" element was defined by the "*Pinching4*" material model. The connection between the gypsum-to-track\stud was the same as those considered for the interaction between stud-to-track elements. To define the interaction between the stud and track components after closure was defined by "*ElasticPPGap*" command using "*Pinching4*" material. The connection between the track and concrete elements was also defined by "*twoNodeLink*" command along with the "*Pinching4*" material for both tension and shear directions. The compression stiffness of concrete was simulated by the "*Elastic-No Tension (ENT)*" command with an initial stiffness of 91360$kips/in$. The contact behavior between the concrete slabs and gypsum boards was defined by parallel springs composed of series "zeroLengthContact3D" and "twoNodeLink" elements at which the "ElasticPPGap" material was assigned to the "twoNodeLink" command (Figure 3). Readers are encouraged to review Rahmanishamsi et al. [2016] to achieve more information in this regard. Figure 4 shows an overall view of the micro-modeling procedure.

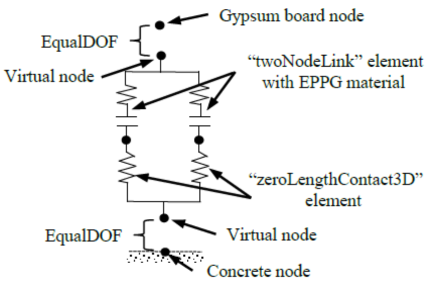

Figure 3 Concrete to gypsum connection

The simulation process mentioned for micro-finite element models was validated by Rahmanishamsi et al. [2016] based on the results of experimental tests implemented at the University of Nevada Reno, and state University at Buffalo [Davies et al., 2011]. Readers can refere to the mentioned reference to see the accuracy of the modeling procedure in capturing the hysteresis parameters of the experimental specimens.

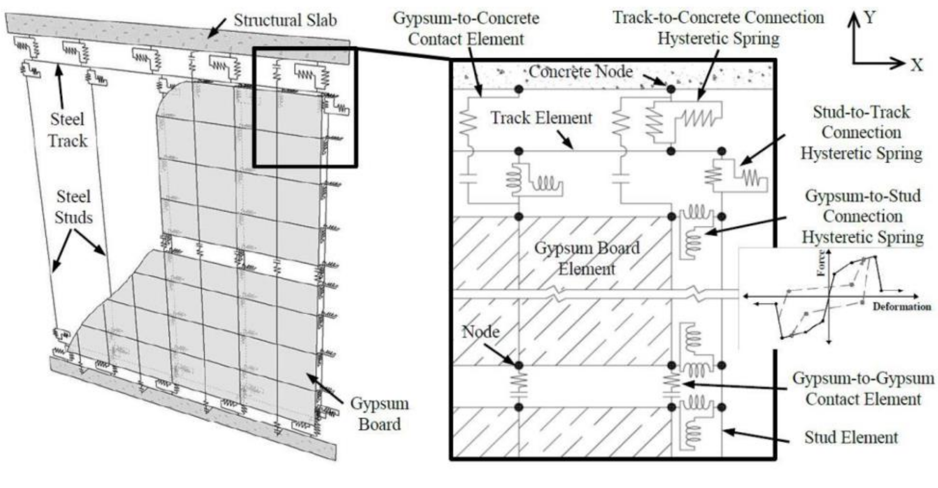

Figure 4 Overall view of the modeling methodology

3. VARIATIONS IN THE CONSTRUCTION OF WALLS

The micro-finite element models were provided for a wide range of gypsum partition walls in terms of various construction details (e.g., stud spacing, dimensions, connection details, and construction qualities). Variable parameters in the micro-models include the following cases:

- The thickness of track\stud elements was 0.019*in* or 0.03*in*.
- Each connection was simulated with three different construction quality (lowest quality, average quality, and best quality).
- Four different edge distances (distance from the edge of the gypsum board to the center of screws (e_1)) of 0.5*in*, 0.75*in*, 1.0*in*, and 1.5*in* were considered (Figure 5a).
- The edge distance in track-to-stud connection (e_2) (Figure 5b) was defined as distances lower and larger than the threshold value of 0.5*in*.
- Six different aspect ratios (height-to-width ratio) of 0.33, 0.5, 1.0, 1.5, 2.0, and 3.0 were considered.

It should be emphasized that the cyclic behavior of gypsum partition walls having 1.2*in* thickness does not depend on the distance from the edge of the track\stud flanges to the center of screws. Totally, thirty-six specimens with variations in the above-mentioned parameters were constructed for each aspect ratio of the walls. These scenarios can be found in Salmasi Javid et al., 2020.

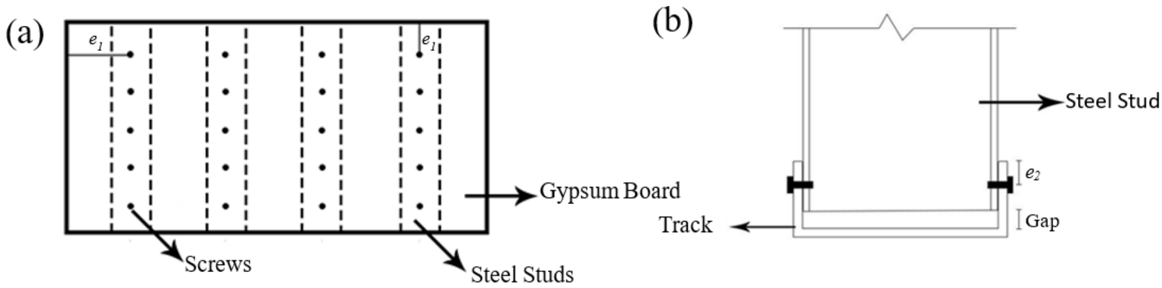

Figure 5 edge distances (a) e_1 parameter (b) e_2 parameter

4. SPRING-BASED SIMPLIFIED MODELS

This paper proposed a simplified spring-based model to capture the hysteresis behavior of gypsum partition walls based on the results of the micro-finite element models. The proposed technique uses a "*zeroLength*" element with the "*Pinching4*" material connected to a rigid truss system to simulate the stiffness and strength parameters of the whole wall. Figure 6 shows the schematic view of the proposed model for a simple frame.

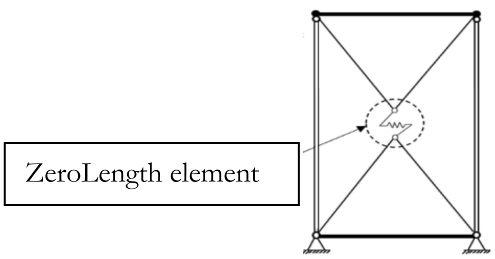

Figure 6 schematic view of the proposed model

It should be noted that the micro-models of the gypsum partition walls are always accompanied by high computational costs and convergence problems, which made it impossible to import these models to the macro-models of the structures. The main objective of the proposed technique is to pave the way for simulating the effect of partition walls on the seismic behavior of the whole building. These simplified models intensively reduce the computational cost related to the micro-models of partition walls and completely eliminate their convergence problem.

5. VERIFICATION

The cyclic performance of the specimens was used as the indicator to validate the accuracy of the proposed modeling technique. For this purpose, the hysteresis curves of the spring-based specimens were compared to the micro-models developed by Rahmanishamsi et al. [2016]. All the specimens were subjected to the cyclic loading protocol shown in Figure 7. This loading protocol is proposed by Davies et al. [2011] for evaluating the cyclic performance of gypsum partition walls. As an example, Figure 7 shows this comparison for a specimen with $THK = 0.03in$, $e_1 \geq 1.5in$, and the lower bound construction quality (Specimen#8). This figure compares the hysteresis curves, moment history, and dissipated energy of the micro-model and spring-based simplified model. As shown, the yield and maximum lateral strength, moment history, and cumulative dissipation energy of both modeling techniques are correlated. This correlation between the micro-models and the spring-based simplified models proves the reliability of the proposed modeling technique.

6. CAPACITY BOUNDS FOR THE WALLS

Since the geometrical properties and construction quality of the nonstructural walls result in having numerous configurations of these systems, it may not be possible for the designer to consider their effect on the seismic performance of building as the details of the wall is not determined perior to the design phase. To resolve the mentioned problem, thirty-six possible scenarios are reduced here to three bounds of maximum, median, and minimum capacity. This process enables the designer to consider the effect of the partition systems by knowing only the size of the wall and deciding about its capacity by interpreting the quality of implementation, materials, etc. In these models, it is assumed that the cyclic behavior of the specimens is symmetric in positive and negative loading direction. Therefore, the force and displacement floating points are obtained by averaging between the abolute of negative and positive values.

Previous studies [Salmasi Javid et al., 2020, 2022] proved that the seismic performance of gypsum partition walls significantly depends on their aspect ratio. The micro-models developed for simulating the cyclic behavior of these walls cover a finite number of aspect ratios. Therefore, the hysteresis parameters of the walls are not available for interstitial aspect ratios. To resolve the mentioned problem, this study proposed a regression-based procedure to obtain the spring-based force parameters. The force parameters of the "Pinching4" material model are estimated for different displacement points. Implementing a regressor on the force values for different aspect ratios requires fixed displacement values for specimens under the regression process. The following section describes the calibration procedure employed here to fix the displacement values.

7. CALIBRATING THE FORCE VALUES

As mentioned, the force values should be available at constant displacement values for specimens with different aspect ratios to execute the regression between the force points. For this purpose, the displacement value corresponding to each force floating point (i.e., ef_1, ef_2, ef_3, and ef_4) of all specimens with the same aspect ratio is defined as the median value of displacements among all specimens in that bin.

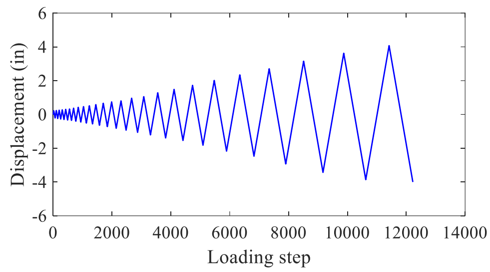

Figure 7 Loading protocol

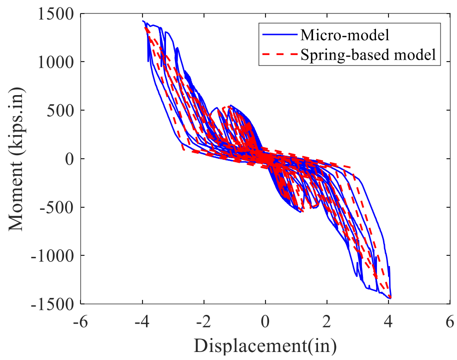

(a) Hysteresis curves

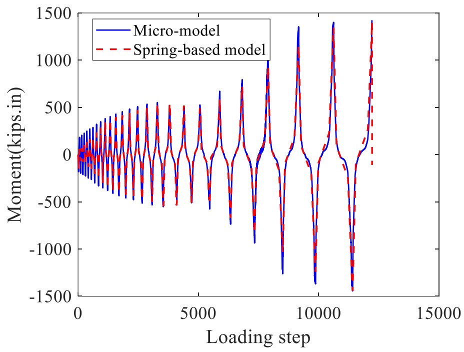

(b) Moment history

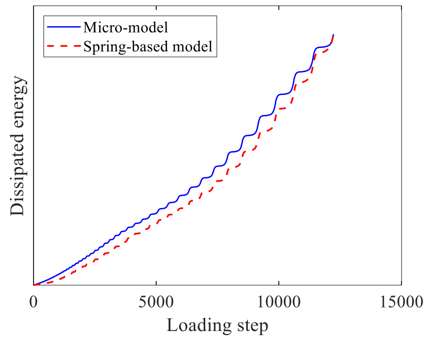

(c) Dissipated energy

Figure 8 Comparison between the hysteresis parameters of the micro- and spring-based models

For example, Figure 9 shows the box plot for the floating displacement values (for specimens with an aspect ratio of 3.0) and the median values of displacement related to each group. Figure 10 compares the changes in the hysteresis curve of an original spring-based specimen to its calibrated model. According to this figure, the cyclic parameters of the model (e.g., initial stiffness, ultimate strength, and dissipated energy) did not affect significant changes during the calibration. Although the mentioned procedure imports imperative error to the cyclic characteristics of the specimens, this error has no significant effect on the hysteresis curves of the models. Moreover, the benefit of the proposed simplified models (low computational cost, eliminating convergence problems, and paving the way for considering the effect of these components on the macro models of buildings) overcomes the cost related to the slight deviation from the original micro-model results.

Table 1 presents the spring-based parameters of gypsum partition walls for the specimens with maximum, median, and minimum capacity after the calibration. In addition, the cumulative dissipated energy of each specimen is compared to the corresponding spring-based model before the calibration. According to this comparison, the maximum difference between the cumulative dissipated energy of specimens after the calibration to their original ones is 12.9%. Thus, it can be concluded that the calibrated models provide adequate accuracy compared to the original specimens.

8. REGRESSION-BASED MODELS

After calibrating the force values of the spring-based models concerning the fixed displacement values, it is now possible to implement a regression process to obtain the force values for interstitial aspect ratios. To do so, two different regression functions (linear and second-order polynomial functions) are used to interpret the force values. Figure 11 shows the goodness of regression functions for ef_1 force parameter. According to this figure, the linear function did not match well to the datapoints compared to the second-order polynomial function.

As shown, the value of R^2 is equal to 0.73 and 0.94 for the linear and second-order regression functions, respectively. Similar trend was observed for the rest of force parameters (i.e., ef_2, ef_3, ef_4). Table 2 summarizes the regression functions obtained for all boundary specimens and force parameters. Generally, the second-order polynomial function presents a more accurate relationship for interpolating the force values compared to the linear function. In addition, according to Figure 11, the linear function results in negative values for some aspect ratios, which seems incorrect as the force values of backbone curves should be positive.

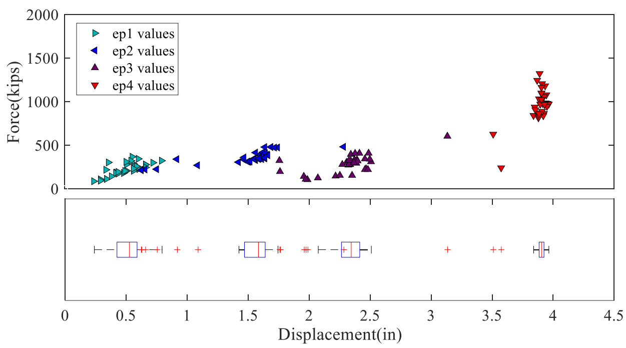

Figure 9 median values obtained for models with aspect ratio of 3.0.

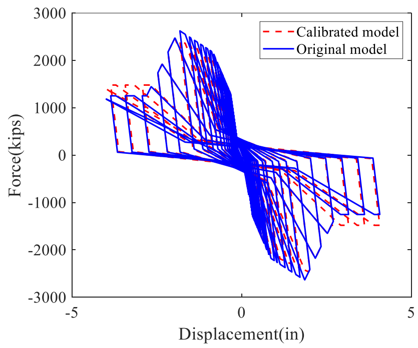

Figure 10 effect of calibration on the hysteresis curves of the spring-based models

9. CONCLUSIONS

This paper presented a spring-based simplified modeling technique for the gypsum partition walls. These models were adopted from the micro-finite element models developed by Rahmanishamsi et al. [2016]. Since the geometrical properties and construction quality of the walls provide a wide range of configurations for these systems, it may not be possible for the designer to consider their effect on the seismic behavior of the buildings. This is because the characteristics of the walls are commonly not known before the design phase of the structure. Herein, the nonstructural walls were categorized into three capacity bounds, i.e., maximum, median, and minimum capacity. This classification enables the designer to consider the effect of nonstructural walls on the seismic performance of the building by finite knowledge about their properties.

Table 1 spring-based simplified models after calibration

Bounds	AS	Stud THK	Track THK	e1	e2	ef1	ef2	ef3	ef4	ed1	ed2	ed3	ed4	rDisp	rForce	uForce	gKLim.	gDLim.	gF	gE	Energy	Error (%)
Minimum Capacity	0.33	0.48	0.48	>=13	>=13	0.505	1.0475	2.2675	3.11	3376.64	4801.64	2223.33	2089.05	0.25	0.45	-0.01	0.3	0.05	0	1	83440.39	1.2
	0.5	0.48	0.48	>=13	>=13	0.5125	1.165	2.1075	3.0575	2032.36	2750.05	1270.57	1275.71	0.58	0.21	-0.04	-0.3	0.1	0	0.5	2.56E+04	1.4
	1	0.48	0.48	>=13	<13	0.33	0.79	1.975	2.645	874.92	1372.67	649.43	675	0.5	0.22	-0.05	-0.5	0.05	0	0.5	18353.41	5.5
	1.5	0.48	0.48	>=13	>=13	0.46	1.2125	2.5825	3.225	663.43	1143.41	363.71	526.15	0.5	0.23	-0.04	-0.6	0.1	0	0.5	13590.94	5.3
	2	0.76	0.76	>=13	Can vary	0.525	1.2225	1.85	3.8275	429.46	663.85	786.31	73.56	0.45	0.6	-0.15	0.6	0.05	0	0.8	8291.11	4.3
	3	0.48	0.48	>=13	>=13	0.5275	1.585	2.345	3.905	215.08	408.82	492.43	242.15	0.5	0.15	-0.04	-0.1	0.01	0	0.5	4429.35	3.5
Median Capacity	0.33	0.48	0.48	>=25	>=13	0.505	1.0475	2.2675	3.11	2840.5	4040.62	5739.7	2902.26	0.45	0.4	-0.1	0.4	0.05	0	1	62498.54	9.5
	0.5	0.76	0.76	>=38	Can vary	0.5125	1.165	2.1075	3.0575	1978.49	2327.23	4002.42	1612.37	0.7	0.2	-0.04	-0.85	0.15	0	0.9	28120.31	8.9
	1	0.76	0.76	>=38	Can vary	0.33	0.79	1.975	2.645	961.77	1737.98	2041.46	1212.46	0.4	0.17	-0.05	-0.7	0.05	0	0.5	25805.82	10.7
	1.5	0.48	0.48	>=38	>=13	0.4625	1.2125	2.5825	3.225	568.12	598.4	1487.72	1169.21	0.65	0.18	-0.04	-0.85	0.15	0	1	11727.74	10.1
	2	0.76	0.76	>=19	Can vary	0.525	1.2225	1.85	3.8275	352.43	287.51	410.252	1116.98	0.52	0.18	-0.08	-0.35	0.05	0	0.3	6336.53	9
	3	0.48	0.48	>=19	<13	0.5275	1.585	2.345	3.905	191.06	351.33	288.015	960.4	0.55	0.18	-0.04	-0.4	0.01	0	0.9	3457.01	5.7
Maximum Capacity	0.33	0.76	0.76	>=38	Can vary	0.505	1.0475	2.2675	3.11	4335.72	5661.99	7956.45	4900.06	0.45	0.4	-0.1	0.2	0.05	0	1	1.19E+05	4.6
	0.5	0.48	0.48	>=25	>=13	0.5125	1.165	2.1075	3.0575	2833.76	3844.19	5249.65	3551.83	0.67	0.22	-0.04	-0.85	0.1	0	1.5	57205.62	0.4
	1	0.48	0.48	>=38	>=13	0.33	0.79	1.975	2.645	1378.53	2038.94	2907.16	1706.09	0.55	0.18	-0.05	-0.5	0.01	0	0.5	37277.09	3.4
	1.5	0.48	0.48	>=38	<13	0.4625	1.2125	2.5825	3.225	1013.99	1187.47	2037.36	1223.8	0.67	0.22	-0.04	-0.85	0.1	0	1.5	21420.42	2.7
	2	0.48	0.48	>=25	>=13	0.525	1.2225	1.85	3.8275	449.72	709.68	685.54	2075.89	0.4	0.18	-0.12	-0.2	0.05	0	0.5	8172.15	12.9
	3	0.48	0.48	>=38	<13	0.5275	1.585	2.345	3.905	350.95	311.71	600.13	1331.53	0.64	0.16	-0.07	-0.85	0.05	0	0.8	5469.48	2.1

Table 2 Results of regression for specimens with boundary capacities

Specimen	Function	Parameter	Regression	R^2
Maximum capacity	Linear	ef_1	$ef1 = -1357AR + 3627$	0.73
	Second-order	ef_1	$ef_1 = 671.9AR^2 - 3433AR + 4555$	0.92
	Linear	ef_2	$ef_2 = -1717AR + 4703$	0.77
	Second-order	ef_2	$ef_2 = 1070AR^2 - 5212AR + 6594$	0.96
	Linear	ef_3	$ef_3 = -2486AR + 6588$	0.76
	Second-order	ef_3	$ef_3 = 1512AR^2 - 7426AR + 9261$	0.94
	Linear	ef_4	$ef_4 = -1194AR + 3843$	0.71
	Second-order	ef_4	$ef_4 = 666.8AR^2 - 3372AR + 5021$	0.86
Median capacity	Linear	ef_1	$ef_1 = -965AR + 2591$	0.74
	Second-order	ef_1	$ef_1 = 631.3AR_2 - 3027AR + 3706$	0.94
	Linear	ef_2	$ef_2 = -1414AR + 3815$	0.74
	Second-order	ef_2	$ef2 = 924.1AR^2 - 4433AR + 5448$	0.95
	Linear	ef_3	$ef_3 = -1845AR + 4957$	0.79
	Second-order	ef_3	$ef_3 = 1054AR^2 - 5289AR + 6820$	0.96
	Linear	ef_4	$ef_4 = -518.1AR + 2215$	0.52
	Second-order	ef_4	$ef_4 = 414.1AR^2 - 722{:}4AR + 1151$	0.73
Minimum capacity	Linear	ef_1	$ef_1 = -1011AR + 2657$	0.69
	Second-order	ef_1	$ef_1 = 422.5AR^2 - 2214AR + 3034$	0.84
	Linear	ef_2	$ef_2 = -1416AR + 3765$	0.69
	Second-order	ef_2	$ef_2 = 967.9AR^2 - 4578AR + 5476$	0.90
	Linear	ef_3	$ef_3 = -633.7AR + 1723$	0.67
	Second-order	ef_3	$ef_3 = 439.8AR^2 - 2070AR + 2500$	0.88
	Linear	ef_4	$ef_4 = -389.1AR + 1504$	0.39
	Second-order	ef_4	$ef_4 = 563AR^2 - 2228AR + 2499$	0.91

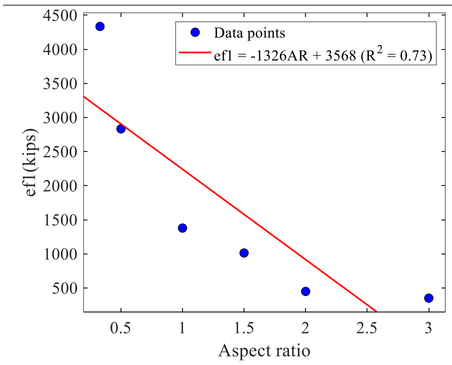

(a) **Linear regression**

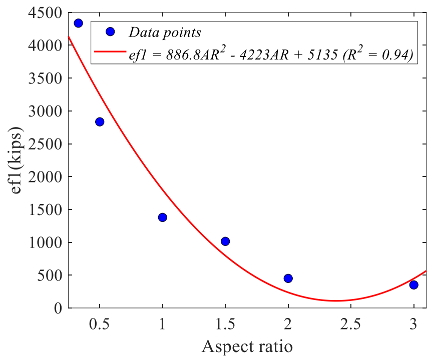

(b) **Second-order polynomial**

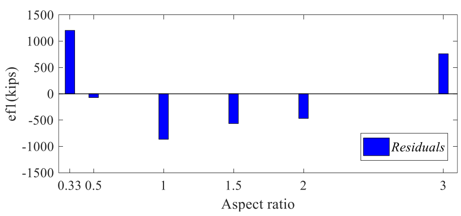

(c) **Residual values for linear function**

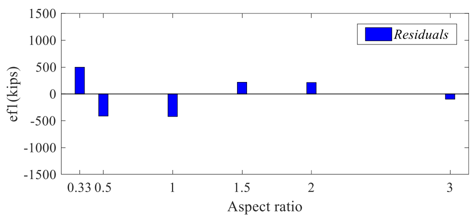

(d) **Residual values for second-order function**

Figure 11 goodness of fittness for the regression functions

Previous studies proved that the seismic behavior of partition walls is highly dependent on their aspect ratio. So far, finite numbers of micro-finite element models with discrete values of aspect ratio are developed for the gypsum partition walls. Therefore, the seismic behavior of these walls is not clear for the walls with interstitial aspect ratios. In this regard, this study proposed a regression-based procedure to estimate the cyclic parameters of the walls with an arbitrary aspect ratio based on the results of the spring-based models. These spring-based models reduce the computational costs related to the micro-finite element modeling technique. In addition, the proposed simplified models pave the way for considering the effect of partition walls on the macro-models of the whole building even for a high number of partition walls. Besides, the spring-based models eliminate the convergence problems related to the micro-finite element models.

References

Araya-Letelier, G., Miranda, E. and Deierlein, G. [2019] "Development and testing of a friction/sliding connection to improve the seismic performance of gypsum partition walls", *Earthquake Spectra*, 35(2), pp. 653–677.

Davies, R., Retamales, R., Mosqueda, G., Filiatrault, A. and Allen, D. [2012] "Effects of cold-formed steel framed gypsum partition walls on the seismic response of a medical facility", Missouri University of Science and Technology.

Davies, R., Retamales, R., Mosqueda, G., Filiatrault, A. and Allen, D. [2011] "Experimental seismic evaluation, model parameterization, and effects of cold-formed steel-framed gypsum partition walls on the seismic performance of an essential facility", *MCEER*.

Fiorino, L., Pali, T. and Landolfo, R. [2018] "Out-of-plane seismic design by testing of non-structural lightweight steel drywall partition walls", *Thin-Walled Structures*, 130, pp. 213–230.

Jenkins, C., Soroushian, S., Rahmanishamsi, E. and Maragakis, E.M. [2016] "Experimental fragility analysis of cold-formed steel-framed partition wall systems", *Thin-Walled Structures*, 103, pp. 115–127.

Kanvinde, A.M. and D.G.G. [2006] "Analytical models for the seismic performance of gypsum drywall partitions", *Earthquake Spectra*, 22(2), pp. 391–411.

Kim, H.-J. and Shin, D.-H. [2021] "Shake table test program of cold-formed steel in-plane partition walls", *Structures*, 30, pp. 503–517.

McKenna, F., Fenves, G.L. and Scott, M.H. [2006] "OpenSees: Open system for earthquake engineering simulation", *Pacific Earthquake Engineering Research Center, University of California, Berkeley, CA., http://opensees. berkeley. edu* [Preprint].

Rahmanishamsi, E. and S.S. and M.E.M. [2016] "Analytical model for the in-plane seismic performance of cold-formed steel-framed gypsum partition walls", *Earthquake Engineering and Structural Dynamics*, 45(4), pp. 619–634.

Salmasi Javid, H., Soroushian, S., Rahmanishamsi, E. and Maragakis, E.M. [2020] "Methodology for the Development of Analytical Seismic Fragility for Full Connection Steel-Framed Gypsum Partition Walls", *Journal of Earthquake Engineering*, pp. 1–18.

Salmasi Javid, H., Mohammadgholiha, M., Soroushian, S., Rahmanishamsi, E. and "Manos" Maragakis, E. [2022] "Generation of numerical-based capacity fragility curves for different aspect ratios of full-connection gypsum partition walls", *Earthquake Spectra*, p. 87552930211067260.

Taghavi, S. and Miranda, M.M. [2003] *Response assessment of nonstructural building elements*. Pacific Earthquake Engineering Research Center.

Wang, X., Pantoli, E., Hutchinson, T.C., Restrepo, J.I., Wood, R.L., Hoehler, M.S., Grzesik, P. and Sesma, F.H. [2015] "Seismic performance of cold-formed steel wall systems in a full-scale building", *Journal of Structural Engineering*, 141(10), p. 4015014.

Wood, R.L. and Hutchinson, T.C. [2012] "A numerical model for capturing the in-plane seismic response of interior metal stud partition walls", *MCEER*, University at Buffalo, State University of New York.

Numerical investigation of the displacement incompatibility between masonry infill walls and surrounding reinforced concrete frames

Livio Pedone[1], Stefano Pampanin[1]

[1] Department of Structural and Geotechnical Engineering, Sapienza University of Rome
Via Eudossiana 18, 00184, Rome, Italy
{livio.pedone, stefano.pampanin }@uniroma1.it

Abstract. In the European building practice, masonry infill panels have been widely adopted as facade elements in Reinforced Concrete (RC) frames in order to provide architectural needs such as thermal and acoustic insulation. During seismic shakings, infill wall panels and the surrounding RC frame have a strong interaction, potentially leading to local brittle failures of both structural and non-structural elements or even to global collapse mechanisms (e.g., soft-story mechanism). In the past years, a significant research effort has been dedicated at the international level to better understand the seismic performance of infilled RC frame structures as well as to develop suitable and practical design/retrofit techniques to reduce the negative effects of infill-frame interaction. However, past numerical and experimental investigations mainly focused on the diagonal compression strut mechanism and associated stress path. On the other hand, a procedure to assess the local infill-frame displacement incompatibility (i.e., detachment due to the relative deformation mechanism) in terms of shape and values is still missing in the literature. Therefore, this paper investigates and discusses the seismic displacement incompatibility between infill walls and the RC frame structure as well as the key parameters affecting the infill-frame detachment. Specifically, the concept of shape functions is introduced and proposed to assess the seismic infill-frame displacement incompatibility, in line with and extending the state-of-the-art investigations on the relative deformation mechanism between seismic-resisting frames and precast flooring units. The proposed methodology can support a displacement-compatible design check of specific connection solutions, in the form of either shear keys and/or steel dowels, as part of either strengthening or decoupling seismic retrofit strategies, as well as of energy rehabilitation solutions, such as external thermal insulation systems, in order to protect these components during earthquakes.

Keywords: Infilled Frame Structures, Infill Walls, Displacement Incompatibility, Shape Functions, Reinforced Concrete Buildings.

1.INTRODUCTION

In the recent past, growing attention has been dedicated to enhance the overall performance of existing buildings, in order to meet recent structural/safety and sustainability requirements at the international level, e.g., Directive (EU) 2018/844 [2018]. In fact, recent catastrophic earthquakes have further highlighted the high seismic vulnerability of existing buildings, often designed for gravity loads only according to pre-seismic-code provisions. Moreover, the built environment is responsible for 36 % of global final energy end-use and 37 % of energy-related carbon dioxide emissions [IEA, 2021].

Focusing on Reinforced Concrete (RC) frame structures with masonry infills, which represent a large part of the European building practice, the overall performance of the facade "non-structural" elements plays a fundamental role in the seismic safety evaluation as well as in the energy consumption of buildings. Although masonry infill panels are typically designed to only provide other-than-structural functions such as thermal and acoustic insulation, it is well known that they have a strong interaction with the surrounding frame during an earthquake, potentially leading to local shear failures (Figure 1, left) or global failure mechanism (e.g., soft-storey mechanism) [Magenes and Pampanin, 2004]. Moreover, it is evident that earthquake damage to "non-structural" infilled facade elements can lead to loss of performance in case of recently implemented energy retrofit solutions such as External Thermal Insulation Composite System (ETICS), even for low-intensity seismic events (Figure 1, right). Therefore, recent works have pointed out that energy and seismic retrofitting should rather be designed and implemented through an integrated multi-performance approach [Calvi *et al.*, 2016; Marini *et al.*, 2017; Buornas, 2018; Di Vece and Pampanin, 2019].

Figure 1. (left) Shear failure of column (Bonefro, Molise 2002; Magenese and Pampanin [2004]); (right) damage to masonry infill panels and external thermal insulation after the Amatrice 2016 earthquake [Santarsiero *et al.,* 2016].

In the past years, the seismic behaviour of infilled RC frame structures has been widely investigated and significant research efforts have been dedicated to study and develop suitable and practical design/retrofit strategies and techniques to reduce the negative effects of infill-frame seismic interaction, based on either decoupling [Tasligedik and Pampanin, 2017; Morandi *et al.,* 2018b] or strengthening [Bournas, 2018; Facconi and Minelli, 2020] approaches. Both decoupling and strengthening retrofit techniques typically require specific construction details such as shear keys or steel dowels to prevent the out-of-plane collapse of infill (in the case of decoupling solutions) or realize an effective connection between the masonry panel and frame in strengthening solutions. It is worth noting that the seismic displacement incompatibility between masonry infill wall and surrounding frames (i.e., the well-known partial detachment between infill panels and the surrounding frame that occurs at the diagonally opposite corners during the seismic shaking) may affect the performance of these structural details (i.e., shear anchors and steel dowels), potentially leading to damage to facade components or results themselves damaged. Moreover, following an energy retrofit intervention comprising for example the use of external thermic insulation systems, the infill-frame displacement incompatibility can lead to damage to the insulation panels since the insulation materials (e.g., expanded polystyrene EPS) can exhibit a brittle failure when subjected to tensile stresses [Tang *et al.*, 2019]. However, past research efforts mainly focused on the diagonal compression strut load path and contact zones; on the other hand, a procedure to assess the local infill-frame displacement incompatibility (i.e., detachment due to the relative deformation mechanism) in terms of shape and values is still missing in the literature.

Therefore, this paper investigates and discusses the seismic displacement incompatibility between masonry infill panels and surrounding frames in terms of shape and detachment values by adopting the concept of shape functions, in line with, and extending, the state-of-the-art investigations on the relative deformation mechanism between seismic-resisting frames and precast flooring units. The paper is structured as follows. In Section 2, the adopted methodology is presented, including a brief review of the displacement incompatibility issue and the concept of shape functions. The description of the case-study structures as well as the adopted modelling strategy, involving two alternative macro-modelling approaches, is reported in Section 3, together with the results and discussion of the performed parametric analysis. Finally, conclusions are given in Section 4.

2. DISPLACEMENT INCOMPATIBILITY: METHODOLOGY

Past studies available in the literature have focused on the displacement incompatibility issue, mainly investigating the relative displacement between different structural members. For instance, Fenwick and Megget [1993] investigated the so-called "beam elongation" effect, i.e. the elongation that can occur in the plastic hinge zones of RC members due to the tensile yielding of the reinforcements and the cycling loads. Moreover, other studies [Matthews *et al.*, 2003; Vides and Pampanin, 2015] focused on the vertical displacement incompatibility between beams and precast flooring units. Yet, very few studies investigated the infill-frame seismic displacement incompatibility in terms of detachment shape and values rather than contact zones and stress path. As an example, quite recently Brodsky *et al.*, [2018] investigated the interaction behaviour in terms of the infill-frame contact regions and interfacial tractions in case of loss of a supporting column.

In order to assess the infill-frame detachment shape and values, this work proposes and adopts the concept of displacement incompatibility shape functions. This concept was introduced by Taylor [2004] and further developed and applied by Vides and Pampanin [2015] to investigate the vertical displacement incompatibility profiles between the seismic resisting frame and the precast flooring unit. Shape functions are defined as the envelope of the maximum (both horizontal and vertical) displacement incompatibility recorded along the interface with the surrounding structural frame. Figure 2 shows the adopted framework to carry out shape functions of displacement incompatibility.

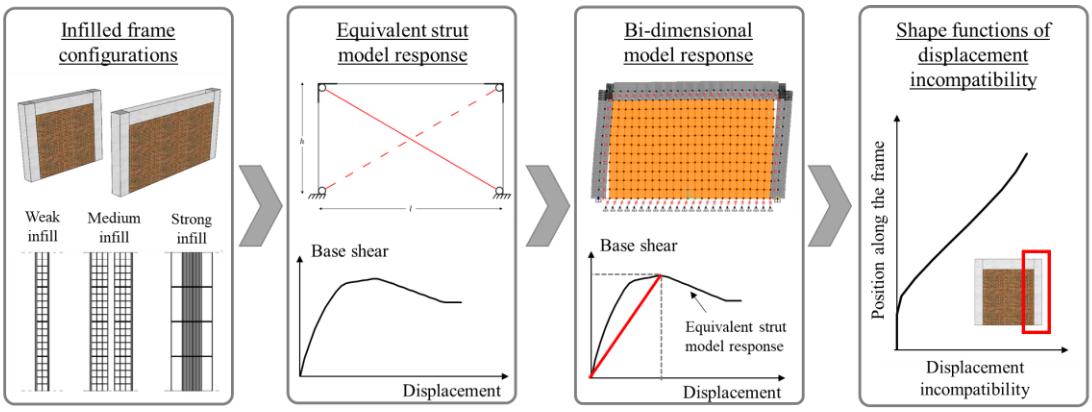

Figure 2. Adopted methodology to evaluate shape functions of displacement incompatibility.

Firstly, geometrical details and material properties of the considered case-study infilled frame structures are defined. Then the seismic behaviour of the structure is assessed by performing nonlinear static (pushover) analysis on numerical models. In order to evaluate the seismic displacement incompatibility through a numerical simulation, the best approach would be to develop a refined Finite Element Method (FEM) model following a micro-modelling approach. These methods allow to provide an accurate description of the structural behaviour of the system by modelling in detail both masonry units and mortar joints. On the other hand, these methods require a significant amount of data, resulting to be complex and time-consuming for their high computation effort [Tarque *et al.*, 2015]. In this research work, a more simplified modelling approach strategy is instead adopted to perform a preliminary investigation on the parameters that strongly affect displacement incompatibility. More specifically, the adopted modelling strategy involves two alternative numerical models of the structure, following the macro-modelling and the meso-modelling techniques. In the first method (i.e., the macro-modelling approach), the masonry infill panel is modelled by an equivalent diagonal strut, while in the meso-modelling approach the infill panel is idealized as a continuous linear bi-dimensional element without distinction between masonry units and mortar joints. Following the provisions reported in Cavaleri and Di Trapani [2015], the two numerical models can be considered as equivalent when they exhibit the same lateral secant stiffness under monotonic loading. Thus, by comparing the two numerical models, the nonlinear behaviour of the bi-dimensional model is introduced by iteratively reducing its stiffness (operatively, by reducing its thickness) until the same lateral secant stiffness of the equivalent strut model is reached for a fixed interstorey drift level. This concept is illustrated in Figure 3.

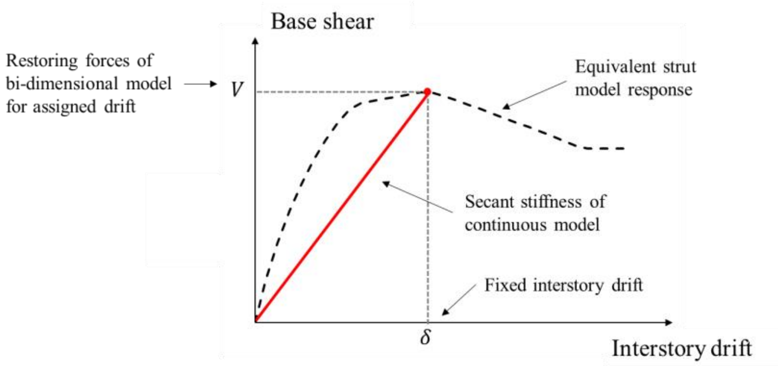

Figure 3. Theoretical representation of the adopted modelling strategy (after Cavaleri and Di Trapani [2015]).

Cavaleri and Di Trapani [2015] also proved that this modelling strategy can provide good accuracy in assessing the overall response of infilled frames as well as the local shear demands on frames. More details about the numerical models developed in this research work are given in Section 3.2. Finally, by evaluating the relative displacement (both in the horizontal and vertical directions) between the masonry infill and the surrounding frame, shape functions of the displacement incompatibility are derived.

In the following section, the proposed framework is applied to different infilled frame structures in order to carry out shape functions of displacement incompatibility and preliminarily assess which parameters strongly affect the infill-frame detachment.

3. PARAMETRIC ANALYSIS

3.1 DESCRIPTION OF THE CASE-STUDY STRUCTURES

Two single-story one-span infilled frame structures, characterized by beam span lengths of 3m and 5m, respectively, and an interstorey height of 3m, are considered to implement the study (Figure 4, left). The RC frame members are representative of a typical pre-1970s existing building in Italy, i.e. designed for gravity load only. Specifically, material mechanical properties, reinforcement and construction details are selected according to available data of an existing school building in Lucera, South Italy, as part of the UEFA/ELENA research project [Pampanin *et al.,* 2020]. Geometrical details of the structural members are shown in Figure 4 (left) and are assumed the same for both structural configurations. The beam-column joints have no stirrups and beam longitudinal bars are anchored with end-hooks. The mean concrete cylindrical strength is equal to 16 MPa, while the mean steel yield stress is equal to 400 MPa. Young's module is equal to 22.85 GPa and 200.0 GPa for concrete and reinforcement steel, respectively.

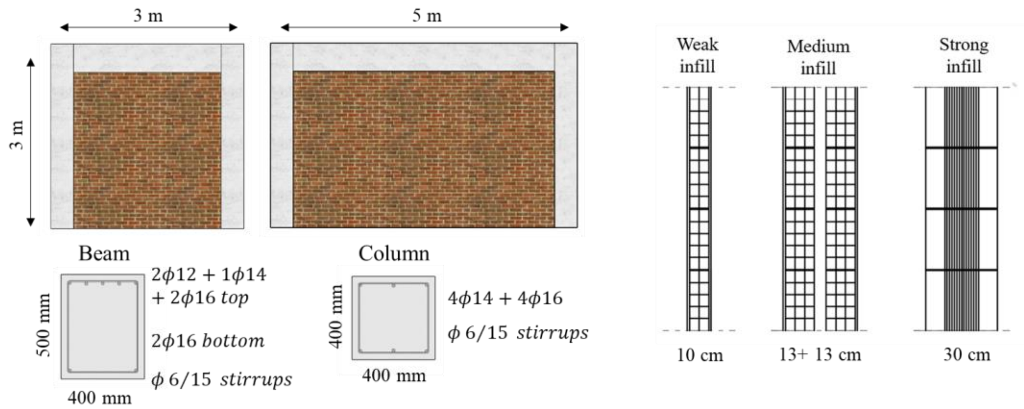

Figure 4. Geometric properties of (left) the infilled frame configurations and (right) the selected masonry infill panels.

For each structural configuration, three different masonry infills are considered: Weak Infill (WI), Medium Infill (MI) and Strong Infill (SI) (Figure 4, right). Specifically, the WI is a single-leaf masonry wall with horizontally hollowed brick; the MI is a double-leaf masonry wall with horizontally hollowed brick divided by an internal cavity; the SI is a single-leaf wall with vertically hollowed brick units. Mechanical proprieties of infill panels are selected according to Hak *et al.* [2012] (more details can be found in the cited paper). Moreover, three different axial load values are applied to the RC columns (i.e., N = 120kN, 270kN and 420kN) to simulate portal frames located at three different story levels in a low-rise building.

3.2 MODELLING APPROACH

As mentioned above, two alternative models are realized for each considered infilled frame configuration: an equivalent diagonal strut and a bi-dimensional model. Concerning the equivalent diagonal strut model, a non-linear lumped plasticity model is implemented in the structural software OpenSees (python library [Zhu *et al.*, 2018]). Details of the adopted modelling approach are shown in Figure 5.

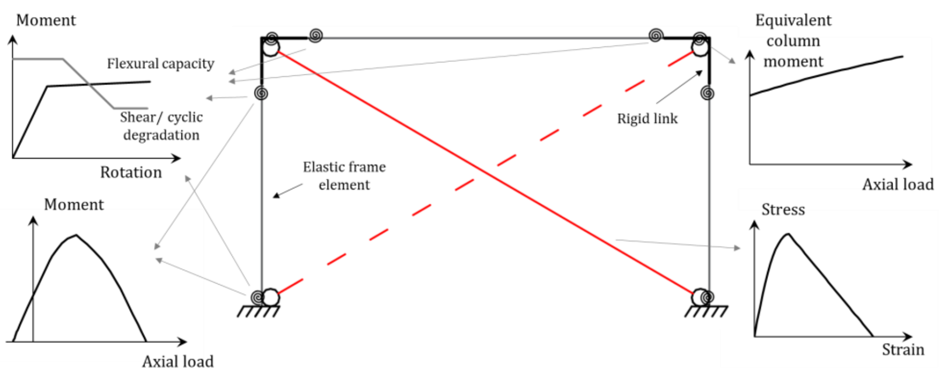

Figure 5. Adopted numerical modelling strategy for the equivalent strut model.

The soil-structure interaction contribution is neglected, and fixed base nodes are considered. Beams and columns are modelled by elastic elements with lumped plasticity at the end sections. Nonlinear behaviour of the plastic hinges is described using proper bi-linear moment-curvature relationships and accounting also for the shear failure mechanism. Panel zones are modelled using rigid arms with additional nonlinear rotational springs to capture the joint non-linear behaviour and failure mechanisms [Pampanin *et al.*, 2003]; these springs are characterized by equivalent column moment vs. joint shear deformation relationships. The infill panel is modelled by an equivalent diagonal strut. The strut properties (i.e., width, length, and thicknesses) as well as the ultimate compression stress are evaluated according to the procedure proposed by Bertoldi *et al.* [1993]. In this model, the thickness and the length of the infill are automatically defined by the panel geometry, while the width is evaluated as a function of the relative stiffness between the infill and frame, λ, obtained according to Stafford Smith [1967]. On the other hand, the ultimate compression stress is assessed considering four different failure mechanisms: 1) compression failure at the centre of the infill, 2) compression failure at the corners of the infill, 3) sliding shear failure, and 4) diagonal tension failure. The ultimate compression stress is defined as the minimum value obtained for the four failure mechanisms. More details about the mathematical formulations of this model can be found in Bertoldi *et al.* [1993]. A fibre section for the equivalent strut is implemented to define the nonlinear behaviour, considering the Kent-Scott-Park stress-strain law [Kent and Park 1971], as suggested by Di Tapani *et al.* [2018]. The ability of this model to provide a good description of the global seismic capacity of infilled-frame structures has been also tested by a comparison with experimental tests available in the literature (Figure 6).

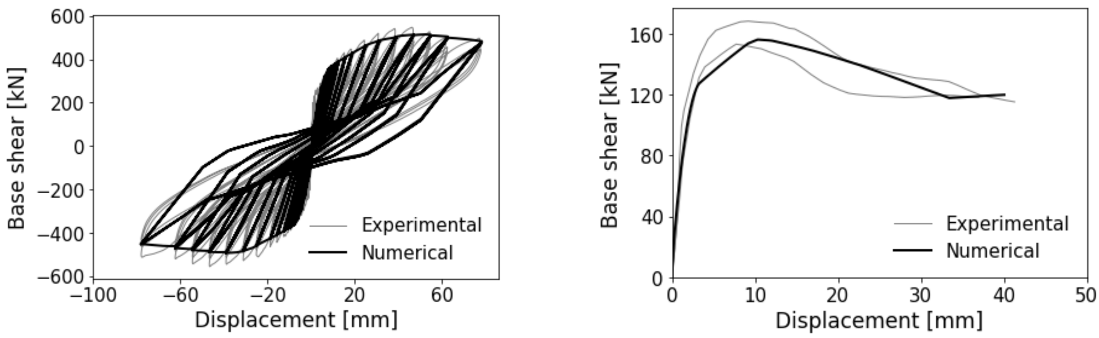

Figure 6. Comparison between experimental and numerical results: (left) cyclic response of the infilled frame tested by Morandi *et al.* [2018a]; (right) monotonic response of the infilled frame tested by Mehrabi *et al.* [1996].

Results show a good agreement between the experimental tests and the numerical results. The force-displacement behaviour is well captured, while the hysteretic behaviour of the numerical model slightly overestimates the energy dissipation of the infilled structure; however, it is out of the scope of this study.

Moving to the bi-dimensional model, beams and columns are modelled as reported previously, while the infill wall is idealized as a continuous element by using elastic orthotropic shell elements. This numerical model is implemented in the structural software SAP2000 [CSI, 2019]. The contact interface between frame and infill is modelled by using gap elements able to transfer compression stresses only. A similar modelling approach can be found also in Cavaleri and Di Trapani [2015] and Doudoumis [2007]. It is worth noting that friction phenomena are herein neglected in the numerical investigation. This choice is deemed reasonable in a preliminary assessment of the detachment mechanism since the definition of a realistic friction coefficient can be challenging, considering that friction stresses progressively vary in the case of cyclic loading. Moreover, past numerical investigations [Fiore *et al.,* 2012] have shown that friction phenomena do not influence the overall behaviour of an infilled frame. A qualitative illustration of the bi-dimensional model is presented in Figure 7.

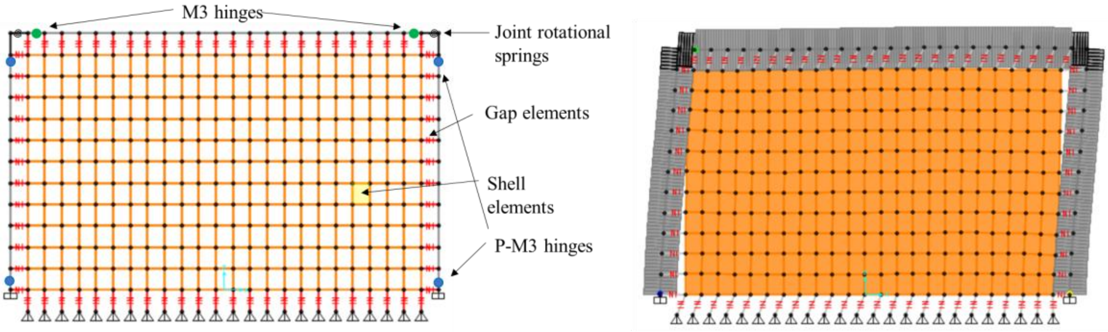

Figure 7. Qualitative illustration of the bi-dimensional model.

3.3 RESULTS AND DISCUSSIONS

Nonlinear static pushover analyses on the equivalent strut model are carried out for each infilled frame configuration. Figure 8 shows the results in terms of global capacity curves (i.e., base shear vs. top displacement).

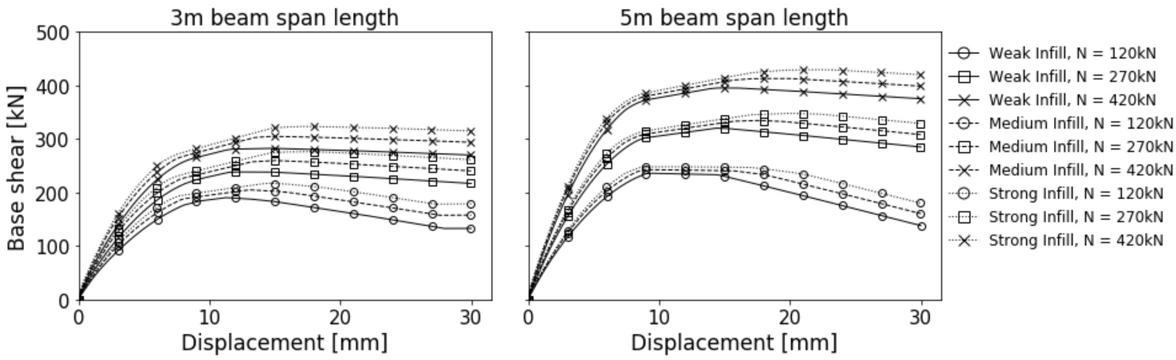

Figure 8. Force-displacement capacity curves for each considered infilled frame configuration.

Results highlight that the beam spam length as well as the axial load on the columns strongly influence the strength and stiffness of the infilled frame structure. Moreover, as expected, the strength and stiffness of the structure increase considering a stronger infill panel. It is worth noting that an ultimate displacement corresponding to an interstorey drift of 1.0% is considered for each configuration since the panel joint shows a critical damage level at this drift level [Pampanin *et al.*, 2002].

For each configuration, shape functions of displacement incompatibility are developed using the continuous bi-dimensional model. Displacement incompatibility is computed as the difference between the displacement of the frame and the infill panel edge both in the horizontal and vertical directions (namely, Horizontal Displacement Incompatibilities, HDI, and Vertical Displacement Incompatibilities, VDI). HDI and VDI are computed at two fixed interstorey drift values (i.e., ϑ=0.4% and ϑ=0.9%) representing the Damage Limit State (DLS) and Ultimate Limit State (ULS) of the infilled frame, according to past numerical and experimental investigations [Magenes and Pampanin, 2004; Hak *et al.*, 2012; Morandi *et al.*, 2018a]. Finally, shape functions are defined by the envelope of displacement incompatibility points. Figure 9 shows the obtained displacement incompatibility shape functions; for brevity, only results related to the HDI between the infill and the right column are reported. In Table 1 the maximum detachment values for both HDI and VDI are listed for each analysed configuration.

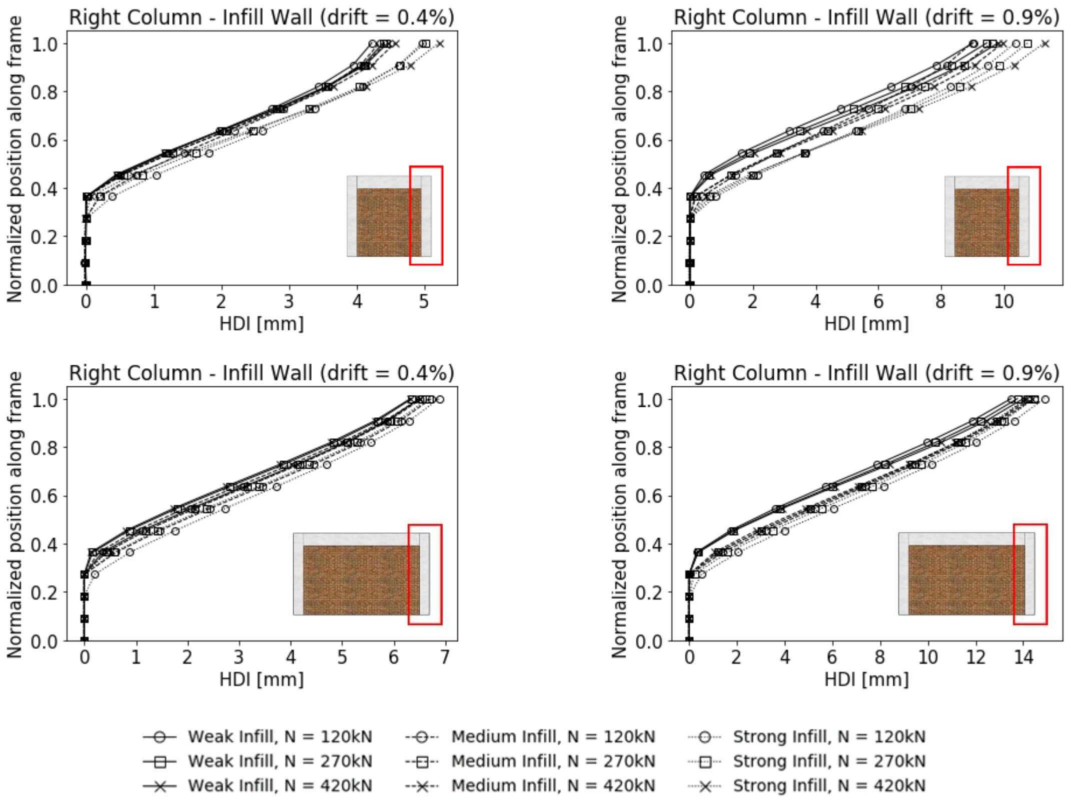

Figure 9. Shape functions of displacement incompatibility between infill wall and column.

Table 1. Maximum displacement incompatibility values for each analysed configuration.

Spec.	h	l	Infill type	N	Δ_{DI} drift 0.4% (mm)			Δ_{DI} drift 0.9% (mm)		
#	mm	mm	-	kN	Col_{sx}	Beam	Col_{dx}	Col_{sx}	Beam	Col_{dx}
1	3000	3000	Weak	120	-2.7	2.5	4.2	-7.1	5.3	9.0
2	3000	3000	Medium	120	-3.1	2.4	4.4	-6.9	5.2	9.5
3	3000	3000	Strong	120	-3.1	2.3	4.5	-6.9	5.2	9.8
4	3000	3000	Weak	270	-2.8	2.3	4.3	-6.5	5.1	9.0
5	3000	3000	Medium	270	-2.9	2.3	4.4	-7.4	5.0	9.6
6	3000	3000	Strong	270	-3.1	2.2	4.6	-7.3	4.9	10.0
7	3000	3000	Weak	420	-3.2	1.8	5.0	-7.7	3.8	10.4
8	3000	3000	Medium	420	-3.2	1.8	5.0	-8.2	3.8	10.8
9	3000	3000	Strong	420	-3.6	1.7	5.2	-8.9	3.7	11.3
10	3000	5000	Weak	120	-5.0	1.8	6.5	-13.2	2.7	13.5
11	3000	5000	Medium	120	-5.4	1.8	6.4	-13.0	3.6	13.8
12	3000	5000	Strong	120	-5.5	1.8	6.3	-12.7	4.6	14.0
13	3000	5000	Weak	270	-4.6	1.8	6.7	-11.2	3.9	14.4
14	3000	5000	Medium	270	-5.1	1.8	6.5	-12.6	4.4	14.2
15	3000	5000	Strong	270	-5.2	1.9	6.5	-12.4	4.6	14.3
16	3000	5000	Weak	420	-4.8	1.5	6.9	-11.6	3.8	14.9
17	3000	5000	Medium	420	-5.2	1.5	6.7	-12.8	3.6	14.5
18	3000	5000	Strong	420	-5.5	1.5	6.5	-13.6	3.6	14.1

Note: Col_{sx} = left column; Col_{dx} = right column; Δ_{DI} = maximum detachment values.

Table 1 shows that in general terms HDI (i.e., horizontal detachment between infill and columns) is more severe than VDI (i.e., vertical detachment between infill and beam). Considering the 5m beam span length, the seismic HDI increases while the VDI decreases when compared to the 3m beam span length. The main differences in the behaviour can be found for the strong infill when compared to weak and medium infills. In fact, generally weak and medium infills show similar behaviour, while strong infill leads to higher values of displacement incompatibility. Considering l=3m, the maximum detachment value is observed for the strong infill with the highest axial load on columns: Δs=5.2mm for interstorey drift ϑ=0.4% and Δs=11.3mm for ϑ=0.9%. Moving to l=5m, similar considerations can be made. The maximum value of detachment is recorded at the top corner in the horizontal direction (HDI), leading to Δs=6.9mm and Δs=14.9mm for interstorey drift ϑ=0.4% and ϑ=0.9%, respectively. As for the l=3m, displacement incompatibility generally increases when considering a stronger infill panel. However, axial load value has a strong influence in this configuration: higher axial load values lead to lower detachment in most of the configurations, especially for VDI and ϑ=0.9%. This is mainly due to the plastic hinges sequence of the structural frame. It is worth remembering that a pre-seismic-code frame structure is considered in this study; hence, the observed failure mode is a mixed sidesway mechanism because of a lack of capacity design principles. However, the panel zone capacity increases as the axial load on columns increases (as experimentally observed in Pampanin *et al.* [2002]), so when N=420kN plastic hinge occurs in the beam for positive bending moment, while when N=120kN shear failure of the panel zone occurs. For these reasons, it is not easy to identify a common behaviour for VDI. However, it is observed that VDI values are always smaller than HDI ones. and thus of lesser concern.

4.CONCLUSIONS

In this paper, a methodology to assess the seismic displacement incompatibility between masonry infill panels and surrounding RC frames has been proposed. The proposed framework involves the definition of shape functions of displacement incompatibility, in line with and extending the state-of-the-art investigations on the relative deformation mechanism between seismic-resisting frames and precast flooring units. A simplified modelling strategy has also been suggested and adopted, in order to allow one to analyse the local detachment mechanism without the need of implementing more refined, but more complex and time-consuming, FEM numerical models according to the micro-modelling techniques. The proposed framework has been applied to different case-study infilled-frame structures through a parametric investigation, to preliminarily evaluate which parameters strongly affect the infill-frame detachment as well as provide a preliminary range of detachment values and identify maximum detachment location along the frame. The proposed concept of shape functions can support the design of structural details such as shear keys or steel dowels, in order to avoid the out-of-plane collapse of infills or realize an effective infill-frame connection in strengthening retrofit techniques, preventing possible local failures. Moreover, shape functions can be used to design adequate construction details for energy efficiency retrofit solutions, such as external thermal insulation systems, since the infill detachment can lead to damage to these solutions.

It is worth mentioning that this research work represents a preliminary investigation of the infill-frame displacement incompatibility, and further research effort is needed to achieve a better understanding of this topic. Firstly, an extensive experimental program coupled with more refined numerical investigations (possibly based on micro-modelling approaches) is deemed necessary. Moreover, the proposed study could be improved by considering a wider class of infilled frame structures; further advancements would consist of developing tables and/or analytical formulations to quickly derive shape functions starting from the geometrical and material properties of the infilled frame structure. Finally, it is worth noting that when plastic hinges occur in the beam, the "beam elongation" effect may affect the infill-frame displacement incompatibility, leading to higher horizontal detachment values. Thus, also the influence of the "beam elongation" effect should be studied through both experimental and numerical investigations.

REFERENCES

Bertoldi, S. H., Decanini, L. D., Gavarini, C. [1993] "Telai tamponati soggetti ad azione sismica, un modello semplificato: confronto sperimentale e numeric," Proceedings of the VI ANIDIS conference, Perugia, Italy.

Bournas, D.A. [2018] "Concurrent seismic and energy retrofitting of RC and masonry building envelopes using inorganic textile-based composites with insulation materials: A new concept," *Compos. Part B: Eng.*, Vol. 148, pp. 166–179.

Brodsky, A., Rabinovitch, O., Yankelevsky, D.Z. [2018] "Determination of the interaction between a masonry wall and a confining frame." *Engineering Structures*, Vol. 167, pp. 214-226.

Calvi, G.M., Sousa, L., Ruggeri, C. [2016] "Energy Efficiency and Seismic Resilience: A Common Approach,". *In: Gardoni P., LaFave J. (eds) Multi-hazard Approaches to Civil Infrastructure Engineering. Springer, Cham.*

Cavaleri, L., Di Trapani, F. [2015] "Prediction of the Additional Shear Action on Frame Members Due to Infills," *Bull. Earthq. Eng.,* Vol. 13(5), pp. 1425–54.

CSI [2019] *SAP2000 Integrated Software for Structural Analysis and Design*. Computers and Structures.

Di Trapani, F., Shing, P. B., Cavaleri, L. [2018] "Macroelement Model for In-Plane and Out-of-Plane Responses of Masonry Infills in Frame Structures," *Journal of Structural Engineering*, Vol. 144 (2).

Di Vece, D., Pampanin, S. [2019] "Combined retrofit solutions for seismic resilience and energy efficiency of reinforced concrete residential buildings with infill walls," *Proceedings of the XVIII ANIDIS conference*, Ascoli Piceno, Italy.

Directive (EU) 2018/844 [2018] *Directive (Eu) 2018/844 of the European Parliament and of the Council of 30 May 2018 Amending Directive 2010/31/Eu on the Energy Performance of Buildings and Directive 2012/27/Eu on Energy Efficiency (Text With Eea Relevance)*, Official Journal of the European Union, European Parliament and Council.

Doudoumis, I. N. [2007] "Finite element modelling and investigation of the behaviour of elastic infilled frames under monotonic loading". *Eng Struct*, Vol. 29(6), pp. 1004–10241

Facconi, L., Minelli, F. [2020] "Retrofitting RC infills by a glass fiber mesh reinforced overlay and steel dowels: experimental and numerical study," *Construction and Building Materials*, Vol. 231, pp. 117133.

Fenwick, R.C., Megget, L.M.[1993] "Elongation and Load Deflection Characteristics of Reinforced Concrete Members Containing Plastic Hinges," *Bull. N. Z. Soc. Earthq. Eng.*, Vol. 26(1), pp. 28–41.

Fiore, A., Netti, A., Monaco, P. [2012] "The influence of masonry infill on the seismic behavior of RC frame buildings," *Eng Struct*, Vol. 44, pp. 133–145.

Hak, S., Morandi, P., Magenes, G., Sullivan, T. J. [2012] "Damage Control for Clay Masonry Infills in the Design of RC Frame Structures," *Journal of Earthquake* Engineering, Vol. 16(1), pp. 1–35.

IEA [2021] *Global Status Report for Buildings and Construction 2021*. Paris: UN Environment and International Energy Agency, France.

Kent, D. C., Park, R. [1971] "Flexural members with confined concrete," *J. Struct Eng.*, Vol. 97(ST7), pp. 1969–1990.

Magenes, G., Pampanin, S. [2004] "Seismic Response of Gravity-Load Design Frames with Masonry Infills," *Proceedings of 13th World Conference on Earthquake Engineering*, Vancouver, B.C., Canada.

Marini, A., Passoni, C., Belleri, A., Feroldi, F., Preti, M., Metelli, G., Riva, P., Giuriani, E., Plizzari, G. [2017] "Combining Seismic Retrofit with Energy Refurbishment for the Sustainable Renovation of RC Buildings: A Proof of Concept," *European Journal of Environmental and Civil Engineering*, Vol. 8189, pp. 1–21.

Matthews, J., Bull, D., Mander, J. [2003] "Hollowcore floor slab performance following a severe earthquake," *Proceeding of fib symposium, Concrete structures in seismic regions*, Athens, Greece.

Mehrabi, A.B., Shing, P.B., Schuller, M.P., Noland, J.L. [1996]. "Experimental Evaluation of Masonry-Infilled RC Frames," *Journal of Structural Engineering*, Vol. 122 (3), pp. 228–37.

Morandi, P., Hak, S., Magenes, G. [2018a] "Performance-Based Interpretation of in-Plane Cyclic Tests on RC Frames with Strong Masonry Infills*," Engineering Structures,* Vol. 156, pp. 503–21.

Morandi, P., Milanesi, R.R., Magenes, G. [2018b] "Innovative Solution for Seismic-Resistant Masonry Infills with Sliding Joints: In-Plane Experimental Performance," *Engineering Structures*, Vol. 176, pp. 719–33.

Pampanin, S., Calvi, G.M., Moratti, M. [2002] "Seismic Behaviour of RC Beam-Column Joints Designed for Gravity Loads," *Proceedings of the 12th European Conference on Earthquake Engineering*, London, UK.

Pampanin, S., Magenes, G., Carr, A. [2003] "Modelling of shear hinge mechanism in poorly detailed RC beam–column joints." *Proceedings of the FIB 2003 symposium*, Athens, Greece.

Pampanin, S., Vallati, A., Currà, E. [2020]. *Analisi Sismo-Energetiche di Edifici Pubblici Nella Provincia di Foggia e Strategie di Interventi Integrati di Miglioramento*, Research Report, UEFA/ELENA Project; 2020.

Santarsiero G, Chiauzzi L, Masi A. [2016] *Analisi del danneggiamento di edifici situati nella zona sud del comune di Amatrice (RI). Confronto pre e post sisma del 240/08/2016*, Reluis report, Italy.

Stafford Smith, B. [1967] "Methods for predicting the lateral stiffness and strength of multi-storey infilled frames," *Build. Sci.*, Vol. 2(3), pp. 247–257.

Tang, N., Dong, L., Huang, D., Xiao, R.. [2019] "Mechanical Performance of Polystyrene Foam (EPS): Experimental and Numerical Analysis," *Polymer Testing*, Vol. 73, pp. 359–65.

Tarque, N., Candido, L., Camata, G., Spacone, E. [2015] "Masonry infilled frame structures: State-of-the-art review of numerical modelling," *Earthq. Struct.,* Vol. 8, pp. 225–251.

Tasligedik, A.S., Pampanin, S. [2017] "Rocking Cantilever Clay Brick Infill Wall Panels: A Novel Low Damage Infill Wall Syste*," Journal of Earthquake Engineering*, Vol. 21 (7), pp. 1023–49.

Taylor, L. [2004] *Vertical Displacement Incompatibility Between Floor Slabs and Seismic Resisting Systems*, BE Thesis, University of Canterbury, Christchurch, New Zealand.

Vides, R., Pampanin, S. [2015] "Towards a performance-based design of precast concrete diaphragms using jointed dissipative connectors: concept and feasibility study." *Proceedings of NZSEE Conference*, Rotorua, New Zealand.

Zhu, M., McKenna, F., Scott, M.H. [2018] "OpenSeesPy: Python Library for the OpenSees Finite Element Framework," *SoftwareX*, Vol. 7, pp. 6–11.

Seismic performance of Point Fixed Glass Facade Systems through Finite Element Modelling and proposal of a low-damage connection system

S. D'Amore[1], S. Bianchi[2], J. Ciurlanti[3] and S. Pampanin[1]

[1] Sapienza University of Rome
Department of Structural and Geotechnical Engineering, Via Eudossiana 18, 00184, Rome, Italy
{simone.damore, stefano.pampanin}@uniroma1.it
[2] Delft University of Technology
Department Architectural Engineering + Technology, Julianalaan 134, 2628 BL Delft, Netherlands
S.Bianchi@tudelft.nl
[3] ARUP
Beta Building, Naritaweg 118, 1043 CA Amsterdam, Netherlands
Jonathan.Ciurlanti@arup.com

Abstract. Among glazed curtain walls, the growing interest in Point Fixed Glass Facade Systems (PFGFS), simply known as "Spider Glazing", is mainly due to their aesthetics, architectural attractiveness and high transparency they can provide when compared to more traditional framed glass facades. PFGFS are in fact punctually attached to the structure by using spider arms and bolted fittings. However, some PFGFS solutions have shown an unexpected moderate seismic vulnerability in recent earthquake events, as a consequence of inadequate connection detailing. As part of current seismic design philosophy, high structural and non-structural damage is accepted under a design-level earthquake. This inevitably leads to high post-earthquake losses in terms of both repair costs and business interruption for the damaged buildings. Therefore, nowadays the need for research efforts towards the development of low-damage technologies for the overall building system, including structural and non-structural components, is increasingly recognized.

This paper aims at investigating the seismic performance of PFGFS through numerical studies at both local-connection level, by advanced non-linear FEM modelling implemented in ABAQUS software, and at global-facade system level, through a simplified lumped plasticity macro-model developed in SAP2000 program. Non-linear static (PushOver) analyses have been carried out to assess the overall in-plane capacity of the facade. Based on the numerical outcomes obtained for a PFGFS consisting of traditional connections (i.e., available on the market), a novel low-damage system has been proposed. This solution comprises horizontal slotted holes for the bolted connection of the spider arms to the supporting structure. A parametric analysis, involving the variation of the slotted hole length, has been finally performed to study the effectiveness of the proposed solution. Results highlight the improvement of the in-plane capacity of the PFGFS, specifically an increase of the maximum allowable inter-storey drift ratio from 1.17% for the traditional system to 2.49% for the low-damage connection.

Keywords: Non-structural components, Glass Facade Systems, Numerical Modelling, Seismic Performance, In-Plane Drift Capacity.

1. INTRODUCTION

Earthquakes that occurred worldwide in the last years have further highlighted the high vulnerability of non-structural components (e.g., architectural elements, mechanical and electrical equipment, contents). Specifically, post-earthquake surveys and reconnaissance on damaged buildings have pointed out how non-structural components can lose functionality even under low-intensity earthquakes, and eventually reach collapse under moderate-to-strong ground motion intensities, leading to a life-safety threat for both occupants as well as pedestrians around the building, [Perrone *et al.*, 2019]. As a result, nowadays it is well acknowledged that such components can highly increase building repair costs, as well as daily inactivity and business interruption (downtime), leading to unsustainable socio-economic (direct and indirect) losses. This justifies the growing research effort, in the last years, towards the implementation of integrated low-damage buildings (both for structural as well as non-structural components) to achieve the goal of a more resilient society against seismic hazard, [Pampanin, 2015; Bianchi *et al.*, 2021]. Specifically, the crucial need for including non-structural components in the design/assessment/loss analysis of buildings is justified when considering the large investment associated with them. For example, Taghavi and Miranda [2003] pointed out that the investment related to non-structural components is 82%, 87% and 92% of the total construction building cost for offices, hotels, and hospitals, respectively. Moreover, such a high value could further increase in the case of Glazed Facade Systems (GFS), being such components among the most expensive.

GFSs are growing in interest due to their high transparency and elegancy. Among GFSs, a relatively novel solution is the Point Fixed Glass Facade System (PFGFS), which allows greater transparency with respect to traditional solutions. GFSs are featured by curtain walls in which mullions and transoms are used. If PFGFSs are used, punctual supports are provided exclusively by spider elements (described in the following section), enhancing the elegance and transparency of the building envelope. Even though recent studies have proved the enhanced performance of PFGFSs with respect to traditional GFSs, recent earthquakes, specifically the 22nd February 2011 Christchurch Earthquake, New Zealand, have proved the vulnerability of such a system under strong earthquakes. Figure 1 shows the extended damage of the building envelope of a modern building in the city of Christchurch, [Baird *et al*, 2011a].

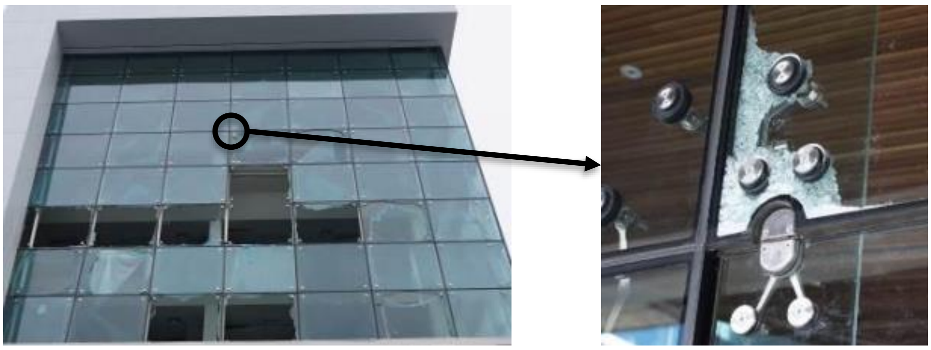

Figure 1. Example of damage in a PFGFS in a modern building located in Christchurch (left), and particular of the damage, due to tensile stress concentration, of the glass panel around the fixing zone (right), [Baird *et al.* 2011].

The main objective of this paper is to investigate the seismic performance of PFGFSs considering the connection systems currently available on the market and to propose an innovative solution, able to improve the seismic performance when the system undergoes moderate-to-severe earthquakes. To achieve these goals, firstly, detailed non-linear 3D Finite Element Models (FEM) is implemented in the software ABAQUS to investigate the local (connection-level) behaviour of the system. After that, using the results from the micro-modelling investigations, a refined lumped-plasticity macro-model is implemented in the software SAP 2000 to define the overall seismic performance of the facade. Finally, an innovative low-damage connection system is proposed, and a comparison (with respect to the traditional connection details) is carried out to investigate the benefits of implementing the latter.

2.DESCRIPTION OF PFGFSs AND THEIR PERFORMANCE

In this paragraph, a brief description of PFGFSs is provided (further information can be found in Inca *et al.* [2019]). PFGFSs generally consist of four components: the supporting structure, glazing support attachments, bolted fixings, and glass panels. The supporting structure generally consists of a light metallic frame to which the spider elements are attached. It is worth noting that using such a component is not mandatory, and the spider elements can be attached directly to the building structure through T-shaped supporting plates. In this case, larger glass panels are used, but as a counterpart, they become much more vulnerable to the in-plane actions [Sivanerupan, 2010]. Figure.2 schematically shows an example of PFGFS.

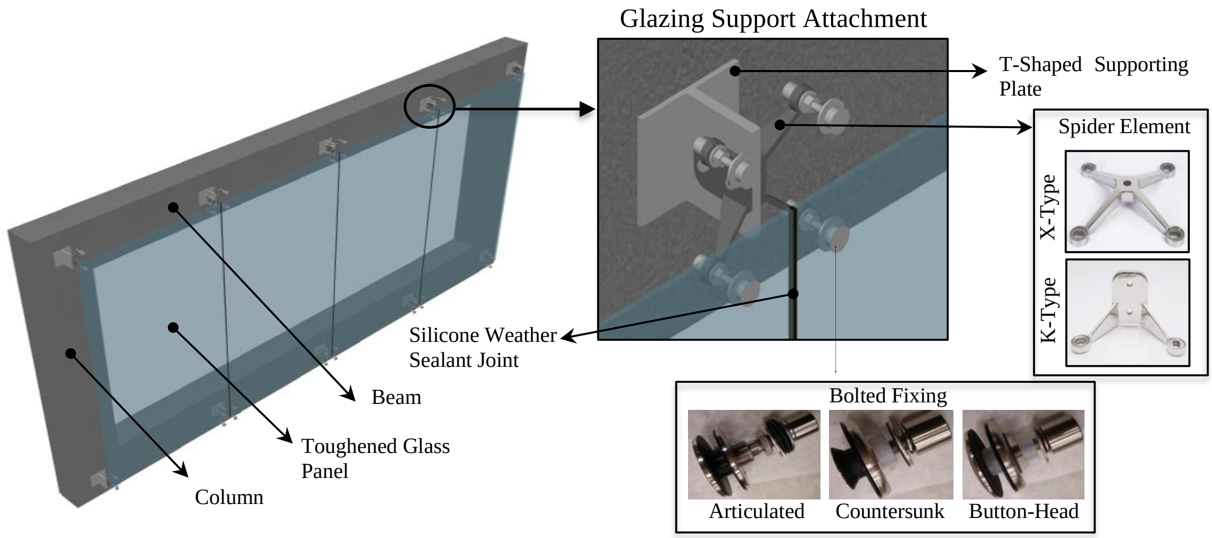

Figure 2. Schematic representation of a PFGFS without supporting structure

The spider elements (e.g., the glazing support attachments), allow to transfer the load to the supporting structure (if used) or directly to the building structure itself. Nowadays, two types of spider elements are available on the market, specifically, the pinned "X-Type" and the sliding "K-Type". The details of such components lead to different capacities in accommodating the in-plane movement of the facade (major details in the following). Further, several bolted fixings are available. These elements are located nearby the corner of the glass panels, and they allow the transfer of the load to the spider element. Bolted fixings can be featured by an articulated system as well as by a fixed one. In the former case, a "spherical joint" allows a higher performance of the facade as a greater rotation and displacement of the glass panel to the fixing can be accommodated without causing excessive stress concentrations. In case a fixed system is used, "countersunk bolts" as well as "button head bolts" are available. In these latter cases, the load is transferred through the bolt to the glass interface, and the system is less performing when compared to the articulated one. Finally, considering the glass panels, toughened or laminated glass is generally used. The main difference is related to the strength of the glass panel itself. In case of laminated glass, two or more panels are bonded together through an intermediate layer (generally polyvinyl butyral, PVB). The resulting "overstrength" should be carefully taken into account in the design phase, as it could affect the correct "hierarchy of strength" and the connection system could become the "weakest link" leading to the potential fallout of the facade, thus resulting in a life-safety threat, [Baird *et al.*, 2011b; Diaferia *et al.*, 2011]. Toughened glass is less resistant, and it is characterized by the property of fragmenting into small pieces in case of rupture.

As pointed out previously, PFGFSs are a relatively novel type of glazed facade. For this reason, limited investigations are available in literature. At the Swinburne University of Technology, Melbourne, Australia, two full-scale displacement-control monotonic tests have been carried out to assess the in-plane capacity of such systems, [Sivanerupan *et al.*, 2014]. The two specimens, featured by the use of X-Type and K-Type spider elements, consist of four 1200x1200mm toughened glass panels 12mm thick, with a silicone weather sealant joint of 8mm. The tests have been carried out pushing the system until the failure of the first glass panel. Further, numerical investigations have been implemented and benchmarked against the experimental results, [Sivanerupan *et al.*, 2016]. The experimental tests, as well as the numerical investigations, pointed out that PFGFSs tend to accommodate the in-plane movement through three main mechanisms, and the difference between the X-Type and the K-Type solution is related only to the first. If X-Type elements are used, the first mechanism is related to the in-plane rigid-body rotation of the spider element itself, while, in case of K-Type, rigid-body translation of the spider element at the base slotted hole connection to the supporting plate is observed. The second mechanism is a rigid body translation related to the built-in standard gaps between the bolts and the holes within the spider arms, as well as between bolts and glass panels. The last mechanism is related to the deformation and yielding of the spider arms, which facilitate the out-of-plane movement of the panels. The out-of-plane movement, together with the diagonal tensile stresses around the bolted connection, bring to a rapid increment of tensile stresses, leading to a brittle failure of the glass panels. The results of the experimental tests highlighted a better performance of the facade system featured by K-Type elements (maximum allowable drift of 5.25%) with respect to the one in which X-Type elements were used (maximum allowable drift of 2.01%). Considering the superior behaviour of K-Type elements, this work focuses on such components as a basis solution to further improve their performance, moving towards a low-damage system.

3.DETAILED FEM MODELLING OF PFGFSs COMPONENTS

This chapter describes the Finite Element Modelling (FEM) approach implemented in the software ABAQUS to assess the behaviour of the PFGFS components, namely the frictional behaviour of the spider element, the bending of the spider arms, the silicone weather sealant joints, and the bolted fixings.

3.1 THE SPIDER ELEMENT

Firstly, a refined 3D non-linear FEM has been developed in ABAQUS to capture the frictional behaviour of the spider element to the supporting plate, as well as the flexural behaviour of the spider arms. After that, the results from the ABAQUS analyses have been used to calibrate a simplified, yet accurate, system of frame/link elements for implementing the macro-model of the overall facade system.

In order to assess the frictional behaviour of the spider element to the supporting plate, simplified assumptions have been considered, allowing a reduction of the computational effort. Specifically, the T-shaped supporting plate has been simplified considering only the part to which the spider elements are attached. Further, this plate has been constrained by fixed support, modelling a rigid connection to the building structure. Finally, in order to study the frictional behaviour, the spider arms have been removed from the model. Figure 3 (left) shows the real connection between the structure and the glazing support attachment (a), as well as the simplified system considered in the analyses (c). The simplified model consists of three parts: i) the supporting plate, ii) the spider element(s), and iii) the bolts. The overall model has been implemented using the quadratic brick element C3D20R featured by 20 nodes with reduced (2x2x2) Gauss integration points.

Two materials have been used into the model: i) the stainless steel AISI 316 modelled as an elastic material and used for the supporting plate as well as the spider element(s), and ii) the stainless steel A4 modelled as an elastic-plastic material and used for bolts. The parameters for implementing the correct material characteristics of bolts depend on their resistance class (CR). Specifically, CR 50, 10mm diameter bolts have been used. The material properties used to implement the plasticity are: the yielding stress σy (210 MPa), the ultimate stress σu (500 MPa), as well as the ultimate strain εu (11.40%).

The frictional behaviour among the parts has been modelled through tangential and normal behaviour within the contact surfaces. For the first one, a frictional coefficient μ for steel-to-steel contact has been selected (μ = 0.30, according to the Italian Building Code [NTC, 2018]). The normal behaviour has been modelled as Hard Contact. Further information about the modelling of frictional interaction are available in the ABAQUS Standard user's manual [2009]. After that, a relative movement between the supporting plate and the spider element(s) has been applied until the gap closure, i.e., when the bolt shanks get in contact with the plate holes. Figure 3 (right) shows the force-displacement curves representative of the frictional behaviour for two assemblies consisting of one (Type A), as well as two (Type B) spider elements. Further, a particular of the mesh used in such analyses is shown. Focusing on the force-displacement curves, it is worth noting how forces increase in the connection until the critical frictional-force is achieved, then the sliding is triggered. After that, the sliding continues until the gap closure, where it is possible to note a sudden increase in stiffness. In this condition, there is a rapid increment of forces which cause a sudden increase of tensile stresses in the glass panels until the failure. These results allow to define multi-linear links for modelling the frictional behaviour into the proposed macro-model of the overall facade system.

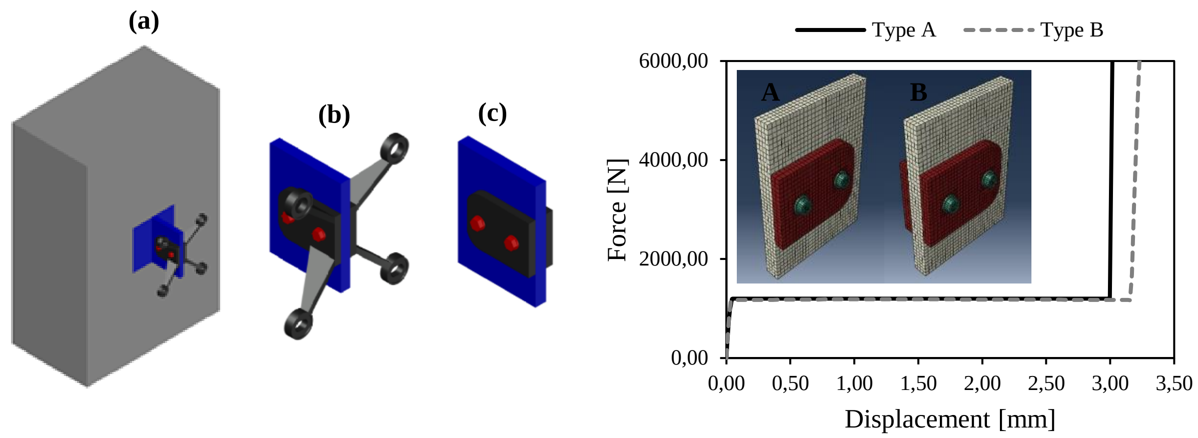

Figure 3. Left: (a) Schematic representation of the real connection, together with the simplified models used for the assessment of the (b) flexural behaviour, as well as of the (c) frictional behaviour; Right: force-displacement curves representing the frictional behaviour of the glazing attachment systems together with the particular of the mesh.

Once the frictional behaviour of the connection had been assessed, the second task focused on the assessment of the flexural behaviour of the spider arms. Specifically, to reach this goal, the aforementioned model was enriched by modelling the spider arms, Figure 3 (left, b) and Figure 4 (left).

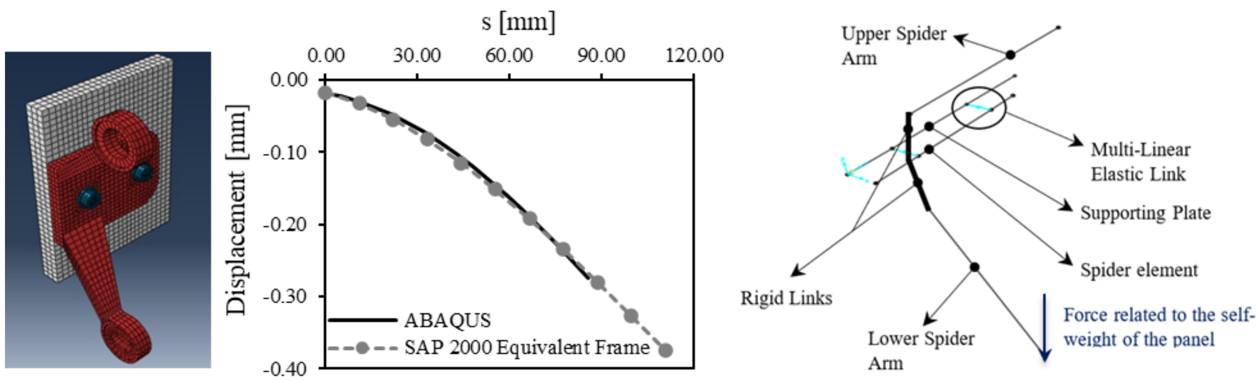

Figure 4. Left: ABAQUS model used to assess the flexural behaviour of spider arms; Centre: calibration of the equivalent frame for spider arms; Right: simplified lumped-plasticity macro-model for the glazing support attachment.

This model allows assessing the flexural behaviour of the spider arms under a vertical force, representing the self-weight of the glass panel. The analysis aims at calibrating the cross-sectional area properties of the equivalent frame to be used in SAP 2000, for modelling the complex geometry of the spider arms. In fact, such an element is featured by variable cross-sectional area properties. Using the results of the ABAQUS model, an iterative procedure has been carried out benchmarking such results with the analyses carried out on a simplified model consisting of the equivalent frame/link elements system. Figure 4 (centre) shows the comparison of the analyses carried out both in ABAQUS as well as in SAP 2000 in terms of the deformed shape of the spider arm when the self-weight force from the glass panel acts. The frame element used for modelling the spider arms consists of a simple rectangular section 30.5mm width and 13.5mm height. Finally, Figure 4 (right) shows the simplified system, used for modelling the glazing attachment system into the lumped-plasticity macro-model. Such an equivalent system consists of frame elements for supporting plate and spider(s) (the same cross-sectional area properties of the real element have been considered), the equivalent frame elements for the spider arms, and multi-linear links for modelling the frictional behaviour. Finally, it is worth noting that in such work, only monotonic (pushover) analyses have been carried out. This justifies the use of multi-linear links as acceptable for modelling the monotonic in-plane behaviour of the facade system. In case cyclic analyses were needed, refined link properties should be accurately calibrated to capture the actual hysteretic behaviour.

3.2 THE SILICONE WEATHER SEALANT JOINT

This paragraph focuses on the behaviour of the silicone weather sealant joint. Specifically, a refined non-linear ABAQUS model has been implemented, and the material characteristics have been calibrated with the experimental results on such a component, as widely investigated in Sivanerupan *et al.* [2016]. The experimental tests have been carried out on 100x100mm specimens consisting of two toughened glass panels (12mm thick) with an 8mm thick silicone weather sealant joint. The specimens have been tested subjecting the silicone to tension, compression and to shear forces.

The refined 2D non-linear model implemented in ABAQUS, used to simulate the experimental tests, consists of both linear (implemented for modelling glass) as well as non-linear (for modelling silicone) shell elements. Glass has been modelled as an elastic material, while silicone has been modelled as an elastic-plastic material for loads cases simulating tension as well as shear, while as a hyperelastic material in case of compression. By means of iterative procedures, the material properties have been defined by calibrating the numerical analyses against the experimental tests. Figure 5 (left) shows the force-displacement curve considering the load cases (i.e., tension, compression, and shear) for an 8mm thick silicone weather sealant joint.

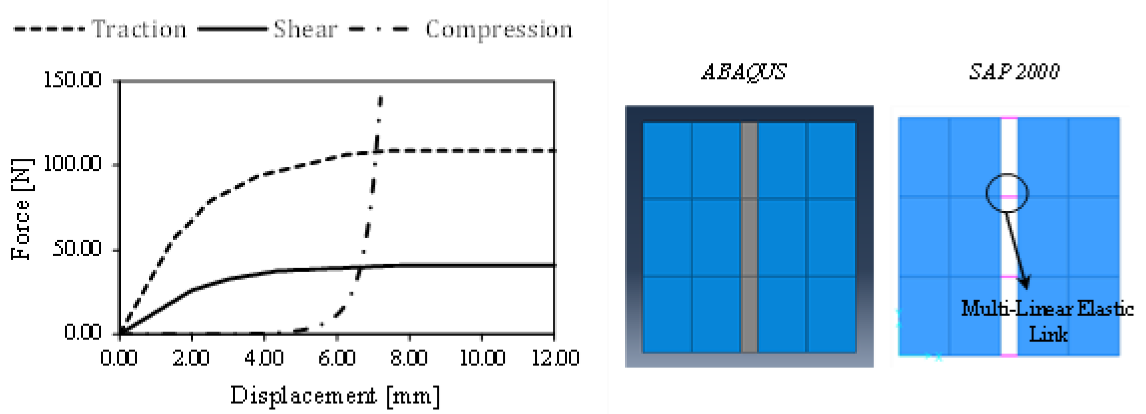

Figure 5. Left: Force-displacement curves representative of the silicone weather sealant joint behaviour; Right: refined non-linear model implemented in ABAQUS together with the simplified one developed in SAP 2000.

Finally, the results of the ABAQUS analyses have been used to calibrate a simplified, yet accurate, model in SAP 2000. Specifically, multi-linear elastic links have been used to replace the complex non-linear shell elements used in ABAQUS. This approach allows for a less computational expensive and more practical analysis. Figure 5 (right) shows the refined non-linear model in ABAQUS as well as the simplified one developed in SAP 2000.

3.3 THE BOLTED FIXINGS

This paragraph focuses on the connection between the glass panel and the spider arm through the bolted fixing. Specifically, countersunk bolts ("fixed" systems) have been adopted in this case. As pointed out previously, higher-performance facade systems could be implemented using "articulated fixings". Nevertheless, the complexity related to the definition of a reliable model of the ball-joint requests further research efforts, and it is out of the scope of this work.

Firstly, a refined 3D non-linear model has been implemented in ABAQUS. The model is similar to those implemented for studying the frictional behaviour of the supporting plate to the spider element connection, and for the flexural behaviour of the spider arm. Also, as in the previous 3D models, the C3D20R hexahedral element has been used for implementing the numerical ABAQUS model. In order to evaluate the frictional behaviour of the bolted fixing to spider arms, the overall model, Figure 6 (left), has been used focusing on the spider arms end. Specifically, a relative displacement between the bolted fixing and the spider arms has been applied until the gap closure, in order to evaluate the force-displacement curves representative of the frictional behaviour. Two analyses have been performed to capture the differences between the two connections. The former analysis focuses on the frictional behaviour of the bolted fixing to the upper spider arm. In this case, the connection consists of a circular hole, and the same relative movement is allowed both vertically as well as horizontally. In the second case (lower connection), there is a horizontally slotted hole, which allows only horizontal movement.

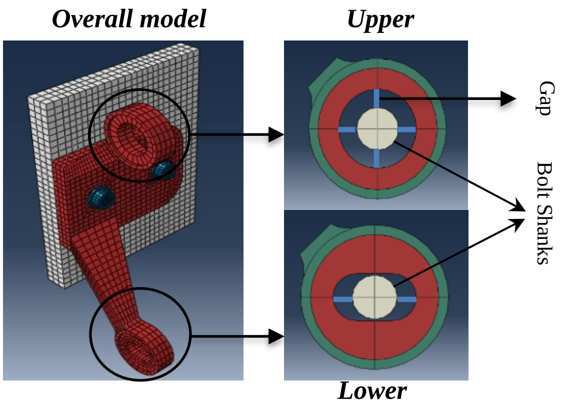

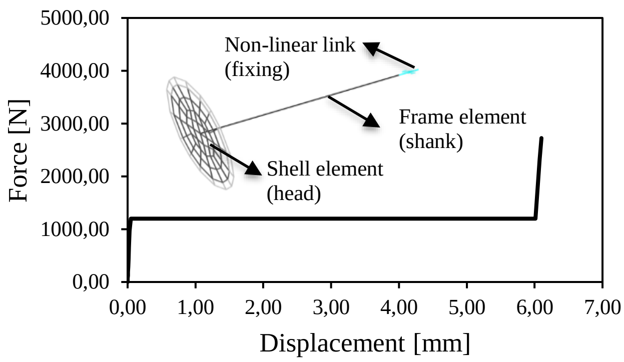

Figure 6. Overall model implemented in ABAQUS with particulars of the upper and lower connection of the bolted fixing to the spider arm (left); force-displacement curve representative of the frictional behaviour of the bolted fixing to the spider arm together with the schematic representation of the simplified model of the bolted fixing.

Finally, as in the previous cases, the results from the ABAQUS micro-model have been used to implement the simplified, yet refined, lumped-plasticity macro-model of the overall facade system. Specifically, such analyses have been used to calibrate a frame/shell/link elements system able to capture the behaviour of the bolted fixing. The simplified model of the bolted fixing consists of shell elements used to model the bolt head, a frame element for modelling the bolt shank, and a multi-linear link for modelling the frictional behaviour of the bolted fixing to the spider arm. Figure 6 (right) shows the force-displacement curve representing the frictional behaviour of the lower connection, together with a schematic of the simplified model implemented for the bolted fixing.

4.SIMPLIFIED MACRO-MODEL OF THE OVERALL FACADE

In this paragraph, the seismic assessment of the overall performance of a PFGFS using traditional K-Type element is assessed and discussed. Referring to the detailed 3D non-linear analyses carried out in ABAQUS at a local (connection) level, a macro-model has been developed in SAP 2000. The PFGFS is coupled with a portion of a Moment-Resisting Frame (MRF) system, modelled through frame elements. Considering the facade, the spider elements, together with the bolted fixings, are modelled by an equivalent frame/non-linear link system. The silicone weather sealant joint is modelled through multi-linear elastic links. Finally, the glass panels are modelled with shell elements. Referring to the glass panels, it is worth noting that a refinement of the mesh has been provided around the bolted fixings. Figure 7 (left) shows the implemented macro-model in SAP 2000, together with the refinement of the mesh.

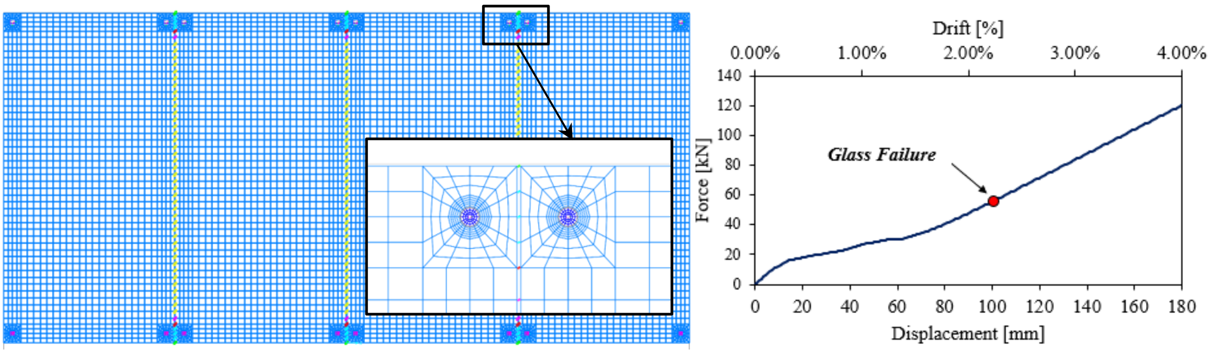

Figure 7. Schematic representation of the traditional as well as innovative solution (left); and stress distribution in bolts for the two configurations.

Non-linear static (pushover) analysis has been performed to define the force-displacement capacity curve of the PFGFS, Figure 7 (right). The principal tensile stresses of the glass panels have been monitored during the analysis in order to assess the glass failure. The failure of the first panel is assumed when the maximum principle tensile stress, f_g, reaches the maximum allowable stress, $f_{g,d}$, according to DT-210 guidelines [CNR, 2013]. These guidelines provide such value according to several parameters (i.e., glass panel dimensions, aspect-ratio, etc.). For the PFGFS assessed herein, four 2000x3800mm, 12mm thick toughened glass panels are considered, and the maximum allowable tensile stress, according to DT-210, the maximum allowed principle tensile stress, $f_{g,d}$, is 82 MPa. The silicone weather sealant joint thickness is 8mm.

The maximum allowable drift value for this PFGFS is 1.17%. It is worth noting that such a value is lower than the5.25% drift capacity observed in the experimental investigations, [Sivanerupan *et al.*, 2014, 2016]. This was expected as the performance of PFGFSs depends on several factors. First, in Sivanerupan *et al.* [2014, 2016], spider elements with vertically slotted holes, enabling for a better performance, rather than with circular holes, were adopted. Further, in those tests, square panels with a length of 1200mm were used. In this case, rectangular glass panels 2000x3800 are adopted, and using larger panels allows for a reduced maximum allowable tensile stress [CNR DT-210, 2013]. These aspects justify a lower performance of the facade systems studied in this work with respect to the tests carried out at Swinburne University.

5. PROPOSAL FOR AN INNOVATIVE LOW-DAMAGE CONNECTION

With the aim of improving the seismic performance of PFGFSs, alternative high-performance attachment systems have been proposed in the last years. Specifically, such components consist of spider elements including vertically slotted holes. These holes allow the connection to slide until the gap closure, so that longer holes lead to an improvement of the in-plane capacity. Nevertheless, strong earthquakes cause bolts yielding during the sliding, and preload losses are expected. If preload losses occur, the bolt is no longer able to counteract the vertical settlement of the facade through the frictional behaviour at the connection level. For this reason, even though the glass panel does not reach rupture, the connection level damage, and the related vertical settlement, lead to potential high economic losses.

For this reason, an innovative low-damage system able to overcome the issues pointed out previously is herein proposed and analytically-numerically investigated. In the low-damage system, horizontally (rather than vertically) slotted holes are introduced, and the supporting system, together with the spider elements, are attached to the structure by rotating themselves 90 degrees. Figure 8 (left) compares the traditional solution (consisting of K-Type spider elements) with the proposed innovative one. A further key difference among the two solutions is the supporting plate. In the former case (traditional solution) a "T-shaped" plate is adopted, while in the low-damage system, a "C-shaped" plate incorporating vertical stiffeners is used. The stiffeners are adopted to reduce the potential high deformations related to the self-weight of the glass panels. As outlined before, the innovative solution is developed to overcome the issues related to the vertical settlement. In fact, even though the preload loss occurs, bolts are still able to support the glass panels through their axial stiffness. Furthermore, as demonstrated by the analyses carried out in ABAQUS, bolts yielding does not occur if the innovative solution is adopted. Specifically, two analyses have been carried out on the attachment systems by applying the same relative displacement, until the gap closure, between the supporting plate and the spider element. Figure 8 (right) shows the analyses results in terms of Von Mises stress distribution. In the traditional case, bolts deform in flexure-shear, yielding locally. If an innovative solution is adopted, the maximum stress developed at the gap closure is about 80 MPa, far from reaching yielding (σy = 210 MPa).

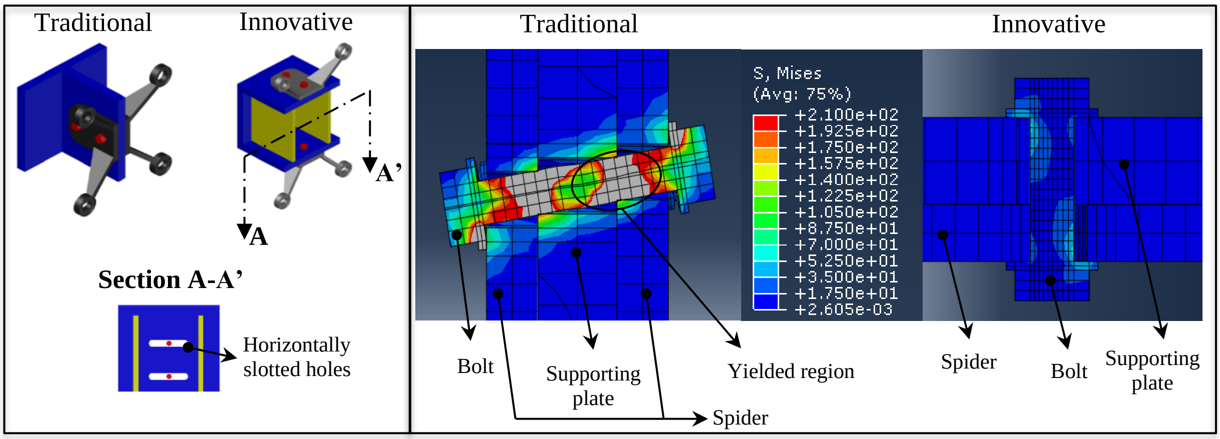

Figure 8. Schematic representation of the traditional as well as innovative solution (left); and stress distribution in bolts for the two configurations.

In addition, a parametric study has been carried out by varying the dimension of the horizontally slotted holes (from 13mm to 80mm). Firstly, ABAQUS FEM analyses have been carried out to define the force-displacement curves at the connection level for implementing the new macro-models of the overall facade. Results in Figure 9 (left) show an improvement of the in-plane capacity of the facade. In fact, using larger horizontally slotted holes enables to reach greater in-plane displacement before the gap closure (which leads to a rapid increment of the tensile stresses) occurs. Nevertheless, it is worth noting that such results refer to a facade system consisting of four rectangular, 2000x3800mm panels. Considering that the maximum allowable tensile stress for glass depends on the panels' dimension and aspect-ratio, [CNR DT-210, 2013], if glass panels with different dimensions are used, such analyses should be repeated. Using 80mm horizontally slotted holes increases the maximum allowable drift to 2.49% (larger than the 1.17% drift achieved by the traditional solution with 13mm circular hole). It is worth noting that the maximum allowable drift defined for the traditional solution (1.17%) is lower when compared to the value of 5.25% observed in the experimental investigations, [Sivanerupan *et al.*, 2014, 2016]. This was expected as the performance of PFGFSs depends on several factors. First, in Sivanerupan *et al.*, [2014, 2016], spider elements with vertically slotted holes, enabling for a better performance, rather than circular holes, have been adopted. Further, in those tests, square panels with a length of 1200mm were used. In this case, rectangular glass panels 2000x3800mm are adopted, and using larger panels allows for a reduced maximum allowable tensile stress [CNR DT-210, 2013]. These aspects justify a lower performance of the facade systems studied in this work with respect to the tests carried out at the Swinburne University.

Finally, another crucial difference between the traditional and the innovative (low-damage) solution is the way they accommodate the in-plane movement of the PFGFS. When a traditional connection system is used, the PFGFS accommodates the in-plane movement through a rocking motion related to the glass panels. If a low-damage system is adopted, instead, the facade is horizontally isolated from the structure, leading to several advantages, such as reduction of the in-plane actions without increasing the system stiffness, [Brueggeman *et al.*, 2000]. Figure 9 (right) schematically shows the difference between the two mechanisms for accommodating the in-plane movement.

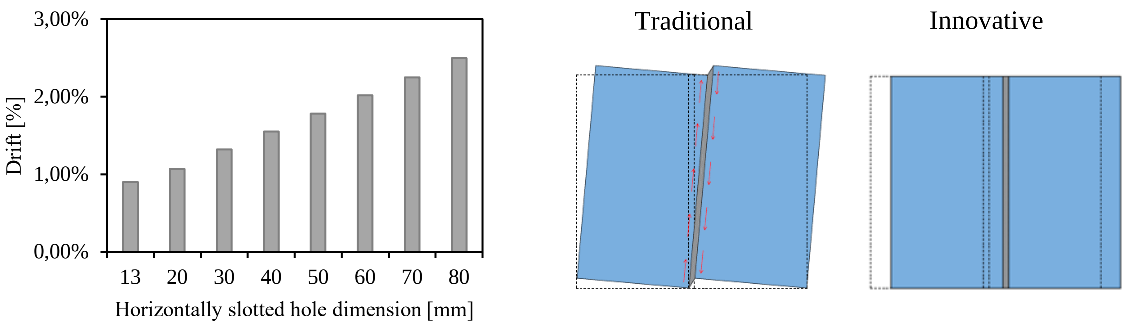

Figure 9. Left: Maximum allowable drift of the innovative system varying the dimension of the horizontally slotted holes; Right: movement accommodation of the facade using traditional or innovative connection systems.

6.CONCLUSIONS

This work assessed the seismic performance of Point Fixed Glass Facade Systems (PFGFSs). Firstly, refined 3D non-linear FEMs have been implemented in ABAQUS to assess the complex local (connection) level behaviour, as well as the behaviour of the silicone weather sealant joint. After that, results from the micro-modelling analyses have been used to define a refined lumped-plasticity macro-model of the facade into the software SAP 2000. The macro-model consists of frame elements, multi-linear springs, and shell elements, and it allows to assess the overall in-plane capacity of the facade. Nowadays, PFGFSs are considered more performing with respect to traditional glazed facade, especially if high-performance attachment details, consisting in vertically slotted holes, are used. Nevertheless, post-earthquake surveys have highlighted the vulnerability of such a system, in fact, traditional attachments have shown yielding and preload losses after strong earthquakes. This compromises the ability to counteract vertical settlements through the frictional mechanism at the connection level, leading to potential high economic losses. Therefore, an innovative low-damage connection system, consisting of horizontally slotted holes, has been proposed and numerically investigated. Refined 3D models have been implemented even for the innovative attachment system, together with the macro-model to assess the overall in-plane capacity of the facade. A parametric study confirmed that the dimension of the horizontally slotted holes strongly affects the in-plane capacity of the facade. Specifically, the maximum allowable drift increases from 1.17% (in case of traditional connection system) to 2.49% when a horizontally slotted hole connection (80 mm length) is used. Currently, a research effort by the authors is focusing on defining other parameters that mostly affect the overall capacity of PFGFSs consisting of the innovative low-damage connection system (e.g., the glass panel size, the silicone weather sealant joint thickness, etc.).

REFERENCES

Baird, A., Palermo, A., Pampanin, S. [2011a]. "Facade damage assessment of multi-storey buildings in the 2011 Christchurch earthquake," *Bull. N. Z. Soc. Earthq. Eng.*, Vol. 44, No. 4, pp. 368-376.

Baird, A., Diaferia, R., Palermo, A., Pampanin, S. [2011b]. "Numerical modelling of local cladding-structure interaction," *Proceedings of the 4th Structural Engineers World Conference*, Cernobbio, Italy.

Bianchi, S., et al. [2021]. "Shake-table tests of innovative drift sensitive non-structural elements in a low-damage structural system," *Earthq. Eng. Struct.*, Vol. 50, No. 9, pp. 2398-2420.

Brueggeman, J. L., Behr, R. A., Wulfert, H., Memari, A. M., Kremer, P. A. [2000]. "Dynamic racking performance of an earthquake-isolated curtain wall system," *Earthq. Spectra*, Vol. 16, No. 4, pp. 735-756.

D.M. 17/01/2018, NTC [2018]. *Norme Tecniche per le Costruzioni*, Gazzetta Ufficiale, n. 42 del 20/02/2018, Supplemento ordinario n.8, Italy, [in Italian].

Diaferia, R., Baird, A., Palermo, A., & Pampanin, S. [2011]. "Numerical study on the seismic interaction between 2D seismic resisting frames and claddings," *Proceedings of the 4th Structural Engineers World Conference*, Cernobbio, Italy.

DT210 [2013], *Istruzioni per la Progettazione, l'Esecuzione ed il Controllo di Costruzioni con Elementi Strutturali di Vetro*, C.N.R., Italy, [in Italian].

Inca, E., Jordão, S., Rebelo, C., Rigueiro, C., Simões, R. [2019]. "Seismic Behaviour of Point Fixed Glass Facade Systems: State of the Art Review," *Eur. j., eng. sci., tech.*, Vol. 2, No. 2, pp. 1-15.

Pampanin, S. [2015]. "Towards the "ultimate earthquake-proof" building: development of an integrated low-damage system", *Chapter in Perspectives on European Earthquake Engineering and Seismology, Ansal A. (ed.); Series: Geotechnical, Geological and Earthquake Engineering*, Vol. 39, Chapter 13, pp. 321-358

Perrone, D., Calvi, P. M., Nascimbene, R., Fischer, E. C., & Magliulo, G. [2019]. "Seismic performance of non-structural elements during the 2016 Central Italy earthquake," *Bull. Earthq. Eng.* Vol. 17, pp. 5655–5677

Sivanerupan, S. [2010]. "In-plane drift capacity of point fixed glass facade systems," *PhD Thesis*, Swinburne University of Technology, Melbourne, Australia

Sivanerupan, S., Wilson, J. L., Gad, E. F., Lam, N. T. K. (2016). "Analytical study of point fixed glass facade systems under monotonic in-plane loading," *Adv. Struct. Eng.*, Vol. 19, No. 4, pp. 611-626.

Sivanerupan, S., Wilson, J. L., Gad, E. F., Lam, N. T. K. [2014]. "Drift performance of point fixed glass facade systems," *Adv. Struct. Eng.*, Vol. 17, No. 10, pp. 1481-1495.

Smith, M. [2009]. *ABAQUS/Standard User's Manual, Version 6.9*, Providence, RI, USA.

Taghavi, S., Miranda, M. M. [2003]. *Response assessment of non-structural building elements*. Pacific Earthquake Engineering Research Center, USA.

Effect of Floor Slab Vibration on Seismic Performance of Suspended Ceiling Systems

Snehasagar Gopagani[1], Andre Filiatrault[2,4], and Amjad J. Aref[3]

[1] Graduate student, Department of Civil, Structural and Environmental Engineering, SUNY Buffalo, Buffalo, New York, USA, 14226.
e-mail: snehasag@buffalo.edu
[2] Professor, University School of Advanced Studies, IUSS Pavia,
Pavia, Italy, 27100.
e-mail: andre.filiatrault@iusspavia.it
[3] Professor, Department of Civil, Structural and Environmental Engineering, SUNY Buffalo, Buffalo, New York, USA, 14226.
e-mail: aaref@buffalo.edu
[4] Emeritus Professor, Department of Civil, Structural and Environmental Engineering, SUNY Buffalo, Buffalo, New York, USA, 14226.
e-mail: af36@buffalo.edu

Abstract. Suspended ceiling systems are heterogenic assemblies constructed with elements of various shapes and sizes such as ceiling tiles, grid runners, hanger wires, wall angles, and lateral restraints. To understand the seismic behaviour of suspended ceiling systems in detail, a considerable amount of shake table testing of large-scale suspended ceilings has been conducted for the past three decades. The observations from these tests resulted in the inclusion of boundary elements such as seismic clips, pop-rivets, perimeter hanger wires, and lateral restraints in seismic resisting design guidelines of suspended ceiling systems. In a full-scale shake table tests conducted at the E-defence facility in Japan, the suspended ceiling systems equipped with lateral restraints showed a greater amount of damage compared with the suspended ceiling systems not equipped with lateral restraints due to the flexible supporting floor slab. This behaviour exhibited by the lateral restraints appears to be opposite to their intended purpose. To better understand this phenomenon in detail, a three-dimensional finite element (FE) model of a ceiling system suspended from a flexible floor slab was developed and validated with available experimental observations. Floor motion records extracted from the FE models of several buildings subjected to the FEMA P695 far-field earthquake ground motions set were considered as input loading. A parametric study was conducted to correlate the fundamental bending frequency of the supporting floor slab with the damage predicted in the suspended ceiling system. The influence of the flexibility of the floor slab on seismic fragility curves of suspended ceiling systems was quantified. The influence of lateral restraints on the seismic performance of suspended ceiling systems was also included in this study.

Keywords: Nonstrucutral components, Suspended ceiling systems, Seismic damage.

1. INTRODUCTION

The large-scale shake table tests on suspended ceiling systems and their observed behaviour in past earthquakes were crucial in developing the seismic resistant design guidelines outlined in the ASTM E580/E580M standard [2020]. However, the influence of the structural system and other nonstructural components on the suspended ceiling system's seismic damage was not explicitly incorporated into these seismic design guidelines. In addition, these seismic design guidelines were developed based on limited available data. Hence, it is vital to understand the effectiveness of these seismic design guidelines in reducing the seismic damage to suspended ceiling systems in various scenarios. The traditional approach of large-scale shake table testing of suspended ceiling systems is time-consuming and costly to generate additional data. Hence a three-dimensional finite element (FE) model of a suspended ceiling system that was developed and validated with experimental data provides a quick and economical alternative to test the robustness of these seismic design guidelines. This study narrows down on quantifying the influence of the flexibility of supporting floor slabs on the seismic damage of suspended ceiling systems. The motivation for this numerical study is that in the limited experimental testing of suspended ceiling systems, it was observed that the flexible supporting floor slab had increased the damage to the suspended ceiling system subjected to seismic loading.

In this study, the authors have utilized seismic fragility curves to compare the influence of the flexibility of the supporting floor slab on the seismic response of suspended ceiling systems. In addition, this study aims to quantify the effect of lateral restraints on the seismic performance of suspended ceiling systems. First, the prominent experimental and numerical studies on suspended ceiling systems that are available in the public literature are briefly reviewed. Then the development and validation of the FE models of suspended ceiling systems with experimental data are discussed. Thereafter, the paper compares the seismic fragility curves developed for these FE models of suspended ceiling systems with different flexural stiffness values of the supporting floor slab. Finally, the paper concludes with comments on the influence of the flexibility of the supporting floor slab and lateral restraints on the seismic response of suspended ceiling systems.

2.LITERATURE REVIEW

The observations from the earliest shake table experiments on suspended ceiling systems conducted by ANCO [1983], Satwant and Granneman [1984], ANCO [1993], and Yao [2000] were the inspiration for the current seismic design guidelines provided in ASTM E580/E580M standard [ASTM 2020]. In the past two decades, the large-scale shake table experiments on suspended ceiling systems of various configurations conducted by Badillo-Almaraz *et al.* [2007], Rahmanishamsi *et al.* [2014], Ryan *et al.* [2016], and Ryu and Reinhorn [2019a] evaluated the effectiveness of these seismic design guidelines. In addition, several tests were also conducted to investigate the interaction between suspended ceiling systems and other nonstructural components, especially by Huang *et al.* [2013] and Qi *et al.* [2020].

Some of the above-mentioned shake table experiments identified the interaction between suspended ceiling systems and supporting floor slabs under seismic loading. As outlined in Ryan *et al.* [2016], a five-story steel moment frame building equipped with base isolators was tested at the E-defence facility in Japan. Along with other nonstructural components, suspended ceiling systems [plan area of 83.61 m^2 (900 ft^2)] were installed with and without lateral restraints on the fourth and fifth stories, respectively. It was observed that the suspended ceiling system equipped with lateral restraints exhibited more damage than the suspended ceiling system not equipped with lateral restraints. This behaviour of lateral restraints was contrary to their intended purpose. It was inferred that the rigid compression struts transferred the large displacements from the flexible supporting floor slab to the suspended ceiling system, causing damage and collapse at lower shaking intensities. In addition, Yao and Chen [2017] conducted shake table tests on the drop hanger system (DHS) ceilings of Taiwan (similar to the suspended ceiling systems in the United States) to understand the effect of vertical accelerations on DHS ceilings. The salient observations were that the suspended ceiling systems were vulnerable to the vertical acceleration effects, and the effectiveness of splay wires and compression struts to resist the horizontal accelerations when the suspended ceiling system is subjected to high vertical accelerations was unclear and needed to be investigated. These experimental studies show that the interaction between the flexible supporting floor slab and the suspended ceiling system under seismic loading needs to be quantified and understood in detail. In addition, the effectiveness of lateral restraints should be evaluated.

Several numerical models of suspended ceiling systems were developed by Yao [2000], Zaghi *et al.* [2016], Echevarria *et al.* [2012], Qi *et al.* [2020], Fiorin *et al.* [2021] and Ryu and Reinhorn [2019b]. Whilst these models successfully predicted the behaviour of undamaged suspended ceiling systems, they could not capture the damage propagation up to the total collapse of suspended ceiling systems. Therefore, a new FE model of suspended ceiling system that can capture the propagation of damage and is able to generate seismic fragility curves for suspended ceiling systems was utilised in this study. This FE model is an incremental development of the general FE model of suspended ceiling systems introduced in Gopagani *et al.* [2022]. So far, seismic fragility curves on suspended ceiling systems were generated based on experimental data by Badillo-Almaraz *et al.* [2007] and Soroushian *et al.* [2016a]. Furthermore, Echevarria *et al.* [2012] and Rezvani *et al.* [2022] developed seismic fragility curves of suspended ceiling systems by employing numerical models. Similarly, the seismic fragility curves in this study were generated based on the proposed FE model of suspended ceiling systems. The following section briefly describes the development and validation of the FE model of the suspended ceiling system.

3.DEVELOPMENT OF FE MODEL

The general FE model of suspended ceiling systems was developed using Abaqus/Explicit solver [Dassault Systèmes. 2019]. The following subsections describe the modelling of the suspended ceiling system components and the validation of FE models of suspended ceiling systems by comparing their numerical predictions with experimental observations. Furthermore, the specific FE models of suspended ceiling systems that were employed in this study are introduced in this section.

3.1 MODELLING THE COMPONENTS OF SUSPENDED CEILING SYSTEMS

The mineral wool ceiling tiles were modelled as three-dimensional (3-D) deformable bodies in Abaqus/Explicit. These ceiling tiles are supported on the assembled grid runner's flanges. Grid runners are classified as main runners and cross runners and manufactured from cold-rolled steel. The grid runners were modelled as two shell structures: a flange of 24 mm (15/16 in.) wide and a web of 38 mm (1.5 in.) high. The main runners are suspended from the supporting floor slab from thin steel hanger wires, modelled with one-dimensional beam elements. The hanger wire's plastic material properties were taken from the experimental study conducted by Soroushian *et al.* [2015]. The grid runners at the perimeter either rest or are connected to the wall angles (modelled with rigid elements) with boundary elements such as pop-rivets or seismic clips. The grid runners and ceiling tiles were positioned on the wall angles with the minimum sliding distance prescribed by the ASTM E580/E580M standard [ASTM 2020]. The splay wires of the lateral restraint systems were modelled as hanger wires, while the compression strut was modelled as a 3-D deformable body with sufficient axial stiffness.

A finite element model of the grid connections was developed, and the responses in axial, major, and minor shear directions were derived and calibrated using a subroutine for the *Pinching4* material model developed by Ding [2015]. The hanger wires, splay wires, and compression struts were connected rigidly to the main runners. The pop-rivets and seismic clips were modelled as nonlinear springs, whose properties were defined based on the experiments conducted by Soroushian *et al.* [2016b]. The contact in the normal direction between two surfaces was modelled as 'Hard contact', and the tangential direction was modelled using friction. Based on the results of a simple pull-out test between a ceiling tile and two grid runners, the coefficient of friction between them was estimated as 0.5. Also, contact damping was defined so that there would be a 50% energy loss when contact occurs between components. The supporting floor slab was modelled with shell elements. The floor slab's elastic material properties and thickness were adjusted to achieve the targeted fundamental vertical frequency. The simply supported boundary conditions were defined on all four sides of the floor slab. The 3-D input accelerations were applied to the wall angles and at the edges of the floor slab.

3.2 VALIDATION OF THE FE MODEL

Assemblies #11 and #12 from the experimental study of Ryu and Reinhorn [2019a] were selected as benchmark suspended ceiling systems for developing a detailed FE model. Both assemblies include a 6.1 m x 6.1 m (20 ft x 20 ft) suspended ceiling system equipped with heavy-duty grid runners and 19 mm (¾ in.) thick 0.6 m x 0.6 m (2 ft x 2 ft) ceiling tiles. Assembly #11(unbraced) and assembly #12 (equipped with lateral restraints) are designed for the seismic categories D and E according to the ASCE 7 standard [ASCE 2022]. Further details on these assemblies are outlined in Ryu and Reinhorn [2019a]. Also, the fundamental vertical frequency of the steel frame on which these suspended ceiling systems were installed was recorded as 22 Hz. The thickness of the supporting floor slab in these FE models of suspended ceiling systems was assigned to achieve this targeted fundamental vertical frequency of 22 Hz.

In the experimental study by Ryu and Reinhorn [2019a], each configuration of the suspended ceiling system was subjected to dynamic loading with increasing intensity until the suspended ceiling system collapsed. The intensity of the artificially generated test motions is related to the mapped maximum earthquake spectral acceleration at short periods, S_S [ASCE 2022]. The predicted damage by the FE models of suspended ceiling systems, such as dislodged tiles, failed grid connections, unseated perimeter runners, failed pop-rivets etc., were converted into equivalent damaged ceiling areas following the FEMA P-58 methodology [FEMA 2018]. The comparison of the percentages of equivalent ceiling area damaged observed in the experiments to the predictions of FE models is shown in Figures 1a and 1b for assemblies #11 and #12, respectively. For both assemblies, the FE models could capture reasonably well the increase in equivalent ceiling area damaged with the increase in S_S observed in the experiments. Hence the FE model can be considered suitable for generating numerical fragility curves for suspended ceiling systems. The probable reasons for the difference between the experimental observations and numerical predictions of the equivalent ceiling area damaged are discussed by Gopagani *et al.* [2022]

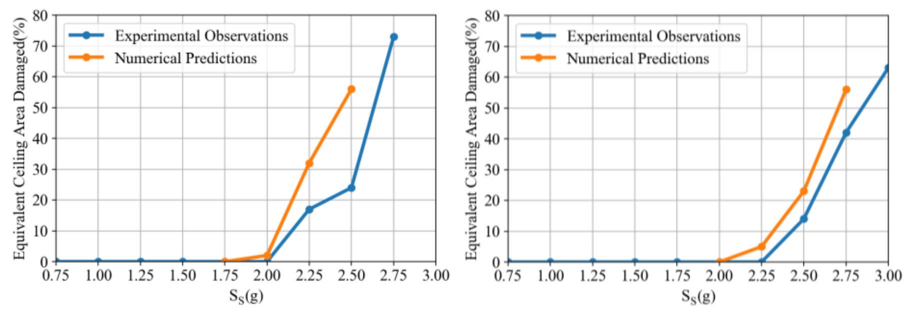

(a) **(b)**

Figure 1: Comparison of experimentally observed and numerically predicted percentage of equivalent damaged ceiling area for (a) Assembly #11 and (b) Assembly #12

3.3 SPECIFIC FE MODEL DEVELOPED FOR THIS STUDY

As shown in Figure 2, the FE model of a suspended ceiling configuration with a square plan area of 7.3 m x 7.3 m (24 ft x 24 ft) and designed for seismic categories D and E according to the ASTM E580/E580M standard [ASTM 2020] was developed for this study. The suspended ceiling system has 144 ceiling tiles of 0.6 m x 0.6 m (2 ft x 2 ft) plan dimensions. The grid runners at the perimeter were fixed to the 50.8 mm (2 in.) wide wall angles on the far sides in both X and Y directions of the suspended ceiling system with pop-rivets. On the other two remaining sides, the grid runners on the perimeter were not fixed to the wall angles, and a minimum sliding distance of 19 mm (0.75 in.) was provided. In addition, stabilizer bars were provided on these two sides. Although the plan area of the above-mentioned suspended ceiling system is less than 92.9 m² (1000 ft²), lateral restraints (not shown in Figure 2) were incorporated for comparison purposes in some of the FE model configurations following the spacing requirements mentioned in ASTM E580/E580M standard [ASTM 2020].

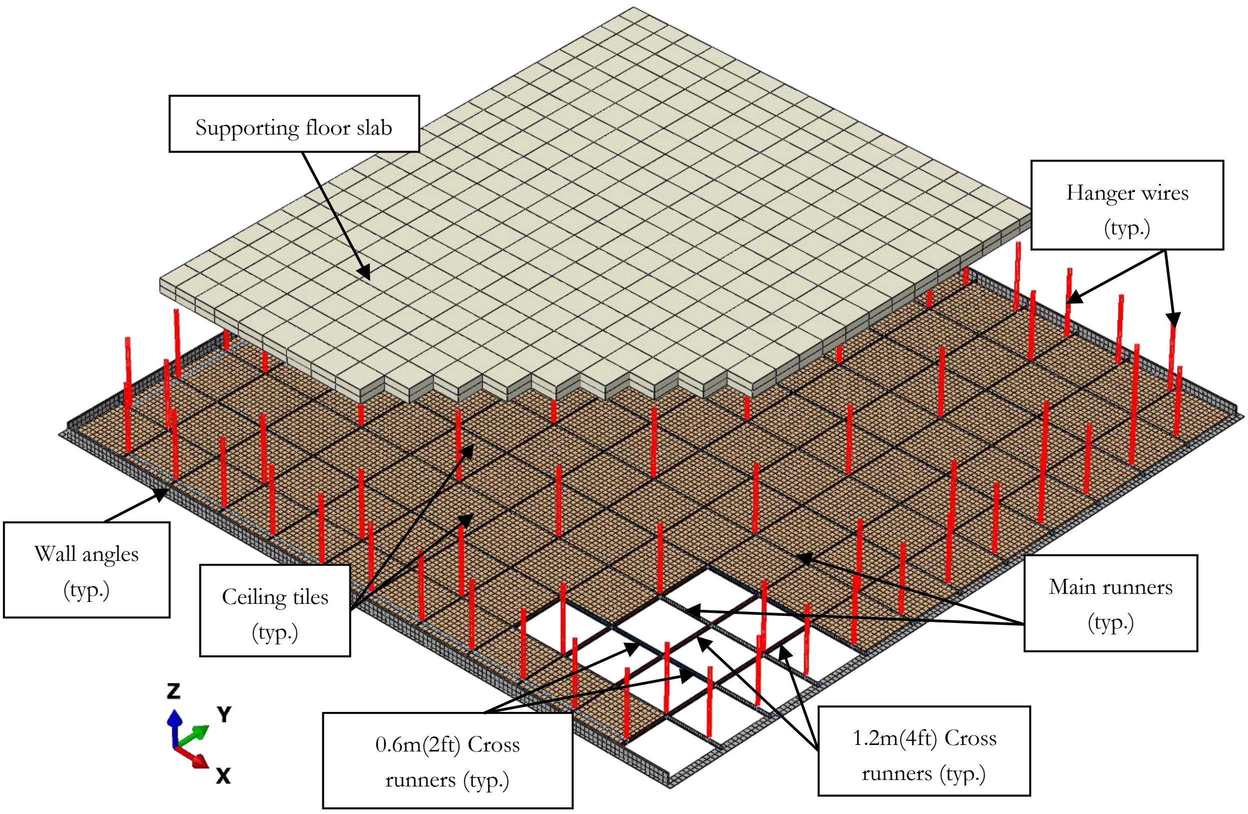

Figure 2: Schematics of the 7.3 m x 7.3 m (24 ft x 24 ft) FE model of suspended ceiling system

4.SEISMIC FRAGILITY CURVES OF FE MODELS OF SUSPENDED CEILING SYSTEMS

This section describes the step-by-step process of developing seismic fragility curves by employing the FE models of suspended ceiling systems developed in this study. At first, the selection of input acceleration motions is explained in detail. The next subsection describes the characteristics of the FE models of suspended ceiling systems analysed. The last subsection presents the seismic fragility curves generated for these configurations of FE models of suspended ceiling systems examined in this study.

4.1 SELECTION OF FLOOR MOTIONS

Analogous to employing ground motions as input loading to develop seismic fragility curves for a building typology, floor acceleration histories were utilised as input loading to develop seismic fragility curves for suspended ceiling systems. The floor acceleration histories were taken from the work carried out by

Chalarca *et al.* [2020]. In this study by Chalarca *et al.* [2020], floor accelerations were recorded for three two-dimensional steel moment-resisting frames of three-story, six-story and nine-story subjected to the 22 pairs of the FEMA P-695 [FEMA 2009] far-field ground motion set. Initially, the horizontal ground motions were scaled to match median response spectra to a specified spectral acceleration at the period of 1s. Then the steel buildings were subjected to these horizontal scaled motions, and the floor acceleration histories were only recorded in the horizontal directions. Due to the large stiffness of the steel moment-resisting frame buildings in the vertical direction, the vertical floor motions around the perimeter of the supporting floor slabs and wall angles were assumed to be similar to the vertical ground motions. Hence, the horizontal floor acceleration histories at the roof level of the six-story steel moment-resisting frame building and the corresponding vertical ground motions (same scaling factor is applied to horizontal and vertical motions) were considered the seismic input for the FE models of suspended ceiling systems. In the FE models of suspended ceiling systems, these floor acceleration histories in all three directions were applied as input at all four edges of the floor slab and to the wall angles.

The steel building models built by Chalarca *et al.* [2020] were inelastic and allowed the building models to yield and eventually collapse. Therefore, the amplitudes of the floor acceleration histories derived from these building models are limited by the force capacity of the structure. To generate data over the full range of the seismic fragility curves, the floor motions corresponding to the largest intensity available were linearly scaled to higher intensities. The median peak floor acceleration was used as the Engineering Demand Parameter (EDP) to construct fragility curves. In contrast to the experiments conducted by Ryu and Reinhorn [2019a], the FE model of the suspended ceiling system was assumed to be initially undamaged for each of the seismic intensities used to construct the numerical fragility curves. The following subsection describes the FE models of the suspended ceiling systems developed in this study.

4.2 FE MODELS OF SUSPENDED CEILING SYSTEMS CONSIDERED IN THE STUDY

The FE model of the 7.3 m x 7.3 m (24 ft x 24 ft) ceiling system suspended from a flexible supporting floor slab was considered in this study. First, the fundamental frequency of the supporting floor slab ω_1, was calculated using the theoretical equation for a simply supported thin plate on all four sides taken from Harris and Allan [2002]:

$$\omega_1 = 5.70 \left[\frac{Et^2}{\rho a^4 (1-\nu^2)}\right]^{\frac{1}{2}} \tag{1}$$

where, E is Young's modulus of the floor slab material (N/m^2 or lb/in^2) , t is the thickness of the floor slab (m or in), ρ is the mass density of the floor slab (kg/m^3 or $lb\,\mathrm{s}^2/in^4$), a is the side length of the square-shaped floor slab (m or in), υ is the Poisson's ratio of the floor slab material. The equation was employed to calculate the desired fundamental vertical frequencies for floor slabs that were corroborated with the FE models of floor slabs. Three fundamental vertical frequencies, 5 Hz, 20 Hz and 40 Hz of the floor slab were considered in this study. The floor slab with the fundamental vertical frequency of 40 Hz represents a rigid floor slab. Similarly, frequencies of 5 Hz and 20 Hz represents the range of fundamental vertical frequencies observed for flexible floor slabs. The vertical floor motions are dominant across all these three frequencies and no frequency-resonance between the excitations and the floor was observed. The floor slab's elastic material properties and thickness were modified to achieve the frequencies mentioned above in the vertical direction. Also, in all the FE models of suspended ceiling systems, the supporting floor slab's boundary conditions were considered simply supported on all four edges. These consistent boundary conditions ensure that the mode shapes for the floor slab will remain similar in all the FE models of suspended ceiling systems.

An additional FE model of the suspended ceiling system was developed by incorporating lateral restraints. For comparison purposes, the supporting floor slab's fundamental vertical frequency in this FE model of the suspended ceiling system was set at 20 Hz. According to the ASTM E580/E580M standard [ASTM

2020], the lateral restraints have a centre-to-centre spacing of 3.6 m (12 ft) in both the orthogonal horizontal directions. In addition, the first lateral restraint should be installed within 1.8 m (6 ft) from the perimeter wall in both the orthogonal horizontal directions. Therefore, four lateral restraints were provided in this FE model of suspended ceiling system based on these spacing guidelines. Typically, the configuration of a lateral restraint is composed of four splay wires installed around a compression strut. Also, the splay wires should be installed at an angle of no more than 45 degrees measured from the plane of the suspended ceiling system. The next subsection presents seismic fragility curves of these four FE models of suspended ceiling systems.

4.3 FRAGILITY CURVES OF SUSPENDED CEILING SYSTEMS

The fragility curves for four FE models of suspended ceiling systems were derived with the previously described floor acceleration motions as input loading. From the FEMA P-58 methodology [FEMA 2018], Damage States (DS) 1, 2, and 3 are associated with 5%, 30%, and 50% of equivalent damaged ceiling area, respectively. DS 1, 2 and 3 correspond to the minimal damage, moderate damage, and a near total collapse of the suspended ceiling system, respectively. Using the horizontal median peak floor acceleration as the EDP, seismic fragility curves generated for these FE models of suspended ceiling systems are provided in Figures 3 and 4. The data points in these plots correspond to the rate of exceedance of a given DS, i.e., the number of floor motions exceeding the prescribed percentage of equivalent damaged ceiling area given a horizontal median peak floor acceleration. The smoothed log-normal fragility curves were obtained through the maximum likelihood procedure [Baker 2015]. Figures 3(a), (b), and (c), compare the resulting seismic fragility curves for DS 1, 2, and 3, respectively, corresponding to the three different fundamental vertical frequencies of supporting floor slabs.

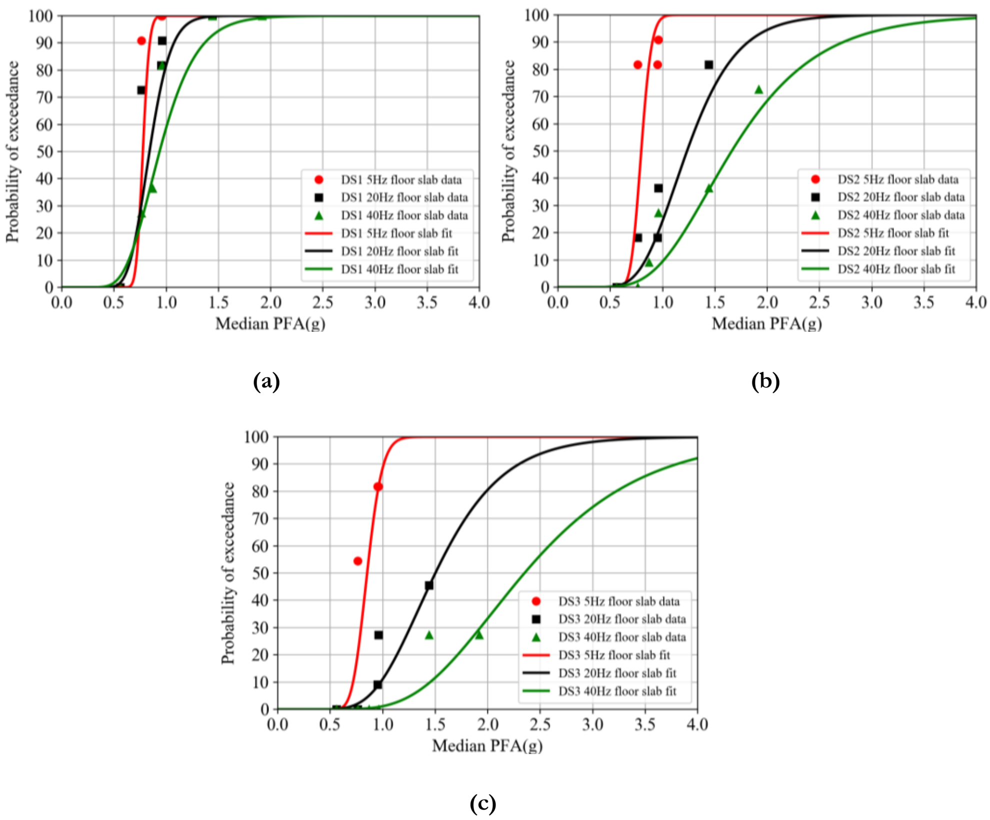

Figure 3: Seismic fragility curves predicted by the FE models of suspended ceiling systems with fundamental vertical frequencies of the supporting floor slab of 5 Hz, 20 Hz, and 40 Hz for (a) Damage State (DS) 1 (b) DS 2 and (c) DS 3.

It is clear from Figures 3(a), (b) and (c) that for any given DS, as the fundamental vertical frequency of the floor slab is increasing, i.e., as the floor slab tends to be less flexible, the seismic intensities at which the FE model of suspended ceiling system exceed a given DS is also increasing. This trend predicted by the FE models of suspended ceiling systems is consistent with the observations from the large-scale shake table experiments [Ryan *et al.* 2016]. Interestingly, the differences between seismic fragility curves for three FE models of suspended ceiling systems are also increasing from DS 1 to DS 3. The numerically predicted median horizontal peak floor accelerations (θ) and log-normal standard deviation (β) values from the seismic fragility curves shown in Figures 3(a), (b) and (c) are reported in Table 1. The corresponding values of θ and β prescribed by the FEMA P-58 methodology [FEMA 2018] for these configurations of suspended ceiling systems [seismic design category D and E, and the area of the suspended ceiling system (53.43 m^2 or 576 ft^2) within 23.22 m^2 (250 ft^2) and 92.99 m^2 (1000ft^2)] are also listed in Table 1.

Table 1: The fragility curve parameters of FE models of suspended ceiling systems

Frequency	5Hz		20Hz		40Hz		FEMA P-58	
Damage State	**θ(g)**	**β**	**θ(g)**	**β**	**θ(g)**	**β**	**θ(g)**	**β**
DS1	0.78	0.06	0.84	0.19	0.94	0.30	1.47	0.30
DS2	0.80	0.10	1.23	0.30	1.66	0.39	1.88	0.30
DS3	0.85	0.13	1.50	0.33	2.35	0.38	2.03	0.30

As the fundamental vertical frequencies of the supporting floor slab decrease, the horizontal median peak floor acceleration (θ) values for a given DS also decreases. This decreasing effect is particularly pronounced for DS 3. For example, the θ value for the 40 Hz fundamental frequency of supporting floor slab is 2.35g, while the corresponding θ value for the 5 Hz fundamental frequency of supporting floor slab is 0.85g, which is a substantial 64% decrease. As discussed above, DS 3 is defined as 50% equivalent damaged ceiling area, in other words, near total collapse of the suspended ceiling grid. Hence it is logical to assume that a flexible supporting floor slab causes the collapse of suspended ceiling systems at lower intensities, which is a consistent observation from the shake table experiments. Also, by comparing the prescribed θ values included in the FEMA P-58 methodology, it is evident that the influence of the flexible supporting floor slab on the seismic response of suspended ceiling systems was not captured. It is important to note that the prescribed fragility curve parameters for suspended ceiling systems included in the FEMA P-58 methodology [FEMA 2018] were generated from engineering judgement based on a limited number of large-scale shake-table experiments and field observations. Interestingly, for all three FE models of suspended ceiling systems, the θ values for the DS 1, i.e., 5% equivalent ceiling damaged area, are close (0.78g – 0.94g). The authors believe it is challenging for the FE model of the suspended ceiling system, to accurately capture the damage under low intensity shaking.

The seismic fragility curves of the FE models of suspended ceiling systems equipped with and without lateral restraints (LRs) for DS 1, 2 and 3 are presented in Figures 4(a), (b), and (c). Note that in both FE models, the fundamental vertical frequency of the supporting floor slab was kept constant at 20 Hz. The inclusion of lateral restraints causes a slight improvement in the performance of the suspended ceiling system. Table 2 lists the numerically predicted median horizontal peak floor accelerations (θ) and log-normal standard deviation (β) values from the seismic fragility curves of the FE models of suspended ceiling systems equipped with and without lateral restraints (LRs) shown in Figures 4(a), (b) and (c). Although there is an increase in the θ values from the inclusion of lateral restraints, the increment is modest (< 15% increase). Note that the ASTM E580/E580M standard [ASTM 2020] seismic design guidelines permit the inclusion of the lateral restraints only for suspended ceiling systems (design categories D and E) whose plan area is greater than 92.9 m^2 (1000 ft^2). Hence the modest gains in θ values shown in Table 2 are consistent with the seismic design guidelines that do not require the suspended ceiling system configuration analysed in this study to be equipped with lateral restraints. More numerical studies, especially on the configurations of suspended ceiling systems with a plan area greater than 92.9 m^2 (1000 ft^2), must be conducted to arrive at a more solid conclusion regarding the effectiveness of the lateral restraints. Note that the predicted log-normal standard deviation (β) values reported in Tables 1 and 2 only include the floor motion record-to-record variability.

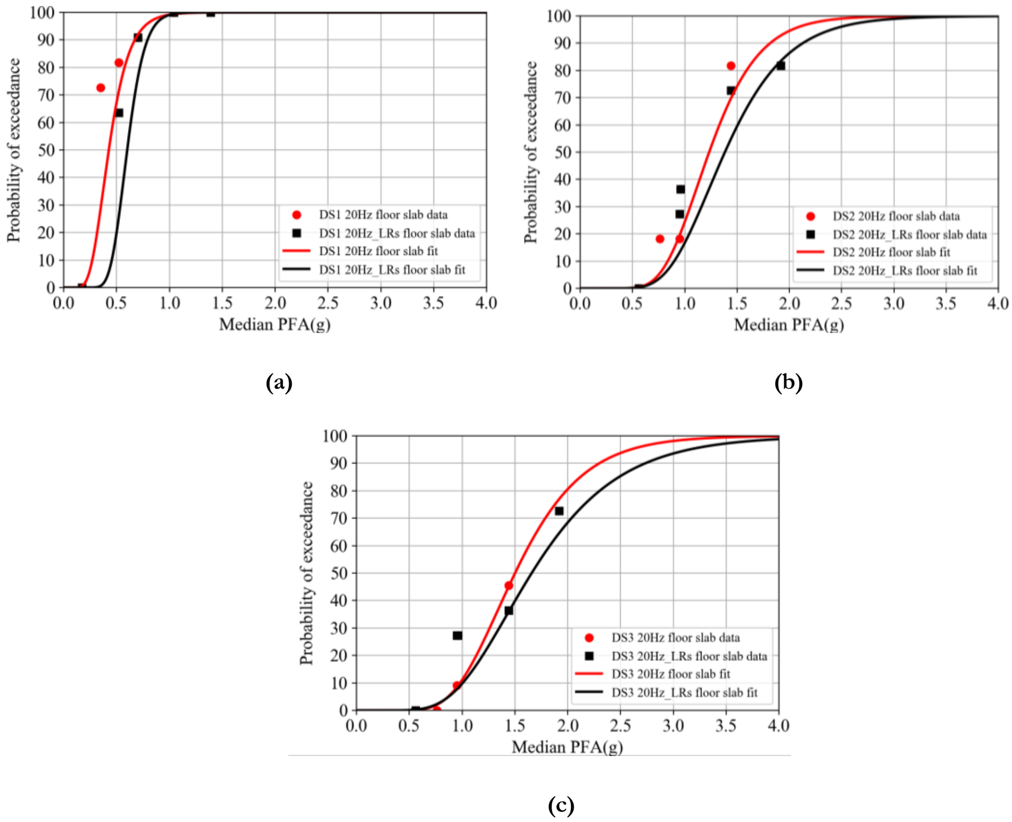

Figure 4: Seismic fragility curves predicted by the FE models of suspended ceiling systems with the fundamental vertical frequency of the supporting floor slab of 20 Hz installed with and without lateral restraints for (a) Damage State (DS) 1 (b) DS 2 and (c) DS 3.

Table 2: The fragility curve parameters of FE models of suspended ceiling systems with and without lateral restraints (LRs)

FE model	Without LRs		With LRs	
Damage State	**θ(g)**	**β**	**θ(g)**	**β**
DS1	0.84	0.19	0.99	0.12
DS2	1.23	0.30	1.38	0.33
DS3	1.50	0.33	1.66	0.39

5. CONCLUSIONS AND FUTURE WORK

To investigate the influence of the flexibility of supporting floor slab on the seismic damage of suspended ceiling systems, a finite element (FE) model of suspended ceiling systems developed and validated with experimental observations was employed in this study. The recorded top floor accelerations of a six-storey steel moment frame building subjected to the FEMA P-695 far-field ground motion set were considered as input for the FE models of suspended ceiling systems. Employing the incremental dynamic analysis and the maximum likelihood fit of the fragility data, the seismic fragility functions for the FE models of suspended ceiling systems with the median horizontal peak floor accelerations as the engineering demand parameter (EDP) were derived. Three different fundamental vertical frequencies of the supporting floor slab, namely 5 Hz, 20 Hz and 40 Hz, were considered in this study. Comparing the numerically predicted median horizontal peak floor accelerations (θ) for the seismic fragility curves, it is evident that as the flexibility of the supporting floor slab increases, the θ values for any given Damage State (DS) decreases, i.e., the probability for a suspended ceiling system to exceed a given DS at a given seismic loading intensity, increases. This trend predicted by the FE models of suspended ceiling systems is consistent with the experimental observations. Furthermore, a modest increase in θ values of the seismic fragility curves is observed when the FE model of the suspended ceiling system is equipped with lateral restraints. This result is consistent with the seismic design guidelines of the ASTM E580/E580M standard, which do not recommend the inclusion of lateral restraints for the configuration of the suspended ceiling system employed in this study.

Validating the FE model of suspended ceiling systems by incorporating grid connection properties derived from experiments and with detailed contact properties between the suspended ceiling system components should bring the seismic fragility curve parameters for the FE model of the suspended ceiling system with the supporting floor slab of fundamental vertical frequency of 40 Hz closer to the prescribed FEMA P-58 values. More numerical studies, especially on the configurations of suspended ceiling systems with a plan area greater than 92.9 m^2 (1000 ft^2), would provide additional insights into the effectiveness of lateral restraints. Furthermore, the effect of lateral restraints on the seismic damage of suspended ceiling systems subjected to larger vertical accelerations must be evaluated. Further studies on several configurations of FE models of suspended ceiling systems will help derive the relationship between the flexibility of the supporting floor slab and the seismic fragility curve parameters. These studies could be conducted with the general FE described in this study without the need of large-scale shake table testing.

ACKNOWLEDGEMENTS

The authors gratefully acknowledge the Italian Department of Civil Protection (DPC) for their financial contributions to this study through the ReLUIS 2019–2021 Project (Work Package 17–Contributi Normativi Per Elementi Non Strutturali). The authors also acknowledge the support and funding received for the graduate study of the first author from the Department of Civil, Structural and Environmental Engineering of the State University of New York at Buffalo. The authors also acknowledge UB Center for Computational Research for the access to their computing clusters. The authors also acknowledge that a few subsections of this paper have been taken from their previous works submitted to the 12th national conference of earthquake engineering [Gopagani 2022] and as a journal paper to the Journal of Structural Engineering (in review).

REFERENCES

ASCE. [2022] *Minimum design loads and associated criteria for buildings and other structures. ASCE/SEI 7,* American Society of Civil Engineers, Reston, VA, USA.

ANCO. [1983] *Seismic hazard assessment of nonstructural ceiling components-Phase I,* ANCO Engineers, Culver City, CA, USA.

ANCO. [1993] *Earthquake testing of a suspended ceiling system*, ANCO Engineers, Culver City, CA, USA.

ASTM. [2020] *Standard practice for installation of ceiling suspension systems for acoustical tile and lay-in panels in areas subject to earthquake ground motions*, *ASTM-E580/E580M*, American Society for Testing and Materials, West Conshohocken, PA, USA.

Badillo-Almaraz, H., Whittaker, A. S., and Reinhorn, A. M. [2007] "Seismic fragility of suspended ceiling systems," *Earthquake Spectra*, Vol. 23, No. 1, pp. 21-40.

Baker, J.W. [2015] "Efficient analytical fragility function fitting using dynamic structural analysis." *Earthquake Spectra*, Vol. 31, No. 1, pp. 579–599.

Chalarca, B., Filiatrault, A., and Perrone, D. [2020] "Seismic demand on acceleration-sensitive nonstructural components in viscously damped braced frames," *Journal of Structural Engineering*, Vol. 146, No. 9, pp. 579-589.

Dassault Systèmes. [2019] *Abaqus analysis user's manual. Version 2019.* Dassault Systemes Simulia, Inc., Providence, RI, USA.

Dhakal, R. P., MacRae, G. A., Pourali, A., and Paganotti, G. (2016). "Seismic fragility of suspended ceiling systems used in NZ based on component tests". *Bulletin of the New Zealand Society for Earthquake Engineering, Special Issue on Seismic Performance of Non-Structural Elements*, Vol. 49, No. 1, pp. 45-63.

Ding, C. [2015] "Monotonic and cyclic simulation of screw-fastened connections for cold-formed steel framing." *MS thesis*, Department of Civil and Environmental Engineering, Virginia Polytechnic Institute and State University, Blacksburg, VA, USA.

Echevarria, A., Zaghi, A., Soroushian, S., and Maragakis, M. [2012] "Seismic fragility of suspended ceiling systems," *Proceedings of 15th World Conference on Earthquake Engineering*, Lisbon, Portugal.

FEMA. [2009] *Quantification of building seismic performance factors. FEMA P-695*, Federal Emergeny Management Agency, Washington, DC, USA.

FEMA. [2018] *Seismic performance assessment of buildings - normative quantity estimating tool. Report P-58,* Federal Emergeny Management Agency, Washington, DC, USA.

Fiorin, L., Brandolese, S., and Scotta, R. [2021] "Experimental and numerical assessment of suspended ceiling joints," *Bulletin of Earthquake Engineering*, Vol. 19, No. 2, pp. 919-962.

Gopagani, S., Perrone, D., Filiatrault, A., and Aref, A. J. [2022] "Finite element modelling for seismic damage estimation of suspended ceiling systems," *Proceedings of 12th National Conference on Earthquake Engineering*, Salt Lake city, UT, USA.

Harris, C. M. and Allan, G. P., [2002] *Harris' shock and vibration handbook. 5th edition*, McGraw-Hill, New York, USA.

Huang, W. C., McClure, G., and Hussainzada, N. [2013] "Seismic interactions between suspended ceilings and nonstructural partition walls," *Coupled Systems Mechanics*, Vol. 2, No. 4, pp. 329-348.

Pourali, A., Dhakal, R. P., MacRae, G., and Tasligedik, A. S., Tasligedik (2015). "Shake table tests of perimeter-fixed type suspended ceilings". *New Zealand Society for Earthquake Engineering Annual Conference,* Rotorua.

Pourali, A., Dhakal, R. P., Tasligedik, S., and MacRae, G., (2018). "Experimental evaluation of the seismic compatibility between low-damage drywall partitions and suspended ceilings". *Proceedings of 11th US National Conference on Earthquake Engineering,* Los Angeles, CA, USA.

Qi, L., Kunitomo, K., Kurata, M., and Ikeda, Y. [2020] "Investigating the vibration properties of integrated ceiling systems considering interactions with surrounding equipment," *Earthquake Engineering & Structural Dynamics*, Vol. 49, No. 8, pp. 772-793.

Rahmanishamsi, E., Soroushian, S., and Maragakis, M. [2014] "System-level experiments on ceiling /piping /partition systems at UNR-NEES site," *Proceedings of 10th National Conference on Earthquake Engineering*, Anchorage, AK, USA.

Rezvani, R., Soroushian, S., Zaghi, A. E., and Maragakis, M. [2022] "Numerical seismic fragility analysis for suspended ceilings with various geometries," *Journal of Building Engineering,* Vol. 54, No. 3, pp. 772-793.

Ryan, K. L., Soroushian, S., Maragakis, E. M., Sato, E., Sasaki, T., and Okazaki, T. [2016] "Seismic simulation of an integrated ceiling-partition wall-piping system at E-Defense. I: Three-dimensional structural response and base isolation," *Journal of Structural Engineering*, Vol. 142, No. 2, pp. 789-796.

Ryu, K. P., and Reinhorn, A. M. [2019a] "Experimental study of large area suspended ceilings," *Journal of Earthquake Engineering*, Vol. 23, No. 6, pp. 1001-1032.

Ryu, K. P., and Reinhorn, A. M. [2019b] "Analytical study of large-area suspended ceilings," *Journal of Earthquake Engineering*, Vol. 23, No. 4, pp. 592-624.

Satwant, S.R., and Granneman, G. [1984] "Experimental investigation of the dynamic behavior of building partitions and supended ceilings during earthquakes," *Proceedings of 8th World Conference on Earthquake Engineering*, San Francisco, CA, USA.

Soroushian, S., Maragakis, E. M., and Jenkins, C. [2015] "Capacity evaluation of suspended ceiling components, Part 1: Experimental studies," *Journal of Earthquake Engineering*, Vol. 19, No. 5, pp. 784-804.

Soroushian, S., Rahmanishamsi, E., Ryu, K. P., Maragakis, M., Reinhorn, A. M. [2016a] "Experimental fragility analysis of suspension ceiling systems," *Earthquake Spectra*, Vol. 32, No. 2, pp. 881-908.

Soroushian, S., Maragakis, M., and Jenkins, C. [2016b]. "Capacity evaluation of suspended ceiling-perimeter attachments," *Journal of Structural Engineering*, Vol. 142, No. 2, pp. 881-908.

Yao, G.C. [2000] "Seismic performance of direct hung suspended ceiling systems," *Journal of Architectural Engineering*, Vol. 6, No. 1, pp. 6-11.

Yao, G., and Chen, W. [2017] "Vertical motion effects on suspended ceilings," *Proceedings of the 16th World Conference on Earthquake Engineering*, Santiago, Chile.

Zaghi, A. E., Soroushian, S., Echevarria, Heiser, A., Maragakis, M., and Bagtzoglou, A. [2016] "Development and validation of a numerical model for suspended-ceiling systems with acoustic tiles," *Journal of architectural engineering*, Vol. 22, No. 3, pp. 881-908.

Study of the Effect of Aspect Ratio of Unbraced Suspended Ceiling Systems on Their Dynamic Responses and Damage Failure Mechanisms

R. Rezvani[1], S. Soroushian[1], A. E. Zaghi[2], and M. Maragakis[3]

[1] Graduate Student, Assistant Professor
Department of Civil and Environmental Engineering, K.N. Toosi University of Technology, Tehran, Iran, 1996715433.
e-mail: rrezvani@email.kntu.ac.ir ; ssoroushian@kntu.ac.ir
[2] Associate Professor
Civil and Environmental Engineering, University of Connecticut, 261 Glenbrook Road, Unit 3037, Storrs, CT 06269-2037.
e-mail: zaghi@engr.uconn.edu
[3] Dean of Engineering
Civil and Environmental Engineering, University of Nevada, Reno/MS 0258, Reno, NV 89557.
e-mail: maragaki@unr.edu

Abstract. The dynamic response of nonstructural systems is the critical factor in performance-based design of structures. Observed from previous low to moderate earthquakes, damage to suspended ceiling systems were one of the main reasons impeding the functionality of buildings. Multiple experimental studies have been performed on these systems to evaluate their vulnerability under seismic events. Although, the effect of the aspect ratio of the system is poorly understood. In this project, a verified numerical modelling methodology is adopted and developed in the OpenSees platform to obtain the effect of the ceiling geometry on their dynamic response. Throughout this paper, nine ceiling specimens are simulated and the corresponding fragility parameters are calculated. Throughout this project, twenty-five time-history input motions are utilized, and the failure ratio of ceilings is obtained. For this purpose, maximum capacity of ceiling components reported in previous experiments done at the university of Nevada-Reno is used to define their failure criteria. Fragility curves obtained from this research are then compared against those presented in the FEMA-P58 fragility guideline for the validation of the outcomes. Finally, fragility curves of all nine specimens are compared to discuss the effect of the aspect ratio of the system on their seismic performance. As the result of this project, it could be understood that unbraced suspended ceiling systems with larger areas are susceptible to more losses during a seismic event. Similarly, higher aspect ratio of the system leads to more damage in such ceiling systems.

Keywords: Nonstructural Elements, Suspended Ceiling Systems, Fragility Analysis, FEMA-P58, OpenSees Software

1. INTRODUCTION

Nonstructural parts of the building refer to those elements which does not carry any lateral or gravitational loading of the structure [Whittaker and Soong, 2003]. Although, these systems are essential for the building operation, they were damaged prior to structural parts of the building during previous earthquakes [Whittaker and Soong, 2003]. Suspended ceiling systems are one of the widely used nonstructural systems. Damage to these components accounts for a major portion of losses during and after an earthquake event including considerable financial losses, impeding the functionality of critical buildings, and in some cases, loss of life. Under the 1989 Loma Prieta earthquake, the 2006 Hawaii earthquake and the 2020 Magna earthquake considerable damage have been recorded on nonstructural systems including suspended ceilings [EERI, 2021]. Falling of ceiling panels, failure of grid tees, buckling, and failure of grid connections were the most common failure mechanisms reported through these events. Figure 1 depicts damage to suspended ceilings during 2017 Iran-Iraq earthquake.

Figure 1. Suspended ceiling damage during 2017 Iran-Iraq earthquake, the hospital of Sarpol-Zahab; Left: Buckling of the grid systems, failure of the grid tees, and falling of ceiling panels;

In order to assess the vulnerability of suspended ceilings and obtain their seismic behaviour, multiple experimental projects and few numerical simulations have been performed. Yao [2000] was one of the first researchers developing numerical method using ANSYS software to capture the response of an experimental test specimen. This modelling technique however simplified, was able to predict components behaviour successfully. Ryu et al. [2012] also conducted both experimental and numerical studies on three suspended ceiling with different geometries using multi-pendulum system. A more detailed method was introduced by Echevarria et al. [2012] in which the effect of uplift of ceiling panels were taken into account. Bothe small and large suspended ceilings were subjected to this simulation and their sensitivity and dynamic response were obtained. A more comprehensive method of simulation was presented throughout the research done by Soroushian et al. [2015c]. In this method, the uplift and pounding of ceiling tiles, as well as the maximum capacity of ceiling components was considered. This method is used to develop a numerical platform in this paper.

In the first part of this paper, a definition of a typical suspended ceiling and fragility curve is provided. Then, the numerical simulation procedure used in this project is explained in detail, and a brief explanation on the fragility curve development method is presented. In the next section, the numerical results are illustrated and fragility parameters of all ceiling samples are calculated. Finally, by comparison between their corresponding fragility curves, the effect of aspect ratio of the system is then investigated and discussed.

2. SUSPENDED CEILING SYSTEMS

Suspended ceiling systems provide coverage for instruments under the structural ceiling and give a modern look to every building. These systems are typically consisting of a grid system of inverted tee beams, ceiling panels, attachments, supporting hangers and a bracing system in high seismic regions. The grid system consists of 2 ft. and 4 ft. cross tees, and main tee runners. At the intersection points, two types of joints can be used, which includes: pop rivet, and seismic clips. Ceiling panels are sat on the flanges of tee beams simply with no additional attachment. In this project, a standard square panel with dimensions of 2 ft by 2 ft are simulated. The entire system is hung up from the structural ceiling using hanger wires. Hanger wires must be installed at 3.99 ft intervals from each other with a minimum of 0.65 ft clearance from the wall. A typical unbraced suspended ceiling system has a clearance of 0.03 ft from the perimeter walls at all boundaries. A schematic view of a typical suspended ceiling system is presented in Figure 2.

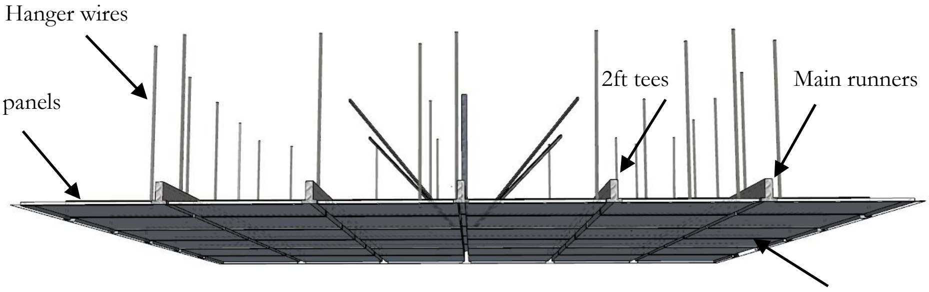

Figure 2. Schematic view of a typical suspended ceiling.

3. FRAGILITY CURVES

In the last few decades, the overall performance of nonstructural elements as well as structural components can be estimated by developing fragility curves [Beck et al., 2002; Badillo et al., 2007; Porter and Kiremidjian, 2000]. These curves are decision making tools which enables engineers to predict future losses to a system in terms of damage portion, cost, and time under a specific condition [Porter and Kiremidjian, 2000]. Cumulative probability functions are used and various methods can be adopted for their development. In general, the relation between Engineering Demand Parameter (EDP), and the probability of exceeding a damage measured (DM) presents fragility curves. Damage states are also defined as a value of DM (damage measured) under each EDP. Suspended ceiling systems are considered as acceleration sensitive systems, as such, the peak floor acceleration (PFA) is accounted for the EDP in this study. According to existing fragility guidelines (i.e., FEMA P-58 [2014]), three damage states including minor DS (more than 5% failure ratio), moderate DS (more than 30% failure ratio), and system collapse (more than 50% failure ratio) are defined. Method B proposed in Porter et al. [2007], presents a procedure in which the maximum EDP is known, and the probability of whether the specimen exceeded the damage state of interest is considered. In this method, all ceiling specimens are taken into account within the development process including the undamaged conditions [Porter et al., 2007]. As such, this method is used for the development of fragility curves in this paper. Equation (1) and Equation (2) represent function giving the probability of exceeding a certain damage level.

$$F_{dm}(edp) \equiv P[DM \geq dm|\ EDP = edp \tag{1}$$

$$F_{dm}(edp) = \emptyset(ln\ (edp/x_m)/\beta) \tag{2}$$

where $\emptyset$ is the standard normal (Gaussian) cumulative distribution function, X_m is the median value of the distribution, and β represents the logarithmic standard deviation. A fragility curve can be developed using two parameters: standard deviation and median value which establish for every damage state. Equation (3) gives the probability of a component in the damage state dm considering EDP=edp.

$$\begin{aligned} P[DM = dm|EDP = edp] &= 1 - F_1(edp) \qquad dm = 0 \\ &= F_{dm}\,(edp) - F_{dm+1}\,(edp) \qquad 1 \leq dm < N \\ &= F_{dm}\,(edp) \qquad dm = N \end{aligned} \tag{3}$$

where N represents the number of possible damage states in a component, and dm=0 denotes the undamaged state. As mentioned earlier, fragility curves of this project are develop using method B [Porter et al., 2007]. The median value and dispersion of the cumulative distribution function are calculated by plotting the linear relation between x and y, where:

$$x = l\,n\,r_i \tag{4}$$

$$y = \emptyset^{-1}\,((m_i + 1)/(M + 1))$$

where $\emptyset^{-1}$ denotes the inverse standard normal distribution; M denotes number of specimens observed; i represents the index of specimens; f_i is the failure indicator for specimen I (1 if the specimen failed, 0 otherwise); m denotes the cumulative value of f_i at each EDP; and r_i represents the input of the fragility curve (demand parameter i). The standard deviation and median value of the distribution are then obtained using Equation (6) and Equation (7), respectively.

$$Y = aX + b \tag{5}$$

$$\beta = (1\,/a) \tag{6}$$

$$X_m = exp\,(-b/a) \tag{7}$$

where β (standard deviation) is the inverse of the slope of the fitted line, and X_m (median value) of the corresponded fragility curve is the value of r_i at the point where y is equal to 0 (Equation (6), and Equation (7)).

FEMA P-58 § 9.31 [Soroushian, 2016b] presents fragility documentation for braced and unbraced suspended ceilings. Table 1 represents fragility parameters of suspended ceiling categories of FEMA P-58 § 9.31 [Soroushian, 2016b]. These data are used in this paper for the validation of the numerical results.

Table 1.Fragility parameters of unbraced suspended ceiling system (FEMA, 2021).

	A< 250			250 < A < 1000			1000 < A < 2500			A > 2500		
	DS1	**DS2**	**DS3**	**DS1**	**DS2**	**DS3**	**DS1**	**DS2**	**DS3**	**DS1**	**DS2**	**DS3**
$\boldsymbol{\theta}$	1.17	1.58	1.82	1.01	1.45	1.69	0.70	1.20	1.43	0.56	1.08	1.31
$\boldsymbol{\beta}$	0.30	0.30	0.30	0.30	0.30	0.30	0.30	0.30	0.30	0.30	0.30	0.30

4.NUMERICAL MODELLING METHOD

The modelling methodology in this paper is adopted from a verified numerical model developed at the University of Nevada Reno [Soroushian et al., 2014; Soroushian et al., 2015c; Soroushian et al., 2015b; Soroushian et al., 2016c] using the OpenSees [2022] software. In this procedure, grid tees are simulated using the "Elastic Beam-Column" command and their self-weight is applied as a distributed load. In this method, grid connections are modelled using ZeroLength elements [Soroushian et. al., 2015b] by incorporating the "Pinching4" material model to account for the strength degradation of these components under cyclic loadings. Thirty-nine parameters are required to define this material model which includes: (1) points defining the backbone curve ePdi/ePNi, ePfi/eNfi; (2) the ratio of reloading to the maximum historic deformation rDispP/rDispN; (3) the ratio of reloading to the maximum historic force rForceP/rForceN; (4) the ratio of negative or positive unloading to the maximum (minimum) monotonic strength uForceP/uForceN; and (5) ratios defining the unloading stiffness degradation gKi. Table 2 represents the thirty-nine parameters used in the modelling process of the grid connections.

Table 2. 39 parameter values of ceiling grid connections.

	Axial	Shear-Minor	Shear-Major	Bending-Minor	Bending-Major
ePf	0.010	0.006	0.143	0.040	0.040
	0.540	0.091	0.186	0.041	0.041
	0.570	0.182	0.181	0.240	0.395
	0.075	0.174	0.183	0.010	0.010
eNf	-0.130	-0.006	-0.060	-0.001	-0.040
	-0.270	-0.091	-0.312	-0.066	-0.041
	-0.190	-0.182	-0.213	-0.090	-0.263
	-0.090	-0.174	-0.084	-0.095	-0.010
ePd	0.0001	0.003	0.120	0.001	0.001
	0.039	0.270	0.225	0..066	0.080
	0.059	0.515	0.420	0.090	0.105
	0.090	0.655	0.595	0.095	0.113
eNd	-0.0125	-0.003	-0.010	-0.001	-0.001
	-0.0375	-0.270	-0.279	-0.066	-0.080
	-0.059	-0.515	-0.415	-0.090	-0.105
	-0.192	-0.655	-0.710	-0.095	-0.113
rDisp	0.080	0.500	0.500	0.800	0.080
	0.080	0.500	0.500	0.800	0.080
rForce	0.001	0.150	0.150	0.0001	0.0001
	0.001	0.150	0.150	0.0001	0.0001
uForce	-0.010	0.070	0.070	0.010	0.010
	-0.010	0.070	0.070	0.010	0.010
gK	0.000	0.500	0.500	0.500	0.500
	0.000	0.500	0.500	0.500	0.500
	0.800	0.750	0.750	0.750	0.750
	1.000	1.000	1.000	1.000	1.000
gD, gF1	1.000	1.000	1.000	1.000	1.000
gD, gF1	**All is 0**				

Ceiling panels are simulated as X-shaped assemblies using ZerolengthImpact3D elements. These strings capture the relative displacement of ceiling panels toward grid tees and the pounding effect on the grid plane. Similarly, these elements are being used at the ceiling perimeter as well.

A 0.03 ft horizontal clearance is considered at all ceiling boundaries of unbraced ceiling systems in the "ZeroLengthImpact 3D" command. The initial gap between tiles and the perimeter wall is also considered 0.01 ft. Ceiling hangers are simulated using the "Truss" element with a bilinear material model "Elastic Perfectly Plastic Gap" (EPPG). Required parameters for this simulation include: (1) the initial module of elasticity (E/k), (2) yield stress (σy), (3) initial gap strain, (4) post-yield stiffness ratio (b = Ep/E), and (5) damage type. The "Rayleigh" damping with a damping ratio of 9 percent is assigned to the suspended ceiling models as well [Soroushian et al., 2015b]. According to previous studies, a friction ratio of 0.5 is assigned to the ceiling panels of this model [Zaghi et al., 2016].

The key feature of this numerical modelling is the elimination process of failed elements. During the analysis, under each time step, the relative displacement of ceiling components is calculated and then compared against their maximum criteria. Every component exceeding its maximum capacity will be removed from the model while the analysis continues. The maximum capacity for element removals is obtained from series of component-level experiments done at the University of Nevada [Soroushian et al., 2015c, 2016c]. These values are illustrated in Table 3.

Table 3. Maximum capacity of the ceiling components (units in ft, lb.)

		2ft Cross Tees	4ft Cross Tees	Main Runner	Hanger Wires
Axial	Positive	0.0160	0.016	-	0.089
	Negative	-0.0029	-0.0029	-	-
Bending - Major	Positive	0.0144	0.011	-	-
	Negative	-0.0144	-0.011	-	-
Bending - Minor	Positive	0.013	0.012	-	-
	Negative	-0.013	-0.012	-	-
Shear - Major	Positive	0.048	0.058	-	-
	Negative	-0.061	-0.079	-	-
Shear - Minor	Positive	0.032	0.045	-	-
	Negative	-0.032	-0.045	-	-
Fixed Boundaries	Positive	0.034	0.050	0.040	-

In this model, failure of every 2 ft cross tees leads to fallen of two ceiling panels. Similarly, when a 4 ft cross tee fails, two additional 2 ft tees and four ceiling panels fall. Excessive uplift can also result in panel dislodgment and elimination. The ratio of failed panels to the area of the ceiling represents failure ratio of the system.

Twenty-five synthetic motions derived from AC156 [2021] are used as the time-history input motions of this model. These motions have been selected in a way in which they match with the benchmark experiments of FEMA P-58 guideline performed at the University of Buffalo [Ryu, 2012].

5. NUMERICAL RESULTS

For the evaluation of the effect of aspect ratio of suspended ceilings on their dynamic behaviour, 9 ceiling specimens with various dimensions have been simulated. Specimens include: 16 x 16, 24 x 24, 42 x 42, 50 x 50, 26 x 16, 42 x 24, 50 x 42, 50 x 24, 50 x 16 square feet. The failure ratio and development procedure of fragility curves for specimen B is presented as a sample specimen in the following. Table 4 represents failure ratio and parameter S for this sample ceiling. Where parameter S represents the value of $(m + 1/M + 1)$. The trending line of x and y data of Equation 4 is illustrated in Figure 3 for this model.

Table 4. Failure ratio of specimen B.

Record Number	PFA (g)	Damage ratio (%)	Parameter S for DS1	Parameter S for DS2	Parameter S for DS3
1	0.200	0.010	0.038	0.038	0.038
2	0.320	0.120	0.076	0.038	0.038
3	0.400	0.300	0.115	0.076	0.038
4	0.560	0.370	0.153	0.115	0.038
5	0.650	0.530	0.192	0.153	0.076
6	0.747	0.650	0.230	0.192	0.115
7	0.840	0.690	0.269	0.230	0.153
8	0.932	0.740	0.307	0.269	0.192
9	1.026	0.750	0.346	0.307	0.230
10	1.110	0.770	0.384	0.346	0.269
11	1.210	0.770	0.423	0.384	0.307
12	1.300	0.800	0.461	0.423	0.346
13	1.440	0.800	0.500	0.461	0.384
14	1.580	0.820	0.538	0.500	0.423
15	1.580	0.820	0.576	0.538	0.461
16	1.770	0.820	0.615	0.576	0.500
17	1.770	0.850	0.653	0.615	0.538
18	1.960	0.850	0.692	0.653	0.576
19	2.050	0.940	0.736	0.692	0.615
20	2.05	0.94	0.769	0.7360	0.653
21	2.23	0.95	0.807	0.769	0.692
22	2.23	0.95	0.846	0.807	0.7360
23	2.23	0.95	0.884	0.846	0.769
24	2.7	0.97	0.923	0.884	0.807
25	2.7	0.98	0.961	0.923	0.846

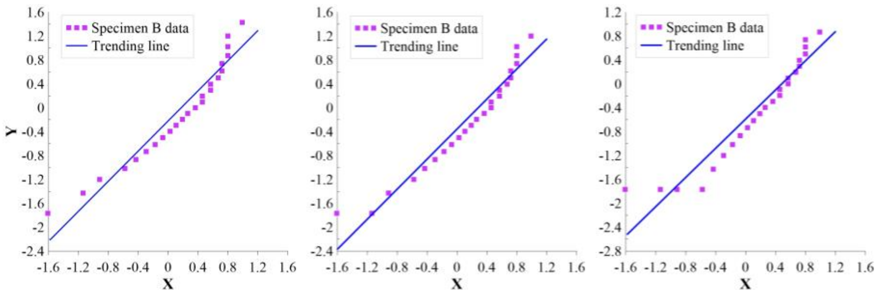

Figure 3. Trending line of specimen B: (a) DS 1, (b) DS 2, and (c) DS 3.

By incorporating the values of failure portion of ceiling specimens corresponding to each PFA, and using Equation 4, a and b parameters for all ceiling specimens are obtained. Using Equation 6 and Equation 7, median and dispersion for each suspended ceiling is calculated. These values are presented in Table 5. Fragility curves for specimens A through I are then obtained, and are compared against those proposed by FEMA P-58 § 9.31 [Soroushian, 2016b]. This comparison is illustrated in Figure 4 through Figure 12. This comparison indicates proper fit between the two sets of results, however, in some cases, the difference is more noticeable.

Table 5. Median and dispersion values of specimen A through specimen I.

	Damage State 1		Damage state 2		Damage State 3	
	median	dispersion	median	dispersion	median	dispersion
A	1.31	All is 0.60	1.64	All is 0.60	2.50	All is 0.60
B	1.28		1.42		1.60	
C	1.01		1.2		1.32	
D	1.00		1.01		1.31	
E	1.32		1.42		1.75	
F	1.23		1.32		1.43	
G	1.21		1.23		1.33	
H	1.21		1.23		1.33	
I	1.23		1.33		1.30	

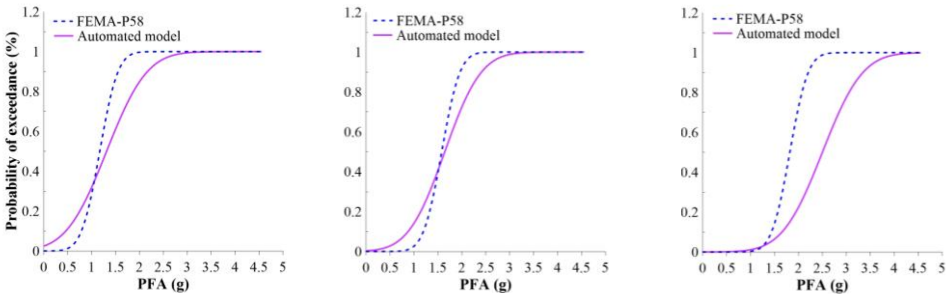

Figure 4.Comparison of fragility curves of the specimen A and FEMA P-58: (a) DS1, (b) DS2, and (c) DS3.

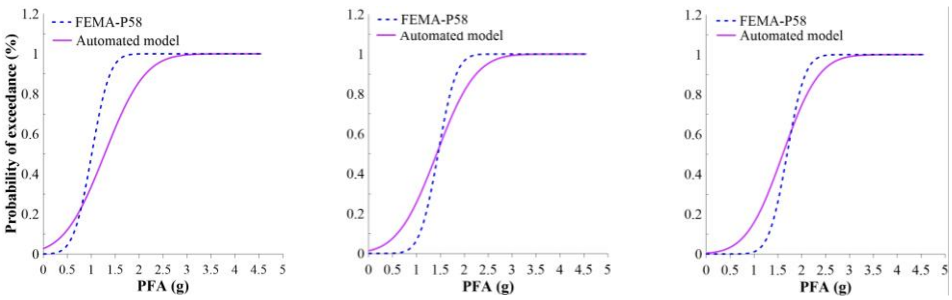

Figure 5. Comparison of fragility curves of the specimen B and FEMA P-58: (a) DS1, (b) DS2, and (c) DS3.

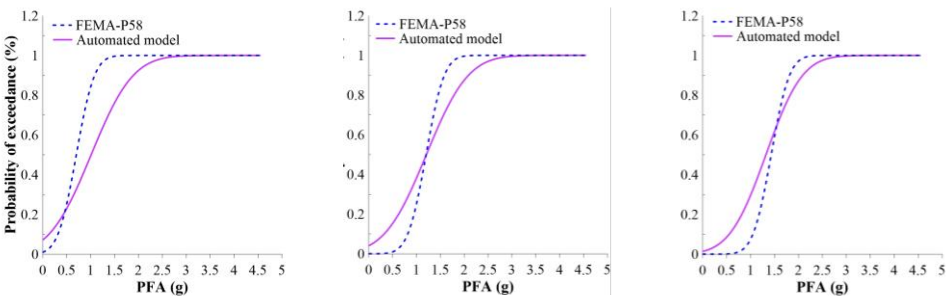

Figure 6. Comparison of fragility curves of the specimen C and FEMA P-58: (a) DS1, (b) DS2, and (c) DS3.

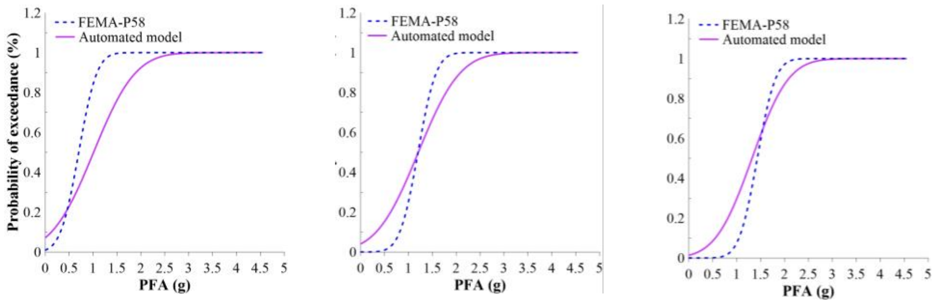

Figure 7. Comparison of fragility curves of the specimen D and FEMA P-58: (a) DS1, (b) DS2, and (c) DS3.

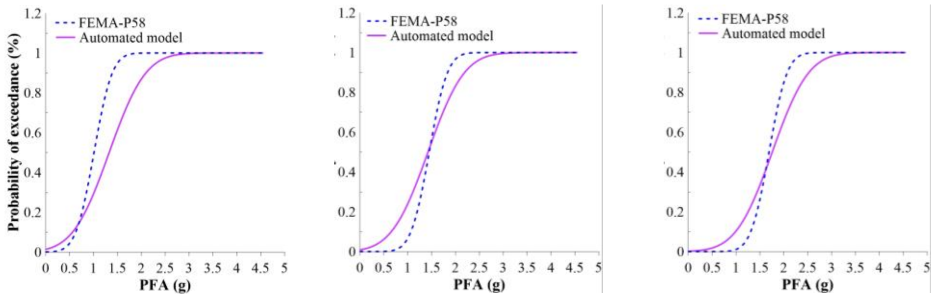

Figure 8. Comparison of fragility curves of the specimen E and FEMA P-58: (a) DS1, (b) DS2, and (c) DS3.

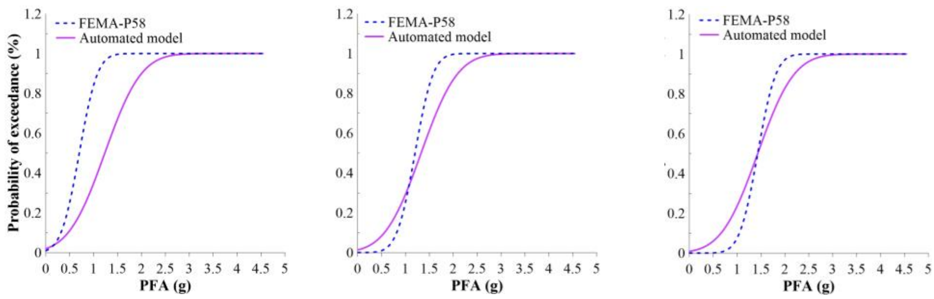

Figure 9. Comparison of fragility curves of the specimen F and FEMA P-58: (a) DS1, (b) DS2, and (c) DS3.

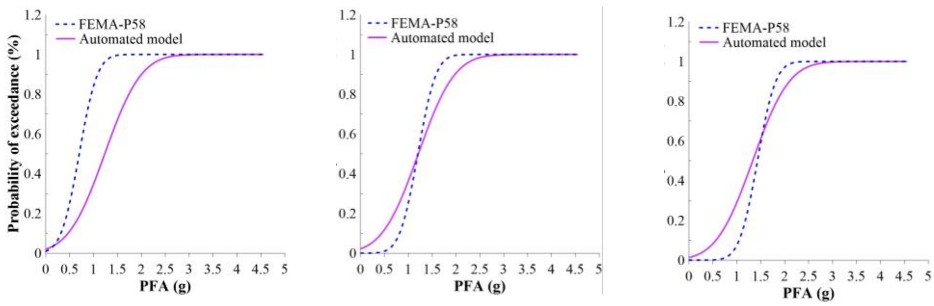

Figure 10. Comparison of fragility curves of the specimen G and FEMA P-58: (a) DS1, (b) DS2, and (c) DS3.

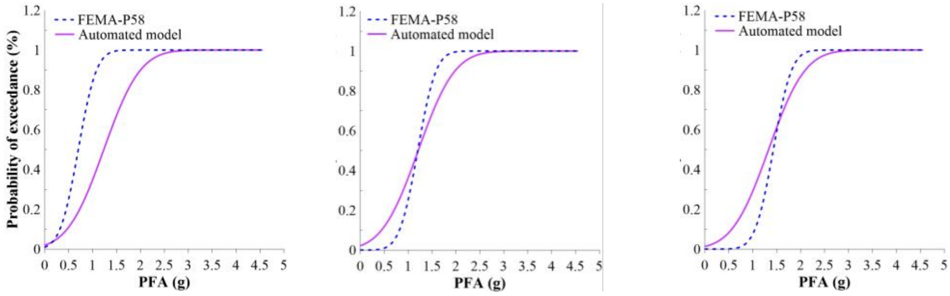

Figure 11. Comparison of fragility curves of the specimen H and FEMA P-58: (a) DS1, (b) DS2, and (c) DS3.

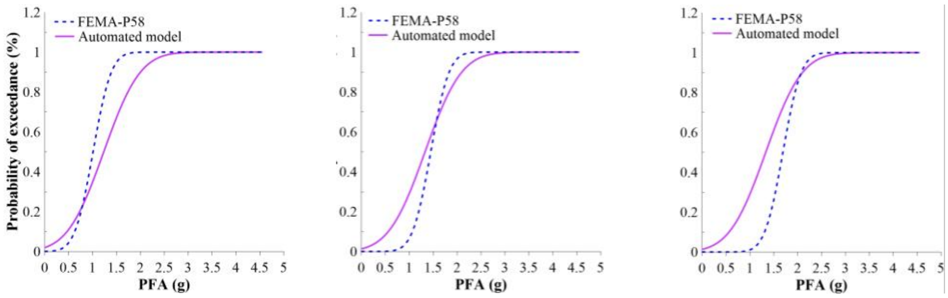

Figure 12. Comparison of fragility curves of the specimen I and FEMA P-58: (a) DS1, (b) DS2, and (c) DS3.

6. SUMMARY AND CONCLUSION

In this paper, the results obtained from a numerical simulation model of suspended ceiling systems are presented and the effect of aspect ratio of the system on their vulnerability against seismic activities are investigated. In this project, nine ceiling specimens with various aspect ratios are considered and the failure ratio of each ceiling model is recorded. a comparison between the specified fragility curves of this project with those presented in FEMA P-58 indicates a proper accuracy of the numerical results. According to the outcomes of this study, following conclusion on the dynamic response of unbraced suspended ceiling systems are gained: a) the vulnerability of unbraced suspended ceiling systems increases in larger ceiling areas, b) the vulnerability of unbraced suspended ceiling systems under seismic events depends on the aspect ratio of the ceiling and this effect must be considered in their seismic design, c) the failure ratio of an unbraced suspended ceiling increases in ceiling specimens with longer longitudinal sides, and d) ceiling specimens with similar longitudinal size have similar vulnerability, regardless of their area. It must be mentioned that these conclusions are made due to the effect of aspect ratio and the area of the system separately, and the effect of combining factors could be investigated in future studies.

REFERENCES

AC156 [2021], Seismic Certification by Shake-table Testing of Nonstructural Components*, ICC Evaluation Service.*

Badillo-Almaraz H., Whittaker A.S., Reinhorn A.M. [2007] "Seismic fragility of suspended ceiling systems" *Earthquake Spectra*.23(1):21–40.

Beck J.L., Porter K.A., Shaikhutdinov R. V., Au S.K., Mizukoshi K., Miyamura M., et al. [2002] "Impact of seismic risk on lifetime property values",*EERL Report*, California Institute of Technology, CA.

Echevarria A., Zaghi A.E., Soroushian S., Maragakis M. [2012] "Seismic fragility of suspended ceiling systems" *15th World Conference on Earthquake Engineering (15WCEE),* p. 24–8.

EERI [2021] *Earthquake Engineering Research Institute Learning from Earthquakes*, USA.

FEMA [2014] "FEMA P-58: Seismic Performance Assessment of Buildings" *Federal Emergency Management Agency*, USA.

OpenSees [2022] *Open System for Earthquake Engineering Simulation*, Berkeley, University of California.

Porter K., Kennedy R., Bachman R. [2007] "Creating fragility functions for performance-based earthquake engineering" *Earthquake Spectra*. 23(2):471–89.

Porter K.A., Kiremidjian A.S. [2000] "Assembly-based vulnerability of buildings and its uses in seismic performance evaluation and risk-management decision-making" *SPA Risk LLC.*

Ryu K.P., Reinhorn A.M., Filiatrault A. [2012] "Full scale dynamic testing of large area suspended ceiling system" *Proceedings, 15th World Conference on Earthquake Engineering*. Lisbon, Portugal.

Soroushian S., Maragakis M., Zaghi A. E., and Echevarria A. [2015c] "Numerical Simulation of Integrated Suspended Ceiling-Sprinkler Systems" *Struct Congress*

Soroushian S. [2016b] "Acoustical Tile or Lay-in Panel Suspended Ceilings", *FEMA P-58*, FEMA P-58/BD 3.9.31.

Soroushian S., Maragakis M., Jenkins C., Zaghi A.E., Echevarria A. [2014] "Analytical simulation of the performance of ceiling-sprinkler systems in shake table tests performed on a full-scale 5-story building", *Structures Congress 2014*, p. 1857–68.

Soroushian S., Maragakis M., Zaghi A. E., and Echevarria A. [2015c] "Numerical Simulation of Integrated Suspended Ceiling-Sprinkler Systems" *Struct Congress.*

Soroushian S., Maragakis E., Jenkins C. [2015b] "Capacity evaluation of suspended ceiling components, part 2: analytical studies" *J Earthquake Eng.*

Soroushian S., Maragakis M., Jenkins C. [2016c] "Capacity evaluation of suspended ceiling-perimeter attachments" *J Struct Eng,* 142(2):4015124.

Soroushian S., Maragakis E., Ryan K.L., Sato E., Sasaki T., Okazaki T., et al. [2016] "Seismic simulation of an integrated ceiling-partition wall-piping system at E-Defense. II: evaluation of nonstructural damage and fragilities" *J Struct Eng.* 142(2):4015131.

Whittaker A.S., Soong T.T. [2003] "An overview of nonstructural components research at three US Earthquake Engineering Research Canters", *Proc, ATC Seminar on Seismic Design, Performance, and Retrofit of Nonstructural Components in Critical Facilities*, p. 271–80.

Yao G.C. [2000] "Seismic performance of direct hung suspended ceiling systems" *J Archit Eng.*,6(1):6–11.

Zaghi A.E., Soroushian S., Echevarria A., Maragakis M., Bagtzoglou A. [2016] "Development and Validation of a Numerical Model for Suspended-Ceiling Systems with Acoustic Tiles" *J Archit Eng,* 22(3):4016008.

On In-plane Shear Stiffness of Ceiling Surface in JPN-US Suspended Ceiling

Reiko Morohoshi[1], Shojiro Motoyui[2]

[1] Graduate student, Tokyo Institute of Technology, Japan
4259 Nagatsuta, Midori-ku, Yokohama, Kanagawa 226-8502, Japan
morohoshi.r.aa@ m.titech.ac.jp
[2] Professor, Tokyo Institute of Technology, Japan
4259 Nagatsuta, Midori-ku, Yokohama, Kanagawa 226-8502, Japan
motoyui.s.aa@m.titech.ac.jp

Abstract. Suspended ceiling system similar to US style of one, which is called "JPN-US ceiling" in this paper, also exists in Japan though unique ceiling system has been developed in Japan. Determining the seismic resistance of the system is different than the US style in two ways. One is that the ceiling surface is set separately with enough gaps to surrounding wall to avoid any interaction. Second, the vertical brace members are installed to control swing of ceiling surface during earthquakes. Especially due to the latter difference, in-plane shear stiffness of ceiling surface becomes one of the most important properties on JPN-US ceiling. In a previous study, our forcus was on the "compression strut" effect of a ceiling panel on in-plane shear stiffness of ceiling surface, and we found out the equivalent axial rigidity of a horizontal brace member which replaced a ceiling panel. However, this axial rigidity of the horizontal brace member was determined by using only the data obtained at the stable region of the experiment. Therefore, the value cannot be applicable when considering the unstable behavior. In this paper, we evaluate the mechanical properties of the in-plane shear stiffness more accurately through the following method. Firstly, we measure the total load-deformation relationship of diagonal unit model. Second step is measuring the amount of compression strain of ceiling panel itself. By the first test and second test, it is possible to know the degree of influence of the axial rigidity of the ceiling panel as a compression strut. We can build a mechanical model in which the stiffness of the panel and surrounding frame can be evaluated separately, and simulate the unstable behavior.

Keywords: Suspended ceiling, In-plane shaer stiffness, Compression strut effect, Numerical model.

1. INTRODUCTION

1.1 BACKGROUND

In recent years, a lot of damages have been reported due to the falling or collapse of non-structural members such as ceiling materials after large earthquakes. During the Kumamoto earthquake in 2016, damages of the suspended ceiling were reported as shown in Photo 1. From the viewpoint of business continuity planning (BCP) in the event of a disaster, ensuring indoor safety and maintaining building functions after an earthquake is a very important issue, but large-scale damages such as ceiling fallings or collapse cause a significant decrease in indoor safety and functions. In some cases, it may lead to the interruption of core businesses and the disruption of supply chains. On the other hand, JPN-US style suspended ceiling is generally adopted inside buildings, and it is widely used in office buildings in Japan. The advantages are good installation workability and high maintainability. Figure 1 shows Japanese standard ceiling installation for seismic method. Braces to reduce the deformation of suspended ceilings and perimeters are provided between the ceiling surface and the surrounding walls. Figure 2 shows basic configuration of the JPN-US style suspended ceiling. It is assembled in a grid pattern using frame elements such as the main tee, cross tee, and sub-cross tee. The panel is placed on surrounding tees as shown in (a). The behavior of this ceiling system is influenced by the in-plane shear deformation of the panel surface. As the panel material and tee frames are separated, the in-plane behavior becomes disintegrated. The joint part of the tee has the shape shown in Figure 2(b), and photo 2 shows the details of joint. As you can see from the photo 2, the plug at the end of the cross tee is inserted into the socket of the orthogonal main tee. Plug-to-socket joints are also applied to cross tee and sub-cross tee joints.

There are some studies on properties of frame member by using the test result of frame joint [R.P.Dhakal et al., 2016] and on the seismic performance using the shaking table test of US-style suspended ceiling [Sato, Tea, Motoyui ,2019 ; Tea, Tola, Motoyui *et al.*, 2019].

(By Prof. Mizutani, Tokyo Polytechnic University)

Photo 1. Damages of the ceiling during KUMAMOTO earthquake in 2016

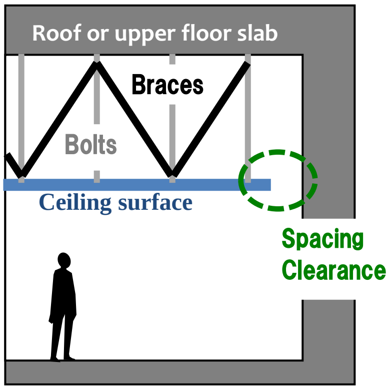

Figure 1. Japanese standard ceiling installation

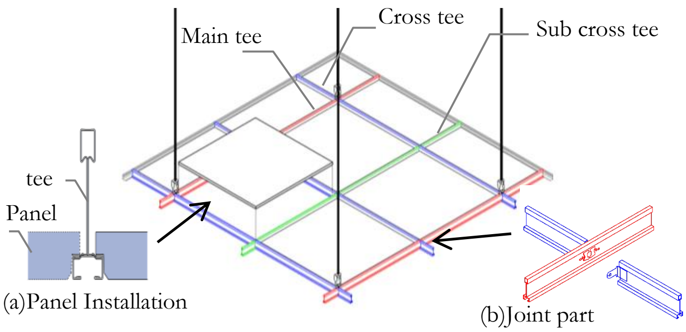

Figure 2. Configuration of JPN-US style ceiling

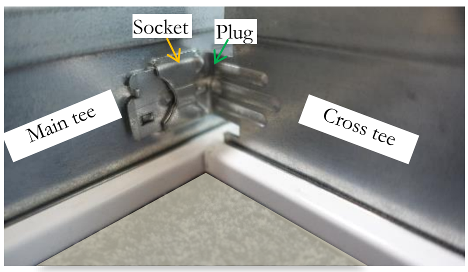

Photo 2. Joint detail between main tee and cross tee

1.2 PREVIOUS EXPERIMENT

In the research on shaking table test [Tea, Tola, Motoyui, *et al.*, 2019], rigidity evaluation is performed based on vibration experiments of the ceiling. Figure 3 shows the outline of the previous experiment. The size of the specimen was 2.4m×2.4m (16 panels of 600mm×600mm with the thickness of 12mm). φ9 bolts of length 1100mm were used for hanging the ceiling placed at an interval of 1200mm. The mechanical model for this specimen in this test could be replaced with a simple Single DOF model as shown in Figure 4. Figure 5 shows the response spectrum which include spectral ratio ($A_1(f)/A_0(f)$) which is the ratio of the amplitude spectrum $A_1(f)$ of the acceleration on the central main bar to the amplitude spectrum $A_0(f)$ of the acceleration on the frame for ceiling installation during each sweep wave (Sweep 20 gal, 40 gal, 60 gal and 80 gal). This model is expected to represent the mechanism of shear deformation of ceiling panels. The shear stiffness K is expressed by equation (1). Since the natural frequency was 1.2Hz, the stiffness K was 16.6[N/mm]. Here, when the in-plane shear stiffness of a single panel (K_p) is represented by a spring, the arrangement of the springs in the ceiling could be represented as shown in Figure 6 and expressed by equation (2).

$$K = (2\pi f)^2 M \tag{1}$$

$$K = \frac{1}{\frac{1}{4K_p}+\frac{1}{4K_p}} = 2K_p \tag{2}$$

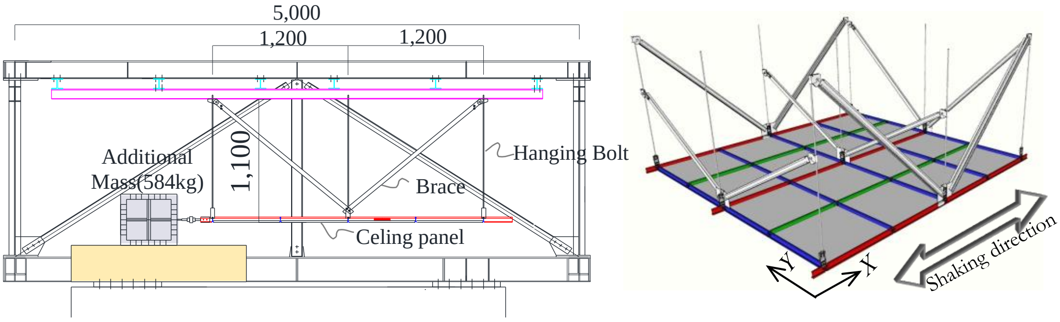

Figure 3. Plan of the shaking table test

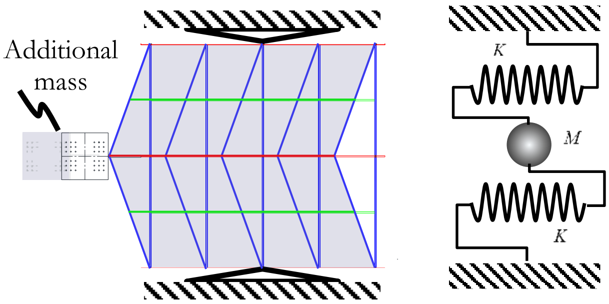

Figure 4. Mechanical model

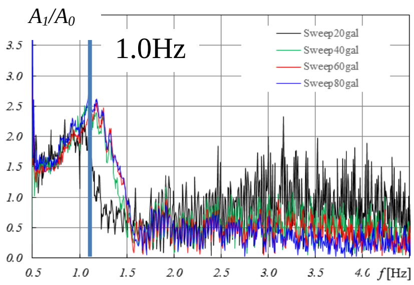

Figure 5. Response spectrum

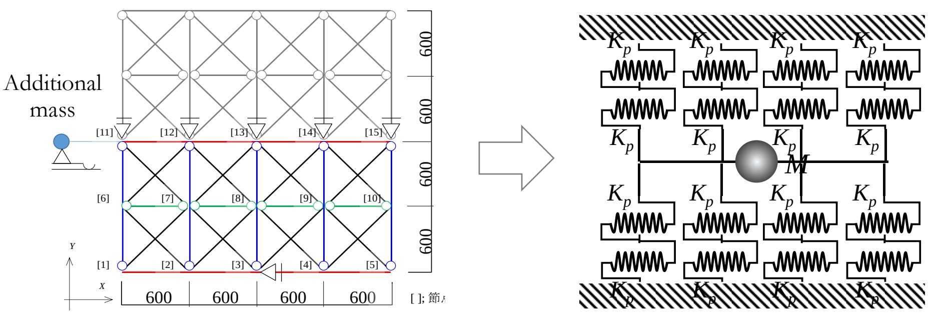

Figure 6. Relationship of springs

Figure 7 shows the compression strut model which axial force-deformation (*N-d*) relationship of the brace. The brace is a truss element with non-tensile resistance characteristics. The in-plane shear siffness of this truss model using the axial stiffness *EA* of the brace can be expressed as equation (4). The equivalent axial stiffness inferred from the result of the natural frequency of the vibration experiment is given as *EA* to the horizontal brace element of the panel as an element related to the stiffness of the ceiling. Figure 8 shows the experimental time-history results of displacement and acceleration, and the numerical analysis results of model with *EA* corresponding to the equivalent stiffness $\overline{K_p}$ as a horizontal brace. Although the time-history analysis using a numerical analysis model based on this simple method captures the behavior in general, it does not fully capture the vibration characteristics due to the complex nonlinear behavior. In this study, with the aim of establishing a numelical model focusing on non-linearity, the basic load-deformation relationship of the in-plane deformation of the JPN-US style suspended ceiling by the unit test is confirmed by static experiments, and axial stiffness of the ceiling panel itself forming the compression strut is verified.

$$\delta = \frac{N\bar{N}}{EA} l = \frac{\sqrt{2}P\sqrt{2}}{EA}\sqrt{2}B = \frac{2\sqrt{2}}{EA}BP \tag{3}$$

$$\overline{K_p} = \sqrt{2}EA/4B \tag{4}$$

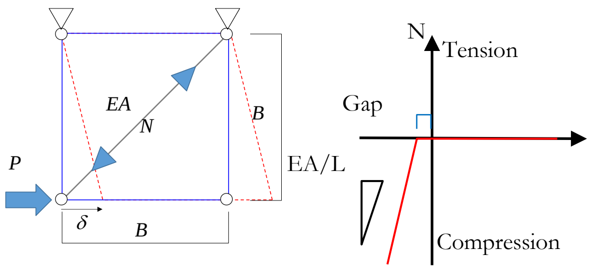

Figure 7. Compression strut model

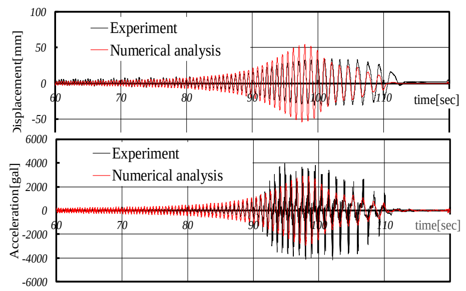

Figure 8. The time-history results

2. FUNDAMENTAL MECHNICAL MODEL

2.1 EXPERIMENT CONCEPT FOR MODELING

As shown in section 1.2, in the conventional model, the elements related to the rigidity of the system ceiling are the horizontal braces of the panel to provide equivalent rigidity. But the frame materials surrounding the panel also have axial forces. $\overline{K_p}$ should be evaluated as a combination of the diagonal stiffness of the panel (K_P) and the stiffness of the frame (K_F), as in equation (5). In this experiment, the unit experiment is planned to be able to estimate the original axis rigidity evaluation of the panel and the rigidity of the frame separately. The stiffness of the frame can be estimated indirectly by measuring the axial strain of the panel together with the load-deformation relationship of the unit. Through the verifications of the two patterns of (a) and (b) in Figure 9, the deformation properties of only the contact part between the panel and the frame, and the deformation properties of the frame in tension can be grasped.

$$\overline{K_p} = 1/(\frac{1}{K_F} + \frac{1}{K_p}) \tag{5}$$

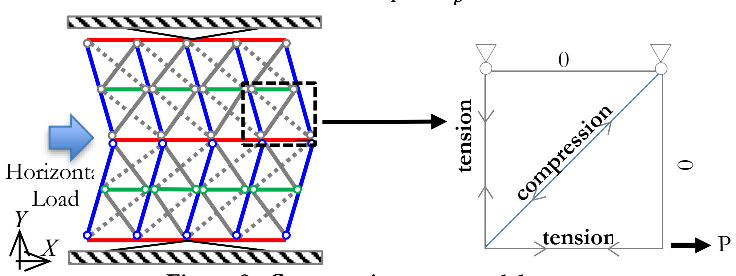

Figure 8. Compression strut model

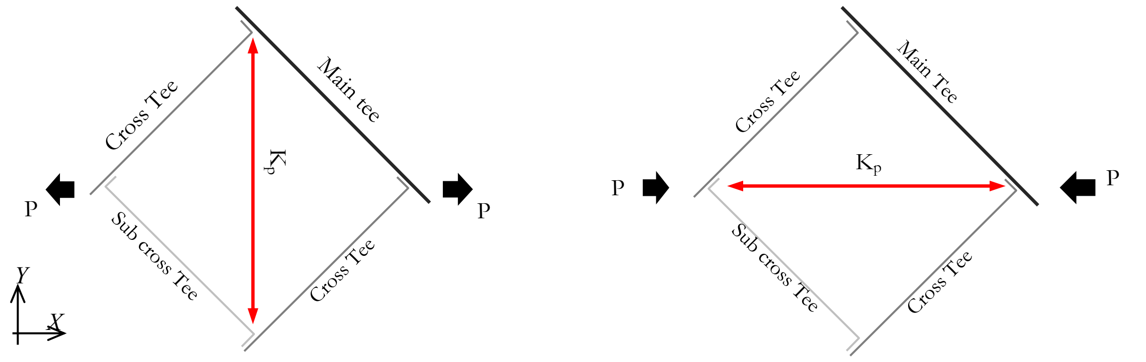

(a) During positive load (b) During negative load

Figure 9. Force applied direction confirmed by experiment

3.PRE-TEST OF THE PANEL

As a preliminary experiment, a diagonal compression test of the panel was performd in order to comfirm the behavior of the panel during compression loading. Figure 10 shows the experimental plan. A panel of size 600mm×600mm is installed diagonally with respect to the loading direction of the tester. A pin boundary condition is assumed at the top and bottom of the panel. The measurement points are in-plane displacement of the panel and out-of-plane displacement at the center of the panel. The applied load is one-way load in the compression direction. Figure 11 shows the load-deformation relationship of the panel. The red line indicates the displacement of tester head in the direction of allplied load and the blue line indicates the displacement of out-of plane by wire-mesurement. The behavior was linear until it reached the maximum load. The initial stiffness seems to be 151N/mm.

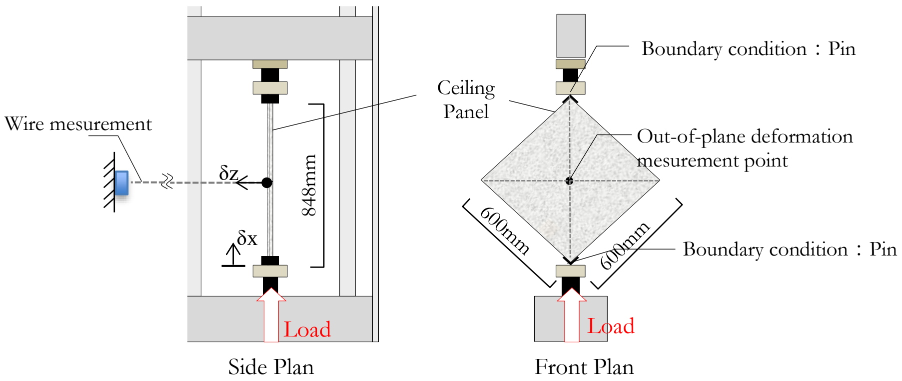

Figure 10. Test specimen

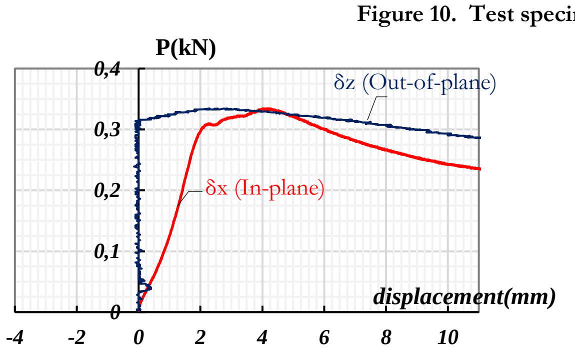

Figure 11. Load- displacement relationship

Photo 3. State of collapse

4.THE DIAGONAL TEST OF THE UNIT MODEL

4.1 OUT LINE OF THE TEST

In this experiment, a diagonal test of the unit model was conducted in order to confirm load-deformation relationship of the unit model and the effective width in forming the compression struts of the ceiling panel, which affects the in-plane shear stiffenss. The load-deformation relationship of the unit is confirmed by experiments using a unit that assumes one ceiling panel. Several test pieces with the diagonal width of the panel as a parameter were used to compare the load-deformation relationship. Figure 12 shows the outline of the specimen. Tee with two diagonal points of the unit is set on a movable pedestal with roller support. As shown in Figure 13, three types of panel widths are prepared as specimens so that the effective width of the panel can be simply confirmed. Displacement meter mounted on the target point distance of the ceiling panel also measures the elasticity of the panel itself. Loading planning involves repeated loading while controlling the load. As the range in which the end of the ceiling panel in the diagonal direction does not fall off with respect to the direction in which the compression struts are formed, the target is 150N when the positive load is applied and 200N when the negative load is applied.

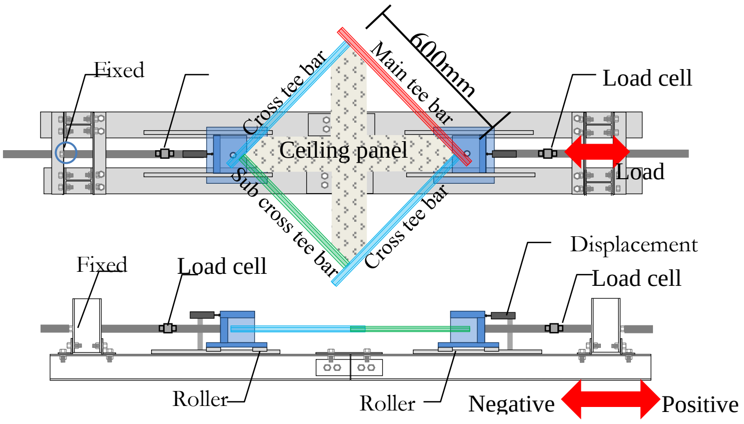

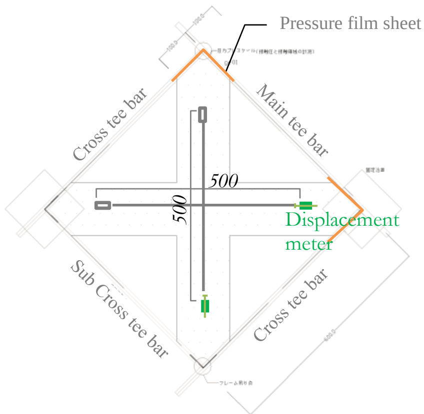

Figure 12. Instrumentation on test specimen

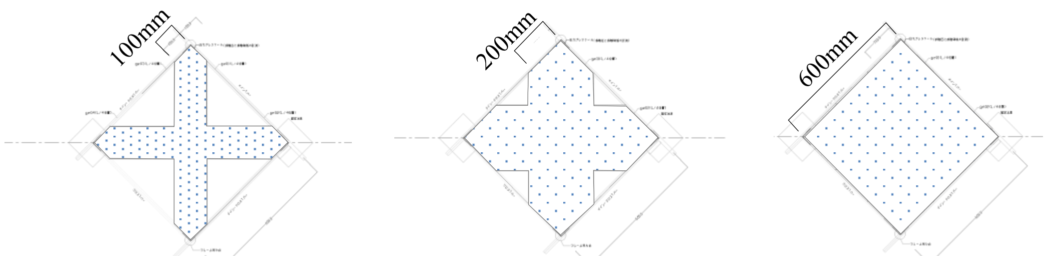

(A) Type-100 **(B) Type-200** **(C) Type-Full**

Figure 13. Parameter of the width of diagonal

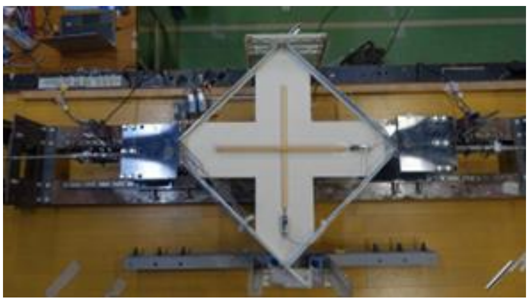

Photo 4. Arrangement of test specimen

4.2 TEST RESULT

Figure 14 shows the Load-deformation relationship. (a) is during negative load, (b) is during positive load. In order to correct the variation due to the initial slip displacement caused by the gap in each model, the point of 20% of the maximam load is corrected as the original of the displacement in this graph. Comparing each panel type with the diagonal width as a parameter, initial stiffness is similar among each specimen. Even a type-100, which has the smallest diagonal width among the three parameters, can sufficiently exhibit shear stiffness as a compression strut, which means the range of width that contributes to the in-plane shear stiffnss is about $100\sqrt{2}$. In case of the negative load, the initial stiffnes is approximately 12N/mm. On the other hand, in the positive load, the initial stiffness is approximately 31N/mm. The stiffness values vary by twice depending on the direction of the compression strut. Characteristics of non-linearity can be seen in all historical loops. Next, Figure 15(a)(b) describe the relationship between strains of the ceiling panel with in-plane and P* which is the load divided by the effective width (141mm) of the test panel. The inclination represents E×t. According to this graph, the value E×t can be approximated by Et=4000(N/mm) both when positive and when negative. Non-Linearity is not noticeable compared to the unit historical loops. The displacement situation of the panel surface almost linear behavior unlike the non-linear hysteresis characteristics such as the triangle in figure 14.

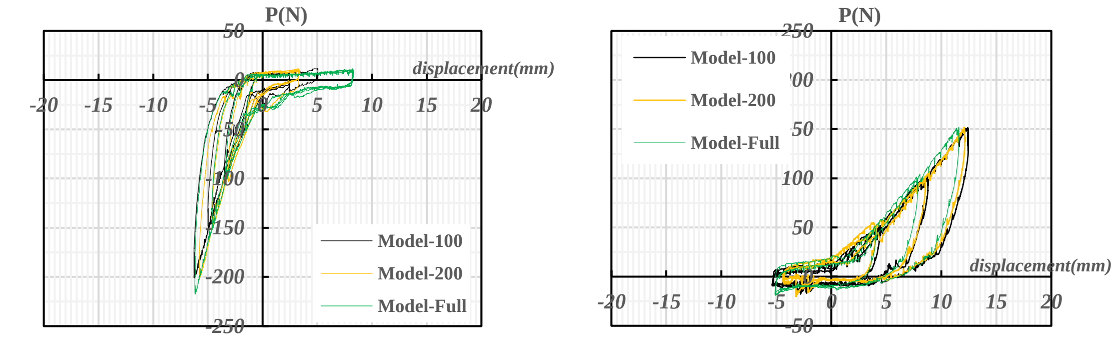

(a) During negative load (b) During positive load

Figure 14. Load-deformation Relationship

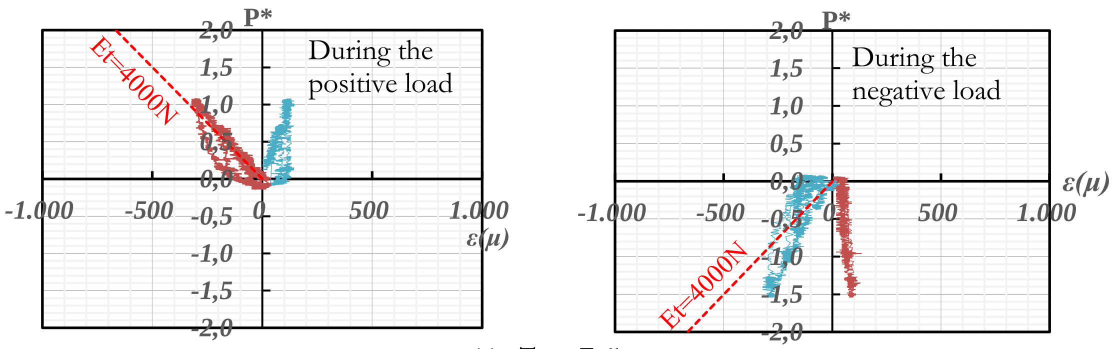

(a) Type-Full

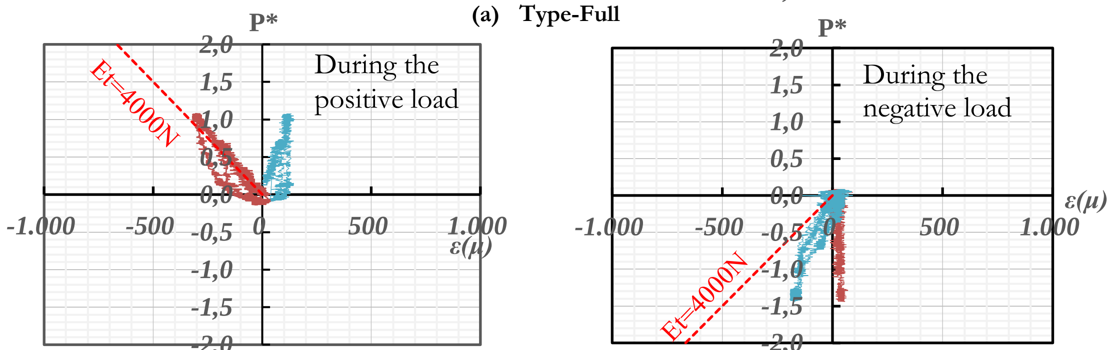

(b) Type-200

Figure 15. Strain of ceiling panel

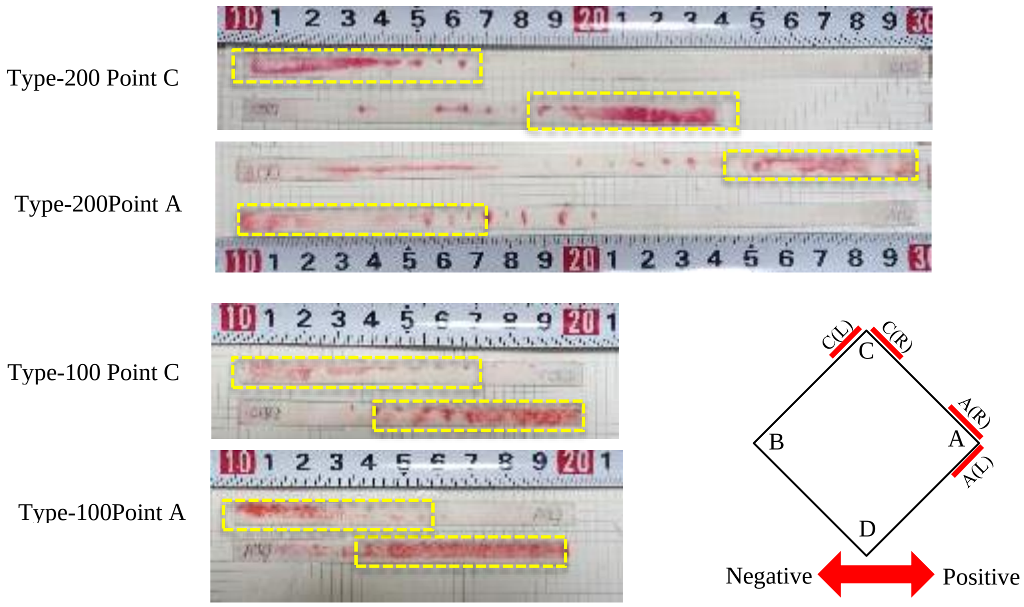

Photo 5. Coloring status of pressure film due to ceiling panel and T-bar contact

Photo.5 shows the measurement results of the contact situation between the ceiling panel and tees by the pressure measurement film. This coloring results are the case of type-100 and type-200. It seems that the coloring width is about 5 to 6 cm for the total width. Therefore, the average width of the compression suruts can be evaluated as $100\sqrt{2}$, but the stress transmission area due to the contact of the ceiling panel with the tee is extremely local.

4.3 Evaluate in-plane shear stiffness

Figure 16 shows the diagram of the load-deformation relationship of the unit, the panel stiffness obtained from the effective width and axial strain, and equivalent stiffness obtained from the natural frequency in previous dynamic experiments respectively. From this figure, the panel axial stiffness is much lager than the initial stiffness of the unit test. According to the equation (5), during the negative load, the initial sitffness of the unit is 31N/mm and the axial stiffness of the panel is 665N/mm, so K_F = 32.5N/mm (=1/31-1/665). On the othe hand, during the positive load, the initial sitffness of the unit is 12N/mm and the axial stiffness of the panel is 665N/mm, so K_F =12.2 N/mm (=1/12-1/665). As a result, the initial stiffness due to the combination of the panel and frame mostly determined by the stiffness of the frame. In addition, the difference in K_F value is possibly caused by the situation that the joints between the main tee and cross tee, or between the cross tee and sub-cross tee at the frame joint have different resistance mechanism in the loading direction. On the other hand, the equivalent stiffness by previous dynamic test is about 1/2 under the tension load and 1/4 under the compression load compared to initial stiffness of unit test.

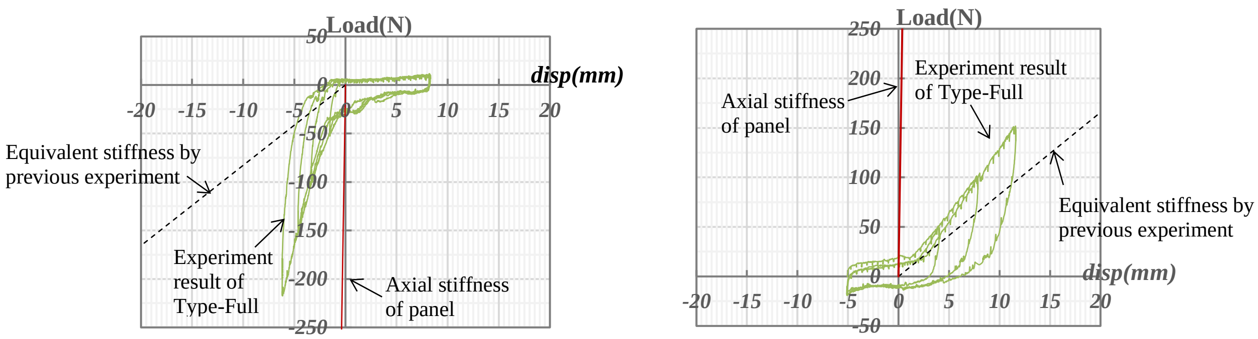

Figure 16. Comparing the stiffness and test results

5.CONCLUSION AND FUTURE WORK

In the in-plane shear stiffness evaluation, we could succesfully distinguish the axial stiffness of the panel diagonal and the stiffness of the surrounding frame by the unit experiment when the compression strut was formed. In particular, the stiffness of the frame joint has a large effect on the overall rigidity of the unit. Since the deformation of the main tee and cross tee, or between the cross tee and sub-cross tee was noticeable in the experiment, it is necessary to consider the frame rigidity focused on the details of each joint. We are planning to conduct element test on joint stiffness and incorporate frame stiffness evaluation.

ACKNOWLEDGEMENTS

This work was supported by JST Program on Open Innovation Platform with Enterprises, Research Institute and Academia and JSPS KAKENHI Grant Number JP16H02375.

REFERENCES

Dhakal, R.P., MacRae G.A., Pourali, A., Paganotti, G. [2016] "Seismic Fragility of Suspended Ceiling Systems Used in NZ Based on component Tests," New Zealand Society for Earthquake Engineering, Vol.49, No. 1.

Shinada, M., Motoyui, S. [2017] "Mechanical Properties of Joint regarding US-style Suspended Ceilings Part 1 Experimental Study of Mechanical Properties," *Summaries of Technical papers of annual meeting Architectural Institute of Japan*, pp. 911-912.

Yasuaki Sato, Kimcheng Tea, Shojiro Motoyui [2019] "Study on In-plane Shaer Stiffness in US-style Suspended Ceiling," *4th International Workshop on the Seismic Performance of Non-Structural Elements (SPONSE)*, pp. 81-90.

Kimcheng Tea, Tola Chhat, Shojiro Motoyui, Fumihiko Sakuraba [2019] "Effect of in-plane shear deformation on dynamic behavior of US-style suspended ceiling Part1 Evaluation of in-plane shear stiffness and proposal of simple numerical analysis model," *Summaries of Technical papers of annual meeting Architectural Institute of Japan*, pp. 1013-1014.

Numerical analysis of suspended ceiling considering pounding behavior between ceiling surface and walls

Minhui Li[1], Shojiro Motoyui[2], Yong Wang[3], Huanjun Jiang[4], Kazuhiko Kasai[5]

[1] Grad.Student, School of Environment and Society, Tokyo Institute of Technology
4259 Nagatsuta, Midori-ku, Yokohama, Kanagawa 226-8502, Japan
li.m.ah@m.titech.ac.jp
[2] Professor, School of Environment and Society, Tokyo Institute of Technology, Japan
4259 Nagatsuta, Midori-ku, Yokohama, Kanagawa 226-8502, Japan
motoyui.s.aa@m.titech.ac.jp
[3] Ph.D. International Joint Research Laboratory of Earthquake Engineering, Tongji University
Shanghai 200092, China
yongwang0305@163.com
[4] Professor, International Joint Research Laboratory of Earthquake Engineering, Tongji University
Shanghai 200092, China
jhj73@tongji.edu.cn
[5] Specially Appointed Professor, Institute of Innovative Research, Tokyo Institute of Technology
Yokohama, Kanagawa 226-8503, Japan
kasai.k.ac@m.titech.ac.jp

Abstract. In the previous study, we executed a full-scale shaking table experiment with a suspended ceiling, which is one of the standard styles in China. In this experiment, the perimeter beams corresponding to the actual walls were installed around the ceiling surface. However, the ceiling surface was not firmly connected to the beam, and according to one of the standard styles of suspended ceilings in China, a gap of approximately 13 mm was artificially set between the ceiling surface and the beam. Due to the presence of the gap, a pounding phenomenon occurred between the ceiling surface and the perimeter beam, and the pounding force at the time of the pounding generated a large acceleration, causing damage to the ceiling surface during the shaking test. Measurement items such as displacement and acceleration at some points and strain of some steel parts were sufficient to macroscopically grasp the dynamic behavior of the current style ceiling, but unfortunately, those measurement items were too few to deeply understand the influence of the pounding force on the dynamic behavior of suspended ceiling. Whereupon in this paper, we first propose a numerical model that can simulate the pounding phenomenon between the ceiling surface and the surrounding beams. On this basis, we show the verification of the model by comparing the numerical analysis results with the experimental results. Even though the present numerical models and calculation methods are very simple, they can simulate pounding phenomena with high accuracy at variable performance. Following accuracy confirmation, we will clarify the effect of the pounding on the axial force of the ceiling steel member and the reason why the ceiling was damaged through the numerical results.

Keywords: Suspended ceiling, Shaking table test, Numerical model, Pounding phenomenon

1. INTRODUCTION

CHN-US style suspended ceilings are developed from US-style ceilings which consist of three kinds of T-shape galvanized steel beams provided in three lengths: 3600mm,1200mm and 600mm, which are called main tees, cross tees, sub cross tees and L-bar which is called wall angle in this paper (as shown in Fig.1). The differences between two types of ceiling are as follows: [1] in US-style ceilings, hanging wires are principal method to hanging ceiling grid, while in the CHN-US style ceilings, hanging bolts are main current, and [2] US-style ceilings are classified as perimeter-fixed, with one or more sides of grid member connected to the wall by setting two screws in the seismic clip which constrained grid element to the boundary, (as shown in Fig.2). However, CHN-US style ceilings are mainly adopted floating systems which keep free boundary condition on both sides, only one screw placed in the slot of the clip, allowing the grid member to slide along its longitudinal direction (as shown in Fig.3). Due to the presence of gap between grid member and adjacent wall angle within the clip, a pounding phenomenon occurred between the ceiling surface and the perimeter beam is inevitable which have highly possible cause serious injury. In fact, during the Lushan earthquake in 2013, damages to the CHN-US style ceiling such as falling of ceiling boards and failure of grid members were reported as shown in Photo.1[1]. These damages have led to the severance of the functionality of facilities and have endangered the safety of people.

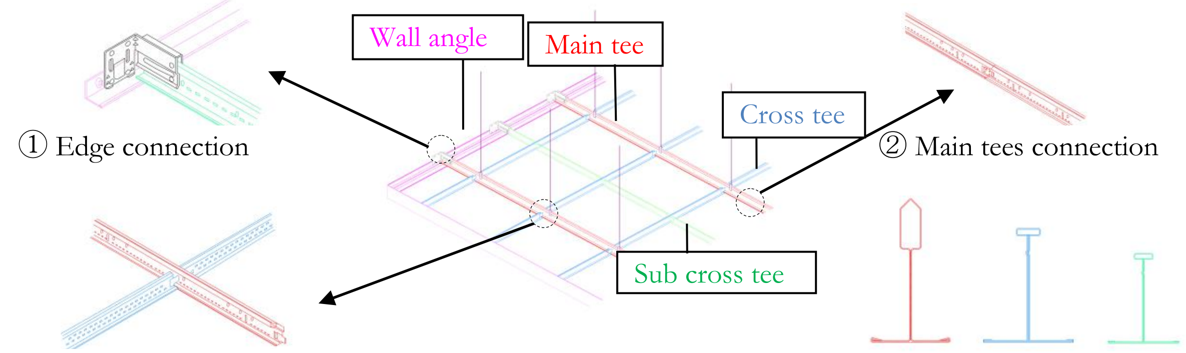

Fig.1 Components of the CHN-US style ceiling

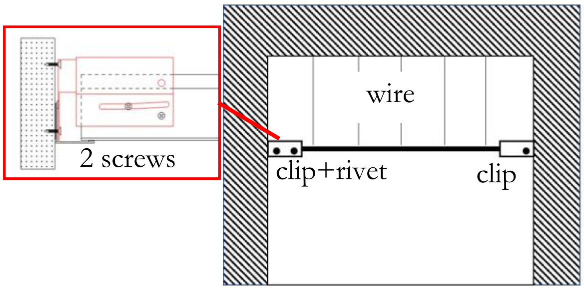

Fig.2 US-style ceiling

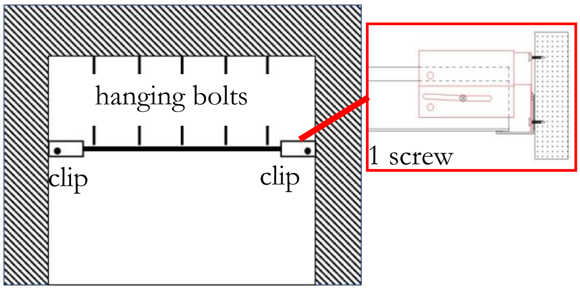

Fig.3 CHN-US style ceiling

Photo.1 Damage of ceiling during Lushan earthquake in 2013

In past, there were some studies on simple methods of appraising axial force based on peak floor acceleration by shaking table tests of perimeter-fixes type suspended ceilings 2) [R.P. Dhakal et al., 2015], the performance of US-style ceiling components such as ceiling joint 3) [Siavash et al., 2015]. However, CHN-US style ceilings are different from US-style ceilings for the ceiling surface can slide along its longitudinal direction freely on both sides. Due to the presence of the gap between the ceiling surface and the wall angle, a pounding phenomenon occurred and it's complicated to simulate by numerical analysis. Therefore, the investigation of the numerical study to simulate the pounding phenomenon still be necessary. To study the analytical method of simulating the essential pounding phenomenon, Motoyui Lab conducted various pounding experiments on gypsum board to simulate pounding (as shown in Photo.2 and Fig.4). By comparing the experimental result with the Hertz model with non-linear damper (which is called Hertzdamp model in this paper) analysis' result and the Voigt model's result, the use of the Hertzdamp model has high accuracy in modeling pounding 4) (as shown in Fig.5~Fig.8), but CHN-US style ceiling surface have different properties from gypsum board, so it's still unclear that the Hertzdamp model could simulate the pounding phenomenon of CHN-US style ceilings. In this study, the pounding occurrence mechanism is clarified by using numerical analysis based on the shaking table test for the CHN-US style ceiling. This paper shows the design and outline of the shaking table test, the characteristic of the test results, and a discussion on how pounding affects the axial force of grid members.

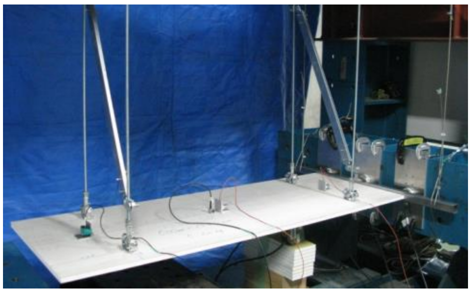

Photo.2 Experiment of the gypsum board pounding behavior

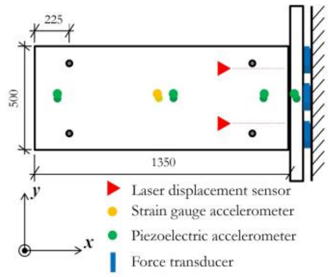

Fig.4 outline of pounding test

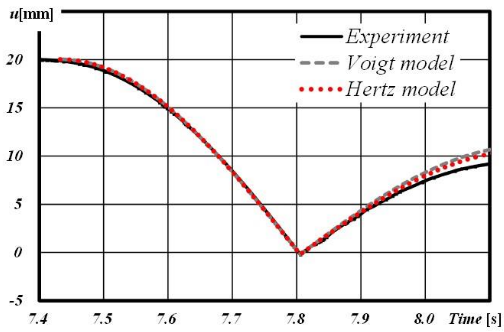

Fig.5 Comparison of displacement

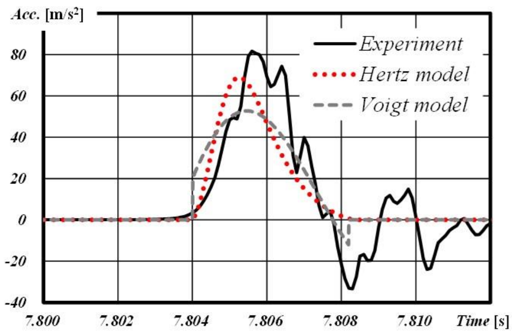

Fig.6 Comparison of acceleration

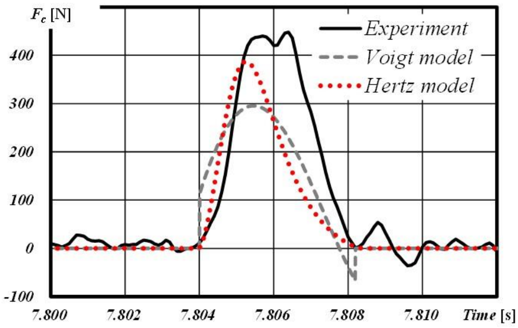

Fig.7 Comparison of pounding force

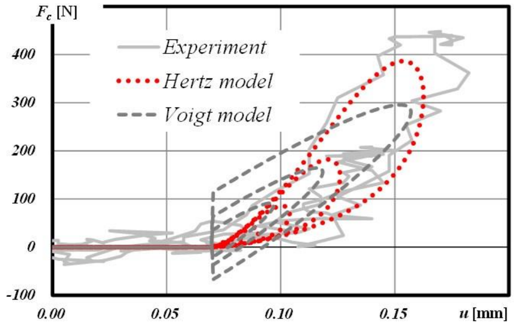

Fig.8 Comparison of displacement-force

2. OUTLINE OF EXPERIMENT

Photo.3 shows the arrangement of the shaking table test [5]. Fig.9 shows the outline of the experiment. The shaking table used in the test assemble with steel platform dimensions of 12840mm×11640m. In order to simulate the boundary condition of the specimen, the perimeter beams were fastened on the platform to represent the surrounding walls (as shown in Photo.4)[5]. The size of the specimen was 12600mm×11400mm (360 lay-in panels of 600mm×600mm with a thickness of 16mm), Φ8 threaded rods of length 1000mm were used for hanging the CHN-US style ceiling (as shown in Photo.5)[5] at an interval of 1200mm. The 3600mm main tees are laid aside parallel to each other at an interval of 1200mm along the Y direction. The cross tees with a length of 1200mm are placed orthogonal to the main tees, sub cross tees were assembled parallel to the main tees(as shown in Fig.9). All sides define the boundary conditions of the ceiling with clips on the wall angles which are called boundary clip in this paper. The grid ends with a nominal gap from the wall angle designed to be able to slide freely within the middle slot of the boundary clip along the longitudinal direction. The total weight of the ceiling was 500kg. The input acceleration applied in the test were sweep waves from 6Hz to 0.8Hz with the acceleration amplitude as the test parameter to explore the failure mechanism of the specimen. The shaking duration was set as 100 seconds. The list of input motions is shown in Table.1.

Photo.3 Arrangement of experiment

No.	Wave	Duration	Acceleration	Impact occurred or not	Failure condition
1	Sweep6-0.8Hz	100s	50gal		
2	Sweep6-0.8Hz	100s	150gal	occurred	
3	Sweep6-0.8Hz	100s	250gal	occurred	Buckling of latches
4	Sweep6-0.8Hz	100s	350gal	occurred	Falling of panel
5	Sweep6-0.8Hz	100s	500gal	occurred	Complete collapse of ceiling

Table.1 The list of input motions

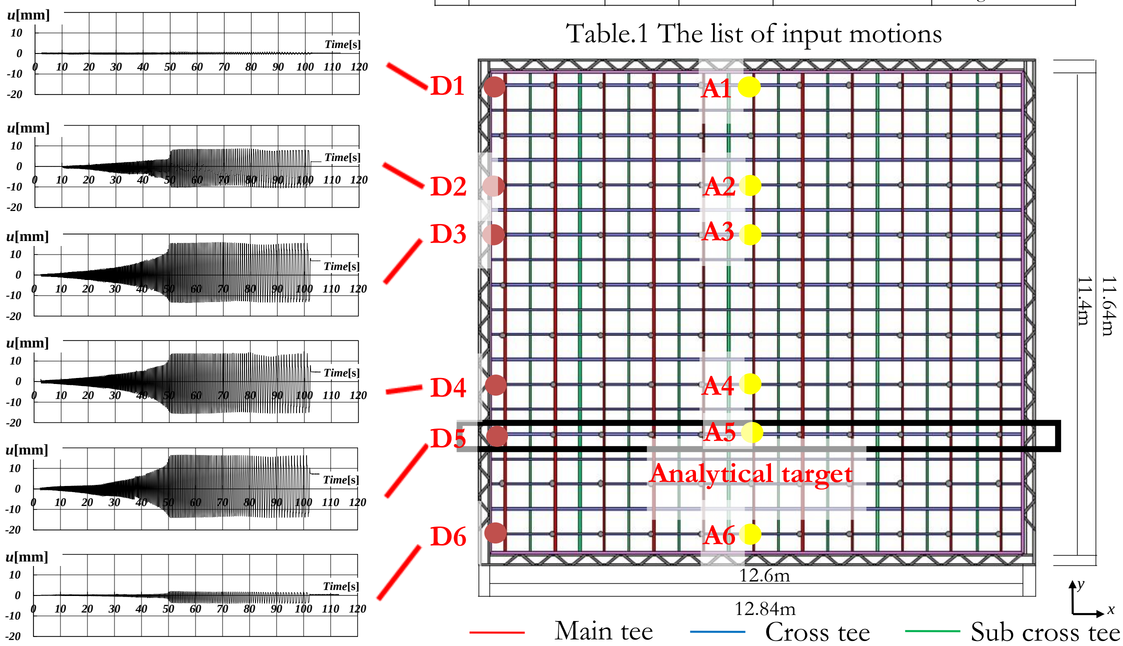

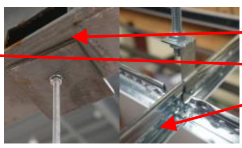

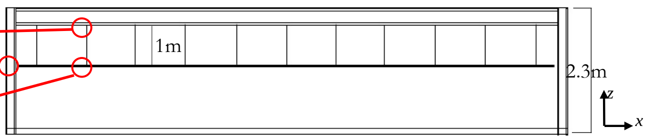

Photo.4 Boundary detail Photo.5 hanging bolt detail Fig.9 Outline of specimen

As shown in the table.1, there was less damage happened but the pounding phenomenon occurred during the sweep of 150gal, so the test result during 150gal will be the investigated target in this paper. Fig.9 also shows the displacement time history from D1 to D6 during the sweep 150gal[6]. The vertical axis is the value of displacement which refers to the relative displacement between the cross tee and perimeter beam. The test result shows that D1 and D6 are significantly less than other displacement results due to being adjacent to the restraint boundary, so there is no pounding phenomenon that occurred in these two rows that are not applicable in this analysis research. Moreover, the characteristic of symmetry can be found in the test result which is from D2 to D5 even though the gap between the grid end and wall angle in each row of the cross tee has an uneven width. Therefore, we only chose the D5 row of the cross tee (as shown in Fig.9) as the analytical target. Fig.10 and Fig.11 show the left end displacement time history D5 and acceleration time history of the middle of the ceiling A5[6]. Two characteristic phases were confirmed from the result of the test. First, the relative displacement between the end of the cross tee and perimeter beam becomes greater gradually but smaller than the gap between the grid end and wall angle where the inertia acting on the grid members is larger than the friction force at the boundary clip on both sides. The acceleration amplification of the middle of the ceiling surface relative to the platform is small since no pounding behavior occurs between the grid end and the wall angle. In the second phase, when the relative displacement between the end of the cross tee and perimeter beam increases to approximate 13.3mm which is the maximum range of the gap between the grid end and wall angle but is limited by perimeter beams, (the maximum of displacement time history D5 exceeds 15mm for the elastic deformation of the ceiling itself) the pounding behavior occurred and the acceleration response of the middle of the grid increases rapidly to 15m/s^2 approximately. Even though the measurement data supplies the fundamental properties of the pounding behavior, it's still insufficient to deeply comprehend the influence of the pounding force on the dynamic behavior of the CHN-US style ceiling.

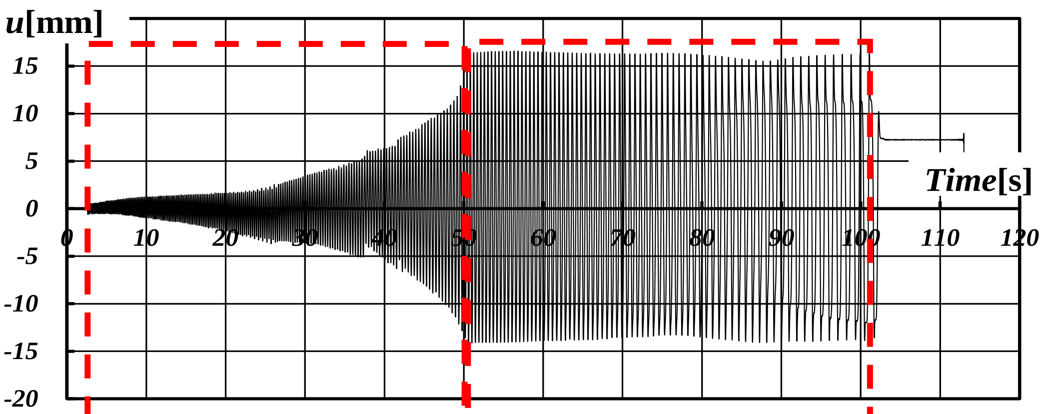

Fig.10 Displacement time history (D5)

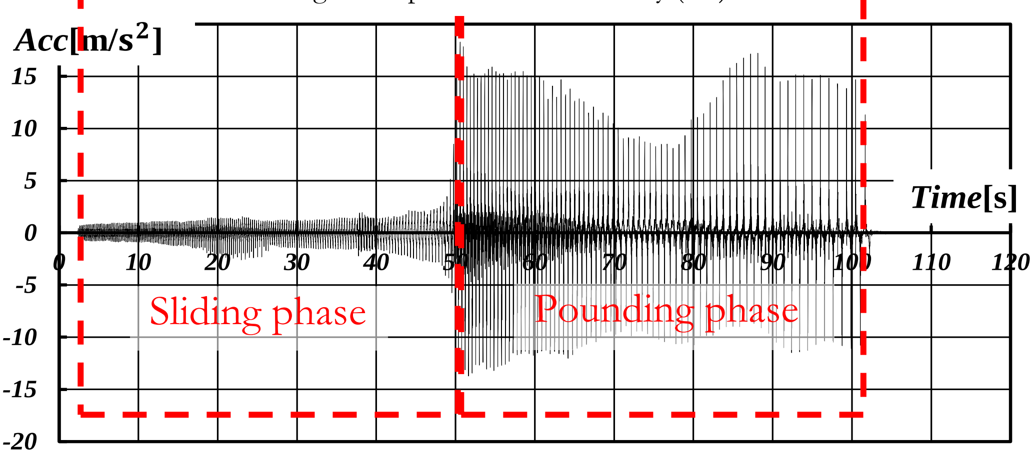

Fig.11 Acceleration time history(A5)

3.SIMULATION BY NUMERICAL MODEL

3.1 OUTLINE OF NUMERICAL MODEL

A simple numerical model was built to simulate the response of the specimen in the shaking table test. In this analysis, 1 row of the cross tee has been chosen as the analytical target (as shown in Fig.12). Fig.13 shows the outline of the numerical model. The total mass of 25kg is allocated to 23 mass points(m_c).

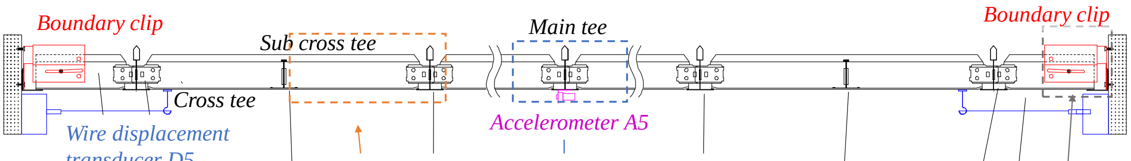

Fig.12 Details of analytical target

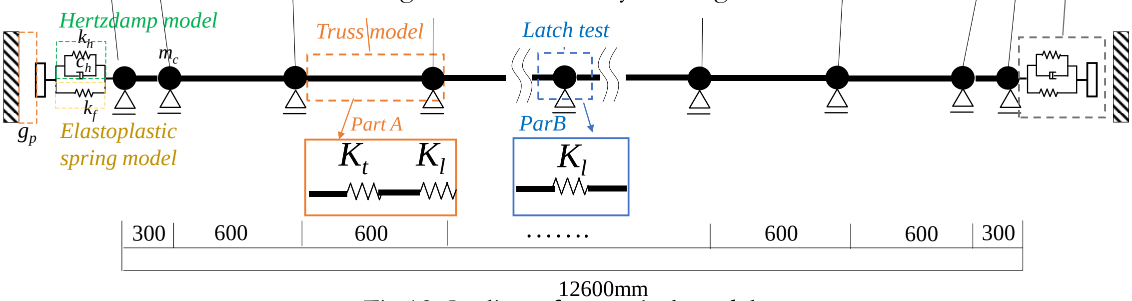

Fig.13 Outline of numerical model

Firstly, a simple truss model was conducted for the cross tee to express the axial stiffness of grid members. Considering that the latch contributed to integral rigidity, the axial rigidity K was calculated as the sum of the rigidity of grid K_t and rigidity of the latch connection K_l (as shown in part A in Fig.13). A tension test of the cross tee and a cyclic test of the latch were designed to evaluate the K_t and K_l. (as shown in Fig.14 and Fig.16). Fig.15 and Fig.17 show the relationship between tension force F_t and strain, the backbone curve of the force F_r-displacement [7].

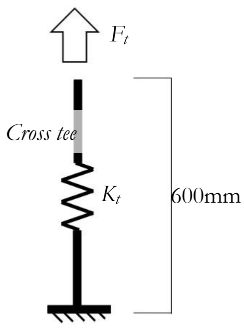

Fig.14 Tension test

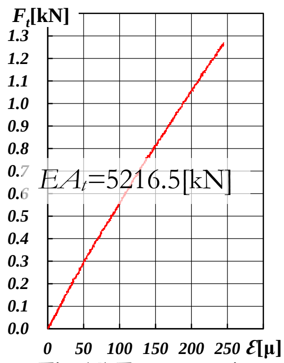

Fig.15 Force-strain

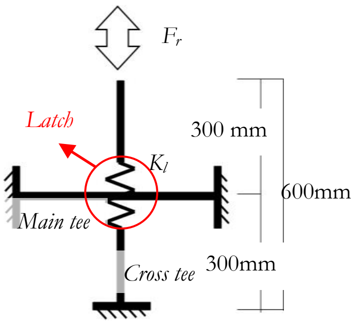

Fig.16 Outline of latch test

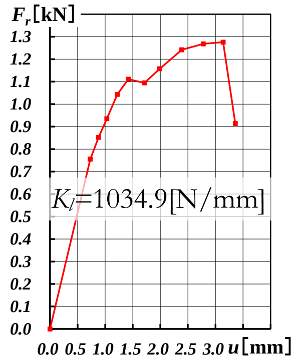

Fig.17 Force-displacement

From the above, the stiffness EA can be defined as follows:

$$\delta = F/K = F(1/K_t + 1/K_l) \qquad \text{where } EA_t = 5216.5[\text{kN}],\ K_t = EA_t/H = 8694.2[\text{kN/mm}] \tag{1}$$

$$EA = KH = 1034.9 \times 600 = 6.2 \times 10^5 [\text{N}] \tag{2}$$

where H is the length of the specimen, for K_t is significantly greater than K_l, K can be considered as K_l

Next, the mechanical properties in the sliding phase need to be clarified, and it can be considered that mechanical properties at the boundary clip are the most significant, so we conducted a mechanical test (as shown in Fig.18) for ensuring their validation of them. From the test result, the mechanical property at the boundary clip can be assumed to be an elastoplastic spring model with slight hardening (as shown in Fig.20(a)). However, results that are obtained by using the parameter values from the test are not close to testing results (as shown in Fig.21(a)) for the stiffness of hanging bolts were not considered in this model, so we also conduct an experiment of hanging bolt test to acquire the stiffness of hanging bolt (as shown in Fig.19). From the test result (as shown in Fig.20(b)), the stiffness K_{bolt} can be defined as follows:

$$K_{bolt}=\frac{12EI}{L^3}+\frac{mg}{L} \tag{3}$$

where E is Young modulus, I is 2nd-moment inertia, and L is the nominal Length of the hanging bolt. Therefore we parallel two elastic spring models at both ends of the ceiling to represent the friction at the boundary clip and stiffness of hanging bolts (as shown in Fig.20(c)). By comparing the numerical and experimental results, the value of K_{bolt} has to be set to 0.67-1.07N/mm (as shown in Fig.21).

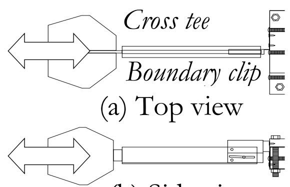

(a) Top view

(b) Side view

Fig.18 Mechanical test

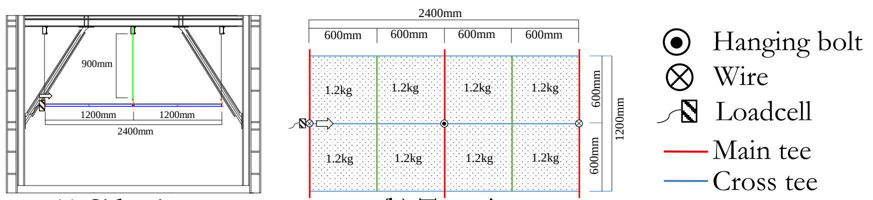

(a) Side view

(b) Top view

Fig.19 Hanging bolt test

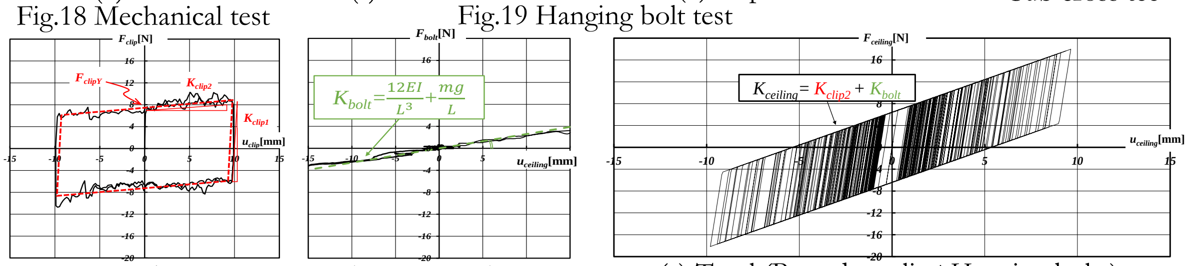

(a) Boundary clip

(b) Hanging bolt

(c) Total (Boundary clip+Hanging bolts)

Fig.20 Elastoplastic spring model

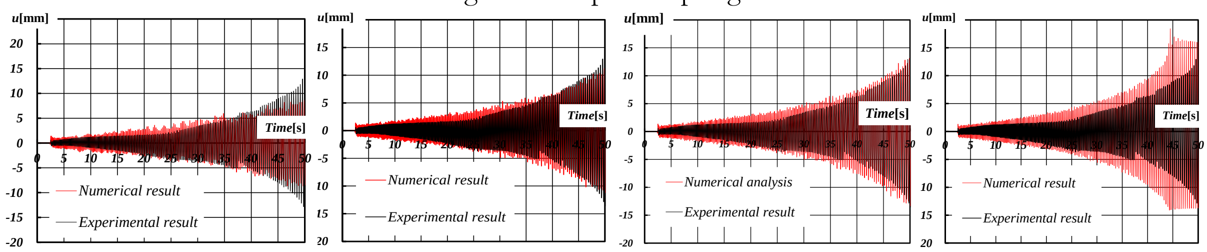

(a) Only clip

(b) K_{bolt}=0.67N/mm

(c) K_{bolt}=1.07N/mm

(d) K_{bolt}=1.77N/mm

Fig.21 Comparison between the numerical and experimental result

Finally, a Hertzdamp model was created to simulate the mechanical properties in the pounding phase. Pounding force F_c representation is:

$$F_c = k_h\delta^{\frac{3}{2}} + c_h\dot{\delta} \quad , \qquad c_h = \frac{8}{5}\frac{k_h(1-e)}{e\dot{\delta}_0}\delta^{\frac{3}{2}} \tag{4}$$

where k_h is the pounding stiffness parameter which depends on the material properties of the colliding structures and the attributes of the contact surface. e is the coefficient of restitution which depends on the materials of colliding structures. Comparing the numerical results with different values of stiffness (as shown in Fig.22), k_h should be set to at least 200N/mm$^{3/2}$. The value of the parameters is shown in Fig.23.

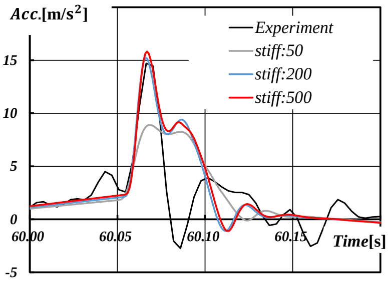

Fig.22 Comparison with different stiffness

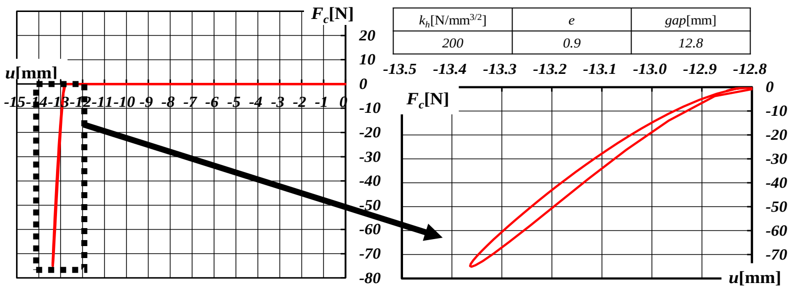

Fig.23 Hertz model with non-linear damper

3.2 VALIDITY OF THE NUMERICAL MODEL

Fig.24~Fig.27 show the response displacement (D4 and D5) of the end of the grid and acceleration of the center of the ceiling (A4 and A5) during the sweep 150gal. By comparing the numerical analysis result (red line) and experiment result (black line), it is confirmed that the numerical analysis result closely matches the experiment result.

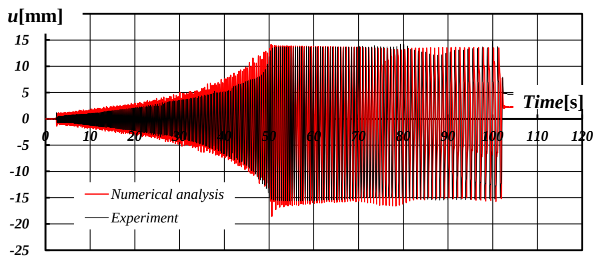

Fig.24 Displacement time history (D4)

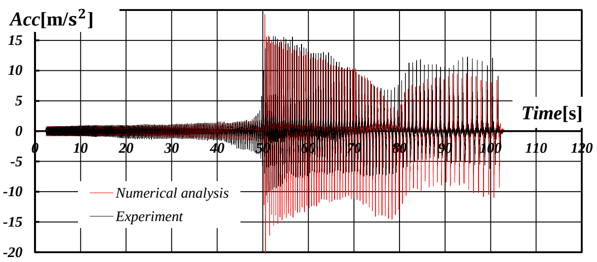

Fig.25 Acceleration time history (A4)

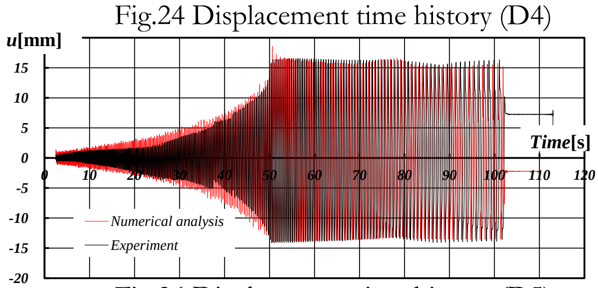

Fig.26 Displacement time history (D5)

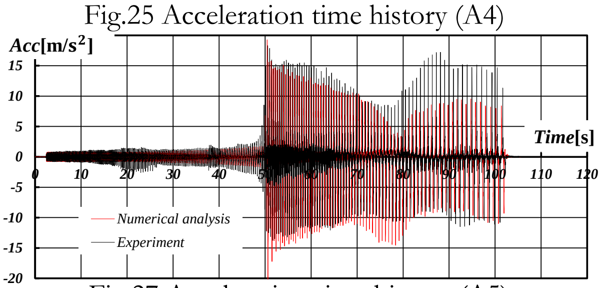

Fig.27 Acceleration time history (A5)

4. EFFECT OF POUNDING ON THE AXIAL FORCE

4.1 RELATIONSHIP BETWEEN THE ACCELERATION AND DISPLACEMENT

Fig.28 shows the acceleration -displacement from numerical analysis results. The vertical axis of Fig.28(a) is the value of the acceleration of the middle of the ceiling, and the horizontal axis is the horizontal in-plane displacement of the ceiling in the shaking direction which is calculated by the relative displacement between grid end and perimeter beam, and the vertical axis of Fig.28(b) is the value of the acceleration of the left end of the grid. Comparing the median acceleration and end acceleration, we figure that the end acceleration is 1.5 times larger than the median acceleration when the pounding phenomenon occurred, so the effect of the excessive acceleration caused by pounding on the axial force of the grid needs to be investigated by numerical studies.

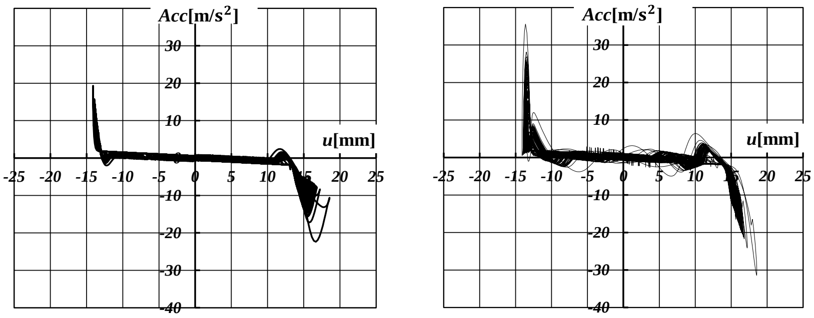

(a)Mid point of the ceiling (b)Left end of the ceiling

Fig.28 Acceleration-displacement

4.2 CHARACTERISTIC OF THE DISTRIBUTION OF IN-PLANE AXIAL FORCE

The research on the effect of pounding on the axial force will be investigated in the analysis result. Fig.29 shows the distribution of inertial force in the ceiling face when a slide occurs. The horizontal axis is the longitudinal direction of the analytical target. From Fig.29, the distribution of the inertial force shows the linear characteristic and the largest inertial force is equal to the predicted inertial force which is calculated as the product of mass and peak acceleration as follows:

$$F_{\text{inertial}}= m\times a_{max}=25\text{kg}\times 1.5\text{m/s}^2=37.5[\text{N}] \tag{5}$$

Fig.31 and Fig.33 show the distribution of in-plane axial force and the acceleration response in the ceiling face before and after the pounding occurs. The horizontal axis is the longitudinal direction of the analytical target. The largest acceleration response at the end of the grid appeared when the pounding happened (red line in Fig.33), but the in-plane axial force is still small at the same time (red line in Fig.31). On the other hand, the largest in-plane axial force appeared and shows the linear characteristic of distribution when the acceleration response at the middle of the ceiling face become the largest after the pounding occurred (blue line in Fig.30 and Fig.32). Therefore, the largest in-plane axial force is not led by the excessive acceleration at the end of the ceiling where the pounding occurred, but by the average maximum in-plane acceleration response.

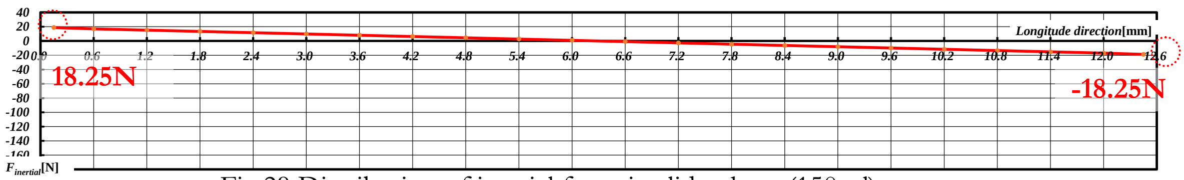

Fig.29 Distribution of inertial force in slide phase (150gal)

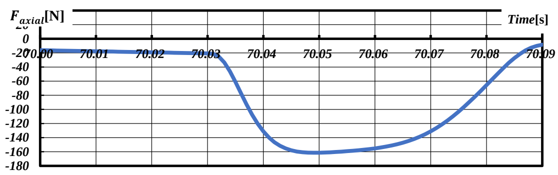

Fig.30 Axial force time history(150gal)

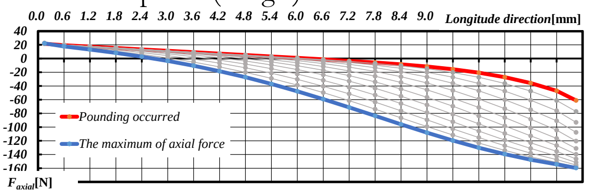

Fig.31 Distribution of axial force(150gal)

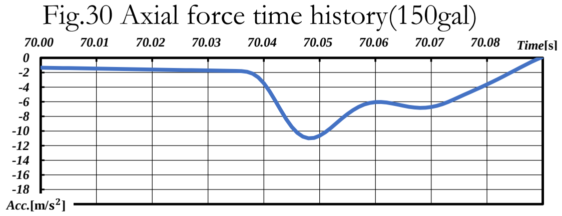

Fig.32 Acceleration time history (150gal)

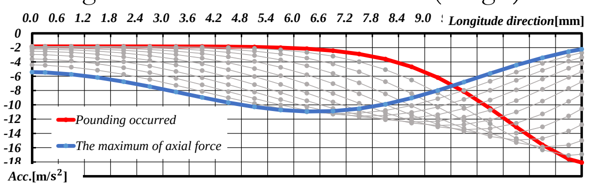

Fig.33 Distribution of acceleration response (150gal)

CONCLUSION

This study aims to investigate the effect of the pounding on the in-plane axial force of the CHN-US style ceiling by using numerical analysis based on the shaking table test. In this research, the validity of the Hertz damp model was confirmed, and the excessive acceleration response on the grid end when the pounding occurred has also been clarified. We figure out the propagation mechanism of both acceleration and in-plane axial force from the numerical result of the acceleration response and in-plane axial force during the pounding that occurred. Through the experiment and numerical analysis, we also find that the kinematic hardening model has high accuracy in modeling the mechanism of the boundary clip, and the influence on the horizontal stiffness from the hanging bolts cannot be ignored in the numerical study.

ACKNOWLEDGEMENTS

This work was supported by JST Program on Open Innovation Platform with Enterprises, Research Institute and Academia and JSPS KAKENHI Grant Number JP16H02375. The authors acknowledge the shaking test conducted and the experiment data investigated by Yong Wang who was a graduate PhD in TongJi University.

REFERENCES

1) LI Qiqi, QU Zhe, XIE Quancai "Seismic damage characteristics and fragility of suspended ceilings in Chinese public buildings" *Key Laboratory of Earthquake Engineering and Engineering Vibration, Institute of Engineering Mechanics, China Earthquake Administration, Sanhe, Hebei 065201, China*

2) A. Pourali, R.P. Dhakal & G.A. MacRae "Shake table tests of perimeter-fixed type suspended ceilings" *2015 NZSEE Conference*

3) Siavash Soroushian, E. "Manos" Maragakis & Craig Jenkins "Capacity Evaluation of Suspended Ceiling Components, Part 1: Experimental Studies" *Journal of Earthquake Engineering, 19:784–804, 2015*

4) Yutaro Sumi, Shojiro Motoyui "Study on basic property for impact behavior and analysis method : Part 1 Impact Behavior of Ceiling with Accidental Spacing in Earthquake" *Architectural Institute of Japan, 987-988, 2014*

5) Huanjun Jiang, Yong Wang, and Kazuhiko Kasai "Shaking table tests on Chinese style suspended ceiling systems" *Proceeding of the 17th World Conference on Earthquake Engineering. Sendai, Japan, 2020.*

6) Yong Wang, Huanjun Jiang, Shojiro Motoyui and Kazuhiko Kasai, Zhiyuan Qin, Youlu Huang "Study on seismic performance of suspended ceiling system with semi-free boundary condition" *Engineering Structures* (*under review*)

7) Huanjun Jiang, Yong Wang, and Chen Wu "Experimental Study on The Axial Behavior of Grid Joint and Splices of Suspended Ceilings" *Engineering Mechanics, 2022, 39(7): 30-38*

Numerical simulation of piping systems connected by grooved fit joints

Tao Wang[1], Lin Qiu[1], and Qingxue Shang[2*]

[1] Key Laboratory of Earthquake Engineering and Engineering Vibration, Institute of Engineering Mechanics, China Earthquake Administration; Key Laboratory of Earthquake Disaster Mitigation, Ministry of Emergency Management, Harbin 150080, China
e-mail: wangtao@iem.ac.cn, 727979239@qq.com
[2] Department of Civil Engineering, Tsinghua University, Beijing 100084, China
e-mail: shangqingxue@outlook.com (*Corresponding author)

Abstract. Piping system is one of the most important non-structural components to reduce the post-earthquake secondary disasters and maintain the post-earthquake normal use of buildings. The seismic damage of piping system will result in loss of firefighting ability or failure of water supply and drainage system in a building. Accurate simulation of mechanical behavior of piping system is helpful to realize its numerical analysis under earthquakes and evaluate seismic performance. In this study, the moment-rotation hysteresis curves of piping-joints connected by grooved fit joints were obtained by quasi-static cyclic tests. The moment-rotation hysteresis models of piping-joints were developed using zeroLength element and Pinching4 uniaxial material in OpenSEES. The model parameters were calibrated using test data. The developed hysteresis models can accurately reproduce the moment-rotation hysteresis curves obtained in the experiments and simulate the moment time history during the loading process. And the trend of the accumulated energy dissipation of the numerical results is consistent with the test results as the increase of the number of cycles. On this basis, the generic moment-rotation hysteresis models of piping-joints were further developed and the recommended values of parameters used to define the generic hysteresis model were obtained. Then numerical model of piping system was developed based on the generic hysteresis model. The numerical results indicated that the numerical model can be used to simulate the nonlinear behavior of piping system under cyclic loading with high accuracy and feasibility.

Keywords: piping system; grooved fit joints; non-structural components; hysteresis model; numerical simulation.

1.INTRODUCTION

Suspended piping system is one of the most critical non-structural systems in a building. Recent earthquakes have demonstrated that non-structural components (NSCs) including piping system of public buildings and critical facilities such as hotels, schools, hospitals, airports, power plants, and industrial units suffered much more damage in comparison with structural components (SCs) (Filiatrault and Sullivan, 2014). During the 1994 Northridge earthquake, pipelines in different piping systems such as HVAC systems, sprinkler piping systems, and water piping systems experienced widespread failures. Leakage of fire sprinkler piping systems forced the temporary evacuation of several hospital buildings after the earthquake. After the 2010 Chile Earthquake, four hospitals in the central south region of the country were inoperable, and 12 hospitals lost almost 75% of their functionalities. Most loss was caused by damages to NSCs such as suspended ceilings, light fixtures, and fire sprinkler piping systems. Two largest airports in Chile were closed as well because of non-structural damages and flooding from failed sprinkler piping systems [Miranda *et al.*, 2012].

The seismic damage of piping systems not only resulted in huge economic loss but also mitigated the functionality of the buildings and facilities. Seismic performance of NSCs and seismic design of NSCs has been started since the early 1980s. Component level quasi-static tests were widely used to determine the force-displacement hysteresis response or moment-rotation cyclic response of piping components [Tian *et al.*, 2014; Wang *et al.*, 2019]. Based on the test results, analytical models of piping components were developed, e.g., numerical models of grooved fit tee joints, threaded tee joints, flexible pipeline connections, cast-iron and copper tee joints, and seismic sway braces for suspended piping systems.

In order to evaluate and understand the dynamic response of piping systems, experiments using shaking tables have been conducted and the test results were used for system level analytical model calibration during the last two decades [Tian *et al.*, 2015a; Zaghi *et al.*, 2012]. Zaghi *et al.* [2012] investigated the seismic performance of welded and threaded hospital piping assemblies by shaking table tests. A simplified computational model was developed using SAP2000 and calibrated with experimental data. Soroushian *et al.* [2014] conducted monotonic and reverse cyclic tests on tee joints and developed nonlinear joint hinge models. These hinge models were then incorporated in an OpenSEES model of a ceiling-sprinkler piping assembly that was tested at the E-Defense shake table facility in 2011. The analytical and experimental response of the fire sprinkler piping system were compared. Tian *et al.* [2015b] developed analytical models for grooved fit tee joints and threaded tee joints. These models were integrated into analytical model of sprinkler piping systems to conduct seismic fragility analysis using floor acceleration histories as inputs.

In addition, Blasi *et al.* [2021] evaluated the seismic demand on two types of piping networks installed in a reinforced concrete (RC) framed building by cascade analysis. The floor acceleration time-histories obtained through non-linear dynamic analysis of infilled and bare frames were used as input for piping systems. Wang *et al.* [2019] conducted probabilistic seismic demand analysis and probabilistic seismic fragility analysis for pipeline system installed to transfer water vertically along the height in 10-story RC building. Ju and Gupta [2015] developed non-linear rotational spring models for Tee-joint piping systems validated using experimental results. The system-level fragility of the complete piping system was evaluated based on nonlinear time history analysis. The interactions between piping systems and the supporting structures were further considered to analyze the effects on piping fragility.

Despite the experimental studies and analytical works have been performed on piping systems, the numerical model of piping system connected by grooved fit joints still needs to be further developed. Considering the fact that there are certain differences in the pipe types, joint types and configuration types adopted in previous studies are selected from different countries, the results are not universal and maybe not suitable for seismic performance analysis of piping systems in China. This paper analyzes the bearing capacity and deformation capacity of the grooved fit piping joints based on the quasi-static test results and the hysteresis model was developed. The pinching4 uniaxial material in OpenSEES is combined with the zeroLength element to reproduce the moment-rotation response of the grooved fit piping joint. The finite element model of the whole piping system is developed then. The proposed piping joint moment-rotation hysteresis model is integrated into the finite element model of piping system.

2.QUASI-STATIC TESTS OF GROOVED FIT PIPING JOINTS

2.1 SPECIMEN

Grooved fit joints, as shown in Figure 1(a)-(c), are a relatively new piping construction product that has gained popularity in earthquake prone areas because of the improved flexibility they provide to fire sprinkler piping systems. Grooved fit joint is composed of pipes with grooves, lathedog-plumbings, rubber gasket and bolts. Dimensions of the joints are presented in Figure 1(b)-(c). Detailed information of the materials and components can be found in Wang *et al.* [2019]. Although this type of joint is massively used in piping construction in China, there's no sufficient investigation on its mechanical behavior, deformation capability and failure mode. A series of quasi-static tests were conducted to examine the seismic performance of the elbow joints and Tee joint. The elbow joint employs a 90° elbow joint connected with two DN150 pipes, as shown in Figure 1(e). The length of each pipe is 840mm. The Tee joint uses a triplet connecting to two DN150 pipes and one DN80 pipe. The length of DN150 pipes is 840mm, while the DN80 is 350mm. Eight Tee joints are divided into two groups. One tests the rotation of DN150 pipes and the other tests the behavior of DN80, as shown in Figure 1(e)-(f), respectively. In each group, there are one monotonic loading test and three cyclic loading tests.

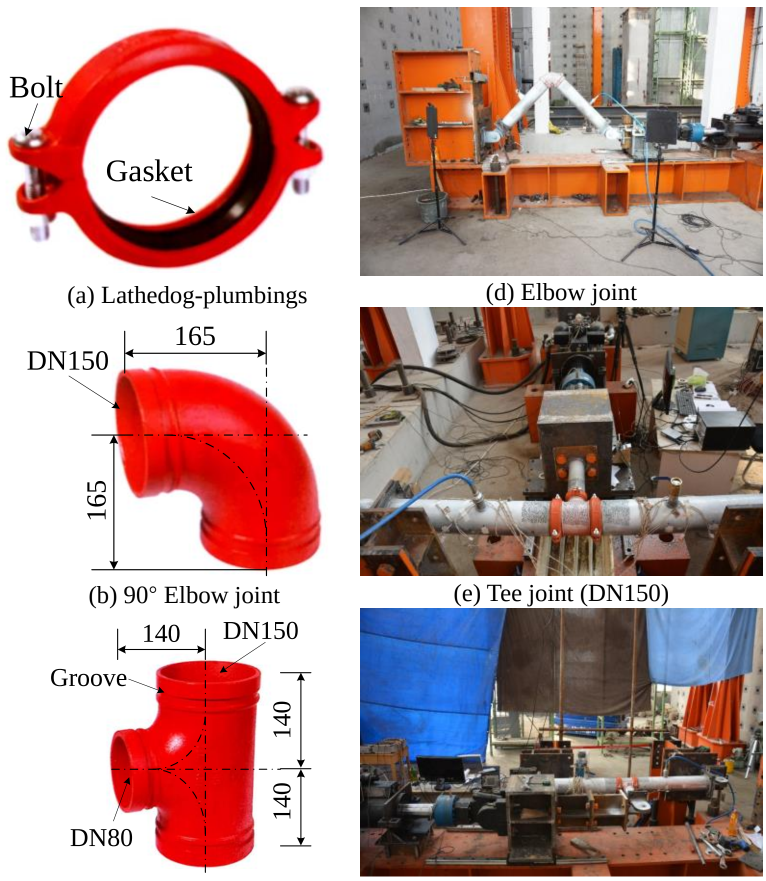

(a) Lathedog-plumbings (d) Elbow joint

(b) 90° Elbow joint (e) Tee joint (DN150)

(c) Tee joint (f) Tee joint (DN80)

Figure 1. Typical grooved fit joint details and experimental set-up

2.2 TEST SETUP AND LOADING PROTOCOL

The functionality examination is one of the objectives of the experiment. The joints were tested with the internal water pressure of 1.6 MPa to capture the leakage during the tests and simulate the working condition of pipes. The pipes full of pressurized water were kept for 24 hours before tests to examine the sealing performance. For Tee joints (DN150) (Figure 1(d)), one hydraulic-servo actuator is employed to realize the quasi-static tests at a low loading speed of 0.5 mm/s. One end of the actuator is fixed on the reaction beam which is securely fixed on the strong floor. The other end is attached to a load jig which is bolted on two linear bearing sliders. The sliders restrain the movement of the load jig in the axial direction only. The end of each DN150 pipe is pinned to one reaction pier fixed on the strong floor, while the end of DN80 is connected to the load jig along the loading direction. Similar set-ups are used to test the Tee joints (DN80) (Figure 1(e)) and the elbow joints (Figure 1(f)). When testing the DN80 connection of the Tee joints, the DN80 pipe is pinned to the load jig perpendicular to the loading direction. The elbow joints are pinned to the load jig at one end and to the reaction beam at the other, as shown in (Figure 1(f)). The axes of the initial positions of the two DN150 pipes of the specimen are 45 degrees from the horizontal line. For each type of joints, three cyclic loading tests were conducted. More details of the test setup are presented in Wang *et al.* [2019]. The specimens were subjected to a cyclic loading following loading protocol suggested by FEMA 461 [FEMA 2007].

2.3 MOMENT-ROTATION CYCLIC RESPONSE OF GROOVED FIT JOINTS

Three damage states including water pressure drop, loss of the ability to maintain water pressure and complete damage of the joints were defined for the tested specimens. However, due to the length limit of this paper, damage state discussion will be omitted. Typical moment-rotation hysteresis curves of different grooved fit joints are shown Figure 2. It can be observed from the hysteresis loops that the moment values would keep increasing even at a large rotation around 0.1 rad. And a pinching effect was introduced by the gaps in the improved configuration. As soon as the loading force was increased, during the load-inversion phase, the gap generated caused relative rotations with near-zero force variation. Furthermore, reduction of the reloading stiffness can be observed after each loading step because the response could be highly influenced by the cumulative damage. It can be seen from the hysteresis curves in Figure 2 that the positive and negative mechanical properties of elbow joints and DN80 joints are almost symmetrical, and the dispersion of peak moment values and corresponding rotation angles are relatively small. For DN150 joints, there is a large difference in the positive and negative mechanical properties (see Figure 2(b)), which is mainly caused by the possible installation errors before the tests, e.g., the inconsistency of the gap between the pipe and the joint between the left and right sides of the joints, which resulted in a certain difference in the positive and negative hysteresis curves. More details of the test results are presented in Wang *et al.* [2019].

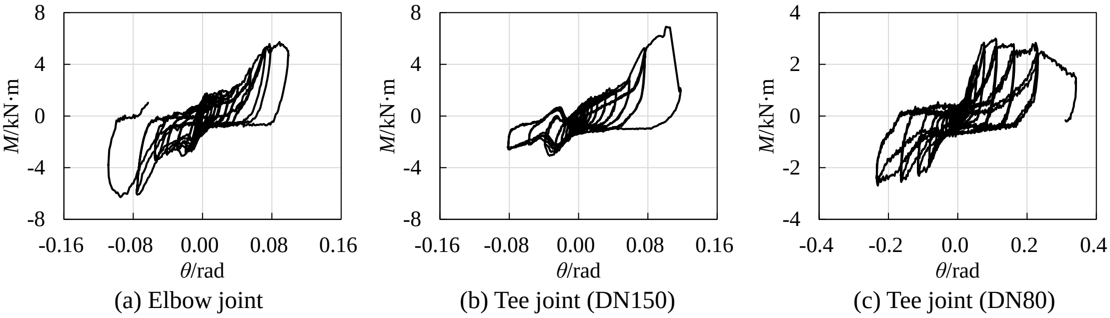

Figure 2. Moment-rotation hysteresis response of different grooved fit joints

3.DEVELOPMENT OF A HYSTERESIS MODEL FOR GROOVED FIT JOINTS

3.1 PINCHING4 UNIAXIAL MATERIAL

The moment-rotation hysteresis response of grooved fit joints shows high nonlinearity. The experimental data presented in Section 2.3 was utilized to develop an analytical hysteresis material model for grooved fit joints. The Pinching4 uniaxial material can consider the strength degradation, stiffness degradation and pinching effect under cyclic reverse loading, and can accurately simulate various complex hysteresis characteristics. The Pinching4 uniaxial material, along with a zeroLength element in OpenSEES platform, was widely used to simulate the force-displacement response of different types of NSCs, e.g., sprinkler piping joints Soroushian *et al.* [2014] and seismic sway braces for pipings Shang *et al.* [2022]. The simulation method used in previous studies was adopted in this study to simulate the moment-rotation hysteresis response of grooved fit joints. The schematic diagram and hysteresis rules of Pinching4 uniaxial material model are shown in Figure 3. The definition of Pinching4 uniaxial material includes the skeleton curve, unloading-reloading path and three material failure criteria (i.e., the unloading stiffness degradation criteria, reloading stiffness degradation criteria and strength degradation criteria). The solid line in Figure 3 is the skeleton curve of Pinching4 uniaxial model, which is composed of multiple lines, while the dotted line demonstrates the unloading-reloading path under cyclic loading, which is composed of three-stage lines. The Pinching4 uniaxial material model requires the definition of 39 parameters to completely define the hysteresis behavior, as presented in Figure 3. Values of (ePdi, ePfi), (eNdi, eNfi) define the shape of the backbone curve, while the rest of the parameters describe the material failure criteria. The pinching parameters (rDispP, rForceP, uForceN, etc.), are based upon the ratio of displacement (Disp) or force (Force) to maximum (P) or minimum (N) historic demands at various points in the unloading (u) or reloading (r) curve. Unloading and reloading stiffness degradation as well as strength degradation can be considered in the model using gKi, gDi, and gFi. In addition, energy degradation parameters (gE) and damage type parameters (dmgType) can be defined. The detailed descriptions of the 39 parameters can be found in Mazzoni *et al.* [2006].

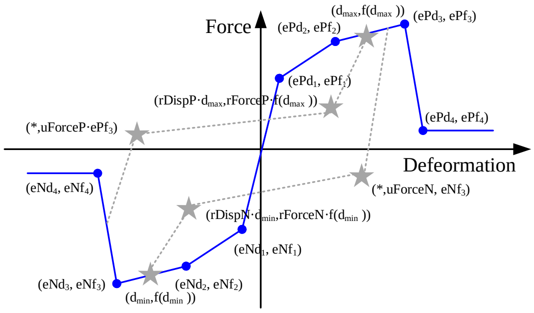

Figure 3. Pinching4 material properties Mazzoni *et al.* [2006]

3.2 VALIDATION OF THE HYSTERESIS MODEL WITH EXPERIMENTAL DATA

Based on the hysteresis curve obtained from the quasi-static tests of grooved fit joints, we calibrate the relevant parameters of Pinching4 uniaxial model and assign the calibrated parameters to the zeroLength element to develop the moment-rotation uniaxial hysteresis model of grooved fit joints. Based on previous research experience, the following principles can be considered for the calibration of Pinching4 parameters: (1) The skeleton curve parameters can be determined according to the characteristic points of the skeleton curve obtained by each specimen in the tests. (2) The unloading-reloading parameters can be determined according to the shape characteristics of the hysteresis curves of the specimens. (3) The failure criteria parameters can be determined according to the unloading stiffness degradation, reloading stiffness degradation, strength degradation and energy degradation of the hysteresis curves of the specimens. In the calibration process, the rotation time histories obtained from the tests were used for displacement control loading. Firstly, the reproduction of the hysteresis curve, the moment time history curve, and the cumulative hysteresis energy dissipation error were considered to calibrate the parameters for each specimen. It is considered to meet the calibration requirements when the peak moment and the maximum cumulative hysteresis energy dissipation errors of each cycle of loading are less than 10%. The calibration results show that the values of the 15 parameters defining the material failure criteria and the parameters defining the energy degradation and damage type are found to be similar for all the specimens. The gKi, gDi, and gFi values are set as 0.1, 0.0, and 0.0, respectively. The gKi, gDi, and gFi values are also set as 0.1, 0.0, and 0.0, respectively. In addition, the gE and dmgType parameters are set as 0.0 and cycle.

The hysteresis curves obtained by Pinching4 uniaxial hysteresis model are compared with the test results in Figure 4. The simulated hysteresis responses of the tested specimens are basically consistent with the test results. The shape of the hysteresis curve obtained by simulation and test is in good agreement. It is indicated that the Pinching4 uniaxial hysteresis model can accurately reproduce the hysteresis response of the grooved fit piping joints. Figure 5 shows the comparison between the time history of bending moment obtained by simulation results of Pinching4 uniaxial hysteresis model and the test results. It can be found that Pinching4 uniaxial hysteresis model can accurately simulate the time history of moment response change of grooved fit joints during the loading process. There is a certain difference between the test results and the simulation results under relatively small rotation angles. The analytical model can basically reproduce the peak moment value in each cycle of loading accurately and error is relatively small. The comparison between the maximum accumulated energy dissipation obtained by Pinching4 uniaxial hysteresis model and the test results was conducted. The error between the simulation results and the test results is within 8%, which is generally in good agreement. Figure 6 shows the accumulated energy dissipation of each loading cycle obtained by analytical results. Compared with the test results, the accumulated energy dissipation increases with the increase of the number of loading cycles, and the results under the same loading cycles are relatively consistent. The comparison indicated that the Pinching4 uniaxial hysteresis model can accurately simulate the accumulated energy dissipation of grooved fit joints and reproduce the change of hysteresis energy dissipation with the increase number of loading cycles. In addition, it should be noted that only one of the three specimes for each type is presented in Figure 2, Figure 4, Figure 5, and Figure 6.

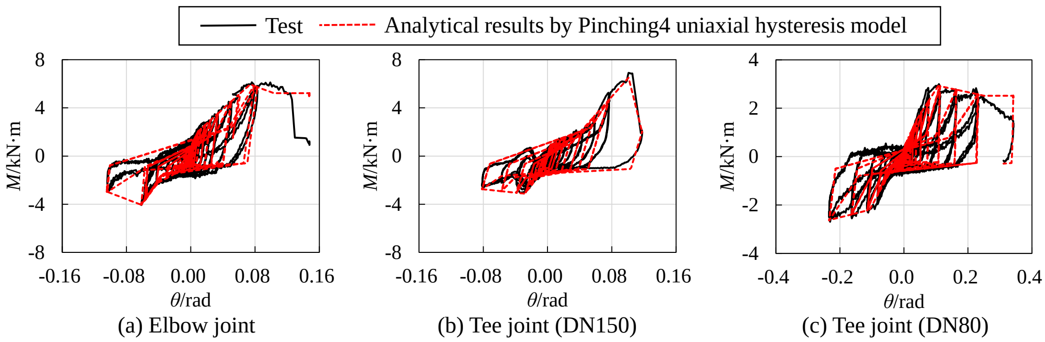

Figure 4. Comparison of hysteresis curves based on Pinching4 uniaxial hysteresis model and test results

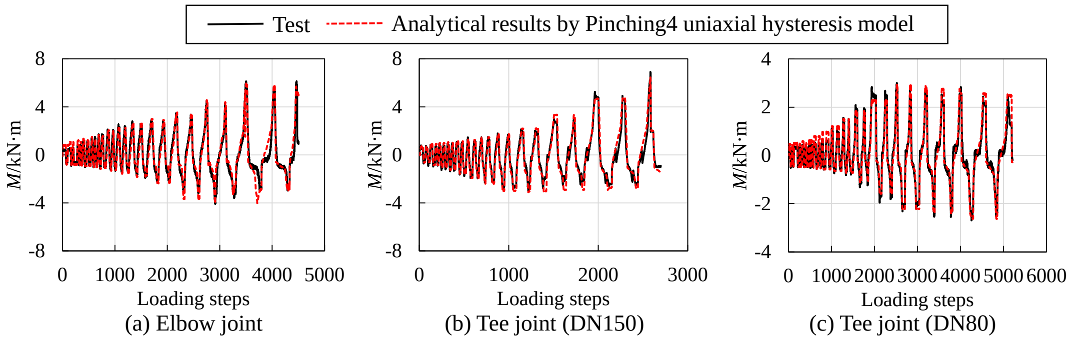

Figure 5. Comparison of moment time history curves based on Pinching4 uniaxial hysteresis model and test results

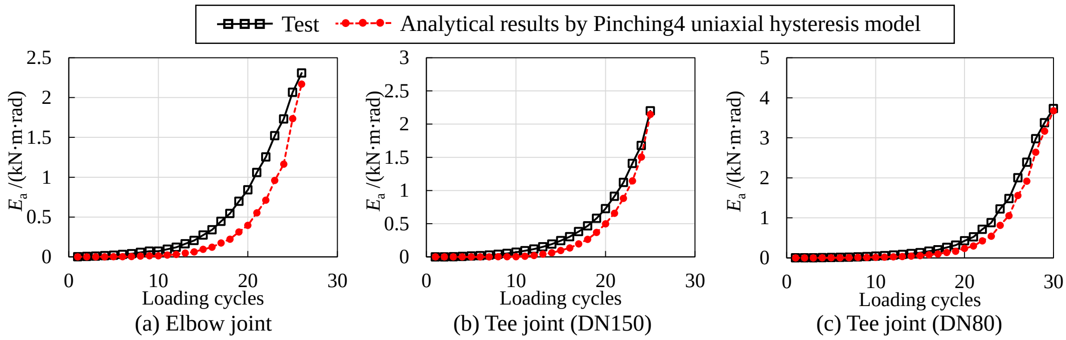

Figure 6. Comparison of accumulated energy dissipation based on Pinching4 uniaxial hysteresis model and test results

3.3 DEVELOPMENT OF A GENERIC HYSTERESIS MODEL

In Section 3.2, the feasibility and accuracy of the moment-rotation hysteresis model are verified based on the comparison between the uniaxial hysteresis model results of Pinching4 and the test results. However, it can also be found that the hysteresis curve obtained in the tests (Figure 2) inevitably has initial defects during the production and installation of the test specimens, which resulted in different test results of the same type of specimens. In ideal condition, the hysteresis curve of the piping joints under positive and negative loading should be symmetrically distributed. However, the test results show that the responses of each specimen under positive and negative loading are different. The test results of the same type of specimens are discrete due to the small size, relatively low bearing capacity and high sensitivity to fabrication and installation accuracy of the test specimens. Therefore, it is necessary to establish a generic hysteresis model to reduce the effects of uncertainties induced from various initial defects in the tests. In this study, there are only three specimens for each type of specimens, the number of specimens is relatively small, and the test results may present inconsistency due to the initial defects. In the calibration process of the generic hysteresis model, a symmetric moment-rotation hysteresis behavior under positive and negative loading of the piping joints were considered. Table 1 shows the calibration results of various parameters for the generic hysteresis models for different types of piping joints. In addition, it should be noted that due to the influence of installation conditions, the relatively small number of test specimens and the assumptions used in this paper, there may be some differences between the calibration results of the parameters and the actual test results. It can be further corrected based on more test results. Figure 7 shows the comparison between the hysteresis curves obtained by the generic hysteresis models and the test results. It can be seen from that the analytical results are in good agreement with the analytical results, indicating that the generic hysteresis model proposed in this study can be used to simulate the hysteresis characteristics of the grooved fit joints.

Table 1. Parameters of generic hysteresis models

Parameter	Elbow joint	DN150	DN80	Parameter	Elbow joint	DN150	DN80
ePf1/kN·m	1.25	1.05	0.35	eNf1/kN·m	-1.25	-1.05	-0.35
ePd1/rad	0.002	0.0004	0.004	eNd1/rad	-0.002	-0.0004	-0.004
ePf2/kN·m	2.05	2.5	1.5	eNf2/kN·m	-2.05	-2.5	-1.5
ePd2/rad	0.007	0.04	0.04	eNd2/rad	-0.007	-0.04	-0.04
ePf3/kN·m	6	6.75	3.25	eNf3/kN·m	-6	-6.75	-3.25
ePd3/rad	0.075	0.11	0.12	eNd3/rad	-0.075	-0.11	-0.12
ePf4/kN·m	4.8	2.1	2.3	eNf4/kN·m	-4.8	-2.1	-2.3
ePd4/rad	0.095	0.125	0.25	eNd4/rad	-0.095	-0.125	-0.25
rDispP	0.6	0.6	0.6	rDispN	0.6	0.6	0.6
rForceP	0.4	0.4	0.35	rForceN	0.4	0.4	0.35
uForceP	-0.1	0.1	0.1	uForceN	0.1	0.1	0.15

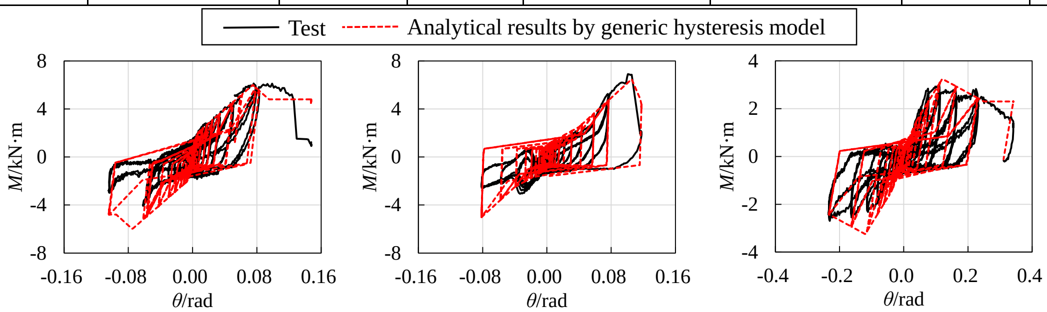

(a) Elbow joint (b) Tee joint (DN150) (c) Tee joint (DN80)

Figure 7. Comparison of skeleton curves based on generic hysteresis models and test results

4.FINITE ELEMENT MODEL OF PIPING-JOINT SYSTEM

4.1 ANALYTICAL MODELS FOR PRIMARY COMPONENTS

The generic hysteresis models of piping joints developed and calibrated in Section 3.3 didn't consider the combination of piping joints and pipeline segment and can not realize the numerical simulation of the whole piping system. Therefore, it is necessary to study how to apply the generic hysteresis models in finite element modeling of piping systems. The finite element model of piping systems is further established in OpenSEES, and its schematic diagram is shown in Figure 8. According to the reported research results, the nonlinear behavior of the pipe segments can be ignored since the moment capacity of the pipe section is much larger than that of the grooved fit joint. The nonlinearity of pipe runs is only concentrated at the rotational degrees of freedom of piping joints. The pipe segments are modeled with ForceBased Beam-Column elements using the elastic cross section properties of the pipes and an elastic material with steel material properties. The modulus of elasticity (E) of the pipe material is taken as 200000 N/mm. The inner diameter of DN150 pipe is 155 mm, the outer diameter is 165 mm while the inner diameter of DN80 pipe is 85 mm, and the outer diameter is 90 mm. The Pinching4 uniaxial material (the parameters are determined in Section 3.3) along with a zeroLength element were used to simulate the moment-rotation response of a piping joint connecting two piping nodes. The axial and shear directions of the zeroLength element are defined by elastic materials, and its material properties can be determined according to the pipe properties. It should be noted that only the elastic material parameters of the axial and shear directions are determined by a previous study [Zhang 2018]. The axial and shear elastic stiffnesses of DN80 are taken as 27802.0 N/mm and 2000000 N/mm, respectively, while that for DN150 are taken as 32958.7 N/mm and 2000000 N/mm, respectively [Zhang 2018].

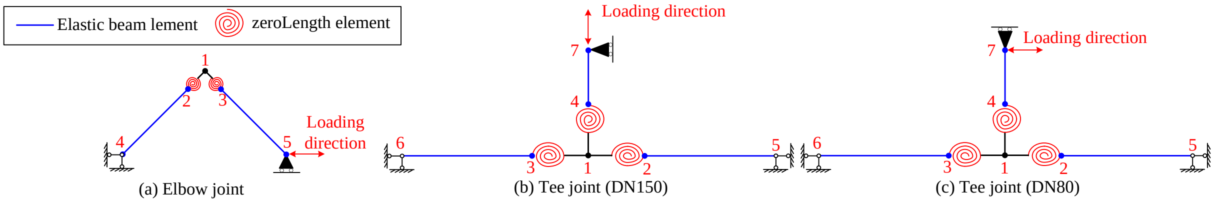

Figure 8. Finite element models of piping system

4.2 VALIDATION OF THE FINITE ELEMENT MODEL WITH EXPERIMENTAL DATA

In the finite element model of piping system, the displacement time histories of the actuator in the tests are used as the input to carry out cyclic loading. The comparison between the moment rotation hysteresis curve at the piping joints obtained by the finite element model and the test results is shown in Figure 9. It can be found that although the control displacement of the loading point is completely consistent with the test, there is a certain gap between the rotation angle at the piping joints obtained by the finite element analysis and the test results. This inconsistency may come from the assumptions used in the modeling process of this study: (1) The tested piping systems are not ideal symmetry system due to the initial defects (e.g., installation error) in the installation process. The failure of the piping joints was all found to be damaged in one side, which resulted in the asymmetric moment-rotation relationship on the left and right sides of the joints. However, the influence of installation error is not considered in the finite element model. It is assumed that the moment-rotation relationship on the left and right sides of the joint is complete symmetrically distributed and unified parameters are used for simulation. (2) In order to improve the applicability of the finite element model of piping system proposed in this study, the generic hysteresis model calibrated in Section 3.3 is used to define the moment-rotation relationship at the rotational degrees of freedom of piping joints, which is not completely matched with each tested specimen. However, in general, the finite element model proposed in this study (Figure 9) can basically simulate the moment-rotation hysteresis response of piping joints.

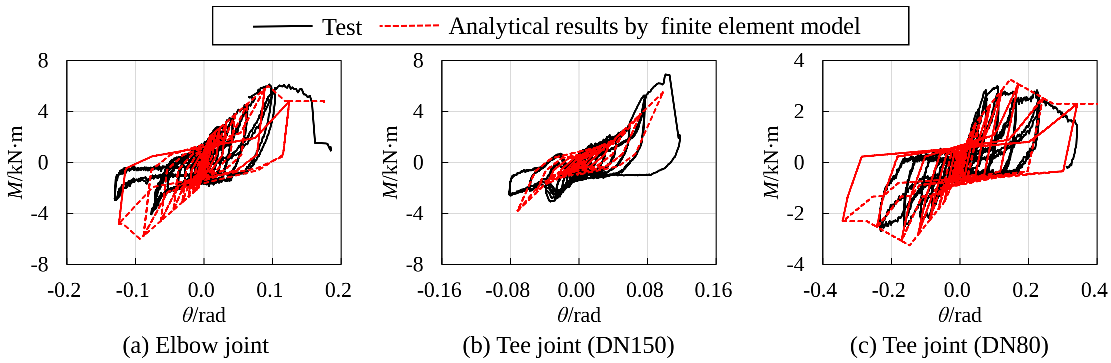

Figure 9. Comparison of hysteresis curves based on finite element model and test results

5.CONCLUSION

The hysteresis model of grooved fit piping joint is developed based on the Pinching4 uniaxial material and zeroLength element in OpenSEES. The parameters of the hysteresis model are calibrated based on the test results in a previous component experiment. The results show that the developed hysteresis model can accurately reproduce the nonlinear hysteresis response of piping joint. In order to reduce the uncertainty induced by initial defects in the tests, a generic hysteresis model is further developed based on the calibration results of each specimen. The generic hysteresis model can be used to simulate the hysteresis characteristics of piping joints. The finite element modeling method of piping system is proposed and the finite element model of piping system is generated based on the generic hysteresis model of piping joint. The proposed finite element model of piping system can basically simulate the hysteresis response of grooved fit joint. The developed finite element model can be used for piping system modeling in a real building. The recorded floor acceleration responses in past earthquakes can be used as input to investigate the seismic demand of the piping system under real earthquakes, and the seismic fragility analysis of the piping system can be carried out in future studies. In addition, it is worth noting that the developed generic hysteresis model in this study is only suitable for the specimens investigated in this test, and the parameters are only valid for the specific size in this study. The feasibility for piping joints with different sizes and materials still needs further study.

6.ACKNOWLEDGMENTS

This research was funded by National Key Research and Development Plan, China (2019YFE0112700), National Natural Science Foundation of China (52208483), National Science Foundation for Distinguished Young Scholars (52125806), China Postdoctoral Science Foundation (2021M701937) and Shuimu Tsinghua Scholar Program (2021SM005).

REFERENCES

Blasi, G., Perrone, D., Aiello, M.A., Pecce, M.R. [2021] "Seismic performance assessment of piping systems in bare and infilled RC buildings," Soil Dynamics and Earthquake Engineering, Vol. 149, 106897.

FEMA. [2007] "Interim protocols for determining seismic performance characteristics of structural and non-structural components through laboratory testing," Federal Emergency Management Agency, Department of Homeland Security (DHS), Michael Mahoney, Project Officer Washington, D.C.

Filiatrault, A., Sullivan, T. [2014] "Performance-based seismic design of non-structural building components: The next frontier of earthquake engineering," Earthquake Engineering and Engineering Vibration, Vol. 13, pp. 17–46.

Ju, B.S., Gupta, A. [2015] "Seismic fragility of threaded tee-joint connections in piping systems," International Journal of Pressure Vessels and Piping, Vol. 132, pp. 106–118.

Mazzoni, S., McKenna, F., Scott, M.H., Fenves, G.L. [2006] "The open system for earthquake engineering simulation (OpenSEES) user command- language manual," OpenSEES user manual.

Miranda, E., Mosqueda, G., Retamales, R., Pekcan, G. [2012]. "Performance of non-structural components during the 27 february 2010 chile earthquake," Earthquake Spectra, Vol. 28, pp. 453–471.

Shang, Q., Qiu, L., Wang, T., Li, J [2022] "Experimental and analytical study on performance of seismic sway braces for suspended piping systems," Journal of Building Engineering, Vol. 57, 104826.

Soroushian, S., Maragakis, M., Jenkins, C., Zaghi, A.E., Echevarria, A. [2014] "Analytical simulation of the performance of ceiling-sprinkler systems in shake table tests performed on a full-scale 5-story building," in: Structures Congress 2014, pp. 1857–1868.

Tian, Y., Filiatrault, A., Mosqueda, G [2014] "Experimental seismic fragility of pressurized fire suppression sprinkler piping joints," Earthquake Spectra, Vol. 30, pp. 1733–1748.

Tian, Y., Filiatrault, A., Mosqueda, G. [2015a] "Seismic response of pressurized fire sprinkler piping systems I: experimental study," Journal of Earthquake Engineering, Vol. 19, pp. 649–673.

Tian, Y., Filiatrault, A., Mosqueda, G. [2015b] "Seismic response of pressurized fire sprinkler piping systems II: numerical study," Journal of Earthquake Engineering, Vol. 19, pp. 674–699.

Wang, T., Shang, Q., Chen, X., Li, J. [2019] "Experiments and fragility analyses of piping systems connected by grooved fit joints with large deformability," Frontiers in Built Environment, Vol. 49. doi:10.1016/j.rcns.2022.06.003.

Zaghi, A.E., Maragakis, E.M., Itani, A., Goodwin, E. [2012] "Experimental and analytical studies of hospital piping assemblies subjected to seismic loading," Earthquake Spectra, Vol. 28, pp. 367–384.

Zhang, T. [2018] "Research on earthquake coupling effects of space truss structure with roofing system and piping system," Master's thesis. Harbin Institute of Technology.

Seismic response analysis of irregular piping networks accounting for vertical acceleration

Gianni Blasi[1], Daniele Perrone[1], Maria Antonietta Aiello[1]

[1]Department of Engineering for Innovation, University of Salento, Italy.

e-mail {gianni.blasi, daniele.perrone, antonietta.aiello}@unisalento.it

Abstract. The evaluation of the seismic performance of piping networks is often difficult due to several parameters, such as complex geometry and input motion properties. Despite several studies have been conducted on this topic, due to the importance of piping networks from a building serviceability standpoint, generalized statements have been hardly obtained. The scope of this study is to investigate several aspects of the dynamic response of different types of irregular piping networks, considering the interaction with the vertical component of the seismic input. A numerical model is developed, accounting for the non-linear behaviour of piping restraint installations and pipe joints. The numerical model is used to perform nonlinear time-history analyses of the system aimed at assessing its dynamic response in a performance-based design framework. The influence of the geometric configuration of the system is investigated by analysing the accelerations and displacements at which the piping networks are subjected.

Keywords: Non-structural components, piping systems, irregular network, vertical seismic action, numerical model.

1 INTRODUCTION

The importance of non-structural components (NSCs) in the seismic performance of buildings is testified by the increasing attention paid by modern seismic codes on this subject (FEMA 412 2002; FEMA E-74 2012; NTC-2018 2018). In the codes, the seismic design/assessment of NSCs in encouraged by providing simplified approaches to compute seismic demand, depending on the ductility capacity, the dynamic properties and the importance of the considered component. On the other hand, several parameters may influence the dynamic response of NSCs, leading to hardships in adopting simplified formulations. In order to overcome the shortcomings of the code procedures in predicting the non-structural seismic demand, recent works proposed simplified procedures accounting for the main parameters influencing the dynamic response of the structure (Vukobratovic and Fajfar 2017; Merino et al. 2020).

In some cases, NSCs have high importance in both serviceability of a building and life-safety (Miranda et al. 2012; Perrone et al. 2018) and the accurate definition of their seismic performance is fundamental. To this regard, piping systems are emblematic, since their operation may be required also in the immediate post-seismic emergency (e.g. fire-fighting systems). For this reason, several research studies were addressed at characterizing the seismic vulnerability of such NSCs, with a focus on fire-protection piping systems in strategic and public buildings. Laboratory tests and numerical analyses were conducted to assess the dynamic behaviour of different piping system configurations (Soroushian et al. 2015b; Tadinada and Gupta 2017) showing failure of pipe joints and piping restraints when subjected to seismic action.

The outcome of the recent research showed major hardships in defining the seismic vulnerability of piping systems, mainly related to the peculiar configurations of the networks, as well as their high irregularity. Despite the high efforts made in characterizing the non-linear response of single components by laboratory testing, such as piping restraining elements (Schneider 1998; Ju and Gupta 2015) or pipe joints (Tian et al. 2013, 2015; Blasi et al. 2018), the definition of simplified models for global analysis is still challenging. In fact, the dynamic properties of piping systems are influenced by a large number of aspects, such as type and location of piping restraints and connections between pipes, presence of vertical and horizontal necks, and so on. It is simply to understand that these aspects are highly connected to specific architectural requirements, which may significantly vary.

In this study, the seismic vulnerability of a fire-fighting piping systems, composed of a main line and two branch lines, is assessed by mean of non-linear dynamic analysis. The piping system is modelled using OpenSees (McKenna et al. 2000), simulating the non-linear hysteretic response of piping restraints and pipe joints to detect damage due to earthquake. Different layouts configurations were considered, varying the location of the branching lines and the number of pipes in the main line, to analyse their influence on the earthquake damage on pipe joints and piping restraints. Numerical time-history analyses were conducted, using, as input motion for the piping systems, floor acceleration time-histories generated from the dynamic analysis of a case study infilled RC frame analysed in a previous work (Blasi et al. 2021).

2 DESCRIPTION OF THE CASE STUDY PIPING SYSTEMS

Two configurations of the piping layout were defined, as shown in **Figure 1**. In both cases, the main line and the two branch lines were composed of 2” and 1” steel pipes, respectively. The dimension of the pipes was defined depending on the required water flow prescribed in (EN 12845 2004). The total length of the main line and both branch lines was equal to 33.0 m. In the first configuration (Model A in **Figure 1**), the first branch line is connected at a distance from the first node of the main line equal to 3.0 meters. In the second configuration (Model B in **Figure 1**), the first and second branch lines are closer compared to Model A. A direct connection of the piping system to the slab of the building was assumed, through gravity and seismic piping restraint installations, characterized by simple cables and trapezes with longitudinal and transverse braces, respectively. In strategic buildings, suspended piping restraints in the main line generally host multiple pipes. Hence, a variation of the total mass of the system and, consequently, its dynamic response, is expected depending on the number of pipes rigidly connected by piping restraints. Since this number is defined based on architectural and serviceability requirements, four configurations were analysed herein, featuring two, four, six and eight pipes with 2" diameter, respectively.

The spacing of seismic restraints was defined based on a simplified seismic design, according to Italian NTC18 (NTC-2018 2018). The equivalent static force, F_{Hr}, acting on the single restraint, was computed according to the formulation:

$$F_{Hr} = \frac{W_{ns} S_{ans}}{q_{ns}} \tag{1}$$

In equation (1), W_{ns} is the piping weight aliquot assigned to the single seismic restraint, evaluated as the product between the pipeline unit weight and the spacing between restraints. S_{ans} is the spectral acceleration demand of the system and q_{ns} is the behaviour factor of the element considered, assumed equal to 1.0. It is worth mentioning that W_{ns} was computed referring to the configuration with higher mass (i.e. with eight pipes along the main line). The mass of the system was computed considering the presence of water in all the pipes in main line and branch lines.

The value of S_{ans} was computed adopting the simplified formulation (2) provided by Italian NTC18 (NTC-2018 2018):

$$S_{ans} = PGA \cdot S_s \left\{ \frac{5 \cdot \left(1 + \frac{z}{h}\right)}{\left[1 + 4\left(1 - \frac{T_{ns1}}{0.8 \cdot T_{f1}}\right)^2\right]} \right\} \tag{2}$$

In equation (2), PGA and S_s are the peak ground acceleration and the soil coefficient, respectively, z and h are the quote of the piping system and the height of the structure, respectively, T_{ns1} and T_{f1} are the fundamental periods of the piping system and the structure, respectively. S_{ans} was calculated according to a conservative approach, assuming $T_{ns1}/T_{f1} = 1$. Based on the simulated design results, the resulting spacing between gravity restraints was equal to 3.0 m, while seismic restraints were included every two gravity restraints (i.e. with 6.0 m spacing).

The numerical model was developed by adopting a lumped plasticity approach. Linear elastic beam elements were used to simulate pipes, including zero-length bi-directional flexural springs (**Figure 1**) to reproduce the hysteretic moment-rotation behaviour at the joint between multiple pipes. The non-linear response of suspended piping seismic restraints was simulated including non-linear zero-length shear springs. Gravity piping restraints were modelled using zero-length axial springs acting in vertical direction (**Figure 1**).

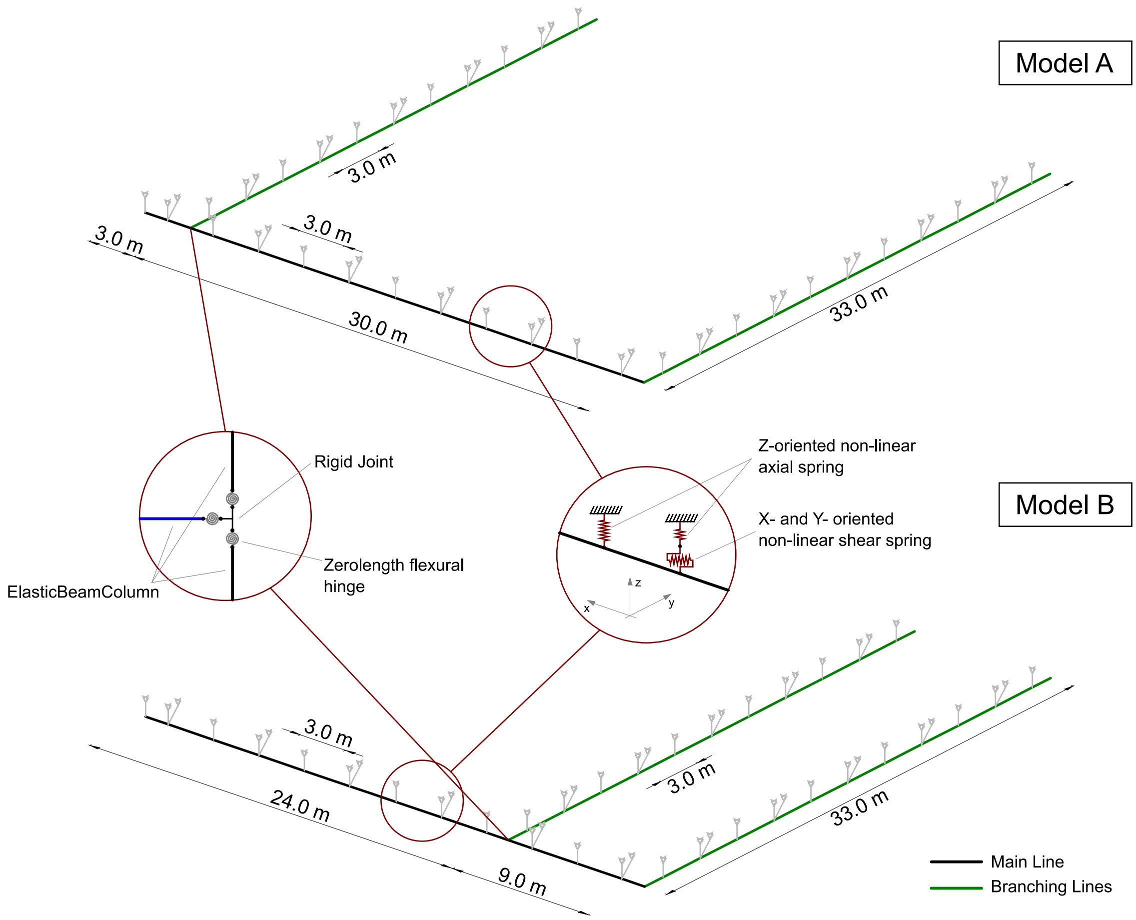

Figure 1. Numerical models developed in OpenSees for time-history analysis.

The mass matrix was defined in the numerical model through a smeared approach, assigning a unit length mass to each linear beam element representing the pipe. The damping of the system was defined adopting the Rayleigh approach (Strutt 1877), by assigning a mass-proportional damping a stiffness-proportional damping to linear elements and lumped hinges, respectively. The damping ratio was assumed equal to 2%, according to the test results obtained by Blasi et al. (Blasi et al. 2018). A summary of the details of the analysed piping networks is provided in Table 1, where suffix -i in the ID code refers to the number of pipes in the main line.

Table 1. Details of the analysed piping networks (i=2, 4, 6, 8).

ID	FP_i	
	Main Line	**Branch lines**
Line length [m]	33.0	33.0
Pipe diameter [mm]	60.3	33.7
Pipe's Young's Modulus [MPa]	194383	194383
Joint type	threaded	threaded
Number of pipes	i	1

2.1 Modelling approach for the non-linear response

In the numerical model adopted in OpenSees, the non-linear response of the pipe connections at pipe-joint interface was simulated using the Pinching4 uniaxial material (Lowes et al. 2003). Two different hysteretic behaviours were defined for 2" and 1" pipe joints, respectively (i.e. for pipe connection in main and branching lines, respectively). The parameters defining the moment-rotation (M-θ) backbone curve and the pinching behaviour were calibrated in order to match the curves obtained from laboratory tests on 2" and 1" pipe joints (Soroushian et al. 2015a; Blasi et al. 2018). The hysteretic M-θ behaviour defined in OpenSees is provided in Figure 2**a** and **b** for 2" and 1" pipe joints, respectively.

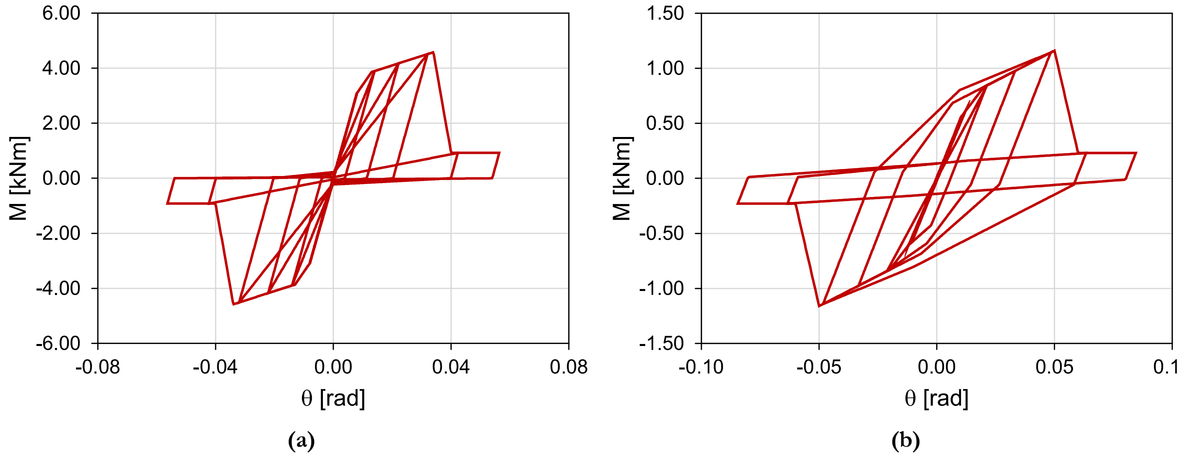

Figure 2. Hysteretic M-θ behaviour in numerical model for (a) 2" and (b) 1" pipe joints.

Both gravity and seismic restraints were simulated including zero-length non-linear springs, acting in vertical and in the two horizontal directions, respectively, and directly connected to the elements simulating the pipes. The mechanical behaviour of gravity supports was defined assuming a tri-linear elastic-hardening-softening Axial force-deformation (F-d) response in tension only (**Figure 3a**). A classical approach was adopted to calibrate the yielding and ultimate point in the F-d bi-linear curve, based on the cross-sectional area of the cables and steel's yielding and ultimate strength, respectively.

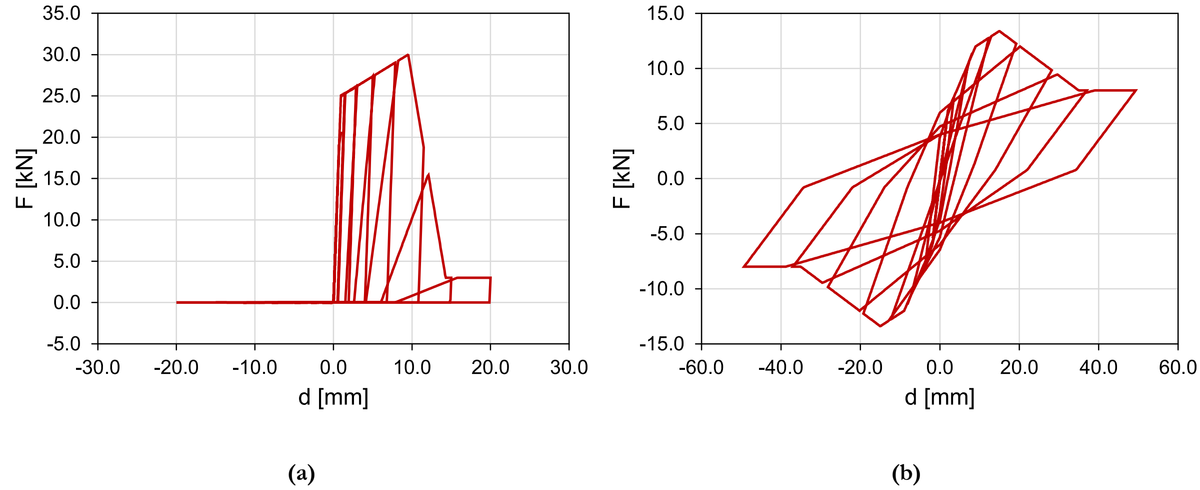

Figure 3. Hysteretic F-d behaviour in numerical model for (a) gravity restraints and (b) seismic restraints.

The softening slope was aimed at simulating tensile failure of the cable, arbitrarily assuming residual strength and deformation values as 10% and 120% of ultimate strength and ultimate deformation, respectively. The F-d behaviour of the lumped springs simulating seismic restraints (**Figure 3b**) corresponds to the X- and Y- lateral response of the braced elements. Similarly to pipe joints, the pinching parameters and the backbone curve points in the F-d curve were calibrated based on laboratory tests results (Perrone et al. 2020).

3 CASCADE ANALYSIS

The floor acceleration time histories employed for the analysis of the piping systems were obtained by a preliminary non-linear dynamic analysis on an eight-storey RC framed building (**Figure 4**), characterized by nine bays at each floor in both principal directions. The inter-storey height and the bay length are equal to 3.4 m and 4.5 m, respectively. The properties of the RC frame elements were defined through a simulate seismic design, according Italian NTC 2018, (NTC-2018 2018). A high seismic hazard zone (Benevento, Campania), a soil type A and a nominal life of the building equal to 100 years were assumed, as prescribed in NTC-18 (NTC-2018 2018) for hospitals. The design peak ground acceleration (PGA) is equal to 0.331 g for a return period equal to 949 years, corresponding to a probability of exceedance equal to 10% in 100 years. The RC frame was modelled considering the infill walls (**Figure 4**), to account for their influence on floor accelerations. More details of the configuration of the building and the modelling approach are available in (Blasi et al. 2021).

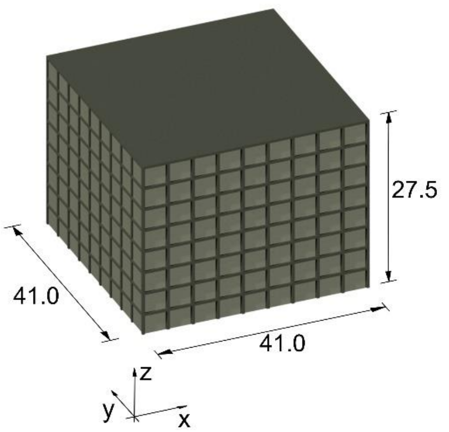

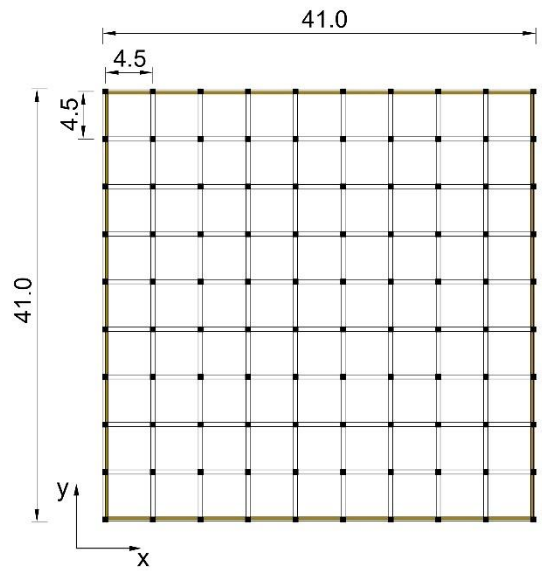

Figure 4. 3D (a) and plan (b) configuration of the RC building analysed.

The seismic input employed for the analysis of the RC frame is composed of a set of 20 unscaled spectrum-compatible ground motions, selected from the European strong-motion database (Ambraseys et al. 2002) using REXEL platform (Iervolino et al. 2010). For each ground motion, the X, Y and Z components of the acceleration were applied in the three principal directions of the structure. The selected set was defined assuming 10% upper and lower deviation tolerance of matching between the average and the design spectrum. The so-defined criterion meets Eurocode 8 provisions (EN 1998-1 2005; NTC-2018 2018). The design spectrum parameters were set as described in the previous section. The 5% damped elastic spectra of the selected ground motions, along with the design spectra and the fundamental period of the frame T_{f1}, are provided in **Figure 5**. It is worth noting that the operation of the building is not required at Life-Safety (LS) performance level; on the other hand, the analysis at this stage might be useful for the damage assessment of the piping system in case of post-elastic response of the structure. Moreover, the stability assessment of NSCs at life-safety performance level is required in modern seismic design codes (e.g. (NTC-2018 2018)).

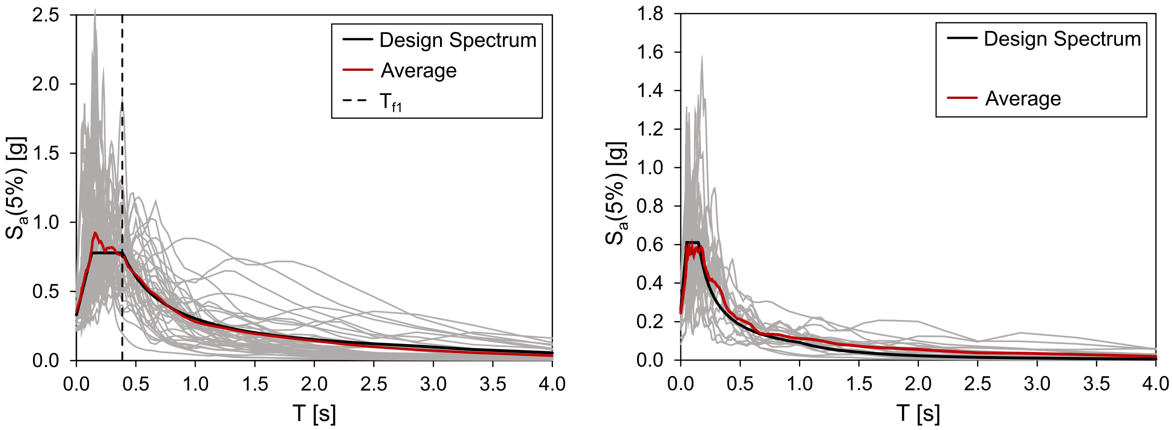

(a) **(b)**

Figure 5. (a) Horizontal and (b) vertical response spectra of the acceleration time histories considered for cascade analysis.

3.1 Nonlinear dynamic analysis results

The seismic vulnerability of the piping systems was investigated by analysing three types of damage: rotation of pipe joints, failure of suspended piping seismic restraints and maximum displacements of the network. The damage rate of pipe joints was expressed as $\boldsymbol{\theta_{max}/\theta_{lim}}$, where $\boldsymbol{\theta_{max}}$ is the maximum rotation obtained from the analysis and $\boldsymbol{\theta_{lim}}$ is the limit rotation. The value of limit rotation is not necessarily equal to the ultimate rotation capacity of the joint prior failure, because leakage of the joints after the attainment of the yielding rotation, $\boldsymbol{\theta_y}$, was observed by Tian et al. (Tian et al. 2013). Since leakage represents loss of operation performance level, the value of $\boldsymbol{\theta_{lim}}$ was set equal to $\boldsymbol{\theta_y}$, according to a conservative approach. In case of suspended piping seismic restraints, the damage rate was computed as $\boldsymbol{\delta_{max}/\delta_{lim}}$, being $\boldsymbol{\delta_{max}}$ the maximum deformation of the braced restraints obtained from the analysis and $\boldsymbol{\delta_{lim}}$ the yielding deformation. Lastly, the maximum displacements ($\boldsymbol{D_{max}}$) at the nodes connected to suspended piping restraints were monitored. These displacements are important for clash detection or for the design of firestops when pipes cross the walls.

The maximum values of $\boldsymbol{\theta_{max}/\theta_{lim}}$, $\boldsymbol{\delta_{max}/\delta_{lim}}$ and $\boldsymbol{D_{max}}$, obtained for each configuration (i.e. FP_2, FP_4, FP_6 and FP_8) of Model A and Model B, are provided in terms of median and Q1-Q3 (i.e. 1^{st} and 3^{rd} quartiles) variation range among the 20 input motions. Figure 6 reports the results of $\boldsymbol{\theta_{max}/\theta_{lim}}$ for 2" and 1" pipe joints (Figure 6a and Figure 6b respectively). Referring to 2" pipe joints, a significantly higher damage is observed for Model A compared to Model B, particularly as the number of pipes in the main line increases (FP_6 and FP_8). In Model A, the median value of $\boldsymbol{\theta_{max}/\theta_{lim}}$ was equal to 0.40, 0.93, 1.43 and 2.36 for FP_1, FP_2, FP_3 and FP_4, respectively. It is worth noting that the value of $\boldsymbol{\theta_{max}/\theta_{lim}} > 1$, obtained for FP_6 and FP_8, means yielding of the pipe joint and, consequently, loss of operation of the system. Hence, the higher mass of main line significantly affected the performance of the system in case of Model A. On the other hand, a negligible influence of this parameter was observed referring to Model B, where the median

$\theta_{max}/\theta_{lim}$ was equal to 0.14, 0.44, 0.37 and 0.42 for FP_1, FP_2, FP_3 and FP_4, respectively. In this case, the value of θ_{max} obtained for was lower than the yielding rotation for all the configurations.

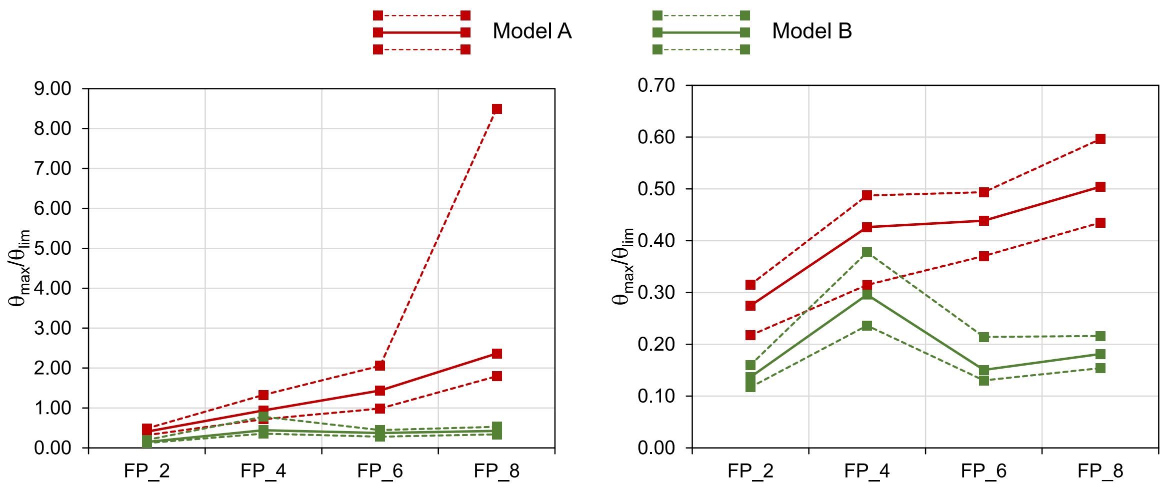

Figure 6. Median values (solid) and Q1-Q3 range (dashed) for $\theta_{max}/\theta_{lim}$ obtained for each configuration in case of 2" (a) and 1" pipes (b).

The higher 2" joints rotation in Model A may be caused by higher participating mass in local mode involving transverse translation of the main line, which led to noticeable relative motion with respect to branching lines. Referring to 1" joints, no significant damage was detected, because the low mass of the branching lines led to negligible relative motion with respect to the main line. On the other hand, the position of the branch line seems to significantly affect the maximum rotation at the joint, particularly in case of FP_6 and FP_8. In fact, the value of $\theta_{max}/\theta_{lim}$ was 50%, 31%, 66% and 64% lower in Model B compared to Model A, for FP_2, FP_4, FP_6 and FP_8, respectively.

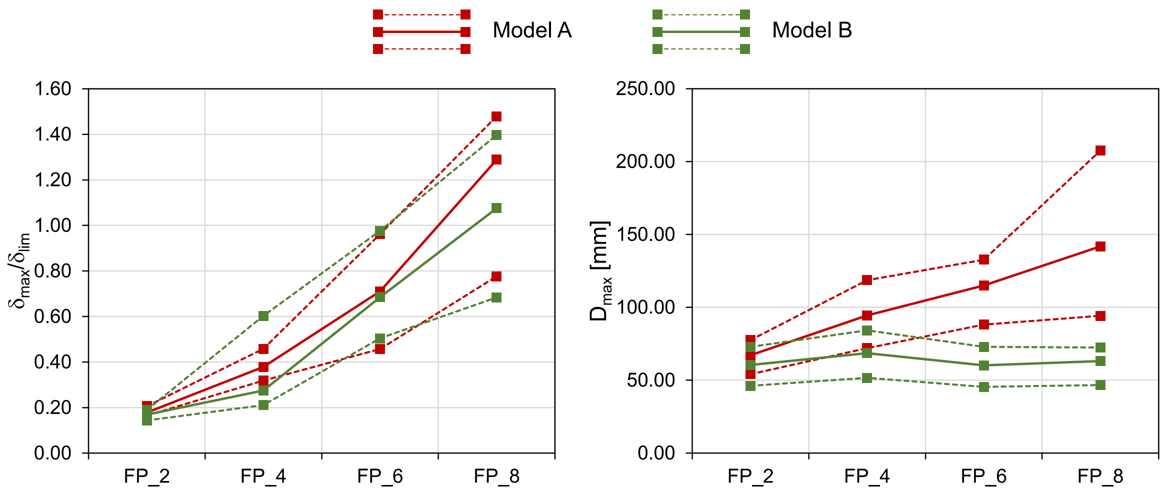

Figure 7. Median values (solid) and Q1-Q3 range (dashed) for (a) $\delta_{max}/\delta_{lim}$ and (b) D_{max}, obtained for each configuration.

Referring to $\delta_{max}/\delta_{lim}$, no significant influence of the position of the branch lines on the results was observed (Figure 7a). Despite higher median values were obtained in Model A compared to Model B, the Q1-Q3 ranges are similar for each configuration considered. It is worth noting that $\delta_{max}/\delta_{lim}$ and the number of pipes in the main lines are almost linearly proportional. This aspect suggests the suitability of straightforward design approaches, assuming the demand on the seismic restraint being linearly proportional to the mass of the pipe line (e.g. equivalent static approach). As expected, yielding of the seismic restraints was observed on case of FP_8, due to the higher mass of the main line. Lastly, the results obtained for the maximum displacement D_{max} of the piping systems are provided in Figure 7b. The influence of the position of branch lines is higher increasing the number of pipes in the main line. In fact, the median value of D_{max} decreased by 48% and 55% in Model B compared to Model A, for FP_6 and FP_8, respectively. Additionally, higher variability of the results is observed in Model A compared to model B.

The maximum displacement was obtained along different directions comparing the two models analysed (Y and X in Model A and B, respectively). As previously discussed, this result may be caused by the higher participating mass, in Model A, obtained for local modes involving transverse translation of the main line. In some cases, the maximum displacements were obtained along the vertical direction, confirming that simplified approaches neglecting the vertical component of seismic acceleration may lead to unconservative results.

4 CONCLUSIONS

The cascade analysis performed in this study was aimed at assessing the influence of the mass and the geometry of a piping layout on its seismic performance. The modelling approach employed allowed to analyse different types of damage in the piping system, such as pipe joints and suspended piping restraints deformations and maximum displacements of the network. Additionally, the vertical component of the earthquake acceleration was considered, in order to obtain a comprehensive assessment of the seismic response of the system subjected to 3-directional floor motion.

The results of the numerical simulation showed an influence of the geometry of the layout on the maximum pipe joints' rotations and the maximum displacements. The position of branch lines influenced the occurrence of pipe-joint yielding in case of high number of pipes in the main line, because of the different participating mass in local modes. The damage on suspended piping restraints, seemed not significantly affected by the geometry of the layout. On the other hand, a clear dependency between the maximum deformation of seismic restraints and mass of the main line was detected. The results obtained in this paper evidence that simplified approaches may be reliable for the design of seismic restraints regardless of the geometry of the layout. However, local modes may lead to noticeable variation of the damage on pipe joints and, consequently, on the operation of the piping system. Additionally, the geometry of the layout was found to influence the maximum displacements of the system, particularly in case of high number of pipes in main line. In some cases, the interaction with the vertical component of the seismic acceleration led to high displacements in the vertical direction, suggesting the need of considering three-dimensional seismic action when dealing with such complex systems.

This work evidences the hardships in analysing the seismic response of piping systems, due to their peculiar configuration. Some aspects were not considered in this work and need further investigation, such as the presence of different types of gravity and seismic restraints and presence of vertical necks, which may significantly affect maximum displacements/joint rotations due to earthquake action.

ACKNOWLEDGEMENTS

The authors gratefully acknowledge the support of "The Laboratories University Network of Seismic Engineering" (RELUIS) thanks to the research project DPC-RELUIS 2022-2024.

REFERENCES

Ambraseys NN, Smit P, Douglas J, et al (2002) Internet site for European strong-motion data. In: Eur. Comm. Res. Gen. Environ. Clim. Program. http://www.isesd.hi.is/ESD_Local/frameset.htm

Blasi G, Aiello MA, Maddaloni G, Pecce MR (2018) Seismic response evaluation of medical gas and fire-protection pipelines' Tee-Joints. Eng Struct 173:1039–1053

Blasi G, Perrone D, Aiello MA, Pecce MR (2021) Seismic performance assessment of piping systems in bare and infilled RC buildings. Soil Dyn Earthq Eng 149:. https://doi.org/10.1016/j.soildyn.2021.106897

EN 12845 (2004) Fixed firefighting systems - Automatic sprinkler systems - Design, installation and maintenance. European Standard

EN 1998-1 (2005) Eurocode 8 - Design of structures for earthquake resistance - Part 1: General rules, seismic actions and rules for buildings. European Standard

FEMA 412 (2002) Seismic restraints for mechanical equipment. Federal Emergency Menagement Agency

FEMA E-74 (2012) Reducing the risks of nonstructural earthquake damage – A practical guide

Iervolino I, Galasso C, Cosenza E (2010) REXEL: Computer aided record selection for code-based seismic structural analysis. Bull Earthq Eng 8:339–362

Ju BS, Gupta A (2015) Seismic fragility of threaded Tee-joint connections in piping systems. Int J Press Vessel Pip 132–133:106–118. https://doi.org/10.1016/j.ijpvp.2015.06.001

Lowes LN, Mitra N, Altoontash A (2003) A Beam-Column Joint Model for Simulating the Earthquake Response of Reinforced Concrete Frames. University of California, Berkeley

McKenna F, Fenves GL, Scott MH, Jeremir B (2000) Open system for earthquake engineering simulation, OpenSEES. University of Berkeley

Merino RJ, Perrone D, Filiatrault A (2020) Consistent floor response spectra for performance-based seismic design of nonstructural elements. Earthq Eng Struct Dyn 49:261–284. https://doi.org/10.1002/eqe.3236

Miranda E, Mosqueda G, Retamales R, Pekcan G (2012) Performance of Nonstructural Components during the 27 February 2010 Chile Earthquake. Earthq Spectra 28:453–471. https://doi.org/10.1193/1.4000032

NTC-2018 (2018) Aggiornamento delle «Norme tecniche per le costruzioni». D.M. 17 gennaio 2018, Italy

Perrone D, Calvi PM, Nascimbene R, et al (2018) Seismic performance of non-structural elements during the 2016 Central Italy earthquake. Bull Earthq Eng 1–23. https://doi.org/10.1007/s10518-018-0361-5

Perrone D, Filiatrault A, Peloso S, et al (2020) Experimental seismic response evaluation of suspended piping restraint installations. Bull Earthq Eng 18:1499–1524. https://doi.org/10.1007/s10518-019-00755-5

Schneider SP (1998) Flexural capacity of pressurized steel pipies. J Struct Eng 124:330–340

Soroushian S, Zaghi AE, Maragakis E, et al (2015a) Analytical seismic fragility analyses of fire sprinkler piping systems with threaded joints. Earthq Spectra 31:1125–1155. https://doi.org/10.1193/083112EQS277M

Soroushian S, Zaghi AE, Maragakis E "Manos," et al (2015b) Seismic Fragility Study of Fire Sprinkler Piping Systems with Grooved Fit Joints. J Struct Eng 141:04014157

Strutt JW (1877) The theory of sound. Macmillan and co., London (UK)

Tadinada SK, Gupta A (2017) Structural fragility of T-joint connections in large-scale piping systems using equivalent elastic time-history simulations. Struct Saf 65:49–59. https://doi.org/10.1016/j.strusafe.2016.12.003

Tian Y, Filiatrault A, Mosqueda G (2013) Experimental Seismic Study of Pressurized Fire Sprinkler Piping Subsystems. Technical Report MCEER-13-0001

Tian Y, Filiatrault A, Mosqueda G (2015) Seismic response of pressurized fire sprinkler piping systems II: Numerical study. J Earthq Eng 19:674–699. https://doi.org/10.1080/13632469.2014.994148

Vukobratovic V, Fajfar P (2017) Code-oriented floor acceleration spectra for building structures. Bull Earthq Eng 15:3013–3026

Modelling One-dimensional Rolling Response of Rigid Bodies on Casters Using Physics Engine Simulation

Cong Xu[1], Quincy Ma[2], and Masahiro Kurata[3]

[1] PhD Candidate, Dept. of Civil & Environmental Engineering, The University of Auckland, NEW ZEALAND
cxu413@aucklanduni.ac.nz
[2] Senior Lecturer, Dept. of Civil & Environmental Engineering, The University of Auckland, NEW ZEALAND
q.ma@auckland.ac.nz
[3] Associate Professor, Disaster Prevention Research Institute, Kyoto Univ., Kyoto 6110011, JAPAN
kurata.masahiro.5c@kyoto-u.ac.jp

Abstract. In hospitals, many contents and medical equipment such as incubators, ventilators and anaesthetic machines are placed on casters. During an earthquake, they may exhibit complex 3-dimensional motion, including rolling, sliding, swivelling, rocking and a combination of the above. There are limited studies on the dynamics of rigid objects on casters. Due to the complexity and sensitivity of this problem, it is difficult to have an accurate yet easy to use model for engineers to predict the seismic performance of building contents. This preliminary study explores the use of physics engine based simulation for the modelling the one-dimensional rolling response of such objects. A subset of 50 simple rolling experiments are reported herein, outlining the process from establishing the rolling resistance relationship to establishing the required parameters required for successful simulations in Unity. A custom programming script has been developed to model the rolling resistance force. A comparison of the Unity simulation results with the physical testing confirms the accuracy of the physics engine simulation and confirms the potential of the use of physics engine simulation for more complex scenarios.

Keywords: Physics engine simulation, Non-structural components, Casters & Wheels, Rolling equipment, Dynamic modelling.

1.Introduction

Hospitals serve an important post-disaster function and are expected to remain operational during and after a major earthquake. Past earthquakes have shown that the performance of non-structural elements (NSEs) significantly affects hospital operations, and recent experience is that NSEs in hospitals have not been performing satisfactorily in earthquakes (FEMA, 2015; Fierro et al., 2011; Gould & Marshall, 2012; Miranda et al., 2012; Motosaka & Mitsuji, 2012). Past surveys showed that up to 80% of the investment of a building lies in non-structural elements and equipment. In cases of hospitals, the portion is even higher and reaches 90% (Taghavi & Miranda, 2003). Because of the large financial investment, NSEs damage typically contributes significantly to buildings' direct economic losses resulting from earthquakes (Miranda et al., 2012). Many NSEs are unanchored for moveability requirements in hospitals, making them prone to overturning during earthquakes. The overturning of partition walls and shelves poses a particularly hazardous condition for patients and other occupants and they can block egress routes. Moreover, damage to medical equipment due to earthquakes can cause significant economic loss. Another concern is that medical equipment on casters or wheels could displace significantly during earthquakes, leading to collision with nearby objects and potentially overturning. Even without apparent damage, the accelerations from collisions can cause some acceleration-sensitive medical equipment to lose functionality. All the above reduce the ability of a hospital to treat injuries and save lives in major earthquakes.

The dynamic response of a rigid object on casters is more complex than it may first appear. A caster is a mechanical assembly comprising one or more wheels, an axle, a fork supporting the axle and wheel(s), and possibly other accessories such as brakes or locking devices (ANSI ICWM, 2018). There can be many different design parameters for a caster amongst all options, including wheel size, arrangement, stem offset, caster angle, wheel material, brakes, swivel or rigid casters, plate or stem mounting and mounting positions. Figure 1 (Left) illustrates the definition of some of these parameters.

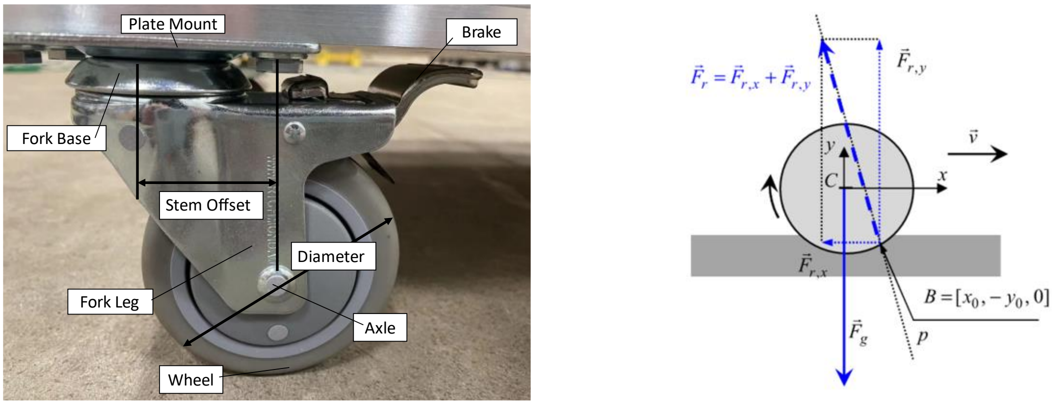

Figure 1 Definitions of caster parameters (Left) and Schematic distribution of elementary forces along the contact surface of a hard rolling cylinder and a soft horizontal underlay (Right) (Vozdecký et al., 2014).

A caster can roll, skid, swivel or a combination of all modes simultaneously. Objects supported on casters can exhibit three-dimensional translation, rotation and rocking motion. All these lead to the complex dynamic motions of the system.

Although extensive studies have covered the dynamics of rocking objects, studies focused on the objects on casters permitted to rock are rare. Chatzis and Smyth (2013) proposed a theoretical model for examining the seismic response of a rigid object with wheels that can swivel and roll on a flexible support medium. They used a concentrated springs model to simulate the deformability of the support medium and a rolling-friction formulation to model the vertical and horizontal reaction forces. Although this theoretical model provided useful insights, it was mathematically complex and not easy for engineers to implement. Other experimental endeavours exist, such as that by Nikfar and Konstantinidis (2017, 2019), which subjected an ultrasound machine on two non-swivelling wheels and two casters and a cart with four casters to earthquake ground motion using a shaking table, and that by Hutchinson et al. (2013), with involved full-scale testing of a five story reinforced concrete building including equipment on casters.

Researchers have also applied classical finite element analysis (FEA) to model the caster rolling problem (Jose Luis Martin, 2015). However, owing to the complex interactions between rocking, rolling and sliding modes, the sensitivity of the problem to parameters selection, the large geometric nonlinearity and the problem's history dependency, simulations often are very computation resource intensive, difficult to validate, and difficult to be transferred from one situation to another.

Physics engine simulation is a modelling technique that relies on Newtonian mechanics to simulate an object's dynamic response (Boeing & Braunl, 2007; Laurell, 2008). It is a powerful and user-friendly tool that has been successfully applied to simulate the motion of the complex system, including robotics (Degrave et al., 2019), civil engineering (Izadi & Bezuijen, 2018), particle simulation (He & Zheng, 2020), medical training (Ricardez et al., 2018), and even disaster simulation (Kim et al., 2016). Physics engine simulation has been shown to be able to accurately model a rigid block's complex rocking behaviour (Ma et al., 2018). However, limited research is available validating its use to simulate the dynamic response of equipment on casters.

This study advances the use of physics engine simulations for accurately modelling rigid bodies on casters. The study focuses on modelling medical equipment on casters and other common objects found in hospitals. This paper presents sets of preliminary characterisation experiments involving the use of three casters types and two different floor coverings. The experiments focus on gaining insight on casters' critical parameters, such as rolling resistance on several floor coverings. This paper sets the scene for future research considering more complex dynamics.

This study utilises Unity, a physics engine based software, to conduct dynamic computer simulations. Unity's simulation results are compared to the experimental results for a rolling trolley to assess Unity's capability. 50 constant force pulling tests are included in this study. A motion capture (MoCap) system measured the 3-dimensional displacement of the trolley during each test.

2.Background

2.1 PHYSICS ENGINE

Physics engines are computer software that simulates the dynamics of physical systems following a modern adaptation of Discrete Element Method. A key tenant of the underlying analysis is dividing a system into interacting bodies and particles. Physics engines are widely applied to game development, virtual reality systems, and the film industry to produce realistic Computer Generated Imagery (CGI). There is generally a trade-off between high precision and the speed of simulation. Physics engines have also been used in accurate scientific applications, such as examples found in computation fluid dynamics and geotechnical engineering (Götz et al., 2010; He et al., 2021). The substantial computational capacity offered by GPUs' parallel processing architecture makes it possible to expedite the rigid body simulation of numerous rigid bodies, which was previously challenging to complete in real-time (Nguyen, 2008). Rolling problems are not well suited to structural finite element framework, due to the large displacement, low stiffness, and changing boundary conditions nature of the problem. Physics engine simulations in contrast are well suited for simulating this type of problems. Basic rolling behaviour can be modelled using Unity's built-in functions.

Physic engines consist of four main subsystems: contact detection, contact resolution, force computation, and state integration (Hecker, 2000). A schematic of these subsystems is shown in Figure 2. Unity uses Nvidia PhysX as its physics engine for 3D projects.

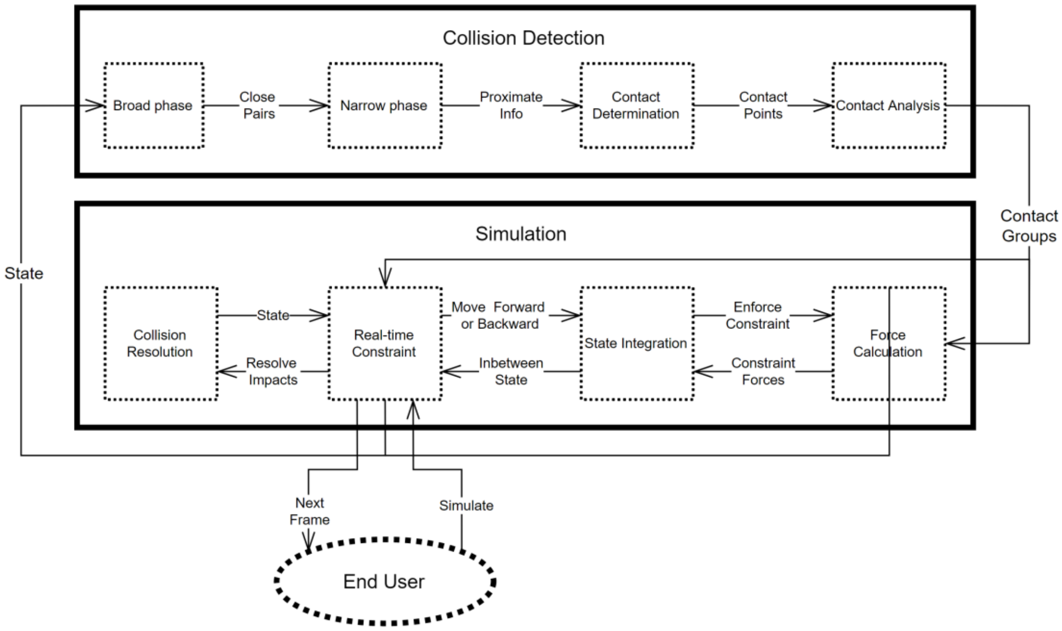

Figure 2 The modules of the physics engines adapted from (Laurell, 2008).

2.2 MOTION CAPTURE SYSTEM

MoCap system uses markers attached to the objects to capture their real-time displacements. For this study, a marker-based motion capture system captured submillimetre-accurate 3D measurements of the caster trolley motion. The system consisted of six Optitrack Prime 41 cameras. It operated on the infrared spectrum and at a sampling rate of 120 frames per second. Using a MoCap system simplified instrumentation and ensured the instrumentation did not influence the specimen motion.

2.3 ROLLING PHYSICS THEORY

The difficulty of simulating the dynamic response of castor objects stems from the compounding challenge of sensitive and nonlinear components. On an individual component level, rolling wheels and twisting casters are low-stiffness and thus prone to numerical instability and initial condition sensitivity. When castors operate in an assembly, this activates additional global degrees of freedom whose responses are strongly history-dependent. For instance, inaccurate tracking of the twisting of a single castor will cause the object to change course and leads to erroneous subsequent motion prediction. Likewise, for incorrect tracking of wheel speed, wheel sliding and interaction with future forcing.

Vozdecký et al. (2014) present a thorough review of several mechanics-based analytical rolling models. These models can be categorised into three groups based on whether the roller and/or the underlay medium deforms during the rolling motion. Some commonly used models include the hard body rolling along a deformable underlay that has symmetric deformation (Bilobran & Angelo, 2013) or a soft body rolling on a hard underlay (Cross, 2015).

Rolling resistance (f_r) is defined in this paper as the generalised nonconservative force that resists the rolling motion as a wheel rolls along a surface. The exact cause of rolling resistance needs to be established. Past research has attributed it to sources such as the deformation and hysteresis of wheels and ground in motion (Wong, 2001), frictional resistance of joints, micro slip and friction on the contact surface and surface adhesion (Ai et al., 2011). Many factors can affect rolling resistance. The most significant factors include wheel load, wheel diameter, wheel material, flooring material, and floor conditions (roughness, cleanliness, slope) (Lippert & Spektor, 2013). This study adopts Equation (1) as the empirical relationship between the rolling resistance force (f_r), the coefficient of rolling resistance (C_r), the wheel radius (R) and the normal force (N) for a rolling wheel.

$$f_r = \frac{C_r}{R} \times N \tag{1}$$

The underlying assumption for the study aligns with the idealised deterministic rolling model as summarised in Vozdecký (2014). This model assumes a rigid wheel is rolling on the deformable ground, with the ground providing an undetermined distribution of elementary forces. Vozdecký model assumes the sum of the elementary forces to a resultant elementary force $\vec{F}$, which drives the wheel acceleration. The rolling resistance force (f_r) in Equation (1) is the x component of the resultant elementary force ($\vec{F}_{r,x}$) in Vozdecký model. A free-body diagram of the forces of the arrangement is shown in Figure 1 (Right).

3.Pulling Test Procedure

A series of pulling tests were carefully conducted in the laboratory. A total of 50 pulling test trials were carried out. These tests cover possible caster types, caster arrangement, flooring and initial conditions combinations for the purpose of establishing simulation parameters for the rolling problem. The test setup was designed to ensure each trial was repeatable and minimise uncertainties in boundary conditions.

The test data aims to calibrate the corresponding settings in a Unity rolling trolley simulation model. The parameters of interest include the static friction coefficient μ_s, kinetic friction coefficient μ_k, coefficient of restitution e, and the twisting resistance force. These correspond to Static Friction, Dynamic Friction, Bounciness and hinge joints' Spring and Damper values in Unity. There is no corresponding setting or mechanism to model rolling resistance in Unity. Thus, a C# script was created to translate the rolling resistance coefficient into a constantly updating force that is applied to each wheel.

Two vinyl floor coverings and three caster types are selected for testing. The floorings are commercial products currently used in new patient wards and corridors in New Zealand hospitals. The selected casters have wheel sizes and materials that are common in practice. All casters in this study can swivel. The detailed caster specifications are presented in Table 1.

Table 1 Casters specifications.

ID	Wheel Material	Wheel Diameter	Wheel Width	Caster Height	Stem Offset
R100	Institutional Rubber	100mm	32mm	131mm	84mm
R125	Institutional Rubber	125mm	32mm	160mm	100mm
P100	Polyurethane	100mm	32mm	131mm	84mm

3.1 EXPERIMENT SETUP

The rolling specimen for the experiment is a 96.5 kg steel trolley, with its centre of mass located at its planar geometric centre 487 mm above the bottom of the base plate. The trolly rest on the floor covering of interest, which is in turn secured to a level concrete floor. Concrete pavers with a mass of 13.6 kg each are placed onto the trolley in some trials to simulate varying wheel normal force. Detailed dimensions of the trolley are shown in Figure 3.

During each test trial, the trolley is set into motion by releasing the trolley restraint abruptly. This allows a drop weight connected with the trolley via a steel cable and pulley arrangement to apply a constant force to the specimen. Figure 3 shows a schematic of the pulling test setup. A load cell is connected in series with the pre-tensioned steel cable, and it records the real-time pulling force acting on the trolley. Two string potentiometers record the displacements of the trolley and the drop weight. An accelerometer sits on top of the trolley and it measures the trolley acceleration during the pulling test.

Six OptiTrack cameras are placed around the specimen as the principal measurement system. One of the cameras is located down low and focuses on capturing the motion of the wheels. The system produces ± 0.10 mm accurate 3D position measurements at 120 Hz, of 12 selected locations of the setup designated by reflective markers.

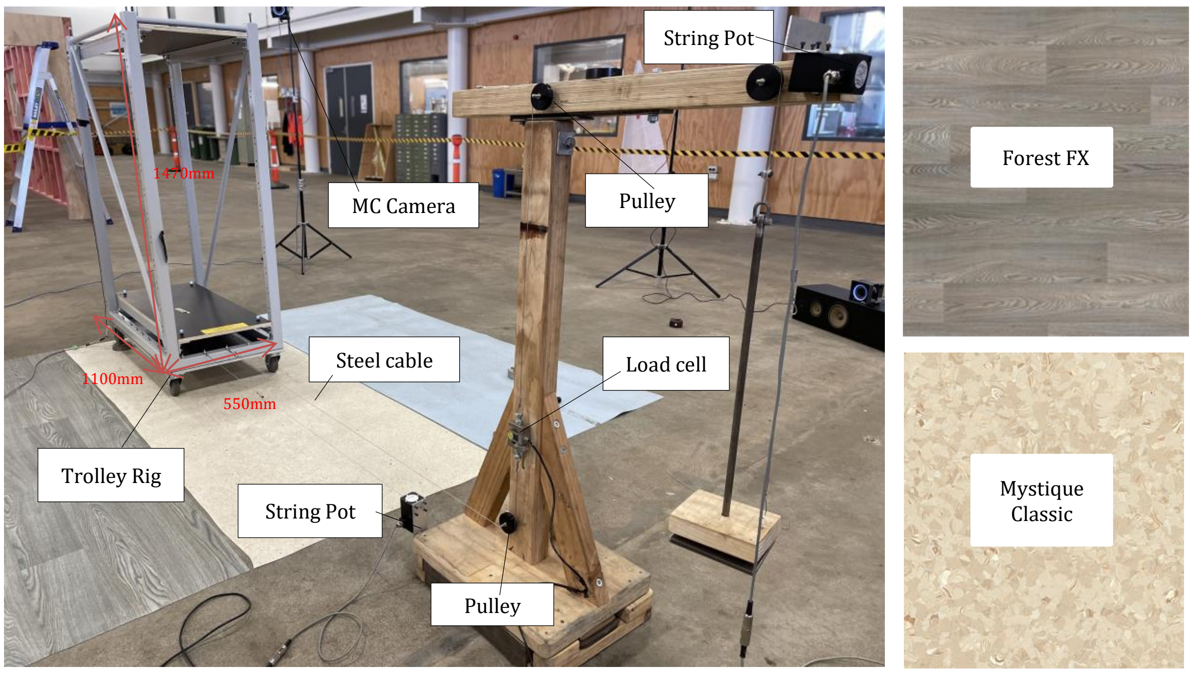

Figure 3 Left: The pulling test setup. Right: Vinyl floor coverings used in the pulling test (Polyflor, 2014).

3.2 RESULTS

There are four phases of trolley motion in a typical test trial.

I. The trolley is held still and in static force equilibrium. The constant force of the drop weight is resisted by blocks placed in front of the casters.

II. The blocks are released and the trolley is set into motion. The trolley accelerates due to the unbalanced force provided by the drop weight via the cable and pulley arrangement. The drop weight falls freely to the ground applying a nearly constant force.

III. The drop weight reaches the ground, and the steel cable no longer applies any force to the trolley. The trolley slowly decelerates due to rolling resistance and other frictional losses while experiencing the very small tension of the string potentiometer.

IV. The test is terminated when either the trolley reaches the end of the flooring or it comes to a rest.

Figure 4 shows the trolley's indicative displacement, velocity and acceleration time history and the cable force time history during a particular test trial.

The rolling resistance force provided by the casters can be evaluated by considering the dynamic forces equilibrium of the system. The condition of which is summarised in the free body diagram and the corresponding equations are shown in Figure 5. It is noteworthy that the string potentiometers' force is accounted for and removed during preliminary data processing, so it is not included in the figure.

The time history response shows that the setup successfully achieved the constant force and constant acceleration condition during the pulling phase (Phase II). Furthermore, the rolling resistance can be calculated from the measured pulling forces and the acceleration data following the equations in Figure 5. Average acceleration over Phases II and III instead of instantaneous values are used for the calculation to minimise the effects of measurement errors.

Figure 6 presents a plot of rolling resistance f_r against the wheel's normal force N. Both figures support the chosen theoretical rolling resistance relationship shown in Equation (1). In these experiments, the floor covering choice has no effect on f_r . Figure 7 (Left) shows the average rolling resistance force plots in the test trials for two wheel diameters with the same wheel material and two different flooring materials. This confirms rolling resistance decreases with wheel diameters. Figure 7 (Right) plots the rolling resistance force against velocity for tests using the R100 casters. Within the test parameters, rolling speed had no effect on f_r.

Figure 8 shows the Unity user interface and the trolley model for this study. The trolley Unity model consists of an assembly of rigid bodies. Figure 9 shows a schematic of how they are connected and related to each other. Hinge joint connections enable the swivelling of the wheel fork and the rotating of each wheel about its axle.

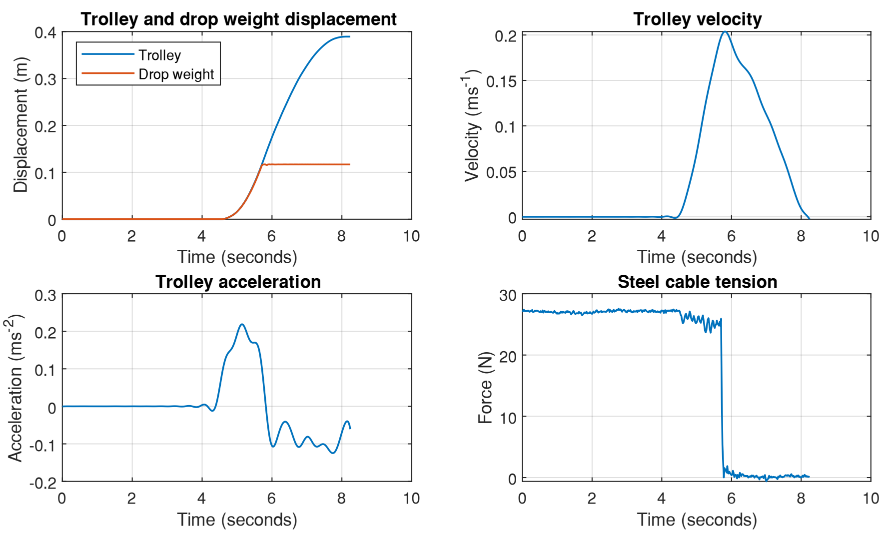

Figure 4 Time history response of a pulling test with 100mm diameter rubber wheel caster.

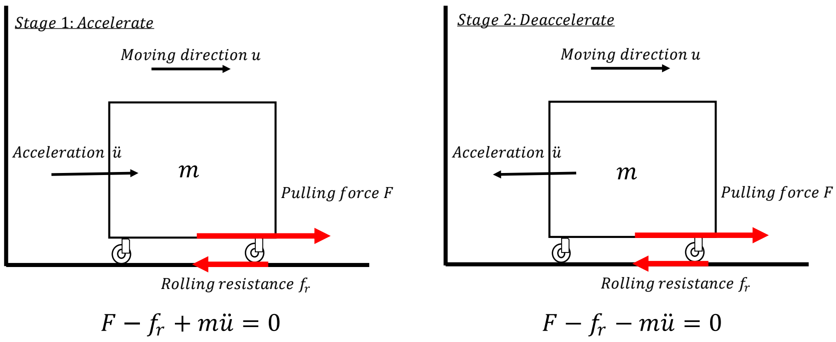

Figure 5 Free body diagram of the trolley.

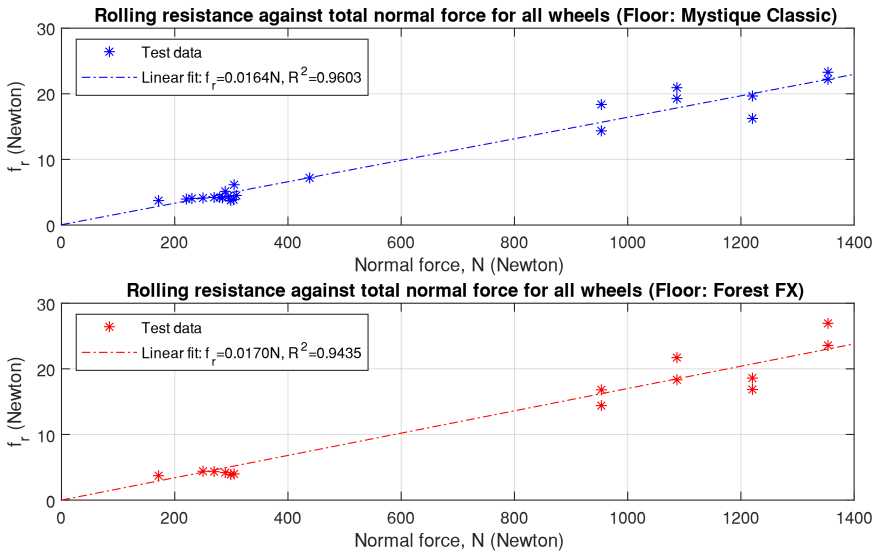

Figure 6 The total normal force on all wheels against rolling resistance.

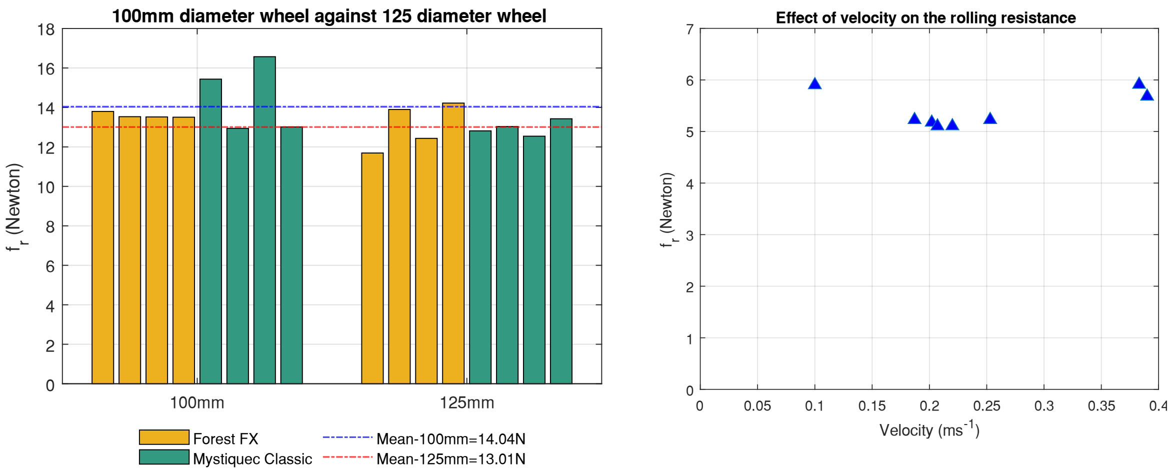

Figure 7: Calculated f_r for two wheel diameters (Left) and different trolley speed (Right).

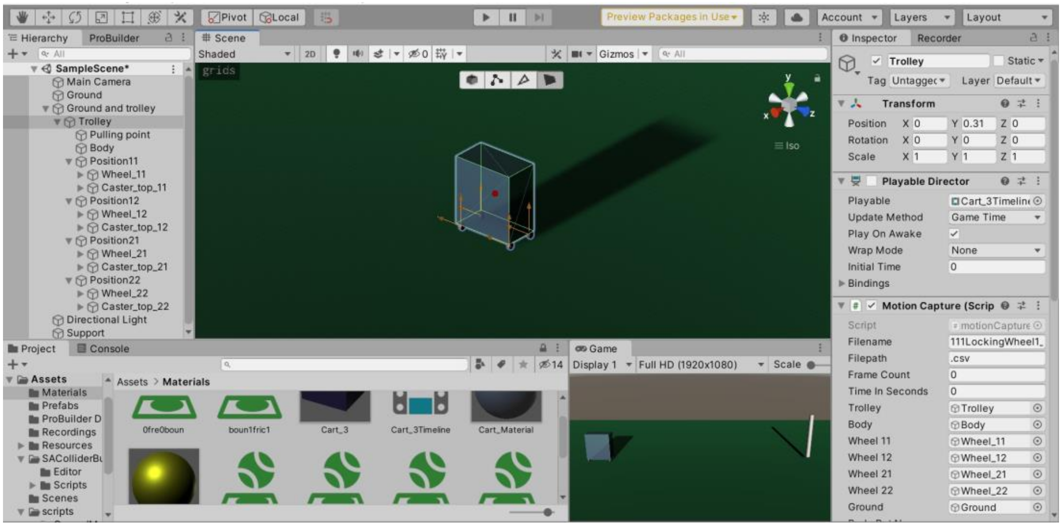

Figure 8 Unity interface and the trolley model.

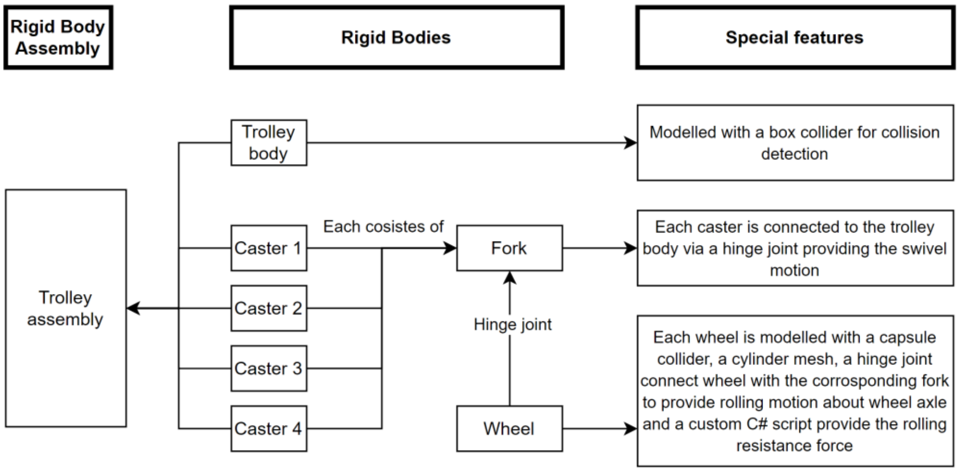

Figure 9 Trolley model hierarchy in Unity.

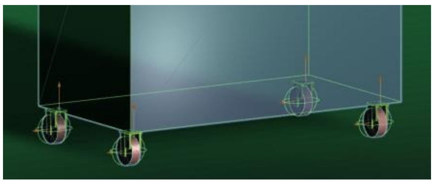

Figure 10 Different colliders used in the trolley model and the use of joints.

4.Physics Engine Model Simulation and Results

4.1 CHOICE OF COLLIDERS

Collisions between objects are key to physics engine simulations. *Collision* takes place when one GameObject makes contact with another GameObject. When a *Collision* event occurs, the function OnCollisionEnter is invoked (Unity, 2020). This enables users to develop custom programming to model bespoke behaviour. Users define a collider for each object in Unity, and colliders define the shape and interfaces where collisions can occur(Unity, 2020). The selection of colliders affects the temporal and spatial accuracy of *collision* detection, and subsequently affects the overall simulation accuracy. There are five choices of standard 3D colliders in Unity: box collider, capsule collider, sphere collider, terrain collider and mesh collider. There is no cylinder collider in Unity. This study has consequently adapted a capsule collider to approximate the rotating wheels. The rotational inertia of the wheel is manually modified using rigid bodies' inertiaTensor property, from that calculated for a capsule to match the correct inertial value for a cylinder. This ensures correct energy transfer in the simulation.

Different parts of the trolley (each GameObject) use different colliders, as shown in Figure 10.

- The trolley's body uses the box collider.
- The wheels use capsule colliders.
- The ground uses the box collider.

4.2 Modelling rolling resistance

Unity does not have a specific parameter or setting for modelling rolling resistance. In this project, a C# script was developed to provide a rolling resistance force f_r to each wheel. The rolling resistance, as shown in Equation 1, has two key factors, i) a dimensionless parameter C_r/R as established by the trendline in Figure 6, and ii) the normal force on each wheel N. Unity's built-in 3D physics engine calculates the normal force on each wheel by detecting collision forces between colliders on the wheel and the ground. Only the vertical component of the collision force is used in the f_r calculation. An "OnCollisionStay" function is triggered whenever the wheel-collider and ground-collider collide and remain in contact for a timestep. This allows the rolling resistance force to be applied to the wheel in the opposite direction of the relative movement between the wheel and the ground.

All phases except for phase I of the pulling tests are simulated in Unity. In Phase II, the constant pulling force measured from the physical experiment is applied to the Unity model. This force is applied for the same duration as the physical experiment. Following this, in Phase III, a constant string potentiometer force is applied the model, consistent with the puling experiment.

4.3 Simulation and Experimental Results Comparison

Figure 11 shows a typical time history comparison between the Unity simulation and the physical experiment results. It shows that the application of hinged joints, capsule colliders and custom-scripted rolling resistance force in Unity can effectively simulate the real trolley motion. The Unity simulation also enables mapping of the energy transfer between the different components during a pulling test, as shown in Figure 11. The WF line represents the work done by the drop weight and the string potentiometer. The WR line represents the work done by the simulated resistance force, and E_{KT} is the kinetic energy of the trolley.

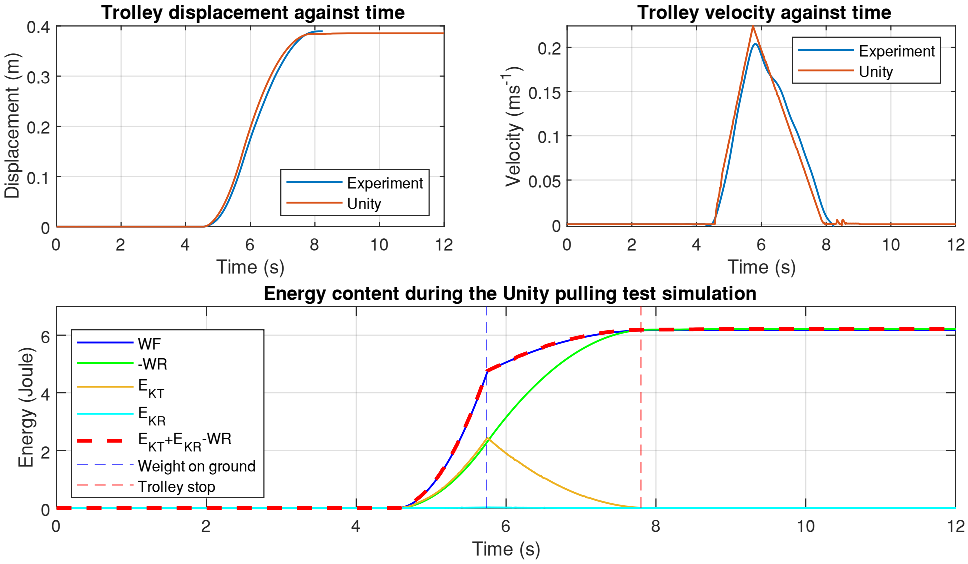

Figure 11 Top: Typical comparison of Unity simulation and physical experiment time histories (Left: displacement, Right: velocity), Bottom: Energy content during a pulling test.

5.Discussion and Conclusion

This study experimentally established the rolling resistance coefficient of a caster trolley on two vinyl floor coverings. A key finding was confirming rolling resistance force is proportional to the wheel's normal force and inversely proportional to wheel diameter. During this experiment, the rolling resistance coefficient did not vary with wheel speed. This study showed advanced energy dissipation behaviour can be simulated through Unity flexible programming functions. Unity accurately simulated the physical pulling tests with the appropriate modifications to its basic settings and functions. The unique arrangement of capsule colliders with hinge joints modelled the caster's behaviour well.

It is worth noting that although Unity was used to only model a simple pulling test in this study, it has the potential to simulate more complex dynamic responses of caster objects subjected to various ground motions. Simulations and experiments with swivelling castor motion and multi-directional rolling motion are not reported in this paper due to length limitations.

6.Acknowledgement

The authors extend their thanks to the undergraduate students, Caleb Knight-Polamalu, Daniel van Dam, Louie Love-Parata, Megan Hoare and William Wang, for their assistance during the experiments. Sincere thanks also to the China Scholarship Council for providing the PhD scholarship for the first author.

REFERENCES

Ai, J., Chen, J.-F., Rotter, J. M., & Ooi, J. Y. (2011). Assessment of rolling resistance models in discrete element simulations. Powder Technology, 206(3), 269–282. https://doi.org/10.1016/j.powtec.2010.09.030

ANSI ICWM. (2018). Vocabulary, Performance and Testing Requirements for Casters and Wheels. Institute of Casters and Wheel Manufacturers (ICWM).

Bilobran, A. L. O., & Angelo, R. M. (2013). Model for the resistance force acting on circular bodies in the imminence of rolling. EPL (Europhysics Letters), 103(5), 56001. https://doi.org/10.1209/0295-5075/103/56001

Boeing, A., & Braunl, T. (2007). Evaluation of Real-Time Physics Simulation Systems. 288. https://doi.org/DOI: 10.1145/1321261.1321312

Chatzis, M. N., & Smyth, A. W. (2013). Three-Dimensional Dynamics of a Rigid Body with Wheels on a Moving Base. Journal of Engineering Mechanics, 139(4), 496–511. https://doi.org/10.1061/(ASCE)EM.1943-7889.0000456

Cross, R. (2015). Rolling to a stop down an inclined plane. European Journal of Physics, 36. https://doi.org/10.1088/0143-0807/36/6/065047

Degrave, J., Hermans, M., Dambre, J., & Wyffels, F. (2019). A Differentiable Physics Engine for Deep Learning in Robotics. Frontiers in Neurorobotics. https://doi.org/10.3389/fnbot.2019.00006

FEMA. (2015). Performance of Buildings and Nonstructural Components in the 2014 South Napa Earthquake, FEMA P-1024. (FEMA P-1024). Federal Emergency Management Agency.

Fierro, E. A., Miranda, E., & Perry, C. L. (2011). Behavior of Nonstructural Components in Recent Earthquakes. Architectural Engineering Conference (AEI) 2011, 369–377. https://doi.org/10.1061/41168(399)44

Götz, J., Iglberger, K., Feichtinger, C., Donath, S., & Rüde, U. (2010). Coupling multibody dynamics and computational fluid dynamics on 8192 processor cores. Parallel Computing, 36(2), 142–151. https://doi.org/10.1016/j.parco.2010.01.005

Gould, N. C., & Marshall, J. D. (2012). Structural and Non-Structural Damage to Industrial Facilities during the February 2011 Christchurch, New Zealand, Earthquake. 1069–1079. https://doi.org/10.1061/9780784412367.095

He, H., & Zheng, J. (2020). Simulations of Realistic Granular Soils in Oedometer Tests Using Physics Engine. International Journal for Numerical and Analytical Methods in Geomechanics, 44(7), 983–1002. https://doi.org/10.1002/nag.3031

He, H., Zheng, J., Chen, Y., & Ning, Y. (2021). Physics engine based simulation of shear behavior of granular soils using hard and soft contact models. Journal of Computational Science, 56, 101504. https://doi.org/10.1016/j.jocs.2021.101504

Hecker, C. (2000). Physics in Computer Games. Communications of the ACM, 43(7), 34–34.

Hutchinson, T., Restrepo, J. I., Conte, J., & Meacham, B. (2013). Overview of the Building Nonstructural Components and Systems (BNCS) Project. Structures Congress 2013, 1485–1498. https://doi.org/10.1061/9780784412848.131

Izadi, E., & Bezuijen, A. (2018). Simulating Direct Shear Tests with the Bullet Physics Library: A Validation Study. PLOS ONE, 13(4), e0195073. https://doi.org/10.1371/journal.pone.0195073

Jose Luis Martin (Director). (2015, May 27). Ansys Tutorial explicit Dynamic. https://www.youtube.com/watch?v=Zeqz_le_xxU

Kim, J. C., Jung, H., Kim, S., & Chung, K. (2016). Slope Based Intelligent 3D Disaster Simulation Using Physics Engine. Wireless Personal Communications, 86(1), 183–199. https://doi.org/10.1007/s11277-015-2788-1

Laurell, B. (2008). The Inner Workings of Real-Time Physics Simulation Engines. IRCSE'08 IDT Workshop on Interesting Results in Computer Science and Engineering., 6.

Lippert, D., & Spektor, J. (2013). Rolling Resistance and Industrial Wheels. Hamilton Caster & Mfg. Co., 11, 8.

Ma, Q. T., Parshottam, S., & Montalla, M. (2018). Modelling rocking behaviour using physics engine simulation. 11th National Conference on Earthquake Engineering 2018, NCEE 2018: Integrating Science, Engineering, and Policy, 2, 1212–1222.

Miranda, E., Mosqueda, G., Retamales, R., & Pekcan, G. (2012). Performance of Nonstructural Components During the 27 February 2010 Chile Earthquake. Earthquake Spectra, 28(1_suppl1), 453–471. https://doi.org/10.1193/1.4000032

Motosaka, M., & Mitsuji, K. (2012). Building damage during the 2011 off the Pacific coast of Tohoku Earthquake. Soils and Foundations, 52(5), 929–944. https://doi.org/10.1016/j.sandf.2012.11.012

Nguyen, H. (Ed.). (2008). GPU Gems 3. Addison-Wesley Professional.

Nikfar, F., & Konstantinidis, D. (2017). Shake Table Investigation on the Seismic Performance of Hospital Equipment Supported on Wheels/Casters. Earthquake Engineering & Structural Dynamics, 46(2), 243–266. https://doi.org/10.1002/eqe.2789

Nikfar, F., & Konstantinidis, D. (2019). Seismic Response of Equipment on Wheels and Casters in Base-Isolated Hospitals. Journal of Structural Engineering, 145(3), 04019001. https://doi.org/10.1061/(ASCE)ST.1943-541X.0002266

Polyflor. (2014, January 13). Classic Mystique PUR Vinyl Flooring Product Range by Polyflor. Polyflor. https://www.polyflor.co.nz/product/classic-mystique-pur/

Ricardez, E., Noguez, J., Neri, L., Escobar-Castillejos, D., & Munoz, L. (2018). SutureHap: Use of a physics engine to enable force feedback generation on deformable surfaces simulations. International Journal of Advanced Robotic Systems, 15(1), 1729881417753928. https://doi.org/10.1177/1729881417753928

Taghavi, S., & Miranda, E. (2003). Response Assessment of Nonstructural Building Elements. Pacific Earthquake Engineering Research Center.

Unity. (2020). Unity - Manual: Unity User Manual 2020.3 (LTS). Available online: https://docs.unity3d.com/Manual/index.html

Vozdecký, L., Bartoš, J., & Musilová, J. (2014). Rolling friction—Models and experiment. An undergraduate student project. European Journal of Physics, 35(5), 055004. https://doi.org/10.1088/0143-0807/35/5/055004

Wong, J. Y. (2001). Theory of ground vehicles (3rd ed). John Wiley.

Seismic Response Analysis of Freestanding Building Contents Exhibiting Rocking, Sliding, and Wall Pounding

Yu Bao[1], Dimitrios Konstantinidis[2]

[1] School of Civil Engineering and Architecture
Wuhan University of Technology, PRC
e-mail: bao.yu@whut.edu.cn
[2] Department of Civil and Environmental Engineering
University of California, Berkeley, USA
e-mail: konstantinidis@berkeley.edu

Abstract. The seismic response of an unanchored rigid block continues to attract significant attention since the pioneering works of Housner and Newmark on the earthquake response of rocking and sliding objects, respectively. In the last two decades studies on rocking have grown, owing to an increased awareness of the overturning risk of slender freestanding objects, such as furniture, equipment, storage casks, etc. The earthquake response of sliding objects has also received marked attention in the last two decades, especially in the context of building contents. The more general response that includes both sliding and rocking has also been studied but to a much lesser extent. Most previous studies on the seismic response of freestanding building contents have assumed that the object moves freely without interacting with neighboring objects. However, this assumption is usually unrealistic; for example, in a building, freestanding furniture such as bookcases and cabinets are nearly always positioned next to a wall, and the presence of the wall can influence the response. Only a few studies have considered the interaction of the object with a boundary: Filiatrault et al. [2004], who carried out a shaking-table test study on bookcase–partition wall systems; Sideris and Filiatrault [2014], who examined the response of pure-sliding objects on inclined surfaces interacting with boundaries; and Bao and Konstantinidis [2020], who investigated the combined rocking-sliding response of a freestanding rigid block (representing a nonstructural component, such as a bookcase or cabinet) with a nearby rigid vertical boundary (representing a wall). The present paper summarizes key aspects of the study by the authors [Bao and Konstantinidis, 2020]. A model of the block that rock-slides and pounds against a wall is presented. The influence of different parameters is evaluated. General conclusions include that decreasing the friction coefficient of the ground, decreasing the clear wall distance, and decreasing the coefficient of restitution of the wall can enhance the stability of the block against overturning.

Keywords: Building Contents, Unanchored, Rocking, Sliding, Overturning, Collisions.

1. INTRODUCTION

A freestanding planar rigid block subjected to base excitation can exhibit five response modes depending on the block's aspect ratio, the friction coefficient at the base, and the excitation intensity: (1) rest; (2) pure sliding; (3) pure rocking; (4) combined sliding-rocking; and (5) free-flight [Shenton 1996]. Several studies have used the rigid block assumption to investigate the seismic risk of unanchored building contents whose response is dominated by pure sliding [e.g., Lopez Garcia and Soong, 2003; Chaudhuri and Hutchinson, 2005; Konstantinidis and Makris, 2005, 2009; Sideris and Filiatrault, 2014; Konstantinidis and Nikfar, 2015; Nikfar and Konstantinidis 2017a,b] or pure rocking motion [e.g., Makris and Konstantinidis, 2003; Makris and Vassiliou, 2012; Vassiliou and Makris, 2013; Dar et al., 2015, Linde et al., 2020; Kazantzi et al. 2022]. Mochizuki and Kobayashi [1976] developed the governing equations of motion for a sliding-rocking block. Subsequently, Ishiyama [1982] and Taniguchi [2002] investigated the complicated response of a rigid block considering different response modes during. Shenton and Jones [1991] presented a general framework to model the impact between the block its base that may occur during base excitation.

Unanchored building contents placed near a wall can pound against the wall during an earthquake. Very few studies have investigated this interaction: Filiatrault et al. [2004], Konstantinidis and Makris [2005], and Sideris and Filiatrault [2014]. The present paper develops an analytical model of a sliding-rocking block with a nearby rigid wall. The equations of motion governing each response mode, as well as the commencing conditions, are presented. An approach based on the principle of impulse and momentum is used in the model to handle the pounding against the wall. The model is used in a case study to evaluate the seismic fragility of a tool cabinet in a nuclear power plant. The influence of different parameters is evaluated by comparing the developed fragility curves. Although the presence of the wall significantly complicates the trends of overturning, some general observations are drawn on the effects of various model parameters.

2. EQUATIONS OF MOTION AND POUNDING AGAINST THE WALL

The problem is schematically shown in Figure 1. The freestanding block has a width of $2B$ and a height of $2H$, or equivalently semi-diagonal $R=\sqrt{B^2+H^2}$ and slenderness $\alpha=\operatorname{atan}(B/H)$. There is a rigid wall to the left of the block. The initial distance between the centroid of the block and the wall is δ_l. The clearance between the block and the left and right walls, respectively, are defined as $\Delta_l=\delta_l-B$ The block has three degrees-of-freedom (the free-flight mode is excluded here): two translations and one rotation. During base excitation, the contact forces at the base are denoted as F_x and F_y. The friction coefficient between the block and the base is denoted as μ, while the wall is assumed frictionless. For the more general case of finite block-wall friction, see Bao and Konstantinidis [2020].

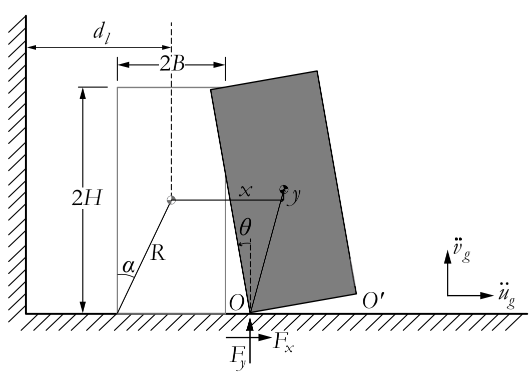

Figure 1. Schematic drawing of a freestanding block placed adjacent to a left side wall

For the block to enter pure rocking motion from the rest mode, the condition $\mu_s \geq \tan\alpha$ must be satisfied. The commencing condition for pure rocking motion is:

$$\left|\ddot{u}_g\right| \geq \tan\alpha\left(\ddot{v}_g + g\right) \tag{1}$$

and the governing equation of motion for pure rocking is:

$$\frac{4}{3}\mathrm{R}\ddot{\theta} = \ddot{u}_g \cos\left(\alpha - |\theta|\right) - S_\theta \sin\left(\alpha - |\theta|\right)\left(\ddot{v}_g + g\right) \tag{2}$$

where $S_\theta = S(\theta)$ denotes the signum function of *θ*. During pure rocking motion, the horizontal and vertical accelerations at the centroid of block are:

$$\begin{aligned} \ddot{x} &= -S_\theta \mathrm{R}\sin\left(\alpha - |\theta|\right)\dot{\theta}^2 - \mathrm{R}\cos\left(\alpha - |\theta|\right)\ddot{\theta} \\ \ddot{y} &= -\mathrm{R}\sin\left(\alpha - |\theta|\right)\dot{\theta}^2 + S_\theta \mathrm{R}\cos\left(\alpha - |\theta|\right)\ddot{\theta} \end{aligned} \tag{3}$$

Therefore, the rocking motion will be sustained provided that the condition $\left|f_x\right| \leq \mu_s\left|f_y\right|$ is satisfied, or,

$$\left|\ddot{x} + \ddot{u}_g\right| \leq \mu_s\left|\ddot{y} + g + \ddot{v}_g\right| \tag{4}$$

If Eq. (4) is violated, the block will switch from pure rocking to combined sliding-rocking motion with the following two equations of motion (recall that the block is constrained from losing contact at the base):

$$\ddot{\theta} + 4p^2 \frac{S_\theta\left[\sin\left(\alpha - |\theta|\right) + \eta\cos\left(\alpha - |\theta|\right)\right]\left[1 + \dfrac{\ddot{v}_g}{g} - 3\cos\left(\alpha - |\theta|\right)\dot{\theta}_p^2\right]}{1 + 3\sin^2\left(\alpha - |\theta|\right) + 3\eta\sin\left(\alpha - |\theta|\right)\cos\left(\alpha - |\theta|\right)} = 0 \tag{5}$$

$$\ddot{x} + 4p^2\mathrm{R}\frac{\dfrac{\eta S_\theta}{3}\left[1 + \dfrac{\ddot{v}_g}{g} - 3\cos\left(\alpha - |\theta|\right)\dot{\theta}_p^2\right]}{1 + 3\sin^2\left(\alpha - |\theta|\right) + 3\eta\sin\left(\alpha - |\theta|\right)\cos\left(\alpha - |\theta|\right)} = -\ddot{u}_g \tag{6}$$

where $p = \sqrt{3g/(4\mathrm{R})}, \eta = \mu_k S_\theta S_{\dot{x}_o}, \dot{\theta}_p = \dot{\theta}/(2p), S_{\dot{x}_o} = S(\dot{x}_o), \dot{x}_o = \dot{x} + \mathrm{R}\cos\left(\alpha - |\theta|\right)\dot{\theta}$. The presence of $S_{\dot{x}_o}$ makes numerical integration of the equations of motion very difficult. To overcome this difficulty, Konstantinidis and Makris [2005] proposed to replace $S_{\dot{x}_o}$ with the Bouc-Wen ODE:

$$\dot{z} = \frac{1}{u_y}\left[-\gamma\left|\dot{x}_o\right||z||z|^{n-1} - \beta\dot{x}_o|z|^n + \dot{x}_o\right] \tag{7}$$

where u_y is the yield displacement, and n, β, and γ are parameters controlling the shape of hysteresis loops. In this study, the following values are used: $u_y = 1.0\times10^{-5}$ m, $\beta = \gamma = 0.5$, and $n = 2$.

The equations of motion for rocking and combined sliding-rocking are not continuous when the rotation angle becomes zero, which indicates impact with the ground. In this study the approach proposed in Shenton and Jones [1991] is adopted to handle the impact of block with the ground, which relates the postimpact velocities of the block with the preimpact ones using the impulse and momentum principle.

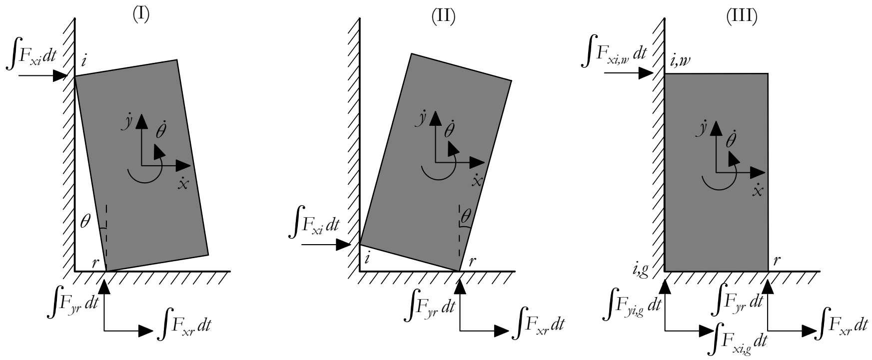

Figure 2. (I) top corner impacting adjacent wall; (II) bottom corner impacting adjacent wall; (III) both corners impacting adjacent wall simultaneously

Pounding (impact) of the block against the wall is assumed to occur over a very short time, so the position of the block does not change but its velocity changes instantaneously. Impulse and momentum theory is used to determine the postimpact velocities of the block. The preimpact and postimpact velocities normal to the impact point *i*, denoted using subscripts 1 and 2 respectively, are related through the coefficient of restitution of the wall e_w. The key point in this approach is to uniquely determine the postimpact velocities without violating any physical constraints. As noted, free-flight mode is excluded here. There are three possible scenarios of pounding, as shown in Figure 2. This section focuses on scenario (I); for a complete description of the approach including scenarios (II) and (III), refer to Bao and Konstantinidis [2020]. With reference to Figure 2(I), the condition for the top corner of the block contacting the wall is given by:

$$x - R\sin(\alpha + \theta) = -\delta_l \tag{8}$$

The two orthogonal components of the velocities at the impact corner *i* and rotation corner *r* before and after the impact can be written as:

$$\dot{x}_{i1} = \dot{x}_1 - R\cos(\alpha + |\theta|)\dot{\theta}_1; \quad \dot{y}_{i1} = \dot{y}_1 - S_\theta R\sin(\alpha + |\theta|)\dot{\theta}_1 \tag{9a}$$

$$\dot{x}_{r1} = \dot{x}_1 + R\cos(\alpha - |\theta|)\dot{\theta}_1; \quad \dot{y}_{r1} = \dot{y}_1 - S_\theta R\sin(\alpha - |\theta|)\dot{\theta}_1 \tag{9b}$$

$$\dot{x}_{i2} = \dot{x}_2 - R\cos(\alpha + |\theta|)\dot{\theta}_2; \quad \dot{y}_{i2} = \dot{y}_2 - S_\theta R\sin(\alpha + |\theta|)\dot{\theta}_2 \tag{9c}$$

$$\dot{x}_{r2} = \dot{x}_2 + R\cos(\alpha - |\theta|)\dot{\theta}_2; \quad \dot{y}_{r2} = \dot{y}_2 - S_\theta R\sin(\alpha - |\theta|)\dot{\theta}_2 \tag{9d}$$

and the principle of linear and angular impulse and momentum requires that:

$$m\dot{x}_1 + \int F_{xi} dt + \int F_{xr} dt = m\dot{x}_2 \tag{10}$$

$$m\dot{y}_1 + \int F_{yr} dt = m\dot{y}_2 \tag{11}$$

$$I\dot{\theta}_1 + \int F_{xr} dt R\cos(\alpha - |\theta|) - S_\theta \int F_{yr} dt R\sin(\alpha - |\theta|) - \int F_{xi} dt R\cos(\alpha + |\theta|) = I\dot{\theta}_2 \tag{12}$$

Substituting Eqs. (10) and (11) into (12) yields:

$$\begin{aligned} I\dot{\theta}_1 - mRS_\theta \sin(\alpha - |\theta|)(\dot{y}_2 - \dot{y}_1) - mR\cos(\alpha + |\theta|)(\dot{x}_2 - \dot{x}_1) \\ + R\left[\cos(\alpha + |\theta|) + \cos(\alpha - |\theta|)\right]\int F_{xr} dt = I\dot{\theta}_2 \end{aligned} \tag{13}$$

Eq. (13) has four unknowns: $\dot{x}_2$, $\dot{y}_2$, $\dot{\theta}_2$, and $\int F_{xr}dt$; therefore, three additional conditions are needed to obtain a unique solution for the postimpact velocities. The first condition uses the restitution coefficient between the block and the wall, $\dot{x}_{i2} = -e_w \dot{x}_{i1}$. With Eqs. (9a) and (9c), the following is obtained:

$$\dot{x}_2 = e_w R\cos(\alpha + |\theta|)\dot{\theta}_1 + R\cos(\alpha + |\theta|)\dot{\theta}_2 - e_w \dot{x}_1 \tag{14}$$

The second condition comes from the no-free-flight assumption. The postimpact vertical velocity at the rotation corner must be zero, $\dot{y}_{r2} = 0$. Thus Eq. (9d) gives:

$$\dot{y}_2 = S_\theta R\sin(\alpha - |\theta|)\dot{\theta}_2 \tag{15}$$

Three additional physical constraints for this problem are:

(1) The impulse at the impact corner must not be less than zero for Case (I). This constraint may be expressed as $S_\theta \int F_{xi}dt \geq 0$, and with Eq. (10) we can have:

$$S_\theta \int F_{xr}dt \leq mS_\theta (\dot{x}_2 - \dot{x}_1) \tag{16}$$

(2) The postimpact horizontal velocity at the impact corner cannot result in penetration into the wall; thus:

$$S_\theta \dot{x}_{i2} = S_\theta \dot{x}_2 - S_\theta R\cos(\alpha + |\theta|)\dot{\theta}_2 \geq 0 \tag{17}$$

(3) There is no net increase in the kinetic energy during impact.

These constraints cannot provide a unique solution to this problem, and it is first assumed that there is sufficient friction, so sliding does not occur at the rotation corner during impact; this is then checked by examining the following condition:

$$\left|\int F_{xr}dt\right| \leq \mu_s \left|\int F_{yr}dt\right| \tag{18}$$

If Eq. (18) is violated, then friction is insufficient to prevent sliding. In either case, the postimpact velocities can be uniquely determined. The following discussion focuses on these two cases.

There is sufficient friction to prevent sliding during impact

If there is sufficient friction to prevent sliding at the rotation corner during impact, then $\dot{x}_{r2} = 0$, giving:

$$\dot{x}_2 = -R\cos(\alpha - |\theta|)\dot{\theta}_2 \tag{19}$$

Combining Eqs. (14) and (19), the postimpact velocities can be written as:

$$\dot{\theta}_2 = \frac{e_w \dfrac{\dot{x}_1}{\dot{\theta}_1} - e_w R\cos(\alpha + |\theta|)}{R\left[\cos(\alpha + |\theta|) + \cos(\alpha - |\theta|)\right]}\dot{\theta}_1 = \xi\dot{\theta}_1;\ \dot{x}_2 = -R\cos(\alpha - |\theta|)\xi\dot{\theta}_1;\ \dot{y}_2 = S_\theta R\sin(\alpha - |\theta|)\xi\dot{\theta}_1 \tag{20}$$

Since Eq. (14) is used, Eq. (17) is automatically satisfied. With all the postimpact velocities available, substituting them into Eq. (13), the impulse at the rotation corner, $\int F_{xr} dt$, can be evaluated as:

$$\int F_{xr} dt = \frac{mRS_\theta \sin(\alpha - |\theta|)[S_\theta \xi R \sin(\alpha - |\theta|)\dot{\theta}_1 - \dot{y}_1] - mR\cos(\alpha + |\theta|)[\xi R \cos(\alpha - |\theta|)\dot{\theta}_1 + \dot{x}_1] - (1-\xi) I\dot{\theta}_1}{R[\cos(\alpha - |\theta|) + \cos(\alpha + |\theta|)]} \tag{21}$$

The above derivation is valid only if $|\int F_{xr} dt| \le \mu_s |\int F_{yr} dt| = \mu_s m(\dot{y}_1 - \dot{y}_2)$ and $S_\theta \int F_{xr} dt \le mS_\theta(\dot{x}_2 - \dot{x}_1)$. Note that $m(\dot{y}_1 - \dot{y}_2)$ is strictly positive, so the absolute sign is dropped.

Provided that friction is sufficient to prevent sliding (i.e., Eq. (18) holds true), if the computed impulse from Eq. (21) results in the violation of Eq. (16), then it is assumed that the impulses at the impact and rotation corners may be expressed as: $\int F_{xr} dt = m(\dot{x}_2 - \dot{x}_1)$ and $\int F_{xi} dt = 0$. With Eqs. (13), (15), and (19), the postimpact velocities can be determined as:

$$\dot{\theta}_2 = \frac{\frac{1}{3}R\dot{\theta}_1 - \cos(\alpha - |\theta|)\dot{x}_1 + S_\theta \sin(\alpha - |\theta|)\dot{y}_1}{\frac{4}{3}R}; \;\; \dot{x}_2 = -R\cos(\alpha - |\theta|)\dot{\theta}_2; \;\; \dot{y}_2 = S_\theta R \sin(\alpha - |\theta|)\dot{\theta}_2 \tag{22}$$

In deriving Eq. (22), since $\int F_{xi} dt = 0$, Eq. (14) which involves the coefficient of restitution of the wall, is assumed invalid. This, however, cannot ensure Eq. (17) is satisfied. Therefore, when the postimpact velocities derived from Eq. (22) violate (17), it is assumed that $\dot{x}_2 = R\cos(\alpha + |\theta|)\dot{\theta}_2$ to ensure compatibility. This leads to an indeterminate case since there are four conditions (i.e., Eqs. (13), (15), (19) and $\dot{x}_2 = R\cos(\alpha + |\theta|)\dot{\theta}_2$) and only three unknowns (i.e., $\dot{x}_2, \dot{y}_2, \dot{\theta}_2$), making it impossible to get a solution that satisfies all the conditions. Consequently, it is proposed that, by ignoring the momentum equilibrium, the only compatible postimpact velocities are zero [Note that although the instantaneous postimpact velocities are zero, the block has finite rotation angle and will begin to move]:

$$\dot{\theta}_2 = 0; \quad \dot{x}_2 = 0; \quad \dot{y}_2 = 0 \tag{23}$$

There is insufficient friction to prevent sliding during impact

If the computed impulse through Eq. (21) cannot meet the condition: $\left|\int F_{xr} dt\right| \le \mu_s \left|\int F_{yr} dt\right| = \mu_s m(\dot{y}_1 - \dot{y}_2)$, then Eq. (19) cannot be used since sliding occurs during impact, but there is a new condition relating the horizontal and vertical impulse at the rotation corner:

$$\int F_{xr} dt = -\mu_k S_{\dot{x}_{r2}} \int F_{yr} dt = \mu_k S_{\dot{x}_{r2}} m(\dot{y}_2 - \dot{y}_1) \tag{24}$$

where $S_{\dot{x}_{r2}} = S(\dot{x}_{r2})$. Substituting Eqs. (14), (15) and (24) into Eq. (13) gives:

$$\dot{\theta}_2 = \frac{\frac{1}{3}R\dot{\theta}_1 + \left[S_\theta \sin(\alpha - |\theta|) - (\cos(\alpha - |\theta|) + \cos(\alpha + |\theta|))\mu_k S_{\dot{x}_{r2}}\right]\dot{y}_1 - e_w R\cos^2(\alpha + |\theta|)\dot{\theta}_1 + (e_w + 1)\cos(\alpha + |\theta|)\dot{x}_1}{\frac{1}{3}R + \left[S_\theta \sin(a - |\theta|) - (\cos(\alpha - |\theta|) + \cos(\alpha + |\theta|))\mu_k S_{\dot{x}_{r2}}\right]S_\theta R\sin(\alpha - |\theta|) + R\cos^2(\alpha + |\theta|)} \tag{25}$$

In Eq. (25), the only unknown is $S_{\dot{x}_{r2}}$. It can be assumed positive, which can then be verified by examining Eq. (9d). The postimpact horizontal and vertical velocities can be found through Eq. (14) and (15) using the angular velocity from Eq. (25). They are not explicitly expressed here.

Similarly, it is also necessary to verify that the second physical constraint (i.e., Eq. (17)) is satisfied. If

$\int F_{xr}dt$ computed from Eq. (24) results in a violation of Eq. (17), the postimpact velocities computed with Eq. (25) are incorrect. Again, the impulses at the impact and rotation corner are assumed as: $\int F_{xr}dt = m(\dot{x}_2 - \dot{x}_1)$ and $\int F_{xi}dt = 0$. With Eqs. (14), (15), and (24), the postimpact velocities are:

$$\dot{\theta}_2 = \frac{\frac{1}{3}R\dot{\theta}_1 - \mu_k S_{\dot{x}_{r2}} \cos(\alpha - |\theta|)\, \dot{y}_1 + S_\theta \sin(\alpha - |\theta|)\, \dot{y}_1}{\frac{1}{3}R + R\sin^2(\alpha - |\theta|) - \mu_k S_{\dot{x}_{r2}} S_\theta R\cos(\alpha - |\theta|)\sin(\alpha - |\theta|)}; \tag{26}$$

$$\dot{x}_2 = \mu_k S_{\dot{x}_{r2}}(\dot{y}_2 - \dot{y}_1) + \dot{x}_1; \quad \dot{y}_2 = S_\theta R\sin(\alpha - |\theta|)\dot{\theta}_2;$$

Similarly, it is necessary to verify Eq. (17): if the postimpact velocities computed through Eq. (26) violate Eq. (17), then the momentum equilibrium is ignored, and the postimpact velocities are evaluated with Eqs. (15), (24) and $\dot{x}_2 = R\cos(\alpha + |\theta|)\dot{\theta}_2$, which gives:

$$\dot{\theta}_2 = \frac{\mu_k S_{\dot{x}_{r2}}\dot{y}_1 - \dot{x}_1}{\mu_k S_{\dot{x}_{r2}} S_\theta R\sin(\alpha - |\theta|) - R\cos(\alpha + |\theta|)}; \quad \dot{x}_2 = R\cos(\alpha + |\theta|)\dot{\theta}_2; \quad \dot{y}_2 = S_\theta R\sin(\alpha - |\theta|)\dot{\theta}_2 \tag{27}$$

The above formulation can be summarized by the flowchart shown in Figure 3.

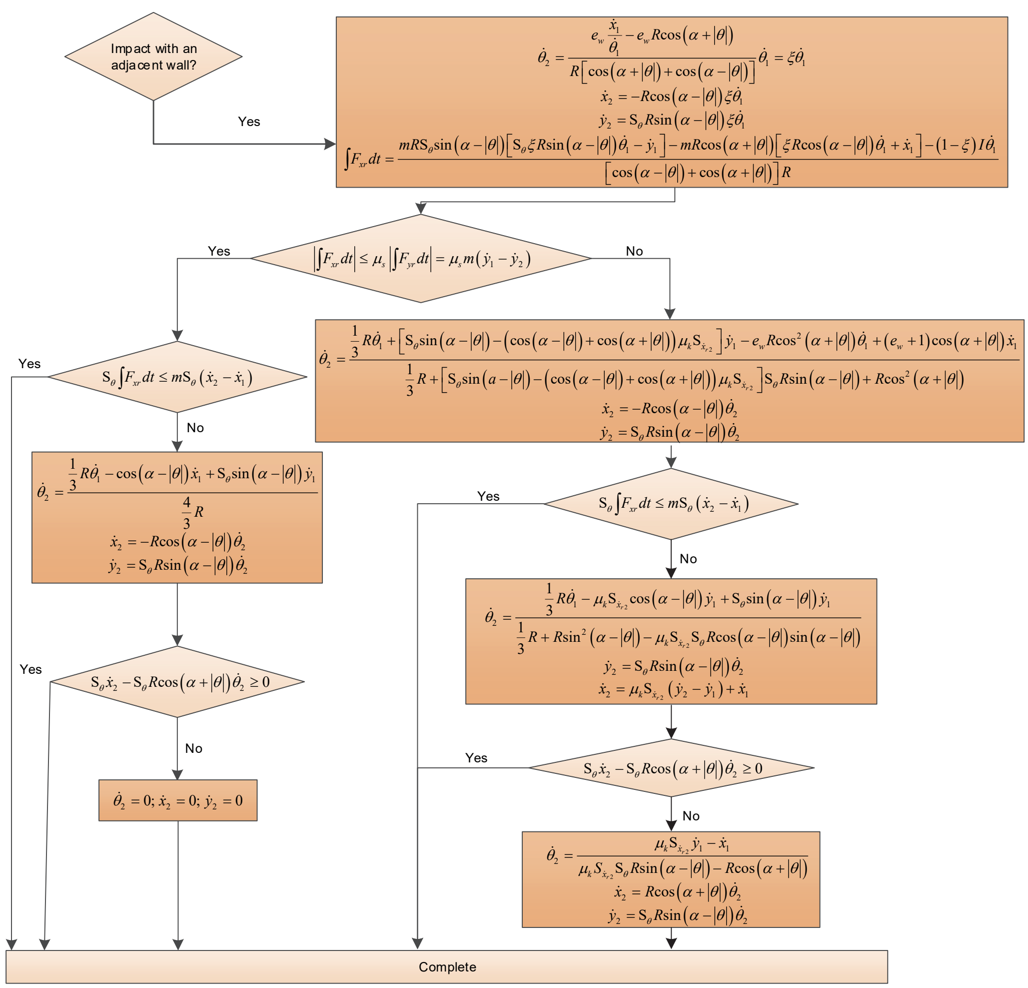

Figure 3. Flowchart of approach to handle top corner impacting an adjacent wall

Figure 4 illustrates the response of a block with p = 2.14 rad/s and a = 0.25 rad as it interacts with a wall to its left. The base motion is the El Centro record from the 1940 Imperial Valley, California, earthquake, scaled by a factor of 2. Also shown are snapshots of the block's position at various times. u_x and $\dot{u}_x$ represent the horizontal sliding displacement and velocity of the rotation corner of the block. The first, second, and fourth dot correspond to the top left corner of the block impacting the wall. It is interesting to note that the three successive impacts with the wall incrementally decrease the clear distance. The negative permanent sliding displacement at the rotation corner indicates that the gap between the block and the wall is reduced from 103 mm in the beginning of the excitation to 26 mm at the end. The incremental slips that occur upon impact are the result of large horizontal velocity spikes at the rotation corner, which can be clearly seen in the $\dot{u}_x$ time history. This example illustrates that the sliding-rocking mode dominates the transient response when there is pounding with the wall.

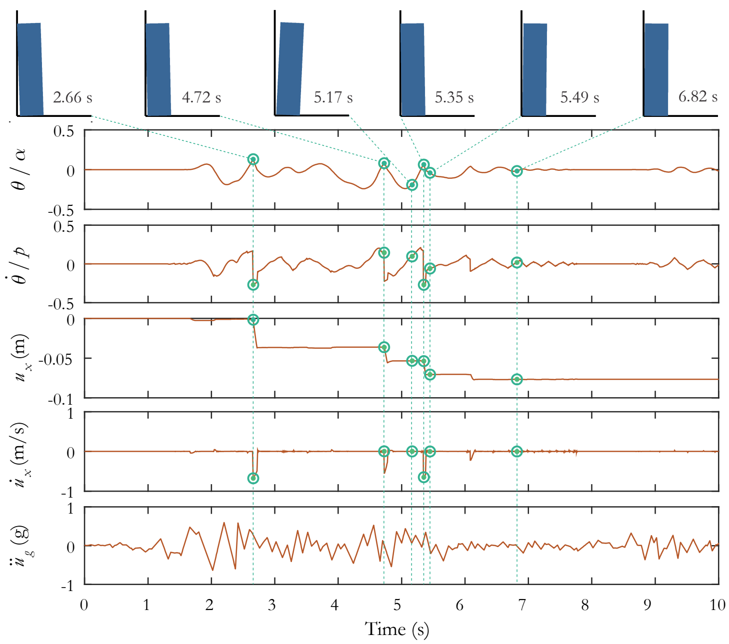

Figure 4. Response of a block with p = 2.14 rad/s and α = 0.25 rad pounding against a wall to its left when subjected to the El Centro motion scaled by a factor of 2 (μ = 0.3, e_w = 1.0, and Δ_l = 103 mm)

3. CASE STUDY: SEISMIC FRAGILITY OF A CABINET IN A NULCEAR POWER PLANT

Recognizing the need for mobility, nuclear standards such as ASCE 43-05 and ASCE 4-16 permit non-safety-critical components in nuclear facilities to be unanchored. This section presents a case study using the developed model to assess the overturning fragility of an unanchored component (a tool cabinet) placed near a wall in a nuclear power plant. The tool cabinet was modeled as a rigid block of uniform mass with dimensions $2B$ = 18 in (45.7 cm) and $2H$ = 84 in (213.4 cm), or equivalently p = 2.619 rad/s and α = 0.211 rad. The wall was assumed to be on the right side of the block. Varied parameters in this case study included: the floor friction coefficient μ = 0.3 and 0.6, the wall coefficient of restitution e_w = 0.25 and 0.75, and the wall clearance $\Delta_r = 0.6$ in (1.524 cm), 3 in (7.62 cm) and 6 in (15.24 cm).

An existing 3D lumped-mass stick model of the internal structure of a representative nuclear power plant reactor building was adapted by Najafijozani et al. [2022] in OpenSees and used to generate acceleration motions at the location where the cabinet was assumed to be situated (elevation of 18.0 m). The internal

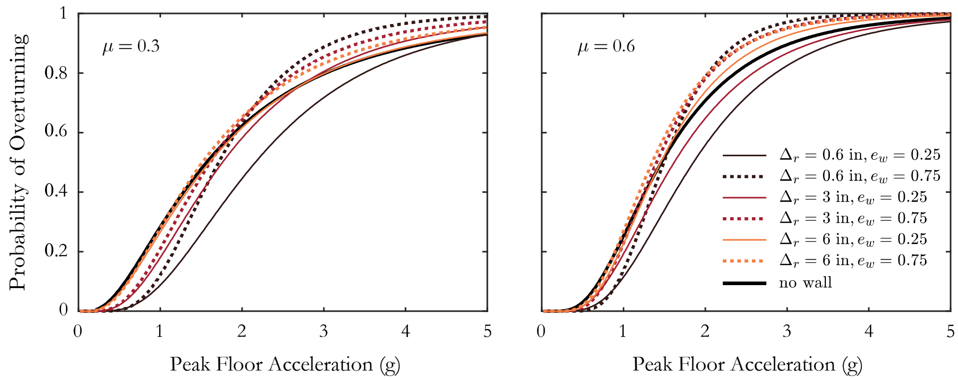

Figure 5. Fragility curves of for the unanchored cabinet for μ = 0.3 (left) and 0.6 (right)

structure had a total height of 39.0 m and a total mass of 50,000 tons and was assumed to be decoupled from the containment structure. Soil structure interaction was not considered. The internal structure was assumed to remain linear and had a fundamental period of 0.14 s. The structure was assumed to be at the Diablo Canyon, California, nuclear power plant site. The design spectrum was established based on the procedures in ASCE 43-05 for a nuclear facility that falls in Seismic Design Category 5 and Limit State D (essentially elastic behavior). A detailed discussion on the selection and scaling of a suite of 20 ground motions is presented in Arshad and Konstantinidis [2022].

Linear response history analysis of the 3D stick model subjected to the ground motion set of 20 X-Y-Z triplets produced absolute floor acceleration time histories, which were then used as input for the analysis of the block. Since the study considered the planar response of the block and the current model did not include free-flight, each horizontal component of the floor motion was applied to the block separately without considering the vertical component. The suite of ground motions was gradually scaled up by 10% increments until all forty motions resulted in toppling of the block. Peak floor acceleration (PFA) was selected as the intensity measure for the development of fragility curves. Although researchers have also examined other IMs [Dimitrakopoulos and Paraskeva, 2015; Kazantzi et al., 2021, 2022], the selection of the most appropriate intensity measure is beyond the scope of this study.

Since we are interested in the overturning probability, which is a binary response, the traditional regression analysis approach where the mean and standard deviation are estimated using the method of moments is not applicable for developing fragility curves. Instead, the fragility curves were developed assuming a two-parameter lognormal distribution, where the two parameters were estimated using the maximum likelihood method. The fragility curves with different combinations of model parameters are presented in Figure 5. It is observed that decreasing the friction coefficient has beneficial effects in reducing the overturning probability. For the case without an adjacent wall, at larger PFA values (>1.5 g) the probability of overturning for $\mu = 0.6$ is notably larger than for $\mu = 0.3$; whereas, somewhat opposite to intuition, for PFA < 1*g* the block with lower friction coefficient is more vulnerable to overturning. Figure 5 suggests that decreasing the wall's coefficient of restitution, e_w, also has beneficial effects, as the fragility curves for e_w = 0.25 are below the ones for e_w = 0.75 for any PFA. Also, by comparing fragility curves with the same Δ_r but different e_w values, it is observed that the effect of the wall's coefficient of restitution becomes more pronounced as Δ_r decreases, as suggested by the larger separation between fragility curves. Figure 5 shows that the combination of smallest clear distance (i.e., Δ_r = 0.6 in) and lowest coefficient of restitution (i.e., e_w = 0.25) results in the lowest probability of overturning of all cases, with or without a wall, and for any PFA. The influence of the clearance Δ_r is more complex compared to other parameters. While an adjacent wall is always beneficial for decreasing the overturning probability for relatively low PFA (< 1 g), for very large PFA (3 to 5 g), larger values of Δ_r (3 and 6 in) generally increase the overturning probability compared to the case with no wall. Whereas Δ_r = 0.6 in and e_w = 0.25 resulted in the lowest fragility, the combination of Δ_r = 0.6 in and e_w = 0.75 results in the highest overturning probability compared to other combinations of parameters when PFA > 2 g; yet, for PFA < 1 g, the fragility curves for Δ_r = 0.6 in are nearly the same—and result in safer response than all others.

The nuances in the stability of the block, including how the presence of the wall increases the stability for low-intensity shaking but, in some cases, decreases it for high-intensity shaking, underline the highly nonlinear nature of the problem. Many past studies have drawn attention to peculiarities in the behavior of the pure rocking block (i.e., without a wall or sliding at its base), including how, under certain conditions, an increase in the input can result in a more stable response [e.g., Makris and Konstantinidis 2003; Makris and Vassiliou, 2013]. It should then come as little surprise that the behavior of a sliding-rocking block, complicated by its interaction with the wall, will also exhibit odd behavior patterns that may be counterintuitive. The observations made in this case study stress the need for in-depth future studies to investigate the effect of different model parameters on the stability of unanchored building contents.

4. CONCLUSIONS

This paper investigated the dynamics of a two-dimensional sliding-rocking rigid block considering wall pounding. The problem has direct applications to the seismic response of unanchored building contents placed near a wall. First, the classical impulse and momentum principle was used to present an approach to account for impacts with an adjacent wall, under the assumption of no free-flight (i.e., that the block always maintains a point of contact with the base). The paper then presented a case study of a cabinet in a nuclear power plant to develop fragility curves and evaluate the effect of different model parameters.

The developed fragilities show that an increased friction coefficient makes the cabinet more likely to overturn. Increased impact damping (represented by lower coefficient of restitution of the wall) has a beneficial effect against overturing. Also, for low levels of peak floor acceleration, placing the component next to a wall has beneficial effects. This observation is consistent with that drawn by Filiatrault et al. [2004] whose shake table tests under relatively low shaking intensity suggested that the pounding of the bookcases with the wall is beneficial. At high levels of peak floor acceleration, the current study shows that the effect of the clear distance on the overturning probability is more nuanced and depends on both the coefficient of restitution and shaking intensity. The smallest clear distance combined with the lowest coefficient of restitution are beneficial without exception, as they result in the lowest probability of overturning, regardless of the shaking intensity. However, other combinations of parameters may result in increased probability of overturning compared to the case without a wall.

Fragility data for unanchored building contents is currently scarce and often not based on rigorous methods. The sliding-rocking block model that considers wall pounding can be used in future studies to evaluate appropriate intensity measures and develop analytical fragility curves for a host of unanchored building contents to support performance-based earthquake assessments.

REFERENCES

Arshad, A., Konstantinidis, D. [2022] "Effect of multi-component excitation on the sliding response of unanchored components in nuclear facilities," *Nuclear Engineering and Design*, Vol. 390, 111707.

Bao, Y., Konstantinidis, D. [2020] "Dynamics of a sliding-rocking block considering impact with an adjacent wall," *Earthquake Engineering & Structural Dynamics*, Vol. 49, No. 5, pp. 498-523.

Chaudhuri, S.R., Hutchinson, T.C. [2005] "Characterizing frictional behavior for use in predicting the seismic response of unattached equipment," *Soil Dynamics and Earthquake Engineering,* Vol. 25, No. 7-10, pp. 591-604.

Dar, A., Konstantinidis, D., El-Dakhakhni, WW. [2016] "Evaluation of ASCE 43-05 seismic design criteria for rocking objects in nuclear facilities," *Journal of Structural Engineering*, Vol. 142, No. 11, 04016110.

Dimitrakopoulos, E.G., Paraskeva, T.S. [2015] "Dimensionless fragility curves for rocking response to near-fault excitations," *Earthquake Engineering & Structural Dynamics*, Vol. 44, No. 12, pp. 2015-2033.

Filiatrault, A., Kuan, S., Tremblay, R. [2004] "Shake table testing of bookcase-partition wall systems," *Canadian Journal of Civil Engineering*, Vol. 31, No. 4, pp. 664-676.

Ishiyama, Y. [1982] "Motions of rigid bodies and criteria for overturning by earthquake excitations," *Earthquake Engineering & Structural Dynamics*, Vol. 10, No. 5, pp. 635-650.

Kazantzi, A.K., Lachanas, C.G., Vamvatsikos, D. [2021] "Seismic response distribution expressions for on-ground rigid rocking blocks under ordinary ground motions," *Earthquake Engineering & Structural Dynamics*, Vol. 50, No. 12, pp. 3311-3331.

Kazantzi, A.K., Lachanas, C.G., Vamvatsikos, D. [2022] "Seismic response distribution expressions for rocking building contents under ordinary ground motions," *Bulletin of Earthquake Engineering*, in press.

Konstantinidis, D., Makris, N. [2005]. "Experimental and analytical studies on the seismic response of freestanding and anchored laboratory equipment," *Report PEER 2005-07*, Pacific Earthquake Engineering Research Center, University of California, Berkeley.

Konstantinidis, D., Makris, N. [2009] "Experimental and analytical studies on the response of freestanding laboratory equipment to earthquake shaking," *Earthquake Engineering & Structural Dynamics*, Vol. 38, No. 6, pp. 827-848.

Konstantinidis, D., Nikfar, F. [2015] "Seismic response of sliding equipment in base isolated buildings subjected to broad-band ground motions," *Earthquake Engineering & Structural Dynamics*, Vol. 44, No. 6, pp. 865-887.

Linde, S.A., Konstantinidis, D., Tait, M.J. [2020] "Rocking response of unanchored building contents considering horizontal and vertical excitation," *Journal of Structural Engineering*, Vol. 146, No. 9, 04020175.

Lopez Garcia, D., Soong, T.T. [2003] "Sliding fragility of block-type non-structural components. Part 1: unrestrained components," *Earthquake Engineering & and Structural Dynamics*, Vol. 32, No. 1, pp. 111-129.

Makris, N., Konstantinidis, D. [2003] "The rocking spectrum and the limitations of practical design methodologies," *Earthquake Engineering & Structural Dynamics*, Vol. 32, No. 2, pp. 265-289.

Makris, N., Vassiliou, M.F. [2012] "Sizing the slenderness of free-standing rocking columns to withstand earthquake shaking," *Archive of Applied Mechanics*, Vol. 82. No. 10-11, pp. 1497-1511.

Makris, N., Vassiliou, M.F. [2013] "Planar rocking response and stability analysis of an array of freestanding columns capped with a freely supported rigid beam," *Earthquake Engineering & Structural Dynamics*, Vol. 42, No. 3, pp. 431-449.

Mochizuki, T., Kobayashi, K. [1976] "A study on acceleration of earthquake motion deduced from the movement of column: an analysis on the movement of column," *Transactions of the Architectural Institute of Japan*, Vol. 248, pp. 63-70. (in Japanese)

Najafijozani, M., Becker, T.C., Konstantinidis, D. [2020] "Evaluating adaptive vertical seismic isolation for equipment in nuclear power plants," *Nuclear Engineering and Design*, Vol. 358, 110399.

Nikfar, F., Konstantinidis, D. [2017a] "Peak sliding demands on unanchored equipment and contents in base-isolated buildings under pulse excitation," *Journal of Structural Engineering*, Vol. 143, No. 9, 04017086.

Nikfar, F., Konstantinidis, D. [2017b]. "Effect of the stick-slip phenomenon on the sliding response of objects subjected to pulse excitation," *Journal of Engineering Mechanics*, Vol. 143, No. 4, 04016122.

Shenton, H.W. [1996] "Criteria for initiation of slide, rock, and slide-rock rigid-body modes," *Journal of Engineering Mechanics*, Vol. 122, No. 7, pp. 690-693.

Shenton, H.W., Jones, N.P. [1991] "Base excitation of rigid bodies. I: formulation," *Journal of Engineering Mechanics*, Vol. 117, No. 10, pp. 2286- 2306.

Sideris, P., Filiatrault, A. [2014] "Seismic response of squat rigid bodies on inclined planes with rigid boundaries." *Journal of Engineering Mechanics*, Vol. 140, No. 1, pp. 149-158.

Taniguchi, T. [2002] "Non-linear response analyses of rectangular rigid bodies subjected to horizontal and vertical ground motion," *Earthquake Engineering & Structural Dynamics*, Vol. 31, No. 8, pp. 1481-1500.

Vassiliou, M. F., Makris, N. [2012] "Analysis of the rocking response of rigid blocks standing free on a seismically isolated base," *Earthquake Engineering & Structural Dynamics*, Vol. 41, No. 2, pp. 177-196.

Evaluation of Seismic Demand on Bridge Nonstructural Components Using ASCE 7

Nathan Girmay[1]; Mirela Tumbeva, Ph.D.[2]; Thanh Do, Ph.D., P.E.[3]; and David R. Ojala, S.E., LEED AP, CWI [4]

[1] Graduate Student, Stanford University
473 Via Ortega, Room 303, Stanford, CA, USA ngirmay3@stanford.edu
[2] Project Engineer, Thornton Tomasetti
301 Howard St, STE 1030, San Francisco, CA, USA, mtumbeva@thorntontomasetti.com
[3] Associate, Thornton Tomasetti
301 Howard St, STE 1030, San Francisco, CA, USA, tdo@thorntontomasetti.com
[4] Associate Principal, Thornton Tomasetti
301 Howard St, STE 1030, San Francisco, CA, USA, dojala@thorntontomasetti.com

Abstract. Bridge nonstructural components, also known as bridge appurtenances or attachments, are not part of the load resisting systems of a bridge structure. Examples of bridge appurtenances include parapets, emergency walkways, Bridge Utility Systems (BUS), signs, and lighting posts attached to the bridge deck. Traditionally, these attachments are designed to resist wind load, live load, and vehicle impact load. However, while these loading types may be thought to control the design, damage to bridge appurtenances in past large earthquakes, such as failure of utility poles and signs, and falling of mounted masts, shows that more attention from the design and research community may be warranted. Current bridge design codes and state Department of Transportation (DOT) provisions do not address the seismic design of nonstructural components. Additionally, the existing AASHTO LRFD specifications for structural supports for signs, luminaires, and traffic signals focus primarily on wind design and fatigue performance and does not include provision for seismic loads. The designer instead is referred to project specific guidelines which typically do not exist. The objective of this paper is to raise awareness on the current state of the practice and discuss possibilities toward a unified approach for seismic design and performance assessment of bridge nonstructural components. As there are no clear procedures for evaluating bridge structural components for seismic loads, it is acceptable to seek guidelines in building codes such as ASCE 7. This paper compares two editions of ASCE 7 and presents two case studies to demonstrate their applicability to the seismic evaluation of bridge nonstructural components. The paper concludes with recommendations and suggestions for future research.

Keywords: Bridge appurtenances, seismic design, code review, seismic demand, earthquake damage.

1. INTRODUCTION

Bridge nonstructural components, also known as bridge appurtenances or attachments, although not part of the load resisting system, have an important role in maintaining bridge functionality. Examples of nonstructural components on bridges include light poles/luminaries, transmission lines, emergency walkways, and Bridge Utility Systems (BUS). Typically, these components are designed to resist wind load, live load, and vehicle impact load. Seismic loads are often not considered as the governing demand, and therefore, may not be explicitly considered. However, damage to bridge nonstructural components in past large earthquakes suggest that these components could be vulnerable to seismic loads and that their performance, as well as impact on the bridge behaviour, need to be investigated. Even if the bridge load-carrying capacity is not compromised, damage such as failure of utility poles and signs, or falling of mounted masts, could delay the functional recovery of the bridge, not only resulting in economic losses but potentially limiting access to food, supplies, and medical attention. In addition, rescue operations could be compromised due to the inability to use the bridge. The bridge and many of the systems it carries are lifelines for the local community and are worth consideration when assessing local seismic resilience.

The objective of this paper is to review the current state of the practice and to discuss a possible unified prescriptive approach for seismic design and evaluation of bridge nonstructural components based around the ASCE 7 framework. We present an extensive literature review and compile a summary of seismic design guidelines from relevant codes, standards, and design criteria, including AASHTO and amendments by different state's Department of Transportation (DOT), and building codes such as ASCE 7. Two case studies are presented to investigate the use of ASCE 7 in seismic demand evaluation of representative bridge nonstructural components, with a focus on comparing the ASCE 7-16 approach to the updated method in ASCE 7-22 and to numerical analysis results. The paper concludes with recommendations and suggestions for future research.

2. PAST SEISMIC PERFORMANCE OF BRIDGE APPURTENANCES

There have been numerous reports of damage to bridge nonstructural components following seismic events. According to Siringoringo *et al* [2020], more than one thousand lighting and utility poles around the Hanshin Expressway were damaged during the 1995 Great Hanshin-Awaji (Kobe) Earthquake (M6.9). Images from the event show yielded barrier mounted light posts and toppled poles over elevated highways. Abé and Shimamura [2014] reported that over 504 electrical power poles and over 10 transformers were damaged following the 2011 Tōhoku Earthquake (M9.0). Some of the damaged poles were mounted on the Shinkansen railway bridge. Seismic damages of BUS, such as potable and wastewater utility lines typically mounted on bridge decks, have also been reported. During the 2010-2011 Canterbury Earthquake Sequence (CES) in New Zealand, severe damage to utility lines was reported despite good structural performance of the bridge structures [Rais *et al* 2015; Palermo *et al,* 2011]. Although the principal source of damage during CES was identified as rotation of the abutments at deck-abutment interface, other damage mechanisms to bridge-mounted utility lines have been recognized. Examples include failure of the pipeline at midspan during the CES and buckling of pipeline during 1994 Northridge Earthquake [Rais *et al*, 2015; Schiff, 1997]. Images from EERI's Virtual Clearinghouse [2016] documenting the Kaikoura Earthquake (M7.5) also show damages to BUS.

The survey of damages discussed above suggests that nonstructural components on bridges are susceptible to earthquakes, and thus, warrant more attention from the engineering community. While seismic behaviour of *building* nonstructural components and their importance to seismic resilience is relatively well-understood, there seems to be a lack of a consensus on seismic design methodologies of *bridge* nonstructural attachments. In addition, while seismic design of bridge *structural* components is relatively well-researched and documented, such as in AASHTO code and other standards by State DOTs, it is the authors' opinion that similar consideration for bridge *nonstructural* components has not been adequately given.

3. STATE OF THE PRACTICE IN SEISMIC DESIGN OF BRIDGE NONSTRUCTURAL COMPONENTS

Current bridge design code [AASHTO, 2020] and/or state DOTs provisions do not specifically address the seismic design of nonstructural components. Additionally, the existing LRFD specifications for structural supports for signs, luminaires, and traffic signals [AASHTO, 2015] focus primarily on wind design and fatigue performance and does not include provisions for seismic loads. Instead, the designer is referred to project-specific seismic guidelines, which may not exist, or which refer to codes or standards intended primarily for building structures. Agencies such as the California Department of Transportation (Caltrans), although having strict requirements and extensive guidelines for seismic design and performance of bridge structural components, does not provide any recommendations for the seismic design of bridge nonstructural components. Similarly, the academic community offers limited research on bridge nonstructural components under seismic loads. Siringoringo *et al* [2020] performed a numerical study on the seismic behaviour of a tapered light pole mounted on a highway bridge. Results show that if the fundamental frequency of the bridge is within the range of ±30% of the fundamental frequency of the light pole, resonance is observed, resulting in larger seismic demand and potential bending failure. Bharil *et al* [2001] proposed general guidelines for bridge water pipe installation including design loads and safety factors for pipe hangers. The paper conservatively recommended using 0.5g for the acceleration coefficient in any lateral direction for the seismic design of these components; however, complete seismic design guidelines were not developed.

In the absence of clearer bridge-specific guidance for seismic design of bridge appurtenances, it is the authors' experience that seismic design is commonly: 1) ignored, under the perhaps incorrect assumption that other design loads and detailing requirements will govern, 2) based on seismic loads used for the base structure, which may ignore possible dynamic interaction between the components and the base structure and the design ground motions, 3) estimated analytically, which can be inaccurate and/or time consuming depending on the method used, or 4) based upon prescriptive provisions in the building code, which may require some judgment to apply to bridges. While numerical analysis may always be the most accurate approach, given that many smaller bridges continue to be designed for earthquakes using prescriptive methods, establishing consensus around a reliable prescriptive method for practitioners would be valuable. We note that Goel [2018] has identified a similar lack of prescriptive guidance for piers and wharves.

As there are no clear bridge-specific prescriptive guidelines for evaluating nonstructural components for seismic loads, it is common to seek guidance in building codes, such as ASCE 7, which contain more robust guidelines for seismic design of nonstructural components. These provisions are frequently referenced (often via reference to local building codes that reference them) by owners in project-specific design criteria and may be applicable (or require consideration alongside AASHTO or other provisions) to design of many nonstructural aspects of vehicular and pedestrian bridges. While ASCE 7 clarifies that the provisions are applicable to building and non-building structures, the provisions and equations were developed in the context of buildings, and therefore their application to bridges and other nonbuilding structures may require some judgment by the designer. However, it is the authors' opinion that ASCE 7 currently provides the best available *framework* for prescriptive seismic design of nonstructural components in general, and the remainder of this paper is dedicated to investigating the potential application of these provisions in the context of bridge design, including key considerations, assumptions, and limitations that may affect the resulting designs.

4. A REVIEW OF ASCE 7 PROVISIONS

The general approach in ASCE 7 is to determine the effective horizontal seismic design force, F_p, acting on the nonstructural component as a function of design peak ground acceleration (PGA). The provisions had been largely unchanged from the time they first appeared in their modern form in ASCE 7-98, through to the version referenced by the building code at time of writing, ASCE 7-16. Using ASCE 7-16, F_p is defined as:

$$F_p = 0.4S_{DS}\left(1 + 2\frac{z}{h}\right)\frac{a_p}{\left(\frac{R_p}{I_p}\right)}W_p \qquad \text{[ASCE 7-16, Ch. 13] (1)}$$

where, S_{DS} = short period spectral acceleration, a_p = component amplification factor, I_p = component importance factor, R_p = component response modification factor, z = structure height at the component attachment level, h = average roof height, and W_p = component operating weight.

Continued poor performance of some nonstructural components and increasing desire for expedited functional recovery has led to a desire for further study and refinement of ASCE 7 provisions [ATC, 2017]. The National Institute for Science and Technology (NIST) GCR 13-917-23 report [Hooper *et al*, 2013] recognized nonstructural components as a crucial area of improvement. This led to further studies including NIST GCR 17-917-44 report [ATC, 2017] which provided recommendations for future work on seismic analysis and design of nonstructural components, as wells as NIST GCR 18-917-43 report [ATC, 2018] which resulted in revisions to existing seismic provisions for nonstructural components in building structures (i.e., ASCE 7-22).

The primary change between the 7-16 and 7-22 provisions is that the equations for deriving F_p were modified to explicitly account for the dynamic characteristics of the structure and its interaction with the nonstructural component. Using ASCE 7-22, F_p is defined as:

$$F_p = 0.4S_{DS}\frac{H_f}{R_\mu}\frac{C_{AR}}{R_{po}}I_pW_p \qquad \text{[ASCE 7-22, Ch. 13] (2)}$$

where, H_f = factor for force amplification as a function of structure height, C_{AR} = component resonance ductility factor, $R_\mu = [1.1R/I_e\Omega_o]^{1/2}$ is the structure ductility factor which shall be greater than 1.3, R_{po} = component strength factor. The factors in both equations are either tabulated in the code or are determined based on the structure and component dynamic properties. The factor H_f is evaluated as follows:

$$H_f = 1 + a_1\left(\frac{z}{h}\right) + a_2\left(\frac{z}{h}\right)^{10} \; where \; a_1 = \frac{1}{T_a} \leq 2.5 \; and \; a_2 = \left[1 - \left(\frac{0.4}{T_a}\right)^2\right] \geq 0 \qquad \text{[7-22] (3)}$$

$$H_f = 1 + 2.5\left(\frac{z}{h}\right) \; when \; structure \; period \; is \; unknown \qquad \text{[7-22] (4)}$$

where T_a is the period of the structure[a]. The code provides Equation (4) as an alternative way to determine H_f if the period of the structure is not readily available. In calculating R_μ, the following factors are defined for the structure: R = response modification factor, I_e = importance factor, and Ω_o = overstrength factor.

[a] ASCE 7 defines T_a as the approximate period as determined using the empirical equations of ASCE 7 (which often yield higher periods than would be determined by analysis), but for nonbuilding structures ASCE 7 does allow T_a to be determined based on a "properly substantiated analysis."

Assuming that it is unreasonable to design for a force that is excessively low or high, both Equations (1) and (2) are limited to minimum and maximum values of $0.3S_{DS}I_pW_p$ and $1.6S_{DS}I_pW_p$, respectively.

Figure 1 breaks down Equations (1) and (2) above and compares the "equivalent" terms**Errore. L'origine riferimento non è stata trovata.**. The first term is the PGA for the design earthquake, estimated as $0.4S_{DS}$ in both versions of ASCE 7, which accounts for the intensity of ground shaking. The second term is the amplification factor from PGA to peak floor acceleration (PFA), which accounts for the dynamic properties of the building. The third term is the component amplification factor from PFA to peak component acceleration (PCA), which accounts for the dynamic properties of the component [ATC, 2018]. These amplification factors convert the ground acceleration to that acting on the component. The last term is associated with the reduction factor, R, which is used to account for energy dissipation due to component and structure nonlinear behaviour. As illustrated in Figure 1, the total seismic coefficient, F_p/W_p, for any nonstructural component is defined as PGA x (PFA/PGA) x (PCA/PFA) x (1/R).

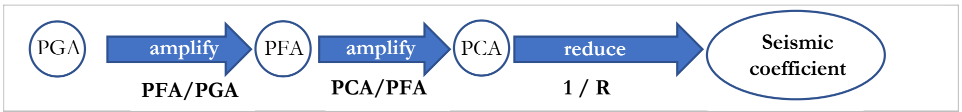

$0.4S_{DS}\ \times$	$\left(1+2\frac{z}{h}\right)$	$\times$	a_p	$\times$	$\frac{1}{R_p}$	=	$\frac{F_p}{W_p}$	**ASCE 7 - 16**
$0.4S_{DS}\ \times$	H_f	$\times$	C_{AR}	$\times$	$\frac{1}{R_\mu}\frac{1}{R_{po}}$	=	$\frac{F_p}{W_p}$	**ASCE 7 - 22**

Figure 1. Conceptual framework for ASCE 7 nonstructural component demand

We acknowledge that this may not reflect how the provisions were actually developed and the terms may not separate as cleanly in practice. For example, in theory, a_p and C_{AR} could approach infinity for structures where the component approaches resonance with the supporting structure and ground motion. However, ASCE 7 commentary [ATC, 2018] implies that a_p and C_{AR} are not purely related to structural dynamics, and both consider component damping and ductility, despite the fact that there is a separate component force reduction parameter. Thus, while separating the equation into the terms described here provides a logical framework for comparing each version of ASCE 7 to our numerical results, both the individual terms and final result of each methodology should be compared. We also note that while the ASCE 7 provisions have a basis in structural dynamic theory, certain assumptions need to be made to create simple equations that produce reasonably economical designs with reliable performance. According to NIST GCR 18-917-43 report [ATC, 2018], instrumentation and analytical data from building structures was used to develop some of the coefficients and set certain bounding values. These underlying assumptions and their possible impact on the results (i.e., conservative versus unconservative) needs to be considered when comparing prescriptive results to pure analysis, and when considering the application of this methodology to non-building structures or even for buildings with relatively unusual characteristics. The relevant assumptions and possible impacts to results will be discussed in this paper.

The following sections will present examples of how each of these terms might be defined by the practicing bridge designer, either prescriptively or numerically, for an archetype bridge and compare the component seismic demands based on guidelines from ASCE 7-16 and ASCE 7-22, and from a linear time history analysis.

5. CASE STUDIES

This section investigates application of ASCE 7-16 and 7-22 provisions through two case studies: a bridge-mounted pipeline and a bridge-mounted light pole. The components are assumed to be mounted on a selected archetype bridge, which is discussed in the following sub-section.

5.1 ARCHETYPE BRIDGE STRUCTURE

Caltrans Seismic Design Criteria (SDC) [Caltrans, 2019] defines three categories of bridges based on the expected post-earthquake damage state and service level (namely ordinary, recovery, and important bridges). The archetype bridge structure in this study, shown in Figure 2, is an ordinary cast-in-place concrete box girder bridge from Caltrans Bridge Design Practice (BDP) manual [Caltrans, 2015]. The bridge structure has three continuous spans with lengths of 126 ft, 168 ft, and 118 ft, respectively. The superstructure is composed of a 6.75 ft deep multi-cell box girder and the substructure includes two bents, each with two 6-ft diameter columns that are 44 ft tall.

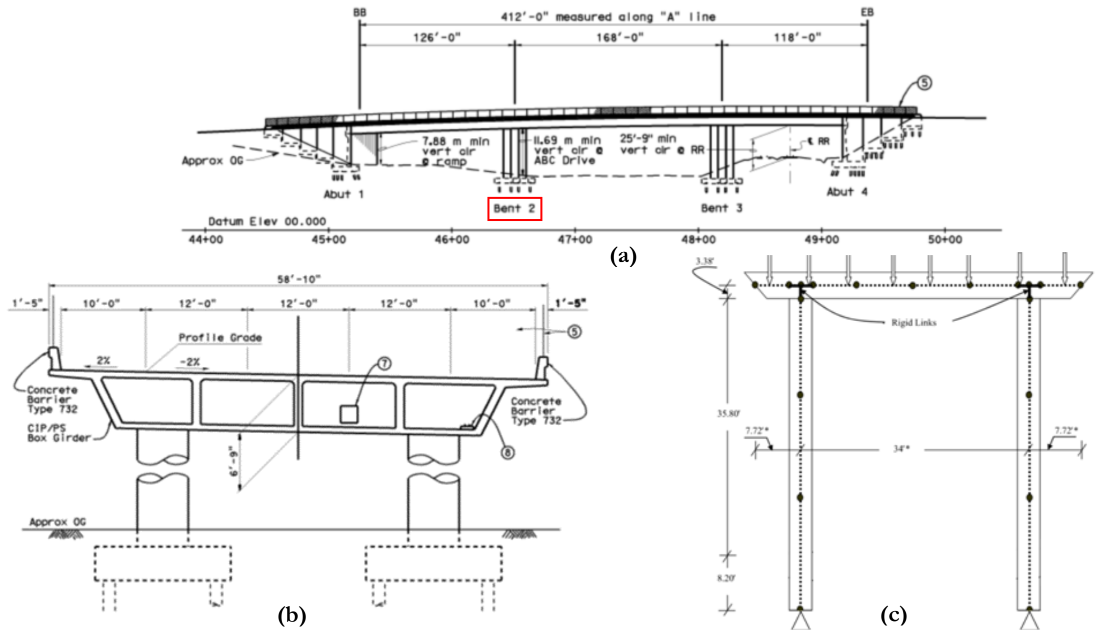

Figure 2. Archetype bridge: (a) elevation view, (b) section view, and (c) structural analysis model [Caltrans, 2015]

5.2 ARCHETYPE NONSTRUCTURAL COMPONENTS

The study considered two archetype nonstructural components: a bridge-mounted pipeline and bridge-mounted light pole. Bridge-mounted utility pipelines can be supported from the bridge deck in various ways. The archetype considered in this paper is a 147 ft long AWWA C151 ductile iron pipeline with a nominal diameter of 20 inches that was installed on Bethel Island Bridge in Northern California [Brick and Tilden, 2019]. The pipeline is supported vertically at every 10 ft by a trapeze that consists of two vertical all thread hanger rods and one horizontal HSS 3x3x1/4. One of the vertical rods is stiffened using Unistrut P1000, and a Unistrut P1000 kicker for lateral bracing is provided every 20 ft. The archetype light pole considered in this paper is the Type 21 pole per Caltrans Standard Plans [Caltrans, 2018]. This pole has a height of 35 ft with a projected arm catching the lighting fixture at 8 ft from centre of gravity. The cross-section is a circular tube tapered linearly along the height with a base diameter of 8.6 inches and top diameter of 3.6 inches. The pole supports 21 lb luminaire per Caltrans authorized materials list.

As summarized in Figure 1, the seismic design force F_p depends on various coefficients typically given in the code. Table 1 summarizes these factors for the two archetype components as given in both ASCE 7-16 and 7-22. Note that the code does not provide factors for poles as they are not typically found in buildings. Thus, the values in Table 1 correspond to an alternative component with similar dynamic properties.

Table 1. ASCE 7 Seismic coefficients for pipe and pole components

Component	Equivalent ASCE 7 Component	Edition	a_p or C_{AR}	R_p or R_{po}	a_p/R_p or C_{AR}/R_{po}
Pipe	Piping and tubing not in accordance with ASME B31, including in-line components, constructed of high-deformability materials, with joints made by welding or brazing	ASCE 7 – 16	2.5	9	0.28
		ASCE 7 – 22	1	2	0.50
Pole	Other flexible architectural components – High deformability elements and attachments	ASCE 7 – 16	2.5	3.5	0.71
		ASCE 7 – 22	1.4	1.5	0.93

5.3 ANALYSIS

In this paper the seismic demand on the archetype nonstructural components is estimated using the following two approaches: 1) prescriptive code-based method using both ASCE 7-16 and ASCE 7-22, and 2) a linear time history analysis. First, the similar terms in the two prescriptive code-based equations are compared. Then, the ASCE 7 results are compared with the more detailed numerical analysis.

An important part of the seismic evaluation of both structural and nonstructural components is the fundamental period. The periods for the archetype bridge, pipeline, and pole are estimated through modal analysis of linear elastic models performed in SAP2000. Sensitivity analysis indicated that the component's periods varied relatively little under reasonable design configurations. Thus, their periods were held constant for this study. However, bridge stiffness can vary significantly based on structural system, anticipated ductility, span length, superstructure/substructure connectivity, etc. Hence, to better understand how the seismic demand changes based on the stiffness of the structure, several fundamental periods of the bridge were investigated through modification of the bridge lateral stiffness, both higher and lower than the baseline period of 2.12 (Case 2) estimated from the Caltrans BDP example discussed above. Table 2 summarizes the component and bridge periods considered in this case study.

Table 2. Fundamental periods of bridges and components considered

	Case 1	Case 2	Case 3	Case 4	Case 5	Case 6
Fundamental period of bridge, T_s (s)	2.98	2.12	1.49	1.22	0.94	0.67
Fundamental period of pipe component, T_p (s)	0.06 (All Cases)					
Fundamental period of pole component, Tp (s)	0.96 (All Cases)					

To further compare the results from the prescriptive equations per ASCE 7, a dynamic study of the bridge-component systems was performed. The natural periods of the archetype components were used to create equivalent lumped mass models that were mounted on the archetype bridge. Ground motions were selected and scaled to Caltrans 2014 Safety Evaluation Earthquake design spectrum for an arbitrary site located in downtown San Francisco (V_{s30} = 270 m/s, Site Class D). A linear time history analysis (THA) using a single ground motion tightly scaled to the design spectrum was performed for each bridge-component system to estimate the resulting maximum accelerations at top of deck and component centre of gravity, which correspond to PFA and PCA, respectively. This permitted the calculation of PFA/PGA and PCA/PFA ratios that are compared to ASCE 7 tabulated values.

We note that ASCE 7-22 Section 13.3.1.5 allows the use of nonlinear time history analysis in lieu of the prescriptive approach. The code requires that the mean demands from a suite of at least seven ground motions be used rather than the single time history used here. Where the component is not explicitly modelled, the PFA is multiplied by C_{AR}/R_{po} to determine the component demands. Because we included the component but modelled the component and structure as elastic, we would consider dividing PFA by the product of R_{po} and R_μ.

5.4 Analysis Results and Discussion

5.4.1 ASCE 7-16 vs. ASCE 7-22

5.4.1.1 *PFA/PGA Amplification Factor*

There is considerable difference in the PFA/PGA amplification factor between ASCE 7-16 and ASCE 7-22. ASCE 7-16 implies that PFA increases linearly based on the point of attachment of the component compared to the height of the structure, up to a maximum of 3 times PGA at the top of structure. In contrast, ASCE 7-22 increases PFA in a more nuanced manner depending on the dynamic characteristics of the structure. PFA depends on the type of lateral resisting system in addition to the mass or stiffness distribution along the height of the structure. ASCE 7-22 attempts to capture these key features by incorporating the period of the structure into the equation. In both ASCE 7 versions, PFA/PGA includes the ratio z/h. Since bridge components are typically mounted at deck level, which could be considered equivalent to "roof level" in a building, it might be natural for the designer to set z/h to unity. Since ASCE 7-16 does not explicitly account for the period of the structure, PFA/PGA has a constant value of 3 when z/h = 1. For ASCE 7-22, PFA/PGA varies and Table 3 summarizes this factor for the range of structure fundamental periods.

Table 3. PFA/PGA per ASCE 7-22

	Fundamental period of bridge, T_s (sec)					
	2.98	**2.12**	**1.49**	**1.22**	**0.94**	**0.67**
PFA/PGA at z/h = 1 (Equation 3)	2.3	2.4	2.6	2.7	2.88	3.1

Note that these are generally less than the fixed value of 3 prescribed by ASCE 7-16 for the period range studied but begin to creep higher than 7-16 for short-period bridges. Equation (3) implies that as the period of the structure approaches 0.4 sec, ASCE 7-22 approaches a maximum amplification of 3.5. Note that an alternate approach to estimate PFA/PGA per ASCE 7-22 is Equation (4), which yields a constant amplification factor of 3.5.

The basis for the PFA/PGA factor in both ASCE 7-16 and ASCE 7-22 is regression on data from instrumented buildings of various heights and structural systems, which ultimately reflects the dynamic characteristics of the structure, such as period, mode shape, and higher mode effect (and likely inherent damping and energy dissipation) [ATC, 2018]. Thus, if the dynamic properties of a given bridge approximate those of buildings (e.g., long- or multiple-span bridges or those whose behaviour is controlled by deck flexibility), ASCE 7 may be valid for estimating amplification, with ASCE 7-22 offering a more nuanced approach. However, for dynamically simple bridges (e.g., rigid deck bridges controlled by bent/pier flexibility) that behave more like a single degree of freedom (SDOF) structure, this amplification may be highly conservative. Therefore, the definition of PFA/PGA, including the assumption that z/h equals unity when the component is mounted on bridge decks, warrants further investigation.

5.4.1.2 *PCA/PFA Amplification Factor*

In ASCE 7-16, the PCA/PFA factors are a step function of either: 1.0 when the component is considered "rigid" (i.e., period less than 0.06s) or 2.5 when the component is considered "flexible" (i.e., period above 0.06s). The updated expression for PCA/PFA factor in ASCE 7-22 still accounts for this ratio of component and building period but in a more nuanced way. In addition to the archetype C_{AR} values provided in Table 1, ASCE 7-22 provides C_{AR} values of 1.0, 1.4, 1.8, 2.2, or 2.8, depending on the ductility and likelihood of the component being in resonance with the supporting structure [ASCE, 2022]. For the archetype bridge structure and components, from Table 1, it is evident that ASCE 7-22 component amplification factors are lower than ASCE 7-16 for both cases considered. We note, however, that values of R_{po} from ASCE 7-22 are also generally lower compared to corresponding values of R_p from 7-16, as discussed further in the next section.

According to ASCE 7, the formulation of a_p and C_{AR} factors accounts for component damping and ductility and is intended to be independent of the supporting structure properties. However, the factors are also intended to limit the design amplification by reducing the probability of component resonance to an acceptably low value [ATC, 2018], and thus have some inherent dependence on the ratio of component period to structure period. Like the PFA/PGA amplification factor, statistical analysis on instrumental data of buildings of various heights and structural systems formed part of the basis for these coefficients (along with properties of representative nonstructural elements). While nonstructural components on both bridges and buildings may have similar properties, the two types of supporting structures may vary in terms of what is considered "typical" and the dynamic properties of each. Survey of documents suggests that typical bridge lateral periods may range from 0.1 sec to 1.2 sec [Dusseau and Dubaisi, 1993; Zelaschi *et al*, 2016; Kuribayashi and Iwasaki, 1973; Feng *et al*, 2011], which is consistent with low- to mid-rise buildings and close to the mean period of components considered in ASCE 7 formulation (which have values of 0.33 sec for flexible and 0.12 sec for rigid components) [ATC, 2018]. Longer span bridges and tall buildings would both likely have periods much longer than this range but would both represent a relatively minor portion of the statistical population. Therefore, it would seem that the building data used to develop the ASCE 7 component amplification factors might still be a good fit for bridges when assessing probability of resonance, but this would warrant further research.

5.4.1.3 *Strength and Ductility Reduction Factor*

ASCE 7-16 provides a single response modification factor, R_p, which accounts for both ductility and overstrength in the component. In contrast, ASCE 7-22 provides a component strength factor, R_{po}, that accounts for the reserve strength in the component, but also requires calculation of a ductility reduction factor, R_μ, that accounts for ductility and overstrength in the supporting structure. Therefore, for purposes of determining the overall demand reduction predicted by each method, it may be more reasonable to compare R_p with the product of R_{po} and R_μ. In this paper, R_μ is calculated to be 2.06 based on AASHTO [2020] values of R = 5.0 and Ω_o = 1.3. Table 4 summarizes the calculated ratio of R_p to the product of R_{po} and $R_{\mu,}$ with values greater than 1.0 suggesting that ASCE 7-16 permits greater reduction for the given structure and component.

Table 4. Comparison of ASCE 7-16 and 7-22 component amplification and reduction factors assuming Rμ = 2.06

Component	Equivalent ASCE 7 Component	$R_p/(R\mu \times R_{po})$	a_p/R_p	$C_{AR}/(R\mu \times R_{po})$
Pipe	Piping and tubing not in accordance with ASME B31, including in-line components, constructed of high-deformability materials, with joints made by welding or brazing	2.19	0.28	0.24
Pole	Other flexible architectural components – High deformability elements and attachments	1.13	0.71	0.45

Table 4 suggests that the total reduction in seismic demand is greater in ASCE 7-16 for both archetype components on this bridge. However, while the reduction permitted in ASCE 7-22 is generally smaller, recall that component ductility is also considered in development of the C_{AR} value and that C_{AR} is generally smaller than the corresponding a_p (see Table 1). This means that a direct comparison of R factors may not tell the full story if various sources of demand reduction have been reshuffled from one coefficient to another. In addition, because the demand reduction potential of the supporting structure is explicitly considered in ASCE 7-22, it is not immediately clear whether ASCE 7-16 or ASCE 7-22 generally predicts lower seismic demands (in terms of allowances for ductility, damping, and overstrength) for any given component without consideration of the supporting structure. A comparison of a_p/R_p with $C_{AR}/(R_\mu R_{po})$ in Table 4 shows little change for the pipe (representative of rigid components) and a more notable change for the pole (representative of flexible components) between the two editions of the code.

Nonetheless, it is important to note that structural demand reduction and overstrength factors can be defined in many ways depending on the design method (force vs displacement) and code used, and that the role of bearings, soil structure interaction, and other sources of demand reduction for bridges may warrant inclusion for bridge applications. Given the importance of this factor to driving overall demands and the fact that ASCE 7 and AASHTO may define and calibrate prescriptive values of R differently, bridge designers need to approach this variable with care if using ASCE 7-22.

5.4.1.4 *Component Seismic Demand*

Considering all factors in the prior sections and their interrelations, it is important to determine the total seismic coefficient predicted for the archetype components and supporting bridge, independent of seismicity (i.e., PGA). This coefficient is calculated using Equations (1) and (2) without the $0.4S_{DS}$ factor. Figure 3 compares the total seismic coefficient independent of seismicity for each component and its variation with the period of the bridge structure.

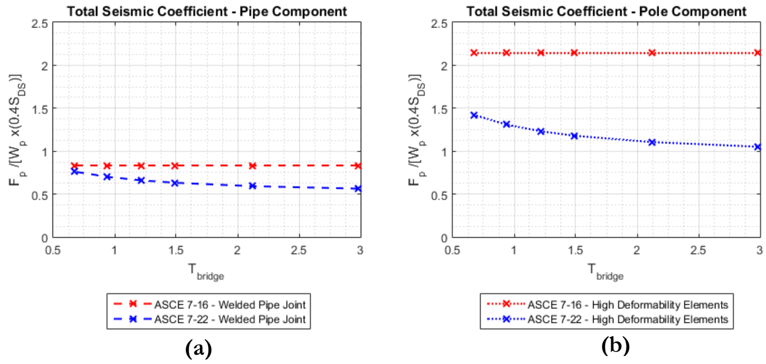

Figure 3. Total seismic coefficients independent of seismicity: (a) Pipe Components, (b) Pole Components

Results in Figure 3 are under the ASCE 7 cap for the seismic design force. Evidently, ASCE 7-22 results in a lower seismic coefficient for both archetype components. A noticeable difference between ASCE 7-16 and 7-22 is that the latter accounts for the impact of the period of the supporting bridge structure on the component demand. As the period of the bridge decreases, ASCE 7-22 equation results in larger seismic demands which is attributed to larger PFA/PGA amplification for short period structures.

5.4.2 ASCE 7 vs. Time History Analysis

In an attempt compare results from prescriptive code provisions to numerical analyses, a linear time history analysis was performed for each bridge-component system. Accelerations at the deck level (PFA) and at the component level (PCA) were extracted. Figure 4 and Figure 5 compare the amplification factors from the dynamic analysis with those from ASCE 7-16 and ASCE 7-22 for different period ratios. Since the THA is linear, the component reduction factors from ASCE 7 are not considered to better compare the dynamic results. Note that the minimum and maximum THA results correspond to an individual ground motion while the THA mean is the average result.

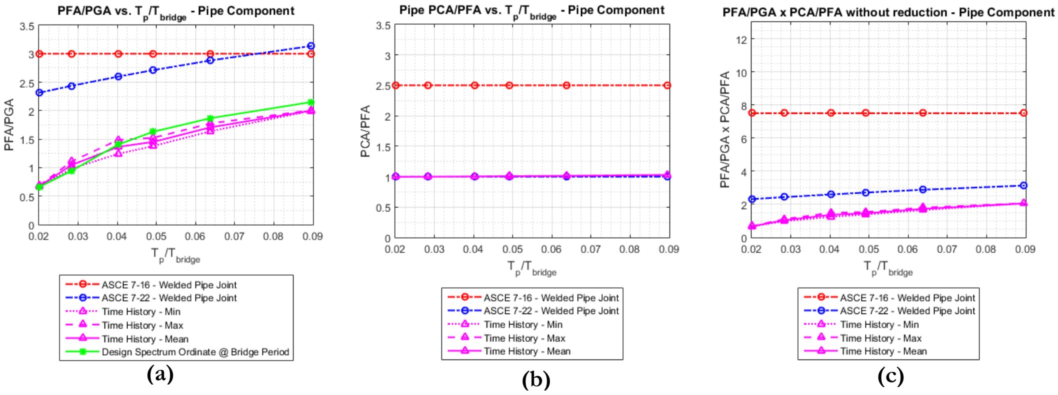

Figure 4. Comparison of amplification for pipe components: (a) PFA/PGA, (b) PCA/PFA, (c) PFA/PGA x PCA/PFA

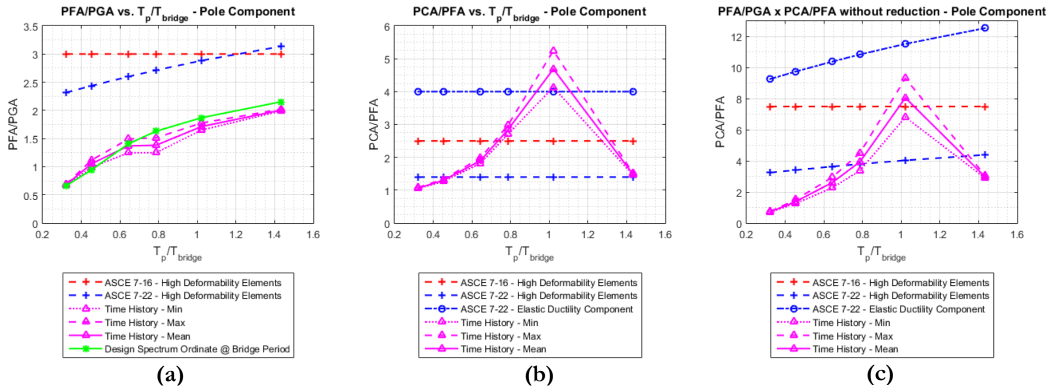

Figure 5. Comparison of factors for pole components: (a) PFA/PGA, (b) PCA/PFA, (c) PFA/PGA x PCA/PFA

Figure 4a and Figure 5a show that both ASCE 7-16 and 7-22 predict PFA/PGA consistently higher than THA for this bridge. This could be attributed to the code equations being based on regression considering the mean response plus some standard deviation [ATC, 2018], as well as the impact of higher mode effects on multi-story buildings. For comparison, we plotted the spectral ordinate of the target response spectrum to which the time history was scaled, which is a close match to the THA, as would be expected given the simple nature of the bridge bent model. Nonetheless, it is evident that ASCE 7-22 PFA/PGA follows the same trend as THA whereas ASCE 7-16 does not, which suggests that ASCE 7-22 correctly considers the impact of supporting structure period, even if the overall amplification suggested through the z/h = 1.0 assumption appears highly conservative. We note that if the user were to assume a value of z/h less than 1.0 (such as 0.5) or remove the amplification term and replace PGA with a conservative value of the design spectral acceleration for the structure, the code demands would fall significantly, and the analysis results would be a much better fit to the code for a dynamically simple structure such as this.

Figure 4b shows that the PCA/PFA for the pipe from the dynamic analysis closely agrees with ASCE 7-22 but is noticeably lower than ASCE 7-16. Similarly, as shown in Figure 4c, the total amplification predicted by THA is closer to the ASCE 7-22 values but much smaller than ASCE 7-16. It is possible that the relationship between the component amplification and reduction factors plays a role here for this particular component type (note that R_p for pipes under ASCE 7-16 was equal to 9). When considering R_p for ASCE 7-16 and the product of R_{po} and R_{μ} for ASCE 7-22, then the results are nearly identical between the two methods and the THA (if the THA results were to be reduced in accordance with ASCE 7-22).

In contrast, Figures 5b and 5c show that PCA/PFA and total amplification for the pole from the THA exceeds the code predicted values for a wide range of period ratio, T_p/T_{bridge}. The noticeable amplification observed for the pole from THA, in contrast to that observed for the pipe, suggests that a pole is more likely to have fundamental period that overlaps with that of the bridge, and thus is more likely to experience resonance. The large difference in the PCA/PFA values for the pole between THA and ASCE 7-22 may, in part, be attributed to a cap placed in the formulation of ASCE 7-22 PCA/PFA, which was developed with an acceptable probability (10 percent) that the component demand is greater than the code prescribed value within a narrow band of period ratio ($0.85<T_p/T_{bridge}<1.25$). Perhaps more importantly, we have noted that component amplification factors in ASCE 7 are not purely dynamic factors and still consider component damping and ductility; in fact, ASCE 7-22 includes an elastic component ductility category with a higher C_{AR} factor, rather than simply reducing the corresponding R_{po} factor for elastic behaviour. Since our THA is a linear elastic analysis and considered only nominal modal damping (5 percent for all modes), using the elastic component $C_{AR}=4.0$ (as permitted by the commentary of the code) gives a result much closer to the mean peak PCA/PFA of 4.7 determined from the THA (Figure 5b). In contrast, the maximum PCA/PFA provided in ASCE 7-16 is 2.5 (even accounting for $T_p/T_{bridge} = 1$ per the commentary). Thus, this suggests that ASCE 7-22 may provide a higher and more accurate estimate for certain flexible bridge components when compared to ASCE 7-16, so long as the designer appropriately categorizes the component ductility when selecting PCA/PFA value.

6. CONCLUSIONS AND RECOMMENDATIONS FOR FUTURE WORK

There are no clear bridge-specific guidelines for prescriptive seismic design of bridge-mounted nonstructural components. The use of ASCE 7 for this purpose was evaluated and differences in demands on archetypal bridge components were compared for two editions of the code, 7-16 and 7-22, for an archetype bridge structure. ASCE 7 amplification factors of archetypal bridge components were then compared with a simplified THA of bridge-component systems. The following conclusions can be drawn from this study:

- Overall, the ASCE 7-22 framework for nonstructural component design appears to be a good candidate for application to bridge structures, with *total* design demands results that match or conservatively envelope, and trend more closely with, the analytical results for this example. In addition, it provides a more nuanced framework based in dynamic principals that should allow designers to more transparently apply engineering judgement to reduce conservativism where supported by first principals or sound analysis. ASCE 7-16, in comparison, both over- and underestimated the analytical results for these case studies but may still yield acceptable results for many bridges.
- The primary source of conservativism between ASCE 7 and the analytical results for this case is the structural amplification factor (i.e. PFA/PGA), especially when z/h is, reasonably, assumed to be 1.0 for deck-mounted components. ASCE 7's amplification equation attempts to conservatively envelope floor spectra for multi-story buildings. While this may yield accurate results for relatively flexible bridges or those with appreciable dynamic response of the deck, this may be overconservative for relatively simple bridges dominated by individual pier response that behave like SDOF structures. In these cases, replacing the PGA (i.e. $0.4S_{DS}$) and the amplification factor with a more accurate value of the floor/deck response (such as the design spectral ordinate for the structure), may be appropriate. It is recommended that suitable bounds on period be selected (considering some level of structure overstrength and elastic response) to assure a reliable design, similar to the T_a cap placed on period for force determination in ASCE 7.
- For the examples chosen, ASCE 7-22 component amplification factors, if selected appropriately, seem to yield better agreement with numerical analysis than similar ASCE 7-16 factors. We note, however, that the ASCE 7-22 C_{AR} factors appear to include assumptions about (a) component overstrength and energy dissipation that may link them to the corresponding component reduction factors and (b) acceptable probability of damage or failure of components whose period approaches that of the supporting structure. These assumptions may or may not yield consistent component reliability in light of typical bridge dynamic response and may not be consistent with the expected reliability of bridge-supported utility components and should be reviewed. Use of a larger component importance factor may be appropriate for critical lifelines.

- A key change to ASCE 7-22 compared to 7-16 is the addition of a structure ductility reduction factor, R_{μ}. While philosophically appropriate to consider, it is unclear how this factor was calibrated for use with typical ASCE 7 lateral system parameters (R and Ω_o) to provide reliable designs, and how potential misapplication of this factor with analytically derived or prescriptively defined (based on other codes like AASHTO or other force- or displacement-based design methodologies) might impact that reliability. When in doubt, use of the minimum structure ductility reduction factor, R_{μ}, of 1.3 recommended in ASCE 7-22 may be conservative and acceptable.

The proposed use of ASCE 7 as a framework for nonstructural component design for non-building structures is by no means new or novel [Goel 2018]. However, engineers should recognize that although believed to be a good candidate for bridges, ASCE 7-22 non-structural provisions were developed for buildings. Thus, designers need to be mindful of this when applying ASCE 7 or interpreting results, pending clearer guidance to practitioners on reliable application of the framework to bridge structures.

The following are limitations with the current study and recommendations for the future:

- This paper considered just two nonstructural components on a single bridge type, with varying lateral stiffness and subjected to two ground motion records, with the intent of simulating a simple component design validation exercise that a bridge designer might undertake. In the future, the scope of the study should account for more components, bridge configurations and structure types, and ground motions with the goal of better validating the ASCE 7 equations for a wider variety of bridges. Additional parameters that impact dynamic properties such as material and construction method should be considered.
- A detailed study of structural amplification (PFA/PGA) for typical bridge structures is warranted to assess the accuracy of the ASCE 7 equations and, if warranted, provide guidance for obtaining less-conservative results.
- The study did not account for nonlinear behaviour in the supporting structure or component. Future studies should consider nonlinear time history analysis and compare results to ASCE 7 accounting for response modification factors.
- The study presented herein focused on seismic response of bridge-component systems in the transverse direction. For bridge decks, vertical acceleration at mid-span as well as longitudinal seismic forces may be significant. Further studies focusing on vertical accelerations and longitudinal loading need to be performed.
- Additionally, it would be important to compare the seismic demands determined herein to typical wind loads to determine if design is ultimately governed by wind or seismic detailing for certain component types.
- We would encourage future refinements to the ASCE 7 nonstructural design framework to more consistently decouple the component dynamic amplification from the corresponding component reduction factors, where feasible, to improve consistency with numerical methods.

REFERENCES

AASHTO [2020], *LRFD Bridge Design Specifications*, American Association of State Highway and Transportation Officials.

AASHTO [2015], *LRFD Specifications for Structural Supports for Highway Signs, Luminaires, and Traffic Signals*, American Association of State Highway and Transportation Officials.

ASCE 7-16 [2017], *Minimum Design Loads and Associated Criteria for Buildings and Other Structures*, American Society of Civil Engineers

ASCE 7-22 [2022], *Minimum Design Loads and Associated Criteria for Buildings and Other Structures*, American Society of Civil Engineers

Abe, M., & Shimamura, M. [2014] "Performance of railway bridges during the 2011 Tohoku Earthquake," *Journal of Performance of Constructed Facilities,* 28(1), 13–23. doi:10.1061/(ASCE)CF.1943-5509.0000379.

Applied Technology Council (ATC) [2017] "Seismic analysis, design, and installation of nonstructural components and systems - background and recommendations for future work," NIST GCR 17-917-44.

Applied Technology Council (ATC) [2018] "Recommendations for Improved Seismic Performance of Nonstructural Components," NIST GCR 18-917-43.

Bharil, R., Pierepiekarz, M., & Chandler, W. [2001]. "Guidelines for bridge water pipe installations," *ASCE Proceedings: Pipelines* 2001, 1-17.

Brick, W., & Tilden, Y. [2019] "Crossing That Bridge Later: Installing a Critical Water Pipeline over an Existing Bridge without Modifications," *Pipelines 2019: Condition Assessment, Construction, and Rehabilitation* (pp. 445-455).

Caltrans [2015] *Bridge Design Practice 4th Edition*, California Department of Transportation.

Caltrans [2018] *Standard Plans*, California Department of Transportation.

Caltrans [2019] *Seismic Design Criteria Version 2.0,* California Department of Transportation.

DIPRA [2016] *Bridge Crossing with Ductile Iron Pipe*, Ductile Iron Pipe Research Association.

Dussfau, R. A., & Dubaisi, H. N. [1993] "Natural frequencies of concrete bridges in the pacific northwest," Retrieved from SCOPUS

Earthquake Engineering Research Institute (EERI), [2016] *Kaikoura, New Zealand Earthquake Virtual Clearinghouse*, available at https://learningfromearthquakes.org/2016-11-13-kaikoura-new-zealand/ (accessed July 2022).

Feng, M. Q., Fukuda, Y., Deng, X., Guan, Y., & Gomez, H. C. [2011] "Long-term Structural Performance Monitoring of Bridges: Hardware Maintenance And, Long-term Data Collection/analysis (No. CEEMF005)," University of California, Irvine.

Goel, R.K. [2018] "Seismic Forces in Ancillary Components Supported on Piers and Wharves," *Earthquake Spectra*, Volume 34, No. 2, pages 741–758, May 2018.

Hooper, J., Holmes, W., Moehle, J., Crouse, C., Pekelnicky, R. and Harris, J. [2013] "Development of NIST Measurement Science R&D Roadmap: Earthquake Risk Reduction in Buildings," NIST GCR 13-917-23.

Kuribayashi, E., & Iwasaki, T. [1973] "Dynamic properties of highway bridges". *Proceedings of the 5th World Conference on Earthquake Engineering* (pp. 938-941).

Palermo, A., Wotherspoon, L., Hogan, L., Kivell, A., Yashinsky, M., Bruneau, M. [2011] "Preliminary findings on performance of bridges in the 2011 Christchurch earthquake." in *Reconnaissance report* 2011.

Rais, A., Giovinazzi, S., & Palermo, A. [2015] "Pipelines at Bridge Crossings: Empirical-Based Seismic Vulnerability Index," *Pipelines 2015*, 1642-1654.

Schiff, A.J. [1997]. "Northridge Earthquake: Lifeline Performance and Post-Earthquake Response." *US Department of Commerce Technology Administration: NIST GCR 97-712*.

Siringoringo, D. M., Fujino, Y., Nagasaki, A., & Matsubara, T. [2021] "Seismic performance evaluation of existing light poles on elevated highway bridges," *Structure and Infrastructure Engineering* 17(5), 649-663.

Zelaschi, C., Monteiro, R., & Pinho, R. [2016] "Parametric characterization of RC bridges for seismic assessment purposes," *Structures* (Vol. 7, pp. 14-24). Elsevier.

Computational Modelling and Seismic Performance of Non-traditional Automated Warehouse Storage System

Lívia Mello[1], Ph.D. and Andy Coughlin, PE, SE[2]

[1] Structural Integrity Associates, Inc.
9710 Scranton Rd, Ste 300, San Diego, CA 92101 USA
e-mail: lmello@structint.com

[2] TRU Compliance, by Structural Integrity Associates, Inc.
233 SW Wilson Ave, Ste 101, Bend, OR 97702 USA
e-mail: acoughlin@structint.com

Abstract. The AutoStore™ system is a warehouse logistics solution and automated modular storage system. Bins containing merchandise are stacked high and close in proximity to one another in an aluminium grid system. Robots travel atop the grid along tracks to move the bins around and fulfil orders. This storage system has many advantages over traditional ones, such as greater space efficiency, fewer staff requirements, and improved speed of fulfilment and restocking. However, due to its complexity, existing prescriptive code recommendations are perceived to be overly conservative and restrictive in evaluating its seismic capacity. Experience from seismic shake table testing demonstrated the structure is more robust than typical code equations would suggest, but the cost becomes prohibitive for testing large-scale grids. Hence, numerical simulation becomes a major tool in evaluating the seismic performance of the system. In this work, a series of nonlinear dynamic analyses of a reference grid were conducted and the dynamic behaviour of different grid configurations were investigated.

Keywords: nonlinear numerical modelling, LS-DYNA, nonlinear dynamic analysis, seismic compliance, seismic performance

1. INTRODUCTION

1.1 BACKGROUND

The AutoStore™ system is an automated warehouse storage system that provides space- and cost-efficient logistics solutions to users with high-performance requirements. The system is assembled as a modular cubic grid; hence it is scalable, simple to build, maintain, and expand.

Plastic storage bins are stacked high and close in proximity to one another in the aluminium-column grid. A bidirectional grid track rests atop of the columns and allows for motorized robotic conveyors to travel along the tracks, move bins around, and deliver them to fulfilment kiosks located along the grid's edges. Once at a kiosk, users can deposit or withdraw inventory as needed. Figure 1 depicts a typical AutoStore™ storage grid.

Figure 1. Overall View of an AutoStore™ System (courtesy of AutoStore™)

The aluminium grid system requires external restraints for lateral stability under operational loads such as robot acceleration and footfall vibrations of maintenance personnel. Building codes also mandate lateral restraint for seismic loads, indoor wind loads, or incidental live loads. Seismic loads can vary greatly from site to site but tend to drive the restrain design in areas of moderate to high seismicity. However, seismic forces calculated in accordance with the equivalent static provisions of ASCE 7-16 [ASCE, 2016] and similar methods in other code jurisdictions [BCJ, 2016] are perceived to be overly conservative and restrictive in evaluating the seismic capacity of the system. Furthermore, experience from shake table testing in Japan in 2016 [Nakagawa, 2016] and at UC Berkeley/PEER in 2019 [Takhirov and Haider, 2019] demonstrate the system is more robust than typical code equations would suggest.

To remove conservatism from code capacity calculations and avoid prohibitive costs of large-scale shake-table testing, numerical simulation becomes a major investigative tool. In this work, a series of high-fidelity nonlinear dynamic analyses of reference AutoStore™ grid were conducted to evaluate its seismic behaviour and performance.

1.2 OBJECTIVES

This work focuses on the computational modelling techniques implemented in the nonlinear dynamic analyses of a non-traditional storage grid system. The results offer insights into its structural behaviour and are expected to assist with future seismic-compliant grid planning. The dynamic analyses are performed following code provisions for seismic certification [ASCE, 2016] adopted by state and local authorities throughout the United States of America but also adaptable to building codes globally. The evaluation of the seismic performance of such a complex system via nonlinear dynamic analysis aids in removing conservatism from static-equivalent design procedures. Designs of mounting systems that meet the seismic capacity derived from these analyses are suitable for acceptance by local building officials with sign-off from an engineer licensed in that jurisdiction.

1.3 NON-DISCLOSURE STATEMENT

Some details of the AutoStore™ grid (such as specifics about the types of material and geometry of the main load-bearing components of the system) are considered sensitive, commercial, or valuable in nature. These were kept undisclosed at the authors' discretion without any loss to the technical relevance of this work.

2. ANALYSIS PROCEDURE

A higher-fidelity finite-element modelling approach using nonlinear explicit analysis in LS-DYNA® was chosen. With this approach, one can model bin separation and sliding, contact between bins and columns, column lift-off, nonlinear material behaviour, and large displacement effects. The level of details assures confidence in the results, but also requires substantial computing power. Another drawback is that long runtimes are inevitable when simulating lengthy time histories in an explicit integration framework. To reduce runtime and increase computational power, all the analyses were executed in Massively Parallel Processing (MPP) [Wang, 2013], which is a type of parallel computing available for LS-DYNA®.

Six grid configurations with different bin sizes and stack heights are considered, as listed in Table 1. For each grid configuration, two main support types are proposed: bare and rigid, totalling 12 models. These two support types bound the behaviour of the grid. However, ultimate seismic capacity is evaluated only for the bare system as it captures the inherent seismic capacity of the structure should the primary support system, regardless of its type, fail.

A third support type, characterized as flexible, is also considered but for model validation purposes only.

The analysis procedure and seismic evaluation goes as follows:

i. Validate the UUT-01 test No. 4 from the 2019 UC Berkeley test program (referred to henceforth as PEER test) [Takhirov and Haider, 2019], which is equivalent to a 330-16 flexible grid system. Acceleration time-histories from the benchmark test are available and shown in Figure 8. The test experienced no damage and no permanent displacement, indicating linear behavior during motion.

ii. Adapt the validated model to apply proper support conditions for both bare and rigid systems. All 12 adapted models are subjected to the same acceleration time-histories above and their seismic performance evaluated.

iii. The same time histories as the previous steps are then used as baseline and scaled to update the demand for different bin heights and stack heights for the bare system, in order to properly approximate the level of failure of each configuration.

Table 1. List of Grid Configurations

Configuration	Bin Height (mm)	Number of Bins per Stack
220-18	220	18
220-24	220	24
330-12	330	12
330-16	330	16
425-10	425	10
425-14	425	14

3. COMPUTATIONAL MODEL

3.1 Overall Description

Figure 2 depicts a typical grid model and list its basic components [AutoStore, 2018]. The column-grid is approximately 4.54 x 9.94 m², with 505 mm and 705 mm on-centre spacings along the x- and y-directions, respectively. Each column is connected to the floor through a foot block. At mid-height, spacers are inserted in between every two adjacent columns. The top tracks sit on top of the column-grid, creating a horizontal grid. Bins are stacked in between each grid cell.

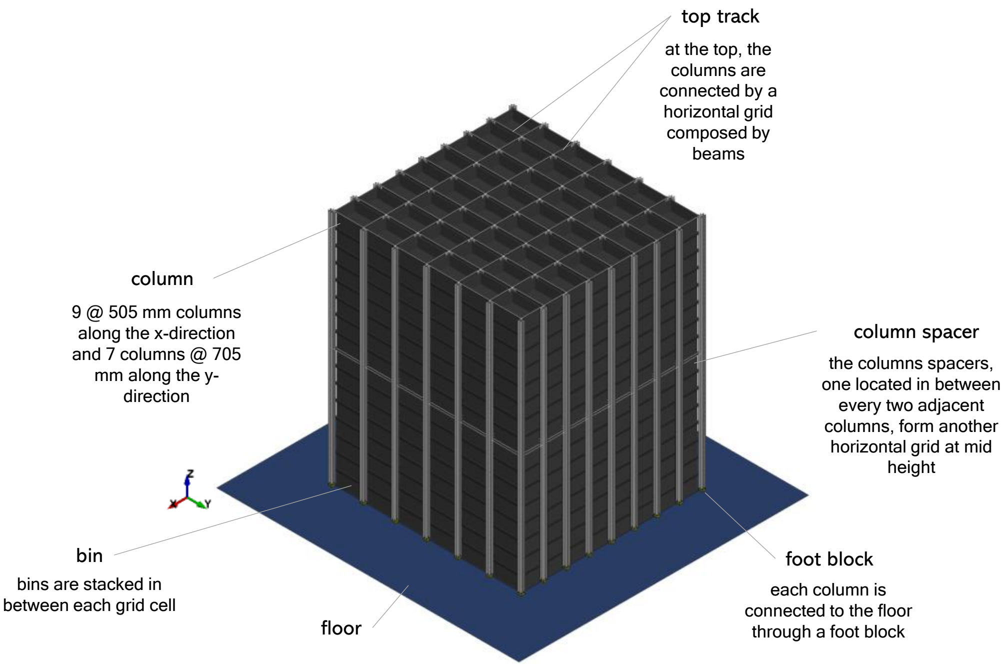

Figure 2. Reference geometry of grid model

3.2 Types of Support Systems

Two main types of support systems are considered: bare and rigid.

Supports matching the PEER test installed conditions are used as a characteristic flexible support model and included for validation purposes only. In the flexible system, the connection between the floor and the base of the perimetral columns is provided by angle-strut brackets which were determined by AutoStore™ to be impractical for their system but provide a good experimental benchmark nonetheless. A similar connection was included in the LS-DYNA model using shell elements. In each bracket, the horizontal plate is constrained to the floor with *CONSTRAINED_EXTRA_NODES_SET, while the vertical plate is tied to the column with *CONTACT_TIED_SHELL_EDGE_TO_SURFACE. The brackets are assumed to be made of elasto-plastic with hardening galvanized steel, defined with *MAT_PIECEWISE_LINEAR_PLASTICITY. Although the contact definitions do not allow for separation between the connected elements (hence connection failure is not considered a failure mode in reinforcement brackets), the brackets can experience plastic deformation up to failure.

For the rigid system, tension-only full-height cross bracings are placed on each side of the model, anchored directly to the floor and the top track through shared nodes [SIA, 2021]. The braces are defined as discrete beams and *MAT_GENERAL_NONLINEAR_1DOF_DISCRETE_BEAM, following the force-displacement curve presented in Figure 4, including unloading-reloading and failure at ultimate axial displacement. Details of the cross-brace design are not presented due to its proprietary nature, and for the purposes of this study its rigidity is intended to represent a variety of low-displacement restraint systems that may be deployed in AutoStore™ grids. In the case of a realistic grid, the braces would be properly spaced throughout the grid.

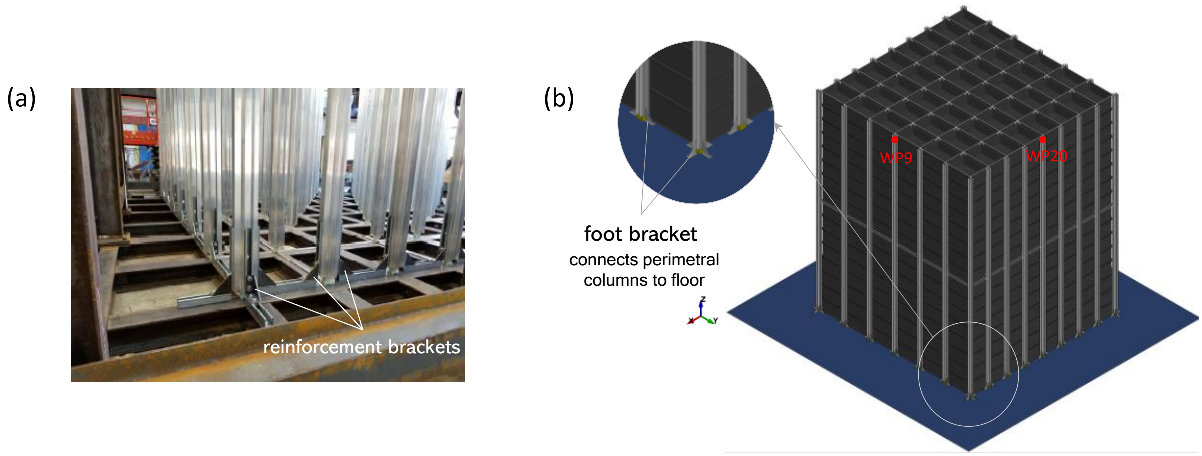

Figure 3. Reinforcement brackets in the flexural system: (a) PEER test; (b) Computational Model

The bare system does not have any additional component to provide lateral support and the column base behaves as a pin connection without resistance to uplift. This support type captures the inherent seismic capacity of the grid, as it represents a self-isolated system. Note that the bare and rigid systems bound the structural behaviour of the model: the former represents a fully unrestrained system, while the latter is nearly fully restrained.

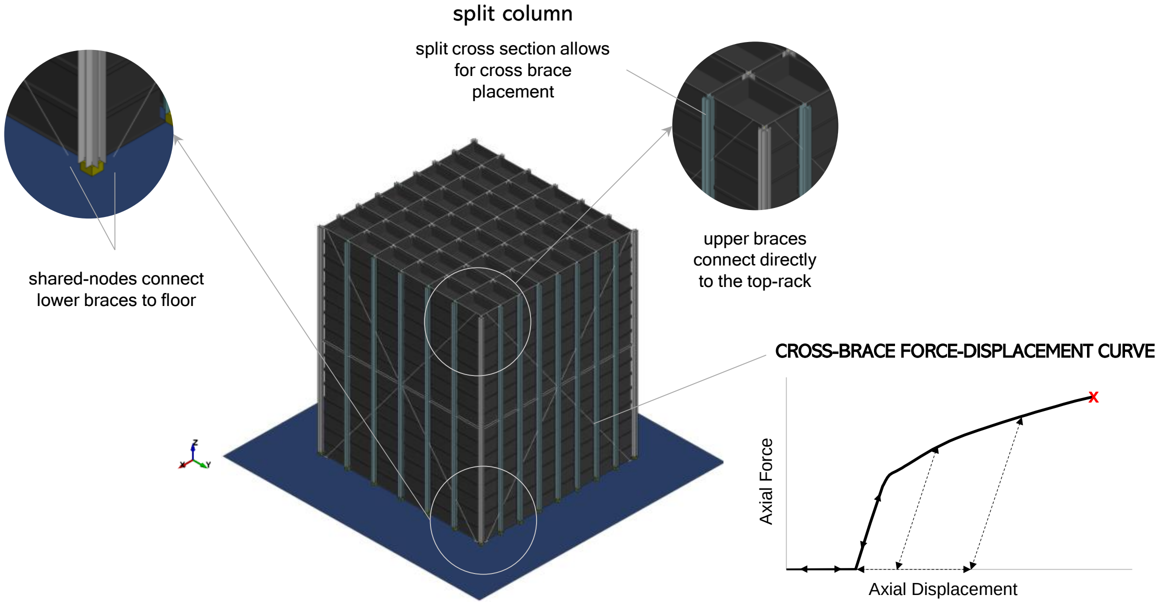

Figure 4. Cross-braces in the computational model

3.3 Columns

The columns are made of shell elements and elasto-plastic aluminium alloy using *MAT_PIECEWISE_LINEAR_PLASTICITY. The height of the columns is adjusted according to the bin stack height.

For modelling purposes, the column cross-section was simplified, which resulted in a slight change in cross-sectional area and overall thickness, but principal moments of inertia remained the same to preserve its flexural behaviour. Both the cross sections of the regular and split-column were simplified. Split columns are part of the rigid system only and they allow for proper placement of the cross-brace. The material density was adjusted to accommodate for the change in the cross-sectional area so that the columns retain their original mass.

3.4 Floor and Foot Blocks

The floor and foot blocks are modelled as rigid (*MAT_RIGID), with shell and solid elements, respectively. The bottom of each block is tied to the floor with *TIED_SURFACE_TO_SURFACE_OFFSET and not allowed to separate. The top of the foot block is shaped so that it gets inserted into the column base, as depicted in Figure 5. This is to simulate possible column lift-off from the track on which the entire grid is built [AutoStore, 2018]: column transfers compressive loads to the block, and subsequently the floor; but if the column lifts enough, it snaps away from the foot block, indicating column-to-floor connection failure. Contact between the column and foot block is defined with *CONTACT_AUTOMATIC_SURFACE_TO_SURFACE.

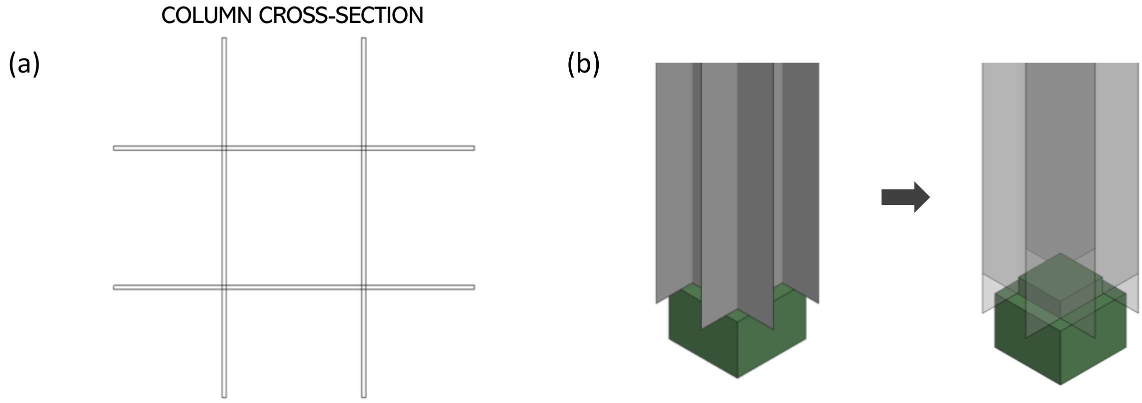

Figure 5. (a) Column cross-section approximation; (b) Column to foot block connection

3.5 TOP TRACK AND COLUMN SPACERS

The top rack is modelled with beam elements and made of elastoplastic aluminium alloy (*MAT_PIECEWISE_LINEAR_PLASTICITY). Similar to the columns, the original X- and Y-track (which run in x and y directions, respectively) cross-sectional profiles were simplified into rectangular shapes with the same moments of inertia, but different cross-sectional areas. Once more, the material density was adjusted to accommodate for the consequent change in cross-sectional area and maintain the top track's original mass.

In an actual grid, the tracks are simply inserted into the columns' hollow cross-section. To simulate this connection, discrete elements with tensile-displacement failure criteria were used to link the track beams to the top of the columns (Figure 6). The discrete element behaviour is defined with *MAT_NONLINEAR_ELASTIC_DISCRETE_BEAM and all translational and rotational force-displacement curves are set to a rigid-like behaviour, except translation in the axial direction. In the axial direction, the elements can resist compression but have low tensile stiffness to mimic the top rack possibly being lifted away from the rest of the structure. In other words, the discrete elements can transfer moments and compressive forces but will fail if extended past their ultimate tensile displacement, characterizing structural failure as the top rack disengages from the rest of the grid. The displacement limit is set to match the same length at which the X- and Y-tracks are inserted into the columns.

Column spacers are placed at the grid's mid-height and connect adjacent columns [AutoStore, 2018] (Figure 6). They are modelled as truss elements made of elastic aluminium alloy. No failure criteria are assigned to these elements, meaning that they cannot disconnect from the columns.

3.6 BINS

Bins are made of shell elements and rigid HDPE plastic modelled with *MAT_RIGID_DISCRETE. This is a material that is discretized into multiple disjoint pieces, often used to model granular material in which the grains behave as individual rigid pieces but interact through an automatic single surface definition [LSTC, 2018]. The modelled bins are shaped as shown in Figure 7 and contact among bins and between bins and columns is defined with *CONTACT_AUTOMATIC_SINGLE_SURFACE. This contact definition considers both static and dynamic coefficient of frictions, which allows for the bins to slide against each other while also impacting the surrounding columns. Common values of friction coefficient for plastic-on-plastic are between 0.2 and 0.3. The bin stacks sit directly on the floor and, similarly to the aforementioned contact definition, they are free to slide against the floor. This interaction between the bottom of the stack and the floor is defined with *CONTACT_AUTOMATIC_SURFACE_TO_SURFACE.

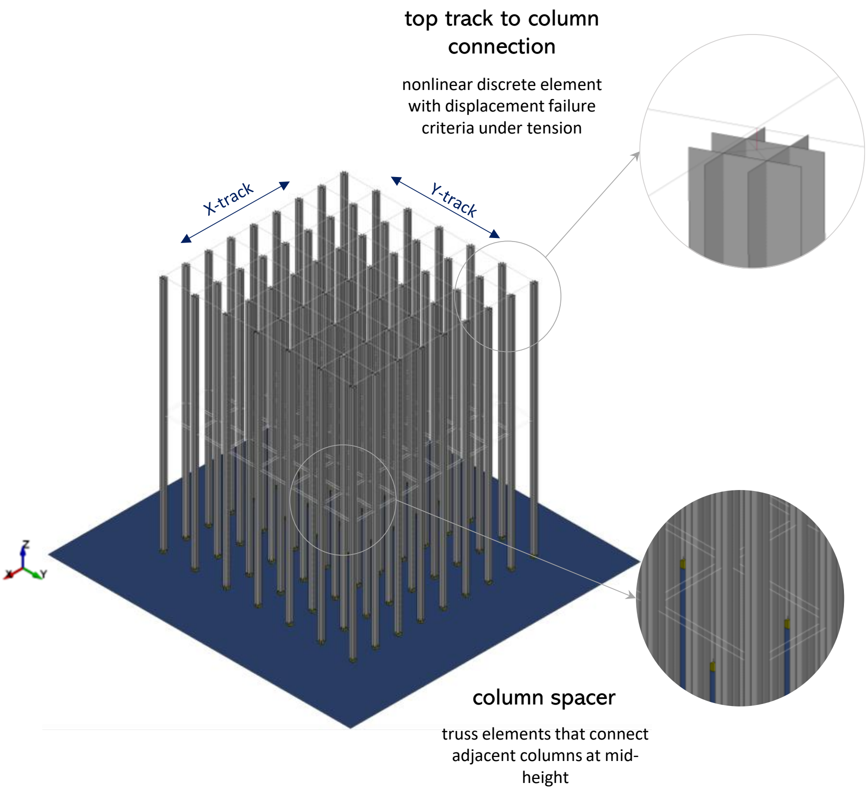

Figure 6. Top track and column spacers

Each bin has an added mass of 23.3 kg [Takhirov and Haider, 2019] to represent the weight of the stored merchandise. This added mass is included with *MASS_NODE_SET and the node set lies on a "false-bottom" layer purposefully placed at the same height as the bin's centre of gravity (Figure 7). Bin height and number of bins per stack vary according to the list of model configurations (Table 1).

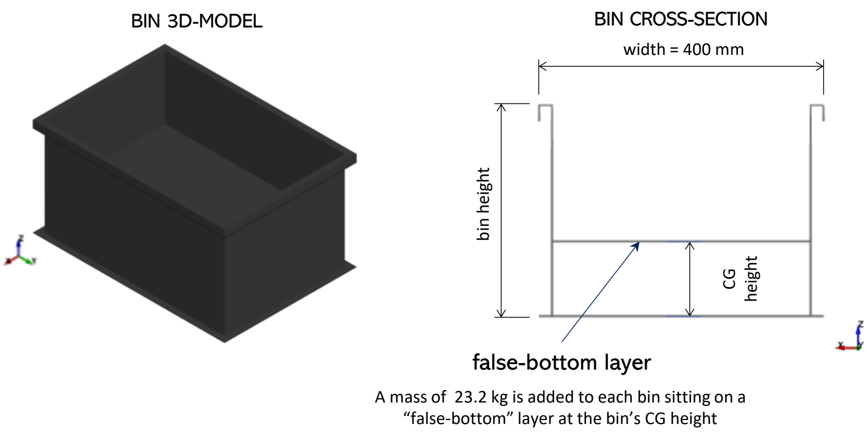

Figure 7. Bin model and added mass

3.7 Load, Boundary Conditions, and Failure Criteria

Preloading due to gravity is applied to the entire model via *LOAD_BODY_Z, followed by the ground motion applied only to the floor, with *BOUNDARY_PRESCRIBED_MOTION_RIGID. The ground motion is based on the acceleration time histories applied in the PEER test UUT-01 No. 4 [Takhirov and Haider, 2019]. This test number experienced no damage and no permanent displacement, indicating linear behaviour during motion. The three mutually orthogonal baseline accelerations (that correspond to S_{DS} = 0.8g) and their respective response spectra (with 5% damping) are shown in Figure 8. They are applied simultaneously and, in the case of the bare system only, scaled (in increments of 0.05g) to update the seismic demand for different bin heights and stack heights and properly approximate the level of failure of the bare model configuration.

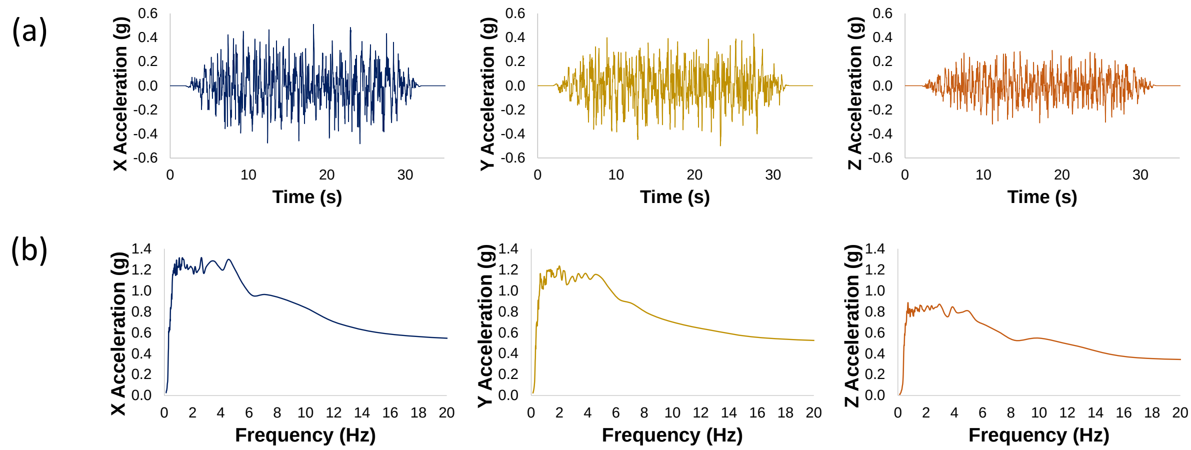

Figure 8. Acceleration histories and response spectra

The ultimate seismic capacity of a grid configuration is presumed to be that at which failure is imminent. Hence, it must be slightly below the seismic level that resulted in a failure state. Structural failure is reached if at least one of the following occurs:

i. One or more columns lift off from their foot block
ii. One or more top rack-to-column connectors fail
iii. Any of the main deformable structural elements (i.e., columns, top rack beams, or cross-braces in the case of a rigid system) present excessive to up to failure deformation.

4. RESULTS

4.1 Model Validation

Model validation is performed by comparing the natural frequency and maximum displacements from the PEER UUT-01 No. 4 test to its equivalent dynamic analysis of the 330-16 flexible system. The test specimen's natural frequencies in the two orthogonal horizontal directions were calculated based on its free vibration response [Clough and Penzien, 1975], captured through its displacement history towards the end of the test run, when the applied ground motion had ceased and the grid was allowed to deform freely. The displacements in question were captured by transducers WP9 and WP20, placed at the top of two mid-grid columns (Figure 3). With the specimen's free vibration response, one can also estimate the damping coefficient of the system [Clough and Penzien, 1975]: 2.8% and 4.7% in the x- and y-direction, respectively.

In the dynamic analysis, an averaged global damping coefficient of 3.5% was assumed and applied with *DAMPING_FREQUENCY_RANGE between 0.5 Hz and 5 Hz.

Table 2 compares the natural frequencies and maximum displacements between the PEER UUT-01 No. 4 test and the dynamic analysis of the 330-16 flexible system. The model's natural frequencies of 0.79 Hz (x-direction) and 0.87 Hz (y-direction) are in the same range as the test grid's: 0.79 Hz and 0.92 Hz in the x- and y-directions, respectively. The model also performs well in capturing the maximum displacement in the y-direction but shows a much larger displacement in the x-direction. Figure 9 compares the entire displacement history between the test and the dynamic analysis and highlights the peak displacements. Note that the model tends to reach higher displacement amplitudes. Due to its high nonlinearity, as well as modelling approximations and simplifications made, it is expected that the simulation does not perfectly agree with the test results. All things considered, the validation results are deemed acceptable.

Table 2. Model Validation Results

		PEER Test	Dynamic Analysis
Natural Frequency, f (Hz)	x	0.79	0.79
	y	0.92	0.87
Maximum Displacement	x	199.6	258.4
	y	193.8	188.3

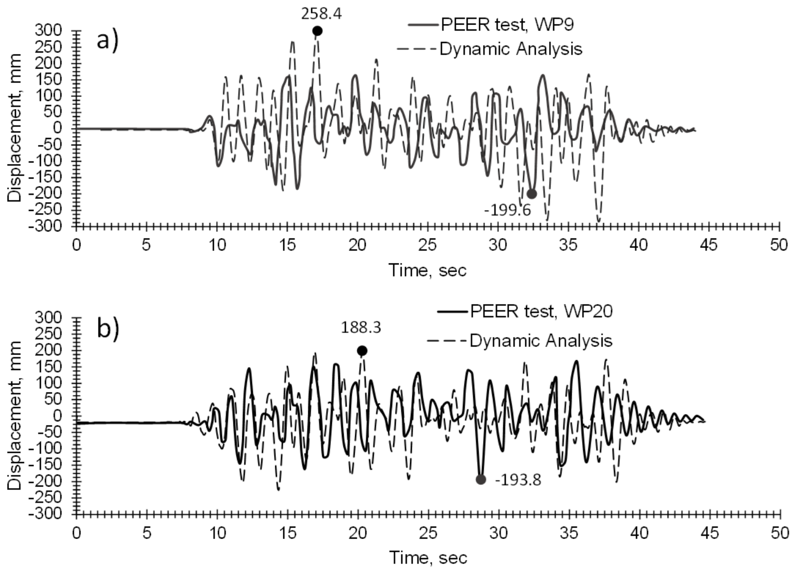

Figure 9. Comparison between displacement histories between PEER UUT-01 No. 4 and 330-16 flexible model, with SDS = 0.8g

4.2 Seismic Performance Evaluation

4.2.1 Bare System vs. Rigid System

Figure 10 compares the maximum displacement at the top of the grid for all six grid configurations of the bare and rigid systems, when subjected to the same acceleration histories as the PEER UUT-01 No. 4 test (Figure 8), with S_{DS} = 0.8g. As expected, the displacements of the rigid system significantly smaller than those of the bare system. Thus, this type of restraint is effective in limiting the grid deformation, which is relevant from an operational standpoint. For comparison, the natural frequencies of the 330-16 configuration of both the bare and rigid systems are, in average between the x- and y-directions, 0.75 Hz and 2.4 Hz, respectively. However, note that 220-24 rigid grid reached a maximum displacement of 57 mm prior to failure of one of the cross-braces. This resulted in even larger deformations and subsequent failure of the other braces. At this point, one may assume the model to behave as a bare system that though the higher displacements pose a limitation on its operational performance, it has some intrinsic seismic capacity regardless of the type of lateral restraint implemented.

4.2.2 Seismic Capacity of the Bare System

Table 3 lists the S_{DS} at failure of each grid configuration of the bare system when subjected to updated acceleration histories, which were scaled up until the grid reached a failure state. In general, an increase in overall height and mass decreases the grid's seismic capacity. For all six configurations, the grid failed due to the top rack disengaging from the columns in at least one location. In some cases, columns that lost their connection to the top grid start to detach from the foot blocks as well. Realistically, and based on the comparison between maximum displacements of the bare and rigid systems, a combination of restraint systems should be implemented to comply with both the operational and seismic requirements.

Table 3. Seismic Capacity of the Bare System

Configuration	S_{DS} at failure (g)
220-18	1.10
220-24	1.05
330-12	1.45
330-16	1.20
425-10	1.35
425-14	1.20

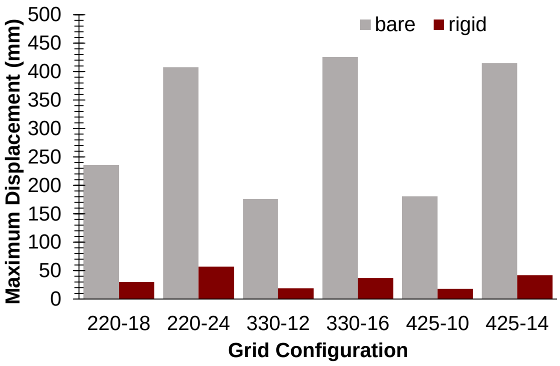

Figure 10. Comparison between bare and flexible systems: maximum displacements at the top of the grid

5.DISCUSSION

Although a level of rigidity is required for reliable operation of the AutoStore™ grid and robots, these results show that the bare system can withstand significant seismic events without failures that would endanger life and limb. A system adequately designed for operational rigidity is expected to attract significant seismic load into its restraint system at the onset of an earthquake, consistent with the non-structural seismic force assumptions of ASCE 7-16 Chapter 13 [ASCE, 2016]. These forces would be expected to quickly overwhelm the restraint system, resulting in its failure and subsequent seismic response of the bare system, whose long period is able to avert much of the seismic energy similar to a base isolation system. The averted (or attenuated) seismic energy, resistance energy of the bare system, and the effects of damping energy combine to achieve a life safety goal consistent with the seismic design goals of building codes in high seismic regions like the U.S. and Japan.

6. CONCLUSION AND FUTURE WORK

Details of the computational modelling approach used in the dynamic analysis of a non-traditional storage system (based on the AutoStore™ grid) were presented. Between the two main restraint systems considered, while the bare system captures the intrinsic seismic capacity of the structure, a combination of restraints is ideal for complying with both operational (i.e., lateral displacement at the top track level) and seismic requirements. Despite the level of detail in the model, which increases confidence in the results, additional numerical analysis and/or experimental tests for different grid sizes and restraint configurations and combinations are suggested. However, given that the numerical dynamic analyses require substantial computing power, future work also includes a proposal for a simpler methodology to arrive at the seismic capacity of a given grid. Preliminary results from detailed finite-element analysis might be used to identify the key dynamic properties of the system, which can then be approximated to a single or multi-degree of freedom system and solved analytically.

REFERENCES

AutoStore. [2018]. *DD Grid 7.0: Installation Manual*, AS-50087-STD-eng, Rev. 0. AutoStore™, Nedre Vats, Norway.

ASCE [2016] *ASCE 7-16: Minimum Design Loads and Associated Criteria for Buildings and Other Structures*. American Society of Civil Engineers, Reston, Virginia, USA.

Clough, R., and Penzien, J. [1975] *Dynamics of Structures*, McGraw-Hill.

LSTC [2018] *LS-DYNA® Keyword User's Manual: Volume II, Material Models*. Livermore Software Technology Corporation, Livermore, California, USA.

Nakagawa [2016] "Grid Earthquake Resistance Test Report", Logistics System Business HQ, Marketing Department, Japan.

SIA [2021] "AutoStore™ Bracing System Analysis and Redesign", 2000472.402.R0. Structural Integrity Associates, Inc., San Diego, California, USA.

Takhirov, S., Haider, A. [2019]. "Seismic Evaluation of AutoStore's Automated Storage System", Report No. PEER – STI/2019-01. Pacific Earthquake Engineering Research Center, UC Berkeley, Berkeley, California, USA.

BCJ [2016] *The Building Standard Law of Japan*. The Building Center of Japan, Tokyo, Japan.

Wang, J. [2013]. *Introduction to MPP Version of LS-DYNA®*. Livermore Software Technology Corporation, Livermore, California, USA.

Case Study to Evaluate the Key Parameters of the Dynamic Response of Floor-Anchored Nonstructural Components

Tal Feinstein[1], Jack P. Moehle[2]

[1] Exponent Inc.
475 14th St #400, Oakland, CA 94612
e-mail: tfeinstein@exponent.com
[2] University of California, Berkeley
Davis Hall, Berkeley, CA 94720
moehle@berkeley.edu

Abstract. Failure of nonstructural components during an earthquake can cause widespread property damage, lead to lengthy downtime of the structure, and pose a life-safety threat to the occupants. Current code provisions aim to minimize the life safety threat by specifying lateral force demands and anchoring requirements. These code requirements are based on a simplified equation that does not fully consider the component attachment's contribution to its overall dynamic response. Previous research suggests that the attachment design changes the boundary conditions and is an important parameter to determine the component dynamic properties. This paper explores the applicability of a mechanics-based numerical modeling approach for floor-anchored nonstructural components attached via steel channel connections. The model considers the interaction between the flexible component response and constrained rocking at the base. The paper presents a case study of eight floor-anchored mechanical and electrical components. The components were chosen from the Health Care Access and Information preapproval database. A suite of 35 ground motions and seven floor motions was used to assess the response of two attachment designs for each of the chosen components. The results of the case study are then used to evaluate the component seismic coefficients used in code provisions to determine the lateral force demand.

Keywords: Seismic Demand, Numerical Model, Equipment, Floor-anchored.

1. INTRODUCTION

The current nonstructural components code provisions are focused exclusively on life safety. ASCE 7 provide lateral force equations based on simplified models considering parameters that are believed to affect the dynamic force amplification of a nonstructural component [ASCE/SEI 2017]. The considered parameters include the site-specific seismic hazard, relative location within the structure, and component-specific properties. The current approach considers a generalized component type behavior, without consideration of its attachment to the structure. Thus, a change in the attachment design of a component would not result in a change of the lateral force demand.

Manufacturers usually predesign equipment without providing information on the properties and build of the component. Thus, the engineer must design an attachment for the equipment based on limited information and with little to no opportunity to modify the component structure itself. An engineer commonly will prefer a ductile attachment design that will limit the force transfer and thereby decrease the overall component demand. Moreover, recent design guidance [NIST 2018] mentions this approach, indicating that providing ductility in the load path between the component and the supporting structure through an angle attachment would be an ideal approach.

Most analyses and experiments that examine the dynamic behavior of nonstructural components are based on an idealized single-degree-of-freedom (SDOF) system with a concentrated mass located at the top of a column [Johnson and Dowell 2017]. Analytical models can incorporate either a linear or a nonlinear force-displacement relationship for the component. In most studies, the deformation is assumed to occur within the component itself, while the component remains fixed based [Anjafi and Medina 2018]. Recent experimental study concluded that the component attachment is also a factor in determining the lateral seismic force demand. The study emphasized the impact of the attachment design on the overall dynamic properties of the nonstructural component [Feinstein and Moehle 2021]. Previous research of medical freezers and battery cabinets showed similar results that highlight the importance of the attachment design on the component dynamic response [Feinstein et al. 2018].

A mechanics-based model to assess the dynamic behavior of floor-anchored nonstructural components was developed, validated with experimental data [Feinstein and Moehle, 2022]. The model accounts for the interaction between the inherent properties of the component and uplift constrained by the attachment design. The attachment force-deformation relationships for a steel channel-based connection are estimated based on an analytical approach and supplemental experimental program. The model proposes a simple approach for the engineer to estimate the contribution of the attachment design to the dynamic amplification of the component.

The newly developed mechanics-based model was utilized to perform a case study of pre-approved equipment. The case study focuses on floor-anchored nonstructural components that have been pre-approved through the program of the Health Care Access and Information (HCAI) formerly known as OSHPD. Eight mechanical and electrical components were chosen for the study. The design force was calculated based on ASCE 7-16, with the target spectrum that is illustrated in figure 1, using 35 ground motions. The components are then simulated using the mechanics-based model to generate the mean component response and compare it with the code demand.

2. METHODOLOGY

The analysis methodology used for this study utilized the mechanics-based model for floor-anchored nonstructural components. The nonstructural component is uncoupled from the structural dynamic response, the mass of the nonstructural component is assumed very small compared to the structure. The ground motions used in the study are recorded motions from the PEER database. Floor motions were generated from numerical models of buildings and taken from recordings of instrumented buildings from the California Strong Motion Instrumentation Program (CSMIP). The properties of the attachment and component in the mechanics-based model were based on practical considerations.

The mechanics-based model runs in the Open System for Earthquake Engineering Simulation (OpenSees) (Mckenna, 2000). Maximum values from the response history are recorded and used to assess the parameter influence on the acceleration amplification of the component. The model is designed in two dimensions and only considers input motions in one direction of motion.

3. INPUT MOTIONS

35 Ground motion recordings were chosen from the PEER database, based on the rupture distance and the moment magnitude, to match an ASCE-7 based spectrum with S_{DS} of 1.5g and S_{D1} of 0.75g. Rrup was limited to 30 km and the moment magnitude (Mw) ranges from a minimum of 6.6 to a maximum of 8. Figure 1 plot the target spectrum with the mean and one standard deviation of the 35 selected ground motions, with 5% damping. The motions were selected to fit the target spectrum in the short period range. The ground motions were taken as recorded.

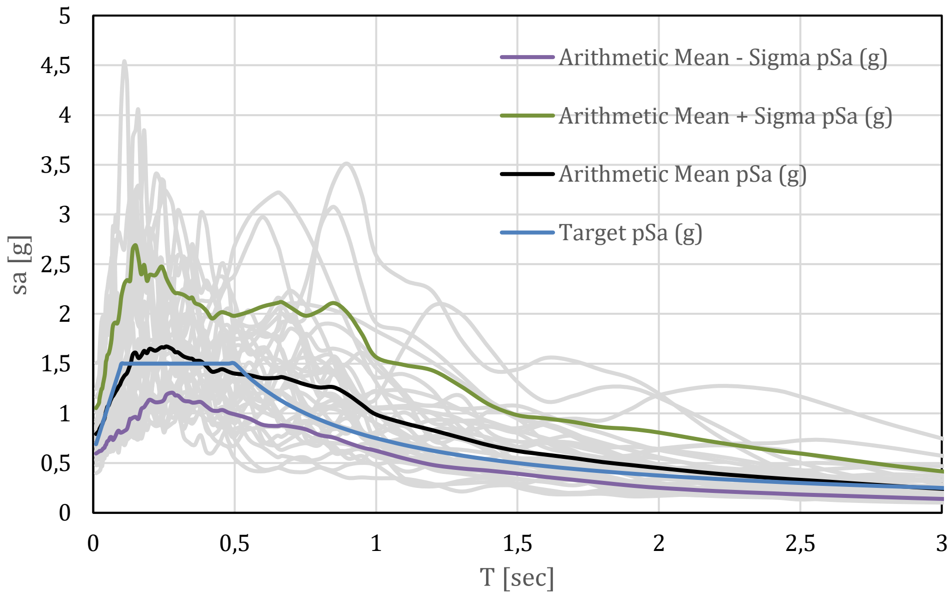

Figure 1. Ground motion selection spectra for input motion study

Floor motions were selected from instrumented structures and numerical building simulations. Figure 2 shows the response spectra for all the chosen floor motions. Figure 2 (A) plots the pseudo acceleration with 3 percent damping. Figure 2 (B) plots the accelerations normalized by the peak floor acceleration of each motion. Based on the response spectra the amplification of the component accelerations can reach up to 8.5. The spectral amplifications of the simulated floor motions are higher than those recorded from instrumented buildings.

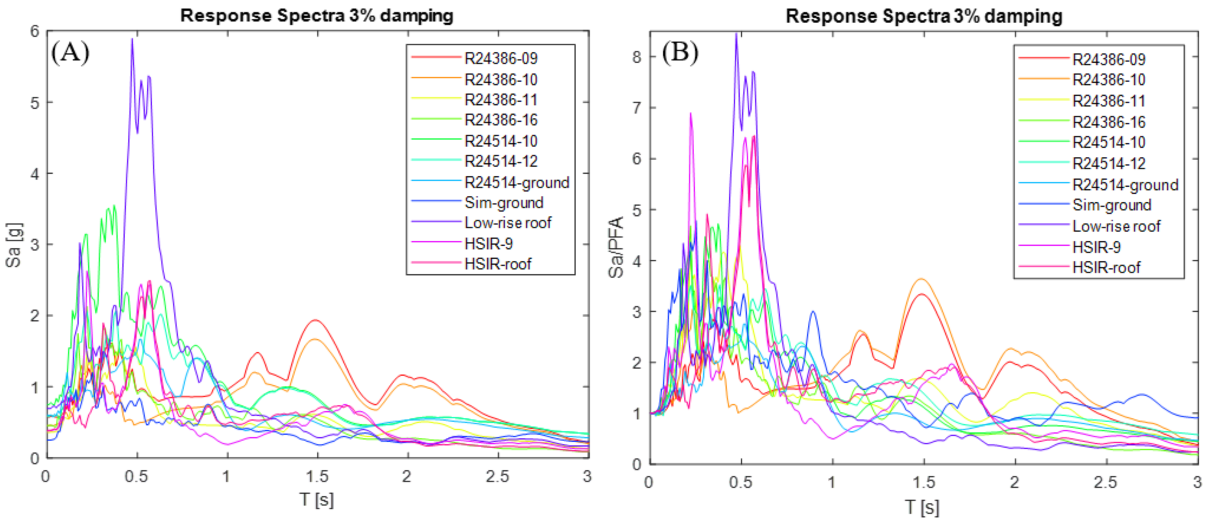

Figure 2. Floor motion spectra (A) pseudo acceleration (B) normalized by the PFA

The recorded floor motions for the study were chosen from the CSMIP database of instrumented buildings. The floor motions were chosen to have a minimum PGA of 0.4g from two structures. Figure 3 details the building plans for the two instrumented buildings that were chosen. Figure 3 (A) describes the locations of the sensors in the Sylmar county hospital. The chosen floor motions were taken in the west-east direction from the third floor and roof floor. The hospital is a 6-story structure with a combined concrete and steel plate shear wall system. The building period of 0.365 sec was taken from Kazanti et al (2020). Figure 3 (B) describes the locations of the sensors in the 7-story hotel in Van Nuys. The hotel structure is a 7-story hotel with a reinforced concrete moment resisting frame structural system. The building period of 0.34 sec was taken from Kazanti et al (2020). The floor motion selected are in the west-east direction from the third, sixth, and roof levels.

Floor motions were also produced from two simulated structures. The HSIR structure consists of two 16-story steel moment frame structures, made of large built-up sections. Floor accelerations at various heights were recorded from a simulated realistic numerical model of the structure, which was developed using OpenSEES [Feinstein et al, 2018]. The HSIR building natural period is 1.54 sec. The second simulated structure was a low-rise consist of a three stories archetype steel structure, with a lateral force resisting system of a special concentric braced frame. The structure was designed as a typical steel structure with a ductile response, using an R value of 6.0 according to ASCE 7-10 (ASCE 7, 2013). The low-rise first natural period is 0.5 sec, floor acceleration history was recorded at the roof level and used as one of the input motions for the study.

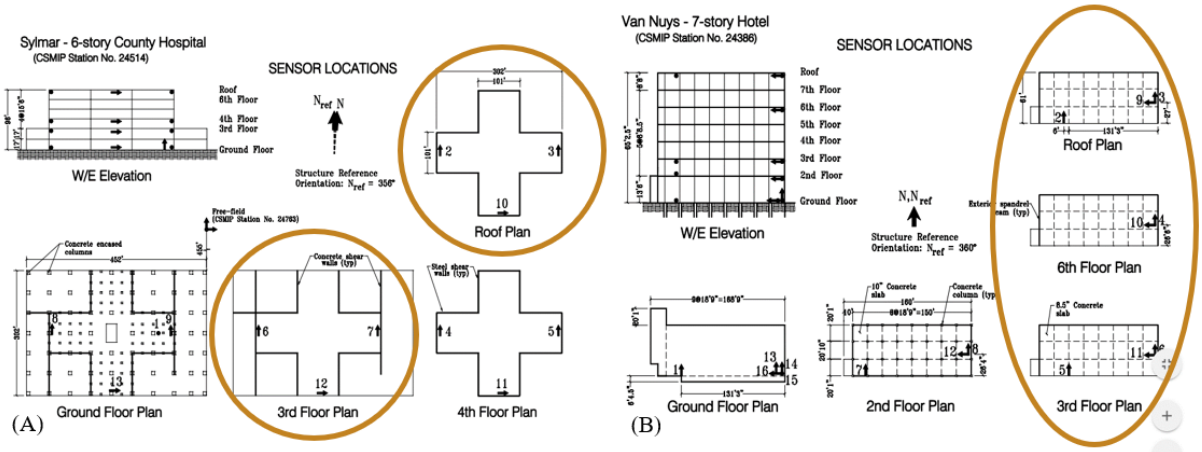

Figure 3. Building details of chosen recorded floor motions

3.1 EFFECTIVE PEAK GROUND ACCELERATION

Nonstructural components usually have short natural periods, and, thus, their response is commonly defined relative to the peak ground acceleration. However, the value of the peak ground acceleration is highly dependent on sharp high-frequency spikes that do not significantly influence the response of typical structural and mechanical systems. Newmark and Hall [1982] described the concept of effective peak ground acceleration as a measure that more closely relates to structural response and the damage potential of an earthquake. As adopted by ATC 3-06 [1978], the effective peak ground acceleration (EPGA) is taken equal to the average spectral pseudo-acceleration ordinates for 5% damping in the period range of 0.1 to 0.5 s divided by 2.5. This concept continues today in ASCE 7 [2017] where the earthquake spectral response acceleration parameter at short periods (S_{DS}) serves as the anchor point for definition of the standard design response spectrum. EPGA defined in this way, perhaps with different damping value more consistent with nonstructural components, may be a better measure of the damage potential for nonstructural components because their fundamental period typically falls within this short-period range.

The EPGA for each individual ground motion was calculated based on the average ground motion 5%-damped spectral response acceleration over a period range of 0.1 to 0.5 s divided by 2.5. Table 2 includes the calculated EPGA for each input motion and demonstrates that the EPGA is usually lower than the PGA as it is less influenced by the high-frequency peaks often present in the ground acceleration record.

4. COMPONENTS

The nonstructural components are listed in table 1. The dimensions and first horizontal period were taken from the HCAI Special Seismic Certification Preapproval (OSP) database. The components were chosen to include a variety of components, with different measurement ratios, and periods ranging from 0.04 sec to 0.17 sec. Figure 4 shows the nonstructural component attached to the shaking table during the pre-approval procedure.

Table 1. Case study equipment info

ID	Component	Weight (lb)	Height (mm)	Width (mm)	Depth (mm)	Period (sec)
1	Transformer	2560	1320	889	940	0.14

2	Switchgear	2696	3226	1219	2184	0.07
3	Ventilator	479	1890	1380	1380	0.11
4	Chiller	2450	1654	870	1410	0.14
5	Battery Cabinet	5185	2133	813	800	0.17
6	Air handling unit	1010	2770	559	2692	0.04
7	Elevator controller	381	1810	700	419	0.08
8	Motor Control center	482	1245*	508	381	0.12

* Center of gravity height

Figure 4. Case study components: (A) Transformer, (B) Switchgear, (C) Ventilator, (D) Chiller, (E) Battery Cabinet, (F) Air handling unit, (G) Elevator controller, (H) Motor Control center [OSP database].

5. ATTACHMENT DESIGN

The lateral force design for the attachment of the case study components was determined with an S_{DS} of 1.5, based on the target spectrum. The component properties were chosen based on ASCE 7-16 table 13.6-1 for the seismic coefficient of mechanical and electrical components. The F_p values were calculated for the ground floor based on equation 1 taken from ASCE 7-16, with $I_p = 1.0$. The minimum lateral force is calculated as $F_{p\,min} = 0.3 \cdot 1.5\ W_p = 0.45W_p$. Table 2 lists the component coefficients for each piece of equipment, and the design forces. The a_p/R_p value for all the components is 0.4-0.42. The corresponding lateral design force on the ground floor is then 0.24-0.25 times the component weight. This force is lower than the lower limit of the equation, thus we would use the lower limit for the design calculations. The attachment design force was determined based on equilibrium with two angle connections, assuming the forces act at the edges of the component. An LRFD combination of the lateral design load and the vertical design load is considered, along with the self-weight in equation 2. The vertical loads are assumed to distribute evenly along the component width.

$$F_p = \frac{0.4 \cdot a_p S_{DS} W_p}{\frac{R_p}{I_p}} \left(1 + 2 \cdot \left(\frac{z}{h}\right)\right) \quad (1)$$

$$F_{att} = F_p \cdot \frac{H}{B} + \frac{0.2 W_p S_{DS} - 0.9 W_p}{2} \; = W_p (0.45 \frac{H}{B} - 0.3) \quad (2)$$

Equation 2 is based on the height of the component, H, the width of the component, B, and the component weight W_p.

Table 2. Design forces for case study components

ID	Equipment	Weight (lb)	a_p	R_p	F_p/W	$F_{anchor}[lb]$	F_{att}[lb]
1	Transformer	2560	1.0	2.5	0.24	2653	943
2	Switchgear	2696	2.5	6.0	0.25	5613	2402
3	Ventilator	479	1.0	2.5	0.24	447	152
4	Chiller	2450	1.0	2.5	0.24	3457	1361
5	Battery Cabinet	5185	1.0	2.5	0.24	10688	4566
6	Air handling unit	1010	2.5	6.0	0.25	4201	1949
7	Elevator controller	381	1.0	2.5	0.24	772	329
8	Motor Control center	482	2.5	6	0.25	919	387

The anchor load is designed with an additional Ω_0 factor of 2.0 for the lateral design force F_p for the components that were chosen. The shear load on the anchors is assumed to evenly distribute between the four anchors, each with a load of $F_p\Omega_0/4$. The battery cabinet will be designed with Hilti HSL-3-G M16, with a utilization of 86 percent of the tension capacity. To simplify the design, the other equipment would be designed using an HSL-3-G M12, with utilization of 5-60 percent of the tension capacity.

The attachment will be designed based on the calculated F_{att} with two geometric designs. First, we will calculate the required M_p for the angle, based on equation 3, with $d = 16mm$ for the battery cabinet, and $d = 12mm$ for all other equipment. We will choose two values for the arm length between the component and the anchor, $b_a = 2\ inch$ and $b_b = 3.5\ inch$. The attachment dimensions are given in figure 5. The attachment will be designed of A36 steel, with $f_y = 36ksi$. The vertical distance v was taken as 2.0 inch for all the attachments.

$$M_p = F_{att}(b - \frac{d}{2})/2 \quad (3)$$

With the calculated M_{pl} we can choose the required thickness of the angle t_{calc}, based on equation 4. We will choose an angle length L of $10\ inch$, or two 5 inch clips. The thickness t_{act} was rounded to the closest 1/16 with a minimum of 1/8 inch.

$$t = \sqrt{\frac{4M_{pl}}{f_y * L}} \quad (4)$$

Table 3 lists the properties of the designed attachment, where ID a and b represents whether the design includes b_a or b_b as the distance from the anchor to the base of the angle. The stiffness parameters were calculated based on the simplified approach detailed in the method described by Feinstein and Meohle [2022]. For this study, the anchor stiffnesses are taken as $k_{an} = 62{,}000 lb/in$ and $k_{an}^{T} = 48000\ lb/in$, based on experimental values. This approach results in seven unique attachment designs.

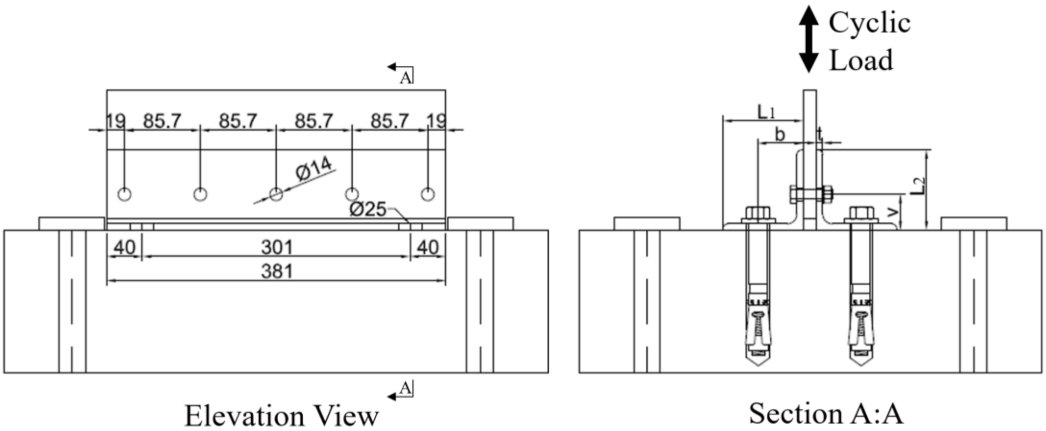

Figure 5. Attachment dimensions

Table 3. Design details of attachment for case study components

ID	M_{pl} $[lb \cdot in]$	t_{calc} $[in]$	t_{act} $[in]$	F_y $[lb]$	F_p $[lb]$	k_0 $[lb/in]$	k_1 $[lb/in]$	k_2 $[lb/in]$
1a	832	0.096	0.125	781	1595	27539	7463	4523
1b	1539	0.131	0.1875	1071	1939	21453	5861	4345
2a	2118	0.153	0.1875	1758	3588	60848	21261	4563
2b	3920	0.209	0.25	1905	3447	41106	12820	4364
3a	134	0.039	0.125	781	1595	27539	7463	4523
3b	248	0.052	0.125	476	862	7238	1815	4413
4a	1200	0.115	0.125	781	1595	27539	7463	4523
4b	2221	0.157	0.25	1905	3447	41106	12820	4364
5a	3847	0.207	0.25	3125	6676	86240	38662	4640
5b	7271	0.284	0.3125	2976	5519	61009	22212	4430
6a	1719	0.138	0.1875	1758	3588	60848	21261	4563
6b	3181	0.188	0.25	1905	3447	41106	12820	4364
7a	290	0.057	0.125	781	1595	27539	7463	4523
7b	537	0.077	0.125	476	862	7238	1815	4413
8a	341	0.062	0.125	781	1595	27539	7463	4523
8b	632	0.084	0.125	476	862	7238	1815	4413

6. RESULTS

The results analyze the component amplification a_c for the range of attachment properties tested. The a_c is calculated as $PCA/EPGA$ for ground motions, and as PCA/PFA for floor motions. The impact of the attachment effective stiffness, displacement ductility, and system effective period are examined.

The mean PCA and mean maximum relative top displacements are calculated for each of the components, based on the results from a suite of 35 ground motions. Additional results are given for the component amplification a_c. The PCA results are compared to the lateral force demand based on ASCE 7-16 and the a_c is compared with the seismic coefficients. The two geometric designs are compared for the eight components considered.

Table 4 summarizes the mean responses for each piece of equipment with two types of attachment designs. The mean of the PCA, mean of the maximum displacement and a_c are calculated for the ground motion suite. The code seismic coefficients are added for reference. The mean spectral acceleration for the ground motion suite, with five percent damping is listed based on the T_{eff}. The mean maximum displacements at the top of the components ranged from 0.26 – 2.9 inch.

The code lateral force F_p can be compared with the mean $PCA.$ The design force was determined by the lower limit of the equation as 0.45 g. The range of PCA is between 2.5 – 3.3 times larger than the code design. When the lower limit is not considered the PCA is 10 times higher than the F_p value that is calculated with equation 1.

Table 4. Mean response results for case study

ID	$PCA\ [g]$	a_c	$Disp\ [in]$	a_p/R_p	T_{eff}	Mean $s_a\ [g]$
1a	1.28	2.11	1.61	0.40	0.17	1.58
1b	1.27	2.08	1.91	0.40	0.16	1.56
2a	1.23	2.02	2.46	0.42	0.09	1.27
2b	1.32	2.12	1.89	0.42	0.08	1.22
3a	1.38	2.31	0.58	0.40	0.13	1.48
3b	1.36	2.27	0.26	0.40	0.12	1.41
4a	1.26	2.09	2.90	0.40	0.16	1.56
4b	1.37	2.24	1.24	0.40	0.15	1.61
5a	1.31	2.15	2.62	0.40	0.18	1.63
5b	1.49	2.40	2.24	0.40	0.18	1.63
6a	1.19	1.97	2.34	0.42	0.05	1.07
6b	1.27	2.06	1.99	0.42	0.04	0.95
7a	1.22	2.05	1.39	0.40	0.09	1.27
7b	1.38	2.35	0.49	0.40	0.08	1.22
8a	1.20	1.99	1.86	0.42	0.13	1.48
8b	1.36	2.23	0.60	0.40	0.12	1.41

Figure 6 (A) plots the a_c for the two different designs vs the effective system period. The a_c ranges from 2-2.5 for all the components, with a mean of 2.16. The amplification values are slightly higher for the long design b, by about 6 percent. This is consistent with the shaking-table results of Feinstein and Moehle [2021]. Figure 6 (B) shows the PCA and the mean spectral acceleration values vs the effective system period. The results suggest that up to an effective system period of 0.1 sec the PCA are larger than the spectral acceleration values, and above 0.1 sec they are lower.

The component is considered to exhibit a nonlinear response of the attachment if the μ value is larger than 1.0. The attachment responded in a nonlinear range in 93 percent of the simulations. The mean a_c of the simulations that responded in the elastic range is 2.01. These results suggest that the elastic response is not driving the mean responses higher.

The amplification a_c results can be used to evaluate the seismic design coefficient a_p/R_p. The code coefficients are about 0.4 for all the components in the case study. The range for the mean a_p is 5 times larger than the coefficients.

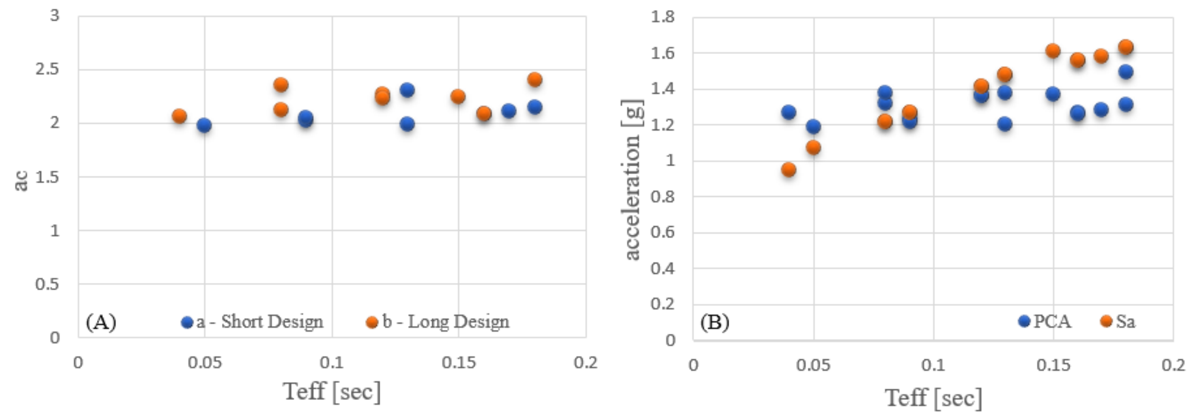

Figure 6. Case study accelerations vs T_{eff} (A) a_c of different designs (B) PCA and S_a

Figure 7 (A) shows the a_c for all the components for the seven floor motions vs the normalized system period by the building's period. The mean of a_c is 2.33 and the results are scattered across the range of 1.0 to 5. Figure 7 (B) plots the mean a_c value for each component for the two attachment designs. The mean results range from 1.9 – 2.7, where for most components the long design b has a higher or similar mean a_c value than the short design a. The long design averages 5% higher than the short design.

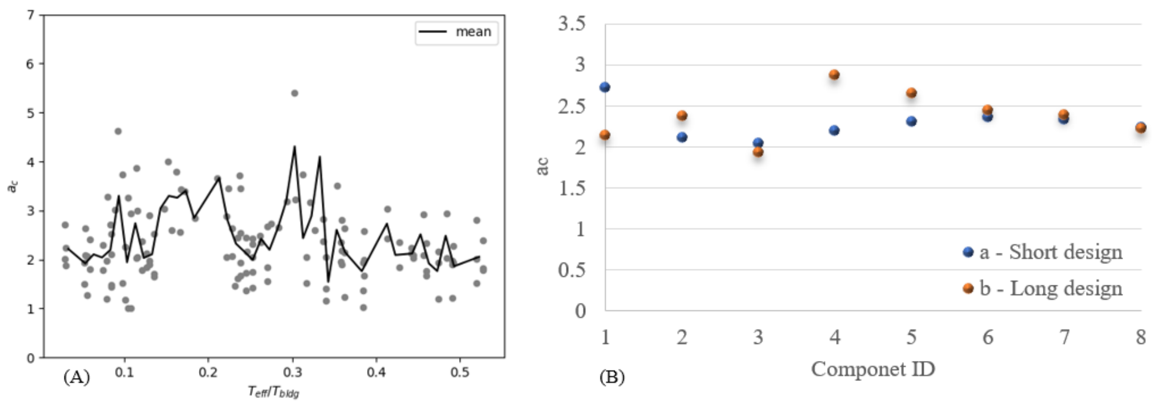

Figure 7. Case study accelerations vs T_{eff} (A) a_c of different designs (B) PCA and S_a

7. SUMMARY

The response of eight mechanical and electrical components was examined using the mechanics-based model developed by Feinstein and Moehle [2022]. A suite of 35 ground motions and 7 floor motions was used to assess the response of two attachment designs for each component.

The design of the attachment was determined by the analytical solution described by Feinstein and Moehle [2022]. Two designs were tested based on the component properties, with two lengths between the anchor location and connection point to the component. The a_c values were in similar ranges for both designs, with slightly higher accelerations for the longer arm design.

The attachment responded in the nonlinear range in 93 percent of the simulations.

Comparison between the simulation results to the code requirements reveals a large discrepancy, with the simulation loads at least 2.5 times larger than the code design based on the lower limit of F_p. The simulation loads were 10 times larger than the value of F_p based on the code equation without accounting for the lower limit.

The mean a_c is 2.16 and 2.33 for the ground motions suite and floor motion suite, respectively. a_c can be compared to the component seismic coefficients ratio a_p/R_p. These mean a_c values are at least 5 times larger than the seismic coefficients ratio for the components included in the case study.

REFERENCES

Anajafi H, Medina RA. [2018] "Evaluation of ASCE 7 equations for designing acceleration-sensitive nonstructural components using data from instrumented buildings." *Earthquake Engineering & Structural Dynamics*., 47(4), 1075-94.

Applied Technology Council, Structural Engineers Association of California. [1978] "Tentative Provisions for the Development of Seismic Regulations for Buildings: A Cooperative Effort with the Design Professions, Building Code Interests, and the Research Community". *Department of Commerce, National Bureau of Standards*.

ASCE/SEI (American Society of Civil Engineers). [2017] "Minimum design loads for buildings and other structures". *ASCE/SEI-7-16*, Reston, VA.

Feinstein T, Mahin S. [2018] "Experimental Performance of Floor Mounted Nonstructural Components Under Seismic Loading". *Proceedings of the 11th National Conference in Earthquake Engineering, Earthquake Engineering Research Institute*, Los Angeles, CA, USA.

Feinstein T, Moehle J.P., Mahin S.A. [2018] "Anchored nonstructural component response to seismic loading - shaking table tests report". *Pacific Earthquake Engineering Research (PEER) Center*, University of California, Berkeley, SEMM, 5.

Feinstein, T, Moehle, J.P. [2021] "Seismic response of floor-anchored nonstructural components fastened with yielding elements". *Earthquake Engng Struct Dyn*. 1– 19. https://doi.org/10.1002/eqe.3553.

Feinstein, T. Moehle, J.P. [2021] "Shaking-Table tests of idealized nonstructural component fastened with yielding elements in Experimental Seismic Performance of Nonstructural Components Fastened with Ductile Elements". *DesignSafe-CI*. https://doi.org/10.17603/ds2-xg94-ds51.

Feinstein, T. Moehle, J.P. [2022] "Seismic response of nonstructural components fastened with yielding elements", *Journal of Structural Engineering*. https://doi.org/10.1061/(ASCE)ST.1943-541X.0003496.

Johnson TP, Dowell RK. [2017] "Evaluation of the overstrength factor for nonstructural component anchorage into concrete via dynamic shaking table tests". *Journal of Building Engineering*. 11:205-15.

Newmark NM, Hall WJ. [1982] "Earthquake spectra and design". *Engineering monographs on earthquake criteria*.

NIST (National Institute of Standards and Technology) [2018], "Recommendations for Improved Seismic Performance of Nonstructural Components", NIST GCR 18-917-43, *prepared by the Applied Technology Council for the National Institute of Standards and Technology*, Gaithersburg, Maryland.

Mckenna, F., Fenves, G.L. [2000] "Open system for earthquake engineering simulation". University of California, Berkeley, CA.

Kazantzi AK, Vamvatsikos D, Miranda E. [2020] "Evaluation of seismic acceleration demands on building nonstructural elements". *Journal of Structural Engineering*. 146(7):04020118.

Effect of Spectral Shape on the Amplification of Peak Floor Acceleration Demands in Buildings

Giulia Scagliotti[1] and Eduardo Miranda[1]

[1] Dept. of Civil and Environmental Engineering, Stanford University, Stanford, CA 94305, USA
e-mail: gscaglio@stanford.edu, emiranda@stanford.edu

Abstract. This study investigates the effect of spectral shape of ground motions on the amplification of peak floor accelerations (PFA) along the height of buildings. Several previous studies that have examined data recorded during earthquakes in instrumented buildings have concluded that the level of amplification in PFA reduces as the level of peak ground acceleration (PGA) increases and that large amplifications are unlikely to occur for moderate or large levels of PGA. These observations are intriguing because there is a consensus that these buildings have responded elastically or practically elastically during the earthquakes recorded so far. If the response is elastic, one would not expect a change in the level of amplification of PFA/PGA since in that case PFA increases at the same rate as the increase in PGA and therefore PFA/PGA remains unchanged with increasing levels of PGA until significant nonlinearity occurs in the building. This investigation carefully re-examines these observations based on recorded data in instrumented buildings. Ground and floor motions recorded in instrumented buildings that have been subjected to various earthquakes with different levels of intensity in California are carefully investigated. Emphasis is placed on the identification of possible reasons for the observed earthquake-to-earthquake variability in the level of amplification of PFAs with respect to PGAs. By examining these variations building by building in each direction separately, earthquake-to-earthquake variations in PFA/PGA are isolated from those related to changes produced by changes in the fundamental period of the supporting structure or by changes in lateral resisting system. Additionally, the effect of the level of PGA experienced by the building is re-evaluated. It is shown that indeed, in many cases, recorded PFA/PGA amplifications show a small decreasing trend with increasing levels of PGA, but that this trend is not really due to the increase in PGA but rather associated with earthquake-to-earthquake variability in the frequency content or spectral shape of the motions at the base of the building, which are primarily the result of specific combinations of magnitude and distance in each of the recorded events. Contrary to the misconception that large amplifications can only occur at low levels of peak ground acceleration, the study shows that strong levels of amplification of PFA/PGA can occur even at larger levels of peak ground acceleration which would produce large levels of PFA.

Keywords: Nonstructural elements, Acceleration demands, Amplification along the height, Spectral shape, Peak floor accelerations.

1. INTRODUCTION

Detailed evaluation of ground motions and building motions recorded during earthquakes in instrumented buildings together with the careful documentation of the performance of non-structural elements during the same earthquakes provide invaluable data to improve design provisions, or for improving guidelines or standards for the evaluation of non-structural elements in existing buildings. Therefore, it is not surprising that several studies have been carried out over the years on the evaluation of recorded data in instrumented buildings. However, depending on how the studies were conducted, they have sometimes arrived at different conclusions and the lack of consensus has contributed to a rather slow progress of seismic code provisions for non-structural elements. This is in part, because non-structural components have typically received much less attention from both the research and practicing engineering communities than the attention devoted to the design of structural elements.

For many years now, there is a practically universal consensus that local sites conditions play a major role in the intensity and frequency content of ground motions and therefore they have a major effect on the level of response and on level of seismic risk of structures. A very large number of empirical observations, study of recorded ground motions as well as analytical studies have led to the explicit incorporation of site conditions for the design of structures in most seismic codes since the 1970s. In some cases, the intensity of design actions can, for example, change by more than a factor of two as a result of a change in site conditions. In other words, there is a consensus that the response of a structure is strongly influenced by the characteristics of the supporting rock/soil in which it is built on. By analogy, one would then intuitively expect that the characteristics of the supporting structure would also have a major influence on the intensity and characteristics of the floor motion on which nonstructural elements are supported on or are suspended from. For example, from basic principles of structural dynamics one would expect that the dynamic characteristics of the supporting structure (e.g., the fundamental period of vibration of the building where the non-structural element is installed) would have a major influence in both the intensity and frequency content of floor motions and therefore on the amplitude and other spectral characteristics of floor spectra. A study conducted by the National Center for Earthquake Engineering Research in 1993 recommended a simplified equation to estimate equivalent static forces for nonstructural elements as a function of the fundamental period of vibration of the supporting structure [Singh *et al.*, 1993]. That study was based on a limited number of analytical studies and did not examined data recorded in instrumented buildings. Nevertheless, it clearly highlighted the importance of the period of vibration of the supporting structure and that study led to its incorporation in the 1994 NEHRP recommended seismic provisions.

Unfortunately, limited or incomplete analyses of recorded data in instrumented buildings have sometimes precluded the timely improvement of seismic provisions of non-structural components. For example, a study examined the validity of the reduction in peak floor accelerations (PFA) for long-period structures by looking at approximately 160 PFAs recorded at roof level in 150 instrumented buildings during 16 California earthquakes [Drake and Bachman, 1996]. The study concluded that recorded data did not support the hypothesis that building seismic-response accelerations decrease with increasing building period, as might be expected from reviewing the shape of typical response spectra. The study speculated that this could be because the design of buildings with fundamental periods greater than 1 s may be governed by drift requirements and may be stiffer than required to meet force requirements. However, there were a series of problems in how the analysis of the data was conducted in that study. For example, the study did not look at the actual fundamental periods of vibration of the instrumented buildings, but only code-estimated periods that are well-known to provide biased estimates (underestimation) in order not to underestimate equivalent static forces on buildings. Also, the study did not look at PFAs from corrected data but only used preliminary uncorrected data and, in many cases, there are significant differences between the two caused by baseline corrections and low-pass filtering of the time series. Furthermore, and more importantly they mixed data of buildings with different lateral resisting systems and did not examine the influence of the magnitude-distance pairs of the events in which the PFA were recorded. These and other aspects of their study masked or partially masked several aspects of the recorded data and did not allow a proper analysis of the influence of the fundamental period of vibration of the recorded data. They mentioned that further study of the issue was warranted, with the possible elimination of the structural-period effect in future versions of the NEHRP recommended seismic provisions. As a result of that study, the recommendation of the NCEER to include the effect of the fundamental period of vibration of the supporting structure was, unfortunately, not incorporated in the 1997 Uniform Building Code (UBC).

A few years later, Miranda and Taghavi [2003a, 2003b, 2005] conducted a study of seismic acceleration demands in buildings by examining data recorded in instrumented buildings in combination with analytical studies of detailed and simplified models of instrumented building and concluded that "*acceleration demands in buildings are sensitive to both the frequency content of the ground motion and to the dynamic characteristics of the supporting structure*". In particular, they showed that the fundamental period of vibration of the structure had a significant influence on acceleration demands on nonstructural components. In particular, they showed that the amplification of PFA with respect to peak ground acceleration (PGA) tended to decrease with increasing fundamental period of the structure. More recently, several other studies have corroborated the influence of the fundamental period of the structure supporting the non-structural element [e.g., Medina *et al.* 2006; Singh *et al.* 2006; Miranda and Taghavi, 2010; Fathali and Lizundia 2011, Wieser *et al.*, 2013]. Based on all those previous studies, which were summarized in the ATC-120 project [ATC, 2018], the latest version of ASCE 7 (i.e., ASCE 7-22) now includes an equation to estimate PFA as a function of the fundamental period of vibration of the supporting structure but, unfortunately, it took nearly 30 years after the NCEER recommendation or 20 years after the comprehensive studies at Stanford for this to be included in seismic provisions used by practicing engineers. This example highlights the adverse consequences of not conducting an adequate evaluation and careful interpretation of seismic motions recorded in instrumented buildings.

A first objective of this study is to re-examine the possible influence of the level of PGA on observed levels of PFA/PGA amplification that have been recorded in instrumented building. Several previous studies that have analyzed data recorded during earthquakes in instrumented buildings have concluded that the level of amplification in PFA reduces as the level of PGA increases and that large amplifications are unlikely to occur at moderate or large levels of PGA.

These observations from previous studies are intriguing and their conclusions perhaps even unlikely given there is a consensus among those who have studied the recorded data that these buildings where the data has been recorded have responded, in practically all cases, elastically or essentially elastically in the earthquakes recorded to date. Therefore, one would not expect a significant change in the level of amplification of PFA/PGA with increase in PGA. This is because, when the response of the structure is elastic, the PFAs increase at the same rate as the increase in PGA and therefore PFA/PGA remains unchanged with increasing levels of PGA until significant nonlinearity occurs in the building. This investigation carefully re-examines these observations by using recorded data in instrumented buildings. Ground and floor motions recorded in instrumented buildings that have been subjected to various earthquakes with different levels of intensity in California are carefully investigated. A second objective of this study is then the identification of other possible reasons for the observed earthquake-to-earthquake variability in the level of amplification of PFAs with respect to PGAs. Unlike previous studies, these variations in the level of amplification are examined in specific directions of individual buildings subjected to various earthquakes in order to isolate earthquake-to-earthquake variations in PFA/PGA from those that might be related to changes from one building to another produced by differences in the fundamental period of the supporting structure, by changes in lateral resisting system or by changes of site conditions. The possible effect of the level of PGA experienced by the building is then carefully re-evaluated. It is shown that indeed, in many cases, recorded PFA/PGA amplifications show a small decreasing trend with increasing levels of PGA, but that this trend is not really caused by the increase in PGA in the ground motion as previous studies have erroneously concluded, but rather they are primarily associated with the earthquake-to-earthquake variability of the frequency content or spectral shape of the motions at the base of the building, which are primarily the result of specific combinations of magnitude and distance in each of the recorded events. Contrary to the misconception that large amplifications can only occur at low levels of peak ground acceleration, the study shows that strong levels of amplification of PFA/PGA can occur even at larger levels of peak ground acceleration, hence possibly leading to large levels of PFA in buildings.

2. BRIEF DESCRIPTION OF PREVIOUS STUDIES

There have been several studies that have investigated the amplifications of PFA along the height of buildings by analyzing data recorded in instrumented buildings in California. Here, only three studies that have arrived at similar conclusions regarding the influence of the level of PGA on PFA/PGA amplifications along the height of buildings will be summarized. Drake and Gillengerten [1994] studied 28 records in three California earthquakes: five buildings with recorded data from the 1984 Morgain Hill earthquake; 12 from the 1989 Loma Prieta earthquake; and 11 from the 1992 Landers earthquake. The maximum PGA in their record set was 0.39g and their largest PFA was 1.24g. They noted that despite the high structural response at upper floor, the buildings in their study exhibited essentially elastic behaviour. They wrote that it was of interest to note that the highest PFA/PGA values were associated with buildings subjected to relatively low intensity ground motions and specified that the same buildings when subject to higher intensity ground motion would experience lower amplification due to increased damping and limited non-linear behaviour.

Fathali and Lizundia [2011] considered a significantly larger data set consisting of data recorded in 151 fixed-base buildings from 73 California earthquakes for a total of 541 "building-earthquake records". Similarly to the previous investigation, they studied PFA normalized by PGA as a function of the normalized height z/h. Consistent with Miranda and Taghavi [2003, 2010] they concluded that PFA/PGA ratios tended to decrease with increasing fundamental period of vibration of the building, but also noted that the level of PGA was also found to be influential on PFA/PGA ratios and proposed simplified equations for the evaluation of PFA demands in existing buildings and for the design of new buildings as a function of the period of vibration of the building but also with decreasing values with increasing level of PGA. In particular, they provided equations for PGA smaller than 0.067g, for PGA between 0.067g and 0.2g and for PGA equal to or greater than 0.2g.

More recently Anajafi and Medina [2018] studied approximately 600 motions recorded in 59 instrumented buildings (i.e., 118 building directions). Similarly to previous studies, they noted that PFA/PGA is influenced by the level of intensity of the ground motion and observed that, while for low intensity ground motions the in-structure amplification factor can exceed the ASCE equation, for higher intensity levels, the ASCE 7 significantly overestimates the magnitude of most in-structure amplification factors. They concluded that as the ground motion intensity increases, normalized acceleration responses significantly decrease, which they wrote shows that the effect of ground motion intensity on floor response spectra is significant. However, they also noted some limitations of their study. In particular, they wrote that this conclusion is based on responses of different buildings with different modal periods and different lateral-load resisting systems such that some of the differences attributed to ground motion intensity could in fact be influenced by differences in fundamental period of vibration of the supporting structure or by mixing PFA/PGA from buildings with different lateral resisting systems. They evaluated the variation of PFA/PGA at roof level in the NS direction of a 13-story moment-resisting frame building in Sherman Oaks California and noted that PFA/PGA decreased from 2.65 to 2.04 and to 1.39, from the 1992 Landers, 1987 Whittier and 1994 Northridge Earthquake, in which PGA of 0.04g, 0.10g and 0.45g were recorded, respectively. Without showing any evidence or analyses, they attributed these reductions in PFA/PGA with increasing PGA to the cracking/nonlinearity in the supporting building due to increasing ground motion intensity level. In their study, they presented a second example consisting of the NS direction of a 10-story residential building in

Burbank in which they observed that with increasing the ground motion intensity from 0.05g to 0.10g, 0.17g, and 0.30g, the PFA/PGA response at roof level changed from 3.30 to 3.13, 1.82, and 2.57, respectively to illustrate a general decreasing trend of PFA/PGA with increasing the PGA but noted that an inconsistency (i.e., an increase in PFA/PGA) was observed when PGA increased from 0.17g to 0.30g.

It is then clear, that even though the three studies arrived at essentially the same conclusion, all three studies also noted some limitations and how they analyzed the recorded data. It is important then to carefully re-evaluate the effect of increasing ground motions in the apparent reduction in PFA/PGA and to identify possible reasons that could explain the observed apparent trend because such trend is not consistent with the consensus that practically all the recorded data is from buildings that exhibited elastic or essentially elastic behavior during the earthquakes. For example, if one conducts an incremental dynamic analysis on a building model having linear elastic behavior, with whatever earthquake ground motion that is used, one would observe that ground and building accelerations (or any response parameter) increases proportionally with the increasing scaling factor applied to the input ground motion. Therefore, one would obtain that, provided the response remains elastic for any ground motion, PFA/PGA would not change with increasing values of PGA.

3. RECORDED BUILDING RESPONSE USED IN THIS STUDY

In order to study the effect of ground motion intensity on amplifications of PFA along the height of buildings, this investigation looked for recorded seismic response of midrise buildings that have recorded data from at least six different earthquake events with moment magnitudes larger than four recorded at a wide range of distances from the building. Unlike lowrise whose acceleration response is typically dominated only by the first translational modes of vibration or in combination with the first torsional mode, the acceleration response of midrise buildings can have a much larger contribution from second translational modes of vibration allowing to study their influence on the level of amplification of floor accelerations along the height of buildings. All data used in this study were recorded in buildings instrumented by the California Strong Motion Instrumentation Program (CSMIP) and all data was downloaded from the Center for Engineering Strong Motion Data (CESMD) website. Contrary to previous studies that mixed data from many buildings with different heights, different lateral resisting systems, different fundamental periods and data from the two orthogonal directions of the buildings, this study looks at the records obtained in each building separately and only one orthogonal direction at the time. This is done in order to not mix changes in the level of in-structure amplification of accelerations (PGA to PFA) produced by other factors such as changes in building height, lateral resisting systems that previous investigations have noted that have an influence in the level of in-structure amplification of accelerations [e.g., Miranda and Taghavi, 2003a, 2003b, 2010]. Furthermore, due to directionality effects, the ground motion intensity is typically different in each orthogonal direction of the building and therefore mixing the data from the two directions also masks the adequate interpretation of the recorded data.

Table 1 summarizes the recorded data used in this investigation. As shown in the table, recorded motions were obtained in four instrumented buildings, three located in the Los Angeles metropolitan region and one located in the San Francisco Bay Area. As mentioned previously, all four buildings are midrise buildings ranging from nine to 14 stories that have recorded at least six earthquakes with moment magnitudes larger than four. For each building, the table summarizes the range of magnitudes and epicentral distances of the recorded events as well as the range of peak ground accelerations and peak floor accelerations at roof level on each of the four buildings.

Table 1. Summary of the characteristics of the four buildings examined

Station Number	Building Location	Stories Number	Number of Earthquakes	Ep. Distance range [km]	Magnitude range	PGA range [g]	PFA_{roof} range [g]	Soil class
14654	El Segundo	14	6	4.6 to 341.9	4.7 to 7.2	0.003 to 0.13	0.010 to 0.246	D
24236	Los Angeles	14	7	16.9 to 347.9	4.4 to 7.2	0.003 to 0.28	0.009 to 0.486	D
24571	Pasadena	9	6	17.7 to 336.8	4.4 to 7.2	0.005 to 0.25	0.012 to 0.425	C
57356	San Jose	10	7	14.4 to 33.4	4.1 to 6.9	0.006 to 0.24	0.014 to 0.365	D

4. EVALUATION OF RESULTS

4.1 EFFECT OF THE LEVEL OF GROUND MOTION INTENSITY

Figure 1 shows the variation of peak floor accelerations at the roof in orthogonal directions of each of the four buildings during each earthquake normalized by the corresponding peak ground acceleration. There is a total of 52 data points in this figure. But as mentioned previously, rather than mixing the data from all buildings which have different fundamental periods of vibration and different lateral resisting systems, here this in-structure amplification of acceleration demands (PFA/PGA) is examined for each building and each

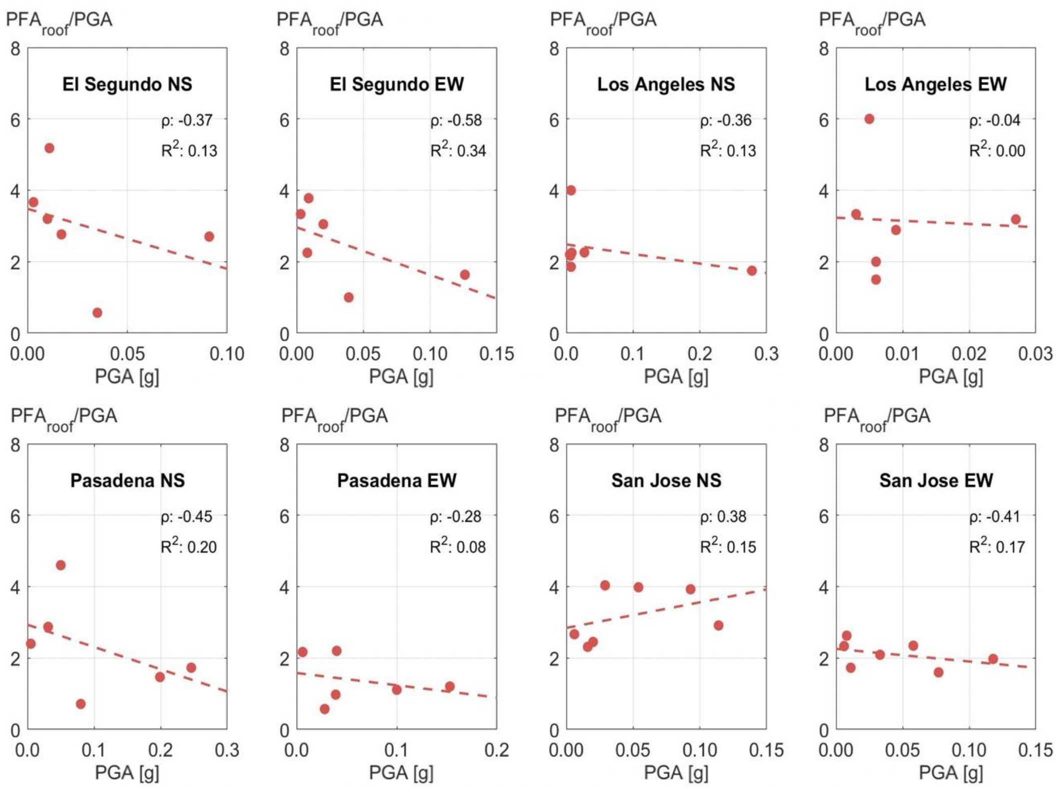

Figure 1. Variation of the peak floor acceleration recorded (PFA) at roof level normalized by peak ground acceleration (PGA) as a function of the level of peak ground acceleration for each direction of the four buildings.

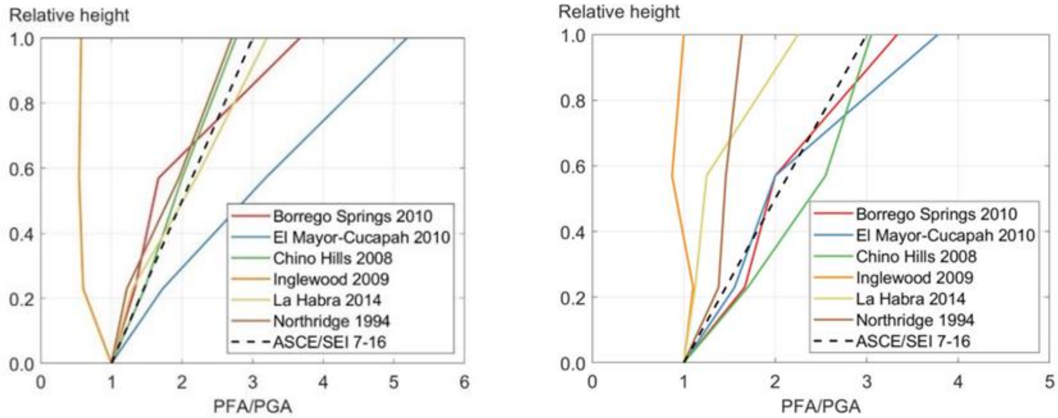

Figure 2. Variation of PFA/PGA along the height of El Segundo building during six different earthquakes in the North-South direction (left) and East-West direction (right).

direction separately. There are four general observations that can be made from this figure: (1) Most of the PGAs are less than 0.05g; (2) there is a large range in the level of amplification varying from values less than one (actually a deamplification of acceleration relative to the one at ground level) all the way to a case of an amplification of more than six; (3) there is large earthquake-to-earthquake variability even within each direction of each building; and (4) there is a general tendency of the level of amplification to decrease with increasing level of PGA. Based on the fourth observation one can perhaps understand why three previous investigations have concluded that large levels of amplification such as three are unlikely to occur at strong levels of ground motion intensity. But in addition to that general descending trend in PFA/PGA with increasing PGA one needs to keep in mind that the descending trend does not occur in all cases (i.e., the NS direction of the building in San Jose has an upward trend) and that in half of the cases, the descending trend has very small downward slope, meaning the effect of PGA does not have a strong influence in the PFA/PGA ratio at roof level. More importantly, for all eight cases there is a large scatter around the linear trend. The correlation coefficient, ρ, and coefficient of determination, R^2, between PGA and PFA/PGA is indicated on the upper right corner of each subplot. The coefficients of determination are, in all cases, relatively small meaning that PGA only explains a small portion of the large variability in PFA/PGA values and therefore it is very likely that there are other factors that are producing the large observed earthquake-to-earthquake variation of the PFA/PGA values in these buildings.

4.2 VARIABILITY OF PFA/PGA IN THE BUILDING IN EL SEGUNDO

In order to examine more carefully the earthquake-to-earthquake variability in the level of acceleration amplification experienced in buildings during earthquakes, it was decided to study one of the buildings in more detail. The building selected for this purpose was the 14-story steel braced office building located in the city of El Segundo just south of the Los Angeles International airport (LAX). The building has records from six earthquakes with magnitudes ranging from 4.7 to 7.2 that had epicenters ranging from as little as 4.6 km to as far as 342 km from the building. Figure 2 shows the variation of PFA/PGA along the height of the building in each of the six earthquakes where a very large earthquake-to-earthquake variability is observed. The largest amplifications occurred during the 2010 El Mayor Cucapah earthquake while the smallest amplifications occurred during the 2009 Inglewood earthquake. For this latter event in the NS direction sensors located above grade recorded PFAs significantly smaller than the one recorded at the base of the building.

Figure 3 shows a map of southern California which indicates the location of the building along with the magnitude and epicenter of each of the six earthquake whose records were analyzed. The largest amplification occurred in the earthquake with largest magnitude, but which occurred very far from the

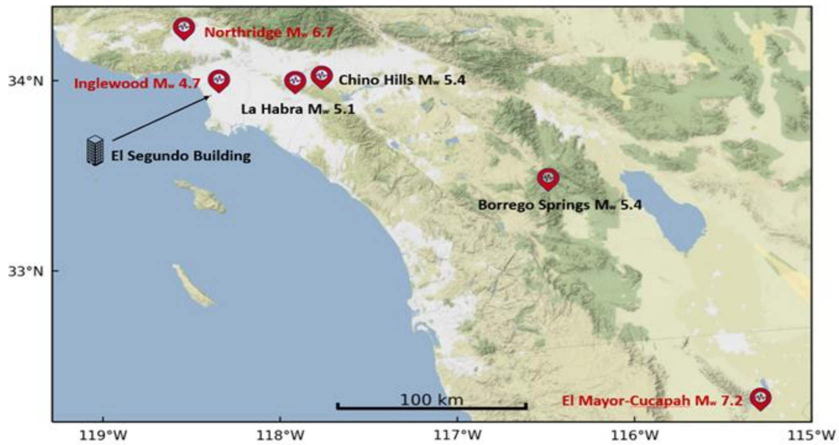

Figure 3. Map of southern California indicating the location of El Segundo building and the epicenter of the six earthquakes whose records were analyzed in this study.

building, while the earthquake that produced no amplifications or deamplifications corresponds to the one with smallest magnitude (only 4.7) but with an epicenter only 4.7 km (less than 3 miles) away from the building. It is well known that magnitude and distance to the source have an important effect on the frequency content of earthquake ground motions so it was decided to investigate if differences in frequency content (i.e., spectral shape) could explain the large earthquake-to-earthquake variability shown in figures 1 and 2 for this building.

4.3 EFFECT OF FREQUENCY CONTENT OF GROUND MOTIONS ON PFA/PGA

Figure 4 shows the variation of PFA/PGA along the height of the building in the NS direction of the El Segundo building during three of the six earthquakes. Only three of the six earthquakes are shown in this figure to make it clearer. One of the earthquakes (the 1994 Northridge earthquake) produced a variation similar to the one in ASCE 7-16 while the 2010 El Mayor Cucapah earthquake produced significantly stronger amplifications than the ones used in ASCE 7-16 while the 2009 Inglewood earthquake much smaller than those in ASCE 7-16, with PFAs actually significantly smaller than the PGA recorded at the base of the building. Also shown in the figure are the 5%-damped response spectra of the motions recorded at the base of the building in this direction in each of the three earthquakes. As shown in this figure, the spectral shapes of these spectra are significantly different from each other. The one corresponding to the 1994 Northridge is closer to mean normalized ground motion spectra for firm soils [e.g., Seed et al. 1976] while the response spectrum of the nearby 2009 Inglewood earthquake consists primarily of high-frequency content with very little energy in low frequencies due to its low magnitude. Meanwhile, the strong but distant 2010 El Mayor Cucapah earthquake has a spectrum characterized by strong energy at low frequencies but with unusually small spectral ordinates in the short period (high frequency) region as the high frequencies have been more strongly attenuated by the long distance that wave had to travel to arrive to the building. The larger attenuation of high-frequency waves than that of low-frequency waves is the results of anelastic attenuation which for this building and earthquake resulted in unusually small contribution of higher modes relative to that occurring in the other two earthquakes. In each spectrum the black dots indicate the spectral ordinates corresponding to the first and second modes of vibration of the building in its NS direction.

In order to evaluate the influence of the frequency content of ground motions on the level of amplification of acceleration, Figure 5 makes use of the ratio of 5% spectral ordinate at the second mode of vibration with respect to spectral ordinate at the first mode of vibration in this direction. These periods of vibration exhibit small variations from one earthquake to another but here they were taken as 1.7s and 0.54s for the first and second mode, respectively. It can be seen as this spectral ratio increases, the level of amplification decreases, but contrary to the large scatter shown when PFA/PGA was plotted as a function of PGA, the level of scatter now is significantly smaller as indicated by the coefficient of determination that is now more than five times larger to that shown in figure 1.

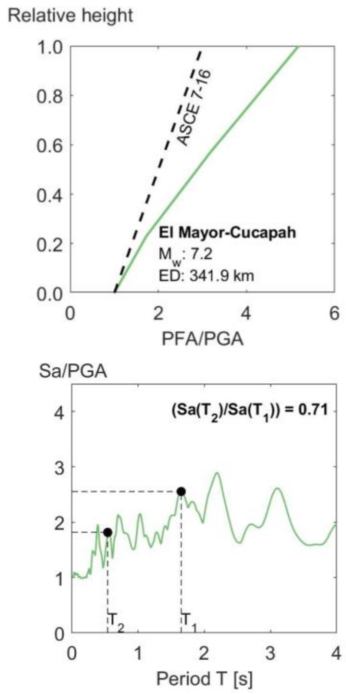

Figure 4. Variation of PFA/PGA along the height (top) and 5% damped response spectra of motions recorded at the base (bottom) in the North-South direction of El Segundo Building for 3 different earthquakes: 2010 El Mayor-Cucapah, 1994 Northridge, and 2009 Inglewood.

Figure 6 shows the variation of the in-structure amplification as measured by the PFA/PGA at the roof in both directions of the four building as a function of the spectral shape metric $Sa(T_2)/Sa(T_1)$ of the ground motion of each earthquake. The correlation coefficient, ρ, and coefficient of determination, R^2, between the spectral shape metric $Sa(T_2)/Sa(T_1)$ and PFA/PGA is indicated on the upper right corner of each subplot. In all cases there is a strong negative correlation between $Sa(T_2)/Sa(T_1)$ and PFA/PGA indicating a clear tendency for PFA/PGA to decrease with increasing $Sa(T_2)/Sa(T_1)$. Furthermore, the coefficients of determination as a function of $Sa(T_2)/Sa(T_1)$ are between 2.3 and 6.4 times larger than those computed when computed using PGA indicating that the proposed spectral shape metric $Sa(T_2)/Sa(T_1)$ is a much better predictor than PGA of the variability of PFA/PGA observed in the data.

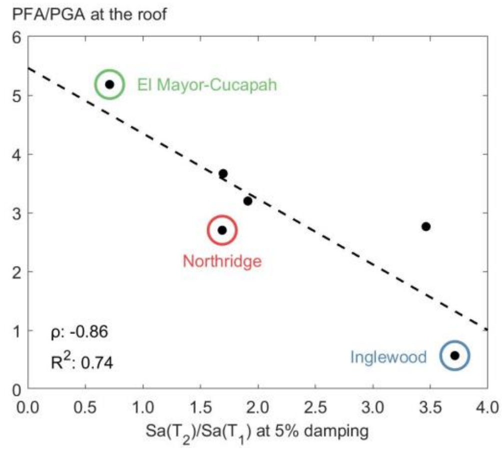

Figure 5. Variation of PFA/PGA at the roof in the North-South direction of El Segundo building during six earthquakes as a function of the spectral shape metric $Sa(T_2)/Sa(T_1)$.

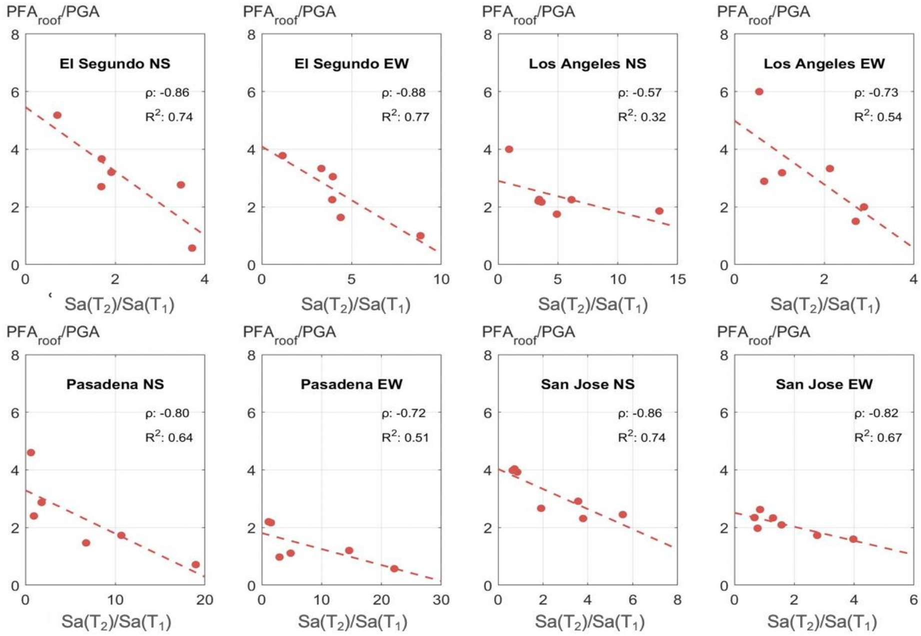

Figure 6. Variation of PFA/PGA at roof level in both directions of the four building as a function of the spectral shape metric $Sa(T_2)/Sa(T_1)$ of the ground motion of each earthquake.

5. SUMMARY AND CONCLUSIONS

The level of amplification of horizontal accelerations in buildings is characterized by a strong earthquake-to-earthquake variability. Previous studies in which recorded data from many different buildings with different fundamental periods and different lateral resisting systems was mixed concluded that the level of amplification depends on the level of ground motion intensity as measured by the peak ground acceleration experience by the building. By studying records obtained in buildings that have been subjected to at least six earthquakes and by evaluating the data from each building and each direction separately, it is shown that changes in the level of amplification of acceleration are primarily due to differences in the frequency content of the ground motion shaking a building. The apparent decrease in level of amplification with increasing level of peak ground acceleration that is observed in the data is a direct result of the combination of magnitudes and distances of the recorded events. Therefore, it would be incorrect to assume that strong levels of amplification are unlikely to occur in buildings during strong earthquake as this could be the result in the case of large magnitude earthquakes developing at short distances of a building.

A relatively simple metric of the spectral shape of a ground motion consisting of the ratio of 5%-damped spectral ordinate at the period corresponding to the second translational mode to that at the period corresponding to the first translational mode is proposed. It is shown that this simple metric of spectral shape is a significantly better predictor (two to six times better) of the level of amplification of peak floor accelerations than using peak ground acceleration.

ACKNOWLEDGEMENTS

The authors acknowledge accessing strong-motion data through the Center for Engineering Strong Motion Data, last visited on 15 Aug 2022. The network providing the data used in this work is the California Strong Motion Instrumentation Program (CSMIP). This work was supported by Ermenegildo Zegna Founder's Scholarship, Foundation Blanceflor and P.E.O. Fund. Additionally, the authors thank Alan Poulos for his assistance in preparing figure 3.

REFERENCES

Anajafi, H., Medina, R.A. [2018] "Evaluation of ASCE 7 equations for designing acceleration-sensitive nonstructural components using data from instrumented buildings," *Earthquake Engineering and Structural Dynamics*, Vol. 47, No. 4, pp. 1075-1094.

Applied Technology Council [2018] "Recommendations for Improved Seismic Performance of Nonstructural Components," *Report NIST GCR 18-917-43*, National Institute of Standards and Technology Gaithersburg, Maryland, USA.

Drake, R. M., Gillengerten, J. D. [1994] "Examination of CDMG Ground Motion Data in support of the 1994 NEHRP Provisions," *Proceedings of the Fifth US National Conference on Earthquake Engineering*, Chicago, USA.

Drake, R. M., Bachman, R. E. [1996] "NEHRP provisions for 1994 for nonstructural components," *Journal of Architectural Engineering*, Vol. 2, No.1, pp. 26-31.

Fathali, S., Lizundia, B. [2012] "Evaluation of ASCE/SEI 7 equations for seismic design of nonstructural components using CSMIP records," *Proceedings of SMIP12 Seminar on Utilization of Strong-Motion Data*, Sacramento, USA.

Fathali, S., and Lizundia, B. [2011] "Evaluation of current seismic design equations for nonstructural components in tall buildings using strong motion records," *The Structural Design of Tall and Special Buildings* Vol. 20, pp. 30-46.

Medina, R. A., Sankaranarayanan, R., Kingston, K. M. [2006] "Floor response spectra for light components mounted on regular moment-resisting frame structures," *Engineering Structures*, Vol. 28, No. 14, pp. 1927-1940.

Miranda, E., Taghavi, S. [2003a] "Towards the prediction of seismic performance of nonstructural elements," *Proceedings of 2003 SEAOC convention*, Lake Tahoe, California, USA.

Miranda, E., Taghavi, S. [2003b] "Estimation of seismic demands on acceleration-sensitive nonstructural components in critical facilities," *Proceedings of the Seminar on Seismic Design, Performance, and Retrofit of Nonstructural Components in Critical Facilities*, Newport Beach, California, USA.

Miranda, E., Taghavi, S. [2005] "Approximate floor acceleration demands in multistory buildings. I: Formulation," *Journal of Structural Engineering*, Vol. 131, No. 2, pp. 212-220.

Miranda, E., Taghavi, S. [2010] "A comprehensive study of floor acceleration demands in multi-story buildings," *Proceedings of ATC and SEI Conference on Improving the Seismic Performance of Existing Buildings and Other Structures,* San Francisco, California, USA.

Seed, H.B., Ugas, C., Lysmer, J. [1976] "Site-dependent spectra for earthquake-resistant design," *Bulletin of the Seismological society of America*, Vol. 66, No. 1, pp. 221-243.

Singh, M.P., Suarez, L.E., Matheu, E.E., Maldonado, G.O. [1993] "Simplified procedure for seismic design of nonstructural components and assessment of current code provisions," *Report NCEER-93-0013*, National Center for Earthquake Engineering Research (NCEER), State University of New York, Buffalo, USA.

Singh, M.P., Moreschi, L.M., Suarez, L.E., Matheu, E.E. [2006] "Seismic design forces. I: Rigid nonstructural components," *Journal of Structural Engineering*, Vol. 132, No. 10, pp. 1524-1532.

Wieser, J., Pekcan, G., Zaghi, A.E., Itani, A., Maragakis, M. [2013] "Floor accelerations in yielding special moment resisting frame structures," *Earthquake Spectra*, Vol. 29, No. 3, pp. 987-1002.

Nonlinear approach on Seismic Design Force of Non-Structural Components for Isolated and Fixed Base Buildings Comparison

S. Shakeri[1], J. Wong[1], T. Hart[2] and M. Halligan[3]

[1] San Francisco State University
sshakeri1@mail.sfsu.edu, jewong@sfsu.edu.
[2] Lawrence Berkeley National Laboratory
thart@lbl.gov
[3] Tomarco/ISAT
mhalligan@isatsb.com

Abstract. Chapter 13 of ASCE 7-22 was significantly updated and now includes building floor accelerations and periods in seismic design anchorage force calculations. One carryover from the previous edition of ASCE 7 is the factor a_i (floor acceleration obtained from dynamic analysis) in the seismic design force (Fp) equation specified in ASCE 7-22 Section 13.1.3.5. The a_i factor can be used to allow the designer to account for reduced floor accelerations from seismic isolation and/or increased damping of the structure. However, the upper and lower limits of Fp used for a fixed based structure still bound the calculation of Fp with the a_i factor, even with the reduction of forces from isolation or damping. In this paper, a series of nonlinear dynamic analyses of a special steel moment frame structure are conducted for quantification and comparison between seismic anchorage resultant forces calculated for a fixed based building versus a seismically isolated building. The result of the analysis indicates that seismic resultant forces (Fp) calculated based on the story acceleration of seismically isolated buildings are much lower compared to ones calculated based on the acceleration of a fixed based building. As a result, the lower Fp limit required by ASCE 7-22 is much higher than the resultant forces calculated for the lower floor levels of a seismically isolated building, which results in the overestimation of anchorage forces of components.

Keywords: Seismic Anchorage Force, Seismically Isolated Building, Nonlinear Analysis, ASCE 7-22, Non-structural.

1. Introduction

Chapter 13 of ASCE7-22 was updated significantly based on key findings from the ATC-120 project (Seismic Analysis, Design, and Installation of Non-structural Components and Systems – Background and Recommendations for Future Work) [ATC,2017]. This project led to the inclusion of building floor accelerations and periods in seismic design anchorage force calculations. In this research discussed herein, the effect of the revised provisions on the design of non-structural components in the seismically isolated building is examined. Accounting for the seismic isolation effect on the seismic design anchorage force is only possible by using the (a_i) factor, the floor acceleration calculated from nonlinear response history analysis, in the alternate equation for Fp specified in ASCE 7-22 Section 13.1.3.5. However, Section 13.1.3.5 also specifies that the lower and upper limits of seismic anchorage force specified for fixed based structures still apply when this Fp equation is used. Since these limits are tied to fixed based structural performance, they prevent designers from fully utilizing the benefits of isolation in designing the anchorage of nonstructural elements.

The more common equation for Fp (without the a_i factor) includes a step function that increases the force up the height of the building. This is to mirror the typical primary behaviour mode for a fixed base building. As a result, the anchorage of a roof top unit such as giant chiller would have to be designed for approximately double the force compared to the force on equipment that are located at the ground floor. However, when the building is base isolated, the floor accelerations at the roof would be similar in magnitude to the forces at the base and would not increase with the building height. Thus, using the actual floor accelerations through the a_i factor for a base isolated building could greatly reduce the calculated force demand on the equipment on the roof.

Establishing resilient equipment anchorage is one of important phases of non-structural design, especially for hospitals, laboratories, scientific buildings, and other facilities that have a large amount of expensive equipment located in them. In this case, accounting for seismic isolation and its effect on the seismic anchorage force more directly will lead to increased accuracy and estimates of the component's behavior, leading to more economical and efficient designs. As a side benefit, building owners may be more willing to include isolation and damping in the structural and/or floor designs if the requirements for non-structural components can be relaxed.

2. Building Model Geometry

A four-story, special steel moment frame with hospital operations near San Jose, California is considered for this study. Since hospitals typically have a high number of non-structural components and are among the most likely buildings to be base isolated, this building type benefits the project's purpose. Figure 1 shows the typical plan of the building and Figure 2 shows the typical elevation of the building. As it is shown, the building is symmetrical with a 90 ft by 90 ft plan and 15 ft height for each story. The building load resistance system is a combination of special moment frames (highlighted with red lines) for the lateral force resistance system and composite-steel concrete slabs for gravity loads.

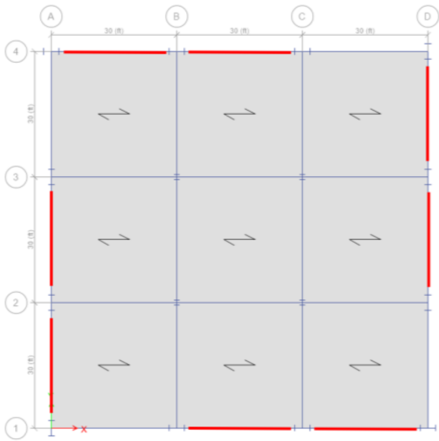

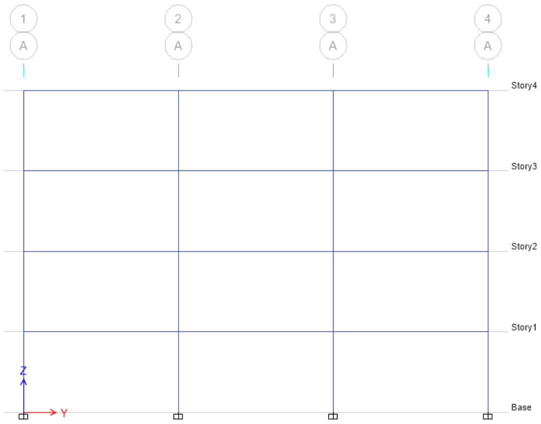

Figure 1. Typical Floor Plan

Figure 2. Typical Floor Elevation

3. Building Loading

Table 1 shows the dead and live loads considered. These loads were drawn from a recently constructed hospital design. Table 2 shows the seismic load parameters calculated using ASCE 7-22[2022].

Table 1. Gravity Loads

Story	Deck Dead Load (psf)	Super Dead Load (psf)	Live Load (psf)
Story 4	65	285	100
Story 3	65	150	100
Story 2	65	150	100
Story 1	65	150	100

Table 2. Seismic Load Parameters

Parameter	Deck Dead Load (psf)
S_{DS}	1.2
S_{D1}	0.56
S_1	0.6
S_{M1}	0.84
C_S	0.225

4.Building Design Summary

The structure was designed based on the provisions of AISC 360 [2016] and AISC 341 [2016]. The sections for the structural elements were designed to met standard design criteria such as strong column weak beam and drift ratio limits. Table 3 shows the designed section summary of structure.

Table 3. Design Summary

Element	Section
Column	W36×652
Moment Frame Beam	W33×291
Gravity Frame Beam	W30×173

5. Seismic Isolator Design

The seismic isolation system is comprised of sixteen lead plug rubber bearing (LPRB) isolators located under each structural column. The isolators were designed based on the displacement response spectra of seven selected ground motions (listed in the appendix) with 10% damping. Figure 3 shows the critical displacement response spectrum. The target period of isolators is set to be 3.5 seconds to make sure that the structure exhibits the rigid body motion that is expected in isolated structures. Considering a 3.5 second period, the ultimate design displacement of the isolators based on the critical displacement response spectrum is 23 in. Table 4 summarizes the isolator parameters. Using isolators will push the period of the structure from 0.9 seconds to 3.5 seconds, which will reduce the maximum probably acceleration from 0.7g to 0.25g as is shown in Figure 4.

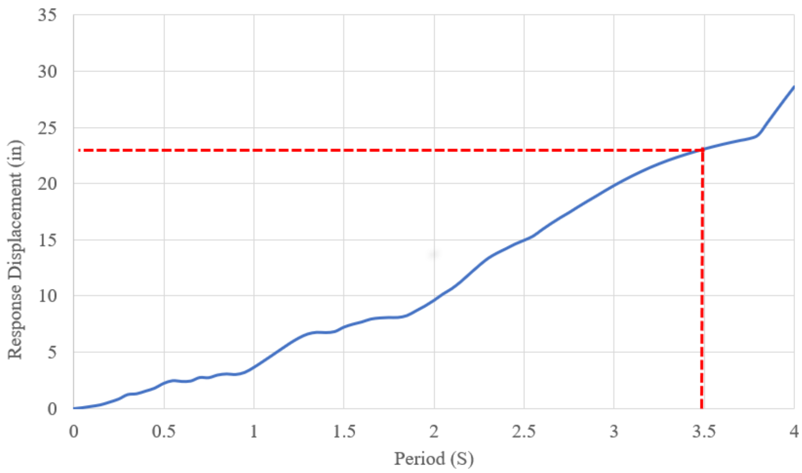

Figure 3. Isolator Displacement Response Spectrum with 10% Damping

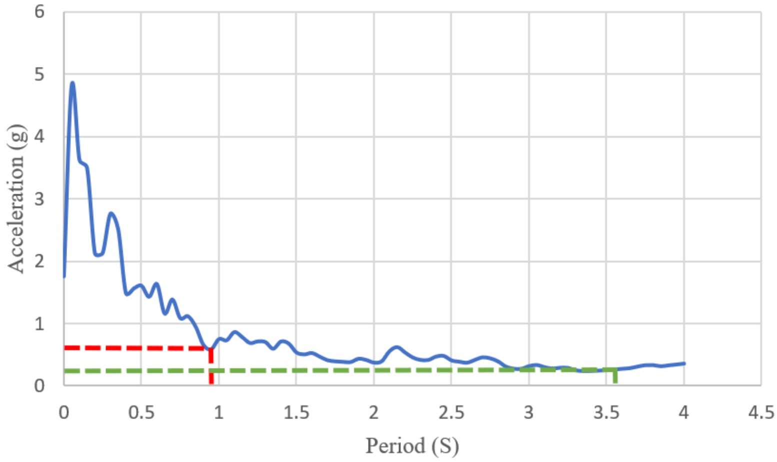

Figure 4. Acceleration Response Spectrum

Table 4. Isolator Parameter to be modelled in OpenSees

Parameter	Symbol	Value
Initial Stiffness	Ki	4.84 kips/in
Yield Strength	Fy	11.15 kips
Yield Displacement	Dy	2.3 in
Characteristic Strength	Qd	3.11 kips
Ultimate Displacement	Du	23 in
Post Yield Stiffness Ratio	α	0.1
Rubber Diameter	D_r	45.2 in
Bearing Height	Tr	26 in
Lead Diameter	R_l	1.62 in

6. Nonlinear Time History Analysis

The 3D fixed based and seismically isolated structures were modelled using OpenSees [McKenna, et. al. (2010)], a finite element analysis software. The beams and columns were defined using elastic beam-column elements. Several gravity beams not participating in lateral load support were modelled using truss section elements to simulate their appropriate behavior. Nonlinearity in the structural system was not considered to ensure that this was reflected in the isolation layer. The Elastomeric Bearing (Plasticity) element was used to model the LPRB isolators based on the properties outlined in Table 4. This element has unidirectional (2D) or coupled (3D) plasticity properties for the shear deformations, and force-deformation behaviors defined by UniaxialMaterials in the remaining two (2D) or four (3D) directions. The Rayleigh Damping function is created considering 2% damping for the structure and 10% damping for isolators based on the 1st and 3rd modes.

The base node that represents the connection of isolator to the ground is fully fixed. The upper part of the base, where the structure sit on the isolators, is fixed in three degrees of freedom (1, 2, and 3) and released in the remaining rotational degree of freedom. In addition, each floor node is constrained by equal degrees of freedom to the centre node of the floor to represent the rigid diaphragm.

To verify the model, a modal analysis was conducted to observe the distribution of modal properties, ensuring that the system has been effectively isolated. The fundamental periods of the fixed base and seismically isolated structures were 0.9 and 3.5 seconds, respectively.

A series of nonlinear time-history dynamic analyses were conducted to record floor level responses, including relative displacements and absolute accelerations. The analyses were conducted uniaxially for a suite of seven ground motions resulting in 14 analyses for each scenario. The ground motions used for the analysis are real time ground motion data obtained from Pacific Earthquake Engineering Research Center (PEER) data base. The ground motion events, and their Peak Ground Accelerations (PGA) are listed in the appendix. The motions were scaled to meet site-specific conditions. Through the dynamic analyses, we were able to review the seismic isolation to ensure it was performing as expected. Figure 6 shows the story drift in isolated building. Based on the result of analysis, maximum building's story drift decreases from 1.7 inch in the fixed base building to 0.5 inch in the isolated building, and the 4th floor's acceleration reduces from approximately 1g to approximately 0.25g, as shown on Figure 7. In addition, as shown in Figure 5, the differences between the accelerations of each floor in the isolated building is near zero, and as shown in Figure 6, the interstory drift at each floor is approximately the same. Therefore, the isolation system was capable of creating nearly uniform responses in the structure with long-period behavior and thus the model could be used for determining the floor accelerations to be used to calculate the seismic anchorage forces.

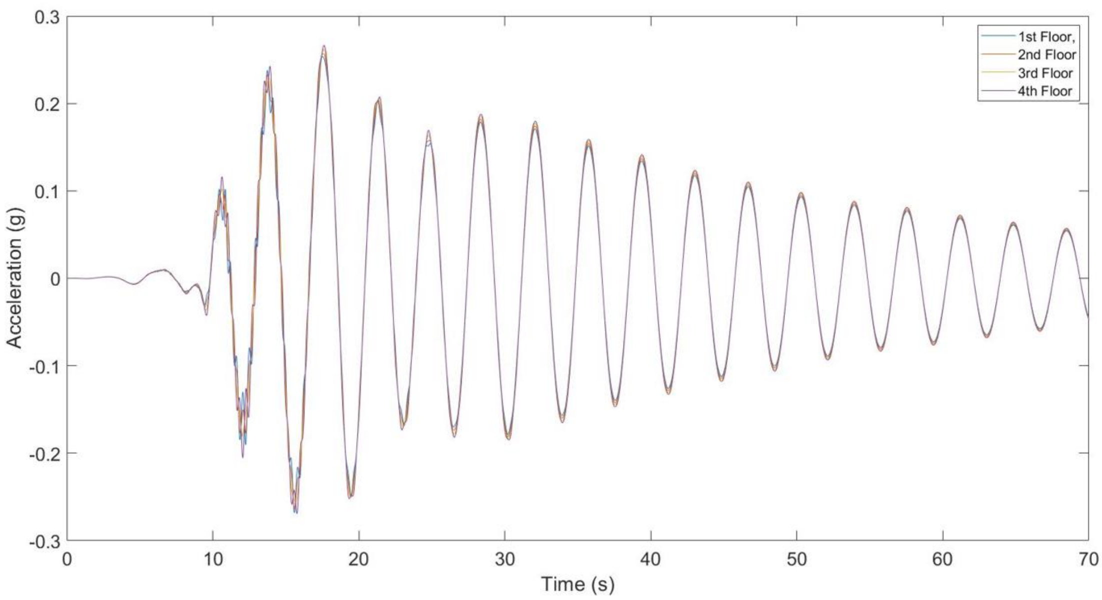

Figure 5. Isolated Building Story Acceleration Comparison-(Bolu 1999 motion-Y direction)

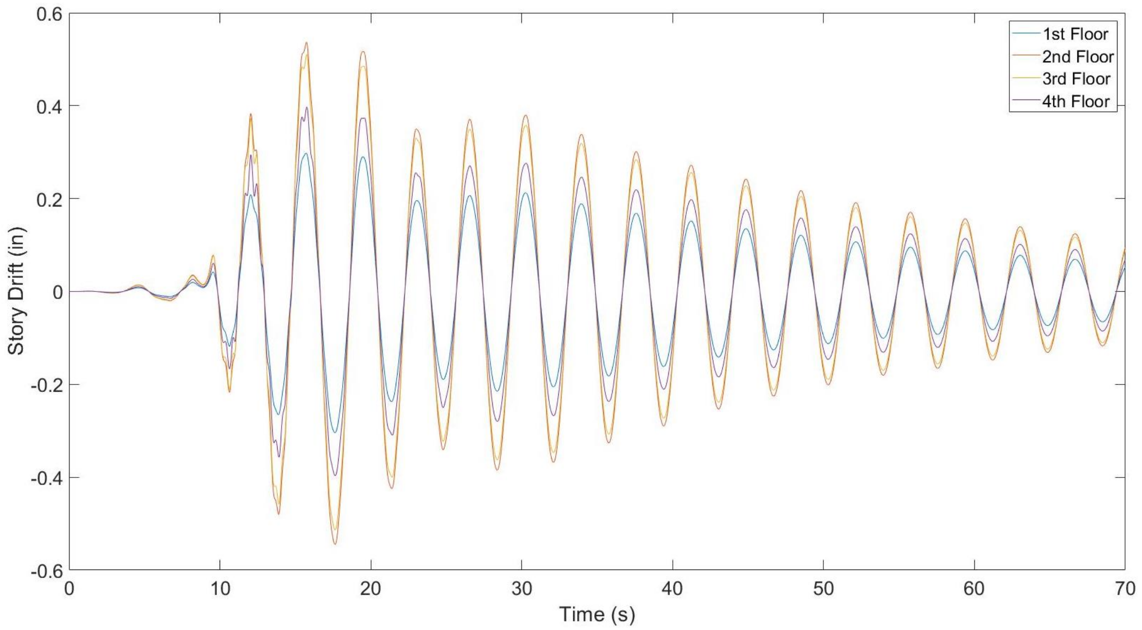

Figure 6. Isolated Building Story Drift Comparison-(Bolu 1999 motion-Y direction)

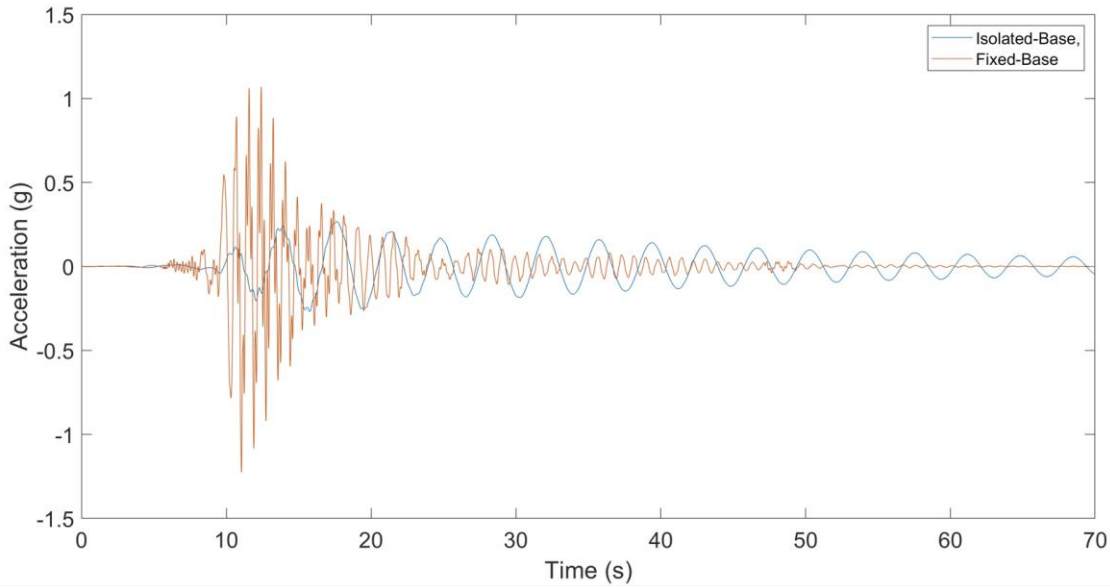

Figure 7. 4th floor acceleration comparison-(Bolu 1999 motion-Y direction)

7.Seismic Design Anchorage Forces

For each building, the seismic anchorage force was calculated using two different equations:

1- Regular design force based on ASCE 7-22 Equation 13.3-1

$$Fp = 0.4S_{DS}I_PW_P.\frac{H_f}{R_u}\frac{C_{AR}}{R_{p0}} \quad (1)$$

2- Seismic design force based on the ASCE 7-22 dynamic analysis Equation 13.3-7

$$Fp = I_PW_P\ a_i\ \frac{C_{AR}}{R_{p0}} \quad (2)$$

In addition to these equations, the maximum and minimum Fp values were calculated as prescribed in ASCE 7-22 via Equations 13.3-2 and 13.3-3:

Equations 13.3-2: $Fp_{(max)} = 1.6S_{DS}I_PW_P$ (3)

Equations 13.3-3: $Fp_{(min)} = 0.3S_{DS}I_PW_P$ (4)

As mentioned in Section 13.3.1 of ASCE 7-22, the Fp force should be calculated considering 100% of the anchorage force in one principal direction plus 30% of the anchorage force in the perpendicular direction. The 100%+30% load combination comparison was conducted as a part of the research and the differences in the calculated Fp forces were comparable to differences calculated using 100% of loads in one direction; therefore, in this study and for comparison purposes, only 100% of each load case is considered and compared with each other. The maximum acceleration (a_i) used in Equation 13.3.7 is the mean maximum acceleration value obtained from the suite of ground motions. For calculating the ratio of C_{AR} to $R_{P0,}$ the "other mechanical or electrical component" group specified in ASCE 7-22 Table 13.6-1 was selected. This results in a value of C_{AR} equal to 1 and R_{P0} equal to 1.5.

8. Results

Tables 5 to 8 and Figures 8 and 9 show the results of the Fp calculations. The Fp in the X direction (calculated based on the dynamic analysis of the X component of motions) for the isolated building is on average 78% less than the lower limit prescribed in ASCE 7-22 Equation 13.3-3 and approximately 60% to 80% less than the force calculated by ASCE 7-22 Equation 13.3-1. A similar result was observed for the Y direction. Fp was on average 52% less than the code prescribed lower limit (Equation 13.3-3) and approximately 20% to 60% less than the forces calculated by Equation 13.3-1. As is shown in Tables 5 and 6, the seismic anchorage forces increase with the height of the structure in the fixed-base model as predicted due to the increasing acceleration in the upper stories. However, the seismic anchorage force in the isolated-base structure is approximately the same at each story, only slightly changing with the increase of height.

Table 5. Fixed Base Model Summary (X Direction)

Story	Average Acceleration (g)	W_P (lb.)	Nonlinear equation (lb.) (13.3-7)	Regular equation (lb.) (13.3-1)	Maximum Force (lb.) (13.3-2)	Minimum Force (lb.) (13.3-3)
4	1.1	1	1.11	0.87	2.88	0.54
3	0.95	1	0.96	0.57	2.88	0.54
2	1.1	1	1.11	0.465	2.88	0.54
1	0.82	1	0.82	0.39	2.88	0.54

Table 6. Isolated Summary (X Direction)

Story	Average Acceleration (g)	W_P (lb.)	Nonlinear equation (lb.) (13.3-7)	Regular equation (lb.) (13.3-1)	Maximum Force (lb.) (13.3-2)	Minimum Force (lb.) (13.3-3)
4	0.118	1	0.118	0.69	2.88	0.54
3	0.111	1	0.111	0.375	2.88	0.54
2	0.113	1	0.113	0.345	2.88	0.54
1	0.115	1	0.115	0.315	2.88	0.54

Table 7. Fixed Base Model Summary (Y Direction)

Story	Average Acceleration (g)	W_P (lb.)	Nonlinear equation (lb.) (13.3-7)	Regular equation (lb.) (13.3-1)	Maximum Force (lb.) (13.3-2)	Minimum Force (lb.) (13.3-3)
4	1.37	1	1.37	0.87	2.88	0.54
3	1.26	1	1.26	0.57	2.88	0.54
2	1.28	1	1.28	0.465	2.88	0.54
1	1.13	1	1.13	0.39	2.88	0.54

Table 8. Isolated Summary (Y Direction)

Story	Average Acceleration (g)	W_P (lb.)	Nonlinear equation (lb.) (13.3-7)	Regular equation (lb.) (13.3-1)	Maximum Force (lb.) (13.3-2)	Minimum Force (lb.) (13.3-3)
4	0.255	1	0.255	0.69	2.88	0.54
3	0.244	1	0.244	0.375	2.88	0.54
2	0.239	1	0.239	0.345	2.88	0.54
1	0.240	1	0.240	0.315	2.88	0.54

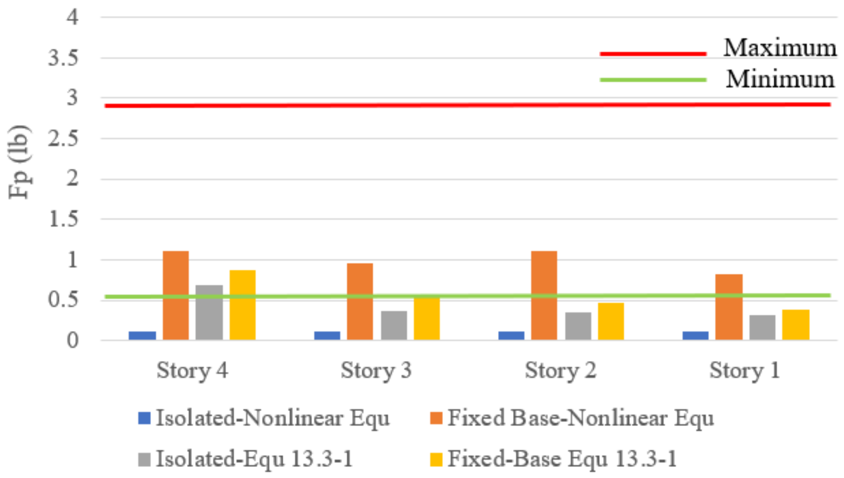

Figure 8. Seismic Design Force Comparison Summary (100%X)

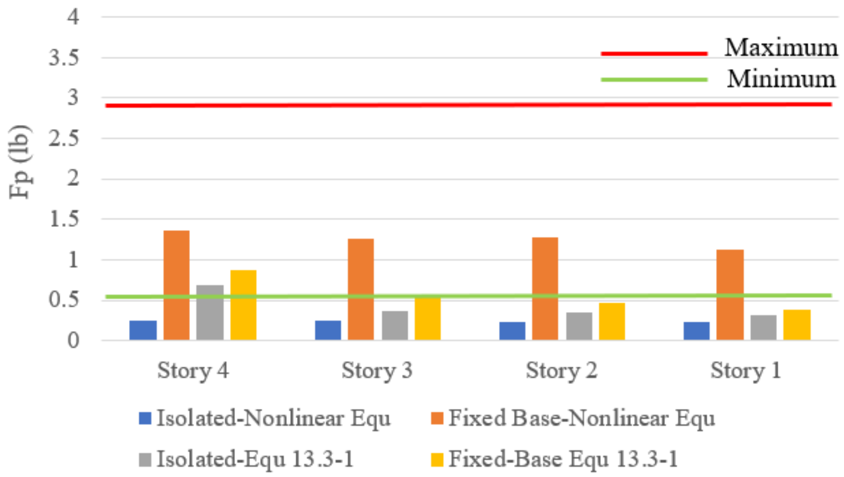

Figure 9. Seismic Design Force Comparison Summary (100%Y)

9.Conclusions

Through this study, the Fp forces were examined for a fixed base and seismically isolated structural scenario. Considering the importance of non-structural components, the results presented observations for consideration in future adjustments to code provisions.

- The Fp forces calculated based on the nonlinear analysis in the isolated structure are considerably less than the minimum Fp force required by the code. Since ASCE 7-22 requires that the minimum design value still be followed even if the building is isolated, it will lead to over designing of anchors for isolated buildings that will unnecessarily increase construction complexity and cost. In addition, although the structural system benefits from the isolators in their design, the nonstructural component does not benefit from that. It is thus suggested that relaxing the minimum Fp requirement for isolated buildings be considered.

- The Fp forces for the fixed base building, calculated by the 13.3-1 equation, linearly increase with height that corresponds with the usage of the height variable. For the seismically isolated system, the use of Equation 13.3-1 also forces the result to gradually increase with height. However, this goes against the general theory behind isolation that relies on rigid behaviour with relatively uniform floor accelerations at each floor. As such, this could be an area of further consideration of the story force distribution in relation to the data produced in this study.

- The new dependency of the Fp value on the period of the structure still does not fully cover the effect of seismic isolation. The nonlinear results, which remove the dependence on the structure's height, might be a better reflection of the Fp forces in seismically isolated buildings. The results are notably consistent with expected rigid body response. This also raises questions regarding the accuracy of the Fp forces in the fixed base buildings since there is fluctuation in the forces without a strong linearly increasing behavior.

- The lower values for Fp for the isolated case versus the fixed case were anticipated, but the higher values for Fp for the fixed base/nonlinear analysis case was unexpectedly higher.

10.References

ASCE7 [2022] *Minimum Design Loads and Associated Criteria for Buildings and Other Structures*, American Society of Civil Engineers, USA.

AISC 360 [2016], *Specification for Structural Steel Buildings,* American Institute of Steel Construction, USA

ATC-120 [2017], *Seismic Analysis, Design, and Installation of Non-structural Components and Systems – Background and Recommendations for Future Work,* Applied Technology Council, USA

11.Appendix

Table A1. Ground Motions Data Base

Motion No	Motion Name	PGA* (X direction)	PGA* (Y direction)
1	Bolu, 1999 Duzce, Turkey earthquake	1.4	1.8
2	Cerro Prieto,1979 Imperial Valley earthquake	2	3.2
3	Hector, 1999 Hector Mine earthquake	1.3	2
4	Nishi-Akaski, 1995 Kobe, Japan earthquake	1.6	2.6
5	Joshua Tree, 1992 Landers earthquake	1.14	2.2
6	LPGC, 1989 Loma Prieta earthquake	1.3	2.6
7	Sepulveda, 1994 Northridge earthquake	1.3	1.4

*PGA stands for Peak Ground Acceleration

Absolute Acceleration Floor Response Spectra for Inelastic Buildings: Quantification of Amplitude Capping and Period Lengthening

Rodriguez D.[1], Perrone D.[1, 2], Filiatrault A.[1], and Brunesi E.[3]

[1] University School for Advanced Studies IUSS Pavia
e-mail: derek.rodriguez@iusspavia.it
daniele.perrone@iusspavia.it
andre.filiatrault@iusspavia.it
[2] University of Salento
[3] European Centre for Training and Research in Earthquake Engineering
e-mail: emanuele.brunesi@eucentre.it

Abstract. In recent years, non-structural elements (NSEs) have gained special relevance in earthquake engineering. The economic losses attributed to NSEs after several seismic events in urban regions have often exceeded that of the structural components, generating an increased attention on their seismic performance. Estimating the seismic demand on NSEs is a challenging task, given that it is influenced not only by the ground motion physical characteristics but also by the dynamic properties of the supporting structure. In this context, floor response spectra (FRS) allow to estimate the seismic demand at which NSEs are prone by considering both ground motion and supporting structure properties in a decoupled manner. Recently, several simplified methods to estimate FRS have been developed for supporting structure responding in the non-linear range. However, most of these methods require detailed information on the supporting structure non-linear response, such as the ductility and displacement demands, which are often not available or laborious to obtain. This investigation aims to quantify the floor spectral acceleration amplitude capping and period lengthening in FRS of supporting structures behaving inelastically in comparison with supporting structures remaining elastic by regression of multiple stripes non-linear and linear time-history analyses of a population of 100 code-compliant reinforced concrete frames designed with a ductility class medium according to Eurocode 8 seismic provisions for a site representative of a medium-to-high seismicity level in Europe. A simplified method is proposed to consider the supporting structure non-linear response in the generation of FRS depending on the seismic hazard intensity level.

Keywords: floor response spectra, inelastic building, acceleration capping, period lengthening.

1. INTRODUCTION

Recent advancements in performance-based earthquake engineering have demonstrated the importance that the seismic design of non-structural elements (NSEs) have in the global performance and associated losses of modern code-compliant facilities. Two of the main issues that justify such a large non-structural influence are the higher vulnerability of NSEs at lower seismic intensities with respect to structural systems and the higher investment associated to NSEs in comparison with the total cost of the structure [Filiatrault *et al.*, 2014].

One of the approaches most commonly used for the seismic analysis of acceleration sensitive NSEs is the floor response spectrum (FRS) method. In this cascading analysis, the dynamic properties and the floor dynamic responses of the supporting structure are estimated without considering the interaction with the NSEs. The structural response at the attachment level is then considered as the input floor motion for the estimation of the dynamic response of the NSE. In recent years, several simplified code-oriented methodologies have been proposed to quickly construct FRS based on the dynamic characteristics of the supporting structure [Vukobratovic and Fajfar, 2017; Calvi and Sullivan, 2014; Welch and Sullivan, 2017; and Merino *et al.*, 2019]. However, for the case of supporting structures behaving inelastically, the majority of these methodologies require detailed information of the supporting structure's non-linear response, such as the ductility and displacement demands and effective periods, which are often obtained through the capacity spectrum method (i.e. N2 Method in Eurocode 8 provisions [CEN, 2004]). This dependency on the capacity spectrum method is often troublesome, given that to conduct this type of analysis, detailed information on the non-linear properties (material and geometric) of the supporting structure is needed, which is not always available. In this paper, a simplified procedure is proposed to estimate FRS for non-linear supporting structures depending on both the floor spectral acceleration amplitude capping and vibration period lengthening. Quantification of the floor spectral acceleration amplitude capping and period lengthening in FRS is conducted for supporting structures behaving inelastically in comparison with supporting structures remaining elastic by means of multiple stripes non-linear and linear time-history analyses of a population of 100 code-compliant reinforced concrete frames designed with a ductility class medium (DCM) according to Eurocode 8 seismic provisions [CEN, 2004] for a site representative of a medium-to-high seismicity level in Europe. Based on these results, regression analyses are conducted to develop prediction equations for the floor spectral acceleration amplitude capping and vibration periods lengthening. The developed procedure is applicable for cases in which detailed information about the supporting structure's non-linear response is not available, such as in the case of the seismic assessment of NSEs in existing supporting structures or regional studies that considers a large number of building assets.

2. SELECTION OF BUILDING POPULATION AND GROUND MOTION SETS

2.1 SELECTION OF BUILDING POPULATION

The frequency content and amplitude of FRS are heavily influenced by the dynamic properties of the supporting structure. Consequently, a target building population that envelopes a wide range of geometric and material properties that mostly affect the dynamic response of a supporting structure must be selected. A building portfolio of 100 code-compliant reinforced concrete frames was considered for this investigation [Perrone *et al.*, 2020]. The building portfolio was generated by means of a Monte Carlo simulation. The parameters that were considered as random variables are: (i) the building height, (ii) the number of bays, (iii) the length of the bays, (iv) the live loads, (v) the unconfined concrete compression strength, and (vi) the characteristic yielding rebar strength. The reinforced concrete frames were designed according to Eurocode 8 seismic provisions [CEN, 2004], assuming a force reduction factor q= 3.75 with a ductility class medium. It should be noted that even though just one ductility class is being considered, the vast majority of buildings in medium-to-high seismicity regions of Europe are designed using a medium ductility class. The selected building site is close to the city of Cassino, a medium-to-high seismicity site of Italy on firm ground conditions.

A non-linear static analysis (pushover analysis) was conducted using a lateral force distribution proportional to the first mode for each of the buildings of the portfolio in order to obtain the yield displacements (Δ_y). The bilinear approximation was used in this investigation to define Δ_y. This bilinear curve was defined by setting the base shear plateau equal to the maximum base shear ($V_{b,max}$) obtained from the pushover curve, while the initial elastic branch is defined by tracing a line from the origin secant to the point at which the pushover curve reaches a value of 40% $V_{b,max}$. Thus, Δ_y is obtained as the intersection point between these two branches.

2.2 GROUND MOTION SELECTION

As will be discussed in Section 3, this investigation uses the displacement ductility demand (μ_Δ) to establish relationships to predict the floor spectral acceleration amplitude capping and the period lengthening for FRS of non-linear supporting structures. Since μ_Δ is a function of the seismic hazard intensity level, several return periods of increasing magnitude must be considered in order to obtain a wide range of μ_Δ values to perform regression analyses.

For the ground motion selection, a far-field site characterised by a medium-to-high seismicity in Italy with a peak ground acceleration on stiff soil equal to 0.21g for a 10% probability of exceedance in 50 years was selected. For the selected site, six return periods of the seismic hazard were considered (100, 140, 200, 475, 975 and 2475-year return periods, respectively). For each return period, hazard-consistent selection of 20 horizontal ground acceleration records was conducted from the PEER NGA-West database [PEER, 2013] based on spectral compatibility with a conditional mean spectrum. The conditional periods for the record selection were obtained based on the eigenvalue analyses of the building portfolio. More details on the ground motion selection can be found in Rodriguez *et al.* [2021] and Perrone *et al.* [2020].

3. DETERMINATION OF FLOOR SPECTRAL ACCELERATION AMPLITUDE CAPPING AND PERIOD LENGTHENING IN FRS OF NON-LINEAR SUPPORTING STRUCTURES

When comparing FRS of linear supporting structures with FRS of non-linear supporting structures there are two key differences that arises. The first one corresponds to the capping of the spectral acceleration amplitude in FRS of non-linear supporting structures due to the finite lateral strength of the structural system that sets down a limit to the floor accelerations that the system can experience. The second difference is the lengthening of the vibration periods of the non-linear supporting structure due to inelastic deformations of the structural elements. Both of these response mechanisms are closely related to the level of inelastic action present in the supporting structure under a seismic excitation. Therefore, to develop prediction relationships for the floor spectral acceleration amplitude capping and period lengthening, a parameter that quantifies the level of the inelastic behaviour in the supporting structure is needed. In this investigation, μ_Δ is used to fulfill this purpose.

In order to determine the capping of the floor spectral acceleration amplitude and the period lengthening, non-linear (NLTHA) and linear (LTHA) time-history analyses were conducted for the entire building portfolio using the ground motions selected in Section 2.2. Using the resulting floor motions, FRS were generated using a non-structural damping ratio equal to 5%. Based on the obtained ensemble of FRS, five adjustment factors are proposed to correct the spectral shape of FRS for linear supporting structures to consider the non-linear behaviour of the supporting structure. Three of these factors adjust the floor spectral acceleration amplitude of the FRS for the first two vibration modes and the peak floor acceleration (PFA), while the remaining two adjust the range of periods that are affected by high acceleration demands in the vicinity of the first two vibration modes of the supporting structure (i.e., the period lengthening due to inelastic response).

3.1 ADJUSTMENT FACTORS FOR THE FLOOR SPECTRAL ACCELERATION AMPLITUDE CAPPING

Three adjustment factors are proposed to modify the spectral floor acceleration amplitude of FRS from linear supporting structures. The first factor, R_1, adjusts the spectral acceleration amplitude in the vicinity of the fundamental vibration period of the supporting structure, and is defined as:

$$R_1 = \frac{S_{FA,n}(T_1)}{S_{FA,e}(T_1)} \tag{1}$$

where $S_{FA,n}(T_1)$ is the maximum value of the spectral acceleration of the non-linear supporting structure in the vicinity of its fundamental period T_1, and $S_{FA,e}(T_1)$ is the value of the spectral acceleration of the linear (elastic) supporting structure at its fundamental period T_1.

The second factor, R_2, adjusts the spectral acceleration amplitude in the vicinity of the second vibration period of the supporting structure, and is defined as:

$$R_2 = \frac{S_{FA,n}(T_2)}{S_{FA,e}(T_2)} \tag{2}$$

where $S_{FA,n}(T_2)$ is the value of the maximum spectral acceleration of the non-linear supporting structure in the vicinity of its second mode period T_2, and $S_{FA,e}(T_2)$ is the value of the spectral acceleration of the linear (elastic) supporting structure at its second mode period T_2.

Finally, the third factor, R_{PFA}, adjusts the PFA (i.e., the spectral floor acceleration value at a non-structural period equal to zero), and it is defined as:

$$R_{PFA} = \frac{PFA_n}{PFA_e} \tag{3}$$

where PFA_n is the peak floor acceleration of the non-linear supporting structure, and PFA_e is the peak floor acceleration of the linear (elastic) supporting structure.

3.2 ADJUSTMENT FACTORS TO CONSIDER THE VIBRATION PERIOD LENGHTENING

Two adjustment factors are proposed to modify the shape of the FRS of a linear supporting structure to consider the period lengthening of the corresponding non-linear supporting structure. The first factor, ΔT_1, adjusts the range of periods that are affected by the maximum floor spectral acceleration at the fundamental mode of vibration of the supporting structure, and is defined as:

$$\Delta T_1 = T_{1,f} - T_1 \tag{4}$$

where $T_{1,f}$ is the point at which the spectral floor acceleration drops to $0.75 * S_{FA,n}(T_1)$ and after which the average spectral floor acceleration remains under this threshold in a period window of 0.25 s. This definition of $T_{1,f}$ was established by minimizing the mean relative difference (MRD) and the maximum error (ME) between the FRS from the NLTHA with the simplified FRS approximation proposed later in Section 3.3. Several iterations were performed until the mean MRD and ME for each supporting structure and each return period were under a threshold deemed acceptable.

The second factor, ΔT_2, adjusts the range of periods that are affected by the maximum floor spectral acceleration at the second mode of vibration of the supporting structure, and is defined as:

$$\Delta T_2 = T_{2,f} - T_2 \tag{5}$$

where $T_{2,f}$ is the point at which the spectral floor acceleration drops to $0.80 * S_{FA,n}(T_2)$ and after which the average spectral floor acceleration remains under this threshold in a period window $T_2 \geq T < T_2 + 0.75 * P_l$, where P_l is equal to ΔT_1 if $T_2 + \Delta T_1 \leq 0.80 * T_1$ and to $0.50 * \Delta T_1$ otherwise. This definition of $T_{2,f}$ was established analogously to the case of $T_{1,f}$.

3.3 Proposed procedure to estimate FRS for non-linear supporting structures

The procedure to estimate the FRS for a non-linear supporting structure consists in calculating the FRS of the corresponding linear supporting structure and correct the shape by using the five adjustment factors presented in Section 3.1 and Section 3.2. The FRS of the linear supporting structure can be calculated by using some of the simplified procedures referenced in Section 1. The rules for the correction of the FRS of the linear supporting structure are the following:

$$S_{FA,m} = S_{FA,e} * R_{PFA} \qquad for\, T < T_2 \tag{6}$$

$$S_{FA,m} = S_{FA,e}(T_2) * R_2 \qquad for\, T_2 \leq T < T_2 + \Delta T_2 \tag{7}$$

$$S_{FA,m} = S_{FA,e} * R_1 \qquad for\, T_2 + \Delta T_2 \leq T < T_1 \tag{8}$$

$$S_{FA,m} = S_{FA,e}(T_1) * R_1 \qquad for\, T_1 \leq T < T_1 + \Delta T_1 \tag{9}$$

$$S_{FA,m} = S_{FA,e} \qquad for\, T \geq T_1 + \Delta T_1 \tag{10}$$

where $S_{FA,m}$ is the floor spectral acceleration of the linear supporting structure with the shape correction to account for the supporting structure non-linear response proposed in equations 6-10.

Figure 1a shows and example of the implementation of the proposed procedure for a building with a fundamental period equal to 0.5 s using a 975-year return period ground motion.

4. DEVELOPMENT OF PREDICTION EQUATIONS FOR THE SPECTRAL ACCELERATION AMPLITUDE CAPPING AND PERIOD LENGTHENING

In order to implement the procedure proposed in Section 3.3 without the need of conducting a NLTHA, prediction equations for the five adjustment factors proposed in Section 3.1 and 3.2 (R_1, R_2, R_{PFA}, ΔT_1 and ΔT_2) to quantify the floor spectral acceleration amplitude capping and the vibration periods lengthening must be developed. By using the results of the NLTHA and LTHA conducted in Section 3, the effect of μ_Δ, the location of the NSE along the building height and the supporting structure fundamental period (T_1) in the five adjustment factors was investigated. Figure 2 shows the results obtained for the five adjustment factors for all the building population and all the return periods plotted against their respective location along the height of the supporting structures. The range of values obtained for each adjustment factor along the height of the supporting structures does not vary significantly. Additionally, the median value obtained at each location along the height of the building remains almost constant for each of the proposed factors. Since the location along the building height does not show a significant effect in the floor spectral acceleration amplitude capping and the period lenghtening, the development of the prediction equations will be performed by using only the roof level values.

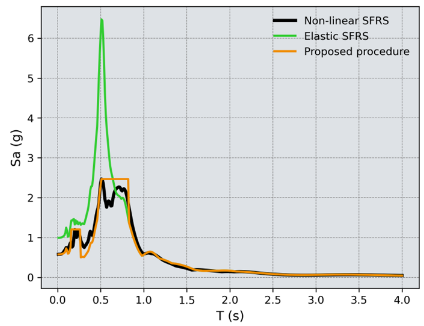

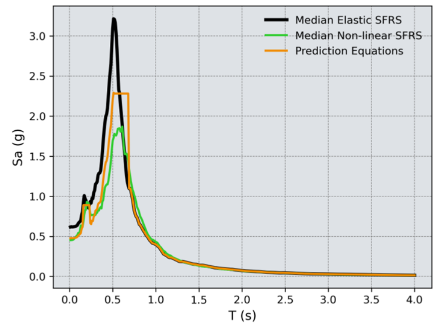

a) b)

Figure 1. Example of implementation of the procedure proposed to estimate the FRS for non-linear supporting structures for: a) A sample building under a 975-year return period ground motion, and b) A sample building under a 475-year return period ground motion set consisting of 20 ground motions using the prediction equations proposed in Section 4

Figure 3a, 3b and 3c show the results obtained for the factors that account for the floor spectral acceleration capping (R_1, R_2 and R_{PFA}) for all the building population and all the return periods plotted against the corresponding μ_Δ in the supporting structure. A decrease in their values is observed as $\mu_\Delta$increases, which is explained by the finite lateral strength of the structural system that sets a limit on the level of floor accelerations that the supporting structures experience as the seismic demand increases. Figure 3d and 3e shows the results obtained for the factors that account for the vibration periods lengthening (ΔT_1 and ΔT_2) against the corresponding μ_Δ and the supporting structure fundamental period. An increase in their values is observed as μ_Δ and building fundamental period increase. The increase with μ_Δ can be explained by the fact that as the displacement demand on the buildings increases, higher inelastic deformations will be experienced by the structural elements, therefore increasing the lengthening of the vibration periods. On the other hand, in the case of the fundamental period of the supporting structure, the increase is related to the fact that under similar levels of period lengthening as a percentage of the fundamental period, the absolute value of the period lengthening will be higher for longer fundamental period structures. Finally, μ_Δ increases with the return period of the seismic hazard, which is expected since as the return period increases, the seismic force demand on the buildings increases as well, producing higher displacements in the seismic force-resisting system.

Regression models were constructed between the five proposed factors and the displacement ductility demand of the buildings. For the case of R_1, R_2 and R_{PFA}, an inverse exponential function was fitted tothe data by means of non-linear regression. Figure 3 shows the fitting of the inverse exponential function to the data along with the standard regression error (S) and the 95% prediction interval. The obtained values of the standard regression error are deemed acceptable considering the level of dispersion present in the data. The obtained expressions for the floor spectral acceleration amplitude capping are as follows:

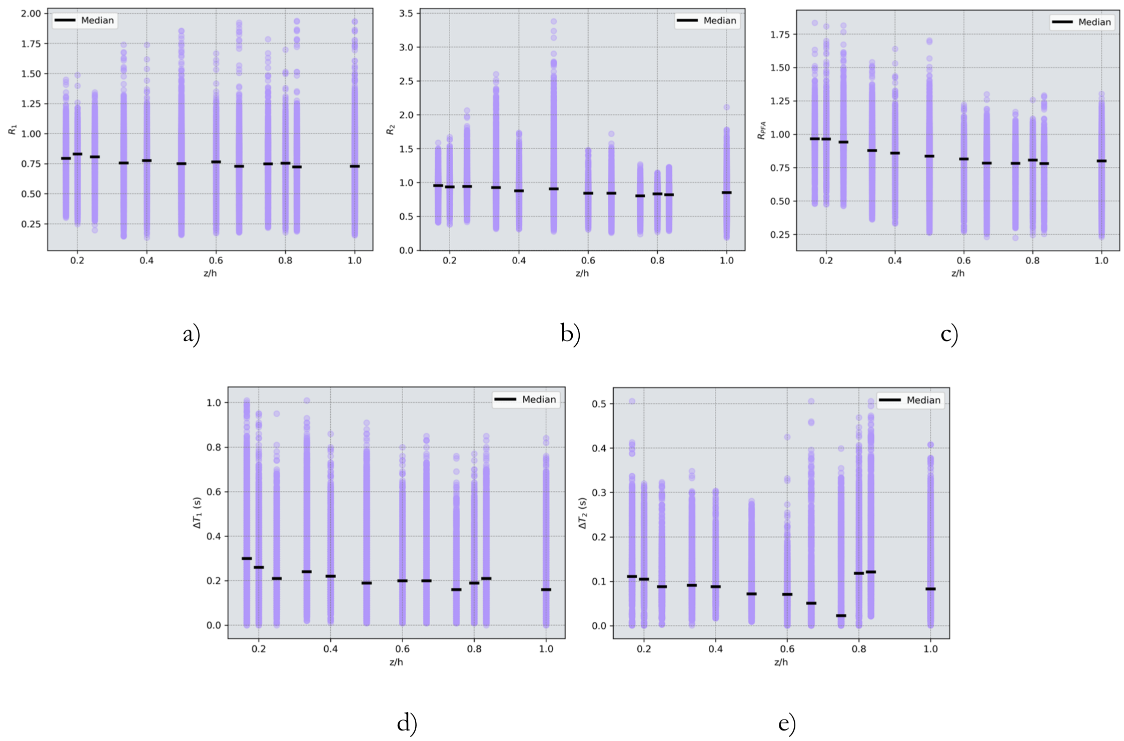

Figure 2. Influence of the location along the building height relative to the roof level (z/h) in a) R_1, b) R_2, c) R_{PFA}, d) ΔT_1 and e) ΔT_2)

$$R_1 = 0.66 * e^{-0.92*\mu_\Delta} + 0.35 \tag{11}$$

$$R_2 = 1.10 * e^{-0.25*\mu_\Delta} - 0.08 \tag{12}$$

$$R_{pfa} = 0.63 * e^{-0.73*\mu_\Delta} + 0.38 \tag{13}$$

With respect to the factors to quantify the first and second mode vibration periods lengthening (ΔT_1 and ΔT_2), a bivariate polynomial was fitted to the data using multivariate non-linear regression. Figure 3d and 3e shows the fitting of the bivariate surfaces along with the standard error of regression. Considering the high dispersion present in the data, the obtained values of the standard error of regression are deemed acceptable. The obtained expressions for period lengthening of the first two modes are:

$$\Delta T_1 = 0.34 * \mu_\Delta^{0.58} * T_B^{0.75} \tag{14}$$

$$\Delta T_2 = 0.19 * \mu_\Delta^{0.33} * T_B^{0.45} - 0.04 \tag{15}$$

Figure 1b shows an example of the implementation of the proposed procedure to estimate FRS of non-linear supporting structures by using the prediction equations 11-15 for a sample building under a 475-year return period ground motion set consisting of 20 ground motion records.

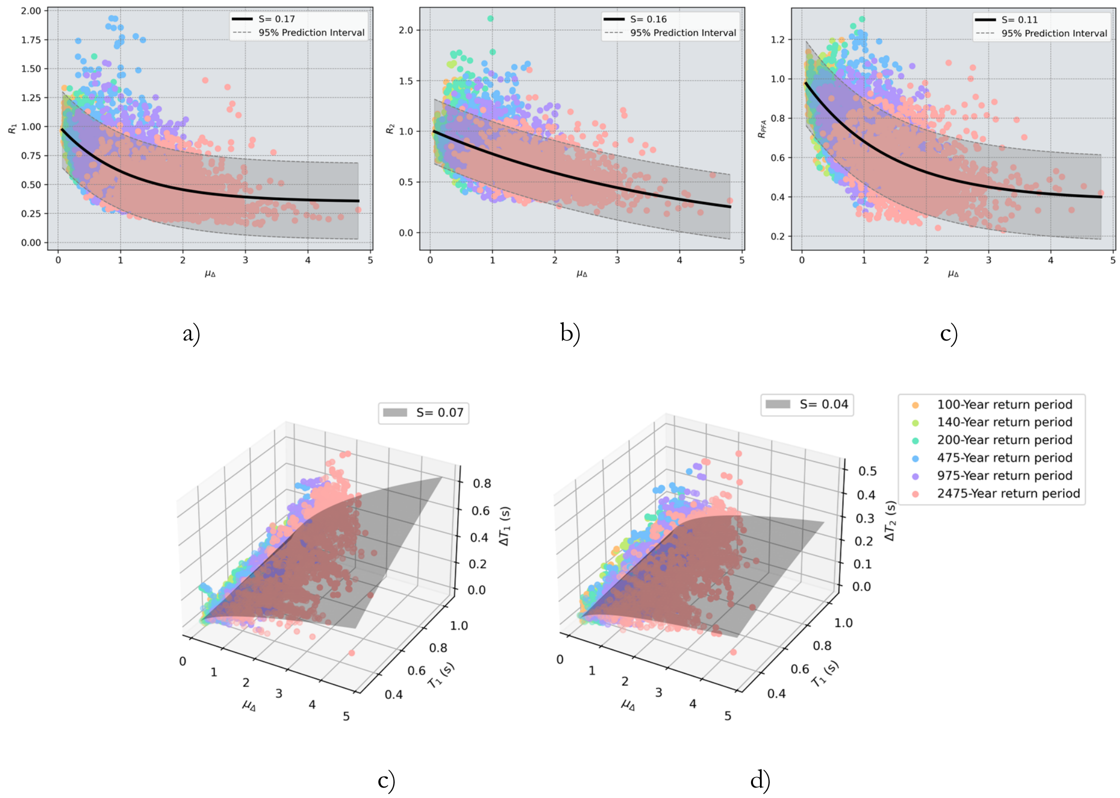

Figure 3. Non-linear regression models using an exponential function for a) R_1, b) R_2 and c) R_{PFA}, and a bivariate surface for d) ΔT_1 and e) ΔT_2)

5.ESTIMATION OF DISPLACEMENT DUCTILITY DEMAND

In order to use the prediction equations proposed in Section 4, μ_Δ is needed. In most of the procedures to estimate FRS mentioned in Section 1, this parameter is obtained through the capacity spectrum method, which requires detailed information of the non-linear geometric and material properties of the supporting structure. This type of information is often not available, as for example in existing structures where the design specifications do not exist, or in regional studies, in which obtaining the complete ensemble of the required non-linear properties and responses of big building portfolios is unfeasible. One way to bypass the need of performing individual capacity spectrum analyses of the supporting structures is to express μ_Δ as a random variable that depends on the seismic hazard intensity level and supporting structure dynamic characteristics. In Section 4, it was determined that μ_Δ has a positive relationship with the seismic hazard level, represented by the ground motion return period. To determine if there is a correlation between μ_Δ and the dynamic characteristics of the supporting structure, the influence of the supporting structure fundamental period in the obtained μ_Δ is investigated. Figure 4 shows the results of the multiples stripes non-linear analyses in terms of $\mu_\Delta$and supporting structure fundamental period for each return period. The Pearson correlation coefficient (ρ) and the coefficient of determination (R^2) of a linear regression performed on the median values are shown. The low values obtained for both the Pearson correlation coefficient and the coefficient of determinaton of the linear regression indicate a poor correlation and relationship between the median μ_Δ and the fundamental period of the supporting structure. Considering the poor correlation between these two parameters, only the influence of the seismic hazard intensity level will be considered to determine an adequate probability distribution to approximate the μ_Δ.

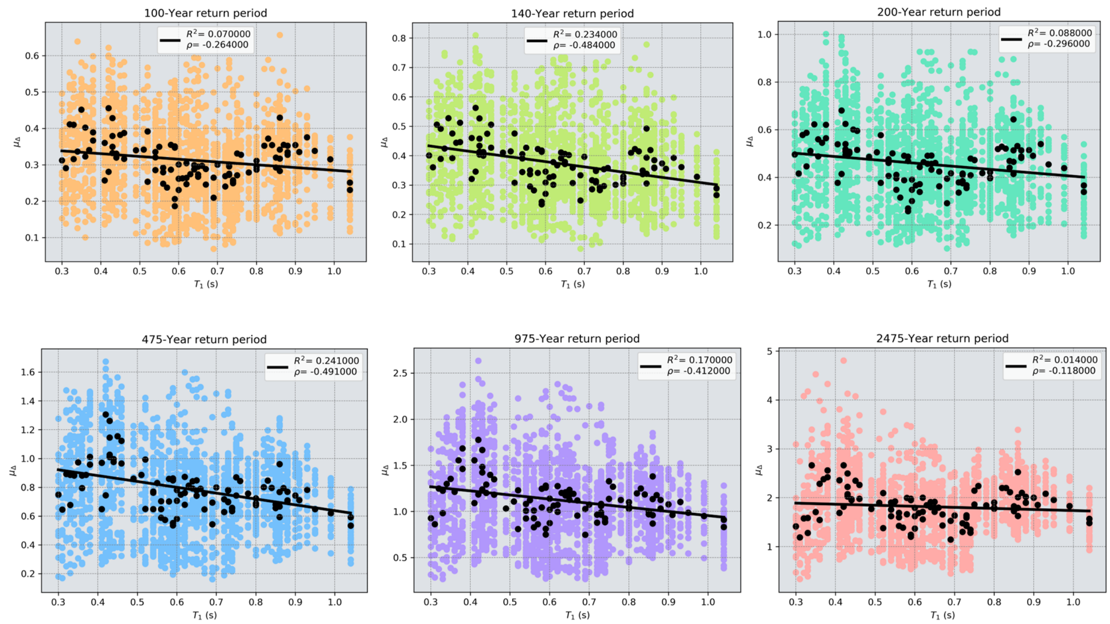

Figure 4. Influence of the supporting structure fundamental period (T_1) in the displacement ductility demand (μ_Δ)

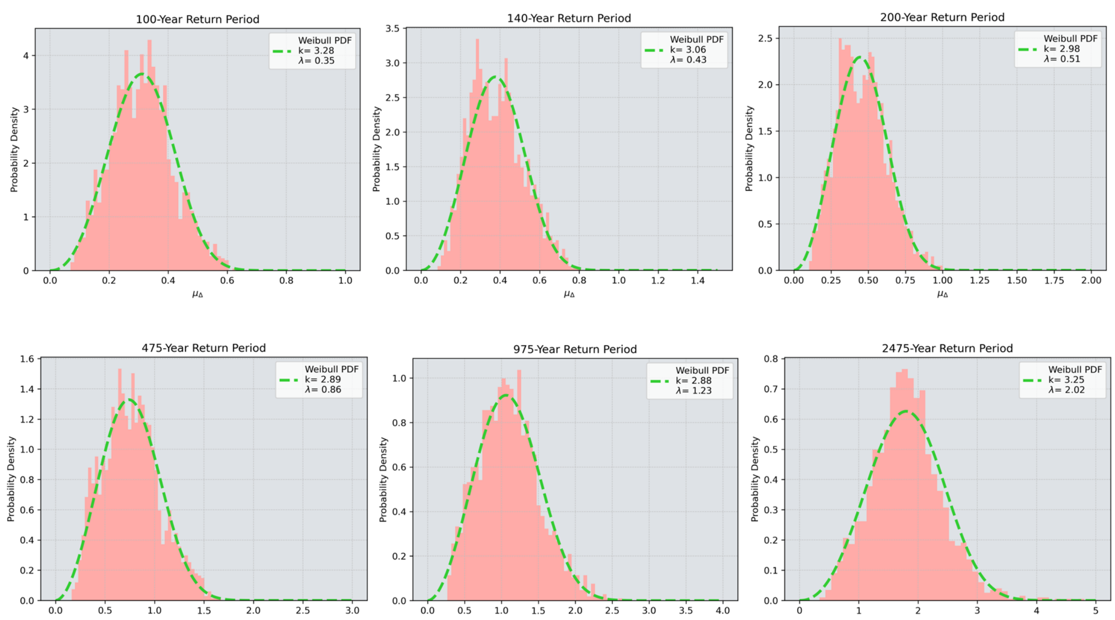

Figure 5. Histograms of the displacement ductility demand data with the fitting of a Weibull probability distribution and the corresponding distribution parameters (k and λ) for each ground motion return period

A probability distribution was fitted to μ_Δ dataset obtained from the multiple stripe non-linear analyses and the pushover curves. By comparing the goodness-of-fit of four probability dsitributions (Normal, Lognormal, Gamma and Weibull) using probability plots, it was determined that the Weibull distribution approximates better the displacement ductility demand data. Figure 5 shows the histograms of μ_Δ for each return period with the fitting of the Weibull distribution and the corresponding distribution parameters (k and λ). The probability plots obtained by fitting a Weibull probability distribution are shown in Figure 6. The Weibull distribution is able to approximate with reasonable accuracy μ_Δ data for all the range of obtained values and return periods, with the exception of the right tail of the 2475-year return period distribution. Since the right tail of the 2475-year return period corresponds to the lowest probability region of the considered sample space, and the Weibull distribution accurately approximates μ_Δ for the rest of the complete ensemble of data, it is considered appropriate for the estimation of μ_Δ.

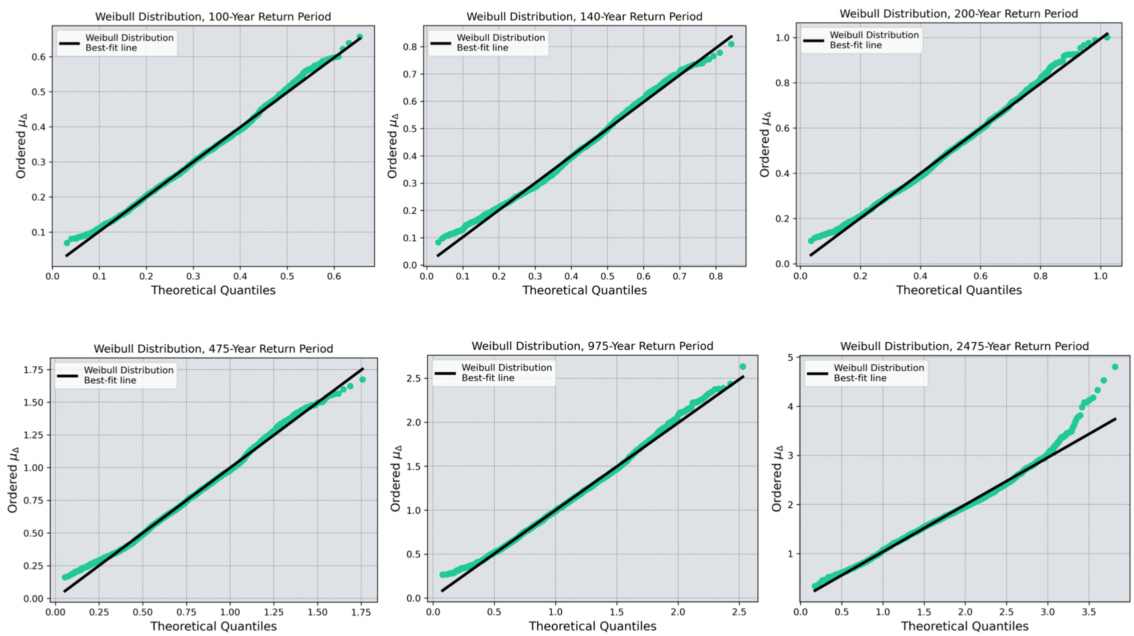

Figure 6. Probability plots for the fitting of the Weibull probability distribution to the displacement ductility demand data for each ground motion return period

6. Conclusions

This study used multiple stripes linear and non-linear time-history analyses, and non-linear static analyses (pushover analyses) to quantify the floor spectral acceleration amplitude capping and vibration period lengthening in non-linear supporting structures designed with a ductility class medium (DCM) according to Eurocode 8 seismic provisions [CEN, 2004]. A method for the estimation of floor response spectra (FRS) for non-linear supporting structures is proposed and prediction equations for both the floor spectral acceleration amplitude capping and vibration period lengthening are developed by means of regression analyses. Finally, a probability distribution is fitted to the displacement ductility demand data in order to express it as a random variable. The floor spectral acceleration amplitude capping increases with the displacement ductility demand, ground motion return period and the supporting structure fundamental period, which is explained by the finite lateral strength of the structural system that sets a limit on the level of floor accelerations that the supporting structures experience as the seismic demand increases. The vibration period lengthening increases with the displacement ductility demand and ground motion return period, which can be explained by the fact that as the displacement demand on the buildings increases, higher inelastic deformations will be experienced by the structural elements, therefore increasing the lengthening of the vibration periods. No significant effect of the location along the building height was documented for both the floor spectral acceleration amplitude capping and the vibration period lengthening. The Weibull distribution was found to give a reasonable approximation of the displacement ductility demand. The proposed method for the estimation of the FRS of non-linear supporting structures is useful in cases in which detailed non-linear geometric and material properties of the supporting structures are unknown or difficult to obtain, and/or in regional studies, in which a large number of building assets must be considered.

AKNOWLEDGMENTS

The work presented in this paper has been developed within the framework of the project "Dipartimenti di Eccellenza", funded by the Italian Ministry of Education, University and Research at IUSS Pavia. The EUCENTRE Foundation is gratefully acknowledged for provided financial support to the first author of this paper. The authors gratefully acknowledge also the Italian Department of Civil Protection (DPC) for their financial contributions to this study through the ReLUIS 2022-2024 Project (Work Package 17 - Contributi Normativi Per Elementi Non Strutturali).

REFERENCES

Calvi, P.M., Sullivan, T.J. [2014] "Estimating floor spectra in multiple degree of freedom systems". *Earthquakes and Structures*. 2014, 7(1):17-38.

CEN, European Committee for Standarddization. EN 1998-1. Eurocode 8: Design of structures for earthquake resistance – Part 1: General rules, seismic actions and rules for buildings. Brussels; 2004.

Filiatrault, A., Sullivan, T. [2014] "Performance-based seismic design of non-structural building components: the next frontier of earthquake engineering," *Earthquake Engineering and Engineering Vibration*. Special Issue on the State-of-the-art and Future Challenges of Earthquake Engineering. 13(1): 17–46. https://doi.org/10.1007/s11803-014-0238-9.

Hunter, J.D. [2007] "Matplotlib: A 2D Graphics Environment". *Computing in Science & Engineering*. 2007. Vol. 9, no. 3, pp. 90-95.

Merino, R.J., Perrone, D., Filiatrault, A. [2019] "Consistent floor response spectra for performance-based seismic design of non-structural elements" *Earthq Eng Struct Dyn*. 2019; 49(3): 261-284, https://doi.org/10.1002/eqe.3236.

PEER NGA-West Database [2013], available on-line: http://peer.berkeley.edu/ngawest.

Perrone, D., Brunesi, E., Filiatrault, A., Nascimbene, R. [2020] "Probabilistic estimation of floor response spectra in masonry infilled reinforced concrete building portfolio". *Engineering Structures*. 2020; 202(2020): 109842.

Rodriguez, D., Perrone, D., Filiatrault, A., Brunesi, E. [2021] "A probabilistic strong floor motion duration model for seismic performance assessment of non-structural building elements". Earthquake Engineering and Structural Dynamics. 2021. 50: 4161-4179. DOI: 10.1002/eqe.3550.

Vukobratović, V., Fajfar, P. [2017] "Code-oriented floor acceleration spectra for building structures". *Bull Earthquake Eng*. 2017, 15:3013-3026.

Welch, D.P., Sullivan, T.J. [2017] "Illustrating a New Possibility for the Estimation of Floor Spectra in Nonlinear Multi-Degree of Freedom Systems". Proceedings of the 16th World Conference on Earthquake, 16WCEE, Paper N° 2632, Santiago, Chile, 2017.

Estimating Floor Acceleration Response Spectra for Self-Centering Structural Systems with Flag-Shaped Hysteretic Behavior

Binod Kumar Shrestha[1], Anil C. Wijeyewickrema[2], Hiroki Miyashita[2], and Niraj Malla[1]

[1]Former Student, Department of Civil and Environmental Engineering, Tokyo Institute of Technology
[2]Department of Civil and Environmental Engineering, Tokyo Institute of Technology
2-12-1 O-okayama, Meguro-ku, Tokyo, 152-8552, Japan
binodstha35@gmail.com, wijeyewickrema.a.aa@m.titech.ac.jp, miyashita.h.ac@m.titech.ac.jp,
nirajmalla67@gmail.com

Abstract. Spectral floor-acceleration demands are necessary for the seismic design of acceleration-sensitive non-structural components (NSCs). Existing studies to estimate floor response spectra (FRS) using empirical equations are based on elasto-plastic and stiffness degrading hysteretic behavior of the primary structure which represents the conventional reinforced concrete and steel moment-resisting frame buildings. In the present study, the FRS for self-centering (SC) structural systems with flag-shaped hysteretic behavior under far-fault ground motions are investigated. The FRS and dynamic amplification factor (DAF) are obtained from nonlinear response history analysis (NLRHA) of SC structural systems, represented as a single-degree-of-freedom system with flag-shaped hysteretic behavior, under far-fault ground motions. The main parameters influencing the amplitude of FRS are discussed, namely the initial vibration period, response reduction factor, and energy dissipation parameter of the primary structure. An empirical equation to predict the maximum dynamic amplification factor is developed considering the influence of all the parameters. Then, an equation to estimate the FRS is proposed and verified by carrying out NLRHA using a different set of far-fault ground motions. The equation to estimate FRS is shown to predict floor acceleration demands with very good accuracy. Furthermore, the mean peak acceleration demand of the secondary structure obtained from the present study, existing empirical equations, and NLRHA are also compared. Results showed better accuracy of the proposed equation for FRS to estimate the NLRHA results than the existing empirical equations. Therefore, it can be concluded that the proposed equation is useful for the seismic assessment, design, and safety check of acceleration-sensitive non-structural components of self-centering structural systems.

Keywords: Dynamic amplification factor, Flag-shaped hysteretic behavior, Floor response spectra, Non-structural components, Self-centering system.

1. Introduction

The adoption of seismic design has greatly reduced damage to the structural elements of buildings. However, damage to secondary structural elements and non-structural components (NSCs) can lead to huge economic losses, due to the associated loss of functionality of important facilities and business downtime after major earthquakes [see, e.g., EERI, 1984; Villaverde,1997; Dhakal et al., 2016; Devin and Fanning, 2019; Wang et al., 2021]. Although existing building codes such as Eurocode 8 [2004] and ASCE 7–16 [2017] provide expressions for determining acceleration demands for the estimation of seismic design force for acceleration-sensitive NSCs, several studies have shown that the peak floor acceleration and floor response spectra (FRS) estimated from such codes are not accurate [see, e.g., Sullivan et al., 2013; Vukobratovic and Fajfar, 2017; Aragaw and Calvi, 2021; Kazantzi et al., 2020; Vukobratovic et al., 2021].

Estimation of FRS using empirical equations based on a single degree-of-freedom (SDOF) system for the primary structure has been reported in previous studies. Oropeza et al. [2010] considered primary structures with an elasto-plastic and modified Takeda hysteretic model, while Sullivan et al. [2013] also considered primary structures using a modified Takeda hysteretic model. Vukobratovic and Fajfar [2015] used the equation of Yasui et al. [1993] in the pre- and post-resonance region and an empirically developed expression in the resonance region for primary structures with an elasto-plastic and stiffness degrading model to estimate the FRS. Welch and Sullivan [2017] modified the equation developed by Sullivan et al. [2018] to estimate the FRS.

Several studies have also extended the approach to estimate the FRS using empirical equations based on SDOF systems to multi-degree-of-freedom (MDOF) systems. For instance, the estimation of FRS for reinforced concrete (RC) frame systems by Calvi and Sullivan [2014], Vukobratovic and Fajfar [2016], and Merino et al. [2020]; for RC walls by Welch and Sullivan [2017] and Vukobratovic and Ruggieri [2021]; and for base-rocking wall buildings by Aragaw and Calvi [2021].

The excellent seismic performance of self-centering (SC) structural systems with flag-shaped hysteretic behavior has been reported previously [see, e.g., Kurama, 2002; Smith et al., 2013; Belleri et al., 2014; Buddika and Wijeyewickrema, 2016; Shrestha et al. 2021]. In the present study, the FRS for SC structural systems with flag-shaped hysteretic behavior under far-fault ground motions are investigated. The FRS and dynamic amplification factor (DAF) are obtained from a nonlinear response history analysis (NLRHA) of SC structural systems with flag-shaped hysteretic behavior. An equation to estimate the FRS is proposed and verified by carrying out NLRHA using a different set of far-fault ground motions.

2. Self-Centering (SC) SDOF System with Flag-Shaped Hysteretic Behavior, Ground Motion Records, and Numerical Modeling

The force-displacement relationship of a self-centering (SC) SDOF system with flag-shaped hysteretic behavior, which is the primary structure, is shown in Figure 1. The nonlinear response history analysis (NLRHA) of the SC flag-shaped SDOF system was carried out with the following parameters: initial vibration period $T_p = 0.1\,\text{s}, 0.3\,\text{s}, 0.5\,\text{s}, 0.75\,\text{s}, 1.0\,\text{s}, 1.5\,\text{s}, 2.0\,\text{s}$; response reduction factor $R = 1, 1.5, 2, 3, 4, 5, 6$; post-yield stiffness ratio $\alpha = 5\%$; energy dissipation parameter $\beta = 0\% - 100\%$ (increments of 20%), which relates the height of the flag in the flag-shaped hysteresis to the yield force (Wiebe and Christopoulos. 2013); and viscous damping ratio $\xi_p = 5\%$. Here, R is defined as the ratio of the elastic demand during the earthquake to the yield strength. Even though $R = 6$ or 7 is used for the design of self-centering structural systems using the force-based design method [Smith et al., 2013; Buddika and Wijeyewickrema, 2016], a wide range of R values were adopted in this study. This was done so that the developed FRS in Section 4 could also be used with the direct displacement-based design method, where the R value depends on the target displacement [Priestley et al., 2007; Yang and Lu, 2018]. It is noted that for SC flag-shaped SDOF systems, a viscous damping ratio $\xi_p = 5\%$ has been used in previous studies [see, e.g., Rahgozar et al., 2016; Zhang et al., 2018; Dong et al., 2020]. The non-structural component (NSC), which is the secondary structure, was represented by an elastic SDOF system with a vibration period $T_s = 0.1\text{ s} - 4.0\text{ s}$ (increments of 0.1 s); and a viscous damping ratio $\xi_s = 5\%$.

For NLRHA, 11 far-fault ground motions were considered from the 22 far-fault ground motion set of FEMA P695 (Table A-4A, FEMA [2009]) and are given in Table 1. Note that as-recorded ground motions are used in this study.

In the present study, the NLRHA was carried out using OpenSees [2017]. The SC flag-shaped SDOF system (primary structure) was modeled using a zero-length element with the SelfCentering material model. The NSC (secondary structure) was represented by an elastic SDOF system and modeled using a zero-length element. The numerical integration of the motion equations was accomplished using the Newmark constant average acceleration method $(\beta_N = 0.25, \gamma_N = 0.5)$.

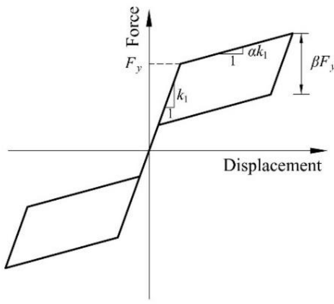

Figure 1. The force-displacement relationship of the self-centering (SC) SDOF system with flag-shaped hysteretic behavior. Note: k_1 = initial stiffness; α = post-yield stiffness ratio; β = energy dissipation parameter; F_y = yield strength.

Table 1. Far-fault ground motions used for the NLRHA (Table A-4A, FEMA [31]).

EQ. No.	Event	Year	Station	Fault Type	M_w	R_{rup} (km)	PGA Component 1 (g)	PGA Component 2 (g)	$\bar{v}_s$ (m/s)
1	Northridge	1994	Beverly Hills-Mulhol	Thrust	6.7	17.2	0.42	0.52	356
2	Northridge	1994	Canyon Country-WLC	Thrust	6.7	12.4	0.41	0.48	309
3	Duzce, Turkey	1999	Bolu	Strike-slip	7.1	12.0	0.73	0.82	326
4	Hector Mine	1999	Hector	Strike-slip	7.1	11.7	0.27	0.34	685
5	Imperial Valley	1979	Delta	Strike-slip	6.5	22.0	0.24	0.35	275
6	Imperial Valley	1979	El Centro Array #11	Strike-slip	6.5	12.5	0.36	0.38	196
7	Kobe, Japan	1995	Nishi-Akashi	Strike-slip	6.9	7.1	0.51	0.50	609
8	Kobe, Japan	1995	Shin-Osaka	Strike-slip	6.9	19.2	0.24	0.21	256
9	Kocaeli, Turkey	1999	Duzce	Strike-slip	7.5	15.4	0.31	0.36	276
10	Kocaeli, Turkey	1999	Arcelik	Strike-slip	7.5	13.5	0.22	0.15	523
11	Landers	1992	Yermo Fire Station	Strike-slip	7.3	23.6	0.24	0.15	354

Note: M_w = moment magnitude; PGA= peak ground acceleration; R_{rup} = distance from recording site to epicenter; $\bar{v}_s$ = average shear wave velocity.

3. Floor Response Spectra and Dynamic Amplification Factor from Nonlinear Response History Analysis (NLRHA)

3.1 Floor Response Spectra

The floor response spectra for self-centering (SC) structural systems with flag-shaped hysteretic behavior were determined using the following procedures:

(a) NLRHA of the prescribed self-centering (SC) SDOF system with flag-shaped hysteretic behavior (primary structure) was used for the set of ground motion records and for the determination of the total floor acceleration response history for each ground motion record. Here, the total floor acceleration response history was the sum of the floor acceleration response history relative to the ground and the ground acceleration response history.
(b) Linear RHA of the elastic SDOF system (secondary structure), using the set of total floor acceleration response histories determined from step (a), was used to generate floor response spectra.
(c) Calculation of the mean floor response spectrum.

The mean normalized floor response spectra (FRS), i.e., A_s / A_p, where A_p, A_s are the peak acceleration demands of the primary structure and the secondary structure, respectively, were calculated for the structural parameters stated in Section 2. The ratio A_s / A_p is also referred to as the dynamic amplification factor (DAF). In Figures 2–3, the mean normalized floor response spectra are shown only for $T_p = 0.5\,\text{s}, 1.0\,\text{s}$, respectively, for $\beta = 0\%, 40\%$, and 80%. It can be observed that when the primary structure is elastic, i.e., $R = 1$, a single peak of the mean normalized FRS at $T_s / T_p = 1$ can be observed. When $R > 1$, the primary structure behaves inelastically and rather than a single peak, the maximum value of the mean normalized FRS remains nearly constant over a wide period range and forms a *spectral plateau*. Moreover, the width of the spectral plateau increases with increase in R and decrease in β, which is due to the higher ductility demand on the primary structure. In most cases, the peak value of the mean normalized FRS increases when R changes from 1 to 2, and then decreases for $R > 2$.

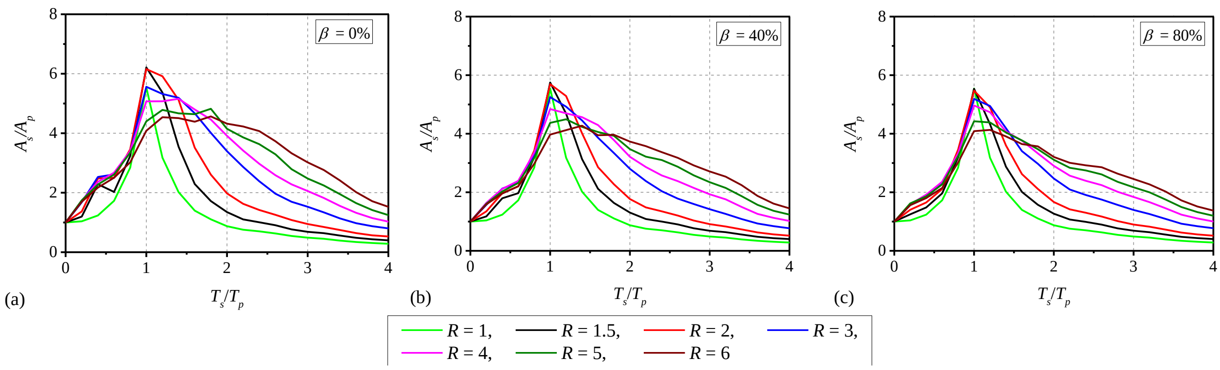

Figure 2. Mean normalized floor response spectra for SC systems with $T_p = 0.5$ s, post-yield stiffness ratio $\alpha = 5\%$; viscous damping ratio $\xi_p = 5\%$; and a secondary structure with viscous damping ratio $\xi_s = 5\%$: (a) $\beta = 0\%$; (b) $\beta = 40\%$; (c) $\beta = 80\%$.

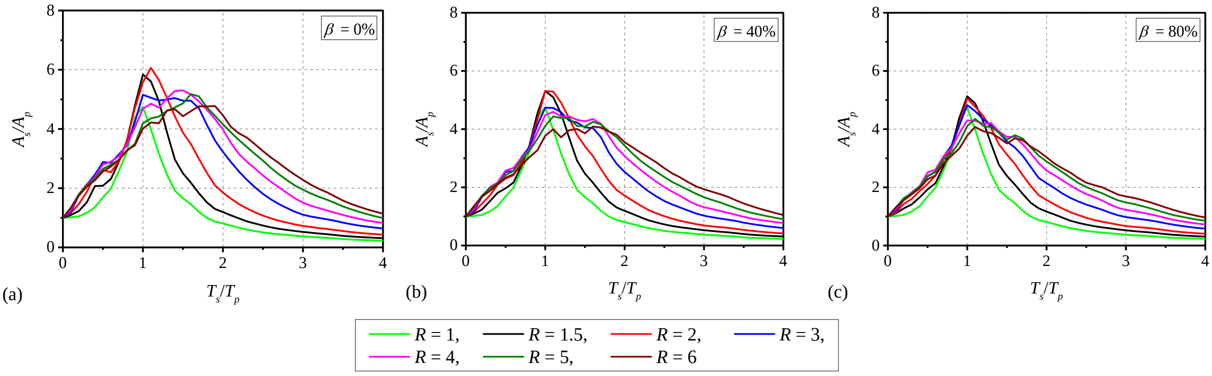

Figure 3. Mean normalized floor response spectra for SC systems with $T_p = 1.0$ s, post-yield stiffness ratio $\alpha = 5\%$; viscous damping ratio $\xi_p = 5\%$; and a secondary structure with viscous damping ratio $\xi_p = 5\%$: (a) $\beta = 0\%$; (b) $\beta = 0\%$; (c) $\beta = 40\%$.

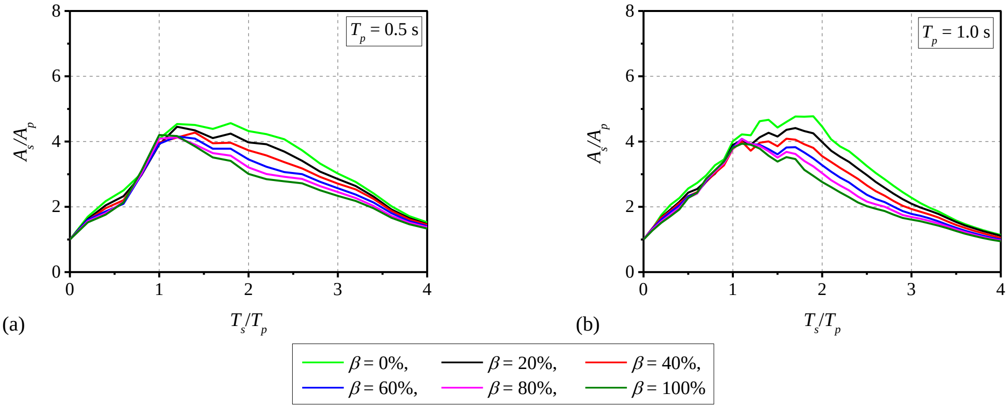

Figure 4. Effect of energy dissipation parameter β on mean normalized floor response spectra for a SC system with $R = 6$, post-yield stiffness ratio $\alpha = 5\%$; viscous damping ratio $\xi_p = 5\%$; and a secondary structure with viscous damping ratio $\xi_s = 5\%$: (a) $T_p = 0.5$ s; and (b) $T_p = 1.0$ s.

To investigate the effects of β more clearly, the mean normalized FRS are shown for a SC system with $R = 6$, $T_p = 0.5\text{s}, 1.0\text{s}$, and $\beta = 0\%, 20\%, \ldots, 100\%$ in Figure 4. The results show that the mean normalized FRS decreases when β increases. A wider spectral plateau is observed with decrease in β.

3.2 Maximum Dynamic Amplification Factor DAF_{max}

Figure 5 shows the maximum values of the mean normalized FRS for $T_p = 0.1\text{s}, 0.3\text{s}, 0.5\text{s}, 0.75\text{s}, 1.0\text{s}, 1.5\text{s}, 2.0\text{s}$, and for $\beta = 0\%, 40\%$, and 80%, also referred to as the maximum dynamic amplification factor DAF_{max}. Note that this DAF_{max} will be used in the equation to estimate the FRS developed in Section 4. It was observed that with increase in T_p, DAF_{max} increased for $T_p \le 0.5$ s, and remained nearly constant for $T_p > 0.5$ s and $R > 1.0$. It was also observed that the DAF_{max} decreased with increasing β. Based on the results of the NLRHA shown in Figure 5, an empirical equation to estimate the DAF_{max} was developed by carrying out nonlinear least-square regression analysis, where the regression coefficients are obtained using the *Levenberg–Marquardt* algorithm (Bates and Watts [1980]), available in SPSS [2017]. The equation for DAF_{max} is:

$$DAF_{max}(T_p, R, \beta; \xi_s) = \begin{cases} \dfrac{1}{\sqrt{\xi_s}}\left(aT_p^b + c\right), & R = 1 \\ \dfrac{0.15(1+\beta)^{-2.6} + 0.85}{\sqrt{\xi_s}}\left(aT_p^b + c\right), & R > 1 \end{cases}, \quad (1)$$

where $a, b,$ and c are constant coefficients determined from the nonlinear regression analysis, separately for each R, and given in Table 2. Note that in the present study, the viscous damping ratio of the secondary structure $\xi_s = 5\%$ (see Section 2). The equation is given for elastic $(R = 1)$ and inelastic $(R > 1)$ primary structures. For verification purposes, in Figure 6, the DAF_{max} obtained from Equation (1) is compared with the NLRHA results obtained using a different set of far-fault ground motions, given in Table 3. The $T_p, R, \alpha, \beta,$ and ξ_p of the primary structure defined in Section 2 were used for the verification. It can be seen that Equation (1) can estimate the DAF_{max} accurately from the NLRHA results for primary structures with different $T_p, R,$ and β.

Table 2. Regression coefficients of the equation for DAF_{max}.

Coefficients	$R = 1.0$	$R = 1.5$	$R = 2.0$	$R = 3.0$	$R = 4.0$	$R = 5.0$	$R = 6.0$
a	−0.020	−0.001	−0.013	−0.021	−0.017	−0.019	−0.018
b	−1.304	−2.358	−1.574	−1.400	−1.382	−1.258	−1.178
c	1.259	1.330	1.350	1.260	1.175	1.108	1.043

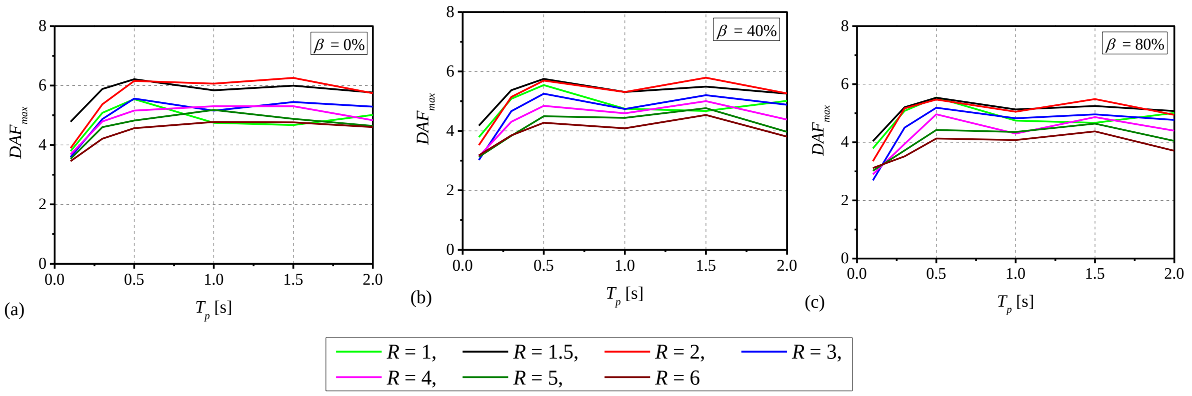

Figure 5. Maximum dynamic amplification factor DAF_{max} for a SC system with post-yield stiffness ratio $\alpha = 5\%$; viscous damping ratio $\xi_p = 5\%$; and a secondary structure with viscous damping ratio $\xi_s = 5\%$: (a) $\beta = 0\%$; (b) $\beta = 40\%$; and (c) $\beta = 80\%$.

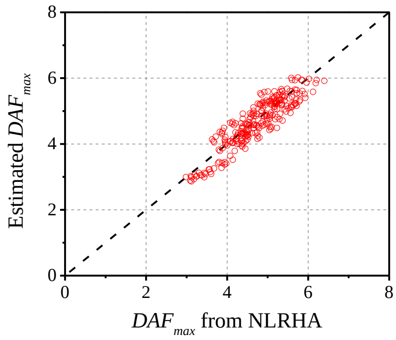

Figure 6. Comparison of the DAF_{max} from the NLRHA results with the estimated DAF_{max} from Equation (1).

3.3 POST-RESONANCE DYNAMIC AMPLIFICATION FACTOR DAF_{pr}

The post-resonance dynamic amplification factor DAF_{pr} will also be used in the equation to estimate the FRS proposed in Section 4. Considering the expression for DAF_{max} given in Equation (1) and the estimation of floor spectra by Welch and Sullivan [2017], the equation for DAF_{pr} is expressed by:

$$DAF_{pr}(T_p, R, \beta; T_s, \xi_s) = \begin{cases} \dfrac{1}{\sqrt{\left(1-\dfrac{T_s}{T_e}\right)^2 + \xi_s}}\left(aT_p^b + c\right), & R = 1 \\ \dfrac{0.15(1+\beta)^{-2.6} + 0.85}{\sqrt{\left(1-\dfrac{T_s}{T_e}\right)^2 + \xi_s}}\left(aT_p^b + c\right), & R > 1 \end{cases}, \tag{2}$$

where the effective period T_e associated with the secant stiffness at the peak response of the primary structure is given by:

$$T_e(T_p, \alpha, \mu) = T_p\sqrt{\frac{\mu}{1+\alpha(\mu-1)}}, \tag{3}$$

(see Welch and Sullivan [2017]), where $\alpha =$ post-yield stiffness ratio (taken as 5% in this study), and the ductility demand μ is computed using the equation for the constant-strength inelastic displacement ratio C_R, given by Zhang et al. [2018] for SC systems as:

$$\mu(T_p, R, \beta) = \left\{1 + (R-1)^{0.515}\frac{0.184 + 0.119(1-\beta)^{1.173}}{T_p^{\,1.478}}\right\}R. \tag{4}$$

Table 3. Far-fault ground motions used for the verification (Table A-4A, FEMA [2009]) of DAF_{max} (Equation 1) and the proposed equation for FRS (Equation 5).

EQ No.	Event	Year	Station	Fault Type	M_w	R_{rup} (km)	PGA Component 1 (g)	PGA Component 2 (g)	$\bar{v}_s$ (m/s)
1	Landers	1992	Coolwater	Strike-slip	7.3	19.7	0.28	0.42	271
2	Loma Prieta	1989	Capitola	Strike-slip	6.9	15.2	0.53	0.44	289
3	Loma Prieta	1989	Gilroy Array #3	Strike-slip	6.9	12.8	0.56	0.37	350
4	Manjil, Iran	1990	Abbar	Strike-slip	7.4	12.6	0.51	0.50	724
5	Superstition Hills	1987	El Centro Imp. Co.	Strike-slip	6.5	18.2	0.36	0.26	192
6	Superstition Hills	1987	Poe Road (temp)	Strike-slip	6.5	11.2	0.45	0.30	208
7	Cape Mendocino	1992	Rio Dell Overpass	Thrust	7.0	14.3	0.39	0.55	312
8	Chi-Chi, Taiwan	1999	CHY101	Thrust	7.6	10.0	0.35	0.44	259
9	Chi-Chi, Taiwan	1999	TCU045	Thrust	7.6	26.0	0.47	0.51	705
10	San Fernando	1971	LA–Hollywood Stor	Thrust	6.6	22.8	0.21	0.17	316
11	Friuli, Italy	1976	Tolmezzo	Thrust	6.5	15.8	0.35	0.31	425

Note: $M_w =$ moment magnitude; PGA= peak ground acceleration; $R_{rup} =$ distance from recording site to epicenter; $\bar{v}_s =$ average shear wave velocity.

4. Equation to Estimate Floor Response Spectra and Verification

4.1 EQUATION TO ESTIMATE FRS

In the present study, the following equation is proposed to estimate the FRS for the primary structure of SC systems:

$$\frac{A_s}{A_p}(T_p, R, \beta; T_s, \xi_s) = \begin{cases} 1+\frac{T_s}{T_p}\left(DAF_{max}-1\right), & 0 \le T_s < T_p \\ DAF_{max}, & T_p \le T_s \le T_e \\ DAF_{pr}, & T_s > T_e \end{cases}. \tag{5}$$

Note that an equation of a similar form was used by Sullivan et al. [2013] for the estimation of FRS for well-detailed RC structures.

The acceleration demand of the secondary structure increased linearly in the pre-resonance region $0 \le T_s < T_p$, remained constant in the resonance region $T_p \le T_s \le T_e$ forming a *spectral plateau* and decreased in the post-resonance region $T_s > T_e$. Note that the effective period T_e increased with the higher inelastic deformation demand of the primary structure, i.e., increase in R and decrease in β, which led to an increase in the width of the spectral plateau.

4.2 VERIFICATION OF THE PROPOSED EQUATION FOR ESTIMATING FRS

For the verification, a primary structure which was a SC structural system with flag-shaped hysteretic behavior, with an initial vibration period $T_p = 0.5$ s, 1.0 s, 1.5 s, response reduction factor $R = 2, 4, 6,$ post-yield stiffness ratio $\alpha = 5\%;$ energy dissipation parameter $\beta = 0\%, 40\%,$ and 80%; and viscous damping ratio $\xi_p = 5\%$; and a secondary structure with a viscous damping ratio $\xi_s = 5\%$ was considered. It is noted that both the primary and secondary structures were modeled by SDOF systems.

Here, 11 far-fault ground motions were considered from the 22 far-fault ground motion set of FEMA P695 (Table A-4A, FEMA [31]), given in Table 3. Note that these 11 far-fault ground motions are not the same ground motions used in Section 2.

The mean floor response spectra were determined from an NLRHA, using the procedure given in Section 3.1. The mean peak acceleration demands of the secondary structure A_s obtained from Equation (5) and NLRHA, are shown in Figures 7–9. For $T_p = 0.5$ s, 1.0 s, the A_s estimated from Equation (5) slightly underestimated the peak acceleration demand of the secondary structure in the resonance region but was mostly conservative in other regions. For $T_p = 1.5$ s, the A_s estimated from Equation (5) slightly underestimated the peak acceleration demand of the secondary structure in the post-resonance region, but was mostly conservative in other regions. It was also observed that the width of the spectral plateau with varying R and β could be estimated well using Equation (5). In general, it can be concluded that the A_s estimated from Equation (5) showed good accuracy when compared with the NLRHA results.

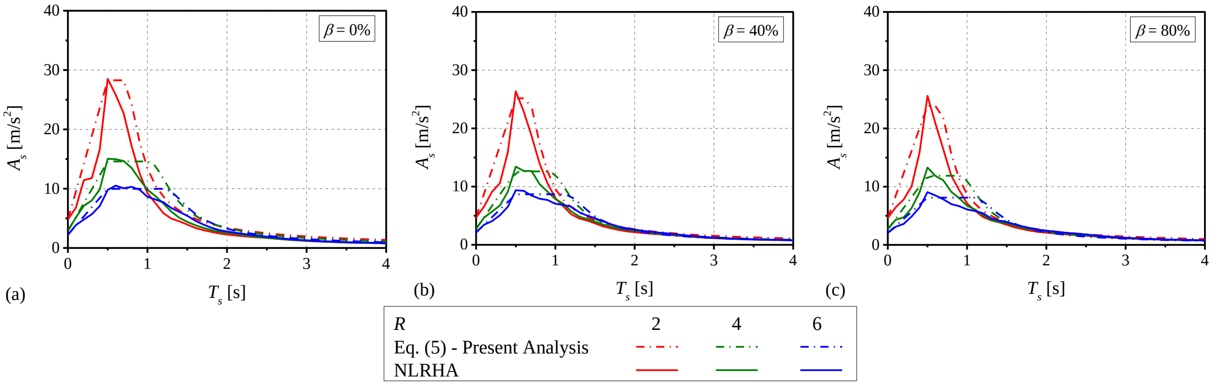

Figure 7. Comparison of the mean floor response spectra from Equation (5) and NLRHA for a primary structure with initial vibration period $T_p = 0.5$ s, post-yield stiffness ratio $\alpha = 5\%$; viscous damping ratio $\xi_p = 5\%$; and a secondary structure with viscous damping ratio $\xi_s = 5\%$: (a) $\beta = 0\%$; (b) $\beta = 40\%$; and (c) $\beta = 80\%$.

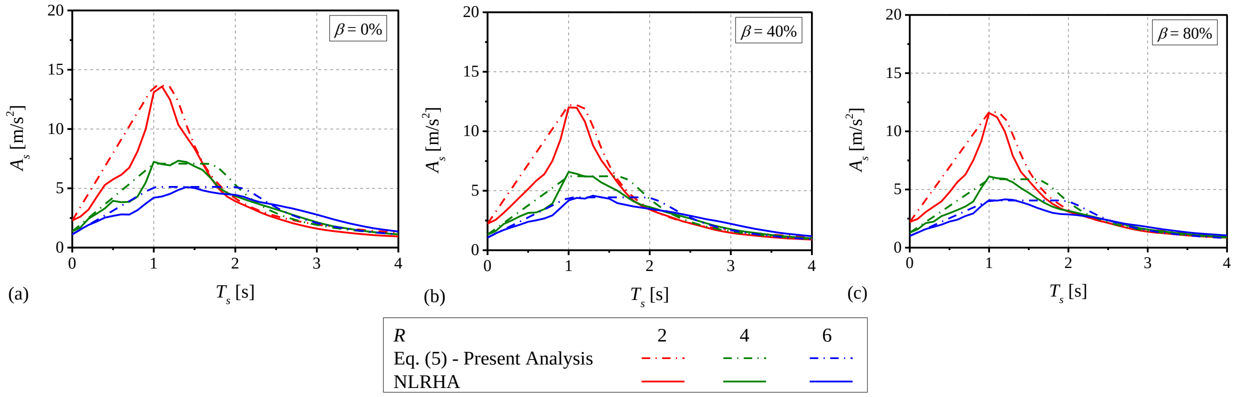

Figure 8. Comparison of the mean floor response spectra from Equation (5) and NLRHA for a primary structure with initial vibration period $T_p = 1.0$ s, post-yield stiffness ratio $\alpha = 5\%$; viscous damping ratio $\xi_p = 5\%$; and a secondary structure with viscous damping ratio $\xi_s = 5\%$: (a) $\beta = 0\%$; (b) $\beta = 40\%$; and (c) $\beta = 80\%$.

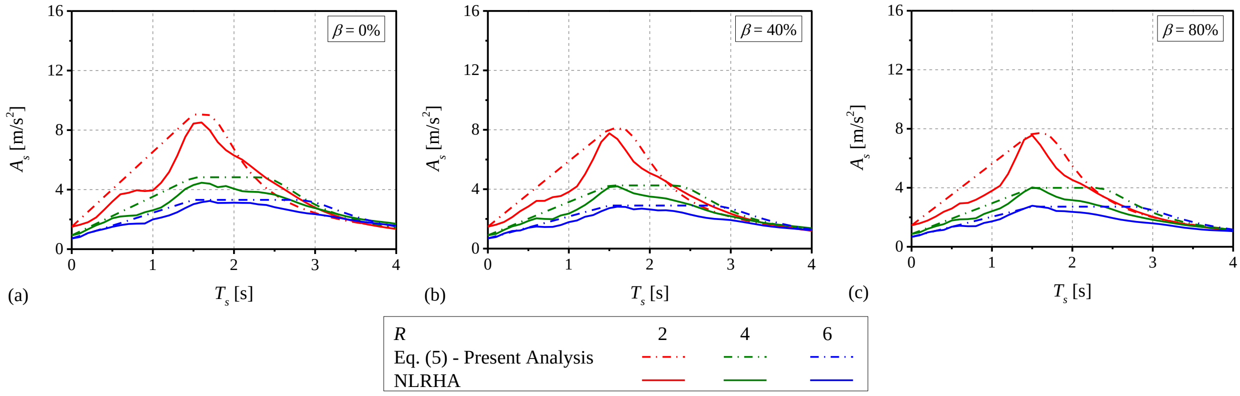

Figure 9. Comparison of the mean floor response spectra from Equation (5) and NLRHA for a primary structure with initial vibration period $T_p = 1.5$ s, post-yield stiffness ratio $\alpha = 5\%$; viscous damping ratio $\xi_p = 5\%$; and a secondary structure with viscous damping ratio $\xi_s = 5\%$: (a) $\beta = 0\%$; (b) $\beta = 40\%$; and (c) $\beta = 80\%$.

4.3 Comparison of the Proposed FRS with Existing Direct Methods

The mean peak acceleration demand of the secondary structure A_s obtained from Equation (5) of the present analysis as well as the existing direct methods of Sullivan et al. [2013] and Vukobratovic and Fajfar [2015] were compared with the NLRHA results in Figure 10. For the comparison, a primary structure with flag-shaped hysteretic behavior, with an initial vibration period $T_p = 1.0$ s, response reduction factor $R = 2$; post-yield stiffness ratio $\alpha = 5\%$; energy dissipation parameter $\beta = 0\%, 20\%, \ldots, 100\%$; and viscous damping ratio $\xi_p = 5\%$; and a secondary structure with a viscous damping ratio $\xi_s = 5\%$ was considered.

It was observed that the A_s estimated from Equation (5) of the present analysis provided a good estimate in the resonance region and slightly overestimated in other regions (see Figure 10). The method of Sullivan et al. [2013] slightly overestimated in the pre-resonance region but underestimated in the resonance region. Moreover, in the post-resonance region, A_s was underestimated for $\beta \leq 20\%$, but showed good accuracy for $\beta > 20\%$. The method of Vukobratovic and Fajfar [2015] underestimated A_s in the pre-resonance region for $T_s < 0.6$s. In the resonance region, underestimation of A_s for $\beta \leq 20\%$, and overestimation of A_s for $\beta > 20\%$ was observed. Furthermore, A_s was underestimated in the post-resonance region. Note that the proposed equation for computing the FRS was developed for SC flag-shaped SDOF systems and shows dependency on β. As a result, the estimated A_s from Equation (5) of the present analysis showed better accuracy than already existing direct methods when compared with the NLRHA results.

5.Conclusions

In this study, the floor response spectra (FRS) for self-centering (SC) structural systems with flag-shaped hysteretic behavior was investigated using nonlinear response history analysis (NLRHA), and an equation for estimating the FRS was proposed. In particular, a primary structure with a post-yield stiffness ratio $\alpha = 5\%$; viscous damping ratio $\xi_p = 5\%$; and a secondary structure with a viscous damping ratio $\xi_s = 5\%$ was considered. The proposed equation was then verified using a different set of far-fault ground motions. Based on this study, the following conclusions can be drawn:

1) The effect of the primary structure initial vibration period T_p, response reduction factor R, and energy dissipation parameter β on the FRS was studied. A single peak was observed on the mean normalized FRS for $R = 1$, but for $R > 1$, the maximum value of the mean normalized FRS was nearly constant over a wide period range and formed a *spectral plateau*. The width of the spectral

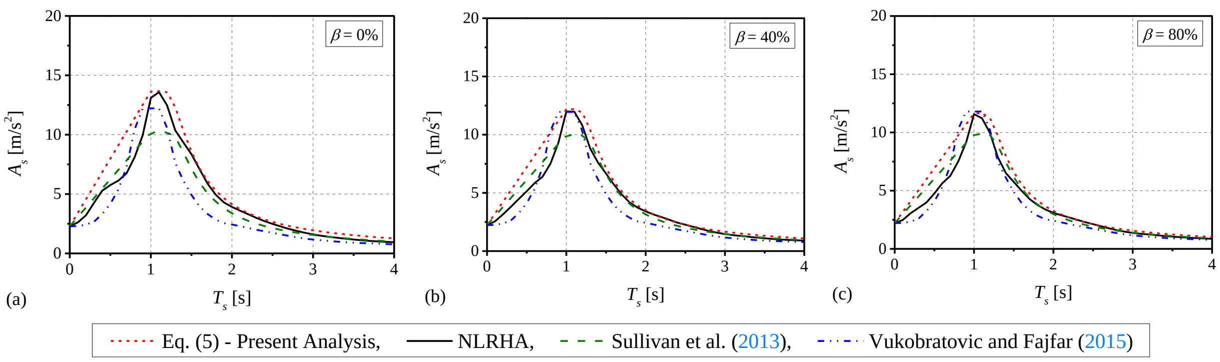

Figure 10. Comparison of the mean floor response spectra from Equation (5) of the present analysis, Sullivan et al. [2013], Vukobratovic and Fajfar [2015], and NLRHA for a primary structure with initial vibration period $T_p = 1.0$ s, response reduction factor $R = 2$; post-yield stiffness ratio $\alpha = 5\%$; viscous damping ratio $\xi_p = 5\%$; and a secondary structure with viscous damping ratio $\xi_s = 5\%$: (a) $\beta = 0\%$; (b) $\beta = 40\%$; and (c) $\beta = 80\%$. Note: The methods of Sullivan et al. [2013] and Vukobratovic and Fajfar [2015] are for primary structures with modified Takeda and elasto-plastic hysteretic behavior, respectively.

plateau increased with increase in R and decrease in β, which was due to the higher ductility demand on the primary structure. In addition, the peak value of the mean normalized FRS increased when R changed from 1 to 2, and then decreased for $R > 2$. The reduction in the mean normalized FRS was observed with increase in β. With increase in T_p, the maximum dynamic amplification factor DAF_{max} increased for $T_p \leq 0.5\text{s}$, and remained nearly constant for $T_p > 0.5\text{s}$ and $R > 1$.

2) An empirical equation for DAF_{max} that can be used to estimate the acceleration demand in the resonance region was developed. This equation showed good accuracy when compared with NLRHA results. In addition, for the post-resonance region, an equation for estimating the dynamic amplification factor DAF_{pr} was also obtained.
3) An equation for estimating the FRS for SC systems with flag-shaped hysteretic behavior was proposed, using the DAF_{max} and the DAF_{pr}. The equation for estimating the FRS was then validated using a different set of far-fault ground motions. It was observed that the equation for estimating the FRS for SC systems with flag-shaped hysteretic behavior showed good accuracy when compared with the NLRHA results.

The results of this study are useful for the seismic design of acceleration-sensitive non-structural components (NSCs).

The equation for estimating FRS developed in the present study is based on SC structural systems with flag-shaped hysteretic behavior, with a primary structure with a post-yield stiffness ratio $\alpha = 5\%$ and viscous damping ratio $\xi_p = 5\%$, and a secondary structure with a viscous damping ratio $\xi_s = 5\%$. Since the damping ratio of the secondary structure strongly influences the FRS, more damping ratios of secondary structures ξ_s should be investigated, and the accuracy of the proposed equation examined. Future studies should also investigate the effect of the post-yield stiffness ratio α and the viscous damping ratio of the primary structure ξ_p on the FRS of SC structural systems with flag-shaped hysteretic behavior.

REFERENCES

Aragaw, L.F.; Calvi, P.M. [2021] "Earthquake-induced floor accelerations in base-rocking wall buildings," *J. Earthq. Eng.*, 25, 941–969.

ASCE 7 [2017] "Minimum Design Loads for Buildings and Other Structures," American Society of Civil Engineers (ASCE): Reston, VA, USA.

Bates, D.M.; Watts, D.G. [1988] "Nonlinear Regression Analysis and Its Applications," Wiley: New York, NY, USA.

Belleri, A.; Schoettler, M.J.; Restrepo, J.I.; Fleishman, R.B. [2014] "Dynamic behavior of rocking and hybrid cantilever walls in a precast concrete building," *ACI Struct. J.*, 111, 661–672.

Buddika, H.A.D.S.; Wijeyewickrema, A.C. [2016] "Seismic performance evaluation of posttensioned hybrid precast wall-frame buildings and comparison with shear wall-frame buildings," *J. Struct. Eng.* (ASCE), 142, 04016021.

Calvi, P.M.; Sullivan, T.J. [2014] "Estimating floor spectra in multiple degree of freedom systems," *Earthq. Struct.*, 7, 17–38.

CEN. Eurocode 8 [2004] "Design of Structures for Earthquake Resistance—Part 1: General Rules, Seismic Actions and Rules for Buildings (EN 1988-1)," European Committee for Standardization: Brussels, Belgium.

Devin, A.; Fanning, P.J. [2019] "Non-structural elements and the dynamic response of buildings: a review," *Eng. Struct.*, 187, 242–250.

Dhakal R. P.; Pourali A., Tasligedik A. S., Yeow T.; Baird A., MacRae G.; Pampanin S., Palermo A. [2016] "Seismic performance of non-structural components and contents in buildings: an overview of NZ research," *Earthq. Eng. Eng. Vib.*, 15, 1–17.

Dong, H.; Han, Q.; Du, X.; Liu, J. [2020] "Constant ductility inelastic displacement ratios for the design of self-centering structures with flag-shaped model subjected to pulse-type ground motions," *Soil Dyn. Earthq. Eng.*, 133, 106143.

EERI [1984]. "Nonstructural Issues of Seismic Design and Construction," Earthquake Engineering Research Institute: Berkeley, CA, USA, Publication 84-04.

FEMA P695. [2009] "Quantification of Building Seismic Performance Factors," Federal Emergency Management Agency (FEMA): Washington, DC, USA.

Kazantzi, A.K.; Vamvatsikos, D.; Miranda, E. [2020] "The effect of damping on floor spectral accelerations as inferred from instrumented buildings," *Bull. Earthq. Eng.*, 18, 2149–2164.

Kurama, Y.C. [2002] "Hybrid post-tensioned precast concrete walls for use in seismic regions," *PCI Journal*, 47, 36–59.

Merino R. J.; Perrone D.; Filiatrault A. [2020] "Consistent floor response spectra for performance-based design of nonstructural elements," *Earthq. Eng. Struct. Dyn.*, 49, 261–284.

OpenSees. [2017] "Open system for earthquake engineering simulation," In Computer Program; University of California: Berkeley, California, USA. Available online: https://opensees.berkeley.edu/ (accessed on April 05, 2017).

Oropeza, M.; Favez, P.; Lestuzzi, P. [2010] "Seismic response of nonstructural components in case of nonlinear structures based on floor response spectra method," *Bull. Earthq. Eng.*, 8, 387–400.

Priestley, M.J.N.; Calvi, G.M.; Kowalsky, M.J. [2007] "Displacement-Based Seismic Design of Structures," IUSS Press: Pavia, Italy.

Rahgozar, N.; Moghadam, A.S.; Aziminejad, A. [2016] "Inelastic displacement ratios of fully self-centering controlled rocking systems subjected to near-source pulse-like ground motions," *Eng. Struct.*, 108, 113–133.

Shrestha, B.K.; Wijeyewickrema, A.C.; Kono, S. [2021] "Seismic performance and collapse safety assessment of post-tensioned hybrid precast concrete infill wall-frames and comparison with reinforced concrete infill wall-frames," *J. Earthq. Eng.*, 1–24 (in press).

Smith, B.J.; Kurama Y. C.; McGinnis, M.J. [2013] "Behavior of precast concrete shear walls for seismic regions: comparison of hybrid and emulative specimens," *J. Struct. Eng.* (ASCE), 139, 1917–1927.

SPSS [2017]. "IBM SPSS Statistics for Windows," Version 25.0; IBM Corp.: Armonk, NY, USA.

Sullivan, T.J.; Calvi, P.M.; Nascimbene, R. [2013] "Towards improved floor spectra estimates for seismic design," *Earthq. Struct.*, 4, 109–132.

Villaverde, R. [1997] "Seismic design of secondary structures: state of the art," *J. Struct. Eng.* (ASCE), 123, 1011–1019.

Vukobratović, V.; and Fajfar, P. [2015] "A method for the direct determination of approximate floor response spectra for SDOF inelastic structures," *Bull. Earthq. Eng.*, 13, 1405–1424.

Vukobratović, V.; Fajfar, P. [2016] "A method for the direct estimation of floor acceleration spectra for elastic and inelastic MDOF structures," *Earthq. Eng. Struct. Dyn.*, 45, 2495–2511.

Vukobratović, V.; Fajfar, P. [2017] "Code-oriented floor acceleration spectra for building structures," *Bull. Earthq. Eng.*, 15, 3013–3026.

Vukobratović, V.; Ruggieri, S. [2021] "Floor acceleration demands in a twelve-storey RC shear wall building. Buildings," 11, 38.

Vukobratović, V.; Yeow, T.Z.; Kusunoki, K. [2021] "Floor acceleration demands in three RC buildings subjected to multiple excitations during shake table tests," *Bull. Earthq. Eng.*, 19, 5495–5523.

Wang, T.; Shang, Q.; Li, J. [2021] "Seismic force demands on acceleration-sensitive nonstructural components: a state-of-the-art review," *Earthq. Eng. Eng. Vib.*, 20, 39–62.

Welch, D.P.; Sullivan, T.J. [2017] "Illustrating a new possibility for the estimation of floor spectra in nonlinear multi-degree of freedom systems," *In Proceedings of the 16th World Conference on Earthquake Engineering,* Santiago, Chile, Paper 2632.

Wiebe, L., Christopoulos, C., Tremblay, R., and Leclerc, M. [2013] "Mechanisms to limit higher mode effects in a controlled rocking steel frame. 1: Concept, modelling, and low-amplitude shake table testing", *Earthquake Engineering and Structural Dynamics*, 42(7), 1053-1068.

Yang, B.; Lu, X. [2018] "Displacement-based seismic design approach for prestressed precast concrete shear walls and its application," *J. Earthq. Eng.*, 22, 1836-1860.

Yasui, Y.; Yoshihara, J.; Takeda, T.; Miyamoto, A. [1993] "Direct generation method for floor response spectra," *In Proceedings of the Transactions of the 12th International Conference on Structural Mechanics in Reactor Technology*, Stuttgart, Germany, Paper no. K13/4:367-372.

Zhang, C.; Steele, T.C.; Wiebe, L.D.A. [2018] "Design-level estimation of seismic displacements for self-centering SDOF systems on stiff soil," *Eng. Struct.*, 177, 431–443.

A Practice-Oriented Floor Response Spectrum Prediction Method for Seismic Design of Non-Structural Elements

Kieran Haymes[1], Timothy J. Sullivan[1], Reagan Chandramohan[1], and Lydell Wiebe[2]

[1] Department of Civil and Natural Resources Engineering, University of Canterbury
Christchurch, New Zealand
[2]Department of Civil Engineering, McMaster University,
Hamilton, Ontario, Canada
e-mail: kieran.haymes@pg.canterbury.ac.nz
timothy.sullivan@canterbury.ac.nz
reagan.c@canterbury.ac.nz
wiebel@mcmaster.ca

Abstract. The development of a practice-oriented method for the prediction of floor response spectra and seismic demands on non-structural elements to facilitate their design is discussed. In New Zealand, the current standards have been observed to provide inaccurate estimates of demands on acceleration-sensitive building components. The simplifying assumptions that underpin the code design approach for parts and components result in the over-prediction of demands on rigid short-period elements, under-estimation of the resonant behaviour of flexible non-structural elements interacting with the modes of the supporting structure, and the prescription of unrealistically large displacement demands for components with long periods. Alternative prediction approaches recently proposed by the authors and others in the literature consider additional dynamic characteristics of both the non-structural element and the supporting structure, thereby improving the accuracy of demand estimates. This method, presented herein, explicitly considers the influence of nonlinear non-structural and inelastic structural behaviour. The approach has been extended for use with low-damage high performance structural systems, including base isolation and controlled rocking steel braced frames. Consultation with practicing engineers in New Zealand is informing further refinement of a methodology for implementation in the New Zealand design standards. The goal of the new methodology is to achieve a suitable balance of simplicity and ease of use with improved specificity and accuracy, and possible means of achieving this are described.

Keywords: Floor response spectrum, design standards, practice-oriented, modal superposition, New Zealand.

1. INTRODUCTION

Widespread non-structural damage occurred throughout New Zealand during the Canterbury earthquake sequence of 2010/11, which caused significant losses in Christchurch [Dhakal, 2010]. Non-structural damage was also observed in the 2013 Grassmere and Seddon and 2016 Kaikōura earthquakes in the northern regions of the South Island, which resulted in damage to buildings in the national capital, Wellington [Baird and Ferner, 2017]. These events, combined with the contemporaneous sentiment that New Zealand's seismic design provisions are robust and maturing in their ability to prevent the loss of life from structural collapse, have driven an increased desire to improve post-earthquake functionality and limit economic and social costs associated with damage. Consequently, the performance of non-structural elements has come into focus.

As research into the seismic performance of non-structural elements increases, it has been identified that improvements could be made to the current New Zealand seismic design approach for non-structural elements [Rashid *et al.*, 2021]. A practice-oriented prediction approach that uses structural modal characteristics has recently been put forward [Haymes *et al.*, 2020], building on previous proposals in the literature [Calvi, 2014; Kehoe and Hachem, 2003; Vukobratović and Fajfar, 2017; Welch and Sullivan, 2017]. More recently, the provisions have been developed to account for non-structural nonlinearity and structural inelasticity within conventional fixed base buildings, steel controlled rocking braced frames, and base isolated buildings. The method has been based upon observations from instrumented buildings, shake table testing, and results from numerical modelling. Although the performance of this approach is promising, successful implementation of revised design provisions in future standards also requires the support of practitioners. To strengthen the close collaboration between academic and industry professionals, a workshop on determining seismic demands on non-structural components was recently held. This paper reviews the recent efforts in New Zealand to improve the assessment of seismic demands on non-structural elements, examines the challenges faced to improve seismic design provisions, and identifies the considerations that are being made to balance the simplicity and ease of use of code provisions with the improved specificity and accuracy that the recently proposed method may offer.

2.THE NEW ZEALAND DESIGN STANDARD APPROACH FOR PREDICTING DEMANDS ON NON-STRUCTURAL ELEMENTS

In New Zealand, the design of non-structural components to resist seismic demands is prescribed by the New Zealand Standard NZS1170.5:2004 with 2016 amendments [Standards New Zealand, 2016b] using a floor response spectrum approach that appears to have been developed from Shelton [2004]. This approach separates the ground motion intensity, amplification of demands with building height, non-structural period, and the effects of non-structural nonlinearity into individually approximated parameters. The horizontal design earthquake action on the non-structural component, F_{ph}, is determined using Equation 1:

$$F_{ph} = C_p(T_p)C_{ph}R_pW_p \leq 3.6W_p \quad (1)$$

where $C_p(T_p)$ is the horizontal design coefficient of the part, which varies as a function of the period of the part, T_p; C_{ph} is the part horizontal response coefficient; R_p is the part risk factor, given as 1.0 for all cases except for where the consequential damage caused by its failure is disproportionately great; and W_p is the weight of the part. The horizontal design coefficient of the part is calculated using Equation 2:

$$C_p(T_p) = C(0)C_{Hi}C_i(T_p) \quad (2)$$

where $C(0)$ is the peak ground acceleration, C_{Hi} is the floor height coefficient for level i, and $C_i(T_p)$ is the part spectral shape factor.

The floor height coefficient captures the variation of peak floor acceleration (PFA) with floor height. This appears to have been introduced from the enveloped peak floor acceleration responses computed from the analytical modelling and instrumented building data described in [Shelton, 2004]. The factor is a function of the height of attachment of the part, h_i, and the height from the base of the structure to the uppermost seismic weight or mass, h_n. This approach appears highly conservative [Uma *et al.*, 2010]. This coefficient is shown in Figure 1a, and computed using Equation 3:

$$C_{Hi} = \begin{cases} 1+\dfrac{h_i}{6} & \text{for all } h_i < 12\text{ m} \\ 1+10\dfrac{h_i}{h_n} & h_i < 0.2h_n \\ 3 & h_i \geq 0.2h_n \end{cases} \tag{3}$$

The part spectral shape factor, $C_i(T_p)$ has a trilinear shape which varies as a function of the period of the part. This factor envelops the floor response spectrum shape that was considered typical at the time. The factor is independent of the modal periods of the structure and has been observed to consequentially underestimate demands on flexible components with periods near long fundamental structural periods [Uma *et al.*, 2010]. This factor amplifies the peak floor acceleration by two, although no amplification develops in rigid components, and thus appears over-conservative [Uma *et al.*, 2010; Sullivan *et al.*, 2013; Filiatrault and Sullivan, 2014]. This possibly reflects code-writers' perceptions that very few components will be truly rigid, and, to avoid negative impacts associated with a designer underestimating the real period of a component, the demands at zero period are set to reflect those more likely at short periods. This approach is also over-conservative at very long non-structural periods, and results in unrealistic corresponding relative displacement demands [Uma, *et al.*, 2010]. The part spectral shape factor is shown in Figure 1b, and described in Equation 4:

$$C_i(T_p) = \begin{cases} 2 & T_p \leq 0.75\ s \\ 2(1.75-T_p) & 0.75\ s < T_p < 1.25\ s \\ 0.5 & 1.25\ s \leq T_p \end{cases} \tag{4}$$

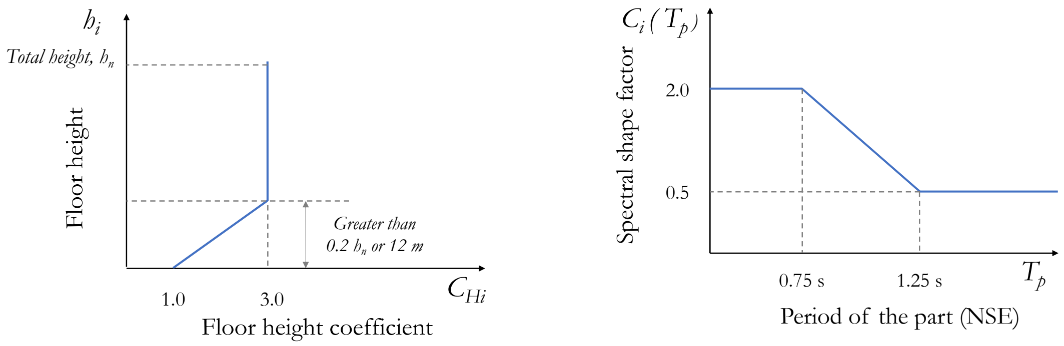

(a) **Floor height coefficient, C_{Hi}** (b) **Spectral shape factor, $C_i(T_p)$**

Figure 1. Design provisions for non-structural elements in NZS1170.5 (Standards New Zealand, 2016b).

The part response factor, C_{ph}, is given in Table 1 and reduces the demands at all component periods with increasing component ductility. The New Zealand standard does not explicitly consider the effects of structural nonlinearity (in contrast to ASCE 7-22 [ASCE 2021]) and applies no limits to the intensities for which this approach can be applied. The part response factor does not have a clear rational basis for rigid components, for which there is no elastic dynamic amplification available to be reduced with ductility.

However, this unconservative reduction counteracts the conservative dynamic amplification prescribed at short periods of the part spectral shape factor, provided the ductility of the part is sufficient.

Table 1. Part response factor, Cph, used in NZS1170.5 (Standards New Zealand, 2016b)**.**

Ductility of the part μ_p	Part response factor C_{ph}
1.0	1.0
1.25	0.85
2.0	0.55
3.0 or greater	0.45

3. A MODAL SUPERPOSITION PREDICTION METHODOLOGY

The floor response spectrum prediction method proposed by Haymes [2022] uses the mode shapes and periods of the building to first compute the peak floor acceleration demands for each mode. Modal methods strictly provide the pseudo-spectral acceleration demand associated with the relative motion of the building to its base. However, the total peak floor accelerations are found to be well predicted by the modal contributions, provided that the building's modes are excited significantly. Peak floor accelerations are required for the design of all acceleration-sensitive non-structural components except those that are very flexible. With the peak floor accelerations estimated, dynamic amplification factors specify the shape of the floor response spectrum contributions of each mode by considering the ratio of the period of the non-structural component to each modal period of the supporting structure. The peak amplification is inversely proportional to the damping ratios of the non-structural component and the supporting structure. The modal contributions are combined using the the square-root-sum-of-squares (SRSS) of all the modal contributions at each non-structural period. A ramped form of the ground response spectrum is added to the relative motions approximated by modal combination to approximate demands at long non-structural periods. Finally, the predicted floor acceleration response spectrum is taken as the maximum of the ground spectral acceleration and the quantity estimated by the sum of the modal combination and the ramped ground response spectrum at each non-structural period. A qualitative example of the construction of a floor acceleration response spectrum using this approach is shown in Figure 2.

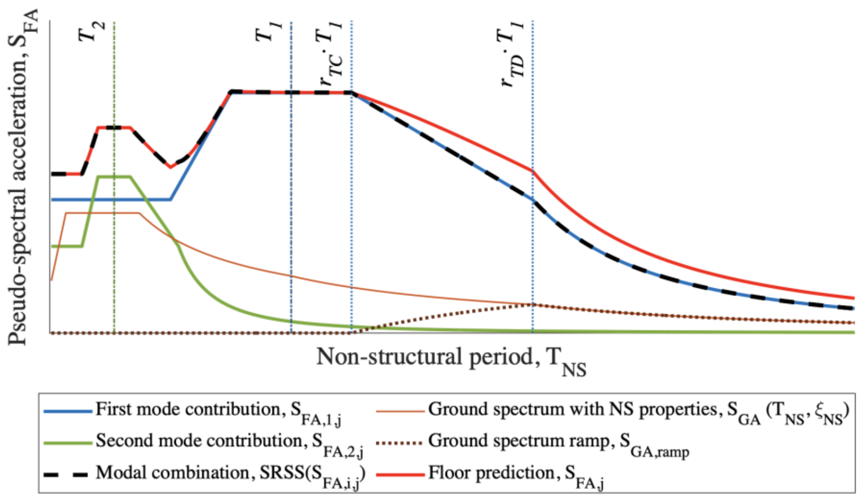

Figure 2. A qualitative example of a floor acceleration response spectrum prediction. The first and second modes are combined using SRSS, and the ground response spectrum ramp is added to produce the predicted floor spectrum.

The contribution of mode i, at floor j, to the floor acceleration response spectrum at the period of vibration of the non-structural component, T_{NS}, is the product of the peak floor acceleration associated with the mode, $PFA_{i,j}$, and the dynamic amplification factor, DAF_i, as computed using Equation 5:

$$S_{FA,ij} = \frac{PFA_{i,j}}{R_i} DAF_i = \left|\Gamma_i \phi_{i,j}\right| \frac{S_{GA}(T_i, \xi_{str})}{R_i} DAF_i \tag{5}$$

where $\Gamma_i \phi_{i,j}$ is the factored mode shape of mode i at floor j; $S_{GA}(T_i, \xi_{str})$ is the spectral acceleration at the ground at structural period T_i considering the damping ratio of the structure, ξ_{str}; and R_i is the modal strength reduction factor.

The dynamic amplification factor, DAF_i, describes the amplification from the interaction between the fundamental mode of vibration of the non-structural element, T_{NS}, and mode of vibration i of the building, T_i. The shape of the dynamic amplification factor is defined by the ratio of the periods of the non-structural component and the modes of the structure, $r_{T,i} = T_{NS} / T_i$. The period ratios r_{TA}, r_{TB}, r_{TC}, and r_{TD} are used to define the piecewise DAF_i function, for which the values of 0.5, 0.75, 1.25 and 2.0 may be adopted, respectively. DAF_i is shown in Figures 3a and 4a, and described by Equation 6:

$$DAF_i = \begin{cases} 1 & r_{T,i} \le r_{TA} \\ \dfrac{r_{T,i} - r_{TA}}{r_{TB} - r_{TA}} (DAF_{max,i} - 1) + 1 & r_{TA} < r_{T,i} < r_{TB} \\ DAF_{max,i} & r_{TB} \le r_{T,i} \le r_{TC} \\ \dfrac{r_{T,i} - r_{TC}}{r_{TD} - r_{TC}} \left(\dfrac{1}{\mu_{NS}} - DAF_{max,i}\right) + DAF_{max,i} & r_{TC} < r_{T,i} < r_{TD} \\ \dfrac{1}{\mu_{NS}\left(1 - r_{TD} + r_{T,i}\right)^2} & r_{TD} \le r_{T,i} \end{cases} \tag{6}$$

where $DAF_{max,i}$ is the maximum dynamic amplification term for mode i, given in Equation 7 after previous work [Sullivan *et al.*, 2013; Vukobratović and Fajfar, 2017; Welch and Sullivan, 2017]:

$$1 \le DAF_{max,i} = \frac{2}{3}[0.5\xi_{str} + \xi_{NS}]^{-2/3} \times \begin{cases} {\mu_{NS}}^{1.5} & i = 1 \\ \mu_{NS} & i \ge 2 \end{cases} \tag{7}$$

where ξ_{NS} is the damping of the component, and μ_{NS} is the ductility of the non-structural component, used in the provisions shown in Figure 3 to describe the influence of non-structural nonlinearity. This permits the seismic design of non-structural components to a minimum yield strength, which is often lower than the corresponding strength required to remain elastic for flexible components, provided component ductility capacity can be demonstrated.

The modal strength reduction factor, R_i, considers the reduction of the demands associated with the modal contributions due to structural inelasticity, quantified using the structural ductility, μ_{str}. The use of the modal strength reduction factor is shown in Figure 4b, is calculated using Equation 8:

$$R_i = \begin{cases} \mu_{str} & i = 1 \\ 1 & i \ge 2 \end{cases} \tag{8}$$

As shown in Figure 4a, the period ratios r_{TC} and r_{TD} define the end of the plateau and the linearly-descending branch of the dynamic amplification factor, *DAF*. Period elongation may be considered by extending these values when computing the floor response spectrum contribution of the fundamental structural mode as a function of effective structural ductility, μ_{eff}. The elongated period ratios $r_{TC,1,inelastic}$ and $r_{TD1,inelastic}$ are given by Equations 9 and 10:

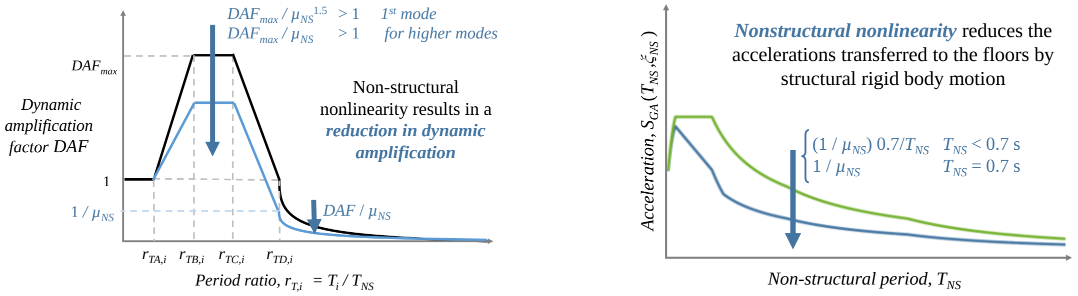

(a) **The dynamic amplification factor, *DAF*, adopts lower values with increasing non-structural nonlinearity.**

(b) The ground response spectrum scaled for non-structural damping reduces with increasing non-structural nonlinearity.

Figure 3. Prediction provisions considering non-structural non-linearity.

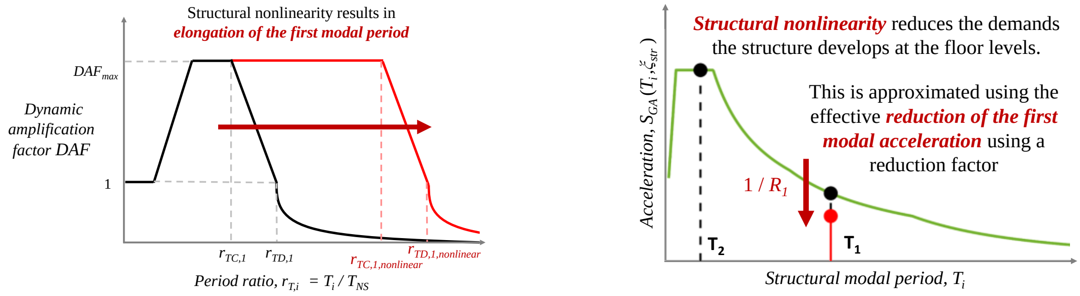

(a) **The period ratios, $r_{TC,1}$ and $r_{TD,1}$, adopt greater values with increasing structural inelasticity due to period elongation occurring in the first structural mode.**

(b) The ground spectral acceleration of the first mode, scaled considering structural damping, reduces with increasing structural nonlinearity.

Figure 4. Prediction provisions considering structural nonlinearity.

$$r_{TC,1,inelastic} = \sqrt{\frac{\mu_{eff}}{1 + \alpha\,(\mu_{eff} - 1)}} + r_{TC} - 1 \tag{9}$$

$$r_{TD,1,inelastic} = \sqrt{\frac{\mu_{eff}}{1 + \alpha\,(\mu_{eff} - 1)}} + r_{TD} - 1 \tag{10}$$

where α is the strain hardening ratio, and μ_{eff} is the effective ductility of the structure that corresponds to the longest non-structural period where dynamic amplification is induced from effects of structural inelasticity, computed using Equation 11:

$$\mu_{eff} = \frac{\mu_{str} + 1}{2} \tag{11}$$

The transition between the behaviour caused by the flexibility of the structural system that influences the spectra at periods near or shorter-than the fundamental period of the structure, and those at long non-structural periods which tend towards the corresponding ground acceleration response spectral ordinates, is considered through the addition of a ramped form of the ground spectral acceleration for periods greater than the plateau of the fundamental modal period ($T_{NS} > r_{TC}T_1$). This ramped ground response spectrum multiplies the ground response spectral ordinates by a linearly increasing function to a maximum value of 1 at the end of the first modal amplification region ($T_{NS} > r_{TD}T_1$), after which it is steady, as given in Equation 12:

$$S_{GA,ramp} = S_{GA}(\xi_{NS}, \mu_{NS}) \begin{cases} 0 & r_{T,1} \leq r_{TC} \\ \dfrac{r_{T,1} - r_{TA}}{r_{TB} - r_{TA}} (DAF_{max,i} - 1) + 1 & r_{TC} < r_{T,1} < r_{TD} \\ 1 & r_{TD} \leq r_{T,1} \end{cases} \quad (12)$$

Finally, the floor acceleration response spectrum, $S_{FA,j}$, is computed using Equation 13 by taking the maximum of the ground response spectrum scaled for non-structural properties, and the sum of the ramped ground response spectrum and the square-root-sum-of-squares (SRSS) combination of the modal contributions.

$$S_{FA,j} = \max\left[S_{GA,ramp} + \sqrt{\sum_i S_{FA,i,j}^{\ 2}} \ , S_{GA}(\xi_{NS}, \mu_{NS}) \right] \quad (13)$$

4. DEMONSTRATION OF PREDICTION PERFORMANCE

The performance of proposed framework and the NZS1170.5 provisions for non-structural nonlinearity are compared in Figure 4. Floor response spectra were computed for the transverse roof record of the University of Canterbury Physics building during the Lyttelton 2011 earthquake [GeoNet, 2022] for 5% non-structural damping and with non-structural ductility values of 1, 1.5, and 3.

The floor response spectrum prescribed by NZS1170.5 is independent of structural periods, instead assuming a spectral shape that is very conservative at most ordinates and fails to predict the amplification of ordinates near resonance with the first and second structural modes in Figure 4a and 4b, respectively. Conversely, the proposed framework can make more accurate predictions of the elastic amplification of ordinates around the structural periods and approximates the reduction with non-structural ductility well. The peak floor acceleration (at T_{NS} = 0) is well predicted by the proposed framework. The spectral shape assumed by NZS1170.5 predicts a peak floor acceleration that is more than twice the observed elastic demand. The NZS1170.5 nonlinear non-structural reduction factors are period-independent, resulting in reductions of peak floor acceleration predictions which do not appear to have any physical basis. Floor response spectral ordinates at T_{NS} > 1 s are significantly over-predicted by NZS1170.5. Conversely, the proposed method, which adopts a reduction of the modal contributions and considers ground response spectra scaled to the corresponding non-structural ductility, provides improved approximations of the observed demand.

5.OBSERVATIONS FROM A WORKSHOP REVIEWING PARTS & COMPONENTS PROVISIONS IN NEW ZEALAND

Based on feedback obtained in a 2022 workshop on parts & components demands [Sullivan and Haymes, 2022], it would appear that practitioners consider the current NZS approach to be conservative. However, research has shown that the NZS approach can produce both conservative and non-conservative estimates, with non-conservative estimates being particularly likely in buildings with long fundamental periods, and for non-structural components with low damping [Haymes *et al.*, 2020; Uma *et al.*, 2010; Welch, 2016]. There is limited evidence that components experience the demands associated with low damping values, however. The Applied Technology Council [2018] limited their proposals to non-structural damping values of five percent, however, based upon the limited characterisation of non-structural damping that is currently available, particularly at high intensities.

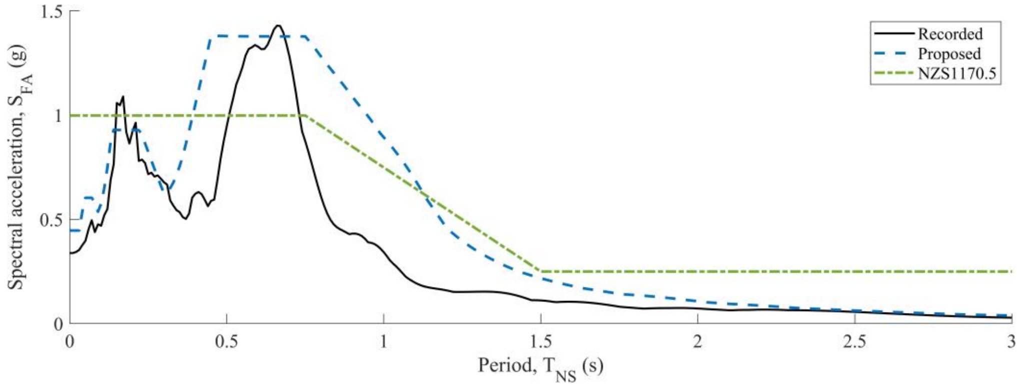

(a) Non-structural ductility of 1.0

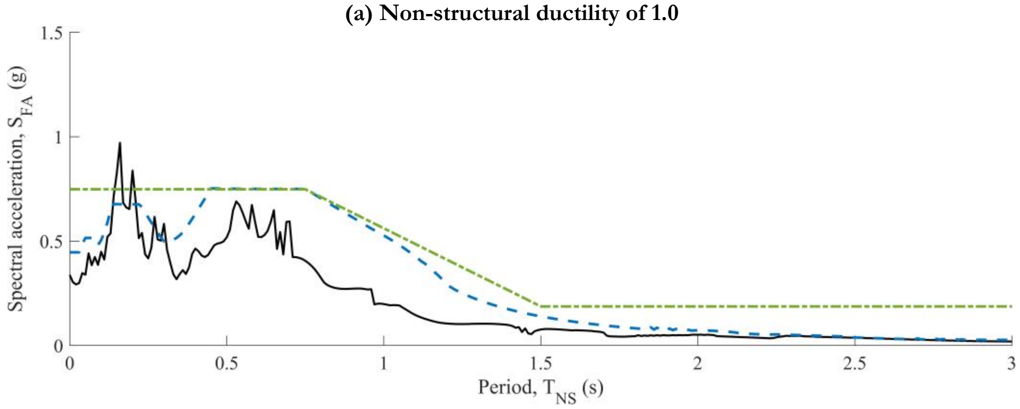

(b) Non-structural ductility of 1.5

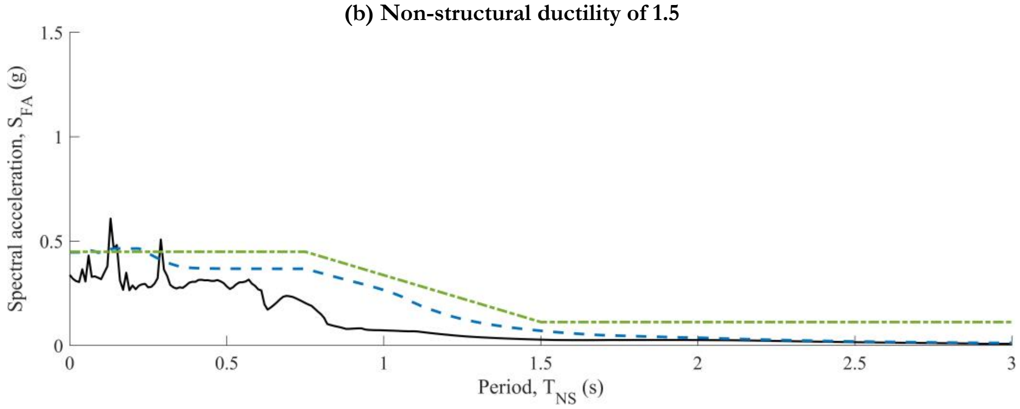

(c) Non-structural ductility of 3.0

Figure 1. Recorded and predicted acceleration floor response spectra for the UC Physics building for the Lyttelton 2011 transverse roof record, at 5% non-structural component damping.

Modal properties of the structural system significantly alter floor response spectra, determining the amplitude of amplified demands, and the non-structural periods at which this occurs. Consequently, prediction methods have been developed using modal superposition to avoid the computational expenditure associated with time history analysis. Practitioners attending the workshop were hesitant for the design standards to include modal analysis, however. The current NZS1170.5 standard is independent of the fundamental structural modal period, which practitioners expressed a desire to maintain. This was based on their notion that the fundamental structural modal period is cannot be estimated easily and reliably by users of the standard. This opinion is held despite the explicit use of this parameter in the non-structural design procedures in Eurocode 8 [European Committee for Standardization, 2004] and ASCE/SEI 7-22 [American

Society of Civil Engineers, 2021]. To this extent, any practice-oriented method should make allowance for uncertainty in the estimation of structural modal periods, as is included within the modal prediction method described in this work and discussed further elsewhere [Haymes *et al.*, 2020].

Some workshop attendees expressed scepticism about the large demands associated with the amplification of the dynamic response of non-structural components with periods near structural modal periods in elastic floor acceleration response spectra. This was based in a belief that most non-structural elements have an inherent ability to develop nonlinearity to reduce these demands. This is perhaps reflective of the commentary to NZS1170.5 [Standards New Zealand, 2016a], where all non-structural elements, except for glazing, are estimated to develop nonlinear responses at the design ultimate limit state. By permitting even small ductility values, large reductions for component periods near resonance of the supporting structure were demonstrated by the authors of this paper as well as by others [Applied Technology Council, 2018; Kazantzi *et al.*, 2020; Vukobratović and Fajfar, 2017], which informed the proposed method. Greater guidance could be developed on how non-structural ductility can be achieved, either through bolt slip, material inelasticity, rocking, or other means, and the degree of nonlinearity that is required to be developed to acquire the desired response.

The current NZS1170.5 approach for estimating parts & components acceleration demands can be applied with greater ease and speed than the proposed prediction approach. The provision of multiple means for compliance, permitting practitioners to determine demands using methods of varying complexity, was discussed in the workshop, where it was noted that multiple approaches are permitted for the determination of seismic loads on structural elements by NZS1170.5. The evolving computational ability of technology was suggested to reduce the significance of computational expenditure, particularly for methods that require relatively few parameters. The adoption of the proposed floor response spectrum prediction method in practice may, therefore, be facilitated by software, an application, or an online tool.

The prediction provisions developed in the ATC-120 project [ATC, 2018], and subsequently adopted in ASCE 7-22, were discussed during the workshop. Attendees acknowledged what appears to be a robust basis for the provisions. Consistent with the existing framework of NZS1170.5, practitioners favour the ability to explicitly consider the influence of first-principle parameters for design, such as the non-structural ductility, to enable more diverse design options. The attendees were reluctant to adopt prescribed values for specific components from tables.

The current code approach does not explicitly consider floor displacement response spectra. The spectral shape factor provides a constant value of 0.5 for non-structural periods greater than 1.25 s, resulting in unrealistically large spectral displacement demands at long periods [Haymes, 2022]. This limits the ability for practitioners to estimate the relative displacement demand on non-structural elements. This may be important for checking clearance requirements, which is common for designing suspended services like distributed sprinkler systems.

Perhaps most importantly, New Zealand engineering practitioners expressed a strong desire for a strong rational basis to be provided to the design approach for non-structural elements that is adopted in future standards. This desire may be interpreted as a mandate for future research into the seismic performance of non-structural elements.

6. CONCLUSIONS

There is an opportunity to improve the provisions given by the New Zealand standard for the seismic demands on non-structural elements. The current approach has been observed to produce predictions that are over-conservative for some components, possibly resulting in surplus capacity, whereas the demands on components with periods near the structural modal periods are often under-predicted.

A floor acceleration response spectrum modal superposition method was developed. This work is differentiated from previous research efforts through its thorough examination of behaviours observed in real world structures, its supplementation with results from rigorous numerical modelling, and the novel means of accounting for non-linearity of both the structure and non-structural components that seeks to strike the right balance between simplicity and accuracy.

Close collaboration between practitioners in the engineering industry and academics in New Zealand is thought to be the most effective way of improving the seismic performance of non-structural components. A recent workshop between industry and academia that was conducted at the University of Canterbury has identified key challenges and industry desires for updated code provisions. This work is ongoing, and the cooperation of these groups to provide a rational basis for practical design procedures promises to improve outcomes.

7.ACKNOWLEDGEMENTS

This project was (partially) supported by QuakeCoRE, a New Zealand Tertiary Education Commission-funded Centre. This is QuakeCoRE publication number 0799. The research has also been supported by the Resilience to Nature's Challenges project, and by the Earthquake Commission (EQC). Their support is gratefully acknowledged.

REFERENCES

American Society of Civil Engineers [2021] "ASCE/SEI 7-22 Minimum Design Loads and Associated Criteria for Buildings and Other Structures." Reston, Virginia.

Applied Technology Council [2018] "Recommendations for improved seismic performance of nonstructural components." NIST.GCR.18-917-43.

Baird, A., Ferner, H. [2017]. "Damage to non-structural elements in the 2016 Kaikōura earthquake." *Bulletin of the New Zealand Society for Earthquake Engineering*; Vol. 50 No. 2, pp. 187–193.

Calvi, P. M. [2014] "Relative Displacement Floor Spectra for Seismic Design of Non Structural Elements." *Journal of Earthquake Engineering*, Vol. 18 No. 7, pp. 1037–1059.

Dhakal, R. P. [2010] "Damage to non-structural components and contents in 2010 Darfield earthquake." *Bulletin of the New Zealand Society for Earthquake Engineering*, Vol. 43 No. 4, pp. 404–411.

European Committee for Standardization [2004] "Eurocode 8: Design of structures for earthquake resistance - Part 1: General rules, seismic actions and rules for buildings."

Filiatrault, A., Sullivan, T. J. [2014] "Performance-based seismic design of nonstructural building components: The next frontier of earthquake engineering." *Earthquake Engineering and Engineering Vibration*, Vol. 13 No. S1, pp.17–46.

GeoNet. [2022] "Structural Array Data." *https://www.geonet.org.nz/data/types/structural_arrays*

Haymes, K. [2022] "Developing Procedures for the Prediction of Floor Response Spectra." *PhD thesis*. University of Canterbury, Christchurch, New Zealand.

Haymes, K., Sullivan, T., Chandramohan, R. [2020] "A practice-oriented method for estimating elastic floor response spectra." *Bulletin of the New Zealand Society for Earthquake Engineering*, Vol. 53 No. 3, pp. 116–136.

Kazantzi, A. K., Miranda, E., Vamvatsikos, D. [2020] "Strength‐reduction factors for the design of light nonstructural elements in buildings." *Earthquake Engineering & Structural Dynamics*, Vol. 49 No. 13, pp. 1329-1343.

Kehoe, B. E., Hachem, M. [2003] "Procedures for Estimating Floor Accelerations." *ATC-29-2 Seminar on Seismic Design, Performance, and Retrofit of Nonstructural Components in Critical Facilities.* Redwood City, California.

Rashid, M., Dhakal, R., Sullivan, T. [2021] Seismic design of acceleration-sensitive non-structural elements in New Zealand: State-of-practice and recommended changes. *Bulletin of the New Zealand Society for Earthquake Engineering*, Vol. 54 No. 4, pp. 243–262.

Shelton, R. H. [2004] "Seismic response of building parts and non-structural components." *Study report, BRANZ Building of Knowledge.* Judgeford, New Zealand.

Standards New Zealand [2016a] "NZS 1170.5 Supp 1:2004 Structural design actions - Part 5: Earthquake actions - New Zealand Commentary." Wellington, New Zealand.

Standards New Zealand [2016b] "NZS 1170.5:2004: Structural design actions, Part 5: Earthquake actions - New Zealand." Wellington, New Zealand.

Sullivan, T. J., Calvi, P. M., Nascimbene, R. [2013] "Towards improved floor spectra estimates for seismic design." *Earthquakes and Structures*, Vol. 4 No. 1, pp. 109–132.

Sullivan, T. J., Haymes, K. [2022] "Report on the Parts & Components Workshop conducted at the University of Canterbury on June 2nd 2022" *EQC report*; University of Canterbury, Christchurch New Zealand.

Uma, S. R., Cousins, W. J., Baguley, D. [2010] "Seismic instrumentation in GNS Science building at Avalon." *GNS Science report*. Lower Hutt, New Zealand.

Uma, S. R., Zhao, J. X., King, A. B. [2010] "Seismic actions on acceleration sensitive non-structural components in ductile frames." *Bulletin of the New Zealand Society for Earthquake Engineering,* Vol. 43 No. 2, pp. 110–125.

Vukobratović, V., Fajfar, P. [2017] "Code-oriented floor acceleration spectra for building structures," *Bulletin of Earthquake Engineering*, Vol. 15 No. 7, pp. 3013–3026.

Welch, D. P., Sullivan, T. J. [2017] "Illustrating a new possibility for the estimation of floor spectra in nonlinear multi-degree of freedom systems." *16th World Conference on Earthquake Engineering.* Santiago, Chile.

Welch, D. P [2016] "Non-structural element considerations for contemporary performance-based earthquake engineering" *PhD Thesis*. Scuola Universitaria Superiore IUSS Pavia, Italy.

Free–field Earthquake Hazard Spectra to Establish Nonstructural Test Requirements for Global Code Compliance

Jeffrey A. Gatscher [1], **and Scott R. Littler** [2]

[1] Fellow Engineer, Schneider Electric, Power Products Division
6700 Tower Circle, Franklin, TN 37067 USA
e-mail: jeff.gatscher@se.com

[2] Principal Technical Expert, Schneider Electric, Energy Management Business
6700 Tower Circle, Franklin, TN 37067 USA
e-mail: scott.littler@se.com

Abstract. Model building codes provide minimum requirements for earthquake resistant design of structures and the equipment servicing these buildings. Every country or regional code that contains earthquake protection provisions includes earthquake hazard spectra used for building seismic design. This paper examines code-based hazard spectra for seventeen global codes to isolate on a code's ground level, free-field hazard spectrum. A free-field hazard spectrum is the response spectrum that is decoupled and independent of the building structure. Next a nonstructural equipment demand spectrum (EDS) can be constructed. The EDS is equivalent to a generic building floor spectrum used for seismic certification testing of equipment. The goal of this paper is to describe the steps to formulate a generic EDS profile. The steps are summarized as follows.

1.) Identify hazard mapping scheme and associated ground motion parameters.
2.) Identify the range of hazard levels as specified on hazard maps.
3.) Construct site hazard spectra for each geotechnical site classification.
4.) Identify any parameters that are either not related to ground motion or are coupled with building structure design and set those parameters to unity.
5.) Identify the peak response acceleration and zero period acceleration (ZPA) for each hazard level for all geotechnical site classifications. Calculate the ratio of peak response to maximum ZPA, herein called BDS_{RATIO}.
6.) Construct EDS profiles for each hazard level and apply building amplification factors.

There is a need to standardize equipment certification practices for essential building applications such that equipment seismic resilience can be a transparent metric. Constructing code-based EDS profiles using common elements of regional hazard spectra will establish the needed objective measure for nonstructural equipment certification. To demonstrate the concept, EDS shape profiles are constructed for seventeen code provisions including: Argentina, Australia, Canada, Chile, China, Colombia, Europe, India, Indonesia, Japan, Mexico, New Zealand, Peru, Russia, Taiwan, Turkey, and United States.

Keywords: global, certification, equipment, testing, spectrum, demand.

1. INTRODUCTION

Nonstructural equipment installations are composed of two design elements: (1) equipment supports and attachments and (2) equipment items. Figure 1 displays an installation drawing showing typical electrical equipment installations highlighting the distinction between supports, attachments, and equipment items. OEM—original equipment manufacturer designed mounting brackets and use of specialized washers (e.g., Belleville conical spring washers) for anchorage are considered part of the equipment item. The OEM is responsible for seismic certification of equipment items. The construction site engineer of record or registered building design professional is responsible for certification of equipment supports and attachments. The focus of this paper is on certification of OEM equipment items (a.k.a. the black box).

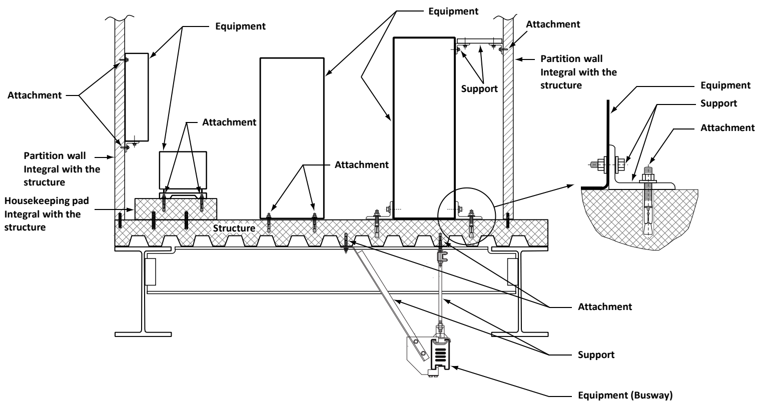

Figure 1. Drawing of equipment installations showing distinction between, supports, attachments and equipment item

Regional building codes and seismic design standards establish minimum earthquake protection requirements for building structures and the mechanical and electrical equipment that service buildings to make a building functional. Certain buildings are classified as essential or critical infrastructure and thus require a higher level of performance to resist earthquake demands. The mechanical and electrical systems servicing essential buildings have a higher level of conformance expectations compared to the systems contained in non-essential infrastructure. Building codes use the concept of an importance factor to designate which building systems and equipment inherit a higher level of performance requirements to resist earthquake demands. The modern-day trend for seismic conformance of "designated important equipment items" in essential infrastructure is certification via shake-table testing, which is the most explicit way to validate post-earthquake equipment functionality.

Model building code seismic provisions provide both a base shear force equation and response spectrum option for building structure design. Today, however, building codes do not include a response spectrum option for equipment certification testing and only include lateral and vertical force equations that are used to properly size equipment supports and attachments for anchorage integrity purposes. Thus, the need is to establish a globalized equipment demand spectrum that is used for equipment item certification via the seismic shake-table testing method.

Fundamentally, all seismic design codes and standards that contain provisions for earthquake resistance are formulated using the same earthquake engineering principles. On the surface country/region-specific codes appear quite different. However, once these codes are broken down into fundamental code constructs, there is great similarity between regional codes and standards, and this similarity provides the impetus to develop an equipment certification methodology that can be universally applied.

Seismic requirements, regardless of code origin, can be broken down into core constructs. These constructs include hazard mapping, site classification, building design response spectrum, and building amplification.

These are the building blocks for creating an equipment demand spectrum to be used for seismic certification testing and are discussed in the following sections. Table 1 identifies the regional building codes and seismic design standards that have been evaluated. These referenced codes reflect the current state editions as of the publication date of this paper.

Table 1. Referenced codes and standards used for seismic certification of nonstructural equipment

Country / Region	Code / Standard Reference ID
Argentina	INPRES-CIRSOC103
Australia	AS 1170.4-2007 AMDT 2:2018
Canada	2020 NBCC
Chile	NCh 433.Of1996
China	GB 50011-2010 (2016)
Colombia	NSR-10 Título A
Europe	Eurocode 8 EN1998-1
India	IS 1893 (Part 1) : 2016
Indonesia	SNI 1726:2019
Japan	Building Standard Law
Mexico	CFE MDOC-15
New Zealand	NZS 1170.5:2004 AMDT 1:2016
Peru	N.T.E. - E.030
Russia	СП 14.13330.2018
Taiwan	CPA 2011 Seismic Design Code
Turkey	TBEC-2018
United States	IBC 2018 / ASCE 7-16

2. Earthquake Hazard Mapping

Hazard mapping is defined as a methodology to prescribe the earthquake hazard risk as ground motion intensity that is a function of the building site's geographic location, site geotechnical classification and assumed earthquake return rate. Commonly referred to as an earthquake hazard map. This is the starting point for EDS development.

An abundance of science is focused on this code construct. As observed in the Figure 2 global seismic hazard map, the earthquake hazard does not respect country or regional boarders. The hazard is global in nature. However, code-based mapping is done country-by-country and region-by-region. The result may be the same, a hazard map used for building structural design, but the methodology to get the map will vary based on the science being applied for a given code.

Some codes use seismic zonal boundaries or micro-zones and provide maps and municipality tables to prescribe ground motion intensity factors and others use latitude-longitude coordinates in conjunction with accessing government geological survey websites. Some code maps are based on a more conservative earthquake return rate (e.g., 2,475 years) and other code maps may use a less conservative return rate (e.g., 476 years). In a perfect world there would be one hazard map covering the globe, today each code's earthquake hazard maps are slightly different but serve the same purpose to quantify the seismic risk at a construction site location.

The objective is to review each code's mapping scheme (i.e., zones, municipality tables, geographic coordinates or other methods) and determine the ground motion parameters that are associated with the various hazard levels. Appendix A provides a summary of the hazard mapping approach taken for each of the Table 1 codes.

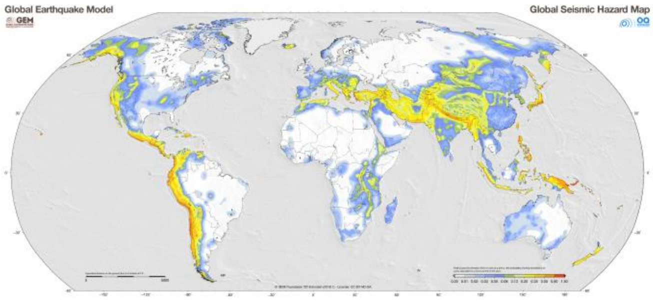

Figure 2. Global Earthquake Model (GEM) Seismic Hazard Map (version 2018.1 - December 2018) by M. Pagani, J. Garcia-Pelaez, R. Gee, K. Johnson, V. Poggi, R. Styron, G. Weatherill, M. Simionato, D. Viganò, L. Danciu, D. Monelli.

3. Site Geotechnical Classification

Site classification is defined as a geotechnical classification assigned to a construction site based on the types of soils present and their engineering properties. The properties of the rock and soil at a building site will affect the input shock wave as it travels from the seismic rupture source to the building foundation. Some locations may contain softer soils and other building sites may consist of harder soils or of bedrock. The site characteristics or soil classification at a building location is one of the common constructs that can be found in codes that contain provisions for earthquake protection.

Typically, there will be three to five rock/soil type categories and each type will affect the input shock wave differently. Thus, a code's earthquake hazard definition needs to account for the different soil/rock types by using site class adjustment factors that get applied to the seismic hazard values prescribed by the code's hazard map. These site class adjustment factors are either directly included in the site hazard response spectrum formulas or included as interpolation tables that get applied.

The assumption made here is to consider all site class adjustments and use the site class that results in maximum ground motion intensity at a construction site location. This conservative assumption ensures that conformance methods will satisfy any site location regardless of the code prescribed soil properties. Code provisions that support site-specific geotechnical analysis are excluded. Appendix A includes the various site classifications adopted by the Table 1 codes.

4. Site Hazard Spectrum

A code's site hazard spectrum is a seismic design response spectrum used for seismic design of buildings and other structures. The site hazard spectrum is typically a multi-stage spectrum (period vs. response acceleration) that is a function of ground motion intensity from earthquake hazard maps, site class factors, spectrum shape factors or formulas and in some cases other factors that are not related to ground motion. The other factors might include building importance factor or building structure response factor. The key is to isolate the factors that control "free-field" ground motion intensity. We want the unmodified, ground-level response spectrum that represents the earthquake hazard independent of the building structure (i.e., decoupled from structures) for a specified earthquake return rate.

The building importance factor should not increase the free-field ground motion. The building importance factor as related to the equipment servicing essential infrastructure implies that equipment should be shake-table tested to validate equipment functionality post seismic event. Likewise, the building response reduction factor (*R* factor) should not decrease ground motion. The assumption made here is to set any site hazard spectrum parameters that are not related to ground motion intensity set to unity. For simplification purposes, a code's free-field site hazard seismic design response spectrum is referred to herein as the BDS—building design spectrum.

The objective is to identify the maximum response acceleration ($BDS_{PEAK\ G}$) for all soil types contained in each building code's earthquake BDS for a given hazard level. Next, we need to identify the maximum ZPA (zero period acceleration) for all soil types. This is the response acceleration magnitude at zero period ($T = 0$) on the BDS. This point on the BDS is commonly referred to as the PGA or peak ground acceleration. The Figure 3 example BDS highlights the difference between maximum response acceleration ($BDS_{PEAK\ G}$) and PGA_{MAX} for the Chile Zone 3 hazard level [Chile NCh 433.Of1996, 2012].

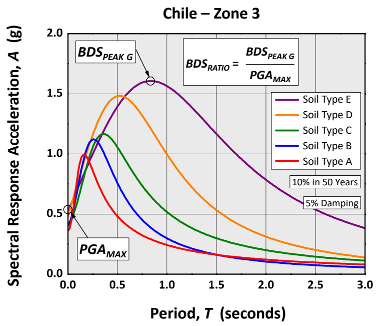

Figure 3. Chile Zone 3 hazard level BDS showing difference between $BDS_{PEAK\ G}$ and PGA_{MAX}

Next, the ratio of maximum BDS response ($BDS_{PEAK\ G}$) over PGA_{MAX} is calculated and is defined in Equation (1) as the BDS response ratio (BDS_{RATIO}). This ratio defines the EDS shape profile for a given code.

$$BDS_{RATIO} = \frac{BDS_{PEAK\ G}}{PGA_{MAX}} \tag{1}$$

The individual BDS assumptions for each Table 1 code and resulting BDS plots at maximum hazard levels are summarized in Appendix A.

5. Building Amplification

Building amplification is defined as the amplification of earthquake ground motion from the building foundation to building roof height based on the dynamic characteristics of building structures and properties of the earthquake shock wave.

The type of building construction will affect the input shock wave as it travels from the foundation, up the building structure, to a location where equipment may be attached. Some buildings are short and stiff and other buildings are taller and more flexible. Every unique building type will respond differently to the input shock wave resulting from seismic events. Equipment installed at building roof elevation will likely experience an amplified input as compared to equipment installed at ground level. Building amplification effects need to be included when constructing an equipment demand spectrum used for equipment certification.

With minor-to-moderate earth-shaking intensity, the building structure may remain linear elastic, and the resulting building amplification at roof elevation would likely be on the order of 3 to 4 times (or greater) the base input for long period structures. With moderate-to-severe shaking intensity, most building structures are designed to have a nonlinear response and will likely experience inelastic response reductions. In this case, the resulting building amplification at roof elevation would likely be on the order of 1 to 2.5 times the base input for long period structures.

The primary goal in equipment certification testing is to demonstrate the maximum seismic withstand capacity (i.e., resilience) for a given product line. This implies the ground motion target for equipment certification is to cover moderate-to-severe earthquake events. A conservative building amplification factor at roof elevation would be on the order of 1.5 to 2 times the base input when considering moderate-to-severe earthquake events. Limiting building amplification over the constant acceleration region will harmonize the EDS with building floor spectra research that reveals roof-level inelastic response reductions for moderate-to-severe earthshaking intensity [US NIST 2018].

The use of a 1.8x limit factor is adopted here for those building codes that do not contain explicit building amplification limit factors. For example, a 1.8x building amplification limit factor is greater than the 1.6x limit factor used today in equipment testing to satisfy the American ASCE/SEI 7-16, 2016 earthquake demands for equipment certification (AC156 test protocol). The ICC-ES AC156, 2020 test protocol has been in use since 2000 and increasing the building amplification limit factor to be greater than 1.6x is a conservative approach to equipment certification practices for essential building applications. The last step is to construct the EDS shape profiles for the Table 1 codes to use for seismic certification testing.

6. Equipment Demand Spectrum

The equipment demand spectrum is defined as a generic broadband response spectrum used for equipment shake-table testing that is a function of BDS parameters, $BDS_{PEAK\,G}$ and PGA_{MAX}, and building height ratio, z/h, for a given regional code or seismic design standard. The z/h height ratio has z as the height in structure at equipment location and h is the average roof height of structure relative to grade elevation. The z/h height ratio ranges from zero at ground to one at roof elevation. The resulting response spectrum is referred to herein as the code's equipment demand spectrum (EDS). The EDS is equivalent to a generic building floor spectrum.

We know the seismic shock wave is impacted by the type of soils present at the building site. We know the building structure will respond to the shock wave as it becomes input to the building foundation. How the building responds is dependent on the structural design and on the magnitude, location, and faulting mechanism of the earthquake, but it's also affected by wave propagation, input direction, velocity, frequency content, and duration of motion.

The bottom line is that it's not possible to pre-determine the exact dynamic characteristics of the earthquake shock wave that becomes input into installed equipment for a given building type at every site location on the globe. A deterministic approach to equipment seismic certification is simply not feasible, nor even possible. The only realistic approach is to apply stochastic principles as the basis for equipment certification.

The EDS should, therefore, be defined as a broadband spectrum using random multifrequency excitation to account for the random nature of earthquake demands. Figure 4 displays a typical random multifrequency input accelerogram used for equipment seismic testing. The total duration of the input motion is 30 seconds (nominal), with the non-stationary character being synthesized by an input signal build-hold-decay envelope as shown in the figure. Looking at this another way might help. If one had the ability to compile seismic records of past earthquakes for every type of building structure ever designed and for all floor elevations within these buildings, and then compile these records onto a single plot, one would likely discover that the resulting composite plot would look very random in nature. The Figure 4 accelerogram is intended to be a composite plot to cover the greatest number of potential earthquake records. The use of random multifrequency input is the only practical way to accomplish that intent and results in a conservative test input motion.

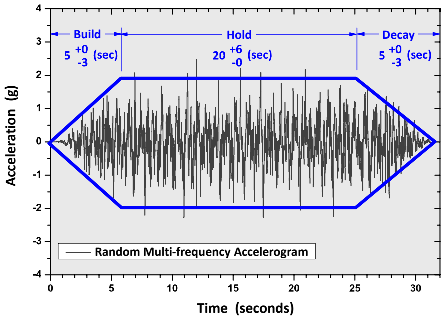

Figure 4. Seismic testing random multifrequency accelerogram used as shake-table drive signal input

The EDS in this sense, must be able to provide input energy content spanning over a wide frequency bandwidth (1 to 35 Hz) to cover the wide variability in geographic locations, building structure types and earthquake characteristics. The Figure 5 spectrum plot presents a generic EDS profile with response acceleration defined by two variables, A_{FLX} and A_{RIG}, and frequency break points defined by four variables, f_1 thru f_4. The EDS response acceleration variables, A_{FLX} and A_{RIG}, are defined in terms of the BDS parameters, $BDS_{PEAK\ G}$ and PGA_{MAX}, and building amplification factors, BA_{FLX} and BA_{RIG}, where the building height ratio, z/h, is either zero at ground level or one at roof elevation.

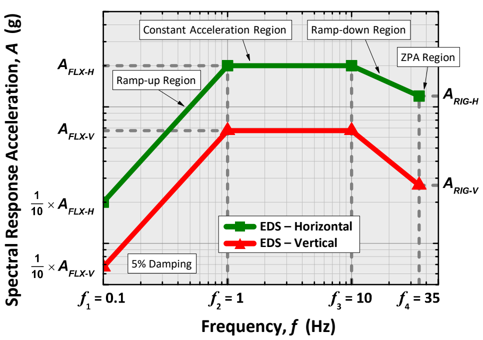

$$A_{FLX-H} = BDS_{PEAK\ G}\left(BA_{FLX}\right)$$

$$BA_{FLX} = \left(1+2\frac{z}{h}\right) \rightarrow \begin{matrix} BA_{FLX}\big|_{MAX} = 1.8 \text{ or} \\ BA_{FLX}\big|_{MAX} = 1.6 \end{matrix}$$

$$A_{RIG-H} = PGA_{MAX}\left(BA_{RIG}\right)$$

$$BA_{RIG} = \left(1+2\frac{z}{h}\right) \rightarrow BA_{RIG}\big|_{MAX} = 3.0$$

$$A_{FLX-V} = \frac{2}{3}\left(BDS_{PEAK\ G}\right)$$

$$A_{RIG-V} = \frac{2}{3}\left(PGA_{MAX}\right)$$

Figure 5. Generic equipment demand spectrum used for certification testing of electrical equipment

The horizontal EDS is limited over the constant acceleration region to be 1.8x ($BA_{FLX}|_{MAX} = 1.8$) or limited to 1.6x ($BA_{FLX}|_{MAX} = 1.6$) for those codes that have prescribed a 1.6x building amplification limit factor. Limiting building amplification accounts for structural inelastic response reductions for moderate-to-severe earthquake demands as noted in US NIST 2018. The constant acceleration region and ZPA region have been expanded compared to the ICC-ES AC156 spectrum to better envelope global BDS profiles. These are conservative modifications to an already conservative AC156 shake-table input spectrum.

The EDS, as described here, provides an objective measure for defining the earthquake demand on nonstructural equipment that service critical infrastructure. EDS shape profiles at ground and roof height elevations are constructed for each of the Table 1 codes. Appendix A, Figures A1 through A17 provide the EDS shape profiles for the Table 1 seismic codes. A global composite EDS can be constructed by enveloping the EDS profiles from the Table 1 codes and using the composite EDS as shake-table testing input for equipment certification. Table 2 summarizes the ground-level EDS parameters at maximum hazard levels for the regional codes sorted by PGA_{MAX} from highest to lowest.

Table 2. Key ground-level EDS parameters for regional codes at maximum hazard levels sorted by PGA_{MAX}.

Country / Region	Code / Standard Reference ID	$BDS_{PEAK\ G}$	PGA_{MAX}	BDS_{RATIO}
Canada	2020 NBCC	2.40	0.97	2.48
Turkey	TBEC-2018	2.41	0.96	2.50
Europe	Eurocode 8 EN1998-1	2.25	0.90	2.50
Russia	СП 14.13330.2018	2.04	0.82	2.50
Mexico	CFE MDOC-15	2.32	0.80	2.90
Indonesia	SNI 1726:2019	2.00	0.80	2.50
United States	IBC 2018 / ASCE 7-16	2.00	0.80	2.50
New Zealand	NZS 1170.5:2004 AMDT 1:2016	1.80	0.80	2.26
Australia	AS 1170.4-2007 AMDT 2:2018	2.21	0.78	2.21
China	GB 50011-2010 (2016)	1.40	0.63	2.22
Chile	NCh 433.Of1996	1.61	0.52	3.09
Colombia	NSR-10 Título A	1.25	0.50	2.50
Peru	N.T.E. - E.030	1.24	0.50	2.50
Japan	Building Standard Law	1.22	0.49	2.50
Taiwan	CPA 2011 Seismic Design Code	1.20	0.48	2.50
India	IS 1893 (Part 1) : 2016	0.90	0.36	2.50
Argentina	INPRES-CIRSOC103	1.05	0.35	3.00

7.Conclusions

By using the response spectrum method to construct a generic, broadband equipment demand spectrum as described herein, a common measuring stick can be implemented across different regional codes and standards. Equipment suppliers can provide seismic certificates of compliance that address country or region-specific earthquake requirements. No building-specific information is required, and certification levels are calculated at both grade and roof height elevations using the maximum peak response accelerations taken from country/region site hazard spectra based on a reference hazard level.

This approach results in a conservative test unit input excitation using random, multifrequency excitation. The method used to transform a country/region BDS requirement into an equipment test requirement (EDS) has been proven effective for over twenty years since industry adoption of ICC-ES AC156 to address the American ASCE/SEI 7 nonstructural earthquake provisions. Adopting this methodology to address other country and regional building codes/standards will render equipment certification a transparent activity that can be objectively approached at a global level. It is believed that with a clear understanding of the principles involved, there will be a well-defined path forward to establish consensus guidelines that can be globally implemented.

The appropriate global standard for capturing the logic presented in this paper would be contained in ISO 13033 [2013]. However, the fundamental difference between logic contained in ISO 13033 and that described herein is how the generic floor spectra are constructed. A nonstructural test spectrum should not be based on the flexibility or rigidity or overstrength of the nonstructural test specimen. The nonstructural test specimen will naturally respond to the broadband input excitation based on its dynamic characteristics. Thus, the nonstructural amplification factors ($k_{R,p,flexible}$ and $k_{R,p,rigid}$ from ISO 13033 Annex G) should not be used to define the input spectrum for nonstructural testing.

Think about it this way, if an equipment item is located outside the building anchored to a grade elevation concrete pad, the appropriate earthquake input for equipment testing is the free-field site hazard spectrum. And if an equipment item is anchored to a building floor up in elevation within the structure, the appropriate earthquake input is the free-field site hazard spectrum multiplied by a generic building amplification factor. The primary reason the building amplification factor is capped off at roof height elevation, over the constant acceleration region of the input spectrum, is to account for inelastic response reductions (i.e., *R* factors) in building structures under moderate-to-severe earthquake demands. The authors support a revision to ISO 13033 to include the EDS concepts presented herein.

REFERENCES

Argentina INPRES-CIRSOC103 (1991); *Argentinean Standards for Earthquake Resistant Constructions*; by the Ministry of Economy and Public Works and Services Argentina; 1991 Edition.

Australia AS 1170.4-2007 AMDT 2:2018 (2018); *Structural design actions, Part 4: Earthquake actions in Australia*; by the Council of Standards Australia; 2018 Edition.

Canada 2020 NBCC (2022); *National Building Code of Canada* 2020; by the National Research Council Canada; 2020 Edition.

Chile NCh 433.Of1996 (2012); *Earthquake resistant design of buildings*; by the National Institute of Normalization Chile; 2012 Edition.

China GB 50011-2010 (2016); *Code for Seismic Design of Buildings*; by the Ministry of Housing and Urban-Rural Construction of the People's Republic of China; 2016 Edition.

Colombia NSR-10 Título A (2017); *Colombian Regulation of Earthquake Resistant Construction*; by the Colombian Association of Seismic Engineering; 2017 Edition.

Europe Eurocode 8 EN1998-1 (2004); *Design of structures for earthquake resistance – Part 1: General rules, seismic actions and rules for buildings*; by the European Union Brussels; 2004 Edition.

India IS 1893 (Part 1) : 2016 (2016); *Criteria for Earthquake Resistant Design of Structures Part 1 General Provisions and Buildings* (Sixth Revision); by the Bureau of Indian Standards, New Delhi, India; 2016 Edition.

Indonesia SNI 1726:2019 (2019); *Earthquake Resistance Planning Procedures for Building and Non-building Structures*; by the National Standardization Agency—BSN, Jakarta, Indonesia; 2019 Edition.

Japan Building Standard Law (2016); *The Building Standard Law of Japan*; by the Building Center of Japan; 2016 Edition.

Mexico CFE MDOC-15 (2015); *Civil Works Design Manual, Earthquake design*; by the Electrical Research Institute, Federal Electricity Commission, Mexico; 2015 Edition.

New Zealand NZS 1170.5:2004 AMDT 1:2016 (2016); *Structural design actions, Part 5: Earthquake actions* – New Zealand; by the Council of Standards New Zealand; 2016 Edition.

Peru N.T.E. - E.030 (2016); *National Building Code, Earthquake-Resistant Design*; by the Ministry of Housing, Construction and Sanitation Peru; 2016 Edition.

Russia СП 14.13330.2018 (2018); *Construction in seismic areas*. Updated version of SNiP II-7-81*; by the Ministry of Construction of Russia; 2018 Edition.

Taiwan CPA 2011 Seismic Design Code (2011); *Seismic Design Code and Commentary for Buildings*; by the Construction and Planning Agency, Ministry of Interior Affair Taiwan; 2011 Edition.

Turkey TBEC-2018 (2018); *Turkey Buildings Earthquake Standard, Earthquake Principles for the Design of Buildings*; by the Disaster and Emergency Management Authority, Ankara, Turkey; 2018 Edition.

United States ICC (2018) *International Building Code*, International Code Council, USA.

United States ASCE (2016) ASCE 7-16: Minimum Design Loads for Buildings and Other Structures, American Society of Civil Engineers, Reston, Virginia, USA.

United States ICC-ES AC156 (2020); *Acceptance Criteria for Seismic Certification by Shake-Table Testing of Nonstructural Components*; by the International Code Council, Inc., Evaluation Service, Country Club Hills, Illinois, USA; 2020 Edition.

United States NIST, (2018). *Recommendations for Improved Seismic Performance of Nonstructural Components*, NIST GCR 18-917-43, by the Applied Technology Council for the National Institute of Standards and Technology, Gaithersburg, Maryland, USA.

Appendix A – Code Summaries at Maximum Hazard Levels

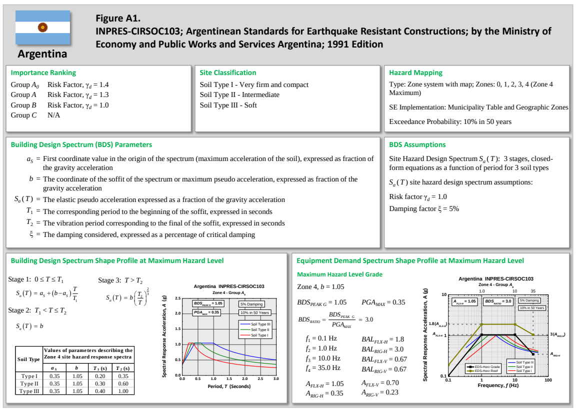

Figure A1.
INPRES-CIRSOC103; Argentinean Standards for Earthquake Resistant Constructions; by the Ministry of Economy and Public Works and Services Argentina; 1991 Edition

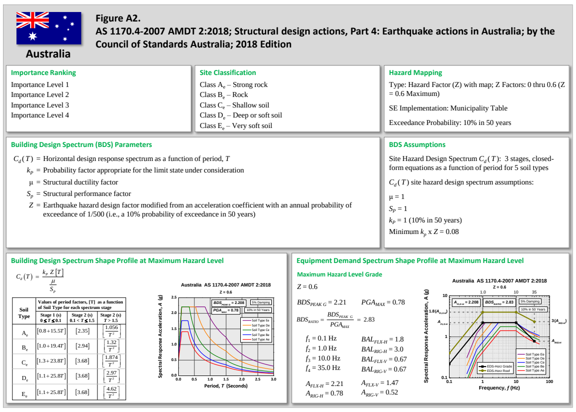

Figure A2.
AS 1170.4-2007 AMDT 2:2018; Structural design actions, Part 4: Earthquake actions in Australia; by the Council of Standards Australia; 2018 Edition

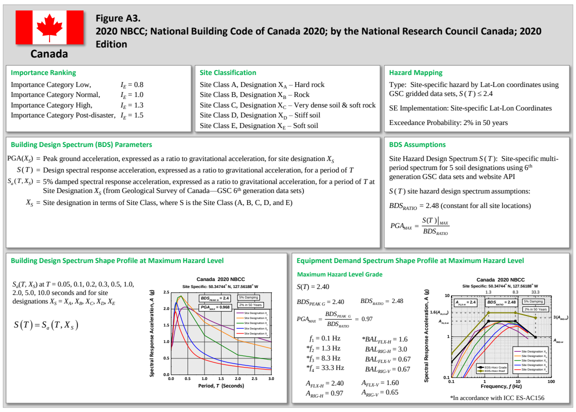

Figure A3.
2020 NBCC; National Building Code of Canada 2020; by the National Research Council Canada; 2020 Edition

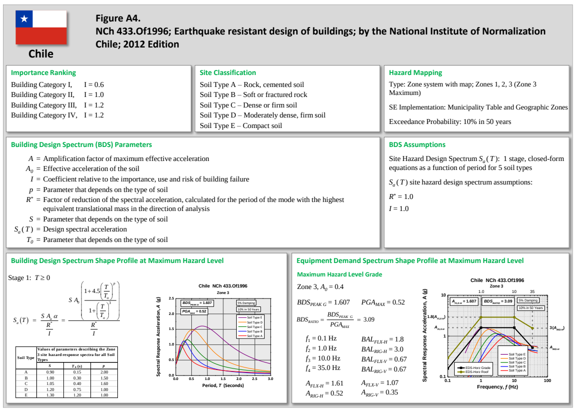

Figure A4.
NCh 433.Of1996; Earthquake resistant design of buildings; by the National Institute of Normalization Chile; 2012 Edition

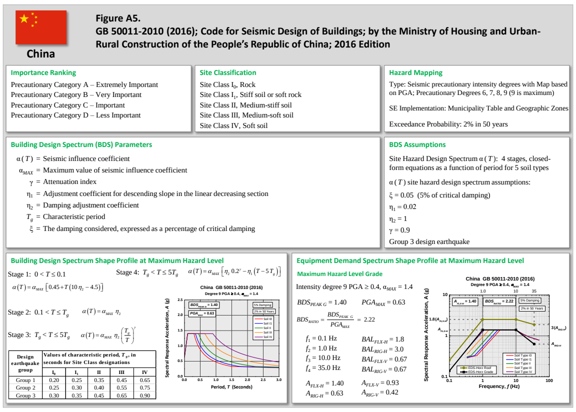

Figure A5.
GB 50011-2010 (2016); Code for Seismic Design of Buildings; by the Ministry of Housing and Urban-Rural Construction of the People's Republic of China; 2016 Edition

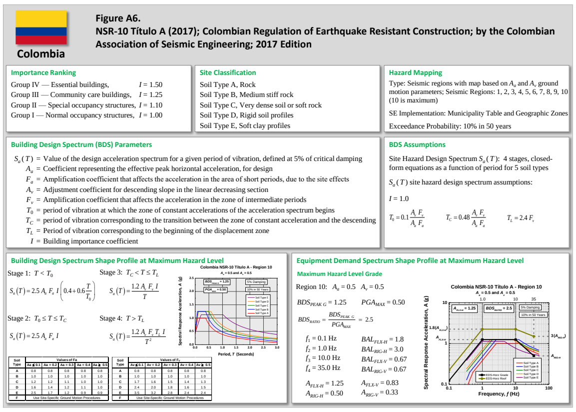

Figure A6.
NSR-10 Titulo A (2017); Colombian Regulation of Earthquake Resistant Construction; by the Colombian Association of Seismic Engineering; 2017 Edition

Appendix A – Code Summaries at Maximum Hazard Levels

European Union

Figure A7.
Eurocode 8 EN1998-1; Design of structures for earthquake resistance – Part 1: General rules, seismic actions and rules for buildings; by the European Union Brussels; 2004 Edition

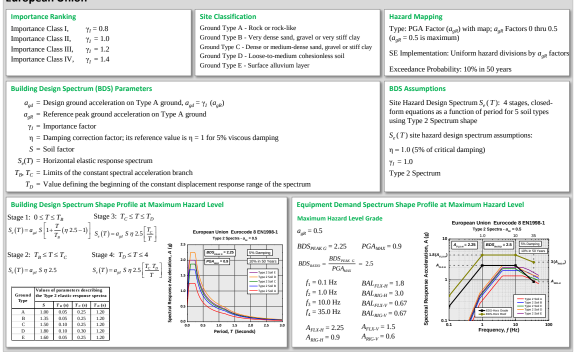

India

Figure A8.
IS 1893 (Part 1) : 2016; Criteria for Earthquake Resistant Design of Structures Part 1 General Provisions and Buildings (Sixth Revision); by the Bureau of Indian Standards, New Delhi, India; 2016 Edition

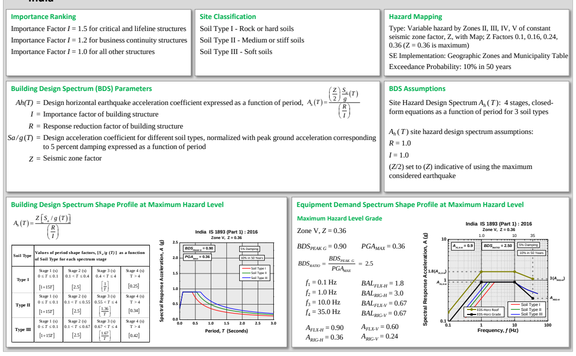

Indonesia

Figure A9.
SNI 1726:2019; Earthquake Resistance Planning Procedures for Building and Non-building Structures; by the National Standardization Agency—BSN, Jakarta, Indonesia; 2019 Edition

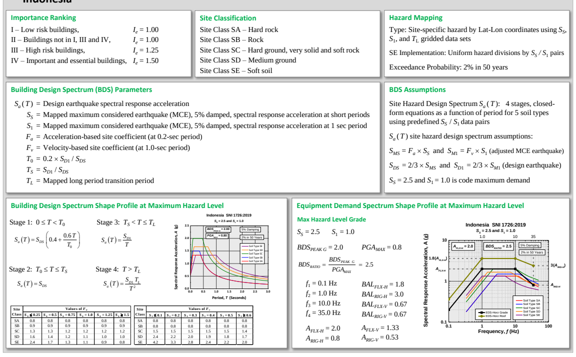

Japan

Figure A10.
Building Standard Law; The Building Standard Law of Japan; by the Building Center of Japan; 2016 Edition

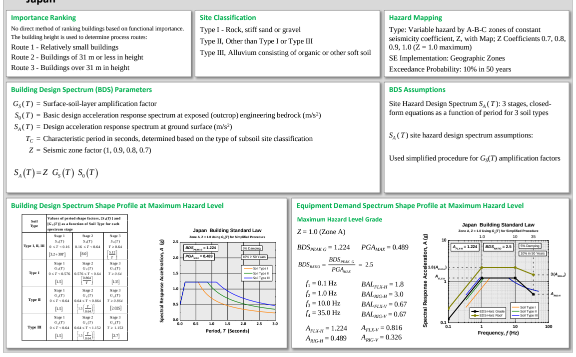

Mexico

Figure A11.
CFE MDOC-15; Civil Works Design Manual, Earthquake design; by the Electrical Research Institute, Federal Electricity Commission, Mexico; 2015 Edition

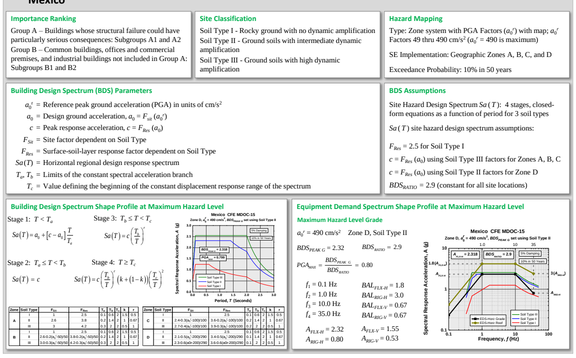

New Zealand

Figure A12.
NZS 1170.5:2004 AMDT 1:2016; Structural design actions, Part 5: Earthquake actions – New Zealand; by the Council of Standards New Zealand; 2016 Edition

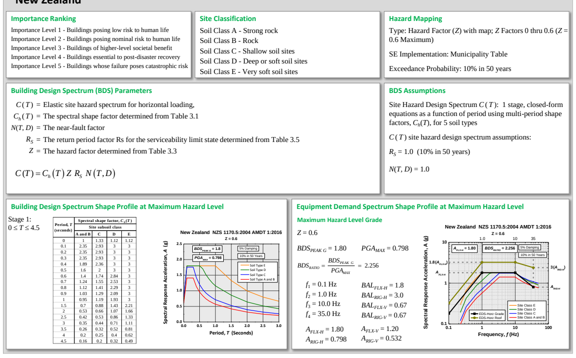

Appendix A – Code Summaries at Maximum Hazard Levels

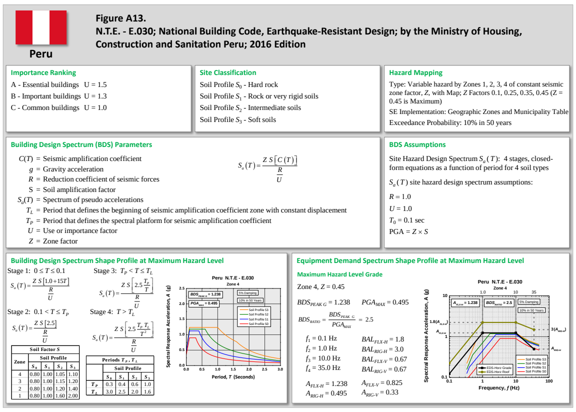

Figure A13.
N.T.E. - E.030; National Building Code, Earthquake-Resistant Design; by the Ministry of Housing, Construction and Sanitation Peru; 2016 Edition

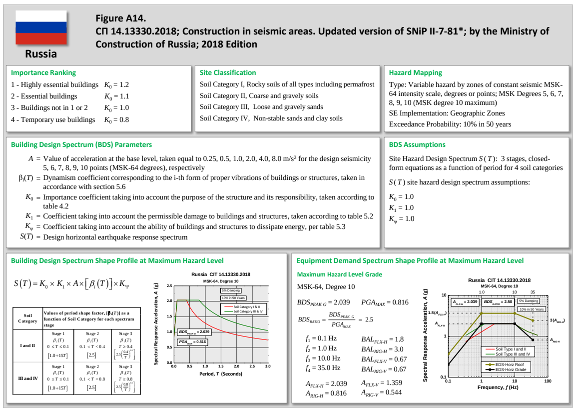

Figure A14.
СП 14.13330.2018; Construction in seismic areas. Updated version of SNiP II-7-81*; by the Ministry of Construction of Russia; 2018 Edition

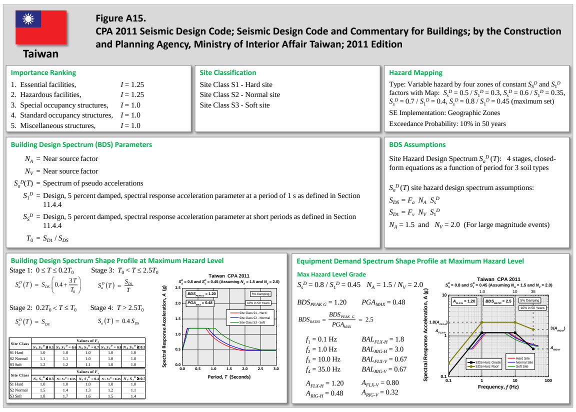

Figure A15.
CPA 2011 Seismic Design Code; Seismic Design Code and Commentary for Buildings; by the Construction and Planning Agency, Ministry of Interior Affair Taiwan; 2011 Edition

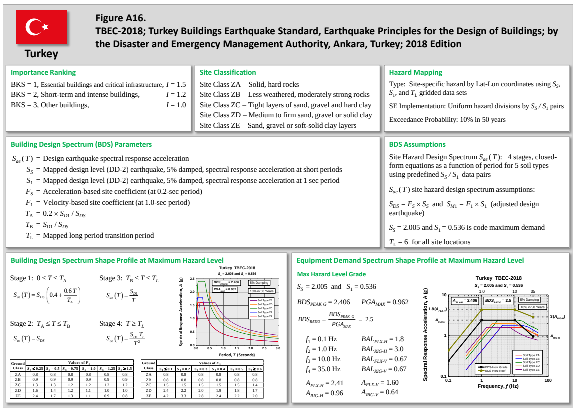

Figure A16.
TBEC-2018; Turkey Buildings Earthquake Standard, Earthquake Principles for the Design of Buildings; by the Disaster and Emergency Management Authority, Ankara, Turkey; 2018 Edition

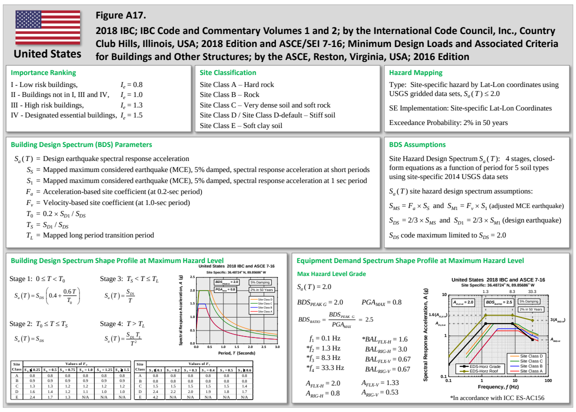

Figure A17.
2018 IBC; IBC Code and Commentary Volumes 1 and 2; by the International Code Council, Inc., Country Club Hills, Illinois, USA; 2018 Edition and ASCE/SEI 7-16; Minimum Design Loads and Associated Criteria for Buildings and Other Structures; by the ASCE, Reston, Virginia, USA; 2016 Edition

Equipment Seismic Performance in the General Docente Ambato Hospital, Ecuador

Oscar S. Sarmiento[1] and Ana G. Haro[2]

[1] Universidad de las Fuerzas Armadas ESPE, Civil Engineering
Av. General Rumiñahui and Ambato, Sangolquí, Ecuador
e-mail: ossarmiento@espe.edu.ec
[2] Universidad de las Fuerzas Armadas ESPE, Earth Sciences and Construction Department
Av. General Rumiñahui and Ambato, Sangolquí, Ecuador
agharo@espe.edu.ec

Abstract. The M 7.8 Muise, Ecuador Earthquake on April 16, 2016, mainly affected Ecuador's central coast, causing meaningful lives and economic losses. Furthermore, this seismic event evidenced critical disruptions in essential facilities throughout the province and cantonal capitals for weeks and months. Indeed, hospitals did not remain operational due to nonstructural components and content damage and did not meet the community's needs. In order to encourage building re-occupancy and functional recovery-based assessment of existing health care facilities in Ecuador, the dynamic response of the General Docente Ambato Hospital located in the central mountains region of Ecuador is established to assess the performance of its most critical equipment. For this purpose, a numerical model of the structure was subjected to the MCE and a representative acceleration record. Once the floors' dynamic responses were processed and transmitted to the selected equipment, their behavior was analyzed through rigid body rocking motion models developed in the past. The results show that the building and its content would suffer severe damage if seismic mitigation strategies were neglected.

Keywords: Damage in hospitals, Hospital equipment seismic response, Rigid body rocking motion.

1. INTRODUCTION

Hospitals are structures that provide essential services to the population, such as safeguarding the well-being and health of citizens. During and after disasters, the provision of these services is of vital importance. The slightest failure in hospital systems and equipment can seriously affect its functionality due to the complexity of hospital operations, making hospitals extremely vulnerable to various natural hazards [FEMA 577, 2007].

The equipment and nonstructural elements of a building can represent a threat to the integrity and life of its users, an economic loss, and a total or partial interruption of its functions. An example of the aforementioned is the Northridge earthquake in 1994, which caused the partial or total suspension of services in 23 hospitals and $3 billion in hospital-related damage [FEMA E-74, 2012].

On April 16, 2016, one of the worst seismic events in the history of Ecuador occurred. This earthquake, with a magnitude of 7.8 on the Richter scale, left a balance of 663 dead and 9 missings and severe damage to elements that make up the country's health network, such as hospitals, clinics, and health centers.

Approximately 8% of the hospital's total cost goes to structural elements. The remaining 92% of the cost goes to nonstructural components and systems: mechanical, electrical, plumbing, architectural, and medical. Indeed, the most significant capital investment in the construction of a hospital is allocated to its nonstructural elements and equipment [Whittaker & Soong, 2003].

Due to this, it is necessary to protect not only the structural elements of a hospital but also its nonstructural elements and equipment, to guarantee that the hospital can fulfill its functions with continuous service to the community. Therefore, during the last century, various investigations have been carried out on the behavior of nonstructural elements and equipment of a building to reduce the risks that these types of elements can generate within a building.

During the last 100 years, the behavior of simply supported rigid blocks on a surface has been studied; Milne in 1885 and Housner in 1963 are the pioneers on this subject. They estimated critical conditions for overturning and generated models of the behavior of a rigid block exposed to a horizontal movement at its base. Subsequently, to generate new models with a greater scope, several studies have been carried out to identify and improve the initial models' limitations [Jaimes et al., 2018].

Spanos et al. [2017] showed that the probability of block toppling depends not only on the geometry of the block and the foundation material but also on the dynamic soil parameters that characterize the random base excitation, leading, in some cases, to conflicting answers. Therefore, if the choice of a foundation material is of interest to protect a block from landslides, a complete numerical analysis must be carried out to properly assess the probability of collapse of that specific block [Spanos et al., 2017].

Estimates show that the earthquake of February 27, 2010, in Chile caused damage of up to USD 30,000 million. The health sector was affected, with 25 establishments seriously damaged, initially estimated at $3.6 billion in direct losses. In 160 seconds, 4,200 beds were lost out of the 26,500 managed by the public sector [Alberto Maturana, 2011].

Anagnostopoulos et al. [2019] present a new and compact mathematical formulation to describe the dynamic roll response of single and double-block systems subjected to gravity and ground excitation. The derived equations describing the impact modes are equivalent to the Housner-derived expression and depend on the angular velocity of the blocks before impact. The integrated model is finally applied to produce normalized rollover maps for double-block systems subjected to single-pulse sinusoidal inputs, revealing the existence of fractal-like behavior. This previously unsuspected feature of multi-block systems is reminiscent of the chaotic behavior exhibited by a classical double pendulum, which suggests that the risk of tipping over can only be probabilistically assessed.

The seismic response of statues with these different boundary conditions varies widely, so accurate characterization is critical. Experimental modal analysis and system identification were carried out on six statues while installed at the Asian Art Museum in San Francisco, California. The statues tested were large, made of stone, and constrained by different comparison mechanisms. Statue-pedestal support systems were quite flexible, with natural frequencies as low as 3 Hz. However, specific systems, which incorporated an embedded base of the statue, were much more rigid, with frequencies around 14 Hz. It should be noted that this type of test requires significant contact and excitation for the statues [Wittich & Hutchinson, 2016].

Simoneschi et al. [2018] developed an active control algorithm based on the post-placement method for rigid blocks from a description of the rocking movement through linearized equations. This approach is an excellent approximation for thin rigid blocks for which the linearized equations can completely describe the rolling motion due to the smallness of the tilt angle. The first analysis revealed the excellent robustness of the control algorithm to a variation of the sampling time and the delay of the actual control devices. In addition, subsequent parametric analyses indicated the proposed control algorithm's effectiveness in reducing the roll angle and protecting against overturning, as well as in the case of blocks with low slenderness. Overturning spectra are obtained in the rigid block case with and without active control.

Zhang & Makris [2001] examined the transient oscillation response of independent rigid blocks subjected to physically achievable trigonometric pulses. Further, this paper shows that under cyclic pulses, an autonomous block can tip over in two ways: (1) exhibiting one or more impacts; and (2) exhibiting no impact. The second mode results in a safe region in the acceleration frequency plane above the minimum overturning acceleration spectrum. Finally, this article concludes that the nonlinear sensitive nature of the problem, in association with the safe region encompassing the minimum overturning acceleration spectrum, further complicates the estimation of the maximum ground acceleration by examining only the objects' geometry regardless of whether it overturned or survived an earthquake.

Bakhtiary & Gardoni [2016] present a probability model to predict the maximum rotation of oscillating bodies exposed to seismic excitations given particular measurements of earthquake intensity. After that, instead of using an iterative solution, which has come to be flawed, a new approximate technique is developed by finding the most representative ground motion intensities. This probabilistic model with the approximate capacity of the wobble blocks is used to estimate the fragility curves of the wobble blocks with specific geometric parameters. Finally, a complete and practical form of fragility curves for design purposes is provided, along with numerical examples.

Berto et al. [2018] compared different methods to evaluate the probability of swinging and overturning independent elements under the action of ground motions of given intensities. First, the main differences between these methods are highlighted and validated based on experimental tests available in the literature using actual seismic records. Then, the different stability criteria are used to obtain overturning stability graphs based on conventional spectra assumed by Eurocode 8. Finally, some considerations are given on each method's applicability conditions.

Highly nonlinear differential equations describing the complex roll and slip instability of a set of multi-rigid blocks freely on the ground under horizontal ground motion are derived analytically using an energy variation approach. It was shown that a minimal slip in a set of two rigid blocks could cause a significant increase in the minimum amplitude of the ground acceleration (considerably stabilized setting). Qualitative analysis also demonstrated that the number of configuration patterns to be examined could be substantially reduced, limiting the computational effort. In addition, some new findings for the roll-slip response for rigid one-block systems are also presented that contribute to the roll-slip analysis of multi-rigid block assemblies [Kounadis, 2018].

Multi-story buildings may have a valuable inventory of items that could be damaged during an earthquake and cause unacceptable losses. Building contents are often modeled as equivalent oscillating rigid blocks. At the same time, their dynamic response depends on the object's geometry, the building's characteristics, and the floor on which the object is located. Vulnerability, risk, and content loss assessment of multi-story buildings have been discussed, which is a complicated task since the response of the block and the structure are coupled, the former being sensitive to acceleration and the latter sensitive to drift. We first discuss a performance-based seismic evaluation framework for sway-block objects. Our risk assessment framework is based on nonlinear response history analysis, while simplified approaches using nonlinear static transfer methods are also possible [Fragiadakis et al., 2017].

According to Vassiliou et al. [2017], to use rocking as a seismic response modification strategy in both directions of seismic excitation, a three-dimensional (3D) rocking model must be developed. This article examines the three-dimensional motion of a bounded rigid cylinder that rises and maintains the rocking and wobbling motion (unstable rocking) without slipping out of its initial position (i.e., a three-dimensional inverted pendulum). First, the modes of cylinder motion are identified and presented. Then, 3D oscillation and oscillation earthquake response spectra are constructed and compared with classical 2D oscillation earthquake response spectra. The 3D-constrained oscillating earthquake response spectra for the considered ground motions appear to have an elementary linear form. Finally, a 2D sway model can lead to unacceptable and unconservative estimates of the 3D sway and sway seismic response.

This research seeks to better understand the behavior of equipment in the "Hospital Docente Ambato" during a seismic event because this type of structure is of vital importance and must be in continuous operation before, during, and even after being affected by an earthquake to continue assisting emergencies and serving the community.

2. METHODOLOGY

A data collection and preliminary analysis of the hospital structure is carried out; for this, it is necessary: a record of accelerations, and a response spectrum, which are representative of the study area and are consistent with the type of structure analyzed.

Information is gathered about the hospital equipment, considered as rigid blocks. From the obtained results, modeling is developed to approximately predict the behavior of each piece of equipment, subject to different excitations and using different analysis models.

2.1 DESIGN SPECTRA

According to the study by Aguiar & Rivas [2018], the analyzed hospital is located on type D soil, for which the spectra with probabilities of exceedance of 2%, 5%, and 10% in 50 years were determined. Figure 1 shows the Maximum Considered Earthquake (MCE) with a probability of exceedance of 2% in 50 years and a return period of 2475 years derived from the acceleration response spectrum defined in the Ecuadorian Seismic Code [NEC-SE-DS, 2015]. This shape obeys the structural characteristics of the hospital, geological properties, hospital location, and the hospital performance objective to continue operating before, during, and after an extreme earthquake.

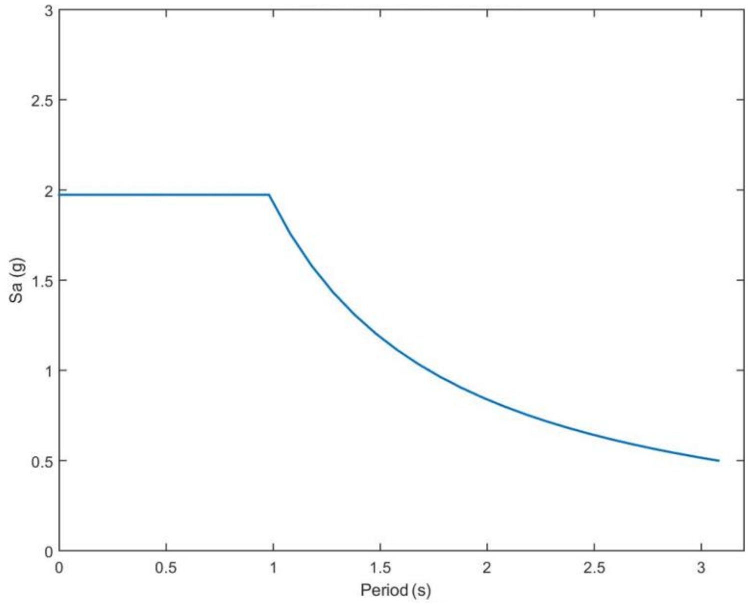

Figure 1. Maximum Considered Earthquake

2.2 SCALED ACCELEROGRAM

Aguiar & Rivas [2018] determined the geological faults capable of generating a high and moderate seismic hazard for the city of Ambato. Based on these failures, a search for acceleration records is performed in the PEER Ground Motion Database, with characteristics similar to those present at the study site. The acceleration record of the 1994 Northridge earthquake recorded at the Santa Monica station was selected, and scaling of this record was performed based on the MCE spectrum. Finally, a new scaled acceleration record is obtained, which is presented in Figure 2.

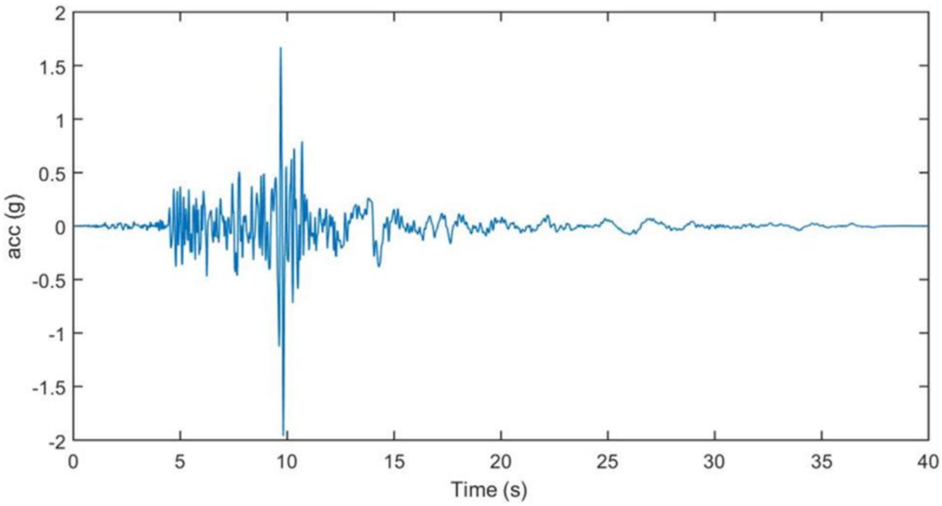

Figure 2. Scaled acceleration record

2.3 BUILDING UNDER ANALYSIS

The hospital, one of the most important in the central highlands of Ecuador, has 336 beds and 54 different areas, including Hospitalization, Imaging, Emergency, Intensive Care, Pharmacy, Surgery, Gynecology, Cardiology, and Psychiatry, among others. The Army Corps of Engineers retrofitted it in 2014 with the central government's investment of USD 38,997,111. The hospital structure consists of three steel blocks, A, B, and C, reinforced with diagonal stiffening elements. The numerical modeling phase was carried out from the structural drawings of the hospital.

The equipment behavior was carried out for block B of the hospital because it is where the most crucial equipment is located, as shown in Figure 3. This block has 5m and 7.5m spans, with mezzanine heights of 4.5m, with a total of 4 stories. It is a structural braced frame system; the entire structure is built in A36 steel.

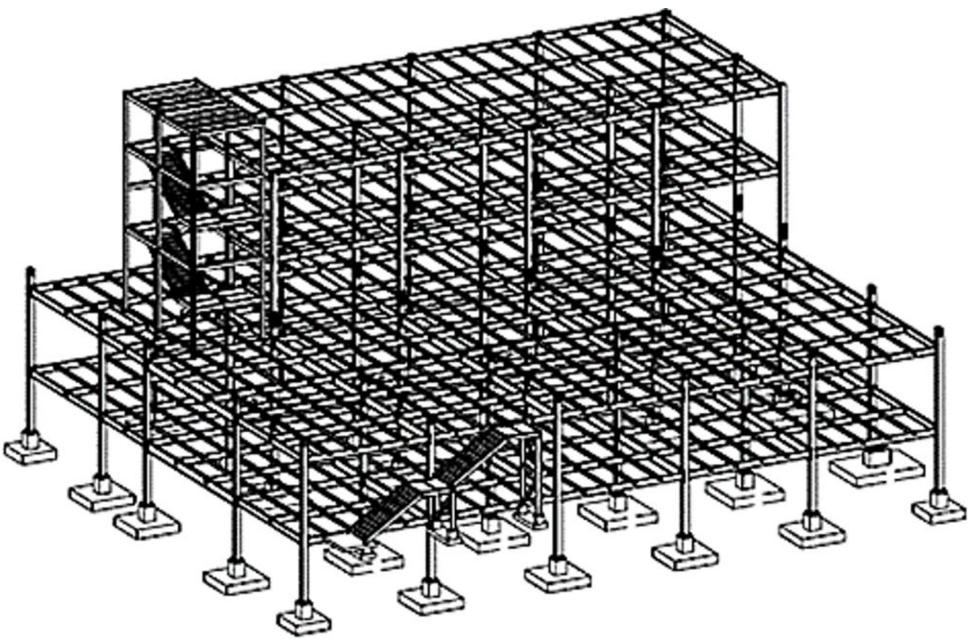

Figure 3. Block B

Sarmiento [2021] performed a linear dynamic structural analysis using the response spectra associated with different exceedance probabilities; each block's inelastic drifts were obtained.

Figure 4 shows the inelastic time history response accelerations at each floor for the structure subjected to the scaled ground motion presented in Figure 2.

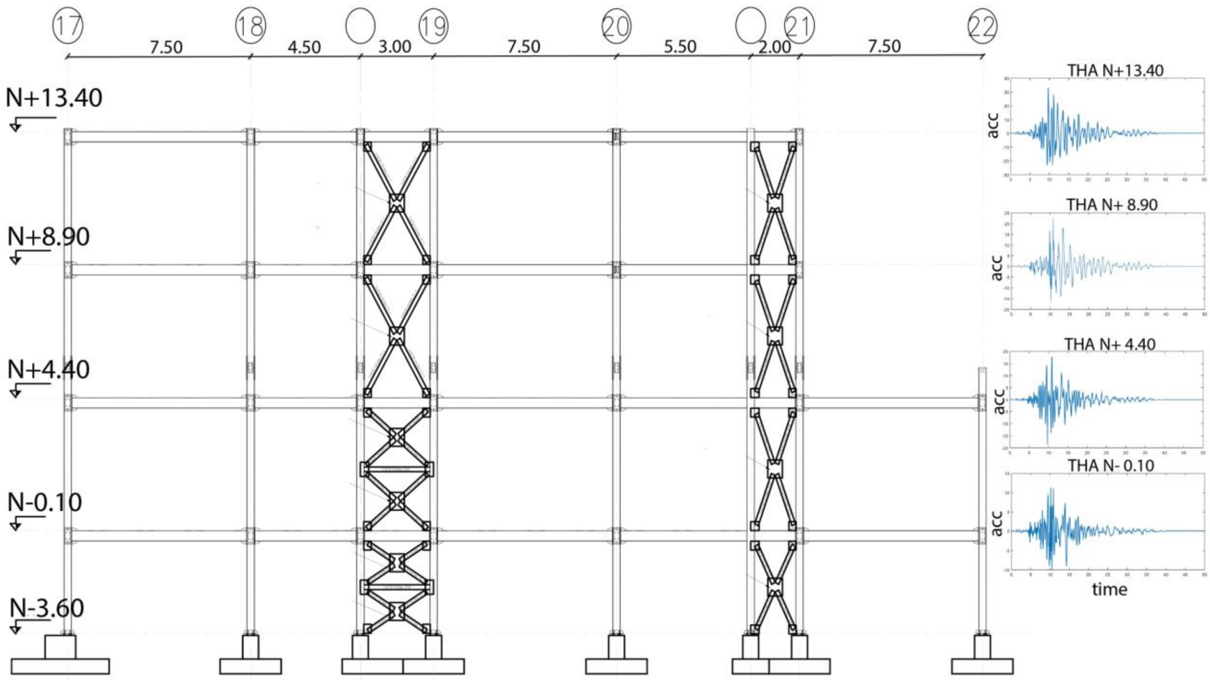

Figure 4. Story Time History Response

2.4 DYNAMIC RESPONSE OF RIGID BODIES

As shown in Figure 5, the rocking of a rigid body occurs when a horizontal excitation of sufficient magnitude is applied to the body, and it begins to rock. The body oscillates between its centers of rotation, points O and O'; if it does not overturn, it continues to rock until it stops [Reinoso *et al.*, 2019].

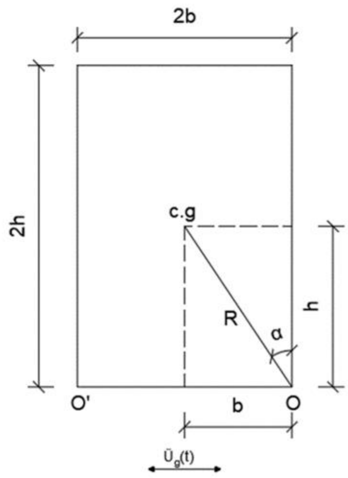

Figure 5. Rigid body model

2.5 OVERTURNING CONDITIONS

A piece of equipment modeled as a rigid body is rocking when it rotates around one of its vertices or centers of rotation and rises. The rocking motion is generated when the inertial force's magnitude of the overturning moment, and the induced rotation caused by excitation in the equipment, are greater than the resistant moment, which depends on the weight of the block [Jaimes *et al.*, 2018].

2.6 CONSIDERED MODELS

2.6.1 George W. Housner Model

Housner [1963] establishes that a rigid body could be modeled, as shown in Figure 5. Based on each body's geometric characteristics, a body's performance is analyzed when it is subjected to different pulses, such as a ground velocity pulse, a square pulse, and a sinusoidal pulse that simulates the movement of the ground generated by an earthquake. For each pulse, equations are generated in which minimum dimensions are defined so that the rigid body does not overturn.

2.6.2 Makris & Roussos Model

Makris & Roussos [1998] consider three acceleration pulses generated by an earthquake and present equations developed for each type of pulse: the cycloidal pulse Type A, Type B, and Type C*n*, where *n* represents the number of cycles of the pulse. The outline of the proposed procedure is to estimate the level of a given ground movement, which is necessary to tip a piece of equipment, based on the model described by Housner [1963]. According to Makris & Roussos [1998], the equipment overturns due to a ground motion when the acceleration to which the equipment is subjected is greater than the acceleration it resists.

2.6.3 Yuji Ishiyama Model

Ishiyama [1982] has studied the conditions for the overturning bodies when these are subjected to horizontal and sinusoidal movements. When a body on a floor is subjected to earthquake excitation, if the excitations become large enough, the body may rock, jump, or start a combination of these movements. Two factors must be taken into account: the horizontal acceleration and the velocity of the floor as criteria for overturning bodies. Also, Ishiyama [1982] presents equations that define the lower limits for acceleration and velocity to overturn a body. Also, it was noticed that the overturning of bodies is slightly affected by the ratio b/h, body size, or surface kinetic coefficient between the body and the surface.

2.7 Selection of Medical Equipment

The equipment analyzed was selected considering the economic value, weight, dimensions, and functioning performed within the hospital; a sample of this equipment is detailed in Table 1. The dimensions correspond to the diagram's nomenclature in Figure 5. Despite the manufacturer's indications and elements, no equipment has anchoring or fastening systems, so they are considered simply supported bodies.

Table 1. Sample of Selected Equipment

Number	Equipment	b (m)	h (m)	Weight (Kg)	Level	Photo
1	Tomograph	0.95	0.90	1200	N-0.10	
2	Autoclave machine	0.5	0.98	2450	N-0.10	
3	X-Ray equipment	0.24	0.70	86	N-0.10	
4	Osmosis plant	0.4	0.75	190	N+4.40	
5	Softening filters	0.25	0.90	300	N+4.40	

6	Recirculation tank	0.53	0.98	5000	N+4.40	

3. RESULTS AND DISCUSSION

When subjected to the different design spectra, Block B depicts lateral displacements such that the drift values are close to 5% for the MCE spectrum, which means severe damage to its structure, nonstructural elements, and operating impairments. Figure 6 shows the inelastic drifts for each hospital block, associated with the different response spectra, with probabilities of exceedance of 2%, 5%, and 10% in 50 years.

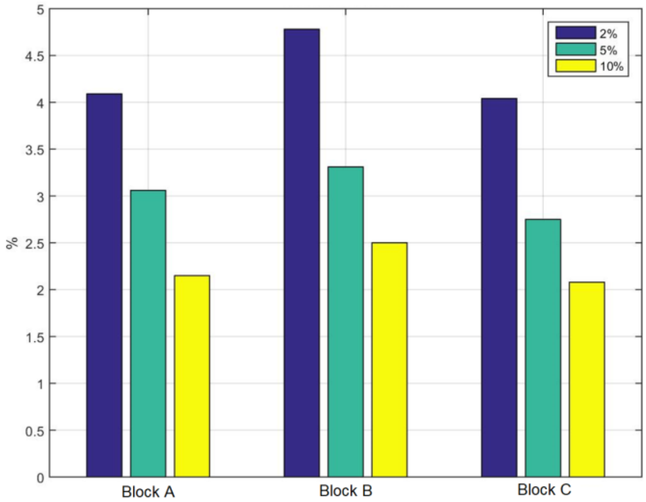

Figure 6. Inelastic drifts by block

The hospital blocks exhibit more significant inelastic drifts as the seismic hazard increases, reaching values close to five percent in Block B, for the MCE earthquake, with a two percent probability of exceedance in 50 years (2% in Figure 6). Maximum absolute accelerations and velocities at each story, subjected to the MCE, and the scaled accelerogram, are presented in Table 2, as well as the period and type of pulse for each corresponding analysis model. The fundamental period for Block B was 1.36 s.

Table 2. Accelerations, velocities, and periods for each story (Block B)

Level	Sa (m/s^2)	T(s) Makris model	Pulse type Housner model	T(s) Housner model	V (m/s) Ishiyama model
N+13.40	33.18	0.53	Cn	0.9	3.48
N+8.90	22.58	0.61	Cn	0.8	2.81
N+4.40	17.68	0.67	A	0.6	2.25
N-0.10	11.35	0.4	B	0.2	1.68

3.1 Equipment Performance

For this study, 20 medical equipment items were selected, including those presented in Table 1 and other items with less economic value but also relevant for the hospital's operations, such as UPS, patient monitors, hemodialysis equipment, ultrasound equipment, and water storage tank. These objects were analyzed depending on their location and distribution at each level.

Figure 7 shows three responses for the MCE corresponding to each model, representing the percentage of the total equipment at each level that would overturn. This graph shows that the equipment on higher levels subjected to larger accelerations would overturn with greater incidence than those on lower levels.

The responses depend on the considered models. For example, the overturning bodies response employing the Housner [1963] model and the Ishiyama [1982] model were the same, whereas the Makris & Roussos [1998] model is quite different. However, the three models report an 80% overturning probability for the hospital equipment located above level N+4.40. Indeed, several essential pieces of equipment would start rocking until overturning.

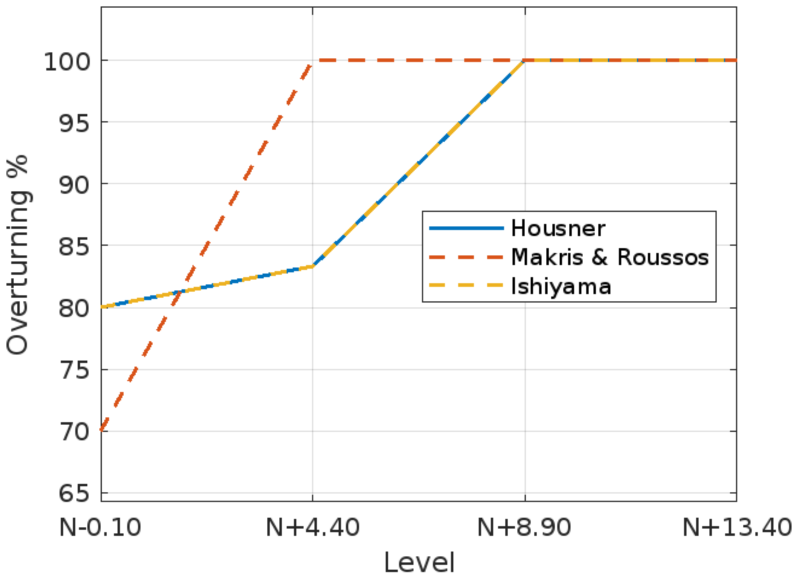

Figure 7. Overturning percentage by story level

4.CONCLUSIONS

A crucial block within a hospital in the inter-Andean region of Ecuador was selected to analyze its structural behavior by simulating a strong earthquake. An MCE response spectrum was considered due to the hospital performance objective. Engineering demands were obtained, such as drifts, accelerations, and velocities. Several medical devices were selected based on their importance within the hospital, and their behavior subject to MCE was analyzed. The equipment was modeled as rigid bodies based on three studies developed in the past about overturning rocking bodies. Relatively similar results were obtained for the equipment located above the first floor level.

For the MCE earthquake, hospital drift values close to 5% are reported, which indicates that the structure and nonstructural elements would suffer severe damage if this earthquake occurred. The equipment selected for this study reported a high probability of overturning, which represents a threat to the hospital's operation and its users' safety, affecting equipment and systems as necessary as the drinking water system, tomography equipment, radiography, and hemodialysis.

The equipment was subjected to different accelerations according to its hospital location. Those on higher levels are the most affected by earthquakes. Above level N+4.40, the equipment overturns with more than 80% for the Housner and Ishiyama models, while 100% for the Makris & Roussos model. Consequently, damages and interruptions arise opposite to the desired continuous functionality.

This study shows the importance of structural and nonstructural element analyses, which has been underestimated in Ecuador until today, especially for buildings requiring continuous functioning before, during, and after significant earthquakes. Indeed, if an MCE or a design-level earthquake occurs, the analyzed hospital would report severe damage, generating extreme failures and interruptions in its operation. Therefore, immediate attention is necessary to reduce the assessed overturning effects.

REFERENCES

Aguiar, R., Rivas, A. [2018] "Microzonificación sísmica de Ambato," *Instituto Panamericano de Geografía e Historia*, Quito, Ecuador.

Alberto Maturana, P. [2011] "Evaluación de riesgos y gestión en desastres. 10 preguntas para la década actual, " *Revista Médica Clínica Las Condes*, Vol. 22, No. 5, pp. 545–555.

Anagnostopoulos, S., Norman, J., Mylonakis, G. [2019] "Fractal-like overturning maps for stacked rocking blocks with numerical and experimental validation," *Soil Dynamics and Earthquake Engineering*, Vol. 125, 105659.

Bakhtiary, E., Gardoni, P. [2016] "Probabilistic seismic demand model and fragility estimates for rocking symmetric blocks," *Engineering Structures*, Vol. 114, pp. 25–34.

Berto, L., Rocca, I., Saetta, A. [2018] "Vulnerability assessment methods for rocking and overturning free-standing elements," *Soil Dynamics and Earthquake Engineering*, Vol. 110, pp. 121–136.

Carlos Zúñiga, S. M. [2010] "Hemodiálisis en tiempo de terremoto informe desde la región del biobío-chile," *Revista Médica Clínica Las Condes*, Vol. 21, No. 4, pp. 638–643.

FEMA 577 [2007] *Design Guide for Improving Hospital Safety in Earthquakes, Floods, and High Winds: Providing Protection to People and Buildings*, FEMA, USA.

FEMA E-74 [2012] *Reducing the Risks of Nonstructural Earthquake Damage*, FEMA, USA.

Fragiadakis, M., Kolokytha, M., Diamantopoulos, S. [2017] "Seismic risk assessment of rocking building contents of multistorey buildings," *Procedia Engineering*, Vol. 199, pp. 3534–3539.

Housner, G. W. [1963] "The behavior of inverted pendulum structures during earthquakes," *Bulletin of the Seismological Society of America*, Vol. 53, No. 2, pp. 403–417.

Ishiyama, Y. [1982] " Motions of rigid bodies and criteria for overturning by earthquake excitations," *Earthquake Engineering & Structural Dynamics*, Vol. 10, pp. 635–650.

Jaimes, M., Fernández-sola, L., Arredondo, C., Reinoso, E. [2018] "Dynamic Rocking Behavior Of Freestanding Symmetrical Rigid Blocks Considering Dynamic Soil-Structure Interaction," *Revista Técnica de la Facultad de Ingeniería Universidad del Zulia*, Vol. 39, No. 3, pp. 112–120.

Kavvadias, I. E., Papachatzakis, G. A., Bantilas, K. E., Vasiliadis, L. K., Elenas, A. [2017] "Rocking spectrum intensity measures for seismic assessment of rocking rigid blocks," *Soil Dynamics and Earthquake Engineering*, Vol. 101, pp. 116–124.

Kounadis, A. N. [2018] "The effect of sliding on the rocking instability of multi-rigid block assemblies underground motion," *Soil Dynamics and Earthquake Engineering*, Vol. 104, pp. 1–14.

Makris, N., Roussos, Y. [1998] *Rocking Response and Overturning of Equipment Under Horizontal Pulse-Type Motions*, Pacific Earthquake Engineering Research Center, USA

NEC-SE-DS [2015] *Peligro Sísmico Diseño Sismo Resistente*, Norma Ecuatoriana de la Construcción, Ecuador.

Reinoso, E., Arredondo, C., Ramos, S. [2019] "Curvas de volteo asociadas a medidas referentes de intensidad sísmica," *XXII Congreso Nacional de Ingeniería Sísmica*, Monterrey, México.

Sarmiento, O. [2021] "Estudio del comportamiento sísmico de contenidos de uso típico en el Hospital General Docente Ambato," *Tesis de grado, Universidad de las Fuerzas Armadas ESPE,* Ecuador

Simoneschi, G., Olivieri, C., de Leo, A. M., Di Egidio, A. [2018] "Pole placement method to control the rocking motion of rigid blocks," *Engineering Structures*, Vol. 167, pp. 39–47.

Spanos, P. D., Matteo, A. Di, Pirrotta, A., Paola, M. Di. [2017] "Nonlinear rocking of rigid blocks on flexible foundation: Analysis and experiments," *Procedia Engineering*, Vol. 199, pp. 284–289.

Vassiliou, M. F., Burger, S., Egger, M., Bachmann, J. A., Broccardo, M., Stojadinovic, B. [2017] "The three-dimensional behavior of inverted pendulum cylindrical structures during earthquakes," *Earthquake Engineering & Structural Dynamics*, Vol. 46, No. 14, pp. 2261–2280.

Whittaker, A., Soong, T. [2003] "An overview of nonstructural components research at three US earthquake engineering research centers," *ATC Seminar on Seismic Design, Performance, and Retrofit of Nonstructural Components in Critical Facilities*, Vol. 29, No. 2, pp. 271–280.

Wittich, C. E., Hutchinson, T. C. [2016] "Experimental modal analysis and seismic mitigation of statue-pedestal systems," *Journal of Cultural Heritage*, Vol. 20, pp. 641–648.

Zhang, J., Makris, N. [2001] "Rocking Response of Free-Standing Blocks Under Cycloidal Pulses," *Journal of Engineering Mechanics*, Vol. 127, No. 5, pp. 473–483.

Effect of Unequal Slab Levels in Adjacent Buildings on the Seismic Demand of Non-Structural Building Components

Prachi Verma[1], Yati Aggarwal[2], and Sandip Kumar Saha[3]

[1] M. Tech Student, School of Civil and Environmental Engineering, Indian Institute of Technology Mandi (IIT Mandi), Mandi-175075, Himachal Pradesh, India
e-mail: t20013@students.iitmandi.ac.in

[2] Research Scholar, School of Civil and Environmental Engineering, Indian Institute of Technology Mandi (IIT Mandi), Mandi-175075, Himachal Pradesh, India
e-mail: d17050@students.iitmandi.ac.in

[3] Assistant Professor, School of Civil and Environmental Engineering, Indian Institute of Technology Mandi (IIT Mandi), Mandi-175075, Himachal Pradesh, India
e-mail: sandip_saha@iitmandi.ac.in

Abstract. Adjacent buildings, especially in unplanned localities, usually have insufficient seismic gap between them with unequal floor levels. It is evident from the post-earthquake reconnaissance studies, such as Mexico city earthquake (1985), Nepal earthquake (2015), etc., that the buildings adjacent to each other experience damage due to pounding during strong earthquakes. Often the adjacent buildings are of different floor heights due to architectural or site requirements. Thus, it is important to study the effect of unequal slab levels, in adjacent buildings, on the seismic pounding. In this study, two adjacent reinforced concrete (RC) frames, 2-story and 4-story with three different slab levels are considered. Finite element modelling of these RC frames is done in ABAQUSv2021 [Abaqus 2011]. Non-linear elastic contact is modelled in between the considered frames. Three different ground motion records are considered to perform non-linear time history analyses. The seismic responses, such as peak interstory drift ratio, peak floor acceleration, pounding force, total energy dissipation, and damage index are studied. It is observed that the responses, such as peak interstory drift and peak pounding force are critical in the frames with unequal floor levels in comparison to those with equal floor levels. Hence, it is concluded that drift-sensitive non-structural building components would be subjected to maximum damage in stiffer buildings with equal slab level interaction whereas in flexible building with two-third slab level interaction. At the same time, peak pounding force is maximum in adjacent buildings with slabs at two-third levels.

Keywords: Damage quantification, Engineering demand parameter, Non-linear time history analysis, Pounding, Seismic response, Unequal slab levels.

1. INTRODUCTION

In populated cities, buildings are constructed close to each other, during an earthquake they may sway out of phase from each other which can lead to collision between them. This phenomenon of collision between adjacent buildings is known as pounding and impact force generated due to collision is known as pounding force. Primary reasons behind seismic pounding are differences in dynamic properties of buildings (owing to different heights, masses and stiffness) leading to out-of-phase sway of the buildings and insufficient separation gap between adjacent buildings to accommodate the displacement demand. In past earthquakes, several incidences of pounding were reported. For example, during the Mexico earthquake (1985), around 40% of severely damaged buildings experienced pounding phenomenon and around 15% of them fully collapsed [Brown and Elshaer 2022]. During Loma Prieta earthquake (1989) there were over 200 pounding occurrences affecting nearly 500 buildings [Kasai and Maison 1996]. In the studies conducted by Cole et. al. [2010] and Cole et al. [2012], during Darfield earthquake (2010) and Christchurch earthquake (2011), respectively, about 6% of the total surveyed buildings were significantly damaged due to pounding. After Gorkha earthquake (2015), a reconnaissance survey of the damaged buildings was conducted by Shrestha and Hao [2018], it was observed that pounding occurred in most of the designed multi-story buildings in Kathmandu Valley even with generous separation gap.

To measure the pounding force (impact) various analytical models have been proposed in the past, such as coefficient of restitution-based stereo-mechanical model, linear spring model, Kelvin model, Hertz model, Hertz damp model and non-linear viscoelastic model [Ye and Li 2009]. In the present study, Hertz model is used to simulate the pounding phenomenon. Several studies by different researchers have been conducted to investigate the responses of buildings undergoing pounding phenomenon [Dogan and Gunaydin 2009; Efraimiadou et al. 2013; Moustafa and Mahmoud 2014; Chenna and Ramancharla 2018; Raheem et al. 2019; Hosseini et al. 2021; Gerami et al. 2021; Lu et al. 2022]. Dogan and Gunaydin [2009] performed stress analysis on a 2-story solid frame at different impact points (floor-to-floor impact and column-to-floor impact) due to pounding. It was observed that column-to-floor pounding was more severe than floor-to-floor pounding. Moustafa and Mahmoud [2014] studied the damage assessment due to pounding between one stiff and other flexible lumped mass SDOF systems under earthquake in terms of ductility, pounding force, input energy from earthquake, dissipated energy in terms of damping and yielding and damage indices, such as Park and Ang [1985], Fajfar [1992], Cosenza [1993], Powell and Allahbadi [1988], etc. They found that a stiffer structure has higher ductility demand, dissipates more hysteretic energy thereby possesses higher damage index in comparison to flexible structure. Chenna and Ramancharla [2018] have studied pounding between adjacent buildings at equal and unequal slab levels and concluded that at dominant period of ground motion, displacement response of stiff structure is more than flexible structure irrespective of equal and unequal heights. On the other hand, if a structure vibrates at non-dominant period of ground motion, then the displacement response of flexible structure is higher than stiff structure.

In most of the earlier reported studies, equal slab level interactions are considered to study pounding between adjacent buildings. Limited studies have been conducted considering the unequal slab levels [Karayannis and Favvata 2005, Zou et al. 2014, Chenna and Ramancharla 2018]. However, there is rarely any literature that reports the effect of pounding between buildings having unequal slab levels on the energy dissipation and extent of damage alongside the peak responses. Therefore, a finite element modelling-based numerical investigation of seismic response of adjacent frames with different slab levels is considered in the present study. The specific objectives of present study are: (i) to perform seismic response of adjacent buildings with three different slab levels in terms of peak interstory drift ratio, peak floor acceleration, and peak pounding force, and (ii) to compare the total energy dissipation and damage index of pounded frames with unequal slab levels.

2. NUMERICAL MODELLING OF REINFORCED CONCRETE FRAMES

In this study, two planar adjacent reinforced concrete (RC) frames of 2-story and 4-story with story height of 3.3m and bay length of 3.2 m are modelled in ABAQUSv2021 [Abaqus 2011]. The cross-section of beam and column is 300mm×300mm and 350mm×350mm, respectively. The diameter of longitudinal rebar and transverse stirrup is taken as 20mm and 10mm, respectively. Clear cover from top and bottom is taken as 40mm. Beam is reinforced with 3 rebars each at top and bottom face, respectively and column is reinforced with 3 rebars on each face. Continuum modelling of RC frames is done in this study. For this, first the geometries of RC beams, RC columns and steel rebars are prepared in Part module of Abaqus. Then, these parts are assembled to get the desired RC frame in Assembly module. Further, in Interaction module, Tie constraints are given at beam column joint to make it a rigid joint. Tie constraint abandon any relative motion between two surfaces. Moreover, embedded region constraints are given between steel rebars and concrete to ensure the grip between steel rebars and concrete as they constrain the translation degrees of freedom of embedded steel.

The separation gap between two RC frames is 2.5mm. Three sets of buildings with different slab levels are developed as shown in Figure 1:

- *Equal slab level*: when the story height of both frames is same, equal slab level interaction is considered. Fundamental periods of 2-, and 4-story RC frames are 0.279s, and 1.055s, respectively.
- *Two-third slab level:* when the story heights of both frames are different, unequal slab level interaction is considered. Here, slab of 2-story frame interacts with the column of 4 story frame at two-third column height. Fundamental period of 2-story RC frame is 0.197s.
- *One-half slab level:* when the story heights of both frames are different, unequal slab level interaction is considered. Here, slab of 2-story frame interacts with the column of 4 story frame at one-half column height. Fundamental period of 2-story RC frame is 0.163s.

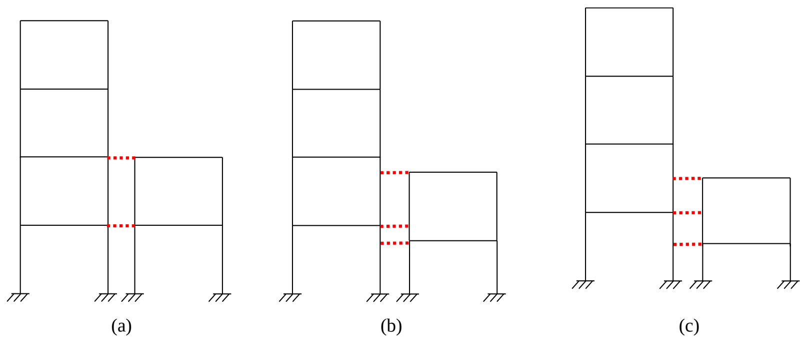

Figure 1: Building sets with different slab levels (a) equal, (b) two-third, and (c) one-half slab levels.

2.1 MATERIAL NON-LINEARITY

Concrete of grade M30 and steel of grade Fe500 are considered for modelling RC frames. Non-linearity in

3

material properties of both concrete and steel is considered while modelling. In concrete non-linearity is accounted for through concrete damage plasticity (CDP) model and for steel elastic perfectly plastic model is considered. CDP model has the potential to simulate the complete inelastic behaviour of concrete both in tension and compression [Hafezolghorani et al. 2017]. Table 1 and Table 2 provide the values of various parameters taken for constitutive modelling of steel and concrete, respectively. Figure 2 shows the stress-strain behaviour of concrete and steel material models, respectively.

Table 1: Material properties of steel.

Parameters	Values
Young's modulus	$2{\times}10^5$ N/mm^2
Poison's ratio	0.3
Yield stress	550 N/mm^2
Plastic strain	0
Density	7850 Kg/m^3

Table 2: Elasticity and plasticity parameters of concrete.

Parameters	Values
Youngs modulus	27386.12 N/mm^2
Poisons ratio	0.2
Density	2400 Kg/m^3
Dilation angle	31
Flow potential eccentricity	0.1
Biaxial by uniaxial plastic strain ratio	1.16
Invariant stress ratio	0.67
Viscosity	0

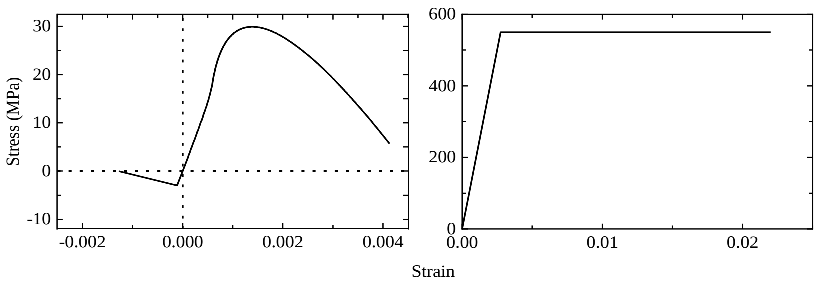

Figure 2: Stress-strain relationship for concrete and steel.

2.2 CONTACT ELEMENT MODELLING

To simulate the behaviour of buildings during pounding and obtain the value of peak pounding force, it is necessary to model the gap between two adjacent buildings. For this purpose, contact elements are used. There are various contact models suggested by researchers in past for modelling gap between adjacent buildings, such as coefficient of restitution-based stereos-mechanical model, linear spring model, Kelvin model, Hertz model, Hertz damp model and non-linear viscoelastic model. In this study, modelling of contact is based on Hertz model. It is one of the popular contact models for representing pounding and is used by many researchers in past [Jing et al. 1991; Pantelides and Ma 1998; Chau et al. 2001; Muthukumar and DesRoches 2006; Mereles et al. 2018].

In Hertz model, non-linear spring having stiffness β is used to model the contact. The value of β depends on the material properties of the building and the geometry of the colliding bodies. For concrete structures, its value ranges from 40 to 80 kN/mm$^{3/2}$ [Jankowski, 2005]. For this study value of β is taken as 80 kN/mm$^{3/2}$. The pounding force *F(t)* during the impact is given by:

$$F(t) = \beta \times \Delta(t)^{3/2} \tag{1}$$

where Δ is the deformation (relative displacement between the adjacent buildings) occurring due to impact and *t* is time instant.

$$\Delta = u_1 - u_2 - g_p \tag{2}$$

where u_1 and u_2 are the displacements of two single of freedom systems (SDOF) with masses m_1 and m_2, respectively and g_p is the gap distance. The contact elements come into function only when the gap ($\Delta \geq 0$) between adjacent buildings becomes zero. These elements are compression-only springs and become inactive in tension.

2.3 GOVERNING EQUATION OF POUNDING

Figure 3 shows two idealized single degree of freedom systems separated by a gap distance of g_p. The SDOF system on left has mass m_1, stiffness k_1 and damping coefficient c_1 whereas, SDOF system on right has mass m_2, stiffness k_2 and damping coefficient c_2. The equation of motion for the system subjected to pounding as be written as:

$$\begin{bmatrix} m_1 & 0 \\ 0 & m_2 \end{bmatrix} \begin{Bmatrix} \ddot{u}_1 \\ \ddot{u}_2 \end{Bmatrix} + \begin{bmatrix} c_1 & 0 \\ 0 & c_2 \end{bmatrix} \begin{Bmatrix} \dot{u}_1 \\ \dot{u}_2 \end{Bmatrix} + \begin{Bmatrix} R_1\,(u_1) \\ R_2\,(u_2) \end{Bmatrix} + \begin{Bmatrix} F \\ -F \end{Bmatrix} = - \begin{bmatrix} m_1 & 0 \\ 0 & m_2 \end{bmatrix} \begin{Bmatrix} \ddot{u}_g \\ \ddot{u}_g \end{Bmatrix} \tag{3}$$

where $\ddot{u}_1$ and $\ddot{u}_2$ are the relative accelerations, $\dot{u}_1$ and $\dot{u}_2$ are the relative velocities and u_1 and u_2 are relative displacements with respect to the ground of the masses m_1 and m_2. R_1, and R_2 are system restoring forces. F is the contact force due to pounding. K_1 is the stiffness of spring which is modelling the contact between adjacent buildings. Pounding occurs when gap between the two buildings closes otherwise pounding (contact) force will remain zero.

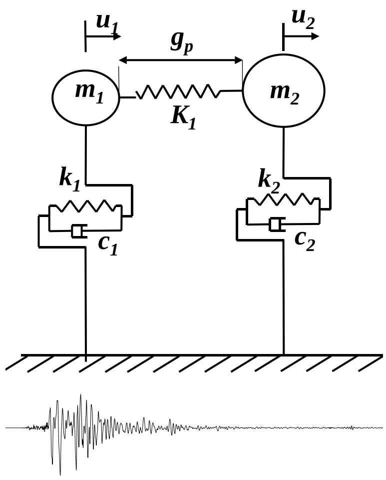

Figure 3: Hertz model for simulating contact between adjacent buildings.

2.4 SELECTION AND SCALING OF GROUND MOTION RECORDS

In this study three unscaled ground motion records, i.e., Imperial Valley (IV) (1940), Loma Prieta (LP) (1989), and Kobe (1995), are used. Details of the ground motion records, such as, magnitude (M_w), station, component, peak ground acceleration (PGA), are listed in Table 3.

Table 3: Details of earthquakes used in the present study.

S. No.	Earthquake	Year	Station	Component	M_w	PGA (g)
1	Imperial Valley	1940	El Centro	North-South	6.95	0.32
2	Loma Prieta	1989	SF Intern. Airport	East-West	6.9	0.24
3	Kobe	1995	KJMA	East-West	6.9	0.83

3. PARK-ANG DAMAGE INDEX

Various damage models have been proposed in past by many researchers in order to account for the damages to structures [Park and Ang 1985; Fajfar 1992; Cosenza 1993; Powell and Allahbadi 1988]. In this study Park-Ang [1985] damage index is used to compute the damage index of RC frames undergoing pounding. Expression for Park-Ang damage index is given as:

$$\mathrm{DI} = \frac{x_m}{x_u} + \beta \frac{EH}{x_u Q_y} \tag{4}$$

where, x_m is maximum deformation under earthquake loading; x_u is the ultimate deformation under monotonic loading; Q_y is the yield strength of the structure. *EH* is the total energy dissipation during excitation. β has constant value for concrete structures, i.e., 0.15.

Park-Ang damage index takes into account the damage due to both ductility (or deformation) and energy dissipation in structures. The first term of the damage index i.e., x_m/x_u represents damage due to ductility (or maximum response) and the second term i.e., $\beta\, EH/x_u Q_y$ represents the damage due to energy dissipation in structure. The values of x_m and *EH* are obtained from non-linear dynamic analysis of structures and the values of x_u and Q_y are obtained by performing non-linear static pushover analysis.

4. RESULTS AND DISCUSSION

4.1 EFFECT ON PEAK INTERSTORY DRIFT RATIO

Peak interstory drift ratio (IDR) is one of the crucial engineering demand parameters (EDP) in earthquake engineering. Typically, damages in structural building components are quantified in terms of peak interstory drift ratio. Figure 4 shows the variation in peak interstory drift ratio along the height of 2-story and 4-story RC frames for equal slab, two-third slab and one-half slab levels under three unscaled ground motions. For 2-story frame, it is observed that when pounding occurs the peak interstory drift ratio increases in comparison to the case when no pounding occurs for all interaction levels of floor. Whereas in 4-story frame, no increase in peak interstory drift is observed for equal and one-half slab levels. However, when slabs are at two-third level, significant increase in peak interstory drift ratio is observed. This significant increase is not corresponding to the level where slabs of 2-story and 4-story frames are interacting. It can be concluded from the results that in the given scenario, stiff buildings (2-story frame) are expected to have more peak interstory drift ratio in comparison to flexible buildings (4-story frame), especially when slab levels are equal. Also, in flexible buildings (4-story frame), when slab is at two-third levels, the peak interstory drift ratio is expected to be higher than no pounding case.

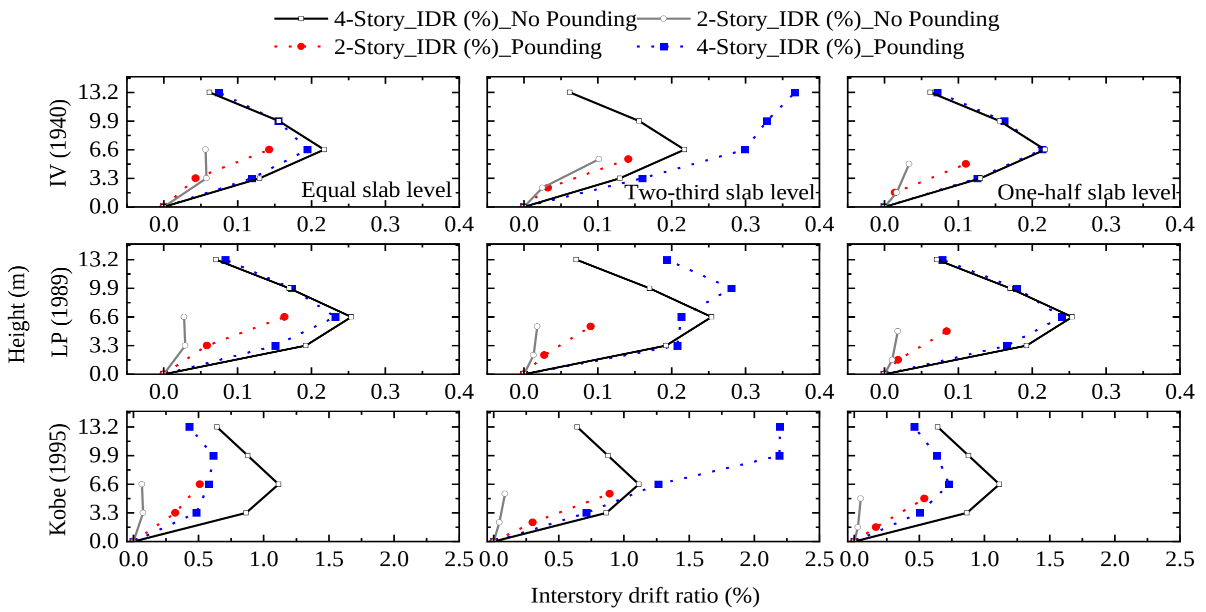

Figure 4: Peak interstory drift ratio along the heights of 2-story and 4-story RC frames for equal, two-third and one-half slab level pounding cases.

4.2 EFFECT ON PEAK FLOOR ACCELERATION

Peak floor acceleration (PFA) is another important EDP as non-structural building components, either mounted on ceiling or resting on floor, are sensitive to floor acceleration. In this section, variation in peak floor acceleration is studied along the height of the RC frames. Figure 5 shows the variation of peak floor acceleration with respect to height of the RC frames for equal, two-third and one-half slab levels. It is observed from Figure 5 that at the location of pounding in RC frames, peak floor acceleration increases many folds. It is also observed that peak floor acceleration is significantly higher when slab levels are equal, because of the interaction among members which are stiffer in-plane. On the other hand, peak floor acceleration is least for one-half slab level where a stiff slab is interacting with comparatively less stiff column. It is also observed from Figure 5 that 2-story frame attracts significantly higher peak floor acceleration in contrast to 4-story frame. It is owing to the fact that 2-story frame is stiff in comparison to 4-story frame.

4.3 EFFECT ON POUNDING FORCE

During an earthquake, when the gap between two adjacent buildings vanishes, they collide with each other, and contact force generates. This contact force is also known as pounding force. Figure 6 shows the time history of pounding force, at roof level of 2-story frame, for equal, two-third and one-half slab levels under Imperial Valley (1940), Loma Prieta (1989) and Kobe (1995) earthquakes. It is observed from Figure 6 that, unlike peak interstory drift ratio, magnitude of peak pounding force is highest when slabs are interacting at two-third level. It was noticed earlier that for 2-story frame, peak interstory drift ratio is maximum when slabs are at equal levels. Typically, peak interstory drift ratio is greater for 4-story frame, in contrast to 2-story frame and at the same time maximum when slabs are at two-third levels. Therefore, it can be concluded that peak pounding force is governed by the peak interstory drift ratio of the whole set of building (maximum among 2-, and 4-story frames).

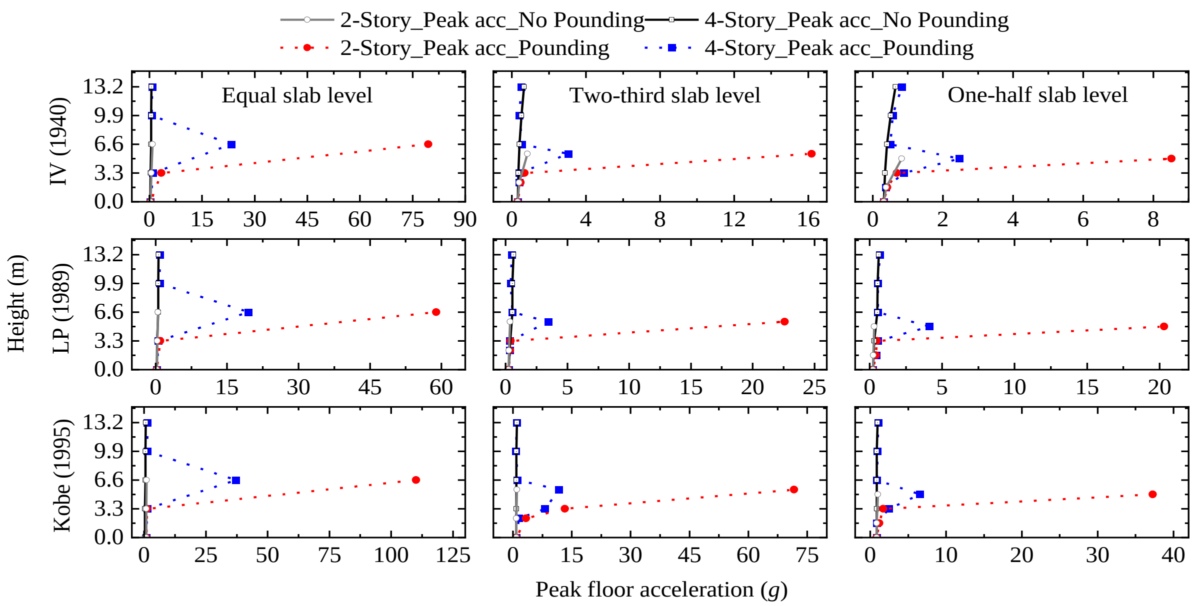

Figure 5: Peak story accelerations for 2-story and 4-story RC frames for equal, two-third, and one-half slab levels.

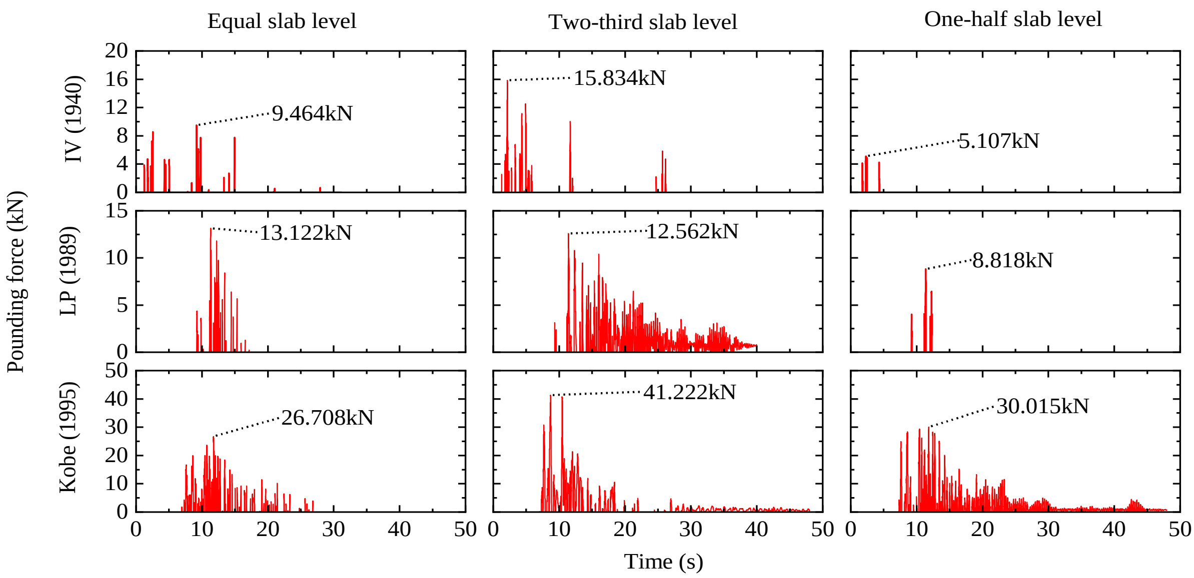

Figure 6: Pounding force time history for equal, two-third and one-half slab levels.

4.4 EFFECT ON ENERGY DISSIPATION

A structure receives input energy in the form of earthquake excitation, dissipated through various mechanisms, such as damping, friction, kinetic energy, etc. It is important to study the energy dissipated by the structure to get an idea of damages induced in the structure. Figure 7 shows the viscous and plastic energy dissipation time history under three earthquakes namely, Imperial valley (1940), Loma Prieta (1989)

8

and Kobe (1995) for equal, two-third and one-half slab levels. It is observed that viscous dissipation energy (VED) is highest in 4-story frame with slabs at two-third level while in 2-story frame insignificant change in viscous energy dissipation is observed. Inelastic deformation in the system contributes to plastic energy dissipation (PED). Plastic energy dissipation is insignificant in 2-story frame in comparison to 4-story frame. Moreover, the magnitude of energy dissipation is very less under Imperial Valley (1940) and Loma Prieta (1989) earthquakes in comparison to Kobe (1995) earthquake owing to their very less intensity.

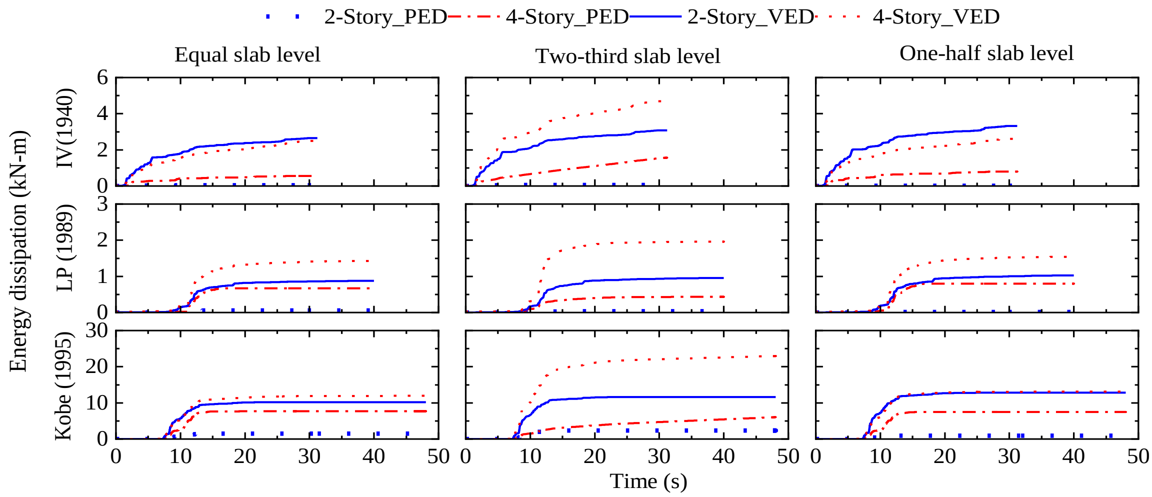

Figure 7: Viscous and plastic energy dissipation for 2-story and 4-story RC frames under equal, two-third and one-half slab levels.

4.5 EFFECT ON DAMAGE INDEX

Park-Ang damage index is calculated for 2-story and 4-story RC frames for different slab level pounding under three ground motions. Damage index of greater than one signifies collapse of the system. It is observed from Figure 8 that the damage index of 2-story frame is greater than 4-story frame. Moreover, damage index is maximum in 2-story frame, when slabs are at one-half levels. Whereas in 4-story frame, damage index is maximum when slabs are at two-third level. Thus, it is concluded that for 4-story frame damage is governed by peak interstory drift ratio response. Whereas for 2-story frame, no uniform trend is seen between the engineering demand parameters and the obtained damage index.

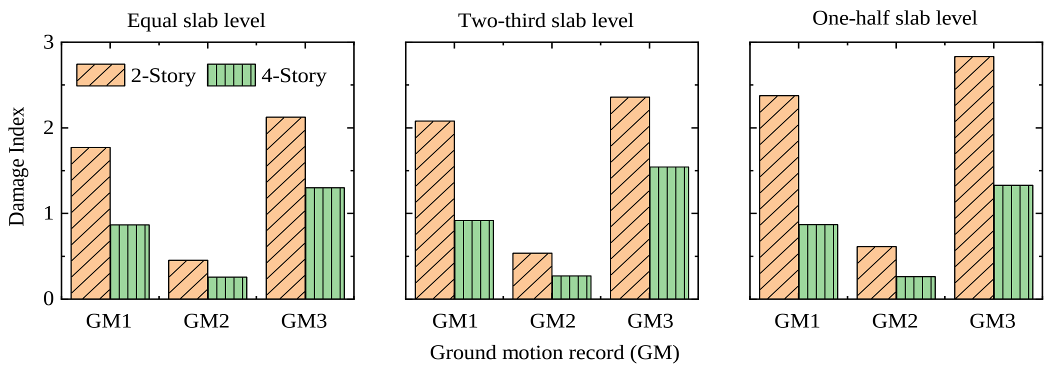

Figure 8: Park-Ang damage index for 2-story and 4-story RC frames under equal, two-third and one-half slab levels.

7. CONCLUSIONS

In this study, seismic response of two adjacent RC buildings is studied with interaction at three slab levels, namely, equal, two-third and one-half. These three sets of building configurations are subjected to three earthquakes, namely, Imperial Valley (1940), Loma Prieta (1989) and Kobe (1995) earthquakes. Non-linear time history analysis is performed and response of buildings in terms of peak interstory drift ratio, peak floor acceleration, peak pounding force, energy dissipation, and damage index is studied. Few major conclusions from this study are as follows:

(i) Drift-sensitive non-structural components would be subjected to maximum damage in stiffer buildings with equal slab level interaction whereas in flexible building with two-third slab level interaction. At the same time, peak pounding force is maximum in adjacent buildings with slabs at two-third levels.

(ii) Acceleration-sensitive non-structural components are expected to face maximum damage when slabs of adjacent buildings are at equal levels.

(iii) During pounding phenomenon adjacent buildings are subjected to different levels of damage. Stiffer buildings undergo higher damage when slabs are at one-half levels whereas flexible buildings undergo higher damage when slabs are at two-third levels.

REFERENCES

Abaqus, G. (2011). Abaqus 6.11. Dassault Systemes Simulia Corporation, Providence, RI, USA.

Abdel Raheem, S. E., Fooly, M. Y., Abdel Shafy, A. G., Taha, A. M., Abbas, Y. A., Abdel Latif, M. [2019] "Numerical simulation of potential seismic pounding among adjacent buildings in series," *Bulletin of Earthquake Engineering*, Vol. 17, No. 1, pp. 439-471.

Brown, T., Elshaer, A. [2022] "Pounding of structures at proximity: A state-of-the-art review," *Journal of Building Engineering*, Vol. 48, pp. 103991.

Chau, K. T., Wei, X. X. [2001] "Pounding of structures modelled as non-linear impacts of two oscillators," *Earthquake engineering & structural dynamics*, Vol. 30, No. 5, pp. 633-651.

Chenna, R., Ramancharla, P. K. [2018] "Damage assessment due to pounding between adjacent structures with equal and unequal heights," *Journal of Civil Structural Health Monitoring*, Vol. 8, No. 4, pp. 635-648.

Cole, G. L., Dhakal, R. P., Carr, A., Bull, D. [2010] "Interbuilding Pounding Damage Observed in the 2010 Darfield Earthquake," Bulletin of New Zealand Society for Earthquake Engineering, Vol. 43, No. 4.

Cole, G. L., Dhakal, R. P., Turner, F. M. [2012] "Building pounding damage observed in the 2011 Christchurch earthquake," *Earthquake Engineering & Structural Dynamics*, Vol. 41, No. 5, pp. 893-913.

Cosenza, E., Manfredi, G., Ramasco, R. [1993] "The use of damage functionals in earthquake engineering: a comparison between different methods," *Earthquake engineering & structural dynamics*, Vol. 22, No. 10, pp. 855-868.

Doğan, M., Günaydin, A. [2009] "Pounding of adjacent RC buildings during seismic loads," *Eskişehir Osmangazi Üniversitesi Mühendislik ve Mimarlık Fakültesi Dergisi*, Vol. 22, No. 1, pp. 129-145.

Efraimiadou, S., Hatzigeorgiou, G. D., Beskos, D. E. [2013] "Structural pounding between adjacent buildings subjected to strong ground motions. Part I: The effect of different structures arrangement," *Earthquake Engineering & Structural Dynamics*, Vol. 42, No. 10, pp. 1509-1528.

Fajfar, P. [1992] "Equivalent ductility factors, taking into account low-cycle fatigue," *Earthquake Engineering & Structural*

Dynamics, Vol. 21, No. 10, pp. 837-848.

Gerami, M., Vahdani, R., Mollaeian, M., Khatami, M. [2021] "Evaluation of Park-Ang Damage Indicator in collisions of two adjacent frames under the near-fault field disturbances," *Journal of Structural and Construction Engineering*, Vol. 7, Special Issue 4, pp. 184-198.

Hafezolghorani, M., Hejazi, F., Vaghei, R., Jaafar, M. S. B., Karimzade, K. [2017] "Simplified damage plasticity model for concrete," *Structural Engineering International*, Vol. 27, No. 1, pp. 68-78.

Hosseini, S. H., Naderpour, H., Vahdani, R., Jankowski, R. [2022] "Evaluation of pounding effects between reinforced concrete frames subjected to far-field earthquakes in terms of damage index," *Bulletin of Earthquake Engineering*, Vol. 20, No. 2, pp. 1219-1245.

Jankowski, R. [2005]. "Non-linear viscoelastic modelling of earthquake-induced structural pounding," *Earthquake engineering & structural dynamics*, Vol. 34, No. 6, pp. 595-611.

Jing, H. S., Young, M. [1991] "Impact interactions between two vibration systems under random excitation," *Earthquake engineering & structural dynamics*, Vol. 20, No. 7, pp. 667-681.

Karayannis, C. G., and Favvata, M. J. [2005]. "Earthquake-Induced Interaction Between Adjacent Reinforced Concrete Structures with Non-Equal Heights," *Earthquake engineering & structural dynamics*, Vol. 34, pp. 1-20.

Kasai, K., Maison, B. F. [1997] "Building pounding damage during the 1989 Loma Prieta earthquake," *Engineering structures*, Vol. 19, No. 3, pp. 195-207.

Kumar, R. P. [1997] "Damage based life of structures in seismic environment," *M. Tech Thesis,* Civil Engg. Dept., Indian Institute of Technology Kanpur.

Kunnath, S. K., Reinhorn, A. M., Park, Y. J. [1990] "Analytical modelling of inelastic seismic response of R/C structures," *Journal of Structural Engineering*, Vol. 116, No. 4, pp. 996-1017.

Lu, Y., Xiong, F., Ran, M. M., Ge, Q., Wang, J. [2022] "Seismic pounding damage to adjacent reinforced concrete frame–shear wall buildings and freestanding contents," *Earthquake Engineering & Structural Dynamics*, Vol. 51, No. 6, pp. 1436-1456.

Mereles, A., Varanis, M., Balthazar, J., Tusset, A. [2018] "Seismic pounding model using hertzian contact," *In X Congresso Nacional de Engenharia Mecânica*, ABCM.

Moustafa, A., Mahmoud, S. [2014] "Damage assessment of adjacent buildings under earthquake loads," *Engineering Structures*, Vol. 61, pp. 153-165.

Muthukumar, S., DesRoches, R. [2006] "A Hertz contact model with nonlinear damping for pounding simulation," *Earthquake engineering and structural dynamics*, Vol. 35, No. 7, pp. 811-828.

Pantelides, C. P., Ma, X. [1998] "Linear and nonlinear pounding of structural systems," *Computers & Structures*, Vol. 66, No. 1, pp. 79-92.

Park, Y. J., Ang, A. H. S. [1985]. "Mechanistic seismic damage model for reinforced concrete," *Journal of structural engineering*, Vol. 111, No. 4, pp. 722-739.

Park, Y. J., Ang, A. H. S., Wen, Y. K. [1985] "Seismic damage analysis of reinforced concrete buildings," *Journal of Structural Engineering*, Vol. 111, No. 4, pp. 740-757.

Park, Y. J., Ang, A. H., Wen, Y. K. [1987] "Damage-limiting aseismic design of buildings," *Earthquake spectra*, Vol. 3, No. 1, pp. 1-26.

Powell, G. H., Allahabadi, R. [1988] "Seismic damage prediction by deterministic methods: concepts and procedures," *Earthquake engineering & structural dynamics*, Vol. 16, No. 5, pp. 719-734.

Shrestha, B., Hao, H. [2018] "Building pounding damages observed during the 2015 Gorkha earthquake," *Journal of Performance of Constructed Facilities*, Vol. 32, No. 2, pp. 04018006.

Ye, K., Li, L. I. [2009] "Impact analytical models for earthquake-induced pounding simulation," *Frontiers of Architecture and Civil Engineering in China*, Vol. 3, No. 2, pp. 142-147.

Zou, L., Li, L., Huang, J., and Huang, K. [2014]. "Seismic Pounding Between Adjacent Buildings of Unequal Floor Height," *Journal of Vibroengineering*, Vol. 16, No. 6.

Seismic Assessment of Acceleration-Sensitive Nonstructural Elements: Reliability of Existing Shake Table Protocols and Novel Perspectives

Danilo D'Angela[1], Martino Zito[1], Chiara Di Salvatore[1], Giuseppe Toscano[1], and Gennaro Magliulo[1,2]

[1] Department of Structures for Engineering and Architecture, University of Naples Federico II
Via Claudio, 21, I-80125 Naples, Italy
{danilo.dangela,martino.zito,gmagliul}@unina.it & chiara.disalvatore88@gmail.com & giuseppe.toscano567@gmail.com
[2] Construction Technologies Institute, National Research Council (ITC-CNR)
Via Claudio, 21, I-80125 Naples, Italy

Abstract. Nonstructural elements (NEs) are typically associated with major seismic risk, as several post-event surveys and literature studies highlighted in the last few decades. NE seismic risk is often expressed in terms of critical functioning disruption, economic losses, and casualties, and this might be significant even in the case of low seismicity sites. In particular, seismic risk can be more critical for NEs than for structural parts, especially frequent seismic events. Shake table testing represents the most reliable method for seismic assessment and qualification of NEs that are sensitive to accelerations (i.e., acceleration-sensitive NEs). However, several protocols and testing inputs were defined in literature and codes but none of them has been assessed in terms of seismic scenario representativity and reliability.

The present study reports the preliminary results of an extensive investigation into the seismic assessment and qualification of NEs through experimental methods and shake table testing. Two reference shake table protocols defined by regulations/codes (AC156 and FEMA 461) are assessed in terms of seismic damage potential/severity considering inelastic single degree of freedom (SDOF) systems and assuming the reliability index as an evaluation parameters. Novel perspectives for developing more reliable shake table protocols and seismic inputs are traced in the light of the preliminary results.

Keywords: Nonstructural elements, acceleration-sensitive, seismic assessment, shake table, seismic input

1. INTRODUCTION

Nonstructural elements (NEs) are generally particularly sensitive to seismic actions and may exhibit a critical behavior also under relatively low intensity earthquakes [Achour *et al.*, 2011; De Angelis and Pecce, 2015; Perrone *et al.*, 2019], especially if they were not designed at all or with regard to seismic actions. NE seismic behavior typically affects facility functioning and can be associated with significant economic losses; moreover, damage of NEs might even cause human losses. Therefore, the seismic assessment of NEs is an issue of paramount importance, especially regarding NEs that are housed within critical facilities [Achour *et al.*, 2011; Cosenza *et al.*, 2015].

The seismic capacity and performance of NEs can be generally assessed by means of analytical, numerical, experimental, observational, and mixed methods. NEs that are critical in terms of their functioning and stability with regard to seismic actions such as fire sprinkler systems [Soroushian *et al.*, 2014] or medical equipment [Di Sarno *et al.*, 2019] should be preferably assessed via experimental methods (e.g., [American Society of Civil Engineers, 2017]), and quasi-static and shake table testing are generally considered to be optimal for assessing displacement-sensitive and acceleration-sensitive NEs (e.g., [Federal Emergency Management Agency (FEMA), 2007)]. Generally, NEs are typically sensitive to both displacements and accelerations, and shake table testing can be reasonably considered to be the best option if the testing setup reproduce realistic NE surroundings/arrangements.

In order to supply robust and representative results, shake table tests are often performed considering seismic inputs compliant with reference testing protocols, and this strictly required when seismic qualification or certification are carried out. As a matter of fact, the seismic response of NEs is strongly conditioned by the record characteristics, and shake table protocol are supposed to provide seismic inputs associated with relatively severe and representative responses. AC156 [International Code Council Evaluation Service (ICC-ES), 2012] and FEMA 461 [Federal Emergency Management Agency (FEMA), 2007] protocols represent the state of the art for seismic assessment and qualification/certification of acceleration-sensitive elements. Other protocols exist but are meant to be used to assess/qualify specific components and equipment, e.g., power substation equipment [Institute of Electrical and Electronics Engineers, 2006] or telecommunication equipment [Telcordia Ericsson, 2017]. However, the level of reliability of existing protocols is not reported by the protocols, as well as this issue was not systematically addressed in the literature, except for a very few studies, that focused on peculiar applications (e.g., [Burningham *et al.*, 2007; D'Angela *et al.*, 2021a]).

The present study reports the preliminary results of an extensive research project aiming at evaluating the current approaches and methods for seismic assessment and qualification of NEs. In this study, the reliability of AC156 and FEMA 461 protocol is assessed with regard to the seismic severity in terms of damage potential to NEs. In particular, rather than the protocols themselves, the associated seismic inputs are investigated by scaling them according to an incremental procedure and considering peak floor acceleration (PFA) as an intensity measure (IM). Elements that can be modeled by single degree of freedom (SDOF) systems have been considered as a case study; these elements correspond to most studied and common acceleration-sensitive elements (e.g., [Akkar and Bommer, 2007; Merino *et al.*, 2020]). Incremental dynamic analyses are performed to assess the seismic response and damage to three case study models. The reliability index associated with the investigated protocols is estimated considering real floor motions as a reference, according to a recently developed methodology [D'Angela *et al.*, 2021a]. Novel perspectives for more reliable seismic assessment of acceleration-sensitive are traced, according to the reliability assessment results.

2. METHODOLOGY

2.1 OUTLINE

The methodology is defined by following steps: (Section 2.2) identification of the shake table protocols to be investigated and development of compliant seismic records, (Section 2.3) definition/selection of reference floor motions to be considered as representative seismic scenarios, (Section 2.4) damage severity analysis of shake table protocols and comparison with reference floor motions (i.e., estimation of reliability index). The methodological approach was derived in [D'Angela *et al.*, 2021a, 2021b] and was enhanced and extended in this study. The readers are referred to the literature studies referred to within the following subsections for further details regarding methods, formulations, and technical/operative aspects.

2.2 REFERENCE PROTOCOLS

The paper focuses on two international protocols: AC156 [International Code Council Evaluation Service (ICC-ES), 2012] and FEMA 461 [Federal Emergency Management Agency (FEMA), 2007]. AC156 is the international reference for seismic assessment and the qualification of acceleration-sensitive elements and referred to ASCE/SEI 7-16 [American Society of Civil Engineers, 2017] also for seismic certification procedures through experimental methods. FEMA 461 is among the most severe protocols for seismic assessment of structural and nonstructural elements by means of shake table testing and also reports the procedure for seismic fragility analysis. AC156 protocol is intended to be a pass or fail test signal, whereas tests according to FEMA 461 protocol are meant to be carried out according to an incremental procedure. Shake table signals for carrying out seismic performance evaluation tests can be generated according to the procedure defined by AC156 protocol even though few features can be defined by the analyst, such as the specific baseline or the octave resolution width. The required response spectra (RRS) related to AC156 are based on the seismic demand formulation provided by ASCE/SEI 7-16. Seismic performance evaluation signals compliant with AC156 were developed in several literature studies [Di Sarno *et al.*, 2019; Magliulo *et al.*, 2012], and further details are omitted for the sake of brevity. FEMA 461 provides a procedure to generate seismic signals, which was developed by Wilcoski *et al.* [1997]. Differently from AC156, FEMA 461 does not provide RRS and implicitly recommends the use of the signals reported in the document. Further details regarding FEMA 461 signals can be found in [D'Angela *et al.*, 2021a]. Figure 1a shows RRS associated with horizontal direction defined by AC156 considering design earthquake spectral response acceleration parameter at short periods (S_{DS}) equal to 0.40 g, where z/h is assumed equal to one (z/h is the ratio between the height location of NE and the building height). S_{DS} equal to 0.40 g represents a relatively severe seismic intensity levels considering European and Italian territory. Figure 1b depicts the spectral responses of two reference seismic signals (latitudinal and longitudinal) defined in FEMA 461.

(a) (b)

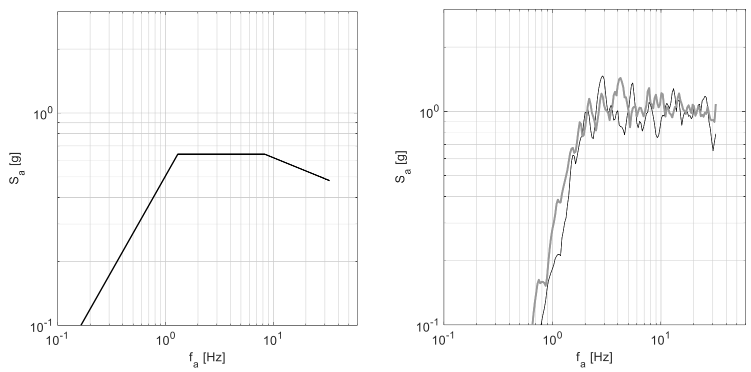

Figure 1. (a) RRS associated with horizontal direction defined by AC156 (International Code Council Evaluation Service (ICC-ES), 2012) considering design earthquake spectral response acceleration parameter at short periods (S_{DS}) equal to 0.40 g and z/h equal to one and (b) spectral responses of two reference seismic signals (latitudinal and longitudinal signals corresponding to thin black and thick gray graphs, respectively) defined in FEMA 461 [Federal Emergency Management Agency (FEMA), 2007].

2.3 REFERENCE FLOOR MOTIONS

Real floor motions (FMs) are considered as a reference for the evaluation of the reliability of shake table protocols. As a matter of fact, capacity estimations based on shake table protocols can be considered as nominal capacities, whereas the capacities compatible with "actual" responses can be derived considering representative seismic and structural scenarios related to earthquake evens and actual buildings, i.e., real floor motions in this context. FMs were recorded in instrumented reinforced concrete (RC) buildings in the US and were provided by CESMD [2017] database. In particular, FMs correspond to real ground motions with PGA not smaller than 0.05 g, selecting the most amplified accelerations over the building's floors. Both near- and far-field records were equally considered, as well as low-, medium-, and high-rise buildings were equally accounted for; the buildings were designed in 1923 – 1975. The selection of the records was derived from literature studies [D'Angela *et al.*, 2022, 2021b]; in particular, FMs are associated with (a) PGA not smaller than 0.05 g, (b) RC buildings designed/constructed from 1923 to 1975 in the US, (c) building floors corresponding to maximum acceleration amplification over the building, provided by CESMD [2017] database. Both near and far field records were considered, as well as low-, medium-, and high-rise buildings were equally included within the building scenarios. Full details regarding the records can be found in [D'Angela *et al.*, 2022, 2021b]. It should be specified that 18 FMs were considered in this study, obtained by removing six records from the record set defined in [D'Angela *et al.*, 2022, 2021b], i.e., records #4, #8, #11, #16, #20, and #24 were removed since they were considered to be excessively mild with regard to the case study models.

2.4 DAMAGE SEVERITY: RELIABILITY INDEX

2.4.1 Outline

The damage severity evaluation of the shake table protocols is based on the estimation of the reliability index, where shake table protocol-based estimations are meant as nominal capacities and real floor motion-based estimations are considered to be compatible with realistic and representative seismic and building scenarios. The case study models and numerical analyses are defined in Subsection 2.4.2 and the damage assessment methodology is defined in Subsection 2.5.3, whereas the computation of the reliability index is illustrated in Subsection 2.5.4.

2.4.2 Numerical modeling and analysis

Case study nonstructural elements consist in elements that are sensitive to accelerations and that are fixed to the structure in a single area/point, which is relatively reduced considering their spatial extension, e.g., cabinets fixed at their bases, antennas, ceiling elements, museum/art objects. The case study elements were modeled considering single degree of freedom (SDOF) systems [Akkar and Bommer, 2007; Merino *et al.*, 2020] provided with nonlinear degrading dynamic behavior. The numerical models were implemented in OpenSees [McKenna *et al.*, 2000] according to lumped plasticity approach. In particular, Ibarra-Medina-Krawinkler model [Ibarra *et al.*, 2005; Ibarra and Krawinkler, 2005] was considered according to consolidated applications within the literature. In particular, the models were assumed to be cantilever elements fixed at their bases, having steel S275 material square hollow sections. The modeling backbone and degrading parameters were derived by [Lignos and Krawinkler, 2010], who developed and calibrated the modeling parameters of steel square hollow sections considering a large and representative set of experimental data. Mass and stiffness-proportional Rayleigh damping was assigned; P-Δ effects were implemented. The formulation is omitted for the sake of brevity, and the readers are referred to the abovementioned study.

Three models were considered in the study, i.e., models, M1, M2, and M3, corresponding to elastic frequencies equal to about 1.0, 1.5, and 3.0 Hz; the geometrical parameters are reported in Table 1, where fel, b, t, H, and m correspond to elastic frequency, cross-section dimension, cross-section thickness, elevation height, and lumped mass. Figure 2a shows the backbone responses (force-displacement) associated with M1, M2, and M3, without P-Δ effects. Figure 2b depicts the definition of DSs for a representative model (M1), where DSs are associated with response considering P-Δ effects; in particular, DS1 to DS3 displacements including P-Δ effects are equal to theoretical (no P-δ effects) ones, $DS4_{Th}$ is related to residual strength achievement over the theoretical response (no P-δ effects), and DS4 is defined by reaching a force equal to 20% of the yielding force over the softening branch including P-Δ effects. F and Δ correspond to shear force and displacement at the mass, respectively. It should be specified that the investigated models are relatively highly flexible, they are representative of relatively low frequency elements and do not account for characteristics uncertainties. Therefore, the results cannot be considered to be exhaustive and cannot be generalized or extended to different case studies.

Table 1. Geometrical parameters of the investigated models

Model	f_{el} [Hz]	b [mm]	t [mm]	H [m]	m [t]
M1	1.02	70	3.0	4.50	0.10
M2	1.52	60	3.0	2.50	0.16
M3	3.04	60	3.0	2.50	0.04

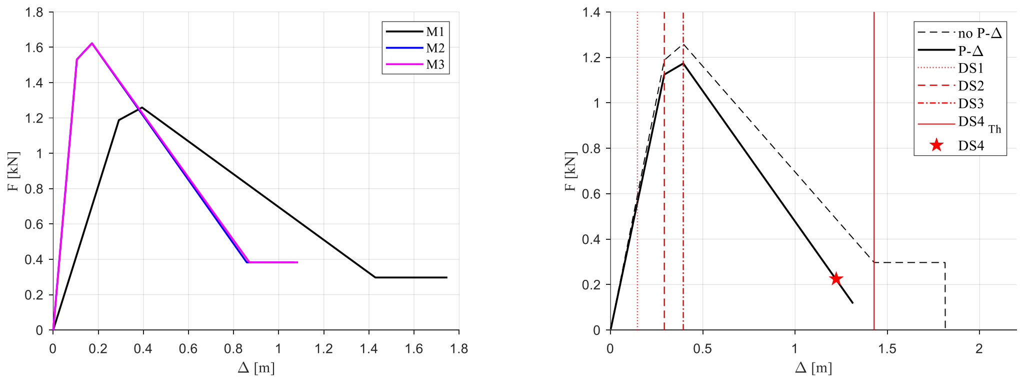

(a) (b)

Figure 2. (a) Backbone shear-displacement responses of the investigated models (M1, M2, and M3) and (b) definition of DSs (DS1, DS2, DS3, $DS4_{Th}$, and DS4) for M1 model.

2.4.3 Damage Assessment

Four damage states (DSs) were defined with regard to the dynamic force-displacement response of the models, considering the mass displacement of the SDOF as a reference. In particular, the displacement capacity thresholds related to DSs were defined considering the degraded static response (including second order geometric nonlinearities): DS1 was associated with halved yielding displacement, DS2 was related to yielding displacement, DS3 corresponded to capping displacement, and DS4 coincides with onset of perfectly-plastic response corresponding to the residual strength condition. Figure 2b schematically depicts the defined DSs, with regard to M1. The top displacement of the mass () was considered as an engineering demand parameter, whereas PFA was used as an IM.

2.4.4 Reliability index

The reliability index β was assessed considering first-order reliability method (FORM) (Schultz *et al.*, 2010). In this context, reliability index defines in a quantitative manner the statistical discrepancy between the capacity estimation associated with the shake table assessment (according to the investigated protocols) and the capacities related to consistently realistic responses (corresponding to a set of representative real floor motions). In particular, protocol-based capacity estimates provided demand measures (S) and FM-based corresponded to capacity measures (R), defining the capacity to demand margin (Z). Accordingly, Φ(-β) defines the failure probability pf, i.e., the probability that the protocol supplies capacities that are larger than the ones associated with FMs, or equivalently, that Z is non positive (where Φ is the cumulative standard normal distribution). The formulations are omitted and can be found in [D'Angela *et al.*, 2021a; Schultz *et al.*, 2010].

Figure 3 shows the correlation between p_f and β. Generally, a lower (upper) bound target/requirement in terms of β (pf) can be reasonably assumed to be equal to 0 (50%) since mean/median values are typically considered when relatively accurate analyses are performed. Overall, it can be assumed that a negative value of β is associated with an unreliable response, whereas a positive values to a reliable; a desirable/optimum range in terms of in terms of β (p_f) might be corresponding to 0 to 1 (~16% to 50%), even though this issue should be defined by codes and regulations (decision-maker issue) and is also conditioned by the use of safety coefficients/factors [D'Angela *et al.*, 2021a].

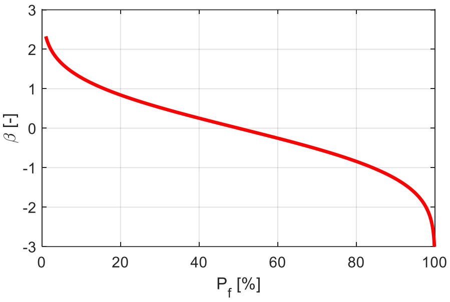

Figure 3. Reliability index β as a function of failure probability p_f.

3. RESULTS: RELIABILITY INDEX

The preliminary results of the reliability assessment are reported in this study. Figure 4 shows the reliability index β associated with DS1, DS2, DS3 and DS4, considering both AC156 and FEMA 461 protocol, assuming various reference FM sets: near field FMs (NF), far field FMs (FF), strong ground motion FMs (SM), all FMs (ALL).

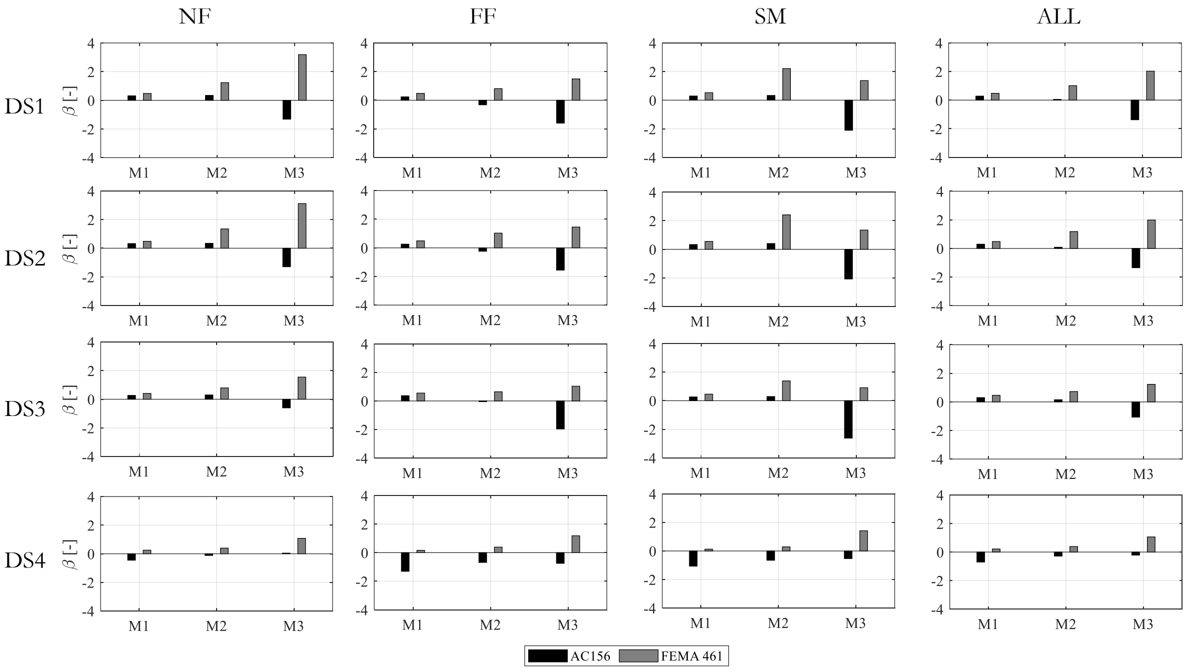

Figure 4. Reliability index β associated with investigated protocols, considering DS1, DS2, DS3, and DS4 and assuming near field FMs, far field FMs, strong ground motion FSs, and all FMs as a reference.

As a first comment, it could be observed that β is overall strongly conditioned by both DS and model. Overall, β decreases as DS severity increases, and a significant reliability drop can be observed passing from DS3 to DS4, whereas the response associated with DS1 and DS2 is more comparable. This can be qualitatively explained by recalling that DS1 and DS2 are associated with elastic response, DS3 with strength capping (displacement) condition, and DS4 with residual strength (displacement) condition; DS1 and DS2 are associated with comparable values of threshold displacements, DS3 displacements are typically slightly larger than DS2 ones, and DS4 ones are significantly larger than DS3 (Figure 2a). Accordingly, the protocols seem to be less reliable as the inelastic response becomes more relevant over the seismic performance; in other words, is it can be expected, the protocols address the elastic or low plastic response better than the inelastic and degrading one, in terms of their reliability.

The set of floor motions also conditions the reliability even though the influence is not regular, e.g., considering M1 and M2 (especially M2), AC156 FF case is associated with a lower reliability than other sets, considering M3, AC156 SM (FF) case results in a lower reliability than other sets for DS1 to DS3 (DS4). While AC156 is unreliable in several cases, FEMA 461 is always reliable. In particular, the critical cases associated with AC156 correspond to (a) all cases for model M3, (b) FF case for model M2, and (c) all DS4 cases but M3 and NF case. However, when β is positive for AC156, it tends to zero. Conversely, the reliability associated with FEMA is often optimal and, in some cases too high; for example, for M3 & NF & DS1/DS2 cases and for M2 & SM & DS1/DS2 β is even larger than 2, reasonably resulting in an excessively conservative capacity estimation. It is worth stressing the that the number of investigated models is relatively reduced and does not represent a wide range of NE scenarios; therefore, the results depicted in Figure 4, as well as the abovementioned comments, cannot be generalized and extended to other cases.

4. NOVEL PERSPECTIVES AND CONCLUDING REMARKS

According to the preliminary results reported in Figure 4, AC156 protocol might be relatively unreliable, whereas FEMA 461 protocol might overall be reliable or excessively conservative in some cases. It should be noted that the analyses did not account for reduction capacities by means of safety factors/coefficients; therefore, after the reduction of the nominal capacities derived according to the protocols, the reliability of FEMA 461 estimations might significantly increase, potentially resulting in relatively antieconomic capacities (relatively too reduced). Therefore, seismic assessment and qualification by means of the AC156 protocol might be associated with overestimated capacities, which might be highly unsafe, especially given that AC156 is the generally most authoritative reference for seismic qualification and certification of NEs. Conversely, capacities estimations obtained according to FEMA 461 might be excessively antieconomic. It is worth stressing that the reported evidence is related to preliminary findings and further studies should be carried out to generalize and extend the specific findings reported in this paper. In particular, further NE case studies should be considered, as well as alternative shake table protocols should also be investigated.

The preliminary evidence points out the necessity of developing a novel protocol, aimed at generic acceleration-sensitive NEs. In particular, a novel protocol could be defined in order to supply more consistent capacities, associated with an optimum reliability. In particular, the protocol could be defined by implementing a procedure that enforces the spectrum-compatibility with a more efficient RRS formulation, also providing optimum reliability indexes and robust safety factors/coefficients. A possible option for a relatively efficient RRS might consist in the simplified formulation provided by Italian building code [Ministero delle Infrastrutture e dei Trasporti, 2019, 2018]. This formulation was developed in [Petrone *et al.*, 2015] with regard to RC frame buildings and was recently found to be relatively reliable and consistent with potential seismic demand scenarios on (RC) frame buildings [Chichino *et al.*, 2021; Di Domenico *et al.*, 2021]. Further studies should account for issues and aspects not addressed in the paper, e.g., explicit assessment of building's nonlinearity influence. The authors are currently working towards the definition of a novel protocol according to the abovementioned perspective, also providing for quantitative validation procedures based on both signal-based analysis and damage potential evaluation

ACKNOWLEDGEMENTS

The study was funded by the Italian Ministry of University and Research (MUR) in the framework of PRIN 2020 project titled "ENRICH project: ENhancing the Resilience of Italian healthCare and Hospital facilities" and by the Italian Department of Civil Protection (DPC) in the frame of the national project DPC – ReLUIS 2022-2024 WP17: "Code contributions for nonstructural elements". Travel expenses for presenting the present paper were partially covered by the Travel Award sponsored by the open access journal Buildings published by MDPI.

REFERENCES

Achour, N., Miyajima, M., Kitaura, M., Price, A. [2011] "Earthquake-Induced Structural and Nonstructural Damage in Hospitals," Earthq. Spectra 27, 617–634. https://doi.org/10.1193/1.3604815

Akkar, S., Bommer, J.J. [2007] "Prediction of elastic displacement response spectra in Europe and the Middle East," Earthq. Eng. Struct. Dyn. 36, 1275–1301. https://doi.org/10.1002/eqe.679

American Society of Civil Engineers [2017] "Minimum Design Loads and Associated Criteria for Buildings and Other Structures," 7th ed. American Society of Civil Engineers, Reston, VA. https://doi.org/10.1061/9780784414248

Burningham, C., Mosqueda, G., Saavedra, R.R. [2007] "Comparison of seismic fragility of free standing equipment using current testing protocols and recorded building floor motions," in: Proceedings, Earthquake Engineering Symposium for Young Researchers. Seattle, WA.

CESMD [2017] "Center for Engineering Strong Motion Data," URL www.strongmotioncenter.org. Download on October 31st 2017

Chichino, B., Peloso, S., Bolognini, D., Moroni, C., Perrone, D., Brunesi, E. [2021] "Towards Seismic Design of Nonstructural Elements: Italian Code-Compliant Acceleration Floor Response Spectra," Adv. Civ. Eng. 2021, 1–18. https://doi.org/10.1155/2021/4762110

Cosenza, E., Di Sarno, L., Maddaloni, G., Magliulo, G., Petrone, C., Prota, A. [2015] "Shake table tests for the seismic fragility evaluation of hospital rooms," Earthq. Eng. Struct. Dyn. 44, 23–40. https://doi.org/10.1002/eqe.2456

D'Angela, A., Magliulo, G., Cosenza, E. [2022] "Incremental Dynamic Analysis of Rigid Blocks Subjected to Ground and Floor Motions and Shake Table Protocol Inputs," Bull. N. Z. Soc. Earthq. Eng. 55. https://www.bulletin.nzsee.org.nz/index.php/bnzsee

D'Angela, D., Magliulo, G., Cosenza, E. [2021a] "Towards a reliable seismic assessment of rocking components," Eng. Struct. 230, 111673. https://doi.org/10.1016/j.engstruct.2020.111673

D'Angela, D., Magliulo, G., Cosenza, E. [2021b] "Seismic damage assessment of unanchored nonstructural components taking into account the building response," Struct. Saf. 93, 102126. https://doi.org/10.1016/j.strusafe.2021.102126

De Angelis, A., Pecce, M. [2015] "Seismic nonstructural vulnerability assessment in school buildings. Nat. Hazards 79, 1333–1358. https://doi.org/10.1007/s11069-015-1907-3

Di Domenico, M., Ricci, P., Verderame, G.M. [2021] "Floor spectra for bare and infilled reinforced concrete frames designed according to Eurocodes," Earthq. Eng. Struct. Dyn. eqe.3523. https://doi.org/10.1002/eqe.3523

Di Sarno, L., Magliulo, G., D'Angela, D., Cosenza, E. [2019] "Experimental assessment of the seismic performance of hospital cabinets using shake table testing. Earthq. Eng. Struct. Dyn. 48, 103–123. https://doi.org/10.1002/eqe.3127

Federal Emergency Management Agency (FEMA) [2007] "Interim protocols for determining seismic performance characteristics of structural and nonstructural components through laboratory testing," Report No. FEMA 461. Washington D.C., USA.

Ibarra, L.F., Krawinkler, H. [2005] "Global collapse of frame structures under seismic excitations (No. 152) ," The John A. Blume Earthquake Engineering Center. Department of Civil and Environmental engineering. Stanford University, Stanford CA.

Ibarra, L.F., Medina, R.A., Krawinkler, H. [2005] "Hysteretic models that incorporate strength and stiffness deterioration," Earthq. Eng. Struct. Dyn. 34, 1489–1511. https://doi.org/10.1002/eqe.495

Institute of Electrical and Electronics Engineers[2006] "693-2006 IEEE Recommended practice for seismic design for substations," Institute of Electrical and Electronics Engineers, New York.

International Code Council Evaluation Service (ICC-ES) [2012] "AC156 Acceptance Criteria for the Seismic Qualification of Nonstructural Components," Brea, California, USA.

Lignos, D.G., Krawinkler, H. [2010] "A steel database for component deterioration of tubular hollow square steel columns under varying axial load for collapse assessment of steel structures under earthquakes," in: Proceedings of the 7th International Conference on Urban Earthquake Engineering (7CUEE) & 5th International Conference on Earthquake Engineering (5ICEE). Tokyo, Japan.

Magliulo, G., Pentangelo, V., Maddaloni, G., Capozzi, V., Petrone, C., Lopez, P., Talamonti, R., Manfredi, G. [2012] "Shake table tests for seismic assessment of suspended continuous ceilings," Bull. Earthq. Eng. 10, 1819–1832. https://doi.org/10.1007/s10518-012-9383-6

McKenna, F., Fenves, G.L., Scott, M.H. [2000] "OpenSees: Open System for Earthquake Engineering Simulation," Pacific Earthquake Engineering Research Center. University of California, Berkeley, CA. Available at: http://opensees.berkeley.edu.

Merino, R.J., Perrone, D., Filiatrault, A. [2020] "Consistent floor response spectra for performance-based seismic design of nonstructural elements," Earthq. Eng. Struct. Dyn. 49, 261–284. https://doi.org/10.1002/eqe.3236

Ministero delle Infrastrutture e dei Trasporti [2019] "Circolare 21 gennaio 2019, n. 7 C.S.LL.PP. Istruzioni per l'applicazione dell'«Aggiornamento delle "Norme tecniche per le costruzioni"," (in Italian).

Ministero delle Infrastrutture e dei Trasporti [2018] "D.M. del 17/01/2018 – "Aggiornamento delle Norme tecniche per le Costruzioni 2018" NTC 2018," (in Italian).

Perrone, D., Calvi, P.M., Nascimbene, R., Fischer, E.C., Magliulo, G. [2019] "Seismic performance of non-structural elements during the 2016 Central Italy earthquake," Bull. Earthq. Eng. 17, 5655–5677. https://doi.org/10.1007/s10518-018-0361-5

Petrone, C., Magliulo, G., Manfredi, G. [2015] "Seismic demand on light acceleration-sensitive nonstructural components in European reinforced concrete buildings," Earthq. Eng. Struct. Dyn. 44, 1203–1217. https://doi.org/10.1002/eqe.2508

Schultz, M.T., Gouldby, B.P., Simm, D., Wibowo, J.L. [2010] "Beyond the Factor of Safety: Developing Fragility Curves to Characterize System Reliability (No. ERDC SR-10-1)," US Army Corps of Engineers. Engineer Research and Development Center.

Soroushian, S., Zaghi, A.E., Maragakis, E. "Manos", Echevarria, A. [2014] "Seismic Fragility Study of Displacement Demand on Fire Sprinkler Piping Systems," J. Earthq. Eng. 18, 1129–1150. https://doi.org/10.1080/13632469.2014.917059

Telcordia Ericsson [2017] "GR 63-05 NEBS Requirements: Physical Protection,".

Wilcoski, J., Gambill, J., Smith, S. [1997] "CERL equipment fragility and protection procedure (CEFAPP)," USACERL Technical Rep. No. 97/58 (No. USACERL Technical Rep. No. 97/58). Champaign, IL.

Development of a code-compliant seismic input for shake table testing of acceleration-sensitive nonstructural elements

M. Zito[1], D. D'Angela[1], G. Maddaloni[2] and G. Magliulo[1,3]

[1] Department of Structures for Engineering and Architecture, University of Naples Federico II, Via Claudio, 21, I-80125 Naples, Italy
{danilo.dangela,martino.zito,gmagliul}@unina.it
[2] Department of Engineering, University of Sannio, Piazza Roma, 21, 82100 Benevento, Italy
giuseppe.maddaloni@unisannio.it
[3] Construction Technologies Institute, National Research Council (ITC-CNR), Via Claudio, 21, I-80125 Naples, Italy

Abstract. Seismic response and performance of acceleration-sensitive nonstructural elements (NEs) significantly depend on the features of the seismic input. Damage severity of real records cannot always be associated with levels of intensity measures, such as peak ground acceleration or Arias intensity, especially if NEs exhibit complex dynamic behavior. In fact, shake table assessment of NEs is often carried out considering artificial seismic inputs that are defined in order to optimize damage severity and seismic representativity. These artificial seismic inputs are typically provided by shake table protocols, which do not often provide details regarding the consistency in terms of seismic hazard and building response; moreover, no literature studies assessed their representativity and damage severity with regard to NEs. The present study reports a novel methodology to generate seismic inputs to be compliant with code seismic demand formulations. These seismic inputs could be primarily used to perform shake table testing but might even be considered as loading histories for implementing numerical analyses. The case study is represented by the Italian building code, which provides a recently developed formulation for determining the seismic demand on NEs. The technical aspects and applicative interventions associated with a robust definition of code-compliant seismic inputs are provided. The potential damage severity of the seismic inputs compliant with Italian building code is estimated and proven to be consistent with seismic demands associated with real severe floor records recorded in instrumented buildings. The study contributes to the literature and practice in terms of technical guidance for defining code-compliant seismic input for shake table testing and seismic qualification. Even though the inputs are developed considering the Italian building code as a reference, the methodology can be easily applied considering other seismic demand formulations.

Keywords: Nonstructural elements, acceleration-sensitive, shake table protocol, Italian building code, seismic assessment, seismic input.

1.INTRODUCTION

Nonstructural elements (NEs) are represented by all those elements that are neither a part of the gravity load resisting system nor a part of the lateral load resisting system but offer functionality to the buildings. The typical examples of NEs in buildings include partitions, masonry walls, cladding, electrical equipment, gas pipes, wastewater pipes, bookshelves, medical equipment, museum artifacts, suspended ceilings, parapets, furniture, tanks, ducts, and elevators. Generally, NEs installed in buildings are sensitive to inertia forces, inter-story displacements, or sometimes to both [FEMA E-74, 2012]. Consequently, based on the sensitivity of their seismic response, these NEs can be grouped under three different categories: (i) force-sensitive (or acceleration-sensitive) NEs, (ii) displacement-sensitive (or interstory-drift-sensitive) NEs, and (iii) combined force-and displacement-sensitive NEs. In past seismic events, numerous buildings reportedly lost their functionalities/operativity solely due to damage in NEs [Baird *et al.*, 2014; Dhakal, 2010; Perrone *et al.*, 2019], though; the structural performance of most of the buildings during these earthquakes was deemed adequate. Past earthquakes that have caused immense damage to NEs include the 2010 Darfield, 2011 Christchurch, and 2016 Kaikōura earthquakes in New Zealand [Baird *et al.*, 2014; Baird & Ferner, 2017; Dhakal, 2010], the 2010 offshore Maule earthquake in Chile [Miranda *et al.*, 2012], 2009 L'Aquila earthquake [Braga *et al.*, 2011], 2012 Emilia earthquake [Magliulo *et al.*, 2014], 2016 Central Italy earthquake [Perrone *et al.*, 2019] and Croatia 2020 Petrinja earthquake in Croatia [Miranda *et al.*, 2021]. Ensuring the operationality and safety of these NEs is essential during an earthquake for guaranteeing the functioning of buildings, especially for critical and strategic facilities such as hospitals [Di Sarno *et al.*, 2019], and they are associated with an extremely large part of building costs [Taghavi and Miranda, 2003]. Thus, assessing the adequacy of existing testing protocols, upgrading and developing new sets of testing protocols to further ensure the seismic safety of NEs is of great interest to the earthquake engineering community.

The present study reports a novel methodology to generate seismic inputs to be compliant with code seismic demand formulations by the Italian building code [MIT, 2019]. The technical aspects and applicative interventions associated with a robust definition of code-compliant seismic inputs are provided. The potential damage severity of the seismic inputs compliant with the Italian building code is estimated and proven to be consistent with seismic demands associated with real severe floor records recorded in instrumented buildings and derived from CESMD database [Partner Data Centers and Networks, 2017]. The study contributes to the literature and practice in terms of technical guidance for defining code-compliant seismic input for shake table testing and seismic qualification/certification. Even though the inputs are developed considering the Italian building code as a reference, the methodology can be easily applied considering other seismic demand formulations.

2. METHODOLOGY

2.1 FRAMEWORK

Shake table input signals are usually expressed as acceleration time histories. The definition of input signals according to existing testing protocols and guidelines is a complex process that often involves different steps and multiple key parameters. Generally, shake table input signals are artificially generated [FEMA 461, 2007; ICC-ES, 2012], but they can also be defined following empirical approaches i.e., considering real earthquakes [IEEE PES, 2018; IEC, 2013]. The seismic input features significantly influence the response of NEs. For example, the seismic input with a time-varying frequency content may have a significant effect on the NEs response, capturing the temporal non-stationarity of realistic earthquake scenarios and ensuring a relatively reliable seismic assessment, [Li *et al.*, 2016; Zhou and Adeli, 2003]. The generation process of the artificially defined input signal is usually based on the definition of the following properties: (a) baseline signal, (c) required response spectra (RRS), (d) compliance/compatibility criteria and rules, and (e) facilities characteristics and capacities. In this study, these features were systematically defined and briefly discussed according to the instructions and recommendations of the most reliable protocols, codes, and literature studies.

2.2 BASELINE SIGNAL

The baseline signal was generated to obtain a nonstationary random signal with an energy content ranging from 1.0 to 32.0 Hz and one-sixth octave bandwidth resolution. The baseline consists of several sinusoidal waves in relation to their phase angle. The baseline signal has a total duration equal to 30 seconds and at least 20 seconds of strong motion. Further details regarding the full procedure can be found in Zito *et al.* [2022].

2.3 REQUIRED RESPONSE SPECTRA (RRS)

2.3.1 Simplified formulation of Italian building code

Equation 1 shows the spectral acceleration (S_a) as a function of the fundamental period of NE (T_a) associated with the simplified formulation for frame buildings provided by the Italian building code [MIT, 2019], where α is the design peak ground acceleration (stiff soil) expressed in *g* units, S is the soil amplification factor, z is the height of the component point of attachment (measured from the building foundations), H is the height of the building measured from the foundations, T_1 is the fundamental building period of the building, and a, b, and a_p are parameters defined according to the fundamental building period. The formulation was derived by Petrone *et al.* [2015, 2016].

$$S_a(T_a) = \begin{cases} \alpha S\left(1+\frac{z}{H}\right)\left[\frac{a_p}{1+(a_p-1)\left(1-\frac{T_a}{aT_1}\right)^2}\right] \geq \alpha S & \text{for } T_a < aT_1 \\ \alpha S\left(1+\frac{z}{H}\right)a_p & \text{for } aT_1 \leq T_a < bT_1 \\ \alpha S\left(1+\frac{z}{H}\right)\left[\frac{a_p}{1+(a_p-1)\left(1-\frac{T_a}{bT_1}\right)^2}\right] \geq \alpha S & \text{for } T_a \geq bT_1 \end{cases} \quad (1)$$

2.3.2 Deriving RRS from simplified formulation

In order to define a formulation for RRS that does not depend on the fundamental building period, Equation 1 was applied considering a wide range of building scenarios, i.e., considering T1 ranging from 0.1 to 2.0 s, which is reasonably compatible with most ordinary buildings over Europe. The RRS formulation was derived by enveloping the set of spectra and is depicted in Figure 1. In particular, the equations defining the envelope depicted in Figure 1 were inspired by the form of Equation 1 and calibrating the key parameters in order to envelope at best the set of Equation 1 curves. The formulation is omitted for the sake of brevity and can be found in Zito *et al.* [2022].

2.4 SPECTRUM-MATCHING PROCEDURE

The spectrum-compatibility procedure was carried out using RSPMatch according to the recommendations provided by Hancock *et al.* [2006]. In particular, the procedure was applied through a time-domain modification of the baseline signal to enforce the RRS spectrum compatibility. The procedure consists of adding to the baseline signal in the time domain some wavelets so that the TRS meets the RRS.

The spectrum compatibility was verified considering different issues. In particular, the test response spectra envelop the RRS ordinates considering a maximum one-sixth-octave bandwidth resolution over the frequency range from 1 to 32 Hz. In the case this did not occur, a maximum of two of the one-sixth octave analysis points may be below RRS, in terms of spectral ordinate, by 10% or less, provided that, for each point, the adjacent one-sixth-octave points are at least equal to RRS.

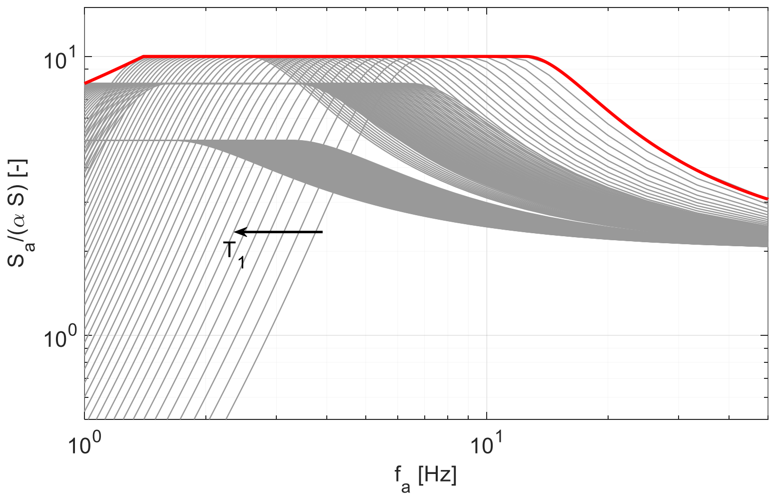

Figure 1. Eq. 1 applied considering a wide range of building scenarios and envelope defining RRS (red line).

2.5 FURTHER PROCESSING AND FACILITY CAPACITIES

As a general rule for shake table testing, the signals to be assigned and reproduced by the earthquake simulator (shake table) should be checked and further processing interventions might be necessary. For technical references regarding AC 156 signals, the readers are referred to Petrone *et al.* [2016]. With particular regard to the present application, the signals derived according to the above-mentioned procedure should be checked to be compatible with the facilities of interest, e.g., shake table and main components (actuators). Among the key parameters to check, the peak displacement represents the most common critical one. In particular, the peak displacement associated with the highest intensity signal should be smaller than the displacement capacity of the shake table. The signal frequency content should be compatible with the frequencies reproducible by the table. Furthermore, it should be checked that the signal performed by the shake table does not induce resonance phenomena, e.g., the resonance of shake table parts, testing infrastructures, or isolated mass. Given the preliminary character of this study, these issues are not addressed in the paper. Further studies will define further processing and facility capacity criteria that reasonably do not affect the consistency and robustness of the signal.

2.6 DEVELOPMENT OF A SET OF COMPLIANT SIGNALS

A set of seven representative input signals, namely new protocol signals (NPSs) was generated to test the consistency and reliability of the procedure. In particular, the input signals were defined considering the target spectra with a S equal to 0.4 g and assuming the z/H ratio equal to one. The time history signals associated with NPSs #1 to #7 are depicted in Figure 2; these signals are compliant with the developed protocol and signal generation methodology. The time histories have (multiple) significantly high peaks; PFA range in 1.45 - 1.88 g, with median values equal to 1.76 g, and coefficient of variation equal to 0.098.

3.SIGNAL PRELIMINARY EVALUATION

3.1 OUTLINE

In this section, NPSs are examined through a multi-level criteria approach: 1) time history assessment, 2) seismic parameter assessment, and 3) spectral assessment. Firstly, the acceleration, velocity, and displacement time histories of NPSs and their spectral response are evaluated. On the second level, few representative seismic parameters typically correlated with seismic damage of dynamic systems are computed for NPSs and are compared with the parameters obtained by considering representative real motions of the floor, referred to as FMs. Finally, the acceleration response spectra of NPS are compared with the response spectra of FMs and existing protocols.

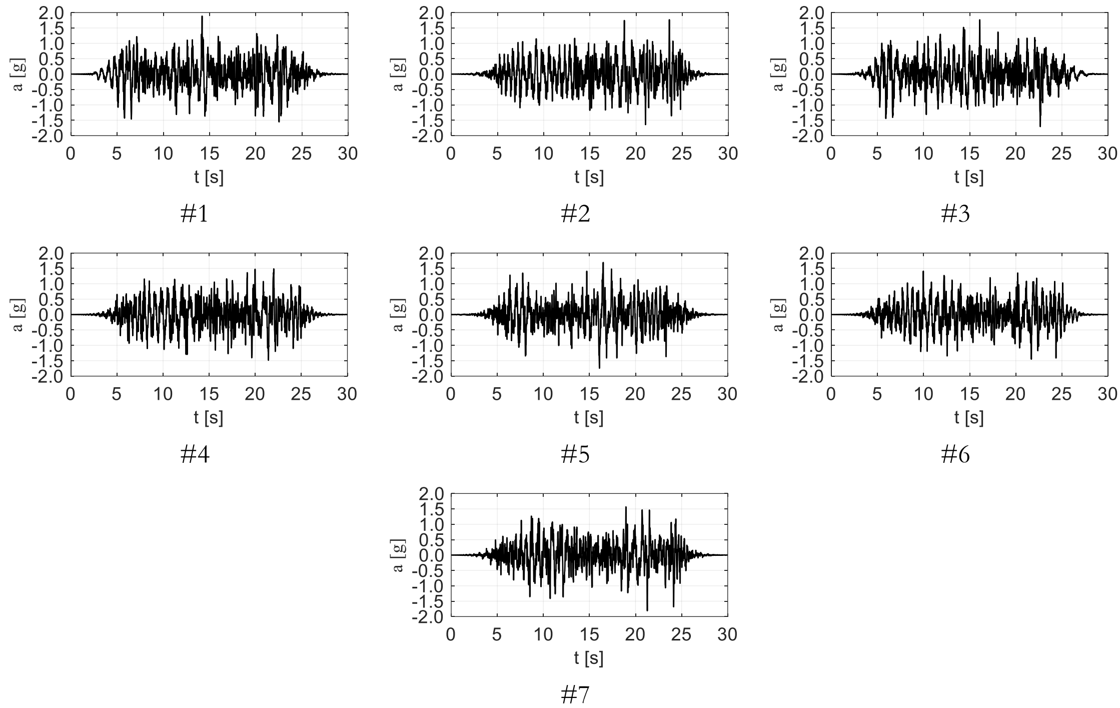

Figure 2. Acceleration time histories related to NPS #1 to #7. NPSs are related to RRS having PGA equal to 0.40 g and assuming z/h equal to one.

3.2 REFERENCE FLOOR MOTIONS

FMs are signals recorded in instrumented US buildings and obtained from CESMD database [Partner Data Centers and Networks, 2017]. FMs are obtained from recordings conducted on concrete buildings designed between 1923 and 1975. FMs are always associated with higher intensity responses on building floors, mostly recorded at the roof level. Two sets of FMs are considered for both seismic parameter and spectral assessment: (set 1 FMs) 24 records with PGA ranging from 0.05 to 0.45 g; (set 2 FMs) seven records with PGA larger than 0.20 g. The number of considered records is relatively representative since sets of seven motions are often considered in the literature, also according to typical regulation requirements (e.g., considering spectral mean value over sever input spectra). Moreover, the considered records equally include near- and far-field motions, considering the same number of low-, medium-, and high-rise buildings as a reference. Further details on the selected floor motions are omitted as the same FM sets were used in D'Angela *et al.* [2021a].

3.3 REFERENCE SHAKE TABLE PROTOCOLS

There are several shake table testing protocols provided by regulations/codes available in the literature. In this study, the most authoritative and reliable existing test protocols available in the literature were considered [D'Angela *et al.*, 2021b]). AC156 [ICC-ES, 2012] is aimed to establish criteria and rules for seismic certification of NEs that are sensitive to the accelerations, i.e., architectural, mechanical, electrical, and other systems attached to structures. This protocol is applicable if NE fundamental frequencies are greater than or equal to 1.3 Hz. FEMA 461 [FEMA 461, 2007] establishes a protocol for shake table testing of structural elements and Nes; the protocol also involves the procedure for PBEE assessment via fragility estimation. FEMA 461 relates to elements that are force-sensitive (or acceleration-sensitive). Finally, ISO 13033 [BS ISO, 2013] defines the method to obtain seismic action and seismic performances of Nes and systems typically anchored.

3.4 SEISMIC PARAMETERS

The parameters considered for the seismic parameter assessment are reported in Table 1. In general, these parameters are usually correlated with the exposed damage to structures and NEs. The parameters used are selected in accordance with the available literature. For further details on these parameters, the reader is referred to the relevant literature (e.g., Table 1).

Figure 3 shows the comparison between NPSs and (set 1 and set 2) FMs in terms of (a) SFMD and (b) PFV/PFA. The results are reported considering each signal and percentile/median thresholds for NPSs and FMs, respectively. Considering both parameters, NPSs provide values that are larger (smaller) than the median (86th percentile) related to set 1 FM ones, whereas NPS values match very well (are larger than) median values of set 2 FM considering PFV/PFA (SFMD). A higher parameter value is usually associated with greater damage potential for the examined parameters. The results obtained demonstrate the reliability and robustness of the protocol methodology. Furthermore, based on the selected seismic parameters, it is confirmed that the protocol loading histories are potentially associated with relatively representative and high damage severity.

Table 1. Seismic parameters and IMs are considered for the assessment of the developed protocol signals. TD is the total duration of the signal, Ia is the Arias intensity [Arias, 1970].

Parameter and formulation		Reference
$\mathbf{SFMD = t_{95} - t_5}$	$t_X = \bar{t} \mid I_a(\bar{t}) = \frac{X}{100} I_a(T_D)$ $I_a(\bar{t}) = \frac{\pi}{2g}\int_0^{\bar{t}} [a(t)]^2 dt$	[Rodriguez *et al.*, 2021; Trifunac & Brady, 1975]
PFV/PFA		[D'Angela *et al.*, 2021b; Kramer, 1996]

SFMD: strong floor motion duration; **PFV/PFA**: peak floor velocity to peak floor acceleration ratio.

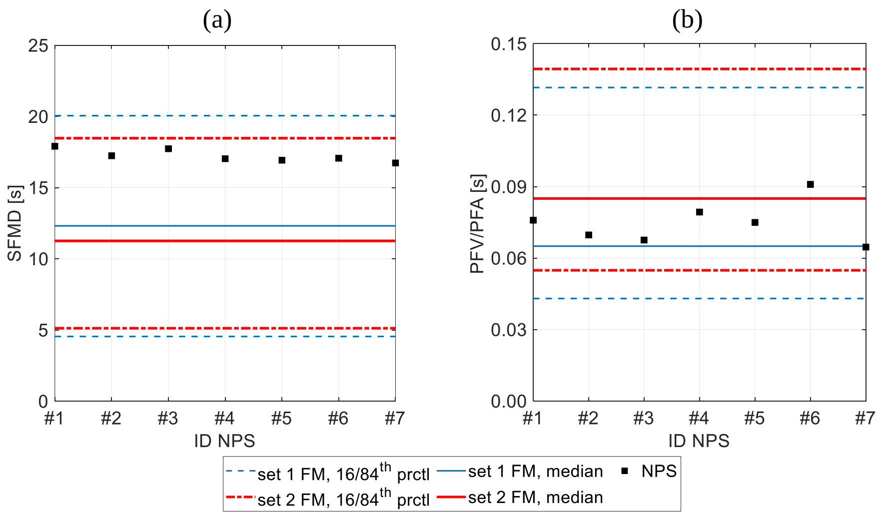

Figure 3. Comparison between NPSs and (set 1 and set 2) FMs considering: (a) SFMD, and (b) PFV/PFA.

3.5 SPECTRAL RESPONSE

Figure 4 depicts spectral comparisons among (a) NPS and most referenced existing shake table protocols and (b) reference FMs and most reference existing shake table protocols, considering PGA equal to 0.50 g. According to Figure 4a, NPS are associated with spectral ordinates that are overall more severe than other protocols, especially over the most amplified response (curve *plateau*). It should be noted that FEMA 461 protocol, which is the only one having larger ordinates corresponding to the amplified region, should be applied considering the spectral ordinate corresponding to the component's period ($S_a(T_a)$) as a reference intensity measure instead of peak floor or ground accelerations, as it is done for other protocols. Therefore, the extremely high severity of FEMA 461 spectra depicted in Figure 4 should be interpreted also considering that the comparison is not fully rigorously consistent by definition.

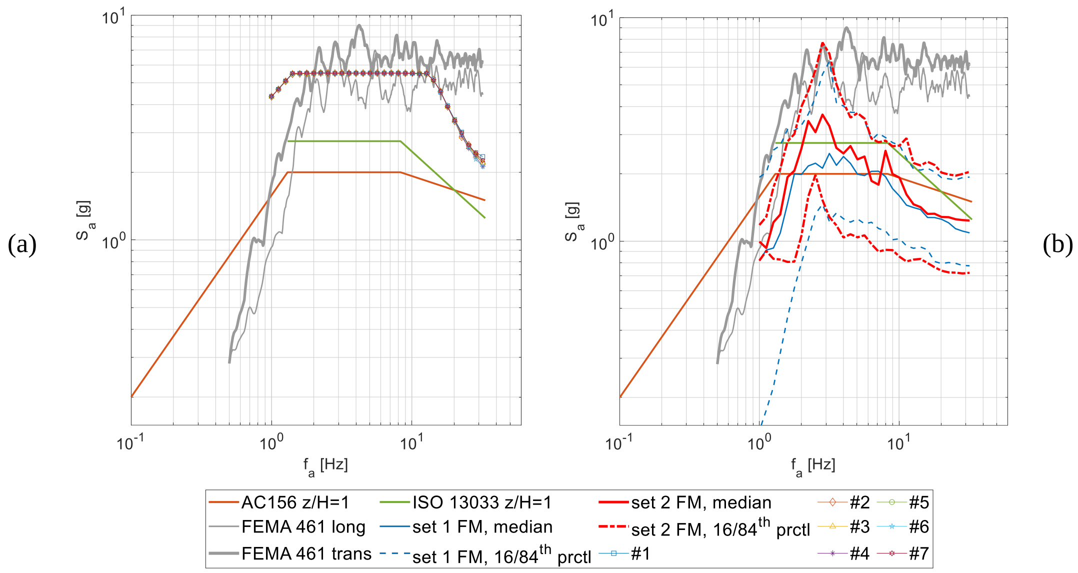

Figure 4. Comparison between RRS/input response spectra related to reference protocols and (a) NPS spectra and (b) FM spectra, considering PGA equal to 0.50 g. All spectra are computed considering 5% damping.

The response of all protocols but the newly defined one (NPSs) and FEMA 461 seems to be less severe in terms of spectral ordinate by considering both Figure 4a and b, especially looking at the upper percentile FM responses. In particular, NPS spectra are overall more severe than most other protocols and FMs over the whole frequency range of interest, and this confirms the potential severity of the developed protocol in terms of elastic spectral response and associated seismic demands. It is worth recalling that the present study reports preliminary results and further analyses, and more comprehensive evaluation and validation processes should be carried out, possibly also considering damage severity and reliability estimations.

4.CONCLUDING REMARKS

The paper disseminates a procedure for developing code-compliant seismic signals for performing shake table tests on nonstructural elements (NEs). In particular, the procedure is implemented and examined considering the seismic demand formulation reported within the Italian building code for frame buildings. The study contributes to the literature towards a more reliable and robust seismic assessment of NEs by means of shake table testing, and the key contributions of the paper are described below.

- The developed framework and methodology can be considered as a reference for developing seismic signals according to given required response spectra (RRS) formulations, towards a more robust seismic assessment of NEs via shake table (methodological and procedural contribution).

- The study supplies a set of seven acceleration time histories compliant with the simplified Italian seismic demand formulation (specific research outcome contribution).
- The developed protocol and signals were proven to be (a) promisingly consistent in terms of seismic parameters and spectral response, considering representative real floor motions, and (b) potentially more severe than alternative reference shake table protocols.

Concluding, it should be mentioned that the provided evidence cannot be considered to be exhaustive and cannot be generalized unless further investigations and validation studies are carried out to this aim.

ACKNOWLEDGMENTS

The study was funded by the Italian Ministry of University and Research (MUR) in the framework of PRIN 2020 project titled "ENRICH project: ENhancing the Resilience of Italian healthCare and Hospital facilities" and by the Italian Department of Civil Protection (DPC) in the frame of the national project DPC – ReLUIS 2022-2024 WP 17: "Code contributions for nonstructural elements".

REFERENCES

Arias, A. (1970). A measure of earthquake intensity in Seismic Design of Nuclear Power Plants (R. J. Hansen, Ed.). Massachusetts Inst. of Tech., Cambridge. Univ. of Chile, Santiago de Chile.

Baird, A., & Ferner, H. (2017). Damage to non-structural elements in the 2016 kaikōura earthquake. Bulletin of the New Zealand Society for Earthquake Engineering (BNZSEE), 50(2).

Baird, A., Tasligedik, A. S., Palermo, A., & Pampanin, S. (2014). Seismic performance of vertical nonstructural components in the 22 February 2011 Christchurch earthquake. In Earthquake Spectra (Vol. 30, Issue 1, pp. 401–425). Earthquake Engineering Research Institute. https://doi.org/10.1193/031013EQS067M

Braga, F., Manfredi, V., Masi, A., Salvatori, A., & Vona, M. (2011). Performance of non-structural elements in RC buildings during the L'Aquila, 2009 earthquake. Bulletin of Earthquake Engineering, 9(1), 307–324. https://doi.org/10.1007/s10518-010-9205-7

Bases for design of structures-Loads, forces and other actions-Seismic actions on nonstructural components for building applications, Pub. L. No. ISO 13033:2013., 1 (2013).

D'Angela, D., Magliulo, G., & Cosenza, E. (2021a). Seismic damage assessment of unanchored nonstructural components taking into account the building response. Structural Safety, 93. https://doi.org/10.1016/j.strusafe.2021.102126

D'Angela, D., Magliulo, G., & Cosenza, E. (2021b). Towards a reliable seismic assessment of rocking components. Engineering Structures, 230, 111673.

Dhakal, R. P. (2010). Damage to non-structural components and contents in 2010 Darfield earthquake. Bulletin of the New Zealand Society for Earthquake Engineering (BNZSEE), 43(4).

Di Sarno, L., Magliulo, G., D'Angela, D., & Cosenza, E. (2019). Experimental assessment of the seismic performance of hospital cabinets using shake table testing. Earthquake Engineering and Structural Dynamics, 48(1), 103–123. https://doi.org/10.1002/eqe.3127

FEMA 461. (2007). Interim Testing Protocols for Determining the Seismic Performance Characteristics of Structural and Nonstructural Components. www.ATCouncil.org

FEMA E-74. (2012). Reducing the Risks of Nonstructural Earthquake Damage-A Practical Guide. http://www.fema.gov/earthquake-publications/fema-e-74-reducing-risks-nonstructural-earthquake-damage

Hancock, J., Watson-Lamprey, J., Abrahamson, N. A., Bommer, J. J., Markatis, A., McCoy, E. M. M. A., & Mendis, R. (2006). An improved method of matching response spectra of recorded earthquake ground motion using wavelets. Journal of Earthquake Engineering, 10, 67–89. https://doi.org/10.1080/13632460609350629

ICC-ES AC156. (2012). Acceptance criteria for seismic certification by shake-table testing of nonstructural components. www.icc-es.org

IEEE Power and Energy Society. (2018). Recommended Practice for Seismic Design of Substations - IEEE 693. IEEE.

Environmental testing - Part 2-57: Tests - Test Ff: Vibration - Time-history and sine-beat method, Pub. L. No. Edition 3.0, 1 (2013).

Kramer, S. L. (1996). Geotechnical earthquake engineering (Prentice Hall, Ed.).

Li, Y., Conte, J. P., & Barbato, M. (2016). Influence of time-varying frequency content in earthquake ground motions on seismic response of linear elastic systems. Earthquake Engineering & Structural Dynamics, 45(8), 1271–1291. https://doi.org/10.1002/eqe.2707

Magliulo, G., Ercolino, M., Petrone, C., Coppola, O., & Manfredi, G. (2014). The Emilia earthquake: Seismic performance of precast reinforced concrete buildings. Earthquake Spectra, 30(2), 891–912. https://doi.org/10.1193/091012EQS285M

Istruzioni per l'applicazione dell'«Aggiornamento delle "Norme tecniche per le costruzioni"» di cui al decreto ministeriale 17 gennaio 2018, 11 23 (2019).

Miranda, E., Brzev, S., & Bijelić, N. (2021). STEER-EERI: Petrinja, Croatia december 29, 2020, Mw 6.4 earthquake Joint Reconnaissance Report (JRR). https://doi.org/10.17603/ds2-1w0y-5080

Miranda, E., Mosqueda, G., Retamales, R., & Pekcan, G. (2012). Performance of nonstructural components during the 27 February 2010 Chile earthquake. Earthquake Spectra, 28(SUPPL.1). https://doi.org/10.1193/1.4000032

Partner Data Centers and Networks. (2017, October 31). Center for Engineering Strong Motion Data (CESMD). Https://Www.Strongmotioncenter.Org/.

Perrone, D., Calvi, P. M., Nascimbene, R., Fischer, E. C., & Magliulo, G. (2019). Seismic performance of non-structural elements during the 2016 Central Italy earthquake. Bulletin of Earthquake Engineering, 17(10). https://doi.org/10.1007/s10518-018-0361-5

Petrone, C., Magliulo, G., & Manfredi, G. (2015). Seismic demand on light acceleration-sensitive nonstructural components in European reinforced concrete buildings. Earthquake Engineering and Structural Dynamics, 44(8), 1203–1217. https://doi.org/10.1002/eqe.2508

Petrone, C., Magliulo, G., & Manfredi, G. (2016). Floor response spectra in RC frame structures designed according to Eurocode 8. Bulletin of Earthquake Engineering, 14(3), 747–767. https://doi.org/10.1007/s10518-015-9846-7

Rodriguez, D., Perrone, D., Filiatrault, A., & Brunesi, E. (2021). A probabilistic strong floor motion duration model for seismic performance assessment of non-structural building elements. Earthquake Engineering & Structural Dynamics, 50(15). https://doi.org/10.1002/eqe.3550

Taghavi, S., & Miranda, E. (2003). Response Assessment of Nonstructural Building Elements - PEER 2003/05.

Trifunac, M. D., & Brady, A. G. (1975). A study on the duration of strong earthquake ground motion. Bulletin of the Seismological Society of America, 65(3), 581–626. https://doi.org/10.1785/BSSA0650030581

Zhou, Z., & Adeli, H. (2003). Time-Frequency Signal Analysis of Earthquake Records Using Mexican Hat Wavelets. Computer-Aided Civil and Infrastructure Engineering, 18(5), 379–389. https://doi.org/10.1111/1467-8667.t01-1-00315

Zito, M., D'Angela, D., Maddaloni, G., Magliulo, G. (2022). A shake table protocol for seismic assessment and qualification of acceleration-sensitive nonstructural elements. Computer-Aided Civil and Infrastructure Engineering (under review).

Mitigate Seismic Rocking Responses and Deformations on the Isolated Equipment-Platforms Sets by Wire Rope Isolators Mounted in Low-Rise Buildings

A. Al Jawhar[1]

[1]Structural Engineer, United States Army Corps of Engineers, Chicago District
231 S. LaSalle St, Suite 1500, Chicago, Illinois 60604
e-mail: ammar.aljawhar@usace.army.mil

Abstract. Even though damaged equipment represents a major cost in earthquake disasters, a validated seismic procedure for designing protective systems for equipment does not exist yet. The objective of this research is to define seismic protective mechanisms based on wire rope isolators (WRIs) for a mounted equipment platform at the roof of a six-story hospital building. The study includes: (1) definition of seismic demands on equipment mounted in low-rise buildings, (2) identification of WRI mechanical properties in different configurations, (3) design of WRI systems to support the equipment, and (4) evaluation of the designs using numerical analysis.
For the seismic demand's definition, an available methodology is adjusted and implemented to generate spectral absolute floor accelerations and then compared with two code-specifications (ASCE7-16, and AC156-ICC). The dynamic characteristics of the systems are selected to avoid the resonance by defining the isolation period which shift away from the natural frequencies of the building. The protective systems are defined to be relatively stiff with an energy-dissipation capacity to mitigate seismic effects. The WRI systems are designed in two configurations: (1) conventional platform with WRIs working in shear/roll horizontally and tension/compression vertically, and (2) platform with inclined WRIs to mitigate the seismic rocking responses of a conventional configuration by reducing or eliminating the eccentricity between the system center of stiffness and the equipment centre of mass. Numerical analyses are conducted using nonlinear time history analysis using SAP2000 to evaluate the design of equipment-platform sets. When the inclined WRIs are implemented, the result of the study shows that rocking responses on the equipment-platform system are significantly reduced to a range of 74% to 95%; furthermore, the equipment deformations are significantly reduced to a range of 50% to 90%. Results from numerical analysis suggest that further investigations are necessary to study the effects of modeling assumptions.

Keywords: Floor seismic demands, floor mounted isolated equipment, wire rope isolator platform, equipment rocking responses, nonlinear time history analysis.

Acknowledgments: The research reported herein was supported by the National Science Foundation (NSF) awarded under Grant No. CMMI-1150462. The author wants to acknowledge the support of Dr. Claudia Marin-Artieda by providing the experimental data and required software and tools to accomplish this research in the graduate school at the Howard University, Washington DC.

1. INTRODUCTION

This paper presents some facts of the research work that described in [Al Jawhar, 2019] to predict the seismic demands on floor mounted equipment attached to a 6-story hospital building. Further, this study defines seismic protective measures based on wire rope isolators (WRI) platforms supporting mounted equipment at the hospital roof, evaluates the design of the WRI platform, and investigates the responses by numerical analysis. The WRI platforms consist of steel plates sandwiched by WRIs and are employed in this research as a seismic isolation/damping interface between the equipment base and the excited floor below. As it is known, the equipment and non-structural components (NSC) in fixed-base buildings experience significant earthquake accelerations. These fixed-base buildings amplify the ground accelerations at every floor throughout the height of the building that may lead to major damage to the NSC. WRI is employed as a seismic protective system because it has sueperior performance characteristics including flexibility in its three main axes, it has stable dynamic properties with ability to mitigate energy by high inherent damping, it has high resistance to chemicals and harsh corrosive environments, and wide range of sizes are available to support different equipment. In critical facilities like hospitals, the indirect losses due to damaged essential equipment can be two to three times greater than the cost of replacing collapsed buildings [Sankaranarayanan, 2007]. Even though hospitals structures are seismically designed, the validated seismic design procedures of protective systems for various essential equipment do not exist.

2. METHODOLOGY

2.1 BUILDING DESCRIPTION

A known current need, the research herein provides for the first time, a validated practical methodology that can be used to design WRI platforms for protection of different equipment attached to essential low-rise buildings at different levels. The selected hospital is a 6-story essential building located in Sylmar neighbourhood of Los Angeles, California. This building is selected for the following reasons: (1) the current study focuses on low-rise buildings with short fundamental periods ranging from 0.3 to 0.5 sec, (2) this building is an essential facility and is expected to respond seismically within the elastic range (linearly), and therefore significant amplification of accelerations on floors are expected, (3) the building is instrumented for recording of seismic motions at different levels; the recorded data of different earthquakes are available at the Center for Engineering Strong Motion Data (CESMD), and (4) the building is located in a high seismic zone. Figure 1 presents the building plan and elevation views and the seismic sensors locations. In 1994, a high seismic event (Northridge) hit this hospital, and even though the primary structure performed well with minimal damage, it transferred significant accelerations to different attached NSC that were subjected to a major damage, which led the hospital to not being functional and evacuated for long time.

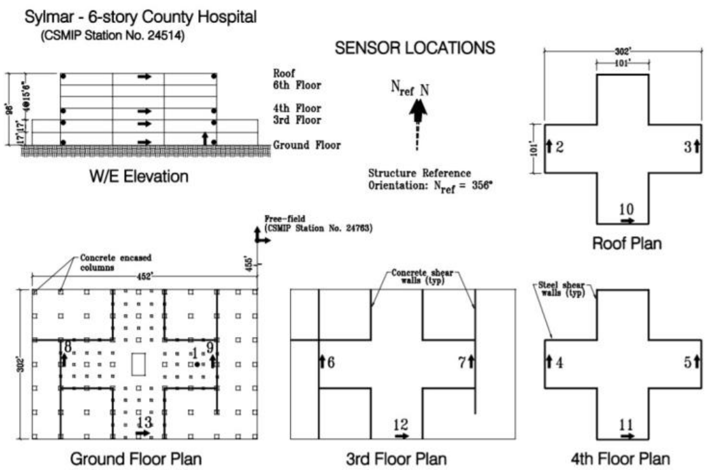

Figure 1. Plan and Elevation Views of the Olive View Hospital (CESMD)

1

2.2 SEISMIC FLOOR RESPONSE

The horizontal design ground spectrum (H-DGS) is constructed based on the location of the hospital building (Latitude 34.324°N, Longitude -118.446°W) and is a class IV (Essential Facility) using the U.S. Seismic Design Maps provided by the U.S. Geological Survey (USGS) as shown in Figure 2. The horizontal seismic floor acceleration demands on the equipment-platform sets are defined based on the procedures reported by Wieser [Wieser, et al., 2012] and adjusted to be used for low-rise buildings at different levels. The Wieser's procedure is proposed to generate the horizontal acceleration amplification envelops at different levels of tall buildings responding in periods of more than 1.0 sec. The generated floor accelerations by this procedure account for the effects of building dynamic properties including the height, fundamental period of the primary structure (T_1) (a parameter that currently is not included in the ASCE provisions), and period ratio of the equipment to the primary structure (T_p/T_1). See Wieser's methodology that is described in the literature of [Al Jawhar, 2019]. In this research, the Wieser's methodology is adjusted to consider the influence of higher modes amplification on the spectral envelopes of low-rise buildings to be used for the design of platforms. This adjusted method is assessed by comparing with a variety of acceleration spectra generated from different resources. To identify the building roof linear response characteristics, the recorded motions are used to develop the roof spectra that are normalized by the ground spectrum. That normalization is used to estimate the amplification of ground accelerations throughout the height of the hospital, and to define the fundamental period (T_1) and higher periods (T_2) and (T_3) that represent the periods at second and third modes, respectively [Marin-Artieda, 2014] as shown in Figure 3.

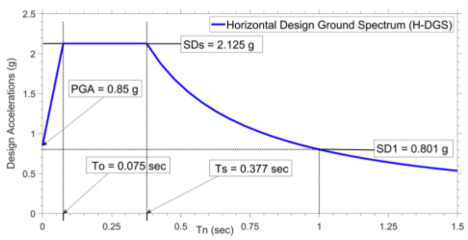

Figure Errore. Nel documento non esiste testo dello

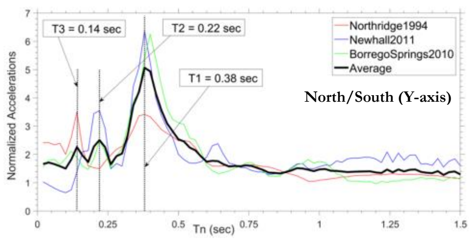

Figure 3. Normalized Roof Accelerations Spectra

2.3 DESIGN OF WRI PLATFORMS

The WRI behaves symmetrically in horizontal directions including shear (S) longitudinally and roll (R) transversely. In the vertical direction, the WRI responds asymmetrically when subjected to tension (T) and compression (C). The dynamic properties of the WRI platforms including fundamental period, effective stiffness, and effective damping ratio are selected. These dynamic properties are determined based on the assumption to avoid tuning (resonance) with the dominant frequencies of the floor accelerations. From the design displacement spectrum that develops based on the adjusted acceleration envelop, a preliminary selection of WRI size and T_p are specified based on the WRI displacement capacity. This preliminary selection is taking into consideration that WRI is to be relatively stiff to achieve high damping. The selected equipment dynamic properties which control the platform design include the weight, geometry, and location of center of mass (C.M.). The rocking response of the isolated equipment due to installing the WRI platform in a conventional configuration is evaluated. This undesirable rocking is controlled by implementing inclined WRIs. Based on the equipment geometry and platform dimensions, the angles of WRIs inclination are defined to minimize the eccentricity between the WRI platform center of stiffness (C.S.) and the C.M.

2.4 NUMERICAL ANALYSIS

A non-linear time history numerical analysis is performed using the computer program SAP2000 to evaluate the design of platforms. A set recorded seismic floor motion is selected from the database of CESMD and scaled up to the adjusted Wieser's design acceleration envelop at the roof level. This scaled set is then applied as input floor excitations to the numerical model. These models are developed to simulate the WRI platforms supporting a cooling tower. To illustrate the effect of different WRI installation configurations, three different platforms are modeled: (1) a fixed platform bolted directly to the floor (FP), (2) a WRI platform in the conventional configuration (CP_{WRI}), and (3) an inclined WRI platform (IP_{WRI}). The WRIs are modelled using two different bilinear models available in SAP2000: (1) a multilinear plastic (MLP), and (2) a plastic Bouc-Wen (PW). The numerical models assume the equipment to be a rigid frame with uniform mass distribution. The maximum responses obtained from the models including the deformations and rocking are evaluated by assessing the performance of the equipment with and without the WRI platforms.

3. RESULTS

3.1 HORIZONTAL SEISMIC DEMANDS ON EQUIPMENT-PLATFORM SET

The Wieser's envelop is developed considering a damping ratio (ξ = 5%) and compared with the normalized spectral accelerations of the recorded motions at the roof in N-S (Y-axis). These motions spectra are scaled up to match Wieser's envelop for assessment as presented in Figure 4. Further, the design (absolute) spectral acceleration is developed by multiplying Wieser's envelope by H-DGS of the hospital as shown in Figure 5.

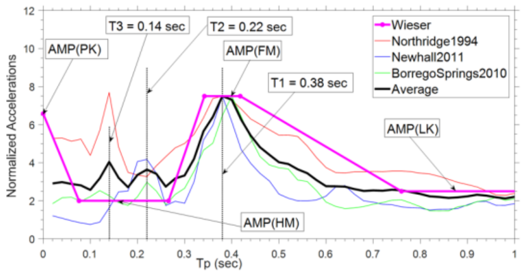

Figure 4. Normalized Spectral Acceleration

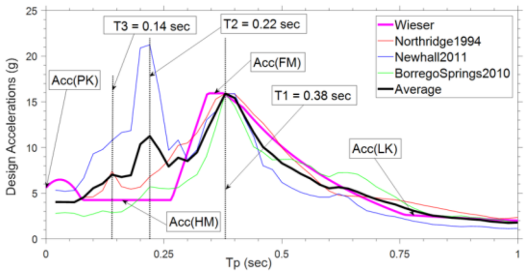

Figure 5. Design Spectral Accelerations

Figure 4 shows that the Wieser's envelope does not reproduce well the seismic acceleration amplification at the higher modes T_2 and T_3 that appear significantly in low-rise buildings. The spectra from recorded motions exhibit higher amplification at higher modes with periods ranging between 0.06 sec and 0.28 sec. Figure 5 shows that the Wieser's approach underestimates the design accelerations at higher modes periods of about 63% of the average recorded accelerations. To better capture the amplification of acceleration at the building floor higher modes, the Wieser's approach is modified. The envelope will have a constant acceleration within the major periods at the peak amplification (AMP_{Pk}), higher mode amplification (AMP_{HM}), and fundamental amplification (AMP_{FM}) as presented in Figures 6. As a result, Figure 6 shows that the adjusted Wieser's approach results in significant design floor accelerations, near 16 g. This is because the hospital building is in a high seismic zone, and the approach assumed that the building responds linearly. Moreover, the adjusted Wieser's amplification envelop at the roof is compared against unscaled spectral amplifications obtained from two code-specifications ASCE 7-16 and AC156-ICC, recorded motions from the Olive View hospital, and records from the experimental work of a five-story building on a shake-table. The recorded motions of the experimental building are evaluated at the University of California, San Diego (UCSD) [Astroza, et al., 2014] and reported on Figure 7 as FB3-ICA50, FB4-ICA100, and FB5-DEN67.

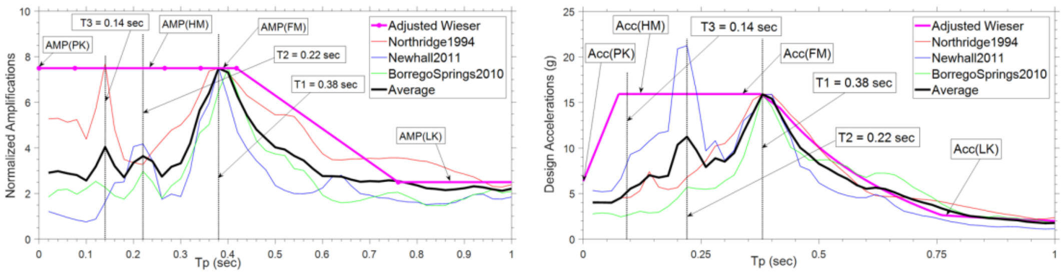

Figure 6. Adjusted Wieser's Approach Versus Recorded Hospital Response Spectra at the Roof, N-S (Y-axis)

3

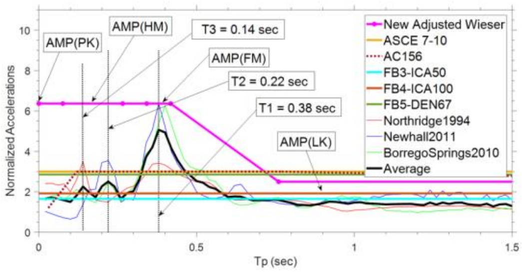

Figure 7. New Adjusted Wieser's Envelope Vs Recorded Motions and Codes Envelopes

Based on the above observations of unscaled spectra in Figure 7, a new modification is implemented to adjust the Wieser's envelope by lowering the constant acceleration amplification value of 7.5 to 6.37. This represents the highest measure of resonance amplification level based on the Newhall2011 response spectra. It is noticeable that the new adjusted Wieser amplification envelop is more practical considering the linear response of essential buildings versus other codes envelopes in ASCE 7-16 and AC156-ICC. These codes are estimated lower amplifications at the fundamental and higher modes. Figure 8 presents the design spectral accelerations and displacements on the mounted equipment-platform systems. These design spectra are developed from the adjusted Wieser's approach, new adjusted Wieser, and two code-specifications ASCE 7-16 and AC156-ICC. The design accelerations of new adjusted Wieser defined reasonable maximum values of acceleration 13.53 g. Even though the essential buildings are usually designed to respond linearly, the spectral amplification of both codes-specifications ASCE 7-16, and AC156-ICC are underestimating the design accelerations values about 53% and 75% considering some nonlinear building responses during seismic events, versus the linear response assumption of new adjusted Wieser's envelope.

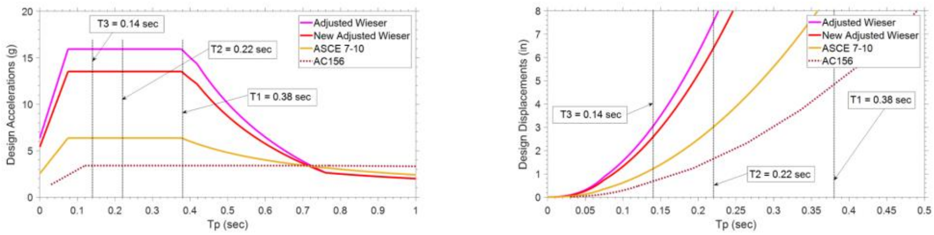

Figure 8. Comparing Design Spectra of the Wieser with the Codes at the Roof, N-S (Y-axis)

3.2 DESIGN OF WRI PLATFORMS SUPPORTING COOLING TOWER

A cooling tower PT2-0709A-1H1 model manufactured by Baltimore Aircoil Company is considered in this study, and it is assumed to be mounted at the roof of the hospital building. Table 1 presents the major data of the equipment including the location of C.M. The steps that are required for the preliminary design of WRI platforms in the conventional configurations are summarized in the following flow-chart, see Figure 9. To start the design of the WRI platform in S/R, the horizontal design spectra for 5% and 10% damping are developed per the new adjusted Weiser approach as shown in Figure 10. According to [Demetriades, et al., 1992], the WRI can offer significant energy dissipation capacity at low deformation levels, and to account for that in this work, an effective damping ratio of 10% is assumed for the WRI platform [Marin-Artieda and Han, 2017]. Further, a vertical design spectrum is developed according to ASCE code requirements to design WRI in T/C as shown in Figure 10. To determine the WRI size, the dynamic characteristics data of WRIs are obtained from the manufacture VMC Group CB Series Helical Wire Rope Isolators for this study.

Table 1. Summary Features of Equipment

Equipment	Cooling Tower
Weight, W, (kip)	6.21
Dimensions, (BxDxH) (in)	107.75 x 87.30 x 136.89
Height of C.M. from Base (in)	66.13
Engine RPM	1800
Forcing Frequency f (Hz)	30

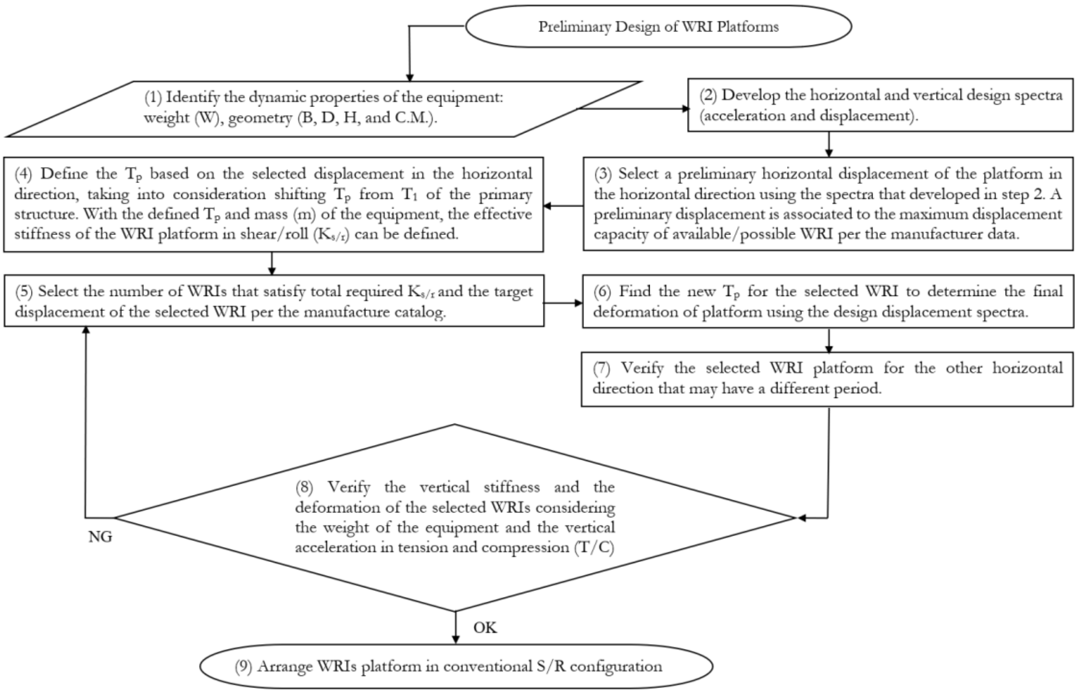

Figure 9. Steps for Preliminary Design of the WRI Platform

Based on the equipment dynamic properties, the WRI CB 1700-15 is selected per the preliminary required platform deformation (D_h = 2 in). Figure 11 presents CB 1700-15 WRI stiffness data (force/deformation). Then, the platform period (T_p = 0.15 sec) and design accelerations (A = 9.79 g) are specified using design spectra. The required total shear/roll stiffness of the platform is calculated ($K_{S/R}$ = 30.15 kip/in) for horizontal direction. Accordingly, eight WRIs ($K_{S/R}$ = 3.77 kip/in, each) are specified to support the cooling tower, which satisfy the required total $K_{S/R}$ of the platform. In addition, the translational periods and deformations are verified considering the actual response of the selected WRI (T_p = 0.13 sec that shifted away from the natural periods of the building T_1, T_2, and T_3 to avoid the resonance) and (D_h = 1.75 in), respectively. Further, the vertical tension and compression stiffness capacity (K_T, K_C) of WRI platform, T_p, and D_v are checked that they conservatively satisfy the required vertical effective stiffness of the platform. Refer to [Al Jawhar 2019] for the results in detail. Finally, the selected WRIs are arranged symmetrically in a conventional configuration as shown in Figure 13. Given the geometry of cooling tower and WRIs arrangement, it is anticipated that the isolated equipment by WRI in conventional configuration may experience a significant rocking response during earthquakes events according to [Demetriades, et al., 1992].

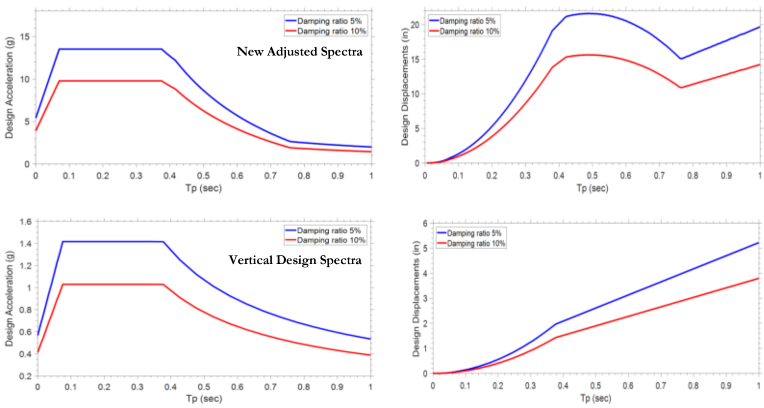

Figure 10. Design Spectra at the Hospital Roof

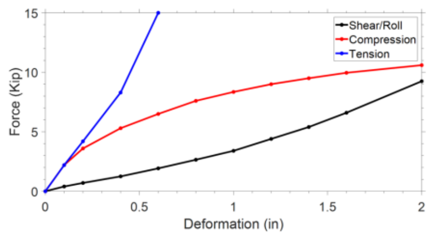

Figure 11. Stiffness Data (Force-Deformation) of WRI CB1700-15 for Cooling Tower

3.3 EVALUATION OF ISOLATED EQUIPMENT ROCKING RESPONSE

The rocking is an undesirable response that may damage the equipment, which is dependent on the properties and geometry of the equipment and platform. The seismic rocking (rotations) of the cooling tower-platform system is evaluated in the vertical planes XZ (Face A) and YZ (Face B) about the horizontal X and Y axes, respectively. See the flow-chart steps to evaluate and control the rocking response in Figure 14. This rocking response may happen due to a combination of the WRIs flexibility in all axes and the location of the equipment C.M. that can create a significant eccentricity with the platform C.S. The Demetriades's methodology described in the literature of [Al Jawhar, 2019], is used to evaluate the effective rocking periods (T_r). Figure 12 presents rocking parameters used to evaluate the T_r that found nearly about 0.05 sec for both directions.

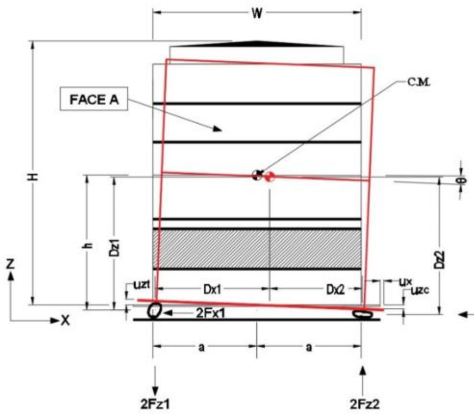

Figure 12. Rocking Parameters

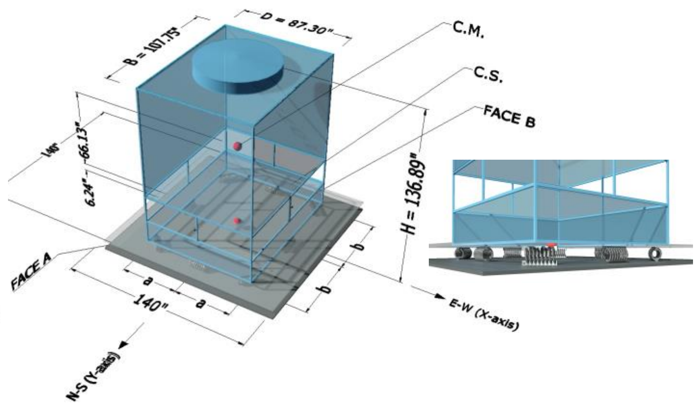

Figure 13. Cooling Tower Isolated with 8 WRIs Platform Conventionally

To control rocking response due to WRI platform in a conventional configuration:

Calculate the horizontal shear forces and the vertical tension/compression forces due to the rocking responses on the platform.

Calculate the moments around the C.M. of the equipment and the rotational stiffness of the WRI platform to evaluate the rocking periods in XZ and YZ planes.

Rotate the WRIs to overcome the rocking response by an angle that eliminate the eccentricity distance between the C.M. of the equipment and the C.S. of the platform.

Find the stiffness of inclined WRI in the global horizontal and vertical axes K_h and K_v.

Calculate the periods and the deformations of the inclined WRIs in the global horizontal and vertical directions.

Finalize the configuration of the inclined WRI platform.

Figure 14. Steps for Final Design of the Inclined WRI Platform

3.4 CONTROLLNG OF ROCKING RESPONSE

The rocking response can be controlled when rotating the WRIs in a specific angle to reduce or eliminate the eccentricity between the C.M. of the equipment and the C.S. of the platform as shown in Figure 15. For the cooling tower, inclined WRIs at a 45° angle is defined to control rocking. This inclination allows the C.S. of the platform and the C.M. to coincide and to decuple translational from the rotational responses because, in theory, the inertia force of the isolated equipment and the reaction forces at WRIs acts through the C.M. The horizontal and vertical stiffness (k_h) and (k_v) of the inclined WRI platform are estimated based on the experimental study of [Marin-Artieda and Han, 2017], that is described in the literature of [Al Jawhar, 2019]. Further, the periods are updated considering the increasing stiffness of the inclined isolators. The inclination of WRI is coupled to the working directions of T/C/S/R. The results of coupled directions T/S/R showed: $k_h = k_v = 14.81$ kip/in, $T_p = 0.07$ sec, platform deformations $U_h = 0.53$ in, and $U_z = 0.06$ in. While the results of C/S/R: $k_h = k_v = 4.96$ kip/in, $T_p = 0.13$ sec, $U_h = 1.5$ in, and $U_z = 0.15$ in.

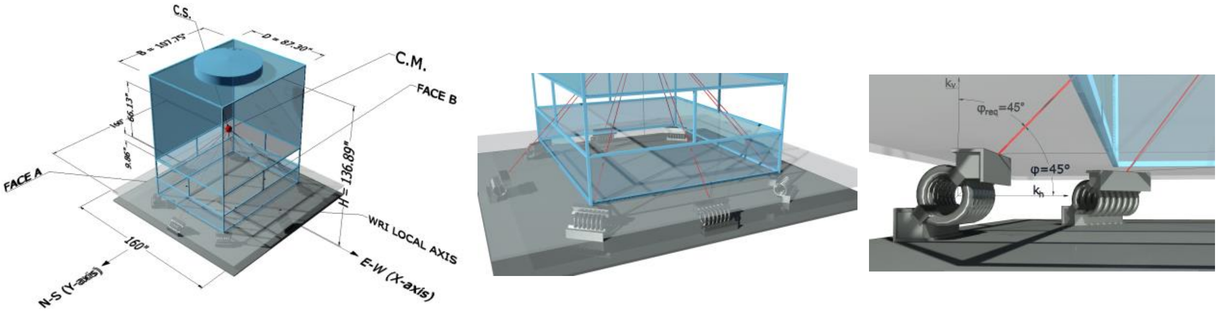

Figure 15. Isolated Cooling Tower with Inclined WRIs Platform at φ = 45°

3.5 NUMERICAL ANALYSIS OF WRI PLATFORMS

A set of recorded acceleration histories are selected from CESMD and used as input floor excitations using nonlinear time history analysis. The accelerations spectra are developed and scaled up to match the new adjusted Wieser design spectrum at the roof as shown in Figure 16. The WRI CB1700-15 data presented in Figure 11 are used to define the properties of multilinear plastic (MLP) link and plastic-Wen (PW) link models that are available in the SAP2000 software.

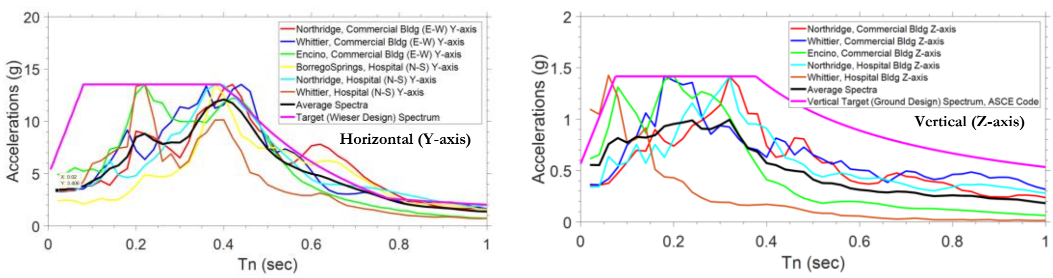

Figure 16. Scaled Recorded Accelerations Spectra at Target Spectrum of the Roof

The PW link element offers the possibility to model symmetric plastic behaviour only in all directions. The inability of the PW link to capture asymmetrical vertical behaviour in T and C of WRIs made the MLP link the only option available in SAP 2000 to capture asymmetric behaviours of the WRIs vertically. However, both links are modelled in this study. The properties of the links are defined including yield strength (F_y), post-yield stiffness ratio (r), and yielding exponent (E_y). The r represents the ratio of plastic stiffness (k_p) to elastic stiffness (k_e). To study the effect of asymmetric vertical behaviour of WRIs, the MLP link is implemented in the models by defining the bilinear stiffness curves in the positive and negative sides using the stiffnesses data k_e and k_p. Table 2 presents the calculated properties of MLP link for WRI CB1700-15.

Table 2. Properties of Multilinear Plastic Link (MLP) for Bilinear Stiffness Curve

WRI CB1700-15 of Cooling Tower									
Horizontal Stiffness (X & Y Axes)					Vertical Stiffness (Z-Axis)				
Behaviour	Nonlinear			Linear	**Behaviour**	Nonlinear			Linear
	$U_{2,3}$ (in)	F (kip)	K (kip/in)	K_{eff} (kip/in)		U_1 (in)	F (kip)	K (kip/in)	K_{eff} (kip/in)
Shear/Roll	-1.94	-8750	k_p = 4.61	4.63	**Tension**	-0.52	-12.80	k_p = 24.62	25.00
	-0.06	-500	k_e = 5.00			-0.08	-2.20	k_e = 27.50	
Shear/Roll	0.06	500	k_e = 5.00	4.63	**Compression**	0.08	2.20	k_e = 27.50	5.30
	1.94	8750	k_p = 4.61			1.92	8.40	k_p = 4.38	

Table 3 shows the stiffness properties of the PW link. Since this link is not able to capture asymmetric geometric nonlinear T/C behaviour, an average vertical effective stiffness (k_{eff}) of T and C for the link is considered in the analysis for the platform. The results of both PW and MLP models are discussed below.

Table 3. Properties of Plastic-Wen Link

WRI CB1700-15 of Cooling Tower					
Behaviour	Nonlinear Properties				Linear
	k_e (kip/in)	F_e (kip)	r	E_y	K_{eff} (kip/in)
Horizontal (S/R) Stiffness (X & Y Axes), $U_{2,3}$	8333	500	0.5412	2	4625
Vertical (T/C) Stiffness (Z Axis), U_1	(1)	(1)	(1)	(1)	15150

(1) Unavailable asymmetrical nonlinear properties in vertical direction

Sample of deformed shapes from multiple vibrational modes of conventional WRI platform (CP_{WRI}) and inclined WRI platform (IP_{WRI}) models using MLP links are presented in Figures 17 and 18, respectively. It is noticed that the second mode of the CP_{WRI} model is controlled by rocking that shows the equipment vertical plane YZ rotating about the horizontal X axes. The second mode of IP_{WRI} model is significantly reduces the rocking and is controlled by translational response in Y-axis. The IP_{WRI} model demonstrated a shorter period due to increasing the horizontal platform stiffness when the WRIs are rotated. This is successfully achieved by shifting T_p from T_1 = 0.38 sec of the primary structure to avoid the resonance.

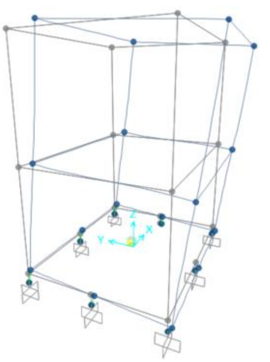

Figure 17. 2nd Mode (Rocking), CP_{WRI} (T_{p2} = 0.32 sec)

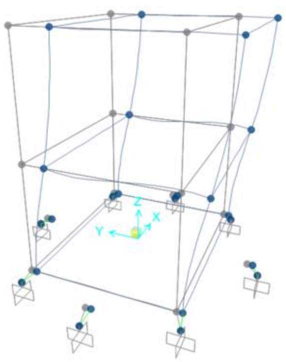

Figure 18. 2nd Mode (Translational), IP_{WRI} (T_{p2} = 0.22 sec)

Figure 19 shows the results of different equipment-platform model responses including the deformations and rocking for the cooling tower supported by FP, CP_{WRI}, and IP_{WRI}. These results data are collected from six recorded motions in X and Y directions. The deformation of equipment is defined as the difference between the top displacement of the equipment relative to the platform displacement. The rocking responses are tracked by observing the maximum rotations of equipment-platform about the X and Y axes. The results show that the deformations are significantly reduced by CP_{WRI}, and IP_{WRI} versus FP in X-axis. Reductions range between 67% to 90%. While on the Y-axis, the WRI platforms reduced the deformations in a range of 50% to 86%. Also, the rocking responses that appeared in CP_{WRI} are significantly reduced in the models supported by IP_{WRI} configuration under all motions. Reductions range between 78% to 94% about the X-axis and 74% to 95% about the Y-axis.

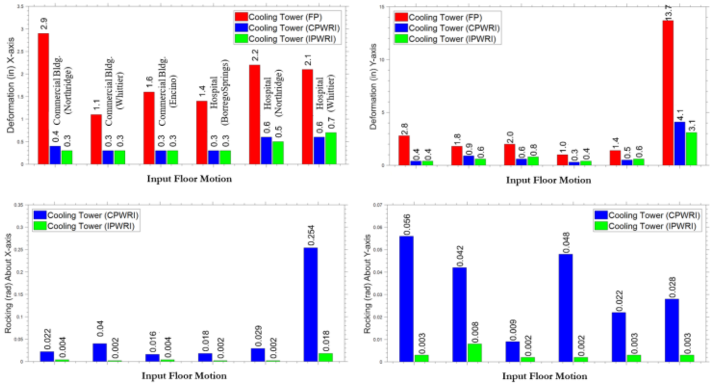

Figure 19. Bar Responses of Cooling Tower Supported by Different Platforms based on MLP

Figures 20 shows a sample of deformations history responses of the cooling tower models under the Northridge commercial building input motion in the X-axis. The histories show that the deformation of FP is reduced by about 86% using the CP$_{WRI}$ and 90% by the IP$_{WRI}$. The results show that the deformation responses from both model links of PW and MLP are similar horizontally. Figure 21 presents the history of rocking (rotational) responses of the isolated cooling tower based on MLP and PW models under the Northridge commercial motions. The figure shows that the rocking response using the IP$_{WRI}$ is reduced by about 84%. Similar rocking response reductions were found for both models, using the PW and MLP links.

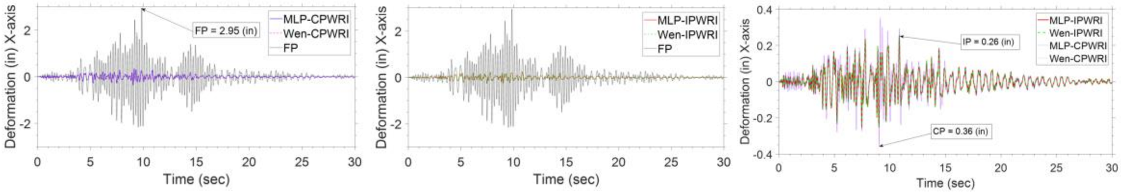

Figure 20. Deformation Histories (Northridge, Commercial Bldg. Motion) of the Cooling Tower

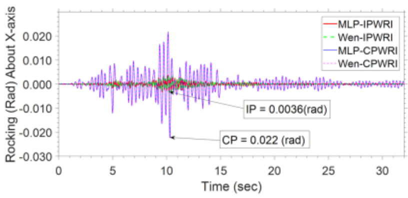

Figure 21. Rocking Histories of Cooling Tower (IP$_{WRI}$ vs. CP$_{WRI}$)

A sample of hysteresis responses (force/deformation) of the CP$_{WRI}$ and the IP$_{WRI}$ in the X-axis using models of the MLP and the PW links under the Northridge commercial motion are presented in Figure 22. The CP$_{WRI}$ shows that the horizontal deformation responses are less than one inch and within the capacity of the WRI CB1700-15. Since the IP$_{WRI}$ exhibits higher stiffness, the platform responses demonstrated smaller deformations of about 55% less than the CP$_{WRI}$, and a larger hysteresis (damping) that represents more energy dissipation capacity. Finally, the responses showed some inconsistencies in the hysteresis results in the vertical direction. It is demonstrated inability of the MLP models to simulate well the asymmetrical vertical behaviour, energy dissipation capacity, and nonlinearity of the WRIs when subject to T and C. These results suggest further investigation is necessary to study WRI platform effects using the MLP model to mitigate equipment responses.

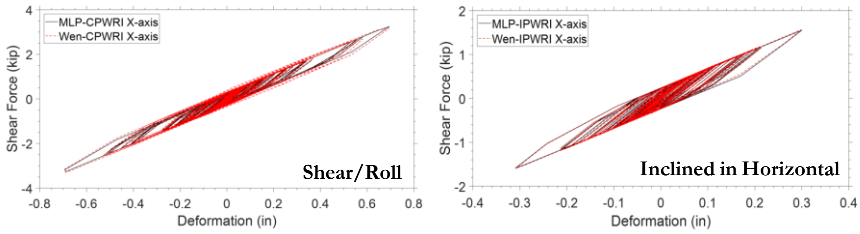

Figure 22. Hysteresis Responses (Force/Deformation) of the WRI CB1700-15

4. CONCLUSIONS

The Wieser's approach is adjusted to better capture the seismic floor acceleration amplification at the higher modes that develop in low-rise buildings. The adjusted Wieser's amplification envelop is developed and compared against the acceleration amplifications obtained from the code-specifications (ASCE 7-16, and AC156-ICC), recorded motions from the selected hospital, and the motions of UCSD experimental building. It is found that both codes-specifications demonstrate significant underestimation of the acceleration amplifications within the range of fundamental and higher modes of essential linearly responding low-rise buildings. These codes consider some nonlinear building behaviours during the earthquake events that are not reflect the actual behaviour of essential low-rise buildings. This nonlinear assumption that may the flexible and tall buildings undergo is considered to include the dissipation of seismic energy that reduces the amplification accelerations. Further, the study discussed that the isolated mounted equipment supported by the WRI platform in a conventional configuration is subjected to significant rocking responses (rotations) due to seismic floor excitations. This rocking response is controlled when rotating the WRIs at a specific angle to reduce or eliminate the eccentricity between the C.M of the equipment and the C.S. of the platform. The results also showed that the vertical and horizontal stiffnesses of the inclined WRIs are increased by the rotation. This increase in stiffness led to lower the WRI platform deformations, produced more energy dissipation capacity, and shifted T_p of the equipment-platform system from the natural periods T_1, T_2, and T_3 of the hospital structure to avoid the resonance. Finally, the numerical analysis for the cooling tower show rocking responses are significantly reduced using the IP_{WRI} in range of 74% to 95%. The deformations of fixed equipment are reduced when supported on the CP_{WRI} and IP_{WRI} by about 50% to 90%. Further, the WRI platforms based on MLP and PW link models produced smaller deformations of about 55% using the IP_{WRI} configuration and larger hysteresis (damping) versus the CP_{WRI} configuration. Results from the numerical analysis suggest that further investigations are necessary to study the effects of the asymmetric WRI platform modeling assumption in the vertical direction using SAP2000.

REFERENCES

Al Jawhar, A. [2019] "Investigating Wire Rope Isolator for Seismic Protection of Floor-Mounted Equipment in a Low-Rise Hospital Building", Department of Civil and Environmental Engineering, Graduate School, Howard University, Washington, DC: ProQuest Dissertations Publishing.

Astroza, R., Pantoli, E., Selva, F., Restrepo, J., Hutchinson, T., & Conte, J. [2014]. "Experimental Evaluation of the Seismic Response of a Rooftop-Mounted Cooling Tower", *Individual Study,* San Diego, CA.

Demetriades, G. F., Constantinou, M. C., & Reinhorn, A. M. [1992] "Study of Wire Rope System for Seismic Protection of Equipment in Buildings", National Center for Earthquake, New York.

Marin-Artieda, C. [2014] "Case Studies on the Assessment of Seismic Protective Systems for Equipment in Multistorey Buildings", *Tenth U.S. National Conference on Earthquake Engineering*, Anchorage, Alaska.

Marin-Artieda, C., & Han, X. [2017] "Energy Dissipation Platforms Based on Wire Rope Isolators for The Seismic Protection of Equipment", *16th World Conference on Earthquake*, 16WCEE 2017, Santiago, Chile: S-E1461893018.

Sankaranarayanan, R. [2007]. "Seismic Response Of Acceleration-Sensitive Non-structural Components Mounted On Moment Resisting Frame Structures". College Park, University of Maryland: ProQuest Dissertations Publishing.

Wieser, J. D., Pekcan, G., Zaghi, A. E., Itani, A. M., & Maragakis, E. [2012] "Assessment of Floor Accelerations in Yielding Buildings", Buffalo, NY: MCEER.

Seismic Demands on Sprinkler Piping Systems: Findings from a Shake Table Testing Program & Relevance to NZ Standards

Muhammad Rashid[1], Rajesh P. Dhakal[1], Timothy J. Sullivan[1] and Trevor Z. Yeow[2]

[1] University of Canterbury
Christchurch, New Zealand
{muhammad.rashid, rajesh.dhakal, timothy.sullivan}@canterbury.ac.nz
[2] Earthquake Research Institute
Tokyo, Japan
trevoryeow@eri.u-tokyo.ac.jp

Abstract. Fire sprinkler piping systems have intricate layouts on building floors that lead to complex distribution of demands in various segments of the system under seismic floor excitation. The New Zealand Standard (NZS) 4541: Automatic Fire Sprinkler Systems [2020] requires sprinkler systems to remain operational at the design limit state and provides a set of empirical analysis and design rules. One vital requirement to achieve a certain seismic performance is a reliable estimation of seismic demands. This paper aims to advance the understanding in the estimation of seismic demands on sprinkler systems to improve the reliability of designs. This objective has been achieved by conducting shake table testing on sprinkler systems typical of New Zealand practices. The investigations demonstrate that seismic demands on piping systems are significantly affected by the dynamic characteristics (period & damping) of the system as well as the frequency content of the floor excitation in addition to its intensity. Scrutiny of the test data reveals the inadequacy of design provisions in NZS 4541 [2020], such as requirements for brace forces and clearance, due to a lack of consideration for dynamic characteristics, frequency content of the floor excitation and the shaking intensity. The tests also provided valuable information on the influence of gravity supports on the dynamic response of the system and their vulnerability to failure under horizontal seismic excitation. Based on the reported findings, recommendations are provided for essential improvements to NZS 4541 [2020] to enhance the reliability of designs conducted in accordance with it.

Keywords: Seismic demands, sprinkler pipes, shake table testing.

1. INTRODUCTION

An automatic fire sprinkler system is an essential non-structural element (NSE) that is provided to suppress building fires to prevent loss of life and damage to property. Fire sprinkler piping systems consist of a network of vertical and horizontal pipes, with hanger rods and braces to resist gravity loads and seismic demands, respectively. Generally, an intricate piping network is required to feed individual sprinklers that are spread across the plenum space. Depending on their function, pipes in a network can be of varying diameters and lengths and are usually interconnected in different configurations.

Damage to fire sprinkler systems during earthquakes can compromise the fire safety of buildings and could also cause flooding damage due to leakage of pipes. Such damages could lead to a disruption in the post-earthquake occupation and functionality of buildings and damage to contents. To avoid such damage in practice, piping networks are braced against seismic demands using proprietary braces to restrain them from deforming excessively in order to prevent leakage of connections and avoid pounding with the surrounding building elements. This is done following a set of design provisions given in the standard for the design and installation of automatic fire sprinkler systems: NZS 4541 Automatic Fire Sprinkler Systems [SNZ 2020]. Table 4.11 of NZS 4541 [2020], referenced by clause 4.3.13.2.1, relates the maximum allowable lateral brace spacing for horizontal pipes of different diameters (≤50mm to 200mm) to pipe lateral force coefficient (i.e., a measure of maximum pipe response acceleration). The technical basis for the relationship between the maximum allowable brace spacing and the lateral force coefficient is, however, not specified in NZS 4541 [2020]. In other words, it is unclear if these spacing requirements have been calibrated to any design criteria.

NZS 4541 [2020] specifies a design force equation to calculate the force demand in braces, which is given by Equation (1) below.

$$F = CW \tag{1}$$

The lateral force coefficient, C, in the above equation is given as follows:

$$C = 2.7C_H Z C_p R_c \leq 3.6 \tag{2}$$

where, W = operating weight of the component, Z = hazard factor, C_H = floor height coefficient, C_p = performance factor, and R_c = component risk factor.

Note that Equations (1) and (2) are based on another standard, NZS 4219, which covers the design, construction and installation of seismic restraints for engineering systems, such as tanks and vessels, piping, ducting, and electrical and communication systems [SNZ 2009]. The force equation in NZS 4219 is in turn a simplified version of the equation to calculate the seismic design coefficient for parts and components in NZS 1170.5: Structural Design Actions - Part 5: Earthquake Actions [SNZ 2004]. For further details, the reader is referred to Rashid *et al.,* [2021]. The coefficient 2.70 presumably accounts for the combined effect of the site hazard coefficient (C(0) in SNZ [2004]) and the dynamic amplification of piping acceleration relative to the peak floor acceleration. In addition to shaking intensity, the magnitude of piping acceleration will be dependent on the dynamic characteristics of the supporting structure and the system attached to it. However, NZS 4219 or NZS 4541 [2020] does not provide any basis for setting the coefficient value at 2.70. Multiple studies on instrumented buildings, numerical models and experimental investigations have shown that the amplifications can be well in excess of 2.0 as discussed in Rashid *et al.,* [2021]. It is not clear whether the 2.7 coefficient would lead to an underestimation or over prediction of the dynamic magnification of piping acceleration relative to the peak floor acceleration.

Additionally, the required clearance to avoid pounding with other elements around a pipe depends mainly on the dynamic characteristics of the pipe, frequency content of the floor excitation and also the movement of the surrounding element. However, in NZS 4541 [2013], the clearance requirements were conditional upon the pipe diameter and were fixed with values of 25mm and 50mm. Consequently, regardless of the demand, the values from NZS 4541 [2013] have been used in practice. This implies that design engineers did not need to estimate the displacement demand on a pipe for specification of clearance requirements. In the recent update to NZS 4541 [2013], NZS 4541 [2020] recommends horizontal clearances of 50mm, 150mm, 50mm and 25mm from restrained components, unrestrained components, penetrations and sprinklers, respectively. There is no explicit clause in NZS 4541 [2020] that requires the determination of displacement of the pipe itself in addition to the movement of the surrounding element to determine the clearances. As will be shown in this paper, the clearances in NZS 4541 [2020] could be exceeded depending on the shaking intensity and the interaction between the piping system and the supporting floor.

Bracing a piping network or providing clearances using empirical design provisions, without any regard to design criteria and the actual seismic demand, leads to a system whose expected global seismic performance cannot be reliably defined. To ensure that adequate bracing and clearances are provided to achieve target performances, it is essential that demands are based on theoretical mechanics or experimental evidence rather than empirical guidelines. To address this need, shake-table tests of sprinkler piping systems typical of New Zealand practice were performed. Results from the testing are discussed in this paper with the aim to provide useful observations on the variations of seismic demands on sprinkler systems and to encourage their possible incorporation in NZS 4541 [2020].

2.DESCRIPTION OF TEST SPECIMENS

The specimens consisted of a distribution pipe (DP) perpendicular to the direction of shaking as shown in Figure 1. The distribution pipe (6.5 m) was connected to a 4.77m long branch pipe (BP) parallel to the direction of shaking. The branch pipe was further connected to arm-over 1, 2 and 3 with lengths of 1.95 m, 1.15 m and 0.6 m, respectively (Figure 1). A total of eight specimens were tested with different variations. Herein, results from three specimens will be discussed with the major difference among these being the diameters of the distribution and branch pipes. The specimens are designated by a combination of the distribution and branch pipe diameters, such as 100-40L, which represents a specimen with a nominal diameter of 100 mm for the distribution pipe and 40 mm for the branch pipe; "L" denotes a certain variation regarding the plenum depth of the pipes, which will not be discussed here. The other two specimens are 65-32L and 40-25L. For further details on the specimen, the reader is referred to Rashid *et al.,* [2022].

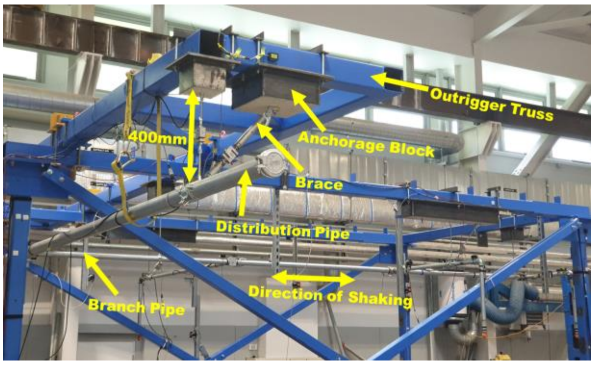

a. Actual image of the specimen mounted on the test frame.

b. Back view of the specimen.

Figure 1: Details of the test specimen.

3. TEST FLOOR MOTIONS

The basic set of floor motions used for testing consisted of recorded floor motions and were divided into two categories: non-resonant and resonant. A non-resonant motion (NRM) is defined here as a motion in which the modal periods of the supporting structure, identified by spectral peaks in the response spectra of floor acceleration response, are not in resonance with the piping period, whereas resonant motion is defined as a motion in which the period of the specimen is in resonance with a spectral peak in the floor motion spectrum. Figure 2 shows the acceleration response spectra of the selected NRM. The period range of interest, marked by the dashed lines, is not in proximity to the modal period of the building on which the motion was recorded (evident as a spectral peak at 0.61s). The response spectra of the selected resonant motions, RM1, RM2, RM3 & RM4, are shown in Figure 2, and it can be observed that the period range of interest is close to the spectral peaks in the spectra. Note that the plots in Figure 2 are not the spectra of the recorded acceleration response on the roof of the test frame. These selected motions were input to the table and the resulting spectra at the roof of the test frame were modified. However, as shown in Rashid *et al.,* [2022], these differences did not affect the suitability of the motions for studying the response of the specimens to non-resonant and resonant cases.

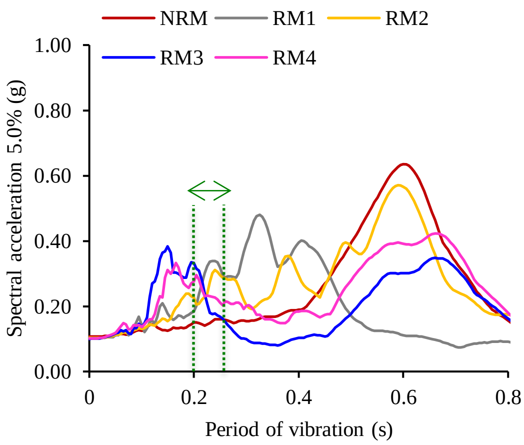

Figure 2: Acceleration response spectra of recorded floor motions selected for testing.

4. OBSERVATIONS ON SEISMIC DEMANDS

4.1 DYNAMIC CHARACTERISTICS, PIPE DIAMETER AND BRACE SPACING

The testing showed that the periods of vibration, and consequently seismic demands, were not dependent on the diameter of pipe only. The periods of vibration of the specimens along the direction of shaking were 0.21s, 0.25s and 0.22s for specimens 100-40L, 65-32L and 40-25L, respectively. The periods of specimens 100-40L and 40-25L are quite close despite the significant difference in the diameters of the constituent distribution pipes. The ratio of the unit mass of the 100 mm pipe to the unit mass of the 40 mm pipe is 3.38; the same ratio for the moment of inertia of the two pipes is 14.25. This implies that with reduction in pipe diameter, the reduction in flexural stiffness is much greater than the reduction in mass, and thus pipes with smaller diameters should have larger periods of vibration. However, the difference between periods is not significant as other sources of flexibility/stiffness were the same in the two specimens. These sources of stiffness were the brace spacing on the distribution pipe, hanger rods on the branch and arm-over pipes and the restraint provided by arm-overs. Consequently, the maximum difference between the peak displacement demands of the distribution pipe in the two specimens was approximately 10 mm as can be seen in Figure 3. Thus it can be said that two systems with the same periods of vibration and subjected to the same floor excitation, can be braced at the same spacing if the design criterion is not to exceed a certain clearance requirement. This is because the demands could be similar due to similar dynamic characteristics. However, Table 4.11 in NZS 4541 (2020) specifies different brace spacing for pipes with diameters of 100 mm and 40 mm at the same design coefficient; for example, spacing values of 7.5 m and 5.4 m are recommended for 100 mm and 40 mm pipes for a design coefficient of 3.0 g.

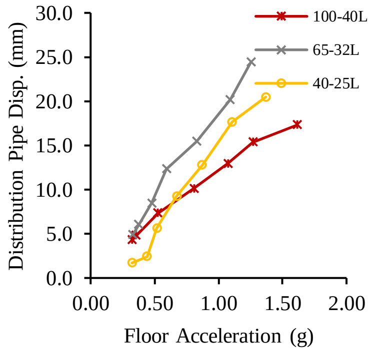

Figure 3: Comparison of the maximum recorded displacements of the distribution pipe for different specimens.

It is important to note that to satisfy the design criterion of displacements being smaller than the leakage threshold, the brace spacing could be different for the same demand as the leakage capacity of pipes of different diameters could be different. Similarly, the criterion of force demand in the brace being less than its capacity, pipes of different diameters could require different brace spacing as they have different masses. To conclude, the correct approach is to consider the dynamic characteristics and the fulfilment of design criteria at the target demands in deciding design variables, such as brace spacing.

4.2 EFFECTS OF FLOOR MOTIONS

4.2.1 Accelerations

The effect of the input motion on the acceleration response of the specimens has been quantified by dynamic amplification factor, which is a ratio of the peak recorded acceleration on the distribution pipe to the peak recorded acceleration on the two ends of the outrigger truss (Figure 1). Figure 4 shows the variation of dynamic amplification factors for different motions at different shaking intensities for the acceleration recorded on the distribution pipe. The variation in the amplification factors could possibly be due to the variations in damping at different shaking intensities. In most cases, the amplification from the NRM was lower than the RMs, which proves that if there is resonance between the piping system and supporting floor, the acceleration demands would, as expected, be larger.

The maximum dynamic amplification factor for acceleration response was observed to be 3.30, 3.50 and 2.10 for specimens 100-40L, 65-32L and 40-25L, respectively. The plots in Figure 4 also show the maximum value of the spectral shape coefficient in NZS 1170.5, $C_i(T_p)$, which characterizes the dynamic amplification factor for NSEs. As stated earlier, Equation (1) is essentially based on NZS 1170.5, and no detail has been provided in NZS 4541 [2020] on what exactly is the dynamic amplification factor. Therefore, the maximum value of $C_i(T_p)$ in NZS 1170.5 has instead been used. It can be observed that NZS 1170.5 underestimates the dynamic amplification of pipe acceleration in most cases. This will have implications for the calculation of force demand in the braces, which would be larger due to higher accelerations in case of resonance. Braces on pipes could thus be under designed if the interaction between the piping system and the supporting floor is not properly taken into account.

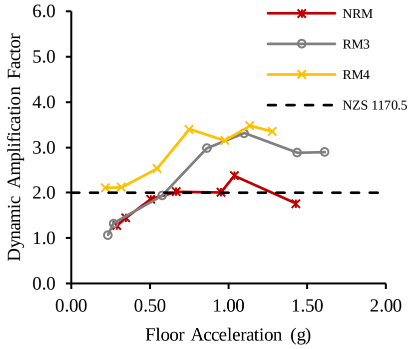

a. 100-40L

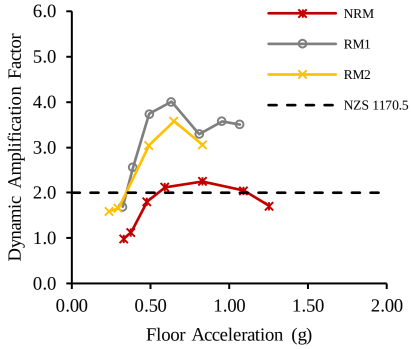

b. 65-32L

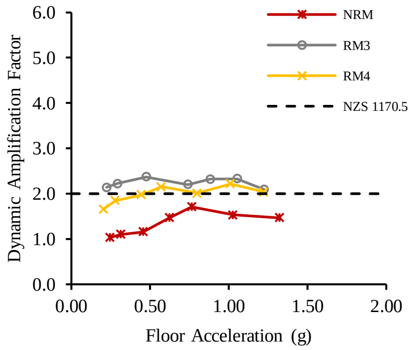

c. 40-25L

Figure 4: Dynamic amplification of the maximum recorded accelerations on the distribution pipe relative to the maximum floor accelerations at different shaking intensities.

4.2.2 Displacements

Similar to accelerations, the RMs exerted larger displacements on the specimens than the NRM as can be seen in Figure 5. The recorded displacement demands on the distribution pipe in response to RMs were found to be 2.0, 1.8 and 1.3 times that recorded for the NRM for specimens 100-40L, 65-32L and 40-25L, respectively. This implies that larger clearances would be required if the period of vibration of a piping system is closer to the modal periods of the supporting structure. The maximum displacement in response to RMs were 37.2mm, 43.8mm and 27.4mm for specimen 100-40L, 65-32L and 40-25L, respectively. It could be inferred from these values that, depending on the shaking intensity, clearance requirements of 25mm-50mm in existing systems designed to NZS 4541 [2013] could easily be exceeded, especially if the pipe and other nearby elements displace in opposite directions.

Similar argument applies to systems designed to NZS 4541 [2020] as the distribution pipe in specimen 65-32L displaced close to 50mm, which is the clearance requirement for restrained components as per NZS 4541. There are no requirements in NZS 4541 [2020] to check the specified clearance values against the displacements resulting from the design force so that the shaking intensity could be taken into account. Given that mutual interaction of sprinkler systems with other elements in the plenum space have resulted in significant damage in the past [Rashid *et al.,* 2018], the stipulation of realistic clearance requirements in NZS 4541 [2020] is highly recommended.

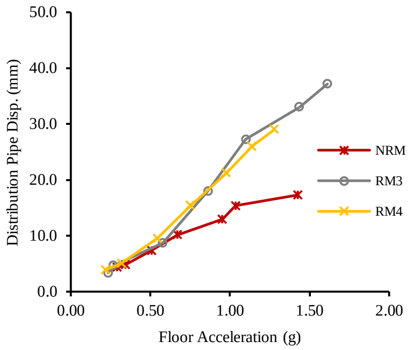

a. 100-40L

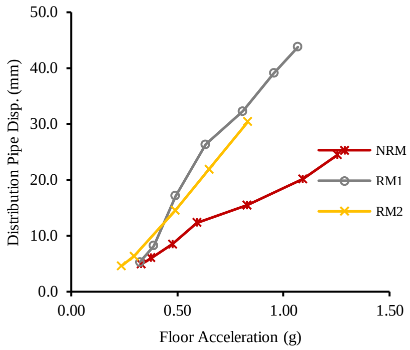

b. 65-32L

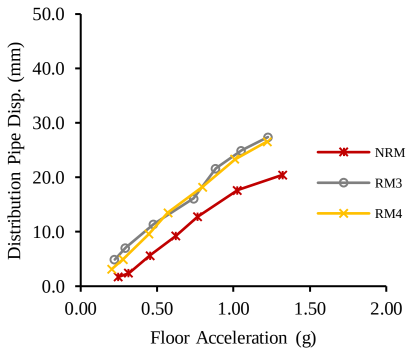

c. 40-25L

Figure 5: Variation of maximum recorded displacements of the distribution pipe with different input floor motions.

4.3 ROLE OF GRAVITY SUPPORTS

Figure 6 shows the deformed shape of a hanger rod on a specimen under a free-vibration pull. The hanger rods, despite being only provided for gravity support, provided partial seismic restraint due to the detailing of their attachments with the pipe and the anchor. This means that hanger rods could be vulnerable to seismic damage with serious implications for the stability of the system under gravity loads.

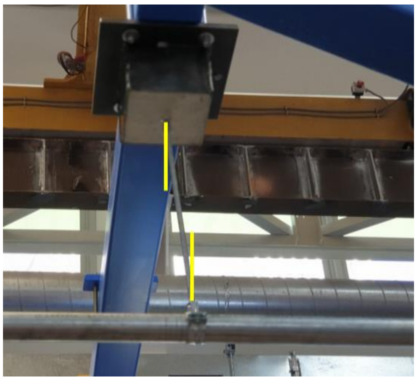

Figure 6: Deformed shape of a hanger rod on a specimen under free-vibration pull.

Specimen 65-32L was re-tested using the NRM after artificially increasing its mass to increase its period of vibration. The additional mass was added in the form of plates bolted to the pipes at the two sides of the distribution and branch pipe connection and along the branch pipe at multiple locations as shown in Figure 7a. The extra mass increased the period of vibration of the specimen from 0.25s to match the period corresponding to the spectral peak in the NRM at 0.61s (Figure 2). The design of hanger rods, for the increased mass, was not revised. This was because the primary target of testing was to observe the demands due to resonance with the spectral peak at 0.61s, which represented the fundamental mode of the instrumented structure. Any increase in the size of hanger rods would have increased the stiffness of the specimen, which would then have required more mass to achieve the period of 0.61s. To avoid this impracticality, testing was carried out with 10 mm hanger rods.

The maximum horizontal displacement of the distribution pipe was 145.8mm, which was almost three times higher than the previous maximum achieved with the actual mass (Figure 7b). This system, in an actual scenario, will require larger clearances than the typical values of 25-50 mm due to its own movement, and the overall clearance could be larger than 150mm if the surrounding element is unrestrained. The maximum horizontal displacements of arm-overs were also much higher than those achieved in the previous tests. From arm-over 1 to arm-over 3, the maximum displacements were 71.2mm, 145.3mm and 147.4mm, respectively. These values indicate that clearances provided around sprinkler heads on the order of 25mm will not be enough to avoid pounding with other nearby elements if the arm-overs are unbraced.

The hanger rods supporting arm-over 2 and the end of branch pipe were fractured at the maximum shaking intensity as shown in Figures 7c and 7d. Due to resonance, these rods were subjected to very high deformation demands, but it must also be kept in mind that these rods were supporting significantly higher gravity loads than would be there in an actual scenario. No other damage was observed in the system. The major lesson from these observations is that hanger rods, with the current detailing practices, should be considered during seismic design of the system.

a. Specimen 65-32L with additional lumped masses.

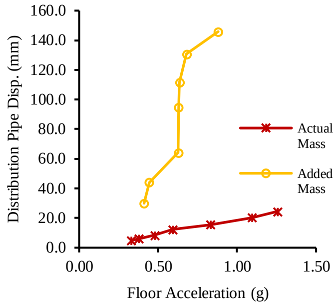

b. Maximum recorded displacements of the distribution pipe at different shaking intensities with and without additional mass.

c. Fractured hanger rod at the end of the branch pipe.

d. Fractured hanger rod at the end of arm-over 2.

Figure 7: Detailing, displacement response and damage modes of specimen 65-32L with additional mass.

5. RECOMMENDATIONS

This paper discussed some important results from a large testing program on sprinkler systems typical of NZ practices. Based on the observations of the experimental campaign, the following recommendations are made for future updates to NZ 4541 with regard to seismic design of suspended piping systems.

i. Brace spacing should be selected based on the fulfilment of design criteria at the estimated design seismic demands.
ii. The clearance requirements need revision and should be related to design demands of the pipe and the surrounding elements.
iii. The existing formulation in NZS 4541 [2020] for design force needs to be modified to account for the dynamic characteristics of the supporting structure and the piping system.
iv. The typical detailing of gravity supports affects the dynamic characteristics of the piping systems and hence these elements could be vulnerable to seismic damage. These elements should be considered during the seismic design of sprinkler systems. Alternatively, the attachments of the hangers should be such that the assembly only provides axial restraint and no lateral restraint.

REFERENCES

Rashid, M., Dhakal, R., and Sullivan, T. [2021]. "Seismic design of acceleration-sensitive non-structural elements in New Zealand: State-of-practice and recommended changes." *Bulletin of the New Zealand Society for Earthquake Engineering*, 54(4), 243-262.

Rashid, M., Dhakal, R., and Yeow, T. [2018]. "Automatic fire sprinkler systems: an overview of past seismic performance, design standards & scope for future research." *2018 NZSEE Conference,* Auckland, New Zealand.

Rashid, M., Dhakal, R. P., Sullivan, T. J., and Yeow, T. Z. [2022]. "Seismic performance characterization of fire sprinkler piping systems through shake table testing (accepted for publication)." *Bulletin of the New Zealand Society for Earthquake Engineering*.

SNZ [2004] *NZS 1170.5 Structural Design Actions, Part 5: Earthquake Actions - New Zealand*, Standards New Zealand, Wellington, New Zealand.

SNZ [2009] *NZS 4219 Seismic performance of engineering systems in buildings*, Standards New Zealand, Wellington, New Zealand.

SNZ [2020] *NZS 4541 Automatic Fire Sprinkler Systems*, Standards New Zealand, Wellington, New Zealand.

Analytical Studies in Support of an Improved Approach to the Design of Acceleration-Sensitive Nonstructural Elements

Athanasia K. Kazantzi[1], Eduardo Miranda[2], Dimitrios Vamvatsikos[1], Ahmed Elkady[3] and Dimitrios Lignos[4]

[1] School of Civil Engineering, National Technical Univ. of Athens, Athens 15780, Greece
e-mail: kazantzi@mail.ntua.gr

[2] Dept. of Civil and Environmental Engineering, Stanford Univ., Stanford, CA 94305, USA
e-mail: emiranda@stanford.edu

[3] Dept. of Civil, Maritime and Envir. Engineering, Univ. of Southampton, Southampton SO16 7QF, UK
e-mail: a.elkady@soton.ac.uk

[4] RESSLab, École Polytechnique Fédérale de Lausanne, Lausanne CH-1015, Switzerland
e-mail: dimitrios.lignos@epfl.ch

Abstract. This paper summarizes a series of analytical studies that were conducted in connection with an improved approach for the design of acceleration-sensitive nonstructural elements. In the new approach, bracing to secure nonstructural elements to the structure is designed and detailed to experience nonlinearities to limit forces acting not only in the nonstructural elements but also in the attachments to the structure and in the attachment(s) to the nonstructural element. The project was sponsored by the Seismology and Earthquake Engineering Research Infrastructure Alliance for Europe (SERA) and involved shake table testing at the University of Bristol to validate the proposed novel approach as well as analytical studies. Prior to the testing, a series of analytical studies were conducted to examine the feasibility of the proposed approach and for selecting motions to be used in the shake table tests. By using exclusively motions recorded in instrumented buildings in California it is shown that acceleration demands in nonstructural elements can easily exceed 2 or 3g, but that by allowing nonlinearity to occur in the bracing element, acceleration and forces can be greatly reduced even with small levels of nonlinearity. In particular, it is demonstrated that given the frequency content of floor motions, which correspond to ground motions amplified and filtered by the structure, the reductions in accelerations and forces are much larger than those that are produced under ground motions for similar levels of nonlinearity. Furthermore, it is shown that the proposed approach not only results in large reductions in forces and accelerations, especially for elements tuned to any of the modal frequencies of the supporting structure but, simultaneously, it can also achieve substantial reductions in lateral deformations with respect to those that would occur on nonstructural elements remaining elastic. Yet, another important advantage of the proposed approach is that force and deformation demands become far less sensitive to the period of vibration of the nonstructural element.

Keywords: Nonstructural elements, Component amplification, Effect of Yielding, Acceleration demands, Force demands, Displacement demands.

1. INTRODUCTION

It is now well-recognized that nonstructural elements represent most of the initial investment in buildings (Taghavi and Miranda, 2003; Filiatrault and Sullivan, 2014) and they play a key role in the functionality of buildings. It is then not surprising that their failure can lead to important consequences such as loss of functionality and large direct and indirect economic losses. A well-known example of the critical role of nonstructural elements on the functionality of buildings is the performance of the Sylmar County Hospital in the 1994 Northridge earthquake, in which despite the fact that the building did not suffer any apparent structural damages, it had to be evacuated and remained inoperable for several months due to extensive repair works required for its contents and nonstructural elements (Naeim, 2004). But additionally, in some cases, failure of the nonstructural elements could also lead to serious injuries and even loss of life. Examples of the latter occurred in the United States, U.S., during the Good Friday 1964 Alaska earthquakes (Ayres, 1973) and during the 1987 Whittier earthquake (Taly, 1988). In both cases, loss of life was attributed to the detachment and fall of architectural façade elements as a result of the earthquake.

Seismic provisions for nonstructural elements have been given much less attention than seismic provisions for the design of buildings and structures. This is mainly because, for many years, the primary goal of earthquake resistant design has been to avoid the collapse of the structure, with much less attention paid to the design of nonstructural elements. Unfortunately, this has led to seismic provisions for nonstructural elements that have many deficiencies. For instance, in the case of structures, there is consensus that local site conditions play a major role in the intensity and frequency content of ground motions and therefore on the level of response and level of seismic risk of structures built on different site conditions. This has led to the explicit incorporation of the effect of site conditions in the design of structures in most seismic codes since the 1970s. In contrast, the role of the supporting structure on the design of nonstructural components has largely been neglected or not properly accounted for. For example, in the U.S. the influence of the fundamental period of vibration of the supporting structure has not been considered in the calculation of design forces of nonstructural elements. Another problem in the field of nonstructural elements, is a fairly generalized misconception that paying attention to load path and providing a bracing element is enough to avoid earthquake damages and therefore design forces are not important. Apparently, this is not true, since practically any moderate earthquake that has struck an urban area has led to a large amount of nonstructural damage and many of this damage has occurred in elements that were braced and in which there was an apparent seismic design. Hence it is clear that simply installing a bracing element is by no means sufficient to secure an adequate seismic behaviour. The bracing elements require a certain strength, stiffness and deformation capacity to lead to an adequate performance. Figure 1 illustrates a couple of examples of this situation. The first example shows diagonal bracing elements, of which one failed as a result of having insufficient force capacity and/or ductility. The other example illustrates a roof mounted vibration-isolated equipment with attachments designed to resist lateral loads. Again, failure occurred as a result of insufficient force capacity and/or insufficient ductility in the elements bracing the equipment to the structure.

The two examples shown in Figure 1 also illustrate how challenging the seismic design of nonstructural components can be. Often nonstructural components are the end end of a long chain of aspects that affect the seismic demands of nonstructural components. Each of these aspects in this conceptual chain is subjected to large uncertainties. For example, there are very large uncertainities in the magnitude and location of future earthquakes. But even if the magnitude and location of a future earthquake were known, estimating the intensity of ground motions at a site is still highly uncertain. For example, for a given type of faulting mechanism, magnitude, distance and site conditions, spectral ordinates have logarighmic standard deviations in the order of 0.6 which means that, for a given earthquake (with known magnitude) at a given distance and site conditions, one could easily see changes in the level of intensity from one site to another at the same distance from the epicenter and in the same site conditions of a factor of four in the level of ground motion intensity. Furthermore, even if the median intensity at a site was to be known, it most likely

Figure 1. Examples of nonstructural elements that had bracing elements with seismic design but nevertheless experienced failure during an earthquake (Photos by Eduardo Miranda).

would have large variations in intensity with changes in direction due to directionality effects (e.g., Poulos and Miranda, 2022). The motion in the structure is influenced by soil structure interaction effects which depend on the local site conditions and type of foundation. The modifications include amplifications or deamplifications of the intensity of the ground motion as well as modification of the dynamic characteristics of the structure, such as periods of vibration, mode shapes and modal damping ratios with respect to those that would occur if the structure was fixed at the base. Depending on the fundamental period of vibration of the supporting structure, its lateral-force resisting systems, its modal damping ratios, the level of intensity and frequency content of the ground motion as well as the peak ground acceleration could be amplified by values in excess of six or be deamplified. Finally, the demands on the nonstructural element are influenced by the location of the element within the structure and by the mass, stiffness, strength and damping of the nonstructural component.

The main objective of this paper is to present a summary of a series of analytical studies conducted by the authors in connection with an experimental study to validate an new approach for the seismic design of nonstructural elements (Elkada et al., 2022; Miranda et al 2018a, 2018b). The proposed approach takes advantage of the unique characteristics of floor motions, which are characterized by ground motions that have been amplified and filtered by the supporting structure. In particular, floor motions are characterized by large amplifications at very specific frequencies that are equal or close to the modal frequencies of the supporting structure. Particular emphasis is placed on the selection of the recorded motions that were used in the shake tests. While the levels of amplifications are very large, it is shown that energy dissipation by means of viscous damping or hysteretic behaviour in a yielding element can produce significant reductions in acceleration and force demands that are much larger than those that would occur in nonstructural components at ground level, in other words, to components subjected to ground motions instead of floor motions. In the proposed approach, bracing elements that are located between the nonstructural elements and the structure are designed and detailed to yield during moderate and large earthquakes. Furthermore, they are designed to be the weakest element in the load path, allowing the design of the nonstructural element and the attachemets (anchors) of the bracing to the nonstructural element and to the structure to be designed for forces that can be estimated as a function of the capacity of the yielding element and therefore their seismic performance becomes more reliable.

2. SELECTION OF INPUT FLOOR MOTIONS

Unlike most shake table tests of nonstructural elements that typically make use of artificial (synthetic) motions to match floor spectra, such as the AC156 floor spectra that was developed to match code provisions and not the characteristics of motions that occur in buildings during earthquake, in this investigation we made exclusive use of floor motions recorded in instrumented buildings in order to employ

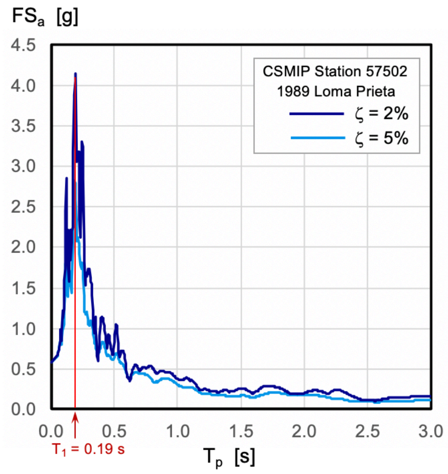

Figure 2. Floor spectra exhibiting large spectral ordinates at periods of vibration near the fundamental period of vibration of the supporting structure that were selected as input for the shake table tests.

motions with realistic amplitude and frequency content. Figure 2 shows the 2% and 5% damped floor response spectra computed for the floor motions recorded at the roof level on two instrumented buildings during the 1989 Loma Prieta earthquake.

The floor spectra on the left correspond to those at roof level of a two-story industrial building in the city of Milpitas, built in 1984, whose lateral-force resisting system comprises tilt-up walls. The peak ground acceleration in this direction was 0.14g which was amplified at roof level to 0.57g. This corresponds to an amplification of nearly four which is what would be expected to occur on average in lowrise buildings. This peak floor acceleration was subsequently amplified for periods of vibration smaller than about 0.5s and strongly amplified to experience accelerations in excess of 2g for periods close to the fundamental period of vibration of the supporting structure which is 0.19s. The floor spectra shown on the right correspond to those at roof level of a four-story reinforced-concrete shear wall commercial building in Watsonville. The peak ground acceleration in this direction was 0.36g which was amplified at roof level to 1.2g, corresponding to an amplification of about three. This peak floor acceleration was subsequently amplified for periods of vibration smaller than about 0.8s and deamplified for periods longer than 0.8s. The levels of acceleration were strongly amplified to experience accelerations in excess of 3g for periods close to the fundamental

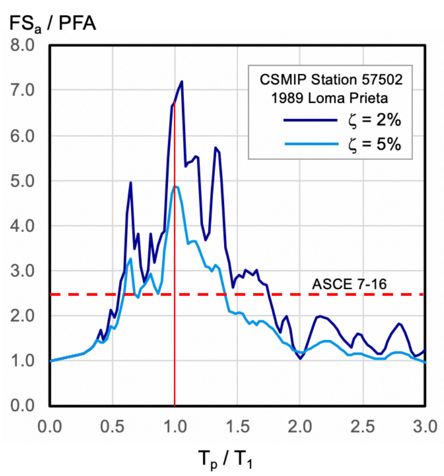

Figure 3. Binormalized floor spectra of recorded motions that were selected as input in the shake table tests which exhibit large amplifications of acceleration (i.e., in excess of four) at periods of vibration near the fundamental period of vibration of the supporting structure (i.e., at T_p/T_1 near one).

period of vibration of the supporting structure, which in this direction is 0.33s. Figure 3 shows the same 2% and 5% damped floor spcetra but now binormalized. In these spectra, the periods of the secondary system, in this case the periods of the nonstructural components, T_p, have been normalized by the fundamental period of the building, T_1. This binormaliztion was first proposed by Miranda (1991) for characterizing seismic demands on structures built on soft soils, whose spectra is also characterized by being narrow banded. The normalization of the abscissas provides the opportunity to study seismic demands not as a function of the period but as function of how close or far a period of vibration is to the predominant period of the ground motion. More recently, Kazantzi et al (2020a, 2020b) used the same normalization to study the seismic demands on nonstructural elements. Meanwhile the normalization of the floor spectral ordinates by peak floor acceleration provides information on the level of amplification of accelerations as the period of vibration of the nonstructural element approaches or gets far from the fundamental period of vibration of the supporting structure. It can be seen that, for nonstructural elements with 5% damping, the amplification for elements tuned or nearly tuned to the first mode of vibration of the supporting structure exceeds four. On the other hand, for nonstructural elements with 2% damping, the amplification of acceleration for elements tuned or nearly tuned to the first mode of vibration of the supporting structure are in the order of 5 or six for the selected motions. Figure 3 also indicates the component amplification factor a_p = 2.5 that is used in ASCE 7-16 for flexible components. As can be seen, the amplifications computed from recorded floor motions for tuned or nearly tuned nonstructural elements greatly exceed those in the U.S. seismic provisions whereas there are other spectral regions where the provisions are very conservative. In the latest version of ASCE 7 (ASCE, 2022) the component amplification factor a_p has been replaced by the so-called component resonance ductility factor, C_{AR}, which varies depending on the type of nonstructural element and on whether the component is supported at or below grade, or is supported above grade by a building structure. The largest value is C_{AR} =2.8 which is assigned to architectural components above grade that are flexible with low-deformability materials and attachments as well as for some vibration isolated equipment above grade. It can be seen that the small increase from 2.5 to 2.8 still falls very short from the levels of amplification computed from recorded floor motions shown in Figure 3.

Examples of 2% and 5% damped floor spectra obtained from motions recorded at roof level of taller instrumented buildings are shown in Figure 4. These motions were selected as possible candidates to be used in the shake table tests as representative of cases in which the nonstructural component is tuned to higher modes of vibration. Station 24370 corresponds to a six-story commercial building whose lateral-force resisting system consists of steel moment resisting frames. The fundamental period of vibration in the NS direction is 1.27s and the second mode where large floor spectral ordinates in excess of 1g are produced is 0.43s. The second example is a thirteen-story office building in the city of Hayward with a fundamental period of vibration of 1.32s and with high acceleration demands for periods near 0.44s and 0.25s which correspond to the second and third translational period of vibration in the EW direction. The third example is a flexible nineteen story office building in Los Angeles whose lateral-force resisting systems consists of

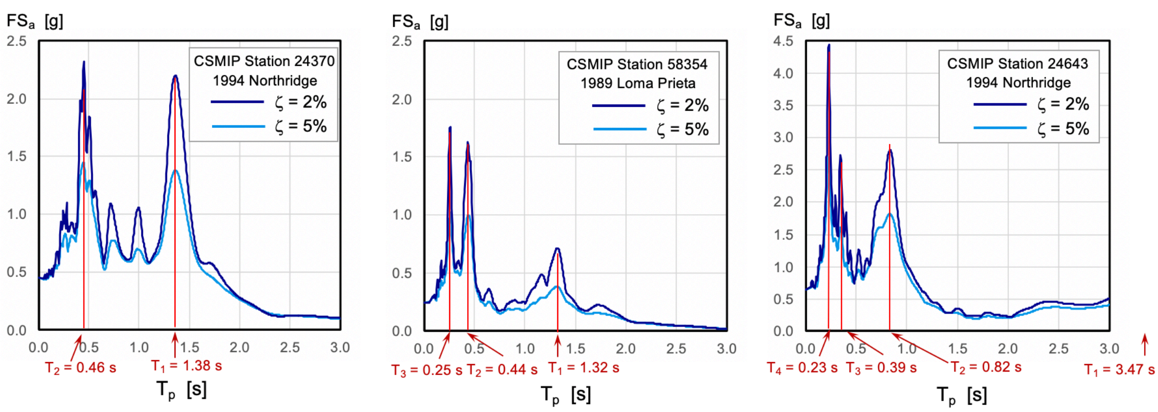

Figure 4. Examples of floor spectra exhibiting large spectral ordinates at periods of vibration near the higher modes of vibration of the supporting structure.

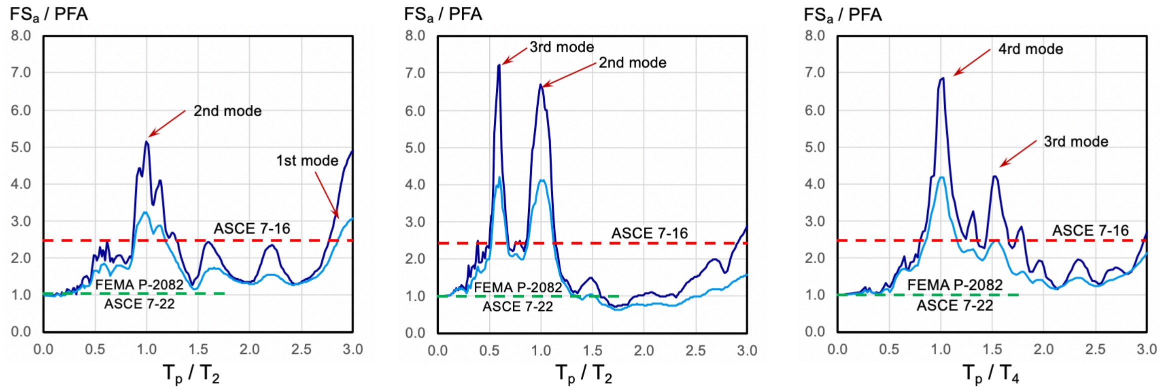

Figure 5. Examples of binormalized floor spectra exhibiting large amplifications of acceleration (i.e., in excess of four) at periods of vibration near higher mode periods of vibration of the supporting structure.

steel moment resisting frames. The fundamental period of vibration is 3.47s and high acceleration demands appear at periods near 0.82s, 0.39s and 0.23s that correspond to the second, third and fourth translational period of vibration in the NS direction of the building. As shown in this figure, unlike the new seismic provisions for nonstructural components stating that large amplifications (referred to in the provisions as "resonance") are unlikely to occur if the period of vibration is less than half of the fundamental period of vibration of the building, this is clearly not the case and in all three examples accelerations in excess of 1g are produced even in periods less than half of the fundamental period of vibration of the buildings. Figure 5 shows the same floor spectra but now in a binormalized form. As can be inferred from Figure 5, contrary to the new U.S. seismic provisions that consider the resonance as unlikely as to stipulate a component resonance ductility factor, C_{AR}=1.0—meaning an acceleration equal to the peak floor acceleration—nonstructural components tuned to higher modes could be subjected to amplifications of acceleration larger than four, suggesting that reducing design forces in this spectral region was not a step in the right direction. The motion recorded at roof level in CSMIP station 24370 at Burbank was selected to be used in the shake table tests at Bristol as a floor motion representative of one that can generate very large amplifications of acceleration for nonstructural elements with periods close to the second mode of vibration of the supporting structure.

Figures 3 and 5 show that the effect of damping of the nonstructural element has very different results depending on how close or far is the period of vibration of the component to one of the modal periods of the supporting structure. As shown in these figures, damping produces much larger reductions in seismic demands for nonstructural elements that are tuned to one of the modal periods of the supporting structure. This is consistent with previous observations by Kazantzi et al. (2020b) who conducted a study on the effect of damping on floor spectra.

Following the preliminary selection of some recorded floor motions, it was needed to verify that these motions were fairly representative of seismic demands that nonstructural elements can be subjected to. In other words, it was necessary to verify that pre-selected motions did not produce unusually low or unusually high amplifications. For this purpose, binormalized floor spectra were compared to statistical studies previously conducted by the first three authors (Kazantzi et al. 2020b). Figure 6 illustrates 113 binormalized floor motions along with their mean, median and 16th and 84th percentiles. The figure on the left corresponds to recorded motions in which the large amplifications occur at a period equal or close to the fundamental period of vibration of the supporting structure while the figure on the right corresponds to recorded motions in which the large amplifications occur at a period equal or close to periods of higher modes of vibration of the supporting structure. As can be inferred by inspecting Figure 6, nonstructural elements with damping ratios of 2% that are tuned to the fundamental period of vibration of the supporting structure are subjected to strong amplifications, 70% of which are between 5.8 and 9.5 with an average amplification of 7.4. The amplifications of the two binormalized floor spectra shown in Figure 3 for 2% damping have peak amplifications of 6.7 and 5.8 indicating that these high levels of accelerations in these example records are by no means unusual but are actually slightly smaller than mean amplifications that have been observed in motions recorded on instrumented buildings in California.

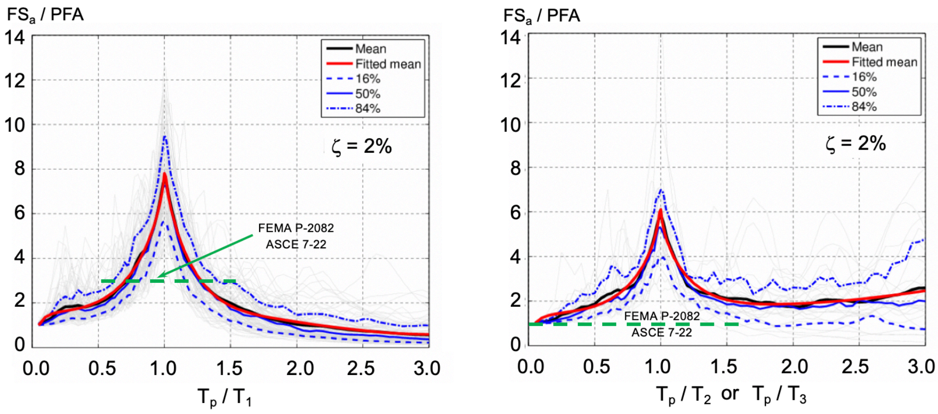

Figure 6. Statistical studies of amplifications of accelerations for flexible components on the left when periods are normalized by the first (fundamental) period of the supporting structure and on the right when normalized to the second or third mode of vibration of the supporting structure.

Meanwhile, nonstructural elements with damping ratios of 2% that are tuned to periods corresponding to higher modes of vibration of the supporting structure are also subjected to strong amplifications, 70% of which are between five and seven with an average amplification of 5.3.

3. EFFECT ON NONLINEARITY IN THE SECONDARY COMPONENT

Figure 7 shows force reduction factors computed from floor motion recorded in instrumented buildings. These reduction factors correspond to relatively small values of nonlinearity as measured by displacement ductility ratios of 1.5 and 2.0. It can be seen that these reduction factors are very different from those computed from ground motions recorded on rock or firm soils. In particular, they are characterized by having large force reductions in secondary systems for approximately the same periods for which large amplifications are produced (i.e., those shown in Figure 6). This means that by allowing only relatively small levels of nonlinearity to take place in the bracing of nonstructural elements that are tuned or nearly tuned to modal periods of the supporting structure it is possible to design for significantly smaller forces than those necessary to keep these elements elastic. For example, by allowing a ductility demand of only 1.5 to take place in components tuned to the first mode, it is possible to design for forces 3.6 times smaller than those necessary to maintain them elastic or 2.4 higher than those that on average could be used for broadband motions for the same level of nonlinearity. If the allowed level of nonlinearity is increased to a ductility of two, the design forces become 6.2 smaller than those necessary to maintain them elastic or 3.2 smaller than those that on average are produced in motions with broadband spectra for the same level of nonlinearity. Hence, the proposed novel design approach is particularly effective in reducing acceleration and force demands in components that are tuned or nearly tuned to modes of vibration of the supporting structure with strong contribution to the response of the structure. For more information on reduction factors for secondary systems, the reader is refered to Kazantzi et al. (2020c).

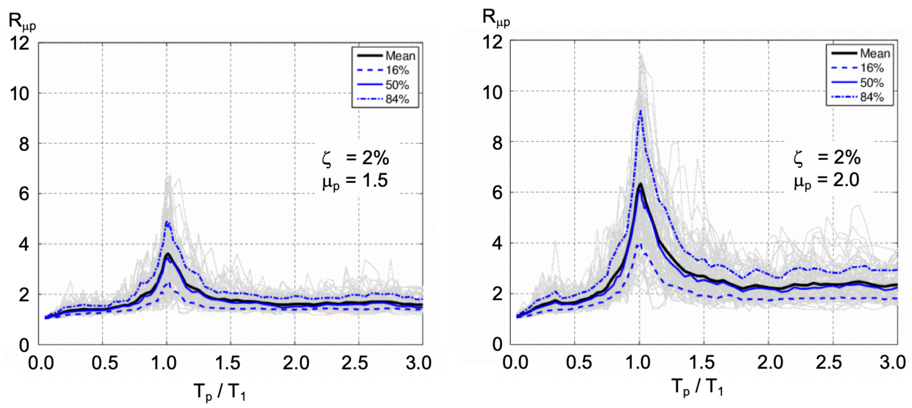

Figure 7. Statistical studies of the effect of level of nonlinearity on force reduction factors of nonstructural elements.

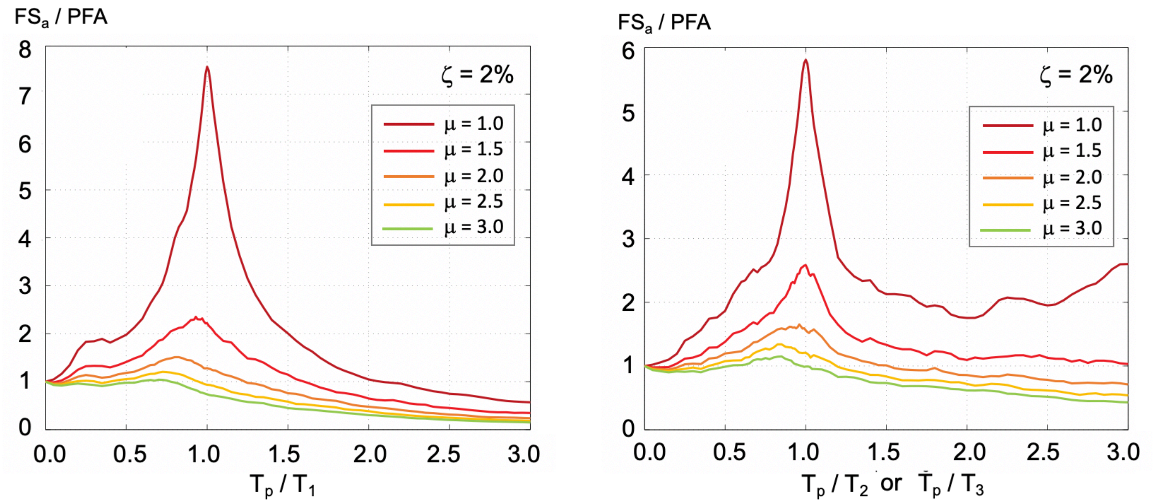

Figure 8. Statistical studies of the effect of level of nonlinearity on levels of amplification of accelerations on nonstructural elements.

Figure 8 shows binormalized floor spectra for different levels of inelastic deformation in the secondary system. The figure on the left depicts the case in which the period is normalized by the first mode of vibration of the supporting structure, whereas the figure on the right corresponds to spectra where the period of the component is normalized by the second or third mode of vibration of the supporting structure. It can be seen that nonlinearity incurs large reductions in horizontal accelerations and equivalent static forces but additionaly acceleration and force demands becomes much less sensitive to changes in the normalized period. This is an important advantage because often the period of vibration of the nonstructural element is not known or is subjected to important uncertainties. Figure 9 shows reductions in forces and in displacements for nonstructural components that are perfectly tuned to the first mode or to higher modes of the supporting structure strongly contributing to the response. It can be seen that even fairly small levels of nonlinearity, such as 1.5 or 2.0, lead to large reductions in forces. However, in addition to large reductions in forces, the proposed approach also leads to important reductions displacement demands. It should be noted that in Figure 9 the displacement demands are normalized with respect to those that would occur in elastic systems showing that they can be reduced to half by allowing a relatively small level of nonlinearity.

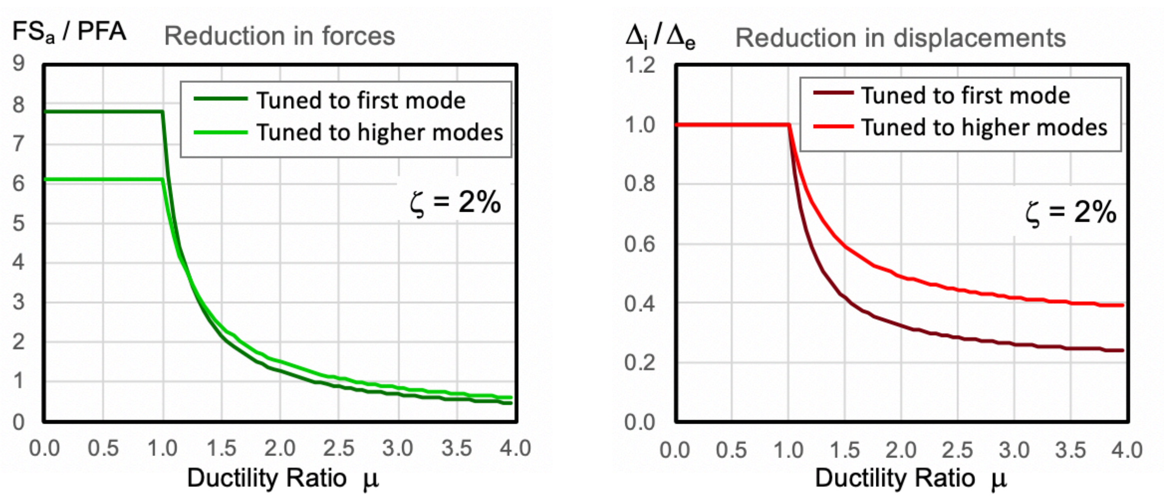

Figure 9. Reductions in forces (left) and in displacement (right) as a function of the level of nonlinearity allowed in nonstructural elements that are perfecty tuned to the first mode or to higher modes of the supporting structure.

4. SUMMARY AND CONCLUSIONS

The seismic design of nonstructural elements is challenging since, in general, there are large uncertainties in estimating force and deformation demands for nonstructural elements and their attachments to the structure in which they are mounted on or are suspended from. Current design provisions make use of oversimplified equations to estimate equivalent static forces that do not properly take into account the main factors controlling the intensity and other characteristics of seismic demands that may occur on nonstructural elements, and therefore, they may greatly overestimate demands leading to overly conservative designs, while in many other cases, they may greatly underestimate seismic demands leading to unconservative designs and nonsatisfactory seismic performance.

There is no doubt that it is possible to develop rational methods for design of nonstructural elements that adequately consider the characteristics of the ground motion, of the supporting structure (lateral strength, lateral stiffness and their spatial distribution in the structure, modal frequencies, damping, etc.) and of the nonstructural element (mass, stiffness, strength, modal frequencies, damping). However, nonstructural elements are typically not designed by structural engineers that are experts in seismic loading. Even, if structural engineers are asked to design these elements they mainly design their bracing and attachments to the structure. Furthermore, nonstructural elements are rarely included in the analytical model of the structure and, more importantly, very little information required to develop detailed models is typically available to the engineers in charge of designing bracing elements of nonstructural elements or their attachments to the structure and to the nonstructural component.

A series of analytical studies have been presented that provide the basis for a new design approach for nonstructural elements in which bracing elements are designed and detailed to yield in the case of moderate and strong earthquakes. The analytical studies allowed the selection of several motions recorded in instrumented buildings that provide severe excitation to nonstructural elements that are representative to those that are expected to occur in nonstructural elements on buildings during moderate and strong earthquake ground motions. The proposed approach is particularly effective for nonstructural elements whose frequencies of vibration coincides with modal frequencies of the structure in which they are mounted on or suspended from. This is true whether the nonstructural element is tuned or nearly tuned to the fundamental mode of vibration or to higher modes of the supporting structure.

The proposed design approach has a number of important advantages with respect to current seismic provisions for the design on nonstructural elements. These advantages are: (1) It can be used with limited information about the supporting structure; (2) It allows to design for significantly lower acceleration and forces; (3) It significantly reduces uncertainties on the seismic forces acting on the nonstructural components, the bracings and attachments, as these forces now depend on the strength of the yielding bracing element which can be estimated with much smaller uncertainty; (4) For components tuned or nearly tuned to modes of vibration of the supporting structure, the proposed approach, in addition to reducing force demands it also leads to important reductions in lateral deformation demands to levels significantly smaller than those that would occur in tuned components responding elastically; and (5) Force and deformation demands become far less sensitive to the ratio of period of vibration of the component to modal periods of vibration of the supporting structure.

ACKNOWLEDGEMENTS

The project was sponsored by the Seismology and Earthquake Engineering Research Infrastructure Alliance for Europe (SERA). This funding is greatly appreciated. Special thanks are also given to Profs Anastasios Sextos and George Mylonakis, Dr. Raffaele De Risi and laboratory personnel at the University of Bristol for their assistance during the shaking table testing. We also thank an anonymous reviewer of this manuscript who provided several sugguestions to improve it.

REFERENCES

Ayers JM, Sun TY, Brown FR. Non-structural damage to buildings, the great Alaska earthquake of 1964: Engineering. National Academy of Science, Washington, DC. 1973.

Elkady A., Vamvatsikos D., Lignos D., Kazantzi A and Miranda E., Experimental study to validate an improved approach to design acceleration-sensitive nonstructural component, Proc. Fifth Intl. Workshop on the Seismic Performance of Nonstructural Elements, Stanford, California, December, 2022.

Filiatrault A, Sullivan T. Performance-based seismic design of nonstructural building components: The next frontier of earthquake engineering. Earthquake Engineering and Engineering Vibration. 2014 Aug;13(1):17-46.

Kazantzi A, Vamvatsikos D, Miranda E. Effect of yielding on the seismic demands of nonstructural elements. In *Proceedings of 16th European conference on earthquake engineering*, Thessaloniki, Greece 2018.

Kazantzi AK, Vamvatsikos D, Miranda E. The effect of damping on floor spectral accelerations as inferred from instrumented buildings. *Bulletin of Earthquake Engineering*. 2020a Mar;18(5):2149-64.

Kazantzi AK, Vamvatsikos D, Miranda E. Evaluation of seismic acceleration demands on building nonstructural elements. *Journal of Structural Engineering*. 2020b Jul 1;146(7):04020118.

Kazantzi AK, Miranda E, Vamvatsikos D. Strength-reduction factors for the design of light nonstructural elements in buildings. *Earthquake Engineering & Structural Dynamics*. 2020c Oct 25;49(13):1329-43.

Miranda E. Seismic evaluation and upgrading of existing buildings. *PhD Thesis*, University of California, Berkeley; 1991.

Miranda E, Kazantzi AK, Vamvatsikos D. New approach to the design of acceleration-sensitive non-structural elements in buildings. *In Proc. 16th European conference on earthquake engineering* 2018a (pp. 18-21).

Miranda E, Kazantzi AK, Vamvatsikos D. Towards a new approach to design acceleration-sensitive non-structural components. *In Proceedings of 11th national conference in earthquake engineering*, Earthquake Engineering Research Institute, Los Angeles, CA 2018b.

Naeim F. Impact of the 1994 Northridge earthquake on the art and practice of structural engineering. The Structural Design of Tall and Special Buildings. 2004 Dec 15;13(5):373-89.

NIST 2018. Recommendations for Improved Seismic Performance of Nonstructural Components, NIST GCR 18-917-43, National Institute of Standards and Technology, Gaithersburg, Virginia; 2018.

Poulos, A. and Miranda, E. Probabilistic characterization of the directionality of horizontal earthquake response spectra *Earthquake Engineering & Structural Dynamics*. 2022.

Taghavi, S., Miranda, E., [2003] “Response assessment of nonstructural building elements,” *Report PEER 2003/05*, Pacific Earthquake Engineering Research Center (PEER Center), University of California, Berkeley.

Taly N. The Whittier Narrows, California Earthquake of October 1, 1987—Performance of Buildings at California State University, Los Angeles. Earthquake Spectra. 1988 May;4(2):277-317.

Simple and Economical Details to Improve the Seismic Resiliency of Large Power Transformers

Neil G. Moore, S.E.
Neil Moore and Associates
4536 French Creek Road, Shingle Springs, California 95682
email: nma@nma-se.com

ABSTRACT: Since the Northridge earthquake where important transformers were damaged, structural engineers have been active in determining the causes. On three essential items, where after free body diagrams were prepared, it became apparent that simple and economical changes to the construction of the transformer would improve its seismic resilience. The three issues are the failures of anchorage, center tensioned porcelain bushings and coil windings. Solutions to each of these failures were already known but not codified adequately in governing documents. These solutions have been known for over 60 years and have been addressed in some manufacturers transformers but not all. Presently the IEEE 693 committee is involved in the codification process. But utilities have the option of specifying these "new" requirements as follows:

- Anchorage: Allow the transformer base plate to thermally move by anchoring a single point on one end while guiding the other end to prevent lateral sliding. Utilizing hold down anchors similar to those used with steel tanks to prevent overturning.

- Center Tensioned Porcelain Bushings: Ensure that there is a seismic restraint mechanism that stabilizes the internal conductor during a seismic event.

- Coil Winding Assembly: Specify Nomex insulation on the windings with plastic spacers between the windings and a hydraulic compression system to ensure that the coil winding assembly is always stable with a pressure monitoring system.

Another issue is the end of life of the transformer and when to remove the transformer from service. Failure of a transformer occurs when it stops functioning or catches fire and/or explodes. One approach to prevent failure would to be monitoring the compression of the coil assembly; when the compression falls below a predetermined value, a signal is provided to the operating staff. If this signal is ignored, then after some time, or when the compression falls below a second predetermined value, the transformer automatically shuts down. Being aware of these problems, the seismic specialist cannot certify that the transformer will operate during and after a seismic event unless the problems are addressed.

KEYWORDS: Anchorage, Approval, Bushings, Coil Windings, End of Life, Free Body Diagram, Seismic Restraint Mechanism

1.1 INTRODUCTION

Transformers are not machines. "A transformer has no internal moving parts, and it transfers energy from one circuit to another by electromagnetic induction." per the Bureau of Reclamation: Transformer Maintenance and Diagnostics[2005]. The electric transformer is the most important unit of any substation and for many years, it has been an enigma to many earthquake engineers as to why there are failures of some of the basic components such as anchorage, center tensioned porcelain bushings and coil windings. Since the Northridge earthquake, where important transformers were damaged, structural engineers have been active in determining the causes. Transformers located in earthquake zones require additional design features to ensure that the transformer functions during and after a seismic event. These features are reviewed, along with a number of other features, for approval by seismic design engineers. Recent reviews and technical documents published by various committees and individuals indicate that this may be possible when focusing on three of the known vulnerabilities. It is interesting that these vulnerabilities have been known for many years and solutions by various manufacturer's are available. Presently the IEEE 693 Recommended Practice for Seismic Design of Substation [2018] committee is involved in the codification process, but utilities have the option of specifying these "new" requirements whether they are codified or not.

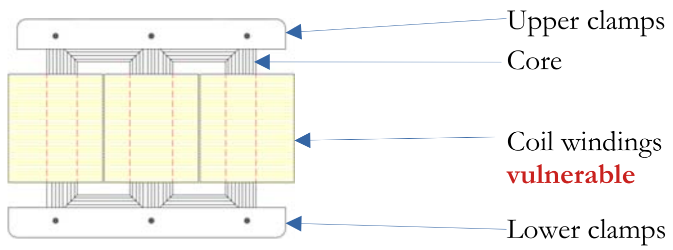

Figure 1.1 Internals of a Transformer

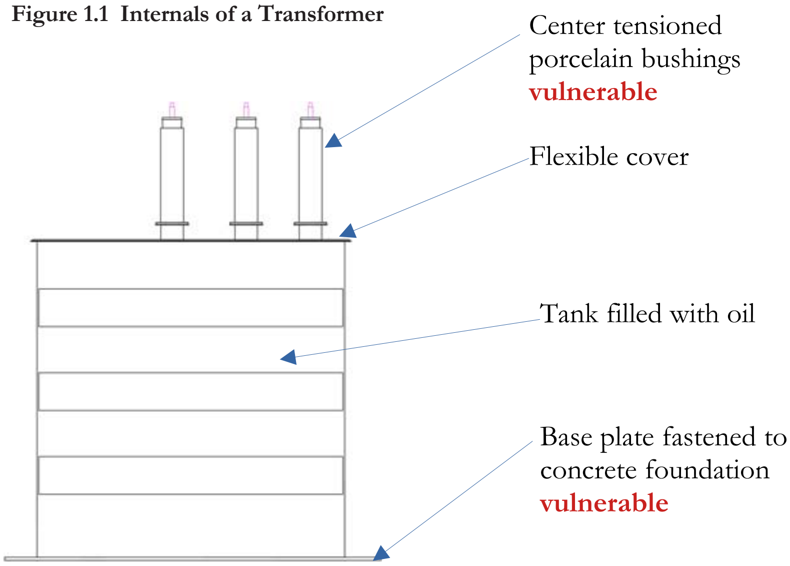

Figure 1.2 Transformer tank with base plate and bushings

1.2 OWNER'S RESPONSIBILITY

The operation of the transformer is the responsibility of the owner and it must have a protocol of defining when the transformer is to be removed from service. Run to failure is not an acceptable option. Without this protocol, the seismic design engineer cannot approve the use of the transformer.

1.3 BASIC STRUCTURAL FUNCTIONS

It is important to understand that the greatest structural loads to a transformer are electric fault forces that have to be resisted by the coil windings, column spacers, insulation, clamping beams, tensioning rods and a permanent compression stabilizing system. Although the transformer engineer provides the design, the seismic design engineer must review and approve the arrangement. Transformers also have thermal characteristics and are designed to function for many years. Internal components that are in the structural load path are wood (hardwood and densified wood), paper insulation or proprietary insulation material, coil wire - either copper or aluminum, and shim/spacer material of various types. Ordinarily structural engineers do not address these materials but they are in the structural load path and have to be considered. In order for differences between standard transformers and transformers specifically designed for earthquake country to be accepted by transformer manufacturers, it is important that these differences be considered.

2. ANCHORAGE

2.1 FAILURES

Transformer base plates that are fastened to the concrete foundation by welding to embedded plates or standard anchor bolts are suspected of distress damage either by broken welds, crushed concrete around the anchor bolt or cracked concrete. Damage can also be hidden by the base plate itself. This is the present recommendation of the IEEE Std 693-2018 *Recommended Practice for Seismic Design of Substations* [2018]. This is caused by thermal forces similar to those affecting steel bridges or steel water tanks such as the sun.

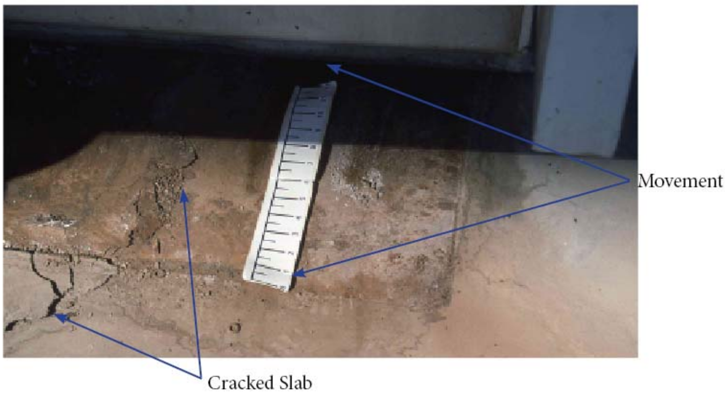

Figure 2.1 Transformer moved 14" during a seismic event

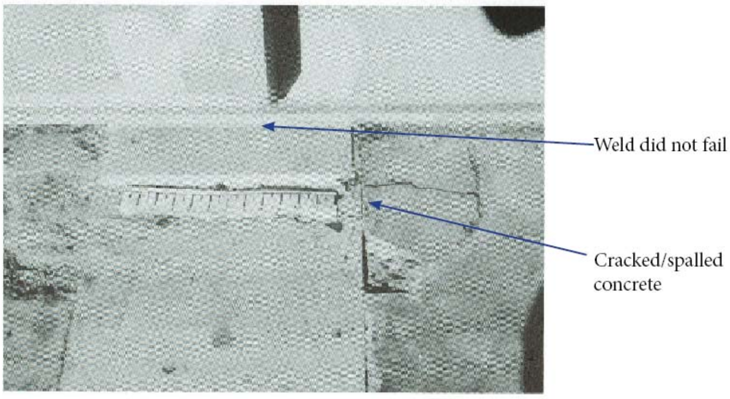

Figure 2.2 Another illustration shows distress but the seismic ground motion was .15g.

2.2 WARNINGS

- The **Guide to Improved Earthquake Performance of Electric Power Systems [1998]**

"Embedment plates must be stiff enough to prevent welds from tearing the plate, to distribute load to headed studs or other means of securing the plate to the foundation slab, and to avoid unacceptable thermal deformation during concrete curing."

2.3 CODES AND TECHNICAL DOCUMENTS

- **ASCE 7-22 [2022] American Society of Civil Engineers Standard Minimum Design**

Section 1.2.3 *"Provision shall be made for self-straining forces arising from assumed differential settlements of foundations and from restrained dimensional changes due to temperature changes, moisture expansion, shrinkage, creep, and similar effects."*

- **Evaluation of Steel Structures with Thermal Restraint [1986]**

Section 6.3.1 states: *"The effects of thermal movements in steel structures are best minimized by modifying connections to allow axial movement."*

- **IEEE 693-2005 [2005] IEEE Recommended Practice for Seismic Design of Substations**

Section 19 Mechanical loads f) *Thermal affects (stresses due to thermal expansion, plus influence on strength properties of materials over the full temperature range from minimum ambient to maximum ambient plus temperature rise due to load heating effects)*

- **IEEE 693-2018 [2018] IEEE Recommended Practice for Seismic Design of Substations**

Section 3.1 Definition normal operating load: *Any force, stress, or load resulting from equipment operation that can reasonably be expected to occur during an earthquake……...*

2.4 SUGGESTED TRANSFORMER ANCHORAGE DESIGN

- **Sliding**

Have one end of the transformer with a single fixed anchor to resist the longitudinal earthquake forces in one direction and about half of the earthquake forces from the transverse direction. The other end is guided such that it is allowed to move in the longitudinal directions and resists about half of the lateral earthquake forces from the transverse direction.

This can be accomplished by embedding two vertical pipe sleeves in the concrete foundation. These pipes would be aligned with the longitudinal center line of the transformer base plate. The transformer base plate would be extended at each end to accommodate a hole at one end and a slot at the other end to accommodate steel pins.

- **Overturning: Transformer profiles are divided into two categories.**

Low profile, which experiences little uplift during a seismic event and does not require uplift connections to the concrete foundation.

High profile which experiences significant uplift forces during a seismic event, and will utilize either anchor rods on both sides of the longitudinal base plate in oversize holes or connections to the jacking pads. In both cases the rods will be connected to the tank some distance above the slab to accommodate thermal movement.

3. BUSHINGS: Center Tensioned Porcelain with Type C Flange (mating surface with non-constrained gasket)

3.1 FAILURES

- Flanges have slipped and allowed oil to escape or ceramic tube above flange has broken/ fractured.

- Unrestrained internal conductor (copper or aluminum tube) wrapped with Kraft paper vibrates and impacts interior surfaces of upper ceramic tube and aluminum flange during the seismic event.

3.2 WARNINGS

- "..........there shall be no slippage, visible oil leak, or broken support flanges." [Gilani, Whitaker, Fenves, Fujisaki 1999]

3.3 CODES AND TECHNICAL DOCUMENTS

- **IEEE 693-18 [2018]:** *Recommended Practice for Seismic Design of Substations*
- **IEC TS 61463 [2016]** *Technical Specification - Bushings - Seismic Qualification*
- **ASCE 7-22 [2022]** *Minimum Design Loads and Associated Criteria for Buildings and Other Structures. Chapter 13 Seismic Design Requirements for Nonstructural Components*
- **Gilani, Whittaker, Fenves, Fujisake [1999]** *Seismic Evaluation and Retrofit of 230-kV Porcelain Transformer Bushing*
- **IEEE Std. C57.19.00 [2004]** *IEEE Standard General Requirements and Test Procedure for Power Apparatus Bushings*
- **IEEE Std. C57.125 [2015]** *IEEE Std. C57.125 [2015] IEEE Guide for Failure Investigation, Documentation, Analysis, and Report for Power Transformers and Shunt Reactors*

3.4 RECOMMENDATIONS

- **Seismic Restraint Mechanism**

Inclusion of an internal seismic restraint mechanism near the flange area to change the vibration mode of the conductor and prevent the slippage. Presently recommended by IEEE 693-2018 [2018]. This detail changes the free body diagram considerably.

Some bushing manufacturer's already have this seismic restraint mechanism and have claimed that they have not had a center tensioned bushing earthquake failure. As it is likely to be a proprietary item and not shown on their submittal drawings, a written statement should be considered.

- **Internal Bushing Stabilization Under Flexible Cover**

Addition of internal turrets braced to change the fastening of the bushing assembly from an out-of-plane seismic moment to the cover, to a couple connection where the resulting forces of the seismic moment are resisted by the in-plane cover and bracing. Recently proposed to bushing manufacturer's and one transformer manufacture for evaluation.

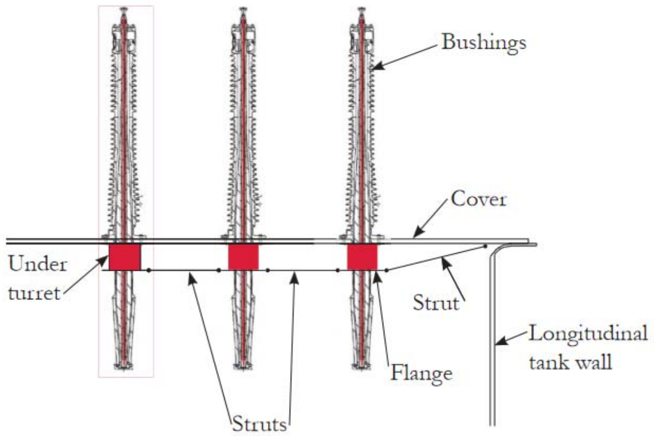

Figure 3.1 Longitudinal Bushing Stabilization

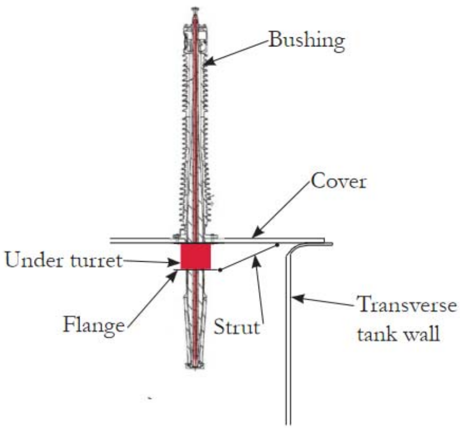

Figure 3.2 Transverse Bushing Stabilization

4. COIL WINDINGS

FAILURES: A PARTICULAR INVESTIGATION

Per Koboyashi, Kido and Kojiro [2019] concerning TEPCO investigations which discusses Seismic Resistance:

- *"-------For example, there was considerable displacement of a transformer winding because of a 23-year old 500kV transformer operating with a high load factor. The winding moved 15 mm (0.59 inches), increasing the gap between the high-voltage and low voltage windings. In addition, the duct spacers collapsed between the pressboard. The seismic acceleration was 890 gal at ground level and 1720 gal at the transformer's center of gravity------"*

- *"------The displacement of the transformer winding coil also was noted in the other transformers, from different manufacturers, located at the same power plant. As a result of the investigation undertaken when the transformer was decommissioned, the clamping force had decreased by approximately 60% and the winding displaced decreased by 40%.*

- *"When the clamping force decreases as a result of thermal degradation, displacement of the winding (can) occur even in the event of a minor earthquake--------"*

4.1 WARNINGS

Insulation and coil spacers are most likely robust enough to resist seismic events in the first few years of the life of a transformer but as the transformer ages, the insulation degrades and becomes weaker and more brittle and vulnerable to shocks; possibly not failing but unexpectedly shortening the life cycle of the insulation. Depending upon the location in earthquake country, some transformers may experience smaller but more frequent events. During the Ridgecrest, California earthquakes, there were almost continuous ground motion events. This illustrates the possibility of incremental damage to local transformers depending upon the age of the insulation.

- **IEEE 693-2018 [2018] Section D.4.1 states:**

  "All components of the load path shall have sufficient rigidity to restrain the core and coil from shifting."

Due to degradation and crushing of various components over the lifetime of the transformer, the coil assembly shrinks and looses the compression forces that provide the structural stability of the coil/radial key spacer columns.

- **Referring to Section 6.1.3 of IEEE Std. C57-140-2017 [2017]**

  " Clamping pressures are transmitted through the columns of radial key spacers. The clamping pressures are normally specified as the pressure exerted onto the radial key spacers. ***There is, however, no industry standard****, and clamping pressures vary widely."*

With the loss of the structural rigidity of the coil/radial key spacer columns, the assembly becomes vulnerable to lateral seismic forces and no longer conforms to IEEE 693-2018 Section D.4.1.

- **According to Section A.2.1 of IEEE Std. C57-125-2015 [2015]**

  "The core clamping system is adjustable on some designs to apply pre-calculated compressive forces on the windings to control axial short-circuit forces. Compressive forces are distributed evenly around the coil stack using jack screws, compression wedges, or spring-loaded, insulating liquid-filled dashpots. The tie bars, tie rods, or lock plates are also insulated from the core and are kept under tension by the clamping system compressive forces on the winding..…"

- **Also, according to Section 6.1.3 of IEEE Std. C57-140-2017 [2017]**

" Some large power transformer designs include dashpots (i.e., oil-filled spring- loaded pistons and cylinders) for coil clamping. This system helps ensure positive clamping pressure even with moderate changes in coil height."

- **IEEE Std. C57.140-2017 - IEEE Guide for Evaluation and Reconditioned of Liquid Immersed Power Transformers**

"Proper coil clamping pressure is required for the winding to withstand axial short-circuit forces. As a result of thermal and mechanical cycling over time, vertical clamping forces (axial) on the coils can be reduced below the level required to hold the coils stable during through-fault events. Inadequate coil clamping pressure has been known as a primary cause of transformer winding failures due to through faults. Coil clamping pressure generally reduces gradually over time at a different rate for different windings or for different layers of the same winding. The primary reason is that total accumulation of cellulose insulation between the fixed top and bottom clamps can take a permanent set over time under static loading and dynamic loading. Mechanical creep characteristics of compressible, non-elastic material are much more pronounced on low-density material such as found in older transformers. For this reason, loss of clamping pressure on coils is more prevalent in older units. Another contributor to the loss of coil clamping pressure is shrinkage of the cellulose, which is caused by thermal cycling due to load variations in service."

- **Per Prevost, Woodcock, Krause [2000]:**

"It is a well-known fact that transformers removed from service at or near their end of life have been found to have little or no pressure remaining on the windings. This observation is not always possible, because when the unit is allowed to reabsorb moisture after being removed from service, the windings can appear tight and lead to the false conclusions that they were tight during operation."

- **McNutt, William [1960]:**

A video of short circuit demonstration and three core limbs installed for viewing. The video shows a test by the GE lab, where they installed different configurations of coil windings on the three legs of a core assembly and tested them with about 25 fault shocks and used a high-speed camera to see what was happening. The first two legs coil windings dramatically bounced up and down and showed large gaps at first two legs with the insulation crushing and the assembly losing its initial compression.

The third leg with insulation, plastic spacers between the windings and a hydraulic system that was able to adjust the compression. This leg survived with little crushing of the insulation around the wire, no crushing of the spacers, and with the hydraulic compression system still functional. Mr. McNutt states that this third leg coil windings assembly is the "ideal" that they recommend.

- **§50.49 *Environmental Qualification of Electric Equipment Important to Safety for Nuclear Power Plants*. United States Nuclear Regulatory Commission**

"(5) Aging. Equipment qualified by test must be precondition by natural or artificial (accelerated) aging to end-of-life installed condition. Consideration must be given to all significant types of degradation which can have an effect on the functional capability of the equipment. If preconditioning to an end-of installed life condition is not practical, the equipment may be preconditioned to a shortened designated life. The equipment must be replaced or refurbished at the end of this designated life unless ongoing qualification demonstrates that the item has *additional life."*

4.3 TRANSFORMER OPERATION

Insulation has a normal degradation curve when the transformer is energized. The expected life of the insulation (and the transformer) can vary from 20 to 75 years. A number of events can shorten the expected life of the insulation as the aging occurs. Such events include faults and/or conditions where the operating temperature is allowed to exceed its design temperature. Faults are addressed by the transformer engineer by designing coils with physical restraints such as large tensioned bolts compressing (clamping) the winding and by the horizontal strapping of the windings. Temperature increase may be an operational decision or a lack of supervision by the user of the transformer. It is assumed that maintenance is performed adequately and that the original insulation material and the workmanship are both of high quality. Refer to IEEE Std. C57.19.100 [2012}

4.4 RECOMMENDED COIL WINDING STRUCTURAL CONSIDERATIONS

- Insulation degradation: Nomex electrical insulation recommended by Mendes. [no date – 74 pages]
- Loss of assembly compression: Inclusion of a permanent spring or hydraulic assembly.
- Failure of clamping connections (top or bottom or both): Structural review by seismic structural engineer.
- Shifting/stability of column stack: Maintain adequate compression.
- Loss of spacer(s): Maintain adequate compression.
- Run to failure: **<u>Do not allow</u>.**
- Gaps between windings (loose windings): **<u>Do not allow.</u>**

4.5 MONITORING FOR END OF LIFE

- Mechanism for providing continuous compression pressure information for operators.
- Alarm for notifying operator that compression approaching inadequate pressure.
- Built-in automatic mechanism for shutting down the transformer if parameters fall below accepted values.

4.6 CONCLUSION

A transformer must be able to remain operational during and after any expected seismic event. Degradation or deterioration of electrical insulation is the most significant failure mode for transformers. Failures of the windings are primarily caused by failures of the insulation system. An immediate, or sometimes postponed, failure of the transformer may result when aged and degraded insulation and loose coil spacers, are subjected to shocks caused by electric faults or seismic events. All transformer maintenance publications focus on insulation life issues. The life of a transformer is predominantly determined by the aging and degradation of the insulation. Solid and paper insulation cannot be repaired, but the rate of degradation can be limited by controlling the transformer usage – such as ensuring routine maintenance and limiting heating above the name plate heat rating. Therefore, a transformer, instead of being a robust piece of equipment, is actually a fragile piece of equipment due to the insulation degradation issue. A permanent system of maintaining compression on the coils assembly as it ages is recommended. This system should also provide adequate warning as well as a means shutting off the transformer at a predetermined condition or set of conditions.

4.7 SIMPLIFIED COIL WINDING ASSEMBLY

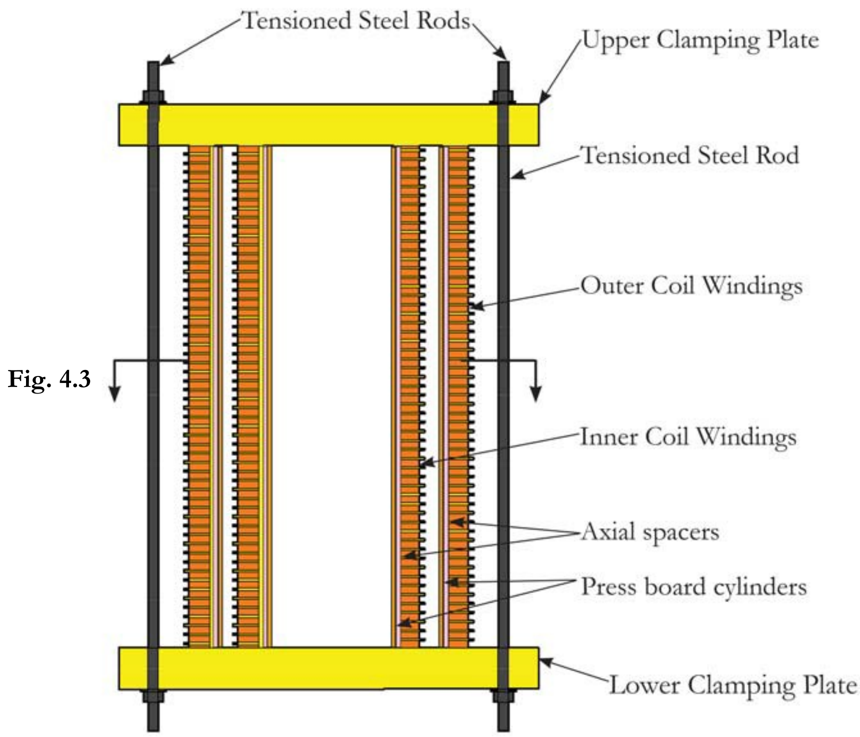

Figure 4.2 Section at Centerline of Coil Key Spacer Columns

4.8 SIMPLIFIED COIL WINDING ASSEMBLY

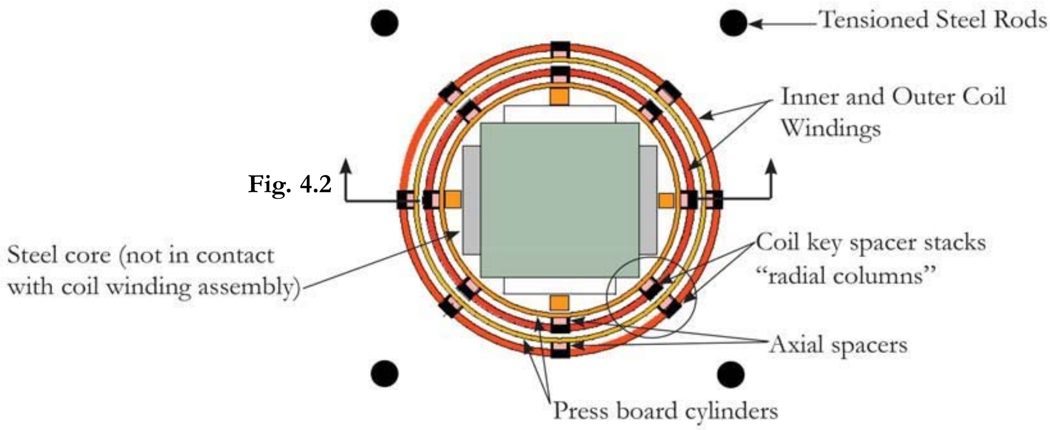

Figure 4.3 Section at Mid Height

4.9 STRUCTURAL ANALYSIS OF RADIAL COIL KEY SPACER COLUMNS

Initial normal compression loading with lateral seismic loading when transformer is new and at ambient temperature.

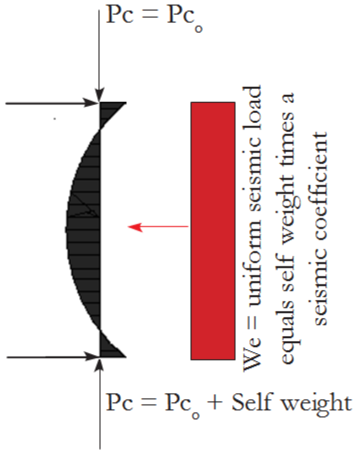

Figure 4.4 – Bending Diagrams for Both the Inner and Outer Coil Winding Assemblies

$$\frac{Pc\text{-}initial}{A} > \frac{Mf}{S} = +Fc \text{ - OK - No Tension} \quad (1)$$

- *Loss of coil winding compression is related to time and heat which can cause "loose coils." The degradation process of the insulation occurs over time and can the shrink the insulation. The thermal elongation of the steel rods occurs when the transformer is energized. As time passes in unknown years, there can be a loss of the compression winding loading. Eventually the compression load is critically reduced or there is no load on the key spacer columns which will result with only a simple uniformly seismic lateral load during a seismic event. Refer Section 4.1 Warnings, IEEE Std. C57.140-2017.*

- ***Loss of compression loading with lateral seismic loading when transformer is energized and old degraded insulation.***

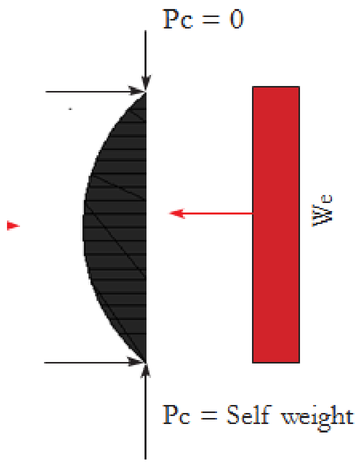

Figure 4.5 - Bending Diagrams for Both the Inner and Outer Coil Winding Assemblies

$$\frac{Pc\text{-}aged}{A} < \frac{Ms}{S} = -Fc \text{ - No good} \quad (2)$$

- **Self Weight:** Coil Winding - Copper or Aluminum. Spacers in the key spacer stack. Insulation Separator Tubes. Vertical Spacers. Circulating Oil in Voids.

- **Structural Properties for Analysis:**

  PC-initial = Initial compression force per Electrical Engineer's analysis, evenly distributed over all coil wire/spacer stack columns.
  Pc-aged = Reduced compression force due to degradation of insulation
  A = Spacer width x effective coil wire width x number of coil wire/spacer circular column stacks.
  Mf = Seismic Fixed End Moment
  Ms = Seismic Simple Beam Moment
  Fc = force
  S = Section modulus of coil wire/spacer column stacks circle.
  We = Uniform seismic lateral load equals self weight x a seismic coefficient.

- **Goal:**

Coil wire/spacer shall have permanent compression of the original design pressure per IEEE 693-18. This requires a compressed key spacer column fixed at both ends to resist a uniformly distributed lateral seismic load.. Referring to Section 6.1.3 of IEEE Std. 57-140-2017, 4th paragraph: "Clamping pressures are transmitted through the columns of radial key spacers. The clamping pressures are normally specified as the pressure exerted onto the radial key spacers. ***There is, however, no industry standard, and clamping pressures vary widely.***"

- **Possible Result:**

The coil key spacers stacks with no compression and may fail during a seismic event. Note that there is some lateral resistance from the strength of the insulation tubes, coil rigidity and the vertical spacers. Coils may move at mid height, especially the inner coil

.

5. CONCLUSION:

The electric transformer is the most important unit of any substation and for many years has been an enigma to many earthquake engineers as to why there are failures of some of the basic components such as anchorage, center tensioned porcelain bushings and coil windings.

Failure of a transformer presents immediate problems for the owner such as obtaining a temporary source of power. It may take two years to purchase a replacement transformer. Transformer failure, in the absence of earthquakes, are usually failures of the insulation and bushings. Transformers do not operate forever and transformers are not machines. There are solutions that have been known for many years that will extend the life of a transformer to its expected life. Unfortunately the solutions are not adequately codified. Codifying the design of the coil windings which includes attention to the type of insulation used and the actual construction of the porcelain bushings needs to be considered. There are other issues such as the end of the transformer life and removal from service requirements and code language concerning the professional structural engineer's length of responsibility.

Transformers in earthquake country complicate the issue because of anchorage failures and noted distress of loose coil windings. The realization is that a transformer although robust at the outset, over time becomes fragile and vulnerable to distress when a seismic event occurs.

ASCE 7-22, Section 13.6 has excellent requirements and commentaries for electrical and mechanical equipment. These requirements particularly address impact of elements, but not the degradation of insulation. Although there are many technical documents that state that the life of a transformer is the life of the insulation, there are no regulations governing this and ***"Long term operational performance of components is beyond the scope of the* [ASCE]*Standard"*** per author's submittal response. Refer to Moore, Neil [2022].

Hopefully ASCE or IEEE 693 will produce a new document specifically for transformers and address the following topics that are not well understood as this time:

- Anchorage failures – lateral movement and overturning

- Center tensioned porcelain bushing failures - stabilization of the inner core, lateral movement of the upper porcelain barrel or brittle failure of the porcelain. Stiffening the cover.

- Coil winding failures – fires and explosions

- End of life language – preventing unexpected failure – either cessation of function or fire/explosion.

- Certification language – legal ramifications and liability insurance for the approving seismic specialist engineer.

The owner's usage and maintenance of the transformer is important and there should be a protocol to avoid cancellation of the seismic specialist's certification if the protocol is not adhered to correctly.

Being aware of these problems, the professional structural engineer cannot certify that the transformer will operate during and after a seismic event unless these problems are addressed. These topics should be further studied with more coordination between the various code committees.

6. REFERENCES

ASCE 7-22 [2022] *Minimum Design Loads and Associated Criteria for Buildings and Other Structures.*
Section 1.3.4 - Self-Straining Forces and Effects Section
13.6.2.1 - Impact
Section 13.6.2.2 - Impact

Evaluation of Steel Structures with Thermal Restraint [1986] Tennessee Valley Authority Nuclear Power DG-6.12
Section 6.3.1 - Thermal Modifications pp. 23

Gilani, Whittaker, Fenves, Fujisake [1999] *Seismic Evaluation and Retrofit of 230-kV Porcelain Transformer Bushing* Pacific Earthquake Engineering Research Center pp. 5

Guide to Improved Earthquake Performance of Electric Power Systems [1998] NIST GCR 98-757 pp. 48, 118, 141

IEC TS 61463 [2016] *Bushings - Seismic qualification* pp. 13, 24, 33-34, 37-38

IEEE Std. 693 [2005] *IEEE Recommended Practice for Seismic Design of Substations pp* pp 5, 22, 83, 88

IEEE Std. 693 [2018] *IEEE Recommended Practice for Seismic Design of Substations pp* 23, 52, 105, 112

IEEE Std. C57.19.00 [2004] *IEEE Standard General Requirements and Test Procedure for Power Apparatus Bushings*
Section 4.2 - Unusual service conditions
Section 4.2.2 - Others conditions that may affect design, testing, and applications

IEEE Std. C57.125 [2015] *IEEE Guide for Failure Investigation, Documentation, Analysis, and Report for Power Transformers and Shunt Reactors* pp. 12, 14, 29, 55

IEEE Std. C57.140 [2017] *IEEE Guide for Evaluation and Reconditioning of Liquid Power Immersed Transformers*
pp. 15-16, 18, 22-23, 43-45

Koboyashi, Kido and Kojiro [2019], *How Transformers Age* [2019]. T&D World magazine pp. 1 - 10 TEPCO (Japan).

McNutt, William [1960s] "Bill McNutt Video Short Circuit Models_000.wmx"
https://drive.google.com/file/d/155yQlqEEGvhJv1ZGjazx0F5vcDIHDw_O/view

Mendes, Jose Carlos [no date - 74 pages]: *Residual Pressing Forces and Short-Circuit Strength, Mechanical Instability, Failure Modes, Solid Insulation Aging and Mechanical Strength Reduction* pp. A-31 and A-32, A-47 and A-48.

Moore, Neil [2-17-22] ASCE 7-22 Transformer Submittal Rejection Responses

Provost, Woodcock, Krause [2000] *The Effects of Winding Clamping Pressure Due to Changes in Moisture, Temperature and Insulation Age* pp. 16 Weidmann Electrical Technology AG

Transformers: Basics, Maintenance, and Diagnostics. Reclamation - Managing Water in the West. [2005] U.S. Department of the Interior, Bureau of Reclamation

§50.49 *Environmental Qualification of Electric Equipment Important to Safety for Nuclear Power Plants*. United States Nuclear Regulatory Commission

Seismic Performance Evaluataion of Braced and Friction-Added Suspended Ceilings Based on Shake Table Testings

Su-Chan Jun[1], Cheol-Ho Lee[1], Chang-Jun Bae[1] and Dong-Seob Lee[1]

[1] Dept. of Architectural and Architectural Engineering, Seoul National University
Seoul 08826, Republic of Korea
e-mail: corrora90@snu.ac.kr, ceholee@snu.ac.kr, changjun0125@snu.ac.kr, zooey2099@snu.ac.kr

Abstract. In this study, shake-table tests on four suspended ceiling specimens were conducted to develop effective seismic retrofit or design methods. First, a braced ceiling specimen was fabricated following the requirements given by ASTM E580 to investigate the limitations and possible side effects resulting from lateral bracing. The braced ceiling specimen suffered substantial damage, comparable to the non-seismic ceiling specimen, mainly due to its lack of diaphragm action in its grid system. Two improving methods were proposed, a strengthening method through grid reinforcements and a rotational friction mechanism addition. The braced ceiling specimen strengthened with grid reinforcements showed a highly improved seismic performance with no damage observed until the end of the test. The grid reinforcements were shown to be effective in developing a rigid diaphragm action within the grid systems, thus spreading the restraining effect of the lateral bracings. The proposed friction-added ceiling exhibited a stable hysteretic behavior under various input motions and effectively enhanced the overall seismic performance. The friction damping parameters, such as the maximum static force, were experimentally calibrated, and an analytical SDOF model of the friction-added ceiling system was developed for inelastic dynamic analysis. A numerical case study, based on an extensive time history analysis of steel moment frame buildings, was also conducted to illustrate the applicability of the friction-added ceiling system.

Keywords: Nonstructural elements, Shake table test, Braced ceilings, Friction damper, Numerical analysis

1. INTRODUCTION

Suspended ceiling is one of the most earthquake-vulnerable nonstructural elements which suffered significant seismic damage during past major earthquakes. The failure of suspended ceiling could lead to severe economic losses by impairing the functionality of buildings and even threaten the life safety of the residents by blocking the path during evacuation.

It is now well recognized from previous studies [for example, Pourali 2017; Pourali et al. 2018] that one of the important causes of suspended ceiling damage is related to the pounding that occurs between the surrounding walls and perimeters of ceiling systems. In order to reduce the pounding effects, ASTM E580 [2017] provides several seismic measures, and they are widely accepted in design codes such as ASCE 7-16 [2017] and also in the Korean seismic design code (KDS 41 17 00) [AIK 2019]. Figure 1 shows the two major requirements given by ASTM E580 for the suspended ceilings installed in high seismic areas (Seismic Design Category D, E, and F) to restrain the movements of ceiling systems. Many previous studies have demonstrated the effectiveness of seismic clips in improving the seismic performance of suspended ceilings, and a variety of clip details have been proposed [Gilani et al. 2008; Huang et al. 2013]. However, in the case of braced ceiling systems, several deficiencies have been reported, which were caused by either high vertical acceleration response [Soroushian et al. 2016] or the low in-plane stiffness of ceiling grids [Ryu and Reinhorn, 2019]. As the braced ceiling systems, in their current detail, are not satisfactory in improving seismic performance, further systematic experimental investigation is required.

In this study, a series of shake table tests were conducted using both the non-seismic (unbraced) and braced ceiling specimens. Based on test results, the limitations and side effects resulting from ceiling braces were analyzed. Then, two seismic performance-improving schemes were proposed, a strengthening scheme through grid reinforcements and a friction-added ceiling where a novel rotational friction mechanism was utilized. Their seismic performance was experimentally evaluated. For friction-added ceiling systems, a simple dynamic analysis model was proposed, and a numerical case study was performed to evaluate the applicability of the proposed ceiling system and draw useful design recommendations based on extensive time history analyses of steel moment frame buildings.

2. EXPERIMETNAL PROGRAM

Shake table tests of four ceiling specimens were performed utilizing two types of test frames. The non-seismic, braced, and the newly proposed friction-added ceiling specimens were tested using a square test frame having an overall dimension of 4.1 m (length) × 4.1 m (width) × 3.2 m (height) (see Figure 2(a)). Shake-table test using a 2-story steel moment frame was also implemented as a part of Korean government-

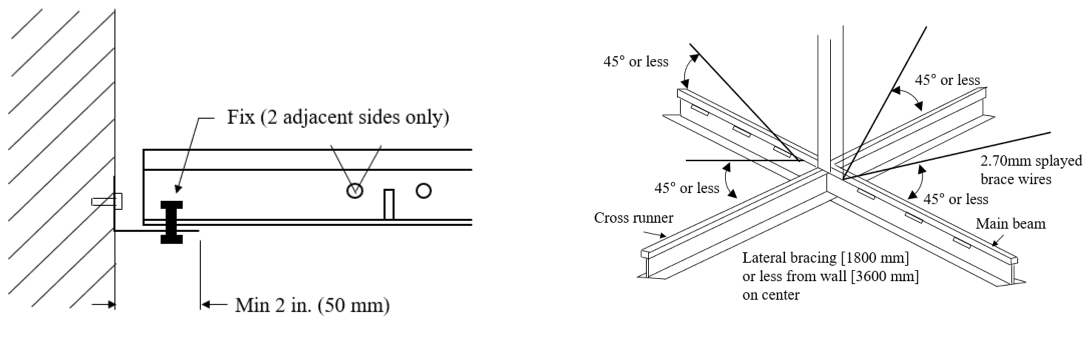

(a) Two side fixed perimeter detail

(b) Lateral braing for large area ceiling systems

Figure 1. Seismic requirements for ceiling installed on SDC D, E, and F building (ASTM E580)

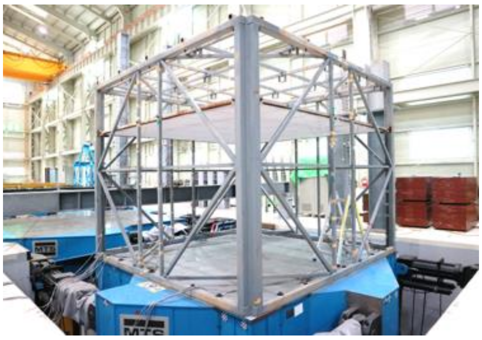

(a) Square test frame

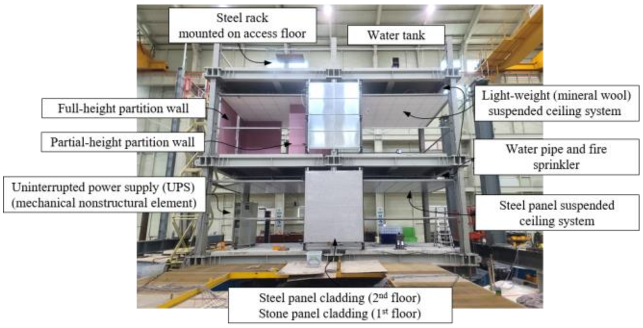

(b) Full-scale 2-story steel moment frame mounted an two isolated shake tables

Figure 2. Overview of test frames utilized for shake-table testing of ceiling specimens

funded joint research project in which 5 universities and more than 10 industry sponsors collaborated to systematically investigate the seismic performance of non-structural elements. A total of 10 types of non-structural specimens were installed in the 2-story steel moment frame, which was mounted on an array of two isolated shake tables (see Figure 2(b)). This study focused on analyzing the performance of the braced ceiling specimen with grid reinforcements (installed on the 2nd floor). The details of each specimen are described below.

2.1 Test Specimens and Measurements

Table 1 summarizes the key information of the tested ceiling specimens. The non-seismic ceiling specimens (Specimen DTL) were fabricated following the minimum perimeter clearance (15 mm) suggested by ASTM E580. The overall specimen and measurement plan are the same as those of DTL-B, except for perimeter clearance and lateral bracing. Specimen DTL-B had lateral bracings fabricated following the requirements for SDC D, E, and F ceilings of ASTM E580. The braces were rigidly designed based on the equivalent static force prescribed by ASCE 7-16 [2017]. A channel section of C-50 × 45 × 0.8 was used as a brace member (Figure 3). The numerically analyzed natural frequency of specimen DTL-B was about 28 Hz.

Specimen DTL-FS-BS represents the braced ceiling specimen installed in the 2-story moment frame where grid reinforcements were added at each bracing location to increase the in-plane stiffness of the ceiling grids (see Figure 4). Through grid reinforcement, the inertial force can be more effectively collected and transmitted to the concrete floor slab. The reinforcement design can be conducted by proportioning the reinforcing member such that lateral displacement smaller than the introduced boundary clearance would occur. The lateral displacement of the reinforcement was calculated by simplifying its behavior as that of the cantilever beam subjected to a uniformly distributed load (see Figure 5). A box channel section of 100 × 20 × 2 (in mm) provided sufficient stiffness to avoid pounding.

Table 1. Four direct-hung lay-in suspended ceiling specimens tested

Specimen	Ceiling size (m)	Excitation	Perimeter clearance (mm)	Plenum depth (m)	Performance-enhancing feature
DTL	3.87 × 3.87	3-dimensional	15	0.75	-
DTL-B	3.87 × 3.87	3-dimensional	20	0.75	Rigid brace
DTL-FS-BS	9.00 × 4.07	1-dimensional	20	0.79	Rigid brace with grid reinforcement
DTL-F	3.87 × 3.87	3-dimensional	20	0.75	Friction damper

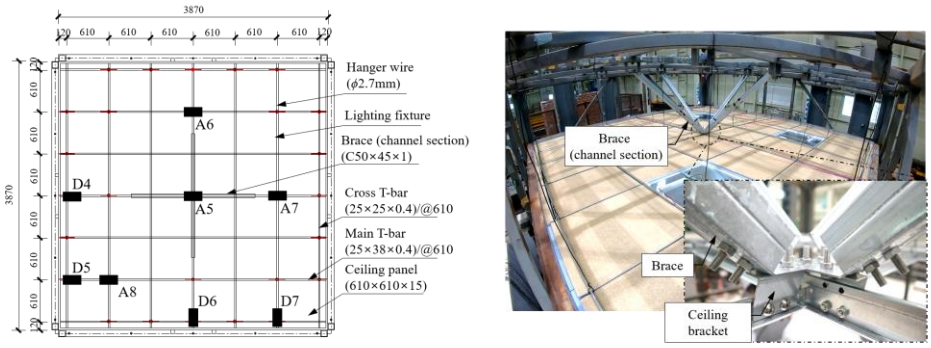

Figure 3. Specimen and measurement plan for braced ceiling specimen (DTL-B)

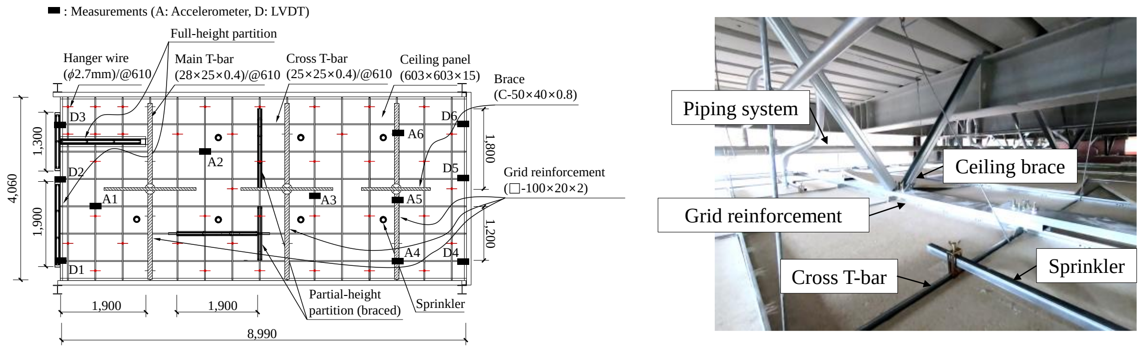

Figure 4. Measurement plan and detailed configuration of braced ceiling specimen with grid reinforcement (DLT-FS-BS)

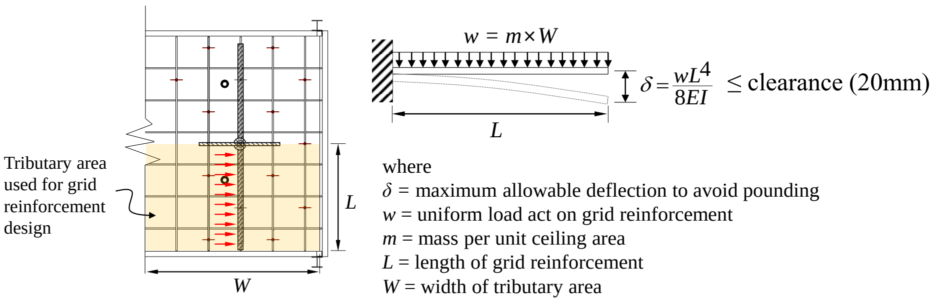

Figure 5. Ceiling grid reinforcement design for inertial force provided from ceiling tributary area

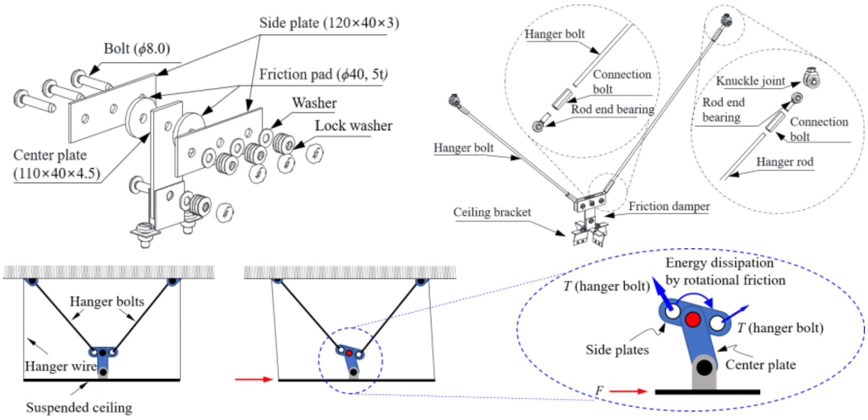

Figure 6. Components and working mechanism of proposed ceiling friction damper

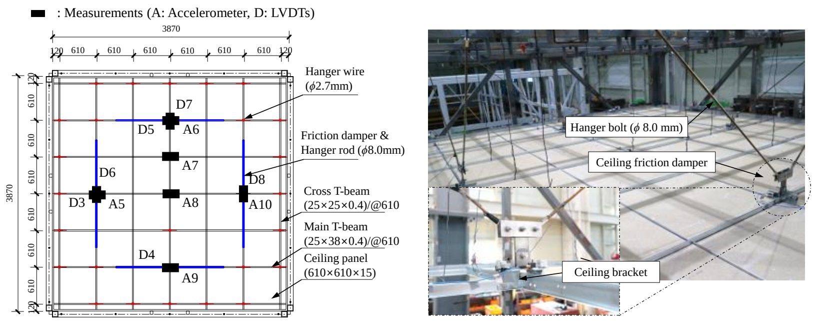

Figure 7. Specimen and measurement plan of friction-added ceiling specimen (DTL-F)

A rotational friction damper was developed and inserted into specimen DTL-F. The friction damper was detailed to be operable under suspended ceiling systems. The damper comprises one center plate, two side plates, circular friction pads made of mild steel plates, and hanger bolts (see Figure 6). When the ceiling is displaced horizontally by the seismic inertial force, the friction forces between the friction pads and the side plates dissipate seismic energy through the relative rotation between the center plate and the side plates. The maximum static friction force depends on the friction coefficient at the faying surface between the steel plates and the clamping force exerted by the center bolts. In this testing program, the clamping force was introduced by fastening the center bolt to a snug-tight condition; fully tightening by hands first, and one or two additional turns using a spud wrench. A total of 4 friction dampers (2 in each orthogonal direction) were installed, as shown in Figure 7.

2.2 TEST INPUT MOTION

Incremental-intensity shake table tests were conducted following ICC-AC 156 [2010] procedure that has been widely used for seismic performance evaluation of non-structural elements. Artificial input motions were generated to envelop the required response spectrum (RRS) specified by ICC-AC 156. The RRS was constructed by considering two parameters; the story height ratio (z/h = 1.0) and the design spectral response acceleration at short period (S_{DS} = 0.50 g), which corresponds to the highest seismic demand according to Korean seismic code (KDS 41 17 00) [AIK, 2019] (see Figure 8). For the 2-story steel frame shake-table test, the story height ratio was not applied as it will be reflected automatically through the dynamic behavior of the frame. Triaxial shake table test was performed for the specimens installed in the square test frame, and uniaxial shake table test was conducted for the test using 2-story steel frame.

3.TEST RESULTS

3.1 SEISMIC PEFORMANCE OF BRACED CEILING SPECIMEN

Despite the lateral bracing provided, approximately 20% of the ceiling panels were dislodged in specimen DTL-B under 225% RRS input (PFA = 2.00 g), and the seismic performance was comparable to that of specimen DTL, implying the ineffectiveness of ceiling lateral bracing in improving the seismic performance. The ineffectiveness was caused by the lack of diaphragm action of the tested ceiling grid. Figure 9 shows the displacement measured at grid line D4 along which the bracing is provided (restrained response), and the response measured at grid line D5 along which the bracing is not available (unrestrained response). Under 100% RRS input (PFA = 0.92 g), large displacement (20 mm) was observed at grid line D5, whereas almost no lateral displacement was observed at grid line D4, clearly indicating that the desirable rigid diaphragm action is rarely mobilized because of inherently low in-plane stiffness of direct-hung lay-in suspended ceiling systems.

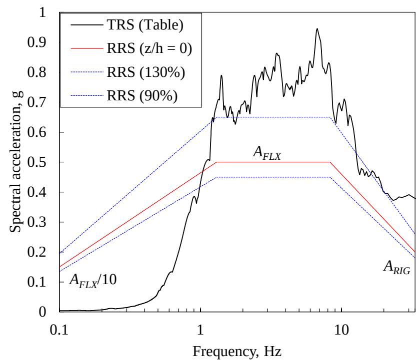

Figure 8. Comparison of RRS and TRS for 2-story steel moment frame shake-table testing

Figure 10 compares the acceleration responses measured from DTL and DTL-B. It can be observed that the unrestrained part of DTL-B was subjected to high horizontal acceleration because of the combined effect of the large displacement response and resulting pounding force. Also, due to the highly increased vertical stiffness caused by the ceiling braces, DLT-B was subjected to increased vertical acceleration, which is surely undesirable side effect.

3.1.1 Ceiling Specimen Installed with Grid Reinforcements

The ceiling specimen with both lateral bracings and grid reinforcements (DTL-FS-BS specimen) showed no damage until end of the test. By introducing grid reinforcements, the rigid diaphragm action of the ceiling grids was developed, and the lateral bracings restrained the relative movements of the ceiling grids.

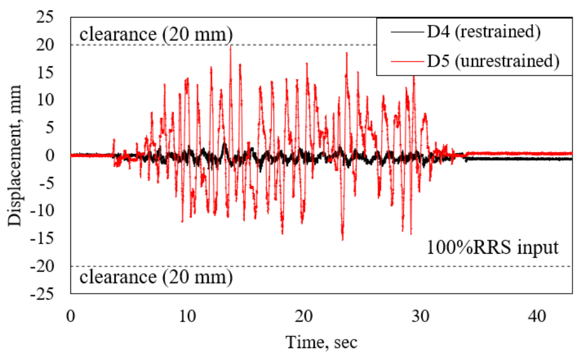

Figure 9. Comparison of displacement response between restrained (D4) and unrestrained (D5) members

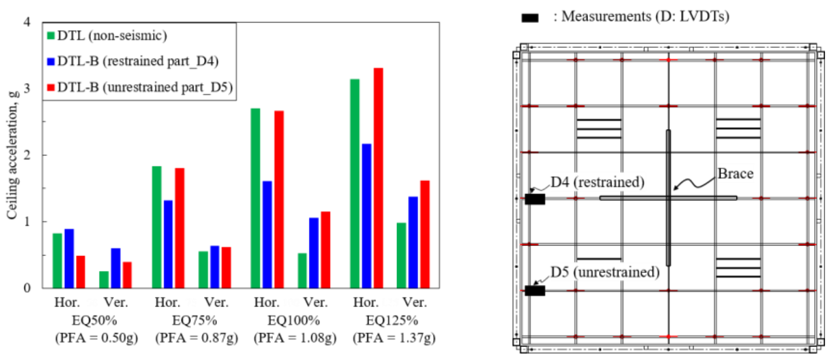

Figure 10. Comparison of measured acceleration from DTL and DTL-B specimens

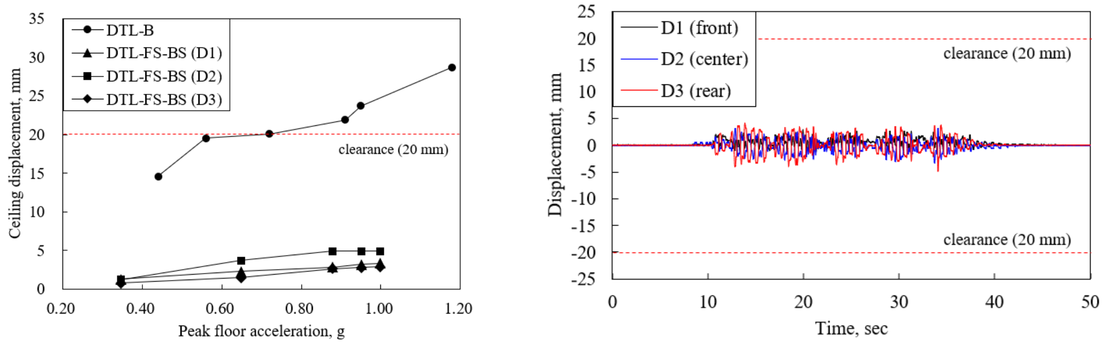

Figure 11. Effect of grid reinforcement on displacement response of DTL-FS-BS specimen

Figure 11 shows the measured displacement of DTL-FS-BS specimen where all the displacements measured in D1 (front), D2 (center), and D3 (rear) were plotted. The displacement response of DTL-B was also presented for comparison. First, it can be observed that DTL-FS-BS specimen responds as a monolithic system where almost no relative displacement within the ceiling grids was observed. The overall displacements of DTL-FS-BS tend to increase as the PFA increases, but they are much less than the clearance (20 mm) introduced at ceiling perimeters and the displacement of DTL-B specimen.

3.2 FRICTION-ADDED CEILING SPECIMEN

Specimen DTL-F showed much improved seismic performance compared to specimens DTL or DTL-B. Only minor damage at the ceiling perimeter was observed at the end of the test. By adding the friction mechanism, the acceleration and displacement response of specimen DTL-F were significantly reduced compared to other specimens (see Figure 13).

In order to assess the robustness and the operability of the proposed damper, a series of preliminary tests were implemented before the main performance evaluation test. The preliminary tests were performed using diverse input motions including sine-sweep with excitation frequency of 1 to 4 Hz, artificial and recorded ground motions. Also, the specimen was tested considering different input conditions: one-dimensional versus three-dimensional excitations.

The objective of these tests was to examine whether the proposed friction damper can develop a consistent frictional behavior regardless of input motion frequency, types of input motions and excitation dimensionality. To comprise more realistic input motions, the floor motions were obtained using the linear dynamic analysis of the SAC steel moment-resisting frame buildings (3-, 9-, and 20-story buildings) using 20 recorded ground motions. Descriptions of the three-dimensional building models and input ground

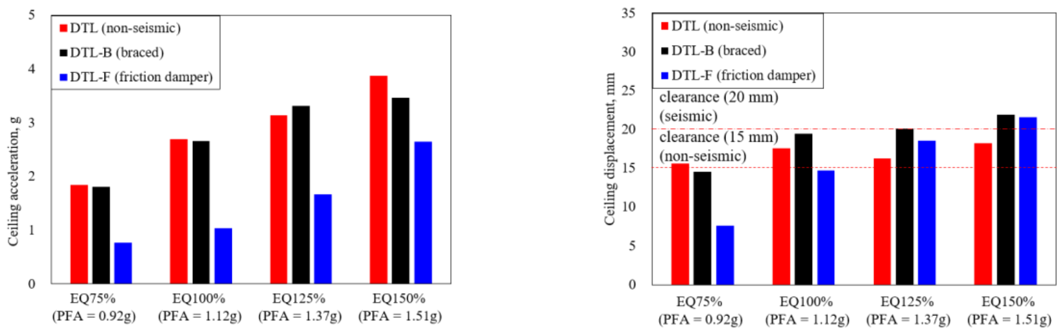

(a) Acceleration (b) Displacement

Figure 12. Reduced response of DTL-F compared to DTL & DTL-B

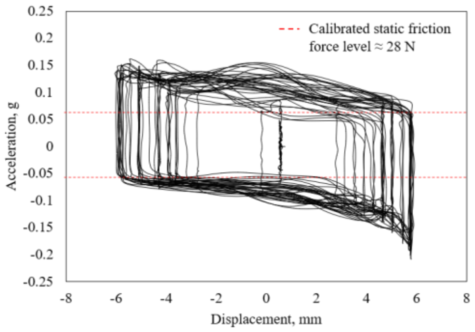

(a) Hysteresis loops measured for 1~2 Hz sinusoidal waves

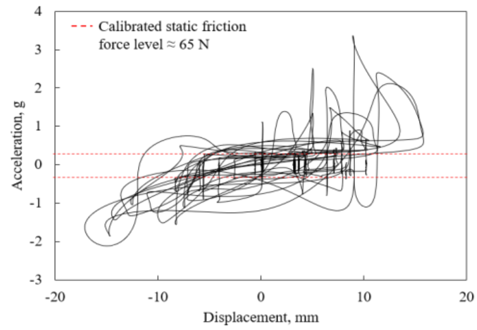

(b) Hysteresis loops measured under Imperial Valley (1979) (LA06) floor motion

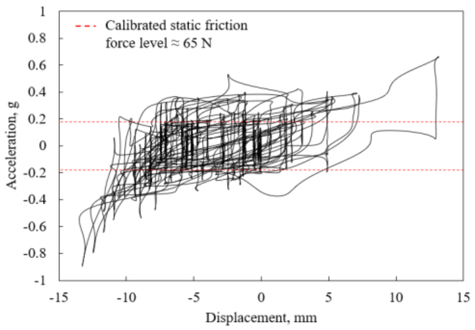

(c) Hysteresis loops measured from uniaxial excitation

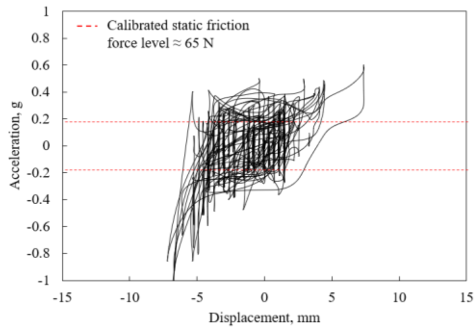

(d) Hysteresis loops measured from triaxial excitation

Figure 13. Stable hysteretic response of DTL-F specimen measured under various input motions

motions can be found in the reference paper [Gupta and Krawinkler, 1999], and detailed discussions about the obtained floor motions are omitted in this paper due to space limitations. The obtained floor motions were applied uni-directionally with their intensity arbitrarily scaled within the shake table operation limit. Test results using Imperial Valley (1979) (LA06) are presented in Figure 14(b).

Figures 14 summarizes the hysteretic responses of specimen DTL-F measured under diverse input condition. The specimen showed consistent frictional responses with stable hysteresis loops under all the input cases. Also, under both uniaxial and triaxial excitation, the damper developed comparable friction forces, demonstrating the robustness of the proposed damping mechanism regardless of the dimensionality of input motions.

3.2.1 Simplified SDOF Model for Friction-Added Ceiling System and Numerical Case Study

A simplified SDOF (single degree of freedom) model with bilinear hysteresis was also developed for the proposed friction-added ceiling system. The envelope of the hysteresis was idealized as two segments. Initial elastic stiffness before the system reaches the maximum static friction force ($F_{friction}$) is calculated based on the lateral stiffness of the damper braces (hanger bolts). The post-friction stiffness is calculated based on the pendulum theory with small deformation assumption, and the equation of motion is,

$$\ddot{\theta} + \frac{c}{m_T L}\dot{\theta} + \frac{g}{L}\theta = 0 \tag{1}$$

Thus, the post-friction stiffness is given as,

$$k_{post} = \frac{g}{L} m_T \tag{2}$$

where c = viscous damping coefficient, g = gravitational acceleration, L = pendulum length (plenum depth of ceiling system), m_T = total mass of ceiling system.

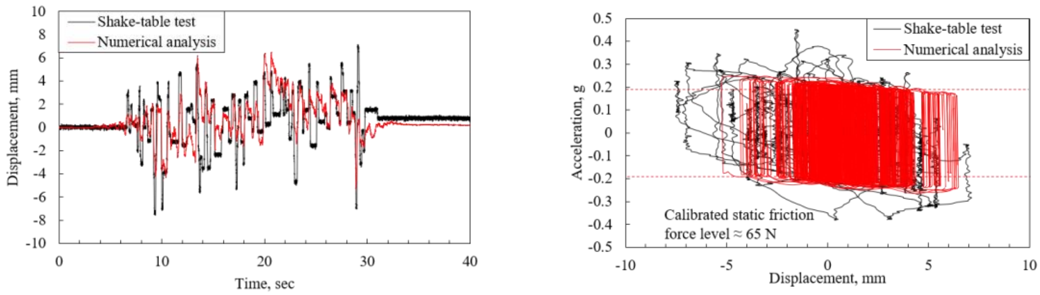

(a) Comparison of numerical and experimental results

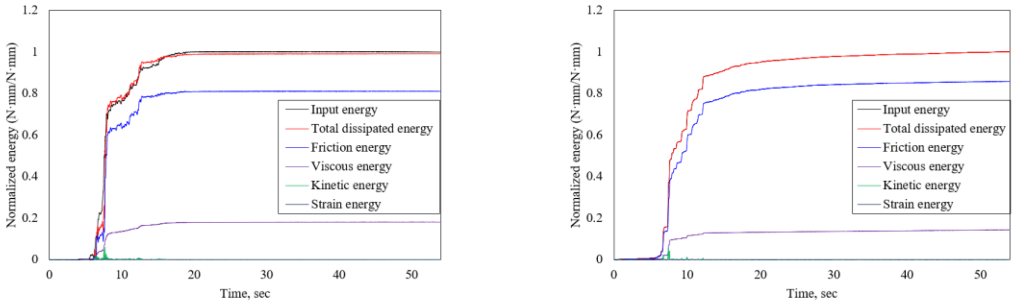

(b) Comparison energy dissipation response using experimental (left) and numerical (right) results

Figure 14. Validation of proposed SDOF model using artificial input motion (ICC-AC 156)

The maximum static friction force ($F_{friction}$) was calibrated on a trial and error basis using the measured displacement and hysteresis loops of specimen DTL-F. The maximum static friction force level identified experimentally was about 65 N, as shown in Figures 16(b). The viscous damping ratio was assumed as 1 percent considering the value reported for unbraced (non-seismic) suspended ceilings [Pourali et al. 2017].

Figures 16 shows that the proposed SDOF model well predicts the overall responses of the friction-added ceiling systems. Also, the proposed model successfully simulates energy dissipation in a close match with shake table test results. The friction-added ceiling is highly effective in dissipating the earthquake input energy, and more than 80% of the input energy was dissipated by the friction damping mechanism.

Based on the floor motions obtained from the dynamic analysis of the three-dimensional steel moment-resisting frames [Gupta and Krawinkler, 1999], extensive nonlinear time history analysis was conducted based on the proposed SDOF model. Newmark's method was implemented using MATLAB to conduct nonlinear dynamic SDOF analysis. The analyzed SDOF ceiling model had the same geometry and configuration as specimen DTL-F (plenum depth = 750 mm, W = 42.5 N/m2), and the maximum static friction force was set as 65 N.

Figure 17 compares the displacement response of friction-added ceiling and non-seismic (free-floating) ceiling systems. First, it can be observed that the displacement responses of non-seismic ceilings are excessively high because of the low critical damping ratio (ζ = 1 %) of suspended ceilings. The actual response of non-seismic ceilings would be less than the analyzed as there exists friction between the ceiling perimeter and wall moldings. However, the effects of perimeter friction were not considered as the damping caused by the perimeter friction needs further investigation to be utilized in numerical analysis.

By introducing a friction damper, the displacement of ceiling systems was much reduced compared to that of non-seismic ceiling systems. Also, it is noted that the median lateral displacement of friction-added ceiling systems is only about 65 mm, implying that it is fully feasible to avoid ceiling pounding.

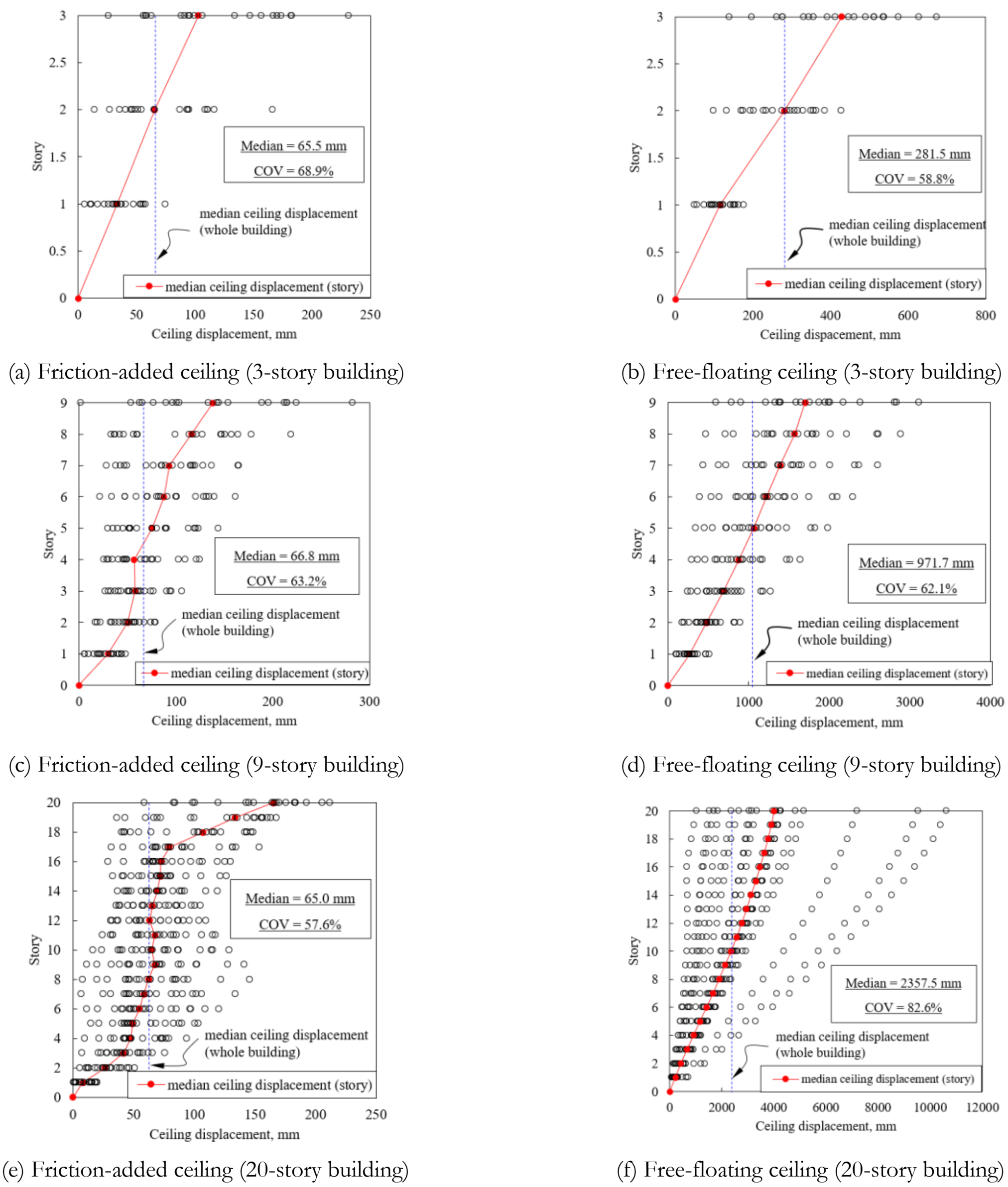

(a) Friction-added ceiling (3-story building) (b) Free-floating ceiling (3-story building)

(c) Friction-added ceiling (9-story building) (d) Free-floating ceiling (9-story building)

(e) Friction-added ceiling (20-story building) (f) Free-floating ceiling (20-story building)

Figure 15. Comparison of ceiling displacement response between friction-added and non-seismic (free-floating) ceiling systems

4.SUMMARY AND CONCLUSIONS

The results of this experimental study can be summarized as follows.

1) The braced ceiling specimen fabricated following current design practice suffered substantial damage comparable to the non-seismic ceiling specimen. The major defect of the braced specimen was the lack of desirable rigid diaphragm action in the ceiling grid caused by its low in-plane stiffness. As a result, the braced specimen was subjected to highly amplified acceleration resulting from the large unrestrained displacement response.

2) The lateral bracing combined with grid reinforcement was shown to be effective in improving the in-plane stiffness of ceiling grids, therefore enhancing the overall seismic performance. No damage was observed until the end of the shake table tests.

3) The friction-added ceiling specimen exhibited much enhanced seismic performance. Only minor damage was observed at the ceiling perimeter. With the addition of the friction mechanism, the acceleration and displacement responses were significantly reduced compared to other specimens.

4) The robustness and the operability of the proposed friction damper were demonstrated using various input motions and excitation conditions. The proposed damper showed consistent frictional behavior with stable hysteretic responses regardless of input motion characteristics and excitation dimensionality.

5) A simplified SDOF model with bilinear hysteresis was developed for the friction-added ceiling system. The proposed SDOF model well predicted the measured acceleration and energy responses. The numerical case study based on the proposed nonlinear SDOF model demonstrated that the displacement of ceiling systems equipped with the proposed friction damper could be suppressed to a level such that ceiling pounding is effectively avoided.

ACKNOWLEDGEMENT

This research was supported by a grant (21AUDP-C146352-04) from Architecture & Urban Development Research Program funded by Ministry of Land, Infrastructure and Transport of Korean government.

REFERENCES

ASTM E580-E80/ASTM-E580M-17 [2017] *Standard Practice for Installation of Ceiling Suspension Systems for Accoutstical Tile and Lay-In Panels in Area Subjected to Earthquake Ground Motions*, West Conshohocken, PA, ASTM International.

ASCE/SEI, 7-16 [2017] *Minimum Design Loads and Associated Criteria for Buildings and Other Structures*, Reston, VA: American Society of Civil Engineering.

Gilani A.S., Glasgow B., Ingratta T. [2008] "Seismic performance of directly hung suspended ceilings with engineered perimeter product," *Proceedings of 14th World Conference on Earthquake Engineering*, Bejing, China.

Huang W.C., Hussainzada N., McClure G. [2013] "Experimental study on the seismic behaviour of suspended ceilings," *Proceedings of the 3rd Specialty Conference on Disaster Prevention and Mitigation.*

Soroushian S., Maragakis E.M., Ryan K.L, Sasaki T., Okazaki T., Mosqueda G. [2016] "Seismic simulation of an integrated ceiling-partition wall-piping system at E-Defense. II: Evaluation of non-structural damage and fragilities," *Journal of Structural Engineering*, Vol. 142, No.2.

Ryu K.P., Reinhorn A.M. [2019] "Experimental study of large area suspended ceilings," *Journal of Earthquake Engineering*, Vol. 23, No. 6, pp. 1001-1032.

ICC [2010] *AC 156 Acceptance Criteria for Seismic Certification by Shake-Table Testing of Non-Structural Components*, International Code Council Evaluation Service, Whittier, CA.

AIK [2019] "Seismic Building Design Code, KDS 41 17 00," Seoul, Korea: Architectural Institue of Korea (in Korean).

Pourali A., Dhakal R.P., MacRae G., Tasligedik A.S. [2015] "Shake table tests of perimeter-fixed type suspended ceilings," Proceeding of the New Zealand Society for Earthquake Engineering Conference, Rotorua.

Pourali A. [2017] "Seismic performance of suspended ceilings," Doctoral dissertation, University of Canterbury, http://dx.doi.org/10.26021/21844.

Pourali A., Dhakal R.P., MacRae G., Tasligedik A.S. [2017] "Fully floating suspended ceiling system: Experimental evaluation of structural feasibility and challenges," Earthquake Spectra, Vol. 33, No.4, pp. 1627-1654.

Pourali A., Dhakal R.P., Tasligedik A.S., MacRae, G. [2018] "Experimental evaluation of the seismic compatibility between low-damage drywall partitions and suspended ceilings," 11th US National Conference on Earthquake Engineering, Los Angeles, Paper No. 1731.

Gupta A., Krawinkler H. [1999] "Seismic demands for performance evaluation of steel moment resisting frame structures," *Report No. 132*. Department of Civil and Environmental Engineering, Stanford University, USA.

Seismic Response of a Braceless Seismic Restraint System for Suspended Nonstructural Elements

Bryan Chalarca[1], André Filiatrault[1], Daniele Perrone[2] and Roberto Nascimbene[1]

[1] University School for Advanced Studies IUSS Pavia
Palazzo del Broletto, Piazza della Vittoria 15, Pavia, Italy
{bryan.chalarca,andre.filiatrault,roberto.nascimbene}@iusspavia.it
[2] University of Salento
Centro Ecotekne Pal. O - S.P. 6, Lecce, Italy
daniele.perrone@unisalento.it

Abstract. Nonstructural elements present a high seismic vulnerability due to their susceptibility to exhibit damage under low seismic intensities. Even though a supporting structure remains unaffected by seismic actions, nonstructural damage can generate large economic losses, loss of functionality, and loss of operability. Similar to structural systems, nonstructural elements can be equipped with seismic protection systems to either reduce their seismic demand or improve their seismic performance. This study explores numerically the implementation of a braceless seismic restraint for suspended nonstructural elements. The proposed system is composed of a vertical hanger connected to a rotational hysteretic damper that provides supplemental damping in the direction of interest to control the seismic response of the suspended nonstructural element without the need for sway braces. A three-dimensional suspended piping system, located on the top floor of a nine-story steel moment-resisting framed building, is considered as case study, including pipes running in both transverse and longitudinal directions. Nonlinear time-history analyses were conducted using the equivalent floor motions obtained from the FEMA P-695 far-field ground motion set. The peak displacements and residual displacements were used to compare the seismic response of the proposed braceless seismic restraint with that of a conventional braced channel trapeze restraint installation. The numerical results indicate that the proposed braceless seismic restraint exhibited smaller median peak displacements compared to those of the conventional braced channel trapeze. Additionally, due to the concentration of the inelastic response in the rotational hysteretic damper, the proposed braceless seismic restraint exhibited comparable residual deformations and smaller, if any, induced damage compared to the conventional braced channel trapeze.

Keywords: Supplemental damping, nonstructural elements, suspended piping system, seismic restraints, hysteretic damper.

1. INTRODUCTION

The seismic performance of nonstructural elements has become a crucial factor of the overall seismic performance assessment of a building. Although recent seismic events have demonstrated that current building codes provide sufficient protection against undesired structural failures or collapse, nonstructural elements continue to represent a significant source of economic losses and limited operativity and occupancy [Miranda *et al.*, 2012; Bevere *et al.*, 2019] due to their high investment cost and seismic vulnerability [Miranda and Taghavi, 2003]. Moreover, the failure of nonstructural elements during seismic events can lead to life safety threats due to the inherent danger of their damage, by blocking evacuation routes, or losing functionality against secondary hazards (*i.e.*, damage to fire protection systems).

Nonstructural elements can be classified based on their vulnerability to seismic actions as acceleration-sensitive, velocity-sensitive, and displacement-sensitive [FEMA, 2018]. Suspended nonstructural elements are classified as acceleration-sensitive nonstructural elements; they are characterized by being suspended from the slabs of the supporting structure (see Figure 1). Vertical hangers, usually steel rods or channel trapezes, carry the gravity loads while diagonal supports, such as sway bracing or braced trapezes, resist the lateral loads. The seismic design of this typology of nonstructural elements is conducted by computing the maximum tributary weight a single support can resist so that a computed shear force based on the elastic properties of the system is not exceeded. However, the current practice (*e.g.*, ASCE 7-16 [2017]) does not require checking the expected inelastic displacements, allowing excessive residual deformations or damage in the support elements. In addition, complex layouts of suspended nonstructural elements (*e.g.*, piping systems, cable trays, *etc.*) could require many anchoring points for gravity and seismic supports, making it difficult to find an efficient distribution of the supporting elements.

Figure 1 Example of suspended nonstructural elements.

This paper explores the implementation of a braceless seismic restraint system for suspended nonstructural elements. The proposed system aims to improve the seismic performance of suspended nonstructural elements by reducing seismic-induced damage and residual deformations on the supporting elements. Moreover, the proposed system requires fewer anchoring points and fewer clearances compared to traditional lateral restraints. The appraisal of the braceless restraint system was carried out numerically by comparing the seismic response of a three-dimensional (3D) suspended piping supported by a conventional braced channel trapeze with that of the proposed braceless restraint system. Both restraint systems were designed following a displacement-based design procedure that allows finding the total number of lateral restraints required by the piping layout to avoid exceeding a target lateral displacement relative to the supporting structure. Finally, the case study piping system was subjected to a set of floor motion records that correspond to the design intensity level. The seismic assessment was carried out by comparing the median peak displacements and median residual displacements along the piping system.

2. SEISMIC DESIGN OF SUSPENDED PIPING SYSTEMS

Suspended piping systems are composed of a piping layout and their respective gravity supports and lateral restraints. They are used to carry gasses, sewage, potable water, and along with sprinklers, compose fire protection systems. The seismic design of suspended piping systems is conducted by applying traditional force-based design procedures based on elastic models and computed shear forces (*e.g.*, ASCE 7-16 [2017]) or by controlling the maximum displacement (*i.e.*, both horizontal and vertical) induced by the dynamic reaction of the piping system to the movement of the supporting structure, avoiding thus excessive deformation of the piping joints or harmful interaction with the supporting structure or surrounding nonstructural elements [Merino *et al.* 2021]. The seismic-induced displacement on the piping systems is controlled by adding lateral restraints, such as braced channel trapezes or sway bracing, which increase the lateral stiffness of the piping system. However, a large flexibility difference between the lateral restraint and the piping lines can lead to local dynamic amplification of the seismic response of the piping [Tatarsky and Filiatrault, 2019]. The proposed braceless seismic restraint reduces this problem by adding supplemental damping instead of increasing the lateral stiffness to control the maximum response of the piping system.

2.1 CONVENTIONAL BRACED CHANNEL TRAPEZE

Braced channel trapezes are a common seismic restraint for suspended piping systems. Two main layouts are used based on the considered direction of the restraint: transverse and longitudinal braced channel trapezes [Perrone *et al.*, 2020a, 2020b]. Both layouts are composed of two vertical and one horizontal steel channels to which the piping lines are attached. The pipes are secured to the horizontal channel by pipe rings. The bracing is typically composed of a single steel channel for the transverse braced trapeze and a pair of steel channels for the longitudinal braced trapeze and are usually inclined at an angle of 45° from the vertical. The section dimensions depend on the application and the applied load with channel depths varying from 21 to 120 mm [Perrone *et al.*, 2020a, 2020b]. Figure 2 illustrates typical braced channel trapezes.

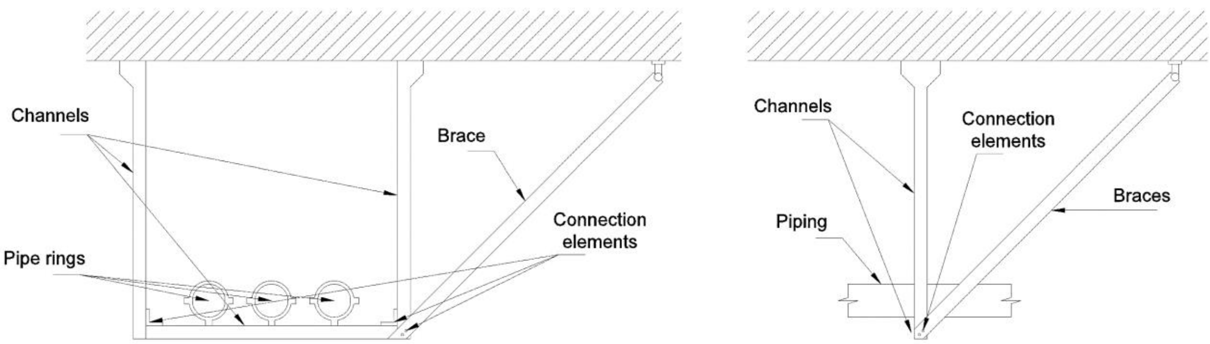

Figure 2 Illustration of typical transverse (left) and longitudinal (right) braced channel trapezes.

Perrone *et al.* [2020a, 2020b] and Merino *et al.* [2021] studied the static inelastic response of braced channel trapezes, finding an asymmetrical response characterized by a strong pinching of the hysteresis loop. The longitudinal braced channel trapeze exhibits a larger strength compared to the transverse braced channel trapeze due to the extra bracing element. The yielding of the connection elements between the different channels is the main source of the inelastic response of the restraint systems. Figure 3 shows typical hysteresis loops of both braced channel trapezes.

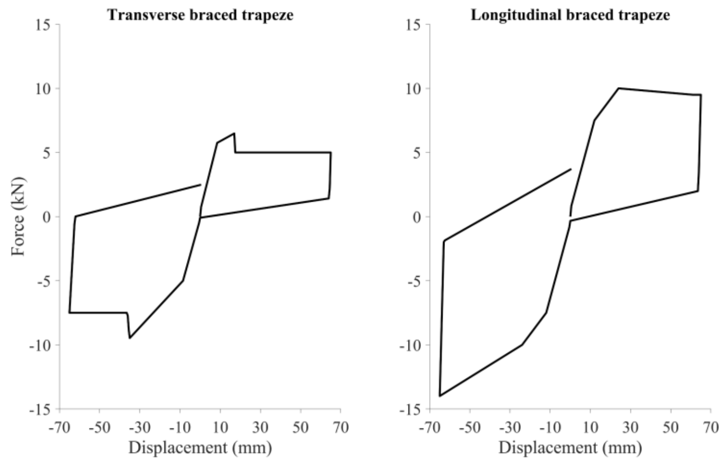

Figure 3 Typical hysteresis loops of braced channel trapezes [Merino *et al.*, 2021].

2.2 BRACELESS SEISMIC RESTRAINT

Figure 4(a) shows the conceptual model of the proposed braceless seismic restraint for suspended piping systems that increases the energy dissipation capacity of the system through the addition of supplemental damping. In addition, the proposed system allows reducing residual deformations and induced damage to the restraint system since the inelastic response of the supporting element is merely generated by the damper element. Another important characteristic of the proposed system is the absence of bracing elements that allows better architectural integration of the suspended piping systems by reducing the area required for restraint installation. Conceptually, the proposed braceless seismic restraint resembles a pendulum composed of one vertical hanger connected to a rotational spring at its upper end that behaves as a hysteretic damper and controls the maximum force and energy dissipation of the system. The hysteretic damper is attached to the supporting structure simulating a pin connection, allowing rotation around the out-of-plane direction with respect to the damper rotation so that the proposed seismic restraint can be used as a transverse or longitudinal restraint. The piping is attached to pipe rings fixed to a horizontal element that connects to the vertical hangers at its bottom end. The inelastic behavior of the rotational hysteretic damper is characterized by an elastic-perfectly-plastic hysteresis loop. This element can be designed to avoid excessive wear or damage during strong seismic events while providing significant supplemental damping. Figure 4(b) shows the idealized hysteresis loop of the rotational hysteretic damper.

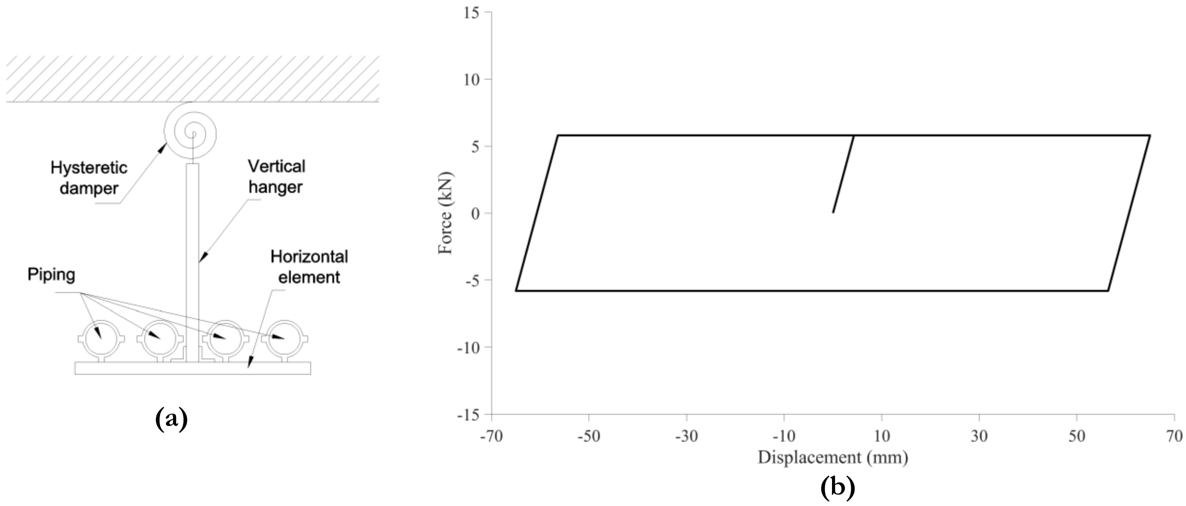

Figure 4 (a) illustration of the proposed braceless seismic restraint and (b) example of the hysteresis loop of the hysteretic damper.

3. NUMERICAL CASE STUDY

3.1 CASE STUDY SUSPENDED PIPING SYSTEM

A 3D case study suspended piping system equipped with the proposed braceless seismic restraints as well as with conventional braced channel trapezes was considered for comparing their seismic responses. The case study piping system was assumed to be part of a suspended water supply system on the top floor of a nine-story building with a drop height of 800 mm. It is composed of three pipelines: cold-water distribution, hot-water distribution, and hot-water recirculation. As shown in Figure 5, the piping layout is composed of one main feed line of 18 m length (Pipe 1) connected to a perpendicular 36 m length cross line (Pipe 2). The unit weight of each water-filled pipe is equal to 0.31 kN/m. The vertical piping (riser) connected to the case study suspended piping system was neglected for simplicity. All pipes are assumed to be made of black standard steel with a diameter of 127 mm (5 in) and a wall thickness of 6.5 mm. All piping connections (*e.g.*, elbows, longitudinal splices, *etc.*) were assumed rigidly welded. More information on the case study piping layout is provided by Filiatrault *et al.* [2018].

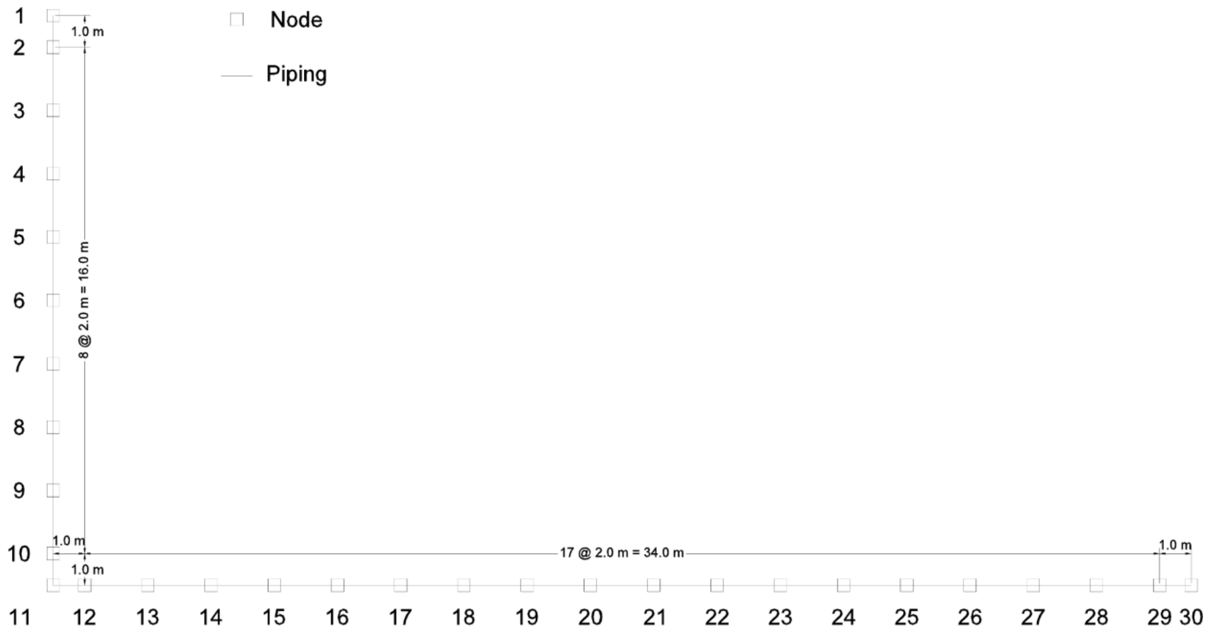

Figure 5 Case study piping layout.

3.2 BUILDING AND FLOOR MOTION RECORDS

The supporting structure was assumed to be a nine-story steel moment-resisting framed building adapted from the FEMA 440 document [2005]. The structural system is composed of five bays in both directions, and it is characterized by a fundamental period equal to 1.89 s. Figure 6 illustrates the supporting building. The supporting building was modeled using the software OpenSees 3.2.2 [McKenna *et al.*, 2010]. Further details on the supporting building and modeling assumptions are reported in Chalarca *et al.* (2020). The supporting building was subjected to nonlinear time-history analysis using the FEMA P-695 [2009] far-field ground motion set. This ground motion set is composed of 22 pairs of horizontal ground motion records that represent the seismicity of the western United States. The records were scaled based on the median spectral acceleration at a period of one second matching the ASCE 7-16 [2017] design spectrum for the city of Los Angeles (US) with a soil type D_{max}. The absolute acceleration time-histories of the top floor were registered for each individual ground motion. This floor motion set was used as the input seismic load for the nonlinear time-history analyses of the case study suspended piping system. Figure 7 shows the 5% damped ground acceleration spectra of the FEMA P-695 far-field ground motion set, the resulting 5% damped top floor absolute acceleration spectra, and top floor relative displacement spectra.

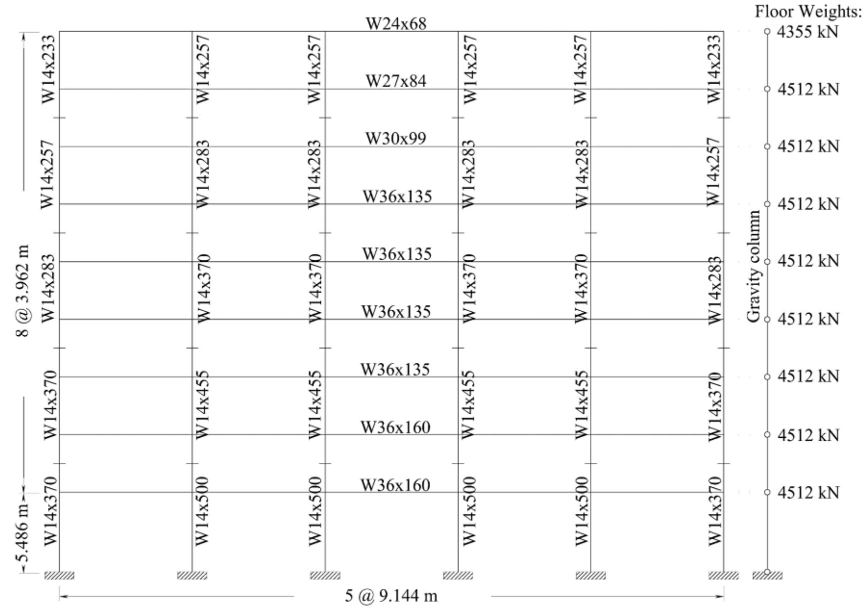

Figure 6 Nine-story supporting building.

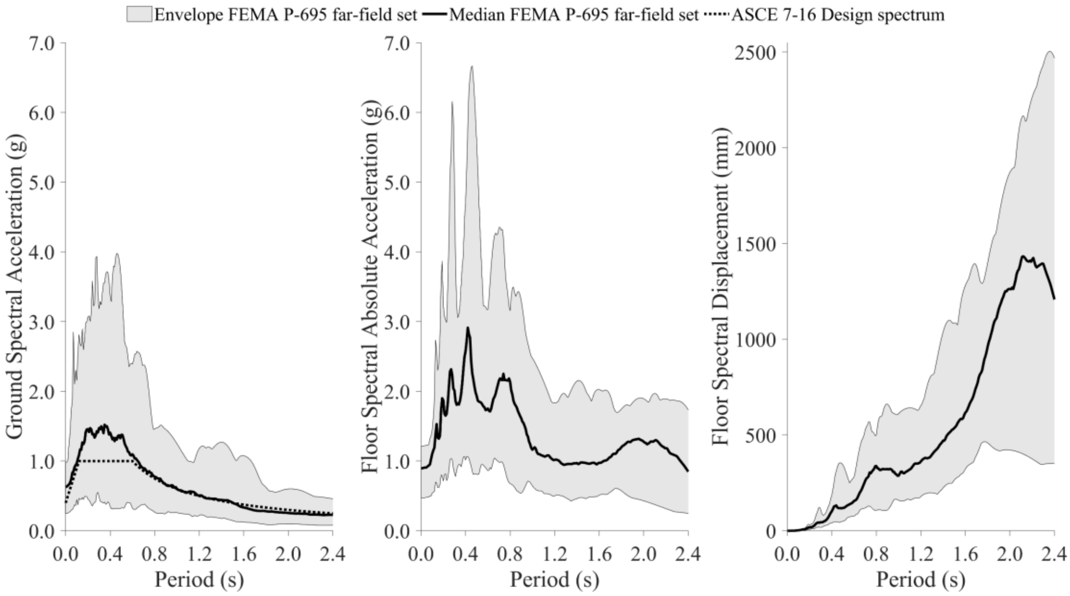

Figure 7 (left) 5% damped ground spectral acceleration of the FEMA P-695 far-field ground motion set, (center) 5% damped top floor absolute spectral acceleration, and (right) 5% damped top floor spectral relative displacement spectra.

3.3 DESIGN OF THE SEISMIC RESTRAINT SYSTEMS

A modified displacement-based design (DBD) procedure for nonstructural elements based on that proposed by Filiatrault *et al.* [2018] was implemented to design both seismic restraints used on the case study suspended piping system. This procedure models each transverse or longitudinal restraint as an elastic SDoF system characterized by an equivalent secant stiffness, secant period, and equivalent viscous damping computed from the nonlinear response of the restraint system at a given target displacement, allowing the calculation of a tributary seismic mass for an individual restraint and therefore, the total number of seismic restraints needed for the suspended piping system can be computed. Considering the recommendation of the New Zealand Standard NZS 4219:2009 [2009], a target displacement of 50 mm was selected as the maximum allowable displacement under the design earthquake to avoid contact with neighboring nonstructural and/or structural elements. The top floor motions obtained from the supporting building analyses were used to conduct the seismic design of the case study suspended piping system. The design procedure for a given seismic restraint system can be summarized as follows:

1. Define the target displacement (*i.e.*, 50 mm for this study).
2. Calculate the equivalent damping of the restraint system (ξ_{eq}) at the target displacement. Merino *et al.* [2021] suggested the following equations for the equivalent damping of the transverse and longitudinal braced channel trapezes, respectively:

$$\xi_{eq} = \frac{1.5}{\pi}\left(1 - \frac{0.0025}{\theta_{tg}}\right)^{7.5} \quad (1)$$

$$\xi_{eq} = \frac{1.6}{\pi}\left(1 - \frac{0.0025}{\theta_{tg}}\right)^{14} \quad (2)$$

where θ_{tg} is the drift of the braced channel trapeze, defined as the lateral displacement of the trapeze (*i.e.*, the target displacement) divided by the drop height of the trapeze (vertical distance from the ceiling to the horizontal channel). On the other hand, the equivalent damping of the braceless seismic restraint was calculated using the classic equivalent viscous damping proposed by Jacobsen [1930] given by:

$$\xi_{eq} = \frac{1}{4\pi}\frac{E_{vd}}{E_{es}} \quad (3)$$

where E_{vd} is the energy dissipated in one cycle of the hysteresis loop, and E_{es} is the recoverable elastic strain energy of the system.

3. Compute the equivalent period (T_{eq}) using the target displacement from the floor displacement spectrum (see Figure 7) calculated for the computed equivalent damping (see Equations 1 to 3).
4. Calculate the equivalent stiffness (k_{eq}) using the target displacement and the backbone curve of the hysteresis models of a given restraint system (see Figures 3 and 4(b)).
5. Compute the tributary seismic mass based on the equivalent period and equivalent stiffness of a single restraint element of a given restraint system.
6. Calculate the number of seismic restraints for each direction (*i.e.*, transverse and longitudinal) for each piping line (*i.e.*, Pipe 1 and Pipe 2) by dividing the total mass by the computed tributary seismic mass.
7. Distributed the seismic restraints along the piping line length.

The braced channel trapezes used in this study were characterized by a channel size equal to 41 mm, a drop height of 800 mm, and a length of the horizontal channel equal to 800 mm. Table 1 lists the properties obtained from the seismic design of the braced channel trapezes. On the other hand, the braceless seismic restraint used in this study was composed of one vertical hanger characterized by a pipe 2.5 xx-strong with a length equal to 800 mm, section modulus equal to 31791 mm^3, yield strength of 0.21 kN/mm^2, and elastic modulus equal to 200 kN/mm^2. To avoid yielding of the vertical hanger, the hysteretic damper was designed with an equivalent activation force equal to 70% of the flexural yielding capacity of the vertical hangers (*i.e.*, 5.8 kN) and an initial stiffness equal to 1.4 kN/mm. Table 1 lists also the properties obtained from the seismic design of the braceless seismic restraint. The number of seismic restraints for each piping line was computed by dividing its total weight by the tributary seismic weight of each system. Based on this modified DBD approach, Pipe 1 requires four transverse and two longitudinal braced channel trapezes, and Pipe 2 requires seven transverse and four longitudinal braced channel trapezes, respectively. In the case of the braceless seismic restraint, Pipe 1 requires three supports for each direction, while Pipe 2 requires five supports for each direction. Figure 8 shows the distribution layout of the braced channel trapezes and braceless seismic restraints for the case study suspended piping system.

Table 1 Properties obtained from the seismic design of the lateral restraint systems.

Seismic restraint system	Target displacement (mm)	Equivalent damping (%)	Equivalent period (s)	Equivalent stiffness (kN/mm)	Seismic weight (kN)
Transverse braced channel trapeze	50	35.1	0.452	0.125	6.35
Longitudinal braced channel trapeze	50	28.8	0.422	0.221	9.80
Braceless seismic restraint	50	58.2	0.535	0.116	8.25

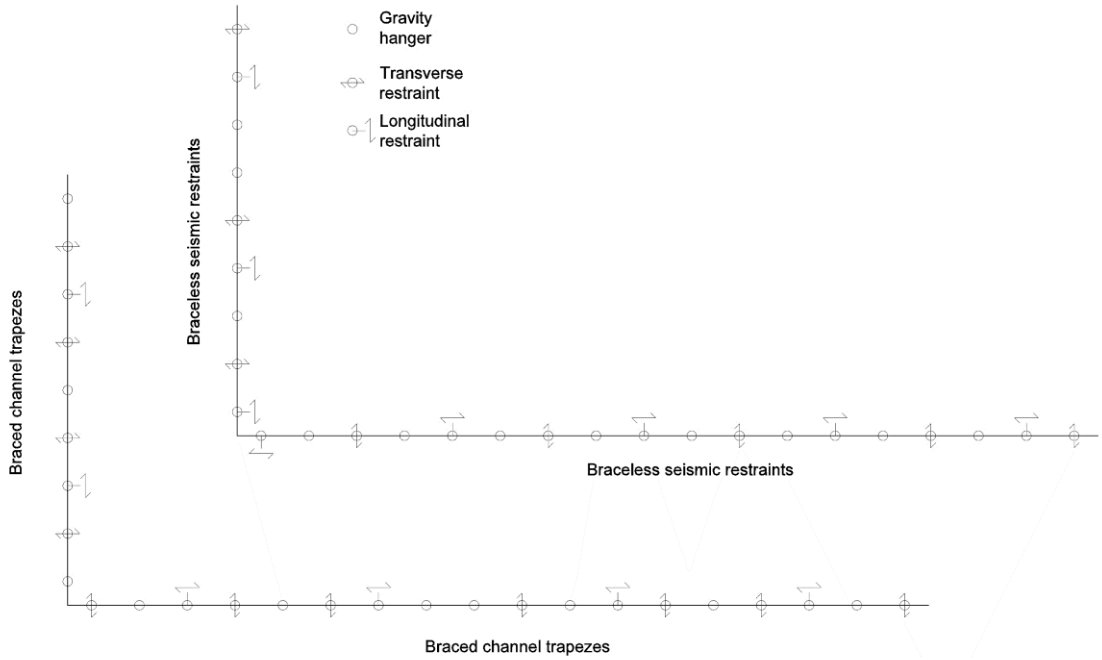

Figure 8 Braced channel trapeze and braceless seismic restraint layouts for the case study suspended piping.

4. SEISMIC ASSESSMENT

The seismic performance of the case study suspended piping system was assessed by comparing the median peak displacements and the residual displacement in both horizontal directions (*i.e.*, transverse and longitudinal) at several locations along the piping line (see Nodes in Figure 5). Both restraint systems, designed in the previous section, were modeled using the software OpenSees 3.2.2 [McKenna *et al.*, 2010] and subjected to nonlinear time-history analysis using the floor motions described in Section 3.2. Each braced channel trapeze, along each transverse and longitudinal direction, was modeled by a shear spring element characterized by the properties proposed by Merino *et al.* [2021]. The braceless seismic restraint was modeled using a rotational spring for the damper and an elastic beam-column element for the vertical hanger. The piping was attached at the end of the vertical hangers simulating a pin connection. For both seismic restraint systems, the gravity hangers were modeled as elastic beam-column elements with idealized pin connections at both ends. Finally, the piping lines were modeled with beam-column elements with fixed connections between pipes [Blasi *et al.*, 2021]. The equivalent seismic masses were assigned to each node while the gravity loads were uniformly distributed along the pipelines. Figure 9 shows the median peak positive and negative displacements of both restraint systems. Furthermore, Figures 10 and 11 shows the envelope and median ± one standard deviation of the peak absolute displacements and residual displacements for both seismic restraint systems in the transverse and longitudinal directions, respectively. The numerical results show that both seismic restraint systems exhibited median peak values below the target displacement of 50 mm at the design intensity level. However, the proposed braceless system showed smaller median peak displacements than those of the braced channel trapezes. In addition, the braceless seismic restraint exhibited a smaller dispersion of the peak displacements in both directions, exceeding in fewer cases the target displacement compared to the braced channel trapezes. Moreover, the layout and properties of the braceless seismic restraints can be further optimized to reduce local displacements. Regarding residual displacements, both restraint systems exhibited similar median residual displacements and dispersion values. However, the distribution of the residual displacements tended to be more uniform on the braced channel trapezes than on the braceless seismic restraints. It is important to highlight that the residual deformation exhibited by the braced channel trapezes was generated by the inelastic response of the system, hence, by induced damage to the support elements. On the other hand, the residual displacement on the proposed braceless seismic restraint was not caused by induced damage to the support elements but by the lack of sufficient recentering force to restore the piping to its initial position. They can be easily restored to their original position by releasing the damper's activation force or applying recentering forces.

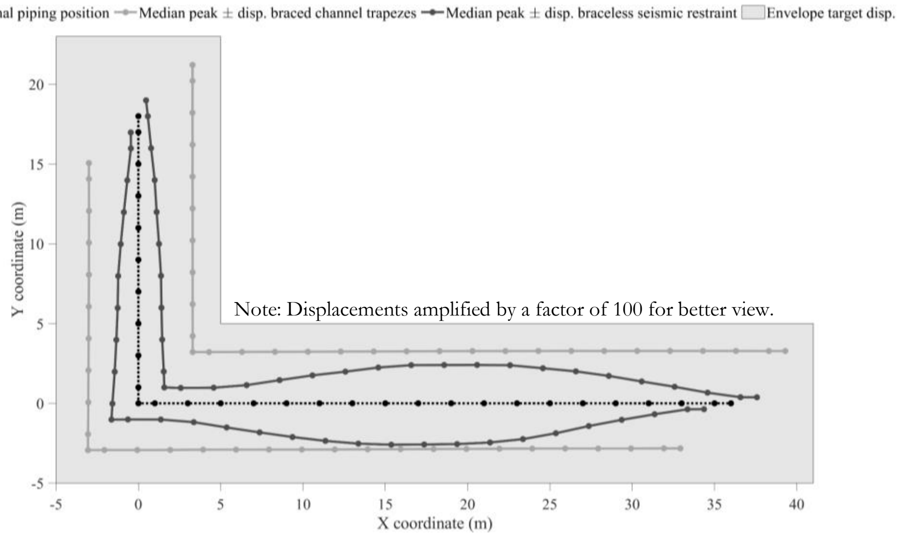

Figure 9 Median peak displacements of both seismic restraint systems.

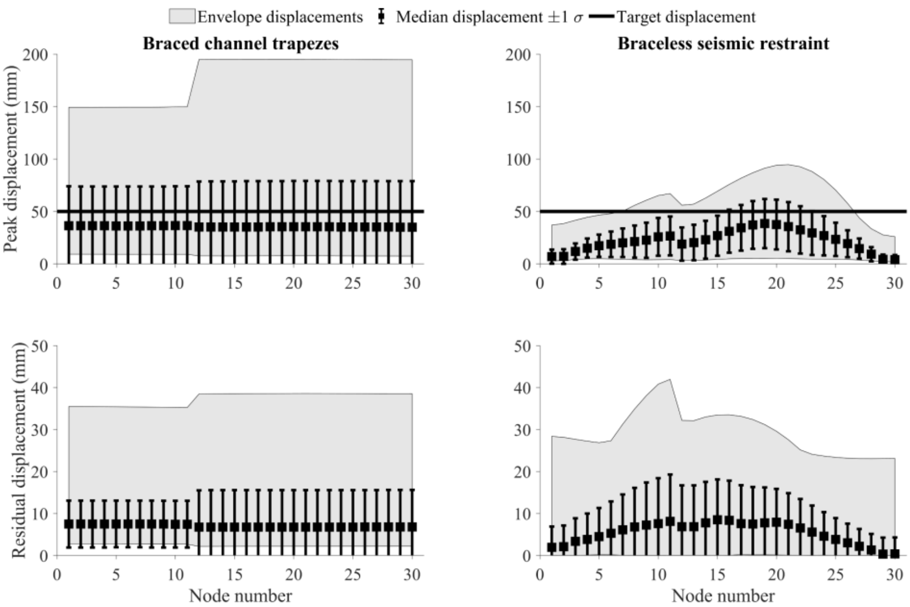

Figure 10 Peak displacements and residual displacements of both restraint systems in the transverse direction.

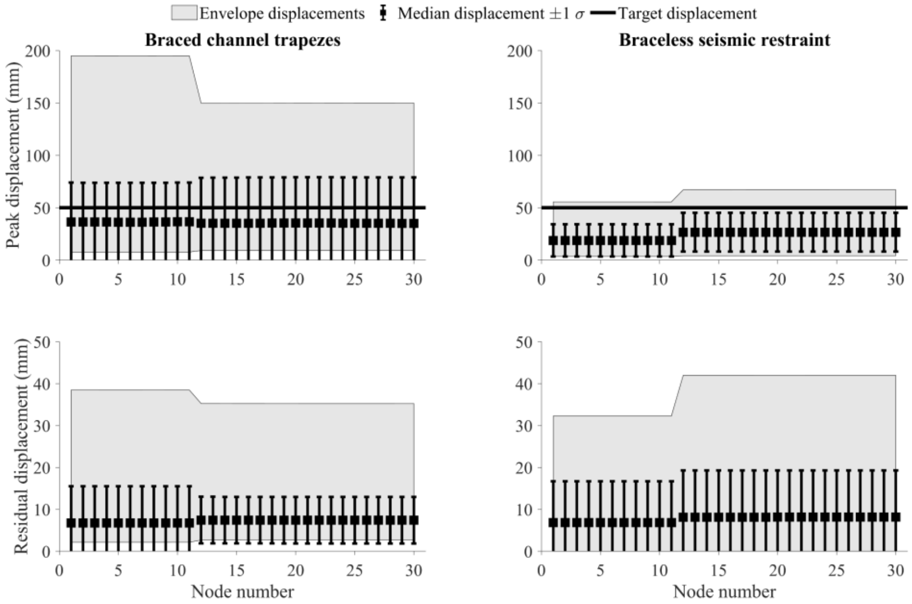

Figure 11 Peak displacements and residual displacements of both restraint systems in the longitudinal direction.

5. CONCLUSIONS

Due to the importance of suspended nonstructural elements on the overall seismic performance of a building, it is necessary to develop seismic restraints that provide sufficient lateral constraint and reduce the induced damage due to the inelastic response of the supporting elements considering the limited clearances available. To address this issue, this study explored the concept of a braceless seismic restraint system that adds supplemental damping to the restraint elements instead of increasing their lateral strength. The proposed system is composed of a rotational hysteretic damper connected to a vertical hanger that provides support to the piping lines. Due to its pendulum-like behavior, the system does not require bracing, reducing the clearances necessary for installation. To assess the performance of the proposed braceless seismic restraint, a case study suspended piping system was assumed to be located on the top floor of a nine-story steel moment-resisting framed building. The case study suspended piping system was designed using conventional braced channel trapezes and the proposed braceless seismic restraints. Nonlinear time-history analyses were conducted using the top floor motions of the supporting building subjected to the FEMA P-695 far-field ground motion set. The performance comparison of both restraint systems was based on the median peak displacements and median residual displacements in the transversal and longitudinal directions measured at several locations along the piping line. The results show that both seismic restraint systems fulfilled the design criterium, exhibiting median peak displacements below the target design displacement. However, the proposed braceless seismic restraint generated median peak displacements smaller than those of the braced channel trapezes. Moreover, the proposed system also had a smaller dispersion in the results. Additionally, both systems showed similar median residual displacements. Nevertheless, the residual displacement represents induced damage in the braced channel trapezes due to inelastic response while for the braceless seismic restraint, the residual displacement represents insufficient recentering force to restore the piping lines to their initial positions.

ACKNOWLEDGMENTS

The authors gratefully acknowledge the funding by the Italian Ministry of Education, University, and Research (PON Grant n.1735/2017, CADS Project) in support of this study.

REFERENCES

ASCE. [2017] *Minimum design loads and associate criteria for buildings and other structures ASCE/SEI 7-16*, American Society of Civil Engineers. United States.

Bevere, L., Ewald, M., Wunderlich, S. [2019] *A decade of major earthquakes: lessons for business*, Swiss Re Institute, Zurich, Switzerland.

Blasi, G., Perrone, D., Aiello, M.A., Pecce, M.R. [2021] "Seismic performance assessment of piping systems in bare and infilled RC buildings," Soil Dynamics and Earthquake *Engineering*, Vol 149, No. 1.

Chalarca, B., Filiatrault, A., Perrone, D. [2020] "Seismic demand on acceleration-sensitive nonstructural components in viscously damped braced frames," *ASCE Journal of Structural Engineering*, Vol 146, No. 9.

FEMA. [2005] *Improvement of Nonlinear Static Seismic Analysis Procedures FEMA 440*, Federal Emergency Management Agency. United States.

FEMA. [2009] *Quantification of building seismic performance factors FEMA P-695*, Federal Emergency Management Agency. United States.

FEMA. [2018] *Seismic Performance Assessment of Buildings FEMA P-58*, Federal Emergency Management Agency. United States.

Filiatrault, A., Perrone, D., Merino, R., Calvi, G.M. [2018] "Performance-Based Seismic Design of Nonstructural Building Elements," *Journal of Earthquake Engineering*, Vol 25, No. 2.

Jacobsen, L.S. [1930] "Steady Forced Vibrations as Influenced by Damping," *ASME Transactions American Society of Mechanical Engineers*, Vol 52, No. 1.

McKenna, F., Scoot, M., Fenves, G. [2010] "Nonlinear finite element analysis software architecture using object composition," *Journal of Computing in Civil Engineering*, Vol 24, No. 1.

Merino, R., Perrone, D., Filiatrault, A. [2021] "Calibrated equivalent viscous damping for direct displacement-based seismic design of suspended piping trapeze restraint installations," *Journal of Earthquake Engineering*, DOI: 10.1080/13632469.2021.1987357.

Miranda, E., Mosqueda, G., Retamales, R., Pekcan. G. [2012] "Performance of nonstructural components during the 27 February 2010 Chile Earthquake," *Earthquake Spectra*; Vol. 28, No. 1.

Miranda, E., Taghavi, S. [2003] "Estimation of seismic demands on acceleration-sensitive non-structural components in critical facilities," *Proceedings of the ATC-29-2 Seminar on Seismic Design*, Newport Beach, United States.

Standards Council. [2009] *Seismic performance of engineering systems in buildings NZS 4219:2009*, Standards Council, New Zealand.

Perrone, D., Filiatrault, A., Peloso, S., Brunesi, E., Beiter, C., Piccinin, R. [2020a] "Experimental seismic response evaluation of suspended piping restraint installations," *Bulletin of Earthquake Engineering*; Vol. 18, No. 1.

Perrone, D., Brunesi, E., Filiatrault, A., Peloso, S., Nascimbene, R., Beiter, C., Piccinin, R. [2020b] "Seismic numerical modelling of suspended piping trapeze restraint installations based on component testing," *Bulletin of Earthquake Engineering*; Vol. 18, No. 1.

Tatarsky, M., Filiatrault, A. [2019] "Seismic response of viscously damped braced thin-wall piping system: a proof-of-concept case study," *Bulletin of Earthquake Engineering*; Vol. 17, No. 1.

Non-Structural Contents Mitigation: Design, Implementation, and Community Outreach

Glen Granholm[1], Steve Austin[2], Katy Briggs[3] and Mark Benthien[4]

[1] Safe-T-Proof™
1207 W. Isabel St, Burbank, CA 91506
gg@safe-t-proof.com

[2] 3M Industrial Adhesives and Tapes Division
3M Center, Building 0220-04-E-02, St. Paul, MN 55144-1000
Sraustin19@mmm.com

[4] SE, Principal, BASE Design
582 Market Street, Suite 1402, San Francisco, CA 94104
katy@basedesigninc.com

[4] Southern California Earthquake Center
3651 Trousdale Pkwy #169, Los Angeles, CA 90089
benthien@usc.edu

Abstract. The need for equipment and furniture being secured during seismic events is well established as critical to reducing injury and loss. There are a variety of methods for attaching and securing these items, thus design professionals are encouraged to consider the following:

- What equipment and furniture will be moved into an office or laboratory, and how does the anchorage/fastening of these items influence the build out of the room?
- The use of high strength adhesives as part of a flexible fastening system as opposed to rigid anchorage utilizing a mechanical attachment.
- The knowledge gap that exists between what is common knowledge to earthquake engineers and misconceptions about earthquakes and earthquake readiness among the public.
- Probable Maximum Loss and the value of participating in education and outreach efforts about non-structural mitigation to ensure accuracy and continuity of messaging.

This body of this paper focuses on just one example: a situation where current developments in the field of non-structural earthquake damage mitigation has advanced beyond the recommendations given in the 2012 FEMA E-74 publication, "Reducing the Risks of Nonstructural Earthquake Damage". After additional considerations are given to the gaps that exist between current engineering best practices and the misperceptions of business and building owners, existing processes for disseminating accurate information about securing non-structural items are reviewed.

Keywords: Non-Structural, Contents, Fastening, Community Education

1. INFLUENCING THE BUILD: FOLLOWING THE ROADMAP OF CALIFORNIA HOSPITALS

The rapid expansion of life science construction throughout California includes not only the building of new structures, but also the decommission and repurposing of existing spaces into laboratories, as described by Kamin [2021]. Many times, in this latter case, the original use for a space was for it to function as an office. The design for remodeling into laboratory uses typically involves taking into consideration anticipated HVAC, power/lighting, and gas system needs. However, the shell of the newly purposed space is often left unchanged, with walls of the space left intact to keep both costs and turnaround time at a minimum.

Quite often when laboratories (or other facilities) are built or repurposed, it is only after equipment is moved in that thought is given to how or if it should be secured. The 2019 California Building Code (CBC) published in ICC [2019] provides guidance on properly building out laboratory workspaces with earthquake considerations in mind, but this guidance can be confusing and is primarily intended to ensure life safety, not the continuation of business operations or the resilience of the facility.

In an attempt to help California hospitals interpret the 2019 CBC and meet state law requiring facilities to stay open following an earthquake, the California Office of Statewide Health Planning and Development (OSHPD, since renamed Department of Healthcare Access and Information, or HCAI) issued a clarification document in 2020 known as a Public Intent Notice. This document, titled "PIN-68 Support and Attachment Requirements for Fixed, Interim, Mobil, Movable, Other and Temporary Equipment" (OSHPD [2020]) has the intent to help structural engineers determine what information needs to be included in construction documents with regards to the seismic anchorage of equipment.

Granted, PIN-68 is guidance for hospitals in the state, and the code requirements for the anchorage of equipment are not applicable to laboratories located in typical life-science and university laboratories. Still, the hospital mandate was put in place to keep facilities open following an earthquake. Thus, PIN-68 provides a roadmap for any facility interested in avoiding closure due to earthquake damage. (See below for information on Probable Maximum Loss and the impact of downtime to businesses).

PIN-68 (p. 1) states that "Section 1617A.1.18 of the CBC modifies the requirements in ASCE/SEI 7-16 (ASCE 7) Section 13.1.4 which exempts nonstructural components from the supports and attachments requirements with exceptions to the exemptions in ASCE 7. This has caused some confusion as there is equipment that was previously required to be anchored that may now remain unanchored or untethered, depending on where the equipment is stored." The phrase "Exceptions to the exemptions" is also confusing, to say the least.

The key to utilizing PIN-68 is to first identify and categorize the different types of non-structural equipment within or planned for a space. The notice states that bracing of these equipment types is no longer limited to the traditional mechanical attachment of equipment (OSHPD [2020] pp 4-5). International Code Council (ICC) testing has expanded the bracing options for securing equipment to the use of adhesive bracing systems, as shown in ICC-ES [2021]. Additionally, shake table testing through the Structural Engineers Association of Northern California (Phipps and McKenney [2015]) confirmed that this type of adhesive bracing can outperform rigid, mechanical attachment.

2.RECENT DEVELOPMENTS IN NON-STRUCTURAL MITIGATION

Securing equipment with flexible fastening that incorporates 3M™ VHB™ Tape (VHB) has showed remarkable results in shake table testing, with limited damage to the equipment anchored compared to equipment anchored using a traditional, mechanical anchorage method. This tape forms a strong adhesive bond, secures multiple types of substrates together, and continues to perform in wide temperature and humidity variations. Additionally, aging tests show an increase in the holding capacity of the bond as time passes, and various pull tests at different strain rates show the adhesive exhibits greater strength in sudden tugging motion (i.e., fast strain rates) common to actual earthquakes.

VHB tapes are acrylic foam pressure sensitive adhesive (PSA) tapes that adhere to the substrates via electrostatic adhesion and viscous flow. They do not damage substrates during attachment as with mechanical fastening (e.g., screws and bolts). Additionally, there is no heat involved and no chemical reactions taking place which allow for a smoother aesthetic when compared to positive attachment methods.

VHB tapes are characterized by having a viscoelastic conformable acrylic foam core with acrylic PSA skins. The acrylic foam provides energy absorption and stress relaxation properties that are beneficial for absorbing energy and reducing fatigue during stress loading. Viscoelastic materials like VHB tape have a modulus and ultimate strength that is strain rate or time dependent. Fast strain rates will exhibit increased modulus and ultimate strength values when compared to slower strain rates. Seismic induced movement is representative of a fast strain rate and therefore, this type of stress loading is where VHB tapes show increased strength values.

The advantages to utilizing adhesive fasteners are many-fold and include eliminating the need to drill into the sides of equipment (thus often voiding the warranty) and allowing for maximum flexibility to move and clean equipment and furniture. As these fastening systems are further developed, it is likely that they will become increasingly common options for the seismic anchorage of heavier and larger pieces of equipment. The factor that limits the weight of equipment that can be secured in this manner will no longer be the adhesive fasteners themselves, but the structure to which these systems are connected.

2A. ADDITIONAL MITIGATION CONSIDERATIONS: WALLS AND FLOORS

Adhesive anchorage systems either connect equipment via a mechanical attachment to the floor structure below or to walls behind the equipment. As discussed above, laboratories and other facilities are often built out in existing office spaces. Yet interior walls in office spaces are typically built with light gauge metal studs with minimal anchorage to the floors above and below. When anchoring equipment to these walls, the strength of the studs themselves and/or the strength of the stud wall connections often limit the capacity of the anchorage system. Consequently, despite advanced technologies in adhesive anchorage, the flexibility that this type of anchorage affords can be limited by the construction of the build out. By constructing stronger interior walls and thicker floor systems, facilities will be positioned to support seismic anchorage loads from larger and heavier equipment secured with adhesive bracing systems. These buildings will also be positioned to accommodate the flexibility that adhesive bracing systems provide, as the structure throughout the space will be able to support the seismic loads imposed by equipment.

Thus, we recommend that heavier gauge metal studs with stronger connections be used to build out rooms for new uses in order to allow the use of flexible, minimally invasive adhesive anchorage systems throughout. Additionally, the existing interior walls that remain in place during facility remodels or conversions should be retrofitted to prepare them for future use as supports for equipment anchorage. This retrofit may include increasing the frequency of anchorage from the bottom track of the wall to the floor below and/or the addition of braces (kickers) from the top track of the wall to the floor above.

If core and shell buildings are being built that may house heavy or large equipment, it is also recommended that the floors of these buildings are constructed with the anchorage of equipment in mind. As when adhesive anchorage systems are connected to interior walls, the strength of these methods of anchorage will often be limited by the strength of the floor system when equipment is anchored to the floor below. Thicker concrete fill over metal deck floors will allow for higher capacities from post-installed anchors (such as expansion or wedge anchors) that connect the adhesive anchorage system to the floor.

Granted, thickening the slab itself in an existing space can often be cost prohibitive. And, securing equipment to existing slabs with the utilization of thru-bolting and blocking below the floor often is expensive and difficult if not impossible to complete. Yet, creative solutions exist that need not break the bank. The addition of top-of-floor metal mounting plates, strategically positioned where free-standing equipment will ultimately be placed, can adequately strengthen the deck to both hold the load and the seismic anchorage needed. In this case, a metal plate is secured to the floor, and equipment is then secured to the metal plate. This solution also works well with equipment positioned in front of windows, where securing to a studded wall is not possible. Such a solution typically adds approximately $500 per plate to install.

Similarly, when addressing wall strengthening factors and the cost to build, all walls do not need to be strengthened– only those to which equipment will ultimately be secured will need stronger gage steel. The cost to install a sixteen or twenty gage stud, as opposed to a twenty-four-gage stud, is not significant. The labor cost should be the same, and the price increase per stud is just a few dollars.

If the wall is open with no drywall in place, the cost to install anchors into the bottom track is also minimal. The anchors themselves cost just a few dollars. Plus, if required, adding kickers to the top track of a partition wall at needed locations adds very little to the overall cost of construction.

Once a room has been adequately prepared structurally for the equipment that will ultimately be moved into the space, there are two additional steps that should be taken before equipment is moved in. First, on the walls that have been strengthened, mount P1000 or equivalent wall c-channel at engineer-recommended elevations. This provides a variety of anchor points that are all secured to the structure. Then, no matter what equipment is moved into the space, it can be secured to these strategically positioned mounting channels.

Secondly, on every bench or table-top where equipment will at some point be placed, install extruded aluminum fastening rails. These rails are multi-directional, can be fabricated to size, and install with no tools utilizing the 3M™ VHB™ Tape (VHB). As with the wall channel, these rails provide a nearly unlimited supply of anchor points, locations to which non-structural elements (tabletop lab equipment) are secured to the structure.

In summary, design professionals are encouraged to consider the following for safe and effective anchorage of equipment and furniture:

1) The equipment and furniture that will be moved into an office or laboratory during the design phase, specifically addressing how the equipment anchorage/fastening should influence the build out of the room.
2) The use of high strength adhesives as part of a flexible fastening system as opposed to rigid anchorage utilizing a mechanical attachment.

3) Wall and floor construction considerations as adhesive fastening advancements continue.

3.BRIDGING THE GAP - CURRENT ENGINEERING KNOWLEDGE VERSUS WIDELY HELD BELIEFS

While the engineering community has done a great job of not only creating but staying abreast of all the latest developments in the field of non-structural earthquake damage mitigation, there are still wide swaths of society that hold onto outdated beliefs and assumptions that could potentially lead to serious consequences in an earthquake.

For example, technical data such as national earthquake probability maps are often misinterpreted. As shown in Figure 1, a map included in Petersen et al [2019], the likelihood of significant earthquake shaking along the California coast is represented by a deep red color. It is often assumed, incorrectly, that this means that the degree of shaking, and anticipated potential damage, will be consistent throughout this red zone. For example, Oceanside (in the southern portion of the state) and South San Francisco as both are in the "red," however the expected seismic forces in Oceanside (.851 S_{DS}) are roughly half of what is expected in South San Francisco (1.574 S_{DS}) according to USGS seismic design data accessed from SeismicMaps.org (SEOAC and OSHPD [2022]). The result? Decisions are made by organizations and institutions assuming that seismic anchorage requirements are consistent across the state.

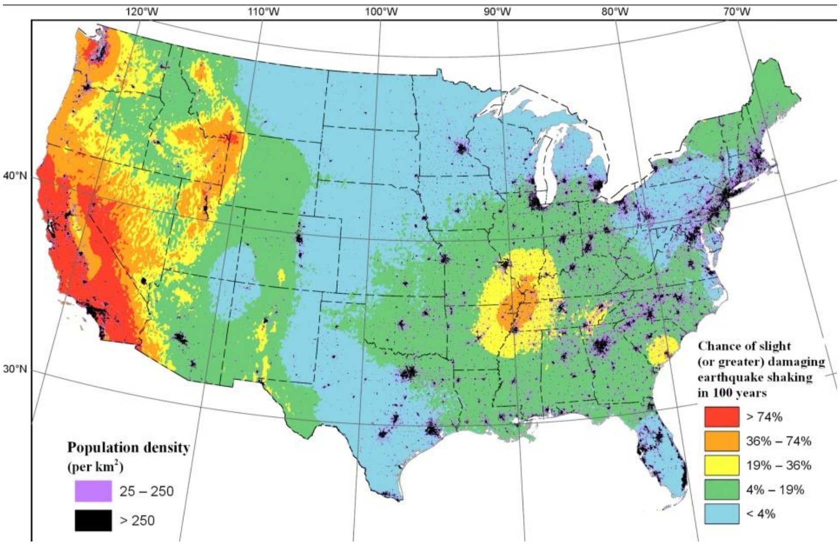

Figure 1. Chance of Damaging Earthquake Shaking in 100 Years, from Peterson et al [2019]

This shows that it is imperative that all involved in the design of a new or converted space be aware of the likely levels of expected seismic forces for its specific location. When a building is located within an area with high S_{DS} values, decisions can be made to help reduce damage due to seismic events and to help reduce costs associated with preventing damage, such as anchoring equipment, and when possible, locating heavier pieces on lower levels of buildings as shaking levels typically increase with building height.

4.START SPREADING THE NEWS–OUTREACH, EDUCATION, AND PROBABLE MAXIMUM LOSS

The considerations and recommendations above are intended to mitigate key sources of loss and business interruption due to earthquakes; the costs to businesses for failing to take such steps to keep their doors open following an earthquake are presented in Yanev [2012] and shown in Tables 1, 2, and 3. He outlines a

Probable Maximum Loss, or PML, anticipated for several life science/pharmaceutical companies in earthquake prone regions.

Table 1 compares the PML to four different pharmaceutical companies, should they decide against taking steps to retrofit their spaces in advance of an earthquake.

Table 1. Property Losses

Site	Building Value ($M)	Building PML	Equipment Value ($M)	Equipment PML	Inventory Value ($M)	Inventory PML	PML Value ($M)
1	143	15	454	30	170	31	76
2	18	2	33	3	28	2	7
3	115	17	55	6	83	13	36
4	44	9	57	6	25	4	19

While those numbers are large, they pale in comparison to the amount of money potentially lost by downtime following an earthquake, as illustrated below in Table 2.

Table 2 – Business Interruption Losses

Site	Annual Exposure ($M)	Business Downtime (Months)	Interruption Loss Estimate ($M)
1	2,776	1.5	347
2	151	1.5	19
3	630	1.5	79
4	503	2	84

And, as a percentage of the total anticipated loss, it is downtime that has the biggest impact, per Table 3 below.

Table 3 – Business Interruption Losses as a Percentage of Total Losses

Site	Total Loss ($M)	% Loss Due to Business Interruption
1	423	82.03%
2	26	73.08%
3	115	68.70%
4	103	81.55%

Yanev's work demonstrates the advantage to businesses to building beyond the requirements laid out in the CBC, simply because downtime, the opposite of resilience, is far and away the biggest potential money drain to businesses after a significant earthquake. This is why a large percentage of businesses that close immediately after an earthquake never reopen, as shown by Blythe [2002].

The engineering community should continue to correct misinformation and misunderstandings about issues related to earthquake resilience, and to consider new approaches. This message can be communicated through structural engineering associations and facility management organizations, and also through earthquake education groups such as Earthquake Country Alliance, which is administered by the Southern California Earthquake Center at USC.

For many years, Glen Granholm (Safe-T-Proof™), has led in-person trainings for the public on how (and why) to properly secure building contents. In partnership with the Earthquake Country Alliance, Granholm has migrated this in-person model to an online, 2-hour "Secure Your Space" training. The program explains key concepts about earthquake fasteners and their use, example images of fallen items, and video tutorials showing proper installation. Since early 2021, ECA has presented five of these trainings to more than 200 attendees (see Earthquakecountry.org/sysjune22 for a recent recording). The purpose is to train people so they can install fastening items in their own home, school, or workplace; ideally, they will also assist others in their communities (as a volunteer or as a paid service) or train them to secure their own space. As shown in this paper, the importance of properly securing new (and existing) laboratory and similar spaces may mean that ECA or others should provide more advanced trainings specific to these settings as well.

In conclusion, the technology now exists to secure laboratory equipment safely and effectively. The structural engineering community in California is well positioned to take the lead in effectively introducing this method of fastening throughout the region and to implement essential pre-move-in space adjustments where needed. Doing so can save money, time, essential research, and ensure continuity of operations. And most importantly, adequately securing non-structural building contents saves lives.

REFERENCES

Blythe, B.T. [2002] *Blindsided: A Manager's Guide to Catastrophic Incidents in the Workplace*, Penguin Group, New York, USA

ICC [2019] *California Building Code,* International Code Council, USA

ICC-ES [2021] *ICC-ES Evaluation Report ESR-4167,* ICC Evaluation Service, USA

Kamin, D. [2021] " '*A Wild 15 Months': Pandemic Spurs Conversion of Offices to Labs*," *New York Times,* July 27, 2021

OSHPD [2020] *Policy Intent Notice 68: Support and Attachment Requirements for Fixed, Interim, Mobile, Movable, Other and Temporary Equipment,* California Office of Statewide Health Planning and Development, Facilities Development Division, USA

Petersen M.D., Shumway, A.M., Powers, P.M. et al [2019] "The 2018 update of the US National Seismic Hazard Model: Overview of model and implications," *Earthquake Spectra*, Vol. 36, No. 1, pp. 5-41

Phipps, M. and McKenney, C. [2015], "Seismic Protection Design for Nonstructural Components: What really happens when it shakes?" Presentation at Spring 2015 SEAONC Quarterly Meeting, San Francisco, USA

SEAOC and OSHPD [2022] *www.SeismicMaps.org,* Website created by the Structural Engineers Association of California and California's Office of Statewide Health Planning and Development

Yanev, P. [2012] "Business Earthquake Resilience," Presentation to Kaiser Permanente, Oakland, USA

Seismic Performance of Electrical Cabinets During Qualification Shake Table Testing

Roberto J. Merino[1], Daniele Perrone[1,2], Andre Filiatrault[1] and Roberto Nascimbene[1]

[1] *University School for Advanced Studies IUSS Pavia*
Palazzo del Broletto – Piazza della Vittoria, Pavia, Italy
e-mail: robertojavier.merinovela@iusspavia.it, daniele.perrone@iusspavia.it, andre.filiatrault@iusspavia.it, roberto.nascimbene@iusspavia.it
[2] University of Salento
Piazza Tancredi 7, Lecce, Italy

Abstract. Damage to non-structural elements during earthquake ground motions can determine the seismic performance of a building in terms of building functionality, economic losses and life safety. Seismic qualification through shake table testing is a comprehensive and simple way of determining the causes of seismic damage to non-structural elements, such as electrical cabinets and quantify their seismic performance. Qualification shake table testing based on triaxial tests was performed to investigate the seismic behaviour of a number of electrical cabinet specimens in the 6DLAB laboratories at the EUCENTRE Foundation in Pavia, Italy. This paper presents the results from qualification shake table testing for two electrical cabinet specimens. One of the tested electrical cabinet specimens has a superstructure that is stronger than its attachment, while the other one has weaker superstructure relative to its attachment. The two electrical cabinet specimens were tested under a recently proposed loading protocol for qualification shake table testing of non-structural elements in Italy. The seismic performance of the two tested electrical cabinet specimens is investigated using their recorded acceleration and displacement time histories as well as through visual inspection using photographs and videos taken during and after the shake table tests. The results of this study highlight the need for further research on the seismic behaviour of electrical cabinets and their modes of failure under earthquake ground motions.

Keywords: electrical cabinets; non-structural elements; nonstructural components; qualification shake table testing; seismic performance

1. INTRODUCTION

The introduction of performance-based concepts to the seismic design of structures has been an important advancement in earthquake engineering during the last two decades. One of the key aspects of this advancement is the acknowledgement that the seismic performance of non-structural elements (NSEs) greatly affects the overall seismic performance of buildings, which can occur in three main ways. First, NSEs can significantly contribute to seismic economic losses in buildings, as has been concluded from recent seismic loss estimation studies [O'Reilly *et al.* 2018]. This is because NSEs represent a majority of the initial investment in several typologies of buildings [Taghavi and Miranda, 2004] and, historically, NSEs have been mostly ignored in the seismic design of buildings until the present day. Second, NSEs that get damaged during earthquakes can pose a life-safety hazard to building occupants or passer-byes, since they can fall [Magliulo *et al.* 2014] or impede the egress of occupants from the damaged building. Finally, damage to NSEs can cause loss of functionality in buildings. In critical buildings, such as hospitals or airport terminals, loss of functionality can hamper emergency recovery and put lives at risk [OSHPD, 1995; Miranda *et al.* 2012], while in commercial and industrial buildings loss of functionality can generate considerable indirect economic losses due to business interruption.

Even though scientific research into the seismic behaviour of NSEs has increased during the past years in terms of analytical studies, experimental studies, and the development of simplified seismic design guidelines [Tao *et al.* 2021], the sheer amount of NSE typologies still requires that the seismic behaviour of several NSE typologies be investigated further both experimentally and analytically. A comprehensive way in which the seismic behaviour of NSEs can be assessed is qualification shake table testing. Qualification shake table testing is not only a simple way in which the seismic performance of NSEs can be assessed and improved on a wide scale [NTC, 2018; ASCE, 2022] but it is also a way in which the seismic behaviour of NSEs can be investigated in depth since this type of testing tries to simulate as close as possible the actual dynamic conditions that a NSE would experience during the occurrence of an actual earthquake ground motion.

This paper investigates the seismic behaviour of two electrical cabinet specimens through qualification shake table testing. The qualification shake table testing of the electrical cabinet specimens was performed on the 6DLAB shake table in the EUCENTRE Foundation located in Pavia, Italy. The electrical cabinet specimens were tested using a loading protocol developed as a part of a seismic classification procedure for NSEs in Italy [Merino *et al.* 2022]. The two tested electrical cabinet specimens have a similar seismic force resisting system but have different structural detailing. The seismic performance of the electrical cabinet specimens is assessed in terms of their acceleration and displacement responses as well as using photographs and videos to record their damage during the testing and their failure modes.

2. DESCRIPTION OF ELECTRICAL CABINET SPECIMENS

This study focuses on the assessment of the seismic behaviour of two electrical cabinet specimens that were tested as part of a larger qualification shake table testing campaign performed in the 6DLAB of the EUCENTRE Foundation located in Pavia, Italy. Table 1 presents the main properties of the two tested electrical cabinet specimens that are referred to in this study as Specimen 1 and Specimen 2. Both electrical cabinet specimens are base-mounted specimens. Both electrical cabinet specimens have a very similar height dimension and a relatively similar width and length dimension. The heigh of both specimens is approximately 2110 mm. Specimen 1 has rectangular plan dimensions with a length of 1013 mm and a width of 611 mm, while Specimen 2 has almost square plan dimensions with a length of 819 mm and a width of 811 mm. The elevation of the centre of gravity above the base is also similar for both specimens and it is at approximately mid height of the specimens. The seismic weight of Specimen 1 is equal to 9.31 kN while the seismic weight of Specimen 2 is equal to 6.11 kN. Finally, white noise tests were conducted for both specimens in order to perform dynamic identification, as described later in Section 4. The initial fundamental frequencies of both specimens in both directions were measured using the results from the white noise dynamic identification tests. As can be observed from Table 1, the measured initial fundamental frequencies of Specimen 1 are higher than those of Specimen 2. These values of measured initial fundamental frequencies demonstrate that even though both specimens have relatively similar geometrical dimensions, Specimen 2 is much more flexible laterally than Specimen 1.

Table 1. Main properties of tested electrical cabinet specimens

	Type of Fixture	Length	Width	Height	Elevation of centre of gravity above base	Seismic weight	Measured Initial fundamental frequency along shorter direction (x dir.)	Measured Initial fundamental frequency along longer direction (y dir.)
Specimen 1	Base-mounted	1013 mm	611 mm	2109 mm	1053 mm	9.31 kN	3.3 Hz	7.5 Hz
Specimen 2	Base-mounted	819 mm	811 mm	2107 mm	1052 mm	6.11 kN	2.2 Hz	4.0 Hz

Figure 1 presents photographs of the two tested electrical cabinet specimens. Figures 1 a) and b) present photographs of Specimen 1 with the cabinet door closed and with the cabinet door open, respectively. Similarly, Figures 1 c) and d) present photographs of Specimen 2 with the cabinet door closed and with the cabinet door open, respectively. Note also that additional weights were added inside the electrical cabinet specimens to simulate the presence of electrical equipment that would be installed in a normal operational situation in a building. The additional weights can be observed in Figures 1 b) and d). Both electrical cabinet specimens were installed on the shake table with their shorter direction aligned with the x axis of the shake table and with the longer direction aligned with the y axis of the shake table. This orientation is shown in Figure 1 using red arrows to represent the direction of the two main axes of the shake table on each photograph. Both tested electrical cabinet specimens have similar seismic force-resisting system (SFRS). Both specimens have an attachment structure, which is located at the base of the specimens, and which is connected to the base of the shake table using rigid anchor bolts. Interior and exterior frame structures are installed on top of the attachment structure. The interior frames support all the additional weights provided by the simulated electrical equipment and are very flexible since the beam-to-upright and base connections tend to behave as pinned connections. During the occurrence of a base movement due to an earthquake ground motion, all the inertial forces generated by the additional weights are transmitted from the flexible internal frame to an external frame using rigid steel elements located at mid height and top of the internal frame. The external frame is a simple frame with only one level but has moment resisting beam-to-upright and base connections, so they are able to resist lateral forces and transmit them to the attachment structure. Steel panel walls are connected to the external frame to create the lateral walls and doors of each electrical cabinet specimen.

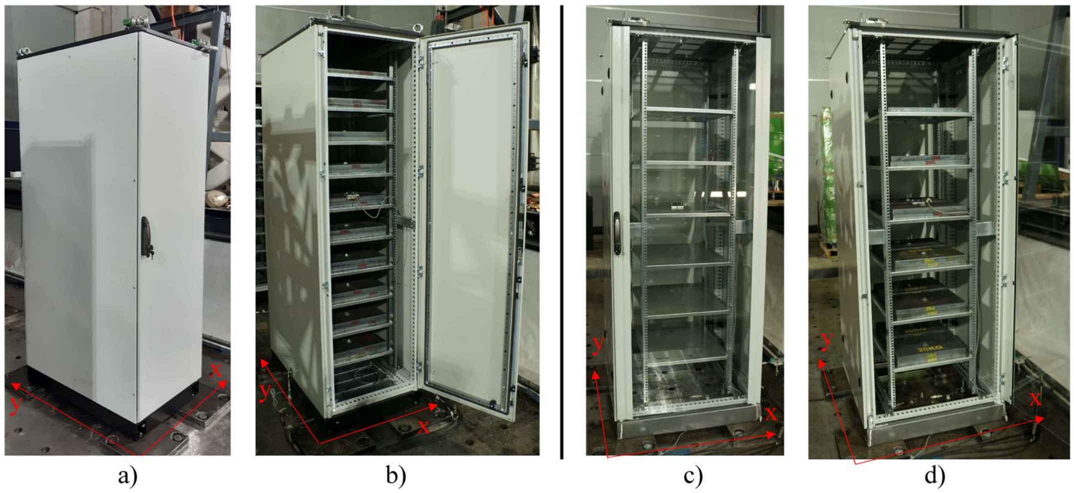

Figure 1. Photographs of tested electrical cabinet specimens: a) Specimen 1 exterior view; b) Specimen 1 interior view, loaded with additional weights; c) Specimen 2 exterior view, unloaded; d) Specimen 2 interior view, loaded with additional weights.

3. INSTRUMENTATION

This section presents the instrumentation that was used to monitor the dynamic response of both electrical cabinet specimens during the qualification shake table testing. The acceleration response of both electrical cabinet specimens was measured using an array of accelerometers distributed throughout each specimen. Three accelerometers were installed on each electrical cabinet specimen: two accelerometers were installed at the top of the specimen on diagonally opposite corners and one accelerometer was installed as close as possible to the specimen's centre of gravity. The displacements of the electrical cabinet specimens relative to the base of the shake table were measured using three string potentiometers installed on a rigid frame, located on the surface of the shake table, and connected to the top of the specimens. Two of the string potentiometers on each specimen were installed horizontally to measure the displacement of the specimens along the x axis of the shake table while one potentiometer was installed at an angle of 45^0 from both the x and y axes of the shake table in order to measure indirectly the displacement of the specimens along the y axis of the shake table. Additionally, the possible uplift of the specimens due to rocking motion was measured using two potentiometers per specimen installed at the base of the specimen on the shake table and connected to a point at around one quarter of the height of the specimens. Figure 2 presents a schematic view of the specific location of the instrumentation on each of the two tested electrical cabinet specimens. Note that the two specimens were not tested simultaneously but they were part of a larger shake table testing campaign of electrical cabinets that included two testing configurations; the first testing configuration included Specimen 1 while the second testing configuration included Specimen 2. Note that the names of the accelerometers and potentiometers in Figure 2 are the original names used throughout the testing campaign of the two configurations of electrical cabinet specimens. This explains why some of the instrumentation names in Figure 2 are repeated for both specimens.

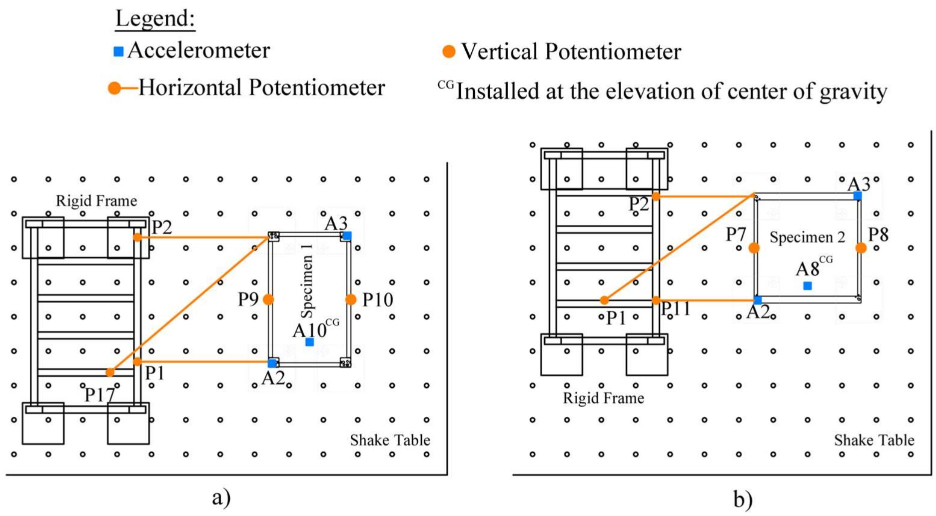

Figure 2. Schematic layout of the instrumentation used to measure the dynamic response of the electrical cabinet specimens: a) Specimen 1; b) Specimen 2.

In addition to the accelerometers and the string potentiometers, video recordings and photographs of the electrical cabinet specimens were taken during and after each testing intensity. This was done so as to define in detail the damage experienced by the electrical cabinet specimens during shake table testing.

4.TESTING PROTOCOL

The testing protocol used to investigate the seismic performance of the electrical cabinet specimens during shake table testing is based on a newly developed seismic classification procedure for NSEs in Italy [Merino et al. 2022]. In this seismic classification procedure, NSEs are classified according to their performance during qualification shake table testing considering four levels of seismic intensity, which are representative of the seismic hazard in the whole Italian territory. The four levels of seismic intensity are represented using a Required Response Spectra (RRS) for each level for the horizontal and vertical directions, as is required for qualification shake table testing. The shape of the RRS is given by the ISO13033 [2013] loading protocol, as shown in Figure 3.

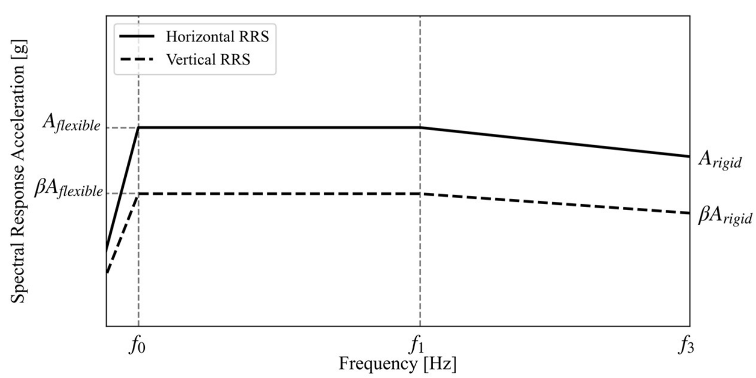

Figure 3. General shape of the RRS from ISO13033 [2013]

The two values of acceleration that determine the seismic intensity of the RRS according to Figure 3, A_{rigid} and $A_{flexible}$, are defined using the formulation used to estimate the acceleration demands on NSEs of

Eurocode 8 [EN1998-1, 2011] and the peak ground acceleration seismic hazard map of Italy. The value A_{rigid} is the acceleration demand on rigid elastic NSEs, and $A_{flexible}$ is the acceleration demand on flexible elastic NSEs. These values of acceleration are defined by Merino *et al.* [2022] as:

$$A_{rigid} = k_{I(u\ or\ s)} \cdot \left[3 \frac{\left(1+\frac{z_i}{H}\right)}{2} - 0.5\right] \tag{4}$$

$$A_{flexible} = k_{I(u\ or\ s)} \cdot \left[3 \left(1+\frac{z_i}{H}\right) - 0.5\right] \tag{5}$$

where $k_{I(u\ or\ s)}$ is the peak ground acceleration at the site, and z_i/H is the ratio between the elevation of the position of the NSE in the supporting structure to the total height of the supporting structure. Note that Merino *et al.* [2022] derived the value of A_{rigid} assuming that the ratio of the non-structural period to the fundamental period of the supporting structure is equal to zero while they derived the value of $A_{flexible}$ by assuming that the same ratio is equal to one. Note also that the loading protocol contemplates a vertical RRS that can be calculated by multiplying the horizontal RRS by a value of β, as can be observed in Figure 3, and always assuming that the value of z_i/H is equal to zero. In other words, no acceleration amplification is considered for the vertical direction, which is equal to assuming that the supporting structure is perfectly rigid in the vertical direction. The value of β is usually taken as 2/3.

The four seismic intensity levels for the qualification shake table testing of the electrical cabinet specimens were defined by creating an $A_{flexible}$ seismic hazard map of Italy using the 475-year peak ground acceleration seismic hazard map of Italy combined with Equation (5). Note that since according to Equation (5), the value of $A_{flexible}$ is maximum for a normalized elevation of the NSE, z_i/H, equal to one, the $A_{flexible}$ seismic hazard map of Italy was created for this value of z_i/H. The resulting 475-year $A_{flexible}$ seismic hazard map of Italy was divided into four regions depending on their value of $A_{flexible}$, the maximum value of $A_{flexible}$ of each of the four regions was then used to define the seismic intensities for the qualification shake table testing of the electrical cabinet specimens. Table 2 presents a summary of the testing sequence used for the qualification shake table tests of the electrical cabinet specimens, including the values of A_{rigid} and $A_{flexible}$ used for each test. Finally, the test input motions for the qualification shake table tests of the electrical cabinet specimens were generated using the criteria prescribed by the AC156 [ICC-ES, 2012] loading protocol.

Table 2. Testing sequence used for the qualification shake table tests of the electrical cabinet specimens.

Sequence No.	Specimen 1	Specimen 2
1	Dynamic Identification- White Noise Test	Dynamic Identification- White Noise Test
2	RRS with A_{rigid} = 0.18 g and $A_{flexible}$ = 0.40 g	RRS with A_{rigid} = 0.18 g and $A_{flexible}$ = 0.40 g
3	RRS with A_{rigid} = 0.36 g and $A_{flexible}$ = 0.80 g	RRS with A_{rigid} = 0.36 g and $A_{flexible}$ = 0.80 g[1]
4	RRS with A_{rigid} = 0.54 g and $A_{flexible}$ = 1.20 g	
5	RRS with A_{rigid} = 0.73 g and $A_{flexible}$ = 1.60 g[2]	

[1]Specimen 2 failed completely for this test. [2]Potentiometers were disconnected from Specimen 1 for this test.

Figure 4 presents the comparison between the RRS and the recorded Test Response Spectrum (TRS) according to the prescriptions of AC156 [ICC-ES, 2012] for some of the shake table tests presented in Table 2. Note that the version of the test input motion that was used to compute the TRS in Figure 4 was the one measured by a tri-axial accelerometer located at the base of the shake table during the tests. Figure 4 shows the matching for Test number 2 of Specimens 1 and 2, and for Test number 4 of Specimen 1. The TRS for all the three orthogonal directions of the shake table matches their respective RRS well for a wide range of frequencies. The only discrepancy is the TRS in the y direction of the shake table goes below the limits of the RRS for frequencies between 15 Hz to 25 Hz for all the three tests presented in Figure 4. This is not a major issue to invalidate the qualification testing, however, since the measured initial fundamental frequencies of the two electrical cabinet specimens in the y direction are considerably lower than 15 Hz.

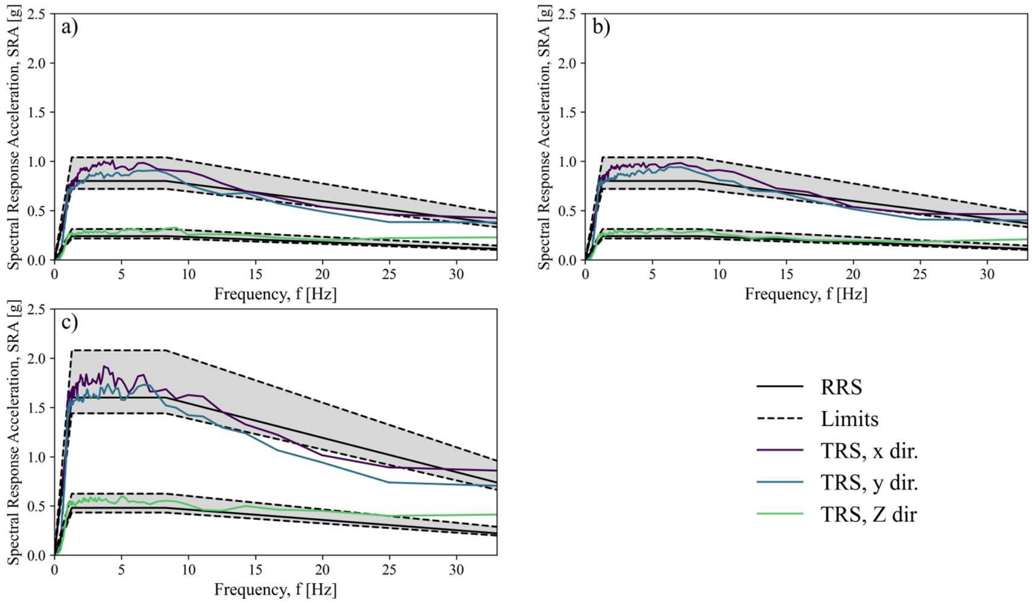

Figure 4. Comparison between RRS and TRS according to the prescriptions of ICC-ES [2012] for: a) Test no. 2 of Specimen 1; b) Test no. 2 of Specimen 2; c) Test no. 4 of Specimen 1.

5. EXPERIMENTAL RESULTS

Figure 5 presents the peak dynamic response of both electrical cabinet specimens in terms of the measured peak accelerations and displacements recorded during the tests using the instrumentation layout of Figure 2 and plotted as a function of the recorded Peak Table Acceleration (PTA) of each test. Figure 5 a) presents the Peak Component Acceleration (PCA) of each specimen measured at the centre of gravity plotted against the PTA for both electrical cabinet specimens and along the two principal axes of the shake table. The dashed line in Figure 5 a) represents a ratio between PCA and PTA equal to 2.2, which is equal to the ratio between $A_{flexible}$ and A_{rigid} calculated using Equations 4 and 5 assuming z_i/H equal to one. As can be observed from Figure 5 a), all of the values of PCA for both electrical cabinet specimens, in both directions, and for all tests are close to the dashed line representing a value of PCA/PTA equal to 2.2. This result indicates that both electrical cabinet specimens have fundamental frequencies between 1.3 Hz and 8.3 Hz, which is the range of frequencies of the plateau of the horizontal RRS of Figure 3. The points that show the greatest discrepancy with the dashed line are the PCAs of Specimen 1 in the x direction, which tend to be over the dashed line. This could be caused by the fact that the TRS is higher than the RRS in the range of frequencies defining the plateau of the spectrum or, as is explained in more detail later, it could also be due to the rocking of the specimen during the last two tests. Figure 5 b) presents the Peak Component Relative Displacement (PCRD) measured at the top of each specimen plotted against the PTA for both electrical cabinet specimens and along the two principal axes of the shake table. The PCRDs of Figure 5 b) are in the range between 10 mm and 200 mm. Even though Specimen 1 achieves the largest PCRD during Test No. 4 (the last test in which the potentiometers were used), Specimen 2 shows larger PCRDs than Specimen 1 for Test No. 3.

Note that after Test No. 3, Specimen 2 had to be removed from the shake table due to excessive damage. Finally, Figure 5 c) presents the Peak Base Potentiometer Vertical Elongation (PBPVE) for both electrical cabinet specimens plotted as a function of the measured PTA. As can be observed from Figure 5 c), the PBPVE of Specimen 1 increases linearly as the PTA increases, while the PBPVE of Specimen 2 remains relatively constant and even decreases slightly as PTA increases. This difference highlights an important distinction between the seismic response of both specimens since Specimen 1 was observed to rock during the tests while Specimen 2 did not.

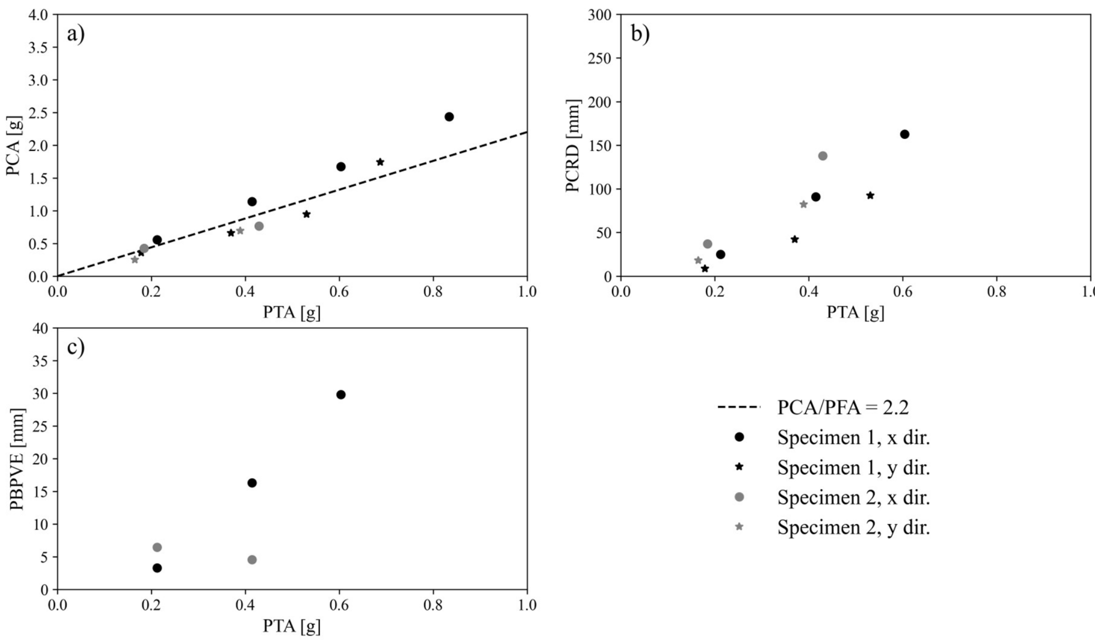

Figure 5. Peak dynamic response of the two tested electrical cabinet specimens plotted as a function of the recorded PTA: a) PCA; b) PCRD; c) PBPVE.

The results presented in Figure 5 are complemented by the photographs shown in Figure 6 of the damages observed to the two electrical cabinet specimens during the shake table tests. Notable damage occurred to Specimen 1 after Test No. 5. Figure 6 a) shows permanent bending damage to one of the lateral walls of Specimen 1, while Figure 6 b) shows the failure of the attachment structure of Specimen 1, both occurred after test No. 5. Specimen 2 presented considerable damages after test No. 3. Figure 6 c) shows how after this test, the lateral walls of Specimen 2 completely collapse as they were ejected violently from their original position.

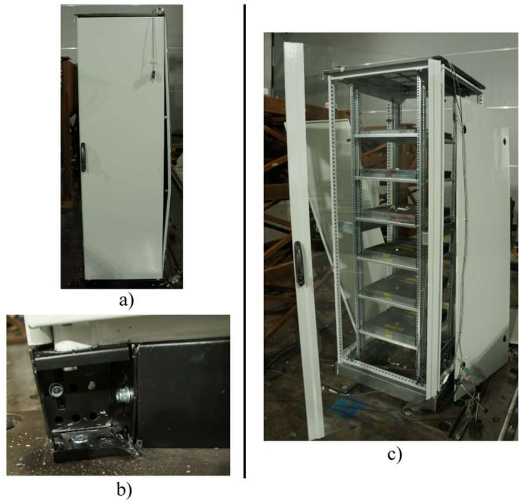

Figure 6. Damage observed to the electrical cabinet specimens during the shake table tests: a) Permanent bending of one of the lateral walls of Specimen 1; b) Failure of the attachment structure of Specimen 1; c) Collapse of the lateral walls of Specimen 2.

Even though both tested electrical cabinet specimens have a similar structure and SFRS, their seismic performance during the shake table tests were markedly different. Specimen 1 was able to withstand a much higher seismic intensity than Specimen 2 since it was able to reach Test No. 5 while Specimen 2 was only able to reach Test No. 3. The damage modes of both specimens were different; rocking was observed between the superstructure and the attachment structure of Specimen 1, while Specimen 2 presented large frame deformations between the top of the specimen and its base without any rocking. The occurrence of rocking in Specimen 1 and not in Specimen 2 can be observed in Figure 5 c) since the PBPVE of Specimen 1 increases linearly with the PTA while the PBPVE of Specimen 2 does not, implying that the vertical elongation of the base potentiometer of Specimen 2 is only due to the internal deformations of the specimen and not due to rocking. Clearly, the external frame of Specimen 1 is much stronger than that of Specimen 2. The external frame of Specimen 1 is strong enough so that the weak link in the system becomes the connection between the whole superstructure and the attachment structure, creating a surface between them in which rocking occurs; this does not occur in Specimen 2 where the external frame is very flexible and weak. This difference results in the failure of the attachment structure of Specimen 1 due to the impact created from rocking and permanent relative deformations of the external and internal frames of Specimen 2. Note, however, that even though Specimen 1 started showing signs of rocking from Test No. 3, its top relative displacements were measured to be lower than those of Specimen 2 for the same intensity. The energy dissipation generated due to the impact created by rocking might have contributed to decrease the relative displacement response of Specimen 1 in relations to Specimen 2. Another difference between the two specimens is the connections between the external frame and the lateral wall panels. For Specimen 1, these connections are stronger than the bending capacity of the lateral wall panels, creating yielding in the panels but no panel dislocation. This is the opposite for Specimen 2, for which the connections between the lateral wall panels and the external frame are much weaker than the bending moment capacity of the panel, creating sudden dislocation of the lateral wall panels from the external frame but no permanent damage in the panels.

6. CONCLUSIONS

This paper investigated the seismic performance of two similar electrical cabinet specimens using the results from a series of shake table tests. The tested electrical cabinet specimens had a similar seismic force-resisting system (SFRS) in which a laterally flexible internal frame, which carries the gravity loads, is connected to a rigid external frame which provides lateral resistance. Both frames were supported by an attachment structure that is rigidly anchored to the base of the shake table. Accelerograms and potentiometers as well as photographs and videos were used to measure and observe the seismic responses of the two specimens during the tests. The loading protocol that was used for the shake table tests consisted of a set of required response spectra that represented sites with different levels of seismicity in Italy for a 475-year return period.

The results from the shake table tests indicated that a better seismic performance of electrical cabinet specimens may be achieved if the external frame of the electrical cabinets is sufficiently rigid and strong. In this case, the electrical cabinet specimen may produce a rocking motion since the connection between the superstructure and the attachment structure becomes the weakest link of the SFRS of the electrical cabinet. This rocking motion of the electrical cabinet, however, seems to be beneficial up to the point in which the electrical cabinet is not at risk of overturning, since the electrical cabinet specimen that rocked during the shake table tests was able to withstand a seismic intensity that was double the one that the electrical cabinet specimen that did not rock was able to withstand. A similar situation occurred with the connections between the lateral wall panels and the external frame. Either the connections are weak, and the panel is ejected during motion, or the connections are strong, and the panel yields and permanently deforms. The results from the shake table tests indicate that the latter is preferable to the former since the specimen for which the lateral wall panels yielded was the one that rocked and was able to withstand higher seismic intensities.

The results from the shake table tests of two electrical cabinet specimens have highlighted the seismic performance of a typology of electrical cabinets. These results could be a first step in developing a hierarchy of failure modes for electrical cabinets based on capacity design principles in which the weakest link of the SFRS of the cabinet is selected in order to maximize its performance in terms of strength, deformations, and energy dissipation during the occurrence of earthquake ground motions. This could be significant step in reducing non-structural seismic losses.

ACKNOWLEDGEMENTS

The authors gratefully acknowledge the funding by Italian Ministry of Education, University and Research (PON Grant n.1735/2017, CADS Project). The authors would also like to acknowledged ETA SpA for providing the electrical cabinet specimens used for the qualification shake table testing. Finally, the authors would also like to thank all the technical staff of the EUCENTRE Foundation, Filippo Dacarro, Paolo Dubini, Francesco Graziotti, Luca Grottoli, Igor Lanese, and Maria Rota, who conducted the shake table tests described in this paper.

REFERENCES

ASCE 7-22 [2022] Minimum design loads for buildings and other structures. *American Society of Civil Engineers*, Reston, Virginia, USA.

Magliulo, G., Ercolino, M., Petrone, C., Coppola, O., Manfredi, G. [2014] "The Emilia Earthquake: the seismic performance of precast concrete buildings," *Earthquake Spectra*, Vol. 30, No.2, pp. 891-912.

Miranda, E., Mosqueda, G., Retamales, R., Peckan, G. [2012] "Performance of nonstructural components during the 27 February 2010 Chile Earthquake," *Earthquake Spectra*, Vol. 28, No. 1, pp. 453-471.

NTC [2018] Aggiornamento delle Norme tecniche per le costruzioni. *Ministero delle Infrastrutture e dei Trasporti*; Roma, Italia.

O'Reilly, G.J., Perrone, D., Fox, M., Monteiro, R., Filiatrault, A. [2018] "Seismic assessment and loss estimation of existing school buildings in Italy," *Engineering Structures*, Vol. 168, pp. 142-162.

OSHPD [1995] "The Northridge earthquake: a report to the hospital building safety board on the performance of hospitals," *Office of Statewide Health Planning and Development, Facilities Development Division,* Sacramento, California, USA.

Taghavi S, Miranda E. [2004] "Response Assessment of Nonstructural Building Elements." *Pacific Earthquake Engineering Research Center*. PEER Report 2003/05. University of California Berkely.

Tao, W., Shang, Q. and Jichao, L. [2021] "Seismic force demands on acceleration-sensitive nonstructural components: a state-of-the-art review." *Earthquake Engineering & Engineering Vibrations*, DOI: 10.1007 Is 11803-021-2004-0.

Merino, R.J., Perrone, D., Filiatrault, A., Nascimbene, R. [2022]. "A Seismic Classification Procedure for Non-Structural Building Elements based on Shake-Table Qualification Testing." *Proceedings of the 3rd European Conference on Earthquake Engineering and Seismology*. Bucharest, Romania.

ISO13033. [2013]. Bases for design of structures – loads, forces and other actions -Seismic actions on nonstructural components for building applications, *International Organization for Standardization*, Geneva, Switzerland.

EN 1998-1. [2011] Eurocode 8 – Design provisions for earthquake resistant structures, EN-1998-1:2011, *Comite Europeen de Normalization*, Brussels, Belgium.

ICC-ES [2012] Acceptance criteria for seismic qualification by shake table testing of nonstructural components and systems, *International Code Council Evaluation Service*, International Code Council AC156, Whittier, CA.

A new testing and evaluation method for seismic rating of non-structural elements

N. Zamani[1], C. Beiter[2], N. D. Perrone[3], A. Filiatrault[4], D. Rodriguez[5], C. Tokas[6]

[1] Codes and Standatrs Senior Manager
Hilti North America, 7250 Dallas Parkway, Suite 1000, Plano, Texas 75024
e-mail: natasha.zamani@hilti.com
[2] Team Leader, Application Research and Technical Data
Hilti Corporation, 9494, Schaan, Liechtenstein
e-mail: clemens.beiter@hilti.com
[3] Assistant Professor
Department of Engineering for Innovation, University of Salento, Lecce, Italy
e-mail: daniele.perrone@unisalento.it
[4] Professor and [5]Ph.D. Candidate
University School for Advanced Studies Iuss Pavia, Italy
e-mail: andre.filiatrault@iusspavia.it, e-mail: derek.rodriguez@iusspavia.it
[6] The Deputy Division Chief Facilities Development
Department of Health Care Access and Information, 2020 West El Camino Avenue, Suite 800,
Sacramento CA 95833
e-mail: chris.tokas@hcai.ca.gov

Abstract. Recent earthquakes have highlighted that poor performance of non-structural elements (NSEs) is one of the main contributors to damages, losses, and business interruption after an earthquake. Such damages can have substantial social or economic implications, particularly for critical buildings such as hospitals. Unlike structural components, there is limited information on the seismic behaviour of NSEs. In this paper, a novel procedure for testing and assessing the seismic performance of non-structural elements and systems is presented. The proposed criteria is based on the outcome of an extensive research project between EUCENTRE and Hilti.The first step in that project was to investigate the existing cyclic loading protocols including FM-1950 and FEMA-461. Experimental and numerical programs were then designed, and various types of suspended sway bracing components and systems were tested and analysed to evaluate their key seismic performance and response parameters. Lastly, a framework for the quantification of seismic performance factors to use in the force-based seismic design of NSE has been proposed. The proposed framework is comparable to the existing FEMA P-695 methodology for the evaluation of seismic performance of structural seismic force-resisting systems. In the proposed approach four performance parameters were defined: the maximum lateral load capacity; the yielding displacement, the ultimate displacement, and the effective ductility ratio. Qualified systems should meet a minimum effective ductility ratio otherwise the lateral load capacity will reduce.

Keywords: Non-structural elements, Seismic performance factors, Effective ductility ratio, Cyclic testing

1. INTRODUCTION

Although significant research has been carried out on the structural safety of buildings under earthquake events, the seismic behavior of non-structural elements (NSEs) has received little attention. Past earthquakes have demonstrated the vulnerability of NSEs to even moderate levels of ground motion. For example, the 1994 Northridge Earthquake caused significant non-structural damage to a number of area hospitals. In these instances, the hospitals remained structurally sound, but required closure due to significant damage to NSEs, primarily water damage and loss of emergency utility function. The losses due to business interruption, which are greatly influenced by non-structural damage, can often equal or exceed losses due to the actual damage to the structure and equipment.

Unlike structural components, there is limited information on the seismic behavior of NSEs. The importance of considering NSEs performance in the overall design and safety of buildings has been recognized by the scientific community in the last years. Although increasing amount of research studies addressing NSEs has been conducted and several new non-structural systems have been proposed by manufacturers, a standardized procedures to test and evaluate NSEs seismic performance is still unavailable. In this regard, an extensive research projects have been conducted by EUCENTRE and Hilti [Filiatrault et al. 2018, Perrone et al. 2020a, 2020b, and 2022] with the aim of better understanding the response of NSEs in seismic events and harmonizing the performance of both non-structural and structural elements in code compliant facilities.

The FEMA P-795 document, "*Quantification of Building Seismic Performance Factors: Component Equivalency Methodology*" [FEMA 2011], provides a standardized methodology for evaluating the seismic performance equivalency of components and subassemblies whose inelastic response controls the collapse performance of a seismic-force-resisting systems (SFRSs). This component equivalency methodology is a statistically based procedure for developing, evaluating, and comparing test data on new components that are proposed as substitutes for selected components in a current code approved SFRSs. The Component Methodology is derived from the general methodology contained in FEMA P-695, "*Quantification of Building Seismic Performance Factors*" [FEMA 2009]. Similar to the general methodology in FEMA P-695, the intent of the Component Methodology is to ensure that code-designed buildings have adequate resistance against earthquake-induced collapse.

In this paper, a framework is proposed to quantify seismic performance factors of NSEs. The FEMA P-795 methodology was used as a reference guide in the development of this framework. In the proposed approach, four performance parameters were defined: the maximum lateral load capacity; the yielding displacement, the ultimate displacement, and the effective ductility ratio. Qualified systems should meet a minimum effective ductility ratio otherwise the lateral load capacity will reduce. The application of the proposed framework has been demonstrated through an illustrative example, which deals with establishing seismic rating for a suspended piping restraint system.

2.REVIEW OF EUCENTRE AND HILTI RESEARCH PROJECT

In absence of detailed seismic design and qualification regulations for NSEs such as installation systems in Europe, Hilti AG, Liechtenstein approached the European Centre for Training and Research in Earthquake Engineering (EUCENTRE), Pavia, Italy to investigate the behavior of installation systems in case of seismic events. Within a three-year research program, an extensive definition phase was followed by hundreds of component and system tests and thousands of numerical simulations. The results of these experimental and numerical investigations led to an extensive behavior understanding and relevant findings are already published and are now summarized in the following paragraphs.

During the initial definition phase, the effect of cyclic loading protocols on the experimental seismic performance evaluation of suspended piping restraint installations was examined [Filiatrault et al. 2018]. Amongst existing loading protocols (ATC-24, SAC, ISO, CUREE-Caltech), the cyclic loading protocols FM-1950 and FEMA-461 were investigated and compared with each other. The results indicates that both loading protocols lead to similar cyclic backbone curves and failure modes for the investigated installation component samples. However, the FEMA-461 loading protocol is more reliable and proper for evaluation of the seismic performance of NSEs such as installation support systems. It provides more consistent details of the specimens' nonlinear characteristics, while depending on the peak strength, details of the nonlinear response of the specimens can be lost by using the FM-1950 loading protocol. Furthermore, the parameters and characteristics of the FEMA-461 protocol were found to be similar to that of the other four displacement-controlled cyclic loading protocols developed for testing structural components and systems (ATC-124, SAC, ISO and CUREE-Caltech) and all are based on statistical studies of nonlinear time-history dynamic analysis (NTHDA) of Single-Degree-of-Freedom (SDOF) systems subjected to various earthquake ground motions. The FM-1950 loading protocol is force-controlled and has been developed specifically for the testing of seismic sway braces of automatic sprinkler systems. It provides much higher energy demand than the other five reviewed cyclic loading protocols. This could lead to unrealistic failure modes (e.g. fatigue) rarely observed in real earthquakes.

Based on these findings the cyclic testing protocol from FEMA-461 was consequently used in the experimental seismic response evaluation of suspended piping restraint installations [Perrone et al. 2019]. Based on the results of a field survey in seismic regions in southern Europe, the following four typologies of suspended piping restraint installations were found to be most common practice and were therefore tested. These supporting typologies were

- Channel trapezes (vertical and horizontal channel) with transverse channel bracing systems,
- Channel trapezes with longitudinal channel bracing systems,
- Rod trapezes (vertical M10 rod and horizontal channel) with transverse rod bracing systems and
- Rod trapezes with longitudinal rod bracing systems.

For each typology three tests were conducted: one monotonic and two cyclic tests according to the FEMA-461 loading protocol. From the results of the tests, the following main conclusions can be drawn:

- All suspended piping restraints exhibited a significant strength capacity.
- No brittle failure occurred in any of the tests. While for the channel trapezes, the deformations were mainly concentrated in the connecting elements, for the rod trapezes significant deformations and buckling of the rods were observed.
- Independent of the failure mode and of the level of damage observed, no specimen lost its gravity load capacity in any test.
- All test specimens exhibited ductile behavior.
- Two performance objectives were identified for the performance-based seismic design of suspended piping restraint installations. The first damage limitation (DL) performance objective ensures the functionality of the building and that the suspended piping restraints can be repaired economically. The second life-safety (LS) performance objective ensures that the life-safety is not jeopardized by ensuring that the suspended piping restraint installations are still able to carry the gravity loads (i.e. the weight of the pipes and their contents) safely.
- The tests showed also that the effective ductility ratio (μ_{eff}), defined as the ratio of the ultimate to the yield displacements observed in each test, is an adequate and conservative Engineering Demand Parameter to predict the performance objectives described above.

Seismic numerical modelling of suspended piping trapeze restraint installations based on component testing was further performed for the above described four pipe suspension typologies [Perrone et al. 2019]. The main objective of this study was to develop reliable numerical models for the prediction of monotonic force–displacement curves to extract performance parameters for performance-based seismic design.

The numerical models were developed based on cyclic test data of the components that make up suspended piping trapezes. The quality of the numerical models' results was assessed against the above benchmark sub-assembly test results.

Based on this, the following main considerations can be drawn:

- No brittle failure occurred in any of the component tests and all components exhibited ductile response.
- Mechanics-based component models were developed for three of the tested components, which reproduced accurately the response of the tested specimens. For the other components the mechanical properties were directly introduced in the sub-assembly models.
- The numerical models were able to reproduce relatively accurately the results of the benchmark sub-assembly tests.
- The comparison between numerically predicted and experimental performance parameters, identified as the most critical for the elaboration of performance-based seismic design procedures for suspended piping restraint installations, demonstrated the effectiveness of the developed mechanics-based numerical models in predicting with acceptable accuracy these performance parameters without the need to conduct sub-assembly tests.

A variety of piping layouts was consequently designed based on state-of-the-art analytical design procedures and thousands of NTHDAwere carried out on these piping layouts. Building floor motions to which NSEs are attached were needed here and a stream-line process to quickly identify floor motion ensembles adequate for the performance evaluation of NSEs under various seismic hazard levels is found to be required. In this project 20 different horizontal ground acceleration records for three return periods, T_r, associated with different performance objectives were selected from the PEER NGA-West database: damage limitation (T_r = 95 years), life safety (T_r = 475 years) and collapse prevention (T_r = 2475 years) and applied on different building typologies to result in meaningful floor motions for the planned time history analysis of the piping layouts. Learning from this exercise, a framework for the quantification of non-structural seismic performance factors, to be used in the force-based seismic design of NSEs, has been proposed [Perrone et al. 2022]. The proposed framework is analogous to the existing FEMA P-695 methodology for the evaluation of seismic performance factors of code-compliant SFRSs. The application of the proposed framework to NSEs was illustrated through a case study example out of the research project that calibrated the behavior factor for suspended piping seismic restraint installations, designed according to the force-based design procedure of Eurocode 8 with a considered partial safety factor of 1.25 (= 1/0.8).

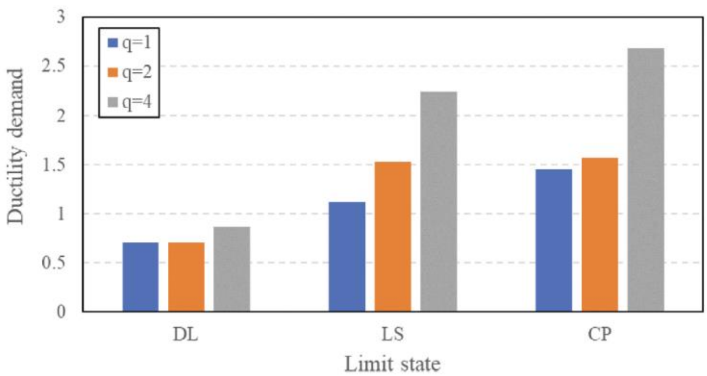

Figure 1: Performance evaluation in terms of meam + one standard deviation ductility demand on sway braced trapezes - Figure courtesy of [Perrone et al. 2022]

Excluding the collapse prevention performance objective as shown in Fig. 1, these results indicate that an effective ductility ratio $\mu_{eff} \geq 1.60$ is required for sway braced installation systems designed with the behavior factor of 2 as indicated in Eurocode 8. Sway braced installation systems showing an effective ductility ratio $\mu_{eff} < 1.12$ should not be used for seismic applications.

3.PROPOSED TESTING AND EVALUATION METHOD FOR SEISMIC RATING OF NSEs

Figure 2 shows a flowchart of the proposed approach for quantifying seismic rating of NSEs. The proposed framework consists of four phases. In phase 1, the cyclic tests are carried out in accordance with the FEMA 461 quasi-static cyclic loading protocol. The results of the cyclic tests are used to define performance parameters employing the provisions of FEMA P-795 (phase 2). In phase 3, acceptable performance level is established, following by quantifying the seismic rating of the NSE under evaluation in phase 4.

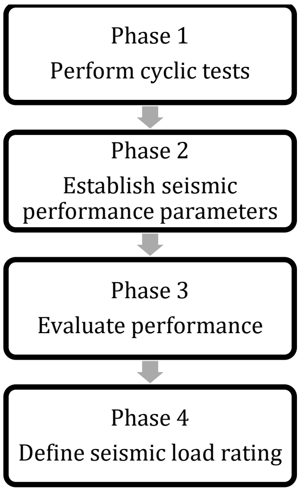

Figure 2: Proposed framework for seismic rating of non-structural elements

3.1 PHASE 1: PERFORM CYCLIC TESTS

The cyclic tests shall be carried out following the FEMA 461 quasi-static cyclic loading protocol. The loading history consists of repeated cycles of stepwise increasing deformation amplitudes (Fig. 3). Two cycles at each amplitude must be completed. The loading history is defined by the following four parameters:

- Δ_0 = the targeted smallest deformation amplitude of the loading history.
- Δ_m = the targeted maximum deformation amplitude of the loading history. It is estimated as the value at which the largest damage level is first observed. This value has to be estimated prior to the test. it can be estimated from a monotonic test, measuring the displacement after 20% decay of the ultimate load, Δ_m.
- n = the number of steps (or increments) in the loading history. It shall be 10 or larger.
- a_i = the amplitude of the cycles, as they increase in magnitude, such that $a_1 = \Delta_0$, $a_n = \Delta_m$, and $a_{i+1} = 1.4a_i$.

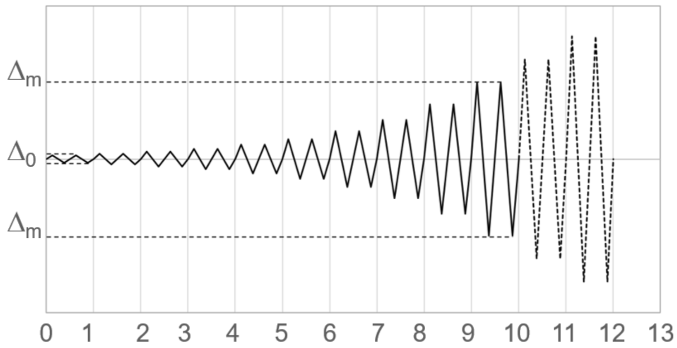

Figure 3: Example of FEMA-461 cyclic loading protocol

If the specimen has not reached the final damage state at Δ_m, the amplitude shall be increased further by constant increment of 0.3 Δ_m. If failure occurs before the 8th loading step, cyclic testing must be repeated starting at smaller Δ_0. Duration for one loading cycle shall not be shorter than 20 seconds to prevent inertia effects.

3.2 PHASE 2: ESTABLISH SEISMIC PERFORMANCE PARAMETERS

The results of the cyclic tests are used to define performance parameters inspired from the FEMA P-795 methodology [FEMA 2011]. Four main parameters are defined as: 1) the maximum lateral load capacity, 2) the effective yielding displacement, 3) the ultimate displacement; and 4) the effective ductility capacity. Figure 4 illustrates an example of cyclic-load test data envelope curve and response parameters.

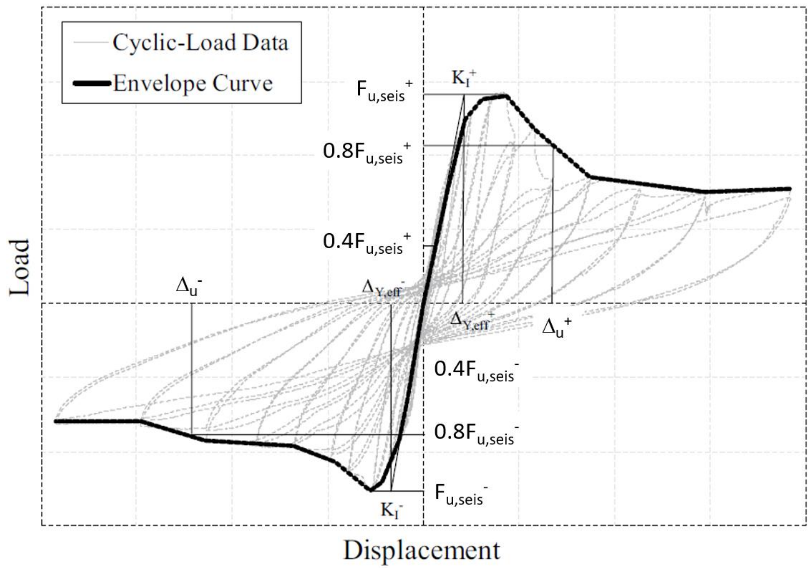

Figure 4: Definition of cyclic test response parameters

$F_{u,seis}$ = Ultimate load in the cyclic test.

K_I= Initial stiffness based on force and deformation at 0.4 $F_{u,seis.}$

$\Delta_{Y,eff}$ = Effective Yield displacement defined as $F_{u,seis}$ / $K_{I.}$

Δ_U = Ultimate deformation corresponding at 0.8 $F_{u,seis}$ in the post peak range.

μ_{eff} = Effective ductility capacity defined as Δ_U / $\Delta_{Y,eff}$

Values of each parameter should be measured from both positive and negative portions of the envelope curve, as illustrated in Fig. 4.

3.3 PHASE 3: EVALUATE PERFORMANCE

In this phase, it is crucial to establish the acceptance criteria that the NSE under evaluation is aiming to achieve. This criterion can be defined based on the acceptable level of damage selected for a specified earthquake intensity level. The achievement of the acceptable performance can be related to many response parameters characterizing the seismic behavior of the NSEs. For this purpose, the effective ductility capacity is considered to be the most suitable response parameter in the performance evaluation. Qualified NSEs should meet a minimum effective ductility capacity otherwise the lateral load capacity will reduce.

Perrone et al. [2022] provides recommendation on required ductility demand for various limit states and behavior factors. Based on those results, minimum effective ductility capacity of μ_{eff} = 1.60 is proposed for this criterion. Also, NSEs exhibiting an effective ductility capacity $\mu_{eff} < 1.12$ should not be used for seismic applications under the consideration of the deformation limitation and life safety performance objective.

3.4 PHASE 4: DEFINE SEISMIC LOAD RATING

Rated load may be expressed in terms of Load Resistance Factor Design (LRFD), where the nominal strength (R_n) is multiplied by a resistance factor (ϕ) less than one, or in terms of Allowable Stress Design (ASD), where the nominal strength is divided by a safety factor (Ω) larger than one.

Minimum of three tests for each NSE is recommended. The nominal strength for the NSE is found by examining the cyclic test data and identifying the smallest ultimate seismic strength from the test samples. Note that tested NSE shall satisfy a minimum ductility capacity of 1.6, otherwise lateral load capacity shall be further reduced by the factor of μ_{eff} /1.60. Also, NSEs with effective ductility capacity smaller than 1.12 are considered unqualified for seismic applications. For load rating, resistance factor is recommended to be taken as ϕ =0.80. Also, the recommended safety factor is Ω =1.8.

4.ILLUSTRATIVE EXAMPLE OF PROPOSED FRAMEWORK

To describe the implementation of the proposed framework presented above, an example is provided in this section. The tested NSE consists of a trapeze with transverse channel bracing. This configuration includes Hilti MQS channels. The distance from the ceiling to the horizontal channel is 800 mm, while the length of the horizontal channel is about 800 mm. The diagonal channel is inclined by an angle of 45 degrees. Figure 5 illustrate the tested specimen configuration.

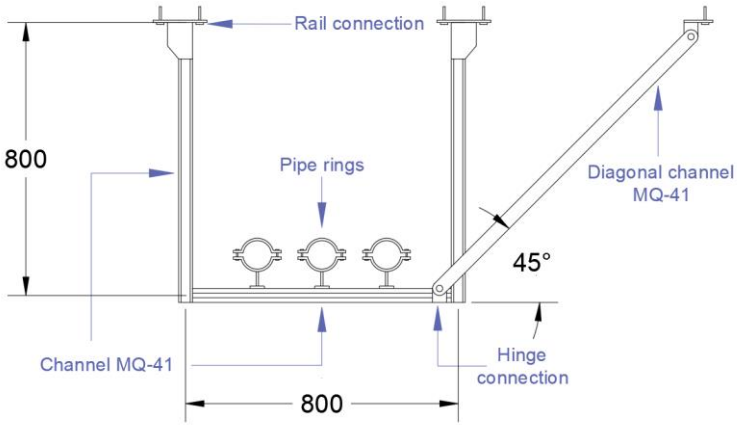

Figure 5: Trapeze with transverse channel bracing system

Two types of tests shall be carried out on the system: monotonic test and cyclic test. The monotonic loading protocol (Fig. 6) consists of a linear ramp until the failure of the testing component or system occurs. The failure is achieved when 20% decay of the maximum load-bearing capacity (after peak force) is observed.

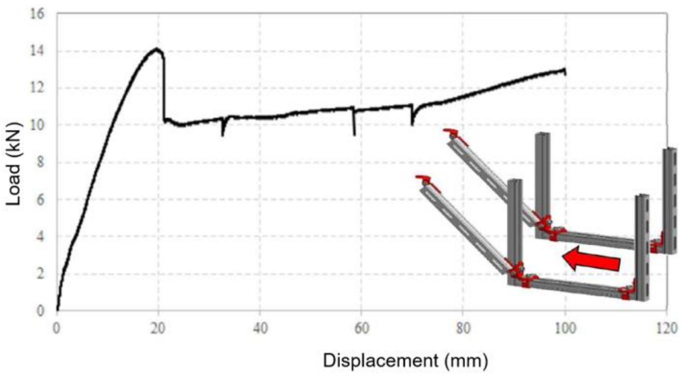

Figure 6: Monotonic force-displacement curve for tested specimen

The target displacements parameters are then estimated based on the performed monotonic test results (Fig. 6). The parameter Δ_m is the deformation at which the most severe damage level is expected. Table 1 shows the ratios a_i/a_n according to FEMA 461. These ratios are a function of the number of steps, considering the expected amplitude at the last step, an, to be equal to Δ_m.

Table 1: Relative loading history deformation amplitude

n	1	2	3	4	5	6	7	8	9	10	11	12	13
a_i/a_n	1.000	0.714	0.510	0.364	0.260	0.186	0.133	0.095	0.068	0.048	0.035	0.025	0.018

Based on monotonic test results, Δ_m is estimated to be about 21.3 mm. For the performed tests in this example, 10 steps were used in the FEMA 461 loading protocol with $a_1 = 0.048\ \Delta_m = 1.03$ mm (this value corresponds to Δ_0). Figure 7 illustrates a FEMA 461 cyclic loading protocol. The values shown in the figure below are normalized with respect to the target maximum displacement, Δ_m.

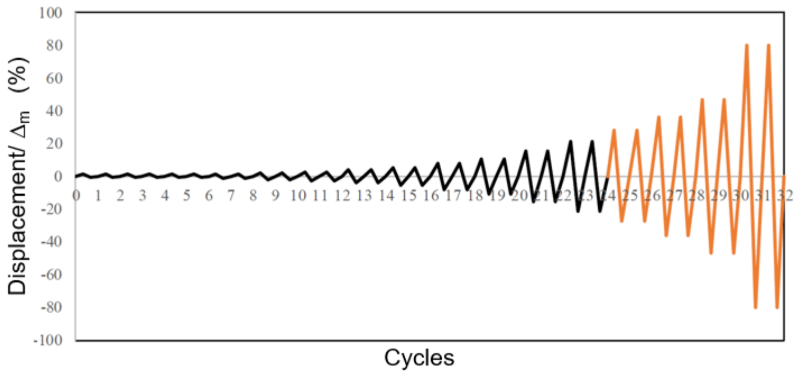

Figure 7: Cyclic loading protocol of the tested specimen

The system was subjected to a various cycle of displacement along its transverse direction as depicted in Fig. 7. The load was imposed in displacement control. It has to be highlighted that the effective necessary cycles calculated from the performance parameters is represented by the black line in Fig. 7. The red line indicates further steps that have been applied since the failure of the specimen was not achieved after 10 steps.

Figure 8 shown the hysteretic force-displacement curves obtained during the test. The maximum loads in compression and tension were 12.9 kN and 18.94 kN, respectively. The maximum displacement was 53 mm in compression and 61 mm in tension.

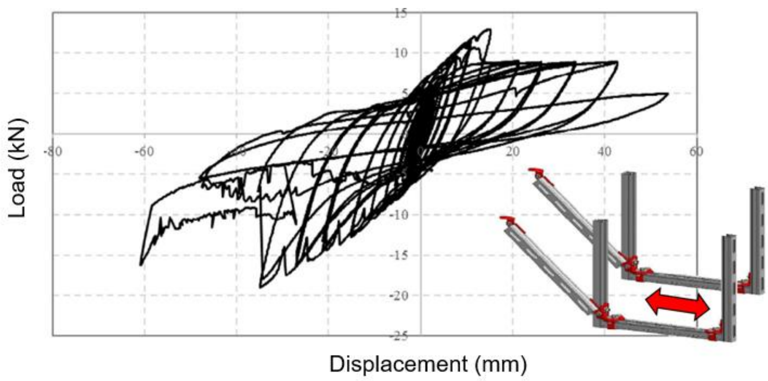

Figure 8: Hysteretic force-displacement curve of the specimen

Table 2 reports performance parameters of the tested system. The overall effective ductility capacity is μ_{eff} =2.09, which is greater than the acceptable range of 1.6. Therefore, no reduction was needed for the lateral load capacity. Lateral load capacity (R_n) was defined as the minimum of maximum tension and compression loads obtained in testing which was Min(12.75kN,18.94kN) = 12.75kN. The rated load for allowable stress design method (ASD) is calculated R_n/Ω = 12.75/1.8 = 7.08 kN, and for Load Resistance Factor Design (LRFD) is calculated as ϕ*Rn = 0.8*12.75 = 10.2kN.

Table 2: Performance parameters of the specimen

$F_{u,seis+}$ (kN)	$F_{u,seis-}$ (kN)	Δ_{u+} (mm)	Δ_{u-} (mm)	Δ_u (mm)	K_I^+ (kN/mm)	K_I^- (kN/mm)	K_I (kN/mm)	$\Delta_{y,eff}^+$ (mm)	$\Delta_{y,eff}^-$ (mm)	$\Delta_{y,eff}$ (mm)	μ_{eff}	R_n (kN)
12.75	18.94	15.29	34.86	25.08	1.49	1.23	1.36	8.56	15.40	11.98	2.09	12.75

5.CONCLUSION

In this paper, a framework for evaluating the seismic performance of non-structural elements (NSEs) and systems is presented. The framework is stablished based on the outcome of an extensive research project between EUCENTRE and Hilti with the aim of understanding seismic behavior of NSEs and providing a standardized test-based procedure to quantify NSEs seismic rating to be used in the design of code compliant facilities.

The proposed framework consists of four phases. In phase 1, cyclic tests are carried out in accordance with the FEMA 461 quasi-static cyclic loading protocol. The results of the cyclic tests are then used to define performance parameters employing the provisions of FEMA P-795 in phase 2. Four main parameters are defined as: the maximum lateral load capacity, the effective yielding displacement, the ultimate displacement, and the effective ductility capacity. In phase 3, acceptable performance level that the NSEs under evaluation is aiming to achieve is established. The effective ductility capacity is considered as the most suitable parameter in the performance evaluation. Qualified systems shall meet a minimum effective ductility of 1.60, otherwise the lateral load capacity will reduce. Also, NSEs exhibiting an effective ductility capacity less than 1.12 are not qualified for seismic applications. In phase 4, the seismic rating of the system under evaluation is defined. Rated load may be expressed in terms of Load Resistance Factor Design (LRFD), where the nominal strength multiplied by a resistance factor ϕ = 0.8 or in terms of Allowable Stress Design (ASD), where the nominal strength divided by a safety factor Ω= 1.8.

6.ACKNOWLEDGEMENTS

The work presented in this paper has been developed within the framework of the project "Dipartimenti di Eccellenza", funded by the Italian Ministry of University and Research at the University School for Advanced Studies IUSS Pavia. The authors gratefully acknowledge the technical staff of the ShakeLab Laboratory at EUCENTRE for conducting the testing program referred to in this paper, and the Italian Department of Civil Protection (DPC) for their financial contributions to this study through the ReLUIS 2019-2021 Project (Work Package 17 - Contributi Normativi Per Elementi Non Strutturali).

7.REFERENCES

FEMA 461 [2007] *Interim testing protocols for determining the seismic performance characteristics of structural and non-structural components*, Federal Emergency Management Agency (FEMA), Washington, D.C.

FEMA P-695 [2009] *Quantification of Building Seismic Performance Factors*, Federal Emergency Management Agency (FEMA), Washington, D.C.

FEMA P-795 [2011] *Quantification of building seismic performance factors: component equivalency methodology*, Federal Emergency Management Agency (FEMA), Washington, D.C.

Filiatrault A, Perrone D, Brunesi E, Beiter C, Piccinin R [2018] "*Effect of cyclic loading protocols on the experimental seismic performance evaluation of suspended piping restraint installations*," Int J Pip Vessels; 166:61–71. https://doi.org/10.1016/j.ijpvp .2018.08.004

Perrone, D., A. Filiatrault, S. Peloso, E. Brunesi, C. Beiter, and R. Piccinin. [2020a] "*Experimental seismic response evaluation of suspended piping restraint installations,*" Bulletin of Earthquake Engineering; 18 (4): 1499–524. https://doi: 10.1007/s10518-019- 00755-5

Perrone, D., E. Brunesi, A. Filiatrault, S. Peloso, R. Nascimbene, C. Beiter, and R. Piccinin. [2020b] "*Seismic numerical modelling of suspended piping trapeze restraint installations based on component testing*," Bulletin of Earthquake Engineering; 18 (7): 3247–83. https://doi: 10.1007/s10518-020-00832-0

Perrone, D., A. Rodriguez, D., Filiatrault., E. Brunesi, C. Beiter, and R. Piccinin. [2022] "*A Framework for the Quantification of Non-Structural Seismic Performance Factors,*" Journal of Earthquake Engineering; https://doi: 10.1080/13632469.2021.1991516

Performance Assessment of Seismically-Damaged Firestopping Systems: A Preliminary Framework

Zhaoyu Ye[1], Anthony K. Abu[2], Charles M. Fleischmann[2], Rajesh P. Dhakal[2]

[1] University of Canterbury
Christchurch, New Zealand
e-mail: vivian.ye@pg.canterbury.ac.nz
[2] University of Canterbury
Christchurch, New Zealand
{anthony.abu, charles.fleischmann, rajesh.dhakal}@canterbury.ac.nz

Abstract. Through-penetration firestopping systems are non-structural passive fire protection elements made up of fire-resistive wall or floor assemblies, penetrating service members and firestop seals. Current evaluation of their performance is based on standard fire testing, without consideration of any other damage that could occur during normal service. Evidence from global earthquakes have however shown that distinct integrity failures may occur in these systems which may limit their effective fire performance, even under relatively minor to moderate earthquakes. If the integrity failures are not picked up the pre-damaged firestopping system could cause significant life and economic losses in future fire events. The effective fire resistance of a pre-damaged firestopping system will depend on the individual contributions of the components of the system and the level of seismic excitation it is exposed to. However, there are no known methodologies to consistently assess the performance of these systems exposed to these hazards during their service life. To address this gap, and to help develop design guidance for firestopping systems in seismic-active regions, this paper proposes a preliminary assessment framework to evaluate the residual performance of non-structural through-penetration firestopping systems after different levels of seismic movement. The framework is developed based on small-scale experimental studies that investigate the thermal performance of a simple firestopping wall assembly after unidirectional seismic damage.

Keywords: Non-structural passive fire protection, Seismic damage, Through-penetration firestopping, Fire after earthquake, Non-standard testing method.

1. INTRODUCTION

Firestopping systems are non-structural fire protection assemblies which are designed to maintain fire resistance when building service components pass through fire separation elements of a building [Gillespie *et al.*, 2007]. A typical firestopping system encompasses three main components: a fire-resistive wall or floor, a penetrating member (e.g. pipe or cable system) and a firestop seal. If the fire-resistive substrate (wall or floor) is completely penetrated throughout its depth, the system can be called a through-penetration firestopping system [ASTM International, 2017], as illustrated in Figure 1.

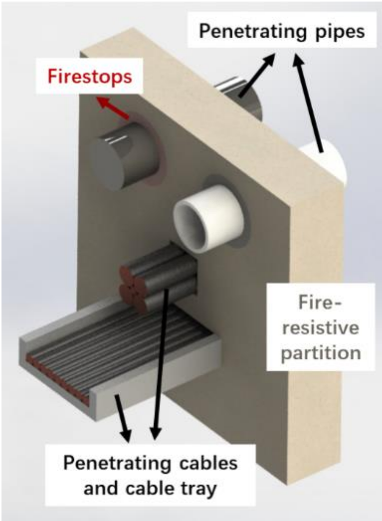

Figure 1. An illustration of through-penetration firestopping system for a wall assembly

These firestopping systems are designed to restrict fire spread across a fire barrier over a given duration, which is universally rated by how long the system survives in the standard furnace test. As a non-loadbearing passive fire protection system, its fire resistance is rated under both integrity and insulation criteria [International Organization for Standardization, 1999; European Committee for Standardization, 2009; ASTM International, 2017]. The integrity criterion fails when movement of flame and/or smoke propagates to the non-fire exposed side of the fire-resistive assembly, while the insulation criterion assesses the temperature rise across that unexposed surface (i.e. thermal penetration). Depending on the particular country, additional assessment criteria (e.g. air leakage, water rating, etc.) may also be included [Underwriters Laboratories (UL), 2015; International Code Council, 2021]. However, conventional standard fire assessments only focus on determining the fire resisting performance of tested systems in an idealized uniformly heated environment, without considering any additional factors that may negatively influence their functionality during their normal usage. For example, the fire testing standard AS 1530.4 [Standards Australia, 2014] states that tests to firestopping system never consider "the ability of penetration sealing systems to withstand stress caused by movements or displacements of the penetrating services".

Nonetheless, a series of site surveys conducted after the 2011 Christchurch earthquake indicated that firestopping systems were severely damaged by the magnitude 6.3 earthquake, with the formation of large gaps between penetrations and firestop seals, as shown in Figure 2. Similar observations were recorded in the 1994 Northridge earthquake, where significant cracks developed between pipe penetrations and stud walls [Federal Emergency Management Agency (FEMA), 2012]. The openings could act as potential paths that channel fire and smoke spread between compartments and ultimately shorten the fire safety of the building. However, these defects are usually neglected during routine inspection and post-disaster remediation because of access constraints and less pronounced cost benefits [Frank *et al.*, 2018]. Without properly mending the problem, the actual (residual) fire resistance of these pre-damaged systems is unknown. Depending on the level of damage as well as the actual components making up the firestopping system, there could be a range of possibilities; sufficient fire resistance, reduced fire resistance or zero fire resistance. Test standards such as ASTM E3037 [ASTM International, 2020a], ASTM E1966 [ASTM International, 2019] and ISO 11600 [International Organization for Standardization, 2003] provide some guidance to estimate the movement capability of firestops during seismic activity, but the residual fire performance of potentially-damaged firestopping systems has not yet been examined. The potential negative impacts of seismic damage on overall performance of fire compartmentation have also not yet been raised in any mandatory fire testing standards. Since the reliability of these "damaged" systems cannot yet be quantified, the overall safety of modern construction is questionable. This is particularly an issue for seismically active countries, such as United States, New Zealand, Japan and so on.

(a)

(b)

Figure 2. Voids created around penetrations in fire rated walls after: (a) the 2011 Christchurch earthquake [Abu, 2012]; (b) the 1994 Northridge Earthquake [Perry et al., 2017]

Compared to structural members, there is a paucity of understanding of seismic capacity and associated dynamic response of most non-structural building elements (NSEs) to date [Stanway *et al.*, 2018]. Apart from diverse external factors (e.g. local seismicity, characteristics of design building, etc.), this deficiency in knowledge could also be attributed to intricate boundary conditions of different NSEs [Ellingwood and Kinali, 2009]. In terms of firestopping systems, which run through a wall assembly, the penetrating members may be classified as acceleration-sensitive members, whose seismic response is influenced by the floor above them [Dhakal *et al.*, 2016]. On the other hand, a non-loadbearing fire partition can be categorised as both drift- and acceleration-sensitive NSE, since its primary response is controlled by relative displacement between two adjacent storeys (i.e. seismic-induced drift); but occasional out-of-plane deformations may also occur depending on the rigidity of the panel [Rahmanishamsi *et al.*, 2017]. Therefore, for firestop seals which are installed between service penetrations and fire-resistive substrates (walls or floors), their seismic performance could be significantly influenced by their interactions with both the penetration and wall panel, with incompatible movements occurring at the interfaces [Pourali *et al.*, 2020]. However, these interactions and resultant damage have not been well-investigated. Knowing the movement capability and deformability of firestop seals would be crucial to determining the overall damage at the interface after seismic events. It is therefore vitally important to determine how each firestopping component would interact with others during earthquake and fire scenarios, to help develop appropriate recommendations for future design.

To improve life safety designs of buildings in earthquake-prone regions, this paper aims to outline a universal assessment framework which would be used to ascertain the performance of general non-structural firestopping systems under fires following earthquakes. It needs to be emphasised that this study investigates scenarios that would normally be classified under low to moderate intensities of earthquakes, which may not immediately cause fires, but may damage the firestopping systems, thereby reducing their resistance against a fire that occurs later. On that basis, the response of firestopping systems under seismic and fire hazards can then be assessed independently in sequence. As a part of a systematic research program to identify the correlation between the level of seismic damage and residual performance of firestopping systems, the key objective of this paper is to present a holistic evaluation methodology.

Firestopping systems can be put together from multiple combinations of their main constituents (firestop seal, penetration and substrate). It is therefore difficult to describe them all with a unified system behaviour. For instance, fire-rated barriers are made by different construction materials (e.g. drywall, masonry-infill, reinforced concrete, etc.) while common service penetrations may include plastic/metallic pipes and cable systems. Besides, in today's market, there are various firestopping solutions that have been well-applied for different service penetrations. For plastic pipes, which are combustible and fragile, intumescent sealants (e.g. silicon or acrylic caulk) are used to fill the increased size of the gap, caused by thermal deformation [Thurston, 1996; Sędłak *et al.*, 2017], while high conductive metal pipes and cable systems use advanced solutions such as speed sleeves and firestop blocks. These act as local insulators to prevent direct contact between penetrations and substrates (i.e. they impede efficiency of heat transfer) [Association for Specialist Fire Protection (ASFP) *et al.*, 2020]. The selection of a firestop seal could also be influenced by other factors such as construction material of fire-resistant assembly, penetration type, size and number of apertures, required fire resistance rating (FRR), aesthetic appeal as well as costs [Sheet Metal and Air Conditioning Contractors' National Association, 2007]. The diversity of firestopping combinations result in some difficulty in predicting their general performance, since each firestopping system setup produces very different thermal or mechanical response. It is neither practical nor economic to evaluate all possible firestopping assemblies. As such, only a basic representative firestopping setup is to be analyzed in this initial study. This basic firestopping system is made up of a fire-resistive concrete partition penetrated by a bare steel pipe. The firestop solution that has been chosen to seal the annular gaps between the perimeter of pipe and the inner surface of wall opening is the thermoplastic non-intumescent acrylic firestop sealant that is available in the current global market. This firestop material has been widely adopted to protect metal penetrations and can be installed across both wall and floor substrates. Depending on installation requirements of individual products, an additional mineral wool insulation layer may be embedded into the depth of the opening, especially for thick fire barriers or to target longer fire resistance times. Figure 3 shows a classic case of this assembly.

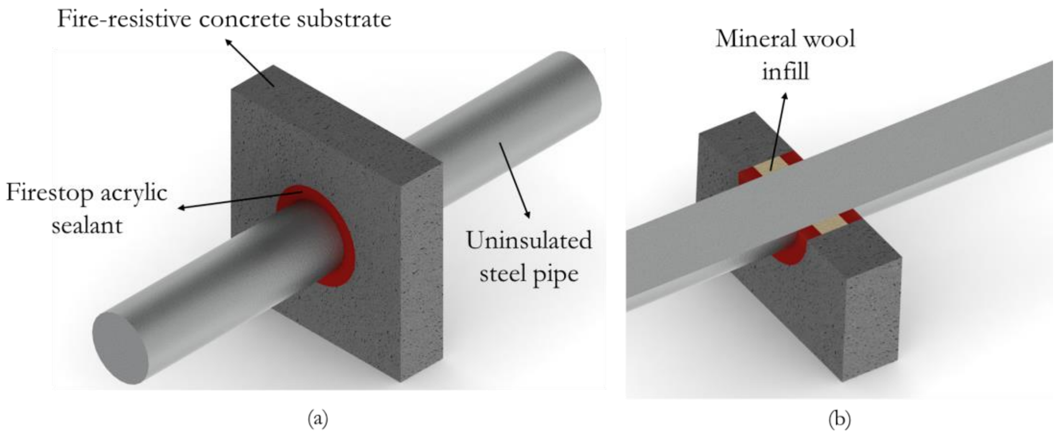

Figure 3. Configuration of selected firestopping system: (a) isometric projection; (b) cross-section view

The whole performance assessment is made up of two parts; a furnace test is performed after a seismic movement test. As an initial study in the field of non-structural seismic-fire research, the seismic actions are uniaxial only: movement along the pipe's longitudinal axis or along its transverse direction. Determination of seismic demand is also not included in the scope of the analysis, as the residual performance of the system is considered directly related to the extent of the resultant physical damage. Although the proposed methodology is developed at small-scale, it should be applicable at full-scale as well. Fragility functions, which will link different levels of seismic damage to residual fire resistance of these firestopping systems will be established. The specific application of the method and findings will be reported in the near future.

2. FORMATION OF ASSESSMENT FRAMEWORK

The proposed assessment method consists of two parts: a dynamic cyclic movement test to produce different levels of mechanical damage in the firestopping system, followed by a furnace test to ascertain the residual fire resistance. The residual fire resistance can then be compared with the original fire resistance of the system to quantify the impact of seismic damage on the functionality of the fire separation. The holistic assessment procedure is summarized in Figure 4. A detailed explanation of the proposed framework is provided in the subsequent sections. The practicality of this methodology will be investigated with small-scale testing at the University of Canterbury (UC) fire engineering lab.

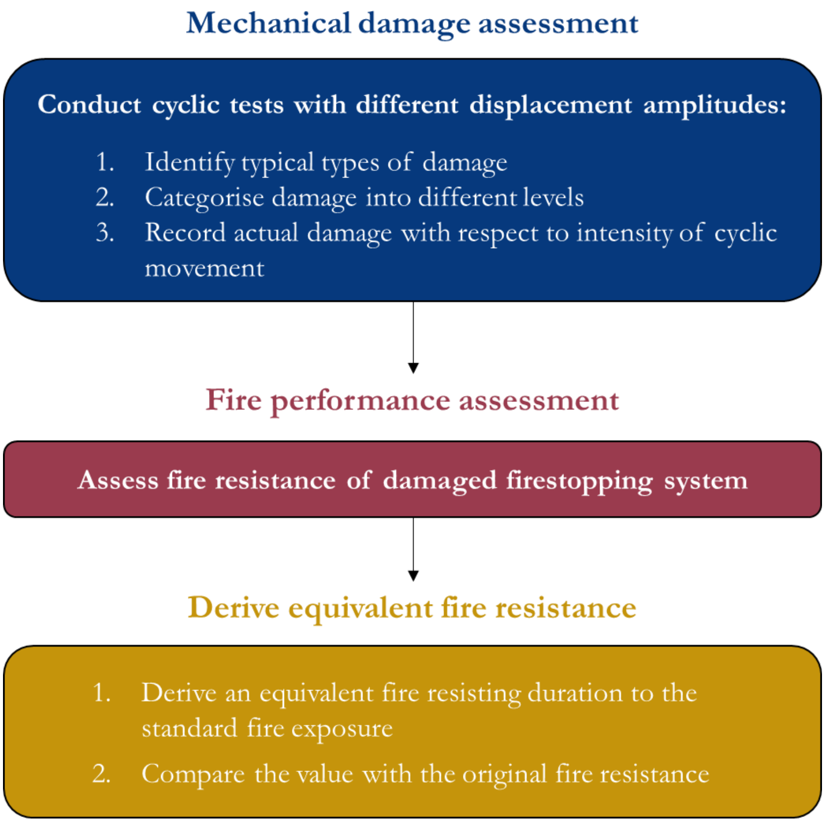

Figure 4. A flowchart of analysis steps

2.1 PHASE I: ASSESSMENT OF SEISMIC-INDUCED DAMAGE

Different firestop materials will produce distinct damage behaviour. In the proposed study, the movement tolerance of the acrylic firestop sealant, which relies on adhesive bonding at contact interfaces, is expected to be large in comparison to other rigid firestop devices, such as firestop collar or speed sleeves, which require additional attachments for their installations [Hilti Inc. (U.S.), 2017; Vali, 2020]. If the relative displacement at the firestop interface becomes significantly large, then the sealant could fail, causing the assembly to lose integrity. Compared to the rigid concrete substrate and metal pipe, the firestop sealant is more likely to damage first when expose to earthquakes. The two most common failure modes of viscoelastic sealants in the literature [Kšiňan and Vodička, 2013] are (see Figure 5):

1. Cohesion failure: fracture developed within the sealant layer
2. Adhesion failure: debonding at the interface between a solid surface and the sealant

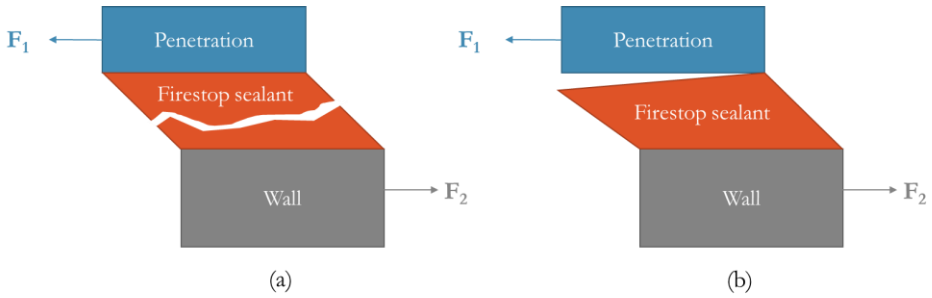

Figure 5. Possible damage patterns at firestop interface when subject to shear movement: (a) cohesion failure; (b) adhesion failure [Nezhad and Stratakis, 2017]

As the aim of this research is to determine the effective fire performance of firestopping systems rather than investigate real seismic behaviour, the mechanical damage assessment is only intended to identify the different levels of damage that could occur at the firestop interface. The size of induced cracks under different intensities of shaking can then be used as the damage measure (DM_s) for the associated seismic effects. By correlating this parameter to a measure of fire response (e.g. the probability of an early failure of fire separation, DM_f), determined in the next stage of assessment, the impact of the seismic damage on functionality of the non-structural passive firestopping system can be quantified.

Since earthquakes are naturally variable, investigating a more general response of the system requires that the cyclic loading sequence does not follow any particular seismic history. Instead, a design displacement protocol is applied to clearly track the resultant deformation or damage of the system at each level of cyclic movement. To develop a reasonable cyclic loading protocol, three important parameters need to be determined: speed of applied motion, the amplitude of movement and the number of repeated cycles for each incremental step.

The applied loading rate would be critical to firestopping systems, especially for elastic firestop sealants, whose structural response is usually sensitive to the strain rate in a non-linear manner [Yu *et al.*, 2001; Takiguchi *et al.*, 2004; Mattos *et al.*, 2016; Gursel and Cekirge, 2019]. Experimental investigations conducted by Modala (2019) indicate that for both brittle and ductile adhesives under shear, the peak strain at failure is likely to reduce under a high loading rate. In addition, very different damage behaviour can occur when there is a change in the velocity of the seismic action. The same conclusion was also drawn in experimental studies by Johar et al. (2015) and Dal Lago et al. (2017). The recommended quasi-static loading rate for evaluating the movement capability of firestopping systems in ASTM E3037 [ASTM International, 2020a], which is not a mandatory testing standard, is between 6.35 and 10.6 mm/s. The imposed motion is considered slow enough to ignore dynamic inertia effects. In contrast, the literature shows that for NSEs in dynamic motion, the frequency of loading can vary from 0.1 to 20 Hz [Retamales *et al.*, 2008; Hutchinson and Wood, 2013; Bianchi *et al.*, 2021], within which 1.5 Hz to 3 Hz was found to "match the 84th percentile of cycles created by real seismic floor motions" [Retamales *et al.*, 2011]. These dynamic loading frequencies are much higher than the quasi-static movement speeds suggested by ASTM E3037. Due to the different material characteristics of firestop products (not just firestop sealants), it is not practical to just use a single movement testing speed for all firestop solutions without validation. Since the effect of displacement rate on the residual performance of these systems has not been well-researched yet, a series of cyclic tests is proposed to compare the consequent damage of typical firestopping systems under different displacement rates. The investigation would at least help to identify whether the quasi-static loading rate suggested in ASTM E3037 is conservative enough. For non-quasi-static loading, a shake table is recommended. Once a critical displacement rate has been determined, it can be maintained for the rest of the damage assessments.

In this project, the magnitude of the displacement is taken as the key variable which should correspond to the level of seismic damage. Because of limited understanding of the seismic response of firestop seals, a monotonic loading test will be carried out to determine appropriate displacement intervals before conducting the cyclic loading tests. This would be based on the material's unique behaviour [Applied Technology Council, 2007], such that

$$\delta_{\text{cyclic, i}} = \chi \cdot \delta_{\text{monotonic}} \tag{1}$$

where δ_{cyclic} and $\delta_{\text{monotonic}}$ stand for the cyclic and monotonic displacements in respective. χ is a ratio in range $0<\chi\leq 1$ and index *i* represents the loading step.

However, in contrast to directly employing a conventional continuous incremental loading protocol (e.g. $\delta_{\text{cyclic displacement at step (i+1)}} = 1.4\ \delta_{\text{cyclic displacement at step (i)}}$ as suggested in FEMA 461), tests with different movement amplitudes would be conducted and analysed independently. It would start with the peak displacement amplitude and then descend with a constant ratio, in order to identify critical displacement magnitudes that correspond to damage initiation and ultimate failure. If significant damage is not noticed at particular displacement steps, then no additional assessments need to be conducted at those displacement levels. The displacement amplitudes that activate critical mechanical damage with visible cracks will then be identified.

Conventionally, ordinary seismic loading protocols usually introduce repeated loading or displacement cycles to account for the cumulative damage caused by the continuous seismic shaking. FEMA 461 [Applied Technology Council, 2007] suggests that for NSEs with low-cycle fatigue features, the number of repeated cycles at the initial displacement should be 10. For subsequent cycles of displacement increments, each displacement amplitude should be repeated in 3 cycles. In the current study, the magnitude of displacement is taken as the dominant variable that should correspond to different levels of seismic damage. The number of repeated cycles for each displacement step is therefore chosen to be constant at three.

After completing the mechanical damage assessments, a range of crack sizes under different dynamic movement intensities will be collected. Then, by placing each "damaged" specimen directly into a furnace test, as described in the following section, the level of reduction of fire resistance of the "earthquake-damaged" firestopping systems shall be obtained.

2.2 PHASE II: DETERMINATION OF REDUCED FIRE RESISTANCE

Fire resistance rating (FRR) of building components is obtained from a standard furnace test [International Organization for Standardization, 1999; ASTM International, 2020b]. During this test, each fire protection component is placed in a uniform heating environment controlled by a nominal furnace time-temperature profile. The test models a post-flashover fire exposure, during which everything in a room is considered to be burning without decay [Buchanan and Abu, 2017].

For fire protection of building elements, FRRs are determined based on their failure time under standard fire exposures, which are assessed based on three criteria: Stability (R), Integrity (E) and Insulation (I). The stability criterion examines the load bearing capacity of structural members at elevated temperature. The integrity criterion examines the effectiveness of the element against flame and smoke penetration, while the insulation criterion is to slow temperature growth on the unexposed side of the element. For a non-loadbearing fire separation system, its fire resistance is determined by the integrity and insulation criteria [International Organization for Standardization, 1999; ASTM International, 2017]. The integrity criterion fails when either a cotton pad ignites on the non-fire side of the fire-resistive assembly, any sustained flaming can be observed on the unexposed surface, or a gap gauge is able to pass through the specimen (i.e. a 6 mm gap gauge can penetrate more than 150 mm across the gap depth, or a 25 mm gap gauge can freely pass to the non-fire end). If any of these integrity failure criteria are observed, it indicates that the penetrated depth of the thermal-induced voids is large enough to allow a possible flame or smoke spread. On the other hand, the insulation criterion assesses the temperature rise across the unexposed surface. This criterion fails when either the average temperature rise of the surface reaches 140 °C, or any part of that surface achieves a temperature rise of 180 °C. For seismically damaged firestopping systems, the resultant cracks throughout the firestopping assemblies are likely to create additional paths for both flame and heat penetration. As such, the corresponding integrity and insulation performance are expected to fail earlier in comparison to their nominal fire resisting period. Based on that, the key objective in this part of the assessment is to identify the residual fire resistance of the through-penetration firestopping system given a level of earthquake damage.

The electrical furnace intended to be used for the study is at bench-scale. It is not capable of replicating the idealized heating environment of the standard fire furnace. The fire tests are therefore carried out under a linear temperature growth profile with a constant heating rate. From previous fire research [Anaut Rufas, 2010; Mihindukulasuriya, 2012; Zarrelli *et al.*, 2012; Bjørge *et al.*, 2018], steady-state heating has been achieved between 1 to 100 °C/min for electrical furnaces, with majority of studies between 5 and 50°C/min. In this study, the 'pre-damaged' firestopping system will exposed to a slow heating rate of 10 °C/min. The gas temperature inside the furnace will become stable once it reaches 1000 °C as shown in Figure 6. Nonetheless, the tested performance of the firestopping system will be compared to the standard fire exposure using the equivalent time approach as described by Nyman [2002].

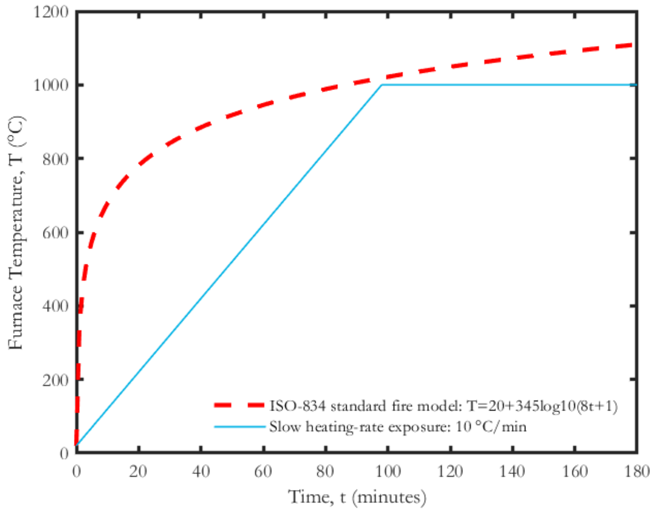

Figure 6. comparison of standard fire curve with the constant slow heating rate

2.3 PHASE III: DERIVATION OF EQUIVALENT FAILURE TIME BETWEEN STANDARD AND NON-STANDARD FIRE EXPOSURES

To help explain Nyman's equivalent time approach [2002], a heat-transfer analysis of a pure concrete wall without any mechanical damage is modelled in the finite element solver ABAQUS [Dassault Systèmes, 2020]. This modelled concrete substrate has a nominal thickness of 75 mm, based on a fire resistance of 60-minutes [European Committee for Standardization, 2004]. An eight-node linear heat transfer brick (DC3D8) was assigned to mesh elements for a thermal analysis. The mesh size was 5 mm to ensure the mesh was considerably fine, while avoiding numerical convergency errors. The heating effects were modelled by the convective and radiant heat transfer at boundaries. As per the recommended heat transfer coefficient values in Eurocode 1 Part 1.2 [European Committee for Standardization, 2002], a convection coefficient of 25 W/m²K with a radiation emissivity of 0.8 was defined at the fire-exposed boundary. By contrast, the convection coefficient was set to be 9 W/m²K on the unexposed end. The rest of the boundaries were all assumed to be adiabatic. The thermal response of the normal-weight concrete was defined by temperature-dependent material properties, including thermal conductivity, specific heat and density values as suggested in BS EN 1992-1-2 [European Committee for Standardization, 2004].

By applying the insulation criterion based on average temperature-rise (i.e. $\overline{T}_{unexposed} \leq 160$ °C from ambient temperature), the numerical results show that the substrate would likely fail its insulation criterion at about 98 minutes under the constant heating rate of 10 °C/min. Then, by plotting a cumulative radiant energy curve for each temperature profile using the Equation (2) below, an equivalent failure time can be estimated by looking for the intersection where the non-fire-exposed side would receive the same amount of energy from the standard fire and the non-standard heating scenarios. The data plotted on Figure 7 shows that by using the above time-equivalence method, the same substrate would fail at 51 minutes when exposed to standard fire condition.

$$E''_{rad} = \varepsilon\sigma \int_0^t T(t)^4 dt \qquad (2)$$

where ε is the emissivty (typically 0.7 for concrete), T(t) is the time-dependent hot gas temperature inside the furnace in unit of Kelvin and σ is the Stefan-Boltzmann constant (5.67×10^{-8} W/m^{2}K^4).

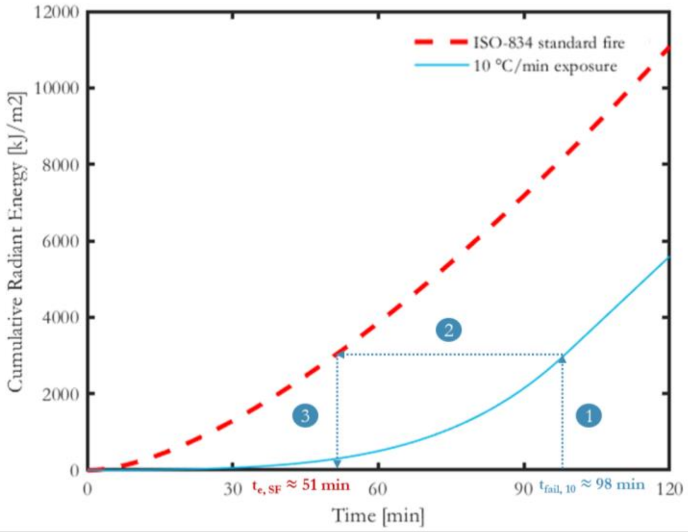

Figure 7. Derivation of equivalent failure time to standard fire exposure

However, the above numerical estimate cannot be treated as reliable failure time until it is confirmed by experimental data. Also, this method is ideal to estimating equivalent insulation performance of fire barriers, but not ideal for integrity failures. The electrical furnace is unable to capture integrity failure under turbulent and high-pressure fires. As such the suitability of the CRE method for earthquake-damaged firestopping systems will need to be further examined at large-scale, which is planned in subsequent studies to this initial investigation described in the current study.

3. EXPERIMENTAL SETUP

The proposed experimental setup for the development of the assessment framework is illustrated as shown in Figure 8. Concrete walls will be fixed in position and attached to the ends of the electric furnace. Displacements will be applied along the axial or lateral directions of the pipe by using a small-scale shaking table. This setup is to help induce relative movements and corresponding damage at the pipe-firestop interface. Once the induced crack widths under each dynamic movement have been recorded, the "damaged" firestopping assembly, attached to the electrical furnace, is exposed to the design heating regime described in Section 2.2. The relevant temperature measurements and other performance indicators (e.g. cotton pad ignition and passage of gap gauges) will follow the rules of AS 1530.4 [Standards Australia, 2014].

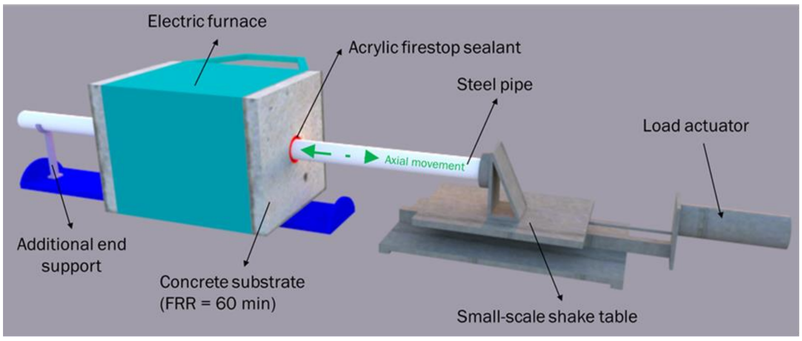

(a)

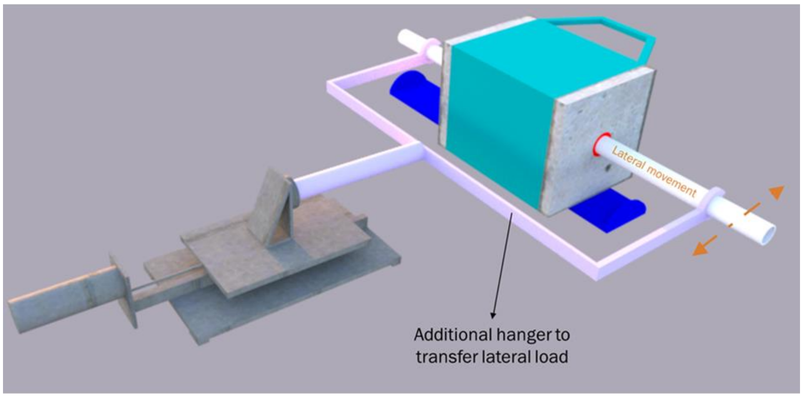

(b)

Figure 8. Illustration of test setup: (a) pipe movement along axial direction; (b) pipe movement along lateral direction

4. POTENTIAL PROBLEMS

The suggested assessment framework is intended to be applied to most firestopping systems, rather than for specific assemblies. As such, the investigation of the most basic firestopping combination that described above shall not be the only firestop sample used for the development of the testing methodology. However, each change in firestop solution may generate different measures and levels of seismic damage, making it challenging to develop a more unified approach for all firestopping systems. Taking intumescent firestop seals as an example, even analogous products could show very different pyrolysis behaviour (e.g. swelling, charring, etc.) under the same temperature, due to the differences in their chemical constituents. In other words, the corresponding residual fire performance of these firestop materials might also be affected by the exact damage that is recorded with each change in firestop solution. Thus, the proposed fragility functions may also be dependent on each firestop solution.

5. CONCLUSION

As a part of a systematic research to identify the reliability of through-penetration firestopping systems in the aftermath of minor to moderate earthquakes, this paper has presented a preliminary framework for assessing the residual performance of a basic through-wall firestopping system after receiving different levels of seismic damage. The proposed methodology is being trialled at small-scale for subsequent full-scale testing. A case study of a typical firestopping assembly consisting of a fire-resistive concrete wall barrier, an uninsulated steel pipe penetration and a commonly used firestop acrylic mastic is discussed in the text to help explain the overall analysis philosophy. It is expected that the methodology will enable the development of fragility functions to explicitly indicate the influence of seismic damage on resultant effective fire resistance of firestopping systems. The validation of the proposed framework has begun. The corresponding outcomes will be released in the near future.

ACKNOWLEDGEMENT

The authors would like to thank Hilti Corporation and the Ministry of Business Innovation and Employment (MBIE) for acknowledging and supporting this research topic.

REFERENCES

Abu A.K. [2012] "Post-Earthquake Fires and Damage to Fire Safety Systems". Christchurch

Anaut Rufas C. [2010] "Characterization of the degradation behaviour of Passive Fire Protector Materials"

Applied Technology Council. [2007] "FEMA 461: Interim Testing Protocols for Determining the Seismic Performance Characteristics of Structural and Nonstructural Components". Redwood City

Association for Specialist Fire Protection (ASFP), Building Engineering Services Association (BESA), Building Services Research and Information Association (BSRIA), Finishes and Interiors Sector (FIS), Gypsum Products Development Association (GPDA). [2020] "Firestopping of Service Penetrations: Best Practice in Design and Installation"

ASTM International. [2017] *ASTM E814-13a: Standard Test Method for Fire Tests of Penetration Firestop Systems*. ASTM International, West Conshohocken

ASTM International. [2020a] *ASTM E3037-20: Standard Test Method for Measuring Relative Movement Capabilities of Through-Penetration Firestop Systems*. ASTM International, West Conshohocken

ASTM International. [2019] *ASTM E1966 - 15(2019): Standard Test Method for Fire-Resistive Joint Systems*. ASTM International, West Conshohocken

ASTM International. [2020b] *ASTM E119: Standard Test Methods for Fire Tests of Building Construction and Materials*. West Conshohocken

Bianchi S., Ciurlanti J., Perrone D., Filiatrault A., Costa A.C., Candeias P.X., Correia A.A., Pampanin S. [2021] "Shake-table tests of innovative drift sensitive nonstructural elements in a low-damage structural system". Earthq Eng Struct Dyn

Bjørge J.S., Gunnarshaug A., Log T., Metallinou M.-M. [2018] "Study of industrial grade thermal insulation as passive fire protection up to 1200° c". *Safety* 4:41

Buchanan A.H., Abu A. [2017] "Structural design for fire safety"

Dal Lago B., Biondini F., Toniolo G., Lamperti Tornaghi M. [2017] "Experimental investigation on the influence of silicone sealant on the seismic behaviour of precast façades". *Bull Earthq Eng* 15:1771–1787. https://doi.org/10.1007/s10518-016-0045-y

Dassault Systèmes. [2020] "ABAQUS 2020 (Version 6.20)". Accessed June

Dhakal R.P., Pourali A., Tasligedik A.S., Yeow T., Baird A., Macrae G., Pampanin S., Palermo A. [2016] "Seismic performance of non-structural components and contents in buildings: an overview of NZ research". *Earthq Eng Eng Vib* 15:. https://doi.org/10.1007/s11803-016-0301-9

Ellingwood B.R., Kinali K. [2009] "Quantifying and communicating uncertainty in seismic risk assessment". *Struct Saf* 31:179–187. https://doi.org/https://doi.org/10.1016/j.strusafe.2008.06.001

European Committee for Standardization. [2009] *BS EN 1366-3:2009 Fire resistance tests for service installations. Penetration seals*. CEN, London

European Committee for Standardization. [2002] *BS EN 1991-1-2:2002: Eurocode 1: Actions on structures -Part 1-5: General actions - Actions on structures exposed to fire*

European Committee for Standardization. [2004] *BS EN 1992-1-2:2004: Eurocode 2: Design of concrete structures - Part 1-2: General rules - Structural fire design*

Federal Emergency Management Agency (FEMA). [2012] "FEMA E-74: Reducing the Risks of Nonstructural Earthquake Damage – A Practical Guide"

Frank K., Baker G., MacIntyre J. [2018] "Assessing the risk of non-compliant firestopping and smokestopping in New Zealand residential buildings undergoing alterations". Wellington

Gillespie P.E., O'Leary P.E., Mattes B., Talbot J., Neese R.K., Wasilewski B. [2007] "Technical Guideline on Through Penetration Firestopping". Chantilly

Gursel A., Cekirge H.M. [2019] "Adhesive Joints Subjected to Impact Loading: A Review". *Int J Mater Eng* 9:16–21

Hilti Inc. (U.S.). [2017] "Firestop Systems Guide for Specifiers"

Hutchinson T.C., Wood R.L. [2013] "Cyclic Load Protocol for Anchored Nonstructural Components and Systems". *Earthq Spectra* 29:817–842. https://doi.org/10.1193/1.4000169

International Code Council. [2021] "International Building Code 2021 (IBC 2021) - Chapter 7: Fire and Smoke Protection Features"

International Organization for Standardization. [1999] *ISO 834-1:1999 Fire-resistance tests - Elements of building construction - Part 1: General requirements*

International Organization for Standardization. [2003] *BS EN ISO 11600:2003+A1:2011: Building construction-Jointing products-Classification and requirements for sealants*

Johar M., Asasaari S.F.M., Tamin N. [2015] "Strain rate-dependent deformation and failure process of adhesive joints". 2015:. https://doi.org/10.1109/IEMT.2014.7123133

Kodur V., Pakala P. [2010] "Energy based time equivalent approach for evaluating fire resistance under design fire exposures". In: Structures Congress 2010

Kšiňan J., Vodička R. [2013] "AN ENERGETIC APPROACH FOR INTERFACE DELAMINATION PROBLEM IN SLIDING MODE WITH COHESIVE OR ADHESIVE CONTACT". *Trans VŠB - Tech Univ Ostrava, Civ Eng Ser* 13:. https://doi.org/10.2478/tvsb-2013-0011

MacIntyre J.D., Abu A.K., Moss P.J., Nilsson D., Wade C.A. [2021] "A review of methods for determining structural fire severity—Part I: A historical perspective". Fire Mater

Mattos H. da C., Nunes L.C. da S., Monteiro A.H. [2016] "Load rate effects in adhesive single lap joints bonded with epoxy/ceramic composites". *Lat Am J Solids Struct* 13:1878–1892

Mihindukulasuriya S.D.F. [2012] "Investigations of heat seal parameters and oxygen detection in flexible packages"

Modala S.S. [2019] "Effect of Strain Rate on Adhesively Bonded Lap Joints with Similar and Dissimilar Adherends"

Nezhad H., Stratakis D. [2017] "Performance of Aerospace Composites in the Presence of Process-induced Defects"

Nyman J.F. [2002] "Equivalent Fire Resistance Ratings of Construction Elements Exposed to Realistic Fires"

Perry C., Phipps M., Hortacsu A. [2017] "FEMA E-74 Presentation Handout". In: Webinar

Pourali A., Tata K., Baird A., Kam W.Y. [2020] "Seismic assessment and restraint of non-structural element-practical solutions and implementation challenges"

Rahmanishamsi E., Soroushian S., Maragakis E., Sarraf Shirazi R. [2017] "Analytical Model to Capture the In-Plane and Out-of-Plane Seismic Behavior of Nonstructural Partition Walls with Returns". J Struct Eng (United States). https://doi.org/10.1061/(ASCE)ST.1943-541X.0001769

Retamales R., Mosqueda G., Filiatrault A., Reinhorn A. [2008] *New Experimental Capabilities and Loading Protocols for Seismic Qualification and Fragility Assessment of Nonstructural Components*

Retamales R., Mosqueda G., Filiatrault A., Reinhorn A. [2011] "Testing protocol for experimental seismic qualification of distributed nonstructural systems". *Earthq Spectra* 27:835–856

Sędłak B., Sulik P., Izydorczyk D., Łukomski M. [2017] "Fire-stop Wraps and Collars with Intumescent Materials-Performance Comparison". In: Procedia Engineering. Elsevier Ltd, pp 961–968

Sheet Metal and Air Conditioning Contractors' National Association. [2007] "Guideline On Through-Penetration Firestopping (Second Edition)"

Standards Australia. [2014] *AS 1530.4-2014: Methods for fire tests on building materials, components and structures - Part 4: Fire-resistance test of elements of construction*. Sydney

Stanway J., Sullivan T., Dhakal R. [2018] "Towards a New Delivery Approach to Improve the Performance of Nonstructural Elements in New Zealand"

Takiguchi M., Izumi S., Yoshida F. [2004] "Rate-dependent shear deformation of ductile acrylic adhesive and its constitutive modelling". *Proc Inst Mech Eng Part C J Mech Eng Sci* 218:623–629

Thurston S.J. [1996] "Modelling Fire Behaviour of Metal Pipe Penetrations Through Concrete Walls". Wellington

Underwriters Laboratories (UL). [2015] *ANSI/UL 1479-2015 Standard for Fire Tests of Penetration Firestops*. Underwriters' Laboratories (UL)

Vali D. [2020] "Defining the Movement Capabilities of Firestops". In: STI Firestop.

https://www.stifirestop.com/news/defining-the-movement-capabilities-of-firestops. Accessed 10 Dec 2021

Wade C., Gerlich J., Abu A. [2014] "The Relationship Between Fire Severity and Time-Equivalence". Wellington

Yu X.X., Crocombe A.D., Richardson G. [2001] "Material modelling for rate-dependent adhesives". *Int J Adhes Adhes* 21:197–210

Zarrelli M., Pullara A., Codda M., Amendola E., Borriello A., Fermi P. [2012] "Fireproof silicone sealants for shipbuilding". *no June* 24–28

Seismic Qualification of Square D Relays Type KPD13 at Laguna Verde Nuclear Power Plant

G. Javio[1], J.F. Guadarrama[2], and V. A. Jarvio[3]

[1] Equipment Qualification Department at Nuclear Research National Institute
Carretera México Toluca-La Marquesa s/n, Ocoyoacac, Estado de México. C.P. 52750 (phone: 0155 5329-7200, Ext. 16014.
gilberto.jarvio@inin.gob.mx
[2] Department of Electrical Engineering at Laguna Verde Nuclear Power Plant
Carretera Cardel-Nautla, Km. 42.5, Mpio. Alto Lucero, Ver., C.P. 91680, phone. 01229 989-9090 Ext. 47511
[3] Technological Institute of Boca del Rio
Veracruz - Cordoba 12, Boca del Río, Ver., C.P. 94290, phone. 01229 690-5010
jose.guadarrama@cfe.gob.mx; vjarvio@hotmail.com

Abstract. The ININ performed a Seismic-Environmental Qualification process applied to 4 SQUARE D Relays Type KPD13 from the Laguna Verde Nuclear Power Plant (LVNPP) to determine an additional ten years to the service's life extension in the control's logic of the Diesel Generators at LVNPP. For a mild environment, the qualification was performed by type testing, following IEEE Std 323-1974 and IEEE Std 344-1975. The environmental qualification was performed in the facilities of the Equipment Qualification Laboratory at the Nuclear Research National Institute, and the seismic qualification was performed in the UNAM Seismic Table. The visual inspections and the functional tests evaluations indicated that the tested specimens met the acceptance criteria established by the LVNPP. The service's life extension of an additional ten years can be established for the Square D Type Relays Type KPD13. It will support a Design Basis Event (DBE) of type OBE and SSE according to the LVNPP specification for its application. The specimens met the acceptance criteria of not presenting "chattering" (Rapid and sustained opening and closing of the contacts of a switch (contact rattling), caused by mechanical vibration or other causes) over 2 ms during the seismic test.

Keywords: Chattering, Operating Basis Earthquake, Safety Shutdown Earthquake, Seismic Qualification.

1.1 INTRODUCTION

Laguna Verde Nuclear Power Plant (LVNPP) requested the Seismic-Environmental Qualification of the Schneider Electric's SQUARE D Relays Type KPD13 to the Qualification and Verification Department of the Quality Equipment from the National Institute of Nuclear Research (ININ) to verify an additional life extension of ten years. The Relays are installed in the control logic of LVNPP, Units 1 and 2. This article presents the results of the seismic qualification tests developed by the ININ. This process was performed using four specimens from the LVNPP, Unit 1 (U1), with an installed life of twenty-five years. The specimens were subjected to a sequence of tests of Seismic-Environmental, following the guidelines established in the IEEE standards [1974], [1975] for a mild environment and Seismic Category I, which for purposes of this article, corresponds to an extension of service life. SQUARE D's specimens, Relays Type KPD13 from Schneider Electric, complied with the operational requirements specified by the LVNPP, for a life extension of ten additional years, to the service life of twenty-five years that they accumulated when previously installed at LVNPP.

1.2 SPECIMENS DESCRIPTION

The test specimens were four Schneider Electric's SQUARE D Relays Type KPD13, plug-in with a 3PDT contact arrangement. The electrical characteristics of the contacts are 10A continuous @ 125DCV. The entire assembly is encapsulated in a transparent cover and mounted on a socket-type connection board brand Curtis model RS-11, which is attached in turn on a mounting rail.

1.3 DEVELOPMENT OF AGING TEST

1.3.1 Development of the Accelerated Thermal Aging Test

Accelerated Thermal Aging was developed using the Arrhenius aging model [Jarvio and Villasana, 2016]

$$t_{aDG} = \left\{ C_1 \left[Exp\left[-\frac{E_a}{K_B}\left(\frac{1}{T_{SDGON} + Ac} - \frac{1}{T_a} \right) \right] \right] + C_2 \left[Exp\left[-\frac{E_a}{K_B}\left(\frac{1}{T_{SDOFF} + Ac} - \frac{1}{T_a} \right) \right] \right] \right\} \tag{1}$$

This model was applied with the following conditions:
Where:

t_s	Qualified Life (years).
t_a	Accelerated thermal aging time (h).
t_{aDG}	Accelerated thermal aging time (h), considering operating conditions in the Diesel Generator Building (DGB).
E_a	Activation energy (eV)
K_B	Boltzmann constant (8.617 x 10^{-5} eV / °K)
T_a	Accelerated thermal aging temperature (° K)
$T_{S\ DGON}$	Service Temperature in DGB when the Diesel Generator (DG) (ON) is 48.8 ° C per specification.
$T_{S\ DGOFF}$	Service Temperature in DGB when the DG (OFF) is 40 ° C per specification.
Ac	Self-heating
C_1	2.5% for five and ten years with DG ON.
C_2	97.5% for five and ten years with DG OFF.

Additionally, a maximum self-heating of 13.2 ° C was taken to calculate thermal aging, obtained by a thermography study of the test specimen in operation. The thermography used as a reference is presented in Figure 1. The points considered are Sp1 and Sp2, with a difference of 13.2 ° C, from which a Self-Heating Temperature of 13.2 ° C was established.

Figure 1. **Thermography of SQUARE D Relay Type KPD13**

The aging time and oven temperature that was applied to the test specimens was:

For five years of qualified life $t_a = 14.13$ days Ta= 100°C
For ten years of qualified life $t_a = 28.25$ days Ta= 100°C

1.3.2 Development of the Mechanical-Electrical Aging Test

The mechanical-electrical aging was developed with the aging parameters established in Table 1 [Jarvio and Villasana, 2016].

Table 1. Mechanical Electrical Aging Parameters of Square D Relays Type KPD13

Group	Years	Cycles	V-coil (DCV)	V-contact (DCV) Resistive	I-contact (A) Resistive
1	5	1000	134	125	0.4
2	10	2000	134	125	0.4

1.3.3 Development of the Radiation Exposure Test

The four specimens were irradiated with a Cobalt-60 source to simulate the usual dose received by the service during five and ten years of life, plus 10% as a trial margin to absorb uncertainties due to dose distribution. In the Irradiator, at a distance from the source, there was an average dose of 0.2 Mrad (in the air) with a dose rate of less than 1 x 106 rad / h (1 Mrad / h), as established by the IEEE standard [1974].

The two groups of test specimens were irradiated, according to the following Total Integrated Dose (TID) [Jarvio and Villasana, 2016]:

For 5 years 2.19×10^2 rad (TID)
For 10 years 4.38×10^2 rad (TID)

1.4 Development of the Seismic Qualification Test

1.4.1 Mounting of Specimens and Orientation

The Seismic Qualification Test of Schneider Electric's SQUARE D Relays Type KPD13 was developed in the Seismic Table of the Engineering Institute at the UNAM under the guidelines of the IEEE standard [1975] and with the test sequence of the IEEE standard [1974].

Tests were developed to monitor the "Chattering" and contact status of the test specimens during the 3 Safety Shutdown Earthquake (SSE). The seismic movement to be reproduced was obtained through the generation of Synthetic Stories (acceleration data), which are a function of the Required Response Spectra (RRS) and, specifically, In-Equipment Response Spectra (IERS)) established in the specification at LVNPP Units 1&2. For this seismic qualification process, the tests were performed using a 10-gauge metal plate mounted on a support, on which the four specimens (previously aged at five and ten years) were installed through a TR2 DIN rail.

The specimens were installed on a Curtis model RS11 socket-type splint board on a TR2 DIN rail screwed to a metal plate by 3/16 screws and flat washers, mechanically coupled to a support using screws. A clamping spring was placed to attach each relay to its terminal board. This steel assembly with mounting structures was designed to be bolted to the Biaxial Seismic Table of the National Autonomous University of Mexico (UNAM). The ININ oversaw the rigid support design and manufacture, meaning it did not present resonances in the frequency range of interest for the effects of the seismic qualification.
The entire assembly (steel support - metallic plate - DIN TR2 with the four relays) was placed and fixed (screwed) to the surface of the Seismic Table of the UNAM on the central part of the same (Figures 2 and 3).

Figure 2. **Installation of SQUARE D Relays Type KPD13, for OBE and SSE Tests (Side to Side/Vertical direction).**

Figure 3. **Installation of SQUARE D Relays Type KPD13, for OBE and SSE Test (Front to Back / Vertical direction).**

Three accelerometers were placed for the seismic test (Operating Basis Earthquake (OBE) and Safety Shutdown Earthquake (SSE)) on the front of the metal plate (Figure 4), at the height of the central part of the specimens, these 3 Accelerometers were: 735 (H (SS)), 737 V and 736 (H (FB).) In addition, 2 accelerometers were integrated into the Seismic Table on 733 (H (SS)) and 734 V. The location of the accelerometers was agreed between the technical staff of the ININ and the UNAM.

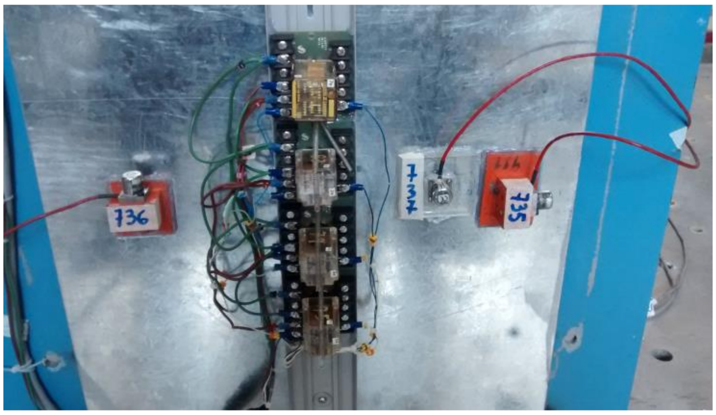

Figure 4. **Installation of the Accelerometers on the Metal Plate of the Bracket Containing the SQUARE D Relays Type KPD13 during the OBE and SSE Test (Side to Side / Vertical and Front to Back / Vertical).**

The assembly's configuration and the specimens' operation were simulated as far as possible as they were installed in the Diesel Generator Control Panels of LVNPP Units 1&2.
The placement of the specimens in the Seismic Table coincided with their designated orientations, such as Side by Side "(greater horizontal dimension of the Control Panels) and "Front to Back "(short horizontal dimension of the Control Panels). How the equipment is mounted on the plant has coincided with the previously programmed movements in the UNAM's Seismic Table.

1.4.2 Seismic Simulation of OBE and SSE Specified by LVNPP

The conditions to which Schneider Electric's SQUARE D Relays Type KPD13 were subjected during the seismic simulation are indicated by Jarvio [2016].
The ININ provided the technical staff of the Seismic Table, the synthetic histories (acceleration data as a function of time) with a duration of 30 seconds for each seismic movement, every five milliseconds (6000 data), one for the test direction "Side to Side", "Front to Back" and one more to its corresponding

Vertical, all of them for the OBE earthquake level. Six similar synthetic stories were also provided for the SSE earthquake level, whose characteristics were that their corresponding Test Response Spectra (TRS) would cover the Required Response Spectra (RRS). These combinations are indicated below.

i. OBE corresponds to the horizontal direction of movement "Side-Side" (SS) and "Front-Back" (FB).
ii. OBE for the direction of Vertical movement.
iii. SSE corresponds to the Horizontal movement direction "Front-Back" (FB) and "Side-Side" (SS).
iv. SSE for the direction of Vertical movement.

Based on the above and within the Seismic Table's limits, the specimens were subjected to 16 independent biaxial movements for 30 seconds each. The synthetic stories generated multifrequency movements with a frequency interval of 0.5 Hz to 40 Hz that, once the mechanical response of the Seismic Table was compensated, generated Test Response Spectra (TRS) that involved the In-Equipment Response Spectra (IERS). A spectrum analyzer analyzed the resulting movement of the Table at 2% damping for the OBE and 3% damping for the SSE. The TRS was plotted in the frequency range of interest.
The sequence of the tests consisted of applying five Horizontal/Vertical movements for the OBE event Side-to-Side direction, later, the support with the specimens was turned 90°, and five horizontal/vertical movements were applied to the OBE event Front to Back direction. Then three horizontal/vertical movements were applied to the SSE event Front-Back direction. The support with the specimens was turned 90° on the Table to finally apply 3 Horizontal/Vertical movements for the SSE event Side-to-Side direction.
During the 3 SSEs, the specimens' functionality parameters were tested so that the appropriate times between tests were given to perform the conducive, take records, photographs, etcetera.
The total number of movements for OBE and SSE was 16 (10 for OBE and 6 for SSE).

1.5 RESULT OF SEISMIC QUALIFICATION TEST

1.5.1 Result of the Multiple Frequency Tests

During the seismic qualification test, the SQUARE D Relays Type KPD13 of Schneider Electric operated in a satisfactory way maintaining its electrical and structural integrity during each of the seismic movements made and covering the In-Equipment Response Spectra (IERS) by the LVNPP.
Table 2 shows each of the seismic movements that were performed [Jarvio and Villasana, 2016].

Table 2. Description of the Seismic Movements of the Schneider Electric Square D Relays Type KPD13

Test No.	Type of Test	Axes	Nominal Level	RRS (IERS)
1-5	MF	SS/V	OBE	LVNPP, U1 & U2
6-10	MF	FB/V	OBE	LVNPP, U1 & U2
11-13	MF	FB/V	SSE	LVNPP, U1 & U2
14-16	MF	SS/V	SSE	LVNPP, U1 & U2

Figures 5 and 6 include the graphs corresponding to the TRS of OBE 1, Side-Side and Vertical directions of the SQUARE D Relays Type KPD13 of Schneider Electric, and corresponds to the accelerometers with the following identification:

i. Accelerometer No. 735 for horizontal movements Side-Side.
ii. Accelerometer No. 736 for horizontal movements Front-Back.
iii. Accelerometer No. 737 for Vertical movements.

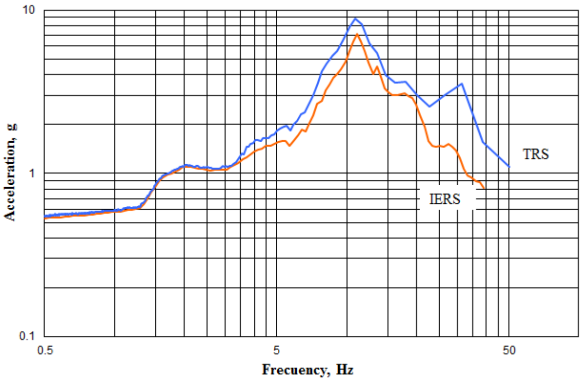

Figure 5. Test Response Spectrum (TRS) and the In-Equipment Response Spectrum (IERS), OBE 1 (Side-Side Direction).

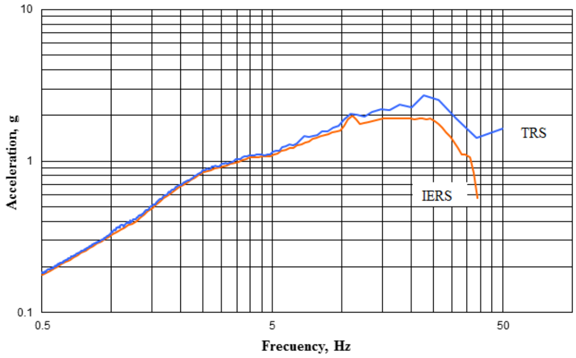

Figure 6. Test Response Spectrum (TRS) and the In-Equipment Response Spectrum (IERS), OBE 1 (Vertical Direction)

For the SSE case, Figures 7 to 9 include the graphs corresponding to the TRS of the SSE 1, Side-Side, Vertical and Front-Back addressed to the SQUARE D Relays Type KPD13 of Schneider Electric and correspond to the Accelerometers identified above.

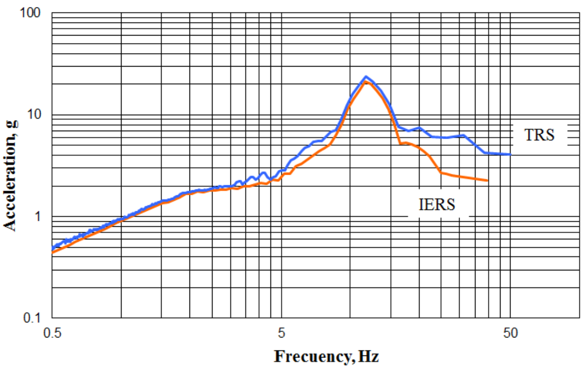

Figure 8. Test Response Spectrum (TRS) and the In-Equipment Response Spectrum (IERS), SSE 1 (Front-Back Direction)

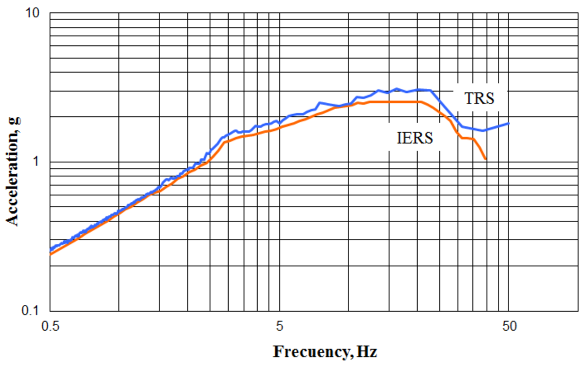

Figure 9. Test Response Spectrum (TRS) and the In-Equipment Response Spectrum (IERS), SSE 1 (Vertical Direction)

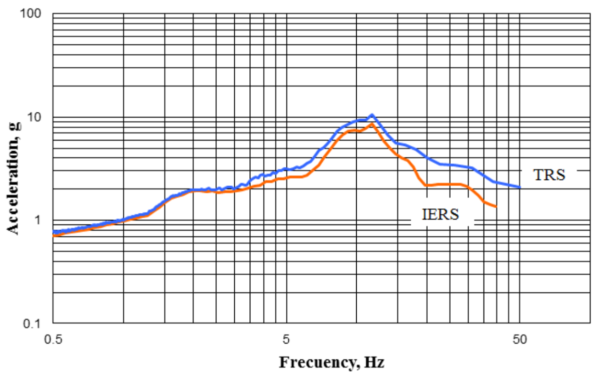

Figure 10. Test Response Spectrum (TRS) and the In-Equipment Response Spectrum (IERS), SSE 1 (Side-Side Direction)

1.5.2 Result of the Function Tests of the Relays During the Seismic Test.

During all the seismic movements performed, the SQUARE D Relays Type KPD13 of Schneider Electric, worked properly and their performance was according to the specified, that is, "Chattering" was not presented; the contacts were changed, maintaining satisfactorily the change of state.

The output graphs' records of the "Chattering" monitoring and contact status of the response instrumented in the specimens generated during the SSE are shown in Figures 11 to 13.

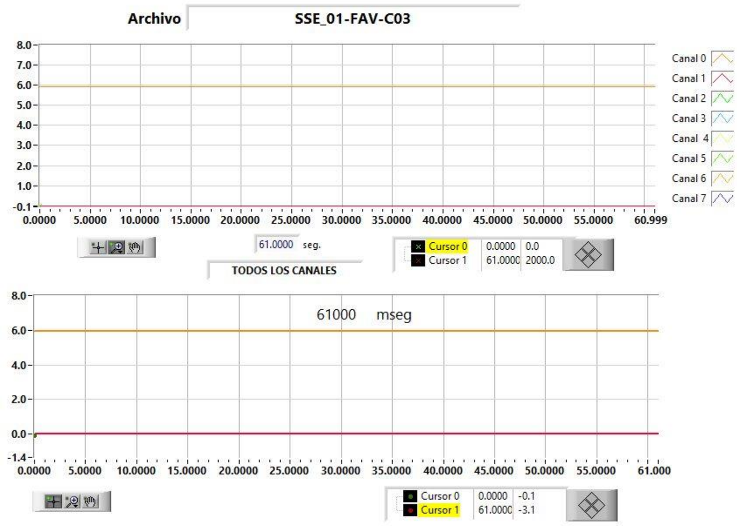

Figure 11. Chattering Graphics during SSE 1 (Direction FB/V, Specimens 1 and 2)

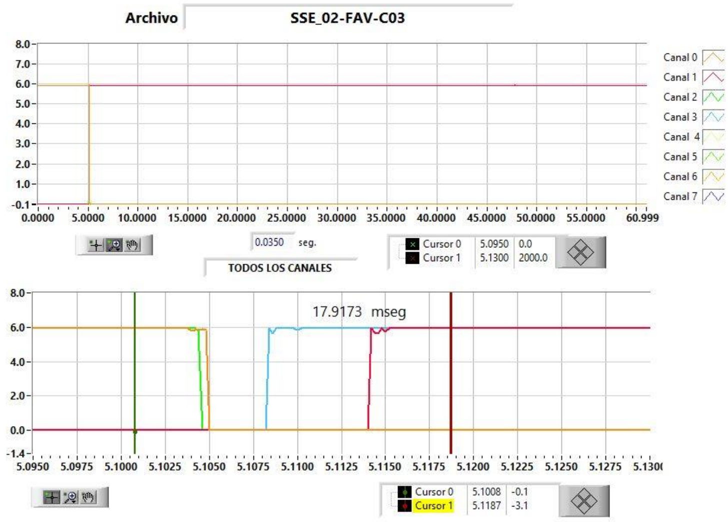

Figure 12. Chattering Graphics during SSE 2 (Direction FB/V, Specimens 1 and 2). The Bottom Graphic Shows the Change of State.

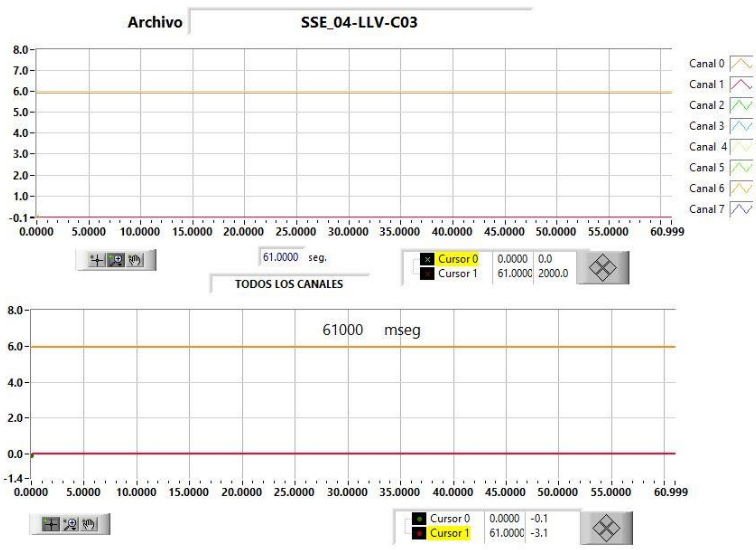

Figure 13. Chattering Graphics during SSE 4 (Direction SS/V, Specimens 1 and 2).

The results of the "Chattering" monitoring and change of contacts are shown in Table 3.

Table 3. Results of "Chattering" and Contacts Monitoring During the Seismic Qualification Test of Square D Relays Type KPD13 of LVNPP, U1

SSE No.	Functional State	Contacts to Monitor	Resistive Load and Source DCV	Compliance with the Functional Acceptance Criteria
1	Relay coil De-energized	1 contact NO 1 contact NC	25 mA y 6VCD	No "Chattering" was presented
2	Energized Relay Coil 100DCV	1 contact NO 1 contact NC	25 mA y 6VCD	No "Chattering" was presented
3	Transition from De-Energized Relay to Energized to 100 DCV, after 15 sec	1 contact NO 1 contact NC	25 mA y 6VCD	Change of Contacts and remained in this state

Based on the results of Table 3, we can say that the acceptance criteria were met, as described below:
In all OBE and SSE, Structural and Electrical Integrity was maintained.
In all OBE and SSE, the TRS involved IERS with a 10% margin from 0.5 to 40 Hz.
In the SSE 1 and 2 "Chattering" was not presented.
In the SSE 3 the change of contacts was presented and remained in that state.

1.6 Evaluation of the Seismic Qualification Test

The SQUARE D Relays Type KPD13 from Schneider Electric operated properly during the seismic movements applied. There were no changes in the status of the relays that could put their operation at risk as shown by Jarvio and Villasana *et al.*, [2016].
The relays continued to function satisfactorily during and until the end of the SSE seismic movements. No "Chattering" was presented during the SSE 1 and 2 movements, and the change of contacts was made keeping in that state during the SSE 3 earthquake.
The specimens maintained their structural, electrical, and functional integrity during each of the seismic movements to which they were submitted, perfectly covering the Response Spectra Required by the LVNPP specifications U1 & U2.
The Test Response Spectra (TRS) for the OBE and SSE, obtained from the tests in the UNAM's Seismic Table, were executed satisfactorily and involved IERS + 10% specified by the LVNPP Units 1&2.
The observations and tests performed on the specimens during all the seismic tests indicated that the specimens were completely functional before, during, and after the Seismic Qualification Process.

1.7 Conclusion

The results' evaluation of the visual inspections and the functional tests indicate that the tested specimens satisfactorily met the acceptance criteria established by the LVNPP. A ten additional years life extension can be established for Schneider Electric's SQUARE D Relays Type KPD13. It will support a Design Basis Event (DBE) of type OBE and SSE according to LVNPP specification for its application in the control logic of the Diesel Generators of the LVNPP Units 1&2. The specimens met the acceptance criteria of not presenting "chattering" greater than 2 ms during the seismic test, as shown by Jarvio and Villasana et al., [2016], and according to the IEEE standards [1978], [2010] and [2013].

Therefore, the Seismic-Environmental Qualification of the SQUARE D Relays Type KPD13 of Schneider Electric has been demonstrated to execute the safety functions assigned in mild environmental conditions, such as Class 1E and Seismic Category I equipment, for its application in the LVNPP, Units 1&2, for ten additional years.

1.7.1 Acknowledgments

The authors are grateful for the support of the ININ colleagues who worked on the development of the Environmental and Seismic Qualification tests: E. Garcia, J. Rodriguez, V. Villasana., B. Ruiz, C. Fernandez, R Ramirez, F. Salgado, I. Suarez, F. Bucio and T. Rivero, R. Argüelles, R. Ramirez, A. Rojas and R. Duran.

1.7.2 References

IEEE. [1974] "IEEE Standard for Qualifying Class 1E Equipment for Nuclear Power Generating Stations". IEEE Std 323-1974 USA.

IEEE. [1975] "IEEE Recommended Practices for Seismic Qualification of Class 1E Equipment for Nuclear Power Generating Stations". Std 344-1975. USA.

IEEE. [1978] "IEEE Standard Seismic Testing of Relays". IEEE Std 501-1978. USA.

IEEE. [2010] "IEEE Standard for Qualifying Class 1E Protective Relays and Auxiliaries for Nuclear Power Generating Stations". IEEE Std C37.105-2010. USA.

IEEE [2013]. "IEEE Standard for Seismic Qualification Testing of Protective Relays and Auxiliaries for Nuclear Facilities". IEEE Std C37.98-2013. USA.

Fernandez, C., Ramirez, R. [2016] "SQUARE D Relays Type KPD13 Performance Tests". *Individual Study*, Nuclear Research National Institute. Mexico.

Jarvio, G. [2016] "Seismic Qualification Test Plan for Service Life Extension of 10 Years of SQUARE D Relays Type KPD13 of LVNPP U1 and U2". *Individual Study*, Nuclear Research National Institute. Mexico.

Jarvio, G., Villasana, V., Ruiz, B. [2016] "Report of Seismic-Environmental Qualification Tests for Service Life Extension of 10 Years of SQUARE D Relays Type KPD13 of LVNPP, U1 & U2". *Individual Study*, Nuclear Research National Institute. Mexico.

Villasana, V., Ruiz, B. [2016] "Environmental Qualification Test Plan for Service Life Extension of 10 Years of SQUARE D Relays Type KPD13 of LVNPP U1 and U2". *Individual Study*, Nuclear Research National Institute. Mexico.

Recent developments in the field of anchoring heavy façades in seismic areas

Matthias Roik[1], Caroline Piesker[1]

[1] Leviat GmbH
Liebigstr. 14, 40764 Langenfeld, Germany
e-mail: matthias.roik@leviat.com, caroline.piesker@leviat.com

Abstract. The design of façade fixings for the bearing of seismic loads was already presented at the last SPONSE workshop. Special attention was paid to the experimental determination of the resistance. For this purpose, the experimental conditions were examined in particular in order to achieve a result that is as generally valid as possible with a manageable amount of effort.

In the meantime, these experiments were further advanced and continuously increased the experience in the design of the corresponding anchoring systems. Tests were continuously performed in three different scales: The micro scale for tests at single anchors, the macro scale, usually provided with shake tables on large specimens and the meso scale for tests on representative façade-areas.

Especially for masonry façades, the "meso-scale" testing method proved to be particularly powerful. It respects the interaction of the different fixing components, i.e. the vertical support, the horizontal fixing parallel and vertical to the façade area as well as the building components like the bricks and mortar. Samples at this scale are usually easier to handle than those at the macro scale, which makes them faster and more economical. In the end, more tests can be carried out, which ultimately improves the quality of the information and enables parameter studies.

Additionally, comparable test methods are also used by approval authorities to issue building approvals.

This paper provides an overview of the calculation methods and test methods. Test methods are introduced as an alternative to large shake table tests. All of them are used to obtain necessary information about the load-bearing behaviour of the entire outer wall and to confirm theoretical assumptions with different experimental effort. The technical background is explained, and the experiment results are illustrated and compared.

Keywords: façades; fixing constructions; heavy façade systems; nonstructural elements, testing methods.

1. INTRODUCTION

A façade, the outer skin of a building, combines aesthetics and function, as shown in Figure 1. It influences the appearance of the building and has also a decisive effect on the building physics, such as thermal insulation.

Façade fixings must support the loads from the façade and safely transfer them to the supporting layer. They also ensure a sufficient distance between the load-bearing and façade layer. Especially in the case of so-called "heavy" façades, i.e. façades with a dead load of more than 100 kg/m² such as masonry, natural stone cladding or concrete slabs. These façade fixings have to transfer high point loads over large wall distances.

In current earthquake standards, façades and their fixings are classified as non-structural components. These components are usually defined as masses that are attached to the structure without their own stiffness. In the event of an earthquake, the fixings are primarily intended to prevent the façade from falling down and to ensure that neither escape routes are blocked nor people are injured.

To assess the seismic application of a fixing, it is imperative to examine all components of a façade to ensure sufficient ductility while maintaining adequate load-bearing capacity. Although some calculation approaches to this topic are known, the load-bearing behaviour of the system is usually determined by tests. During the 4th SPONSE Workshop 2019 in Pavia, different test scales have already been explained and evaluated by Roik, Piesker [2019]. In the following, the test methods in macro, micro and meso scale will be briefly presented again.

This paper introduces a general meso-scale test procedure according to CAHIER 3725 [2013], as it is carried out to obtain a Technical Experimentation Assessment (ATEx) for seismic fixings in France. A test on a seismic fixing system for masonry façades is presented and the test results are shown.

It is highlighted, how this type of test combined with the technical assessment allows - besides an evaluation of the considered fixing system and its suitability for certain seismic zones - the validation of a calculation method to determine the individual number of seismic anchors for deviating projects by scaling. By offering a standardised test, based design method to facade designers, that is accepted by e.g. insurance companies, these tests represent an important connection between research and practice.

Figure 1. sketch of a rear ventilated façade

2. "HEAVY" FAÇADES

The considered external wall constructions with heavy façade consist of a load-bearing layer, insulation layer, air layer and a façade with a weight of more than 100 kg/m², e.g. made of masonry, natural stone or concrete. Accordingly, the façade fixings must pass through the insulation and act either as cantilever beams or as tensile straps with spacers.

2.1 BRICKWORK FAÇADES

The dead load of a brickwork façade is supported by angles or brickwork support brackets attached to the load-bearing layer. Horizontal loads perpendicular to the façade, like wind loads, must be taken by separate horizontal anchors such as wall ties.

2.2 NATURAL STONE FAÇADES

Natural stone façades consist of stone slabs with a thickness of at least 30 mm, which are usually supported at four points in the vertical or horizontal joint by grout-in anchors or bolted anchors. For larger wall distances or if non-load-bearing areas of the load-bearing layer have to be bridged, special channel substructures are used. Natural stone anchors are usually capable of transferring dead loads as well as wind loads to the supporting layer.

2.3 CONCRETE FAÇADES

There are two main types of precast concrete façades: Façade panels and sandwich panels.

Concrete façade panels are manufactured separately and fixed to the supporting structure after this has been erected. Vertical loads (e. g. dead load) are carried by the support anchors, while horizontal loads perpendicular to the façade surface are transferred by spacers.

Sandwich elements, on the other hand, consist of a load-bearing layer and a façade layer, which are manufactured simultaneously with intermediate insulation and are connected to each other by means of sandwich ties.

Examples of heavy façades and their fixings are shown in figure 2 till figure 7. This paper will mainly focus on brickwork façades in the following.

Figure 2. building with brickwork façade

Figure 3. building with natural stone façade

Figure 4. building with concrete façade

Figure 5. example of brickwork façade support

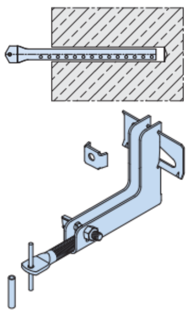

Figure 6. examples of natural stone anchors

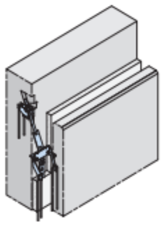

Figure 7. example of concrete façade fixing

3. LOAD-BEARING BEHAVIOUR OF FAÇADE ANCHORS

3.1 STATIC RESISTANCE

Load-bearing anchors of heavy façades serve, on the one hand, to ensure the wall distance between the supporting layer and the façade, which may be larger than 300 mm. On the other hand, they absorb the loads acting on the façade and safely transfer them to the supporting layer. In the static load case, only the dead load of the façade and horizontal loads perpendicular to the façade, such as wind, have to be considered. Horizontal forces parallel to the façade can usually be neglected.

Serviceability is achieved by complying with maximum deflections.

3.2 SEISMIC RESISTANCE

In areas with seismic risk, the effects of earthquakes must be taken into account to ensure free escape routes in the event of an earthquake and to avoid personal injury.

In earthquake standards, façades are usually classified as non-structural components designed for horizontal loads acting in the centre of gravity of the façade in the most unfavourable direction, as shown in figure 8.

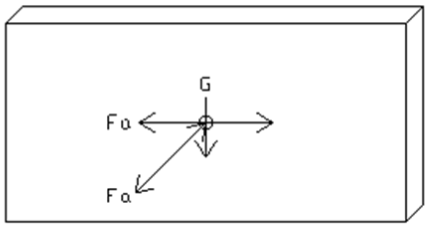

Figure 8. sketch of a façade with dead load (G) and possible directions of seismic loads (Fa)

To avoid additional loads due to constraints, façades are supported in a statically determined manner and are suspended in a self-stabilising manner as far as possible. For use under seismic loads, the horizontal displacements must be limited to the serviceability limits, which often requires additional bearings. As a result, the façade fixings must be a) supplemented with additional fixings or b) the existing supports must be strengthened with additional horizontal supports.

The suitability of these additional horizontal supports can be assessed in tests at different scales (macro, meso, micro).

4. GENERAL TEST METHODS FOR SEISMIC RESISTANCE

4.1 MACRO-SCALE TESTS

The essence of a macro-scale test is that either whole buildings or large parts of buildings are investigated. For the application of comparative seismic loads, shaking tables are usually used, but other load applications can also be used, such as vibration exciters or dynamic acting jacks. The structure, including fixings and façade, at a scale of 1:1 is loaded with a series of artificial or natural earthquakes of increasing intensity while the applied loads and the resulting deformations are recorded (see figure 9).

The advantage of this type of test is the possibility to determine for a specific construction what earthquake intensity can be sustained while complying with the serviceability limits.

The main disadvantages of macro-scale tests are that they are time-consuming, cost-intensive and do not allow conclusions for deviating constructions.

4.2 MICRO-SCALE TEST

In a micro-scale test, a single anchor is tested without its connection to the façade (figure 10).

The anchor is attached to the structure, e.g. concrete, and loaded with a horizontal load in the most unfavourable direction, as specified in the common seismic standard. The additional dead load of the façade, if any, to be taken by the anchor is simulated by a mass suspended from the anchor cantilever. Since there is no standard regulating the test procedure for façade systems under seismic loading, the tensile or shear tests can be carried out, for example, following ETAG 001, Annex E [2013].

This micro-scale test is advantageous in order to be able to quickly and easily check anchor modifications that are necessary or interesting for further development with little time and money. It allows quick conclusions to be drawn about the seismic suitability and the deformation behaviour of a particular anchor and its connection to the supporting structure.

A disadvantage is the lack of consideration of the connection of the fastening to the façade, for which accordingly no statements can be made in tests at this scale.

4.3 MESO-SCALE TEST

In order to not only test a single anchor as in the micro-scale tests, a special "meso"-scale was developed which allows the analysis and verification of all components of a façade system.

A representative façade area is fixed with suitable anchors and static equivalent loads are applied, determined according to common earthquake standards. Such a test set-up shows figure 11.Since there is no standard regulating the test procedure for façade systems under seismic loading, the test procedure can be chosen based on ETAG 001, Annex E [2013], increasing loads are applied one after the other and loads as well as deformations are documented.

With the help of meso-scale tests, different fixing systems can be comprehensively tested and compared, i.e. not only the fixing itself, but also the connection to the supporting layer and to the façade, according to various criteria such as load-bearing capacity, deformation or ductility. They are easy to carry out and allow important statements at lower costs and time, thus enabling the assessment of the earthquake resistance of a corresponding overall construction.

In the following, further meso-scale tests are described that were carried out on brickwork façades in France at the CSTB institute according to the procedure of Cahier 3725 [2013]. Based on the achieved test results, a method for scaling the number of seismic anchors for different seismic loads was developed.

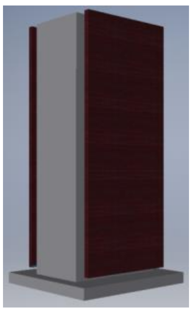

Figure 9. macro-scale test (shake table)

Figure 10. micro-scale test (single anchor)

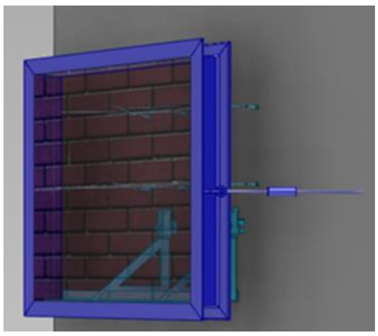

Figure 11. meso-scale test (reference façade)

5. METHODS FOR SEISMIC ASSESSMENT OF BRICKWORK FAÇADE FIXINGS IN FRANCE

A French ATEx (Technical Experimentation Assessment) is a technical assessment procedure carried out on any innovative product or system. It provides preliminary, test-based feedback on the implementation of products or systems and enables to validate innovative design approaches and thus helps innovators to promote new systems or outstanding architectural design approaches. The so gained results provide information to project managers, insurance companies or technical inspectors, that they need to appreciate the risks to be expected, and to convince them of supporting the innovation.

In order to prove a seismic fixing system in France it is necessary to obtain such an ATEx according to the test procedures of CAHIER 3725 [2013]. The tests can be assigned to the meso-scale and are carried out on a façade system to be validated, which is attached to a concrete support layer and loaded either horizontally parallel to the façade or horizontally perpendicular to the façade, as illustrated in Figures 12-13.

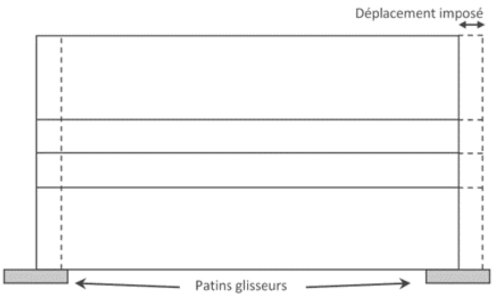

Figure 12. principle sketch for the parallel seismic test according to CAHIER 3725 [2013]

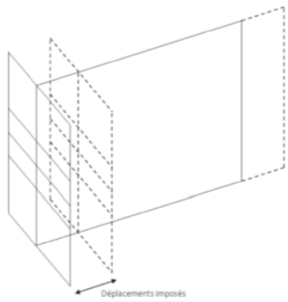

Figure 13. principle sketch for the perpendicular seismic test according to CAHIER 3725 [2013]

	Phase 1	Phase 2	Phase 3	Phase 4	Phase 5	Phase 6	Phase 7	Phase 8
	Accélération a_i en m/s²							
f en Hz	3,5	5	6,4	8	9,3	11,2	14	16,5
1								
2	22,2 20 cycles	31,7 20 cycles	40,5 20 cycles	50,7 20 cycles				
3					26,2 20 cycles	31,5 20 cycles	39,4 20 cycles	46,4 20 cycles
4								
5	3,5 20 cycles	5,1 20 cycles	6,5 20 cycles					
6				5,6 20 cycles				
7					4,8 20 cycles	5,8 20 cycles		
8	1,4 20 cycles						5,5 20 cycles	6,5 20 cycles
9		1,6 20 cycles						
10			1,6 20 cycles					
11				1,7 20 cycles				
12					1,6 20 cycles			
13						1,7 20 cycles		
14							1,8 20 cycles	
15								1,9 20 cycles

Figure 14. accelerations, amplitudes and cycles of the test phases of the seismic test according to CAHIER 3725 [2013]

For the parallel and the perpendicular test, a concrete supporting layer of the appropriate test rig is designed according to the CAHIER 3725 [2013] specifications. The considered brick façade is to be fixed to the supporting layer with the fixing system to be tested.

In accordance with the CAHIER 3725 [2013] test programme, eight test phases of increasing intensity, each with three amplitudes at defined load frequencies, are applied to the test object and measured values are recorded (see Fig. 14). After each phase, any damage to the façade or the fixing system is documented. The test ends either after eight phases or as soon as the first brick falls down.

As a conclusion from this rule, it becomes clear that not only the fixing system itself, but also the connection to the load-bearing layer or façade, as well as the masonry bricks and mortar and the quality of the wall itself contribute to the success of the test.

On the one hand, the test can be used to directly determine the suitability of a system for the maximum achieved acceleration. On the other hand, the required number of anchors can be scaled for structures with lower expected acceleration in the event of an earthquake based on the test result and a calculated dimensioning, which has been verified by the expert group. The calculated design therefore is based on the principles of Eurocode 8 (DIN EN 1998-1 [2010]), Eurocode 6 (DIN EN 1996-1-1 [2013]) and their national annexes for France. Test procedure and design method are described in detail in the following chapter.

6. MESO-SCALE TESTS ON A BRICKWORK SUPPORT SYSTEM ACCORDING TO CAHIER 3725 [2013]

The applicability of a seismic brickwork fixing system was tested in a parallel and a perpendicular meso-scale seismic test according to the test procedure of CAHIER 3725 [2013].

A perforated brick façade of 105 mm thickness with standard mortar joints was fixed to the concrete test walls with a wall distance of 220 mm. To fix the façade to the concrete wall, the following elements were used:

- brickwork support brackets with a drop (dimensioned for dead load of the façade), see Figure 15
- straight wall ties to support horizontal loads perpendicular to the façade (wind, seismic) designed according to requirements, see Figure 16
- seismic anchors to support horizontal loads parallel to the façade (seismic) designed according to requirements, see Figure 17
- flexible reinforcement at the top and bottom of the façade.

A drawing of the test set-up is illustrated in Figure 18 for the parallel test and in Figure 19 for the perpendicular test. Figure 20 and Figure 21 show the test walls before the test started.

The test procedure is shown in Figure 14. It consists of eight test phases with three series of 20 load cycles each. Every test phase represents a certain acceleration a_i. Based on formula (1), the amplitudes A for each series of a test phase were calculated, which are applied to the component at specified frequencies f.

$$A(f, a_i) = a_i / (2 \cdot \pi \cdot f)^2 \tag{1}$$

Figures 22 and 23 show the considered façades after the tests.

Figure 15. tested brickwork support bracket with drop

Figure 16. tested bricks, straight wall ties and flexible masonry reinforcement

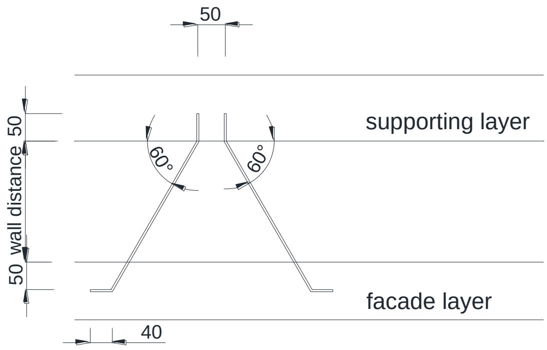

Figure 17. sketch of a seismic anchor

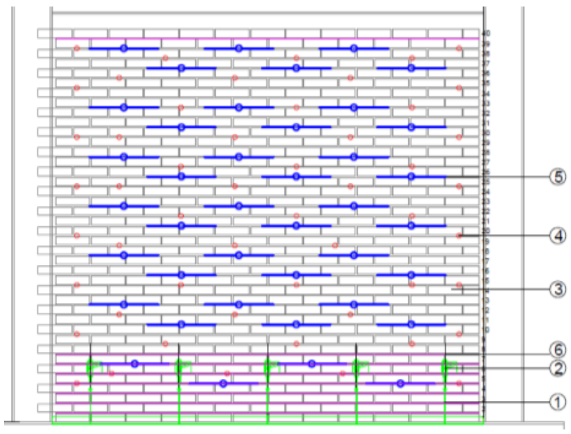

Figure 18. sketch of test set-up for the horizontal parallel seismic test acc. to CAHIER 3725 [2013] with (1) support brackets bolted (2) to the support layer, (3) bricks, (4) straight wall ties, (5) seismic anchors, (6) flexible reinforcement

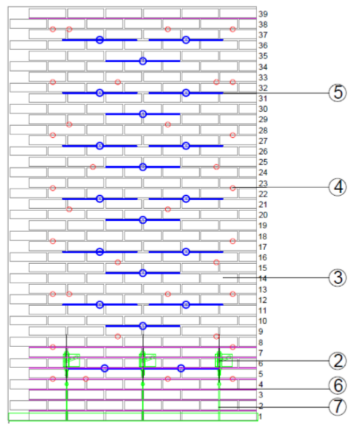

Figure 19. sketch of test set-up for the horizontal perpendicular seismic test acc. to CAHIER 3725 [2013] with (7) support brackets bolted (2) to the support layer, (3) bricks, (4) straight wall ties, (5) seismic anchors, (6) flexible reinforcement

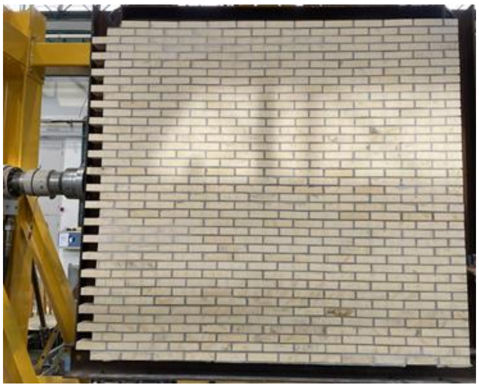

Figure 20. test set-up for the horizontal parallel seismic test acc. to CAHIER 3725 [2013]

Figure 21. test set-up for the horizontal perpendicular seismic test acc. to CAHIER 3725 [2013]

Figure 22. test wall after the horizontal parallel test acc. to CAHIER 3725 [2013]

Figure 23. test wall after the horizontal perpendicular test acc. to CAHIER 3725 [2013]

To determine the domain of application of the seismic brickwork system in the different seismic zones, for different building categories and soil, the acceleration ai for these several options are calculated for France according to EN 1998-1 and compared to the achieved test acceleration in the following. The used formula for the maximum acceleration a_i according DIN EN 1998-1 [2010] / CAHIER 3725 [2013] taking into account a behavior factor qa of the façade of qa = 1 is the following:

$$a_i = 5{,}5 \cdot a_{gr} \cdot \gamma_I \cdot S \tag{2}$$

In equation (2) a_{gr} represents the ground acceleration, γ_I the importance factor for the building category and S the soil factor. The maximum accelerations a_i are compared to the test accelerations from the seismic test according to CAHIER 3725 [2013] and the scope of application of the system is determined. For the considered fixing system the applicability determined by the test is shown in Figure 24.

Applicability of the Leviat seismic brickwork fixing system

		building category			
		I	II	III	IV
Seismic zone	1				
	2			all soils	all soils
	3		all soils	soil A-C	soil A
	4		soil A	soil A	
	5				

no seismic provisions required acc. to CAHIER 3725

not covered by the Leviat seismic brickwork fixing system

Figure 24. applicability of the tested seismic brickwork fixing system

The number of seismic anchors distributed across the area for the test setup was determined by calculation, based on the expected test accelerations and the static load-bearing capacity of the seismic anchors. Using the accelerations a_i of the wall, horizontal equivalent seismic loads F_a were calculated according to CAHIER 3725 [2013] and Eurocode 8 (DIN EN 1998-1 [2010]) by multiplying the accelerations a_i by the mass m of the façade (formula (3). The number n of seismic anchors required can be determined by dividing the seismic equivalent load F_a by the resistance force R_d of a single seismic anchor (formula (4)).

$$F_a = a_i \cdot m \tag{3}$$

$$n = \frac{F_a}{R_d} \tag{4}$$

In the same way, the required number of seismic anchors per façade slice can be determined for the individual conditions of a project site.

7. SUMMARY AND OUTLOOK

The bearing behaviour of façade fixings can be examined either by calculation or by appropriate tests. While relatively accurate calculation methods are available for the calculation of the façade system, fastening and supporting structure, the test is still the most meaningful method for determining the load-bearing capacity and ductility.

Although the most common test method is the macro-scale shake table test, simpler test methods, like single anchor or micro-scale tests or tests on a representative façade area, so called meso-scale tests, are more beneficial.

A so-called Technical Experimentation Assessment. (ATEx) was issued for the validation of a new Leviat seismic fixing system. The tests can be assigned to the meso-scale and are carried out on a façade system to be validated, which is attached to a concrete support layer and loaded either horizontally parallel to the façade or horizontally perpendicular to the façade.

Testing and test results of a seismic brickwork fixing system in a parallel and a perpendicular meso-scale seismic test according to the test procedure of CAHIER 3725 [2013] was described. The tests were supplemented by an individual mathematical determination of the number of anchors for a building to be constructed in an earthquake zone. This calculation was validated by the good accordance of the test result with the pre-assumptions.

The test procedure and test set-up are firmly defined in CAHIER 3725 [2013]; every fixing system that is to be used in France for buildings in seismic zones has to be validated by these tests. In this way, the project participants obtain results for different systems that are easily comparable, and obtain information about suitability and the expected risk - with tests whose effort is manageable due to the meso-scale.

REFERENCES

CAHIER 3725 [2013] *Seismic on cladding / façades*, CSTB, France.

DIN EN 1996-1-1 [2013] *Eurocode 6: Design of masonry structures - Part 1-1: General rules for reinforced and unreinforced masonry structures*, DIN German Institute for Standardization e.V., Germany.

DIN EN 1998-1 [2010] *Eurocode 8: Design of structures for earthquake resistance - Part 1: General rules, seismic actions and rules for buildings*, DIN German Institute for Standardization e.V., Germany.

ETAG 001, Annex E [2013] *Metal Anchors for Use in Concrete, Annex E: Assessment of Metal Anchors under Seismic Action*, European Organization for Technical Approvals, Belgium.

Roik, M., Piesker, C. [2019] "Streamlining the test methods for seismic verification of façade anchors," *Proceedings of 4th International Workshop on the Seismic Performance of Non-Structural Elements (SPONSE)*, Pavia, Italy.

The Influence of High-Dispersion Nonstructural Component Fragility Curves in Damage and Loss Uncertainty

Ioannis Vouvakis Manousakis[1], Dimitrios Konstantinidis[2]

[1] Department of Civil and Environmental Engineering
University of California, Berkeley, USA
e-mail: ioannis_vm@berkeley.edu
[2] Department of Civil and Environmental Engineering
University of California, Berkeley, USA
e-mail: konstantinidis@berkeley.edu

Abstract. The current FEMA P-58 fragility database contains very few occupancy-specific equipment and content fragility curves derived from expert opinion. The methodology outlines a "judgment-based" approach that relies on limit-state calculations for fragility development that can be used for those nonstructural components. Although the implementation is straightforward, the resulting fragility curves have high dispersion. This study quantifies the contribution of uncertainty coming from "judgment-based" equipment and content fragility curves to the uncertainty of the loss measures and compares it against the contribution of other sources of uncertainty. We conducted variance-based sensitivity analysis on the FEMA P-58 performance evaluation results of various code-conforming steel special moment-resisting frame archetypes, considering two occupancy scenarios: Office, for which fragility curves from the existing database are used, and Healthcare, using fragility curves developed with the judgment-based approach for medical equipment and contents. The study quantifies the uncertainty in building response, component quantities, component fragilities, component repair costs, building replacement cost, building collapse, and excessive residual drift fragilities. The results show that the high dispersion of the judgment-based nonstructural component fragility curves of the healthcare case makes them the most significant contributor to the variance of the repair cost distribution. For all cases considered, building response, structural and nonstructural component fragilities, and building collapse and excessive residual drift fragility curves are the highest contributing sources of uncertainty, and their contributions depend on the level of shaking. Since excessive variance in the predicted loss measures is undesirable, the study underscores the need to develop more precise fragility curves for occupancy-specific nonstructural components. It also serves as a proof of concept for using variance-based sensitivity analysis to reveal the sources of uncertainty that contribute the most to the variance of the performance evaluation results.

Keywords: Uncertainty Quantification, Variance-Based Sensitivity Analysis, Damage and Loss Estimation, FEMA P-58, Nonstructural Component Fragility.

1. INTRODUCTION

Advances in Performance-Based Earthquake Engineering (PBEE) have enabled the estimation of earthquake-induced losses, providing a new tool for stakeholders to better understand how their decisions can affect the seismic vulnerability of their assets. The FEMA P-58 methodology [FEMA, 2012a] can produce probabilistic estimates of post-hazard repair cost, downtime, casualties, environmental impacts, and probability of red tagging. Nonstructural component (NSC) performance is crucial in PBEE assessments, as most earthquake-induced losses in recent earthquakes that struck developed countries have been attributed to nonstructural damage [Filiatrault et al., 2001; Chock et al., 2006]. FEMA P-58 loss assessments consider the performance of NSCs using fragility curves and consequence functions.

Despite the growing use of the methodology, few studies have focused on how uncertainty propagates from the various parameters involved in the intermediate calculations of the damage and loss estimation methodology to the output space. Cremen and Baker [2021] used Variance-Based Sensitivity Analysis (VBSA) to rank the relative importance of uncertainty in ground shaking intensity, lateral system type, first-mode vibration period, building age, nonstructural component quantities, and occupancy type, to the FEMA P-58 loss estimates. However, the context of the study was more related to applying the methodology for broader natural hazards assessment rather than assessing the performance of a particular building having known attributes.

Meanwhile, the current fragility curve database, provided as part of the supporting material of FEMA P-58, contains several structural, architectural, electrical, mechanical, and plumbing components, most of which have been developed based on expert opinion and observation of past post-earthquake performance, rather than physical testing or analytical investigations. Moreover, the database contains a very modest collection of occupancy-specific equipment and contents suited to office occupancy scenarios (e.g., modular office workstations, desktop computers, bookcases, and filing cabinets). The FEMA P-58 reports provide a straightforward approach for expanding the database, termed "judgment-based" and demonstrated in the fifth volume [FEMA, 2012c], which requires making subjective assumptions and results in fragility curves with high dispersion. High uncertainty reduces the confidence of decision-makers in the analysis results and weakens their incentive to achieve anything more than code conformance. When uncertainty reduction is the objective, it is helpful to know what source of uncertainty contributes the most, as reducing the uncertainty of that source would have the greatest impact on lowering the output variance.

This study demonstrates a method to decompose the variance of FEMA P-58 damage and loss estimation results to all associated contributing sources. We aim to answer how much of the uncertainty in the earthquake-induced monetary loss is attributed to the uncertainty in building response, nonstructural component quantities, structural and nonstructural component fragility and repair cost, building collapse fragility, and building replacement cost conditioned on a sequence of earthquake intensity measures. We also seek to determine the degree of influence of high-dispersion component fragility curves on the loss estimates.

2. PERFORMANCE EVALUATION

2.1 BACKGROUND

The FEMA P-58 methodology involves a series of distinct analysis steps. For a time-based assessment, where the goal is to quantify the expected losses considering all possible earthquake intensities, these are conducting a probabilistic seismic hazard analysis (PSHA) to quantify earthquake risk, identifying a sequence of shaking intensities that represent distinct hazard levels ranging from frequent earthquakes that cause minimal damage to rare ones that cause significant loss, developing target spectra and selecting suites of representative ground motion records for each hazard level, and conducting nonlinear time-history analysis to obtain the structural response. Finally, damage and losses are estimated via a Monte-Carlo simulation (MCS) approach, using the obtained structural analysis results and predefined probability distributions for the fragility and damage consequence of all components of the building that are capable of producing losses, as well as overall-building-related distributions representing the likelihood for collapse or total loss due to excessive residual drift.

2.2 Archetype Buildings

We considered four steel Special Moment-Resisting Frame (SMRF) structural archetypes, designed according to ASCE 7-22 for a conceptual site in Berkeley, California. All archetypes share the same plan layout, shown in Figure 1 (a). The plan layout was adapted from the building layouts considered in the fifth volume of FEMA P-58, studying the expected seismic performance of code-conforming buildings [FEMA, 2012c]. The plan layout is regular, having four bays in one direction and five bays in the other. Lateral load-carrying capacity is provided by four identical SMRFs located in the perimeter of the plan. The SMRF beam-column connections are pre-qualified reduced beam section (RBS) connections, denoted with triangles in Figure 1 (a). Steel members were proportioned considering AISC 360-16, AISC 341-16, and AISC 358-16. Some basic attributes of the four designs are shown in Table 1. 3D models were developed in OpenSees [McKenna et al., 2010] to obtain the structural response of the archetypes. Nonlinear response was captured through a concentrated plasticity implementation, following ATC guidelines [PEER/ATC, 2010]. All frame elements were modeled as linear elastic, with nonlinear behavior simulated by adding nonlinear springs. This simplified approach was chosen as capable of capturing component-level cycling deterioration without requiring excessive computation time. Gravity columns were pinned at the base. Nonlinear springs were added at the two ends of gravity beams, in the direction of strong-axis bending, to simulate the effects of gravity shear-tab connections, using the pinched hysteretic model proposed by Elkady and Lignos [2015]. The model parameters depend on the plastic flexural capacity of the beam and were derived from calibration based on test data. RBS beams were modeled similarly, using a model proposed by Lignos and Krawinkler [2011] and Elkady and Lignos [2014]. The model accounts for the composite action between the floor and the supporting beams. Panel zone behavior was modeled explicitly using a method proposed by Gupta and Krawinkler [1999].

2.3 Performance Evaluation Results

PSHA was conducted using the Open-Source Seismic Hazard Analysis Software (OpenSHA)

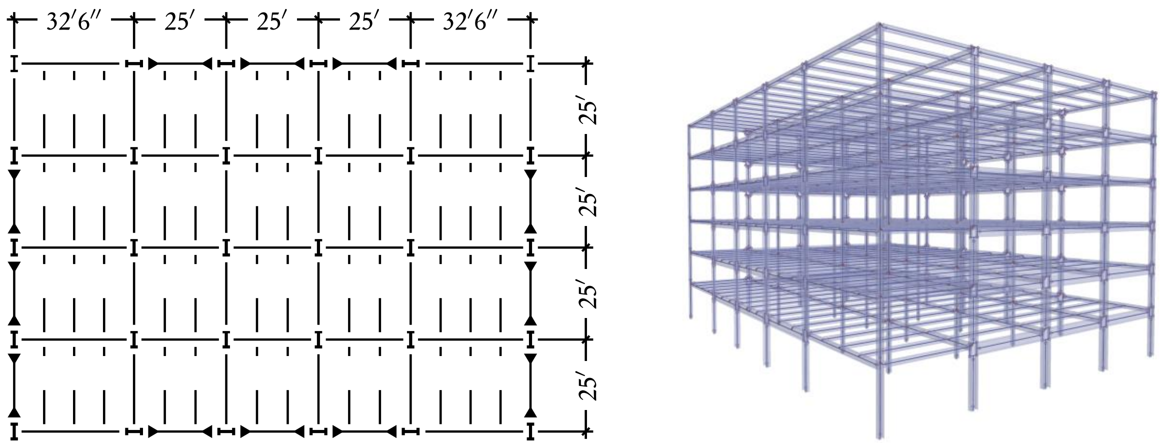

(a) **(b)**

Figure 1. (a) Plan layout of the archetype buildings, (b) Archetype 6-II OpenSees model perspective

Table 1. Archetype building design attributes

Code	Number of Stories	Risk Category	1st Mode Period[(1)] $\bar{T}$ (s)	Design Drift (%)	Seismic Weight (kip)	Median Collapse $Sa(\bar{T})$ (g)
3-II	3	II	0.93	2.0	2395	3.35
6-II	6	II	1.34	2.0	4750	1.74
3-IV	3	IV	0.77	1.5	2395	5.32
6-IV	6	IV	1.07	1.5	4750	2.87

(1) Average of the first-mode vibration periods at the two primary directions of the building

[Field et al., 2003]. The obtained hazard curves for a RotD50 spectral acceleration corresponding to the average first-mode period of the examined archetypes are shown in Figure 2 (a). As shown in the figure, 16 hazard levels were considered. A uniform hazard spectrum (UHS) was generated for each hazard level using OpenSHA. While a conditional mean spectrum (CMS) would presumably provide a better target spectrum for a single building, a UHS permitted using the same suite of ground motions for each hazard level across all archetypes, enabling comparison. 14 ground motion records were selected from the PEER NGA-West2 ground motion database and scaled to match the target spectrum of each hazard level. A multi-period loss function was chosen, aiming to retrieve records that match the entire shape of the target spectra. The target spectrum, the selected ground motion suite mean and standard deviation, and the individual records corresponding to hazard level 16 are shown in Figure 2 (b).

To conduct damage and loss estimation, two performance models were assembled for each archetype, corresponding to two occupancy type scenarios: office and healthcare. Structural component fragilities were defined considering the structural layout and configuration of each archetype. Architectural, mechanical, electrical, and plumbing component quantities were assigned using the Normative Quantity Estimation Tool, provided as part of the supporting electronic materials of FEMA P-58. The fragility and consequence parameters for office components were obtained from the FEMA P-58 component fragility database. Since medical component fragilities are not available in the FEMA P-58 fragility database, the medical component fragilities, damage state definitions, and loss data used in FEMA P-58 vol. 5 [FEMA, 2012c] were used in this study, with modified quantities and locations to fit the examined archetypes. Medical components consist of anchored acceleration-sensitive and mobile velocity-sensitive equipment. As done in FEMA P-58 vol. 5, the median value of the fragility curves was derived using FEMA P-58

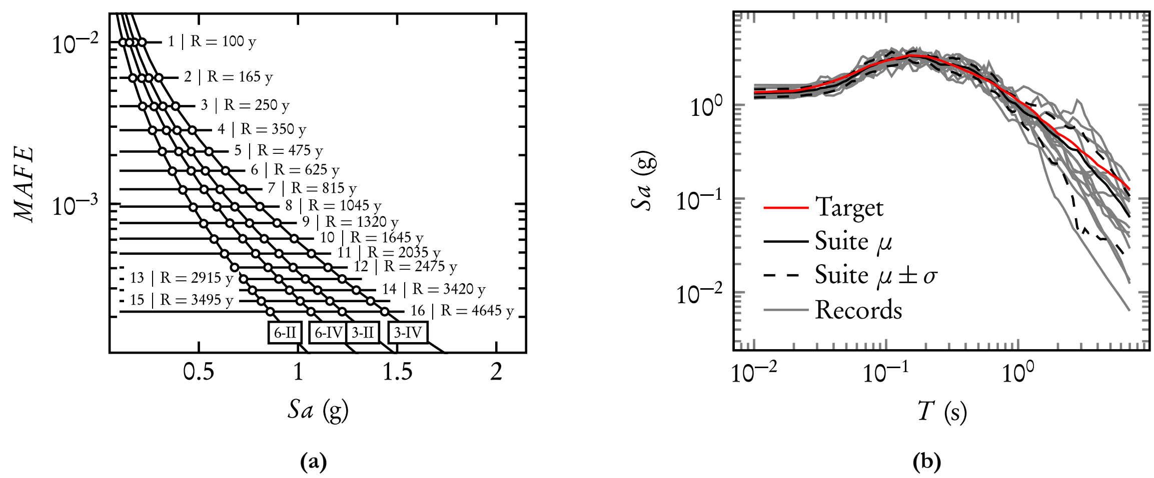

Figure 2. (a) Hazard curves and identified hazard levels, (b) Target spectrum and selected ground motion suite mean, standard deviation and record spectra for the 16th hazard level

vol. 1 Equations 3-2 and 3-15 [FEMA, 2012a], for acceleration-sensitive and velocity-sensitive components, respectively, and a dispersion of 0.5 was assigned. Except for the occupancy-specific components, the rest of the components used for the two occupancy scenarios are the same for any given archetype to provide a baseline for comparing the effects of the different occupancy-specific components. The mean building replacement cost for the two occupancy scenarios was derived assuming a unit cost of 250 USD/ft^2 for the office occupancy and 400 USD/ft^2 for the healthcare occupancy. Building replacement cost was assumed to be lognormally distributed with a coefficient of variation of 0.1. Collapse fragilities were developed using SPO2IDA [Vamvatsikos and Cornell, 2006] to obtain median values, with an assigned dispersion of 0.6. This collapse fragility development approach, proposed in FEMA P-58 vol. 1, sec. 6.3, was chosen as it is likely to be used extensively in practice due to its simplicity. A residual drift fragility curve, considering global behavior (as opposed to individual stories), having a median of 1% and a dispersion of 0.3, was used for all archetype buildings. A building replacement threshold of 1.0 was assumed for all performance evaluations. Therefore, excluding cases of collapse or excessive residual drift, the building was considered a complete loss only if the component repair cost exceeded the building replacement cost. Lower replacement threshold values are more realistic, and FEMA P-58 suggests using a value of 0.4. A lower replacement threshold leads to more cases of building replacement caused by excessive component damage, which amplifies the expected repair cost and the relevance of the variance associated with building contents to the variance of the repair cost. Modelling uncertainty, β_M, is used to amplify the variability in building response to account for uncertainty in the ability of the used model to capture the real behavior or the material properties and construction quality of the physical building being modelled. We assumed average building analysis and construction quality ($\beta_M = 0.353$).

Performance evaluation analyses were conducted using an instance of *pelicun* [Zsarnoczay, 2019] which we modified for the purposes of the present study to support VBSA calculations. Figure 3 shows the mean and standard deviation of the repair cost for each archetype, occupancy type and hazard level. Note that Risk Category II and IV cases only differ in the structural model, while the same performance model is used. Even so, we observe that the mean losses are effectively the same while the standard

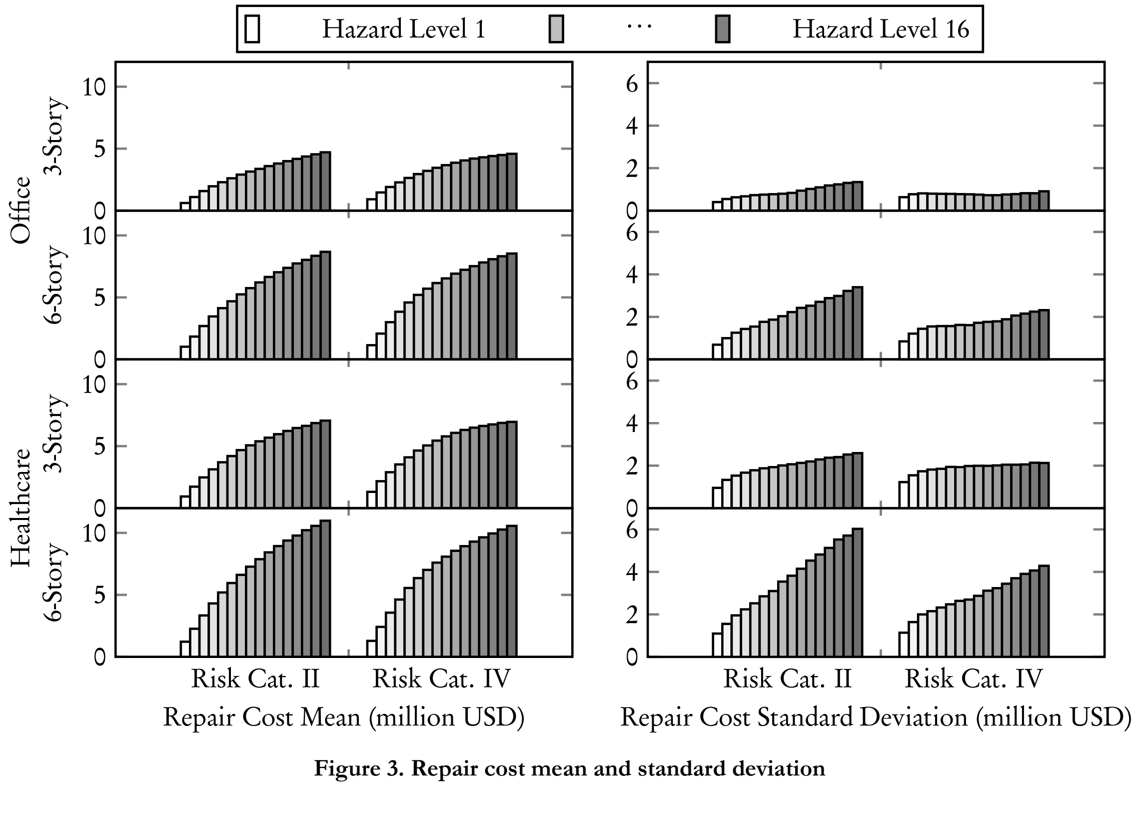

Figure 3. Repair cost mean and standard deviation

deviations are reduced, with the taller archetypes exhibiting a stronger reduction. These effects are due to the stiffer design of the Risk Category IV archetypes, of which the response for any given hazard level had a smaller standard deviation and was characterized by lower drifts and higher accelerations compared with the response of the Risk Category II archetypes. The difference in the standard deviation between the healthcare and the office occupancy cases is entirely attributed to the different occupancy-specific components and specifically to the higher dispersion of the medical equipment.

3.VARIANCE-BASED SENSITIVIY ANALYSIS

3.1 BACKGROUND INFORMATION

The goal of VBSA is to quantify how much of the variance of the output of a probabilistic model, $\mathrm{Y} = h(\mathrm{X}_1, \mathrm{X}_2, \ldots, \mathrm{X}_n)$, is attributed to the contributions of its individual random variable inputs, X_i, and their interactions. It is a global method, meaning that it considers the entire range of possible values of the examined inputs to assess their contribution to the output variance. Saltelli et al. [2008] described the earlier development, provided theoretical background, and offered a practical numeric implementation of VBSA. For the benefit of the reader, this section will provide a brief overview of some basic definitions.

The following expression defines the *first-order sensitivity index* of input X_i:

$$s_i = \frac{\mathrm{V}_{\mathbf{X}_{-i}}\left[\mathrm{E}_{\mathrm{X}_i}\left[\mathrm{Y} \mid \mathrm{X}_i = x\right]\right]}{\mathrm{V}[\mathrm{Y}]} \tag{1}$$

where $\mathrm{V}_{\mathbf{X}_{-i}}[\cdot]$ denotes the variance under the distribution of all inputs except X_i, and $\mathrm{E}_{\mathrm{X}_i}[\cdot]$ the expectation under the distribution of input X_i. By the law of total variance, $s_i \in [0,1]$. A value close to one indicates that the variance of input X_i contributes substantially to the output variance. A low value, however, does not rule out the possibility of interactions between input X_i and other inputs having a high contribution. Higher-order sensitivity indices can capture these interaction effects. The *total-order sensitivity index* of input X_i captures the first-order as well as all higher-order effects involving that input, defined as follows:

$$s_T = \frac{\mathrm{E}_{\mathbf{X}_{-i}}\left[\mathrm{V}_{\mathrm{X}_i}\left[\mathrm{Y} \mid \mathbf{X}_{-i}\right]\right]}{\mathrm{V}[\mathrm{Y}]} \tag{2}$$

where $\mathrm{V}_{\mathrm{X}_i}\left[\cdot\right]$ denotes the variance under the distribution of input X_i, $\mathrm{E}_{\mathbf{X}_{-i}}\left[\cdot\right]$ the expectation under the distribution of all inputs except X_i, and $\mathbf{X}_{-i}$ represents all inputs except X_i.

A low value of the total-order sensitivity index of an input indicates that its variance has no contribution to the variance of the output, and it could be fixed to its mean without affecting the results. The above definitions apply to a single input, X_i. However, models can have many inputs that can be arranged into groups. Grouping allows quantifying the effects of the joint distribution of some random variables on the output variance and helps bring down the number of the resulting indices. It is accomplished by partitioning the input space, $\mathbf{X}$, into the group of inputs of interest, $\mathbf{X}_g$, and the rest of the inputs, $\mathbf{X}_{-g}$. Similar to the single-input case, the effective first-order sensitivity index for the group is defined as

$$s_g = \frac{\mathrm{V}_{\mathbf{X}_{-g}}\left[\mathrm{E}_{\mathbf{X}_g}\left[\mathrm{Y} \mid \mathbf{X}_g\right]\right]}{\mathrm{V}[\mathrm{Y}]} \tag{3}$$

and the effective total-order sensitivity index of the group is defined as

$$s_{T,g} = \frac{\mathrm{E}_{\mathbf{X}_{-g}}\left[\mathrm{V}_{X_g}\left[\mathrm{Y} \mid \mathbf{X}_{-g}\right]\right]}{\mathrm{V}[\mathrm{Y}]} \tag{4}$$

Research efforts have yielded methods to efficiently estimate the sensitivity indices numerically, via MCS approaches. This study used the method outlined by Saltelli et al. [2010], the details of which are omitted here for brevity.

3.2 SENSITIVITY ANALYSIS RESULTS

All random variables involved in the FEMA P-58 repair cost estimation process were partitioned into six groups. The EDP group consists of random variables used for sampling simulated engineering demand parameters. The C-DM group contains all random variables used for sampling fragility threshold values for structural and nonstructural component damage state determination. Those values determine the engineering demand parameter capacity associated with the exceedance of each damage state of a component. The C-DV group contains all random variables used for accounting for the uncertainty in the repair cost of building components. The C-QNT group consists of random variables used to sample component quantities. The B-DM group is similar to the C-DM group, but the associated random variables correspond to building collapse and excessive residual drift fragility curves. Finally, B-DV is a single random variable that accounts for the building replacement cost uncertainty. While building replacement cost is assumed to be constant in the FEMA P-58 framework, randomness in that quantity was considered in this study to investigate the extent of its contribution to the output variance and assess the soundness of the current practice of fixing that quantity to its expected value.

Using the notion of the first-order and total-order sensitivity indices of groups of random variables, VBSA was performed for the groups. The first-order and total-order sensitivity indices of each group were obtained for all hazard levels. A 95% bootstrap confidence interval was generated for each sensitivity index. The results are shown in Figure 4. Results are plotted for each hazard level in ascending order looking from left to right. The bottom and top of each bar indicate the first-order and total-order sensitivity indices, respectively, as the total-order indices always exceed the first-order indices. The thickness of each bar quantifies interactions between the considered group and the rest of the groups. When interpreting the results, it is helpful to keep in mind that the sensitivity indices are quantities normalized by the same output variance for any given hazard level. Therefore, if most of that output variance is attributed to one group, the rest of the groups will have lower sensitivity indices.

In all cases, uncertainty in the component repair cost (C-DV), component quantities (C-QNT), and building replacement cost (B-DV) contribute much less to the variance of the result compared to the other groups. Comparing the results of the two occupancy scenarios, we observe that the EDP group sensitivity indices generally exceed those of the C-DM group for the office occupancy in most cases, while the opposite is true for the healthcare case. The amplification of the C-DM contribution results from the crudely defined equipment and content fragility curves of the healthcare occupancy, as all other performance evaluation inputs are the same. We also observe that the uncertainty in building replacement cost, represented by B-DV, has a negligible contribution to the results across all considered scenarios in this study. These results justify the practice of considering the building replacement cost as a fixed quantity. This, however, would not necessarily be the case if the variance of the building replacement cost was high. We used a reasonably small variance as it is expected that in a critical practical application, enough market research should precede a performance evaluation to lower the uncertainty in cost-related quantities as much as possible. Finally, we observe that the contribution of uncertainty related to the building fragilities becomes important at high shaking intensities. As most cases of building replacement were triggered by building collapse, this highlights the need to use a more precise collapse fragility development process. It should be noted, however, that using a building replacement threshold of 0.4 can reduce the relevance of the building fragility curves, as the increased number of realizations of building replacement due to excessive component damage amplifies the effects of uncertainty associated with component performance.

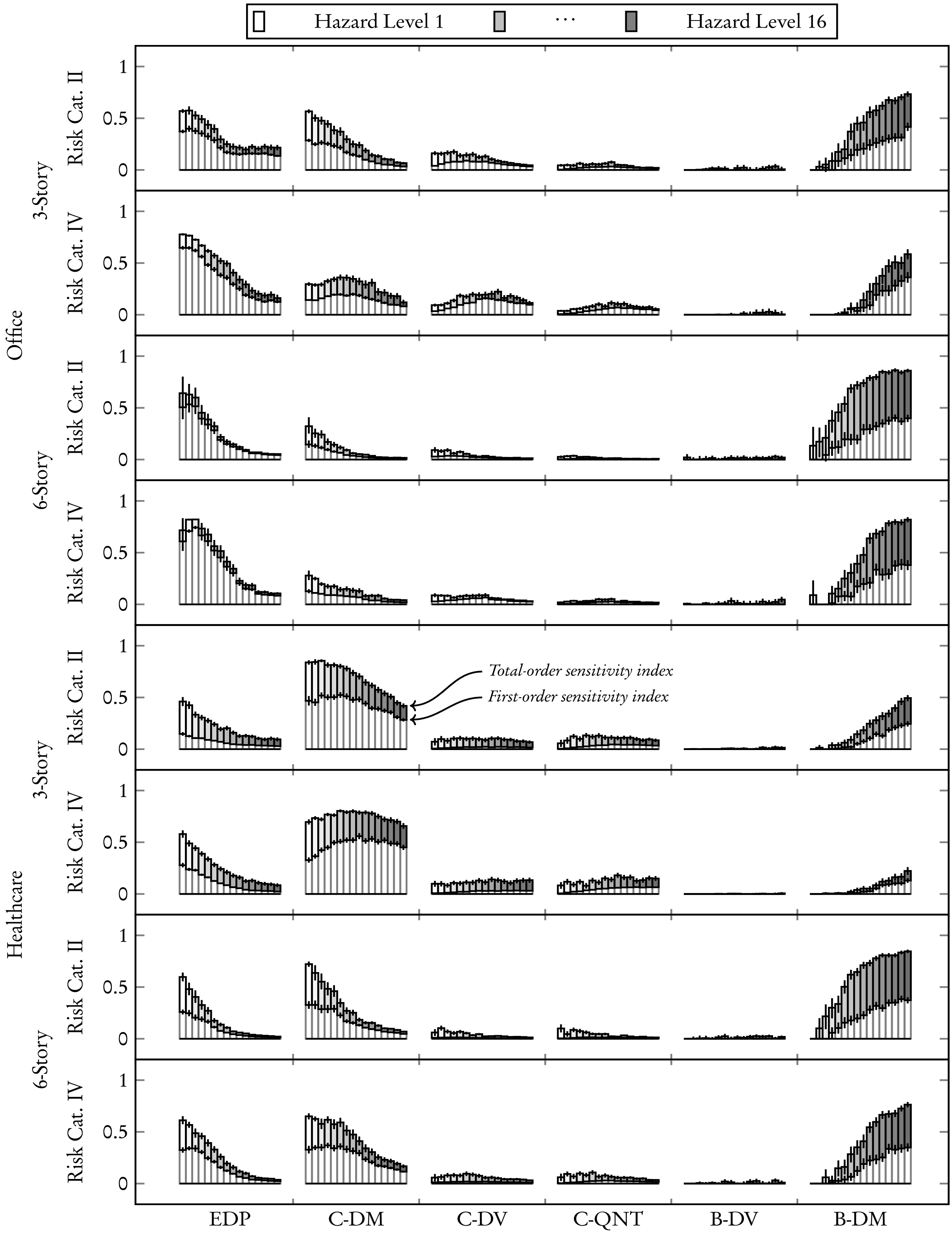

Figure 4. VBSA results assuming average building analysis and construction quality (β_M = 0.353). The bottom and top of the bars correspond to the first-order and total-order sensitivity indices, respectively. Error bars show a 95% bootstrap confidence interval.

4. CONCLUSIONS

This study utilized variance-based sensitivity analysis to demonstrate the level of contribution of each of the sources of uncertainty that are considered in the damage and loss estimation framework of the FEMA P-58 methodology: uncertainty associated with the response of the building conditioned on the level of shaking, the likelihood of collapse or excessive residual drift that would prevent the building from being repairable, the damage potential of its structural and nonstructural components, their quantities and the cost associated with repairing that damage, and the replacement cost of the building if it cannot be repaired. We aimed to quantify the level of contribution of uncertainty introduced by using judgment-based equipment and content fragility curves.

The results show that there is no single source of uncertainty that consistently ranks higher than the rest across all examined configurations, occupancies, and shaking intensities. However, considering the examined cases, uncertainty in building response (resulting from different ground motion inputs and modelling uncertainty), structural and nonstructural component fragility (i.e., dispersion of the component fragility curves), and building fragility (i.e., dispersion of the fragility curves used to distinguish cases in which the building can be repaired versus being a complete loss) generally contribute the most. The highest contributing source depends on the level of earthquake shaking, the specified modelling uncertainty, the building replacement threshold, and the quality of the defined performance model. VBSA provides a tool to reveal the most predominant contributor and guide efforts to increase the precision of the loss estimates.

While substantial research has been conducted to predict building collapse and irreparability, limited tools are available for quantifying the fragility of building components and equipment that would provide a more refined performance model to reduce uncertainty. By enabling comparison between the two occupancy scenarios, the study demonstrated that using judgment-based nonstructural component fragility curves with high dispersion to expand the available fragility database, as outlined in Chapter 7 of FEMA P-58 vol. 2 and implemented in vol. 5 [FEMA, 2012a,b], greatly increases the contribution of the uncertainty in the component fragilities to the uncertainty of the estimated repair cost, with the potential for those fragility curves to become the limiting factor for the accuracy of the result. Their high contribution may be amplified when the framework is applied to essential buildings, such as healthcare facilities, where modelling and construction qualities are superior. Analyses with a building replacement threshold of 0.4, which are not shown here for the sake of brevity, suggest a further increase in their contribution.

This study should not be interpreted as an attempt to capture the effects of uncertainty associated with the seismic hazard of the site or the structural properties and modelling accuracy of the examined buildings to the performance evaluation results. The goal was to follow the steps outlined in FEMA P-58 for a time-based assessment and provide insight into the effects of the uncertainty introduced from the random variables involved in the damage and loss estimation framework applied to the considered case studies. The above effects remain an open question.

REFERENCES

Chock, G. et al. [2006]. “Compilation of Observations of the October 15, 2006, Kiholo Bay (Mw 6.7) and Mahukona (Mw 6.0) Earthquakes, Hawaii,” Earthquake Engineering Research Institute, Oakland, California.

Cremen, G., Baker, J.W. [2021] “Variance-based sensitivity analyses and uncertainty quantification for FEMA P-58 consequence predictions,” *Earthquake Engineering & Structural Dynamics*; Vol. 50, No. 3, pp. 811–830.

Elkady, A., Lignos D.G. [2014]. "Modelling of the composite action in fully restrained beam-to-column connections: Implications in the seismic design and collapse capacity of steel special moment frames," *Earthquake Engineering & Structural Dynamics*, Vol. 43, No. 13, pp. 1935–1954.

Elkady, A., Lignos D.G. [2015]. "Effect of gravity framing on the overstrength and collapse capacity of steel frame buildings with perimeter special moment frames," *Earthquake Engineering & Structural Dynamics*, Vol. 44, No. 8, pp. 1289–1307.

FEMA [2012a]. "Seismic Performance Assessment of Buildings: Methodology." Federal Emergency Management Agency, Vol. 1, Washington, D.C.

FEMA [2012b]. "Seismic Performance Assessment of Buildings: Implementation Guide." Federal Emergency Management Agency, Vol. 2, Washington, D.C.

FEMA [2012c]. "Seismic Performance Assessment of Buildings: Expected Seismic Performance of Code-Conforming Buildings" Federal Emergency Management Agency, Vol. 5, Washington, D.C.

Field, E.H., Jordan, T.H., Cornell, C.A. [2003] "OpenSHA: A developing community-modelling environment for seismic hazard analysis," *Seismological Research Letters*, Vol. 74, No. 4, pp. 406–419.

Filiatrault, A., Uang C.M., Folz B., Christopoulos C., Gatto K. [2001] "Reconnaissance Report of the February 28, 2001 Nisqually (Seattle-Olympia) Earthquake," Tech. rep. SSRP-2001/02. Department of Structural Engineering, University of California, San Diego.

Gupta, A., Krawinkler, H. [1999] "Seismic Demands for Performance Evaluation of Steel Moment Resisting Frame Structures," Tech. rep. 132, John A. Blume Earthquake Engineering Center, Stanford, California.

Lignos, D.G. and Krawinkler H. [2011] "Deterioration modelling of steel components in support of collapse prediction of steel moment frames under earthquake loading," *Journal of Structural Engineering*, Vol. 137, No. 11, pp. 1291–1302.

McKenna, F., Scott, M., Fenves, G. [2010] "Nonlinear finite-element analysis software architecture using object composition," *Journal of Computing in Civil Engineering*, Vol. 24, No. 1, pp. 95–107.

PEER/ATC [2010]. "Modeling and acceptance criteria for seismic design and analysis of tall buildings," Tech. rep. 72-1. Redwood City, California.

Saltelli, A, Annoni, I., Azzini, F., Campolongo, M., Ratto, M., Tarantola, S. [2010] "Variance based sensitivity analysis of model output. Design and estimator for the total sensitivity index," *Computer Physics Communications*, Vol. 181, No. 2, pp. 259–270

Saltelli, A., Ratto, M., Andres, T., Campolongo, F., Cariboni, J., Gatelli, D., Saisana, M., Tarantola, S. [2008] *Global sensitivity analysis: the primer*, John Wiley & Sons, New York, New York.

Vamvatsikos, D., Cornell, C.A. [2006] "Direct estimation of the seismic demand and capacity of oscillators with multi-linear static pushovers through IDA," *Earthquake Engineering & Structural Dynamics*, Vol. 35, No. 9, pp. 1097–1117.

Zsarnoczay, A. [2019] *pelican* (v1.1.0). DOI: 10.5281

Seismic performance of acceleration sensitive non-structural elements in stiff self-centring structural systems

Wilson W. Carofilis[1], Eugene Kim[2], and Donghyuk Jung[3]

[1] Dept. of Civil & Environmental Engineering, University of Waterloo
200 University Ave W E2-3320 Waterloo, ON, Canada
e-mail: wcarofil@uwaterloo.ca
[2] Dept. of Civil & Environmental Engineering, University of Waterloo
200 University Ave W CPH 3611B Waterloo, ON, Canada
kekim@uwaterloo.ca
[3] School of Civil, Environmental and Architectural Engineering, Korea University, Korea
jungd@korea.ac.kr

Abstract. Resilience-based design philosophies which aim to minimize the downtime following a disaster is becoming more widely embraced by engineers and society in general. Self-centring buckling-restrained braces have been shown to be an effective way to improve a building's seismic resilience by reducing lateral displacements and residual deformations. However, one potential drawback for such systems is the increased lateral stiffness leading to increased peak floor accelerations which may impact acceleration sensitive non-structural elements such as ceiling systems, piping/ducts, and electrical systems. Damage to these components can significantly affect building safety and function resulting in large economic losses and long-term or permanent displacement of population after a seismic event. Furthermore, such non-structural components may be crucial to the operation of essential facilities such as hospitals. To assess the vulnerability of non-structural elements and develop mitigation measures, this paper analytically investigates the seismic performance of acceleration sensitive non-structural components in moment resisting steel frame buildings with and without self-centring buckling restrained braces. First, non-structural elements are classified according to their importance in regaining at least partial building functionality after an earthquake. Then, floor response spectra are determined for each storey and compared to the unbraced frame configuration to identify the period range with higher spectral floor demands and examine the components that are likely to be damaged. Based on the numerical simulation results, a loss estimation analysis and resilience assessment are carried out to determine the overall building performance. The outcomes demonstrate that although self-centring buckling restrained braces can substantially enhance the overall structural behaviour of buildings, non-structural elements need to be protected through equivalent retrofitting measures to ensure overall seismic resilience.

Keywords: seismic performance, acceleration sensitive, partial functionality, spectral response, loss estimation.

1. INTRODUCTION

Although a building is structurally safe after an earthquake, damage to non-structural elements (NSEs) such as ceiling systems, piping/ducts, and electrical systems can compromise its normal operation and render it unoccupiable for an extended period of time. Even frequent earthquakes (i.e., low intensity ground motions) can significantly influence the functionality of critical facilities such as hospital buildings [Gabbianelli *et al.*, 2020]. Moreover, recent studies [Sousa and Monteiro, 2015; O'Reilly *et al.*, 2018] have shown that damage to NSEs can account for a large fraction of the total economic losses in earthquakes, particularly in lower intensity events. This supports the findings of Miranda and Taghavi [2003] and Bevere *et al.*, [2019] who reported that losses associated to NSEs can represent around 60-80 % of the total financial losses in buildings.

As outlined by Merino *et al.*, [2019], NSEs can be classified into two groups according to their response sensitivity. The first group is displacement or drift sensitive NSEs. The damage experienced by these elements is most closely related to inter-story drifts in the supporting structure. Wall partitions and glazing facades are good examples of displacement sensitive NSEs [Merino *et al.*, 2019]. The other group is acceleration sensitive NSEs, for which damage in earthquakes is primarily induced by inertia forces arising from horizontal and vertical accelerations of the supporting structure. Some acceleration sensitive NSEs are piping systems, ceiling systems and anchored or free-standing mechanical equipment [Merino *et al.*, 2019]. A building's functionality and occupiability depends on the operation of these NSEs. It is possible that a building experiences only minor structural damage but sustains severe damage to NSEs in an earthquake, leading to long-term loss of functionality. An example of this is the Santiago International Airport which was closed for several days following the 2010 Chile earthquake because of severe damage to NSEs (e.g., piping systems interacting with ceiling systems) [Miranda *et al.* 2012].

The performance of NSEs in earthquakes is gaining more attention as resilience-oriented approaches are becoming more relevant as a beyond-code philosophy surpassing not only traditional seismic design criteria but also performance-based approaches. The two key components in seismic resilience of buildings are 1) reducing the damage sustained, and 2) rapidly restoring initial conditions. Consequently, this also implies decreasing any possible damage to NSEs. The importance of NSEs for regaining the primary function of buildings is strongly emphasized by Almufti and Willford [2013] in the resilience-based earthquake design initiative (REDi) guidelines. For primary function, a building requires restoration of power, water, fire sprinklers, lighting, and heating, ventilation, and air conditioning (HVAC) systems while also ensuring that elevators are back in service. In residential buildings, functional recovery is primarily related to occupant comfort and health, thus requiring lights, water, heating, and air conditioning [Almufti and Willford, 2013].

Despite the role of NSEs in building functionality, seismic performance has traditionally been defined solely by the performance of the lateral system with retrofit measures focusing on increasing their lateral strength capacity. Nevertheless, conducting such structural interventions can generate other complications. For example, O'Reilly and Sullivan [2018] observed that the expected annual losses (EAL) in existing reinforced concrete (RC) frames is substantially increased when the lateral force resisting system is strengthened and/or stiffened. This approach may serve to improve the collapse capacity and to reduce losses from drift sensitive components, but a stiffer building also means higher floor acceleration demands. Therefore, more damage to acceleration sensitive NSEs can be expected to increase the net EAL. This also affects the overall resilience of buildings as more damaged NSEs would lengthen the time needed to repair and restore the building's functionality. Self-centring structural systems are affected by the same issue. For instance, Carofilis *et al.*, [2022a] examined the performance of steel moment resisting frames with self-centring buckling restrained braces (SCBRBs) with iron-based shape memory alloys (Fe-SMA) and found that while SCBRBs substantially reduce lateral displacements and residual deformation, floor accelerations are considerably increased.

This paper builds on the work of Carofilis *et al.*, [2022a] to more closely examine the performance of NSEs in structurally retrofitted buildings and quantify their impact on the overall seismic resilience. A three-storey steel moment frame building is analysed with and without SCBRBs to compare the demands and a loss assessment is carried out to determine the fraction and contribution of acceleration and drift sensitive NSEs to the total economic losses. Based on the analysis results, NSEs contributing the most to the economic losses are identified and the effectiveness of three NSE retrofit scenarios are assessed in terms of improvement to recovery time. Results show that retrofits to NSEs not only lead to substantial reductions in economic losses but also in the time needed to restore building functionality, contributing significantly to enhancing its seismic resilience.

2.SCBRBs MODEL

SCBRBs are efficient energy dissipative systems used to control structural damage under earthquake actions [Miller *et al.*, 2012; NIST 2015]. The self-centring ability and energy absorption of these systems can considerably reduce the damage to other main structural elements such as beams and columns [Miller *et al.*, 2012]. The SCBRB conceptualized in the study of Carofilis *et al.*, [2022a] relies on the shape memory effect of Fe-SMAs acting as prestressed tendons to provide the self-centring effect. Fe-SMAs are a relatively new development and only possess the shape memory effect (i.e., heat-activated material behaviour which allows it to recover plastic strains and return to original shape), but at a fraction of the cost of other SMAs (e.g., Ni-Ti SMAs). More details about the design and modelling of SCBRB with Fe-SMA device can be found in Carofilis *et al.*, [2022a].

Figure 1 illustrates the case study building which consist of a three-storey 2D steel moment resisting frame adopted from the study by Chalarca [2020] and FEMA 440 [2005]. The model was developed in OpenSees [Mckenna *et al.*, 2010] applying the modelling techniques and assumptions of Chalarca [2020]. The building is characterized by brittle beam-column joint connections typical of the pre-Northridge seismic designs. The fundamental period of the bare frame and braced frame (SCBRB with Fe-SMA) is 0.37 seconds and 0.79 seconds respectively. Figure 1 also illustrates the idealized behaviour of the SCBRB which follows a bilinear behaviour during the loading phase and a trilinear behaviour during the unloading stage. This behaviour produces good self-centring properties and shows negligible residual deformations at unloading, which are produced in the steel core of the brace system [Liu et al., 2018]. The self-centring ability of the SCBRB system comes primarily from the pretension of the Fe-SMA tendons while the energy dissipation is provided by yielding of the steel core.

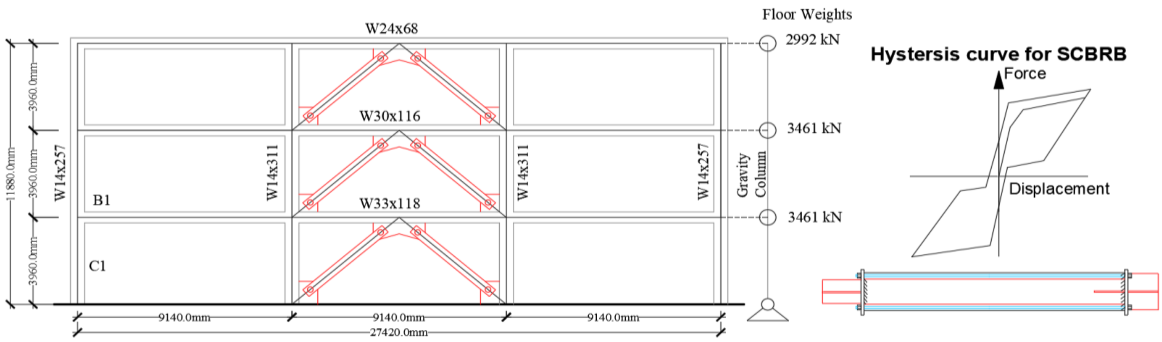

Figure 1. Building model configuration

The FEMA P-695 [2009] far-field ground motion set composed of 44 individual records are shown in Figure 2. They represent the seismicity of western United States. The records were scaled such that the median spectral acceleration at a period of one second matches the ASCE 7-16 [2017] design spectrum for the city of Los Angeles with a soil type Dmax. Figure 2 includes the acceleration response spectra for all ground motion records as well as the median and design spectra for the design earthquake (DE).

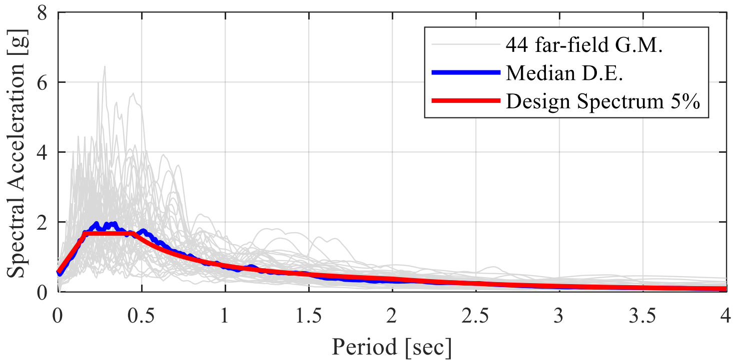

Figure 2. 5% damping FEMA P-695 far-field and ASCE 7-16 design acceleration spectra selection

3.PERFORMANC OF NON-STRUCTURAL ELEMENTS

3.1 NSEs Assessment Overview

Floor acceleration spectra are commonly used for the seismic design and assessment of acceleration sensitive NSEs (e.g., mechanical, electrical, plumbing, and architectural) [Vukobratović and Fajfar, 2017]. Floor response spectra are estimated through nonlinear time-history analyses, which also give information about other demand parameters such as peak floor accelerations (PFAs), peak storey drifts (PSDs), and residual storey drifts (RSDs). It is important to note that NSEs are not directly excited by the earthquake ground motion. Instead, demands on NSEs are a result of the building's dynamic response to the earthquake ground motion. As such, the floor response spectra and the displacement response time history of the building are used to estimate the peak demands on NSEs.

3.2 Floor Response Spectra

Figure 3 compares floor acceleration and displacement spectra of the bare and braced frames at each storey. It is observed that the floor spectral acceleration in the first storey is comparable for the bare and braced frame (SCBRB) in the short period range (< 0.15 seconds) which suggests stiff NSEs on the first floor with natural periods shorter than 0.15 seconds would be subjected to similar demands regardless of whether the structure is braced or not. On the other hand, for subsequent storeys the spectral floor accelerations are higher in the braced frame given the much larger stiffness of this system particularly for the period range of 0.3-0.8 seconds. The peaks of the floor acceleration spectra in the bare frame corresponds to its first three periods of vibration, while for the braced frame the peaks are shifted to the right of its fundamental period (0.37 seconds). Addition of the SCBRB changes the vibration modes in the building and the period associated to the peak floor spectral acceleration becomes dominant compared to the fundamental period of the braced building. This effect is especially pronounced in the second and third storeys where the peak is located around 0.5 seconds which is 1.34 times the fundamental period of the braced frame. From these floor acceleration response spectra, it is clear that in the building with the braced frame, NSEs with natural periods in the range of 0.3-0.8 seconds will be subjected to significantly higher spectral floor accelerations than in the unbraced bare frame. For NSEs with long natural periods, the spectral accelerations are comparable in the bare and braced frame models. In the first storey, this is true for non-structural periods longer than 1 second, whereas in the second and third storeys it is true for non-structural periods exceeding 2 seconds. With or without bracing, NSEs with long non-structural periods generally do not present a concern since the floor acceleration will generate low inertia forces.

In terms of the floor displacement, the floor displacement response spectra show that the displacement demand on NSEs with non-structural periods between 0.3-0.8 seconds will be significantly greater when the frame is braced. As a result, these elements in the SCBRB system are likely to suffer more damage due large demands. Therefore, the seismic performance of stiff drift sensitive NSEs (e.g., masonry walls, interior walls, or partitions walls) must be improved in order to mitigate any possible damage related to large displacement demands. In general, SCBRB reduces the displacement demand on NSEs with non-structural periods larger than 0.8 seconds, especially on the second and third storeys.

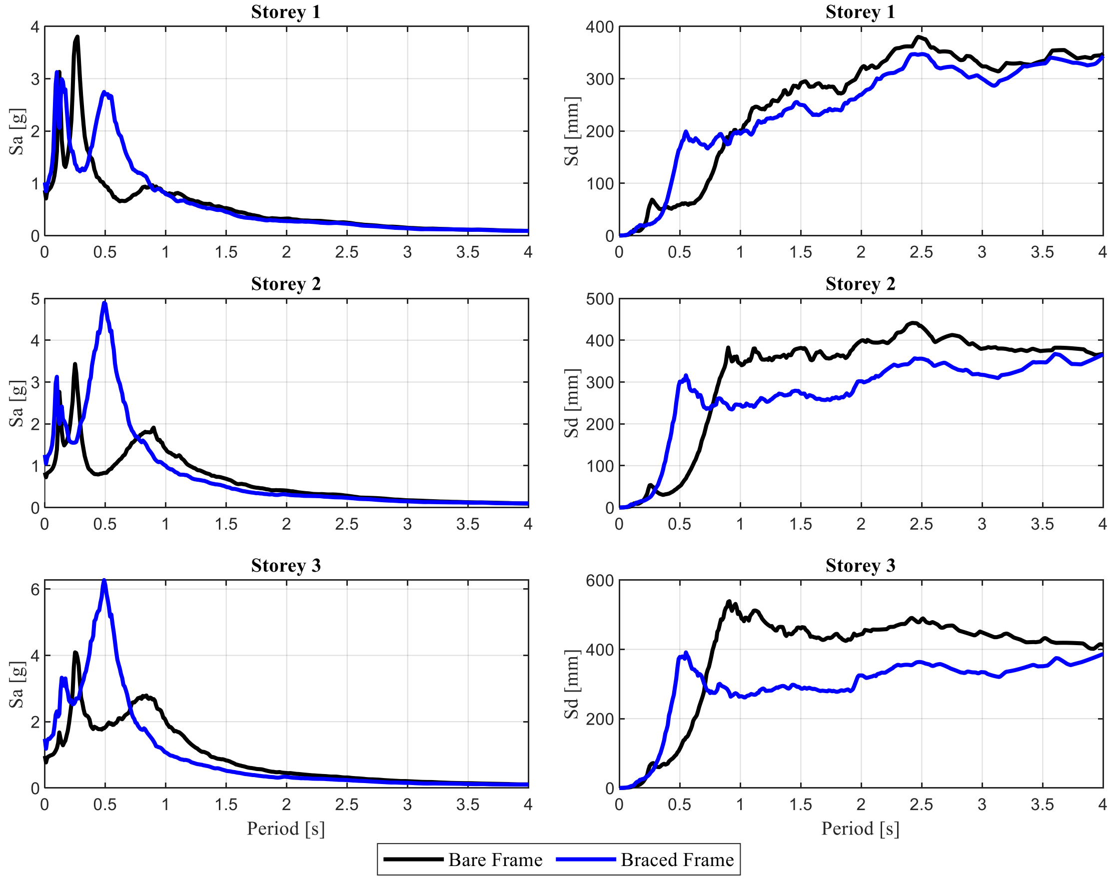

Figure 3. Floor response spectra

Based on the seismic floor demands, the seismic demands on NSEs can be estimated and NSEs can be properly designed or seismically retrofitted. The impact of an earthquake can also be quantified through loss assessment analysis. In the subsequent sections, earthquake damage to NSEs and the effect of retrofitting NSEs will be estimated based on expected economic losses.

4.LOSS ASSESSMENT

A loss assessment was carried out for the DE demand applying the procedure specified by FEMA P58-1 [2012], where the demand distribution for selected ground motion intensities is characterized by median values and dispersions. The normative quantities were adopted from the structural and nonstructural inventory reported in Chalarca [2022]. The building layout was adopted from the case study building in FEMA P58. The best-estimate analytical model was used for analysis and the calculated dispersions were determined accounting for modelling uncertainty on the building typology and seismic hazard. This accounts for uncertainties in the actual properties of structural elements (e.g., material strength, section properties, among other features). For the case study building, a modelling uncertainty $\beta c = 0.4$ was assumed [FEMA P58-1, 2012] since this value is representative of steel buildings designed and built before the Northridge earthquake. On the other hand, the ground motion record-to-record variability was measured as dispersion of all 44 records. The specialized software PACT [FEMA P58-3, 2012] for loss assessment was used to quantify the earthquake risk in terms of direct financial losses and downtime. PACT can perform an intensity-based analysis to calculate the possible consequences of an earthquake (e.g., repair cost, repair time), taking as inputs the response of the building (e.g., time history analysis). Consequence functions in PACT relate potential distribution of losses with respect to damage states of each building component and are calculated *n* times (i.e., realization). For this study a total of 1000 realizations were adopted. To determine whether a repair is practical, PACT uses the maximum residual drift ratio and building repair fragility curves. The damage states associated with residual drifts ranges from the onset of damage to NSEs to near collapse of the structure. The median storey drifts in PACT are approximate and based on a combination of judgment and limits. FEMA P 58-1 [2012] provides descriptions of the damage states according to residual storey drift ratio. For example, for a 0.2% residual storey drift ratio a building may require adjustment and repair to non-structural and mechanical components. For a residual storey drift of 0.5%, some structural and non-structural repairs may be needed. For a 1% of residual storey drift major structural realignment is required, however, the repair of the structure may not be economically and practically feasible. This highlights the importance of reducing residual drifts to control economic losses and the subsequent repair activities to restore a building's primary functionality.

The maximum peak storey drift ratio of the bare and braced frames are 1.4% and 0.71%, respectively with residual drifts of 0.4% and 0.11%. The wall partitions used in the loss assessment (C1011.001a PACT Library) have three damage states: light, moderate, and severe damage which correspond to median peak storey drifts of 0.5%, 1%, and 2.1%. It is evident that the bare frame experiences a damage level between DS2 and DS3. As a result, some actions like removing and replacing of some components may be needed in the recovery process. In contrast, the braced frame shows a damage level between DS1 and DS2 which will only require minor repairs. Additionally, PACT provides an assumed fragility function for residual drift ratio that uses a median value for irreparability of 1% residual storey drift and a dispersion of 0.3. This value is slightly larger than the residual drift observed in the two models. However, the residual drift in the braced frame is only one-quarter of the bare frame which is a substantial improvement.

PACT provides a fragility database with information about damage, fragility curves, and consequences curves for many structural and non-structural components that relate the median intensity of a given damage state with respect to the input demands. The fragility functions are derived from a large quantity of test data [FEMA P 58-1, 2012]. Repair cost and repair time consequence function provided in PACT have been developed by professional cost estimators using component damage state repair descriptions for a reference location in the United States at a reference time 2011 [FEMA P 58-1, 2012]. However, one of the main limitations of this software is that the fragility database is based on peak floor demands. Thus, the input values for the loss assessment are given by PFA, PSD and RSD. This means that PACT does not account for the amplification demands of the floor response spectra associated to the non-structural periods. Even though PFA, PSD and RSD are not the most ideal criteria to evaluate the seismic performance of NSEs, these parameters are acceptable to obtain a close estimate of the economic losses. A total replacement cost of 15,000,000 USD for the case study building [Chalarca 2020] was adopted for the loss assessment analysis.

FEMA E-74 [2012] provides several measures to properly address the seismic performance of NSEs. These measures depend on the spectral demands (either floor acceleration or displacement). However, for simplification, improvement of NSEs is considered in the loss assessment by assuming that a retrofitted NSE will have superior seismic performance resulting in a larger median value for the fragility curves. In other words, the fragility curve of a retrofitted NSEs is replaced with a fragility curve of higher performance from the PACT library. Noting that Almufti and Willford [2013] define functional recovery after an earthquake as the restoration of power, water, fire sprinklers, lighting, HVAC systems, and elevators three NSE retrofit scenarios were identified to quantify the effect of NSE retrofits on earthquake losses. Table 1 summarizes the three scenarios. In all three cases, the building is assumed to be braced with SCBRBs.

Table 1. Description of non-structural elements seismically improved

Model	Retrofitted Components
C1	Wall partitions
C2	C1 and access floor, suspended ceiling, independent pendant lighting, elevator, heating hot water piping, sanitary waste piping, HVAC galvanized, HVAC drops, concrete tile roof, chiller, cooling tower, air handling unit, motor control centre
C3	C1, C2, and fire sprinkler water piping, fire sprinkler drops standard threaded steel, sanitary waste piping

Figure 4 shows the results of the loss assessment in terms of expected loss ratio (i.e., expected economic losses/total replacement cost of the building) for five models: 1) the bare frame (unbraced), 2) braced frame (SCBRB), and the three cases listed in Table 1 (C1, C2, and C3). The retrofit measures comprising C1 to C3 are based on FEMA E-74 and involve engineering and non-engineering approaches such as providing proper support and introducing anchors and braces. The total expected loss ratio for each building is distinguished into contributions from drift sensitive structural elements (DS), drift sensitive NSEs (DNS), and acceleration sensitive NSEs (ANS).

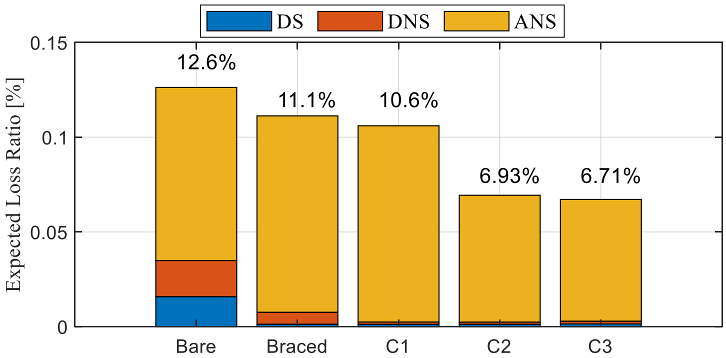

Figure 4. Expected loss ratio for design earthquake (DE) level

For all five buildings, the largest contribution to the economic losses comes from acceleration sensitive NSEs. Notably, the largest expected losses are in the bare frame which is expected to sustain a greater level of structural damage than the braced buildings. The SCBRB considerably reduces the PSD which reduces the losses due to both displacement sensitive structural and non-structural elements. However, as noted with the peak floor acceleration spectra, the SCBRB increases the PFA. As a result, in the braced frame without NSE retrofits, although the overall losses are reduced by 12% compared to the bare frame, the contribution of the acceleration sensitive NSEs to the overall expected losses is greater by 13% compared to the bare frame. Improving the seismic performance of just the wall partitions (a drift sensitive NSE) in C1 reduced the expected loss ratio by 16% compared to the bare frame. In comparison, with retrofits to acceleration sensitive NSEs the expected loss ratio was reduced considerably by 45% and 47% respectively in C2 and C3 in relation to the bare frame. Compared to C2, the additional improvements in C3 only yielded a marginal reduction in the expected loss, suggesting the seismic upgrades identified in C2 may be sufficient from a strictly economic standpoint. However, for regaining primary function, the components identified in C3 must also be retrofitted.

5. SEISMIC RESILIENCE ASSESSMENT

The REDi guidelines [Almufti and Willford, 2013] provide a framework to assess the seismic resilience of buildings through a rating classification system. As outlined in Carofilis *et al.,* [2022b] this framework can be adopted to estimate the functionality curve of buildings and their downtime associated to a given seismic intensity. The functionality curve describes the recovery path for a building from the initial damage caused by an earthquake to restoration back its original undamaged condition. Downtime is defined as the total time (i.e., delay time plus repair time) needed to return to initial building functionality. REDi modifies the outputs derived from PACT to incorporate more realistic repairs strategies and delays due to external factors that affect the initiation of repairs known as impeding factors (e.g., post-earthquake building inspections, securing financing for repairs, mobilizing engineering services, obtaining permits, mobilizing contractors and necessary equipment). Additionally, this framework considers the utility disruption time (e.g., water, gas, electricity supply) which is very likely to occur for the DE level.

5.1 REPAIR GROUPS

Seismic resilience can be estimated through a functionality curve which relates the loss of functionality and the time needed to restore a building's original conditions (recovery path). The loss of functionality characterizes the damage experienced by a building due to a seismic event, which can be represented by the expected economic losses. To restore a building's original functionality a repair sequence or activities must be performed which will gradually improve functionality until normal operation conditions are restored. NSE repairs are typically initiated only after structural repairs are completed since the structural integrity of the building must first be ensured for occupant safety. It is assumed that NSE repairs are carried out simultaneously. For the case study building, the building components are further classified into seven repair groups based on repair sequences defined by Almufti and Willford [2013]. The repair groups are structural repairs (S), interior repairs (A), exterior repairs (B), mechanical repairs (C), electrical repairs (D), elevator repairs (E), and stair repairs (F). Figure 5 shows the contribution of each repair group to the overall economic losses. It can be seen that the largest contribution to economic losses comes from interior repairs which represent almost half of the total economic losses. When the SCBRBs is implemented, no structural repairs are needed, which demonstrates the effectiveness of this system in reducing structural damage. With retrofits to acceleration sensitive NSEs, losses associated with interior repairs are considerably reduced in C2 and C3 but a slight increase in external repairs is noted.

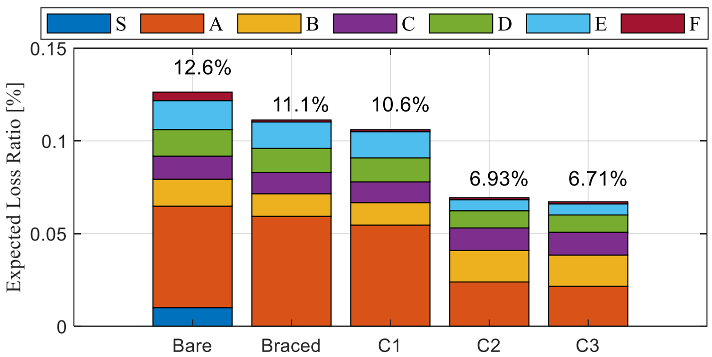

Figure 5. Expected loss contribution according to repair groups

5.2 RECOVERY PATH

Seismic resilience can also be defined in terms of the degree of recovery along a recovery path from a damaged state to a fully operational state [Cimerallo *et al.*, 2010]. After an earthquake, the recovery path generally follows an irregular pattern since the functionality of a building is restored gradually as different repair activities are conducted. Determining the recovery path and a resilience index is the goal in detailed seismic resilience assessments. However, in this study a simplified linear recovery path is used to compare the different retrofit scenarios in terms of the initial loss in functionality and the total recovery time or downtime. The reason for this is to highlight the influence of NSEs in the functionality and recovery time of stiff self-centring structural systems.

Loss of functionality is directly related to the expected losses since it describes the damage experienced by the building's components. Lower economic losses mean a greater level of functionality is maintained as shown in Figure 6. Moreover, the REDi guidelines [Almufti and Willford, 2013] provides estimates of delay time and provides a framework to estimate repair times, the sum of which represents the total downtime for a building following an earthquake (Figure 6). The delay time is associated to restoring water, energy and/or gas supply to the building, as well as the activities required prior the beginning of the repair process. For the DE in this study, the delay time for the bare frame resulted is approximately 89 days, whereas the other models with SCBRB would likely require approximately 84 days. This difference is mainly due to the fact that less structural damage is expected when the frame is braced thus requiring less time for structural inspections. A median value of 2 days was adopted for the possible post-earthquake inspection. Likewise, engineering mobilization was characterized by assuming engineering contracts of 2 weeks to conduct any review design. The financing was assumed to come from insurance (6 weeks). In terms of contractor mobilization, it was assumed 3 weeks. Finally, for permitting, it was considered as 1 week. All these median values were adopted from the REDi guidelines which are based on previous earthquake recovery scenarios [Almufti and Willford, 2013]. Additionally, for better visualization of the functionality curve it was assumed that the seismic event happened after 10 days of the initialization of the observation period.

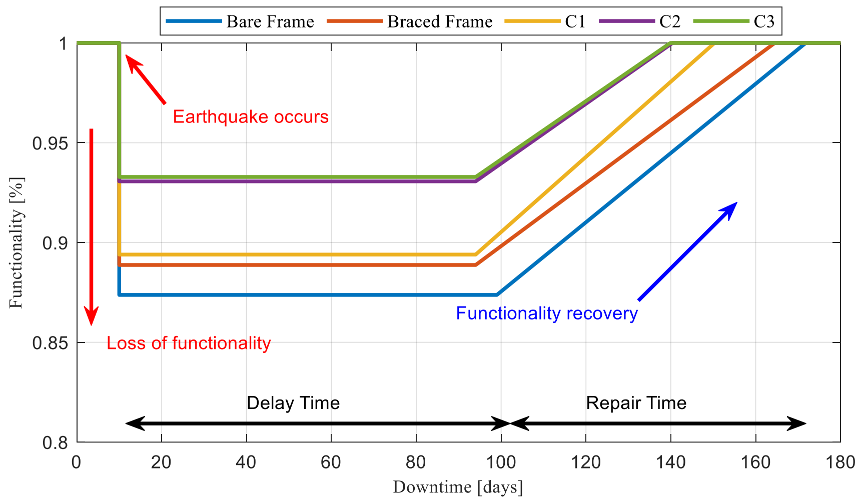

Figure 6. Functionality recovery curves for the different models

The total downtime to restore the building with the unbraced bare frame to its original condition is 162 days (89 days of delays and 73 days of repairs). In comparison, adding the SCBRB reduces the down time to 155 days (84 days of delays and 71 days of repairs) since no structural inspection are required and the drift sensitive NSEs experience lower displacement demand. However, as noted above, damage to acceleration sensitive NSEs are slightly increased in this case. Moreover, upgrades to NSEs further reduces the total downtime. C1 results in a downtime of 140 days (84 days of delays and 56 days of repairs), while C2 and C3 yield a downtime of 130 days (84 days of delays and 46 days of repairs). As observed in the loss assessment, C3 only provides a marginal reduction in losses over C2. As such, the expected downtime is not significantly different between C2 and C3. This is also reflected in the loss of functionality following the earthquake seen in Figure 6. Although C3 does not have a significant impact on the overall resilience of the building, the NSEs considered in C3 are critical for occupant health and safety. As discussed above, fire sprinklers are an essential NSE primary function in a building. Post-earthquake fires are a common hazard [Almufti and Willford, 2013]. Similarly, without a functioning sanitary system, buildings would be difficult to occupy and/or provide normal operation activities.

One limitation of this study is the use of the 2013 version of REDi which is based on studies (e.g., emergy plans) reported prior to 2013. On the other hand, ATC 138 [ATC 2021] is based on more recent data (comprising studies and seismic events up to 2020). REDi presents impeding factors as a lognormal distribution with median and standard deviations while ATC 138 defines median values with upper and lower bounds. Thus, using ATC 138 may result in a more realistic recovery time. Additionally, ATC 138 also describes damage clean up and temporary repairs related to the main repairs, which provides a more realistic sequence of repair activities.

Another limitation of this study is that it only focuses on one earthquake level (DE). Carofilis *et al.* [2022] investigated the benefits of SCBRB under larger seismic intensity (i.e., maximum considered earthquake (MCE)) and found a braced frame experiences substantially reduced peak storey drift and residual drift but higher peak floor acceleration. Thus, a subsequent step in this research is to explore the recovery time of the same frames subjected to MCE.

6.CONCLUSIONS

This study investigated the effect building retrofits with self-centring buckling restrained braces (SCBRBs) can have on the performance of non-structural elements (NSEs) in earthquakes and quantified the impact of NSE damage on economic losses and post-earthquake recovery. The main conclusions are as follows:

- SCBRBs have been shown to be an effective retrofit method for improving the structural performance of buildings. However, the added stiffness provided by the bracing can lead to larger seismic demands on some NSEs, particularly those that are acceleration sensitive. Similarly, NSEs with high stiffness (e.g., wall partitions) that are drift sensitive can experience more damage due to amplification of the floor displacements. SCBRBs can substantially reduce lateral displacements and improve the seismic performance of most of the other drift sensitive NSEs.
- A large fraction of the expected losses in an earthquake can come from acceleration sensitive NSEs, which not only increases economic losses but also impacts the seismic resilience. Analysis showed that a brace frame system with SCBRB may sustain economic losses and downtime comparable to a bare unbraced frame system.
- In order to substantially increase the seismic resilience of SCBRB systems, it is not necessary to improve the seismic performance of all NSEs but only the ones contributing the most to the expected losses, as well as to enhance the components considered as essential to regain partial functional operation in a building and ensure comfort/safety to the occupants. By conducting such actions, the expected losses and downtime can be reduced by up to 50% compared to an unbraced system with no NSE retrofits.

REFERENCES

Almufti, I.,Willford, M. [2013] *REDi rating system, resilience-based earthquake design initiative for the next generation of buildings*, Version 1.0.

ASCE [2017] Minimum design loads and associate criteria for buildings and other structures, ASCE/SEI 7-16, American Association of Civil Engineering, USA.

ATC [2021] Seismic performance assessment of buildings volumne 8 – methodology for assessment of funcation recovery time, ATC 138-3 Repot, Applied Technology Council, Redwood City, California. Bevere, L., Ewald, M., Wunderlich, S. [2019] "A decade of major earthquakes: lessons for business," *Report, Swiss Re* Institute, Switzerland.

Carofilis, W., Kim, E., Jung, D., Pinargote, J. [2022a] "Numerical evaluation of self-centering buckling-restrained braces with prestressed iron-based shape memory alloy tendons," CSCE 2022 Annual Conference, Whistler, British Columbia.

Carofilis, W., Clemett, N., Gabbianelli, G., O'Reilly, G., Monteiro, R. [2022b] "Seismic resilience assessment in optimally integrated retrofitting of existing school buildings in Italy," *Buildings,* Vol. 12, No. 845

Chalarca, B. [2022] "Implementation of fluid viscous dampers as a seismic protection system and its effects on the structural and nonstructural seismic sesponse," Doctoral thesis, University School for Advanced Studies IUSS Pavia, Italy.

FEMA 440 [2005] *Improvement of nonlinear static seismic analysis procedures,* Federal Emergency Management Agency, USA.

FEMA P-695 [2009] *Quantification of building seismic performance factors,* Federal Emergency Management Agency, USA.

FEMA E-74 [2012] *Reducing the risk of nonstructural earthquake damage – a practical guide*, USA

FEMA P58-1 [2012] *Seismic performance assessment of buildings: volume 1*, USA.

FEMA P58-3 [2012] *Seismic performance assessment of buildings volume 3 - performance assessment calculation tool (PACT) Version 2.9.65*, USA.

Gabbianelli, G., Perrone, D., Brunesi, E., Monteiro, R. [2020] "Seismic acceleration and displacement demand profiles of non-structural elements in hospital buildings," *Buildings*, Vol. 10, No. 12, pp. 243.

Liu, L., Zhao, J. and Shuang, L. [2018] "Nonlinear displacement ratio for seismic design of self-centering buckling-restrained braced steel frame considering trilinear hysteresis behavior," *Engineering Structures*, Vol. 158, pp. 199-22.

McKenna, F., Scott, M.H., Fenves, G.L. [2010] "Nonlinear finite-element analysis software architecture using object composition," *Journal of Computing in Civil Engineering*, Vol. 24, No. 1, pp. 95–107.

Merino, R.J., Perrone, D., Filiatrault, A. [2019] "Consistent floor response spectra for performance-based seismic design of nonstructural elements," *Earthquake Engineering and Structural Dynamics*, No. 1, pp. 1-24.

Miller, D.J., Fahnestock, L.A, Eatherton, M.R. [2012] "Development and experimental validation of a nickel-titanium shape memory alloy self-centering buckling-restrained brace," *Engineering Structures*, Vol. 40, pp. 288-298.

Miranda, E., Taghavi, S. [2003] "Estimation of seismic demands on acceleration-sensitive nonstructural components in critical facilities," *ATC-29-2 Seminar on Seismic Design*, *Performance, and Retrofit of Nonstructural Components in Critical Facilities*, United States.

Miranda, E., Mosqueda, G., Retamales, R., Pekcan, G. [2012] "Performance of nonstructural components during the February 27, 2010 Chile Earthquake," *Earthq. Spectra*, Vol. 28, pp. S453–S471.

NIST [2015] *Seismic design of steel buckling-restrained braced frames: a guide for practicing engineers*, GCR 15-917-34, NEHRP Seismic Design Technical Brief No. 11, produced by the Applied Technology Council and the Consortium of Universities for Research in Earthquake Engineering for the National Institute of Standards and Technology, Gaithersburg, MD.

O'Reilly, G.J., Perrone, D., Fox, M., Monteiro, R., Filiatrault, A. [2018] "Seismic assessment and loss estimation of existing school buildings in Italy," *Eng. Struct.* Vol. 168, pp. 142–162.

O'Reilly, G.J., Sullivan, T.J. [2018] "Probabilistic seismic assessment and retrofit considerations for Italian RC frame buildings," *Bulletin of Earthquake Engineering*, Vol. 16, No. 3, pp. 1447–85.

Sousa, L., Monteiro, R. [2018] "Seismic retrofit options for non-structural building partition walls: Impact on loss estimation and cost-benefit analysis," *Eng. Struct.* Vol. 161, pp. 8–27.

Vukobratović, V., Fajfar, P. [2017] "Code-oriented floor acceleration spectra for building structures," *Bulletin of Earthquake Engineering*, Vol. 15, No. 1, pp. 3013-3026.

Impact of masonry infill variability on the seismic demand of non-structural elements

Mucedero G. [1]**, Perrone D.**[2] **and Monteiro R.** [1]

[1] University School for Advanced Studies IUSS
{gianrocco.mucedero,ricardo.monteiro}@iusspavia.it

[2] University of Salento
daniele.perrone@unisalento.it

Abstract. Recent earthquakes demonstrated that most of the observed economic losses were due to the high vulnerability of non-structural elements (NSEs), rather than to the damage of the structural counterpart. Although the seismic performance of NSEs is currently recognised as a key issue in the performance-based seismic design and loss estimation of buildings, the accurate evaluation of the seismic demand to which the former are subjected is still an open issue. Some methodologies are available in the literature to estimate, for instance, Floor Response Spectra (FRS), however the effect of masonry infill variability is not adequately quantified. This study aims to quantify the impact of different masonry infill typologies on FRS in existing infilled reinforced concrete (RC) frames, representative of buildings designed according to the Italian codes in force between 1970 and 1980. Nonlinear time history analyses are carried out for different case-study RC frames, selected from a vast building portfolio, accounting for different geometrical configurations and number of storeys. To account for the infill-related variability and, thus, uncertainty, a macro-level distinction of common infill types, in terms of shear strength, is used. Absolute acceleration FRS are then computed and statistically characterised, based on the observed infill-to-infill-related variability. In order to quantify the effects of different masonry infill typologies on the maximum seismic demand at the resonance period of the NSEs, the component amplification factor is defined and investigated. Finally, the seismic demand variability on both rigid and flexible NSEs is presented in a statistical fashion, underlying the importance of understanding the masonry infill variability.

Keywords: Floor response spectra, Buildings portfolio, Masonry infills, Non-structural elements, Seismic Demand.

1. INTRODUCTION

The earthquake-related economic losses observed in the last decades were often attributed, for a good share, to damage to non-structural elements (NSEs), as reported in post-earthquake surveys [O'Reilly et al., 2018; Perrone et al., 2019]. NSEs represent all the systems and elements attached to the floors and walls of a building that are not part of the vertical and lateral load-bearing structural systems, but they are subjected to the same dynamic excitation during a seismic event. As reported by [Miranda and Taghavi, 2003], NSEs represent the largest portion of the total investment in typical buildings. At the same time, the damage to NSEs can also represent a threat to life mostly because of falling hazards. Due to the numerous typologies of NSEs installed in a building, their vulnerability could significantly affect the immediate functionality because they generally exhibit damage at low (serviceability) seismic intensities, while the supporting structures mainly respond in the elastic range. This issue is paramount for strategic facilities, such as hospitals and schools, that should remain operational in post-earthquake emergency situations. In Italy, for instance, the actual repair costs of reinforced concrete (RC) residential buildings damaged following the 2009 L'Aquila Earthquake, involved majorly the repair of infills and partitions [Di Ludovico et al., 2017]. Indeed, hollow clay brick walls, typical of Mediterranean construction standards, are characterised by brittle behaviour, which resulted in significant damage [Del Vecchio et al., 2020].

The lack, or in some cases the questionable accuracy, of code prescriptions and code-compliant guidelines [Eurocode 8, 2004], has oriented the recent past research efforts towards the development of simplified methodologies to predict absolute acceleration and displacement floor response spectra (FRS) for elastic and inelastic single-degree-of-freedom (SDOF) and multi-degree-of-freedom (MDOF) systems [Calvi, 2014; Calvi and Sullivan, 2014; Merino et al., 2020; Petrone et al., 2015; Sullivan et al., 2013; Vukobratović and Fajfar, 2015]. Such methodologies are particularly useful, given that accurate FRS estimates require complex and demanding nonlinear time-history analysis (NLTHA). Petrone et al. [2015] proposed a methodology to predict absolute acceleration FRS calibrated using a set of RC moment resisting frames designed according to [Eurocode 8, 2004] and subjected to frequent (serviceability-level) earthquake ground motions. Sullivan et al. [2013] proposed a simplified approach to predict absolute acceleration FRS for linear and nonlinear SDOF structures, which was subsequently extended to linear and nonlinear MDOF systems [Calvi and Sullivan, 2014]. Another approach, proposed by Vukobratovic and Fajfar [2015], was calibrated for both elastic and inelastic SDOF and MDOF structures. In the case of MDOF structural systems, the resulting FRS were obtained combining the contribution of individual vibration modes and a significant influence of higher modes on FRS was observed. Other methodologies were also developed by Calvi [2014] to evaluate relative-displacement FRS and by Merino et al. [2020] to predict consistent absolute acceleration and relative displacement FRS, which can be used when displacement-based seismic design methodologies of NSEs are adopted.

For what concerns the presence of masonry infills, few studies have investigated their influence on FRS in RC buildings [Lucchini et al., 2014; Surana et al., 2018]. Lucchini et al. [2014] investigated the influence of masonry infills and damping models on FRS in nonlinearly analysed buildings, pointing out that the infill walls can significantly affect the peak floor acceleration profile and FRS at a given intensity. More recently, Surana et al. [2018] studied the effect of unreinforced masonry infills on the inelastic FRS of RC frame buildings; the outcomes demonstrated that the influence of masonry infills cannot be neglected in the evaluation of FRS, especially for frequent earthquakes, for which the uncracked stiffness of the infills tends to be considered. Recently, Perrone et al. [2020], by means of Monte Carlo simulation, analysed a database of European masonry-infilled RC frames and computed absolute acceleration and relative displacement FRS at different floor levels for both bare and infilled frame archetypes using NLTHA. As a result, a preliminary seismic demand model for NSEs in masonry infilled RC frames, to be used for regional scale applications, was proposed. More recently, Di Domenico et al. [2021] proposed a simplified code-oriented formulation for the assessment of floor response spectra of infilled reinforced concrete framed structures, as a useful tool for the seismic assessment of acceleration-sensitive non-structural components.

With such considerations in mind, this paper deals with the evaluation of absolute acceleration FRS of RC infilled frames, with the aim of quantifying, in a more thorough manner, the impact of masonry infills variability (i) on the FRS and (ii) on the seismic demand on NSEs. A fully integrated building stock, recently assessed by means of nonlinear static analysis in [Mucedero et al., 2021], is considered as case-study. Once the building stock was defined, NLTHAs were performed to record the acceleration time histories at two different floor levels (first and roof floor) and to compute the FRS. Then, the comparison of FRS for the Life Safety Limit State (LSLS) is presented. The impact of masonry infills on seismic demand of NSEs was estimated through the component amplification factor (β), defined as the ratio between the maximum floor spectral acceleration ($S_{fa,max}$) and the peak floor acceleration (PFA) at T_{NSE}=0s (where T_{NSE} is the vibration period of the NSE). Finally, according to the frequency range of NSEs (flexible components 1.3Hz < f < 8.3Hz, rigid components f > 8.3Hz) provided in [AC156, 2010], two periods of vibration (0s and 0.76s) were selected, corresponding to the first period of vibration of rigid and flexible components, respectively, and the variation in their seismic demand due to the masonry infill variability, i.e. different assumed infill typologies, was quantified.

2. CASE-STUDY BUILDING STOCK

A building portfolio representing existing masonry-infilled RC residential buildings in Italy built between 1960 and 1980, decades with massive construction of such a building typology and during which an update of the seismic design guidelines was introduced, was used as a source to define the case-study. The portfolio accounts for both the building geometrical layout and infills variability, characterized from statistical data collected from [ISTAT, 2001] and from databases comprising information regarding experimental tests carried out on different masonry infill typologies [Blasi et al., 2021; De Risi et al., 2018]. The variability in the following parameters is included: plan dimension, number of floors, inter-storey height, span length, material properties of RC elements and of masonry infills.

For this specific study, the specific construction period (1970-1980) was selected and the corresponding mechanical properties of the materials were obtained from the results of in-situ tests on existing buildings or from data collected in laboratory archives [Masi et al., 2014; Verderame et al., 1950]; it was chosen to use 20 MPa and 350 MPa for concrete strength and yielding strength, respectively. As regards the masonry infill properties, based on the results provided by Mucedero et al. [Mucedero et al., 2020], a macro-level distinction of the infills in terms of shear strength was adopted. Five masonry infill typologies, from weak to strong, were thus selected as representative of the existing masonry infill typologies used in RC residential buildings built between 1970 and 1980 in Italy (Table 1).

Table 1: Selected masonry infill typologies.

Type	Macro classification	t_w [mm]	E_{wv} [MPa]	E_{wh} [MPa]	G_w [MPa]	f_{wv} [MPa]	f_{wlat} [MPa]	f_{wu} [MPa]
1	Weak	80	1873	991	1089	2.02	1.18	0.44
2	Weak-Medium	240	1873	991	1873	1.5	1.11	0.25
3	Medium-Strong	300	3240	1050	1296	3.51	1.5	0.3
4	Medium-Strong	350	5299	494	2120	4.64	1.08	0.359
5	Strong	150	6401	5038	2547	8.66	4.18	1.07

tw: thickness; Ewv: elastic modulus vertical direction; Ewh: elastic modulus horizontal direction; Gw: shear modulus; fwv: vertical strength; fwlat: lateral strength; fwu: shear sliding strength.

The design of the buildings was carried out using a simulated design approach, according to the codes in force between 1970 and 1980 [Ministerial Decree, 1975]. The case-study building portfolio comprised a total of 108 geometrical configurations, given by the combination of the different variables. In specific, the length

L_y of the analysed 2D masonry infilled RC frames was in the range 8-25 m. The span length varies between 3 m and 5 m, with increments of 1 m, while the height of the buildings varies between 3 m and 18 m, with increments of 3 m (the inter-storey height). Seven discrete building lengths were selected from the range of L_y (8-25 m) and combined with equally discrete possible different span lengths, leading to 18 different geometrical configurations (labelled as ID-1 to ID-18). Each of these was then combined with six different building heights, leading to 108 geometrical configurations, and with the five masonry infill typologies, leading to 540 uniformly infilled frames.

2.1 NUMERICAL MODELLING

An advanced nonlinear numerical model was developed to account for most of the phenomena that may occur in the buildings during an earthquake, such as: material and geometrical nonlinearity, flexible joints with likely shear failure, behaviour of poorly detailed and non-ductile RC frame members, premature shear failure, deficiencies in concrete core confinement due to stirrup spacing, inelasticity concentrated in the structural element ends, amongst others. The numerical models were developed using OpenSees [McKenna et al., 2000]. The flexural elements (i.e. beams and columns) were modelled through force-based beam-column elements with a modified Radau plastic hinge integration scheme, as suggested by Scott & Fenves [Scott and Fenves, 2006], where the nonlinearity is lumped at the ends of the element and an aggregation section, V-γ and M-θ, was introduced. The flexural behaviour was defined through the moment-curvature relationships proposed in [O'Reilly and Sullivan, 2015], whereas the shear behaviour was modelled according to [Zimos et al., 2017]. To capture the nonlinear behaviour of joints, a zero-length spring coupled with a rotational hinge was adopted, which represents the shear joint behaviour; its hysteretic behaviour was calibrated according to different experimental tests [Braga et al., 2009; Melo et al., 2012; Pampanin and Calvi, 2002]. Regarding damping, 5% tangent stiffness proportional Rayleigh damping at the fundamental periods was adopted. The uniaxial nonlinear Pinching4 Material model has been adopted to simulate the hysteretic behaviour of the masonry infills; all the parameters defining the equivalent strut's hysteretic behaviour were not selected a priori but rather calibrated considering the specific features of each masonry infill typology, defined according to the numerical modelling validation recently carried out by [Mucedero et al., 2020]. The masonry infills were considered perfectly connected to the surrounding RC frame. More details on the numerical modelling approach and validation of the response of masonry infilled RC frames using experimental testing results are provided in [Mucedero et al., 2020].

2.2 SEISMIC HAZARD MODELLING AND GROUND MOTION RECORD SELECTION

The OpenQuake [Silva et al., 2014] software was used to perform the seismic hazard computations, adopting the SHARE Project [Giardini et al., 2014] source model and the GMPE proposed by [Boorea and Atkinson, 2008]. The hazard curve corresponding to the average spectral acceleration (AvgSa), the chosen intensity measure (IM), for the period range 0.01-2.0 s for the city of L'Aquila (Italy) was derived and, accordingly, a total of 30 pairs of ground motion records were selected from the PEER NGA-West database [Ancheta et al., 2013]. One IM level was selected, corresponding to return period (Tr) equal to 500 years, which is close to the Tr at which corresponds the Life Safety Limit State (LSLS) and equal to 475 years, as defined in [Eurocode 8, 2004].

3. DERIVATION OF FLOOR RESPONSE SPECTRA

The results of NLTHAs of the 2D frame buildings were used to derive absolute acceleration FRS (AFRS). The 5%-damped AFRS were evaluated by subjecting the building portfolio to the selected set of ground motions and then using numerical techniques to compute the FRS from floor acceleration time-histories recorded along the structure's height. For the sake of brevity, only the AFRS of the first and roof storeys, for a selected IM level (Tr=500 years), are presented. The results of the eigenvalue analyses carried out to characterise the dynamic properties of the case-study building portfolio, as well as the variability due to different typologies of masonry infills, are comprehensively presented in [Mucedero et al., 2021], through median, 16^{th} and 84^{th} percentiles of the first elastic period of vibration, T_1.

Figure 1 plots the median AFRS (MAFRS) and the area defined by the 16^{th} and 84^{th} percentiles for the first (Figure 1a) and roof (Figure 1b) levels. The MAFRS are reported for all considered masonry infill typologies. The grey-filled areas in Figure 1 are representative of the record-to-record variability, the geometry variability and the infill-to-infill variability.

The impact of masonry infill properties is less significant for the first storey AFRS, except for the two-storey RC frames, while it is significant at roof level. For the two-storey buildings, the higher values of the Sfa are obtained for weak and weak-to-medium masonry infills, whereas for taller buildings the trend is reversed, with the highest values generated by medium-to-strong and strong masonry infills. The median Sfa, due to the different infill typologies, is in the range of [0.91÷1.51g] and [0.57 ÷2.69g], respectively, for AFRS at first and roof level. Moreover, as regards the envelope of the 16^{th} and 84^{th} percentiles, the variability is quite different as a function of the period of the NSEs considered. Given three different non-structural periods, T_{NSE}, and considering the AFRS recorded at roof level for the selected IM level, the maximum differences between the 16^{th} and 84^{th} percentiles are in the following ranges: (i) [0.74÷3.02g] for Sfa (T_{NSE}=0.2s), (ii) [0.19÷1.4g] for Sfa(T_{NSE}=0.5s), and (iii) [0.007÷0.23g] for Sfa(T_{NSE}=1.0s). This variability also increases with the number of storeys, particularly for shorter T_{NSE}. Considering the six-storey buildings, the peak value of MAFRS at the roof level decreases of almost 43%, when comparing infill type 5 (strong) with infill type 1 (weak). This trend is quite similar also in the case of four-storey buildings, with peak values of MAFRS that decrease almost 40÷44%, when comparing infill type 5 with infill type 1. For lower buildings (two-storey buildings), when changing infill type 1 to infill type 5, the MAFRS peak decreases of almost 40%, respectively. Overall, regardless of the level at which the FRS is recorded, the variability surrounding the MAFRS is therefore quite significant. Additionally, the variability due to masonry infills' properties is less significant for T_{NSE} longer than 1 s.

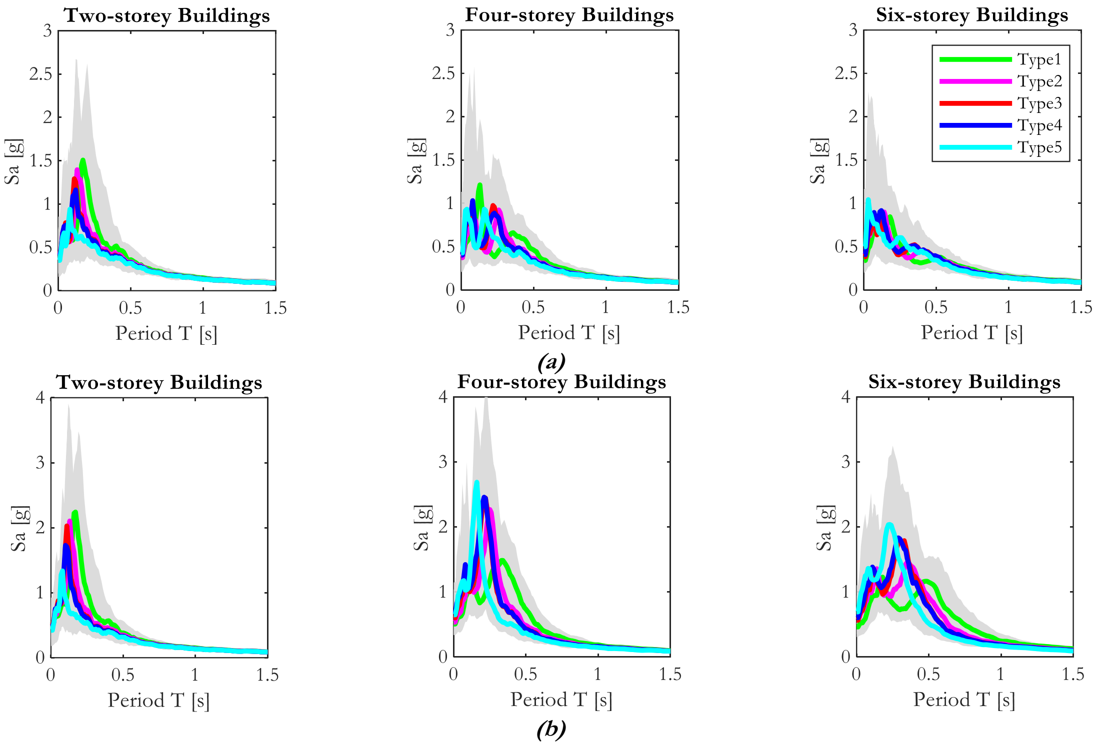

Figure 1: Acceleration floor response spectra, ξ=5%, at (a) first level and (b) roof level for the infilled frame structural typology. Median values of FRS for each infill typology over the entire building portfolio, by aggregating all the IDs, and envelope (grey-filled area) of 16^{th} and 84^{th} percentile for each infill typology.

4. COMPONENT AMPLIFICATION FACTORS

In order to assess the seismic demand to which the NSEs are subjected, many factors should be taken into account, such as damping and the period of vibration of both the primary structure and the NSEs, the influence of the inelastic response of NSEs and of the supporting structure, among others. In this sense, a useful parameter to understand such seismic demand, also adopted in some codes and guidelines, is the component amplification factor (β). It is defined as the ratio between the maximum floor spectral acceleration and the PFA. As for the FRS, β has been calculated at the first and roof storeys, for the selected IM level (Figure 2).

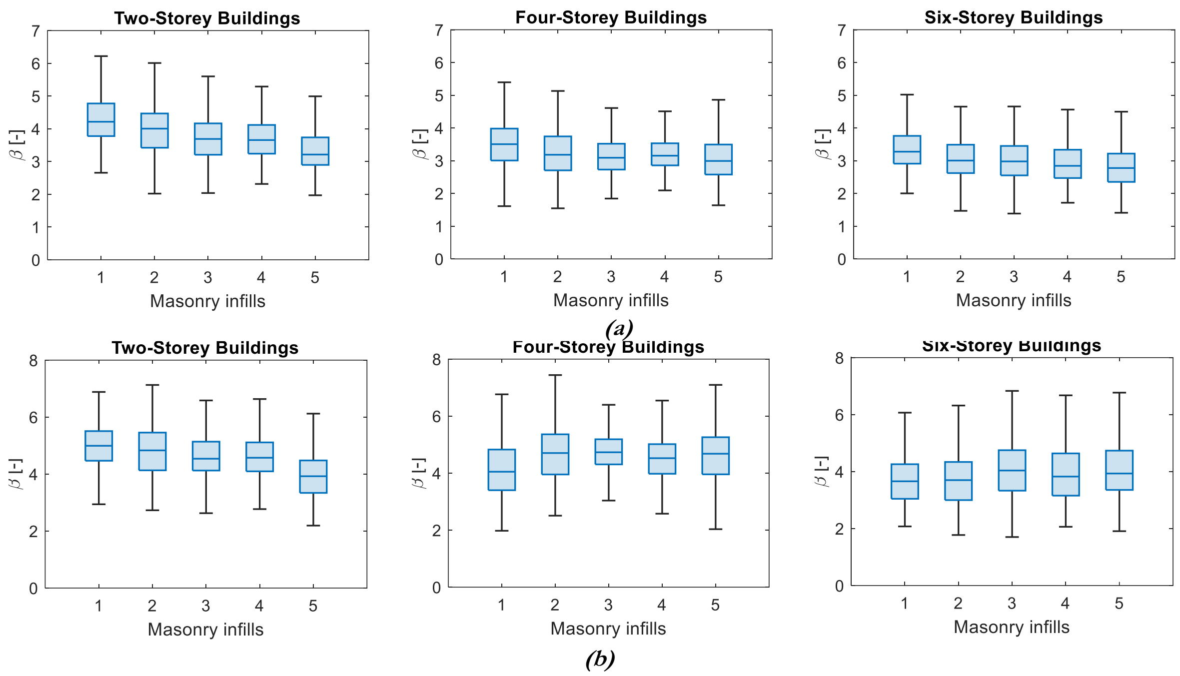

Figure 2: Component amplification factor (β) for different buildings height at (a) first level and (b) roof level, as a function of the masonry infill typologies.

Figure 2(a) reports the values of β at the first level for different building heights, as a function of the masonry infill typologies. The factor β is in the range of [1.97÷6.22], [1.55÷5.39] and [1.38÷5.018] for two-, four- and six-storey buildings, respectively. Looking at the median values, for two-storey buildings, β seems to decrease with the increase of the stiffness and strength of the masonry infills, from weak to strong masonry infills, and it is in the range of [3.21÷4.22]; the same trend is also noticed increasing the building height, although the difference in the median β values are less pronounced, ranging between [2.99÷3.5] and [2.77÷3.27] for four- and six-storey buildings, respectively. Globally, β for NSEs located at the first level seems to be higher for weak masonry infills, independently of the building heights, and to decrease when increasing the stiffness and strength of the masonry infills.

As regards the roof level, as shown in Figure 2(b), β is in the range of [1.97÷6.22], [1.55÷5.39] and [1.38÷5.018] for two-, four- and six-storey buildings, respectively. Looking at the median values, for two-storey buildings, β seems to decrease when increasing the stiffness and strength of the masonry infills, from weak to strong masonry infills, and it is in the range of [3.21÷4.22]; the same trend is also noticed increasing the building height, although the differences in the median β values are less pronounced, with median values in the range of [2.99÷3.5] and [2.77÷3.27] for four- and six-storey buildings, respectively. Globally, β for

NSEs located at the roof level seems to be higher for strong masonry infills, expect for two-storey buildings, and to increase when increasing the stiffness and strength of the masonry infills.

The AC156 [2010] guideline, which provides a testing protocol for seismic qualification of NSEs by shake table testing, distinguishes NSEs into two categories, according to their natural frequency (f): flexible components if 1.3Hz < f < 8.3Hz and rigid components if f > 8.3Hz. To evaluate the variability in seismic demand due to different masonry infill typologies on these two categories, two periods of vibration ($T_{NSE,1}$=0s and $T_{NSE,1}$=0.76s) were selected, corresponding to the first period of vibration of rigid and flexible components, respectively. The seismic demand Sfa($T_{NSE,1}$) at the selected IM level on rigid ($T_{NSE,1}$=0s) and flexible ($T_{NSE,1}$=0.76s) NSEs located at first level and roof level are presented through the box plots in

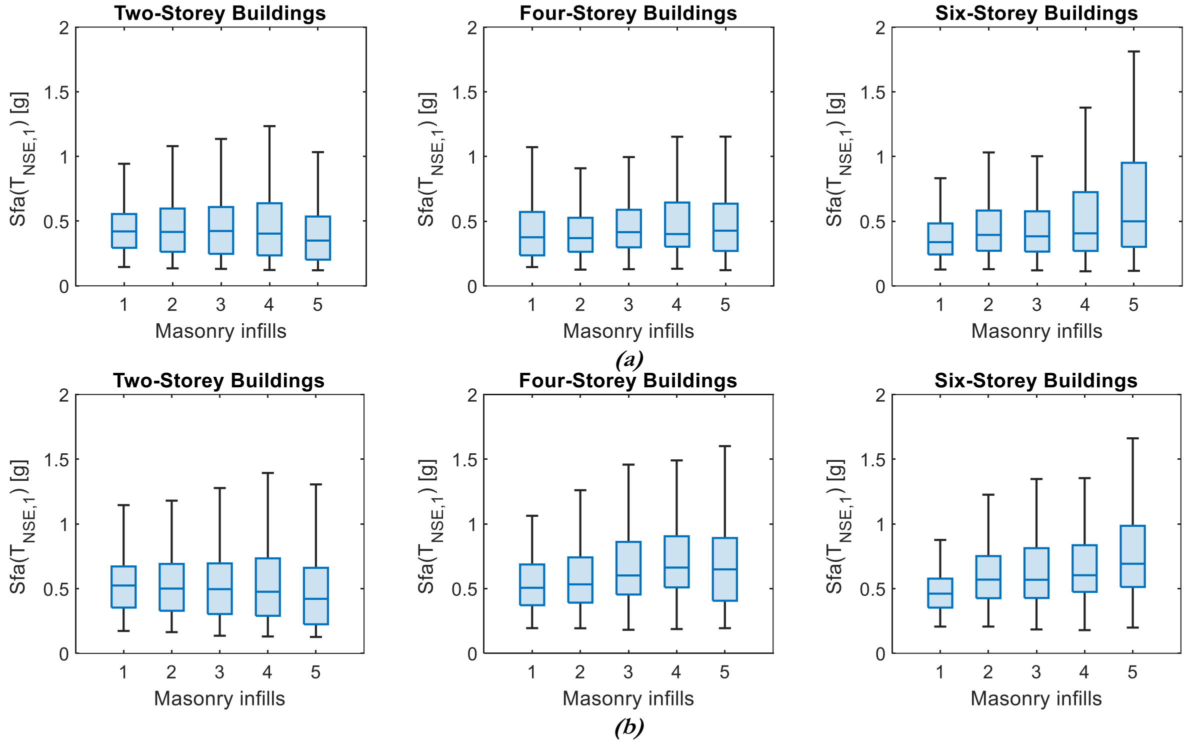

Figure 3 and Figure 4, respectively.

It can be seen how, for the rigid NSEs, Sfa($T_{NSE,1}$), in four- and six-storey buildings, becomes increasingly higher when increasing the stiffness and strength of the masonry infills, regardless of the location of the NSEs in the buildings; the median values of Sfa($T_{NSE,1}$) at first and roof level are in the range of [0.37÷0.43g] and [0.50÷0.65g], respectively, for four-storey buildings, whereas are in the range of [0.33÷0.50g] and [0.46÷0.69g] for six-storey buildings. Moving from weak to strong masonry infills, the seismic demand on the NSEs located at the first level increases of almost 16% and 51% for four-and six-storey buildings, respectively, while of almost 30% and 50% for those located at roof level. This trend is not observed in two-storey buildings and the median value of Sfa($T_{NSE,1}$) on the NSEs seems practically unaffected by the masonry infill typologies, and is in the range of [0.35÷0.42g] and [0.42÷0.52g] for the first and roof levels, respectively. The seismic demand decreases of almost 16% and 19%, going from weak to strong masonry infills, for the NSEs located at first and roof level, respectively.

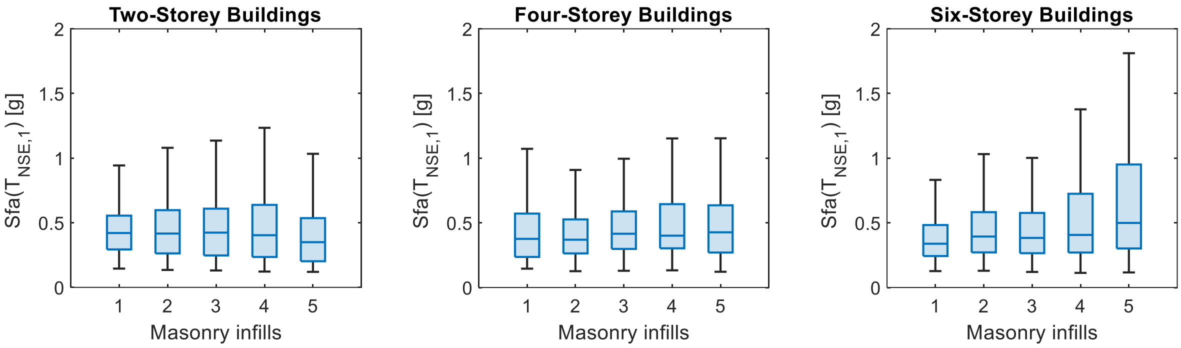

(a)

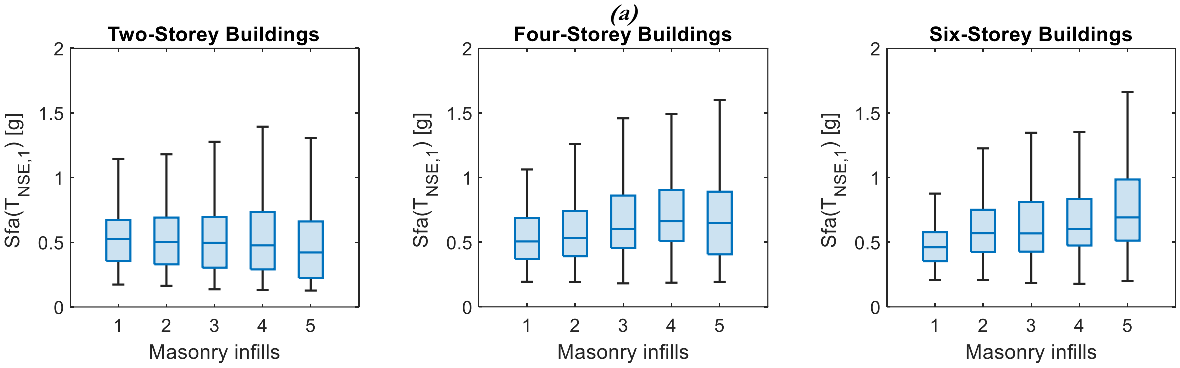

(b)

Figure 3: Sfa($T_{NSE,1}$) on NSEs with $T_{NSE,1}$=0s and located at (a) first level and (b) roof level.

Regarding Sfa($T_{NSE,1}$) on flexible NSEs, the trends are presented in Figure 4. Conversely to the trend noticed for the case of rigid NSEs, the seismic demand becomes increasingly lower when increasing the stiffness and strength of the masonry infills, regardless of the location of the NSEs in the buildings. In particular, the median values of Sfa($T_{NSE,1}$) at first and roof level are in the range of [0.18÷0.22g] and [0.19÷0.29g], respectively, for four-storey buildings, whereas are in the range of [0.19÷0.23g] and [0.24÷0.47g] for six-storey buildings, with lower values obtained with medium-strong and strong masonry infills. Going from weak to strong masonry infills, the seismic demand on the NSEs located at the first level decreases of almost 18% for four-and six-storey buildings; the impact of the masonry infill typologies on the seismic demand is much more pronounced for the NSEs located at the roof level, with a reduction of almost 34% and 49% for four-and six-storey buildings, respectively. This trend is also found in two-storey buildings, though not as significantly as for four- and six-storey buildings, and the median values of Sfa($T_{NSE,1}$) are in the range of [0.17÷0.19] for both first and roof level, with a reduction of almost 11% of Sfa($T_{NSE,1}$), going from weak to strong masonry infills.

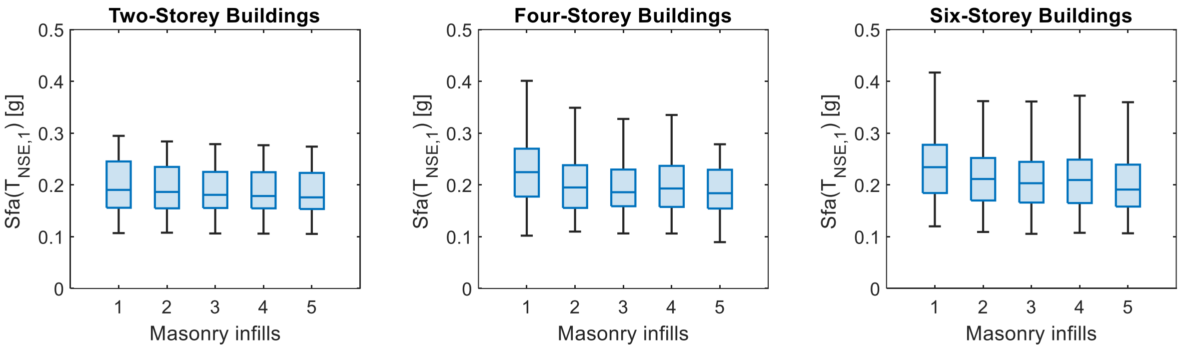

(a)

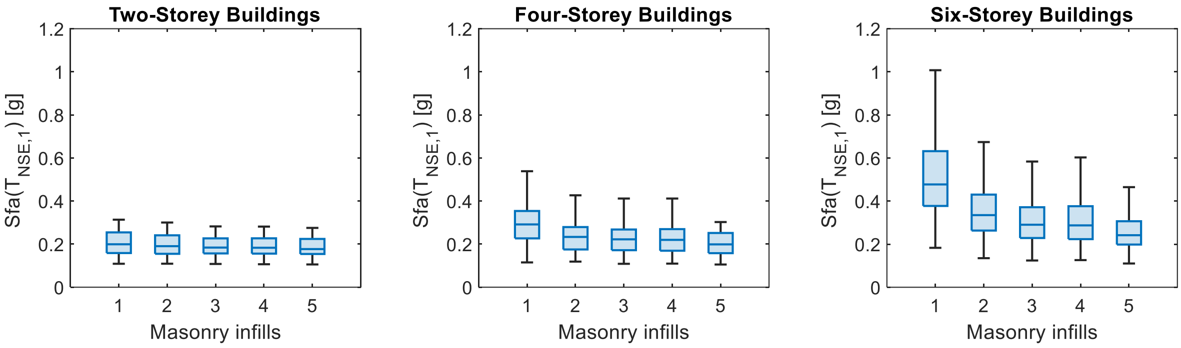

(b)

Figure 4: Sa($T_{NSE,1}$) on NSEs with $T_{NSE,1}$=0.76s and located at (a) first level and (b) roof level.

5. CONCLUSIONS

Significant efforts have been made in the recent past to investigate the influence of masonry infills on the seismic performance of existing RC buildings. However, less attention has been paid to the evaluation of the role of their variability on peak floor accelerations and floor response spectra, as well as on the variability of the seismic demand on non-structural elements (NSEs). To address this gap, this study investigates the influence of different typologies of masonry infills on the absolute acceleration floor response spectra (AFRS) and on specific parameters describing the seismic demand on NSEs, such as the component amplification factor (β). A macro-level distinction of masonry infills that defines five typologies, representative of the infill properties commonly adopted in the European context, has been used to characterise their variability. The results of this study quantitatively pointed out how the impact of the variability in the masonry infills on the AFRS is high, although different trends are observed for low-rise and medium-rise buildings. In particular, for low-rise buildings, the highest spectral floor acceleration (S_{fa}) values are due to weak and weak-to-medium masonry infills, whereas for medium-rise buildings (four- and six-storey buildings) the trend is reversed, with the highest values generated by medium-to-strong and strong masonry infills. These results can be used, for instance, to correctly define the seismic demand imposed on NSEs and, consequently, to realistically perform their seismic design or to assess the expected annual losses. By means of the derived AFRS, it is noticed that the component amplification factor (β), if the NSEs are located at the first level, is higher for weak masonry infills and it decreases when increasing the stiffness and strength of the masonry infills, while it is the opposite for NSEs located at the roof level, with β that seems to be higher for strong masonry infills and to increase when increasing the stiffness and strength of the masonry infills. Moreover, this study further demonstrates that the variability related to the masonry infills induces significant dispersion on the AFRS and shows how neglecting the masonry infill variability can be highly misleading and lead to results that are not realistic, particularly for seismic demand on NSEs. Indeed, through the results presented in a statistical fashion, it is highlighted how the impact of different masonry infill typologies on the seismic demand of rigid or flexible NSEs is quite significant, at least for medium- and high-rise buildings, while low-rise buildings seem practically unaffected by such variability. While the seismic demand on rigid NSEs was seen to be much higher in case of medium-strong and strong masonry infills, on flexible NSEs, it was much higher in case of weak masonry infills. Moreover, due to the masonry infills variability, the seismic demand on NSEs could be underestimated or overestimated even up to 50%. Finally, further efforts are still required to investigate the impact of masonry infills variability on the seismic demand on NSEs and to improve the existing simplified methodologies to compute the AFRS in order to account for such effect.

REFERENCES

AC156. [2010]. International Code Council Evaluation Service Inc. [ICC-ES]. Acceptance Criteria for Seismic Qualification by Shake-Table Testing of Nonstructural Components and Systems.

Ancheta, T. D., Darragh, R. B., Stewart, J. P., Seyhan, E., Silva, W. J., Chiou, B. S. J., Wooddell, K. E., Graves, R. W., Kottke, A. R., Boore, D. M., Kishida, T., & Donahue, J. L. [2013]. PEER NGA-West2 Database, Technical Report PEER 2013/03. May 2013.

Blasi, G., De Luca, F., Perrone, D., Greco, A., & Antonietta Aiello, M. [2021]. MID 1.1: Database for Characterization of the Lateral Behavior of Infilled Frames. Journal of Structural Engineering, 147(10), 4721007. https://doi.org/10.1061/(asce)st.1943-541x.0003117

Boorea, D., & Atkinson, G. [2008]. Ground-Motion Prediction Equations for the Average Horizontal Component of PGA, PGV, and 5%Damped PSA at Spectral Periods between 0.01 s and 10.0 s. Earthquake Spectra, 24. https://doi.org/10.1193/1.2830434

Braga, F., Gigliotti, R., & Laterza, M. [2009]. R/C Existing Structures with Smooth Reinforcing Bars: Experimental Behaviour of Beam-Column Joints Subject to Cyclic Lateral Loads. The Open Construction and Building Technology Journal, 3(1), 52–67. https://doi.org/10.2174/1874836800903010052

Calvi, P. M. [2014]. Relative Displacement Floor Spectra for Seismic Design of Non Structural Elements. Journal of Earthquake Engineering, 18, 1037–1059.

Calvi, P. M., & Sullivan, T. J. [2014]. Estimating floor spectra in multiple degree of freedom systems. Earthquake and Structures, 7(1), 17–38. https://doi.org/10.12989/eas.2014.7.1.017

CEN, Eurocode 8 – Design provisions for earthquake resistant structures, no. EN-1998-1:2004, Comite Europeen de Normalization, Brussels, Belgium [2004].

De Risi, M. T., Del Gaudio, C., Ricci, P., & Verderame, G. M. [2018]. In-plane behaviour and damage assessment of masonry infills with hollow clay bricks in RC frames. Engineering Structures, 168, 257–275. https://doi.org/10.1016/j.engstruct.2018.04.065

Del Vecchio, C., Ludovico, M. D., and Prota, A. [2020]. Repair costs of reinforced concrete building components: From actual data analysis to calibrated consequence functions. Earthquake Spectra, 36(1), 353–377. https://doi.org/10.1177/8755293019878194

Di Domenico, M., Ricci, P., and Verderame, G. M. [2021]. Floor spectra for bare and infilled reinforced concrete frames designed according to Eurocodes. Earthquake Engineering and Structural Dynamics, eqe.3523. https://doi.org/10.1002/eqe.3523

Di Ludovico, M., Prota, A., Moroni, C., Manfredi, G., and Dolce, M. [2017]. Reconstruction process of damaged residential buildings outside historical centres after the L'Aquila earthquake: Part I—"light damage" reconstruction. Bulletin of Earthquake Engineering, 15(2), 667–692. https://doi.org/10.1007/s10518-016-9877-8

Giardini Woessner J. Danciu L., D. [2014]. Mapping Europe ' s Seismic Hazard. 95(29).

ISTAT. [2001]. http://dati-censimentopopolazione.istat.it/Index.aspx

Lucchini, A., Mollaioli, F., and Bazzurro, P. [2014]. Floor Response Spectra for Bare and Infilled Reinforced Concrete Frames. Journal of Earthquake Engineering, 18(7), 1060–1082. https://doi.org/10.1080/13632469.2014.916633

Masi, A., Digrisolo, A., and Santarsiero, G. [2014]. Concrete Strength Variability in Italian RC Buildings: Analysis of a Large DataBase of Core Tests. Applied Mechanics and Materials, 597, 283–290. https://doi.org/10.4028/www.scientific.net/AMM.597.283

McKenna F Filippou FC Mazzoni S, F. G. [2000]. Open system for earthquake engineering simulation (OpenSees). https://opensees.berkeley.edu/wiki/index.php/Main_Page

Melo, J., Varum, H., Rossetto, T., and Costa, A. [2012]. Cyclic response of RC beam-column joints reinforced with plain bars: An experimental testing campaign. 11.

Merino, R. J., Perrone, D., and Filiatrault, A. [2020]. Consistent floor response spectra for performance-based seismic design of nonstructural elements. Earthquake Engineering and Structural Dynamics, 49(3), 261–284. https://doi.org/10.1002/eqe.3236

Ministerial Decree. [1975]. D.M. 05/07/1975 Amendments to ministerial instructions June 20, 1896, relating to the minimum height and to the main sanitation requirements of the living quarters, (in Italian).

Miranda, E., and Taghavi, S. [2003]. Estimation of Seismic Demands on Acceleration-sensitive Nonstructural Components in Critical Facilities. 347−360, Proceedings of the Seminar on Seismic Design, Performance, and Retrofit of Nonstructural Components in Critical Facilities, ATC 29−2,.

Mucedero, G., Perrone, D., Brunesi, E., and Monteiro, R. [2020]. Numerical Modelling and Validation of the Response of Masonry Infilled RC Frames Using Experimental Testing Results. Buildings, 10(10), 182. https://doi.org/10.3390/buildings10100182

Mucedero, G., Perrone, D., and Monteiro, R. [2021]. Nonlinear static characterisation of masonry-infilled RC building portfolios accounting for variability of infill properties. Bulletin of Earthquake Engineering, 19(6), 2597–2641. https://doi.org/10.1007/s10518-021-01068-2

O'Reilly, G. J., Perrone, D., Fox, M., Monteiro, R., and Filiatrault, A. [2018]. Seismic assessment and loss estimation of existing school buildings in Italy. Engineering Structures, 168(August 2017), 142–162. https://doi.org/10.1016/j.engstruct.2018.04.056

O'Reilly, G., and Sullivan, T. [2015]. Influence of modelling parameters on the fragility assessment of pre-1970 italian rc structures. Proceedings of the 5th International Conference on Computational Methods in Structural Dynamics and Earthquake Engineering (COMPDYN 2015), 788–809. https://doi.org/10.7712/120115.3430.1245

Pampanin, S., and Calvi, G. M. [2002]. Seismic behaviour of R.C. Beam-column joints designed for gravity loads. 12th European Conference on Earthquake Engineering, 726, 1–10.

Perrone, D., Brunesi, E., Filiatrault, A., and Nascimbene, R. [2020]. Probabilistic estimation of floor response spectra in masonry infilled reinforced concrete building portfolio. Engineering Structures, 202, 109842. https://doi.org/10.1016/j.engstruct.2019.109842

Perrone, D., Calvi, P. M., Nascimbene, R., Fischer, E. C., and Magliulo, G. [2019]. Seismic performance of non-structural elements during the 2016 Central Italy earthquake. Bulletin of Earthquake Engineering, 17(10), 5655–5677. https://doi.org/10.1007/s10518-018-0361-5

Petrone, C., Magliulo, G., and Manfredi, G. [2015]. Seismic demand on light acceleration-sensitive nonstructural components in European reinforced concrete buildings: Seismic demand on acceleration-sensitive nonstructural components. Earthquake Engineering and Structural Dynamics, 44(8), 1203–1217. https://doi.org/10.1002/eqe.2508

Scott, M. H., and Fenves, G. L. [2006]. Plastic Hinge Integration Methods for Force-Based Beam–Column Elements. Journal of Structural Engineering, 132(2), 244–252. https://doi.org/10.1061/(ASCE)0733-9445(2006)132:2(244)

Silva, V., Crowley, H., Pagani, M., Monelli, D., and Pinho, R. [2014]. Development of the OpenQuake engine, the Global Earthquake Model's open-source software for seismic risk assessment. Natural Hazards, 72(3), 1409–1427. https://doi.org/10.1007/s11069-013-0618-x

Sullivan, T. J., Calvi, P. M., and Nascimbene, R. [2013]. Towards improved floor spectra estimates for seismic design. Earthquakes and Structures, 4(1), 109–132. https://doi.org/10.12989/eas.2013.4.1.109

Surana, M., Pisode, M., Singh, Y., and Lang, D. H. [2018]. Effect of URM infills on inelastic floor response of RC frame buildings. Engineering Structures, 175, 861–878. https://doi.org/10.1016/j.engstruct.2018.08.078

Verderame, G. M., Ricci, P., Esposito, M., and Sansiviero, F. C. [1950]. Le caratteristiche meccaniche degli acciai impiegati nelle strutture in c.a. realizzate dal 1950 al 1980. 8.

Vukobratović, V., and Fajfar, P. [2015]. A method for the direct determination of approximate floor response spectra for SDOF inelastic structures. Bulletin of Earthquake Engineering, 13(5), 1405–1424. https://doi.org/10.1007/s10518-014-9667-0

Zimos, D., Mergos, P., and Kappos, A. [2017]. A model for non-linear dynamic analysis of sub-standard reinforced concrete members. Proceedings of the 6th International Conference on Computational Methods in Structural Dynamics and Earthquake Engineering (COMPDYN 2015), 1656–1666. https://doi.org/10.7712/120117.5520.17845

Overlooked Nonstructural Component Flexibility Design Issues

Brian E. Kehoe[1]

[1] Wiss, Janney, Elstner Associates, Inc.
2000 Powell Street, Suite 1650, Emeryville, CA 94608
e-mail: bkehoe@wje.com

Abstract. Nonstructural components are required to be anchored or braced to the structural framing to resist seismic forces. Design procedures, such as those in ASCE 7-16 Minimum Design Loads and Associated Criteria For Buildings and Other Structures, prescribe criteria for the force level for designing nonstructural anchorage. Other design criteria are also prescribed, such as allowance for relative displacements within structures and between structures. Because of the wide variety of nonstructural components that can exist in a building and the numerous types of systems that can be used to anchor or brace nonstructural components, designers or installers of those components may overlook some aspects of the details of the anchorage or bracing that may affect the behavior of the nonstructural components. Examples of existing installations are discussed where conditions, such as the relative flexibility of the nonstructural support, changes in the support conditions along the length of a distributed system, relative displacement of the nonstructural components, and unintended restraint conditions are described. Some considerations of the building response on the behavior of the building are also discussed. While building code provisions cannot account for all possible conditions that may be encountered, recommendations are made for provisions that can be included in design codes to encourage designers to account for many of these conditions.

Keywords: Nonstructural, Dynamics, Flexibility, Distributed Systems, Supports.

1. Introduction

1.1 BACKGROUND

The seismic response of nonstructural components can represent significant monetary contributions to the damage associated with a building during an earthquake and can impact the post-earthquake functionality [ATC, 2017]. Although nonstructural components represent a wide variety of systems, including architectural, mechanical, and electrical, the building codes for the seismic design of nonstructural components often simplifies the expected behavior of these components. Although building code provisions for the seismic design of nonstructural components have been regularly updated, there are conditions where they may not effectively provide a design engineer with the tools to account for the actual behavior of the components.

1.2 BUILDING CODE REQUIREMENTS

Building codes in the United States have included seismic design provisions for nonstructural components since the early 1960s [UBC, 1961]. When introduced in these older building codes, nonstructural components were referred to as "parts or portions of buildings." Typically, seismic design provisions contain requirements for calculating lateral forces for the nonstructural components and may also include design requirements for nonstructural components to allow for relative displacement of structural components without unintended restraint being provided by the nonstructural components.

This study focuses on the nonstructural seismic design provisions in the American Society of Civil Engineers standard ASCE/SEI 7-16 *Minimum Design Loads and Associated Criteria for Buildings and Other Structures* (ASCE 7-16) [ASCE, 2016]. The concepts discussed in this study however may be applicable to the seismic design provisions in other modern building codes.

1.2.1 Nonstructural Seismic Forces

Seismic forces on nonstructural components are determined using an equation that calculates an equivalent lateral force. The lateral force equation for ASCE 7-16 is shown in Equation (1).

$$F_P = 0.4 S_{DS} \frac{a_p}{\left(\frac{R_p}{I_p}\right)} \left(1 + 2\, {}^{z}\!/_{h}\right) W_p \tag{1}$$

In this equation, the lateral force on the nonstructural component, F_p, is proportional to the weight of the component, W_p, and based on several factors. The term $0.4S_{DS}$ represents the ground acceleration. The term $(1+2z/h)$ represents the variation of the floor acceleration over the height of the building, where z is the elevation where the component is attached to the structure and h is the height of the structure. The terms a_p, and R_p are factors that represent the dynamic amplification and response modification factors, respectively. The term I_p is an importance factor for the component.

The dynamic amplification factor for the components are tabulated in ASCE 7-16 and are based on the generic type of components. The dynamic amplification factor, a_p, consists of two specific values, 1.0 and 2.5 for components that are considered as rigid and flexible, respectively. Similarly, the response modification factors are tabulated in ASCE 7-16 based on the type of component, with some variation for components based on their deformability.

1.2.2 Accommodating Seismic Displacements

The nonstructural seismic design provisions in the ASCE 7-16 building code include requirements for accommodating seismic relative displacements. These provisions address three conditions:

i. Displacement for nonstructural comopnents attached at connection points on the same structure at two different heights. For this condition, the nonstructural component needs to accommodate the calculated building relative deflection between the elevations where the component is attached.

ii. Relative displacement for nonstructural components attached at connection points on separate structures or structural framing systems. For this condition, the nonstructural component needs to accommodate the differential displacement of the two structures at the points of attachment.

iii. For the connections of exterior nonstructural walls to the structural framing, the connections are to be designed to accommodate the calculated seismic displacements through mechanisms such as sliding or bending of threaded rods.

There are no explicit requirements to determine design displacements that need to be accommodated for other attachment conditions for nonstructural components.

2.Nonstructural Component Characteristics

Nonstructural components represent a wide variety of items associated with a building. The seismic behavior of the nonstructural components can generally be defined by several important characteristics. These characteristics are typically considered as binary, with little or no consideration regarding where the component lies within the spectrum.

2.1 RIGID VS. FLEXIBLE

The rigidity of a nonstructural component affects whether the component can become excited and vibrate independently of the structure to which it is attached. This is referred to as the dynamic amplification factor. A flexible component can vibrate in resonance with the structure and amplify the input acceleration from the structure. In contrast, a rigid component will experience a response that is essentially equal to the acceleration response of the structural framing to which the component is attached.

The flexibility of the nonstructural component is defined by the period of vibration or natural frequency of the component. Traditionally, a period of 0.06 seconds (16.67 Hertz) is used to differentiate between rigid and flexible nonstructural components with rigid components being those with a fundamental period of vibration less than 0.06 seconds [Lizundia, 2019]. Cantilever elements, such as parapets and chimneys are considered flexible and components such as tanks, pumps, and exterior wall elements are considered rigid [ASCE, 2016].

For many nonstructural components, the vibrational characteristics are not known. For some components that can be considered single degree of freedom systems, the period of vibration can be estimated using principals of dynamics assuming that the mass and stiffness are known. ASCE 7-16 includes a simple formula based on dynamics for calculating the period of vibration, as shown in Equation (2).

$$T_P = 2\pi\sqrt{\frac{W_P}{K_P g}} \tag{2}$$

In this equation, T_P is the fundamental period of vibration of the component, W_P is the weight of the component, and K_P is the stiffness of the component.

In ASCE 7-16, tables are provided to prescribe the factor to use for establishing whether a nonstructural component is rigid or flexible based on the type of component.

The characterization of a component as rigid or flexible considers the potential for dynamic amplification of the component response relative to the response of the structure at the point where the component is attached. Where the period of vibration of the component is close to the fundamental period of vibration of the structure, the response of the nonstructural component will be amplified. Components where this amplification could occur are considered to be flexible. If the period of vibration of the component is very low or very high relative to the building period, dynamic amplification does not occur. The implied comparison of the component period to the building period that would indicate whether a component is rigid or flexible would compare the period of vibration of the component to the fundamental period of vibration of the structure.

2.2 DESCRETE COMPONENT VS. DISTRIBUTION SYSTEM

Nonstructural components are often simplified as either a discrete item or as a distributed system. Discrete items are treated as a mass that is attached to the structure at a single location. The response of these components is generally characterized as a lumped mass with a single value of stiffness.

Distributed systems are components that are attached to the structure at multiple locations. Some attachments may provide gravity load support, and some may provide gravity and lateral support. Examples of distributed sytems are pipes, ducts, conduits, and cable trays. In practice, theses distributed systems are treated as being flexible relative to the lateral supports and therefore, lateral forces from the distributed systems are applied to the lateral supports based on the tributary length of the distributed system to each support.

2.3 ACCELERATION SENSITIVE VS. DEFORMATION SENSITIVE

The building code recognizes that damage to nonstructural components may be the result of shaking of the component during an earthquake. These components are described as being acceleration sensitive. For these components, the design of the component and its attachment to the structure are based on the seismic design force.

For other components, the primary source of damage to the component may be the result of the deformations imposed on the nonstructural component due to lateral displacement of the building. For these components, the design of the component attachment is based on the relative displacement that needs to be accommodated by the component.

3.Nonstructural Configuration and Installation

The configuration of nonstructural components are often not as easily defined into categories as would be indicated by the building code design provisions. Nonstructural components can be very complex pieces of equipment or systems that include multiple elements. As a result, some nonstructural components cannot be as easily classified as rigid vs. flexible, discrete vs. distributed, and acceleration sensitive vs. deformation sensitive. For some components, the behavior may be different depending on the direction being considered for the component. The dynamic behavior of some nonstructural components may also vary depending on the characteristics of the component support system.

Based on the author's experience in evaluating nonstructural components, there can be many installation conditions that may result in characterizations of nonstructural components based on building code assumptions that do not correspond with the as-constructed conditions.

3.1 FLEXIBLE DISCRETE COMPONENT INSTALLATIONS

Characterizing a nonstructural component's dynamic amplification as rigid or flexible based solely on the type of equipment can be misleading. Many types of mechanical equipment are considered as being rigid with a dynamic amplification factor prescribed by the building code as 1.0. If that mechanical equipment is attached directly to the floor, the characterization as rigid may be correct. However, if that same mechanical equipment is supported on framing, the response of the system, including the mechanical equipment may result in the overall behavior as being flexible instead of rigid.

An example where the mechanical equipment that would typically be considered as rigid is shown in Figure 1. In this installation, the equipment is anchored to the concrete floor slab. The installation of a different installation of a similar mechanical equipment is shown in Figure 2. In this installation, the equipment is supported on steel framing that would provide some flexibility and therefore the component could experience dynamic amplification. The response of the two pieces of equipment could be different because of the differences in the method of attachment to the structure.

Figure 1. Example of rigid mechanical equipment

Figure 2. Support framing for a similar rigid mechanical equipment shown in Figure 1

As another example, a steel tank would typically be considered to be a rigid nonstructural component if the tank is supported directly on the structural framing of a floor. If that tank is supported by framing, as shown in Figure 3, some of which may be the structural framing and some that may be nonstructural bracing, the response may be complex and would likely experience dynamic amplification. Therefore, the assumption of the tank being rigid with no dynamic amplification may under-predict the seismic response of the tank.

Figure 3. Example of tank supported on a combination of structural framing and nonstructural bracing.

3.2 RIGIDITY ORIENTATION

Some nonstructural components are characterized as rigid; however, the rigidity may apply to only one horizontal direction. Stairs for example, are considered as rigid with a dynamic amplification factor of 1.0 in ASCE 7-16. The construction of some stairs may be more appropriate characterized as flexible, as shown in Figure 4. In this example, the stiffness of the stairs in the direction perpendicular to the stringers relies on the two stringers, which are steel channel sections, in weak axis bending. These stairs would be expected to respond flexibly in the weak axis of the stringers and could experience dynamic amplification. In the weak axis, the moment of inertia is about 0.06 times the moment of inertia in the strong direction. This leads to a factor of about 4 difference in the natural frequency.

Figure 4. Stair with steel stringers relying on weak-axis bending for stiffness.

As another example, an exterior precast concrete cladding panel would typically be characterized as a rigid component with an amplification factor of 1.0 using ASCE 7-16. These cladding panels are typically attached to the floor framing at the top and bottom of the cladding panels, as shown in Figure 5. Depending on the ratio of the panel thickness to the vertical span between supports, a precast concrete panel that is less than 8 inches thick would have a period of vibration greater than 0.067 seconds for a vertical span of about 12 feet and should be considered flexible.

Figure 5. Exterior precast concrete wall panels with connections to the floor at the top and bottom of the panels.

For the in-plane direction, a cladding panel that is solid and squat may be considered to be rigid. Where the cladding panels are perforated with large window openings, as shown in Figure 6, the in-plane response may approximate that of a moment frame and therefore be considered flexible.

Figure 6. Example of precast concrete cladding panels with window openings.

Similarly, a cabinet constructed with light-gauge steel that contains mechanical or electrical equipment would be considered flexible by ASCE 7-16 with a dynamic amplification factor of 2.5. This assumes that the cabinet is free-standing and anchored only at the base. If the cabinet is anchored at the base and also anchored at the top to a structural wall, the response would instead be relatively rigid and may not experience dynamic amplification.

3.3 DISTRIBUTED SYSTEM SUPPORT STIFFNESS

As described above, distributed systems are generally designed as flexible relative to the support framing and therefore the lateral design loads are distributed based on tributary area. While there are many distributed systems for which this approach is valid, there are some installations of distributed systems for which this approach may not be valid.

A cable tray that is supported by rods from the framing below and braced with diagonal struts is often considered a flexible system spanning between rigid bracing elements. Structures with significant quantities of cables may require a gridwork of cable trays rather than the simple linear system that is assumed in the building cade for a distributed system. Linear cable tray systems may be considered flexible, similar to other distributed systems, such as piping and ducts. However, where there are intersecting cable trays, the entire system may instead create a rigid horizontal plane rather than flexible linear elements. Figure 7 shows an example of a portion of a large installation of cable tray framing with multiple levels of cable trays and diagonal bracing in both directions between the cable trays. A simple tributary length approach to distributing lateral loads to the bracing elements may not adequately represent the actual behavior of this system.

Figure 7. Example of a system of interconnected cable trays with internal bracing

For some distributed systems, the stiffness of the system may not be flexible relative to the lateral support framing. The example in Figure 8 shows a large diameter (42 inches) plastic duct that is supported on and laterally braced by a series of steel frames. The steel framing that braces the duct are 2-inch (5 cm) square hollow structural steel sections that cantilever more than 10 feet (3 meters) from the floor framing below. The relative stiffness of the duct may be greater than the lateral stiffness of the supports.

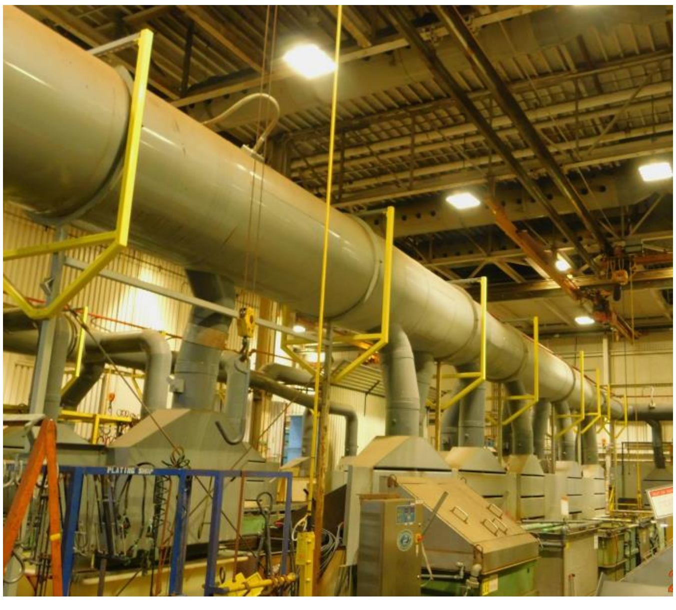

Figure 8. Example of large diameter plastic ducts supported by and laterally braced by tall cantilever steel framing.

3.4 ACCOMMODATING RELATIVE DISPLACEMENTS

ASCE 7-16 provides requirements for specific conditions where relative displacements need to be accommodated by nonstructural components. There are many conditions where the attachment of nonstructural components should be designed to accommodate relative displacement between portions of the component.

Note in Figure 8 that there are vertical branches of the duct attached to equipment below with no accommodation of differential displacement of the duct relative to the equipment. Excessive lateral displacements of the large duct may result in damage to the vertical branches of the duct or damage to the equipment to which the ducts are attached. ASCE 7-16 includes requirements for independent bracing of in-line equipment and the allowance for flexible connections but does not provide requirements to allow for differential movement between the duct and equipment not attached "in-line."

Design provisions for accommodating interstory drifts are typically applied to architectural components, such as exterior walls and partitions. These would also be applied to distributed systems, such as pipe risers. Seldom are these provisions considered to be applicable to mechanical or electrical equipment. An example of this condition is shown in Figure 9, where server racks are attached to the floor and the tops of the rack are braced to the floor framing above. Relative interstory displacement could cause distortion of the rack for which it may not be able to accommodate.

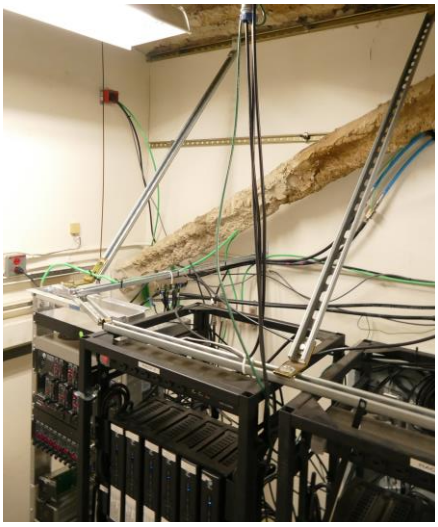

Figure 9. Top of server racks anchored to the floor framing above in addition to the base attachment.

3.5 DISTRIBUTED VS. DISCRETE COMPONENTS

In complex installations of nonstructural components, there may be no clear distinction between elements that are treated as discrete components and those that are distributed systems. Interconnected components may encompass large areas with varying stiffnesses. The installation shown in Figure 10 includes server racks, which would typically be considered discrete nonstructural components and cable trays, which would typically be considered distributed components. Complex systems of interconnected components may require considerations such as the variations in stiffness of the components and their bracing and the strength and stiffness of the connections between the components.

Figure 10. Example of complex system of interconnected components

4.Conclusions and Recommendations

For discrete nonstructural components, the potential for dynamic amplification should not depend on the generic type of component. Component flexibility is a function of the component and the system of bracing and supports that are used to connect the component to the structural framing. Seldom would a component with framing between the component and structure respond rigidly. This would also include components with integral legs. Even when a nonstructural component is directly attached to the structure, the component may have inherent flexibility if the component is constructed of an assembly of parts. Building codes should consider mechanical and electrical components that are constructed with light gauge steel framing as flexible if attached only at the base. Exterior wall components should be considered as flexible in the out of plane direction unless the stiffness can be demonstrated to be rigid.

Some nonstructural components may be constructed and attached in a way that allows them to respond differently in two orthogonal directions. Building codes should require the design engineer to assess the flexibility of the component separately in both orthogonal directions of the component.

Distributed systems should be designed for lateral forces considering the relative stiffness of the supports and the relative stiffness of the distribution system and the bracing for that system. Building codes should require the design engineer to consider the relative flexibility of the component and the support bracing when distributing lateral loads.

REFERENCES

ASCE/SEI [2016] *Minimum Design Loads and Associated Criteria for Buildings and Other Structures*, American Society of Civil Engineers, USA.

ATC [2017], Seismic Analysis, Design, and Installation of Nonstructural Components and Systems – Background and Recommendations for Future Work, NIST GCR 17-917-44, National Institute of Standards and Technology, USA

ICBO [1961] *Uniform Building Code*, International Conference of Building Officials, USA.

Lizundia, Bret [0219] Proposed Nonstructural Seismic Design Force Equations, *2019 SEAOC Convention Proceeding*s, Structural Engineers Association of California, USA.

Seismic Design Optimization of Sprinkler Piping Restraint Installations with Dynamo

Milena Casto[1], Daniele Perrone[2], Roberto Nascimbene[1], Andre Filiatrault[1], Maria Antonietta Aiello[2]

[1] University School for Advanced Studies, Piazza della Vittoria n.15, Pavia,
milena.casto@iusspavia.it
roberto.nascimbene@iusspavia.it
andre.filiatrault@iusspavia.it

[2] University of Salento
S.P. 6, Lecce - Monteroni - Lecce
daniele.perrone@unisalento.it
antonietta.aiello@unisalento.it

Abstract. The damage observed during recent earthquakes pointed out the need for the seismic design of non-structural elements to mitigate the seismic risk at which buildings are prone and to guaranty the immediate occupancy after low to moderate seismic events. Non-structural elements installed without seismic detailing often experienced damage at low seismic intensities with significant consequences on the functionality of critical facilities, such a hospitals. Sprinklers piping systems, according to the common non-structural elements classification, belong to the building utility systems (or mechanical and electrical equipment) category, which is of paramount importance for maintaining life-safety and continuous operation of strategic structures. This paper proposes a Building Information Modelling (BIM)-based tool developed to optimize the seismic design of sway bracing in sprinkler piping systems. The tool is developed in Dynamo, a visual programming tool implemented in Revit, a well-known BIM commercial software. The Dynamo's workflow allows to design the sway bracing according to different code prescriptions and to minimize the cost of the lateral supporting systems by automatically optimizing the shape, the size and the spacing of the sway braces. In order to demonstrate the effectiveness of the proposed tool, two case studies are presented. The case studies consist in the seismic design of the sway braces, according to the NFPA13 Standard, for a sprinkler piping system suspended from the top floor of a generic building located in two Italian regions characterized by different seismicity.

Keywords: Non-Structural Elements, Cost Optimization, Sprinkler piping systems, Building Information Modelling, Design Automatization, Nonstructural Components

1. INTRODUCTION

The damage observed following recent seismic events repeatedly demonstrated the seismic vulnerability of non-structural elements (NSEs). Even if the structural systems are designed to guarantee immediate occupancy after a seismic event, the failure of NSEs, such as partitions, ceiling systems, and piping systems, could significantly affect the performance and the functionality of buildings. International building codes and guidelines often classify NSEs in three main categories: architectural components, building utility systems (or mechanical and electrical equipment) and building contents. Among these non-structural categories, piping systems are of paramount importance in order to guarantee the immediate post-event functionality of critical facilities, as demonstrated by the damage reported following many earthquakes worldwide [Miranda *et al* 2012, Fleming 1998, Perrone *et al* 2018]. The poor seismic performance of piping systems, and in particular of pressurized fire sprinkler piping systems, was generally due to inadequate sway bracing supporting systems. Inadequately or improperly restrained piping systems may suffer damage as a result of large differential displacements between pipelines, excessive piping joint rotations and impact with adjacent structural and NSEs. Therefore, a particular attention should be given to the design of sway bracing systems. However, this could be a difficult task for practitioners due to the lack of knowledge in terms of seismic design of NSEs, as well as to the complexity of the piping layouts in ordinary and critical facilities. In this context, the use of Building Information Modelling (BIM) could significantly help to introduce into practice the seismic design of NSEs. BIM is a digital representation of the physical and functional characteristics of a facility, and it is used to manage the entire construction process (design, construction and management across the entire lifecycle) [Vitiello *et al* 2019]. BIM has become important thanks to the development of digital tools widely used in the Architecture, Engineering, and Construction (AEC) industry to present and manage information on structural systems and processes [Shafie Panah *et a*l 2021]. The growing interest within the AEC industry in using BIM is mainly related to the interoperability of the BIM models, which allows the real time data sharing between different actors involved in the design process. There are many positive aspects in using BIM, as for instance the ability to associate to each element in the model accurate information beyond geometric detailing (i.e. costs, materials, maintenance, energy performance, etc.). This aspect could significantly help in optimizing the design process on one hand and to deal with the maintenance of the building during the entire life cycle on the other hand. This paper describes a BIM-based tool, based on the methodology proposed by Perrone and Filiatrault [2017], for the automatic seismic design of sway bracing in fire sprinkler piping systems. The tool is developed in Dynamo [Autodesk, 2019], a visual programming add-in implemented in Revit [Autodesk 2000] a well-known commercial BIM software. The proposed tool allows to design the sway bracing according to different code prescriptions and to minimize the cost of the lateral supporting systems by automatically optimizing the shape, the size and the spacing of the sway braces.

2. USE OF BIM FOR DESIGN OPTIMIZAZION

BIM is defined by international standards as “a shared digital representation of physical and functional characteristics of any built object which forms a reliable basis for decision” [I.S.O Standard 2010]. BIM has been gaining acceptance in the construction industry for many applications, such as constructability analyses, design checks, commissioning, life-cycle assessment, among others [Volk *et al* 2013]. BIM not only changes how building drawings are created, but also dramatically alters all of the key processes involved in the AEC industry: how the client’s programmatic requirements are achieved; how design alternatives are analyzed to optimize architectural, structural and energy aspects; how multiple teams collaborate during the design process within a single discipline as well as across multiple disciplines; how the building is actually constructed, including the fabrication of different components by sub-contractors; and how, after construction, the building facility is operated and maintained [Eastman *et al* 2011]. The conceptualization of BIM has been discussed in the literature since the 1970s, however its application has started only after the

1990s, when the improvement of computer capabilities allowed the data sharing within the AEC community, as shown by Volk *et al* [2014], Eastman *et al* [2011], and Nederveen *et al* [1992]. In addition to utilising BIM for AEC processes, recent research proposed the use of BIM in the facility management (FM) over its entire life cycle Vitiello *et al* [2019]. The spreading of the BIM methodology is demonstrated by its introduction in building codes worldwide. In fact, some governments have mandated the use of BIM in public projects involving bridges, tunnels, and railways, as well as for strategic facilities such as hospitals and schools. The United Kingdom has required the use of BIM in all government projects since 2016, while the Italian government recently published a decree of law requiring the use of BIM methodology starting from 2025 for the design of all public buildings. The BIM methodology can be used to facilitate the design process in both existing and new design buildings. Effective information management generates accurate documentation on existing buildings, containing requirements and criteria aimed at automating performance assessment and decision-making on possible refurbishment. In this regard, the use of digital documents gives the opportunity to upgrade and expand the data, with savings in long-term resources. A building information model can also function as a web database that documents the inherent attributes of the parametric architectural objects [Bruno *et al* 2018]. For the design of new buildings, BIM is an essential tool to expedite and optimize the design. In this context, the use of BIM for seismic risk mitigation in buildings has the potential to change traditional design practices, especially for the seismic performance assessment of NSEs. According to Welch *et al* [2014], BIM could assist in the assessment and mitigation of seismic risk in three different ways: 1. BIM could provide valuable data on characteristics of both structural and NSEs within a building to permit a reliable seismic risk assessment as well as a detailed seismic design, 2. BIM automatize the diagnosis of the building performance using the data received from structural health monitoring technologies, and 3. BIM could enable the realisation of an emergency management hub within a building management system for implementing control processes to monitor and eventually shutdown damaged mechanical services (e.g. gas pipes) following an earthquake. The use of BIM within a seismic assessment framework, especially for NSEs, can provide crucial information necessary to improve the quality of analysis results. The use of BIM can also provide records regarding the installation costs at the time of construction as well as manufacturer details [Bercerik-Gerber 2012 , Azhar *et al* 2008] of mechanical and service equipment that can significantly reduce the inventorying process prior to conducting a seismic loss assessment. A lifecycle cost analysis of buildings exposed to seismic risk is a critical issue in structural engineering and a careful evaluation should be undertaken, as reported by Vitiello *et al* [2019]. The major of a buildings construction cost are attributed to NSEs, therefore an optimization of these investments is necessary at the design stage. Within the last few years, a number of studies have been carried out to apply BIM for the design of structures and NSEs. Vitiello *et al* [2019] developed a tool, for new and existing buildings, to perform an economic loss assessment of a facility and to optimize the lifecycle cost analysis starting from a BIM model in a closed chain system. When combined with structural monitoring and control technologies within a building automation system, BIM can provide a platform that could allow for an unparalleled line of protection against secondary earthquake hazards. Charalambos *et al* [2014] displayed the damage states of structural elements and NSEs under different earthquake scenarios using colour codes in the BIM model. This visualization provides non-technical stakeholders with new insights into the seismic risk of their building design. TohidiFar *et al* [2021] combined Bayesian Networks and BIM visualization to display the expected status of a hospital's utility systems after a disaster. Valinejadshoubi *et al* [2020] estimated the seismic risk level of NSEs in buildings using FEMA-E-74 [FEMA 2012] and visualized it on a BIM model. This model automatically updated the seismic risk by changing the locations and types of NSEs. Lastly, a simple methodology has been developed to automatically perform the seismic design of sway braces for pressurized fire suppressant sprinkler piping system based on information extracted from a BIM model [Perrone and Filiatrault 2017].

3. A BIM-BASED FRAMEWORK FOR THE OPTIMIZATION OF THE SEISMIC DESIGN OF SWAY BRACING SYSTEMS IN SPRINKLER PIPING SYSTEMS

In this study, a BIM-based tool for the optimization of the seismic design of sway bracing systems in sprinkler piping system is proposed. The tool is implemented in Dynamo. Dynamo for Revit is an open-source visual programming software based on code blocks for quick data entry and object creation. Code blocks are a unique feature in Dynamo that brings together visual programming with DesignScript, which is a text-based language for computational design. No specific IT (Information Technology) knowledge is required to use Dynamo. Therefore, it is easy and intuitive for all practitioners and Revit's users.

Figure 1 illustrates the general framework of the proposed tool. The BIM-based seismic design optimization procedure consists of three main phases: 1) Collecting required information on the piping layout from the Building Information Model, 2) Evaluate the seismic demand on the sprinkler piping system, and 3) Design the sway bracing system (with traditional and optimized design options) and update the original Building Information Model. The tool can be directly executed in the Revit environment allowing to automatically update the existing Building Information Model with the designed sway bracing system. The detailing available in the Building Information Model significantly facilitates the design process, which allows for the modification of the properties of the BIM Objects based on the design requirements.

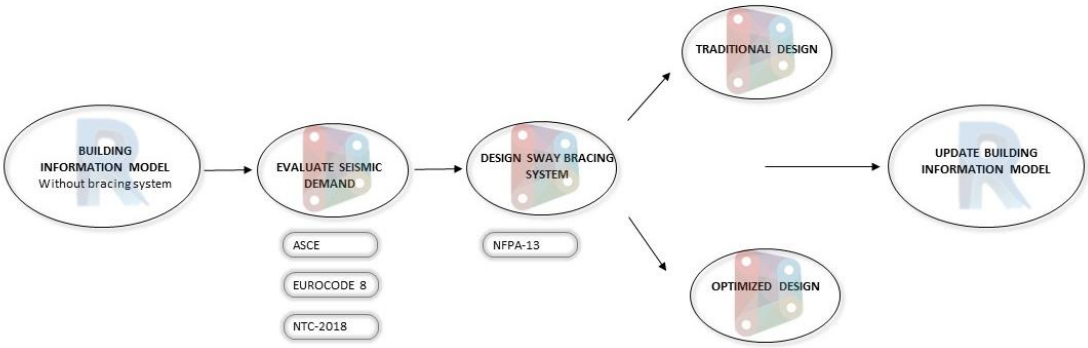

Figure 1. Framework for the automatic seismic design of sway bracing for sprinklers piping systems using BIM.

The proposed tool allows for the evaluation of the seismic demand according to three different codes: ASCE 7-22 [Minimum Design Loads for Buildings and Other Structures 2022], Eurocode 8 [EN 1998-1 2005] and NTC18 [NTC 2018]. In this part of the workflow, only the spectral acceleration at which the piping system is subjected to is calculated, while the spacing between the sway bracing is calculated in the third step of the procedure (Figure1). In the "Design Sway Bracing System" code block in Figure 1, the workflow takes advantage of all the Building Information Model capabilities. In fact, the tool is able to automatically recognize the properties of the pipelines required for the design of the sway bracing. For example, the tool is able to distinguish between the main and branch lines and to evaluate the geometrical and mechanical properties of the pipelines (Figure 2). In order to start the design process, it is required to select a pipeline in the Building Information Model. The is able to automatically recognize all pipes characterized by similar properties in the piping layout and is able to extract the properties required for the design of the sway braces.

Figure 2: Overview of the Design Sway Bracing code block

Then, the "Design Sway Bracing System" code block branches out in two different design options. In the first case, the conventional design process is followed: the practitioner selects the preferred brace typology (size, shape and inclination) and the tool automatically evaluates the spacing and updates the Building Information Model. In the second case, a design optimization is performed: the practitioner can choose between different optimal solutions calculated by the tool in order to optimize the costs of the supporting system. In both cases, the prescriptions of NFPA-13 [2022] are followed. The optimization of the sway bracing seismic design consists of three steps (Figure 3): 1) Include the cost of the sway braces in the properties of the BIM Objects, 2) Calculate the required spacing (S) for all the sway bracing typologies allowed by NFPA-13 [2022], and 3) Compare S with the maximum allowable spacing (L). If $S > L$, for all sizes in a given sway bracing typology, the workflow automatically returns the lowest size; if $S < L$, the tool performs a cost optimization. For each sway bracing size, and for all sway bracing typologies allowed by NFPA-13, the total cost of the sway bracing system is calculated and the size which leads to the lowest total cost of the lateral supporting system is suggested. The design procedure was implemented using a special node in Dynamo, called "Python script". This node allows programming with the Python language when a particular action is required. The node "Python script" was used to implement the complete design process including the check of all design prescriptions provided by NFPA-13 [2022]. At the end of the design process, the designer can select the preferred sway bracing typology based on the cost optimization and the design tool will automatically update the Building Information Model and it will create an Excel file with the properties and the cost of the sway bracing system.

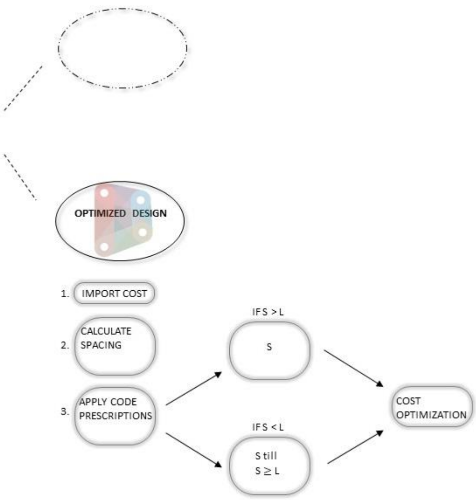

Figure 3: Overview of the Optimized Design code block.

It is worth to be noted that to apply the proposed design tool, the BIM Objects representing the different typologies of sway bracing allowed by NPFA-13 for sprinkler piping systems should contain all the properties required for the design process. To deal with this issue, specific BIM Object families were created and included in the package of the design tool.

4. ILLUSTRATIVE EXAMPLE

In this section, two illustrative examples are presented to investigate the effectiveness of the proposed BIM-Based tool to perform the seismic design of sway braces in sprinkler piping systems. The two case studies differ only for the seismicity of the sites in which the supporting building is located. This variation allowed to investigate the effectiveness of the design tool when the design is governed by code prescriptions or by cost optimization. In Case Study 1, the building is assumed to be located in Lecce (Italy) with a design peak ground acceleration (PGA) on firm soil equal to 0.05g (with a return period of 475 years). In Case Study 2 the building is located in Cassino (Italy). This site is characterized by a PGA on firm soil equal to 0.16g (with a return period of 475 years). These values are representative of a low (Case Study 1) and a medium-high (Case Study 2) seismic zone in Italy.

A hypothetical sprinkler piping system installed in a five-storey RC school building was analysed in this study. Figure 4 shows the sprinkler piping system layout installed at each floor of the building. The sprinkler piping system consists of one main line with a diameter equal to 150 mm and five branch lines, each with a diameter equal to 75 mm. The structural system consists of three RC frames along the longitudinal direction and two transverse RC frames in the lateral direction. The interstorey height is equal to 3.3 m (with the exception of the ground floor that is characterized by a height of 3.7m) for a total height of the building equal to 21.7m. The structure is composed of two identical modules separated by a thermal joint.

Although the BIM-based tool automatically performs the calculations for the sprinkler piping systems installed at each floor, in the illustrative examples, only the results of the seismic design of sway braces installed in the piping system located at the top floor are discussed.

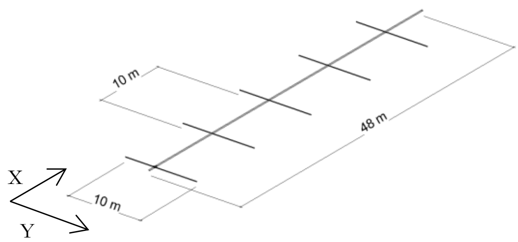

Figure 4: Layout of piping system

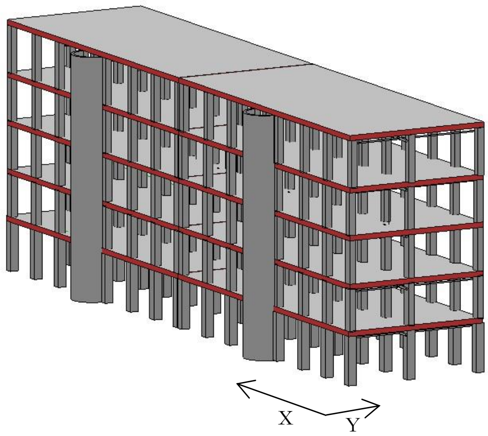

Figure 5: Building information model developed in Revit software

All the prescriptions provided in Chapter 18 of NFPA-13 [2022] are followed in the design process and are fully implemented in the proposed BIM-based tool. The piping system should be braced to resist the horizontal seismic loads in both transverse and longitudinal directions. NFPA-13 [2022] provides tables defining the maximum horizontal loads of the sway braces (Tables 18.5.11.8(a-f) in NFPA-13) based on the sway bracing typology, the slenderness ratio, the material and the inclination of the brace. The slenderness ratio and the inclination of the sway braces are generally governed by architectural constraints. In the analysed case studies, the sway braces are assumed inclined at 45° from the vertical and the piping layout is suspended at a distance from the slab (downdrop) equal to 50 cm. Five typologies of sway braces are considered in NFPA-13: Pipe Schedule 40, Angles, Rods (all thread), Rods (threaded at ends only), and Flats. For each bracing typology, the maximum horizontal loads for different sizes are provided. The proposed BIM-based tool account for all sway brace typologies considered by NFPA-13 and it also allows the inclusion of user-defined piping support installation systems.

To calculate the seismic demand on the sway braces, the formulation proposed by NTC18 [NTC 18-Aggiornamento delle "Norme Tecniche per le Costruzioni"] was considered in this illustrative example. According to NTC18, the equivalent horizontal static design force on a NSE can be calculated as follows:

$$F_a = \frac{S_a}{q_a} W_a \tag{1}$$

where W_a is the operating weight of the NSE, q_a is the behavior factor (varying between 1.0 and 2.0 based on the type of NSEs) and S_a is the floor spectral acceleration. NTC18 provides different formulations to calculate S_a based on the structural typology of the supporting building. In the analysed case studies, the simplified formulation provided by NTC18 for RC moment resisting frames was adopted. In particular, the following parameters were assumed in the design process to evaluate F_a:

- W_a is equal to 0.14 kN/m (operational weight of water filled pipes increased of 10% to account for the weight of sway braces and other fittings);

- q_a is assumed equal to 2;

- S_a is equal to 0.77g for Case Study 1 and to 1.28g for Case Study 2. In the evaluation of S_a, it was assumed $T_a/T_1=1$, where T_a is the fundamental period of the NSEs and T_1 is the fundamental period of the supporting structure;

- $z/H=1$ (piping system at the top floor), where z is the height at which the NSEs is installed, and H represents the total height of the supporting structure.

Because the actual costs of the proprietary sway braces were not available, some assumptions were made in the cost optimization by referring to the material costs available in the Italian cost list for construction. Please note that the costs of the special connections, such as anchor and pipe rings, as well as the labour costs and the bracing anchorage costs are not included in the evaluation.

Table 1 summarizes the results of the seismic design of the sway braces in the transverse direction of the main line carried out using the proposed BIM-Based tool. The highlighted results represent the best solution in term of spacing, shape and costs (in Euro).

For Case Study 1, the spacing between adjacent sway braces is governed by code prescriptions for all sway brace typologies and sizes. In particular, the maximum spacing in the transverse direction is fixed equal to 12 m. Based on this consideration, the design tool automatically provides to the user the smallest size for each sway brace typology (highlighted in bold in the table) without evaluating the cost of the sway braces for all possible configurations. At the same time, the sway brace typology characterized by the lowest cost is suggested to the user (highlighted in red). In this case, the cheapest solution is characterized by Rods (all threaded) with a diameter equal to 10 mm.

For Case Study 2, in which the site is characterized by higher seismicity, only the spacing of sway braces is governed by the code prescriptions for all sizes. In this case, the cost optimization tool evaluates the cost for each sway bracing typology and for all sizes. This is necessary because it is not obvious which will be the cheapest solution. For example, in the case of all thread rod sway braces, the most economical solution is rod diameter of 16 mm, because reducing the size of the rods implies an higher number of sway braces. The BIM-based tool provides a list of the optimized sway braces sizes based on cost optimization. In particular, for Case Study 2, the cheapest solution is characterized by all thread rods with a diameter equal to 16 mm.

		Case Study 1					***Case Study 2***				
Brace Shape	**Size (mm)**	**Spacing (m)**			**Number of sway braces**	**Cost (€)**	**Spacing (m)**			**Number of sway braces**	**Cost (€)**
		Tool	**Limit**	**Selected**			**Tool**	**Limit**	**Selected**		
Pipe Schedule 40	**25**	164	12	**12**	4	**115.4**	11	12	**11**	5	**125.9**
	32	220	12	12	4		15	12	12	4	189.2
	40	226	12	12	4		17	12	12	3	221.8
	50	460	12	12	4		30	12	12	3	462.2
Angles	**40x40x6**	218	12	**12**	**4**	**105.4**	14	12	**12**	**4**	**105.4**
	50x50x6	315	12	12	4		20	12	12	4	107.2
	65x50x6	350	12	12	4		22	12	12	4	125.4
	65x65x6	398	12	12	4		25	12	12	4	146.2
	80x65x6	435	12	12	4		27	12	12	4	200.6
	80x80x6	480	12	12	4		30	12	12	4	231.3
Rods(all thread)	**10**	25	12	**12**	4	**76.8**	10	12	10	7	131.6
	15	45	12	12	4		10	12	10	6	110.4
	16	68	12	12	**4**		12	12	**12**	**4**	**94**
	20	105	12	12	4		12	12	12	4	147.6
	22	140	12	12	4		12	12	12	4	178.8
Rods (threaded at ends only)	**10**	38	12	**12**	4	**81.2**	10	12	10	5	**97.5**
	15	45	12	12	4		11	12	11	5	103.4
	16	102	12	12	4		12	12	12	5	115.6
	20	148	12	12	4		14	12	12	4	159.6
	22	200	12	12	4		13	12	12	4	190.8
Flats	**40x6**	125	12	**12**	4	**100.3**	10	12	10	5	**120**
	50x6	165	12	12	4		14	12	12	4	128
	50x10	16	12	12	4		16	12	12	4	168

Table 1. Results of the Illustrative Examples for main line bracing in the transverse direction

Once the user selects the final solution, the tool automatically updates the existing Building Information Model with the designed sway bracing system. Figures 6 and 7 show the updated Building Information Models for Case Study 1 and 2, respectively.

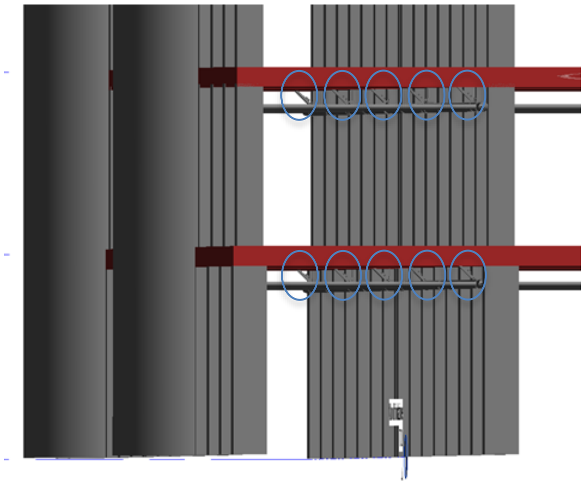

Figure 6: Building Information Model for Case Study 1

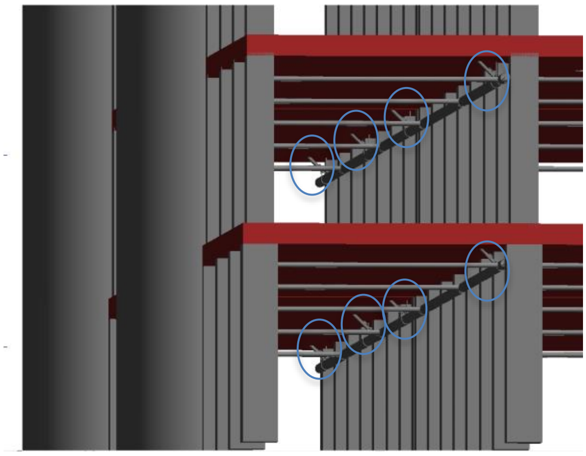

Figure 7: Building Information Model for Case Study 2

5. CONCLUSION

The damage observed following recent seismic events demonstrated the seismic vulnerability of non-structural elements (NSEs) even under low seismic intensities and the need for the harmonization of the structural and non-structural seismic performance. However, the seismic design of NSEs is still difficult to be introduced into practice due to lack of knowledge and often to an unclear definition of the designers' responsibilities. In this context, the use of Building Information Modelling (BIM) could significantly help in the implementation of the performance-based seismic design of NSEs. In this paper, a BIM-based tool for the seismic design of sway braces in sprinkler piping system was proposed. The tool automatically provides the best solution in terms of typology and size of the sway braces, based on cost optimization, and it updates the original Building Information Models using the capabilities of Dynamo. The effectiveness of the proposed methodology was appraised through two illustrative examples. The obtained results clearly demonstrated the benefit of developing BIM-based tools also for other NSE typologies to facilitate the introduction into practice of the performance-based seismic design of NSEs. As a logical progression of the work for updating the current framework, the issue related to the clash detection will be investigated and included in the automatic procedure. At the same time, the tool will be extended to different typologies of NSEs also performing the cost optimization as a function of the use of the buildings.

6. ACKNOWLEDGEMENTS

The authors gratefully acknowledge the funding by Italian Ministry of Education, University and Research (PON Grant n.1735/2017, CADS Project).

REFERENCES

Autodesk 2000 "Autodesk Revit v. 2022.1" Revit: BIM software for designers, builders, and doers.

Autodesk 2019 " Dynamo Revit v.2.12.1" Automatically installed as part of Revit since Revit 2020.

Azhar, S., Hein, M., Sketo, B. [2008] "Building Information Modeling (BIM): Benefits, Risks, Challenges". Associated Schools of Construction (ASC) 44th Annual Conference. Auburn, Alabama.

Bercerik-Gerber, B., Jazizadeh, F., Li, N., Calis, G. [2012] "Application areas and data requirements for BIM-enabled facilities management". Journal of Construction Engineering and Management, Vol 138 No. 3, pp. 431- 442.

Bruno, S.;De Fino, M.;Fatiguso, F. [2018] "Historic Building Information Modelling: performance assessment for diagnosis-aided information modelling and management" *Automation in Construction,* Vol 86, pp. 256-276.

Ciotta, V.; Asprone, D.; Manfredi, G.; Cosenza, [2021] E. "Building Information Modelling in Structural Engineering: A Qualitative Literature Review." *CivilEng,* Vol 2, pp. 765-793.

Eastman, C., Teicholz P., Sacks, R., Liston, K., [2011] "BIM Handbook A Guide to Building Information Modeling for Owners, managers, designers, Engineers, and Contractors" Second edition, Wiley.

EN 1998-1 [2005] " Eurocodice 8 - Progettazione delle strutture per la resistenza sismica - Parte 1: Regole generali, azioni sismiche e regole per gli edifici"

FEMA [2012] "Reducing the Risks of Non-Structural Earthquake Damage—A Practical Guide"

Fleming, R.P. [1998] "Analysis of fire sprinkler system performance in the Northridge Earthquake" *Report No. NIST-GCR-98-636, U.S. Department of Commerce, Building and Fire Research Laboratory. National Institute of Standards and Technology, Gaithersburg, MD.*

I.S.O Standards[2010], ISO 29481-1:2010(E): Building Information Modelling-Information Delivery Manual-Part 1: Methodology and Format.

Minimum Design Loads for Buildings and Other Structures [2022] (ASCE/SEI 7-22) *American Society of Civil Engineers.*

Miranda, E., Mosqueda, G., Retamales, R., Pekcan, G. [2012] "Performance of Nonstructural Components during the 27 February 2010 Chile Earthquake". Earthquake Spectra Vol. 28 No. S1, pp. S453-S471.

NFPA-13 [2022] "Standard for the Installation of Sprinkler System" *National Fire Protection Association.*

NTC [2018] Aggiornamento delle "Norme Tecniche per le Costruzioni". Supplemento Ordinario n.8 alla Gazzetta ufficiale del 20.02.2018, Rome, Italy.

Perrone D, Calvi, P.M., Nascimbene, R, Fischer, E, Magliulo, G [2018] "Seismic performance and damage observation of non-structural elements during the 2016 Central Italy Earthquake." *B Earthq Eng,* Vol. 33 pp. 1-25.

Perrone D., Filliatrault A. [2017] "Automated seismic design of non-structural elements with building information modelling" *Automation in Construction,* Vol. 84, pp. 166-175.

Shafie Panah, R.; Kioumarsi, M. [2021] "Application of Building Information Modelling (BIM) in the Health Monitoring and Maintenance Process: A Systematic Review." *Sensors,* Vol. 21, No. 3.

TohidiFar, M. Mousavi, A. Alvanchi [2021] "A hybrid BIM and BN-based model to improve the resiliency of hospitals' utility systems in disasters" *International J. Disaster Risk Reduction,* Vol. 57 pp. 102176.

Van Nederveen, G.A., Tolman F.P., [1992] "Modelling multiple views pn buildings" *Automation in Construction,* Vol. 1, No. 3, pp. 215-224.

Vitiello, U., Ciotta, V., Salzano, A., Asprone, D., Manfredi, G., Cosenza, E. [2019] "BIM-based approach for the cost-optimization of seismic retrofit strategies on existing buildings" *Automation in Construction,* Vol. 98, pp. 90–101.

Volk, R., Stenge,l J., Schultmann, F. [2014] "Building Information Modeling (BIM) for existing buildings — Literature review and future needs" *Automation in Construction,* Vol. 38, pp. 109–127.

Welch, D. & Sullivan, T. & Filiatrault, Andre. [2014]. "Potential of Building Information Modelling for Seismic Risk Mitigation in Buildings." *Bulletin of the New Zealand Society for Earthquake Engineering*, Vol. 47, pp. 253-263.

Whittaker. A., Hamburger, R.O., Comartin, C., Mahoney, M., Bachman, R. [2004] "Performance-Based Engineering of Buildings and Infrastructure for Extreme Loadings". Technical paper submitted to the Applied Technology Council, ATC-58 project.

Improving Seismic Restraint Design Implementation

Andrew Baird[1], Craig A. Muir[1], Atefeh Pourali[1], and Weng Yuen Kam[2]

[1] Beca Ltd
e-mail: andrew.baird@beca.com, craig.muir@beca.com, aty.pourali@beca.com,
[2] Beca Carter Hollings & Ferner (S.E. Asia)
e-mail: kam.wengyuen@beca.com

Abstract. Surveys of the installation of non-structural elements (NSE) in New Zealand commercial buildings has shown poor levels of compliance with seismic restraint design codes. These observations, as well as the damage to NSE in recent earthquakes, has led to greater regulatory pressure to ensure a seismic restraint design is undertaken in New Zealand building projects. It is now common for such design to be completed earlier in a project, typically in parallel with other design disciplines. This early design involvement has led to better implementation of seismic restraint design and overall project outcomes by allowing for a better ability to coordinate, cost and address constructability issues. However, early design involvement also creates new challenges for both engineers and contractors.

This paper presents recommended approaches to improve the implementation of seismic restraint design. Examples include the use of technology to coordinate (3D BIM modelling) and to improve installation efficiency (virtual installation modelling); establishing strategies that consider the interactions between building services, partition, ceiling and building seismic response more holistically; understanding construction sequencing, amongst others. The paper also shares lessons learnt regarding challenges that commonly arise due to early design involvement, and suggested approaches for how these are dealt with. For example, identifying which elements benefit from being included in early design packages and what elements are best left to be detailed during construction collaboratively between the engineer and contractor.

Keywords: non-structural elements, seismic restraint design, constructability, lessons-learnt, practical implementation

INTRODUCTION

Earthquake damage to non-structural elements such as ceilings, partitions, building services, etc. has been well documented for many years in New Zealand, USA, and other seismic regions worldwide [Dhakal, 2010; Braga *et al.*, 2011; Baird, & Ferner, 2017; Perrone *et al.*, 2019]

Research has also shown that it is common for losses associated with damage to non-structural elements and building contents to represent the majority of overall losses in an earthquake [Kircher, 2003; Bachman, 2004; Miranda *et al.*, 2012]. This outcome is not overly surprising when considering the primary intention of design standards is to protect life-safety, as opposed to reduce the losses of non-structural or content damage. This outcome is also reflected in injury statistics, where the majority of direct injuries in recent New Zealand earthquakes are minor and are due to falling contents or non-structural elements [Yeow *et al.*, 2019].

Clearly there is a need to improve the status quo. The earthquake engineering community, as well as society in general, are becoming increasingly aware of the potential losses associated with non-structural damage and demanding more is done [Schouten, 2013]. One of the key factors considered necessary in improving the seismic performance of non-structural elements (SPONSE) is the early involvement of engineers and architects to collaborate to prevent damage to non-structural elements [CERC, 2012]. Consequently, it is now common for seismic restraint design to be completed earlier in a project, typically in parallel with other design disciplines. However, even with momentum in both research and design, there is anecdotal evidence that poor installations of seismic restraint of non-structural elements continues to occur [Pennington, 2017].

It is evident that in order to improve real world SPONSE outcomes, it is vital that improvements from research and design are implemented in practice and construction. This paper outlines some of the opportunities and challenges that arise from early design involvement, and recommended approaches for how these can improve the implementation of seismic restraint design.

SEISMIC RESTRAINT DESIGN

– BACKGROUND

The selection of most non-structural elements is made during the construction phase in New Zealand. This is one of the main contributing factors to seismic restraint design historically being undertaken "just-in-time". That is – the seismic restraint design is undertaken following the selection of elements, possibly during installation of the element in the building. While this approach does provide advantages in terms of installation efficiencies, it also means that any design for these elements is completed after the regulatory building consent approvals process has been completed.

The result of this in practice was that services, partitions, and ceilings in existing buildings have very poor levels of compliance with seismic restraint design codes. The majority of non-structural elements in New Zealand commercial buildings are inadequately seismically restrained as shown in Figure 1 [MBIE, 2016].

These observations, as well as the damage to NSE in recent earthquakes in New Zealand (Darfield 2010, Lyttelton 2011, Seddon 2013 and Kaikoura 2016), has led to greater regulatory pressure to ensure a seismic restraint design is undertaken in New Zealand building projects. Consequently, it is now common in New Zealand building projects for such design to be completed earlier in the project, typically in parallel with other design disciplines.

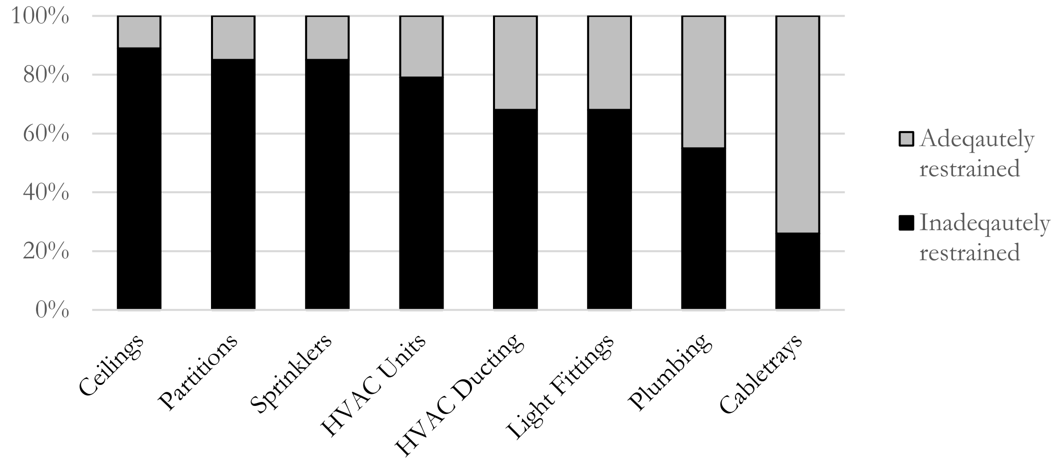

Figure 1. Proportion of non-structural elements adequately restrained in New Zealand commercial buildings [MBIE, 2016]

While this can provide better project outcomes in terms of costing, consenting and constructability of non-structural elements (which will be elaborated on in the subsequent section) it also presents challenges due to the industry not yet being matured in its approach to early seismic restraint design.

– EARLY DESIGN INVOLVEMENT

Seismic restraint design occurring in parallel with other well-established design disciplines is a relatively recent development in building design in New Zealand. These well-established disciplines such as structural, building services, and architectural design each have their own mature industries where the approach to design is well understood by both designers and contractors. For these main disciplines, there are well established industry standards, e.g., design stage outputs, scope splits, standard details, etc. [NZCIC, 2016].

Seismic restraint design also lies at the intersection of these various well-established disciplines. As such, it is subject to the forces of each discipline, e.g., meeting the requirements of architects and their sub-contractors for the design of ceilings and partitions, while at the same time meeting the requirements of building service engineers and their individual sub-contractors. Seismic restraint design is very much multi-disciplinary, and this highlights the importance of an approach which understands and considers the requirements of various disciplines. This will be further elaborated on when discussing recommended approaches to seismic restraint design.

Early seismic restraint design is still in its formative years in New Zealand and a standard industry approach does not yet exist. There is an established industry approach in specific sectors internationally e.g. the public healthcare sector in California under the OSPHD and the nuclear industry under the IAEA Safety Standard [SSC, 2000; IAEA, 2021]. In New Zealand, different design engineers will provide very different design products in terms of level of detail and thought that goes into design solutions based on what they consider appropriate. The forces of each discipline on each project will also vary widely on each project, for example, an early seismic restraint design will often need to provide the seismic restraint requirements of partitions significantly earlier than that of reticulated HVAC ducting since the former will often be frozen some months in advance of the latter. The partition restraint design will also often impact the HVAC ducting layouts. Consequently, the timing requirement of seismic restraint design outputs can vary greatly between disciplines. The above factors present challenges, but also opportunities. These opportunities and challenges will be discussed in the following section.

– Opportunities

There are several key benefits to early seismic restraint design involvement, but the central theme to these is improving implementation of the design during construction. Three important opportunities to improve implementation that arise from early seismic restraint design are discussed in this section.

- **BIM Modelling**

The role of Building Information Modelling (BIM) continues to grow in importance in building design and construction. This importance coupled with improvements in the modelling tools themselves creates a significant opportunity to early seismic restraint design.

For example, seismic restraints elements, e.g. braces, can infer the data of the building service element that they are restraining, e.g. height, weight, material, etc. When this information is coupled with design calculation scripts, seismic restraint layouts and calculations can be efficiently produced with a degree of automation. Restraint layouts and engineering calculations can also be easily regenerated following changes to services layouts. The 3D modelled braces can then be used to spatially coordinate and collaborate with other disciplines to resolve clashes and ensure acceptable visual appearance where restraints are exposed, such as in Figure 2 below.

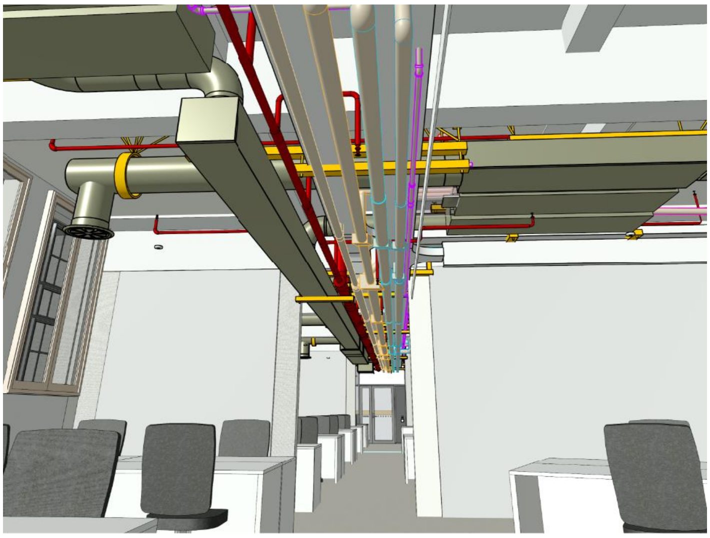

Figure 2. 3D models of seismic restraints (yellow) of exposed building services

Early forms of seismic restraint design often consisted of mark-ups of architectural or building services drawings. These were often cumbersome to produce, and not easily updated to reflect changes in building service layouts. They relied on other disciplines being well progressed with their design, i.e., drawings were required, and they were not easy for other design disciplines to take into consideration.

The use of BIM and agile modelling tools allows the seismic restraint designer to insert themselves into the design process, collaborate to solve constructability issues and influence other disciplines. The mechanical engineer can now see a partition brace clashing with their duct in a 3D model and re-route their duct accordingly. These sorts of clashes may have meant a brace didn't get installed using a historical 'just-in-time' design approach or led to significant remediation costs, but with BIM modelling the issue can be solved before anything is built.

It is not difficult to imagine how further advances in efficiency tools can lead to models being able to self-resolve clashes by flipping, shifting, and adjusting braces. When such solutions do not solve the clash, this can then be highlighted to the designer. This process alone provides huge value by highlighting to the designer where problematic areas exist so they can redirect and prioritise their attention.

A 3D seismic restraint model also allows for improved installation efficiency. The designer's model can be passed to the contractor to visualise the installation during construction coordination. It is commonplace to observe installers having a digital device alongside them to check the virtual installation. In future this may become an augmented reality type installation.

- **Integrated Design Solutions**

Early seismic restraint design involvement allows for integrated design solutions that consider the seismic interactions between building services, partition, ceiling, and structure more holistically. Such solutions often lead to overall cost-savings and significantly simplify the seismic restraint requirements.

Integrated design solutions are nearly impossible to achieve if they do not originate early in the project design life since they need to consider the requirements of a number of disciplines. An example is shown below for a heavily serviced building containing laboratory spaces. The architect's desire was to leave as much of the structure and services exposed as possible. The requirement to expose services, along with the congested service reticulation led to the need to develop a strategy for the seismic restraint of building services that was coordinated, tidy and efficient.

The concept of a system of inverted frames hung from the floor above was proposed. This frame required services to be routed via the frames down what was called a services 'racetrack'. Several iterations of frames were required to fit the services in the 'racetrack', to maintain adequate clear height, to limit loads on the structural floor and to ensure an acceptable appearance. One such early concept is shown in Figure 3 (left). While the development of integrated solutions sometimes requires more coordination between disciplines, they improve the implementation of seismic restraint design by front-loading the problem-solving to the design phase rather than construction phase. It is more efficient to accommodate for significant non-structural elements demands on the structure during the design phase as opposed to making up for it in construction phase where the structure is already finalised and built.

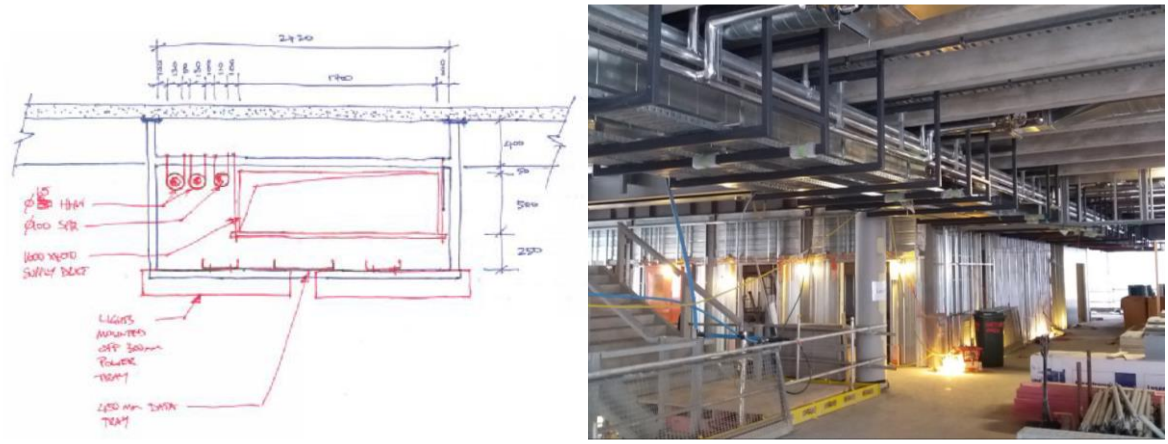

Figure 3. Concept of inverted frames supporting and restraining reticulated building services in 'racetrack' (left). Inverted frames and services during installation (right)

- **Consenting and Tendering**

Seismic restraint design that is undertaken prior to building consent and tender improves the likelihood that a compliant design is appropriately costed by the contractor. Contractors have historically allowed for the cost of seismic restraints as provisional sums or via risk-based pricing since very little information existed at the time of tender. This could lead to under-pricing the extent of seismic restraint works or tagging out of the work altogether. By having a better understanding of the quantum of restraints at tender, this allows for clearer and more accurate procurement, reducing the risk that there is not adequate budget for seismic restraints to be installed.

– CHALLENGES

Shifting the design of seismic restraints from the construction phase into the design phase can create new challenges that need to be overcome for early design effort to be successful. Some key challenges are discussed in this section. Refer to the following section for more detailed recommended approaches that help overcome these challenges.

▪ Design Timing

Seismic restraint design is heavily reliant on other disciplines progressing their respective designs before it can proceed. This can lead to a 'catch-22' situation; trying to collaborate with other disciplines while adequate information to proceed in not yet available, but if a design does not proceed the other disciplines will not have anything to coordinate with.

This challenge can be overcome by collaborating closely with other disciplines and timing the design based on how the project design is proceeding. This timing can vary from project to project depending on how the project is progressing. For example, it will be common for main service runs to be designed and modelled before branch runs are confirmed. Rather than waiting for modelling and documentation to be completed, it is usually better to proceed with the design and modelling of the seismic restraint of frozen main runs, but to wait until branch runs are frozen at a later date. Alternatively, a project may proceed from area to area, so in this case it would be necessary for the seismic restraint design to follow this scheme.

Similarly, different disciplines will freeze their designs at different times in the design programme. It is recommended to focus on elements with reduced flexibility first when progressing seismic restraint design. For example, partition layouts are often the first to freeze to confirm room layouts, and since the spatial positioning of partition braces do not have as much flexibility as other elements it is useful to progress the partition restraint strategy, including deflection head height and modelling of partition restraints as soon as room layouts have been confirmed.

▪ Inconsistency in Design Outputs

Inconsistency between seismic restraint design outputs arises from a lack of maturity and standardisation within the industry. If a client does not understand what they are paying for, and if gaining building consent is their key driver, then there is an incentive to choose the cheapest design on offer. This leads to a 'race to the bottom' in design fees and scope, which logically excludes more advanced service offerings such as BIM modelling and integrated design solutions. Consequently, the opportunities offered by early design involvement are often not capitalised on because these can be seen as an additional cost to the project. In reality, this cost will still exist, but it will instead be lumped within the contractor's fee.

Inconsistency in design also makes it harder for contractors. When the output from designers – such as drawings and model (if provided) vary in quality and appearance, it is obviously more difficult for the contractor to understand and price. This can be detrimental to the improved accuracy in tendering discussed earlier, since if designs are too difficult to understand then the contractor may refer to their previous strategies because they feel more comfortable with that approach, as opposed to pricing off an unfamiliar drawing style.

It is evident that industry guidelines are required to inform designers of what they should be providing at different design stages and create standardised delivery models appropriate for different project types. This is important to help build contractors' confidence and familiarity so they can accurately price at tender.

- **Confusion in Scope**

The design of some elements may not benefit the project by being shifted from the construction phase into the design phase. For example, the design of hold-down fixings for a lightweight piece of equipment does not require coordination with other disciplines and the cost is minor and likely well understood by the contractor. Conversely, the fixings for a heavy air-handling unit require close coordination with the structural engineer since the loads will likely influence the structure and if inadequate it could lead to significant increased costs. In other instances, it may simply not be possible to progress the design until the equipment is selected and its size and weight is available.

Similarly, there can be significant confusion over how to include or exclude elements which include both gravity and seismic demands. Gravity dominant elements such as plant room framing are traditionally designed or selected by sub-contractors to suit the building service gravity requirements and spatial constraints on site. It is therefore likely inefficient for the design engineer to define these frames during the project design phase, and rather to work alongside the contractor to ensure the solution they propose is adequate for both gravity and seismic demands.

At its essence this challenge is an issue of timing and scope. It is overcome by identifying which elements benefit from being included in early design and what elements are best left to be designed and detailed during construction collaboratively between the engineer and contractor. Similarly, to the previous challenge, it is evident that industry guidelines are required to help standardise the approach to various elements.

RECOMMENDED APPROACHES

This section presents recommended approaches to improve the implementation of seismic restraint design when undertaken in parallel with other design disciplines.

– Standardising Delivery

As discussed in the previous section, some of the key challenges to overcome relate to design timing, inconsistency in design and confusion in scope. These challenges have similarities in that they would all benefit from a more standardised approach to seismic restraint design.

One aspect of this is determining what is most suitable and appropriate to provide at each stage in the design. The most relevant example to refer to in New Zealand is the NZCIC Design Guidelines. These are widely adopted interdisciplinary guidelines that clearly define and communicate to all parties involved in a project the following:

- responsibilities and deliverables each party will provide at each project stage,
- the scope of services the various parties provide to the Client,
- the interactions and coordination required between all parties.

These guidelines are recommended for use in all building projects and were developed following concerns over the impact of poor documentation on the building industry in New Zealand [NZCIC, 2016]. Unfortunately, they do not yet include seismic restraint as a design discipline.

Based on our experience, we have proposed a very high-level approach to standardising seismic restraint design at each design phase as shown in Figure 4 on the following page.

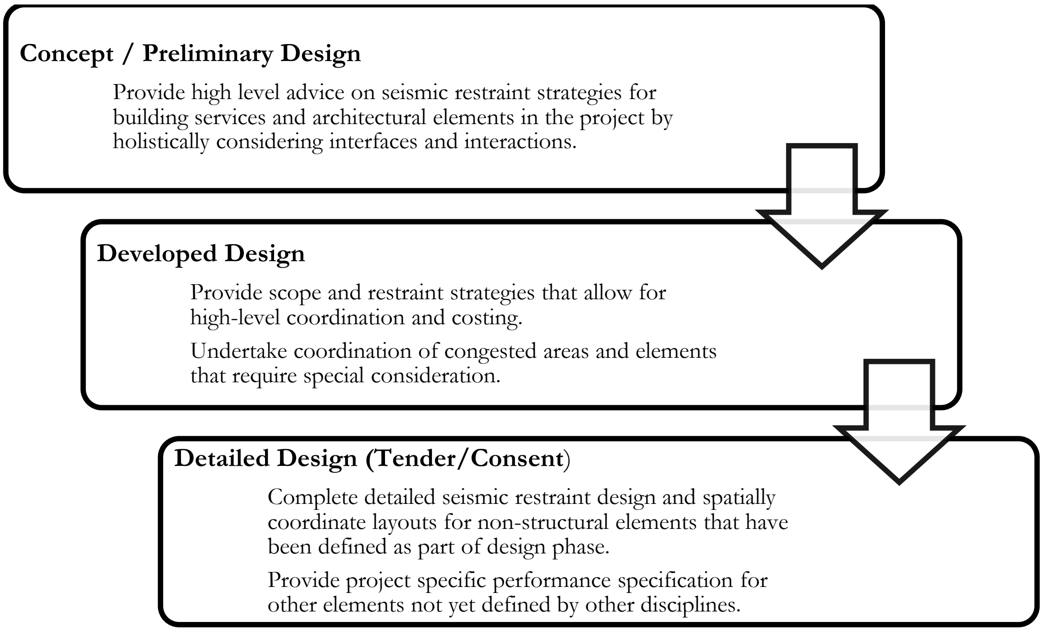

Figure 4. High-level approach to seismic restraint design at each design phase

This high-level approach includes a consideration of how best to collaborate with other disciplines at each design stage. For example, at Developed Design there may still be insufficient information available to undertake an accurate seismic restraint design, however this represents a critical opportunity for coordination with other disciplines. It is therefore recommended that the seismic restraint developed design adopts the form of a simple, well targeted deliverable that identifies the restraint strategies across the project at a high-level to facilitate coordination with other disciplines. An example of this type of deliverable is shown in Figure 5 for partition walls. This outlines different partition restraint strategies that may be employed in different areas to suit that particular area.

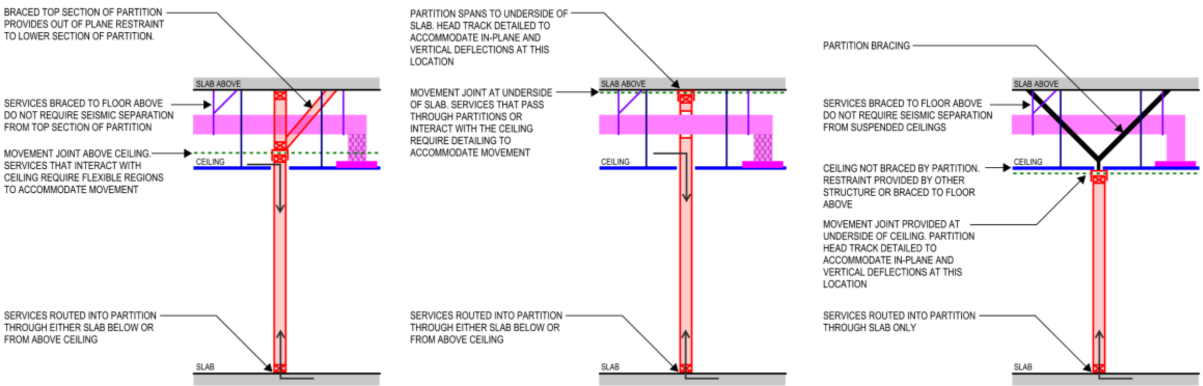

Figure 5. Example of seismic restraint partition strategies for discussion and coordination with architects and building service engineers

– Scope Delineation

Delineating the responsibilities of the design engineer and the contractor is vital to improve accountability. Improving accountability is seen as being a key driver to improving implementation. Therefore, it is recommended that a design responsibility matrix is defined for each non-structural element. A standardised industry approach to seismic restraint design would benefit from including such a matrix. As discussed in the previous section, various non-structural elements will require different involvement from the design engineer and contractor depending on a number of factors, e.g. gravity dominant, proprietary items, design-build items, etc. An example responsibility matrix is shown below for linear services supported from above and from below.

Table 1. Example of scope delineation between designer and contractor for linear

NSE Group	Designer (pre-tender)	Contractor (post-tender)	Designer (post-tender)
Linear services, e.g. pipes, ducts, cable trays supported from **above**	Seismic brace and fixing details. Seismic brace layouts & maximum brace spacings. Spatial planning for seismic restraints, flexibility & clearances. Coordination of seismic loads with structural designer.	Gravity support design or selection. Selection of flexible elements and vibration isolators for combined thermal, gravity & seismic displacements. Construction phase set-out & coordination.	Review Contractor's layout, support & detail submissions & if/where appropriate, update/ complete design
Linear services, e.g. pipes, ducts, cable trays supported from **below**	Coordination of significant seismic point loads with structural designer.	Design of supports for gravity & seismic actions. Selection of flexible elements and vibration isolators for combined thermal, gravity & seismic displacements. Construction phase set-out & coordination.	Review Contractor's support structure design (calcs & details) w.r.t. seismic actions.

– INTEGRATING SEISMIC RESTRAINT DESIGN DURING CONSTRUCTION PHASE

Outputs from early seismic restraint design include indicative plan layouts, project specific details, standard details, and performance specifications for undefined elements. Finalisation of seismic restraint layouts cannot take place until building services sub-contractor construction phase design and equipment selection. It is therefore necessary to integrate the sub-contractor design and selections with the seismic restraint design. We recommend the following approach for this integration:

- Undertake an initial briefing meeting with the contractor, building services, ceiling and partition subcontractors to discuss general principles to be followed, shop drawings process, standard details to be used and agreed procedures for areas where standard details may not apply.

- Once seismic restraint design layouts are issued for construction, the subcontractors will need to incorporate the seismic restraint design intent layouts onto their shop drawings to confirm final layouts are compatible with the subcontractor construction phase design layouts and selections.

- The main contractor's non-structural elements seismic coordinator will work with all subtrades to coordinate the seismic bracing design with the finalized sub-contractor design.

- The designer will review sub-contractor shop-drawing submissions to check seismic restraint design intent is considered and incorporated.

The main contractor plays a critical role in the coordination and management of seismic restraints across the various trades. We recommend the contractor identifies a 'Seismic Restraint Installation Coordinator' who is responsible for coordinating the final locations of seismic restraints to non-structural elements. This coordinator can also consider other design factors that have likely not been explicitly considered in the seismic restraint design, such as thermal expansion, pressure/thrust, vibration, acoustics, etc.

CONCLUSION

Early seismic restraint design involvement provides opportunities to improve implementation. However, it also creates new challenges that need to be overcome for early design effort to be successful. The successful implementation of early seismic restraint design is considered by the authors as the most important step in getting improved seismic performance outcomes. In essence, the only way to improve the resilience of our built environment is by ensuring the research and design effort makes it into our buildings. If the advantages gained by early design involvement are not useful for the contractor, or not taken into consideration by the contractor, then these advantages are lost – negating the benefit of early seismic restraint design.

This paper has presented on recommended approaches to improve early seismic restraint design implementation from a New Zealand design engineers' perspective. These approaches include standardising delivery, delineating scope between designer and contractor, and integrating seismic restraint design during construction. It is evident that seismic restraint design requires continued input and collaboration between designer and contractor, and that the industry would benefit from establishing a standardises approach.

REFERENCES

Bachman, Robert E. [2004]. The ATC 58 Project, Plan for Non-structural Components, Performance-Based Seismic Design: Concepts and Implementation, *Proceedings of the International Workshop*, Bled, Slovenia, 28 June – 1 July 2004.

Baird, A., & Ferner, H. [2017]. Damage to non-structural elements in the 2016 Kaikōura earthquake. *Bulletin of the New Zealand Society for Earthquake Engineering*, Vol. 50, No. 2, pp. 187–193.

Braga, F., Manfredi, V., Masi, A., Salvatori A., Vona, M. [2011]. Performance of non-structural elements in RC buildings during the L'Aquila, 2009 earthquake. *Bulletin of Earthquake Engineering*, Vol. 9, pp. 307–324.

CERC. [2012]. Canterbury Earthquakes Royal Commission - Final Report

Dhakal, R. P. [2010]. Damage to non-structural components and contents in 2010 Darfield earthquake. *Bulletin of the New Zealand Society for Earthquake Engineering*, Vol. 43, No. 4, pp. 404–411.

IAEA [2021]. "Seismic Design for Nuclear Installations". Iaea Safety Standards Series No. SSG-67. International Atomic Energy Agency Vienna, 2021

Kircher, C. [2003]. "ATC-29-2: It makes Dollars and Sense to Improve Non-Structural System Performance". Applied Technology Council, USA.

Pennington, P. [2017]. "Auckland DHB: 40% of hospital fittings 'poorly restrained'". *Stuff*. https://www.rnz.co.nz/news/national/335991/auckland-dhb-40-percent-of-hospital-fittings-poorly-restrained

Perrone, D., Calvi, P.M., Nascimbene, R. [2019]. Seismic performance of non-structural elements during the 2016 Central Italy earthquake. *Bulletin of Earthquake Engineering*, Vol. 17, pp. 5655–5677.

MBIE [2017]. "Survey of Seismic Restraint of Non-Structural Elements in Existing Commercial Buildings." KOA, NZ.

Miranda, E., Mosqueda, G., Retamales, G., Pekcan, G. [2012] Performance of nonstructural components during the 27 February 2010 Chile earthquake. *Earthquake Spectra* Vol. 28, pp. S453–S471.

NZCIC [2016]. New Zealand Construction Industry Council Guidelines

Schouten, H. [2013]. "Call for more controls for ceilings, fittings." *Stuff*. http://www.stuff.co.nz/dominion-post/business/commercial-property/8800732/Call-for-more-controls-for-ceilings-fittings

SSC [2000]. A History of the California Seismic Safety Commission – "Living where the Earth Shakes", California Senate Office of Research, Sacramento, Califoronia, USA

Yeow, T., Baird, A., Ferner, H., Ardagh, M., Deely, J., Johnston, D. [2020]. Cause and level of treatment of injuries from earthquake damage to commercial buildings in New Zealand. *Earthquake Spectra*, Vol. 36, pp. 1254–1270.

Practical Considerations for Non-structural Bracing Design of Multiple Suspended Utilities in Congested Areas of Facilities

John P. Masek, MS,PE,SE[1]; Paul McMullin, PhD.,PE,SE[2]; and Blake Larsen[3]

[1] VIE Consultants Inc.
South Ogden, Utah
e-mail: jpmseismic1@gmail.com

[2] McMullen Engineering, LLC
Sandy, Utah
e-mail: Paul@mcmullineng.com

[3] CFC, Inc.
West Haven, Utah
blake@cfcdelivers.com

This paper presents practical considerations for seismic bracing design and construction of nonstructural systems in highly congested areas of facilities. Mechanical and electrical design engineers, as well as structural engineers of record (SEOR's), typically delegate the design of nonstructural seismic bracing design by the use of performance specifications. The SEOR typically provides limitations of allowable loads that can be transmitted to the structure by seismic braces and also provides limitations to where seismic bracing can be attached. Often, multiple third-party bracing firms are involved in each project, so that the bracing systems may differ from mechanical ductwork, mechanical piping, process piping, electrical conduit, electrical cable tray, and other suspended mechanical, electrical, and plumbing (MEP) systems. This deferred submittal approach can be effective for open accessible areas in facilities. However, in corridors, or other congested areas with multiple suspended utilities, this approach can result in difficult situations, with several MEP trades competing for limited space to fit in seismic bracing. Additionally, in these congested areas, relative deflection limitations in ASCE7-16 [ASCE/SEI, 2016] are difficult to comply with, due to the close proximity of MEP systems. The authors have observed several ways to improve coordination between the SEOR, the MEP design firm of record, and third-party bracing design firms. A fully coordinated BIM model can assist with coordination. However, many projects do not have such a BIM model, either because it is not part of the designer's scope, or since final MEP layout, and subsequentially the seismic bracing design, occurs after the project is bid and awarded to a contractor. This paper presents guidelines for SEOR's and MEP design engineers in developing performance specifications and design documents that accommodate practical bracing installation restrictions.

Keywords: Nonstructural Seismic Bracing, BIM, Mechanical Systems, Electrical Systems, Computer Systems

INTRODUCTION

Nonstructural systems in buildings and facilities include items such as electrical conduit and cable tray, mechanical piping & ductwork, (both suspended and base mounted), and platform or base mounted mechanical and electrical equipment. These are collectively referred to as mechanical, electrical, and plumbing (MEP) systems in this paper. Building or facility owners also may install process related specialty equipment, computer systems, and telecommunication equipment. In many cases, seismic design requirements of suspended non-structural items, as well as base mounted equipment items, are delegated to third party entities though the use of performance specifications. In this scenario, the third party companies prepare nonstructural seismic design documents and submit them to the structural engineer of record (SEOR) and the MEP engineer(s) of record for review and approval. Multiple solutions exist for installation of seismic bracing in difficult congested areas of buildings. This paper presents a few of the many approaches the authors have used in recent projects. By reviewing these concepts, engineers designing facilities may gain further insight that is helpful in preparing project design drawings and specifications. Specifically, careful thought should be given to how (or if) the engineers and contractors (for delegated submittals) can install bracing in locations (as shown and within load limitations given in contract drawings/specifications developed by the SEOR and MEP engineers). Facility design engineers are encouraged to reflect upon reasonable non-structural bracing load limitations (to use in specifications) when designing main structural members, as well as secondary systems such as interior walls, ceilings, and supplemental structural members. Such activities can reduce project schedule delays and minimize change orders related to nonstructural seismic bracing.

As of the date of this paper, the current building code that is applicable to seismic bracing design for suspended mechanical, electrical and plumbing systems in the United States is the 2018 International Building Code (IBC) [ICC, 2018] and (by reference in the IBC) ASCE 7-16 (ASCE/SEI, 2016]. Individual states, counties, or other local government agencies, and in some cases cities themselves, will have additional requirements that are added to IBC and ASCE 7 design and installation requirements. Some owners of high value facilities, such as data centers, hospitals, or utilities, may have seismic requirements that are supplemental to IBC and ASCE 7 requirements. The Federal government mostly adopts IBC and ASCE 7 requirements, but also may require further seismic design measures for more critical facilities.

This paper presents observations and recommendations that are intended to be helpful to SEORs, MEP design engineers, facility owners, and review and approval authorities in developing and implementing performance specifications (as well as preparing facility design documents), such that these design documents contain practical non-structural accommodations. Recommendations have been developed based on the authors' experience completing non-structural bracing and equipment anchorage design for hundreds of facilities in the United States over the past forty years. This paper does not address base mounted equipment anchorage. This paper also does not address seismic qualification of equipment. These topics, while important, are beyond the scope of this particular paper.

BUILDING INFORMATION MODELLING (BIM) AS A TOOL FOR SEISMIC BRACE INSTALLATION COORDINATION

A fully coordinated BIM model can assist with seismic bracing design and installation. However, many projects do not have such a BIM model, either because it is not part of the designer's scope, or since final MEP layout (and seismic bracing design) occurs after the project is bid and awarded to a contractor. Even if a BIM model does exist, inputting large amounts of data (as final MEP layouts are determined) can result in brace installation schedule delays and related costs. That is not to say that such models are not useful for certain projects; however, the authors have observed the BIM models are not a panacea for seismic bracing installation coordination. Often multiple third-party bracing firms are involved in each project, so that the bracing systems may differ from mechanical ductwork, mechanical piping, process piping, electrical conduit, electrical cable tray, and other MEP systems. Since multiple firms can be involved in nonstructural seismic bracing design, overall responsibly for the entire MEP system can be unclear [NIST, 2017]. This (deferred submittal) approach in less complex open accessible areas of facilities. However, in corridors (or other congested areas) with multiple suspended utilities, this (deferred submittal) approach can result in difficult situations, with several MEP trades competing for limited space to fit in seismic bracing.

STANDARD BRACING DETAIL USE AND ADAPTION OF STANDARD DETAILS FOR AREAS WITH MODERATE ACCESS LIMITATIONS

Many public domain resources exist illustrating conceptual seismic bracing details for suspended MEP systems. [FEMA 2005, 2012], [NEHRP/FEMA P-2082 [2020]. These details are useful in explaining basic design intent. Basic details can also be adapted for seismic bracing of suspended utilities in areas where good access exists to install bracing. Even in congested areas of facilities, with many suspended utilities in close proximity to each other, access is sometimes available for installation of straightforward bracing configurations. Examples of straightforward seismic bracing installations are shown in Figures 1-2.

Figure 1. Example of Installed Simple Seismic Brace Installation with Minimal Adjacent Utility Interference

Figure 2. Example of Installed Simple Seismic Brace for a Trapeze with Minimal Adjacent Utility Interference

CUSTOMIZED DETAILS IN AREAS WITH MODERATELY RESTRICTIVE ACCESS FOR INSTALLATION

Moderate variations of standardized details are also often applicable for brace installations in locations with moderate access limitations. The authors have found that it is effective to have deferred submittals include alternative details and descriptive variations (along with standard details). An illustration of one such variation is shown in shown in Figures 3 and 4. In these figures, transverse braces are installed within the trapeze vertical hangers (instead of extending outward from the trapezes). Bracing within trapezes can also be used for multiple-tier trapezes. These and other variations can be anticipated in advance and included on deferred submittals. Additionally, deferred submittal documents usually require showing the location of seismic braces on MEP drawings. If a BIM model does not exist, this is commonly done on 2-D plan drawings. The authors have found it helpful to show likely permutations (from standard details) on the deferred submittals, even if it is not known definitely where specialty conditions will apply. When preparing deferred submittal calculations, it is recommended that calculations be included for these anticipated alternate details. This approach allows the reviewers (SEOR and MEP engineers) to approve anticipated variations, and the contractor to implement approved variations, without the costly and time consuming process of additional submittals (for cases when anticipated variations can be used). As an additional recommendation, the authors advise preparing seismic bracing calculations and drawings in a manner with allows some variation of brace location (without resubmittal of seismic bracing drawings and calculations for each case when a variation is required). This can be done by identifying locations that are congested and specifying alternative brace locations and configurations that are allowed and which are consistent with submitted seismic calculations.

RELATIVE DISPLACEMENT CONSIDERATIONS

Relative displacements between suspended nonstructural systems have been the significant contributing cause of damage during many seismic events [M. Phipps, 2017]. In the 1994 Northridge California Earthquake, eight acute care hospitals within the affected area from the earthquake were evacuated. Six of them were evacuated due to nonstructural damage, such as extensive water damage from burst pipes, fire sprinklers, and other nonstructural systems [Tokas, 2011]. Nonstructural elements can be generally classified into two categories: "acceleration-sensitive" or "displacement-sensitive" nonstructural elements [FEMA, 2012]. Suspended utility systems are both acceleration and displacement sensitive. In the view of the authors, modern seismic design codes in the United States generally provide adequate provisions for calculating seismic forces and designing for acceleration-sensitive nonstructural components. Seismic design standards in the United States (ASCE 7-16, and state and local supplements) also require that seismic design of suspended nonstructural components account for relative displacement effects. Among other requirements, ASCE 7, Section 13.6.4.2 states: "Component supports shall be designed to accommodate the seismic relative displacements between points of support determined in accordance with Section 13.3.2". Best practices reports cite the need for consideration of relative displacements of nonstructural systems [NIST 2017, 2018]. In practice, this can be very difficult to accomplish for nonstructural components in highly congested corridors or other confined areas. The authors agree that compliance with the relative displacement requirements in ASCE 7 is needed, to the extent that this is reasonably possible. As one example, bracing of nonstructural elements using long cable or strut braces (to structural floors located (in many cases) ten or more feet above the braced item) may be ineffective (due to both a brace installation access restrictions and due to flexibility of long brace members). One possible solution to this challenge is to design bracing that is connected to closely adjacent structural elements, or nonstructural walls. If braces are attached to nonstructural walls, these walls must be designed for imposed nonstructural loads (from suspended utility bracing). Where applicable (i.e. congested corridors) the need to design nonstructural walls for imposed suspended utility bracing loads can be anticipated and accounted for by the overall project SEOR.

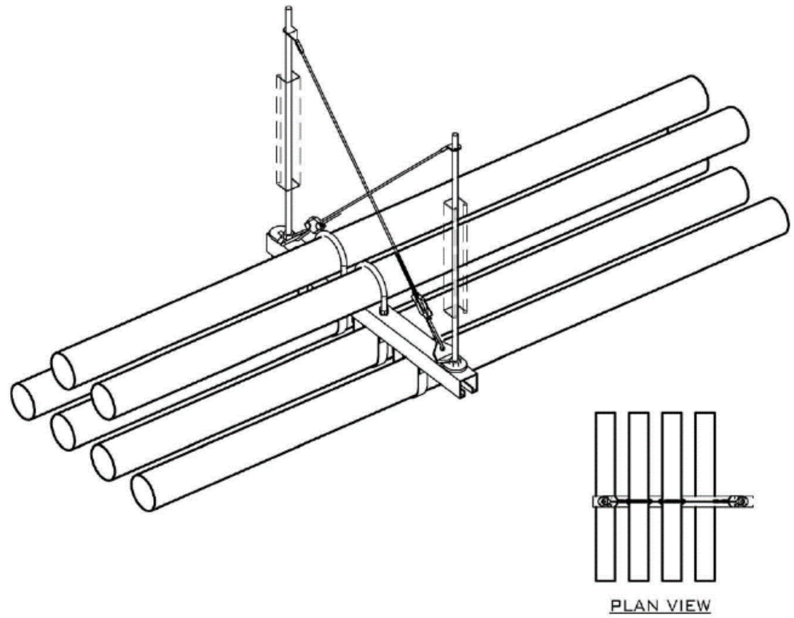

Figure 3. Example of Seismic Trapeze Brace for Use When Interferences Exist on Both Sides

Figure 4. Installed Cross Brace on Trapeze Brace for Use When Interferences Exist on Both Sides

CUSTOMIZED DETAILS IN AREAS WITH VERY RESTRICTIVE ACCESS FOR SEISMIC BRACE INSTALLATION

Seismic bracing installation in highly congested areas of facilities can present challenges, simply due to the fact that it is physically impossible to fit bracing through the complex assembly of piping, ductwork, electrical systems, and specialty process piping that are in very close proximity to each other. Often, these highly congested areas are known in advance because they are shown on design drawings developed by the MEP engineers. In the absence of a coordinated BIM model, seismic bracing is designed and installed by each trade. An example of a hallway in a new airport terminal is shown in Figure 5. In this figure, a very dense concentration of suspended MEP systems is shown on contract documents. Original design documents and specifications did not allow seismic brace attachment to concrete masonry unit (CMU) walls. Through a cooperative effort between the SEOR and the nonstructural seismic design engineers, it was agreed that bracing installation to the structural steel (far above the hallway) was not feasible. CMU wall capacity was evaluated and found adequate for installation of seismic bracing (that is attached to these CMU walls). (Refer to Figures 6 and 7). Involvement of a nonstructural seismic design implementation specialist is one way to address such issues in advance. Another possibility is for the SEOR to design such walls (for possible seismic bracing attachment loads) as a part of the original design. In a similar situation on this same project, brace installation to overhead structural steel was not feasible due to the presence of many utilities (above and on each side) of the conduit run for which seismic bracing was to be designed and installed (Figure 8). A variation of this design using cable bracing is shown in Figure 9. In this case, the capacities of the steel stud walls were calculated, and it was determined that the steel stud walls had sufficient capacity for seismic bracing to be attached to them. The examples (referred to above) exist at a large new commercial airport (Ip (Importance Factor) =1.25 for the structure, and both Ip =1.0 or Ip =1.5 for suspended systems). In Ip=1.0 buildings (offices, commercial buildings), as well as Ip =1.5 buildings (hospitals, critical services buildings) hallways are often constructed with multiple suspended utility systems. In these hallways, steel stud framed walls often exist. Attachment to these stud walls can be a practical solution for installation of seismic bracing. The authors note that in all cases where bracing is to be attached to walls, the capacity of these walls to resist additional seismic loads from utility bracing must be verified.

Figure 5. Excerpt from design drawing, with markups of seismic bracing loads for the hallway areas

Figure 6. Highly congested MEP systems in a hallway in a utility area of a modern airport

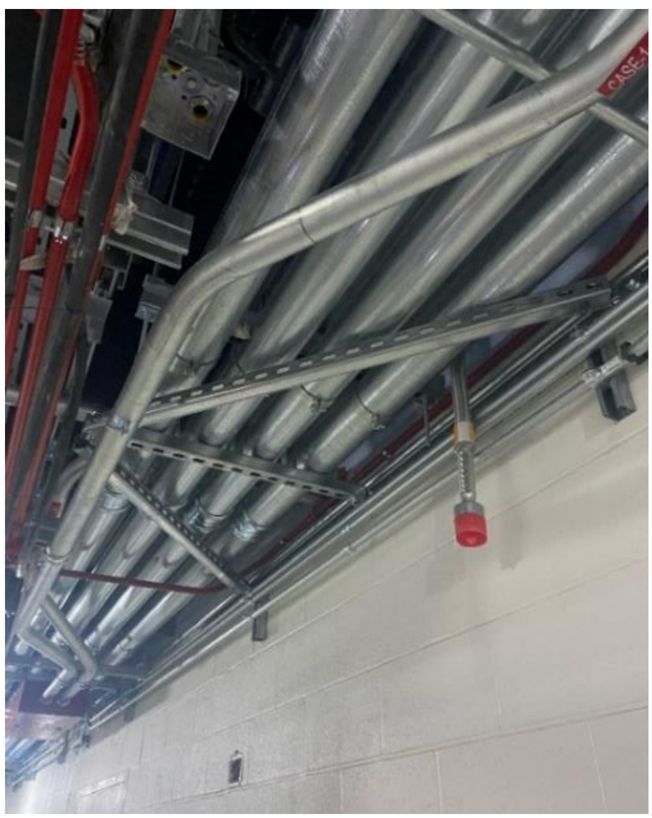

Figure 7. Seismic bracing attached to CMU wall

Figure 8. Seismic strut bracing attached to steel stud wall

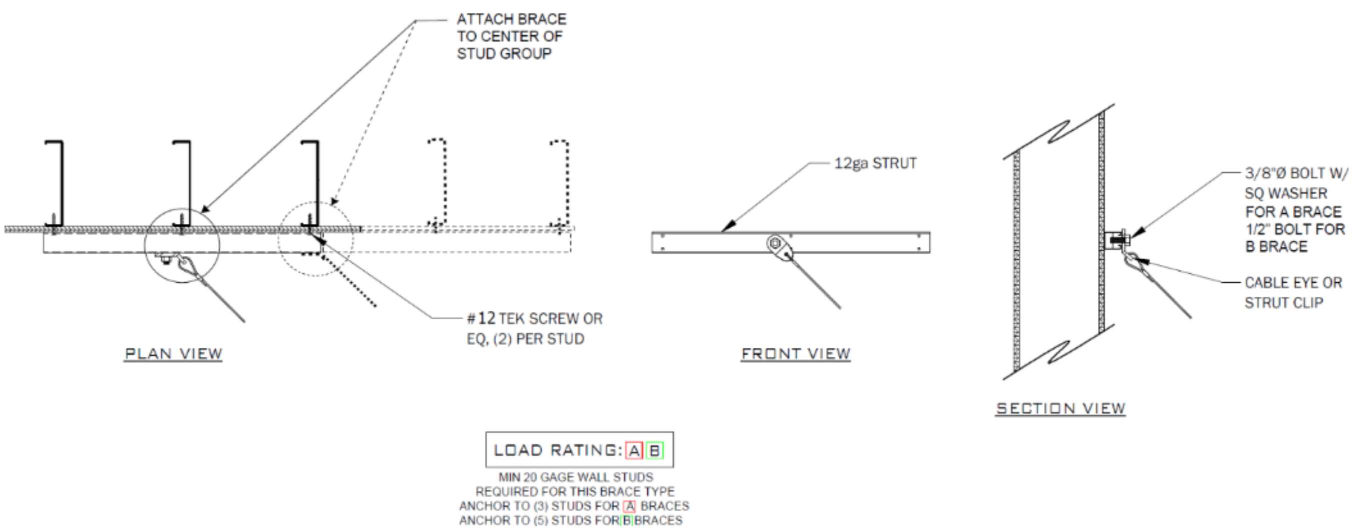

Figure 9. Seismic cable bracing attached to steel stud wall

An additional example of a facility where customized seismic bracing installations may be needed is within computer rooms of data centers. Within these data centers, rooms referred to as "hot-rooms" often exist. These rooms are enclosed with semi-airtight ceilings and walls. The computer equipment within these rooms may have cooling plenum structures that enclose for all or a portion of the computer equipment within these rooms. Normal seismic bracing (extending up to the structure above) is many times disallowed (because air tightness must be maintained to specified levels). In such cases, the authors have found that by coordinating properly with the SEOR and MEP engineers (involved in air plenum design) economical and effective seismic bracing solutions can be designed. These solutions can meet seismic bracing design requirements, limit seismic loads to acceptable values for primary and secondary structures, and also conform to MEP air tightness requirements. While many solutions have been used by the authors, two will be provided in this paper for illustration purposes. One solution involved forethought by the SEOR, in which hanging steel posts were designed and attached to structural steel at the roof level. These posts extended into the computer "hot-rooms". As illustrated in Figure 10, seismic bracing was then attached to these hanging posts. An alternate seismic bracing method in computer "hot-rooms" consists of designing the secondary steel (for plenum supports) to also accommodate seismic bracing loads for electrical systems. This concept is shown in Figure 11.

Figure 10: Attachment of seismic supports to "hanging posts" designed by the SEOR

Figure 11: Attachment on nonstructural seismic supports to "hot-room" plenum steel

HOW THE STRUCTURAL ENGINEER OF RECORD (SEOR) AND MEP DESIGN ENGINEERS CAN ASSIST SPECIALTY SEISMIC BRACING DESIGN ENGINEERS

The mechanical and electrical design engineers, as well as the structural engineer of record (SEOR), typically delegate non-structural seismic bracing design by the use of performance specifications. The SEOR typically provides limitations of allowable loads that can be transmitted to the structure by seismic braces and also provides limitations to where seismic bracing can be attached. Both the SEOR and MEP engineers of record should consider seismic performance specification completeness, as well as the reasonableness of load limitations. Use of BIM models can be beneficial in preplanning potential seismic bracing loads and locations. BIM modeling alone (if a BIM model exists) is not a panacea for non-structural seismic bracing coordination. The final layout of MEP systems is most often the responsibility of MEP contractors who are selected well after the overall construction documents are completed. Therefore, even in cases where there are BIM models, the final MEP layout is typically the responsibility of the electrical or mechanical contractors. The SEOR is responsible for the design of structural systems including primary and secondary beams, slabs, columns, structural walls, and structural lateral force resisting systems. Steel stud partition walls may be designed by the SEOR or may be designed in a deferred submittal. Design of secondary steel, such as plenum enclosures may also be a delegated design. In areas where concentrated MEP systems exist (especially where it can be foreseen that limited access for seismic bracing installation may be an issue) careful consideration should be given to the reasonableness of load limitations specified for seismic brace attachments to secondary systems, such as concrete block partition walls or steel stud partial walls. Design/build approaches can also be used to coordinate nonstructural seismic brace installation. However, design/build approaches are not used or not allowed by many owners. Design/bid/build, or other contracting mechanisms, would benefit by careful thought concerning if the contract documents accommodate practical and economical seismic brace installation.

REFERENCES

ASCE/SEI 7-16 [2016], *American Society of Civil Engineers/Structural Engineering Institute*, Minimum Design Loads and Associated Criteria for Buildings and Other Structures, USA

ASCE/SEI 41-17 [2017], *American Society of Civil Engineers/Structural Engineering Institute,* Seismic Evaluation and Retrofit of Existing Buildings, USA

ATC-69 [2008], *Applied Technology Council,* Reducing the Risks of Nonstructural Earthquake Damage, State-of-the-Art and Practice Report, USA

FEMA [2005], *Federal Emergency Management Agency*, Earthquake Hazard Mitigation for Nonstructural Elements, Field Manual, USA

FEMA [2012], *Federal Emergency Management Agency*, Seismic Performance Assessment of Buildings: Volume 1- Methodology, USA

NEHRP/FEMA P-2082 [2020], *National Earthquake Hazards Reduction Program, Federal Emergency Management Agency (NEHRP*), Recommended Seismic Provisions for New Buildings and Other Structures, USA

NIST GCR 17-917-44 [2017], *National Institute of Standards and Technology, U.S. Department of Commerce*, Seismic Analysis, Design, and Installation of Nonstructural Components and Systems-Background and Recommendations for Future Work, USA

NIST GCR 18-917-43 [2018], *National Institute of Standards and Technology, U.S. Department of Commerce*, Recommendations for Improved Seismic Performance of Nonstructural Systems, USA

IBC [2018], *International Code Council,* 2018 International Building Code, USA.

Phipps, M., et.al. [2017], *Future Developments in the Seismic Analysis and Design of Nonstructural Components for Buildings*, 16th World Conference on Earthquake Engineering, Chile

Tokas, C. [2011], *Nonstructural Components and Systems – Designing Hospitals for Post-Earthquake Functionality*, 2011 Architectural Engineering (AEI) Conference, USA

Seismic response analysis of precast structures with closure external panels

Davide Bellotti[1], Francesco Cavalieri[1], and Roberto Nascimbene[1,2]

[1] European Centre for Training and Research in Earthquake Engineering (EUCENTRE)
Via Ferrata 1, 27100 Pavia, Italy
e-mail: davide.bellotti@eucentre.it; francesco.cavalieri@eucentre.it; roberto.nascimbene@eucentre.it
[2] University School for Advanced Studies (IUSS)
Palazzo del Broletto, Piazza della Vittoria 15, 27100 Pavia, Italy
e-mail: roberto.nascimbene@iusspavia.it

Abstract. The major seismic vulnerabilities in precast industrial buildings observed in the recent past earthquakes consist in the overturning and the collapse of closure external panels. The aim of this work is to assess the seismic vulnerability of existing single-storey precast buildings, designed in accordance with past Italian code provisions and with increasing seismic hazard levels, in the case of explicit modelling of external panels. The considered case studies are single-storey precast industrial buildings representative of the Italian building stock in the 1970s and 1990s, assumed to be located in two Italian cities subjected to different hazard levels. The structures are characterised by two different cladding systems, namely masonry infills (representative of the '70s) and reinforced concrete precast panels (typically used in the '90s). Several nonlinear pushover analyses were carried out on the corresponding three-dimensional numerical models created in OpenSees. The results provided insights into the influence of the two types of closure panels under investigation on the global structural behaviour, with respect to the Usability Preventing Damage and Global Collapse performance levels.

Keywords: Precast, Industrial buildings, Seismic assessment, Pushover, Masonry infills, Cladding panels.

1. INTRODUCTION

In the recent earthquakes that hit Italy (Abruzzo 2009, Emilia-Romagna 2012 and Central Italy 2016), significant damage was observed in existing structures, among which precast buildings [Belleri *et al.*, 2015; Bournas *et al.*, 2014; Fischinger *et al.*, 2014; Toniolo and Colombo, 2012; Magliulo *et al.*, 2014; Savoia *et al.*, 2017; Bosio *et al.*, 2020]. Particular attention should be therefore placed on the matter concerning the seismic safety of structures constituted of precast elements. The surveys carried out following the earthquakes, and reported in the above-cited works, made it possible to highlight how the main and most widespread damages were due to: a) loss of support of the horizontal structural elements (beams and roof elements), falling from the supporting elements (columns and beams, respectively), caused by the absence of mechanical connections; b) overturning of the closure external panels due to the collapse of the connection with the structure; c) loss of verticality of the columns following the expulsion of the concrete cover at the base with consequent instability of the bars due to a lack of transverse reinforcement; d) damage to the steel storage racks not properly braced, which interacted with the structure and contributed to the overall damage. The closure external panels in precast structures, unlike the other structural elements, can be classified as non-structural elements having aesthetic and technological functions (thermal and acoustic insulation). The most common solutions found in the Italian inventory of the last decades are the lightweight reinforced concrete (RC) precast horizontal or vertical panels with ordinary or prestressed steel reinforcement. Concerning the precast buildings built before the 1980s, the most frequently used typology of external closure was masonry infills, often with the presence of ribbon windows [e.g. Bellotti *et al.*, 2014; Babič and Dolšek, 2016].

The main damages suffered by the closure panels following recent Italian earthquakes were due to the poor connection between these panels and the precast structure. This happened, concerning the precast reinforced concrete panels, due to the low resistance or the low constraint effect of the steel connections with the structure. As a result, extended damage was observed in older buildings during recent seismic events: the connections often suffered from serious damage and the panels collapsed due to overturning (Figure 1a). In other cases, the collapse occurred due to the seismic interaction with other types of non-structural elements, such as steel racks adjacent or directly restrained to the precast panels (Figure 1b).

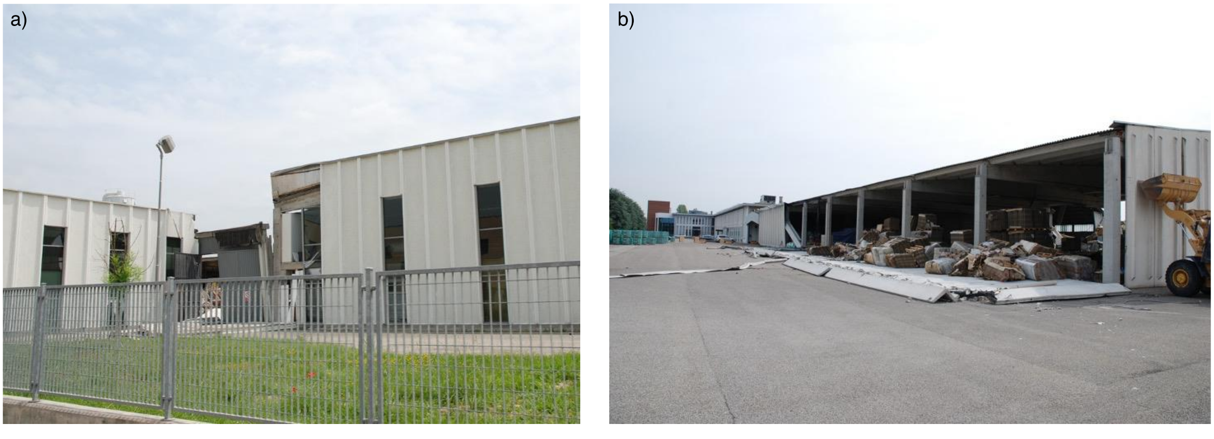

Figure 1. Collapse of external RC precast cladding panels during the 2012 Northern Italy earthquake (Emilia-Romagna): a) due to overturning; b) due to the interaction with steel racks

The masonry infills in precast buildings contribute to the stiffness of the structure even if they are often not adequately constrained to the load-bearing system. Following the recent earthquakes, their presence has affected, positively or negatively, depending on their arrangement, the response of the entire structure. It is important to note that the closure is often irregular, with openings and the presence of ribbon windows. In the latter case, the "squat column" effect may occur. In the presence of frictional connections between beams and columns, the friction force is often lower than the shear capacity of the column, whose drift is reduced by the infills, and this causes the sliding of the beam with respect to the column. Cases have also been observed in which the squat (or short) column collapsed due to flexure/shear mechanisms (Figure 2a), or the infills collapsed due to their weakness (Figure 2b).

Figure 2. Collapse of external masonry infills during the 2012 Northern Italy earthquake (Emilia-Romagna): a) with additional collapse of the short column; b) due to the weakness of the infills

Few researchers to date investigated the seismic behaviour of existing precast buildings with explicit modelling of their closure external panels, thus taking into account the structural failure of masonry infills and precast panel connections [e.g. Babič and Dolšek, 2016; Zoubek *et al.*, 2016; Bosio *et al.*, 2022]. In this work, which is based on the outcomes of the Italian RINTC project [2015-2021; see also Iervolino *et al.*, 2018, 2019], the seismic response of existing Italian precast structures built in the '70s and '90s was analysed. To this aim, three-dimensional numerical models were created in OpenSees [McKenna *et al.*, 2000], featuring the presence of frictional or dowel (i.e. with protruding bars) beam-column connections, as well as explicitly modelled infills/panels, thus highlighting the actual contribution offered by non-structural elements, which are instead typically modelled solely as participating masses.

2. CASE STUDY BUILDINGS

The definition of the case studies was carried out by selecting the typology of single-storey RC precast structures that is most frequently used for industrial buildings in Italy. Such a typology is composed of a series of parallel single-storey portals representing two different construction periods: the '70s, when the closure external panels were typically masonry infills, and the '90s, when the panels were typically made of precast reinforced concrete.

The first case study is a single-storey precast structure representative of the Italian construction period of the '70s, located in Naples and designed on the base of gravity loads only (Figure 3). The geometry consists of a single span with total plan size of 20 × 54 m^2. The columns have a 0.35 × 0.35 m^2 cross-section and a 6 m height. The main beams in the transverse (x) direction have a span of 20 m and a double slope (10% inclination) with an I-section variable in both height and thickness. The secondary beams in the longitudinal (y) direction are 6 m long with a tee cross-section. The beam-column connections are friction-based. The roof is characterised by the presence of cast-in-place concrete topping (5 cm thickness) with continuous steel reinforcement between the double-tee roof elements and the reinforcement stirrups protruding from the beams. The external closure is present on all sides of the building and is constituted of masonry infill panels creating a ribbon window of a 1.5 m height.

The second case study is representative of the Italian construction period of the '90s, located in L'Aquila and characterised by a rectangular plan with a total size of 15 × 24 m^2 (Figure 4). The columns have a 0.55 × 0.55 m^2 cross-section and a 6 m height. The main beams in the transverse (x) direction have a span of 15 m and a double slope (10% inclination) with an I-section variable in both height and thickness. The secondary beams, oriented along the longer side in plan (i.e. *y* direction), are made up of elements in prestressed concrete with a tee cross-section and 6 m long. This building features beam-column dowel connections. A bridge crane is present, with the height of the supporting corbels assumed to be 4.5 m; the overhead crane runs on two beams with a HEA400 section. The roof system is constituted of precast double-tee elements with a 5 cm thick cast-in-situ slab; as regards the connection between the roof elements and the main beams, it was assumed that they are connected with bolted steel plates: for these reasons, and according to EC8 [CEN, 2004], the roof may be considered rigid in its plane. The external closure, also in this case present on all sides of the building, is constituted of vertical RC precast panels.

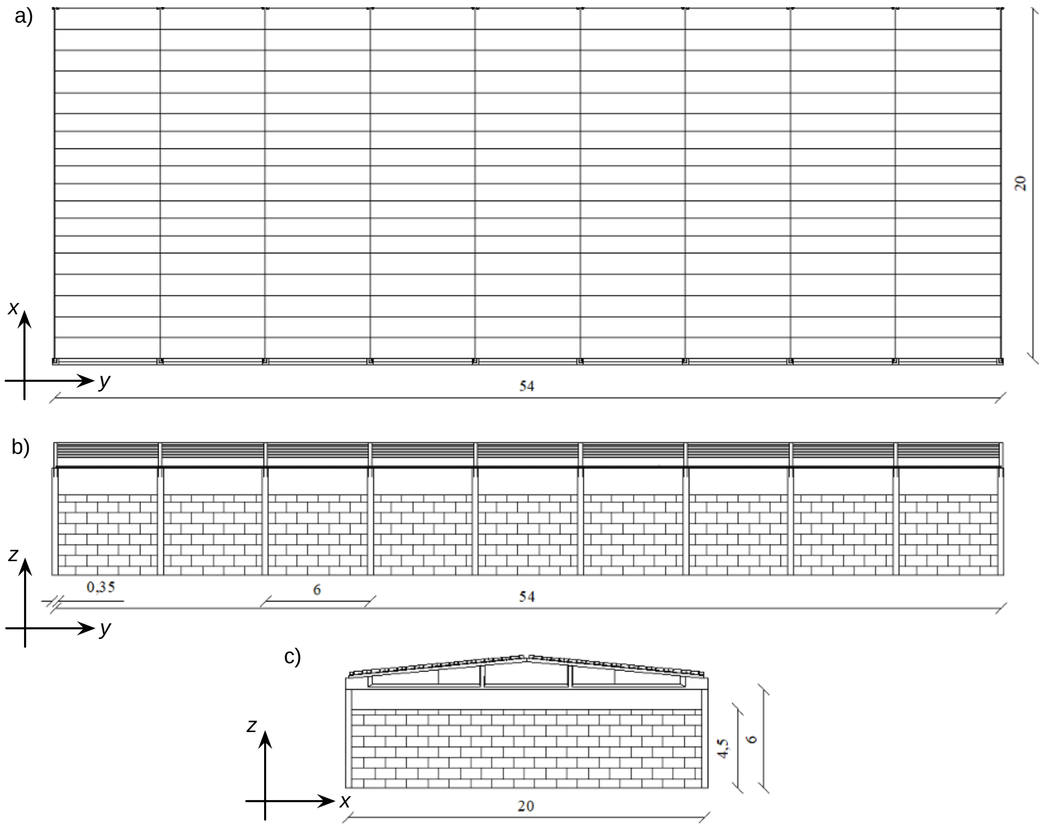

Figure 3. a) Top, b) side and c) frontal view of the '70s case study building (Units: m)

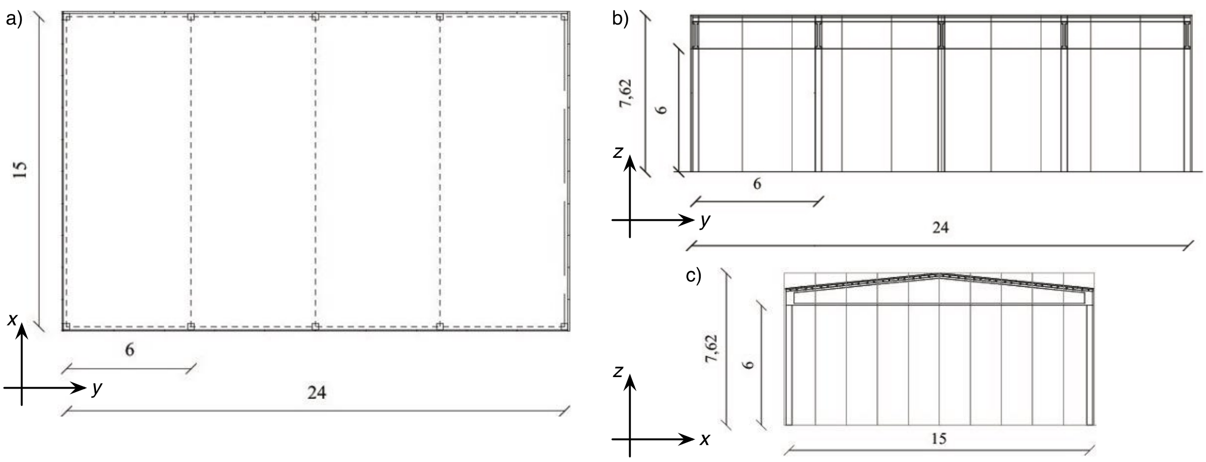

Figure 4. a) Top, b) side and c) frontal view of the '90s case study building (Units: m)

3. MODELLING ASSUMPTIONS

As already said in the Introduction, 3D numerical models of the case study buildings were created in OpenSees. In these building models (three models per case study, as explained in Section 4), a concentrated plasticity approach with a plastic hinge at the base of the columns was used to describe the global structural nonlinear behaviour; in the adopted model, the stiffness of the entire element is obtained by connecting in series the stiffness of the rotational spring and the one of the column element. The plastic hinge model was defined using the "Modified Ibarra-Medina-Krawinkler Deterioration Model with Peak-Oriented Hysteretic Response" (*ModIMKPeakOriented*) material, as implemented in OpenSees, whose mechanical parameters were assigned according to Bosio *et al.* [2022]. Beam-column frictional connections in the '70s building were modelled by means of the *Flat Slider bearing* element of OpenSees, which allows the translation in both the principal horizontal directions at the attainment of the friction force computed following the Coulomb model. The friction coefficient was evaluated according to the model proposed by Magliulo *et al.* [2011] for neoprene–concrete friction, as a function of the normal stress acting on the sliding surface. Similarly, beam-column dowel connections in the '90s building were modelled explicitly. Two elements were introduced (in parallel) between the two nodes (sharing the same position) representing the generic beam-column joint, namely a *Flat Slider bearing* element and a *zeroLength* element. The former simulates the shear friction resisting mechanism acting together with the dowel, whilst the second one represents the dowel and features a bilinear behaviour along the two principal horizontal directions: the latter behaviour, which includes post-yielding hardening and post-capping degradation, was modelled by means of the *ModIMKPeakOriented* material. A simulated design of the dowel was carried out in accordance with the 1980s code provisions, resulting in 1 ϕ24 mm steel bar for each joint. The parameters of the force-displacement relationship characterising the dowel, and assigned within the *ModIMKPeakOriented* material, were evaluated following Bressanelli *et al.* [2021], on the base of experimental results [Ferreira and El Debs, 2000]. The properties of the roof system of both buildings, as described in Section 2, justify the adopted assumption of rigid diaphragm for the roof in the models for both buildings, although with the adoption of two different modelling strategies. In particular, in the '70s building models, the roof elements were explicitly introduced as elastic (rigid) elements (see Figure 5a), rigidly connected to the beams; on the other hand, for the '90s building models, the roof elements were only considered as loads, a master node was introduced in the roof centroid and linked to the other nodes of the plane by a *RigidDiaphragm* constraint of OpenSees.

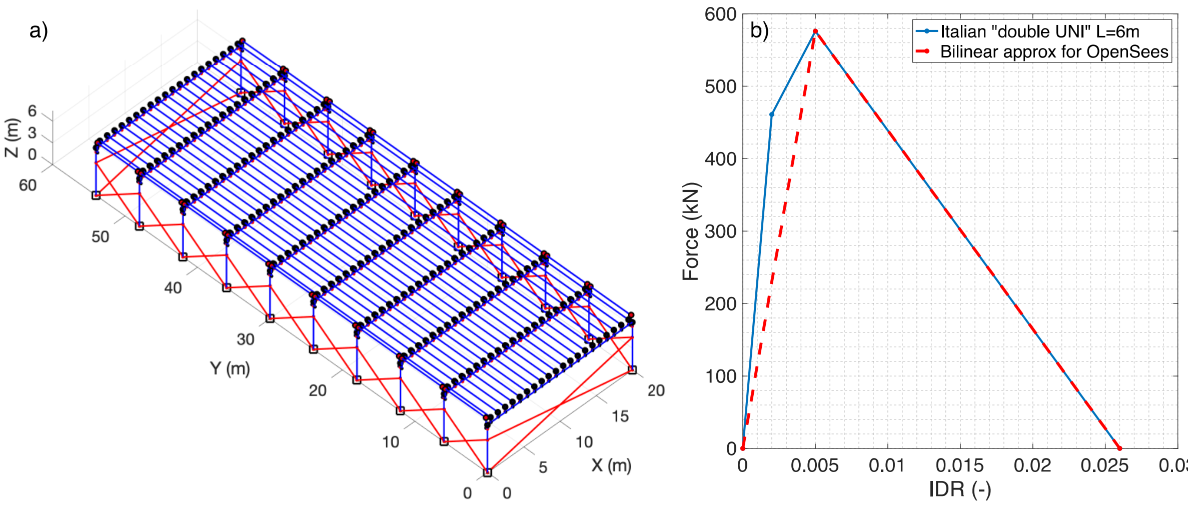

Figure 5. a) Three-dimensional drawing of the OpenSees model of the '70s case study building; b) Trilinear behaviour of masonry infills and implemented bilinearisation

The external cladding system was obviously introduced following different modelling strategies for the two case studies. Concerning the '70s building model, depicted in a 3D view in Figure 5a), the infills were modelled following the work by Liberatore *et al.* [2018], in which different sets of experimental tests available in the literature were used to evaluate the reliability of several models based on the equivalent strut approach. The nonlinear response follows the failure modes proposed by Decanini and Fantin [1986]: cracks are due to diagonal tension/compression, joint sliding and corner compression. The trilinear behaviour was bilinearised and calibrated according to the type of infill masonry of interest herein, namely Italian "double-UNI", with thickness 24 cm; Figure 5b) shows the behaviour for the infill panels having a width of 6 m and a height of 4.5 m.

Regarding the strength of the double-UNI masonry, the values are those adopted in the work of Bosio *et al.* [2022], where the possible reduction of stiffness and ultimate strength of the panel due to the presence of openings was neglected. The obtained stress and strain values were introduced in OpenSees using the *Concrete01* material. Two *twoNodeLink* elements with the latter material and embedding the infill's mass were employed to model two diagonal compression-only connecting struts, whose deformation as a function of the lateral drift was retrieved on the base of the expressions proposed by Hak *et al.* [2012, 2013]. Given the presence of a ribbon window on all sides of the case study building, an additional lumped plastic hinge was introduced, through a *zeroLength* element, at the intersection between the upper end of the equivalent strut and the column, so as to model the behaviour of the upper part of the column (i.e. the short column), failing in flexure.

As regards the '90s case study structure, whose OpenSees model is depicted in Figure 6, for the RC cladding panels a model similar to the one proposed by Magliulo *et al.* (2015) for vertical panels was implemented. Specifically, the generic vertical panel was explicitly modelled as two elastic elements with high stiffness, each embedding a half of the panel's mass, which is uniformly distributed along its height. The elements are restrained at the base through a fixed connection in the direction parallel to the plane of the panel and a pinned connection (i.e. a hinge) in the out-of-plane direction, whilst another hinge at the node of attachment to the beam ensures that the panel behaves as a pendulum in the out-of-plane direction. In this way, the influence of the vertical panels on the response of the precast structure only depends on the in-plane properties of the anchors of connection to the beam, in the upper part of the panels.

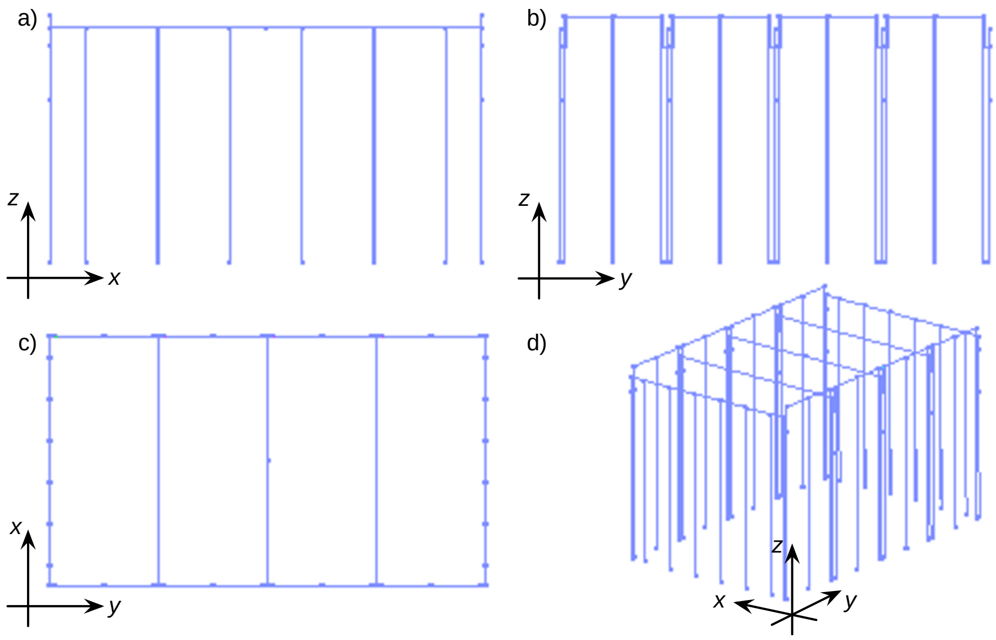

Figure 6. OpenSees model of the '90s case study building: different views

The anchors typically adopted to connect vertical panels to beams are hammer-head strap connections, which allow the presence of a gap, of size d_{gap}, between the panel and the beam. Such connections are characterised by a hysteretic response, for which the force-displacement relationship proposed in the study by Zoubek *et al.* [2016] was herein taken as reference. According to the latter, the complete cyclic response is simulated by combining in series/parallel three different hysteretic materials, already included in the software tool OpenSees, namely *ElasticPP*, *ElasticPPgap* and *Hysteretic*. The *ElasticPP* material simulates the friction between the hammer-head strap and the concrete beam, the *ElasticPPgap* material is used to increase the stiffness due to the head of the strap becoming stuck inside the panel's slot, and then the *Hysteretic* material is added to represent the nonlinear response of the head of the strap.

This OpenSees model was modified in the current endeavour to overcome numerical issues encountered in the *ElasticPP* and *ElasticPPgap* materials, while still reproducing accurately the experimental results reported by Zoubek *et al.* [2016]. In particular, in the first branch of the curve, up to d_{gap}, the *Multinear* material was adopted; on the other hand, for the second branch, from d_{gap} to the failure, the *Hysteretic* material was added (with the *Multinear* being still enforced), whose parameter *pinchX* was calibrated (and set to 0.65) so as to avoid a completely peak-oriented behaviour and thus closely reproduce the experimental results. These two materials, namely *Multinear* and *Hysteretic*, were then joined into a parallel material of OpenSees (equal strains, additive stresses and stiffnesses), the latter being assigned to a *zeroLength* element modelling the connection. The parameter values of the two adopted materials were assigned with a view to reproduce the backbone curve proposed by Babič and Dolšek [2016] for the type of anchor of interest herein (called "Fastening A" in that study). Such a backbone is characterised by four points, whose force-displacement values are considered either constant or uniformly distributed: in the latter case, the mean of the uniform distribution was adopted in this work. Figure 7 shows the obtained cyclic response, in terms of force-displacement relationship, of the implemented model, together with the four points of the backbone curve, characterised by the force-displacement values reported in Table 1. It has to be remarked that the first backbone point represents the attainment of the friction force in the connection, a condition causing the hammer-head strap to freely (i.e. with zero stiffness) slide in the panel's slot up to d_{gap} (i.e. to point #2): based on the experimentally observed large initial slope, the displacement of point #1 was assigned the very small conventional value of 1 mm.

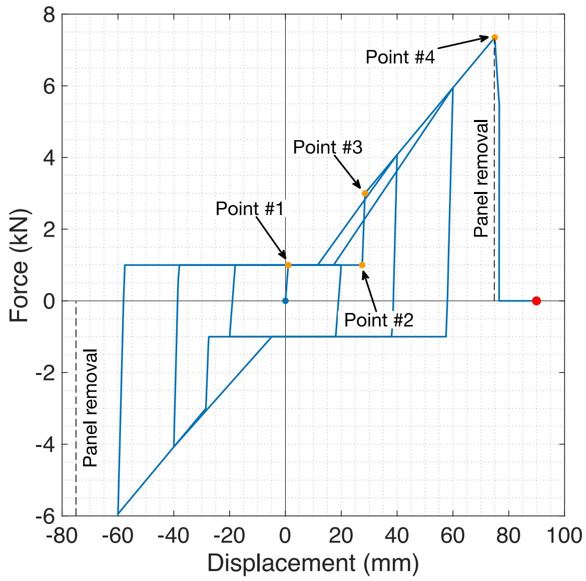

Figure 7. Force-displacement relationship of the *zeroLength* element employed to model the panel's connection

To model the in-plane failure of the panel-beam connection and the consequent removal of the generic vertical panel, the pushover analyses in OpenSees were carried out on a step-by-step basis (rather than calling the analyze command with the total number of steps), monitoring at each step the force that is transmitted by the connection. When the force demand equals (in absolute value) the capacity, corresponding to the force value (i.e. 7.35 kN) of point #4 in the backbone, the *zeroLength* element modelling the connection is deleted by invoking the *remove element* command, and a new *zeroLength* element characterised by an *Elastic* material with very small stiffness is created between the same two nodes. In this way, all panels remain connected to the beams, thus avoiding difficulties with the numerical stability of the analysis, but actually no longer influence the structural behaviour. Apart from the *zeroLength* replacement, the panel masses in the connection nodes, as well as the panel recorders, are also removed from the model, and the analysis is then resumed.

Table 1. Force-displacement values of the four points of the adopted backbone curve of the panel's connection

Point #	Force (kN)	Displacement (mm)
1	1.00	1.00
2	1.00	27.50
3	3.00	28.50
4	7.35	75.00

4. ANALYSES AND RESULTS

The OpenSees models of the considered case study buildings were subjected to nonlinear static (pushover) analyses in both principal directions. Only the longitudinal (y) direction is of interest herein, given the larger number of infills/panels involved and consequently the higher expected contribution of the cladding system to the global structural behaviour.

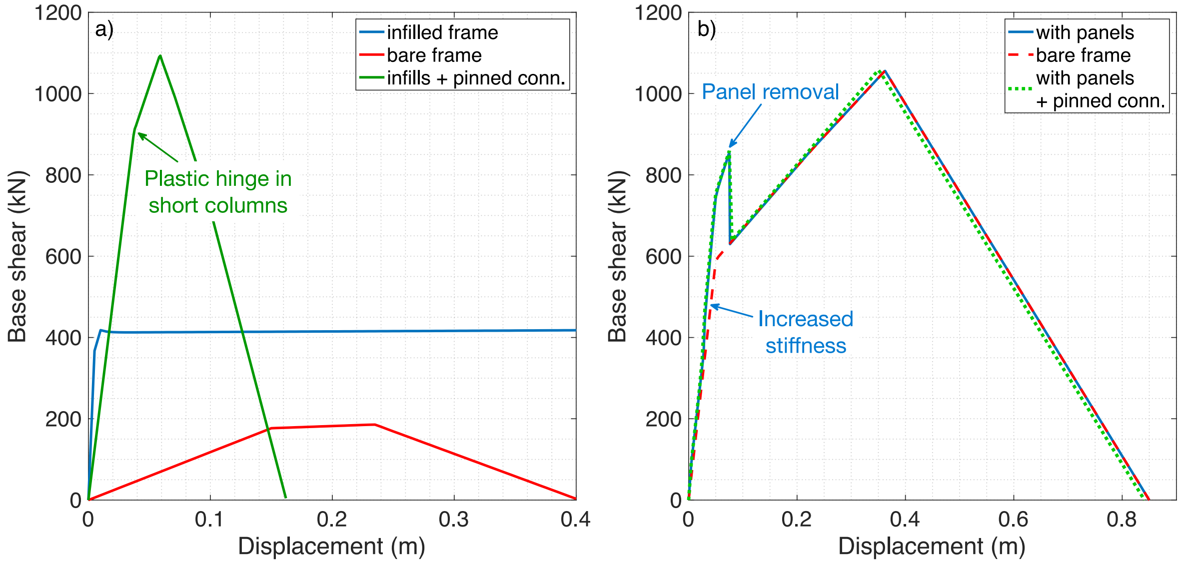

Figure 8. Results of the nonlinear static analyses: a) '70s building models; b) '90s building models

Concerning the '70s building (see Figure 8a), pushover analyses were undertaken on three models, namely i) the regular infilled model with beam-column frictional connections, ii) the bare frame model, and iii) an additional one with infills and pinned beam-column connections (simulating the implementation of a generic retrofit option), in place of frictional ones. From the pushover curves, it is first evident how the behaviour of the bare frame (curve displayed in red in Figure 8a) is governed by the plastic hinges at the base of the columns, with the base shear never reaching the friction force in beam-column connections. The infilled frame (curve in blue) has a much larger initial stiffness and resistance than the bare frame, but its base shear is then limited (to a value of around 400 kN) by the attainment of the friction force in beam-column connections: in the latter condition, the pushover curve becomes flat, indicating that the beam freely slides until loss of support. On the other hand, the green curve related to the model with infills and pinned beam-column connections shows a much larger resistance compared to the regular model, as expected, as well as a slightly different initial stiffness: the latter divergence is due to the different static scheme, as rotations around both the principal directions are allowed by pinned connections, but prevented by *Flat Slider bearing* elements (according to the implemented settings). It is interesting to note that in this third model (featuring pinned connections), given that the masonry infills do not collapse and the lower (main) parts of the columns do not yield, the "squat column" effect occurs, with the formation of a plastic hinge (indicated by a change of slope in Figure 8a) in the short columns adjacent to ribbon windows: such an effect has therefore an impact on the Global Collapse (GC) limit state, which is attained for a column displacement (or drift) causing a 50% drop of the peak base shear in the degrading branch of the pushover curve [RINTC, 2015-2021].

For the '90s building as well (see Figure 8b), pushover analyses were undertaken on three models, namely i) the regular model with cladding panels and explicitly modelled beam-column dowel connections, ii) the bare frame model, and iii) an additional one with panels and pinned beam-column connections (thus not capturing the possible dowel's yielding and collapse). As observed for the '70s models, the behaviour of the bare frame (curve displayed in dashed red in Figure 8b) is governed by the plastic hinges at the base of the columns, with the base shear never reaching the dowel's capacity. The pushover curve of the regular model (in blue) shows an increased initial stiffness with respect to the bare frame; it is noted that this increase is considerably lower than what expected if the panels were inserted within the structural frames, a behaviour also observed in the experimental tests carried out by Brunesi *et al.* [2015]. It is evident how the panel-beam connections along the y-direction collapse soon after the yield point of columns, for a displacement of 0.075 m, corresponding to a column drift of 1.25%: such a value is slightly larger than the threshold of the Usability Preventing Damage (UPD) limit state, assumed to be 1% [RINTC, 2015-2021], and quite similar to the value experimentally observed by Brunesi *et al.* [2015]. After the panel removal, the curve shows a sharp reduction of base shear, after which it then follows the curve of the bare frame, as expected. Since dowels do not collapse, the blue curve is practically superimposed to the dotted green one, related to the model featuring panels and pinned beam-column connections: the slight divergences are due to the different static scheme, as also highlighted for the '70s building case.

5. CONCLUSIONS

In the framework of the Italian RINTC project [2015-2021], aimed at evaluating the seismic risk of existing buildings with various structural typologies, this work investigated the seismic performance of existing single-storey precast industrial buildings, designed in accordance with past Italian code provisions, in the case of explicit modelling of closure external panels. Two precast buildings were considered as case studies, characterised by two different cladding systems, namely masonry infills (representative of the '70s) and RC precast panels (typically used in the '90s). The corresponding 3D numerical models created in OpenSees were subjected to pushover analyses. It was confirmed that masonry infills can increase the global structural stiffness, but their influence is also limited by the attainment of the friction force in beam-column connections. It was also shown that, in the presence of a retrofit option that prevents beam sliding, modelled by means of pinned joints, the "squat column" effect may take place, with the formation of a plastic hinge in the short columns adjacent to ribbon windows. On the other hand, the influence of RC panels on the global structural behaviour appeared to be not so relevant, given the very limited increase of initial stiffness and the fact that the collapse of the panel-beam connections occurs soon after attaining the UPD limit state and the yielding of columns. It is finally worth noting that the panel-beam connection collapse may occur for a drift even smaller than expected, given that, due to construction tolerances in real-world buildings, the connections may be not centred within the available stroke in the panel's slot, and may therefore fail prematurely in one of the two directions.

ACKNOWLEDGEMENTS

This research study was developed within the activities of the Italian national project DPC-ReLUIS-EUCENTRE RINTC 2015-2021, funded by the Italian Department of Civil Protection (DPC). Note that the opinions and conclusions presented by the authors do not necessarily reflect those of the funding entity.

REFERENCES

Babič, A., Dolšek, M. [2016] "Seismic fragility functions of industrial precast building classes," *Engineering Structures*, Vol. 118, pp. 357-370. DOI: https://doi.org/10.1016/j.engstruct.2016.03.069.

Belleri, A., Brunesi, E., Nascimbene, R., Pagani, M. [2015] "Seismic Performance of Precast Industrial Facilities Following Major Earthquakes in the Italian Territory," *Journal of Performance of Constructed Facilities*, Vol. 29, No. 5, 04014135. DOI: 10.1061/(ASCE)CF.1943-5509.0000617.

Bellotti, D., Casotto, C., Crowley, H., Deyanova, M.G., Germagnoli, F., Fianchisti, G., Lucarelli, E., Riva, S., Nascimbene, R. [2014] "Capannoni monopiano prefabbricati: distribuzione probabilistica dei sistemi e sottosistemi strutturali dagli anni sessanta ad oggi," *Progettazione sismica*, Vol. 5, No. 3, pp. 41-70. DOI: 10.7414/PS.5.3.41-70 (in Italian).

Bosio, M., Belleri, A., Riva, P., Marini, A. [2020] "Displacement-Based Simplified Seismic Loss Assessment of Italian Precast Buildings," *Journal of Earthquake Engineering*, Vol. 24(sup1), pp. 60-81. DOI: 10.1080/13632469.2020.1724215.

Bosio, M., Di Salvatore, C., Bellotti, D., Capacci, L., Belleri, A., Piccolo, V., Cavalieri, F., Dal Lago, B., Riva, P., Magliulo, G., Nascimbene, R., Biondini, F. [2022] "Modelling and Seismic Response Analysis of Non-residential Single-storey Existing Precast Buildings in Italy," *Journal of Earthquake Engineering*. DOI: 10.1080/13632469.2022.2033364.

Bournas, D.A., Negro, P., Taucer, F.F. [2014] "Performance of industrial buildings during the Emilia earthquakes in Northern Italy and recommendations for their strengthening," *Bulletin of Earthquake Engineering*, Vol. 12, No. 5, pp. 2383-2404. DOI: https://doi.org/10.1007/s10518-013-9466-z.

Bressanelli, M.E., Bellotti, D., Belleri, A., Cavalieri, F., Riva, P., Nascimbene, R. [2021] "Influence of modelling assumptions on the seismic risk of industrial precast concrete structures," *Frontiers in Built Environment*, Vol. 7, 629956. DOI: https://doi.org/10.3389/fbuil.2021.629956.

Brunesi, E., Nascimbene, R., Bolognini, D., Bellotti, D. [2015] "Experimental investigation of the cyclic response of reinforced precast concrete framed structures," *PCI Journal*, Vol. 60, No. 2, pp. 57-79. DOI: https://doi.org/10.15554/pcij.03012015.57.79.

CEN [2004] "EN 1998-1:2004. Eurocode 8: Design of structures for earthquake resistance - Part 1: General rules, seismic actions and rules for buildings," European Committee for Standardization.

Decanini, L.D., Fantin, G.E. [1986] "Modelos simplificados de la mampostería incluida en pórticos. Características de rigidez y resistencia lateral en estado límite," *Proceedings of 6th Jornadas Argentinas de Ingeniería Estructural*, Buenos Aires, Argentina, Vol. 2, pp. 817-836 (in Spanish).

Ferreira, A., El Debs, M.K. [2000] "Deformability of beam-column connection with elastomeric cushion and dowel bar to beam axial force," *Proceedings of 2nd International Symposium on Prefabrication*, Helsinki, Finland.

Fischinger, M., Zoubek, B., Isakovic, T. [2014] "Seismic Response of Precast Industrial Buildings," in: Ansal, A. (eds) Perspectives on European Earthquake Engineering and Seismology. Geotechnical, Geological and Earthquake Engineering, Vol. 34. Springer, Cham. DOI: https://doi.org/10.1007/978-3-319-07118-3_4.

Hak, S., Morandi, P., Magenes, G. [2013] "Damage Control of Masonry Infills in Seismic Design," *Research Report EUCENTRE No. 01.2013*, IUSS Press, Pavia, Italy.

Hak, S., Morandi, P., Magenes, G., Sullivan, T.J. [2012] "Damage control for clay masonry infills in the design of RC frame structures," *Journal of Earthquake Engineering*, Vol. 16(sup1), pp. 1-35.

Iervolino, I., Spillatura, A., Bazzurro, P. [2018] "Seismic reliability of code-conforming Italian buildings," *Journal of Earthquake Engineering*, Vol. 22(sup2), pp. 5-27. DOI: https://doi.org/10.1080/13632469.2018.1540372.

Iervolino, I., Spillatura, A., Bazzurro, P. [2019] "RINTC-E project: towards the assessment of the seismic risk of existing buildings in Italy," *Proceedings of COMPDYN 2019 - 7th International Conference on Computational Methods in Structural Dynamics and Earthquake Engineering*, 24-26 June 2019, Crete, Greece.

Liberatore, L., Noto, F., Mollaioli, F., Franchin, P. [2018] "In-plane response of masonry infill walls: Comprehensive experimentally-based equivalent strut model for deterministic and probabilistic analysis," *Engineering Structures*, Vol. 167, pp. 533-548. DOI: 10.1016/j.engstruct.2018.04.057.

Magliulo, G., Capozzi, V., Fabbrocino, G., Manfredi, G. [2011] "Neoprene–concrete friction relationships for seismic assessment of existing precast buildings," *Engineering Structures*, Vol. 33, No. 2, pp. 532-538. DOI: 10.1016/j.engstruct.2010.11.011.

Magliulo, G., Ercolino, M., Manfredi, G. [2015] "Influence of cladding panels on the first period of one-story precast buildings," *Bulletin of Earthquake Engineering*, Vol. 13, No. 5, pp. 1531-1555.

Magliulo, G., Ercolino, M., Petrone, C., Coppola, O., Manfredi, G. [2014] "The Emilia Earthquake: Seismic Performance of Precast Reinforced Concrete Buildings," *Earthquake Spectra*, Vol. 30, No. 2, pp. 891-912. DOI: https://doi.org/10.1193/091012EQS285M.

McKenna, F., Fenves, G.L., Scott, M.H. [2000] "OpenSees: Open System for Earthquake Engineering Simulation," *Software*, University of California, Berkeley, USA. Available at: http://opensees.berkeley.edu (last accessed 30 July 2022).

RINTC [2015-2021] "Implicit seismic risk of code-conforming structures in Italy," *Joint project*, ReLUIS and EUCENTRE, funded by the Italian Department of Civil Protection (DPC).

Savoia, M., Buratti, N., Vincenzi, L. [2017] "Damage and collapses in industrial precast buildings after the 2012 Emilia earthquake," *Engineering Structures*, Vol. 137, pp. 162-180. DOI: https://doi.org/10.1016/j.engstruct.2017.01.059.

Toniolo, G., Colombo, A. [2012] "Precast concrete structures: the lessons learned from the L'Aquila earthquake," *Structural Concrete*, Vol. 13, No. 2, pp. 73-83. DOI: https://doi.org/10.1002/suco.201100052.

Zoubek, B., Fischinger, M., Isaković, T. [2016] "Cyclic response of hammer-head strap cladding-to-structure connections used in RC precast building," *Engineering Structures*, Vol. 119, pp. 135-148. DOI: https://doi.org/10.1016/j.engstruct.2016.04.002.

Assessment of the Effects of Non-Structural Walls (NSWs) on the Dynamic Properties and Interstory Drifts of a Case Study Building

Rola Assi[1], Ayman Ramadan[1]

[1] Department of construction engineering, École de technologie supérieure (ÉTS)
1100 Notre-Dame St. W, Montreal, Quebec H3C 1K3
rola.assi@etsmtl.ca , ayman.ramadan.1@ens.etsmtl.ca

Abstract. This article evaluates the effects of non-structural walls (NSWs), consisting of masonry and curtain walls, on the mode shapes, fundamental periods, damping ratios, and lateral stiffness of a case study building located in Montreal. As well, interstory drifts are computed under the effect of synthetic earthquake time histories compatible with Montreal's uniform hazard spectrum (UHS) and having a 10% chance of being exceeded in 50 years.

Ambient vibration measurements (AVMs) were conducted at the bare frame (BF) and full frame (FF) stages of the building's construction. Then, two linear-finite element models of the building representing both construction stages were developed in the ETABS 2017® software [CSI, 2017] and calibrated using the in-situ dynamic characteristics extracted from the AVMs.

It was found that the building's fundamental period decreased by -12.4% when the NSWs were added to it. The mode shapes remained the same at both construction stages and were not affected by the presence of masonry walls only on the ground floor. In addition, the damping ratio increased by +53%, from +1.98% (bare frame) to +3.03% (full frame).

It was ascertained that masonry walls contribute more to the stiffness and damping ratio than do curtain walls. Moreover, a parametric study showed that the effect of masonry walls on fundamental periods and damping ratios is directly proportional to their quantity in the building.

As well, it was observed that adding masonry walls to the first three floors leads to a -64.7% to -77.6% reduction of interstory drifts at all floors in the longitudinal direction, and to a -40.7% and -79.1% reduction in the transversal direction.

Keywords: Non-structural walls, Ambient vibration measurements, Finite element models, Interstory drifts.

1. INTRODUCTION

When an earthquake occurs, the components of a building are subjected to significant forces and displacements propagating in all directions. These include both structural components (SCs) and non-structural components (NSCs). According to the national building code of Canada (NBC) NRC [2015], NSCs must be considered in calculating the fundamental period of a building if they decrease its value by more than 15%. Nevertheless, structural engineers tend to model only the load bearing components of a structure (columns, beams, slabs, and concrete cores, etc.) while neglecting the NSCs (masonry walls, prefabricated panels, facades, windows, equipment, and furniture, etc.), and choose to account for NSCs by adding their mass at floor levels in the analysis model. NSCs thus only participate in increasing the mass of the building, and their contribution to lateral stiffness is mostly ignored in practice.

Masonry walls are considered to be non-structural walls (NSWs) which are frequently used as interior and exterior walls in both reinforced concrete and steel structures. Their ubiquity is attributable to the many advantages they provide, such as ease of construction, high versatility, and excellent durability. The presence of masonry walls has an appreciable effect on the dynamic behaviour of structures since it increases a building's mass and stiffness. Recent studies have demonstrated that this presence modifies the dynamic properties and interstory drifts of a building. Asgarian [2012] studied the effect of masonry walls on the seismic response of an eleven-storey reinforced concrete frame building. He found that the presence of masonry walls reduces the building period by -40% and decreases the drift demand by -77% in the longitudinal direction, and by -80% in the transversal direction. Pokhrel et al. [2019] investigated the effect of masonry walls on the interstory drift of a symmetrical four-storey frame reinforced concrete building, and found that adding masonry walls to the first three floors leads to a -42.5% to -97% decrease of the interstory drift. For their part, Amanat et Hoque [2006] investigated the fundamental periods of a regular 35 m RC frame building having infills through finite element modeling and modal analysis. They found that varying the amount of masonry walls in the building has a significant effect on the period.

Curtain walls are the outer coverings of a building used to keep the weather out and the occupants in. They are mostly used in building envelopes systems in contemporary architecture owing to factors such as their aesthetic quality, transparency and natural illumination. Typically, they are NSWs since they carry only their own dead load. Nonetheless, these walls can influence the dynamic properties of a building. Li et al. [2011] studied the effect of curtain walls on 30-storeys high-rise reinforced concrete shear wall building and found that curtain walls increase the lateral stiffness of the building by +1.2%. Moreover, Bonne [2018] studied a 4-storey building with concrete cores, and found that curtain walls decrease the fundamental period of the building by -6%, and increase the stiffness by +11%.

Hence, the behavior of these NSWs under dynamic loads must be considered to assess their effect on the dynamic response of the supporting structure as well as the engineering demand parameters by developing full 3-D finite element models of the structure with and without NSWs. This paper aims to gain a better understanding of the effect of curtain walls, and masonry walls on the elastic response of buildings during earthquakes. More precisely, investigate the effect of masonry walls and curtain walls on the mode shapes, fundamental periods, damping ratios, and lateral stiffness of a supporting structure as well as on the interstory drifts used for the design of deformation-sensitive NSCs.

The paper presents a description of the studied building, the modelling assumptions of the building at two construction stages (bare frame stage and full frame), the calibration of numerical models using AVMs, the evaluation of relative mass and stiffness contribution of NSWs, as well as their effect on the dynamic properties (fundamental period and damping ratios). In addition, a parametric study consisting in varying the quantity of masonry walls was conducted to assess the effect of their amount on the dynamic properties and interstory drifts of the building.

2. DESCRIPTION OF THE BUILDING

The building selected in this study, *La maison des étudiants* (MDE), is part of the campus of École de technologie supérieure in Montreal and it is composed mainly of offices, classrooms, and workspaces. The MDE is 23.2 m in height with an almost rectangular trapezoidal shape at the base. It has one level in the basement, five floors above ground in addition to a mezzanine between the ground and second floors; it also has a steel structure consisting of a mechanical room on the roof used for its water treatment, electricity, and mechanical ventilation. The MDE was designed according to the 2010 edition of the National Building Code of Canada [NRC, 2010]. It is an irregular reinforced concrete structure with SCs consisting of reinforced concrete slabs, beams, columns and concrete cores. The lateral load resisting system (LLRS) is a conventional construction of reinforced concrete cores with limited ductility (R_d = 1.5, R_o = 1.3). The building is located on a very dense soil known as Site Class C according to NBC 2015 [NRC, 2015]. Figure 1 shows the 3-D views of the MDE at the bare frame and full frame stages.

Figure 1 3-D views of the MDE at the bare frame and full frame stages

3. MODELLING OF THE MDE AND NSWs, AVMs, AND CALIBRATION OF THE FEM

In this section, the modelling assumptions of the selected building and its NSWs are described. In addition, the ambient vibration measurements, as well as the calibration of the building's finite element models (FEM) are presented.

3.1 Finite element modelling (FEM) of the MDE building and its NSWs

The bare frame SCs (concrete cores, columns, beams, and slabs) and full frame consisting of the bare frame plus the NSWs were modelled in ETABS 2017® [CSI, 2017] software . The concrete precast floor slabs of thickness 275 mm were modelled as rigid diaphragms with compressive strength of 30 MPa and unit mass of 2400 kg/m^3. The concrete cores were modelled using 4-node wall elements (mesh size 500*500 mm) with compressive strength of 30 MPa and unit mass of 2400 kg/m^3. Masonry walls and curtain walls were modelled according to the architectural plans and using 4-node wall elements (500*500 mm). The masonry walls (compressive strength of 15 MPa and unit mass of 1600 kg/m^3) were separated from the surrounding structure by a *gap element* (10 mm) to avoid a direct connection with the structure. The stiffness of this element was calculated using Equation 1 proposed by Dorji et Thambiratnam [2009].

$$\mathrm{K_g} = 0.0378 * \mathrm{K_i} + 347 \tag{1}$$

$$\mathrm{K_i} = \mathrm{E_i} * \mathrm{t_i} \tag{2}$$

where K_g is the axial stiffness of the contact element (110232 and 191200 N/mm); K_i (Equation 2) is the stiffness of the infill wall in (N/mm); E_i is the young elastic modulus of the infill wall (15300 MPa), and t_i is the thickness of the infill wall (190 or 330 mm). The out-of-plane behaviour of the masonry walls was neglected since the risk of wall buckling under service conditions was low. As for curtain walls, the interface between the structure and the aluminum frame was modelled using gap elements (5mm). The aluminum frame is composed of mullions and transoms which are rigidly connected. The space between the glass panels and the aluminum frame was simulated by an elastoplastic Wen link [Caterino et al., 2017] and the buckling of the glass panels was ignored. All the SC and NSW sections were considered as uncracked sections for the calibration of the building's finite element model because it is a relatively new construction and ambient loading (wind in this case) is considered as a service load. On the other hand, the seismic response was calculated based on cracked section properties, with the effective stiffness I_e assumed equal to 0.75 I_g for shear walls, 0.4 I_g for beams, and 0.7 I_g for columns [CSA-A23, 2014], where I_g denotes the gross stiffness.

Only the mass of the other NSCs, consisting of mechanical and electrical systems, ceilings and partition walls, were considered in the numerical models. Figure 2 shows the numerical models of the bare and full frames, with the blue shells representing curtain walls and the green ones representing masonry walls.

a) b)

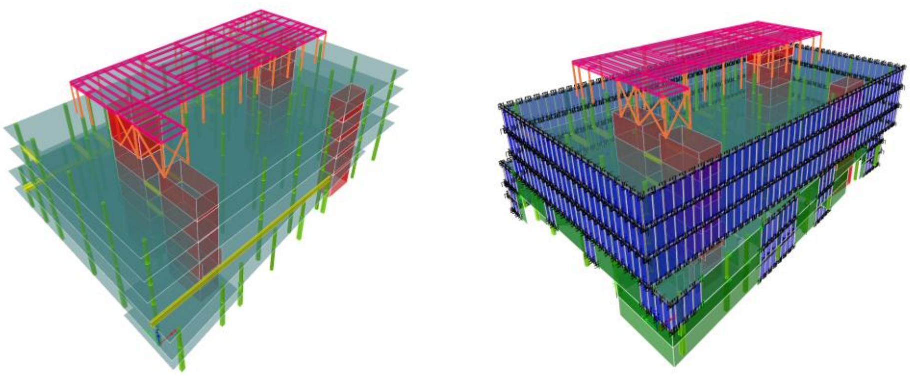

Figure 2 3-D Isometric views of the building's numerical models: a) bare frame; b) full frame

3.2 Calibration of the finite element models (FEM) using ambient vibration measurements (AVMs)

FEM must be calibrated with experimental test data such as AVMs [Brincker et Ventura, 2015] to minimize deviations from the ground truth. Therefore, AVMs were conducted at multi-floor levels to obtain the modal properties of the MDE and calibrate its finite element models at the bare and full frame stages. The modal parameters were determined using the stochastic subspace identification (SSI) method due to its user-friendly implementation in the ARTeMIS Extractor software [ARTeMIS Modal, 2018], and the engineering tool called "stabilization diagram" implemented in ARTeMIS [ARTeMIS Modal, 2018] was used to handle bias errors in the estimates of modal parameters including natural frequencies and damping ratios.

Before starting the recording of AVMs, it is imperative to define a north reference to be respected throughout the acquisitions and to check that each sensor is levelled before each setup [Brincker et Ventura, 2015]. A setup corresponds to the recording of the signals by all the sensors when the latter are positioned together in the building. A configuration corresponds to how the sensors are positioned in the building to capture its modes of deformation. In this research, one setup was conducted for the bare frame due to synchronization issues between the sensors, and 24 setups were conducted for the full frame at different positions on the floors over the entire building in order to capture its lowest natural frequencies. Figure 3a shows a configuration of the sensors on the 5th floor of the building at the full frame stage while Figure 3b shows the distribution of sensors (triangles) over all floors, as well as the presence of a reference sensor on the 5th floor.

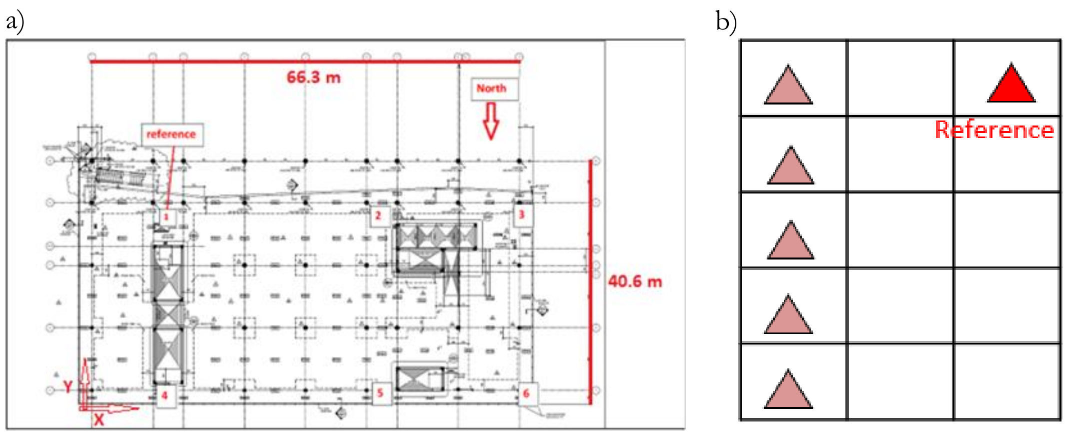

Figure 3 a) Configuration of the 6 sensors on the 5th floor; b) elevation view showing the distribution of the sensors over all floors

The manual calibration technique was used to update the FE models. For the bare frame, the self-weights of concrete members and the additional loads (paving and slope concrete) were increased by +4% and +3%, respectively. For the full frame, the weight of glass and masonry was decreased by -20%, the weight of aluminum and of additional applied loads (mechanical equipment, ceilings, and partitions) was decreased by -5%, the modulus of elasticity of glass and masonry was increased by +20%, and the modulus of elasticity of aluminum was increased by +5%. Table 1 shows that the calibrated models reflect the behaviour of the MDE at both stages of construction since the natural periods of the models coincide with those of the AVMs, within an acceptable margin of ±10%.

Table 1 Comparison of the periods obtained by AVMs and calibrated FE models at bare and full frame stages

	Mode	Shape	AVMs	Calibrated model	
			T (s)	**T (s)**	**Diff (%)**
Bare frame	1	Transversal translation + torsion	0.53	0.48	-8%
Full frame	1	Transversal translation + torsion	0.46	0.47	+2.61%
	2	Longitudinal translation	0.40	0.40	0%

3.3 Effect of NSWs on fundamental periods, damping ratios, and mode shapes

The fundamental periods and damping ratios obtained from AVMs at both stages of construction were compared to assess the effect of NSWs on the building, as shown in Table 2, where the bare frame properties are considered as the reference.

Table 2 Comparison of the periods and damping ratios obtained by AVMs at different stages of construction

		Bare frame		Full frame		Difference	
Mode	**Shape**	**T (s)**	**ζ (%)**	**T (s)**	**ζ (%)**	**ΔT (%)**	**Δζ (%)**
1	Transversal Translation+torsion	0.53	1.98	0.46	3.03	-12.4	+53.3

A comparison of the bare and full frames showed a -12.4% reduction in the building's fundamental period. Similar observations were found by Devin et al. [2015], who studied a four-storey reinforced concrete frame office building, by comparing the building's periods consisting only of its structural components (bare frame) and once it was in service (full frame). They observed that adding NSCs decreased the fundamental period by -31.8%.

The damping ratio increased by +53%. The results obtained in this research for the full frame stage (first mode) are very close to the damping ratio used in common practice for the elastic analysis of new buildings (ζ=3%). In fact, the values of damping ratio can change depending on the damping model that is adopted. Devin et Fanning [2012] carried out full-scale forced vibration testing on a 4-storey reinforced concrete shear-core office building, they found that the equivalent viscous damping ratio varied from 2.3% at bare frame stage to 3.5% after adding cladding elements and building completion (ready for occupation).

The displacement normalized mode shapes obtained from the numerical models at the centre of mass for each floor remained unchanged at both stages of construction. This can be explained by the presence of masonry walls only on the ground floor and to a negligible contribution of curtain walls.

3.4 Relative contribution of NSWs to stiffness

The stiffness and mass of the calibrated numerical model at the bare frame stage were used as a reference to estimate the relative contribution of the masonry and curtain walls to the stiffness (K_1/K_2, Equation 3) and mass (m_1/m_2), as shown in Table 3, where K_1, f_1, and m_1 are respectively the stiffness, frequency, and mass of the bare frame + masonry walls or bare frame + curtain walls model, and K_2, f_2, and m_2 are the characteristics of the bare frame model.

$$\frac{k_1}{k_2} = \left(\frac{f_1}{f_2}\right)^2 \frac{m_1}{m_2} \tag{3}$$

Table 3 Stiffness and mass contribution of masonry walls and curtain walls in both building directions

	Masonry walls		Curtain walls	
	Transversal direction (Y)	**Longitudinal direction (X)**	**Transversal direction (Y)**	**Longitudinal direction (X)**
m_1 (tonne)	15 104	15 104	14 276	14 276
f_1 (Hz)	2.08	2.56	2	2.38
T_1 (s)	0.481	0.39	0.5	0.42
m_2 (tonne)	12 827	12 827	12 827	12 827
f_2 (Hz)	2.07	2.63	2.07	2.63
T_2 (s)	0.483	0.38	0.483	0.38
m_1/m_2	1.18	1.18	1.11	1.11
T_1/T_2	0.996	1.03	1.04	1.1
k_1/k_2	1.19	1.12	1.04	0.91

Table 3 shows that masonry walls increase the building's stiffness by +19% and +12% in the transversal and longitudinal directions, respectively. This minor contribution is explained by the presence of masonry walls on the ground floor only, in both directions. Zhou et al. [2020] studied the effect of masonry walls on the lateral stiffness of 3 high-rise reinforced concrete shear wall buildings, and found that the presence of masonry walls increases the lateral stiffness of the building by a range of +30% to +50 %. Their mass contribution is +18% over the entire building.

On the other hand, the curtain walls increase the building's stiffness by +4% in the transversal direction. Their mass contribution is +11% over the entire building.

Therefore, it can be concluded that masonry walls contribute more to the building's stiffness than do curtain walls. Since masonry walls were only present at the ground floor level in the present case study, a parametric study was therefore conducted to assess how the dynamic properties of the building are affected when the masonry walls are present on multiple floors. Moreover, since these components are deformation-sensitive, their effect on the interstory drift is discussed as well.

4. PARAMETRIC STUDY OF THE EFFECT OF MASONRY WALLS ON DYNAMIC PROPERTIES

A parametric study was conducted to assess the effect of masonry walls on the fundamental period, damping ratio, mass and stiffness of the bare frame. The study consisted of four cases: the masonry walls present on the ground floor only (20% infill); on the ground and 2nd floors (40% infill); on the ground, 2nd and 3rd floors (60% infill); and on all floors (100% infill). Figures 4a, 4b and 4c illustrate a 3-D isometric view, a plan view of masonry walls in the ground floor, and a plan view of masonry walls in the 3rd, 4th and 5nd floors.

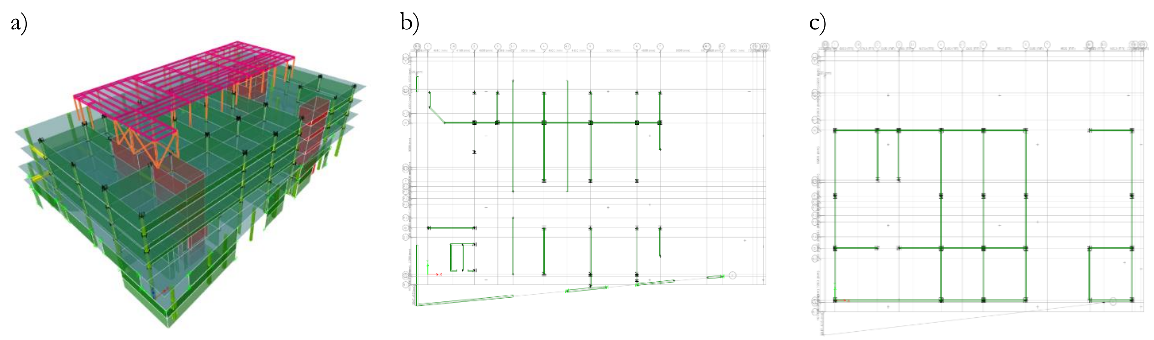

Figure 4 Masonry walls on all floors: a) 3-D isometric view; b) Plan elevation view in the ground floor c) Plan view in 3rd, 4th, and 5th floors

The calibrated model of the bare frame model was taken as a reference for comparison. The parameters and results obtained in the transversal direction are presented in Table 4 and Figure 5.

Table 4 Results of the parametric study

	20% infill	40% infill	60% infill	100% infill
m_1 (tonne)	15 104	15 308	15 648	16 636
f_1 (Hz)	2.08	2.23	2.38	2.46
T_1 (s)	0.481	0.45	0.42	0.41
m_2 (tonne)	12 827	12 827	12 827	12 827
f_2 (Hz)	2.07	2.07	2.07	2.07
T_2 (s)	0.483	0.483	0.483	0.483
m_1/m_2	1.18	1.19	1.22	1.3
T_1/T_2	0.996	0.93	0.87	0.84
k_1/k_2	1.19	1.38	1.61	1.84

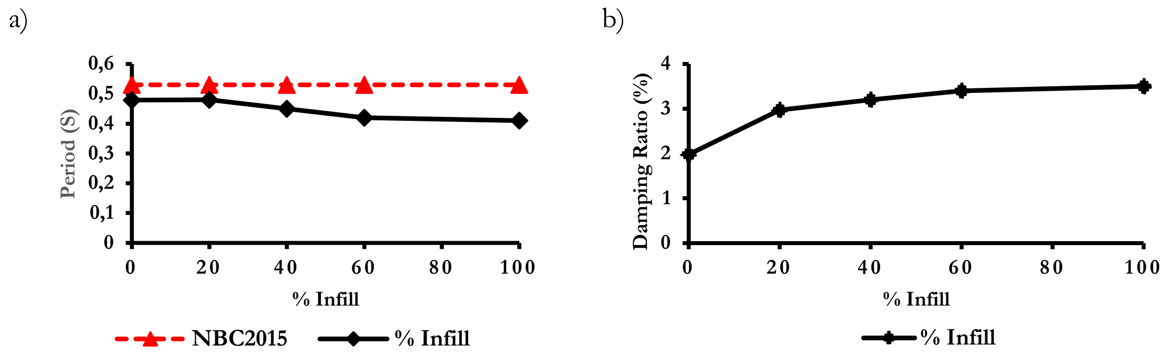

Figure 5 Relation between the density of masonry walls and their contribution to: a) the building's fundamental period b) the damping ratio

Table 4 shows that by adding masonry walls to the building, the stiffness increased by +19% to +84%, and the mass increased by +18% to +30%. Su et al. [2005] studied the effect of masonry walls on the dynamic properties of a 41-storey reinforced concrete shear wall building, and found that adding masonry walls to all floors rigidify the building by +61% in the longitudinal direction and by +82% in the transversal direction. Moreover, Li et al. [2011] noticed that adding masonry walls to all stories increased the stiffness of a 30-storey building with reinforced concrete shear walls by +60%. Figure 5a shows the change in building fundamental period with the increase of percentage of infill masonry walls compared to NBC2015 [NRC, 2015] equation [$(T(s)= 0.05*h^{0.75})$ where h is the height of the building (23.2m)] directed. In addition, adding masonry walls decreased the fundamental period by -0.4% to -16% and increased the damping ratio of the building by 50% to +76% (Figure 5b). Therefore, we can conclude that masonry walls should be considered in the seismic analysis of a medium-rise building when they are present on all its floors.

5. EFFECT OF MASONRY WALLS ON INTERSTORY DRIFT

5.1 Numerical models and ground motions

Elastic time history analysis was conducted on 4 building cases: bare frame (BF) only; BF with 20% masonry infill; BF with 40% masonry infill, and BF with 60% masonry infill. The building cases were subjected to 12 synthetic earthquake records selected and scaled to match 5% damped Montreal target spectrum having a 10% chance of being exceeded in 50 years [Atkinson, 2009]. Four Magnitude-distance (M-R) scenarios were defined with a suite of 3 ground motions considered for each scenario. The first scenario included records with a moment magnitude M_w = 6.0 at a fault distance R ranging between 10 and 30 km (Figure 6). The second scenario included records with M_w = 7.0 at distances ranging 20 and 70 km (Figure 6).

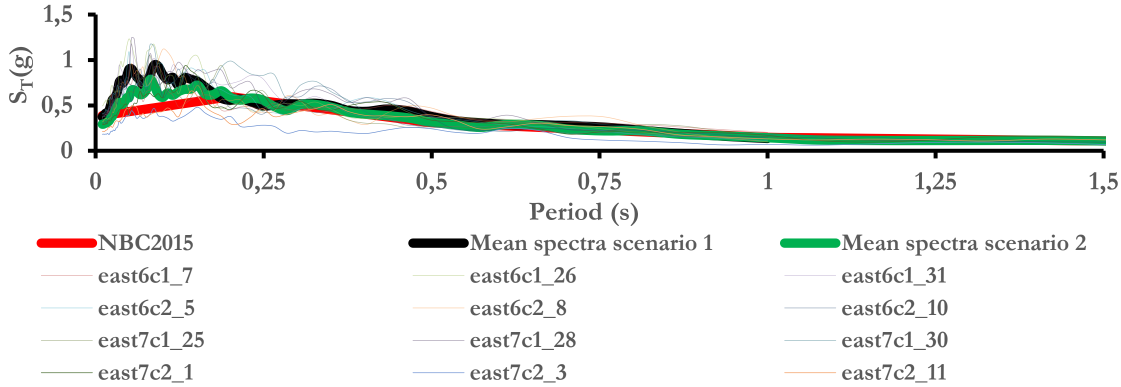

Figure 6 Acceleration response spectra of the selected and scaled individual ground motion time histories

The nomenclature of the record (east6c1_7) indicates that it pertains to eastern Canada, with a magnitude of 6, soil type C, and 1 refers to the proximity to the source of the earthquake (1 refers to near-field and 2 refers to far-field). The last number (7) is the number of the record.

5.2 Computed interstory drifts

In this subsection, the effect of adding masonry infill walls on the interstory drift will be investigated. The interstory drift results are shown in Figure 7 by calculating the 84th percentile (median+σ) values.

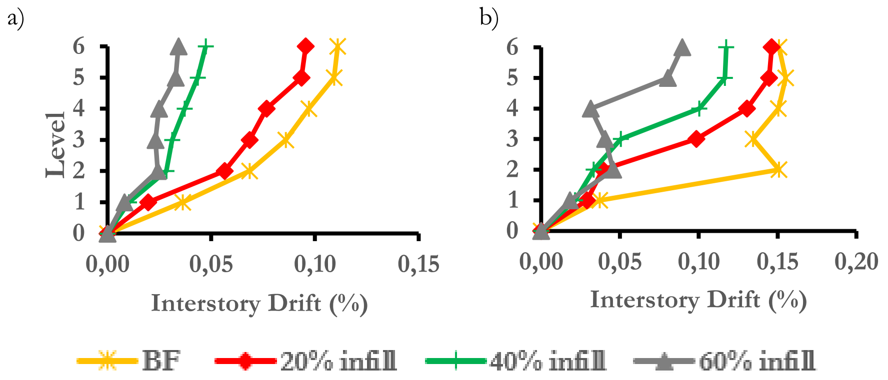

Figure 7 Interstory drifts: a) longitudinal direction; b) transversal direction

Figure 7 highlights that adding masonry walls reduces the interstory drift of the building on all floors, but the rate of decrease is much lower in greater infill coverage (Figure 7a). Also, the effect of infills is more noticeable in the upper floors as the interstory drift trends in the lower two stories are rather close for all cases. It can also be noticed that for the 40% and 60% infills, values of interstoy drift are almost uniform along the building height. For the 60% infill case, the interstory drift was reduced by -64.7% to -77.6% in the longitudinal direction, and by -40.7% to -79.1% in the transversal direction. Similar observations were found by Pokhrel et al. [2019], who studied the effect of variation of infill wall amount on the interstory drifts of a four-story prototype RC frame building. Moreover, it can be noted that the interstory drifts obtained are less than the FEMA356 [2000] immediate occupancy (IO) limit of 1%, which can be explained by the fact that the building is rigid (T < 0.5s).

CONCLUSION

Two 3-D finite element models of a medium-rise shear wall building were developed at the bare frame and full frame stages of construction and calibrated with AVMs to minimize the differences between the FE models and the ground truth. An analysis of the AVMs data showed that adding NSWs reduces the building's fundamental period by -12.4% and increases the damping ratio by +53%. Results from finite element models showed that masonry walls contributed to the building's stiffness in both directions (+19% and +12% in the transversal and longitudinal directions, respectively). However, the curtain walls contributed to the building's stiffness in the transversal direction to a much less extent (+4%). Therefore, this study shows that masonry walls contribute more to the stiffness of buildings than do curtain walls. Moreover, the parametric study consisting of analyzing the bare frame with various % of masonry infill walls shows that adding masonry walls to the building increases its stiffness (by +19% to +84%) according to their amount in the building and decreases the fundamental period (by -0.4% to -16%) with an almost constant rate as the percentage of infill increases. On the other hand, this increase in stiffness leads to higher peak floor acceleration which will affect the acceleration sensitive components such as ceilings, mechanical pipes and machinery, and might disclose unconservative estimates of economic losses. Moreover, it is widely recognized that damaged NSCs may not only result in major economic loss and the potential loss of functionality of buildings due to damage of critical NSCs, but may also increase the occupants' risk of life safety [Ray-Chaudhuri et Hutchinson, 2011]. Therefore, a better prediction of the peak floor acceleration leads to a better design or retrofitting strategy for anchoring, supporting, or bracing the NSCs.

In addition, it was shown that adding masonry walls to all floors (100% infill) decreases the fundamental period by -16%, which implies that in such a case, masonry walls should be considered in calculating the fundamental period of the building to comply with NBC provisions in case of 100% infill.

Finally, the effects of different amounts of masonry walls on interstory drifts of the MDE building were assessed under the effect of selected and scaled synthetic earthquake records matching Montreal's uniform hazard spectrum (5% damping) with a return period of 475 years. It was concluded that adding masonry walls reduced the interstory drift at all floors of the building and in both directions (by -64.7% to -77.6% in the longitudinal direction, and by -40.7% to -79.1% in the transversal direction). In addition, it was observed that the interstory drifts obtained were less than the FEMA356 [2000] immediate occupancy (IO) limit of 1% for both horizontal directions.

REFERENCES

Amanat, K. M., Hoque, E. [2006] "A rationale for determining the natural period of RC building frames having infill", *Engineering Structures,* Vol. 28, No. 4, pp. 495-502.

ARTeMIS Modal, S. [2018], *Structural Vibration Solutions*, Aalborg, Denmark.

Asgarian. [2012] "Impact of seismic retrofit and presence of terra cotta masonry walls on the dynamic properties of a hospital building in Montreal"*, Individual Study,* McGill University, Canada.

Atkinson, G. M. [2009] "Earthquake time histories compatible with the 2005 National building code of Canada uniform hazard spectrum", *Canadian Journal of Civil Engineering,* Vol. 36, No. 6, pp. 991-1000.

Bonne, A. [2018]. "Caractérisation de l'effet des composants non structuraux sur les propriétés dynamiques des bâtiments", *Individual Study*, École de technologie supérieure, Canada.

Brincker, R., Ventura, C. [2015]. *Introduction to operational modal analysis*. John Wiley & Sons.

Butterworth, J., Lee, J. H., Davidson, B. [2004]. "Experimental determination of modal damping from full scale testing", *13th World Conference on Earthquake Engineering, Vancouver, Canada*.

Caterino, N., Del Zoppo, M., Maddaloni, G., Bonati, A., Cavanna, G., Occhiuzzi, A. [2017] "Seismic assessment and finite element modelling of glazed curtain walls", *Structural Engineering and Mechanics,* Vol. 61, No. 1, pp. 77-90.

CSA-A23. [2014], *CSA Standard,* CAN/CSA-A23. 3-14, Design of concrete structures, Canada

CSI. [2017], 17.0. 1: ETABS Documentation. *Computer and Structures Inc.,* Berkeley, CA, USA.

Devin, A., & Fanning, P. [2012] "Impact of nonstructural components on modal response and structural damping". *Topics on the Dynamics of Civil Structures, Volume 1* (pp. 415-421). Springer.

Devin, A., Fanning, P., Pavic, A. [2015] "Modelling effect of non-structural partitions on floor modal properties", *Engineering Structures,* Vol. 91, pp. 58-69.

Dorji, J., Thambiratnam, D. P. [2009] "Modelling and analysis of infilled frame structures under seismic loads", *The open construction and building technology journal,* Vol. 3, No. 1.

FEMA356. [2000] *Pre-Standard and Commentary for the Seismic Rehabilitation,* Federal Emergency Management Agency, Washington (DC).

Li, B., Hutchinson, G. L., Duffield, C. F. [2011] "The influence of non-structural components on tall building stiffness", *The Structural Design of Tall and Special Buildings,* Vol. 20, No. 7, pp. 853-870.

NRC. [2010] *National building code of Canada*, National Research Council, Canada

NRC. [2015] *National building code of Canada*, National Research Council, Canada

Pokhrel, A., Gautam, D., Chaulagain, H. [2019] "Effect of variation on infill masonry walls in the seismic performance of soft story RC building", *Australian Journal of Structural Engineering,* Vol. 20, No. 1, pp. 1-9.

Ray-Chaudhuri, S., & Hutchinson, T. C. [2005] "Effect of nonlinearity of frame buildings on peak horizontal floor acceleration". *Journal of earthquake engineering*, 15(1), 124-142.

Su, R., Chandler, A. M., Sheikh, M. N., Lam, N. [2005] "Influence of non-structural components on lateral stiffness of tall buildings", *The Structural Design of Tall and Special Buildings,* Vol. 14, No.2, pp. 143-164.

Probabilistic Evaluation of Post-earthquake Functional Recovery of a Seismically Isolated RC Building

Jean-Piers Chavez[1], Juan Murcia-Delso[2], Elena Oliver-Saiz[3], Francisco López-Almansa[4]

[1]PhD Candidate, Civil and Environmental Engineering Department, Universitat Politècnica de Catalunya (UPC BarcelonaTech), Campus Nord UPC, 08034 Barcelona, jean.piers.nicolas.chavez@upc.edu
[2]Assistant Professor, Civil and Environmental Engineering Department, Universitat Politècnica de Catalunya (UPC BarcelonaTech), Campus Nord UPC, 08034 Barcelona, juan.murcia-delso@upc.edu
[3]Assistant Professor, Architecture Technology Department, Universitat Politècnica de Catalunya (UPC BarcelonaTech), Campus Sud UPC, 08028 Barcelona, elena.oliver@upc.edu
[4]Professor, Architecture Technology Department, Universitat Politècnica de Catalunya (UPC BarcelonaTech), Campus Sud UPC, 08028 Barcelona, francesc.lopez-almansa@upc.edu

Abstract. All earthquakes throughout history have taught us that damage to non-structural elements and content has serious repercussions on the direct economic cost of damage and functionality. In essential buildings such as hospitals, rapid functional recovery is essential to safeguard the lives of the occupants and the injured who arrive after the earthquake. This study presents the detailed evaluation of the functional recovery of a RC seismically isolated 8 story hospital building located in an area of high seismicity. The study is carried out using the probabilistic analytical framework F-Rec, which has been recently proposed in the literature for the evaluation of the functional recovery of buildings after an earthquake. This framework complements the FEMA P-58 performance evaluation methodology allowing a complete and detailed evaluation of post-earthquake functionality, duration of damage and the path of functional recovery, considering structural and non-structural elements and content. In this study, a non-linear model of the building is created in OpenSees and the seismic response is studied for three hazard scenarios, Service Level Earthquake (SLE), Design Based Earthquake (DBE) and Maximum Considered Earthquake (MCE). Based on the results of the non-linear analyses, the damage losses are calculated using the FEMA P-58 tool, while the building recovery process is evaluated using the F-Rec framework. The efficient functional recovery time and route are analyzed for each scenario. The results show that the F-Rec framework is a viable tool for the evaluation of the post-earthquake functionality of isolated hospital buildings, but that there is a need to develop specific fragility and recovery curves for medical equipment.

Keywords: Functional Recovery, Non-Structural Elements, Seismic Isolation, Probabilistic Recovery Curve, Hospital Building.

1. INTRODUCTION

Lessons learned from past earthquakes indicate that hospitals or health centers are the most important buildings after a seismic event. To date, structural seismic performance and design is a well-studied subject, and there are advanced techniques that allow structural protection of this type of building. However, seismic performance today is still a delicate and little studied issue due to the complexity involved in understanding what would be the best methodology that allows continuous functionality of all components and non-structural elements after an earthquake. One of the most notable events in history is the Loma Prieta earthquake in 1989 with Mw=6.9, which caused great economic and human losses due to damage to the content and non-structural elements. As a solution, seismic base isolation is currently the most accepted and effective means of protecting this type of essential building. The safety of the occupants has been the main objective of the system, therefore, guaranteeing zero damage to the structure is essential and also minimizing accelerations and speeds, which are the cause of damage to non-structural elements and highly expensive components.

As medical technology advances, hospital-type buildings are becoming more expensive due to the implementation of new medical equipment and the high performance that hospitals in general must have. The seismic design of this type of buildings is controlled by the seismic performance design methodology based on a set of strict performance criteria for the structure and the non-structural elements and contents, ensuring life, the non-probability of collapse and continuity of use. However, seismic resilience and functional recovery time after an earthquake are not considered in structural design as the tools and methodologies to assess these parameters were not available until recently. Everything mentioned refers to a hospital-type building on a fixed base, however, considering the same building, but on an isolated base, there is still no information that explains how the functional recovery curve is, taking into account that the performance of the building isolated is very different from a building on a conventional basis.

Currently the most significant methods for modeling the post-earthquake recovery of buildings, these being the REDi model that complements the FEMA P-58 methodology and estimates the recovery time (downtime), without explicit consideration of the post-earthquake functionality of the building in a limit state, this being one of its main disadvantages. On the other hand, recently there is a new tool called F-Rec (Figure 1) that suggests a complete and detailed evaluation of the seismic performance of buildings considering all the structural and non-structural components/systems of the building and the calculation of performance metrics relevant to the building and evaluation of the entire recovery process, including the post-earthquake functionality of the building along with the duration and path of functional recovery. The new framework for modeling functional recovery is in line with the PBEE (probabilistic performance-based earthquake engineering).

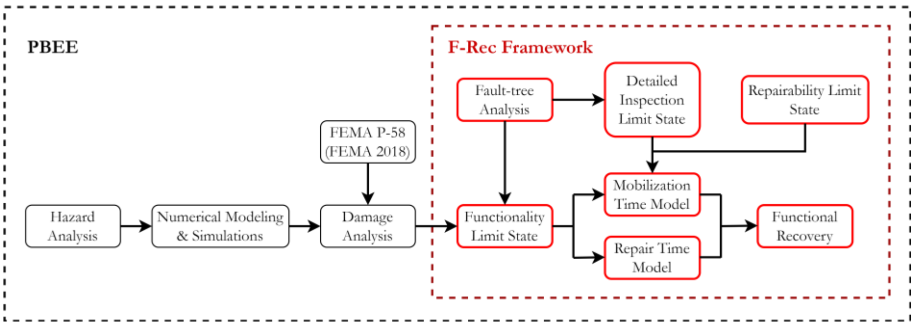

Figure 1. F-Rec framework for modelling functional recovery in conjunction with PBEE/FEMA P-58 methodology (Terzic et al. [2021]).

2. RESEARCH METHODOLOGY

The present study applies the new probabilistic functional recovery method F-Rec proposed by Terzic et al. [2021] to an essential hospital-type building with a regular structure of 8 floors. The building has been designed in a zone of high seismic hazard and includes base isolation. First, the seismic response of the building is analyzed for a set of far-field seismic records selected following FEMA P-695 [2010] recommendations. To this end, nonlinear time-history dynamic analyses of the typical building frame are conducted using OpenSees (Open System for Earthquake Engineering Simulation) platform (McKenna [2000]). The story drift and accelerations demand obtained from the analyses are used to estimate probabilities of damage in structural and non-structural components following the FEMA P-58 methodology through the PACT software [2018b]. Fault trees and component recovery functions are then used to evaluate the functional recovery of the building following the F-Rec method. The main result obtained by applying this new method is the functional recovery curve which provides information on the post-earthquake functionality expressed as a percentage of the area within the building with preserved functionality.

3. BUILDING DESCRIPTION AND DESIGN

The analyzed building has eight floors and is located in Los Angeles. It has a height of 32 m and a total weight of 62229 kN. The building has reinforced concrete moment-resisting frames in each direction and is isolated at the base using elastomeric isolators with a central lead core (Figure 2).

The structure has been designed for a CD type soil and has a seismic risk category IV. The spectral acceleration parameter for short periods is $S_S = 2.22$ and the acceleration parameter for a period of one second is $S_1 = 0.74$, in accordance to current ASCE 7-22 recommendations. The basic design spectrum (DBE) shown in Figure 3 has been considered for the analysis and design of the building. The design is carried out using the method of forces and the final drifts are verified with nonlinear analysis to comply with the HAZUS damage-drift relationship methodology [2013]. The ductility reduction factor R have been taken as 1.5 following ASCE 7-22. The columns have square sections with side of 0.60 m and are spaced 5 m on the X axis and 4.30 m on the Y axis. The beams are 0.35 m wide by 0.75 m high, and the slabs are solid with a thickness of 0.25 m. The design of all the structural elements has been carried out to maintain the building structure elastic against a maximum considered earthquake (MCE), the cross sections are the minimum to be used to obtain drifts and accelerations below the limit of structural and non-structural damage.

(a) 3D Model of the hospital building frame (b) Elevation view

Figure 2. Scheme of hospital building structure

4. GROUND MOTION SELECTION

A set of 44 seismic records has been used from the FEMA P-695 far-field ground motions set, comprising 22 pairs of earthquakes records for C/D type soils ($V_{s30} = 365$ m/s). The building site is located at a longitude = -118.2074° and latitude = 34.042°. The set consists of large magnitude (magnitude 6.5 M_w or greater) slip or reverse earthquakes, of which 16 earthquakes were recorded in type D soil (rigid soil) and 6 earthquakes in type C soil (very rigid soil), which coincide appropriately with the location of the building. Each seismic record went through the process of baseline correction, bandpass filtering and scaling to 3 levels of seismic hazard, service earthquake (SLE), design earthquake (DBE) and maximum considered earthquake (MCE). SeismoSignal software [2022] was used for the filtering and correction process and SeismoMatch [2022] for scaling and spectral adjustment, the adjustment and scaling process was carried out for the entire response spectrum, considering not to be below 90 % and 110 % of the target spectrum. Shown in Figure 3 are the 44 earthquakes and the spectra for each level of seismic hazard, respectively.

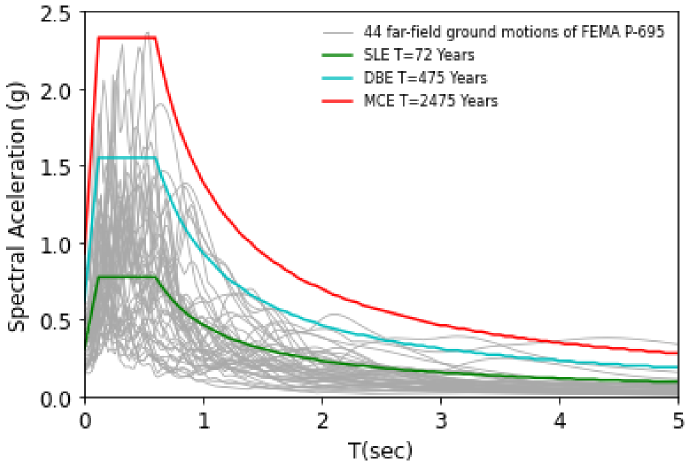

Figure 3. Design spectra and individual spectra of 22 pairs of unscaled records

5. STRUCTURAL MODELING

5.1 BUILDING MODELING

The central main frame was chosen in the X axis of the building for the modeling, Figure 4b shows the scheme of the model developed in the OpenSees [2000]. All building elements were modeled to allow entering the plastic range using forceBeamColumn elements with distributed plasticity. The analysis was performed in two dimensions and the total tributary weight was evenly distributed among the six nodes corresponding to each floor, including the base floor. According to Ryan and Polanco [2008], the damping for an isolated building has to be only proportional to the stiffness, thus avoiding applying excessive artificial damping at frequencies lower than the fundamental frequency of the superstructure. The fundamental period of the fixed base building analyzed here is 1.00 s, inserting the seismic isolation system, the period of the building is 3.10 s.

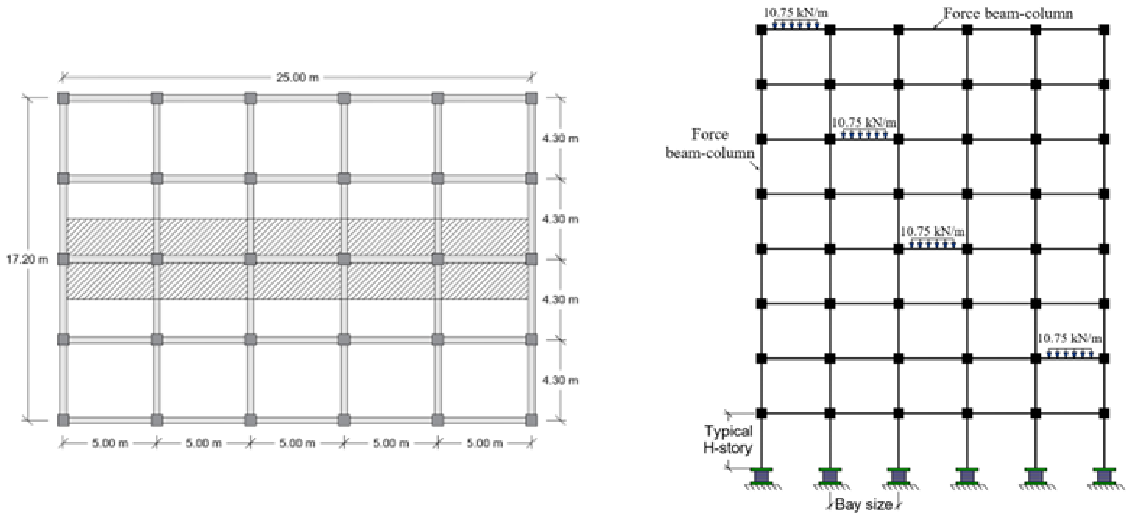

(a) Plan view with a tributary area of the main frame (b) Frame model in OpenSees

Figure 4. Building modeling

5.2 SEISMIC ISOLATION MODELING

Lead rubber bearings (LRB) were used as isolators. The lateral response of the LRB is represented by a bilinear load-displacement law, following the approach of Erduran et al. [2011], consisting of an assembly of an elastic column, an elastic-perfectly plastic horizontal spring and a nonlinear vertical elastic spring, as shown in Figure 5. The general properties of these isolators are shown in the following table:

Table 1. Properties of LRB isolators

Device	K_l (kN/m)	Q_d (kN)	α_1	D_{ext} (m)	H_t (m)	ξ_D (%)
LRB	11298.30	105.75	0.02	1.00	0.40	20

$Q_d = Characteristic\ Strength$

$\xi_D = Equivalent\ Damping\ Ratio$

$D_{ext} = Outer\ Diameter$

$H_t = Total\ Height$

$\alpha_1 = Ratio\ of\ Initial\ Stiffness\ to\ Post-yield\ Stiffness$

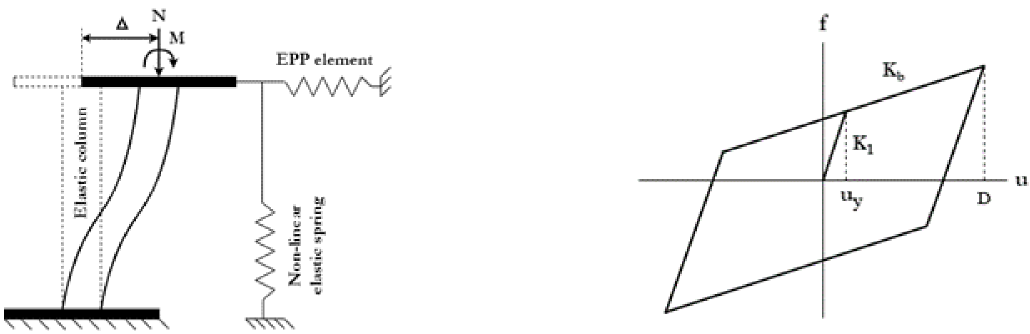

(a) Column model with lateral and vertical non-linear spring (b) Resultant lateral force–displacement hysteresis of the model

Figure 5. LRB hysteretic model

6. NONLINEAR ANALYSIS RESULTS

The results of the nonlinear time-history dynamic analyses for the three hazard levels are shown in Figure 6. The plotted results correspond to the mean values of the peak story drift values, peak floor accelerations and residual story drift at each level as obtained from the 44 seismic records. As a reference, these results are compared with the recommended limits in REDi [2013], which indicates that a hospital has a platinum category with downtime of maximum 72 hours. The HAZUS [2013] indicates that the maximum drift for an essential building should be 0.33 % to avoid structural damage and acceleration 0.30 g to avoid non-structural damage. It can be observed that for the service earthquake (SLE) the maximum value of the average peak story drift is 0.16 % (second story) and the maximum average value of the peak acceleration is 0.1 g (eighth floor). For the design earthquake (DBE) and maximum considered earthquake (MCE), the maximum value of the average peak story drift is 0.232 % and 0.378 %, respectively, in the second story, while the maximum average value of the peak acceleration is 0.175 g and 0.33 g, respectively, in the eighth floor. It can be seen that thanks to the isolation system, the drifts are relatively small even for the MCE. Accelerations are also greatly reduced thanks to the isolation system; it is observed that they are very similar at all levels. Finally, Figure 6d shows the hysteretic loop of a central isolator for an MCE earthquake, where it is observed that the maximum displacement is 0.75 m.

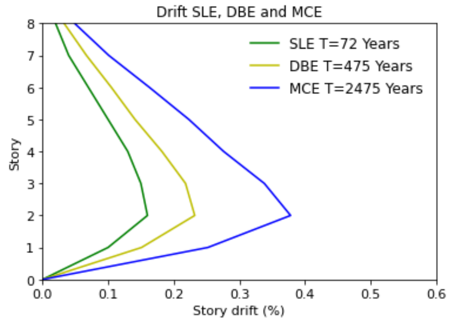

(a) Mean values Drift

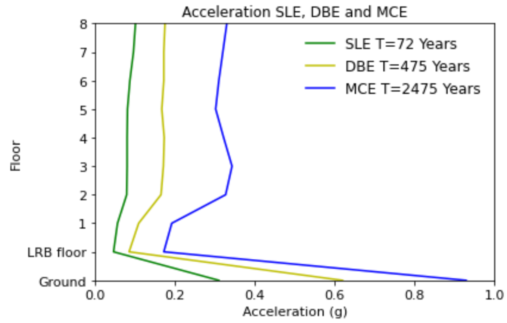

(b) Mean values Accelerations

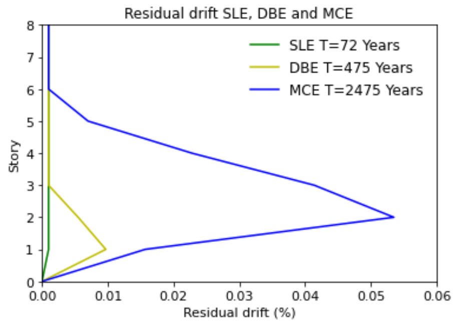

(c) Mean residual drift

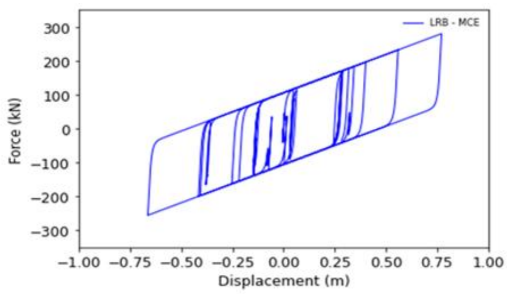

(d) Hysteretic model example for an isolator in MCE

Figure 6. Non-linear response of hospital building

7. PERFORMANCE AND FUNCTIONAL RECOVERY EVALUATION

7.1 PERFORMANCE EVALUATION PER FEMA P-58

The results of the nonlinear analyses obtained in section 6 were incorporated into the FEMA P-58 PACT software, which creates a performance model for the evaluation of damage to structural and non-structural elements. The performance model in PACT includes fragility curves suitable for all types of structures, architecture, and mechanical components in the building. To evaluate the damageability performance in a probabilistic way, Monte Carlo simulations of building response and damage are conducted considering 2000 realizations for each level of seismic hazard. For the calculation of the residual drift, the recommendations of volume 1 of the FEMA methodology P-58-1 [2018a] will be taken, in this case since it is a building with seismic isolation, the structural damage is null, which it is more important to evaluate the damage in the nonstructural elements and content. In the FEMA volume 1 methodology, 4 states of damage are indicated (DS1, DS2, DS3 and DS4), for this work it will be considered to limit the residual drift to the DS1 state, which indicates that structural realignment is not necessary for the stability of the building, however, the building may require adjustments and repairs to mechanical and non-structural components that are sensitive to the alignment of the building. Figure 6c shows how the residual drifts appear at the DBE and MCE earthquake levels, but with very low values.

The types and quantities of structural elements (beams, columns and slabs) have been determined from the building design and introduced in PACT. The non-structural components and general building equipment (elevators, stairs, exterior walls and partitions, roofs, water system, medical gas systems, etc.) are modeled in their respective locations and their quantities are determined using FEMA P-58 recommendations and hospital architecture research references by Yu et al. [2019] and Elfante et al. [2019]. In PACT, each component of the building is associated with a fragility curve that correlates the seismic demand (story drift or acceleration) with the probability that this element reaches a particular state of damage. In figure 7a it can be seen how the structural system presents zero damage for the 3 levels of seismic hazard evaluated, thanks to the base isolation. In Figure 7b, 7c y 7d, it can be seen that for the dividing walls there is a 15 % and 25 % partial loss for DBE and MCE earthquakes, respectively. However, for the ceiling there is a 15 % partial loss only for the MCE earthquake and for the piping there is no loss in the 3 hazard levels.

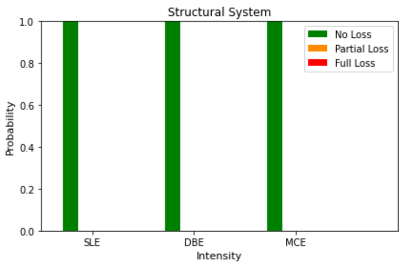

(a) Probability of structural system damage

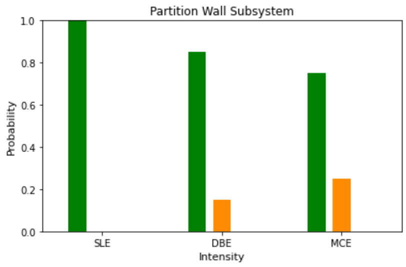

(b) Probability of the partition wall damage

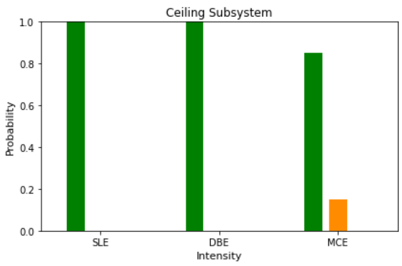

(c) Probability of the ceiling damage

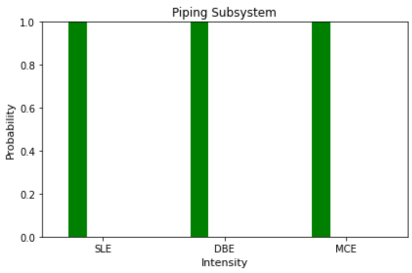

(d) Probability of the piping damage

Figure 7. Damage states without medical equipment

A second model of the model has been defined in PACT by also considering basic medical equipment for a hospital with an operating room. In the chapter 3 Figure 2b presents the distribution of operating rooms in the building. The fragility functions for this medical equipment were not available by default in the software and have been defined from the investigations by Yu et al. [2019] and Elfante et al. [2019]. As shown in Figure 8b, the IV Pole equipment in ward rooms presents a probability of partial loss of 55 %, 70 % and 90 % for SLE, DBE and MCE respectively. For the hospital bed there is a partial loss of 40 % for the MCE earthquake (Figure 8d). For the operating rooms, damage is only seen in the trolley carts with a partial loss of 10 %, 20 % and 30 % for SLE, DBE and MCE earthquakes, respectively (Figure 8d).

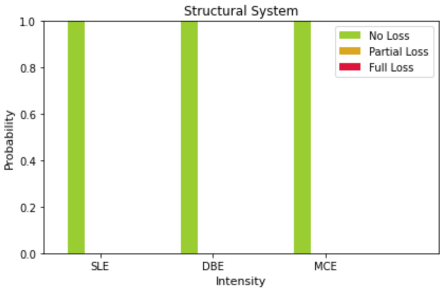

(a) Probability of structural system damage

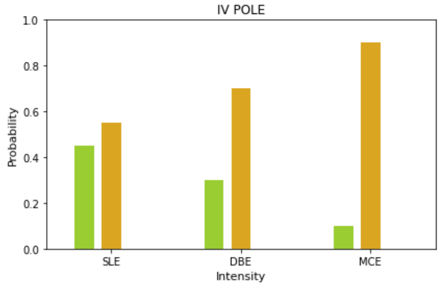

(b) Probability of the IV Pole damage

(c) Probability of the trolley cart damage

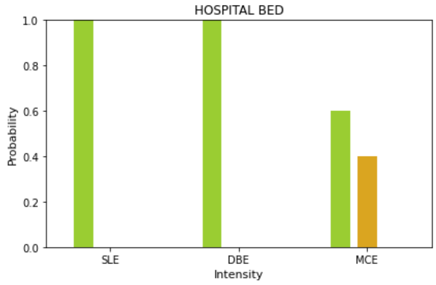

(d) Probability of the hospital bed damage

Figure 8. Damage states with medical equipment

7.2 FUNCTIONAL RECOVERY EVALUATION

The functional recovery analyses are conducted based on the results of the damage assessment obtained with the FEMA P-58, the fault trees of the building and its subsystems, and the limit state functions of the building components that define probabilistically the damage thresholds affecting the building. This study uses fault trees proposed for components of basic and essential medical care in a hospital. Figure 9 shows the process that has been followed for the evaluation and recovery of the isolated hospital building.

Data for the evaluation of damage and functionality in core elements in the F-Rec tool (Terzic and Villanueva [2021]) were originally obtained from recommendations from facility managers, builders, and structural engineers. It is worth mentioning that the present study considers two models for recovery evaluation: one neglecting basic medical equipment and the other considering it.

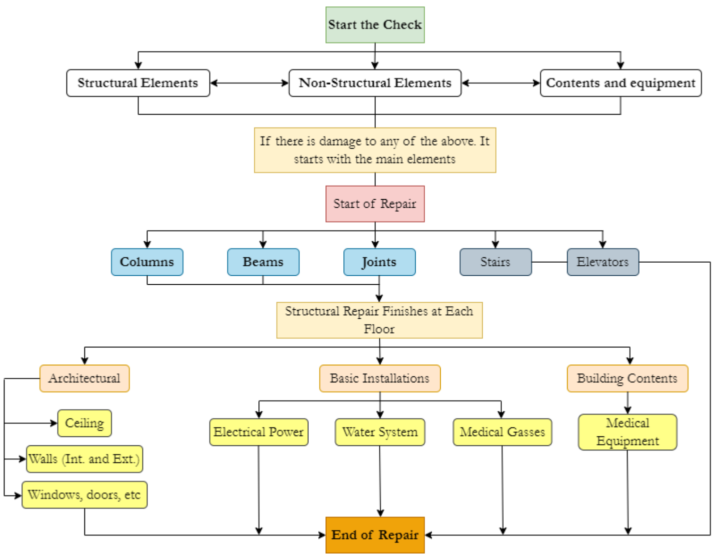

Figure 9. Proposed flowchart for evaluation and functional recovery of the isolated hospital

Figure 10 shows the functional recovery curves for the 3 levels of seismic hazard when neglecting medical equipment. This figure provides the median and the 90th percentile that show the change in the capacity of the building from the occurrence of the earthquake (time = 0) until the building fully recovers its function. Figure 11 shows also the cumulative distribution functions of functional recovery time for the 3 hazard levels. The building is expected to fully regain its function in 12.00 hours for frequent earthquakes (SLE), it takes 21.36 hours for rare earthquakes (DBE), and 2.28 days for very rare earthquakes (MCE).

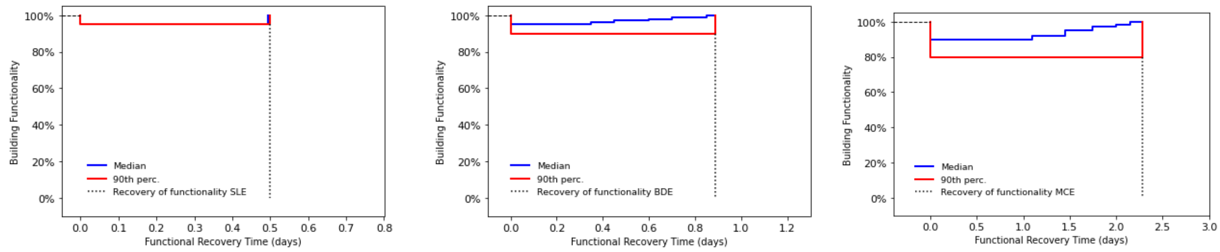

(a) SLE hazard level (b) DBE hazard level (c) MCE hazard level

Figure 10. Functional recovery evaluation without medical equipment

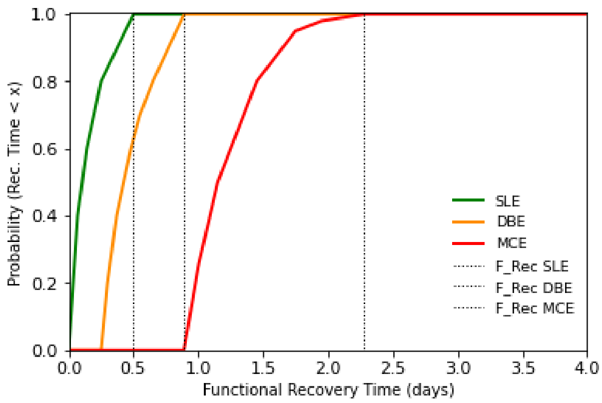

Figure 11. Functional recovery evaluation results at three considered hazard levels without medical equipment

Figure 12 shows the functional recovery curve for the 3 levels of seismic hazard in the hospital considering the influence of the medical equipment. As shown in Figure 13, the building is expected to fully recover its function in 1.08 days for frequent earthquakes (SLE), 2.40 days for rare earthquakes (DBE) and 5.00 days for very rare earthquakes (MCE). Hence, the expected recovery time increase by a factor of 2 to 5 when considering medical equipment

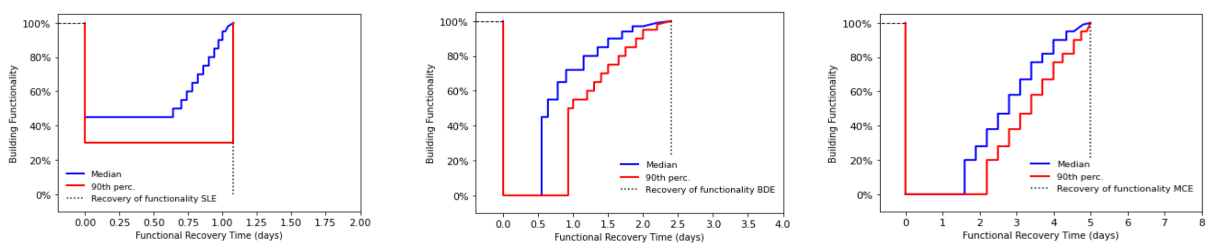

(a) SLE hazard level (b) DBE hazard level (c) MCE hazard level

Figure 12. Functional recovery evaluation with medical equipment

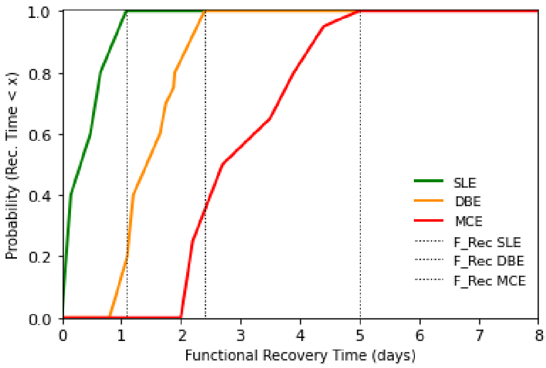

Figure 13. Functional recovery evaluation results at three considered hazard levels with medical equipment

8. CONCLUSIONS

The present study has investigated the functional recovery of an eight-story hospital with base isolation located in an area of high seismicity. Based on the results of nonlinear analyses, damage impaired losses are calculated using FEMA P-58 tools, while the building's post-earthquake functionality along with the path of the building's functional recovery are evaluated using the recently-proposed F-Rec framework.

The results of the present study indicate that post-earthquake functionality of the building with base isolation is mainly governed by the performance of the non-structural elements and equipment. Full functional recovery is expected to be achieved at 12 hours, 21 hours and 2.3 days for SLE, DBE and MCE, respectively when neglecting medical equipment. When considering basic medical equipment, recovery times increase to 1 day, 2.4 days and 5 days for SLE, DBE and MCE, respectively. Based on these results, it is concluded that a detailed assessment of the medical equipment damage is necessary for an accurate estimation of the functional recovery of this type of buildings. Hence, it is critical to develop specific fragility and recovery functions for such equipment.

ACKNOWLEDGEMENTS

This research was conducted with the support from the Secretariat for Universities and Research of the Ministry of Business and Knowledge of the Government of Catalonia and the European Social Fund.

REFERENCES

Applied Technology Council (ATC-138-3) [2021], Seismic Performance Assessment of Buildings Volume 8 – Methodology for Assessment of Functional Recovery Time, Redwood City, California 94065.

Elfante, P.B., Sy, A.W., Tan, N.J., et al. [2019] "Seismic fragility assessment of non-fixed hospital equipment," *DLSU Research congress,* Manila, Philippines.

Erduran, E., Dao, N.D., and Ryan, K.L. [2011]. "Comparative response assessment of minimally compliant low-rise conventional and base-isolated steel frames." *Earthquake Engineering Structures*, Vol. 11, No. 40, pp. 1123–1141.

Federal Emergency Management Agency (FEMA) [2018a], *FEMA P-58-1: Seismic performance assessment of buildings, volume 1–methodology*. Washington, DC.

Federal Emergency Management Agency (FEMA) [2018b], *FEMA P-58-2: Performance Assessment Calculation Tool (PACT)*. Washington, DC.

Federal Emergency Management Agency (FEMA) [2013], *HAZUS-MH 2.1:* Multi-Hazard Loss Estimation Methodology. Washington, DC.

Federal Emergency Management Agency (FEMA) [2010], *FEMA P-695: Methodology for quantification of building seismic performance factors*. Washington, DC.

McKenna, F.; Fenves, G. L.; Scott, M. H.; and Jeremic, B. [2000] "Open System for Earthquake Engineering Simulation (OpenSees)," Pacific Earthquake Engineering Research Center, University of California, Berkeley, CA.

Resilience-based Earthquake Design Initiative for the Next Generation of Buildings [2013]. Redi Rating System. U.S.A

Ryan, K., Polanco, J. [2008] "Problems with Rayleigh damping in base isolated buildings." J. *Structural Engineering*, Vol. 134, No. 11, pp. 1780–1784.

SeismoSoft. SeismoMatch [2022] - A computer program for response spectrum matching from: www.seismosoft.com. U.S.A

SeismoSoft. SeismoSignal [2022] - A computer program for signal processing of strong-motion data from: www.seismosoft.com. U.S.A

Terzic, V., Villanueva, P.K. [2021] "Framework for modelling post-earthquake functional recovery of buildings," *Engineering Structures*, Vol. 246, No. 113074, pp. 1-15.

Terzic, V., Villanueva, P.K., Saldana, D., Yoo, D.Y. [2021] *F-Rec Framework: Novel Framework for Probabilistic Evaluation of Functional Recovery of Building Systems, PEER Report 2021/06*. UC Berkeley: Pacific Earthquake Engineering Research Center.

Yu, Peng., Wen, W., et. al. [2019] "A framework to assess the seismic resilience of urban hospitals," *Advances in Civil Engineering*, Vol. 2019, No. 7654683, pp. 1-11.

Comparison of seismic loss and floor response spectra of low-rise buildings with various types of braced frames

Amir Banihashemi[1], Lydell Wiebe[1], André Filiatrault[2], and Paul Steneker[3]

[1] McMaster University
1280 Main St W, Hamilton, ON L8S 4L8
e-mail: baniham@mcmaster.ca, wiebel@mcmaster.ca
[2] University School for Advanced Studies IUSS Pavia
Piazza della Vittoria, 27100 Pavia, Italy
andre.filiatrault@iusspavia.it
[3] WSP Canada Inc.
150 Slater, Ottawa, Canada
e-mail: paulsteneker@gmail.com

Abstract.

Over the last decades, there has been increasing awareness of the importance of minimizing seismic losses in buildings caused by both damage to nonstructural components and demolition because of excessive residual drifts. A desire to avoid residual drifts has led to the development of many new self-centering devices and seismic force-resisting systems (SFRSs). This study examines how the chosen SFRS affects overall seismic losses, especially when self-centering systems are considered. For this purpose, a six-story steel building's seismic loss assessment is compared when it is designed using three different SFRSs: a special concentrically braced frame (SCBF), a buckling-restrained braced frame (BRBF), and a controlled rocking braced frame (CRBF). This study reveals that while the six-story SCBF and BRBF built to current state-of-the-art seismic building design codes meet expectations regarding life safety and structural collapse, expected demolition losses due to residual drift can lead to more than half of the total expected annual seismic loss. Conversely, the six-story CRBF has minimal seismic losses due to residual drift and structural repair costs. While this comes at the cost of higher demands on acceleration-sensitive nonstructural components, the total seismic loss for the CRBF is lower than for the SCBF and BRBF designs. Furthermore, the findings suggest that traction elevators, curtain walls, mechanical equipment including chillers and air handling units, and wall partitions are the components that contribute to more than 80% of the nonstructural seismic loss. Finally, examining the floor response spectra of the three systems suggests that peak floor accelerations may not be an ideal engineering demand parameter for predicting seismic loss related to acceleration-sensitive nonstructural components since they do not account for spikes that may happen in the high-frequency range of floor response spectra due to higher mode effects.

Keywords: Concentrically braced frame, Buckling-restrained braced frame, Controlled rocking braced frame, Seismic loss, Floor response spectra, Nonstructural elements.

1.INTRODUCTION

While current seismic design codes target low collapse probability, they have not been developed with the intent of minimizing seismic losses in buildings. Earthquake-induced loss in a building can stem from four sources: (i) collapse of the building, (ii) demolition of the building related to excessive residual drift, (iii) repair of damaged structural components, and (iv) repair of damaged nonstructural components. Therefore, seismic loss minimization can be achieved by a combination of improving the structural performance of buildings and reducing damage to nonstructural components.

Conventional seismic force-resisting systems (SFRSs) for steel buildings such as special concentrically braced frames (SCBFs) and buckling-restrained braced frames (BRBFs) exhibit seismic loss due to all sources listed above. The asymmetric hysteretic behaviour of braces in buildings with SCBFs can lead to local story collapse due to plastic deformation concentrations [Hwang and Lignos, 2017], or to large residual drifts or global structural collapse [Tremblay *et al.*, 1996; Tremblay *et al.*, 1995]. Erochko *et al.* [2011] studied buildings with different heights from 2 to 12 stories designed with BRBFs. They showed that the BRBFs can experience large residual drifts, with values between 0.8% and 2% under design basis excitations.

Controlled rocking braced frames (CRBFs) have been proposed as an alternative SFRS to minimize seismic loss. CRBFs reduce structural losses and provide self-centring behaviour to avoid residual drifts by uplift and rocking, while their response can be controlled with energy dissipation devices and post-tensioning strands. Additionally, during high-intensity earthquakes, this type of frame has a low collapse probability due to its large displacement capacity [Steele and Wiebe, 2021]. However, acceleration-sensitive nonstructural components may experience greater demand due to higher mode effects in CRBFs, which could raise the overall seismic loss [Buccella *et al.*, 2021]. Dyanati *et al.* [2017] compared the economic effectiveness of six-story and 10-story buildings designed using SCBFs and CRBFs. They employed probabilistic seismic engineering demand parameter models to evaluate the seismic loss and followed FEMA [2014] and Ramirez and Miranda [2009] to define the capacities of the drift-sensitive and acceleration-sensitive components, respectively. They discovered that employing CRBFs was advantageous for the six-story building, but not for the ten-story building.

In this study, a six-story steel building is designed separately with an SCBF, a BRBF, and a CRBF. Engineering demand parameters (EDPs) for different seismic intensity levels are calculated using multiple stripe analyses. Then, considering twenty-two different nonstructural components selected from FEMA-P58-3 [FEMA, P-58-3, 2018], the expected annual loss is evaluated for each type of system and compared. Finally, the floor response spectra that develop with these systems are also compared.

2.DESIGN OF PROTOTYPE STRUCTURES

In this study, a six-story steel building was designed separately with three different SFRSs: an SCBF, a BRBF, and a CRBF. According to ASCE 7-16 [American Society of Civil Engineers (ASCE), 2017], the building is assumed to be located on a site class D with stiff soil and in a seismically active area with mapped short periods and 1-second spectral accelerations of S_s=1.5 g and S_1=0.6 g, respectively. The building has a footprint of 54.9 m × 36.6 m, with a 4.57 m story height and seismic weights of 10200 and 6430 kN for the floors and roof, respectively. Four frames with a width of 9.15 m each were designed to resist seismic forces in each direction.

The SCBF and BRBF buildings were designed based on ASCE 7-16 and AISC 360-16 [American Institute of Steel Construction (AISC), 2016)]. For the equivalent force approach, response modification factors (*R*) of 6 and 8 were employed for the SCBF and BRBF buildings, respectively. Steel members of the SCBF and

BRBF buildings were designed in two steps: (i) design of braces to act as fuse elements in resisting lateral loads, and (ii) capacity design of other steel members to remain elastic upon yielding and buckling of the braces.

The building incorporating CRBFs was designed based on a two-step procedure developed by Wiebe and Christopoulos [2015]. In this procedure, the base rocking joints are designed first, including post-tensioning (PT) and energy dissipation (ED), after which all other steel members are capacity designed for elastic response under a defined level of seismic loads. To design the base rocking joints, R was taken as 8 and the target energy-dissipation parameter (β), which is defined as the ratio of the height of the CRBFs' flag-shaped hysteresis to the linear limit, was taken as 90%. Additionally, the ratio of the prestress to the ultimate stress, η, was targeted to be 50% when designing the PT, which was placed in line with the column at each end of each frame. The frame members were designed using the dynamic capacity design procedure developed by Steele and Wiebe [2016]. In this procedure, the frame members' forces are a combination of the forces from frame rocking when the ultimate base rotation occurs and higher mode forces, which were computed from modal analysis using a truncated spectrum at the maximum considered earthquake (MCE) level.

3.GROUND MOTION SELECTION AND NUMERICAL MODELLING

The far-field ground motion records of FEMA-P695 [FEMA P-695, 2009] were used for the time-history analyses. The set of ground motions was scaled according to ASCE 7-16 to minimize the sum of squares of differences between the design response spectrum and the median acceleration spectrum of the records over a range of 0.2 times the first-mode period of the CRBF building to 2.0 times the first-mode period of the BRBF building (Figure 1). OpenSees [2011] was used to perform the time-history analyses of the 44 scaled ground motions for each designed building. The performance of each building was evaluated by multiple stripe analyses [Baker, 2015] using five different intensity stripes: one quarter of the design earthquake (DE), half of the DE, the DE, the MCE, and twice the MCE.

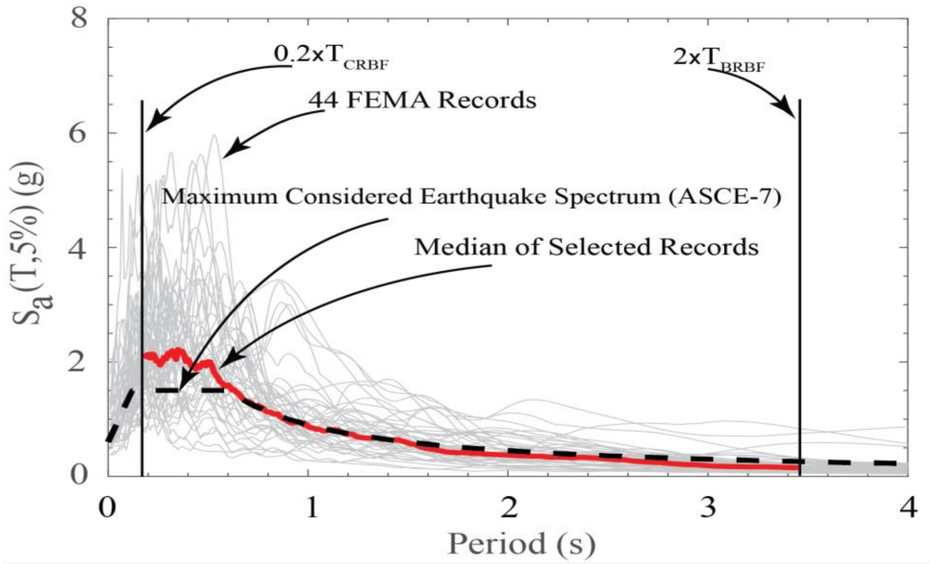

Figure 1. Design response spectrum and scaled ground motions.

A schematic of the numerical model of the SCBF building is shown in Figure 2 (a). Brace members were modelled with multiple force-based beam-column elements in OpenSees with an initial out-of-straightness of 0.1% of the member length to capture buckling response. The braces were pinned at both ends to simulate a flexible gusset plate connection. Other frame members, including beams and columns, were also modelled using nonlinear beam-column elements.

Figure 2 (b) shows a schematic of the numerical model of the BRBF building. Brace members were modelled using the Steel4 material model in OpenSees with general validated parameters for buckling-restrained braces proposed by Zsarnóczay [2013]. The braces were modelled as pinned at both ends. Beam and column members were modelled using nonlinear beam-column elements.

A schematic of the numerical model of the CRBF building is shown in Figure 2 (c) based on the model suggested by Steele and Wiebe [2021]. At the base of each column, vertical and horizontal gap components were introduced to allow the CRBF to uplift and rock. The energy dissipation devices were modelled as friction dampers using an elastic perfectly plastic model with a very high initial stiffness. The post-tensioning strands were represented by corotational truss elements with a multilinear material model prestressed with an initial stress material model. All frame members were modelled with force-based beam-column elements in OpenSees using multiple elements with an initial out-of-straightness to capture buckling response. Also, at the ends of each brace, designed gusset plates were modelled using fibre elements.

A leaning column was included in the models of all three types of frames in order to account for P-Delta effects from the other gravity frames of the building. Each floor's mass was lumped at the nodes of the leaning columns, which were laterally constrained to the centre joints of the frames. Inherent damping of all three types of frames was modelled using 5% Rayleigh damping in modes one and three, as determined using the fixed-base periods.

4.INITIAL CONSTRUCTION COST AND LOSS ASSESSMENT

Using RSMeans [2020], the initial cost of the six-story SCBF office building was estimated to be $16 million based on a reference time in 2011. The initial cost of the BRBF and CRBF buildings was assumed to be 2% more expensive than the SCBF building as they require more advanced and additional components. Using the normative quantity estimation tool from FEMA-P58-3 [FEMA P-58-3, 2018], twenty-two nonstructural components were estimated and examined, including drift-sensitive and acceleration-sensitive components with the number of quantities for each performance group on each floor. Moreover, all anchorages for types of equipment that require them were assumed to be designed so that they would not be damaged before the buildings collapsed. Therefore, they were not taken into account for the loss assessment. Special concentric braced frames with HSS braces were designed to AISC standards and buckling restrained braces were employed from FEMA-P58-3 to evaluate damages in braces of the SCBF and BRBF buildings, respectively. For the CRBF building, inter-story drift comprises both a rigid body deformation due to its rocking behaviour and an additional deformation of the frame itself. Therefore, to quantify the damage to bracing in the CRBF, the maximum compression deformation of the braces was used as the engineering demand parameter (EDP) in the damage fragility curves rather than inter-story drift [Banihashemi and Wiebe, 2022]. The FEMA-P58-3 library was used to allocate the structural and nonstructural components' damage and consequence models. Also, a lognormal distribution with a median of 0.01 and a logarithmic standard deviation of 0.3 was employed to calculate the demolition loss resulting from excessive roof drift. The Pelicun software [Zsarnóczay, 2019], developed by the Computational Modelling and Simulation Center (SimCenter), was used to carry out the seismic loss analyses.

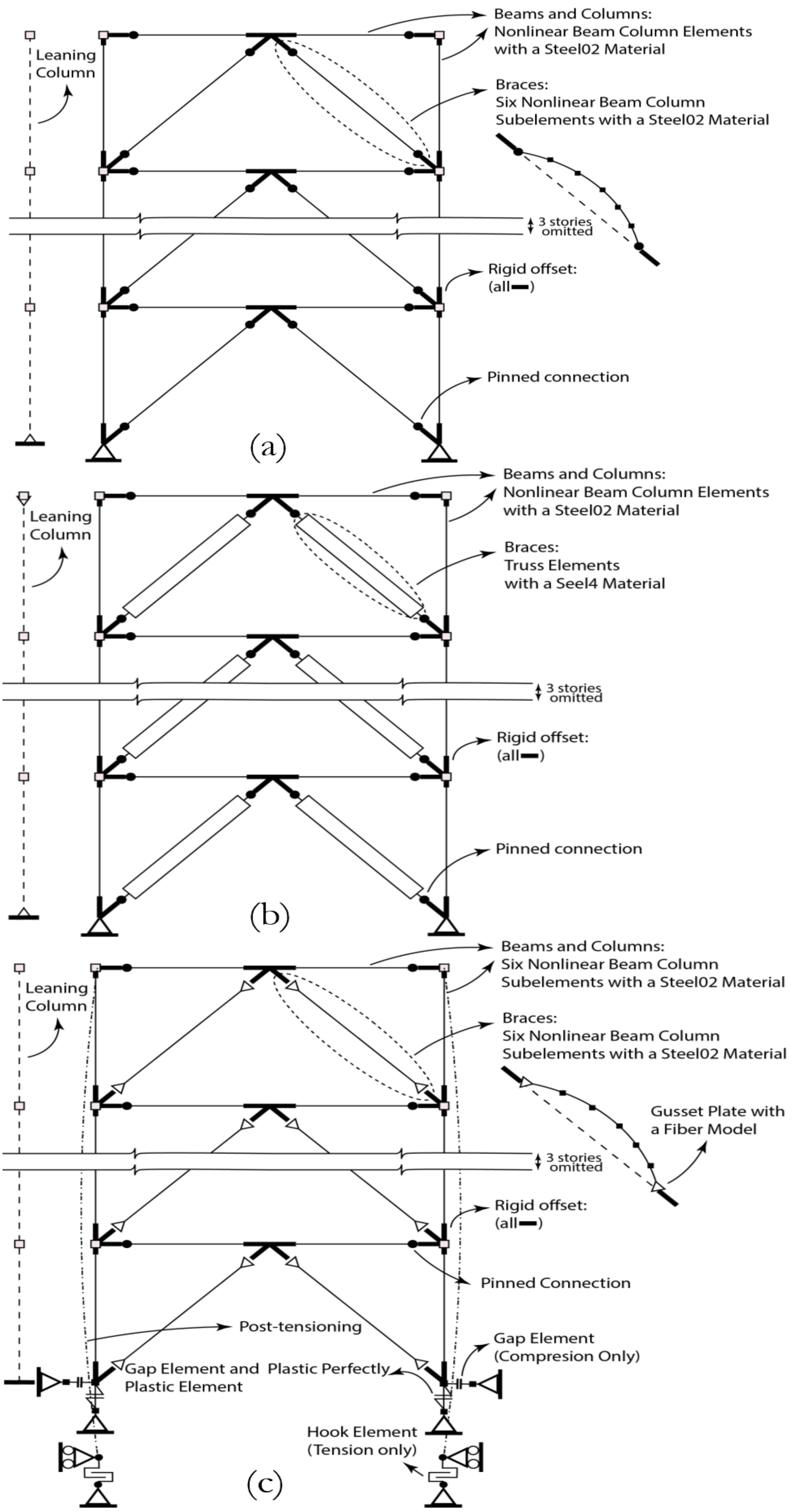

Figure 2. The schematic numerical modelling: (a) SCBF, (b) BRBF and (c) CRBF buildings.

5.RESULTS AND DISCUSSION

5.1 STRUCTURAL PERFORMANCE

The median inter-story drifts and accelerations at the DE level for the three types of designed buildings are presented in Figure 3 (a) and (b). Comparing inter-story drifts shows that for most floors, the drift for the SCBF building is less than for the two other types of buildings. However, for the CRBF building, the inter-story drifts are larger than those of the two other types of frames for most floors, while the distribution of median drift throughout the structure's height is almost uniform. The acceleration demands on the CRBF buildings are greater than those on the SCBF and BRBF buildings for most floors, notably at the roof, where mechanical equipment such as chillers and air handling units are located. The comparison of the collapse fragility curves of the three buildings is shown in Figure 3 (c), with the ratio of the demand intensity to the MCE-level intensity (i.e. $S_a(T_1,5\%)/S_{MT}$) on the x-axis. All three buildings have an acceptable collapse probability of less than 10% at the MCE level. Nonetheless, the CRBF building shows a higher capacity as it has a lower probability of collapse for intensity levels greater than the MCE level.

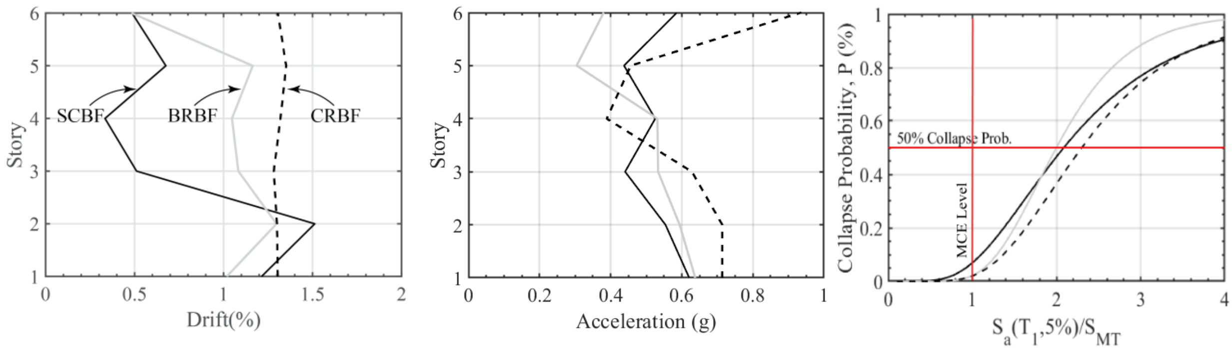

Figure 3. Structural performance of the designed buildings: (a) median inter-story drifts at the DE level, (b) median story accelerations at the DE level and (c) collapse fragility curves.

5.2 LOSS ASSESSMENT

Figure 4 compares normalized expected annual losses of the three buildings. The results show that the CRBF and SCBF buildings have the lowest and largest normalized expected annual losses (EALs), respectively. The findings also reveal that structural components and demolition losses account for more than half of the overall seismic losses for the SCBF and BRBF buildings. The CRBF building, on the other hand, has most of its seismic loss from damage to nonstructural components.

Comparing the portion of seismic loss due to collapse shows that all three buildings have a similar contribution of approximately 0.04% of the total building value, though this contribution is slightly smaller for the CRBF building than for the other designed buildings. As indicated in Figure 3 (c), the CRBF building has a s lower collapse probability for most considered intensities compared to the two other buildings.

The seismic loss due to demolition is the largest contributor to losses in the SCBF and BRBF buildings, with a normalized EAL of 0.1%. In contrast, this portion of the loss for the CRBF building is very small because this kind of frame benefits from elastic self-centring behaviour. For the SCBF building, seismic loss due to the repair of structural components is another large contributor, with a normalized EAL of approximately 0.1%. This portion of the loss for the BRBF building is smaller than for the SCBF building. Because buckling-restrained braces (BRBs) have a large displacement capacity, the median capacity fragility curve for the BRBs based on FEMA-P58-3 is 2% drift, which happens only at high-intensity level earthquakes. Additionally, the CRBF building has negligible structural repair cost since this type of frame mitigates energy through rocking rather than through damage to structural elements, and all CRBF steel frame elements were capacity designed to not yield or buckle while the frame is rocking.

Comparing the three types of buildings for seismic loss due to drift-sensitive nonstructural components shows that the SCBF and CRBF buildings have the smallest and largest portion, respectively. This result was also suggested by Figure 3 (a) when comparing inter-story drift at the DE level; however, drifts for all intensities are used to calculate normalized EALs. Also, comparing seismic loss due to acceleration-sensitive nonstructural components shows that these components are more vulnerable to damage in the CRBF building than the others, with repair costs for acceleration-sensitive components leading to a normalized EAL of 0.03% in the CRBF building. Among the three considered buildings, the BRBF building has the lowest contribution to EAL from acceleration-sensitive nonstructural components.

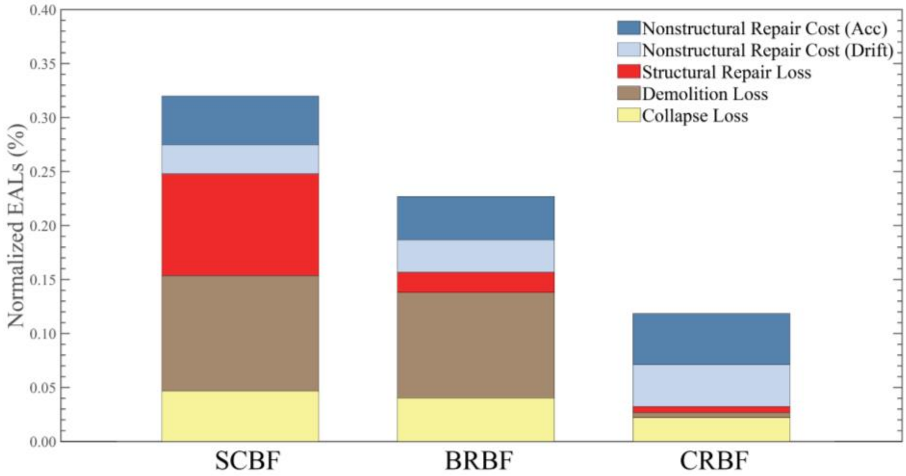

Figure 4. Comparing normalized expected annual losses for the three designed buildings.

Figure 5 shows the seven types of nonstructural components that contribute the most to the total seismic loss in each building. The nonstructural component type that contributes the most for the SCBF building is the traction elevator, whereas the most contributing type is the wall partition for the BRBF and CRBF buildings. The traction elevator is of particular importance not only because it has a single damage state with a median acceleration capacity of only 0.39 g, indicating this component is damaged for more than half of records even at the DE level for all three buildings (Figure 3 (b)), but also because the repair costs when it is damaged are relatively high. Also, the wall partition type has three damage states, where the fragility curves have a median capacity that ranges from 0.2% to 0.9% drift. Based on this range, even at the DE level (see Figure 3 (a)), wall partitions in all three buildings can significantly crack or crush based on the fragility curves suggested by FEMA-P58-3.

Another nonstructural component type that contributes significantly to the total seismic loss is the curtain wall. Although the first damage state of this component has a median capacity of 2% drift, its contribution is high because of the high number of units and unit repair cost. The air handling unit is another nonstructural component type that contributes notably to the total seismic loss for the SCBF and CRBF buildings. Even though the first damage state of this component has a median acceleration capacity of 1.54 g, the component's unit repair cost can be more than $16,000. Independent pendant lighting, chiller and raised access floor are other nonstructural components in this group of seven that can contribute much to the total repair cost.

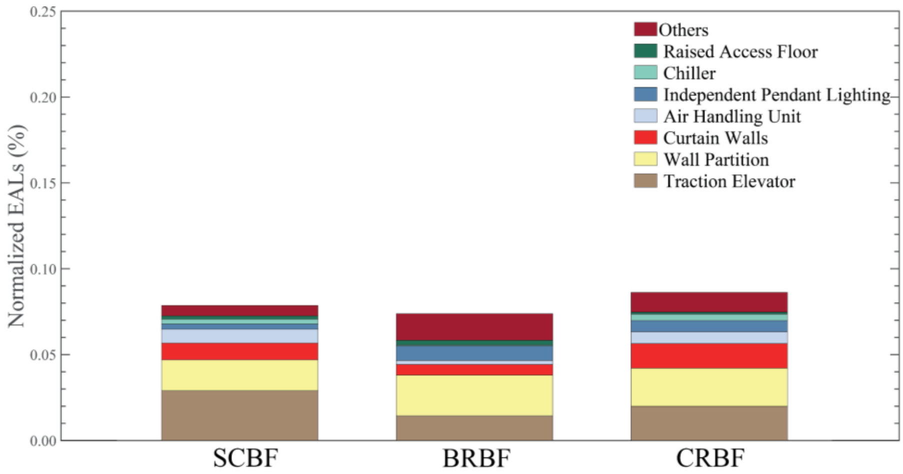

Figure 5. Nonstructural components contribute more to total seismic losses.

5.3 COMPARISON OF FLOOR RESPONSE SPECTRA

Current seismic loss estimation methodologies are based on peak responses such as peak inter-storey drift ratios or peak floor accelerations. However, floor response spectra can be employed to provide more detailed demand characterization for acceleration-sensitive nonstructural components. Figure 6 compares the median top floor absolute acceleration response spectra (Sa) with 5% damping of the three buildings at two intensity levels: 1/2 DE and DE.

The median peak floor accelerations (PFA) for the top floor of all three buildings, which can be determined from the spectra at very short periods, are relatively similar for the 1/2 DE intensity level (Figure 6 (a)). However, depending on the type of SFRS and the period of a nonstructural component, the median acceleration demand on the component might change. For instance, an acceleration-sensitive component with a period of 0.25 s might experience a median acceleration of more than 2 g if installed on the roof of the CRBF building (Figure 6 (a)). In comparison, this same component would experience a median acceleration of less than 1.5 g if installed on the roofs of the SCBF and BRBF buildings.

Brace members in SCBF and BRBF buildings may experience buckling or yielding when the shaking intensity rises, such as at the DE level, which results in the capping of the floor acceleration spectrum between the initial and elongated period of the building. However, as the CRBF building mitigates the induced-earthquake energy through the rocking mechanism, the capping is not observed in the spectrum. Instead, large spikes can be observed near the second period of the CRBF building. This result also is in agreement with that by Buccella *et al.* [2021]. Considering Figure 6 (b), using PFA to estimate the seismic loss of acceleration-sensitive nonstructural components suggests that those installed in the CRBF building will consistently be damaged more than those installed in the SCBF and BRBF buildings. However, comparing the floor spectra suggests that the damage to a component installed in the CRBF building could be much greater or lesser than when installed in the SCBF or BRBF building, depending on the relevant period of the nonstructural component.

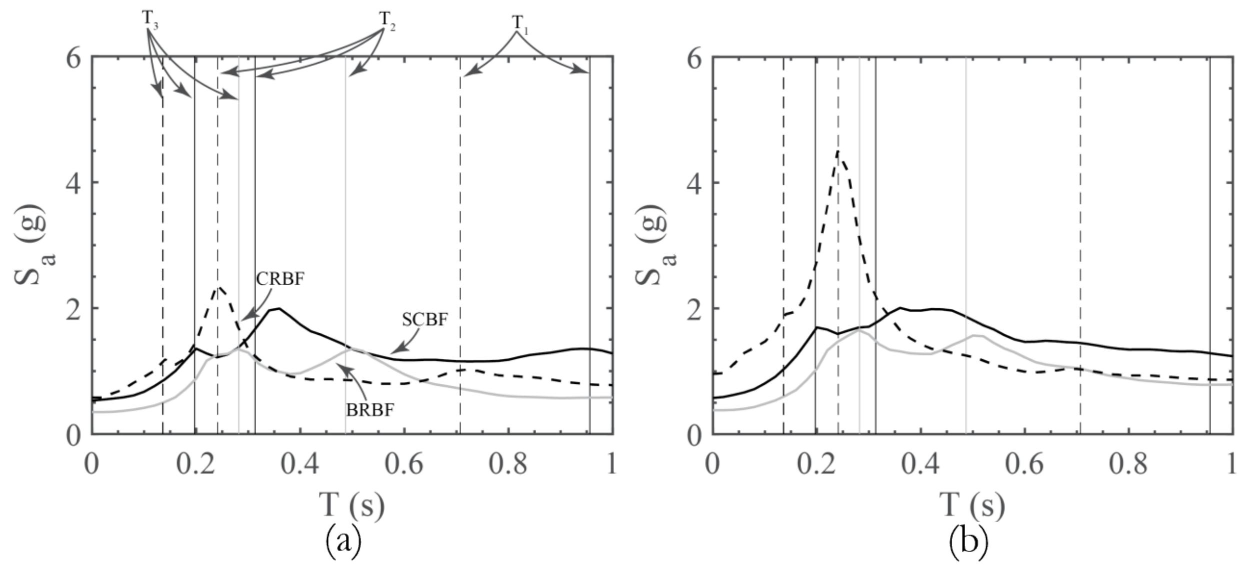

Figure 6. Median top floor absolute acceleration response spectra: (a) 1/2DE level, (b) DE level.

6.Conclusion

A six-story building was designed separately with three different seismic force-resisting systems (SFRSs): a special concentrically braced frame (SCBF), a buckling-restrained braced frame (BRBF), and a controlled rocking braced frame (CRBF). Performing seismic loss assessment showed that the SCBF and CRBF buildings had the largest and lowest expected annual loss, respectively. The findings revealed that the total seismic loss for the BRBF and SCBF buildings was 1.5 times and twice as large as for the CRBF building, respectively. The primary reasons for the reduction of seismic loss in the CRBF building compared to the other two SFRS are: 1) the CRBF has self-centring behaviour, which reduces losses due to demolition loss because of excessive residual drift, and 2) the CRBF mitigates earthquake energy through a rocking mechanism, which reduces losses due to structural repair. However, the CRBF building had a larger calculated seismic loss due to acceleration-sensitive nonstructural components because of its greater acceleration demands compared to the other two systems. Overall, the findings confirmed that using CRBFs as an SFRS can be an attractive alternative to minimize the total seismic loss in buildings.

Current seismic loss estimation methodologies use peak floor accelerations (PFAs) to estimate the demands in acceleration-sensitive components regardless of their natural periods. The median top floor absolute acceleration response spectra, which are period-dependent, and top floor median PFAs of the three buildings were compared. Two phenomena were observed that raise questions about using PFAs as an appropriate engineering demand parameter (EDP) for the evaluation of seismic loss of nonstructural components. First, it was observed at half of the design earthquake (DE) intensity level that although PFAs were close to each other for all three buildings, this was not true at all periods. Second, at a higher intensity, such as DE level, a flattening in the spectrum of the SCBF and BRBF buildings occurred due to buckling and/or yielding of the brace members. However, because of the different mechanics involved in CRBFs, a large spike occurred in the top floor acceleration spectrum at the second modal period of the CRBF building. Comparing the PFAs of the three buildings at either intensity level does not reflect the differences in floor spectra at any given period. This suggests a need for further study of suitable EDPs for predicting losses to acceleration-sensitive nonstructural components.

REFERENCES

American Institute of Steel Construction (AISC). [2016] "Specification for structural steel buildings," *ANSI/AISC Stand. 360-16*. Chicago, IL, USA.

American Society of Civil Engineers (ASCE). [2017] "Minimum design loads and associated criteria for buildings and other structures," *American Society of Civil Engineers*, Reston, VA.

Baker, J. W. [2015] "Efficient analytical fragility function fitting using dynamic structural analysis," *Earthquake Spectra,* Vol. 31, No 1, pp. 579–599.

Banihashemi, A., and L. Wiebe. [2022] "Design of Low-Rise Controlled Rocking Braced Frames for Life Cycle Costs," *International Conference on the Behaviour of Steel Structures in Seismic Areas*, pp. 746-754, Springer.

Buccella, N., L. Wiebe, D. Konstantinidis, and T. Steele. [2021] "Demands on nonstructural components in buildings with controlled rocking braced frames," *Earthquake Engineering and Structural Dynamics*, Vol. 50, No. 4, pp. 1063-1082.

Dyanati, M., Huang, Q., and D. Roke. [2017] "Cost-benefit evaluation of self-centring concentrically braced frames considering uncertainties, " *Structure and infrastructure engineering*, Vol. 13, No. 5, pp. 537-553.

Erochko, J., Christopoulos, C., Tremblay, R., and Choi, H. [2011] "Residual drift response of SMRFs and BRB frames in steel buildings designed according to ASCE 7-05," *Journal of Structural Engineering,* Vol. 137, No. 5, pp. 589-599.

FEMA P-695. [2009] "Quantification of Building Seismic Performance Factors," Washington, D.C.: Federal Emergency Management Agency.

FEMA P-58-3. [2018] *Seismic Performance Assessment of Buildings, Volume 3–Supporting Electronic Materials and Background Documentation: 3.1 Performance Assessment Calculation Tool (PACT).* Version 3.1.2, Washington, D.C.: Federal Emergency Management Agency.

FEMA. [2014] "HAZUS-MH. 2.1 technical manual: Earthquake model Washington, D.C.: Federal Emergency Management Agency.

Hwang, S.-H., and D. G. Lignos. [2017] "Effect of Modeling Assumptions on the Earthquake-Induced Losses and Collapse Risk of Steel-Frame Buildings with Special Concentrically Braced Frames," *ASCE Journal of Structural Engineering*, Vol. 143, No.9, pp. 04017116–1.

OpenSees. [2011] "Open system for earthquake engineering simulation (OpenSees), v2.5.0," *Berkeley, CA, Pacific Earthquake Engineering Research Center.*

Ramirez, C. M., and E. Miranda. [2009] "Building-specific loss estimation methods and tools for simplified performance-based earthquake engineering (Report No. 171)" *John A. Blume Earthquake Engineering Center*, Stanford University.

RSMeans. [2020] "Commercial Renovation Cost Data," *Reed Construction Data, Norwell, MA, 569.*

Steele, T. C., and L. D. A. Wiebe. [2021] "Collapse risk of controlled rocking steel braced frames considering buckling and yielding of capacity-protected frame members," *Engineering Structures*, Vol. 237, pp. 111999.

Steele, T. C., and L. DA Wiebe. [2016] "Dynamic and equivalent static procedures for capacity design of controlled rocking steel braced frames," *Earthquake Engineering and Structural Dynamics*, Vol. 45, No. 14, pp. 2349-2369.

Tremblay, R., A. Fliatrault, M. Bruneau, M. Nakashima, H. G. Prion, and R. DeVall. [1996] "Seismic design of steel buildings: lessons from the 1995 Hyogo-ken Nanbu earthquake," *Canadian Journal of Civil Engineering*, Vol. 23, pp. 727-756, NRC Research Press Ottawa, Canada.

Tremblay, R., P. Timler, M. Bruneau, and A. Filiatrault. [1995] "Performance of steel structures during the 1994 Northridge earthquake," *Canadian Journal of Civil Engineering*, Vol. 22, No. 2, pp. 338-360.

Wiebe, L., and C. Christopoulos. [2015] "Performance-based seismic design of controlled rocking steel braced frames. I: methodological framework and design of base rocking joint," *Journal of Structural Engineering*, Vol. 141, No. 9, pp. 04014226.

Zsarnóczay, Á. [2019] "NHERI-SimCenter/pelicun: pelicun v2.0.0 (Version v2.0.0). Zenodo."

Zsarnóczay, Á. [2013] "Experimental and Numerical Investigation of Buckling Restrained Braced Frames for Eurocode Conform Design Procedure Development," *Individual Study*, Budapest University of Technology and Economics.

Wooden infills influence on the seismic performance of steel structures

Mattia Calò[1], Gianrocco Mucedero[2], Vanni Nicoletti[3] and Giammaria Gabbianelli[1]

[1] Department of Civil Engineering and Architecture, University of Pavia
Via Adolfo Ferrata 3, 27100, Pavia, Italy
mattia.calo01@universitadipavia.it; giammaria.gabbianelli@unipv.it
[2] University School for Advanced Studies IUSS Pavia
Piazza della Vittoria 15, 27100, Pavia, Italy
gianrocco.mucedero@iusspavia.it
[3] Department of Construction, Civil Engineering and Architecture, Marche Polytechnic University
Via Brecce Bianche, Ancona, 60131, Italy
v.nicoletti@univpm.it

Abstract. Infill walls are one of the most common non-structural elements worldwide adopted to build external and internal partition walls in framed structures. As well-known, infill walls may trigger undesirable effects on the building's seismic performance (e.g., soft-storey mechanism, shear failure of poorly detailed columns), reducing the building's overall ductility and leading to possible collapses. Furthermore, the infill damage can lead to a loss of building functionality and occupancy, which in turn leads to downtime and indirect economic losses. For these reasons, infill presence should be considered during the design process of new buildings and in assessing the existing ones.

Conversely to masonry enclosure walls, few studies have investigated wooden infills, which represent an attractive solution compared to the classical ones, and their effects on the structural response of steel buildings are currently recognised as a key issue. With such consideration in mind, this paper deals with the evaluation of the wooden infill effects on the seismic performance of a real framed building located in Italy. The building is a two-storey steel frame structure with steel-concrete composite floors and with external infills built with wooded panels. At first, dynamic tests were performed on the bare and infilled building with the aim of investigating the infills contribution to the dynamic properties of the structure. Moreover, the modal parameters identified through in situ dynamic tests are adopted to calibrate the numerical model and to obtain more trustworthy numerical outcomes. Therefore, nonlinear dynamic analyses were performed, establishing the infills contribution to the seismic performance of the structure, with a focus on low return period earthquakes. Numerical outcomes highlighted the impact of the wooden infills on the dynamic response and structural behaviour of the two-storey building analysed, though not as significantly as could be expected in case of masonry enclosure walls.

Keywords: Infilled steel structures, Wooden infills, In situ dynamic tests, Nonlinear dynamic analyses, Multiple-stripe analyses.

1. INTRODUCTION

Infill walls in framed structures are one of the most common non-structural elements worldwide adopted to build external and internal partition walls [Nicoletti *et al.*, 2022a; Mucedero *et al.*, 2021]. Their widespread use is due to many advantageous aspects, along with the constructive easiness, the high versatility and the possibility to easily realise acoustical and thermal insulation by adding insulation layers to these elements. Moreover, the infill layout and openings can be modified during the building life usually without the need of changing the structural members and, hence, without the need to perform a structural assessment. In designing new framed buildings and assessing the existing ones, it is common practice to neglect the presence of these non-structural elements and to consider them only in terms of added masses and loads on the bare structure. However, this simplified assumption that leads to reasonable and acceptable simplifications in the structural design can also lead to disregarding detrimental interactions between structural and non-structural elements which can trigger undesirable effects on the building's seismic performance (e.g., soft-storey mechanism, shear failure of short unconfined columns), reducing the building's overall ductility and leading to possible collapses [Furtado *et al.*, 2019; De Angelis and Pecce, 2019]. Therefore, it is evident the need to consider infills also in terms of added stiffness and consequently to adopt suitable techniques to model these non-structural elements within building numerical models. The simplest way to model infills within a structural frame is by means of macro-modelling techniques, such as using one or multiple diagonal struts, that also allow taking into account the linear and nonlinear behaviour of the non-structural component [Stafford-Smith and Carter, 1969; Mainstone, 1974]. However, due to the wide range of variability surrounding the infill properties, the standardisation of parameters through which these struts are modelled is rather tricky to be used worldwide; the parameters defining the equivalent strut's hysteretic behaviour should not be selected a priori, but rather calibrated considering the specific features of each masonry [Mucedero *et al.*, 2020]. With such consideration in mind, to the authors' best knowledge at least, the possibility to perform tests on real infilled structures may conduce to an in-deep knowledge of the building behaviour and to an improvement of the modelling strategies, both for structural and non-structural elements. Among others, vibration-based tests and, in particular, Ambient Vibration Tests (AVTs) are nowadays gained wide usage since they are fast and easy to perform in real buildings, also without the interruption of the building occupancy and functionality [Nicoletti *et al.*, 2022b]. These tests, in conjunction with Operational Modal Analyses (OMAs), allow the identification of the actual dynamic behaviour of the tested building under its operative conditions. The identified dynamic behaviour can be adopted for many purposes, along with the calibration of numerical models that can be used to develop analysis and seismic assessment of buildings.

This paper proposes an investigation of the wooden infill effects on the seismic performance of a real framed building located in Italy. The considered building is a two-storey steel frame structure with steel-concrete composite floors and external infills built with wooded panels, herein also called Oriented Strand Board (OSB). The building has an irregular plan shape, with maximum dimensions of 35 x 40.3 m, and a total height of about 7 m. In Figure 1 the ground floor plan and some pictures relevant to the building during its construction process and to the adopted wooden infills are illustrated. For what concerns the paper contents, the real dynamic behaviour identified through AVTs is illustrated in Section 2, where also a comparison between the bare and infilled frame dynamics is proposed. The real dynamic behaviour is also used as a benchmark for the calibration of the numerical model (well described in Section 3) that was developed to perform the seismic analyses, whose results are reported in Section 4. In particular, nonlinear dynamic analyses are performed to investigate the infill contribution to the seismic performance of the building case study with a focus on low return period earthquakes. Also, the record selection for the nonlinear analyses is discussed in Section 3.

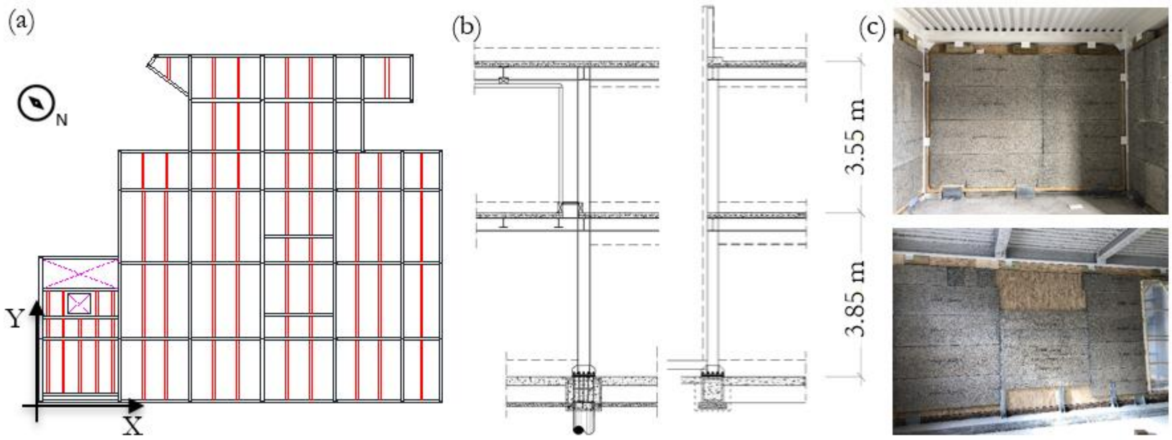

Figure 1. Building case study: (a) ground floor plan, (b) elevation scheme, (c) adopted wooden infills

2.INVESTIGATION OF BUILDING DYNAMIC PROPERTIES

The real building dynamic properties were investigated by performing in situ dynamic tests in key stages of the construction process, namely at the end of the bare frame construction and when all the perimetric wooden infills were mounted. Two AVTs were performed, both adopting the same instrumentation and sensors layout. In detail, four high-sensitivity and high-resolution accelerometers were deployed on the first floor and on the roof floor slabs, two measuring in X and two in Y directions on each floor. All sensors were connected by means of coaxial cables to 3-channels Data Acquisition (DAQ) modules mounted on a USB chassis. A notebook equipped with dedicated software was adopted to store data and to real-time checking the dynamic tests. The two tests were performed by measuring the accelerations produced by the so-called ambient noise for a time length of about 20 minutes for each test. This sensors layout permitted to investigate the global dynamic behaviour of the building, which is identified through the OMA methodology, exploiting the use of the Stochastic Subspace Identification – Principal Component (SSI-PC) [Van Overschee and De Moor, 1996] technique. After the identification procedures, eleven and nine global vibration modes are identified considering the bare and the infilled structure, respectively. The relevant periods and damping ratios are listed in Table 1 for the bare frame and in Table 2 for the infilled building, whilst in Figure 2 the mode shapes relevant to the fundamental vibration mode for the bare and infilled structure are depicted. The latter modes mobilize the majority of the modal participating mass and, as can be seen from Figure 2, their deformed shapes are mainly translational in Y direction, with a slight couplement with the torsional rotation.

Comparing results before and after the infills construction, it is evident that all periods shortened after infill installation, demonstrating a lateral stiffness increment provided by the non-structural elements; in detail, for the fundamental mode, the period reduction is about 7%.

Table 1. Periods and damping ratios identified for the bare frame.

Mode n.	1	2	3	4	5	6	7	8	9	10	11
Period [s]	0.42	0.32	0.29	0.27	0.23	0.19	0.17	0.15	0.14	0.10	0.09
Damping ratio [%]	0.40	0.52	0.72	0.84	0.54	0.46	0.63	0.32	0.33	0.52	0.94

Table 2. Periods and damping ratios identified for the infilled frame.

Mode n.	1	2	3	4	5	6	7	8	9
Period [s]	0.39	0.28	0.22	0.18	0.14	0.13	0.12	0.10	0.08
Damping ratio [%]	1.38	1.89	1.84	2.03	2.20	1.84	0.98	1.35	1.29

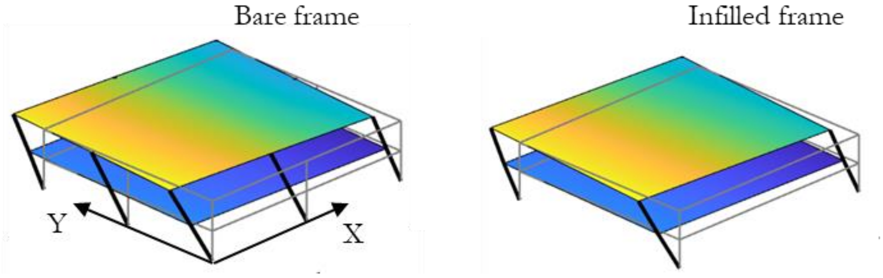

Figure 2. Mode shapes of the fundamental vibration mode before and after the infill construction

Conversely, the damping ratios generally increase when the infills are accounted for, demonstrating an increase in the building dissipative capabilities, albeit they are quite low (maximum damping of 2.20%).

3.NUMERICAL MODEL

The three-dimensional numerical model of the steel structure was developed in the finite element software SeismoStruct [SeismoSoft, 2022]. In accordance with the case study, a steel material belonging to class S355 [EN1993-1-1, 2014] with a bilinear hysteretic behaviour was adopted. As regards the columns and beams, a displacement-based beam-column element with two integration points was selected [Reissner, 1981], enabling the use of fibre cross sections, with an approximate number of 150 fibres for each section. In such a way, the model was able to reproduce accurately the material nonlinearities induced by the seismic actions. To capture the geometrical nonlinearities and P-delta effects, the corotational formulation [Correia and Virtuoso, 2008] provided by the software SeismoStruct [SeismoSoft, 2022] was included in the model. In addition, as a consequence of the high stiffness of the slabs, a floor constraint, i.e. a rigid diaphragm, was included on each floor. Regarding the connections between columns and beams, and between columns and the ground floor, full-stiffness/full-strength joints were modelled, following the indications of the building design. Moreover, in order to perform nonlinear time-history analyses, 3% tangent stiffness proportional damping was set for the first mode of vibration resulting from eigenvalue analysis [Petrini *et al.*, 2008]. In Figure 3 the three-dimensional numerical model developed in SeismoStruct [SeismoSoft, 2022] is depicted, with the reference orientation system considered for the analyses.

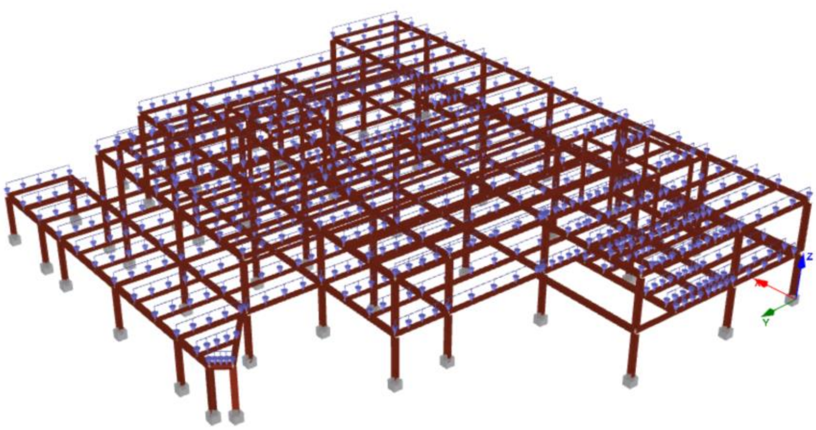

Figure 3. Numerical model of the steel structure case study developed in the finite element software SeismoStruct [SeismoSoft, 2022]

Concerning the modelling of the wooden infills, the indications of Pintarič and Premrov [2013] were followed. In particular, similarly to the modelling of masonry infills [Mucedero *et al.*, 2020, 2021], the stiffness contribution of the wooden infill is considered using a braced frame with one fictive diagonal. Regarding the thickness of the wooden panels, it was considered equal to 18 mm, for both the internal and external OSB panels, according to the original drawing of the building. For further details regarding the numerical modelling please refer to Pintarič and Premrov [2013], whereas for the standard values of wooden infills, refer to Dataholz [2022].

3.1 CALIBRATION OF THE NUMERICAL MODEL

Before performing seismic analyses, the developed numerical model was adjourned and validated in order to faithfully represents the real dynamic behaviour of the building, the latter obtained from in situ dynamic tests (AVTs). The calibration procedure is based on the comparison between the numerical and experimental mode periods: if these quantities match each other well, the model is considered calibrated. Obviously, to compare the building's numerical dynamic behaviour with the experimental one, some modifications are strictly necessary; for example, the loads (and consequently the masses) applied to the model must be modified to account for the actual loads effectively acting on the building at the time of the test executions. For this reason, live and permanent loads are deleted since only the structural part of floors was present during tests. Moreover, for the model with infills, the stiffness of the non-structural components was modified (reduced by 50%) to account for the presence of the openings (windows and doors) since the adopted infill model [Pintarič and Premrov, 2013] considers only full filled panels. The periods obtained by the bare and infilled numerical models are compared with the experimental ones in Figure 4. Here it is possible to observe that these models are well calibrated because differences between periods are almost negligible for the first vibration modes (the first five and three for the bare and infilled models, respectively), while they slightly increase for the superior ones. However, for the considered building, the first modes are those with the higher participant mass percentages, so they are those of greater interest for the subsequent seismic analyses. Accordingly, both models accurately reproduce the actual building dynamic behaviour, so they can be considered validated.

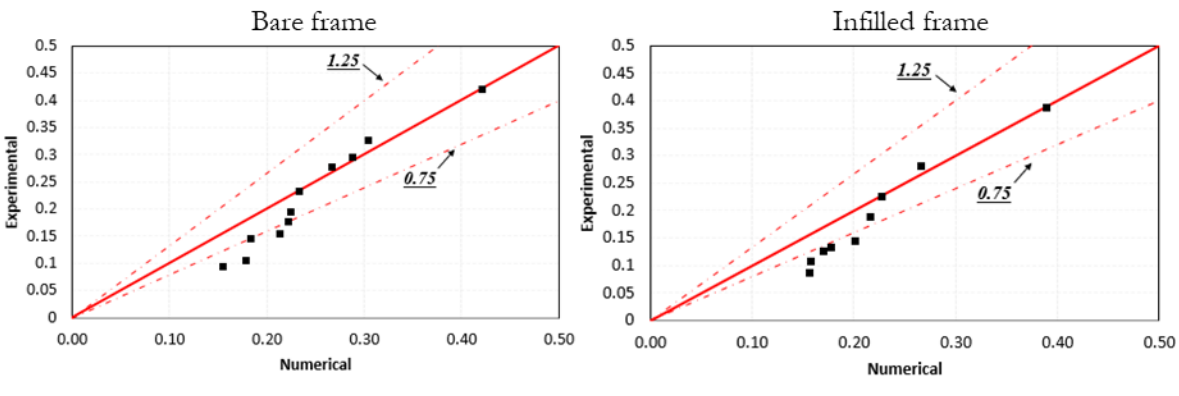

Figure 4. Comparisons between numerical and experimental periods for the bare structure and the infilled building during the construction process

3.2 RECORD SELECTION

The Probabilistic Seismic Hazard Analysis (PSHA) was performed to obtain the seismic inputs for the nonlinear time-history analyses. The PSHA for the city where the building stands, which is classified as a medium-high seismic zone according to the Italian code [NTC18, 2018], was carried out with the dedicated tool REASSESS V2.1 [Chioccarelli *et al.*, 2019]. The selection foresaw a category soil C, in accordance with the Eurocode 8 [EN1998-1, 2011] classification. Considering the indications of the Italian Standard [NTC18, 2018], office buildings with regular crowd of people can be classified with an importance class II, which leads to a nominal life of 50 years. It should be noted that the knowledge of the nominal life of the structure permits defining the Return Period (RP) associated with the probability of exceedance of the seismic actions related to different limit states. As a matter of fact, the commonly adopted limit states, i.e. Immediate Occupancy (IO), Damage Control (DC), Life Safety (LS) and Collapse Prevention (CP), are associated with the probability of exceedance of 81%, 63%, 10% and 5%, respectively (i.e. four different RPs). This leads to defining the seismic actions with an RP of 30, 50, 475 and 975 years for the four above-mentioned limit states, respectively. However, since this study aims to investigate the influence of wooden infills at low seismic intensities, the RP of 50 years, which is associated with the Damage Control (DC) limit state, was considered. For the adopted RP, a total of 20 pairs of ground motion records in two horizontal components were selected; as Intensity Measure (IM), the Average Spectral Acceleration (AvgSA) proposed by [Kohrangi *et al.*, 2017] was assumed, with the advantage of performing a single selection suitable for both the modelling with and without the wooden infills. The records' scaling factors varied between 0.5 and 2.0, and the compatibility of the AvgSA was imposed in the range of periods between 0.05s and 1.1s. Note that for both models, the first fundamental periods, including the masses for the seismic combination [NTC18, 2018], are about 0.71s and 0.61s for the bare and infilled building, respectively. Figure 5 illustrates the Uniform Hazard Spectrum (UHS), Conditional Spectrum (CS), median spectrum ± standard deviation and single spectra of the selected records.

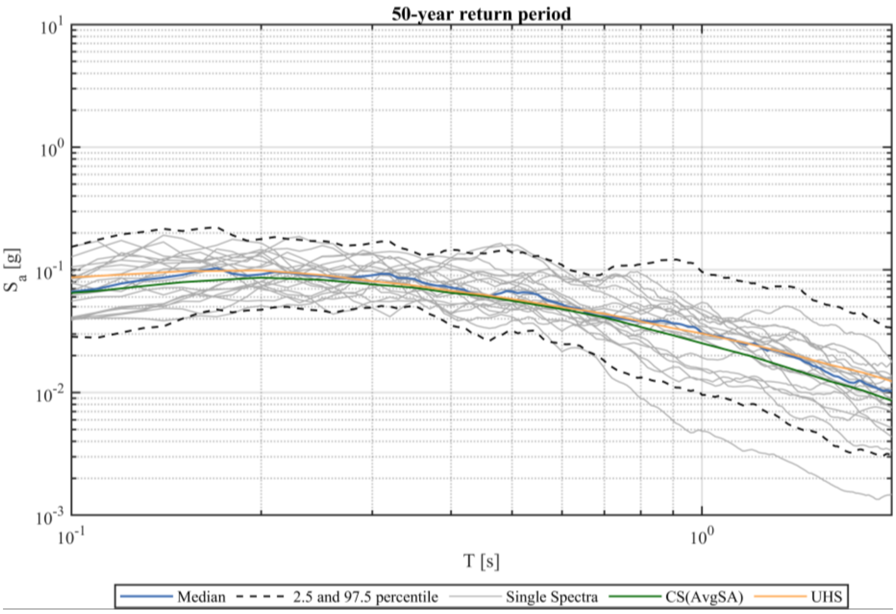

Figure 5. UHS, CS(AvgSA), median spectrum, median spectrum plus standard deviation and single spectra for the return period of 50 years

4. RESULTS OF THE NONLINEAR TIME-HISTORY ANALYSES

Nonlinear time-history analyses were performed in order to investigate the influence of the wooden infills in the seismic response of the building. For these analyses, both the numerical models (the bare and the infilled ones) are further modified from the calibration phase, adding all the loads that are commonly considered in the design of new structures (permanent and live loads). The acceleration and displacement time-histories derived for each floor of the structure were processed to obtain peak acceleration and drift profiles, both for X and Y directions; this endeavour permits the quantification of the structural seismic response and performance for the selected RP (50 years).

4.1 INTERSTOREY DRIFT PROFILES

The interstorey drift ratio (IDR) profiles and the IDR values (represented by the square markers) for each record are presented in Figure 6; moreover, the results are presented in a statistical fashion with the mean (μ) and the dispersion (μ ± the standard deviation (σ)) of the IDR values for the OSB and the bare structure configurations. The representation of σ provides an insight of the dispersion due to the aleatory uncertainties (or equivalently randomness due to record-to-record variability) in the IDR profiles when a building is subjected to different ground motions records. As far as the X direction is considered, the mean IDR for the first and second floors of the OSB structure configuration are 0.037% and 0.053%, respectively, whereas 0.038% and 0.056% for the bare structure configuration. As regards the dispersion, the IDR values for the first and second floors are respectively 0.051% and 0.072% for the OSB and, respectively, 0.056% and 0.078% for the bare structure configuration. Therefore, μ + σ defines an IDR increment with respect to the μ IDR of 38% (σ=0.014) and 36% (σ=0.019) for the first and second floors of the OSB structure configuration and an increment of 47% (σ=0.018) and 39% (σ=0.022) for the bare structure configuration. Therefore, the OSB determines a slight reduction in terms of mean IDR profile, though not as significantly as could be noticed in case of classical masonry enclosure walls; moreover, higher dispersion was noticed in the results of bare structural configuration with respect to that obtained for the OSB counterparts.

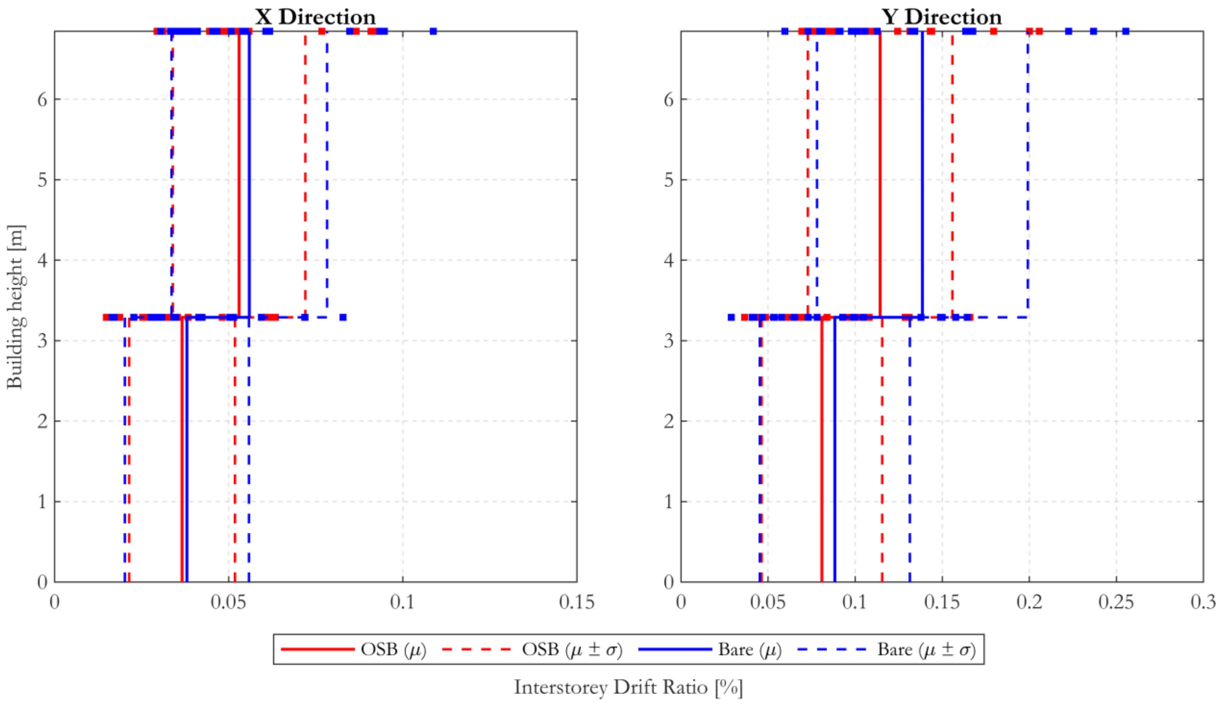

Figure 6. Interstorey drift profiles for the X and Y directions of the building

As concerns the Y direction, similar considerations can be observed. The mean IDR values for the first and second floors for OSB model are 0.081% and 0.114%, whereas, for the bare structural configuration, the values are 0.088% and 0.139%. Considering the dispersion (μ + σ), for the OSB structure, the IDR values are instead about 0.116% and 0156% for the first and second floors, respectively, and for the bare structure are 0.131% and 0.199%. In this case, the differences in IDR are also significant for the mean values, for which for the second floor there is an increment, for the bare model, of 22%. The increment in terms of μ + σ with respect to μ is equal to 43% (σ=0.035) and 37% (σ=0.042) for the OSB frame on the first and second floor, and 49% (σ=0.043) and 43% (σ=0.060) for the bare frame in the first and second floor, respectively. Also in Y direction, the dispersion of IDR in the OSB structure configuration is less than that obtained for the bare frame counterparts.

4.2 PEAK-FLOOR ACCELERATION PROFILES

As regards the peak floor acceleration (PFA) profile, a similar format to the drift profiles was adopted and plotted in Figure 7. As can be easily deducted, there is no distinction between the models if the peak ground acceleration is taken into account. On the contrary, for both directions, a distinction has to be made between the two numerical modelling approaches for the first and second floors. The PFA mean μ for the first floor in the X direction is 0.455g and 0.429g for the OSB and bare models, respectively. The standard deviation σ is about 0.143g and 0.123g, again for the OSB and bare frames, respectively. The same outcomes for the second floor are 0.779g and 0.726g (μ) and 0.302g and 0.296g (σ). Such results entail the fact that the stiffening effect of the infills increases the peak floor accelerations, notwithstanding it can not be appraised a significant increase of the PFA dispersion.

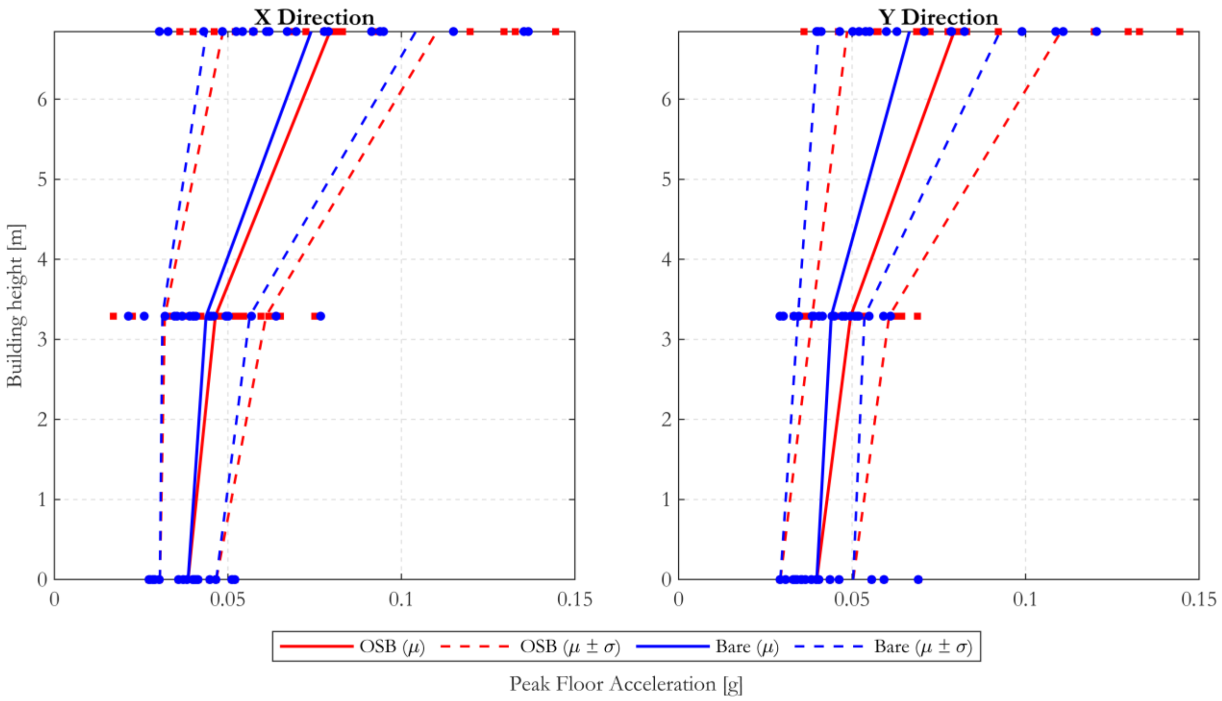

Figure 7. Peak floor acceleration profiles for the X and Y directions of the building

Again, similar considerations can be made in direction Y, for which the mean PFAs are 0.487g and 0.779g for OSB structure on the first and second floors and 0.432g and 0.653g for the bare structure on the first and second floors, respectively. In this case, the standard deviations are 0.109g and 0.302g (OSB model) and 0.094g and 0.256g (bare model) for the first and second floors, respectively. For this direction (Y), the presence of the wooden infills increases the peak floor acceleration by 13% and 19% for the first and second floors.

5. CONCLUSIONS

This paper proposed an investigation of the wooden infill effects on the seismic performance of steel frame buildings. The study was conducted with reference to a real case study located in Italy, which consisted of a two-storey steel frame structure with steel-concrete composite floors and with external infills built with wooded panels. An in-situ experimental campaign was performed, consisting of ambient vibration tests performed in key stages of the building construction, namely at the end of the bare frame construction and after the infill mounting. These tests allowed the identification of the building's dynamic properties, which were used to investigate the contribution of infills to the lateral stiffness of the whole building, as well as to calibrate and validate the numerical model developed to perform the seismic analyses. The numerical model of the whole building was developed with the commercial finite element software SeismoStruct and, in detail, two numerical models were considered: the first one referring to the bare frame and the second one to the infilled structure in which the wooden infills were modelled with diagonal strut elements.

In order to conduct a correct comparison among the two different models, a suitable record selection independent of a single conditional period, different for each model, was performed. In particular, the average spectral acceleration as intensity measure was selected, enabling the adoption of a quite wide range of conditional spectral periods for computing the target spectrum. Therefore, such approach permits to perform nonlinear time history analyses, for the two models, with the same seismic input, allowing a direct comparison of the outcomes.

Comparing the identified dynamic properties before and after the infill construction, it is possible to assert that the global lateral stiffness increases due to the infills contribution, as demonstrated by the lower vibration mode periods obtained after the infill positioning. Nevertheless, the stiffness increase provided by the wooden panels is not so high since the fundamental period slightly reduces (about 7%).

As regards the numerical analyses, the interstorey drift profiles highlighted the beneficial effect of the wooden infills in reducing the mean interstorey drift ratio. In addition, it should be noted that the infill contribution also reduces the dispersion of the interstorey drift ratio, slightly stabilising the seismic response of the structure. However, the drift reduction of the wooden panels is not comparable with the one generally provided by the traditional masonry infills. As a counterpart of such result, the expected high increase of the peak floor acceleration values with the masonry infills is not seen in this study with the more flexible wooden panels, giving hence a glimpse of its potentiality and feasibility in seismic applications.

However, further investigations are necessary to corroborate the present findings, explore the nonlinear response of wooden panels, estimate the differences in floor absolute acceleration response spectra, and understand the consequences of its adoption considering the economic losses.

REFERENCES

Chioccarelli, E., Cito P., Iervolino I., Giorgio M. [2019] "REASSESS V2.0: Software for Single- and Multi-Site Probabilistic Seismic Hazard Analysis," *Bulletin of Earthquake Engineering*. https://doi.org/10.1007/s10518-018-00531-x.

Correia, A.A., Virtuoso, F.B.E. [2008] "Nonlinear Analysis of Space Frames". *III European Conference on Computational Mechanics*. https://doi.org/10.1007/1-4020-5370-3_107.

Dataholz [2022] "Catalogue of Reviewed Timber Building Components," https://Www.Dataholz.Eu/En.Htm. 2022.

De Angelis, A., Pecce, M.R. [2019] "The Structural Identification of the Infill Walls Contribution in the Dynamic Response of Framed Buildings," *Structural Control and Health Monitoring* 26 (9). https://doi.org/10.1002/stc.2405.

EN1993-1-1. 2014. *Eurocode 3: Design of Steel Structures - Part 1-1: General Rules and Rules for Buildings*. European Committee for Standardisation, Brussels, Belgium.

EN1998-1. 2011. *Eurocode 8: Design of Structures for Earthquake Resistance - Part 1: General Rules, Seismic Actions and Rules for Buildings*. European Committee for Standardisation, Brussels, Belgium.

Furtado, A., Vila-Pouca N., Varum H., Arêde, A. [2019] "Study of the Seismic Response on the Infill Masonry Walls of a 15-Storey Reinforced Concrete Structure in Nepal," *Buildings* 9 (2). https://doi.org/10.3390/buildings9020039.

Kohrangi, M., Bazzurro, P., Vamvatsikos, D., Spillatura, A. [2017] "Conditional Spectrum-Based Ground Motion Record Selection Using Average Spectral Acceleration," *Earthquake Engineering and Structural Dynamics*. https://doi.org/10.1002/eqe.2876.

Mainstone, R J. [1974] "Supplementary Note on the Stiffness and Strength of Infilled Frames," Watford, U.K.

Mucedero, G., Perrone, D., Monteiro, R. [2021] "Nonlinear Static Characterisation of Masonry-Infilled RC Building Portfolios Accounting for Variability of Infill Properties," *Bulletin of Earthquake Engineering* 19 (6). https://doi.org/10.1007/s10518-021-01068-2.

Mucedero, G., Perrone, D., Brunesi, E., Monteiro, R. [2020] "Numerical Modelling and Validation of the Response of Masonry Infilled RC Frames Using Experimental Testing Results," *Buildings*. https://doi.org/10.3390/buildings10100182.

Nicoletti, V., Arezzo, D., Carbonari, S., Gara, F. [2022a] "Dynamic Monitoring of Buildings as a Diagnostic Tool during Construction Phases," *Journal of Building Engineering* 46. https://doi.org/10.1016/j.jobe.2021.103764.

Nicoletti, V., Arezzo, D., Carbonari, S., Gara, F. [2022b] "Vibration-Based Tests and Results for the Evaluation of Infill Masonry Walls Influence on the Dynamic Behaviour of Buildings: A Review," *Archives of Computational Methods in Engineering*. https://doi.org/10.1007/s11831-022-09713-y.

NTC18. 2018. *Norme Tecniche per Le Costruzioni. DM 17/1/2018*. Gazzetta Ufficiale della Repubblica Italiana, Italian Ministry of Infrastructure and Transport, Rome, Italy.

Petrini, L., Maggi, C., Priestley, M J.N., Calvi, G.M. [2008] "Experimental Verification of Viscous Damping Modeling for Inelastic Time History Analyzes," *Journal of Earthquake Engineering*. https://doi.org/10.1080/13632460801925822.

Pintarič, K., Premrov, M. [2013] "Mathematical Modelling of Timber-Framed Walls Using Fictive Diagonal Elements," *Applied Mathematical Modelling* 37 (16–17): 8051–59. https://doi.org/10.1016/j.apm.2013.02.050.

Reissner, E. [1981] "On Finite Deformations of Space-Curved Beams," *ZAMP Zeitschrift Für Angewandte Mathematik Und Physik* 32 (6). https://doi.org/10.1007/BF00946983.

SeismoSoft. 2022. 'SeismoStruct - Earthquake Engineering Software Solutions'. *Official Reseller Mosayk Srl, Www.Mosayk.It.*

Stafford-Smith, B., Carter, C. [1969] "A Method for Analysis for Infilled Frames,". *Proceedings of the Institution of Civil Engineers* 44 (1). https://doi.org/10.1680/iicep.1969.7290.

Van Overschee, P., De Moor, B. [1996] "Subspace Identification for Linear System: Theory - Implementation – Applications," *Conference Proceedings of the International Conference of IEEE Engineering in Medicine and Biology Society* 2008.

Customized Tools for Assessing Nonstructural Element Vulnerabilities in Hospitals in Nepal and Myanmar

Janise Rodgers[1], Hari Kumar[1], William Holmes[2], Yeshey Lotay[1], Dinesh Joshi[1], and Upama Ojha[1]

[1] GeoHazards International
6701 Koll Center Pkwy, Suite 250, Pleasanton, CA 94566
e-mail: rodgers@geohaz.org, hari@geohaz.org, yeshey@geohaz.org, joshi@geohaz.org, upama@geohaz.org
[2] Consultant, Oakland, CA
wholmes@ruthchek.com

Abstract. Hospitals depend on the performance of non-structural elements to protect staff and patients, and to maintain medical service delivery during the critical post-earthquake period when injured people seek care. In many Global South countries with high earthquake risk, non-structural elements in most hospitals have not been seismically protected, or have been protected only in very recently built hospitals. Economically addressing the potential impacts of non-structural elements on the seismic performance of these hospitals is an essential part of the overall process of improving facility seismic performance. We developed two customized rapid screening tools, for Nepal and Myanmar, which are intended to provide an economical and time-efficient method to identify major vulnerabilities across a portfolio of hospital buildings; provide key inputs for program-level decision-making; and provide individual facility assessments focused on potential impacts to essential medical service delivery. These tools are locally customized versions of the World Health Organization's Global Hospital Safety Index (HSI). The Global HSI is a checklist-based tool with a scoring system, which covers hazards (Module 1), and structural (Module 2) and non-structural (Module 3) aspects of hospital buildings along with the hospital's emergency and disaster preparedness (Module 4).

Key modifications to the lengthy non-structural module included: (a) addressing hospitals with multiple medical buildings (the Global HSI assumes major services are in a single building, which is typically not the case in South Asia) by developing a weighting system to combine individual building scores based on importance of medical functions in the building; (b) splitting the module into facility-wide and building specific portions; and (c) updating the checklist items to account for common systems and equipment present in local hospitals. The non-structural module received significant use and testing, in particular by the authors, prior to customization, and further testing of the customizations is anticipated after the COVID-19 pandemic.

Keywords: Hospital, Index, Safety, Screening, Checklist/Tool.

1. BACKGROUND

1.1 NON-STRUCTURAL SEISMIC VULNERABILITIES IN HOSPITALS

Hospitals depend on an array of building systems, medical equipment, architectural elements and contents to provide a functional, infection-controlled, and safe environment in which personnel can deliver medical services. These non-structural elements are critical for hospital function but are often vulnerable to earthquake damage. Numerous hospitals have experienced substantial losses in functionality due to non-structural damage despite minimal structural damage in past earthquakes, including in the 1994 M6.7 Northridge [Schultz et al., 2003]; 2010 M8.8 Maule, Chile [Kirsch et al., 2010; Mitrani-Reiser et al., 2012]; and 2011 Christchurch [Jacques et al., 2014] earthquakes. Figure 1 provides an example. In addition, hospital non-structural components and systems in a number of high-hazard, low- and middle-income countries are typically not seismically protected because building codes either lack non-structural provisions or incorporated them very recently [Achour et al., 2011; Rodgers et al., 2012; Dixit et al., 2014]. A number of studies discuss the impacts of non-structural component damage on hospital facility resilience [e.g., Myrtle et al., 2005; Bruneau and Reinhorn, 2007; Jacques et al., 2014; Fallah-Aliabadi et al., 2020].

Figure 1. Damage to suspended ceilings, lighting, and associated building systems in a hospital corridor, 2010 M8.8 Maule, Chile earthquake (Photo: William T. Holmes)

1.2 THE HOSPITAL SAFETY INDEX (HSI)

Amid ongoing concerns about the safety and functionality of hospitals during earthquakes and other natural hazard events, global initiatives such as the World Health Organization (WHO)'s Hospitals Safe from Disasters initiative and Safe Hospitals Initiative [World Health Organization, 2015] have highlighted the need to assess the risks from natural hazards that hospitals face. To help address the need for a rapid and inexpensive method of performing initial assessments, following the 2005 World Conference on Disaster Reduction in Kobe, Hyogo Prefecture, Japan, the Pan American Health Organization (PAHO) developed and published the Hospital Safety Index, or PAHO HSI [PAHO, 2008]. (WHO Europe also published a different checklist-based rapid assessment tool [WHO Europe, 2006]).

In 2014, WHO developed the Global Hospital Safety Index, or Global HSI, [World Health Organization and Pan American Health Organization, 2015] by modifying the original PAHO HSI to support its use worldwide. The Global HSI screens hospitals for threats to safety and functionality from hazards. It collects basic hospital information (e.g., services, numbers of beds and staff) and has four checklist-based modules:

- Module 1: Hazards Affecting the Safety of the Hospital and the Role of the Hospital in Emergency and Disaster Management
- Module 2: Structural Safety
- Module 3: Nonstructural Safety
- Module 4: Emergency and Disaster Management

Both the PAHO HSI and Global HSI are multi-hazard, with a focus on seismic and to a lesser extent wind, with some consideration of flooding and fire, primarily in the non-structural module. Module 1 on hazards is intended to comprehensively capture natural, technological, sociological and environmental hazards to the hospital and its catchment areas, and is not directly connected to Modules 2-4. The Global HSI scoring system that generates index scores for Modules 2-4 individually and then combines them into a facility-wide index score between 0 and 1. Facilities are then placed in three broad categories: A (0.66-1) carry out measures medium to long term; B (0.36-0.65) intervention needed in short term; and C (0-0.35) urgent intervention needed. Module 3 is intended to provide vulnerability information for a wide range of non-structural components and systems. Figure 2 shows an example of the Global HSI Module 3 checklist format and typical questions.

3.3 Critical systems	**Safety level**			**Observations (evaluators' comments)**
	Low	**Average**	**High**	
3.3.1 Electrical systems				
38. Capacity of alternate sources of electricity (e.g. generators) *Safety ratings: Low = Alternate source(s) is(are) missing or covers less than 30% of demand in critical areas, or can only be started manually; Average = Alternate source(s) covers 31–70% of demand in critical areas and starts automatically in less than 10 seconds in critical areas; High = Alternate source(s) start(s) automatically in less than 10 seconds and cover(s) more than 70% of demand in critical areas.*	☐	☐	☐	
39. Regular tests of alternate sources of electricity in critical areas *Safety ratings: Low = Tested at full load every 3 months or more; Average = Tested at full load every 1 to 3 months; High = Tested at full load at least monthly.*	☐	☐	☐	
40. Condition and safety of alternate source(s) of electricity *Safety ratings: Low = No alternate sources; generators are in poor condition, there are no protective measures; Average = Generators are in fair condition, some measures provide partial protection and security; High = Generators are in good condition, well-secured and in good working order for emergencies.*	☐	☐	☐	

Figure 2. Excerpt from Module 3 Checklist (from WHO Evaluator's Guide, 2015)

Module 3 has subsections for architectural elements, egress and access, critical systems (electrical, telecommunications, water supply, fire protection, waste management, fuel storage, medical gases, heating, ventilation and air conditioning), and equipment and supplies (office, storeroom, medical and laboratory). Beyond providing a score, the questions can be used as an educational tool for hospital administrators, who may be unaware, for example, that WHO recommends that hospitals have on-site water storage sufficient to provide 300L per bed per day for three days.

The HSI family of hospital assessment methodologies has limitations typical of other rapid visual assessment methods: findings are based on visual inspection only, without engineering calculations, non-destructive testing, or intrusive/destructive testing or material sampling. The original PAHO and Global HSI also have several other limitations, discussed in detail in subsequent sections.

1.3 Prior use of the Hospital Safety Index leading up to customization efforts

GeoHazards International (GHI) began using the non-structural module of the PAHO HSI in 2012 (without scoring) as part of a methodology for initial seismic vulnerability assessments of Bhutan hospitals for WHO [e.g., Rodgers et al., 2012], and for assessment of non-structural component and system vulnerabilities of Kathmandu, Nepal hospitals for WHO under the Nepal Risk Reduction Consortium [e.g., Mitra et al., 2013]. Following this, GHI continued using the non-structural module in assessments, and also began working with WHO on the Global HSI.

GHI and WHO conducted two field tests of the nearly-final Global HSI in August 2014 in Honiara, Solomon Islands and in December 2014 in Kathmandu, Nepal, just a few months before the April 28, 2015 M7.8 Gorkha earthquake. The field tests resulted in several recommendations, including to address hospitals with multiple medical buildings and to consider modifying the structural module (Module 2) to better address vulnerabilities specific to structural system type. These were not implemented by WHO during the 2015 Global HSI finalization and dissemination process, primarily due to time and resource constraints. In late 2016, WHO requested that GHI compare pre-earthquake Global HSI findings with 2015 earthquake impacts, which took place with site visits and field interviews in early 2017. Hospitals assessed had not experienced in 2015 the strong ground motions assumed during the 2014 Global HSI field test, but the comparison produced several additional recommendations for changes.

Based on the findings from GHI's comparison of Global HSI findings and 2015 earthquake damage, and consultations with the Government of Nepal, it was determined that the HSI could be useful for Nepal, though it would need customization to local conditions. Customization efforts in Nepal began with joint assessments of four hospitals in the westernmost part of the country in January 2019 by GHI and engineers from the Department of Urban Development and Building Construction (DUDBC) and the Nepal Engineers Association (NEA). GHI then worked with WHO, the Ministry of Health and Population, DUDBC, and NEA to develop a customized version of the HSI for Nepal in 2019.

After conducting a small project to reduce risks from damage to non-structural components and systems in Myanmar hospitals, in 2020 GHI worked with the Federation of Myanmar Engineering Societies, Myanmar Earthquake Committee, and UN-Habitat Myanmar to prepare a customized HSI for Myanmar. The project team made additional customizations and adaptations to the Nepal-customized version. Subsequent sections discuss this work in Nepal and Myanmar in greater detail.

2.IDENTIFIED CUSTOMIZATION NEEDS

The efforts described in the background section generated substantive recommendations for modifications to the Global HSI, initially focused on changes necessary for Nepal but applicable to similar contexts, particularly elsewhere in South Asia. These customization needs included the following, focusing on the non-structural module (Module 3):

Multiple buildings: The Global HSI assumed most medical services were in a single hospital building but this is not the case in many hospitals in South Asia and elsewhere. Essential medical services can be dispersed across multiple buildings with varying structural types, ages and non-structural components and systems. The HSI lacked a method to consistently combine structural and non-structural module scores across multiple buildings (the guidance simply stated that evaluators were to "average" across buildings with no details provided). A related issue was that the non-structural module combined both sitewide and building-specific items, which needed to be split apart to properly address multiple buildings.

Water system vulnerabilities: The non-structural module did not address several readily field-observable vulnerabilities including seismic protection for pipes or drinking water treatment equipment. In many South Asia hospitals, drinking water is treated or filtered on site.

Unreinforced masonry partitions: The scoring system underestimated the potentially severe impacts to medical service delivery from damage to the unreinforced brick partitions and infill walls that are very common in South Asia. At Kathmandu's Bir Hospital, two of seven inpatient Operation Theatres (OTs) and one of two outpatient OTs were out of service for more than a month after the 2015 earthquake, due mainly to partition damage [Mitrani-Reiser et al., 2016], despite modest shaking and lack of concrete frame damage in the affected buildings. Partition damage has a greater functional impact than a number of other architectural items with which it is equally weighted in the scoring.

Country-level customizations: Architectural elements and building systems can vary by country as well as by geographic region. The non-structural module needs specific review against common local components and systems when customizing to a particular country.

A number of other recommendations were made for substantive changes to the structural module including replacing it with a structural-type-specific checklist such as the Nepal Department of Urban Development and Building Construction (DUDBC) seismic vulnerability checklist (based on FEMA 310) or the ASCE-41 Tier 1 [ASCE, 2017], and adding a flood, wind and wildfire checklist with content from FEMA 577 [FEMA, 2007]; and changes to the hazards module such as local customization (for example, to remove coastal hazards for landlocked countries).

3. HSI CUSTOMIZATION FOR NEPAL

To customize the HSI for Nepal, a 5-day charrette-style tool development workshop was held in Kathmandu December 1-5, 2019, and attended by engineers, medical doctors and other participants. For the HSI modules on hazards, structural safety and nonstructural safety (Modules 1,2 and 3, respectively), GHI led technical discussion and group writing sessions with local professionals to develop the tool rapidly and with stakeholder consensus. (Adaptations to Module 4 on preparedness were led by WHO and other professionals.) Following the workshop, GHI implemented the customizations to Modules 1-3, and tested and modified them using January 2019 data from buildings assessed with WHO and DUDBC.

Though not the primary topic of this paper, customization efforts in Nepal had as a substantial impetus the replacement of the original Global HSI structural module (Module 2) with a modified DUDBC structural assessment checklist originally based on FEMA 310 Tier 1 checklists, the precursor to ASCE 41-17 Tier 1 checklists. Using the modified DUDBC checklist necessitated developing an HSI-compatible scoring system for it, which serves a starting point for subsequent structural module customizations. The decision was made to prepare the scoring system for a single "High" level of seismic hazard, because it was difficult to justify lower levels of hazard with current scientific knowledge.

The customization effort included the following major changes to the non-structural module (Module 3):

- Divided the checklist into two parts, a hospital-wide checklist (Module 3A) and a building-specific checklist (Module 3B) because some items, such as exits and vulnerability of architectural elements and finishes, will be unique to each building;
- Developed adjustments to the scoring system to account for multiple buildings in the building-specific checklist (Module 3B) to combine scores for Module 3B, using a procedure based on essential functions in each building;
- Provided guidance to only use the Module 3B checklist for buildings with the most essential functions (Group 1 in Table *2*) to keep assessment fieldwork manageable;
- Developed method of combining scores from Modules 3A and 3B to arrive at an overall Module 3 score, which could then be combined with scores from other modules;
- Added explanatory text for several items that had been unclear in the previous version;
- Included lightning protection;
- Included building-specific fire protection assessment; and
- Incorporated lessons from the previous hospital assessments in Nepal and other places.

Table 1 shows the topics from the original Module 3 covered in the non-structural facility-wide checklist (Module 3A) and the individual buildings checklist (Module 3B). Fire protection is important both for normal use conditions and to help prevent fire following earthquake.

Table 1. Contents of customized Modules 3A and 3B, including division of topics from the original single Module 3. Items in bold are new items added during customization.

Original Module 3 Category	**Module 3A Nonstructural Safety Hospital-wide**	**Module 3B Nonstructural Safety for Individual Buildings**
3.1 Architectural safety	Safe conditions for movement outside buildings	All other items including past damage; doors, exits; windows; corridors, stairs and ramps; envelope and cladding; roofing; architectural ornamentation; railings and parapets; internal walls and partitions; ceilings; floor coverings; interior evacuation routes
3.2 Infrastructure protection, access and physical security	Location of critical services; exterior emergency evacuation routes, **assembly sites**; hospital access routes	Physical security of building, equipment, staff and patients
3.3 Critical systems		
3.3.1 Electrical	Alternate sources (generators); electrical equipment, cables, ducts; redundancy in grid connection; control panels, overload breaker switches; lighting system for critical areas, internal and external areas; substation; emergency maintenance and restoration	None
3.3.2 Telecommunications	Antennas; internet and telephone; alternate communications systems; equipment, cables; effects of external telecom systems; site safety; internal communication systems; emergency maintenance and restoration	None
3.3.3 Water supply	Water reserves; tank locations; distribution system condition; alternate supply; supplementary pumping; emergency maintenance and restoration	**Seismic protection of water distribution system**
3.3.4 Fire protection	Water supply for fire suppression; emergency maintance and restoration	Passive fire protection system; fire/smoke detection systems; manual

Original Module 3 Category	Module 3A Nonstructural Safety Hospital-wide	Module 3B Nonstructural Safety for Individual Buildings
		and automatic fire suppression systems; **fire evacuation routes**
3.3.5 Waste management	Nonhazardous, hazardous wastewater; liquid waste; non-hazardous, hazardous solid waste; emergency maintenance, restoration	None
3.3.6 Fuel storage	Fuel reserves; above-ground tanks, cylinders; location away from buildings; fuel distribution system; emergency maintenance and restoration	None
3.3.7 Medical gases	Safe location for tanks, cylinders; distribution system; alternate sources; emergency maintenance and restoration	Medical gas cylinders and equipment in the building
3.3.8 HVAC	None	Enclosures; protection for ducts, pipes, valves; air-conditioning systems; incl. negative pressure areas; emergency maintenance and restoration
3.4 Equipment and supplies		
3.4.1 Office and storeroom furnishings, equipment	None	Shelving, shelf contents, computers and printers
3.4.2 Medical and lab equipment, supplies	Medical equipment in operating theaters, recovery rooms, emergency care unit, intensive or intermediate care unit, emergency burn care, radiation therapy, nuclear medicine, other services; radiology, imaging equipment; laboratory equipment, supplies; pharmacy equipment, furnishings; sterile services equipment, supplies; sterilized instruments; medicines and supplies; specific medical equipment for emergencies, disasters; medical gas supply; mechanical volume ventilators; electro-medical, life support equipment; supplies, equipment for cardiopulmonary arrest	None
Other	None	**Lightning protection system**

The issue of how to address multiple buildings affected both the the structural and non-structural modules. The project team utilized work done previously by Mr. Holmes in support of California hospital safety legislation to develop a method assigning a weight to each building by summing up points for the essential functions each building contains, and normalizing by the total essential function points for the entire facility to obtain a weight between 0 and 1. The weighted contribution of each building's individual module scores to the overall facility score for that module depends on the building's essential medical functions, meaning that the vulnerability of buildings with many essential functions will affect the overall facility score much more than those that do not. Table 2 shows the four essential function exposure groups, points and directions for checklist completion developed during the Nepal customization.

Because Module 3B is completed only for buildings containing essential services in Group 1, weights used to combine Module 3B scores will differ from those for the entire facility. The essential function points for each building will be the same, but evaluators total up only the essential function scores for buildings under Group 1. The normalized essential function weight for Module 3B is determined by dividing each building's essential function score by the total score for buildings with Group 1 services. To determine an overall Module 3B score, the weighted individual Module 3B scores are added together. This would then be added to the total Module 3A score using a suggested weight of 50% Module 3A and 50% Module 3B; this weight could be adjusted in future customizations, but must be clear. This strategy also aids evaluators in prioritizing field time spent filling out checklists just for buildings with critical tasks and conducting qualitative observations of other buildings, both of which should increase program efficiency and cut costs.

Table 2. Essential function exposure groups and medical servies

Group 1: Most essential	Group 2: Next most essential	Group 3: Needed	Group X: Qualitative assessment only
Assign 20 points for each service listed below. Complete Module 2 and Module 3B checklists if building has any of the services below:	Assign 10 points for each service listed below. Complete Module 2 checklists if building has any of the services below:	Assign 5 points for each service listed below. Complete Module 2 checklists if building has any of the services below:	Do not complete checklists, but provide a qualitative opinion on the building's vulnerability to collapse or significant earthquake damage that would affect life safety:
• Emergency / Trauma Department • Operation Theatres (OTs) / Surgery • ICUs / NICU / other critical care beds – 20 points for each 10 beds or fraction thereof • CSSD / sterilization services • Radiology • Labor and Delivery / Obstetrics (ongoing essential service) • Utility buildings housing generators and other essential onsite utilities • Blood bank • Disaster stores (if present) • Backup generator	• Pharmacy store and medical store • Wards (general beds) – 10 points for each 50 beds or fraction thereof • Laboratories • Designated patient surge areas (for use during a disaster)	• Administrative buildings • Key staff quarters (such as Medical Superintendent) • Canteen (to prepare food for staff and patients) • Ordinary pharmacy (not store) belonging to hospital • Mortuary • Other key utility services: water, main electrical switchgear and transformer, oxygen plant/ medical gas	• Outpatient Department (OPD) • Other staff quarters • Nutrition rehabilitation center or clinic • HIV / ART clinic • Family planning • Public health offices • Other clinics, offices, and other services not listed above

4. HSI CUSTOMIZATION FOR MYANMAR

GHI worked with the Federation of Myanmar Engineering Societies (MES), Myanmar Earthquake Committee (MEC) and UN-Habitat Myanmar to customize a version of HSI for Myanmar, based on the Global HSI and a Nepal-customized version. The Fed. MES, MEC members were the main stakeholders and formed a working group to guide efforts to develop and customize the tool for Myanmar. The customization process was carried out entirely through virtual collaboration, because travel was not possible due to the COVID-19 pandemic and drastic changes in Myanmar's political situation. Government agencies such as the health ministry were not involved because they were under the control of the military.

Using the Nepal-customized HSI as a starting point, GHI and the working group determined several needs for additional customization to address Myanmar conditions, which included specific building types and varying seismic hazard levels. These modifications primarily impacted Modules 1 and 2. In contrast to Nepal, where a single level of "High" earthquake hazard could be justified for the entire country, Myanmar's seismic hazard varied from low-moderate to very high. In Module 1, GHI introduced Seismic Hazard Categories tied to hazard provisions in the Myanmar National Building Code [MES, 2016]. GHI reviewed the scoring system for the Myanmar version [MES et al., 2019] of the FEMA P-154 Rapid Visual Screening tool [FEMA, 2015], including seismicity/seismic hazard levels used, and developed a scoring system for the Myanmar-customized HSI based on the Nepal-customized HSI, using the P-154 scoring to inform the scoring system development. The team also adjusted and clarified the checklist language in instances in which it was not clear. Due to similarities in hospital systems, finishes, equipment and other nonstructural aspects across countries, there were no changes to Module 3A and few changes to Module 3B:

- Updated specific provisions, such as the distance of fire evacuation routes, to align with provisions of the Myanmar building code;
- Added explanatory text and terms familiar to Myanmar to clarify items found to be unclear during virtual checklist testing; and
- Incorporated lessons from the previous non-structural risk assessments of Yangon and Mandalay General Hospitals.

The scoring system for Module 3, which had not been customized for Nepal except to allow for multiple buildings, was not modified to accommodate multiple hazard levels. The non-structural (Module 3) received significant use and testing of checklist by the authors through virtual non-structural mitigation training for the participants from different agencies in Myanammar.

5. DISCUSSION AND CONCLUSIONS

The HSI customization efforts aimed to provide a cost- and time-effective way for identifying significant vulnerabilities across a portfolio of hospital facilities, as well as to provide individual facility evaluations with an emphasis on possible effects on the delivery of vital medical services. Particularly for non-structural components and systems, the customized HSI provides basic vulnerability information about a wide variety of systems important for hospital function after earthquakes. The customized checklists provide assessors with a framework to offer suggestions to hospital administrators and assistance in decision-making to increase the likelihood that the hospital will continue to operate in the case of natural catastrophes.

The customization process in both countries provided opportunities to adapt the Global HSI to local conditions in response to both local recommendations for changes and to implement improvements considered previously (but for which resources were not available in earlier efforts). These efforts produced substantial improvements to the Global HSI, which can be applied in future assessments, and used as the basis for customization in other countries. For the non-structural module, these improvements included dividing the existing checklist into sitewide and building-specific portions, and providing clear guidance on how to address multiple buildings with essential medical functions, common at hospitals in many countries. These customizations also included more information about fire safety, important for reducing the potential for fire following earthquake in the hospital.

Despite this progress, substantial future work remains. Due to the COVID-19 pandemic, neither tool has been field-tested, but that should be done once national health systems again have sufficient bandwidth for assessment programs. Work on the non-structural module in particular identified shortcomings in the fire safety provisions, which are currently being rectified through development of fire safety checklists by GHI, WHO's Regional Office for South East Asia, and technical partners. The new fire safety information will need to be integrated into the Global HSI, along with other planned updates.

REFERENCES

Achour, N., M. Miyajima, M. Kitaura, and A. Price. [2011] "Earthquake-Induced Structural and Nonstructural Damage in Hospitals," *Earthquake Spectra*, Vol. 27, No. 3, pp. 617–634. https://doi.org/10.1193/1.3604815.

ASCE. [2017] *Seismic Evaluation and Retrofit of Existing Buildings*, American Society of Civil Engineers, Reston, VA.

Bruneau, M., and A. Reinhorn. [2007] "Exploring the Concept of Seismic Resilience for Acute Care Facilities," *Earthquake Spectra*, Vol. 23, No. 1, pp. 41–62. https://doi.org/10.1193/1.2431396.

Dixit, A. M., R. Yatabe, R. Guragain, R. K. Dahal, and N. P. Bhandary. [2014] "Non-structural earthquake vulnerability assessment of major hospital buildings in Nepal," *Georisk: Assessment and Management of Risk for Engineered Systems and Geohazards*, Vol. 8, No. 1, pp. 1–13. https://doi.org/10.1080/17499518.2013.805629.

Fallah-Aliabadi, S., A. Ostadtaghizadeh, A. Ardalan, F. Fatemi, B. Khazai, and M. R. Mirjalili. [2020] "Towards developing a model for the evaluation of hospital disaster resilience: a systematic review," *BMC Health Service Research*, Vol. 20, No. 1, p. 64. https://doi.org/10.1186/s12913-020-4915-2.

FEMA. [2007] *Design Guide for Improving Hospital Safety in Earthquakes, Floods, and High Winds*, Federal Emergency Management Agency, Washington, DC.

FEMA. [2015] *Rapid Visual Screening of Buildings for Potential Seismic Hazards: A Handbook, Third Edition*. Federal Emergency Management Agency, Washington, DC.

Jacques, C. C., J. McIntosh, S. Giovinazzi, T. D. Kirsch, T. Wilson, and J. Mitrani-Reiser. [2014] "Resilience of the Canterbury Hospital System to the 2011 Christchurch Earthquake," *Earthquake Spectra*, Vol. 30, No. 1, pp. 533–554. https://doi.org/10.1193/032013EQS074M.

Kirsch, T. D., J. Mitrani-Reiser, R. Bissell, L. M. Sauer, M. Mahoney, W. T. Holmes, N. Santa Cruz, and F. de la Maza. [2010] "Impact on Hospital Functions Following the 2010 Chilean Earthquake," *Disaster Medicine and Public Health Preparedness*, Vol. 4, No. 2, pp. 122–128. https://doi.org/10.1001/dmphp.4.2.122.

MES. [2016] *Myanmar National Building Code (MNBC) 2016*, Federation of Myanmar Engineering Societies.

MES, MEC, and MGS. [2019] *Guideline for Rapid Visual Screening of Buildings for Potential Seismic Hazards*, Myanmar Engineering Society, Myanmar Earthquake Committee and Myanmar Geoscience Society, published by UN-Habitat, Yangon.

Mitra, K., H. Kumar, J. E. Rodgers, and W. T. Holmes. [2013] *Initial Seismic Vulnerability Assessment of Equipment, Utilities, Architectural Shell and Contents at National Academy of Medical Sciences (Bir Hospital), Kathmandu, Nepal*, GeoHazards International, Menlo Park, California.

Mitrani-Reiser, J., M. Mahoney, W. T. Holmes, J. C. de la Llera, R. Bissell, and T. Kirsch. [2012] "A Functional Loss Assessment of a Hospital System in the Bío-Bío Province," *Earthquake Spectra*, Vol. 28, Suppl. 1, pp. 473–502. https://doi.org/10.1193/1.4000044.

Myrtle, R. C., S. F. Masri, R. L. Nigbor, and J. P. Caffrey. [2005] "Classification and prioritization of essential systems in hopsitals under extreme events," *Earthquake Spectra*, Vol. 21, No. 3, pp. 779–802.

PAHO. [2008] *Hospital safety index: guide for evaluators*, PAHO, Washington, DC.

Rodgers, J. E., W. T. Holmes, L. T. Tobin, H. Kumar, and K. D. Tshering. [2012] *Initial Seismic Vulnerability Assessment of Jigme Dorji Wangchuck National Referral Hospital, Thimphu, Bhutan*, GeoHazards International, Palo Alto, California.

Schultz, C. H., K. L. Koenig, and R. J. Lewis. [2003] "Implications of Hospital Evacuation after the Northridge, California, Earthquake," *New England Journal of Medicine*, Vol. 348, No. 14, pp. 1349–1355. https://doi.org/10.1056/NEJMsa021807.

WHO Europe. [2006] *Health facility seismic vulnerability evaluation: A handbook,* Disaster Preparedness and Response Programme, Division of Country Support, Country Policies, Systems and Services, World Health Organization, Regional Office for Europe, Copenhagen.

World Health Organization. [2015] *Comprehensive safe hospital framework*, World Health Organization, Geneva.

World Health Organization and Pan American Health Organization. [2015] *Hospital safety index: guide for evaluators,* World Health Organization, Geneva.

Managing Seismic Risk in the San Francisco Legal Arena: Performance Gap Claims Based on Curtain Walls and Other Non-Structural Elements

(SPONSE)

Mark N. White[1]

[1] Law Offices of Mark N. White
P.O. Box 5339, Berkeley, CA 94705
e-mail: mark.white@mnwhitelaw.com

Abstract. In San Francisco, after the Loma Prieta earthquake of October 1989, more than 30 million square feet of high-rises have been designed and built. A majority of them share the following characteristics: the stated performance target was Risk Category Two (ASCE-7); the principal use was residential; and in order to obtain necessary regulatory approval, the owner's design team had to demonstrate to the satisfaction of a peer review panel that the constructed high-rise would sustain only minor damage, suspend operations for a very short time and perform virtually elastically during (and after) a foreseeable service level earthquake. For each such high-rise, this performance prediction may become the starting point for future legal claims akin to the "performance gap" theories of liability developed in the ***Millennium Tower*** litigation.

Most of the designs for these high-rises utilize non-structural curtain walls or a functionally equivalent system. It is probable that some of the post-Loma Prieta high-rises will sustain significant damage to those non-structural systems during service-level (or lighter) earthquakes, when peak ground acceleration at the site exceeds 0.20 PGA. The resulting down-time and costs to repair will almost certainly lead to legal claims against some of the owners and some of the design professionals, based on variations of the "performance gap" theories employed in the ***Millennium Tower*** litigation. In order to improve management of such seismic risk in the legal arena, long before the next significant earthquake, owners and design professionals should develop the testimony that will demonstrate that they acted reasonably in assessing seismic vulnerabilities and developing mechanisms in the field to derive satisfactory seismic capacity in their curtain wall systems and other non-structural elements of their high-rise facility.

Keywords: Curtain wall; performance gap; seismic risk management; testimony.

1. INTRODUCTION

In San Francisco, since 2008, the Department of Building Inspection ("DBI") has conditioned permission to construct most new high-rises on a pre-construction demonstration by the design team that "critical non-structural elements," including "exterior curtain wall and cladding systems," will remain intact during and after a foreseeable service level earthquake. [City, AB-083, sections 4.1 and 4.2] Among other things, DBI expects "that the building cladding will remain undamaged and that egress from the building will not be impeded when the building is subjected to the service-level ground motion." [City, AB-083, section 4.2 (Commentary)] Should the curtain wall system for one of these high-rises fail to meet such performance standards during and after a service-level (or smaller) earthquake, legal claims will be asserted against certain owner entities and certain members of their design team. This paper will discuss ways that legal exposure for such claims can be reduced long before San Francisco and its newer high-rises are subjected to foreseeable earthquakes that challenge non-structural cladding systems, including curtain walls.

2. PERFORMANCE TARGETS FOR POST LOMA PRIETA HIGH-RISES

After the 1989 Loma Prieta earthquake (October 17, M 6.9), more than 50 "New Tall Buildings," comprising more than 30 million square feet of new occupiable space, were built in the heart of San Francisco, virtually all with a height of greater than 160 feet, using "Non-Prescriptive Seismic-Design Procedures," as those terms are used by the DBI. This group of facilities will be referred to as "Post Loma Prieta High-Rises" and as will be shown below, ***most that were designed and built after 2008 have been predicted to provide "essentially elastic seismic performance at the service-level ground motion."*** [City, AB-083] When any of these high-rises fails to deliver elastic seismic performance in a foreseeable service-level (or lighter) earthquake, legal claims will inevitably be made requiring discovery of the reasons for substandard performance. Put another way, owners and design teams of such high-rises will be required to describe, under oath, the way that performance targets and structural design approaches were chosen, for both lateral force resisting elements and or architectural elements, such as cladding systems. This paper is intended to rationalize changes in the way that owners and design professionals make those choices and preserve the evidence that illustrates them.

2.1 The Portfolio of Post Loma Prieta High-Rises in San Francisco

At least 26 Post Loma Prieta High-Rises were permitted and completed for residential occupancy after 1989. See Table 1 for details. [ATC, 2018] Of these 26, the reported "structural system" for 18 towers is "RC Shear Wall," with no supplemental braced frame or moment frame systems, as opposed to the reported supplemental systems in the other eight. The occupiable area of these 26 residential high-rises is in excess of 13 million square feet.

The situation is similar for the 28 non-residential high-rises that were completed after the October 1989 Loma Prieta earthquake. See Tabl 2 for details. [ATC, 2018] Of these 28, the reported "structural system" for nine towers is "RC Shear Wall," with no supplemental systems, as opposed to the reported systems for the other 19, which either had supplemental systems or employed non-RC Shear Wall systems. The occupiable area ofthese 28 non-residential high-rises is in excess of 16 million square feet.

Accordingly, in the heart of San Francisco, after the Loma Prieta earthquake in 1989, in these 54 new high-rises, roughly 30 million square feet of new occupiable space was added, with an aggregate retail market value of in excess of $25 billion in 2022 dollars. [See, e.g., Li, 2018]

2.2 HIGH-RISE RESILIENCY AND THE REALITY OF REDUCED PROPERTY DAMAGE TARGETS AFTER LOMA PRIETA

Since 1989, ASCE 7 has been modified to require greater protection of property, above and beyond traditional life-safety standards. This shift is reflected in local Western urban ordinances, such as San Francisco's Community Safety Element to its General Plan, as well as Federal NEHRP legislation (passed in December 2018) which finances research and "an effective earthquake hazards reduction program," in order to achieve "the purpose of Congress . . . to reduce the risks of life and property from future earthquakes and increase resilience of communities" (28 United States Code section 7702). Expectations have grown that newer high-rises will sustain less death, destruction and downtime in foreseeable earthquakes, and this extends to their constituent architectural elements, such as curtain walls.

These evolving standards shape the legal risk profile of owners of Post Loma Prieta High-Rises. ***Salesforce Tower*** is one example; it is the tallest and most visible high-rise in San Francisco (61 stories and 1,070 feet in height). Salesforce Tower was assigned ASCE Risk Category III, with an Importance Factor of 1.25, but the possibility of infeasible repairs after an MCE was nonetheless identified by its design team:

> "For this Occupancy [sic] Category III structure, the probability of collapse is lower than that expected for a comparable Occupancy [sic] Category II structure. ASCE 7-10 sec. C1.3.1 suggests that code-compliant designs have a probability of collapse given occurrence of MCE shaking of 10% and 6% respectively for Occupancy [sic] Categories II and III. . . . ***Extensive structural damage may occur; repairs to structural and non-structural systems are required and may not be economically feasible***." [DBI permit records] (Italics and emphasis added.)

The underlying logic employed by the structural design team for the Salesforce Tower is spelled out in their June 2017 article in Structure Magazine. [Klemencic, *et al.,* 2017] "Given the scale of Salesforce Tower, the calculated number of building occupants will far exceed the building code threshold of 5,000 people, triggering the building's consideration under Occupancy [or Risk] Category III. Category III buildings require additional safety for wind and seismic demands, thus prompting new challenges for the engineering team." Id. at p. 45. Part of the extra seismic capacity required for Risk Category III high-rises is implemented "by applying code-defined seismic forces that have been amplified by an Importance Factor (1.25 for Category III buildings)." Ibid. Consistent with ASCE 7 Commentary, the Salesforce structural design team "targeted a reduction to 6% (from 10%) of the probability of collapse under a Maximum Considered Earthquake (MCE) ground shaking." Id. at p. 46. "Since the vertical elements of the tower's seismic force-resisting system include only shear walls . . . , the City of San Francisco's Administrative Bulletin 083 (AB-083) . . . applied." Id. at pp. 46-47. As a result, the structural design team chose a performance target of ***elastic performance in service-level earthquakes.*** "The lateral design of Salesforce Tower was driven by seismic loading in conditions for three levels of ground shaking: ***Elastic performance targeted for service-level shaking (with a mean recurrence interval of 43 years). . . ."*** Id. at p. 47. (Italics and emphasis added.) The structural design team reported that during the peer review process, it was able to demonstrate, among other things, that as-designed, the "***wall shear demands remain elastic***, and vertical wall strains are quite modest with only limited yielding predicted." Ibid. (Italics and emphasis added.). As noted in the Introduction above, the design team was also required to demonstrate that in service level earthquakes, "the building cladding will remain undamaged and that egress from the building will not be impeded."

2.3 AB-083 AND ITS ROLE IN HYPOTHETICAL LITIGATION

What if Salesforce Tower sustains substantial damage and is shut down in a service level earthquake (say PGA 0.20)? If we assume, in this hypothetical, that innocent bystanders are injured as a result of the unacceptableperformance (assume that cladding detaches and associated components hit the passers-by), then the likelihood is high that a skilled lawyer for each victim would persuade a judge (or jury or both) to consider whether an owner and members of its design team should be held legally culpable because the seismic performance of each high-rise fell short of predicted seismic performance—a performance gap theory of liability. Similar arguments would be made by tenants who sustain financial losses arising from downtime before repairs are completed.

The potentiality of this theory comes into focus if we take a closer look at Administrative Bulletin 083 (March 25, 2008, amended 2020) ("AB-083"). [City, AB-083]

In AB-083 DBI mandated virtual elasticity as the performance target in service-level earthquakes for "New Tall Buildings" that were designed using "Non-Prescriptive Seismic-Design Procedures" Ibid. "Tall Building" is defined as a structure with an "*hn* greater than 160 feet above average adjacent ground surface." Section 1. Service-level ground motion is defined as "having a 43-year mean return period (50% probability of exceedance in 30 years)." Section 4.2. With regard to the "primary structural system," the latter section requires the project design team ***"to demonstrate acceptable, essentially elastic seismic performance at the service-level ground motion."*** (Italics and emphasis added.) The design team must demonstrate no more than "minor yielding," requiring no more than "minor repair." [City, AB-083, Commentary at 83-5] Specifically, ***"essentially elastic seismic performance"*** includes a prediction of no worse than "minoryielding of ductile elements of the primary structural system, provided such results do not suggest appreciable permanent deformation in the elements, strength degradation, or significant damage to the elements requiring more than minor repair." Ibid.

In addition, "it is expected that the ***building cladding will remain undamaged*** and that egress from the building will not be impeded when the building is subjected to the service-level ground motion." Ibid. "The evaluation ***shall demonstrate that the elements being evaluated exhibit serviceable behavior***." Ibid. (Italics and emphasis added.)

Thus, in our hypothetical involving serious damage to the Salesforce Tower, a judge will likely find that an actionable performance gap exists between (i) what owner's design team predicted in the service level scenario and (ii) what the completed high-rise delivered in the field, when exposed to 0.20 PGA. Automatic legal immunity for defendants is unlikely.

Adherence to the requirements of AB-083 is obtained through a Peer Review process denominated "Structural, Geotechnical, and Seismic Hazard Engineering Design Review" spelled out in DBI's Administrative Bulletin 082 ("AB-082"). [City, AB-082] The extent to which members of the Peer Review team require the design team to justify the substance of their compliance with applicable performance targets has increased since AB-082's original adoption in 2008. These refinements were, in part, the results of lessons learned from the complex civil litigation in San Francisco Superior Court involving unexpected settlement at the ***Millennium Tower*** (58 story, 605 foot height). Publicly available information indicates that legal fees in those cases already exceed $50 million and that the first phase of remedial work, currently ongoing, will cost more than $100 million. [See, e.g., Matier & Ross, 2018]

3. LESSONS OF THE *MILLENNIUM TOWER* LITIGATION, HARBINGER OF PERFORMANCE GAP LAWSUITS AFTER FUTURE EARTHQUAKES

The ***Millennium Tower*** litigation is a precursor of the above-described hypothetical earthquake-driven litigation. It continues to be played as the parties struggle to finalize a $100 million partial resolution of the underlying performance failure. Several lawsuits arose from unexpected settlement experienced by the Millennium Tower, and those disputes entangled to varying degrees other substantial facilities, including Salesforce Tower and the Transbay Transit Center.

The gist of the charging allegations of these cases is that since commencement of construction, the amount of settlement sustained by the Millennium Tower far exceeds that predicted by members of the project design team and that such information was wrongfully concealed from both the association and unit purchasers (among others) before sales of individual units took place. The actionable situation is a settlement ***performance gap***: settlement in the field far exceeds that predicted by members of the design team before structural construction commenced.

Because the Millennium Tower has experienced unexpected and excessive settlement and tilt, and lack of stabilization of the settlements, in-depth investigation was undertaken to determine whether it meets the minimum structural and seismic safety requirements expected under San Francisco and California building codes. [Deierlein, *et al.,* 2017 at pp. 2 and 11

Based on current, publicly available information, it would be expected that some experts in the ***Millennium Tower*** litigation could testify along the following lines:

> The original design anticipated one inch of settlement under Millennium Tower by the time of construction completion, and additional long-term settlement due to compression of the underlying clay layers of five inches. Settlement was expected to be uniform over the Tower foundation area. [Deierlein, *et al.,* 2017 at p. 2]
>
> Contrary to the predicted performance, it appears that the Millennium Tower settled six inches at the time of construction completion, instead of one inch. And, as of July 2017,settlement was on the order of 17 inches instead of the five predicted for the long-term. Moreover, settlement has not been uniform and the Tower leans to the west on the order of 14 inches and leans to the north on the order of six inches as of July 2017. This isroughly twice what would be considered acceptable construction tolerance for out-of-plumb. [Deierlein, *et al.,* 2017 at pp. 1, 5, 11]
>
> A voluntary seismic upgrade and foundation stabilization program

> for the Millennium Tower is predicted to reduce post-2017 settlement to a few additional inches through 2060, rendering the structural and foundation systems in compliance with AB-083 and local building codes, upon completion in September 2022. [Deierlein, *et al.,* 2022 at p. 4]

The ***Millennium Tower*** litigation reveals patterns that unfolded in the seminal ***Myrick*** litigation [White & Yanev, 2020], and that will unfold in future cases arising from unsatisfactory high-rise performance during foreseeable earthquakes. Take our Salesforce Tower hypothetical: before the substandard performance during a service level earthquake, assume the tower owner becomes aware of troublesome mechanisms (tangible vulnerabilities) in elements of the lateral force-resisting system and in the cladding system; and further, before the flaws are corrected, innocent bystandersare harmed by them during the earthquake. In turn, hypothetically, this leads to litigation which requires evidentiary disclosure of performance targets implicitly or explicitly adopted by the structural team and the tower owner; they, in turn, will be required to testify under oath whether they, individually, were aware ofthe tangible vulnerabilities before the earthquake, and if so, what was done about it. Able adverse counsel will ask tough questions, including whether the tangible vulnerabilities tended to undercut adopted performance targets, and whether the actual harm in the field was reasonably foreseeable. Needless to say, legal counsel defending the owner and the design team will predict both how expert testimony will play out and how the judge and jury will respond to it. [White & Yanev, 2020]

Another pattern that will emerge after future severe earthquake shaking in the heart of San Francisco is controversy over whether Post Loma Prieta residential high-rises were designed with sufficient seismic capacity for structural as well as cladding systems. In a hypothetical collapse of a new residential high-rise (or separation of the cladding system), able counsel for innocent victims will likely develop the argument that Importance Factor 1 was not enough under ASCE 7 and that instead of meeting the functional equivalent of Risk Category II, the structural design team should have used stricter requirements analogous to those of Risk Category III, which in turn would have increased the Importance Factor to 1.25. Most judges will be reluctant to accept the defense argument that meeting code minimum automatically immunizes design professionals and owners from potential liability, in light of the contrary holding in the ***Myrick*** litigation***.*** [White & Yanev, 2020]

4. CONCLUSION

Another lesson learned from the ***Millennium Tower*** litigation is that the best practice is for the Peer Review team and DBI to preserve all documents generated during the design review process. The better argument is that such project-related materials should be preserved because, once circulated with the Peer Review team, they are covered by California's Public Records Act and by San Francisco's Sunshine Ordinance. When a vulnerability is discovered after construction commences, the design review materials actually used during construction often efficiently illuminate the source of the problem and facilitate its correction before property is damaged or personal injuries are sustained in foreseeable earthquakes. Collecting and retaining these design review materials is an essential part of DBI's ongoing program to improve the earthquake resiliency of its high-rise stock, which necessarily includes migration from avoidance of collapse to reduction of property damage.

REFERENCES

Applied Technology Council [2018] *San Francisco Tall Buildings Study,* 201 Redwood Shores Parkway, Suite 240, Redwood City, California 94065, USA.

City and County of San Francisco, Department of Building Inspection [2008] Administrative Bulletin 082, *Guidelines and Procedures for Structural, Geotechnical, and Seismic Hazard Engineering Design Review*, 10 pages (March 25, 2008, revised 2016 and 2018).

City and County of San Francisco, Department of Building Inspection [2008] Administrative Bulletin 083, *Requirementsand Guidelines for the Seismic Design of New Tall Buildings using Non-Prescriptive Seismic-Design Procedures*, 7 pages (March 25, 2008, revised 2014 and 2020).

Deierlein, G.G., Schotanus, M, Vahdani, S., Shields, C. [2017] *Structural Safety Review of the Millennium Tower* 14 pages (delivered to Naomi N. Kelly, City Administrator, City and County of San Francisco on July 28, 2017).

Deierlein, G.G., Schotanus, M, Shields, C. [2022] *Engineering Design Review [Millennium Tower]* 5 pages (delivered to Richard Tam, Building Plans Engineer, Department of Building Inspection, City and County of San Francisco on June 15, 2022).

Goodyear, C. [December 8, 2005] "Rincon Hill's Huge Towers Put On Hold / S.F. Building Agency Withholds Permit Over Seismic Concerns," *San Francisco Chronicle,* San Francisco, California, USA.

Klemencic, R, Valley, M, Hooper, J [June 2017] Salesforce Tower, *Structure Magazine,* pp. 45-48, accessed February 9, 2020 at https://www.structuremag.org.

Li, R [July 22, 2018] "San Francisco's 10 Most Valuable Buildings," *San Francisco Chronicle,* San Francisco, California, USA.

Matier & Ross [September 25, 2018] "As Millennium Tower Sinks, Legal Fees Keep on Rising," *San Francisco Chronicle,* San Francisco, California, USA.

White, M.N., Yanev, P. [2020] "The Evolution of Managing Seismic Risk in American Urban Centers after the Loma Prieta Earthquake: Changes in California Authorities and Federal Statutes After 1989," *17th World Conference on Earthquake Engineering, Paper No. 0184,* Sendai, Japan pp. 3-5.

TABLE 1 POST LOMA PRIETA HIGH-RISES PERMITTED AND COMPLETED FOR RESIDENTIAL USE AFTER 1989, THROUGH 2017 [ATC, 2018]						
HIGH-RISE NAME	**ADDRESSS**	**YEAR COM-PLETED**	**PERMIT DATE**	**STORIES ABOVE GRADE**	**HEIGHT (FEET)**	**AREA (SQUARE FEET)**
BridgeView	400 Beale Street	2003	1999	26	358	449,567
The Watermark	501 Beale Street	2004	2004	22	225	149,000
The Metropolitan at 355 1st St	355 1st Street	2005	2000	28	240	597,982
The Metropolitan at 333 1st St	333 1st Street	2005	2000	21	178	141,960
The Paramount	680 Mission Street	2005		41	475	681,251
Infinity I North	301 Main Street	2006	2006	36	350	409,556
Infinity II South, aka 300 Spear Street	338 Spear Street	2006	2006	41	401	454,990
One Rincon Hill South	425 1st Street	2008	2006	56	550	757,137
Millennium Tower	301 Mission Street	2009	2005	58	605	1,100,000
One Hawthorne Street	1 Hawthorne Street	2010		25	239	290,607
Trinity Place Apartments	1188 Mission Street	2010		24	223	328,055
LUMINA II	338 Main Street	2012	2012	37	381	487,000
LUMINA I	301 Beale Street	2012	2012	42	429	487,000
Jasper	45 Lansing Street	2013	2012	40	430	471,334
Ava 55 Ninth	55 9th Street	2014	2011	18	187	308,000
NEMA North Tower	1411 Market Street	2015	2014	39	352	951,676
399 Fremont Street	399 Fremont Street	2016		42	400	596,400
340 Fremont Street	340 Fremont Street	2017	2005	42	400	290,000
The Harrison, aka One Rincon Hill North	401 Harrison Street	2017	2013	47	450	485,000
1500 Mission - Residential	1500 Mission Street	2017	2017	39	397	767,200
Solaire (Transbay Block 6)	299 Fremont Street	2017		33	330	476,705
500 Folsom	500 Folsom Street	2017	2017	42	402	743,500
Oceanwide Center II	526 Mission Street	2017	2017	54	605	631,638
MIRA, aka Folsom Bay Tower	160 Folsom Street	2018	2017	40	400	480,000
33 Tehama Street	33 Tehama Street	2018	2018	34	366	278,097
The Avery aka 450 Folsom	450 Folsom Street	2019		56	550	906,472

TABLE 2

POST LOMA PRIETA HIGH-RISES PERMITTED AND COMPLETED FOR NON-RESIDENTIAL USE AFTER 1989, THROUGH 2017 [ATC, 2018]

HIGH-RISE NAME	ADDRESS	YEAR COM-PLETED	PERMIT DATE	STORIES ABOVE GRADE	HEIGHT (FEET)	AREA (SQUARE FEET)
121 Spear Street	121 Spear Street	1990	1985	24	280	572,535
600 California Street	600 California Street	1991		20	270	403,629
505 Montgomery	505 Montgomery Street	1992		24	420	308,297
160 Spear Street	160 Spear Street	1993		19	250	289,253
Four Seasons Hotel	757 Market Street	1998	1998	36	449	1,110,500
W Hotel	181 3rd Street	1999	1997	31	298	289,040
101 2nd Street	101 2nd Street	1999		25	340	441,412
199 Fremont Street	199 Fremont Street	1999	1998	28	350	400,000
150 California Street	150 California Street	2000		23	317	247,500
GAP Building	2 Folsom Street	2001		15	222	780,000
JPMorgan Chase	560 Mission Street	2001		31	434	779,000
33 New Montgomery Street	33 New Montgomery St	2001		19	287	240,000
55 2nd Street	55 2nd Street	2002		25	330	404,437
St. Regis San Francisco	125 3rd Street	2007	2000	42	449	736,000
InterContinental San Francisco	888 Howard Street	2008	2007	35	350	564,614
555 Mission St	555 Mission Street	2008		35	487	625,524
706 Mission Street	706 Mission Street		2010	44	480	57,482
SF PUC Headquarters	525 Golden Gate Avenue	2012		15	187	277,511
1190 Mission at Trinity Place	1190 Mission Street	2013		22	215	338,053
535 Mission Street	535 Mission Street	2014	2014	27	378	355,000
222 2nd Street	222 2nd Street	2016	2016	26	367	523,150
Salesforce East, aka 350 Mission Street	350 Mission Street	2017	2011	30	384	490,000
181 Fremont	181 Fremont Street	2017	2013	58	746	706,617
Salesforce Tower	415 Mission Street	2017	2014	61	1,070	1,370,000
Oceanwide Center I	50 1st Street	2017	2017	61	850	1,432,872
33 8th at Trinity Place	33 8th Street	2017		19	229	961,816
350 Bush Street	350 Bush Street	2017	2017	21	259	420,000
1500 Mission	1500 Mission Street	2017	2017	19	255	573,560
Park Tower	250 Howard Street	2017	2018	45	568	743,000

Applied Technology Council Directors

ATC Board of Directors (1973-Present)

Milton A. Abel	(1979-1985)
Dan Allwardt	(2010-2013)
James A. Amundson*	(2010-2016)
James C. Anderson	(1978-1981)
Victoria Arbitrio*	(2011-2018)
Thomas G. Atkinson*	(1988-1994)
Steven M. Baldridge	(2000-2003)
Albert J. Blaylock	(1976-1977)
David C. Breiholz	(2004-2006)
Melissa Burton	(2019-2025)
Patrick Buscovich*	(2000-2009)
James R. Cagley*	(1998-2004)
H. Patrick Campbell	(1989-1990)
Lyle P. Carden	(2018-2024)
Arthur N. L. Chiu*	(1996-2002)
Anil Chopra	(1973-1974)
Richard Christopherson*	(1976-1980)
Lee H. Cliff	(1973)
Kelly Cobeen	(2021-2024)
Leighton Cochran	(2011-2017)
Michael L. Cochran	(2018-2024)
John M. Coil*	(1986-87, 1991-97)
Eugene E. Cole	(1985-1986)
Anthony B. Court	(2001-04, 2016-22)
Edwin T. Dean*	(1996-2002)
Robert G. Dean	(1996-2001)
Gregory G. Deierlein	(2003-2009)
James M. Delahay*	(1999-2005)
Edward F. Diekmann	(1978-1981)
Burke A. Draheim	(1973-1974)
John E. Droeger	(1973)
Donald O. Dusenberry*	(2018-2024)
Michael D. Engelhardt*	(2014-2020)
David A. Fanella	(2010-2011)
Nicholas F. Forell*	(1989-1996)
Douglas A. Foutch	(1993-1997)
Paul Fratessa	(1991-1992)
Sigmund A. Freeman	(1986-1989)
Maria E. Moreyra Garlock	(2020-2023)
Nancy L. Gavlin*	(2011-2016)
Ramon Gilsanz*	(2005-2012)
Barry J. Goodno	(1986-1989)
Mark R. Gorman	(1984-1987)
Melvyn Green	(2001-2002)
Lawrence G. Griffis*	(2002-2008)
Kurtis R. Gurley	(2011-2018)
Gerald H. Haines	(1981-82, 1984-85)
William J. Hall	(1985-1986)
Ronald O. Hamburger	(1999-2000)
Robert W. Hamilton	(2002-2005)
James R. Harris*	(2004-2010)
Gary C. Hart	(1975-1978)
Erleen Hatfield	(2011-2017)
Robert H. Hendershot	(2000-2001)
Lyman Henry	(1973)
Richard L. Hess	(2000-2003)
James A. Hill	(1992-95, 2003-04)
Ernest C. Hillman, Jr.	(1973-1974)
Eve Hinman	(2002-2008)
Ephraim G. Hirsch	(1983-1984)
Douglas C. Hohbach*	(2015-2021)
William T. Holmes*	(1983-1987)
Warner Howe	(1977-1980)
Edwin T. Huston*	(1990-1997)
David Hutchinson	(2004-2010)
Jeremy Isenberg	(2002-2005)
Paul C. Jennings	(1973-1975)
Carl B. Johnson	(1974-1976)
Carrie J. Johnson*	(2017-2023)
Edwin H. Johnson	(1988-89, 1998-01)
Stephen E. Johnston*	(1973-75, 1979-80)
Christopher P. Jones*	(2001-2008)
Joseph Kallaby*	(1973-1975)
Donald R. Kay	(1989-1992)
T. Robert Kealey*	(1984-1988)
H. S. (Pete) Kellam	(1975-1976)
Andrew B. Kennedy	(2013-2019)
Ryan A. Kersting*	(2017-2023)
Helmut Krawinkler	(1979-1982)
Steven Kuan	(2006-2009)
James S. Lai	(1982-1985)
Mark H. Larsen	(2003-2006)
Gerald D. Lehmer	(1973-1974)
Roberto T. Leon*	(2012-2018)
Christopher W. Letchford	(2017-2023)
Marc L. Levitan	(2006-2010)

James R. Libby	(1994-1998)
Charles Lindbergh	(1989-1992)
R. Bruce Lindermann	(1983-1986)
Bret Lizundia*	(2009-2015)
L. W. Lu	(1987-1990)
Walter B. Lum	(1975-1978)
Kenneth A. Luttrell	(1991-1999)
James O. Malley*	(2016-2022)
Newland J. Malmquist	(1997-2000)
Melvyn H. Mark	(1979-1982)
John A. Martin	(1978-1982)
Stephen McReavy	(1973)
John F. Meehan*	(1973-1978)
Andrew T. Merovich*	(1996-2003)
David L. Messinger	(1980-1983)
Bijan Mohraz	(1991-1997)
William W. Moore*	(1973-1976)
Manuel Morden	(2006-2012)
Ugo Morelli	(2004-2006)
Gary Morrison	(1973)
Robert Morrison	(1981-1984)
Ronald F. Nelson	(1994-1995)
Joseph P. Nicoletti*	(1975-1979)
Sissy Nikolaou	(2017-2020)
Bruce C. Olsen*	(1978-1982)
Gerard Pardoen	(1987-1991)
Robert B. Paullus, Jr.	(2014-2017)
Stephen H. Pelham*	(1998-2005)
Norman D. Perkins	(1973-1976)
Richard J. Phillips	(1997-2000)
Maryann T. Phipps	(1995-96, 1999-02)
Sherrill Pitkin	(1984-1987)
Chris D. Poland	(1984-1987)
Edward V. Pollack	(1973)
Egor P. Popov	(1976-1979)
Robert F. Preece*	(1987-1993)
David O. Prevatt	(2018-2023)
H. John Price*	(2004-2011)
Ahmad Rahimian	(2021-2023)
Lawrence D. Reaveley*	(1985-91,2000-03)
Jose Restrepo	(2022-2025)
Philip J. Richter*	(1986-1989)
John M. Roberts	(1973)
James Robinson	(2005-2008)
Charles Roeder	(1997-00, 2009-12)
Spencer Rogers	(2007-2013)
Arthur E. Ross*	(1985-91, 1993-94)
C. Mark Saunders*	(1993-2000)
Walter D. Saunders*	(1975-1979)
Wilbur C. Schoeller	(1990-1991)
Samuel Schultz*	(1980-1984)
Donald R. Scott*	(2009-2015)
Lawrence G. Selna	(1981-1984)
Daniel Shapiro*	(1977-1981)
Joseph B. Shepard	(2008-2014)
Jonathan G. Shipp	(1996-2000)
Howard Simpson*	(1980-1984)
Robert Smilowitz	(2008-2011)
Thomas L. Smith	(2008-2014)
Mete Sozen	(1990-1993)
William Staehlin	(2002-03, 2013-19)
Scott Stedman	(1996-1997)
Donald R. Strand	(1982-1983)
James L. Stratta	(1975-1979)
Edward J. Teal	(1976-1979)
W. Martin Tellegen	(1973)
John C. Theiss*	(1991-1998)
Seth Thomas	(2022-2025)
Charles H. Thornton*	(1992-00, 2005-11)
James L. Tipton	(1973)
Christos Tokas	(2019-2025)
Ivan Viest	(1975-1977)
Ajit S. Virdee*	(1977-80, 1981-85)
J. John Walsh	(1987-1990)
Williston L. Warren, IV	(2012-2018)
Robert S. White	(1990-1991)
James A. Willis*	(1980-81, 1982-86)
Thomas D. Wosser	(1974-1977)
Loring A. Wyllie	(1987-1988)
Kent Yu	(2015-2018)
Edwin G. Zacher	(1981-1984)
Theodore C. Zsutty	(1982-1985)

*ATC President

ATC Executive Directors (1973-Present)

Jon A. Heintz	(2015-present)
Ronald Mayes	(1979-1981)
Christopher Rojahn	(1981-2015)
Roland L. Sharpe	(1973-1979)

Applied Technology Council

ATC Sponsors, Supporters, and Contributors

Sponsors

James R. and Sharon K. Cagley
Rutherford & Chekene
John M. Coil
Computers & Structures, Inc.
Degenkolb Engineers
Gilsanz Murray Steficek
Sang Whan Han
Edwin T. Huston
KPFF Consulting Engineers
Nabih Youssef & Associates
Robert B. Paullus
Rojahn-King Family
Structural Engineers Association of California
Charles H. Thornton
Walter P. Moore & Associates

Supporters

Erleen Hatfield

Contributors

Omar D. Cardona
Lawrence D. Reaveley
John C. Theiss

ATC Projects and Report Information

ATC conducts applied research and technology transfer projects for which a consensus of engineering opinion is necessary or beneficial. ATC's primary audience includes engineering design professionals, federal, state, and local government entities, and other stakeholders in the global hazard mitigation community. In its nearly 50-year history, ATC has conducted more than 150 projects and published more than 300 major reports and publications.

ATC reports have identified and encouraged needed structural engineering research at the national level, contributed to the development and evolution of building codes and standards, and served to define seismic and other engineering design practice in the United States and the world. Because ATC products are consensus-based and non-proprietary, they are immediately accepted by the profession and hold lasting value to engineering practitioners. Although technology continues to evolve, many older reports remain useful as a historical reference or as a guide for current engineering practice.

A complete listing of ATC Projects and Report Information is available at www.ATCouncil.org.